Computational Geomechanics

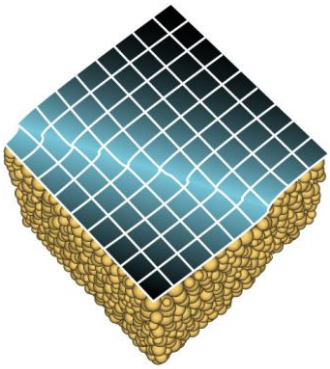

Edited by

S. Pietruszczak & G. N. Pande

Published by
International Centre for Computational Engineering (IC^2E)
Rhodes, Greece & Swansea, UK

Organizing Committee

Co-organizers

Technical Advisory Panel

PROCEEDINGS OF THE 3rd INTERNATIONAL SYMPOSIUM ON COMPUTATIONAL GEOMECHANICS (COMGEO III), Krakow, Poland, 21-23 August, 2013

Computational Geomechanics
COMGEO III

Editors

S. Pietruszczak
McMaster University, Hamilton, Canada
G.N. Pande
Swansea University, Swansea, UK

IC²E Rhodes, Greece; Swansea, UK

IC²E *International Centre for Computational Engineering (IC²E) is a 'not for profit' organisation registered as an educational institution in the Aegean island of Rhodes, Greece.*

Published by: ***IC²E*** - International Centre for Computational Engineering
www.ic2e.org

ISBN: 978-960-98750-2-8

Table of Contents

3 Modelling of thermo-hydro-mechanical coupling and other transient problems

4 Application of numerical techniques

4.1 Foundations; piles, anchors

4.2 Slopes/embankments and dams

4.3 Other applications

Preface

Over the last few decades a rapid progress has been made in many areas of computational geomechanics and a broad spectrum of software is now readily available to the engineer. However, engineers are facing new challenges as demand for sustainable alternative means of energy production and solutions to environmental problems are being sought all over the world. Only computational methods can provide viable solutions of complex geotechnical and geo-environmental problems being faced by engineers of today. Need for co-operation and dialogue amongst all concerned at the highest technical level has never been greater than now.

The International Centre for Computational Engineering (IC^2E) - a not for profit educational charity - is a unique independent organisation that is well placed to play an important role in promoting exchange of views, developing state-of-the art reports and giving unbiased advice to stake holders, private sector, governmental and non-governmental organisations.

Following the first two Symposia on "Computational Geomechanics" (ComGeo) held in Nice (France) and in Dubrovnik (Croatia), ComGeo III is being organised in Krakow, Poland, 21 -23 August 2013 under the umbrella of IC^2E. ComGeo series of Symposia is a sequel to "Numerical Models in Geomechanics" NUMOG series which was launched in 1982 and included 10 international meetings that were organized over a period of 25 years. Each meeting had a limited number of participants and the focus was on preserving a high technical standard as well as an informal style. ComGeo series aims to maintain the same format, however, the scope of this series is much broader and will include new emerging research areas as and when needed.

The proceedings of ComGeo III on this USB flash drive contain over 70 papers, which were selected for presentation at the Symposium. Accepted papers are organized in four major sections:

1. *Constitutive relations for geomaterials*
2. *Numerical algorithms: formulation and performance*
3. *Modelling of thermo-hydro-chemo-mechanical and other transient problems*
4. *Application of numerical techniques to practical problems*

The proceedings include many papers written by internationally recognized experts in their respective fields and all papers are of a high international standard. All papers included here will be archived in a downloadable form in the e-Library of IC^2E (http://www.ic2e.org), for wider dissemination.

We are grateful to the members of the Technical Advisory Committee, for their co-operation and helpful suggestions.

S. Pietruszczak
G. N. Pande

July 2013

MICROCRACKS-INDUCED DAMAGE MODELLING FOR TRANSVERSELY ISOTROPIC ROCKS

Séverine Levasseur
Département ArGEnCo, Université de Liège, Liège, Belgium

Hélène Welemane
Ecole Nationale d'Ingénieurs de Tarbes, Université de Toulouse, Tarbes, France

Djimédo Kondo
Institut d'Alembert, Université de Paris VI, Paris, France

ABSTRACT: *In the present study, a new micromechanical damage model is proposed for transversely isotropic rocks. The originality of this model lies in the fact that it accounts not only for the coupling between material structural anisotropy and damage-induced one, but also for the opening/closure status (the so-called unilateral effects) of evolving microcracks. Taking advantage of a recent study by Goidescu et al. (2013), a closed-form expression of the overall free energy of the microcracked medium is presented. This expression is implemented in an appropriate thermodynamics framework which allows formulating a complete constitutive damage model. The salient features of the model such as the coupling between anisotropies and its effect on the damage yield function and on the tangent operator are illustrated and validated on the identification of a transversely isotropic argillite. It is shown that under direct tensile loading (including off-axis tests), the theoretical mechanical response predicted by the proposed model well captures experimental data. Owing to the above results, the response of the material is studied along a tension loading followed by an unloading and a reloading in compression in order to illustrate the so-called unilateral damage effects due to microcracks closure.*

1 INTRODUCTION

The inelasticity of rock behaviour under mechanical loading generally results from damage phenomena due to evolving microcracks. To model this, both phenomenological and micromechanical approaches have been developed in the last decades in the framework of Continuum Damage Mechanics (CDM) (see for instance Krajcinovic 1996; Lemaitre & Chaboche 1990; Costanzo et al. 1996; Ju & Lee 1991; Kachanov 1982; Levasseur et al. 2011; Pensée et al. 2002; Zhu et al. 2008). However despite their interest, the above cited models concern mainly materials which are isotropic in their undamaged state. The modelling of coupling between initial and damage-induced anisotropies can only be found in studies devoted to brittle matrix composites, like Cazacu et al. (2007) and Halm et al. (2002) for purely macroscopic models or Baste (2001) and more recently Monchiet et al. (2012) in the context of micro-macro models. But, this class of models still need to be completed in order to properly account for unilateral effects due to microcracks closure. These effects are of paramount importance and necessary for the modelling of quasi brittle geomaterials generally subjected to tensile loading as well as to compression. In

this way, Goidescu et al. (2013) recently established closed-form expressions of the overall free energy of orthotropic materials weakened by microcracks, either open or closed. The present study takes advantage of these recent results to formulate a complete model with coupling between initial anisotropy and evolving unilateral damage due to 2D systems of open or closed microcracks under frictionless conditions.

For this purpose, the closed-form expression of the macroscopic free energy is recalled in this paper to constitute the thermodynamic potential of damaged geomaterials. Based on a discrete damage representation defined by microcrack densities, the state laws are deduced providing the macroscopic stress as well as the damage energy release rate. It follows a damage yield function associated to each microcracks family and the damage evolution law from the classical normality rule of CDM. This allows to establish the complete rate formulation of the anisotropic constitutive damage law with microcracks closure effects. After a simple calibration step, the ability of the model to account for the coupling between the initial anisotropy and microcracks-induced one is assessed first by comparing its prediction to available data on the behaviour of an argillite subjected to a tensile loading (Liao et al. 1997). Then, the response of the material during tensile and compressive loads confirms the ability of the model to account for the unilateral behaviour induced by the microcracks opening and closure.

Notations: Standard tensorial notations is used throughout the paper. Lower bold script letter describes vector, bold script capital letter is associated to second-order tensor and mathematical double-struck capital letter denotes fourth-order tensor. The following vector and tensor products are exemplified: $(\mathbf{A}.\boldsymbol{b})_i = A_{ij}b_j$, $(\mathbf{A}.\mathbf{B})_{ij} = A_{ik}B_{kj}$, $(\mathbb{A}:\mathbf{B})_{ij} = A_{ijkl}B_{kl}$, $(\mathbb{A}:\mathbb{B})_{ijkl} = A_{ijpq}B_{pqkl}$. Einstein summation convention, applied for the repeated indices and Cartesian coordinates are used. As usually, small (respectively large) characters refer to microscopic (resp. macroscopic) quantities. $\mathbf{I}$ and $\mathbb{I}$ are, respectively, the second and fourth order identity tensors, the components of the former is represented by the Kronecker symbol (δ_{ij}) while for the latter one has $I_{ijkl} = (1/2)(\delta_{ik}\delta_{jl} + \delta_{il}\delta_{jk})$.

2 MICROCRACKS-INDUCED DAMAGE MODEL

2.1 Representative volume element (r.v.e.)

Micromechanical formulation of damage model requires the homogenization of the microcracked material by defining a representative volume element *r.v.e.* of the material (noted Ω). The virgin matrix is constituted of an elastic orthotropic solid matrix s (occupying a domain Ω^s) and an arbitrary oriented system of microcracks families (denoted r and occupying a domain Ω^r). This *r.v.e.* is subjected to uniform stress boundary conditions:

$$\boldsymbol{T_d} = \boldsymbol{\Sigma}\cdot\boldsymbol{n}(\boldsymbol{z}) \quad \forall \boldsymbol{z} \in \partial\Omega \tag{1}$$

$\boldsymbol{z}$ denoting the vector position, $\boldsymbol{T_d}$ the surface density force, and $\boldsymbol{\Sigma}$ the macroscopic stress tensor. The local constitutive equation in the heterogeneous medium follows elastic relation:

$$(\boldsymbol{z} \in \Omega) \quad \boldsymbol{\sigma}(\boldsymbol{z}) = \mathbb{C}(\boldsymbol{z}) : \boldsymbol{\varepsilon}(\boldsymbol{z}) \tag{2}$$

with $\boldsymbol{\sigma}(\boldsymbol{z})$ the local stress tensor and $\mathbb{C}(\boldsymbol{z})$ the heterogeneous stiffness tensor such as:

$$\mathbb{C}(\boldsymbol{z}) = \begin{cases} \mathbb{C}^s & \text{in matrix } (\Omega^s) \\ \mathbb{C}^r & \text{in microcracks domain } (\Omega^r) \end{cases} \tag{3}$$

In the two dimensional approach considered in this paper, the solid matrix stiffness has an orthotropic structure with symmetry axes corresponding to the orthonormal basis ($\boldsymbol{e_1}$,$\boldsymbol{e_2}$) defined in Figure 1 and is described by means of the structural fabric tensor $\mathbf{A} = \boldsymbol{e_1} \otimes \boldsymbol{e_1}$, such as:

$$\mathbb{C}^s = a_1 \mathbf{I} \otimes \mathbf{I} + a_2 \mathbf{I} \overline{\otimes} \mathbf{I} + a_3 \mathbf{A} \otimes \mathbf{A} + a_4 (\mathbf{A} \otimes \mathbf{I} + \mathbf{I} \otimes \mathbf{A}) \tag{4}$$

where

$$\begin{array}{ll} a_1 = \mathbb{C}^s_{2222} - 2\mathbb{C}^s_{1212} & a_2 = 2\mathbb{C}^s_{1212} \\ a_3 = \mathbb{C}^s_{1111} + \mathbb{C}^s_{2222} - 2\mathbb{C}^s_{1122} - 4\mathbb{C}^s_{1212} & a_4 = \mathbb{C}^s_{1122} - \mathbb{C}^s_{2222} + 2\mathbb{C}^s_{1212} \end{array} \tag{5}$$

and

$$\begin{array}{lll} \mathbb{C}^s_{1111} = \dfrac{E_1}{1 - \upsilon_{12}\upsilon_{21}}, & \mathbb{C}^s_{2222} = \dfrac{E_2}{1 - \upsilon_{12}\upsilon_{21}}, & \mathbb{C}^s_{1212} = G_{12}, \\ \mathbb{C}^s_{1122} = \mathbb{C}^s_{2211} = \dfrac{\upsilon_{21} E_1}{1 - \upsilon_{12}\upsilon_{21}} & \text{with} & \dfrac{\upsilon_{12}}{E_1} = \dfrac{\upsilon_{21}}{E_2} \end{array} \tag{6}$$

in which E_1 and E_2 are the Young moduli in principal anisotropic directions related respectively to $\boldsymbol{e_1}$ and $\boldsymbol{e_2}$, G_{12} is the shear modulus and υ_{12} and υ_{21} are Poisson ratios related to ($\boldsymbol{e_1}$,$\boldsymbol{e_2}$) verifying the symmetry : $\dfrac{\upsilon_{12}}{E_1} = \dfrac{\upsilon_{21}}{E_2}$.

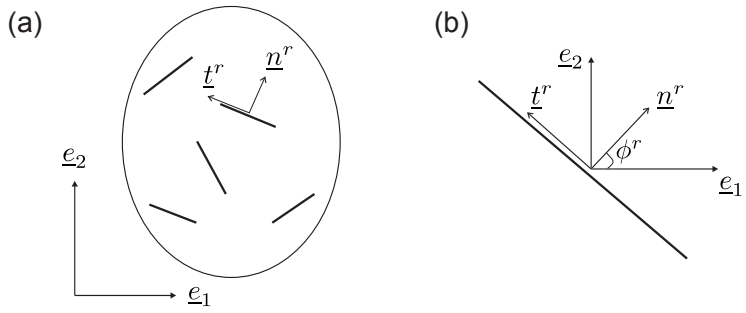

Fig. 1. (a) Representative volume element in two-dimensional case; (b) crack coordinate system

2.2 Thermodynamic potential of the transverse isotropic medium weakened by an arbitrarily oriented distribution of microcracks

According to Goidescu *et al.* study (2013), the macroscopic thermodynamic potential of the anisotropic medium weakened by an arbitrarily oriented distribution of microcracks can be expressed as a function of the macroscopic strain tensor $\mathbf{E}$ (the observable state variable of the problem) and of the set of damage variables d^r, noted $\boldsymbol{d}$, associated to all microcracks families ranging from 1 to N (the internal state variables of the problem). Note that the contribution of open (N_o sets) and closed families of microcracks (N_c sets) are distinguished ($N = N_o + N_c$):

$$\begin{aligned} \Psi(\mathbf{E}, \boldsymbol{d}) = & \frac{1}{2} \mathbf{E} : \mathbb{C}^s : \mathbf{E} \\ & - \sum_{r=1}^{N_o} d^r \{ H^r_{nn} (\mathbf{N}^r : \mathbf{E})^2 + 2 H^r_{nt} (\mathbf{N}^r : \mathbf{E})(\mathbf{T}^r : \mathbf{E}) + H^r_{tt} (\mathbf{T}^r : \mathbf{E})^2 \} \\ & + \sum_{r=1}^{N_c} \frac{d^r}{H^r_{nn} H^r_{tt} - H^{r2}_{nt}} \{ H^r_{nn} H^{r2}_{nt} (\mathbf{N}^r : \mathbf{E})^2 + 2 H^{r3}_{nt} (\mathbf{N}^r : \mathbf{E})(\mathbf{T}^r : \mathbf{E}) \\ & \qquad + H^r_{tt} (2 H^{r^2}_{nt} - H^r_{nn} H^r_{tt}) (\mathbf{T}^r : \mathbf{E})^2 \} \end{aligned} \tag{7}$$

in which

$$\mathbf{N}^r = \mathbb{C}^s : (\boldsymbol{n}^r \otimes \boldsymbol{n}^r), \qquad \mathbf{T}^r = \frac{1}{2}\mathbb{C}^s : (\boldsymbol{n}^r \otimes \boldsymbol{t}^r + \boldsymbol{t}^r \otimes \boldsymbol{n}^r) \tag{8}$$

are two second order symmetric tensors, and H^r_{nn}, H^r_{nt} and H^r_{tt} are scalar parameters that depend on the virgin matrix properties and on the crack orientation $\phi^r = (\boldsymbol{e_1}, \boldsymbol{n}^r)$ as:

$$H^r_{nn} = C(1 - D\cos 2\phi^r), \quad H^r_{nt} = CD\sin 2\phi^r, \quad H^r_{tt} = C(1 + D\cos 2\phi^r) \tag{9}$$

with scalars C and D related to the initial stiffness components:

$$C = \frac{\pi}{4}\frac{\sqrt{\mathbb{C}^s_{1111}} + \sqrt{\mathbb{C}^s_{2222}}}{\sqrt{\mathbb{C}^s_{1111}\mathbb{C}^s_{2222} - (\mathbb{C}^s_{1122})^2}}\sqrt{\frac{1}{\mathbb{C}^s_{1212}} + 2\frac{\sqrt{\mathbb{C}^s_{1111}\mathbb{C}^s_{2222}} - \mathbb{C}^s_{1122}}{\mathbb{C}^s_{1111}\mathbb{C}^s_{2222} - (\mathbb{C}^s_{1122})^2}} \tag{10}$$

$$D = \frac{\sqrt{\mathbb{C}^s_{1111}} - \sqrt{\mathbb{C}^s_{2222}}}{\sqrt{\mathbb{C}^s_{1111}} + \sqrt{\mathbb{C}^s_{2222}}} \tag{11}$$

The transition between open and closed cracks is described by $g(\mathbf{E}, \boldsymbol{n}^r)$ function:

$$g(\mathbf{E}, \boldsymbol{n}^r) = H^r_{nn}\mathbf{N}^r : \mathbf{E} + H^r_{nt}\mathbf{T}^r : \mathbf{E} \tag{12}$$

If $g(\mathbf{E}, \boldsymbol{n}^r) > 0$ microcracks are open, while they are closed if not.

The above formulation of equation (7) can also be written in the following global form:

$$\Psi(\mathbf{E}, \boldsymbol{d}) = \frac{1}{2}\mathbf{E} : \mathbb{C}^{hom} : \mathbf{E} \tag{13}$$

with

$$\mathbb{C}^{hom} = \mathbb{C}^s - \sum_{r=1}^{N} 2d^r\{\mathcal{C}^r_1\mathbf{N}^r \otimes \mathbf{N}^r + \mathcal{C}^r_2[\mathbf{N}^r \otimes \mathbf{T}^r + \mathbf{N}^r \otimes \mathbf{T}^r] + \mathcal{C}^r_3\mathbf{T}^r \otimes \mathbf{T}^r\} \tag{14}$$

in which constants $\mathcal{C}^r_1$, $\mathcal{C}^r_2$ and $\mathcal{C}^r_3$ are defined in case of open cracks (index o) as:

$$\mathcal{C}^r_{1_o} = H^r_{nn}, \qquad \mathcal{C}^r_{2_o} = H^r_{nt}, \qquad \mathcal{C}^r_{3_o} = H^r_{ttn} \tag{15}$$

while for closed cracks (index c) one has:

$$\mathcal{C}^r_{1_c} = -\frac{H^r_{nn}H^{r^2}_{nt}}{H^r_{nn}H^r_{tt} - H^{r^2}_{nt}}, \quad \mathcal{C}^r_{2_c} = -\frac{H^{r^3}_{nt}}{H^r_{nn}H^r_{tt} - H^{r^2}_{nt}}, \quad \mathcal{C}^r_{3_c} = -\frac{H^r_{tt}(2H^{r^2}_{nt} - H^r_{nn}H^r_{tt})}{H^r_{nn}H^r_{tt} - H^{r^2}_{nt}} \tag{16}$$

Then from equation (13), the first state law which gives the macroscopic stress tensor $\boldsymbol{\Sigma}$ can be obtained by derivation:

$$\boldsymbol{\Sigma} = \frac{\partial\Psi}{\partial\mathbf{E}} = \mathbb{C}^{hom} : \mathbf{E} \tag{17}$$

as well as the second state law which provides the expression of the damage energy release rate F^{d^r}:

$$F^{d^r} = -\frac{\partial\Psi}{\partial d^r} = \mathbf{E} : (\mathcal{C}^r_1\mathbf{N}^r \otimes \mathbf{N}^r + \mathcal{C}^r_2[\mathbf{N}^r \otimes \mathbf{T}^r + \mathbf{T}^r \otimes \mathbf{N}^r] + \mathcal{C}^r_3\mathbf{T}^r \otimes \mathbf{T}^r) : \mathbf{E} \tag{18}$$

Both the homogenized stiffness tensor $\mathbb{C}^{hom}$ and the damage energy release rate F^{d^r} are then affected by the anisotropic properties of the solid matrix and depends on the orientation of the considered microcracks family. This is at the origin of the complex coupling between initial anisotropy and damage-induced one, as already discussed in Goidescu et al. (2013).

2.3 Damage yield function

Based on classical thermodynamics arguments in CDM, the following general form is adopted for the damage criterion corresponding to each family of microcracks:

$$f(F^{d^r}, d^r) = F^{d^r} - \mathcal{R}(d^r) = 0 \tag{19}$$

The function $\mathcal{R}(d^r)$ represents the resistance to the damage evolution by microcracks growth. Following Marigo (1985) proposition for brittle damage in the context of isotropic matrix, such global form has been considered for $\mathcal{R}(d^r)$:

$$\mathcal{R}(d^r) = \mathcal{K} + \xi d^r \tag{20}$$

for which we introduce a dependence of the initial threshold with loading orientation as:

$$\mathcal{K} = \mathcal{K}_0 exp(\omega\psi) \tag{21}$$

$\mathcal{K}_0$, ω and ξ are then material parameters relative to initial threshold and its evolution with damage, ψ corresponds to the angle between orthotropy axis e_1 and macroscopic stress principal direction. Exponential term is aimed at shifting the yield surface from constant value $\mathcal{K}_0$ according to the direction of load. From equation (18), one can see that the damage yield function for each family r of microcracks $f(F^{d^r}, d^r) = 0$ is strongly sensitive to matrix anisotropy, microcracks orientation and their opening-closure state. Once the yield surface is reached, density d^r increases as described in the next section.

To illustrate the global form of criterion given by equation (19), Figure 2 shows for one microcrack family orientation ϕ^r=20^o, the initial yield surface (d^r=0) in the macroscopic strain spaces (E_{11}, E_{22}), (E_{11}, E_{12}) and (E_{22}, E_{12}) associated to orthotropy axis ($\mathbf{E} = E_{11}\boldsymbol{e}_1 \otimes \boldsymbol{e}_1 + E_{12}(\boldsymbol{e}_1 \otimes \boldsymbol{e}_2 + \boldsymbol{e}_2 \otimes \boldsymbol{e}_1) + E_{22}\boldsymbol{e}_2 \otimes \boldsymbol{e}_2$); for simplicity only the source term $\mathcal{K}$ is considered (ω=0). Application is done on an orthotropic medium studied by Liao et al. (1997) and analysed in section 3: E_1 = 60 GPa, E_2 = 27 GPa, G_{12} = 13 GPa, ν_{12} = 0.22, and $\mathcal{K}$=12 kJ/m^2. One can see on this figure that damage criterion is reached earlier for open cracks than for closed cracks characterizing more damaging capabilities in case of open cracks than in case of closed cracks. This feature of microcracks growth stability is clearly observed during experimental tests (see for instance laboratory data compiled on concrete by Zhu et al. (2009) in case of isotropic material).

2.4 Damage evolution law and rate form of the constitutive model

For a given family of microcracks, the consistency condition, $\dot{f}^r = 0$, provides the damage evolution in the following form:

$$\dot{d}^r = \frac{1}{c_1}\dot{F}^{d^r} = \frac{2}{c_1}\mathbf{E} : \mathbb{B}^r : \dot{\mathbf{E}} \tag{22}$$

with

$$\mathbb{B}^r = \mathcal{C}_1^r \mathbf{N}^r \otimes \mathbf{N}^r + \mathcal{C}_2^r[\mathbf{N}^r \otimes \mathbf{T}^r + \mathbf{T}^r \otimes \mathbf{N}^r] + \mathcal{C}_3^r \mathbf{T}^r \otimes \mathbf{T}^r \tag{23}$$

And, by differentiating the macroscopic stress-strain relation given by (17), the macroscopic stress increment is expressed as:

$$\dot{\boldsymbol{\Sigma}} = \mathbb{C}_t^{hom} : \dot{\mathbf{E}} = \left[\mathbb{C}^{hom} - \frac{1}{c_1}\mathbf{E} : \left(\sum_{r=1}^{N} \mathbb{B}^r \otimes \mathbb{B}^r\right) : \mathbf{E}\right] : \dot{\mathbf{E}} \tag{24}$$

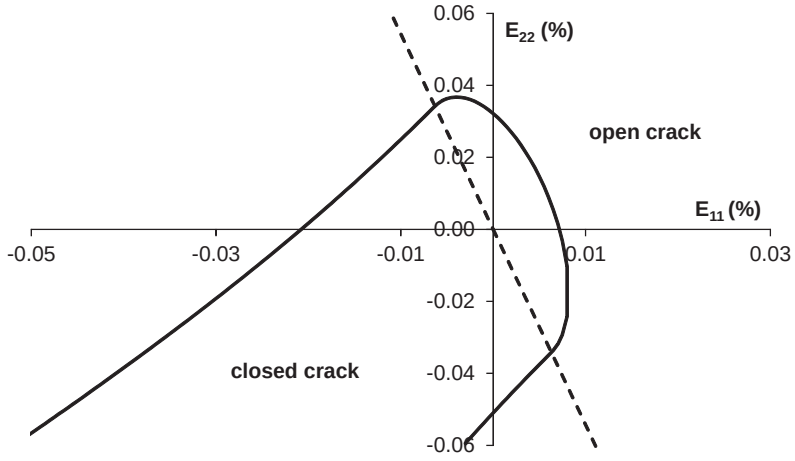

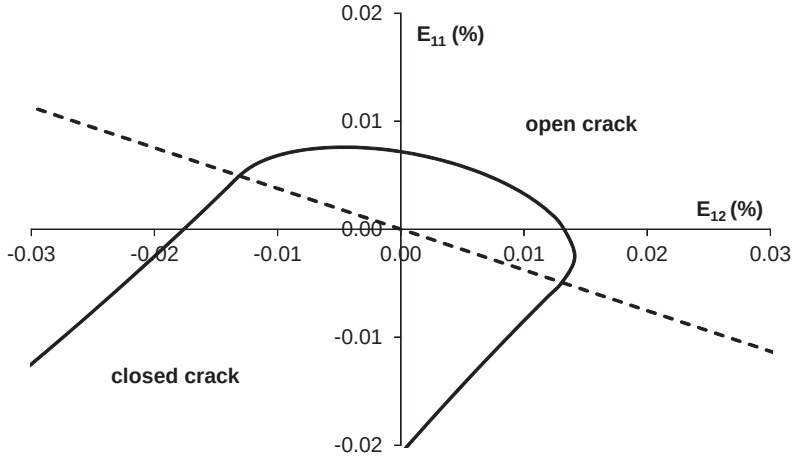

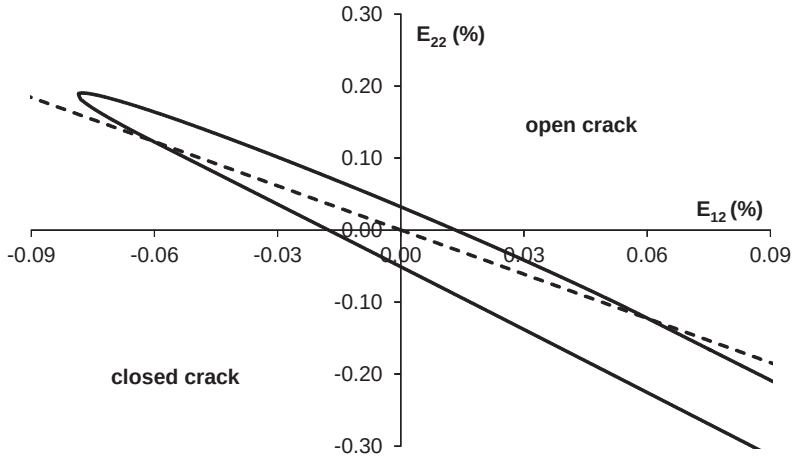

Fig. 2. Initial damage yield surface in the (E_{11}, E_{22}), (E_{11}, E_{12}) and (E_{22}, E_{12}) strain spaces for a microcrack orientation ϕ^r=20^o (dashed lines denote the hypersurface separating the domain of open and closed microcrack)

3 APPLICATIONS

3.1 Simulation of uniaxial tensile test on argillite

Let consider the orthonormal basis (x, y) as the calculation coordinate frame. The virgin material behaviour is modelled as a linear transversely isotropic elastic material in the material axis (e_1,e_2) defined by means of $\psi = (x, e_1)$ angle (see Figure 3). To validate the damage model proposed in this paper, we consider uniaxial tensile tests along y axis carried out on a transversely isotropic argillite of Taiwan by Liao et al. (1997) for several anisotropy orientations from $\psi = 0^o$ to $\psi = 90^o$. Modelling is based on 2D plane strain approach. Owing to symmetry considerations, only one quarter of the sample is considered. Vertical displacements are locked on the bottom and horizontal displacements are locked on the left side. The tensile loading is applied on the top of the sample. All simulations are made using $N = 60$ families of microcracks with uniform distribution of unit normals n^r in the space. The corresponding generalized Hooke's law takes the form:

$$\mathbf{E} = \mathbb{S}^s : \boldsymbol{\Sigma} \tag{25}$$

in which the matrix of components of $\mathbb{S}^s = \mathbb{C}^{s^{-1}}$ in Voigt notation is:

$$\mathbb{S}^s = \begin{pmatrix} \dfrac{1}{E_1} & -\dfrac{\upsilon_{21}}{E_2} & 0 \\ -\dfrac{\upsilon_{12}}{E_1} & \dfrac{1}{E_2} & 0 \\ 0 & 0 & \dfrac{1}{G_{12}} \end{pmatrix} \tag{26}$$

For the considered argilite, elastic moduli have been specified on section 2.3. Moreover, we assume an initial isotropic damage value $d^r = 0.01$ and parameter ξ of equation (20) has been identified from the initial threshold obtained during tensile tests (Liao et al. 1997; see Levasseur et al. 2013). This leads to $\xi = 10kJ/m^2$ whereas the dependence of the parameter $\mathcal{K}$ defined in equation (21) given in table 1.

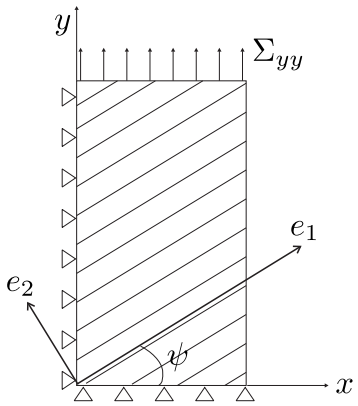

Fig. 3. Geometry of uniaxial tensile test in relation with loading orientation ψ

The results of this model calibration are shown in Figure 4 for ψ=0^o, 45^o, 60^o and 90^o (see Levasseur et al. (2013) for others loading orientations). The stress-strain curves (Σ_{yy}, E_{yy}) are then well captured by the model and the evolutions of damage seem realistic. As observed in the

Table 1. Evolution of $\mathcal{K}$ with loading orientation ψ

$\psi\ (^o)$	0	30	45	60	75	90
$\mathcal{K}\ (kJ/m^2)$	0.2	0.2	0.3	0.6	6	10

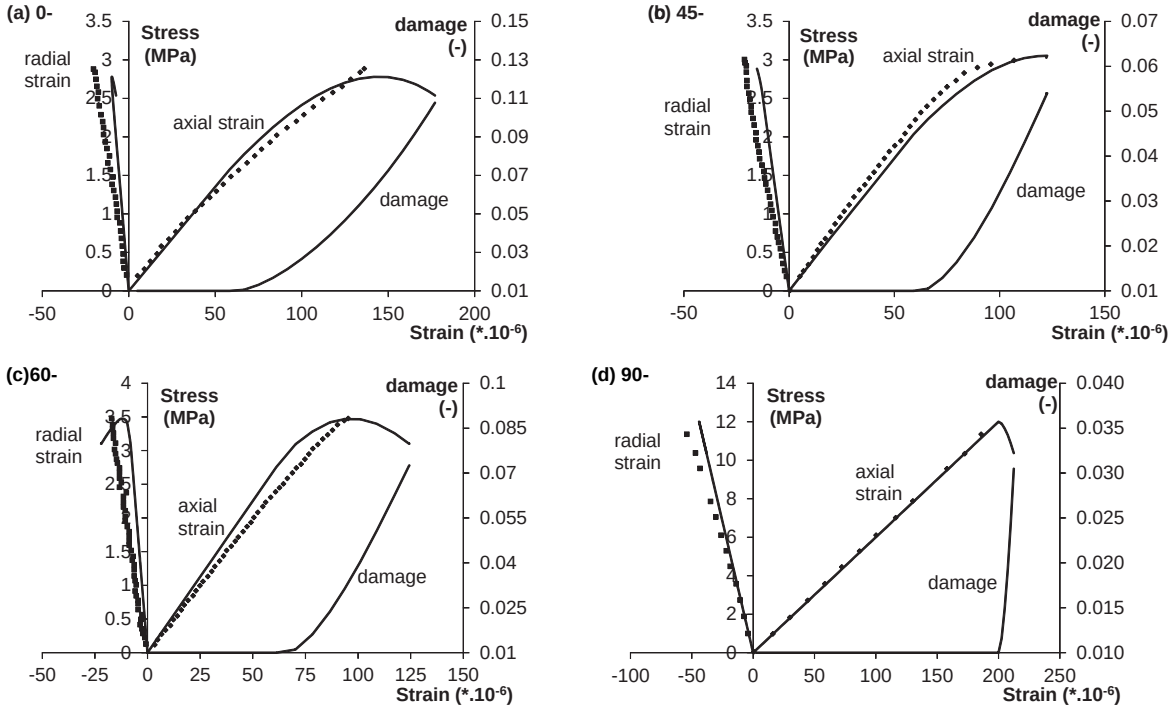

Fig. 4. Axial stress-strain $\Sigma_{yy} - E_{yy}$ curves and damage evolution as function of axial strain E_{yy} for 4 orthotropic axis orientations: 0^o, 45^o, 60^o and 90^o (symbols: lab measurements; full lines: numerical results)

laboratory tests on specimen with low inclination ψ, the predicted stress-strain curves exhibit apparent non linearity before failure; for specimen with high inclination ψ, the stress-strain curves are quasi-linear. In agreement with experimental observations, the influence of microcracks indicates that the tensile behaviour decreases when the anisotropy angle ψ increases. For specimen with low inclination, damage appears gradually causing a more pronounced non linear behaviour of argillite. For specimen with high inclination, damage occurs more suddenly. Numerically, this leads to the non convergence of the model due to the sudden important damage level reached in this latter case.

Similarly to stress paths in elasto-plasticity theory, a "damage path" can be drawn in strain spaces. For instance, Figure 5 presents the "damage paths" in the orthotropic principal strain space (E_{11}, E_{22}) for one microcrack orientation ϕ=20^o and two anisotropy orientations ψ=0^o (corresponding to a loading case along anisotropy axis) and ψ=60^o (corresponding to a loading out of anisotropy axis). Figure 5 puts in evidence that once strain state reaches damage criterion, the yield surface evolves linearly with damage both in open and closed crack domains due to equation (20) and similarly in all directions. Then, final damage surface is homothetic to the initial one.

3.2 Analysis of microcracks closure effect: tension-compression loading

The modelling of tensile loading followed by an unloading and reloading in compression allows to study unilateral effect. Indeed, we can then evaluate how progressive closure of open

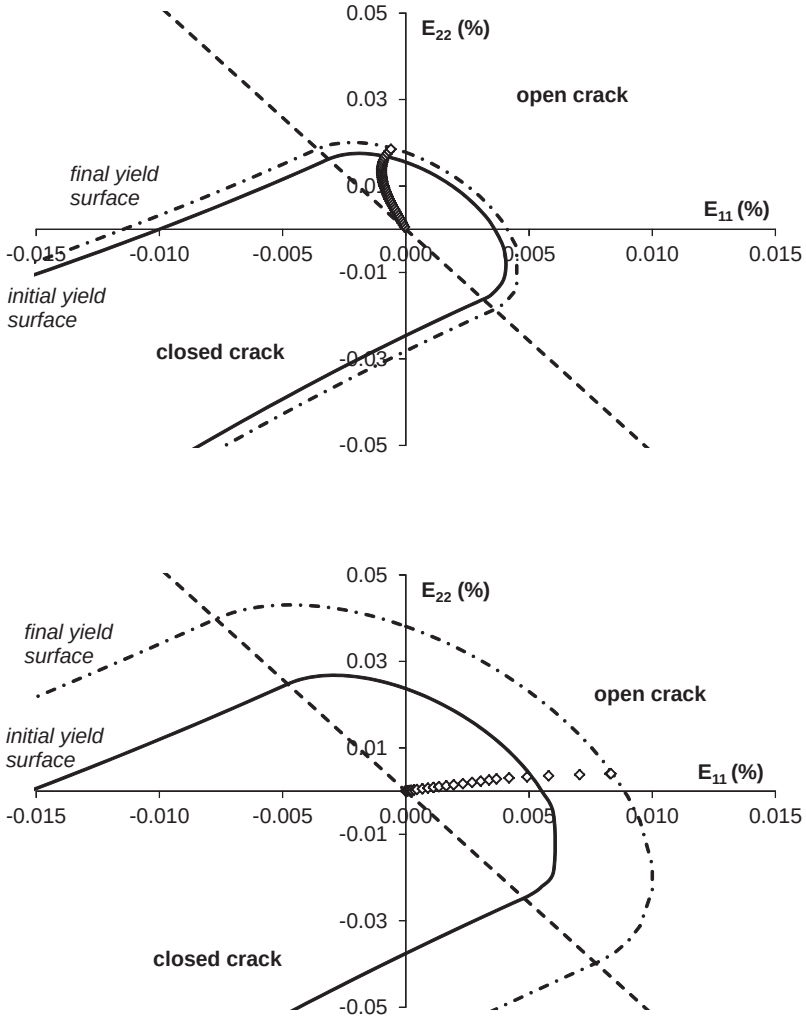

Fig. 5. Initial ($d^r = 0.01$, full lines) and final ($d^r_{\psi=0^o} = 0.0194$ and $d^r_{\psi=60^o} = 0.121$, dash lines) damage yield surfaces $f(F^{d^r}, d^r)$=0 in (E_{11}, E_{22}) space for loading orientations ψ=0^o (top) and ψ=60^o (bottom) for one crack orientation ϕ^r=20^o; tensile loading path is represented by diamond symbols

microcracks generated during the tension loading step affects the macroscopic material response during the compression phase. Figure 6 presents the axial stress-strain curve corresponding to the described loading path for loading orientation ψ=0^o. In the same figure, the evolution of overall damage variable ($\sum_{r=1}^{N} d^r$) with strain is given. The obtained stress-strain curve shows continuous response at the tension-compression transition when axial stress is equal to zero (corresponding to the opening/closure transition) despite the discontinuity of the macroscopic elastic properties. In fact, during tension-compression loading damage yield surface evolves as follows (see Figure 7):

- As long as loading does not reach damage criteria, damage is constant and stress-strain relation is linear;
- When damage criterion is attained for a given family of microcracks, damage evolves providing on one hand, the non linearity of stress-strain curve due to the degradation of stiffness tensor and, on the other hand, the growth of damage surface;

- During unloading phases, the loading path comes into the elastic convex domain and no more damage evolves since the yield surface is reached once again during reloading phase.

Same kind of results is obtained whatever the loading orientation ψ.

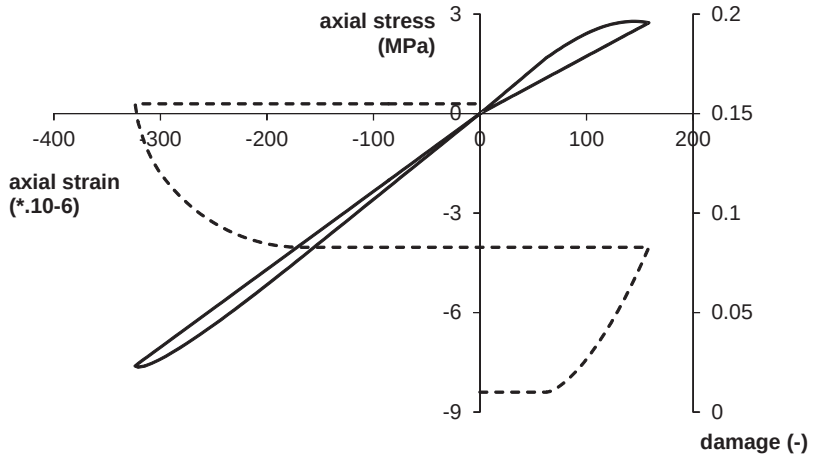

Fig. 6. Simulation of tensile loading followed by unloading and reloading in compression in the case of loading orientation ψ=0^o (full line : axial stress-strain curve $\Sigma_{yy} - E_{yy}$; dashed line : overall damage evolution with axial strain)

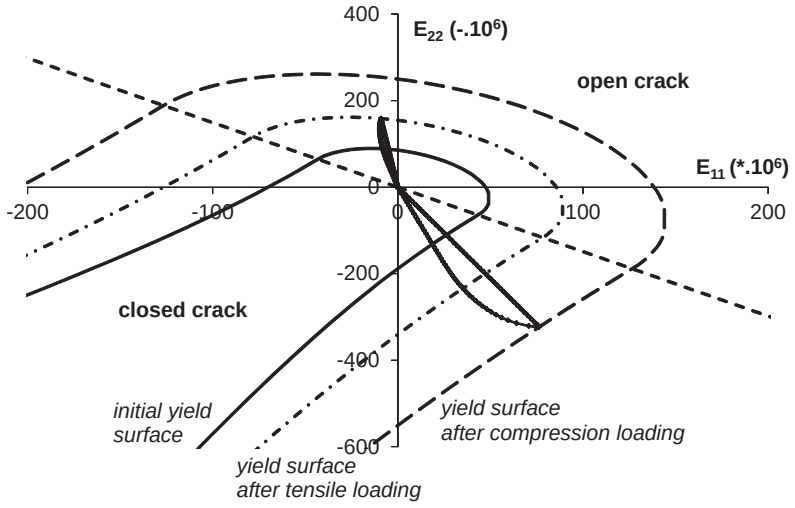

Fig. 7. Evolution of damage yield surface $f(F^{d^r}, d^r)$=0 in (E_{11}, E_{22}) strain space for loading orientation ψ=0^o and for one crack orientation ϕ^r=45^o due to tension-compression loading ; loading path is represented by diamond symbols

4 CONCLUSIONS

Taking advantage of the recent study by Goidescu et al. (2013), this paper presents a full 2D anisotropic micromechanical damage model accounting for unilateral effects in transversely

isotropic rocks. Applied to argillite, it is shown that the initial anisotropy of the rock strongly affects the damage initiation and growth and subsequently the macroscopic response of the material through the stiffness degradation. Furthermore, depending of the inclination of the load, damage can occur gradually or suddenly, leading either to non linear or to quasi-linear behaviour of argilite, as observed during experiments. Moreover, by a systematic analysis of damage criterion in strain spaces, an appropriate description of damage evolution process and of the opening/closure consequences of microcracks is provided.

ACKNOWLEDGEMENTS

The authors would like to thank the F.R.S.-FNRS, the national funds of scientific research in Belgium, for their financial support in FRFC project.

REFERENCES

Baste, S. (2001). Inelastic behaviour of ceramic-matrix composites. *Composites Science and Technology 61*, 2285–2297.

Cazacu, O., Soare, S., & Kondo, D. (2007). On modeling the interaction between initial and damage-induced anisotropy in transversely isotropic solids. *Mathematics and Mechanics of Solids 12(3)*, 305–318.

Costanzo, F., Boyd, J., & Allen, D. (1996). Micromechanics and homogenization of inelastic composite materials with growing cracks. *Journal of the Mechanics and Physics of Solids 44*, 333–370.

Goidescu, C., Welemane, H., Kondo, D., & Cruescu, C. (2013). Microcracks closure effects in initially orthotropic materials. *European J. of Mechanics, A/Solids 37*, 172–184.

Halm, D., Dragon, A., & Charles, Y. (2002). A modular damage model for quasi-brittle solids - interaction between initial and induced anisotropy. *Arch. Appl. Mech. 72*, 498–510.

Ju, J. & Lee, X. (1991). Micromechanical damage model for brittle solids. Part 1: Tensile loading. Part 2: Compressive loading. *Mechanics of Materials 117(7)*, 1495–1536.

Kachanov, M. L. (1982). A microcrack model of rock inelasticity. Part 1: Frictional sliding on microcracks. Part 2: Propagation of microcracks. *Mechanics of Materials 1*, 19–41.

Krajcinovic, D. (1996). *Damage mechanics*. North-Holland.

Lemaitre, J. & Chaboche, J.-L. (1990). *Mechanics of Solid Materials*. Cambridge University Press.

Levasseur, S., Collin, F., Charlier, R., & Kondo, D. (2011). A two scale anisotropic damage model accounting for initial stresses in microcracked materials. *Engineering Fracture Mechanics 78*, 1945–1956.

Levasseur, S., Welemane, H., & Kondo, D. (2013). A microcrackes-induced damage model accounting for unilateral effects: application to transversely isotropic rock. *in preparation*.

Liao, J., Yang, M., & Hsien, H. (1997). Direct tensile behavior of a transversely isotropic rock. *Int. J. Rock Mech. Min. Sci. 34(5)*, 837–849.

Marigo, J.-J. (1985). Modeling of brittle and fatigue damage for elastic material by growth of microvoids. *Eng Fract Mech 21(4)*, 861–874.

Monchiet, V., Gruescu, C., Cazacu, O., & Kondo, D. (2012). A micromechanical approach of crack-induced damage in orthotropic media: application to a brittle matrix composite. *Engineering Fracture Mechanics 83*, 40–53.

Pensée, V., Kondo, D., & Dormieux, L. (2002). Micromechanical analysis of anisotropic damage in brittle materials. *J. Eng. Mech. 128*, 889–897.

Zhu, Q., Kondo, D., & Shao, J. F. (2009). Homogenization-based analysis of anisotropic damage in brittle materials with unilateral effect and interactions between microcracks. *Int. J. Num. Anal. Meth. Geomech. 33*, 749–772.

Zhu, Q., Kondo, D., Shao, J. F., & Pensée, V. (2008). Micromechanical coupling of anisotropic damage in brittle rocks and application. *Int. J. Rock Mech. Mining Sci. 45*, 467–477.

PRINCIPAL CAUSES OF AGING AND RATE EFFECTS IN SANDS: STATIC FATIGUE AND PRESSURE DISSOLUTION

R.L. Michalowski & S.S. Nadukuru
Department of Civil and Environmental Engineering, University of Michigan, Ann Arbor, U.S.A.

ABSTRACT:
The occurrence of time effects in sand has been known for decades, but the cause of this behavior is still a mystery. The practical consequence of this behavior is, for instance, a time-dependent increase in the bearing capacity of a pile driven into a granular soil. Experimental work indicates that delayed fracturing of microscopic features at inter-granular contacts can be a major contributor to time effects in sand. Experiments revealed that the discrete character of the process at the grain contacts leads to a step-wise process of deformation. Often referred to in material science as static fatigue, the process of delayed micro-fracturing was identified as the source of creep in rocks. An analogous process takes place at contacts between sand grains. The most recent experimental work reveals that the presence of environmental factors, moisture in particular, is of primary importance. Pressure dissolution of grain minerals at contacts affects both the properties of inter-granular contacts and also the force chains in the granular assembly. Consequently, the macroscopic stress state in the soil mass can be altered, leading to surprising effects at the macro scale. A series of test results will be reported to support the hypothesis.

1 INTRODUCTION

Time and rate effects are common in soils, not only in clays, but also in sands. At the macroscopic scale the rate effects manifest themselves as viscous behavior, but the nature of this behavior is not revealed by the phenomenological description. The rate effects and aging are both time-dependent effects that are well-defined at the macroscopic scale (continuum); however, once this behavior is considered at different spatial scales, the distinction between the two may not be as clear.

Attention to the time effects in sand was brought in the paper of Mitchell and Solymar (1984), indicating that the cone penetration resistance of sand deposits may decrease after dynamic compaction, but it will increase gradually in time following compaction. Early explanation of this phenomenon included an existence of particle bonding, which would be damaged during dynamic disturbance, but would form again in time after the disturbance. Since then, the explanation of the phenomenon shifted toward phenomena occurring during *secondary compression* (Mitchell 2008). Another example of time effects in sand is manifested in an increase in bearing capacity of piles driven into granular soils in time following installation (Chow et al. 1998, Jardine et al. 2006). Despite wide literature on the

subject (e.g., Schmertmann 1991, Mesri et al. 1990), the time effects in sand remain unresolved.

We will propose a hypothesis capable of explaining some of the time effects in sand, and we will demonstrate some experimental evidence in support of this hypothesis.

2 THE HYPOTHESIS

Sand is typically considered at the macroscopic (continuum) scale as an elasto-plastic material, or, in a discrete modeling, as an assembly of grains with inter-granular interactions being elastic with a limit set by frictional sliding. Such approach is common, for instance, in the discrete element models. Two Scanning Electron Microscope images of sand surfaces are presented in Fig. 1.

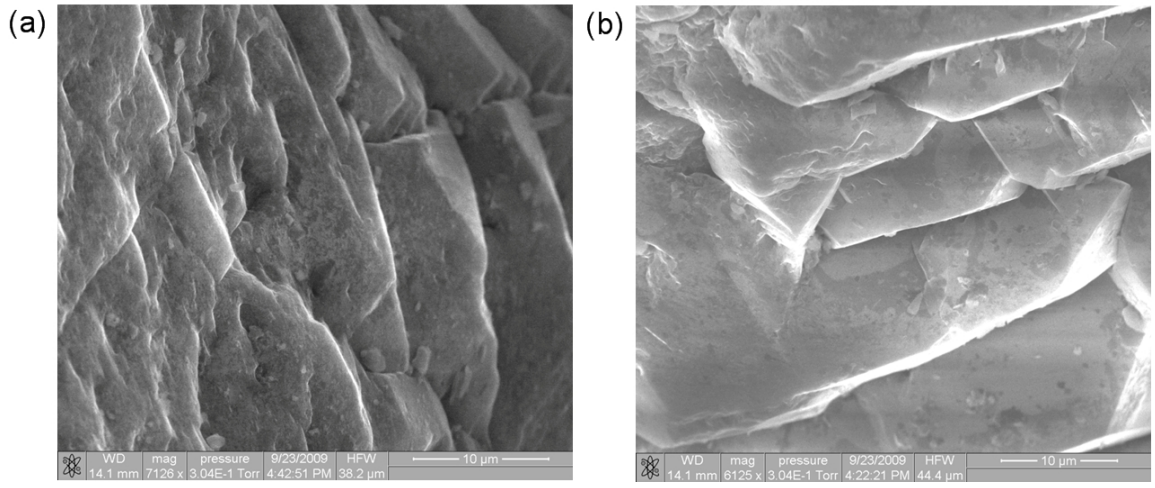

Figure 1. Scanning Electron Microscope images of Flint Shot sand.

When grains with surface micromorphology as in Fig. 1 come into contact and a load is transfer through the contact, the primary response is fracture of the microscopic features on the surfaces between the two grains. Part of this process is in direct (immediate) response to the load, but delayed fracturing occurs afterwards at a constant contact force. It is this delayed fracturing that we identify as the primary cause of time effects: the predominant mechanism contributing to time effects in sand is the delayed fracture of the micro-morphological features on surfaces of grains in contact (asperities, crystalline fragments, or mineral *debris*). This hypothesis was recently suggested in Michalowski and Nadukuru (2010, 2011, 2012); it is hypothesis is different from that advocated by Lade and his co-workers (Lade and Karimpour 2010) in that the emphasis here is not on the fracture of grains, but only the microscopic features on the surfaces of grains.

The process of delayed fracture will be also referred to as *static fatigue* (Charles 1958, Scholz 1968, 1972).

3 SINGLE CONTACT INTERACTION

To demonstrate fracturing of asperities on the grain surface an experiment was performed with three grains mounted on a standard SEM pin stub, at the corners of an equilateral triangle, and loaded with a force of 0.2 N. The areas of grains where contacts were expected

to occur were scanned, and they were rescanned after 15 minutes, and after 1 week of loading. An asperity that was part of the contact on one of the grains is shown in Fig. 2.

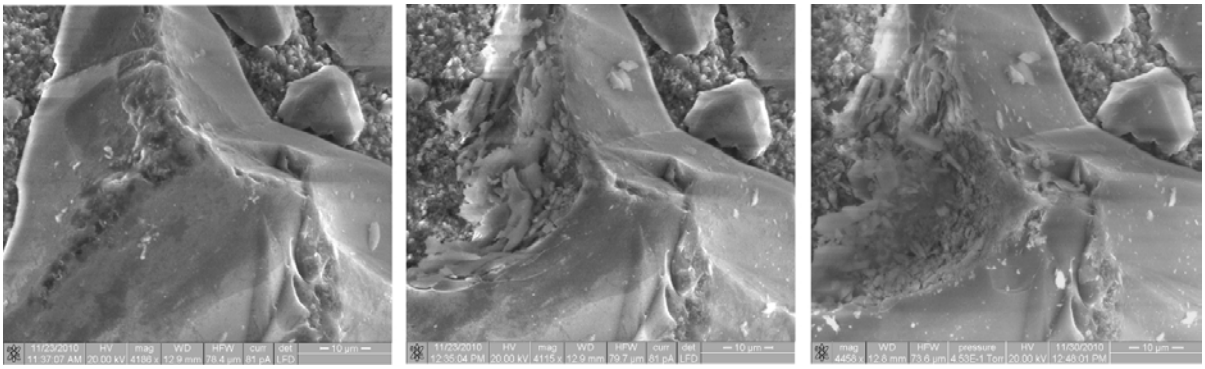

Figure 2. SEM images of silica grain asperity; total image width 80 μm: (a) before loading; (b) after 15 min of loading with a force of 0.67 N; (c) after 1 week of loading (after Michalowski and Nadukuru 2012).

While the images in Fig. 2 are a good demonstration of the damage, the test was not focused on the quantitative measures. To quantify the behavior of two grains in contact, a devise was constructed that allows loading the contact with a known force and measure the relative displacements of the two grains in time. This device is presented in Fig. 3(a); during testing, the device was placed in environmental chamber with constant temperature of 20°C and relative humidity of 20%.

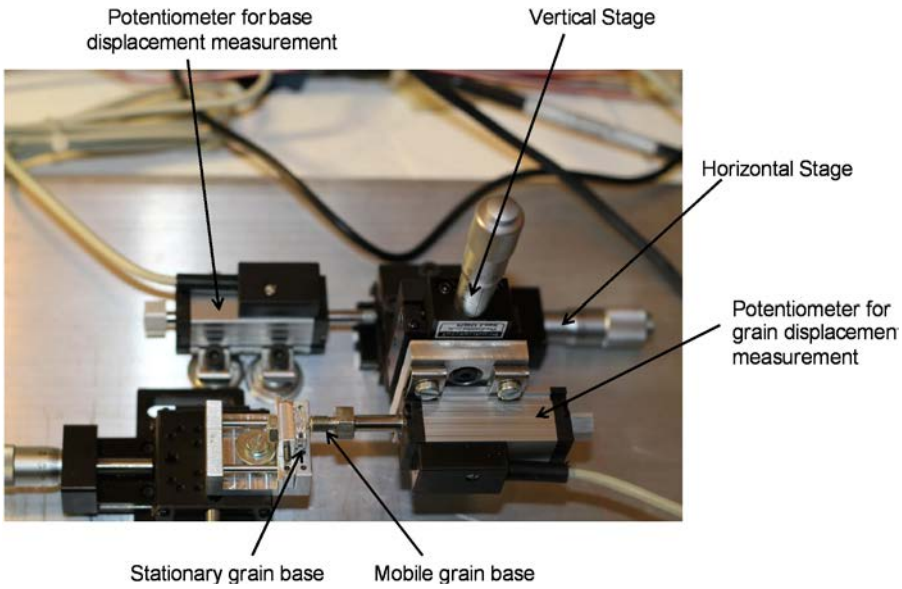

Figure 3. An apparatus for measuring time-dependent behavior of a contact between two grains.

The preliminary measurement of the contact time-dependent behavior is demonstrated in Fig. 4. It is evident that two grains in contact loaded with a force converge together in time. Figure 4(a) illustrates a large (over 200 μm) relative displacement upon application of the

3-Newton force at the contact. Figure 4(b) shows an increase in relative displacement in the following 42 hours at the constant contact load. This additional relative displacement appears to be small (slightly less than a micron), but measurable, and it is significant from the standpoint of a single contact response. We claim that the change in the relative distance of the two grains (grain convergence) will cause a change in the contact properties that will, in turn, affect the behavior of the grain assembly.

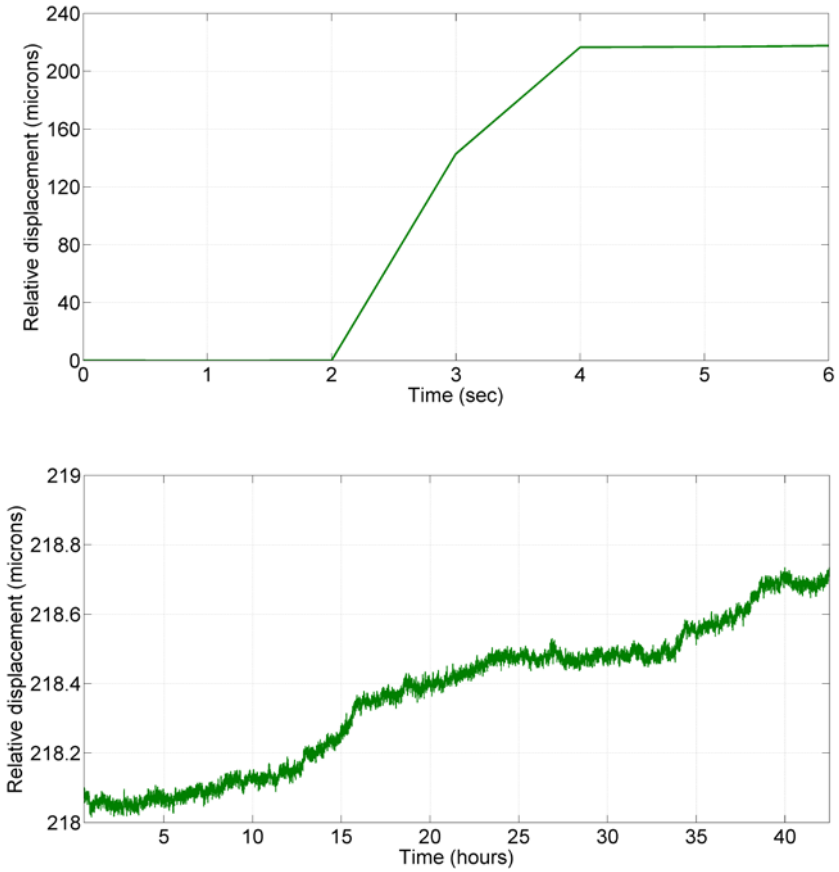

Figure 4. Preliminary results from a single contact test: (a) large convergence upon initial loading, and (b) time-dependent convergence of two grains caused by fatigue of the contact.

4 EXPERIMENTS ON CONFINED SAND SPECIMENS

If inter-granular contacts are indeed affected by static fatigue, then one might expect the grains to *converge* (come closer together), giving rise to an increase in the contact stiffness. This increase will then propagate through the spatial scales and will be manifested at the macroscopic scale as an increase in elastic moduli. This was confirmed in the tests of Afifi and Woods (1971), who demonstrated that the shear modulus increases in time when sand is subjected to sustained load. Consequently, one would expect a change in horizontal stress in a confined sand specimen that is loaded with a constant vertical stress. This conjecture comes from consideration of the elastic energy. The elastic energy stored in a unit volume of sand can be expressed in terms of the average (macroscopic) stresses and strains as

$$W_e = \frac{1}{2}\,\bar{\sigma}_{ij}\,\bar{\varepsilon}^{e}_{ij}\;; \qquad i,j = 1,2,3 \tag{1}$$

where $\bar{\sigma}_{ij}$ and $\bar{\varepsilon}^{e}_{ij}$ are the average stress and average elastic strain tensors, respectively. For simplicity, we assume the sand to be isotropic at the macroscopic scale with strains described by the Hooke's law

$$\bar{\varepsilon}^{e}_{ij} = C_{ijkl}\;\bar{\sigma}_{kl} \tag{2}$$

where C_{ijkl} is the elastic constitutive tensor

$$C_{ijkl} = \frac{1}{E}\Big[(1+\nu)\delta_{ij}\delta_{jl} - \nu\delta_{kl}\delta_{ij}\Big] \tag{3}$$

E and *v* are the Young's modulus and Poisson's ratio, respectively. Specifying directions *1*,*2*,*3* to coincide with the principal directions, and using the Hooke's law in eq. (2), the strain energy in eq. (1) can be expressed as

$$W_e = \frac{1}{2E}\left(\bar{\sigma}_1^2 + \bar{\sigma}_2^2 + \bar{\sigma}_3^2\right) - \frac{\nu}{E}\left(\bar{\sigma}_1\bar{\sigma}_2 + \bar{\sigma}_2\bar{\sigma}_3 + \bar{\sigma}_3\bar{\sigma}_1\right) \tag{4}$$

It is clear from the form of eq. (4) that if the elastic modulus increases, preservation of the elastic energy will require an increase in the mean stress; for instance, in a natural deposit with the vertical load governed by gravity, the horizontal stresses need to increase to preserve the strain energy.

The increase in elastic modulus at the macroscopic scale is associated with changing stiffness at the contacts. The latter is due to delayed fracturing of the microscopic features (asperities) at grain surfaces, thus producing larger contact areas and firmer (stiffer) interaction. The process of fracturing requires expenditure of energy to overcome energy barriers to crack propagation. Part of that energy may come from the strain energy, thus reducing it by some amount. It is likely, however, that the horizontal stresses will still increase. Hence a radial stress in a cylindrical sand specimen subjected to constant (time-independent) vertical load

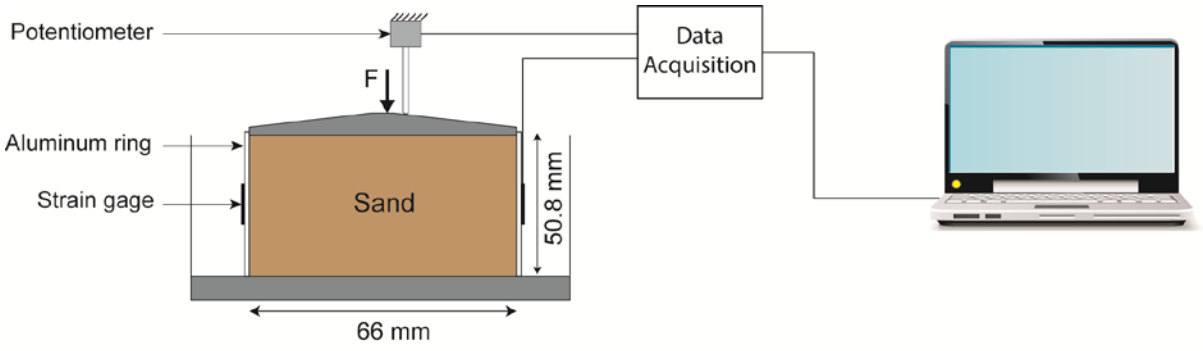

Figure 5. Experimental soft ring setup.

should be increasing in time. This conjecture is tried on specimens of sand placed in an aluminum ring that will deform, should the radial stress increase. An experimental setup is illustrated schematically in Fig. 5.

The soft ring is made of aluminum of about 0.1 mm in thickness, and small changes in radial stress produce the circumferential deformation that is measurable by strain gauges installed on the outside surface if the ring. This deformation is then used to calculate changes in radial stress. The specimens were deposited in the ring using a funnel, with the resulting porosity in the range of 0.41 to 0.43. The settlement of the specimen was measured with a potentiometer, and the signals from the strain gauges and the potentiometer were recorded on a portable computer continuously with frequency of 0.1 Hz and 1 Hz, respectively. The entire assembly was placed in an environmental chamber with constant temperature of 20°C and constant relative humidity of 20%.

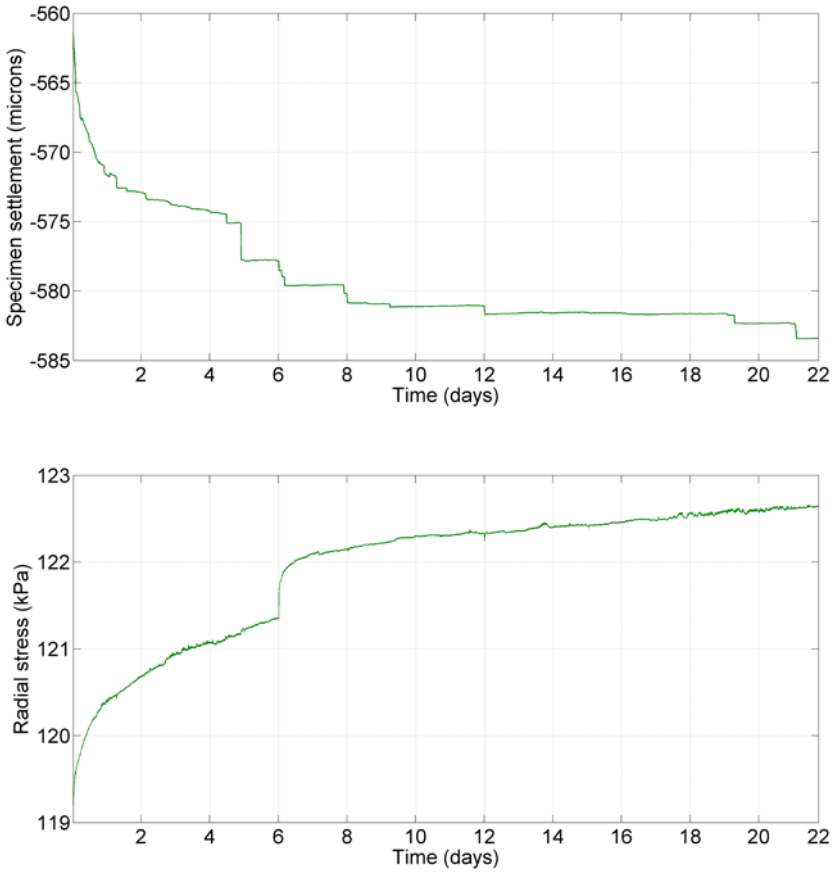

Figure 6. (a) Settlement of silica sand specimen after initial ½ hour of loading, and (b) increase in radial stress as function of time (constant vertical stress of 230 kPa).

After application of vertical load of 230 kPa, the nearly-immediate settlement of the specimen (50 mm in height) exceeded 500 μm, with the reading of about 565 μm after ½ hour of loading. Subsequently, the specimen settled another 10 μm in 5 days. In the following 17 days the specimen settled another 8 μm, with the time-settlement curve having a clear step-wise characteristic. The radial stress in the specimen increased to 119 kPa after the vertical load of 230 kPa was applied, and it raised another 3.5 kPa in the following 22 days. A distinct sudden increase in radial stress at 6 days was caused by an external excitation, which was

registered by geophones installed in the environmental chamber (in subsequent experiments an accelerometer was used to register any external disturbance). It is rather surprising that this disturbance did not cause a comparable anomaly in the settlement function.

The experiment indicates that the horizontal stress does indeed increase in time while the vertical load remains constant. This is consistent with the hypothesis that static fatigue at inter-granular contacts leads to an increase in sand stiffness at the macroscopic scale. The settlement of the specimen has a rather interesting step-wise characteristic. If only a few contacts in the grain assembly were subjected to fatigue, then the settlement of the specimen would not be possible, because of the redundancy of contacts. In order for the grain system to deform (settle), there needs to be enough contacts that have fatigued, so that instability in the system can occur allowing for grain "adjustments" ("restructuring"). The steps in the step-wise settlement function in Fig. 6(a) are associated with these "restructuring" events. They occur each time after sufficient number of contacts have "aged" (or fatigued), allowing formation of a mechanism. This is a plausible explanation of the process.

5 INFLUENCE OF ENVIRONMENTAL FACTORS

It has been well established that environmental factors, such as moisture, have crucial effect on the process of subcritical fracturing (Cuallar et al. 1987). The experiment described in the previous section is now repeated with a specimen that is saturated with distilled water.

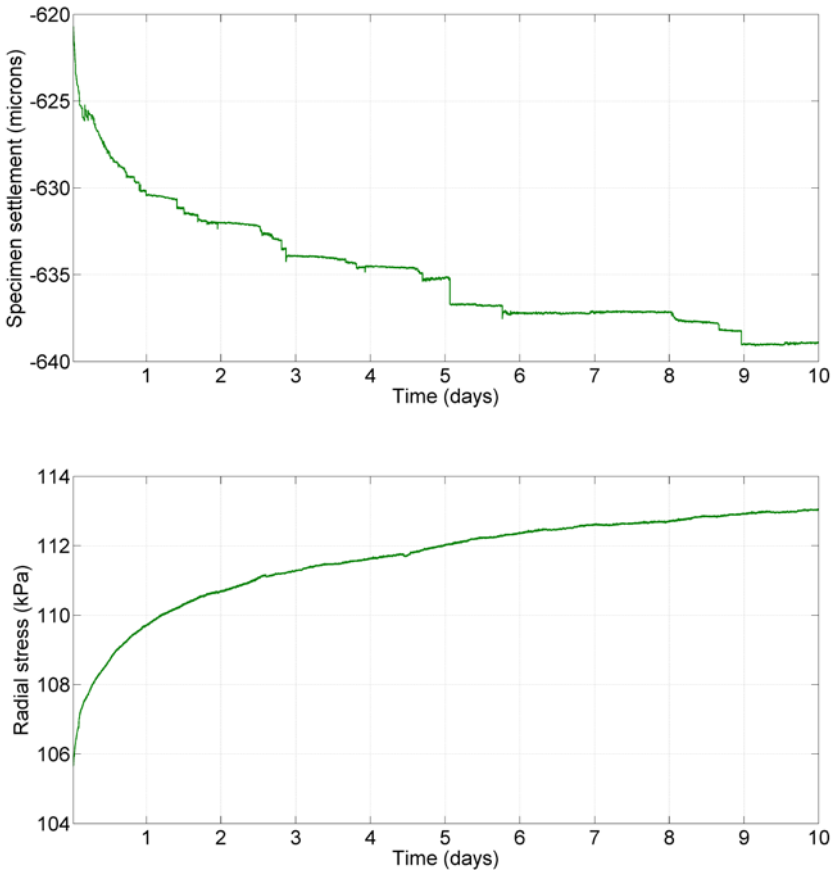

Figure 7. (a) Settlement of silica sand specimen saturated in distilled water (pH 6.8) after initial ½ hour of loading, and (b) increase in radial stress as function of time (constant vertical stress of 230 kPa).

The settlement appears to have a similar step-wise characteristic, and its magnitude in the first 10 days (excluding first ½ hour) is quite similar. The rate of increase of the horizontal stress, however, is substantially different. In the time interval from ½ hour after load application to 6 days, the dry specimen experienced an increase in horizontal stress of about 2 kPa, whereas the specimen saturated with distilled water experienced an increase more than three times larger. This difference could be caused by higher rate of fracturing at contacts causing a faster increase in the contact stiffness. This is consistent with the earlier findings (Cuallar et al. 1987) indicating that a presence of moisture accelerates the process of static fatigue.

The subsequent experiment was performed with distilled water mixed with 2 Normal HCl acid, resulting in pH of 6.6 solution. While the settlement is similar to that for dry

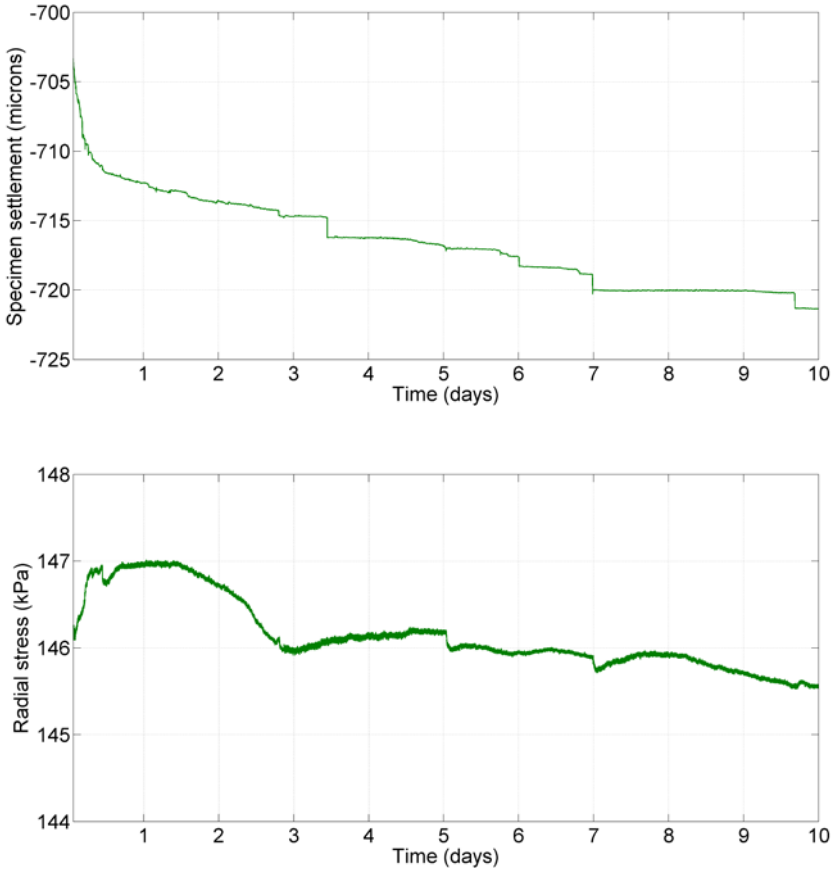

Figure 8. (a) Settlement of silica sand specimen saturated in a slightly acidic solution (2N HCl solution in distilled water resulting in pH 6.6) after initial ½ hour of loading, and (b) increase in radial stress as function of time (constant vertical stress of 230 kPa).

specimen and that for specimen saturated with distilled water, the radial stress function is very different from the other two. After an initial increase in horizontal stress, a reduction tendency appeared after one day and continued for another 9 days. This behavior is consistent with softening of the contacts, and the slightly acidic environment may soften the mineral. It is clear from eq. (4) that preservation of strain energy requires reduction in radial and circumferential stress if the Young's modulus is reduced. Another possible cause behind this outcome is pressure dissolution of mineral in the acidic environment. Pressure dissolution

causes loss of mass from the contact, which is likely to cause stress relaxation in a confined specimen. The original increase in the radial stress (in a day following the first ½ hour of loading) was about 1 kPa, and the reduction was 1.5 kPa in the subsequent 9 days. This is a very small reduction, but it is clearly contrary to the outcome of the test with the air-dry sand or the sand submerged in distilled water. The conjecture that pressure dissolution is responsible for this outcome still needs more evidence, but it is a very plausible explanation of the observed outcome.

6 CONCLUSIONS

While the time and rate effects in sand have been reported by many, the nature of these effects remains enigmatic. The hypothesis presented indicates delayed fracturing of micro-morphological features on grain surfaces at contacts as the major contributor to these effects. This process is also referred to as static fatigue. Environmental factors, such as moisture, have a chief influence on the process. Moisture can accelerate static fatigue, whereas acidic environment can contribute to dissolution of minerals, which affects the behavior of sand at the macroscopic scale.

Acknowledgement

The work presented in this paper was supported by the National Science Foundation through grants CMMI-1129009 and CMMI-0724022. This support is greatly appreciated. The authors also would like to thank The University of Michigan Electron Microbeam Analysis Laboratory, for the use of their Quanta 3D Scanning Electron Microscope supported by the National Science Foundation, grant No. DMR-0320740.

REFERENCES

Afifi, S.S. and Woods, R.D. (1971). “Long-term pressure effects on shear modulus of soils.” ASCE *J. Soil Mech. Found. Div*., 97**(**10), 1445-1460.

Charles, S.J. (1958). “Static fatigue of glass. I.” *Journal of Applied Physics*, 29(11), 1549-1553.

Chow, F. C., Jardine, R. J., Brucy, F., and Nauroy, J. F. (1998). "Effects of Time on Capacity of Pipe Piles in Dense Marine Sand." *Journal of Geotechnical and Geoenvironmental Engineering*, 124(3), 254-264.

Cuallar, E., Roberts, D. and Middleman, L. (1987). “Static fatigue lifetime of optical fibers in bending.” *Fiber and Integrated Optics*, 6(3), 203 - 213

Jardine, R. J., Standing, J. R., and Chow, F. C. (2006). "Some observations of the effects of time on the capacity of piles driven in sand." *Geotechnique*, 56(4), 227-244.

Lade, P.V. and Karimpour, H. (2010). “Static Fatigue Controls Particle Crushing and Time Effects in Granular Materials.” Soils and Foundations, 50(5), 573-583.

Mesri, G., Feng, T.W. and Benak, J.M. (1990). “Postdensification penetration resistance of clean sand.” *J. Geotech. Eng.*, 116(7), 1095-1115.

Michalowski, R.L. and Nadukuru, S.S. (2010). “Stress corrosion cracking and relaxation of deviatoric stress after dynamic compaction of sand.” *37th Solid Mechanics Conference*, (*SolMech 37*), Keynote, Sept. 6-10, 2010, Warsaw, Poland (extended abstract).

Michalowski, R.L. and Nadukuru, S.S. (2011). “Stress corrosion cracking and multi-scale process of delayed increase in penetration resistance after dynamic compaction of sand.” Geo-Frontiers 2011, March 13-16, 2011, Dallas, TX.

Michalowski, R.L. and Nadukuru, S.S. (2012). “Static fatigue, time effects, and delayed increase in penetration resistance after dynamic compaction of sand.” *Journal of Geotech. Geoenv. Engineering*, **138**, No. 5, 564-574.

Mitchell, J.K. and Solymar, Z.V. (1984). “Time-dependent strength gain in freshly deposited or densified sand.” *J. Geotech. Eng.*, 110(11), 1559-1576.

Mitchell, J.K. (2008). “Aging of sand – a continuing Enigma?” *6th Int. Conf. on Case Histories in Geotechnical Engineering*. Arlington, VA, Aug. 11-16, 2008, 1-21.

Schmertmann, J.H. (1991). “The mechanical aging of soils.” *J. Geoecht. Eng.*, 117(9), 1288-1330.

Scholz, C.H. (1968). “Mechanism of creep in brittle rock.” *J. Geophys. Res.*, 73(10), 3295-3302.

Scholz, C.H. (1972). “Static fatigue of quartz.” *J. Geophys. Res.*, 77(11), 2104-2114.

A WATER RETENTION MODEL FOR COMPACTED CLAYEY SOILS

A.C. Dieudonne
ArGEnCo Department, Univeristy of Liege, Liege, Belgium
F.R.I.A., Fond de la Recherche Scientifique - FNRS, Brussels, Belgium

S. Levasseur, R. Charlier
ArGEnCo Department, Univeristy of Liege, Liege, Belgium

G. Della Vecchia
Department of Civil and Environmental Engineering, Politecnico di Milano, Milan, Italy

C. Jommi
Department of Civil and Environmental Engineering, Politecnico di Milano, Milan, Italy
Department of Geosciences and Engineering, TU Delft, Delft, The Netherlands

ABSTRACT: *The paper presents a water retention model accounting for the evolution of the aggregated structure of compacted clays along generalized hydromechanical stress paths. In this model, the retention mechanisms of both microstructural and macrostructural levels are described separately using an expression of the type proposed by van Genuchten (1980). From the water retention model, a theoretical pore-size distribution (PSD) can be derived. Experimental PSD data on two compacted clays subjected to various wetting, drying and loading paths are exploited to provide a physical based calibration of the parameters of the water retention model. Not only they emphasize the evolution of some parameters, such as the air-entry pressure, along generalized stress paths but they also provide a quantification of these processes. On this basis, simple evolution laws are proposed. Finally, the water retention model is validated against other experimental data on the same materials compacted at different dry densities. The proposed formulation succeeds in tracking simultaneously the evolution of the fabric pattern and the hydraulic state of compacted clays along generalized stress paths.*

1 INTRODUCTION

In recent years, particular attention has been paid to the behaviour of compacted clays in relation to their use as engineered barriers in deep geological repositories for nuclear waste (Pusch 1992; Komine & Ogata 1994; Delage et al. 1998; Wiebe et al. 1998; Romero et al. 1999; Collin et al. 2002; Lloret et al. 2003; among others). In this context, the engineered barrier experiences a complex behaviour owing to the strong multiphysical processes taking place. Initially unsaturated, the compacted clay experiences hydration from the saturated host rock. During this process, it tends to expand and develops swelling stresses, hence modifying the water transfer properties of the material (see, for instance, Loiseau et al. 2002; Villar & Lloret 2002; Ye et al. 2009).

Because the final effectiveness of the seal is believed to depend on this transient phase, the conceptual understanding of the water retention mechanisms appears as a key issue. It is now admitted that the behaviour of compacted clays is better understood when the effects of the

aggregated structure is taken into account, and numerous studies have focused on the evolution of the clay fabric along generalized stress paths (see for instance Romero et al. 1999; Cuisinier & Laloui 2004; Della Vecchia 2009; Monroy et al. 2010; Wang et al. 2012).

Although the influence of structure on the behaviour of compacted clays has been recognized, only a few water retention models have taken it explicitly into account. Indeed classical approaches for modelling the water retention behaviour are based on parameters to be fitted using experimental data.

Durner (1994) modelled successfully the water retention behaviour of a sandy loam, distinguishing explicitly in the formulation the existence of two structural levels. The same approach was later used by Gitirana Jr. & Fredlund (2004) on a pelletized diatomaceous soil and on a residual, highly collapsible clay from Brasilia. Romero & Vaunat (2000) distinguished an intra-aggregate water region and inter-aggregate water region to model the retention behaviour of Boom Clay. However none of these Authors have considered explicitly the evolutionary character of the soil fabric along hydromechanical stress paths. Early attempts to include the evolution of microfabric into a water retention model are the ones proposed by Simms & Yanful (2002, 2004) and by Romero et al. (2011) and Della Vecchia et al. (2013). Simms & Yanful (2002, 2004) proposed indeed water retention models explicitly derived from the pore-size distribution. As Romero et al. (2011) and Della Vecchia et al. (2013) are concerned, they extended the framework of Romero & Vaunat (2000) in order to account for swelling of clay aggregates and identified micro- and macrostructural domains by defining a discriminating pore size.

In this paper, a water retention model, together with a pore-size density model, are proposed to model the behaviour of compacted clayey materials. Micro- and macrostructural domains both cover the whole range of pore sizes, and thus the whole range of suction values. Experimental data on compacted Boom Clay from Della Vecchia (2009) and on compacted London Clay from Monroy et al. (2010) are used to calibrate and later validate the model. Although considered as moderately active, theses clays were selected to grasp the problem of the evolving microstructure along generalized stress paths.

2 WATER RETENTION AND PORE-SIZE DENSITY MODELS

Explicitly accounting for the aggregated structure of compacted clayey materials, the water retention model is written as the superposition of two elementary curves. The retention mechanisms of each structural level are described separately using an expression of the type proposed by van Genuchten (1980). In this way, the total water ratio e_w (defined as the volume of water per unit volume of solid) includes a contribution e_{wm} from the intra-aggregate water and a contribution e_{wM} from the water stored in the macropores. Using the indices (m) and (M) to refer respectively to the microstructural and macrostructural properties, the water retention model writes:

$$e_w(s) = e_{wm} + e_{wM} = e_m \left[1 + \left(\frac{s}{s_0^{(\mathrm{m})}} \right)^{n^{(\mathrm{m})}} \right]^{-m^{(\mathrm{m})}} + (e - e_m) \left[1 + \left(\frac{s}{s_0^{(\mathrm{M})}} \right)^{n^{(\mathrm{M})}} \right]^{-m^{(\mathrm{M})}} \quad (1)$$

where e and e_m are the total and microstructural void ratios, s_0 is a parameter related to the air-entry pressure[1], and n and m are model parameters. The parameter n is associated to the rate

[1] Note that the notion of air-entry value is not defined in van Genuchten's formulation. However, for sake of simplicity, s_0 will be referred as the air-entry pressure in this paper.

of desaturation of the soil while m is linked to the curvature of the water retention curve in the high suction range.

Considering the Washburn equation (Washburn 1921), relating suction s to an equivalent pore diameter x, a theoretical pore-size density (PSD) model can be derived directly from equation (1):

$$PSD \equiv \frac{\partial e_w}{\partial \log x} = -\frac{4\sigma \cos\theta_w}{2.3\, x} \frac{\partial e_w}{\partial s} \tag{2}$$

where $\sigma = 0.07275\ N/m$ is the air/water surface tension and $\theta_w = 0^\circ$ is the water-solid contact angle.

The model parameters s_0, n and m can thus be interpreted linking them to the pore-size density function. The value of s_0 is related to the position, on the x-axis, of maximum value of the PSD function, while n and m are associated to the width and the shape of the pore-size distribution.

3 CALIBRATION OF THE PSD MODEL

3.1 Calibration procedure

Experimental data on compacted Boom Clay from Della Vecchia (2009) and on compacted London Clay from Monroy et al. (2010) are used to calibrate the pore-size distribution model. Mercury intrusion porosimetry data are exploited to this aim. In total, 24 experimental PSD curves are fitted with equation (2) in a systematic way in order to highlight the influence of various hydromechanical stress paths, such as wetting, drying and loading under constant water content, on the model parameters. The calibration procedure includes three main steps:

- The definition of a law for the evolution of the microstructural void ratio along generalized hydromechanical paths. In order to achieve this first step, the experimental PSD curves of the as-compacted materials are first calibrated. Their model parameters are then used as starting point for the calibration of the other experimental curves.
  A good correlation is found between the microstructural void ratio e_m and the water content e_w and the following relationship is proposed:

  $$e_m = \beta_0 e_w^2 + \beta_1 e_w + e_{m,0} \tag{3}$$

  where β_0 and β_1 quantifies the swelling tendency of the aggregates and $e_{m,0}$ is the microstructural void ratio of the dry material. Note that this equation is similar to the one proposed by Romero et al. (2011), except that it suggests a continuous evolution of the microstructural void ratio with the water ratio.
  The model parameters for Boom Clay and London Clay are presented in Table 1.
- Basing on the prediction of (3) for e_m, a second calibration is performed, trying to keep fixed the greatest number of parameters. As a result, parameters $n^{(\mathrm{m})}$, $m^{(\mathrm{m})}$ and $m^{(\mathrm{M})}$ are kept almost constant during generalized stress paths.
- A final calibration step, using equation (3) and imposing constant values for $n^{(\mathrm{m})}$, $m^{(\mathrm{m})}$ and $m^{(\mathrm{M})}$. This final calibration highlights the evolution of the microstructural air-entry value $s_0^{(\mathrm{m})}$ with the microstructural void ratio e_m (Fig. 1(a)). Moreover, the macro-structural air-entry pressure is found to change along with the ratio of macrostructural to total void ratios (Fig. 1(b)).

Table 1: Evolution of the microstructural void ratio with the water ratio. Model parameter values for Boom Clay and London Clay.

	β_0	β_1	$e_{m,0}$
Boom Clay	0.2	0.05	0.33
London Clay	0.35	0.08	0.27

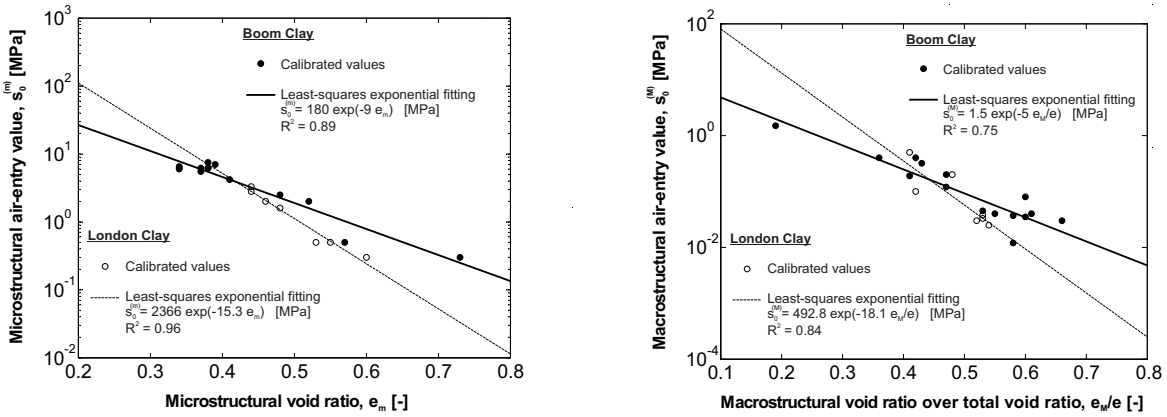

(a) (b)

Fig. 1: Variation of the model parameters along hydromechanical stress paths. (a) Dependence of the microstructural air-entry pressure with the microstructural void ratio. (b) Dependence of the macrostructural air-entry pressure with the ratio of the macrostructural void ratio over the total void ratio.

3.2 Structural changes along wetting paths

Experimental data on London Clay from Monroy et al. (2010) are used to highlight the effects of wetting on the structure. Fig.2(a) presents the evolution of the PSD during a wetting path from the as-compacted material (suction close to 1000 kPa) up to full saturation of the material. Hydration occurred under a nominal load of 7 kPa.

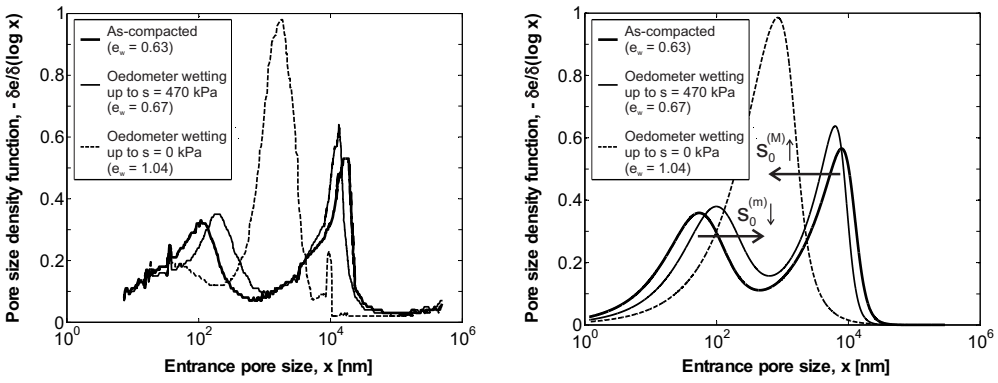

(a) (b)

Fig. 2: Structural changes along wetting paths. (a) Experimental data on London Clay (Monroy et al. 2010). (b) Model fitting.

It can be observed that wetting induces progressive increase of the micropores sizes, hence invasion of the macropores. As the microstructural mode displaces towards larger pore-size values, the microstructural air-entry pressure decreases (Fig.2(b)). On the contrary, invasion of the macropores induces an increase in the macrostructural air-entry pressure as the inter-aggregate volume is decreased.

3.3 Structural changes along drying paths

Data on Boom Clay Della Vecchia (2009) are used to highlight the influence of drying paths on the structure. Samples were prepared by static compaction at a water content of 15%, and then saturated under oedometer conditions at almost null vertical stress.

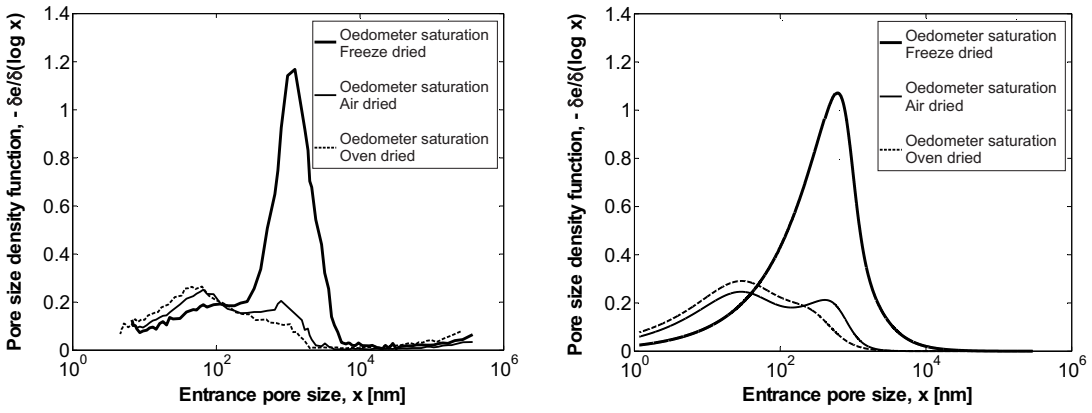

Fig. 3: Structural changes along drying paths. (a) Experimental data on Boom Clay (Della Vecchia 2009). (b) Model fitting.

As shown in Fig. 3, the drying process induces a shrinkage of the material. Assuming that freeze-drying does not induce changes in sample fabric, this shrinkage seems to affect not only the porous volume but also the pore-size distribution. Indeed the decrease in micro- and macrostructural porous volume is associated with a shift of the pores towards smaller sizes. As far air-entry values, this corresponds to an increase in $s_0^{(\mathrm{m})}$ and $s_0^{(\mathrm{M})}$.

3.4 Structural changes along loading paths

Experimental data from Della Vecchia (2009) are used to highlight the influence of loading on the structure. Fig.4 presents the pore-size distributions of the as-compacted material and the material subjected to both triaxial and oedometer compression under constant water content.

It can be observed that loading induces a progressive decrease of the macrostructural pore volume, starting from the largest macropores, while the microstructure is hardly affected.

Similar results are observed on London Clay (Monroy et al. 2010), and over wider ranges of void ratios, on FoCa clay (Lloret et al. 2003), on Spethwhite kaolin (Tarantino & De Col 2008), Barcelona Silty Clay (Buenfil et al. 2005) and on a compacted scaly clay from Italy (Airo Farulla et al. 2011; Della Vecchia et al. 2012), among others.

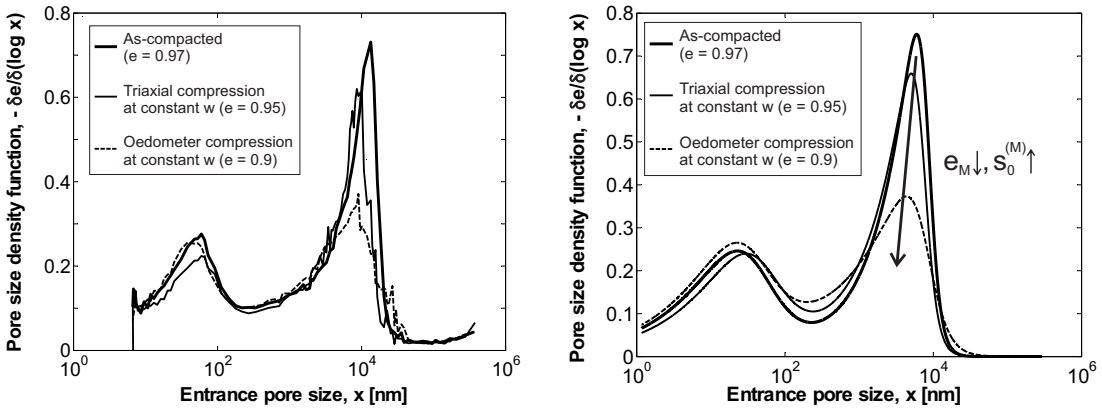

Fig. 4: Structural changes along loading paths. (a) Experimental data on Boom Clay (Della Vecchia 2009). (b) Model fitting.

4 VALIDATION OF THE WATER RETENTION MODEL

The proposed water retention model is validated against experimental data on compacted Boom Clay from Romero et al. (2011). Note that the mercury injection process is assimilated to a desorption path and the model should therefore be used to predict the retention behaviour of the material upon drying. Theoretical predictions of the water retention model are calculated from equations (1). The key issue in the formulation of the model is to assign, when meaningful, evolution laws to the parameters. Exploiting the calibration of the PSD model presented in the previous section, the parameters $s_0^{(\mathrm{m})}$ and $s_0^{(\mathrm{M})}$ are assumed to evolve exponentially (in the considered range of values) respectively with the microstructural void ratio e_m and with the ratio $(e - e_m)/e$, representing the ratio between the macrostructural and the total void ratios:

$$s_0^{(\mathrm{m})} = \alpha_1^{(\mathrm{m})} \exp\left(-\alpha_2^{(\mathrm{m})} e_m\right) \tag{4}$$

$$s_0^{(\mathrm{M})} = \alpha_1^{(\mathrm{M})} \exp\left(-\alpha_2^{(\mathrm{M})} \frac{e - e_m}{e}\right) \tag{5}$$

where e_m is given by equation (3) and α_1 and α_2 are model parameters.

In accordance with the calibration of the PSD model, the parameters $n^{(\mathrm{m})}$, $m^{(\mathrm{m})}$ and $m^{(\mathrm{M})}$ are set constant. Although $n^{(\mathrm{M})}$ is find to vary along generalized stress paths, a constant value is given in the water retention model. All parameter values are presented in Table 2.

Table 2: Model parameter values for Boom Clay.

Microstructural characteristics				**Macrostructural characteristics**			
$n^{(\mathrm{m})}$	$m^{(\mathrm{m})}$	$\alpha_1^{(\mathrm{m})}$	$\alpha_2^{(\mathrm{m})}$	$n^{(\mathrm{M})}$	$n^{(\mathrm{M})}$	$\alpha_1^{(\mathrm{M})}$	$\alpha_2^{(\mathrm{M})}$
1.65	0.35	180 MPa	9	2.0	0.16	1.5 MPa	5.0

The performance of the model is presented in Fig. 5. It can be observed that the model predictions compare favourably with the experimental data on Boom Clay compacted at different void ratios. The model succeeds in tracking the increase of air entry pressure with decreasing

void ratio. Moreover, for high suction values, the model tends to reach a unique relationship between water ratio and suction, regardless of the current value of void ratio. In this domain, the water retention behaviour is indeed dominated by the behaviour of the microstructure. On the contrary, for low values of suction, the water retention curve is sensitive to mechanical actions.

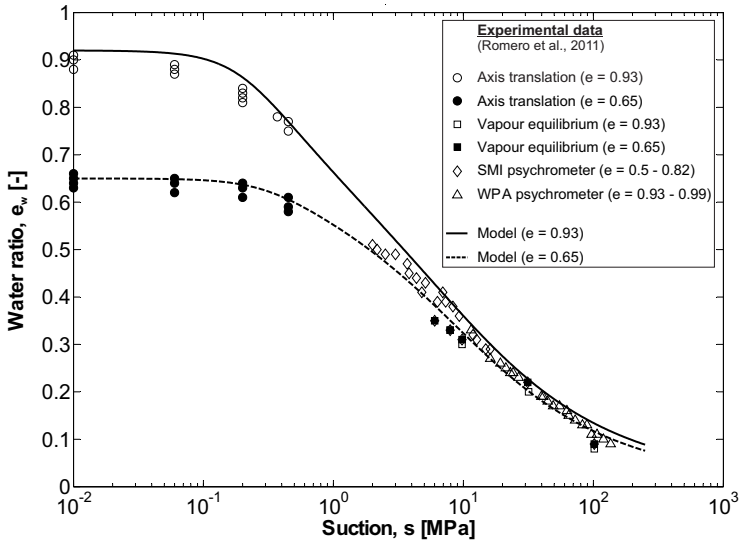

Fig. 5: Comparison between experimental main drying paths for compacted Boom Clay (Romero et al. 2011) and model predictions at different void ratios

5 CONCLUSIONS

The paper presents a water retention model for compacted clayey soils, accounting for the evolution of their aggregated structure along generalized hydromechanical stress paths. Microstructural and macrostructural water retention mechanisms are distinguished and described separately. According to experimental evidence, a law is proposed for the evolution of the microstructural void ratio with the water content.

The water retention model is used to derive a theoretical pore-size distribution which is used to calibrate the model parameters on experimental PSD curves from the literature. As the mercury intrusion process can be assimilated to a drying path, the attention is focussed on the main drying branch of the retention domain. The evolution of some parameters along generalized hydromechanical stress paths is highlighted and quantified. The water retention model is then validated against experimental data on the same materials compacted at different dry densities.

The proposed model captures important features of the retention behaviour of compacted clayey soils, such as:

- The increase in microstructural porous volume with increasing water content;
- The increase in air-entry pressure for decreasing macrostructural voids;
- The existence, in the high suction range, of an intra-aggregate water region which is almost not sensitive to the total void ratio.

ACKNOWLEDGEMENTS

The authors acknowledge the Belgian FRS-FNRS for its financial support during the stay of the first Author at the Politecnico di Milano.

REFERENCES

Airo Farulla, C., Battiato, A., & Ferrari, A. (2011). The void ratio dependency of the retention behaviour for a compacted clay. In *Unsaturated Soils*, pp. 417–422.

Buenfil, C., Romero, E., Lloret, A., & Gens, A. (2005). Hydro-mechanical behaviour of a clayey silt under isotropic compression. In *Proc. 2nd Int. Workshop on Unsaturated Soils, Anacapri*, pp. 331–342.

Collin, F., Li, X., Radu, J., & Charlier, R. (2002). Thermo-hydro-mechanical coupling in clay barriers. *Engineering Geology 64*, 179–193.

Cuisinier, O. & Laloui, L. (2004). Fabric evolution during hydromechanical loading of a compacted silt. *Int. J. Num. Anal. Meth. Geomech. 28*, 483–499.

Delage, P., Howat, M., & Cui, Y. (1998). The relationship between suction and swelling properties in a heavily compacted unsaturated clay. *Engineering Geology 50*, 31–48.

Della Vecchia, G. (2009). *Coupled hydro-mechanical behaviour of compacted clayey soils*. Ph. D. thesis, Politecnico di Milano.

Della Vecchia, G., Airo Farulla, C., & Jommi, C. (2012). Modelling the water retention domain of a compacted scaly clay. In *Unsaturated Soils: Research and Applications*, pp. 55–62.

Della Vecchia, G., Jommi, C., & Romero, E. (2013). A fully coupled elastic-plastic hydromechanical model for compacted soils accounting for clay activity. *Int. J. Num. Anal. Meth. Geomech. 37*, 503–535.

Durner, W. (1994). Hydraulic conductivity estimation for soils with heterogeneous pore structure. *Water Resources Research 30*, 211–223.

Gitirana Jr., G. & Fredlund, D. (2004). Soil-water characteristic curve equation with independent properties. *J. of Geotech. and Geoenv. Engng., ASCE 130*, 209–212.

Komine, H. & Ogata, N. (1994). Experimental study on swelling characteristics of compacted bentonites. *Can. Geotech. J. 31*, 478–490.

Lloret, A., Villar, M., Sanchez, M., Gens, A., Pintado, X., & Alonso, E. (2003). Mechanical behaviour of heavily compacted bentonite under high suction changes. *Géotechnique 53*, 27–40.

Loiseau, C., Cui, Y., & Delage, P. (2002). The gradient effect on the water flow through a compacted swelling soil. In J. Juc, T. de Campos, & F. Marinho (Eds.), *Unsaturated Soils. Proceedings of the 3rd International Conference on Unsaturated Soils (UNSAT 2002)*, Recife, Brazil, pp. 395–400.

Monroy, R., Zdravkovic, L., & Ridley, A. (2010). Evolution of microstructure in compacted london clay during wetting and loading. *Géotechnique 60*, 105–119.

Pusch, R. (1992). Use of bentonite for isolation of radioactive waste products. *Clay Minerals 27*, 353–361.

Romero, E., Della Vecchia, G., & Jommi, C. (2011). An insight into the water retention properties of compacted clayey soils. *Géotechnique 61*, 313–328.

Romero, E., Gens, A., & Lloret, A. (1999). Water permeability, water retention and microstructure of unsaturated compacted boom clay. *Engineering Geology 54*, 117–127.

Romero, E. & Vaunat, J. (2000). Retention curves for deformable clays. In C. Tarantino, A. & Mancuso (Ed.), *Experimental Evidence and Theoretical Approaches in Unsaturated Soils*, Balkema, Rotterdam, pp. 91–106.

Simms, P. & Yanful, E. (2002). Predicting soil-water characteristic curves of compacted plastic soils from measured pore-size distribution. *Géotechnique 52*, 269–278.

Simms, P. & Yanful, E. (2004). Estimation of soil-water characteristic curve of clayey till using measured pore-size distribution. *J. Environ. Engng. 130*, 847–854.

Tarantino, A. & De Col, E. (2008). Compaction behaviour of clay. *Géotechnique 58*, 199–213.

van Genuchten, M. (1980). A closed-form equation for predicting the hydraulic conductivity of unsaturated soils. *Soil Sci. Soc. Am. 44*, 892–898.

Villar, M. & Lloret, A. (2002). Variation of the intrinsic permeability of expansive clays upon saturation. In K. Adachi & M. Fukue (Eds.), *Clay Science for Engineering*, A.A. Balkema, Rotterdam, pp. 259–266.

Wang, Q., Tang, A., Cui, Y., Barnichon, J., & Ye, W. (2012). Hydraulic conductivity and microstructure changes of compacted bentonite/sand mixture during hydration. *International Journal of Applied Clay Science*.

Washburn, E. (1921). A method of determining the distribution of pore sizes in a porous material. *Proc. Nat. Acad. Sci. 7*, 115.

Wiebe, B., Graham, J., Tang, G., & Dixon, D. (1998). Influence of pressure, saturation, and temperature on the behaviour of the unsaturated sand-bentonite. *Can. Geotech. J. 35*, 194–205.

Ye, W., Cui, Y., Qian, L., & Chen, B. (2009). An experimental study of the water transfer through confined compacted gmz bentonite. *Engineering Geology 108*, 169–176.

COUPLING BETWEEN MECHANICAL AND WATER RETENTION BEHAVIOUR IN UNSATURATED SOILS

M. Lloret-Cabot
Centre for Geotechnical and Materials Modelling, University of Newcastle, Newcastle, NSW, Australia

D. Sheng
Centre for Geotechnical and Materials Modelling, University of Newcastle, Newcastle, NSW, Australia

ABSTRACT: *The importance of incorporating appropriate coupling mechanisms between the mechanical and the water retention behaviour in a constitutive model of unsaturated soils has been demonstrated in a number of studies (e.g. Wheeler et al., 2003; Sheng & Zhou, 2011; Zhou et al., 2012). For example, the experimental results of Romero (1999) on Boom clay show that the water retention behaviour exhibits a significant dependence on the void ratio, or the data from Sharma (1998) demonstrates that the occurrence of different degrees of saturation at the same value of suction, as a consequence of hydraulic hysteresis, can influence the mechanical response of the soil.*

This paper analyses how the experimentally observed coupled behaviour in unsaturated soils is incorporated in two well-established constitutive models. A brief introduction of the considered models is presented first, followed by a description on how these models account for the coupling between water retention and mechanical behaviour. In order to investigate further the proposed relationships for the couplings, a number of fictitious stress paths are simulated to analyze the volumetric and water retention predictions given by each of the models used.

1 INTRODUCTION

The unsaturated condition of the soil is present in many civil engineering constructions as it is the common condition of the soil above the water table level, where most of the engineering structures interact. It is, therefore, important to understand soil's behaviour when not fully saturated and to take it into account in the project design, during the construction stage and also during the life of the civil structure, in order to better protect constructions from potential risks. In general, the soil below the water table level is saturated while the soil above is under the effect of capillary pressures. The location of the water table level, however, can vary with climate or weather, generally rising during wet seasons and lowering during drought periods. This variability, inducing wetting/drying cycles on the soil, may also have a significant influence on soil's mechanical behaviour. It is, then, important to improve our current understanding of these mechanisms influencing soil response, in order to determine their relevance on the design/construction/life-time stages of a civil engineering structure.

The work presented in this paper concentrates on constitutive modelling of unsaturated soils with particular emphasis on the experimentally observed coupling between mechanical and water retention behaviour. Two well-established constitutive models of unsaturated soils are considered to discuss how the interactions between mechanical and water retention

responses are incorporated in their respective formulation: the constitutive model proposed by Wheeler et al. (2003) and the constitutive model proposed by Sheng et al. (2008a). The latter model, will be referred to as SFG model, as suggested in the original work. A general introduction of each constitutive model is presented first, followed by a discussion on the proposed coupling relationships. A demonstration of some of the model capabilities is finally presented by showing the model predictions under a number of isotropic stress paths.

2 WHEELER ET AL. (2003) MODEL

The constitutive model proposed by Wheeler et al. (2003) is formulated in terms of the mean Bishop's stress p^* and the modified suction s^*:

$$p^* = p - \left(S_r u_w + \left(1 - S_r\right) u_a\right) \tag{1}$$

$$s^* = \left(u_a - u_w\right) n \tag{2}$$

where p is the mean total stress, u_a is the pore air pressure, u_w is the pore water pressure and n is the porosity.

Three yield curves are considered to describe unsaturated soil behaviour under isotropic stress conditions (Figure 1a). Yielding on the Loading Collapse yield curve (LC) causes volumetric strain which, in turn, induces a coupled upward movement of the Suction Increase (SI) and Suction Decrease (SD) yield curves. This coupled movements of SD and SI are controlled by a coupling parameter k_2 and are not accompanied by plastic changes of S_r (Wheeler et al., 2003). A consequence of the coupled movements on the SD and SI yield curves (as a result of yielding on the LC) is a shift in the main wetting and drying retention curves of the model (Figure 1b) to higher suctions.

Yielding on the SI yield curve causes plastic reduction of S_r which produces a coupled upward movement of the SD yield curve and an outward movement of the LC yield curve (involving no plastic changes of the volumetric strains). Yielding on the SD yield curve causes plastic increments of S_r which produces a coupled downward movement of the SI yield curve and an inward movement of the LC yield curve (again, involving no plastic changes of the volumetric strains). The coupled movements of the LC yield curve (as a consequence of yielding on the SI or SD yield curves) is controlled by a second coupling parameter k_1.

The expressions of the three yield curves are given below:

$$F_{LC} = p^* - p_0^* = 0 \tag{3}$$

$$F_{SI} = s^* - s_I^* = 0 \tag{4}$$

$$F_{SD} = s_D^* - s^* = 0 \tag{5}$$

where p_0^* is the hardening parameter (i.e. Bishop's pre-consolidation pressure) that defines the position of the F_{LC} (Figure 1a), s_I^* and s_D^* are the hardening parameters defining the locations of the F_{SI} and F_{SI} yield surfaces respectively.

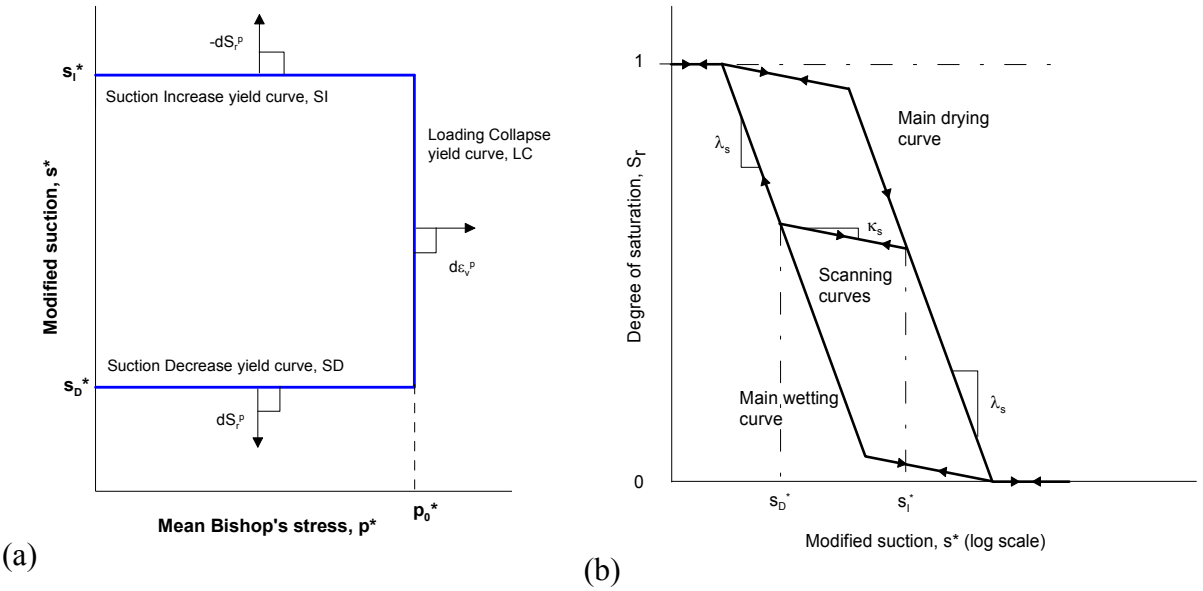

Fig. 1. (a) Yield curves for isotropic stress states of the Wheeler et al. (2003) model; (b) water retention behaviour (Wheeler et al., 2003).

3 SFG MODEL

For isotropic stress conditions, the SFG constitutive model is formulated in terms of the mean net stress $\overline{p}$ and the matric suction s.

The elastic domain is illustrated in Figure 2a and is defined by the following expressions:

$$F_{LC} = \overline{p} - \overline{p}_y(s) = 0 \tag{6}$$

$$F_{SI} = s - s_I = 0 \tag{7}$$

$$F_{SD} = s_D - s = 0 \tag{8}$$

where s_I and s_D define the location of the drying and wetting yield curves respectively and are related to the saturation suction s_{sa}, the air entry value s_{ae}, the water entry value s_{we} and the residual suction s_{re} (see Figures 2a and 2b). The expression of $\overline{p}_y(s)$ takes the following form:

$$\overline{p}_y(s) = \begin{cases} \overline{p}_{y0} - s & s \le s_{sa} \\ \overline{p}_{y0} - s_{sa} - s_{sa} \ln \dfrac{s}{s_{sa}} & s > s_{sa} \end{cases} \tag{9}$$

where $\overline{p}_{y0}$ is the yield stress at zero suction (Figure 2a).

Also a yield stress $\overline{p}_0(s)$ describing the apparent tensile strength for $s > 0$ is defined as:

$$\overline{p}_0(s) = \begin{cases} -s & s < s_{sa} \\ -s_{sa} - s_{sa} \ln \dfrac{s}{s_{sa}} & s \ge s_{sa} \end{cases} \tag{10}$$

For an unsaturated soil that is compressed or compacted at a higher suction than the saturation suction, a new yield stress $\overline{p}_{yn}(s)$ is defined and it takes the following form (Sheng et al., (2008a):

$$\overline{p}_{yn}(s)=\begin{cases}\overline{p}_{yn0}-s & s<s_{sa}\\ \dfrac{\overline{p}_{yn0}}{\overline{p}_{y0}}\left(\overline{p}_{y0}+s-s_{sa}-s_{sa}\ln\dfrac{s}{s_{sa}}\right)-s & s\geq s_{sa}\end{cases} \tag{11}$$

where $\overline{p}_{yn0}$ is the new pre-consolidation pressure at zero suction (see Figure 2a).

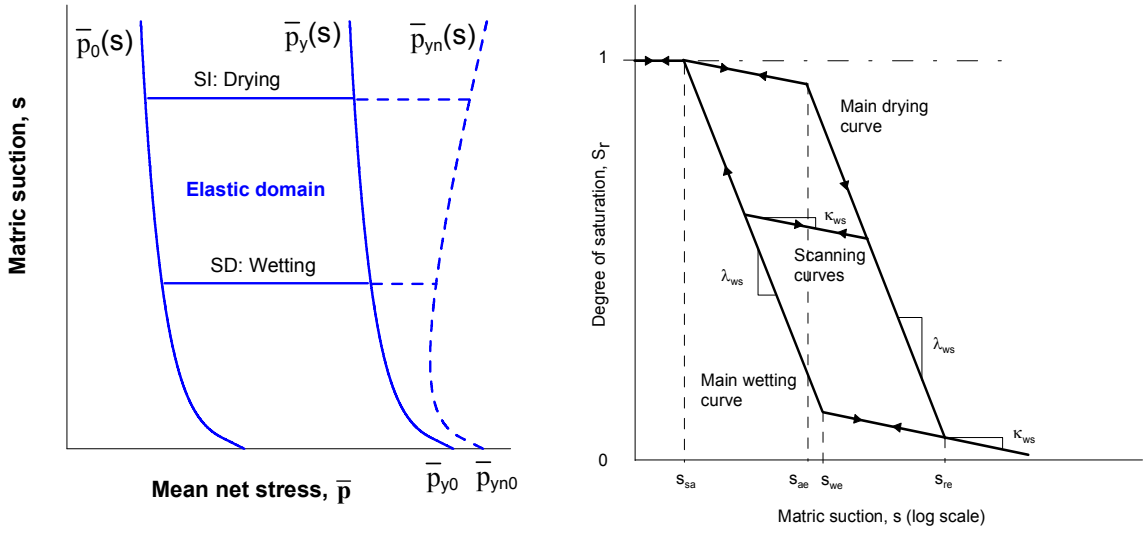

Fig. 2. (a) Yield curves for isotropic stress states of the SFG model; (b) water retention behaviour (Sheng et al., 2008a).

4 COUPLING OF MECHANICAL AND WATER RETENTION BEHAVIOUR

This section is aimed at discussing how the interactions between water retention and mechanical behaviour are described at constitutive level and for isotropic stress conditions. These influences are observed in both directions. Mechanical behaviour influences water retention behaviour (essentially through variations of the void ratio *e*) and water retention behaviour influences mechanical behaviour (mainly through variations of the degree of saturation S_r). The two existing constitutive models presented earlier are used in this section to illustrate the discussion.

4.1 Influence of mechanical behaviour on water retention behaviour

Variations of the void ratio change the capacity of the soil to retain water. In fact, as highlighted in Wheeler et al. (2003) and more recently by Zhou et al. (2012), changes in size of voids and of passageways between voids modifies the suction necessary to flood or empty the voids. These variations of *e* are essentially controlled by the stress-strain relationships and therefore the mechanical behaviour influences the S_r-*s* relationships. A shift of the main drying and wetting curves in the water retention plane is typically observed if the void ratio changes. For example, the main drying and wetting retention curves are shifted to higher suction values when the void ratio decreases as the required suction to flood or empty the voids tends to increase with decreasing void ratio. These influences have been observed by

several authors (e.g. Romero, 1999; Romero & Vaunat, 2000; Jommi, 2000; Gallipoli et al., 2003a; Tarantino & Tomobolato, 2005; Nuth & Laloui, 2008; Tarantino, 2009; Masin, 2010) and different approaches to incorporate them in a constitutive relationship have been proposed (Vaunat & Romero, 2000; Gallipoli et al., 2003a; Wheeler et al., 2003; Sheng et al., 2008a; Sheng & Zhou, 2011; Zhou et al., 2012). This paper concentrates on how these interactions are incorporated in two of these models: the Wheeler et al. (2003) and the SFG (Sheng et al., 2008) models.

A useful approach to illustrate this aspect of unsaturated soil behaviour was proposed in Sheng & Zhou (2011) and is summarised by the following equation:

$$dS_r = Eds + Fd\overline{p} \tag{12}$$

where E and F are two general functions that, in the framework of SFG model, are specified as:

$$E = \frac{-\lambda_{ws}}{s} \tag{13}$$

$$F = A\frac{S_r}{n}\left(1 - S_r\right)^m \tag{14}$$

where A is a general function associated with the volumetric behaviour (as further described in the next section), m is a fitting parameter (Sheng & Zhou, 2011), λ_{ws} can take a value of zero, κ_{ws} (slope of a scanning curve in the S_r:ln$s$ plane) or λ_{ws} (slope of a main drying/wetting curve in the the S_r:ln$s$ plane) depending on the suction value and the suction stress path (see Figure 2b).

Similar expressions, although more complicated, can be found when looking at how the degree of saturation changes are described within the Wheeler et al. (2003) model (see Ravendiraraj, 2009; Lloret, 2011). However, when using this model, it is simpler to express the changes of degree of saturation in terms of the stress state variables of the model (Equations 1 and 2). For example, if elastic behaviour is considered:

$$dS_r = -\kappa_s \frac{ds^*}{s^*} \tag{15}$$

where κ_s is the slope of a scanning curve in the S_r:lns^* plane. If yielding on SD or SI is occurring, the increments of S_r are given by:

$$dS_r = -\lambda_s \frac{ds^*}{s^*} \tag{16}$$

where λ_s is the slope of the main wetting/drying curve in the S_r:lns^* plane. Finally, if simultaneous yielding on SD (or SI) and LC is occurring the increments of S_r are given by:

$$dS_r = -\frac{\kappa_s ds^*}{s^*} - \frac{\left(\lambda_s - \kappa_s\right)}{\left(1 - k_1 k_2\right)}\left(\frac{ds^*}{s^*} - k_2\frac{dp^*}{p^*}\right) \tag{17}$$

where k_1 and k_2 are the two coupling parameters introduced earlier.

4.2 Influence of water retention behaviour on mechanical behaviour

There is also an influence in the other direction. This is the water retention influencing the mechanical behaviour. The degree of saturation influences (in addition to suction) the mechanical response because it describes the number of inter-particle contacts affected by meniscus water bridges (Sharma, 1998; Gallipoli et al., 2003b; Wheeler et al., 2003). According to Wheeler et al. (2003) model, these meniscus water bridges have a stabilising effect on the soil skeleton that is lost when an individual void is flooded with water.

Sheng & Zhou (2011) also provided a second useful relationship to account for the influence of the water retention behaviour in the mechanical behaviour:

$$d\varepsilon_v = Ad\bar{p} + Bds \tag{18}$$

where again A and B are two general functions that need to be specified. According to the SFG model they can take the following form:

$$A = \begin{cases} \dfrac{\kappa_{vp}}{\bar{p}+s} & \text{if elastic} \\ \dfrac{\lambda_{vp}}{\bar{p}+s} & \text{if plastic} \end{cases} \tag{19}$$

$$B = \begin{cases} \dfrac{\kappa_{vs}}{\bar{p}+s} & \text{if elastic} \\ \dfrac{\lambda_{vs}}{\bar{p}+s} & \text{if plastic} \end{cases} \tag{20}$$

where λ_{vp}, κ_{vp}, κ_{vs} and λ_{vs} are soil parameters (Sheng et al., 2008). In particular, κ_{vs} and λ_{vs} take the following form:

$$\kappa_{vs} = \begin{cases} \kappa_{vp} & s < s_{sa} \\ \kappa_{vp}\dfrac{s}{s_{sa}} & s \geq s_{sa} \end{cases} \tag{21}$$

$$\lambda_{vs} = \begin{cases} \lambda_{vp} & s < s_{sa} \\ \lambda_{vp}\dfrac{s}{s_{sa}} & s \geq s_{sa} \end{cases} \tag{22}$$

where κ_{vp}, λ_{vp}, are the elastic and elasto-plastic indices due to net stress (Sheng et al., 2008a).

Again, when using the Wheeler et al. (2003) model, the variations of volumetric strains are easier described in terms of p^* and s^*. For elastic behaviour:

$$d\varepsilon_v = \kappa\frac{dp^*}{vp^*} \tag{23}$$

where κ is the slope of a swelling in the e:lnp^* plane. If yielding on LC the increments of dε_v are given by:

$$d\varepsilon_v = \lambda \frac{dp^*}{vp^*} \tag{24}$$

where λ is the slope of the normal compression line for saturated conditions. Finally, if simultaneous yielding on SD (or SI) and LC is occurring the increments of $d\varepsilon_v$ are given by:

$$d\varepsilon_v = \kappa \frac{dp^*}{vp^*} + \frac{(\lambda - \kappa)}{v(1 - k_1 k_2)} \left(\frac{dp^*}{p^*} - k_1 \frac{ds^*}{s^*} \right) \tag{25}$$

4.3 Application

Figure 3 illustrates the two stress paths considered in the simulations. Both stress paths start at the same initial stress state A which is assumed to be on the main wetting curve (i.e. for the Wheeler et al. (2003) model, s_A^* is equal to the hardening parameter s_D^* whereas for the SFG model the values of the parameters λ_{ws} and s_{sa} are taken ensuring that point A also lies on the SD yield curve). The first stress path is referred to as Test 1 and comprises an isotropic loading at constant suction of 300 kPa varying mean net stress from 50 kPa to a 400 kPa (i.e. AB in Figure 3). The second stress path considered (i.e. Test 2) involves an initial wetting at a constant mean net stress of 50 kPa varying suction from 300 kPa to 200 kPa (path AC in Figure 3). This wetting path is followed by an isotropic loading at a constant suction of 200 kPa to reach a mean net stress of 400 kPa (path CD in Figure 3).

Figure 3 also includes the respective initial and final yield curves considered in each model. In addition, the intermediate position of the SD yield curve (after the initial wetting AC) is also illustrated for the SFG model (Figure 3a) and for the Wheeler et al. (2003) model (Figure 3b). The initial sate and the soil parameters involved (for each of the models considered) are summarized in Table 1.

Table 1. Initial state and soil parameters

Initial state	SFG	Wheeler et al. (2003) model
e=1.169	κ_{vp}=0.03	κ=0.03
S_r=0.618	λ_{vp}=0.165	λ=0.135
s=300 kPa	κ_{ws}=0.02	κ_s=0.03
$\overline{p}$ =50 kPa	λ_{ws}=0.117	λ_s=0.12
n=0.539	m=0.15	k_1=0.62
p^*=234.8 kPa	-	k_2=0.76
s^*=161.7 kPa	$\overline{p}_{y0}$ =94 kPa	p_0^*=285 kPa
-	s_{sa}=10 kPa	s_D^*=161.7 kPa

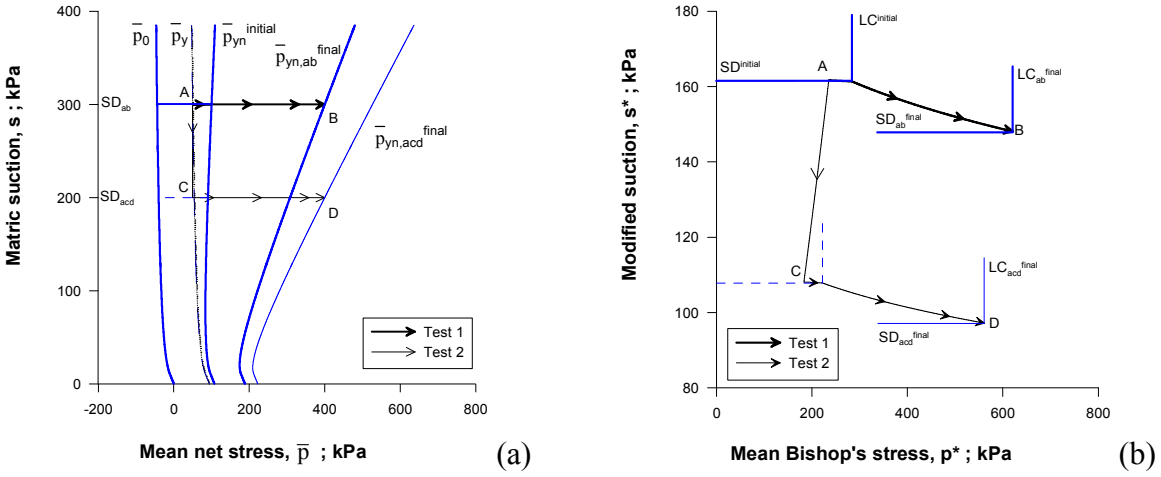

Fig. 3. Stress paths and yield curves: (a) SFG model in mean net stress and matric suction; (b) Wheeler et al. (2003) model in mean Bishop's stress and modified suction.

All simulations are presented in Figure 4. In each of the figures, model simulation of Test 1 is indicated by a thicker line, whereas the model simulation of Test 1 is indicated by a thinner line. Figures 4a and 4c show the variation of S_r and Figures 4b and 4d show the variation of e, both variables are plotted against mean net stress.

The predicted response of the first stress path considered (i.e. Test 1), when using the Wheeler et al. (2003) model, is qualitatively the same to the response predicted for the loading part of Test 2 (Figures 4a and 4b). During the loading part of both stress paths, the model predicts yielding on the SD yield curve because of the reduction of s^*. This variation on s^*, increases the degree of saturation, but this increase is very small (as illustrated in Figure 4a) because the modified suction changes are also very small during this initial part (see also Figure 3b). This is true until the loading stress path reaches the LC yield curve in Y (Figures 4a and 4b). From this point onwards simultaneous yielding on SD and LC yield curves is predicted resulting in large plastic increases of degree of saturation (Figure 4a) and large plastic decreases of void ratio (Figure 4b). During the initial wetting AC, the model predicts yielding on the SD yield curve, and hence large plastic increases of S_r. No yielding on the LC yield curve takes place during this wetting and, consequently, an elastic swelling is predicted by the model as a result of the decrease in mean Bishop's stress (Figures 3b and 4b).

When using the SFG model, the predicted response of Test 1 is also qualitatively similar to the model predictions of the loading part of Test 2 (Figures 4c and 4d). During the loading part of the stress paths, the model predicts elastic behaviour. No yielding on the SD yield curve takes place as the matric suction is kept constant during the loading (Figure 3a). As a consequence the variations of both, void ratio and degree of saturation, are relatively small. Again, this is true until the loading stress path reaches the LC yield curve in Y (Figures 4c and 4d). From this point onwards, yielding on the LC yield curve is predicted resulting in large decreases of e (Figure 4d) which cause a large increase of S_r (Figure 4c), controlled by the function F in Equation 12. During the initial wetting AC, the SFG model also predicts yielding on the SD yield curve and hence plastic increases of S_r. No collapse compression is neither predicted by the SFG model as the LC yield curve is not reached during the wetting AC. The predicted elastic swelling is, however, very small as a consequence of the parameter κ_{vs} which, for the particular case presented here, takes a very small value (see Equation 22).

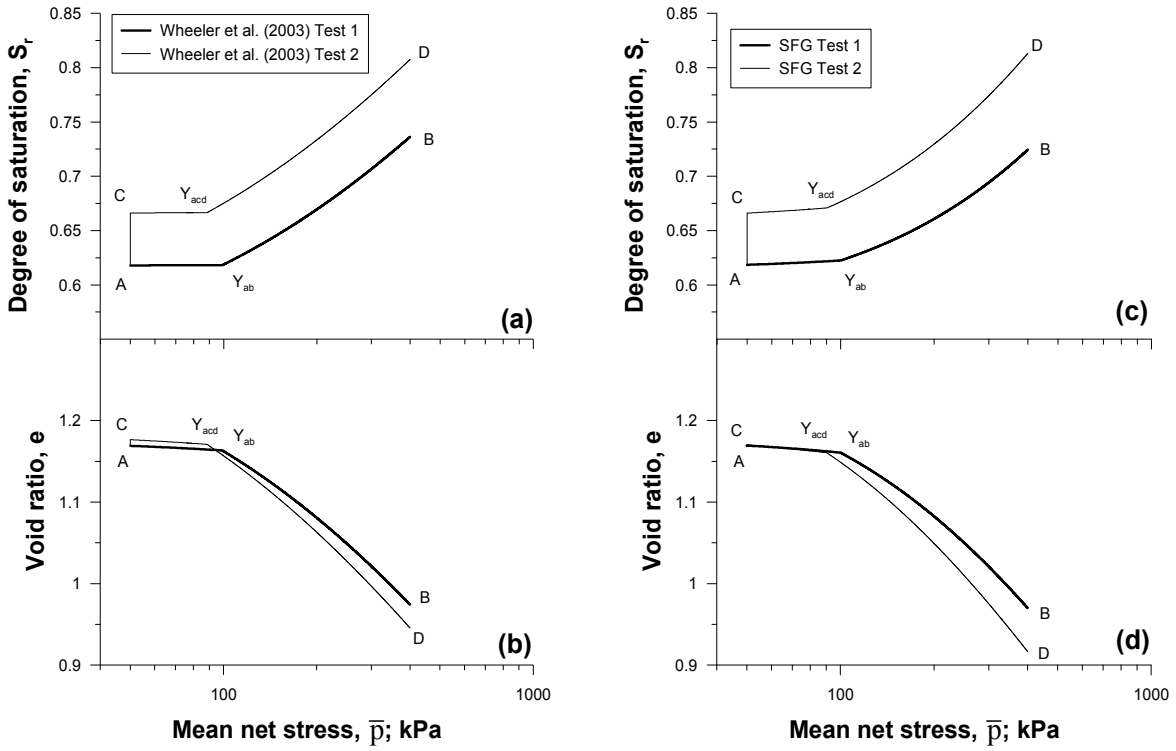

Fig. 4. Model predictions: (a) Wheeler et al. (2003) model predictions in the ln $\overline{p}$:*e* plane; (b) Wheeler et al. (2003) model predictions in the ln $\overline{p}$:S_r plane (c) SFG model predictions in the ln $\overline{p}$:*e* plane; (d) SFG predictions in the ln $\overline{p}$:S_r plane.

5 CONCLUSIONS

Two existing constitutive models for unsaturated soils have been adopted to discuss how the couplings between mechanical and water retention behaviour are incorporated in their constitutive relationships. In particular, the models used are the one proposed by Sheng et al. (2008), the SFG model, and the model proposed by Wheeler et al. (2003). A demonstration of some of the models' capabilities has been presented by simulating a number of isotropic stress paths involving irreversible volumetric and water retention behaviour. For the particular case of the stress path considered, both models are able to reproduce similar results although adopting substantially different approaches.

REFERENCES

Gallipoli, D., Wheeler, S.J. & Karstunen, M. (2003a), "Modelling the variation of degree of saturation in a deformable unsaturated soil". Géotechnique. Vol. 53(1), 105-112.

Gallipoli, D., Gens, A., Sharma, R.S. & Vaunat, J. (2003b), "An elasto-plastic model for unsaturated soil incorporating the effect of suction and degree of saturation on mechanical behaviour". Géotechnique. Vol. 53(1), 123-135.

Jommi, C. (2000), "Remarks on the constitutive modelling of unsaturated soils". Experimental evidence and theoretical approaches in unsaturated soils (eds. A. Tarantino and C. Mancuso), Rotterdam: Balkema, 139–153.

Lloret, M. (2011), Numerical Modelling of Coupled Behaviour in Unsaturated Soils, PhD Thesis, University of Strathclyde, UK.

Lloret-Cabot, M., Sánchez, M. & Wheeler, S.J. (2013), "Formulation of a three-dimensional constitutive model for unsaturated soils incorporating mechanical-water retention couplings". Int. J. Num. Anal. Meth. Geomech., DOI: 10.1002/nag.2176.

Masin, D. (2010), "Predicting the dependency of a degree of saturation on void ratio and suction using effective stress principle for unsaturated soils". Int. J. Num. Anal. Meth. Geomech. Vol. 34(1), 73-90.

Nuth, M. & Laloui, L. (2008), "Advances in modelling hysteretic water retention curve in deformable soils". Computers & Geotechecnics. Vol. 35(6), 835-844.

Raveendiraraj, A. (2009), Coupling of mechanical behaviour and water retention behaviour in unsaturated soils, PhD thesis, University of Glasgow, UK.

Roscoe, K.H. & Burland, J.B. (1968), On the generalised stress-strain behavior of wet clay. Engineering Plasticity (eds Heyman J & Leckie FA), Cambridge University Press, Cambridge, 535-609.

Romero, E. (1999), Characterisation and thermo-hydro-mechanical behaviour of unsaturated Boom clay: an experimental study, PhD Thesis, Universitat Politècnica de Catalunya, Barcelona, Spain.

Romero, E. & Vaunat, J. (2000), "Retention curves of deformable clays". Experimental evidence and theoretical approaches in unsaturated soils (eds. A. Tarantino and C. Mancuso), Rotterdam: Balkema, 91-106.

Sharma, R.S. (1998), Mechanical behaviour of unsaturated highly expansive clays, PhD Thesis, University of Oxford, Oxford, UK.

Sheng, D., Fredlund, D.G., & Gens, A. (2008a), "A new modelling approach for unsaturated soils using independent stress variables". Canadian Geotechnical Journal. Vol. 45, 511-534.

Sheng, D., Gens, A., Fredlund, D.G. & Sloan S.W. (2008b), "Unsaturated soils: From constitutive modelling to numerical algorithms". Computers and Geotechnics. Vol. 35, 810-824.

Sheng, D. & Zhou, A. (2011), "Coupling hydraulic with mechanical models for unsaturated Soils". Canadian Geotechnical Journal, Vol. 48, 826-840.

Sivakumar, V. (1993), A critical state framework for unsaturated soil, PhD thesis, University of Sheffield, UK.

Tarantino, A. (2009), "A water retention model for deformable soils". Géotechnique, Vol. 59(9), 751-762.

Tarantino, A. & Tombolato, S. (2005), "Coupling of hydraulic and mechanical behaviour in unsaturated compacted clay". Géotechnique, Vol. 55(4), 307-317.

Vaunat, J., Romero, E. & Jommi, C. (2000), "An elasto-plastic hydro mechanical model for unsaturated soils". In Experimental evidence and theoretical approaches in unsaturated soils (eds. A. Tarantino and C. Mancuso), Rotterdam: Balkema, 121-138.

Wheeler, S.J. & Sivakumar, V. (1995), "An elasto-plastic critical state framework for unsaturated soil". Géotechnique. Vol. 45(1), 35-53.

Wheeler, S.J, Sharma, R.S. & Buisson, M.S. R. (2003), "Coupling of hydraulic hysteresis and stress-strain behaviour in unsaturated soils". Géotechnique. Vol. 53(1) 41-54.

Zhou, A.N., Sheng, D. & Carter, J.P. (2012), "Effect of initial density of water retention behaviour". Géotechnique. Vol. 64(4), 669-680.

MODELING OF PROGRESSIVE FAILURE IN GEOTECHNICAL STRUCTURES SUBJECTED TO WATER INFILTRATION

S. Pietruszczak & E. Haghighat
Department of Civil Engineering, McMaster University, Hamilton, Ont., Canada

ABSTRACT: *The primary focus here is on modeling of fracture propagation in soils with apparent cohesion subjected to a period of intense rainfall. In this case, a micromechanically-based description represents an overwhelming task due to a very complex system of mineralogical and chemical factors. This is particularly evident at the range of irreducible saturation. Recognizing this limitation, the approach followed here is based on the framework of chemo-plasticity. The formulation incorporates an assumption that the injection of water triggers a volume change (swelling/collapse) that is coupled with a reduction in suction pressures which, in turn, results in degradation of the strength and deformation properties. The modeling of localized failure mode is based on a constitutive law formulated through volume averaging in the neighborhood of the embedded discontinuity. The latter is enhanced by employing the level set method. The governing equations are applied to examine the stability of a slope in cohesive soils, subjected to a period of intense rainfall.*

1 INTRODUCTION

Increased precipitation often leads to a loss of stability of geotechnical structures. Examples include here the natural slopes and embankments constructed in cohesive soils. In recent years, several case histories have been documented, both in Canada as well as in other parts of the world (e.g., in China, Korea, Malaysia, South America), whereby the failure of engineered and/or natural slopes was related to the loss of apparent cohesion triggered by the local weather conditions (Blatz et al., 2004; Griffiths & Lu, 2005; Chen & Zhang, 2006). The primary difficulty in modeling the loss of stability due to a heavy rainfall lies in assessing the in-situ conditions and in describing the coupling between the time-dependent process of water infiltration and the evolution of the stress/pore pressure field. The problem is typically analyzed by integrated software in which the transient seepage is coupled with traditional limit equilibrium slope stability analysis (Schmertmann, 2006; Tsaparas et al., 2002; Cho & Lee, 2001). Alternatively, the frameworks for unsaturated soil are implemented in which the suction pressure is considered as a state parameter and an optimization technique is used to search for a critical slip surface (e.g., Schmertmann, 2006). In general, the conventional methods for assessing the stability of unsaturated soils, based on the limit equilibrium approach, significantly underestimate the safety factors. Therefore, more accurate techniques are required.

The specification of properties of unsaturated clayey soils is difficult. This is particularly the case when dealing with low degrees of saturation, i.e. within the range of irreducible

saturation, as the latter involves a very complex system of mineralogical and chemical factors. In clays, the bond strength increases rapidly with decreasing water content. The water in the vicinity of minerals, however, has quite different properties which cannot, in fact, be quantified due to complex chemical interactions. Therefore, the assessment of suction pressures and their evolution is difficult, which is the main reason why the developments in the area of mechanics of unsaturated soils have not found their utility in a parallel development of design methodologies. Recognizing the above limitations, a different approach is pursued here. In particular, at the range of irreducible saturation (cf. Nitao & Bear, 1996), when the water phase is discontinuous, the behavior of the material is described based on a phenomenological framework of chemo-plasticity (cf. Pietruszczak, 1996; Hueckel, 1997; Pietruszczak et al., 2006). Within this framework, an increase in water content due to wetting is said to trigger a reduction in the interparticle bonding and the corresponding degradation of strength and deformation properties at the macroscale. At the stage when the water phase becomes continuous, the behaviour can then be defined in mechanical terms alone; for example, by employing an averaging procedure in which the compressibility of the pore space is expressed as a function of properties of constituents (free water and air) and the microstructure of saturation (Pietruszczak & Pande, 1995; Pietruszczak & Pande, 1996).

The research presented here is an extension of the work recently reported by Pietruszczak & Haghighat (2013), and it is focused on the development of a general methodology that includes modeling of the onset and propagation of failure in geotechnical structures subjected to water infiltration. In the next section, a brief overview is given pertaining to the evolution of microstructure of saturation during the infiltration process. In the subsequent section, the formulation of the problem is discussed, viz. chemo-plasticity, including the notion of modeling of localized deformation. Two numerical examples are given. The first one, aimed at illustrating the proposed methodology, deals with simulation of a biaxial test on dense sand. The second one involves a transient hydro-mechanical analysis investigating the stability of a slope in cohesive soils subjected to a period of intense rainfall. In solving the problem, the evolution of the phreatic surface is monitored and coupled with mechanical analysis incorporating the propagation of localized damage triggered by the chemical interaction.

2 ON MICROSTRUCTURE OF SATURATION IN GRANULAR SOILS

During the infiltration process the microstructure of saturation undergoes a progressive evolution, which should be accounted for in the course of specification of hydraulic/mechanical properties of the material. In general, referring to Fig.1, four different types of microstructure can be distinguished in partially saturated soils (Wroth & Houlsby, 1985):

(A) At very low degrees of saturation, the gas phase is continuous while the liquid phase is discontinuous (i.e., the liquid phase is present only within the interparticle contact areas)
(B) At higher degrees of saturation, both the gas and the liquid phase remain continuous
(C) As the degree of saturation is further increased, the gas phase becomes discontinuous (e.g., bubbles embedded in the liquid phase)
(D) Large bubbles may be entrapped in saturated matrix (‘gassy’ soil).

The common types are (A) to (C) and during the infiltration process the microstructure will abruptly change from one type to another. The last structure (D) is formed when the gas (produced by decomposition of organic matter) pushes against the soil skeleton creating gas voids of a size that is much larger than the average particle size.

It should be noted that for soil types B, C and D the liquid (water) phase is continuous and has known mechanical properties. In this case, for each specific geometric arrangement of the microstructure of saturation, the mechanical properties can be defined in terms of properties of the skeleton, air and the free water. In this case, the formulation incorporates the degree of saturation as well as the 'average pore size' which is considered to be an independent characteristic dimension (c.f. Pietruszczak & Pande, 1995; Pietruszczak & Pande, 1996). Alternatively, the problem has also been phrased using the notions of unsaturated soil mechanics (Alonso et al., 1990) whereby the suction pressure is introduced as an independent state variable. Note, however, that the latter approach does not make any explicit reference to the type of microstructure.

At the range of irreducible saturation, which is of main focus here, the water phase is discontinuous and the soil microstructure is of the type A. In this case, the specification of properties, particularly in clayey soils, is difficult as the problem involves complex physical-chemical interactions and the properties of water in the vicinity of minerals cannot be easily quantified. Thus, the control/measurement of suction pressures is rather problematic and the problem cannot be approached as purely mechanical one. In view of these difficulties, the approach adopted here for the type A soil is based on the phenomenological framework of chemo-plasticity which is preferred to the classical notions of unsaturated soil mechanics.

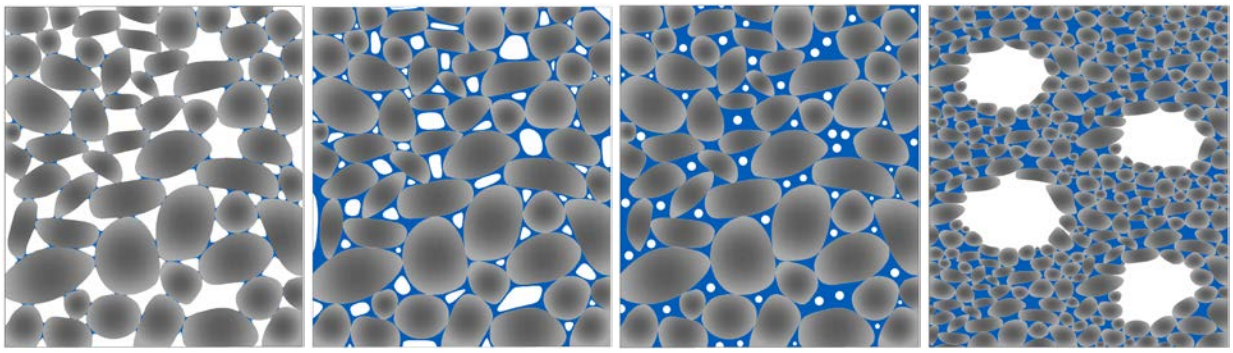

Figure 1. Microstructure of partially saturated soils: Soil types A through D

3 FORMULATION OF THE PROBLEM

3.1 Chemo-plasticity framework

The general approach for modeling the evolution of properties of clays in the presence of the interparticle bonding is based on the framework of chemo-plasticity. The particular formulation outlined here is analogous to that described in the recent article by Pietruszczak & Haghighat (2013). Within this approach, the progress in chemo-mechanical interaction is monitored by a scalar parameter ζ, which may be interpreted as the change in the initial suction pressure u_s^0, at the irreducible wetting fluid saturation, in REV; i.e. $\zeta \propto (u_s^0 - u_s)/u_s^0$, so that $\zeta \subset [0,1]$.

The evolution law can be taken in a simple linear form

$$\frac{\partial \zeta}{\partial t'} = B(1-\zeta); \quad dt' = \mathrm{g}dt \tag{1}$$

where $\mathrm{g} \subset [0,1]$ depends on the chemical composition of the clay minerals and water, and B is a material constant. In the elastic range, the constitutive relation takes the form

$$\varepsilon_{ij}^{e} = C_{ijkl}^{e}\,\sigma_{kl} + \epsilon\,\zeta\,\delta_{ij} \tag{2}$$

Here, σ_{ij} is the *effective* stress, C_{ijkl}^{e} is the elastic compliance operator and the last term represents the volumetric strain due to wetting, with ϵ being the maximum expansion/contraction in the stress-free state. Note that the differential form of eq. (2) may be expressed as

$$\dot{\varepsilon}_{ij}^{e} = C_{ijkl}^{e}\,\dot{\sigma}_{kl} + \left(\partial_{\zeta} C_{ijkl}^{e}\,\sigma_{kl} + \epsilon\,\delta_{ij}\right)\dot{\zeta} \tag{3}$$

In order to specify the plastic strain rates, the functional form of the yield criterion $f = 0$ is assumed to be affected by the chemical interaction, i.e.

$$f = f\left(\sigma_{ij}, \kappa, \zeta\right) = 0; \quad \kappa = \kappa(\varepsilon_{ij}^{p}); \quad \dot{\varepsilon}_{ij}^{p} = \dot{\lambda}\frac{\partial \psi}{\partial \sigma_{ij}} \tag{4}$$

where $\kappa = \kappa(\varepsilon_{ij}^{p})$ is the hardening parameter and $\psi = \psi(\sigma_{ij}, \zeta)$ is the plastic potential function. Employing now the consistency condition, the plastic multiplier $\dot{\lambda}$ can be defined as

$$\dot{f} = 0 \;\Rightarrow\; \dot{\lambda} = \frac{1}{H}\left(\frac{\partial f}{\partial \sigma_{ij}}\dot{\sigma}_{ij} + \frac{\partial f}{\partial \zeta}\dot{\zeta}\right); \quad H = -\frac{\partial f}{\partial \kappa}\frac{\partial \kappa}{\partial \varepsilon_{ij}^{p}}\frac{\partial \psi}{\partial \sigma_{ij}} \tag{5}$$

Thus, invoking the additivity postulate and using the equations (3)-(5), the constitutive relation may be expressed as

$$\dot{\varepsilon}_{ij} = C_{ijkl}\,\dot{\sigma}_{kl} + b_{ij}\dot{\zeta}; \quad b_{ij} = \partial_{\zeta} C_{ijkl}^{e}\,\sigma_{kl} + \frac{1}{H}\frac{\partial f}{\partial \zeta}\frac{\partial \psi}{\partial \sigma_{ij}} + \epsilon\,\delta_{ij}; \; C_{ijkl} = C_{ijkl}^{e} + \frac{1}{H}\frac{\partial \psi}{\partial \sigma_{ij}}\frac{\partial f}{\partial \sigma_{kl}} \tag{6}$$

Note that the inverse form, defining the stress rates for given strain rates, can be expressed as

$$\dot{\sigma}_{ij} = D_{ijkl}\left(\dot{\varepsilon}_{kl} - b_{kl}\dot{\zeta}\right); \quad D_{ijkl} = C_{ijkl}^{-1} \tag{7}$$

3.2 Description of localized deformation

In this work, the propagation of localized failure is modeled by employing the volume averaging to estimate the properties of an initially homogeneous medium intercepted by a shear band/interface (Pietruszczak & Mroz, 1981; Pietruszczak, 1999). The constitutive relation incorporates the properties of constituents (i.e., intact material and interface) as well as a characteristic dimension associated with the structural arrangement. This approach is later enhanced by incorporating the level set method, similar to that used in Extended Finite Element Method (Stolarska et al., 2001; Sukumar et al., 2001), in order to capture a discrete nature of the shear band propagation process.

A discontinuous motion within a representative volume ΔV which contains a discontinuity surface Γ, can be defined as

$$\mathrm{v}_i(x_i, t) = \hat{\mathrm{v}}_i(x_i, t) + \mathcal{H}_{\Gamma}\,\tilde{\mathrm{v}}_i(x_i, t) \tag{8}$$

where, $\mathrm{v}_i(x_i, t)$ and $\hat{\mathrm{v}}_i(x_i, t)$ are continuous functions and $\mathcal{H}_{\Gamma}$ is the Heaviside step function. Denoting the velocity discontinuities across the interface as $\dot{\mathrm{g}}_i = [\![\mathrm{v}_i]\!]$, a symmetric part of the velocity gradient $\mathrm{v}_{i,j}^{s}$ can be expressed

$$\mathrm{v}^s_{i,j} = \hat{\mathrm{v}}^s_{i,j} + \mathcal{H}_\Gamma\, \tilde{\mathrm{v}}^s_{i,j} + \delta_\Gamma\, (\dot{\mathrm{g}}_i\, n_j)^s \tag{9}$$

where, δ_Γ is the Dirac delta function. The procedure for assessing the equivalent properties within a representative volume ΔV intercepted by a shear band is based on averaging scheme, viz.

$$\frac{1}{\Delta V}\left(\int_{\Delta V} \mathrm{v}^s_{i,j}\, dV\right) = \frac{1}{\Delta V}\left(\int_{\Delta V} \left(\hat{\mathrm{v}}^s_{i,j} + \mathcal{H}_\Gamma\, \tilde{\mathrm{v}}^s_{i,j}\right) dV + \int_{\Delta V} \delta_\Gamma\, (\dot{\mathrm{g}}_i\, n_j)^s\, dV\right) \tag{10}$$

which implies

$$v^s_{i,j} = \hat{v}^s_{i,j} + k\, \tilde{v}^s_{i,j} + \chi\, (\dot{g}_i\, n_j)^s \tag{11}$$

Here, $v_{i,j}$'s and $\dot{g}_i$ are volume averages of the respective variables defined in eq.(10), $\chi = \Delta A / \Delta V$ and $k = (\Delta V^+ - \Delta V^-)/\Delta V$, while ΔA is the surface area of the interface/shear band within the representative volume. Note that the decomposition (11) may be simplified by assuming that the discontinuity divides the representative element into two approximately equal volumes, in which case there is $k \to 0$. Identifying now the symmetric parts of the displacement gradients with the corresponding strain rates, one can write

$$\dot{\varepsilon}_{ij} = \dot{\bar{\varepsilon}}_{ij} + \dot{\tilde{\varepsilon}}_{ij}\,; \qquad \dot{\bar{\varepsilon}}_{ij} = \hat{v}^s_{i,j} + k\, \tilde{v}^s_{i,j}\,;\ \dot{\tilde{\varepsilon}}_{i,j} = \chi\, (\dot{g}_i\, n_j)^s \tag{12}$$

In eq.(12), $\dot{\bar{\varepsilon}}_{ij}$ defines the strain rate in the intact material, while $\dot{\tilde{\varepsilon}}_{ij}$ is the strain rate due to discontinuous deformation along the interface averaged over the representative volume. In general, $\dot{\varepsilon}_{ij}$ may include both elastic and plastic components.

Within the context of the chemo-plasticity framework, as discussed in the previous section, the average stress rates in the intact material can now be defined as

$$\dot{\bar{\sigma}}_{ij} = D_{ijkl}\left(\dot{\bar{\varepsilon}}_{kl} - b_{kl}\dot{\zeta}\right) \quad \Rightarrow \quad \dot{\sigma}_{ij} \simeq \dot{\bar{\sigma}}_{ij} = D_{ijkl}\left(\dot{\varepsilon}_{kl} - \dot{\tilde{\varepsilon}}_{kl} - b_{kl}\dot{\zeta}\right);\quad \dot{\tilde{\varepsilon}}_{ij} = \chi\, (\dot{g}_i\, n_j)^s \tag{13}$$

The stress rate $\dot{\bar{\sigma}}_{ij}$ is subjected to the continuity condition that requires

$$\dot{\bar{\sigma}}_{ij} n_j = \dot{t}_i = K_{ij}\, \dot{g}_j \tag{14}$$

where t_i is the traction along the interface and K_{ij} defines the stiffness properties of the interfacial material. Note that the latter can be described using the plasticity formalism

$$\dot{t}_i = K_{ij}\, \dot{g}_j\,;\ \ f_\Gamma = f_\Gamma(t_i, \kappa);\quad \dot{g}^p_i = \dot{\lambda}\frac{\partial \psi_\Gamma}{\partial t_i};\ \ \kappa = \kappa(g^p_i) \tag{15}$$

where, $\dot{g}^p_i$ is the plastic part of the velocity discontinuity, f_Γ, ψ_Γ are the yield and plastic potential functions, respectively, and κ is the softening parameter. Combing representations (13) and (14) leads, after some algebraic transformations, to the localization rule

$$\dot{g}_i = n_p E^{-1}_{ij} D_{jpkl}\left(\dot{\varepsilon}_{kl} - b_{kl}\dot{\zeta}\right); \qquad E_{ij} = K_{ij} + \chi D_{iklj}\, n_k n_l \tag{16}$$

which defines the local velocity discontinuities in terms of average macroscopic strain rates. Note that for a standard rate-independent plasticity there is $\dot{\zeta} \to 0$ and the representation given in Pietruszczak (1999) is recovered.

The strategy for monitoring the propagation of shear band within the context of finite element (FE) analysis is similar to that explained in the companion paper that deals with

modeling of fracture process in brittle materials (Pietruszczak & Haghighat, 2013). The interface is traced using the level set method, so that it is represented as a polygon of line segments passing through elements in which the shear band develops. The characteristic dimension χ is then evaluated based on the geometry of the element and that of the propagating localization zone.

4 APPLICATION OF CHEMO-PLASTICITY FRAMEWORK TO MODELING OF SOIL INFILTRATION

In order to trace the evolution of phreatic surface during the rainfall infiltration, the problem is defined by invoking a coupled formulation for flow through unsaturated porous media. Within this framework, the porous material is considered as a mixture of solid grains and voids; the latter filled with water and/or air. For the mathematical details pertaining to FE formulation of the initial boundary-value problem the reader is referred to the original article (Pietruszczak & Haghighat, 2013).

The numerical simulations presented here are based on the classical plasticity approach incorporating the notion of deviatoric hardening (Pietruszczak, 2010). Within this approach, the loading surface $f = f\left(\sigma_{ij}, \kappa, \zeta\right)$ is defined as

$$f = \sqrt{3}\bar{\sigma} - \eta\, h(\theta)\left(\sigma_m + c\cot\phi\right) = 0; \qquad \eta = \eta_f \frac{\kappa}{A+\kappa} \tag{17}$$

Here, $\sigma_m = -\sigma_{ii}/3$, $\bar{\sigma} = \left(s_{ij}s_{ij}\right)^{1/2}$ and $\theta = \sin^{-1}(-3\sqrt{3}J_3/2\bar{\sigma}^3)/3$; where s_{ij} is the stress deviator and $J_3 = \frac{1}{3}s_{ij}s_{jk}s_{ki}$. The parameter θ represents Lode's angle and the function $h(\theta)$ implemented here is that proposed by (Willam & Warnke, 1974). Furthermore, in eq.(17), ϕ is the friction angle, c is the cohesion and the hardening effects are attributed to accumulated plastic distortions, i.e. $\dot{\kappa} = \left(\dot{e}^p_{ij}\,\dot{e}^p_{ij}\right)^{1/2}$ where e_{ij} is the strain deviator. Note that in the hardening function given above, A is a material constant and η_f defines the value of η at failure, i.e. $\eta \to \eta_f$ for $\kappa \to \infty$. Assuming that the condition at failure are consistent with Mohr-Coulomb criterion, we have $\eta_f = 6\sin\phi/(3-\sin\phi)$. Furthermore, the flow rule is assumed to be non-associated and the plastic potential function is taken in the form

$$\psi = \sqrt{3}\bar{\sigma} + \eta_c(\sigma_m + c\cot\phi)\ln\frac{\sigma_m + c\cot\phi}{\sigma_m^0} = 0 \tag{18}$$

where, $\eta_c = const.$ is a material constant.

In order to incorporate the deviatoric-hardening model within the chemo-plasticity framework, the strength parameters η_f and c, as well as the Young's modulus E, are assumed to undergo a progressive degradation in the course of chemical interaction. The evolution laws are taken in a simple linear form

$$\eta_f = \eta_f^0\left(1 - G_1\zeta\right); \quad c = c^0\left(1 - G_2\zeta\right); \quad E = E^0\left(1 - G_3\zeta\right) \tag{19}$$

where G's are material constants and the kinetics of the interaction process, viz. evolution of ζ, is governed by eq.(1) .

In the localized regime, the interfacial constitutive relation is derived by invoking the classical Coulomb criterion and attributing the strain softening effects to irreversible sliding along the interface. Thus,

$$f_\Gamma = |t_i m_i| - \mu(\gamma)(t_i n_i + c) = 0; \quad \psi_\Gamma = |t_i m_i| = const. \tag{20}$$

where n_i is a unit vector normal to the shear band/interface, m_i is an arbitrary vector normal to n_i, c is the cohesion and μ defines the frictional properties. The latter are assumed to degrade as a function of discontinuity in tangential component of velocity $\dot{\gamma} = \dot{g}_i^p m_i$, i.e.

$$\mu(\gamma) = (\mu_0 - \mu_r) + \mu_r \exp(-\alpha\gamma) \tag{21}$$

where α is a constant and μ_r defines the residual value of μ.

In what follows, two numerical examples are given. The first one is aimed at illustrating the proposed methodology and involves a numerical simulation of the onset and propagation of a shear band in a sample of dense sand subjected to axial compression under plane strain conditions. The second example deals with a coupled hydro-mechanical analysis, which involves assessment of slope stability under conditions of an intense rainfall.

4.1 Modeling of localized deformation in a biaxial test on dense sand

The numerical analysis carried out here involves the simulation of a biaxial (plane strain) test conducted on a dense Ottawa sand at the confinement of 100kPa (Khalid et al., 2000). The sample had the dimensions of $83.3 \times 152.4 \times 80.8$ mm and the deformation was recorded by digital monitoring of nodal displacements of the grid that was imprinted on the membrane surface (see Fig.2).

The simulations were carried out assuming that the material remains elastic prior to the onset of localization. The latter was defined as $\eta \to 0.99\eta_f$ in the Mohr-Coulomb criterion (16). In the softening regime, the response was said to be associated with localized deformation mode, viz. eq.(15), whereby the behaviour of the shear band material was defined through eqs.(19) and (20). The key material properties, as reported by Khalid et al. (2000), were as follows

$$E = 23\,MPa, \ \nu = 0.3, \ \phi = 48.2^\circ$$

while for the interface, the following material constants were employed

$$k_N = k_T = 1000\ \text{N/mm}; \quad \mu_r = 0.6\mu_0; \quad \alpha = 0.2\ \text{mm}^{-1}$$

where k_N, k_T are the elastic moduli.

Note that since prior to the onset of localization the material is said to be elastic, the value of *E* represents the secant Young's modulus. For the localized deformation mode, the simulations were completed assuming that the shear band orientation was 57^0 with respect to the horizontal, which was the actual value measured in the experiment. In general, however, this value should be determined through an independent criterion, such as that associated with the bifurcation properties of the constitutive relation (cf. Rudnicki & Rice, 1975).

The boundary conditions involved no friction at the end platens while the localization was triggered by introducing an inhomogeneity in the center of the specimen (25 % increase in the value of E).The main results of simulations are presented in Fig.2. The figures on the left show the deformation mode, both the predicted and experimentally observed, while the figure on the right gives the corresponding material characteristics. The results of simulations are, in general, fairly consistent with the experimental data.

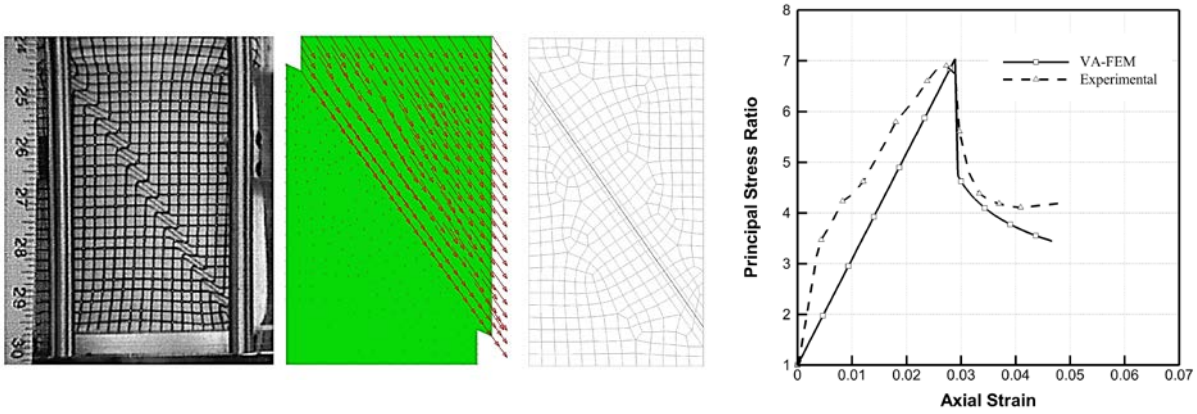

(a) (b)

Figure 2. Shear band formation in biaxial plane strain test: a) cracking pattern and post localization deformation mode; b) Load-deflection curve

4.2 Modeling of shear band initiation and propagation in clayey slopes subjected to a heavy precipitation

The analysis presented here is an extension of the recent work reported by Pietruszczak & Haghighat (2013). The study involves a slope in a cohesive soil (silty clay) subjected to a period of an intense rainfall. The slope has the geometry typical of engineered slopes in Singapore; it is also representative of shallow slopes in the province of Manitoba (Canada) that underwent a translational failure in the late 1990's.

In order to trace the evolution of the phreatic surface, a transient coupled analysis incorporating unsaturated flow was conducted. In the simulations, the history of infiltration was monitored and the framework of chemo-plasticity (Section 2.1) was used to model the degradation of mechanical properties of clay. The overall stability of the slope was assessed by examining the time history of the onset and propagation of localized damage. The simulations were carried out assuming the same material parameters as in the original reference, i.e.

$$E = 100\,MPa;\ \ \nu = 0.35;\ \eta_f = 0.98;\ \ \eta_c = 0.77;\ \ c = 20\,kPa;\ \ A = 1.0\times10^{-5}$$

The constants governing the kinetics of the chemical interaction and the rate of degradation were taken as

$$G_1 = 0.10;\ \ G_2 = 0.75;\ \ G_3 = 0.10;\ B = 460.0\,\text{sec}^{-1}$$

while the parameters defining the shear band properties were selected as

$$k_N = k_T = 1000.0\,\text{MN/m};\ \ \mu_r = 0.6\mu_0;\ \ \ \alpha = 100.0\ \text{m}^{-1}$$

The soil permeability was assumed as $1\times10^{-5}\,\text{m/sec}$. The transition to localized deformation was defined again in terms of the critical ratio of η/η_f as $\eta \to 0.95\eta_f$, while the local orientation of the shear band was assumed to be at $45^0 + \phi/2$ with respect to the direction of the minor principal stress .

The loading process incorporated two stages. The first one involved the solution due to own weight of the material, while the second one dealt with the simulation of the infiltration process and its coupling with the mechanical response. The total height of the slope was taken as $H = 10\,m$. The gravity load was applied incrementally in five layers, in order to

reflect the construction sequence. By the end of first stage, the maximum value of η / η_f was in the range of 0.8, indicating that no localized deformation developed (see Pietruszczak & Haghighat, 2013). Fig.6 presents the boundary conditions for the second stage of the analysis, i.e. the infiltration process. In this phase, the slope was said to be exposed to a heavy rainfall (i.e., precipitation in excess of 0.75 cm per hour). The boundary conditions for this stage of analysis are shown in Fig.3. Along the ground surface, the water pressure was assumed to increase linearly from an initial value of $-5\,kPa$, which corresponds to $S = 5\%$, to zero in a period of 4*hr* and then was maintained constant. Such boundary conditions are analogous to those assumed in the article by Borja and White (2010) and imply that the horizontal surfaces can absorb water at the rate which depends on the permeability, while the water cannot congregate along the slope.

The infiltration analysis was performed for a period of 30 days. Fig.4 shows the distribution of the degree of saturation at the end of rainfall, while Fig.5 presents the corresponding contours of η / η_f and those of accumulated plastic distortions, respectively. It is evident here that, in the area around the toe of the slope, there is $\eta / \eta_f \to 1$. Finally, Fig.6 shows the predicted shear band formation .The latter is indicative of a failure mechanism forming in this region.

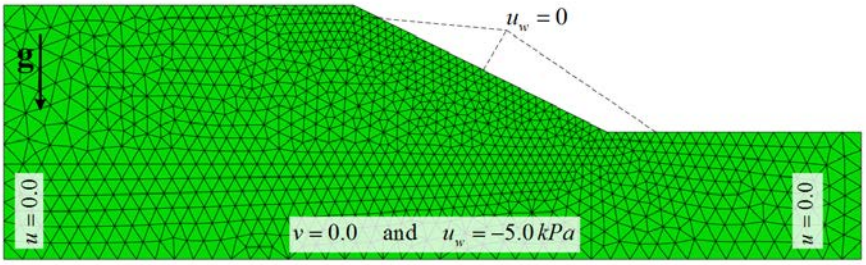

Figure 3. Geometry and boundary conditions for the infiltration analysis

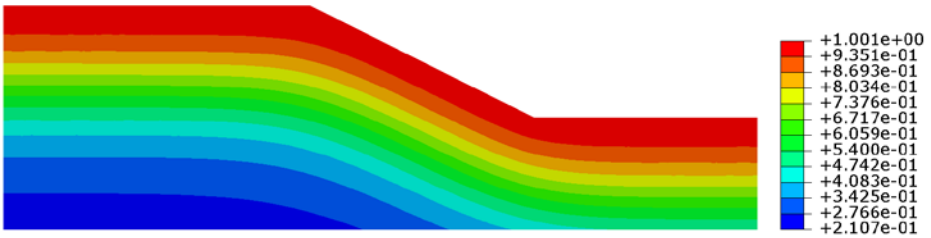

Figure 4. Saturation at the end of rainfall (30 days)

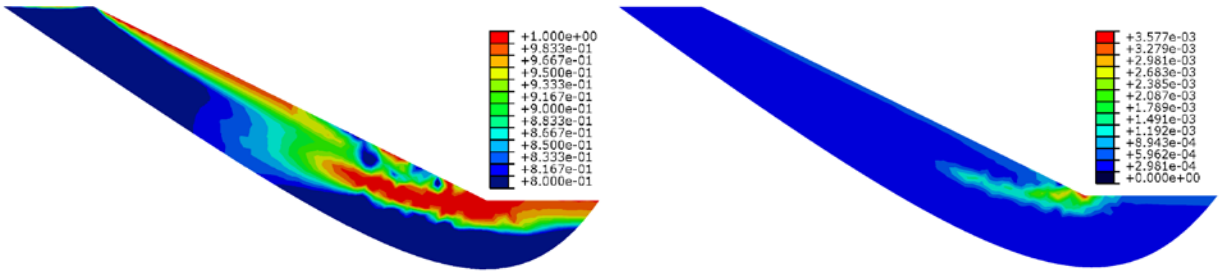

(a) (b)

Figure 5. a) Value of η / η_f at the end of rainfall; b) Equivalent plastic strain at the end of rainfall (30 days)

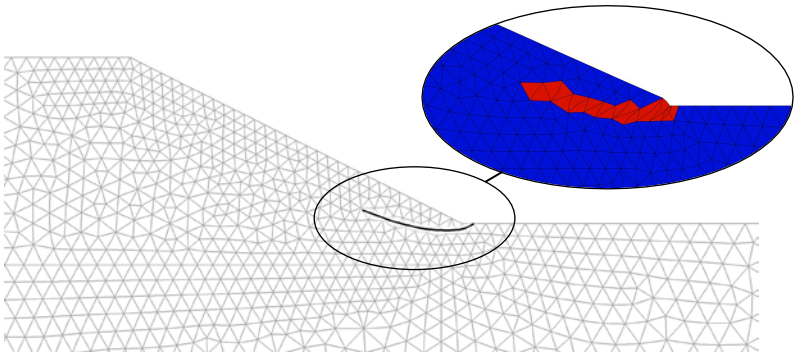

Figure 6. Shear band pattern and deformed mesh (scale factor=200)

5. FINAL REMARKS

In this paper, the problem of shear band propagation in cohesive-frictional materials has been investigated. The primary focus was on modeling of fracture process in soils with apparent cohesion subjected to a period of intense rainfall. The approach was based on employing (at very low degrees of saturation) the framework of chemo-plasticity, whereby the injection of water was assumed to trigger a reduction in initial suction pressures which, in turn, resulted in degradation of the strength and deformation properties. The modeling of fracture propagation at the macroscale incorporated a constitutive law formulated through volume averaging in the neighborhood of the embedded discontinuity. This methodology was enhanced by coupling with the level set method that has been previously used for the same class of problems within the context of the Extended Finite Element approach. A new analytical formulation has been presented for the decomposition of strain rates in the presence of a discontinuous motion.

Besides the coupled hydro-mechanical analysis dealing with environmental loads, another illustrative example has been provided that focused on the evolution of localized damage triggered by mechanical load. In particular, the propagation of fracture was examined within the context of a sample of dense sand subjected to biaxial compression under initial hydrostatic pressure. The results of simulations clearly demonstrate the ability of the volume averaging approach to describe the process of onset and propagation of localized deformation in geomaterials.

REFERENCES

Alonso, E.E., Gens, A. and Josa, A. (1990), "A constitutive model for partially saturated soils". Géotechnique, 40(3), 405–430.

Blatz, J.A., Ferreira, N.J. and Graham, J. (2004), "Effects of near-surface environmental conditions on instability of an unsaturated soil slope". Can. Geotech. J., 41(6), 1111–1126.

Borja, R.I. and White, J.A. (2010), "Continuum deformation and stability analyses of a steep hillside slope under rainfall infiltration". Acta Geotechnica, 5(1), 1–14.

Chen, Q. and Zhang, L.M. (2006), "Three-dimensional analysis of water infiltration into the Gouhou rockfill dam using saturated unsaturated seepage theory". Can. Geotech. J., 43(5), 449–461.

Cho, S.E. and Lee, S.R. (2001), "Instability of unsaturated soil slopes due to infiltration". Computers and Geotechnics, 28(3), 185–208.

Griffiths, D.V. and Lu, N. (2005), "Unsaturated slope stability analysis with steady infiltration or evaporation using elasto-plastic finite elements". Int. J. Numer. Anal. Meth. Geomech., 29(3), 249–267.

Hueckel, T. (1997), "Chemo-plasticity of clays subjected to stress and flow of a single contaminant". Int. J. Numer. Anal. Meth. Geomech., 21(1), 43–72.

Nitao, J.J. and Bear, J. (1996), "Potentials and their role in transport in porous media". Water Resources Research, 32(2), 225–250.

Pietruszczak, S. (2010), "Fundamentals of Plasticity in Geomechanics", CRC Press.

Pietruszczak, S. (1999), "On homogeneous and localized deformation in water-infiltrated soils". International Journal of Damage Mechanics, 8(3), 233–253.

Pietruszczak, S. (1996), "On the mechanical behaviour of concrete subjected to alkali-aggregate reaction". Computers & Structures, 58(6), 1093–1097.

Pietruszczak, S. and Haghighat, E. (2013), "Assessment of slope stability in cohesive soils due to a rainfall". Int J Numer Anal Meth Geomech.

Pietruszczak, S. and Mroz, Z. (1981), "Finite element analysis of deformation of strain-softening materials". Int. J. Numer. Meth. Engng, 17(3), 327–334.

Pietruszczak, S. and Pande, G. (1995), "On the mechanical response of partially saturated soils at low and high degrees of saturation". Numerical models in Geomechanics, 33–39.

Pietruszczak, S. and Pande, G.N. (1996), "Constitutive relations for partially saturated soils containing gas inclusions". Journal of geotechnical engineering, 122(1), 50–59.

Pietruszczak, S., Lydzba, D. and Shao, J.F. (2006), "Modelling of deformation response and chemo-mechanical coupling in chalk". Int J Numer Anal Meth Geomech, 30(10), 997–1018.

Rudnicki, J.W. and Rice, J.R. (1975), "Conditions for the localization of deformation in pressure-sensitive dilatant materials". Journal of the Mechanics and Physics of Solids, 23(6), 371–394.

Schmertmann, J.H. (2006), "Estimating slope stability reduction due to rain infiltration mounding. Journal of geotechnical and geoenvironmental engineering", 132(9), 1219–1228.

Stolarska, M., Chopp, D.L., Moës, N. and Belytschko, T. (2001), "Modelling crack growth by level sets in the extended finite element method". Int. J. Numer. Meth. Engng, 51(8), 943–960.

Sukumar, N., Chopp, D.L., Moës, N. and Belytschko, T. (2001), "Modeling holes and inclusions by level sets in the extended finite-element method". Computer Methods in Applied Mechanics and Engineering, 190(46), 6183–6200.

Tsaparas, I., Rahardjo, H., Toll, D.G. and Leong, E.C. (2002), "Controlling parameters for rainfall-induced landslides". Computers and Geotechnics, 29(1), 1–27.

Willam, K.J. and Warnke, E.P., "Constitutive model for the triaxial behaviour of concrete", IABSE Seminar on Concrete Structures Subjected to Triaxial Stresses III-1, 184, 1974.

Wroth, C.P. and Houlsby, G.T. (1985), "Soil Mechancis - Property characterization and analysis procesures". 11th ICSMFE. San Francisco, 1–55.

MODELLING GRANULAR MATERIALS THROUGH COORDINATION NUMBER AND FABRIC ANISOTROPY AT THE PARTICLE SCALE

M. Pouragha & R. Wan
Department of Civil Engineering, University of Calgary, Calgary, AB, Canada

ABSTRACT: *Granular materials involve microphysics at the various scales that give rise to distinct behaviours of geomaterials such as steady states, plastic limit states and unstable material behaviour. Incorporating such characteristics is one of the biggest challenges in constitutive modelling of granular materials. With this motivation, we use coordination number and fabric as the most important underlying micro-elements for defining the state of the material at the macroscopic level. In order to deal with the highly nonlinear functional dependencies at the micro level, the correlation between coordination number and fabric anisotropy has to be formulated at the particle level, rather than on an average sense. This is the essence of the proposed work which investigates the evolutions of coordination number (connectivity) distribution and anisotropy (contact normal) distribution curves with deformation history and their correlations through DEM (Discrete Element Modelling). These results enter as joint probability distribution functions into homogenization expressions during upscaling to a continuum constitutive model. More interestingly, these expressions can also be regarded as geometrical constraints used in entropy maximizing approaches. The end product of this work is a better understanding of the microstructure or fabric at critical state, which is a long standing question in geomechanics.*

1. INTRODUCTION

Micro-statistical approaches to modelling granular material behaviour often involve integrating over probability distribution functions (PDF) of micro-variables during homogenization in order to arrive at expressions in terms of macroscopic variables such as stress and strain. Most of these approaches pre-assume that statistical micro-variables are probabilistically independent from each other so that the corresponding PDF's can be conveniently integrated. However, ignoring such interdependencies comes at the cost of losing the sophistication required for capturing distinct granular material phenomena such as asymptotic behaviour (so-called Critical State) whereby deformations are sustained with yet stationary internal state variables.

Coordination number as the mean number of contacts per particle is intimately linked with fabric anisotropy which describes contact normal distribution. Indeed, Discrete Element Modelling (DEM) studies show that at Critical State, a characteristic coordination number is reached that determines an anisotropy limit (Troadec, et al., 2002). While the above is useful in defining limit states, it is more meaningful to investigate statistically the evolutions of both coordination number and fabric anisotropy toward these states during deformation history. From such a consideration, it follows that mechanisms of plastic deformations at the

macroscopic level may well be deciphered if we describe how fabric anisotropy develops with coordination number through their respective probability distribution functions.

In order to construct such probability distribution functions, we develop a novel method that assigns both a local coordination number and a local contact fabric to each particle based on the idea of Dirichlet tessellation in the 2D case. Then, the interdependency between these two local variables is investigated through DEM in a biaxial test for both loose and dense granular assemblies. The concept provides a means for distinguishing between the different deformational regimes during deviatoric loading of a granular assembly (Pouragha, et al., 2012) in view of analyzing failure and material instability issues.

2. DEM SIMULATIONS

DEM biaxial simulations have been carried out using PFC2D on a dense (2D porosity of 0.1) and a loose (2D porosity of 0.21) sample comprising around 20,000 particles with a narrow particle diameter D distribution between 16 mm and 20 mm, and a normal stiffness (K_n) to confining pressure (p) ratio of $K_n/(Dp)$ in the order of 10^5. The latter refers to a relatively stiff contact, hence representing rigid particles. As in a conventional biaxial test, the horizontal stress is kept constant, while the top and bottom boundaries of the sample are moved toward each other with a constant speed. At the same time, a servo-control mechanism modifies the movement of lateral boundaries in order to keep the lateral stress constant to its target value. The loading rate and simulation procedures followed are such that a quasi-static condition is maintained throughout the entire loading history.

The respective stress-strain including volumetric strain responses showing typical post-peak and dilation behaviours are illustrated in Fig. 1 together with contact fabric distribution at some selected points (early, peak and ultimate stages). At the microscopic scale, it is clearly shown that contact normals tend to align themselves along the major direction of loading to the detriment of contact losses in the horizontal direction.

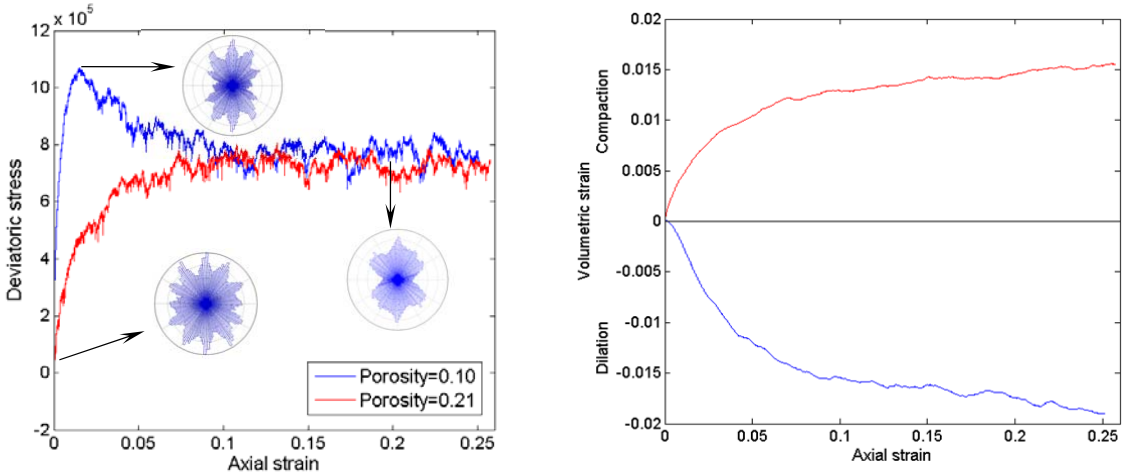

Figure 1. DEM simulation of granular assembly for dense and loose packings

In addition to basic results conveyed in Fig. 1, other field variables such as shear strain and local second order work were analyzed at the various strategic axial strains (initial stage: 0.5%, peak: 1.5% and ultimate: 20%) chosen during loading history; see Fig. 2. The shear strains were calculated from particle kinematics during a time increment and homogenization.

As such, they reflect the local strains within the specimen, especially the development of patterned deformation structures such as localized shear zones as depicted in Figs. 2a,b,c. The linkage between these localized shear zones and failure is provided through the calculation of the second order work (Hill, 1958) which signals the potential for material instability, and hence failure on a broad sense. Herein, the second order work has been computed at the local level (particle contact) simply as the product of the contact force increment and contact displacement increment (branch) vectors, thereby letting us evaluate local instabilities. Figures 2d,e,f show zones of negative local second order work signaling local instabilities that clearly correlate with localized shear zones. It is worth noting that even far away before peak condition; there are local violations of the second order work as a result of local instabilities. At both peak and post peak, zones of violation of second order work become prominent with adjoining areas having positive second order work.

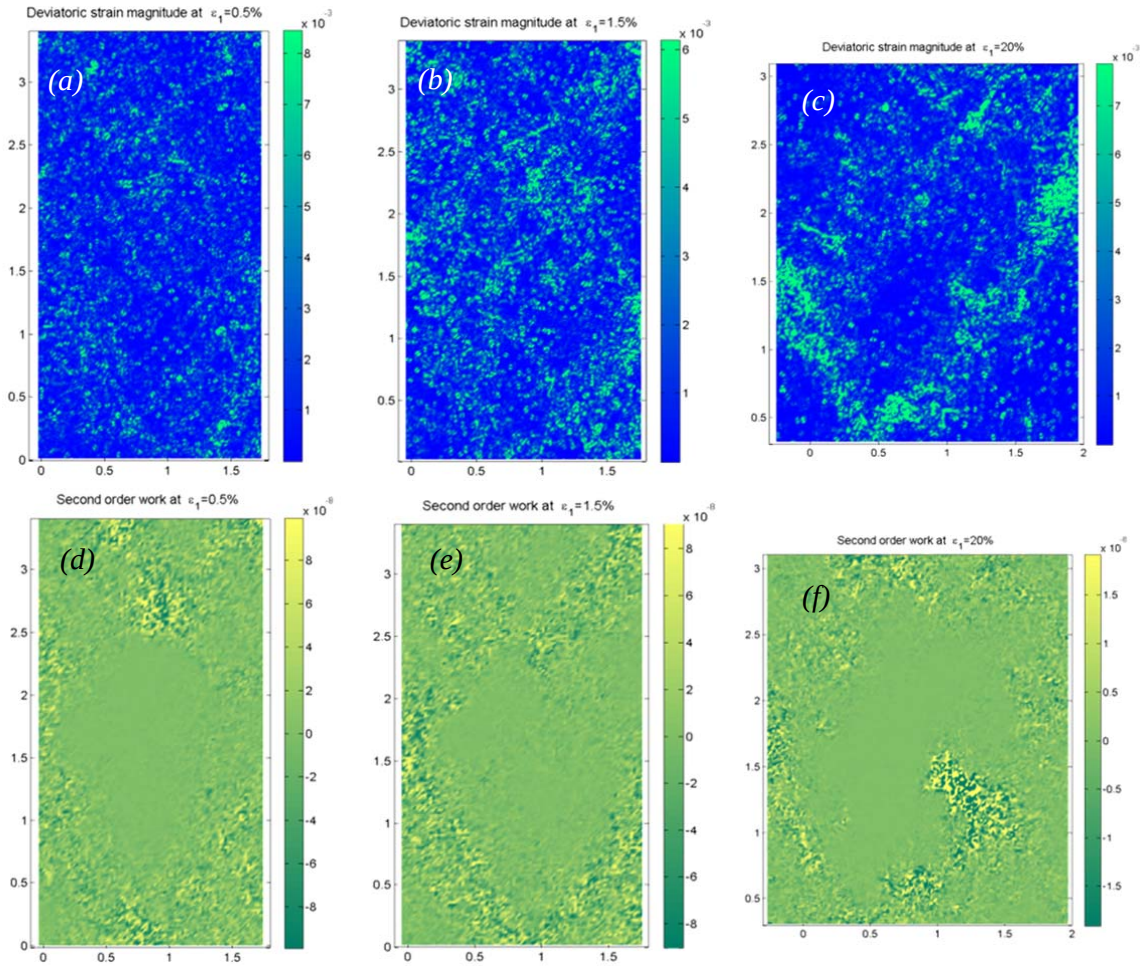

Figure 2. Snapshots of shear strains and second order work at strategic points during loading history for dense sample

With the above brief presentation of DEM results as background, the following analysis aims at defining the local parameters such as coordination number and contact fabric anisotropy touched upon earlier in the introduction. In analyzing their distribution throughout the sample via their respective probability density function, we anticipate to be able to describe the underlying microphysics of deformations presented in Fig. 2.

We next extract a circular Representative Element Volume (REV) of around 6500 particles from the central part of the sample. Dirichlet tessellation is then carried out on the REV using a new computational algorithm that we implemented in MATLAB. Figure 3 gives a snapshot of part of the above REV with the tessellation representing the cells of influence around each particle within the network. This tessellation provides the network upon which local coordination number and local fabric anisotropy will be defined and computed.

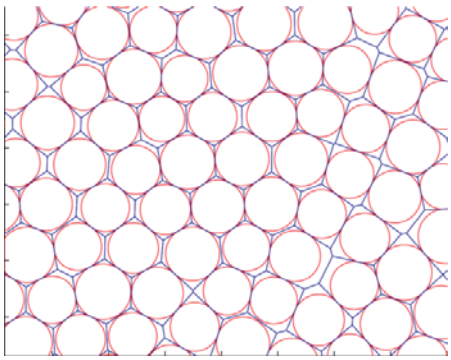

Figure 3. Snapshot of tessellated REV with network for local coordination and fabric anisotropy calculations

3. LOCAL PARAMETER DEFINITIONS

We start with the issue of a contact between a pair of particles in order to introduce the definition of coordination number on a local level. Despite the trivial notion of "contact", both the detection and identification of a contact in an actual granular assembly can become ambiguous since there may be particles touching each other with no appreciable interparticle forces. On the other hand, the discrete nature of the contact formation and breakage makes it difficult to incorporate a local coordination evolution into any analytical solution in order to depict the kinematics at the micro-level. To remedy this problem, a particular definition of coordination number as calculated on the Dirichlet tessellation is introduced so that it now becomes a continuous variable for which a PDF can now be constructed.

The Dirichlet tessellation principle is recalled in Fig. 4 wherein a boundary is found between two particles such that the tangents to the particles are equidistant to that boundary. As such, the tessellation gives rise to a network of contiguous cells enclosing each particle based on closest distance considerations. Hence, each cell represents the zone around a given particle within which interactions with the nearest neighbouring particles are likely to occur. If all particles are assumed to be in contact, regardless of the arrangement of particles, the ratio of the cell area to the area of the particle can be analytically written as follows:

$$A_{cell} = \frac{z}{\pi} \tan \frac{\pi}{z} \tag{1}$$

where z is the number of contacts around the central particle. Eq. (1) can now be conveniently used to express coordination number based on the area of the cell rather than actual interparticle contacts.

Recalling the ambiguity raised earlier in defining a contact, one might argue that if two particles are very close but not touching, they are still being considered as a contact in the Dirichlet tessellation, and hence in the calculation of coordination number. This over counting of contacts may be justified since in the process of replacing an original irregularly shaped particle assembly with equivalent circular or spherical particles, some actual contacts

may be lost in the process. In addition, an overestimation of coordination numbers generally tends to decrease anisotropy. Therefore, when integrating expressions containing PDF's of coordination number and contact fabric anisotropy during homogenization, this overestimation is mitigated on an average sense.

Now that the Dirichlet tessellation has been introduced, it is natural to define a local anisotropy a_c as the geometrical anisotropy of the Dirichlet cell, i.e.

$$a_c = \frac{r_{\max} - r_{\min}}{r_{\max} + r_{\min}} \tag{1}$$

where $r_{\max}$ and $r_{\min}$ are the major and minor axes of the cell (Fig. 4).

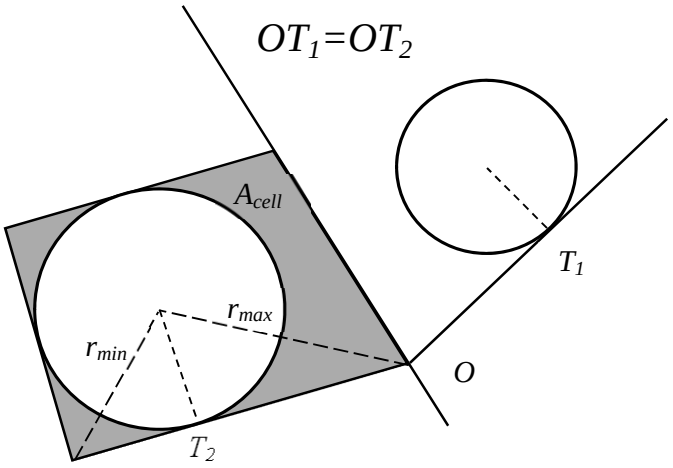

Figure 4. Dirichlet tessellation basic principle

4. LOCAL INTERDEPENDENCY

4. 1 Coordination number distribution – connectivity curve

It has been mathematically proven that the distribution of the cell areas for similar tessellations generally follows a Gamma distribution function (Kiang, 1966; Aste, et al., 2007), which has been also observed here in our DEM simulations. By contrast, the coordination numbers as calculated from cell areas closely follow a Gaussian distribution in accordance with previous studies where the commonly defined coordination number is believed to follow a normal distribution; see Fig. 5 (Rosato & Yacoub, 2000).

It is interesting to note that the Gaussian nature of the local coordination number distribution is verified throughout loading history as shown in Fig. 5. These so-called connectivity curves define an upper limit for coordination number which is imposed by geometrical hindrances, with a lower limit being controlled by statistical equilibrium considerations. For instance, equilibrium of particles cannot be attained with less than two contacts in the 2D case, which can be verified in Eq. (1) where there is a singularity when the coordination number approaches two.

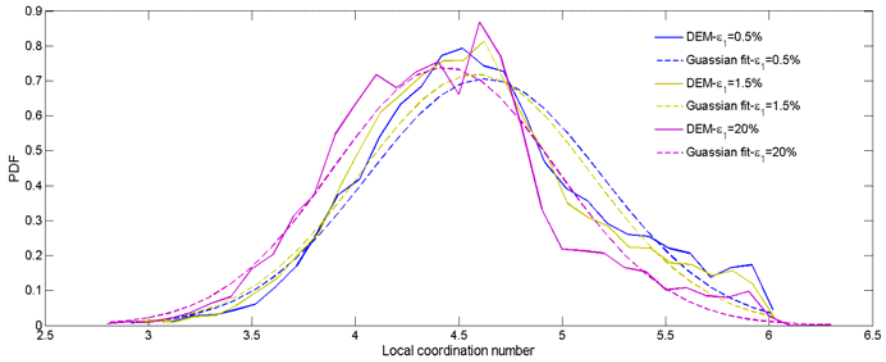

Figure 5. Connectivity PDF and Gaussian fit at different stages of deformation

4.2 Local anisotropy

For calculation purposes, the contact normal distribution $p(\theta)$ can be conveniently expanded as a Fourier series and retaining the first harmonic,

$$p(\theta) = \frac{z}{2\pi}(1 + a_c \cos 2\theta) \tag{3}$$

from which the maximum contact density per radian can be found as $z / 2\pi(1 + a_c)$.

On the other hand, for a virtually mono-dispersed granular assembly, the contact points may not have an angular distance less than $\pi / 3$, which leads to a contact density limit of $3/\pi$. Assuming that contact probability function is not a function of location, a local limit for the degree of anisotropy emerges as:

$$a_c^{\max} = \frac{6 - z}{z} \tag{4}$$

which is a function of coordination number z.

The above local limit in degree of anisotropy was simply derived considering only one layer of interacting neighbours, while more layers may be involved in the rearrangement of particles. As such, the maximum anisotropy given in Eq. (4) must be adjusted by using a scaling factor α, i.e.

$$a_c^{\max} = \alpha \frac{6 - z}{z} \tag{5}$$

Using DEM results, we next verify this limiting degree of anisotropy that arises purely from a geometrical constraint and which has important ramifications to plastic deformations. Figure 6 illustrates the plot of local coordination number and local anisotropy for each individual particle within the granular assembly as calculated from DEM simulation of the biaxial test at peak condition for the dense case. Eq. (5) nicely fits the DEM results within an acceptable degree of accuracy for a value of $\alpha = 0.45$. It is noted that this value does not change during loading history and even for various different packing densities. However, there might be a correlation between α and grain size distribution which is beyond the scope of this study.

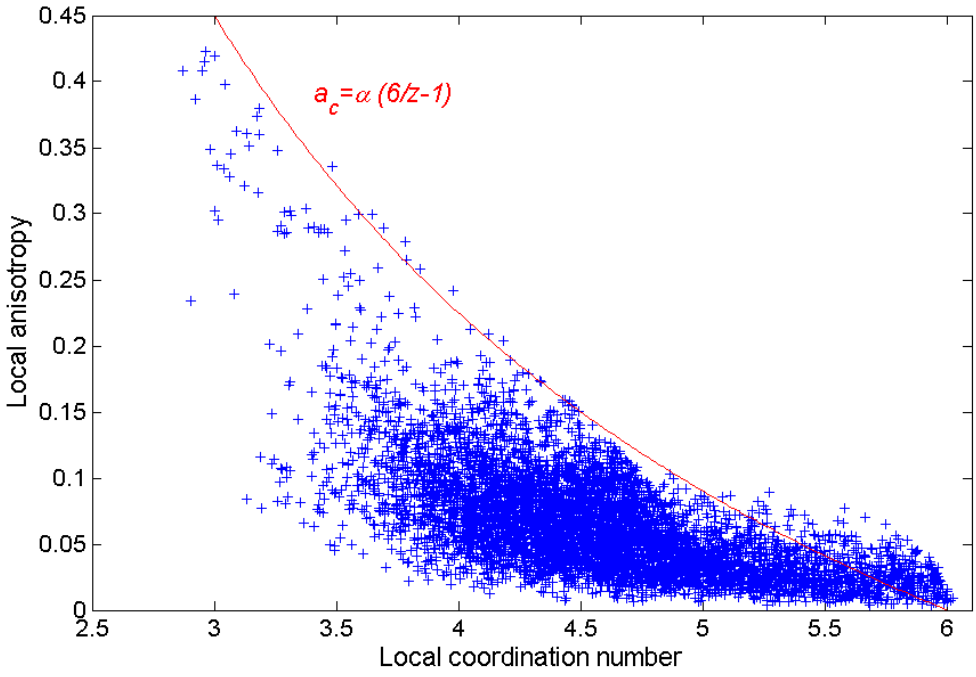

Figure 6. Population plot of local anisotropy and. local coordination within the assembly at peak condition

5. ASYMPTOTIC STRENGTH BEHAVIOUR

The plot shown in Fig. 6 provides the background material to explain the micro kinematics during loading history. When a granular assembly undergoes deviatoric loading, it first tries to accommodate for the deviatoric deformation through rearrangement of the contact distribution around particles, thereby mobilizing shear strength (Fig 7a). However, when the contact anisotropy reaches its geometrical limit, and the degree of anisotropy can no longer be increased, another mechanism takes control in which the deviatoric deformation results from convection of particles. More precisely, a particle moves from a neighbourhood to another, while its original location is being taken by another particle such that the net anisotropy does not change (Fig. 7b). The situation resembles a periodic boundary condition in a local sense where Eulerian strain can be seen as the convection of mass at the boundaries. It is worth mentioning that there is no strength mobilization due to the second mechanism of deformation, i.e. convection of particles. As such, deviatoric deformations can be sustained without any increase in strength, suggesting the notion of asymptotic behaviour. These two regimes are to some extent similar to those defined by Bagi (1996) for biaxial and shear tests. However, in our study, a combination of the two regimes is considered to describe the deformational behaviour throughout the test.

Further insights in the interpretation of asymptotic behaviour can be obtained by examining Fig. 6. The plot shows that there is only a small population of particles with high local anisotropy at the low range of coordination numbers, while most of the particles tend to have low anisotropies with coordination numbers in the higher range. Hence, during loading history, the mean anisotropy of the assembly of particles increases as deviatoric strength is mobilized with less and less particles contributing to anisotropy growth. Figure 8 shows the identification of two regimes of deformation at the micro scale, i.e. particle rearrangement and convection, which emerge when notions of connectivity and limiting local anisotropy are superimposed. It is seen as mean anisotropy in the granular assembly during deviatoric

loading, that the population of particles still mobilizing anisotropy decreases with more particles following the convection type of kinematics (Fig. 7b). As such, from a continuum level, the rate of shear strength mobilization gradually decreases with deviatoric strain toward an asymptotic value.

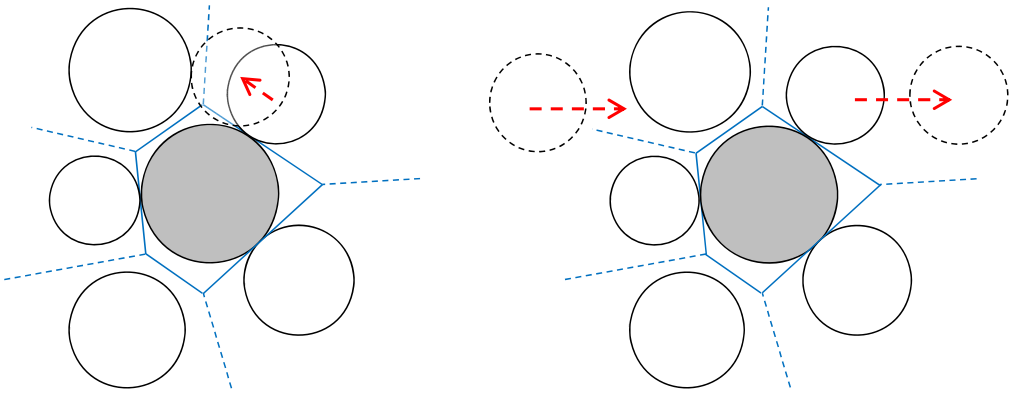

Figure 7. Two different regimes in deformation; *(a)* anisotropy mobilization, *(b)* periodic boundary condition with constant anisotropy

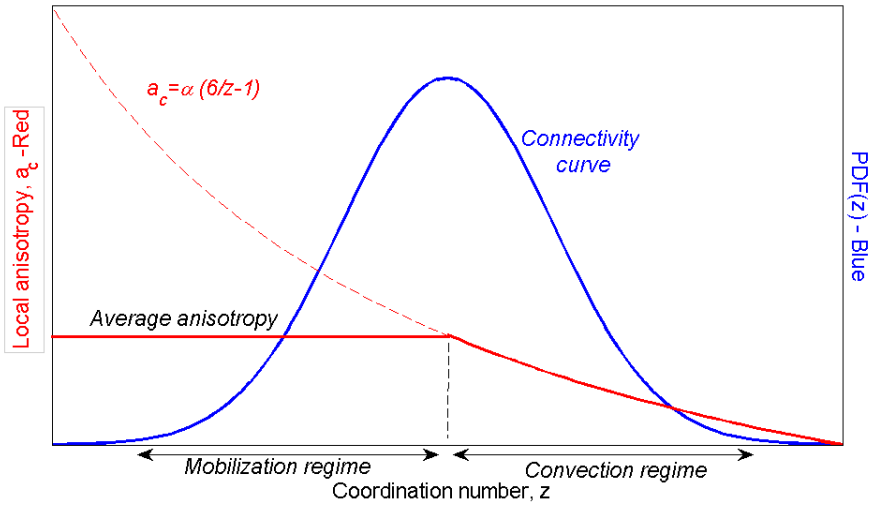

Figure 8. Particle rearrangement versus particle convection as a function of anisotropy

Finally, to illustrate the significance of the results of this work, changes in local coordination number and local anisotropy have been upscaled to strains at the continuum level through homogenization calculations on the Dirichlet tessellation and finally lead to the matricial relationship (Pouragha, et al., 2012):

$$\begin{Bmatrix} \dot{\varepsilon}_v \\ \dot{\varepsilon}_s \end{Bmatrix} = \begin{bmatrix} A_{vz} & A_{vc} \\ A_{sz} & A_{sc} \end{bmatrix} \begin{Bmatrix} \langle \dot{z} \rangle \\ \dot{a}_c \end{Bmatrix} \tag{6}$$

where $\dot{\varepsilon}_v$ and $\dot{\varepsilon}_s$ are volumetric strain and deviatoric strain increments respectively. It is anticipated that the evolution of material instability can be analyzed from the singularity of

the coefficient matrix in Eq. 6 which expresses the micromechanical response of the granular material due to imposed deformational loadings at the boundaries.

Figure 9 shows analytical calculations of average anisotropy and coordination number with strains as compared with the DEM calculations for the dense packing case. It is clear that the analytical model which is based on statistical information on micro-variables reproduces nicely the DEM simulation results. Most importantly, the model can capture asymptotic behaviour through the incorporation of limiting local anisotropy and particle convection mechanism. It is worth mentioning that such an approach to relate deformation to micro-statistical variables was proposed by Kruyt (2012), but using a relatively phenomenological expression in comparison with our study.

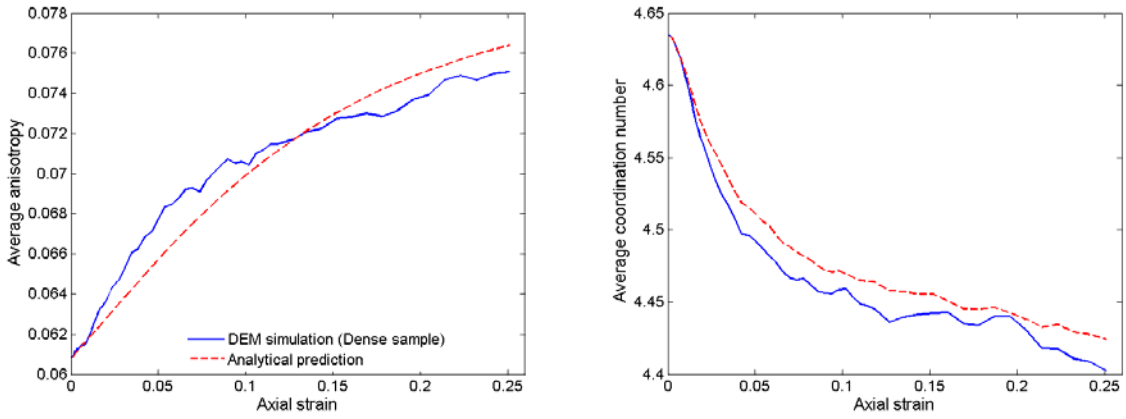

Figure 9. Comparison of analytical model results with DEM for the dense packing case

6. CONCLUSIONS

As major findings of the present study, we conclude that a micro-statistical approach based on strain provides an analytical formulation which can explain the salient deformational characteristics of granular materials. Recently, there have been some investigators who have followed similar approach, but results have not been conclusive yet. The newly defined micro-variables such as local anisotropy and local coordination number at the particle level convey information about spatial void distribution that can be easily upscaled to obtain strain at the continuum level. It turns out that the above micro-variables also carry the information about local forces, and hence the loop can be closed whereby a stress-strain relationship at the continuum level can be derived ultimately. This is currently under implementation.

ACKNOWLEDGEMENT

The first two authors acknowledge the Natural Science and Engineering Research Council of Canada and the Computer Modelling Foundation for their financial support through a NSERC-CRD project.

REFERENCES

Aste, T., Matteo, T. D., Saadatfar, M., Senden, T. J., Schroter, M., & Swinney, H. L. (2007), "An invariant distribution in static granular media". A Lett. J. Explor. Front. Phys., Vol. 79, 24003-p1-p5.

Bagi, K. (1996), "Stress and strain in granular assemblies". Mech. Mater.,Vol 22, 185-177.

Hill, R. (1958), “A general theory of uniqueness and stability in elastic-plastic solids”. J. Mech. Phys. Solids,Vol 6(3), 236–249.
Kiang, T. (1966), “Random Fragmentation in Two and Three Dimensions”. Z. Astrophys., Vol. 64, 433-439.
Kruyt, N. (2012), “Micromechanical study of fabric evolution in quasi-static deformation of granular materials”. Mech. Mater.,Vol. 44, 120–129.
Pouragha, M., Wan, R., & Harthong, B. (2012), “Micromechanical Description of Strain in a Granular Material due to Fabric Evolution”. Proceeding of 49th Annual Technical Meeting of Society of Engineering Science. Georgia tech, Atlanta.
Rosato, A. D., & Yacoub, D. (2000)’ “Microstructure evolution in compacted granular beds”. Powder Technol.,Vol. 109, 255–261.
Troadec, H., Radjai, F., Roux, S., & Charmet, J. C. (2002), “Model for granular texture with steric exclusion”. Phys. Rev. E ,Vol. 66, 041305.

ON MODELING CROSS-ANISOTROPIC ELASTICITY OF SOILS WITH A MICROSTRUCTURE TENSOR

B. Schädlich
Institute for Soil Mechanics and Foundation Engineering, Graz University of Technology, Graz, Austria

H.F. Schweiger
Institute for Soil Mechanics and Foundation Engineering, Graz University of Technology, Graz, Austria

ABSTRACT: *Anisotropic shear strength in multilaminate, microplane and microstructural constitutive models has been modeled by various authors with a microstructure tensor, which gives shear strength parameters depending on the spatial orientation of the stress vector on the contact plane. It is straightforward to use the same approach also for anisotropic elasticity by varying stiffness parameters with spatial orientation. In that case, however, physical constraints on local stiffness parameters limit the possible range of macroscopic stiffness parameters. The paper compares the range of macroscopic cross-anisotropic stiffness predicted by the microstructural approach with experimental results for various soils. It is shown that not all mechanically admissible and experimentally observed combinations of macroscopic parameters can be described by physically meaningful (i.e. positive) microscopic parameters. Furthermore, local strain distributions obtained with the microstructural approach are compared with the direct projection of strains, highlighting significant differences between the two. The reasons for these discrepancies and possible alternative approaches for modeling cross-anisotropic elasticity are discussed.*

1 INTRODUCTION

Formulating material behavior at microstructural level (i.e. at the contact planes between individual grains) offers some advantages over conventional invariant based constitutive models: Anisotropic strength properties can be incorporated in a physically meaningful manner, rotation of principal stress axes and anisotropic hardening is accounted for automatically. This class of constitutive models comprises multilaminate, microplane and micromechanical models. These models are based on the concept, that the macro-mechanical material behavior can be related to processes at the micro-mechanical scale. If the material is considered as an assemblage of discrete, solid particles, elastic deformations can be assigned to the particles, and plastic deformation can be attributed to inter-particle sliding.

An important issue in this class of models is consistency between local and global material parameters. In the case of elastic stiffness parameters, local parameters usually cannot be measured directly, but need to be correlated to macroscopic quantities by so called micro-macro-relations. Such mathematical relationships can be found analytically by comparing local and macroscopic strain increments for a general macroscopic stress increment.

All these models involve some kind of contact plane, on which local stresses and strains are evaluated. The orientation of such a plane i is defined by its normal vector $\mathbf{n}_i$, whose orientation with respect to the global coordinate system x, y, z is given by the angles α_i and β_i (Fig. 1). In order to uniquely define the direction of the local stresses and strains parallel to

the integration plane, local unit vectors $\mathbf{s}_i$ and $\mathbf{t}_i$ are introduced, with $\mathbf{n}_i$, $\mathbf{s}_i$ and $\mathbf{t}_i$ forming a system of mutually orthogonal local axes. While the choice of $\mathbf{s}_i$ and $\mathbf{t}_i$ is in principle arbitrary (provided they are mutually orthogonal), it is convenient to choose $\mathbf{s}_i$ and $\mathbf{t}_i$ parallel to the dip and strike direction of plane *i*, respectively (Eq. 1)).

$$\mathbf{n}_i = \begin{bmatrix} n_{1,i} \\ n_{2,i} \\ n_{3,i} \end{bmatrix} = \begin{bmatrix} \cos\alpha_i \\ \sin\alpha_i \cdot \cos\beta_i \\ \sin\alpha_i \cdot \sin\beta_i \end{bmatrix}, \quad \mathbf{s}_i = \begin{bmatrix} s_{1,i} \\ s_{2,i} \\ s_{3,i} \end{bmatrix} = \begin{bmatrix} -\sin\alpha_i \\ \cos\beta_i \cdot \cos\alpha_i \\ \sin\beta_i \cdot \cos\alpha_i \end{bmatrix}, \quad \mathbf{t}_i = \begin{bmatrix} t_{1,i} \\ t_{2,i} \\ t_{3,i} \end{bmatrix} = \begin{bmatrix} 0 \\ -\sin\beta_i \\ \cos\beta_i \end{bmatrix} \tag{1}$$

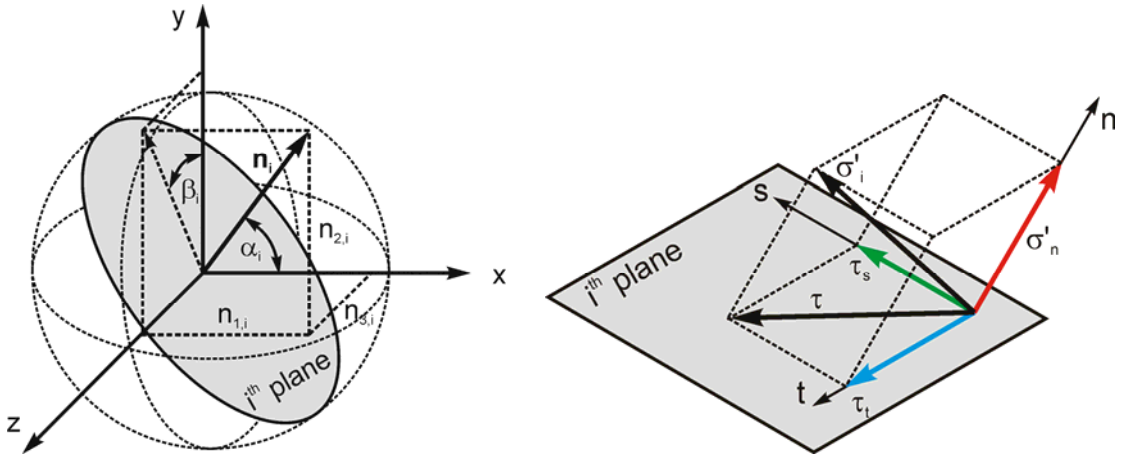

Fig. 1. Definition of integration plane orientation and local stress components

The multilaminate concept employs the static constraint, i.e. local stresses are projections of macroscopic stresses (Eq. 3)), whereas local strains are in general no projection of macroscopic strains. The transformation matrix $\mathbf{T}_i$ contains the derivatives of local stresses with respect to the macroscopic stress components and changes with plane orientation.

$$\boldsymbol{\sigma}' = \begin{pmatrix} \sigma'_{xx} & \sigma'_{yy} & \sigma'_{zz} & \tau_{xy} & \tau_{yz} & \tau_{xz} \end{pmatrix}^T \tag{2}$$

$$\boldsymbol{\sigma}'_i = \left(\mathbf{T}_i\right)^T \cdot \boldsymbol{\sigma}' = \begin{pmatrix} \sigma'_n & \tau_s & \tau_t \end{pmatrix}^T \tag{3}$$

$$\mathbf{T}_i = \frac{\partial \boldsymbol{\sigma}'_i}{\partial \boldsymbol{\sigma}'} = \begin{bmatrix} n_{1,i}^2 & n_{1,i} \cdot s_{1,i} & n_{1,i} \cdot t_{1,i} \\ n_{2,i}^2 & n_{2,i} \cdot s_{2,i} & n_{2,i} \cdot t_{2,i} \\ n_{3,i}^2 & n_{3,i} \cdot s_{3,i} & n_{3,i} \cdot t_{3,i} \\ 2n_{1,i} \cdot n_{2,i} & n_{1,i} \cdot s_{2,i} + n_{2,i} \cdot s_{1,i} & n_{1,i} \cdot t_{2,i} + n_{2,i} \cdot t_{1,i} \\ 2n_{2,i} \cdot n_{3,i} & n_{3,i} \cdot s_{2,i} + n_{2,i} \cdot s_{3,i} & n_{3,i} \cdot t_{2,i} + n_{2,i} \cdot t_{3,i} \\ 2n_{1,i} \cdot n_{3,i} & n_{3,i} \cdot s_{1,i} + n_{1,i} \cdot s_{3,i} & n_{3,i} \cdot t_{1,i} + n_{1,i} \cdot t_{3,i} \end{bmatrix} \tag{4}$$

For elastic material, the local compliance matrix $\mathbf{C}_i$ delivers the relation between local strains and local stresses (Eq. 5)). In the case of isotropic linear elasticity $\mathbf{C}_i$ is equal for all planes. The diagonal structure of $\mathbf{C}_i$ (Eq. 6)) involves the assumption, that local shear and normal deformations are decoupled.

$$\boldsymbol{\varepsilon}_i = \begin{pmatrix} \varepsilon_n & \gamma_s & \gamma_t \end{pmatrix}^T = \mathbf{C}_i \cdot \mathbf{d}\boldsymbol{\sigma}_i \tag{5}$$

$$\mathbf{C}_i = \begin{pmatrix} C_n & 0 & 0 \\ 0 & C_t & 0 \\ 0 & 0 & C_t \end{pmatrix} \tag{6}$$

Macroscopic strains are obtained by transforming local strains back into the macroscopic coordinate system and integrating over the surface of the unit sphere.

$$\boldsymbol{\varepsilon} = \begin{pmatrix} \varepsilon_{xx} & \varepsilon_{yy} & \varepsilon_{zz} & \gamma_{xy} & \gamma_{yz} & \gamma_{xz} \end{pmatrix}^T = \frac{3}{4\Pi} \cdot \int_{\alpha} \int_{\beta} \left(\mathbf{T}_i \cdot \boldsymbol{\varepsilon}_i \right) \cdot \sin\alpha \cdot d\beta \cdot d\alpha \tag{7}$$

2 CROSS-ANISOTROPIC ELASTICITY

In most cases the concept of cross anisotropy or transverse isotropy is utilized to describe the anisotropic stiffness characteristics of natural soils (e.g. Kuwano & Jardine, 2002; Gasparre et al., 2007). Cross anisotropy exhibits one axis of symmetry, which for most naturally deposited soils and sedimentary rocks equals the vertical axis. Assuming a bedding plane parallel to the y-z-plane, the stress-strain behavior can be formulated according to Eq. 8).

$$\begin{pmatrix} \Delta\varepsilon_{xx} \\ \Delta\varepsilon_{yy} \\ \Delta\varepsilon_{zz} \\ \Delta\gamma_{xy} \\ \Delta\gamma_{yz} \\ \Delta\gamma_{xz} \end{pmatrix} = \begin{pmatrix} \frac{1}{E'_v} & \frac{-\nu'_{vh}}{E'_v} & \frac{-\nu'_{vh}}{E'_v} & 0 & 0 & 0 \\ \frac{-\nu'_{vh}}{E'_v} & \frac{1}{E'_v} & \frac{-\nu_{hh}}{E_h'} & 0 & 0 & 0 \\ \frac{-\nu'_{vh}}{E'_v} & \frac{-\nu_{hh}}{E_h'} & \frac{1}{E'_h} & 0 & 0 & 0 \\ 0 & 0 & 0 & 1/G_{vh} & 0 & 0 \\ 0 & 0 & 0 & 0 & \frac{2(1+\nu'_{hh})}{E'_h} & 0 \\ 0 & 0 & 0 & 0 & 0 & 1/G_{vh} \end{pmatrix} \cdot \begin{pmatrix} \Delta\sigma'_{xx} \\ \Delta\sigma'_{yy} \\ \Delta\sigma'_{zz} \\ \Delta\tau_{xy} \\ \Delta\tau_{yz} \\ \Delta\tau_{xz} \end{pmatrix} \tag{8}$$

with E'_v … Effective Young's modulus in vertical direction
E'_h … Effective Young's modulus in horizontal direction
G_{vh} … Shear modulus in all vertical planes
ν'_{hh} … Poisson's ratio linking horizontal loading and horizontal strain perpendicular to loading direction
ν'_{vh} … Poisson's ratio linking vertical loading and horizontal strain

3 MICROSTRUCTURE TENSOR

Anisotropic shear strength in multilaminate or conceptually similar micromechanical models has been described previously by introducing a so-called microstructure tensor (Pietruszczak & Mroz, 2000). With this approach anisotropy is taken into account by evaluating the microstructure tensor for the direction of the local shear stress, which results in local material parameters varying with plane orientation. The type of anisotropy is defined by the structure of the microstructure tensor, while the magnitude of anisotropy is described by a scalar

valued anisotropy parameter. For cross anisotropy with a vertical axis of symmetry the variation of the local parameter α_u can be derived as

$$\alpha_u = \alpha_0 \cdot \left(1 - \frac{A_r - 1}{A_r + 2} \cdot \left(1 - 3 \cdot (u_v)^2\right)\right) \tag{9}$$

with α_u directional dependent local parameter
α_0 mean value of the local parameter
$A_r = \alpha_v / \alpha_h$ ratio of local anisotropy
u_v vertical component of the unit vector in which α_u is calculated.

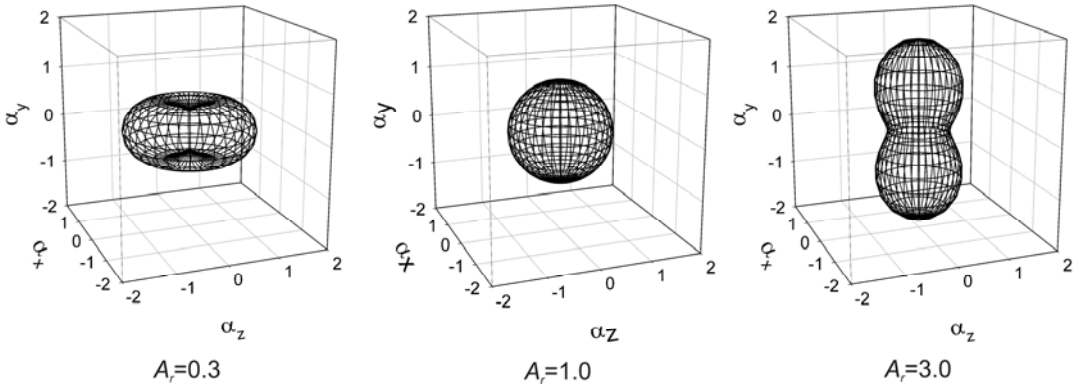

Fig. 2. Spatial distribution of the cross-anisotropic parameter for different values of parameter A_r (Schweiger et al. 2009)

Applying that approach to elastic stiffness results in local stiffness (or compliance) varying with plane orientation and the orientation of the local stress vector. For macroscopic cross-anisotropic stiffness it is plausible to assume that local stiffness parameters also vary in a cross-anisotropic manner, and that the macroscopic and local axis of symmetry coincide. In that case the local normal and tangential compliance parameters can be written as

$$C_n = C_{n0} \cdot \left(1 - \frac{A_{r,Cn} - 1}{A_{r,Cn} + 2} \cdot \left(1 - 3 \cdot (n_v)^2\right)\right), \tag{10}$$

$$C_{ts} = C_{t0} \cdot \left(1 - \frac{A_{r,Ct} - 1}{A_{r,Ct} + 2} \cdot \left(1 - 3 \cdot (s_v)^2\right)\right), \tag{11}$$

$$C_{tt} = C_{t0} \cdot \left(1 - \frac{A_{r,Ct} - 1}{A_{r,Ct} + 2} \cdot \left(1 - 3 \cdot (t_v)^2\right)\right). \tag{12}$$

C_n is the normal compliance, C_{ts} and C_{tt} are the tangential compliances in **s**- and **t**-direction, n_v, s_v and t_v are the components of the normal and tangential vectors (Eq. 1)) in the direction of the macroscopic axis of symmetry (here equal to the vertical axis). As n_v, s_v and t_v are related to the plane orientation angle α, the local compliances also depend on plane orientation. The tangential stiffness in general differs in **s**- and **t**-direction on one plane, as the microstructure tensor is evaluated for different directions. It is implicitly assumed, that the

local compliance exhibits a diagonal structure, such that local stresses and strains are decoupled.

$$\mathbf{C}_i(\alpha,\beta)=\begin{pmatrix} C_n(\alpha,\beta) & 0 & 0 \\ 0 & C_{ts}(\alpha,\beta) & 0 \\ 0 & 0 & C_{tt}(\alpha,\beta) \end{pmatrix} \tag{13}$$

The global compliance matrix **C** is obtained by equating the macroscopic strain increment **dε** with the integral over all local strain increments. The analytical integration over the surface of the unit sphere delivers a relationship between local and global compliance (Eq. 14)). The structure of **C** is symmetric and cross-anisotropic with a y-z bedding plane (x has been taken as the vertical axis), which validates the assumption concerning congruence of local and global anisotropy.

$$\mathbf{C}=\frac{3}{4\Pi}\cdot\int_{\alpha}\int_{\beta}\left[\mathbf{T}_i(\alpha,\beta)\cdot\mathbf{C}_i(\alpha,\beta)\cdot\mathbf{T}_i(\alpha,\beta)^T\right]\cdot\sin\alpha\cdot d\beta\cdot d\alpha \tag{14}$$

The elements of **C** can be related to the cross-anisotropic constants of Eq. 8), which gives global parameters in terms of local compliances and anisotropy ratios:

$$E'_v=\frac{35}{9\cdot C_{n0}\cdot\dfrac{5\cdot A_{r,Cn}+2}{A_{r,Cn}+2}+6\cdot C_{t0}\cdot\dfrac{3+4\cdot A_{r,Ct}}{A_{r,Ct}+2}} \tag{15}$$

$$E'_h=\frac{35}{9\cdot C_{n0}\cdot\dfrac{A_{r,Cn}+6}{A_{r,Cn}+2}+3\cdot C_{t0}\cdot\dfrac{11+3\cdot A_{r,Ct}}{A_{r,Ct}+2}} \tag{16}$$

$$G_{vh}=\frac{35}{12\cdot C_{n0}\cdot\dfrac{3\cdot A_{r,Cn}+4}{A_{r,Cn}+2}+3\cdot C_{t0}\cdot\dfrac{23+19\cdot A_{r,Ct}}{A_{r,Ct}+2}} \tag{17}$$

$$\nu'_{vh}=\frac{C_{t0}\cdot\left(4\cdot A_{r,Ct}+3\right)\cdot\left(A_{r,Cn}+2\right)-C_{n0}\cdot\left(3\cdot A_{r,Cn}+4\right)\cdot\left(A_{r,Ct}+2\right)}{2\cdot C_{t0}\cdot\left(4\cdot A_{r,Ct}+3\right)\cdot\left(A_{r,Cn}+2\right)+3\cdot C_{n0}\cdot\left(5\cdot A_{r,Cn}+2\right)\cdot\left(A_{r,Ct}+2\right)} \tag{18}$$

$$\nu'_{hh}=-\frac{C_{t0}\cdot\left(A_{r,Ct}-8\right)\cdot\left(A_{r,Cn}+2\right)+C_{n0}\cdot\left(A_{r,Cn}+6\right)\cdot\left(A_{r,Ct}+2\right)}{C_{t0}\cdot\left(3\cdot A_{r,Ct}+11\right)\cdot\left(A_{r,Cn}+2\right)+3\cdot C_{n0}\cdot\left(A_{r,Cn}+6\right)\cdot\left(A_{r,Ct}+2\right)} \tag{19}$$

Eq. 15)-19) deliver isotropic macroscopic parameters, if the local anisotropy ratios $A_{r,Cn}$ and $A_{r,ct}$ are set to unity. It should be noted, that these micro-macro relations are non-unique. While it is possible to derive global parameters for a chosen set of local compliances and anisotropy ratios, this is not possible in reverse. Evidently, four local variables cannot be uniquely determined such that a chosen set of five global parameters is matched without introducing some artificial coupling between the global parameters.

The relationship between local anisotropy ratio and global parameters is plotted in Fig. 3. The chosen ratio of local normal vs. shear contact stiffness $C_{n0}/C_{t0} = 3/8$ is equivalent to $\nu' = 0.2$ at $A_{r,Cn} = A_{r,ct} = 1.0$ (isotropy). For $A_{r,Cn} < 1$ a horizontal plane is stiffer in normal

compression than a vertical one, which increases E'_v and decreases E'_h compared to the isotropic case. Consequently, the anisotropy ratio E'_h/E'_v decreases and approaches ~0.46 at $A_{r,Cn} = A_{r,ct} = 0.0$. For higher values of $A_{r,Cn}$ the ratio E'_h/E'_v reaches values of 1.7-2.2. G_{vh}/G_{hh} follows a reverse trend with a limiting value of ~1.62 at $A_{r,Cn} = A_{r,ct} = 0.0$ and values of 0.4-0.6 at $A_{r,Cn} = 5$. Varying the anisotropy ratios for local shear and normal stiffness independently by assuming $A_{r,Ct}/A_{r,cn} \neq 1.0$ changes the range of macroscopic anisotropy ratios only slightly.

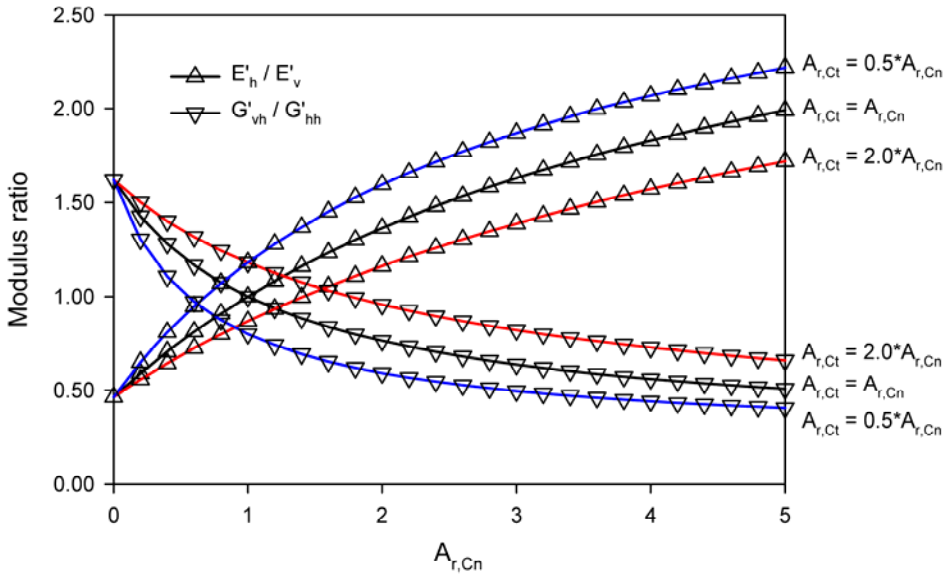

Fig. 3. Relationship between global and local anisotropy ratio

The Poisson's ratio ν'_{vh} is virtually independent of the local anisotropy ratio for a given ratio of C_{n0}/C_{t0} (Fig. 4). On the other hand, the Poisson's ratio ν'_{hh} is very sensitive to changes in $A_{r,Cn}$ and in the ratio $A_{r,Cn}/A_{r,ct}$.

These results do not change significantly when C_{n0}/C_{t0} is varied. This is consistent with results presented by Yimsiri & Soga (2000), who used a similar approach to account for spatial distribution of particle contacts in their microstructural model. The microstructure approach apparently predicts a strong correlation between E'_h/E'_v, G_{vh}/G_{hh} and Poisson's ratios. It is therefore not possible to obtain $E'_h/E'_v < 1$ and $G_{vh}/G_{hh} < 1$ with the same set of local parameters. Furthermore, high values of E'_h/E'_v enforce low values of ν'_{hh}.

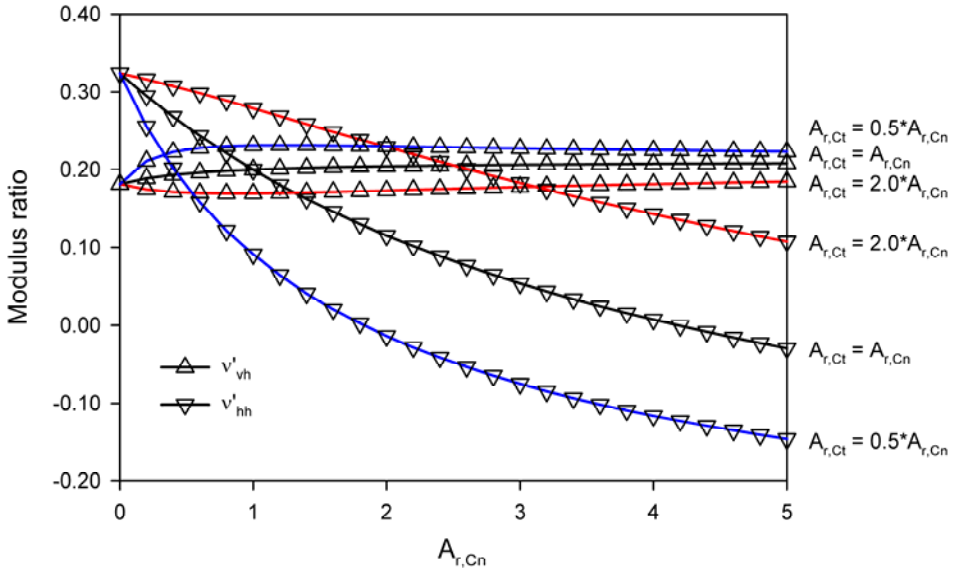

Fig. 4. Relationship between global Poisson's ratios and local ratio of anisotropy

Experimental data on cross-anisotropic soil stiffness within the quasi-elastic range (i.e. at very small strains) suggest that such strong correlations do not exist (Fig. 5, Fig. 6). In order to reproduce measured values of E'_h/E'_v, G_{vh}/G_{hh} and ν'_{hh}, for some soils (e.g. Ham River Sand, London Clay) negative local stiffness would be required in some directions, which obviously is physically meaningless.

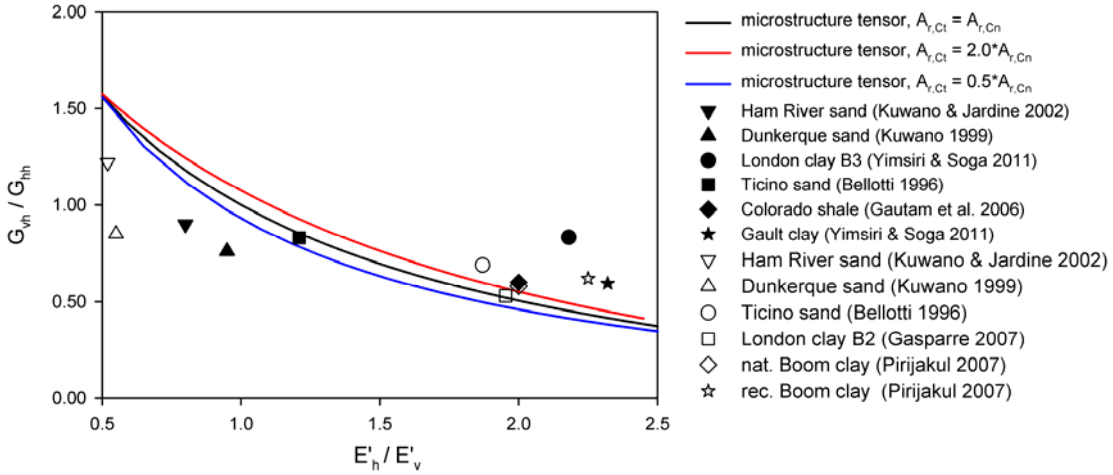

Fig. 5. Comparison of experimental ratios of anisotropy with predictions by the microstructure tensor approach (full symbols: isotropic stress states, empty symbols: anisotropic stress states)

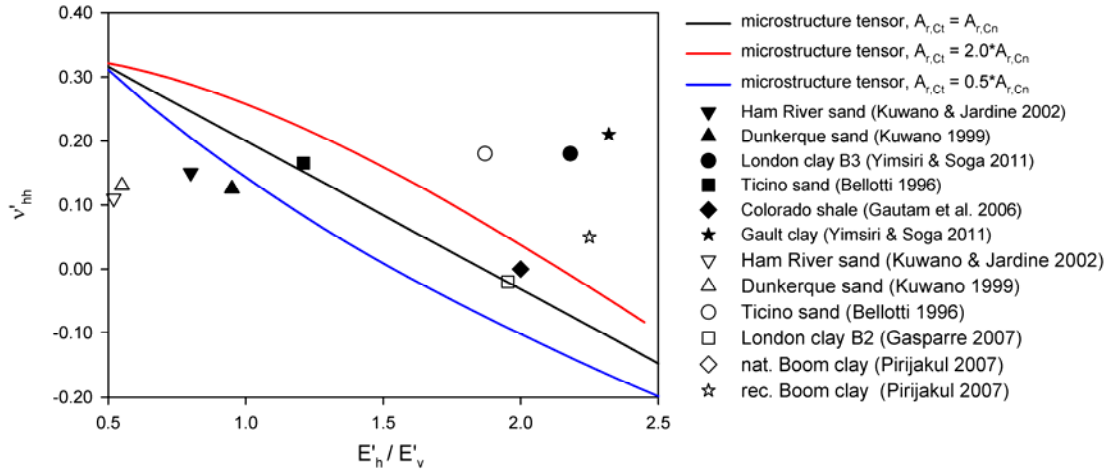

Fig. 6. Comparison of experimental Poisson's ratios ν'_{hh} with predictions by the microstructure tensor approach (full symbols: isotropic stress states, empty symbols: anisotropic stress states)

4 LOCAL STRAIN DISTRIBUTION

A cross-anisotropic elastic material with a vertical axis of symmetry is loaded by stress increments of $\Delta\sigma'_h = \Delta\sigma'_v = -100$ kPa (isotropic compression) and $\Delta\sigma'_h = +100$ kPa, $\Delta\sigma'_v = -200$ kPa (triaxial compression). For these stress conditions the local normal and shear strain distributions predicted by the microstructural approach can be derived analytically using Eq. 5). Local parameters for the microstructural approach are assumed as $A_{r,Cn} = 5$, $A_{r,Ct} = 2.5$, $C_{t0} = 0.0001$ and $C_{n0} = 3/8 \cdot C_{t0}$. The resulting global cross-anisotropic parameters are obtained from Eq. 15)-19) and summarized in Tab. 1.

Tab. 1. Cross-anisotropic elastic material parameters

E'_v [kPa]	E'_h [kPa]	G_{vh} [kPa]	ν'_{vh}	ν'_{hh}
11 531	19 840	5 911	0.185	0.108

These parameters were then used to calculate the macroscopic strain increment (Eq. 8)) and project the macroscopic strains directly into the different orientations using the kinematic constraint:

$$\mathbf{d\varepsilon}_i = \mathbf{T}_i^T \cdot \mathbf{d\varepsilon} = \left(d\varepsilon_n \quad d\gamma_s \quad d\gamma_t\right)^T \tag{20}$$

Plotting the resulting strain distributions for both approaches over orientation angle α (with $\alpha = 0$ denoting a horizontal plane) reveals significant differences (Fig. 7, Fig. 8). In isotropic loading, the microstructural approach predicts a more extreme normal strain distribution than the direct strain projection, but no local shear strains at all. This is due to the decoupling of local normal stresses and local shear strains, with the latter originating only from local shear stresses (which are zero in isotropic loading). The direct strain projection delivers maximum shear strains at $\alpha = \pm 45°$ to the vertical axis. In triaxial loading, the direct projection delivers the more extreme distribution of local normal strains and less shear strain than the microstructural approach.

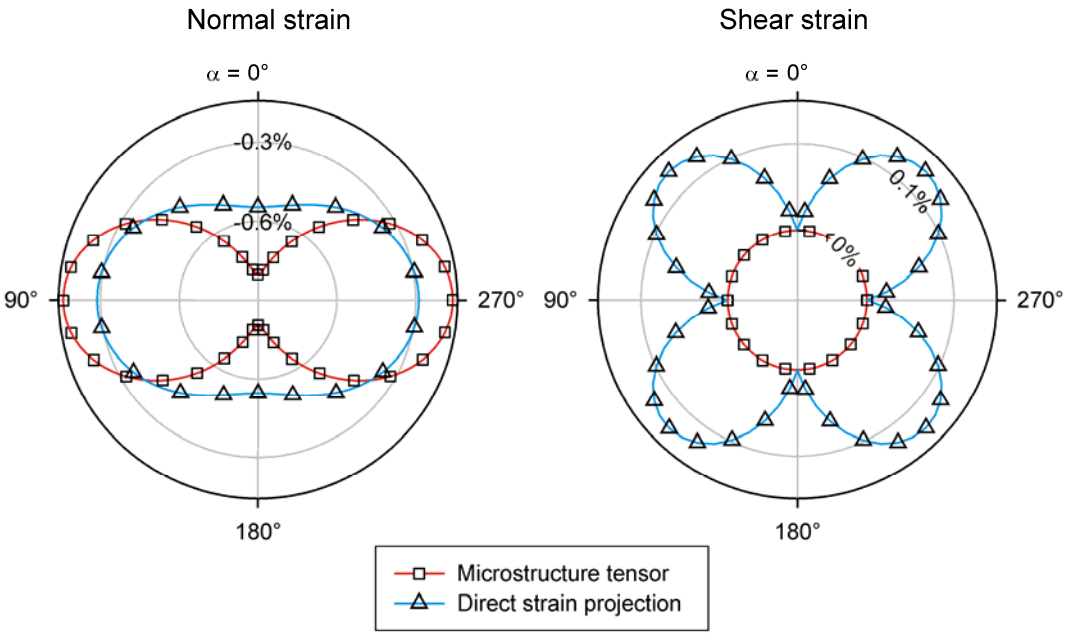

Fig. 7. Distribution of local strains in isotropic compression

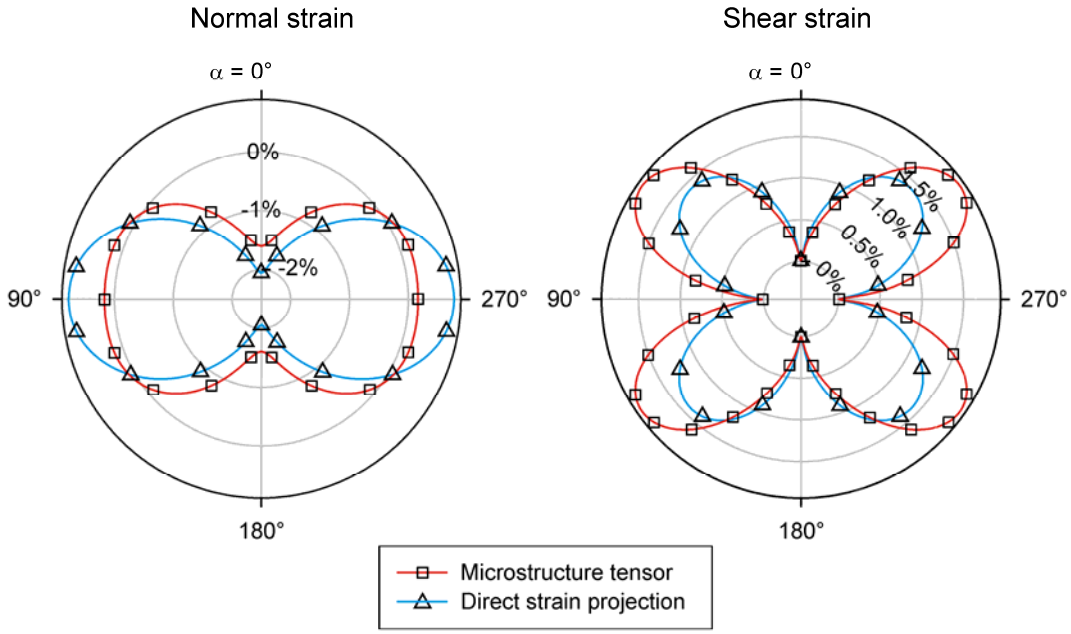

Fig. 8. Distribution of local strains in triaxial compression

5 DISCUSSION AND CONCLUSIONS

Application of the microstructure tensor approach for cross anisotropic elasticity suffers from three major drawbacks:

1. It is not possible to relate stiffness parameters on the micro level to macroscopic parameters in a unique way. It is only possible to derive macroscopic parameters once a set of microscopic parameters has been chosen. This limits the practical applicability of

the microstructural approach, as local stiffness parameters and their spatial variation are in general not known.

2. The possible range of macroscopic parameter combinations is limited by the condition of strictly positive local stiffness parameters. It is not possible to obtain $E_h/E_v < 1$ and $G_{vh}/G_{hh} < 1$ at the same time, even though experimental data on small strain stiffness suggest that this can be the case for some soils.
3. Local stresses and strains fulfill either the static or the kinematic constraint, but not both. With the decoupled local compliance used in the microstructure approach, no local shear strains are obtained in isotropic compression, as $\tau = 0$ on all planes. However, isotropic compression of a cross-anisotropic material results in different macroscopic strains in and perpendicular to the axis of symmetry, which indicates the presence of shear strains within the material.

It has been shown by Bažant & Prat (1988) that an additional split of the local normal stress in a volumetric and deviatoric component (V-D-split) is able to enforce the double constraint for isotropic elasticity. That is however, not sufficient for cross-anisotropic elasticity, as local shear stresses and strains remain 0 in isotropic loading even with the V-D-split. Shear strains in isotropic compression can only be obtained by coupling shear strains and normal stresses on local level, which requires non-zero off-diagonal terms in the local compliance matrix. Besides the difficulty of relating these coupling terms analytically to macroscopic parameters, the physical meaning for coupling shear strains and normal stresses within an elastic particle-to-particle contact model appears questionable. The discrepancy between experimental results and the numerical parameter range indicates that cross-anisotropic elasticity cannot be modeled with a microstructure tensor for all soil types.

These discrepancies may be traced back to the assumption that any deformation at a single particle contact exclusively results from stresses at that contact. In reality stresses are acting on the particle in other directions, and due to the local particle deformability local strains arise in directions which may not be loaded at all.

A more promising approach is offered by the spectral decomposition of the macroscopic compliance matrix (Cusatis et al. 2008), in which the global stress state is split into spectral components using the eigenvectors of the global compliance matrix. Local stresses are found by projecting these components separately into the different directions. Local strains are then calculated by multiplying the local spectral stresses with the corresponding eigenvalues of the macroscopic compliance matrix. Local compliance matrices can also be derived, but the local stress state needs to be split into six components to carry out the necessary transformations (Schädlich & Schweiger 2012).

ACKNOWLEDGEMENT

The financial support for the first author of this study by FWF Austria (grant no. P21225-N13) is gratefully acknowledged.

REFERENCES

Bažant, Z.P. & Prat, P.C. (1988), “Microplane model for brittle-plastic material. I. Theory, Journal of Engineering Mechanics”, Vol. 114(10), 1672-1688.

Bellotti, R.; Jamiolkowski, M.; Presti, D.C.F. & O'Neill, D.A. (1996), “Anisotropy of small strain stiffness in Ticino sand”. Géotechnique, Vol. 40(4), 115-131.

Cusatis, G.; Beghini, A. & Bažant, Z.P. (2008), “Spectral stiffness microplane model for quasibrittle composite laminates - Part I: Theory”. Journal of Applied Mechanics, ASME, Vol. 75(2), 021009.

Gasparre, A.; Nishimura, S.; Minh, N.A.; Coop, M.R. & Jardine, R.J. (2007), “The stiffness of natural London Clay”. Géotechnique, Vol. 57(1), 33-47.

Gautam, R. & Wong, R.C.K. (2006), "Transversely isotropic stiffness parameters and their measurement in Colorado shale”. Canadian Geotechnical Journal, Vol. 43(12), 1290-1305.

Kuwano R. (1999), “The stiffness and yielding anisotropy of sand”. Ph.D. Thesis, Imperial College, London, U.K.

Kuwano, R. & Jardine, R.J. (2002), “On the applicability of cross-anisotropic elasticity to granular materials at very small strains”. Géotechnique, Vol. 52(10), 727-749.

Pietruszczak, S. & Mroz, Z. (2000), “Formulation of anisotropic failure criteria incorporating a microstructure tensor”. Computers and Geotechnics, Vol. 26(2), 105-112.

Piriyakul, K. (2007), “Anisotropic stress-strain behaviour of Belgian Boom clay in the small strain region”. Ph.D. Thesis, Ghent University, Ghent, Belgium

Schädlich, B., & Schweiger, H.F. (2012). “A multilaminate constitutive model accounting for anisotropic small strain stiffness”. International Journal for Numerical and Analytical Methods in Geomechanics, in print.

Schweiger, H.F.; Wiltafsky, C.; Scharinger, F. & Galavi, V. (2009), “A multilaminate framework for modelling induced and inherent anisotropy of soils”. Géotechnique, Vol. 59(2), 87-101.

Yimsiri, S. & Soga, K. (2000), “Micromechanics-based stress-strain behaviour of soils at small strains”. Géotechnique, Vol. 50(5), 559-571.

Yimsiri, S. & Soga, K. (2011), “Cross-anisotropic elastic parameters of two natural stiff clays”. Géotechnique, Vol. 61(9), 809–814.

XFEM-BASED GEOMECHANICAL MODELLING OF POROUS MEDIA AT SMALL SCALE

B. Sonon, B. François, T.J. Massart
Building, Architecture & Town Planning CP 194/2, Université Libre de Bruxelles (ULB), Av. F.D. Roosevelt 50, 1050 Brussels, Belgium

ABSTRACT: *The numerical characterization of the geomechanical behaviour of geomaterials (soils, rocks or concrete) at small scale requires the consideration of the complex 3D geometries of their microstructures. It implies (i) difficulties to generate complex 3D Representative Volume Elements (RVEs), and (ii) major problems to discretize properly such RVEs to solve mechanical problems. We present here an integrated framework allowing morphological studies thanks to an efficient RVE generator coupled with an XFEM setting for three-dimensional mechanical simulations. Based on level set functions and "controlled" Random Sequential Packing algorithms, a dedicated tool for the generation of RVEs has been developed. The efficiency of the method is maximized by constraining the sequential addition process with a global level set function. The obtained RVEs respect the microstructural characteristics of the materials (grain size distribution, proportions of phases…). This microstructure generation tool is illustrated by the generation of 3D RVEs corresponding to various heterogeneous geomaterials. The microstructure is then discretized using a regular mesh using level set-based extended finite element (XFEM) approaches, which allow uncoupling the meshing operations from the presence of the (complex) fine scale material interfaces. Finally, fine scale constitutive laws, including plasticity, are used in computational homogenisation procedures to model the progressive mechanical degradation of the material under stress. This is illustrated by the numerical simulation of the mechanical behaviour of a clayey sand and a rock-type material.*

1 INTRODUCTION

Heterogeneous geomaterials possess complex microstructures. The main difficulties encountered in multi-scale modeling of geomaterials, at small scale, are related to the complexity of the geometry, the natural disorder and the variety of contributing multi-physical phenomena. The computational homogenisation of such microstructures requires specific tools to take this complexity into account, both from the point of view of the availability of representative volume elements, and from the point of view of the discretization technique. In this work, those two specific aspects are addressed through the development of generic tools for the generation of controlled microstructure, based on a topology-independent geometrical representation (level set) (Sethian, 1999) and a heterogeneity independent discretization methodology, consisting in a level set-based extended finite element description (XFEM) (Sukumar et al., 2001, Moes et al., 2003). A fine-scale plastic constitutive law is used to model the progressive mechanical degradation under mechanical loading. The scale transition to obtain the macroscopic stress-strain

relationship from the computation at micro-scale is obtained through a periodic homogenization scheme (Kouznetsova et al., 2001, 2002, Massart and Selvadurai, 2012).

2 PERIODIC HOMOGENEIZATION

Scale transition techniques are used to obtain the average (macroscopic) material properties of a homogeneous equivalent material based on microstructural descriptions including fine-scale heterogeneities and the constitutive laws of each phase. Consequently, the experimental parameter identification is transferred to lower scales on which phenomenologically simpler laws can be used.

The averaged mechanical properties of a heterogeneous material can be deduced by loading a Representative Volume Element (RVE) containing the main microstructural features of the material, and solving the corresponding equilibrium problem. When a macroscopic strain E is applied to a RVE, the displacement of a point inside the RVE is given by

$$\vec{u}(\vec{x}) = E.\vec{x} + \vec{u}_f(\vec{x}) \tag{1}$$

where $\vec{x}$ is the position vector within the RVE and $\vec{u}_f$ is a fluctuation field caused by the heterogeneity of the material. Assuming that the macroscopic strain is the volume average of the fine-scale strain field ε resulting from the above equation, and accounting for a periodic fluctuation, the Hill-Mandel condition (energy equivalence between the fine-scale and macroscopic descriptions)

$$\Sigma : \delta E = \frac{1}{V}\int_V \sigma : \delta\varepsilon \; dV \tag{2}$$

implies that the macroscopic stress tensor is obtained as the volume average of the microstructural stress tensor. Considering the periodicity of the fluctuation field, the macroscopic stress tensor can next be identified based on the cell tying forces at nodes controlling the macroscopic loading as

$$\Sigma = \frac{1}{V}\int_V \sigma \; dV = \frac{1}{V}\sum_{a=1}^{4} \vec{f}^{(a)} \vec{x}^{(a)} \tag{3}$$

where the summation spans the nodes controlling the RVE loading, $\vec{f}^{(a)}$ and $\vec{x}^{(a)}$ are, respectively, the nodal force and the nodal displacement of the node (a). The periodicity of the microfluctuation field can be enforced by homogeneous linear connections between corresponding faces. In a three-dimensional body, four controlling points (denoted 1 to 4 in Fig. 1) are used to apply the macroscopic stress or deformation modes of the boundary of the RVE, provided identical meshes are used on the opposite faces of the RVE.

The RVE equilibrium problem under the macroscopic stress loading is then solved by imposing forces $\vec{f}^{(a)}$ at the controlling points, which represent the action of the neighboring continuum on the RVE. The displacements of the controlling points, energetically conjugated to the imposed controlling forces, can be used to extract the macroscopic strain. A full description of the homogenization scheme can be found in Massart and Selvadurai (2012).

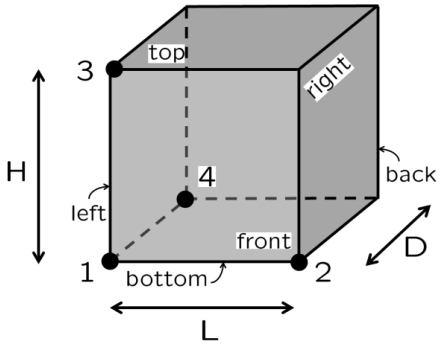

Fig 1. Control points for macroscopic quantities control on a RVE for upscaling principles

3 MICROSTRUCTURE GENERATION

The numerical modeling of the geomaterial behaviour at micro-scale requires, first, a proper representation of the microscopic morphology (at the particle scale). Two alternatives can be adopted to consider a representative microstructure: (i) the extraction of a real microstructure from the image analysis of full-field experimental methods of material observations (e.g. Computed X-Ray Tomography) (Hashemi et al., 2013) or (ii) the computed generation of microstructure respecting some constraints (e.g. prescribed volume fractions and/or grain size distributions) (Sonon et al., 2012). The main advantage of the second method is that representative microstructures can be randomly generated providing a large number of possible morphologies for a same set of constraints. Also, it does not require sophisticated techniques of sample observations.

In the present work, a specific methodology for the computed generation of microstructures has been developed. The RVE generator tool is mainly designed for granular media, possibly cemented, bridged or coated by a matrix material as well as polycrystalline media. It is based on distance fields and level set functions as presented in Sonon et al. (2012) for 2D RVEs, and extended in Sonon et al. (2013) for 3D simulations.

Three tools are combined to build an RVE starting from a random distribution of inclusions (inclusion packing, Section 3.1) that can be morphed (inclusion morphing, Section 3.2) to achieve specific features, and completed with a specific binding phase (Coating/bridging paste, Section 3.3).

3.1 Inclusion packing

The inclusion packing is the first step of the RVE generation method that gives the basis for the microstructural spatial arrangement. It allows incorporating prescribed volume fractions and grain size distributions as input parameters. The geometry used for the shape of inclusions is arbitrary and can be randomly generated through a parameterization or explicitly defined from existing data (e.g. in order to use data from Computed X-Ray Tomography).

The problem of filling a container with a given volume fraction of inclusions while respecting prescribed size distributions and grain shapes is achieved here using a Random Sequential Addition (RSA) of inclusions (Cooper, 1988), improved by the use of distance fields. The method is called LS-RSA (for Level-Set controlled Random Sequential Addition, Sonon et al. (2012)). With this original method, the efficiency of the sequential addition of inclusion is drastically improved using distance fields. Instead of a purely random trial position, a set of discrete positions satisfying a priori the non-overlapping and neighboring distance conditions is used to select new inclusion locations. Consequently, trial positions are

never rejected, as it is often the case for the classical RSA algorithm (mainly when dense packing must be reached).

The available zone for the addition of the next inclusion is built using the nearest neighbor distance function $LS_1(\vec{x})$ (see Fig. 2a) which is maintained on a structured grid of points $\vec{x}_n$ at each inclusion addition. The radius r of the smallest enclosing circle (or sphere) of the new inclusion is used as an indicator of its size. The positions on the grid leading to overlap with existing inclusions can be excluded for the random inclusion positions by allowing selection only among the points of the grid satisfying the condition (Fig.2a)

$$LS_1(\vec{x}_n) > r \tag{4}$$

This allows the addition of a new inclusion at each trial, and the generation cost is therefore not linked to any probability relative to the actual density, but rather to the number of added inclusions. Additional neighboring distance conditions can be enforced using $LS_1(\vec{x})$ such as for instance

$$nn_{\min} + r < LS_1(\vec{x}_n) < nn_{\max} + r \tag{5}$$

where $nn_{\min}$ and $nn_{\max}$ are the minimum and maximum distance imposed from the first neighbor of the added inclusion (Fig. 2a). To increase packing density, the spatial organization has to be optimized by minimizing the distances of the added inclusion to its second nearest neighbor in 2D and its third nearest neighbors in 3D. The corresponding distance functions $LS_2(\vec{x})$ and $LS_3(\vec{x})$ are used for this purpose with the same type of condition (Fig. 2b).

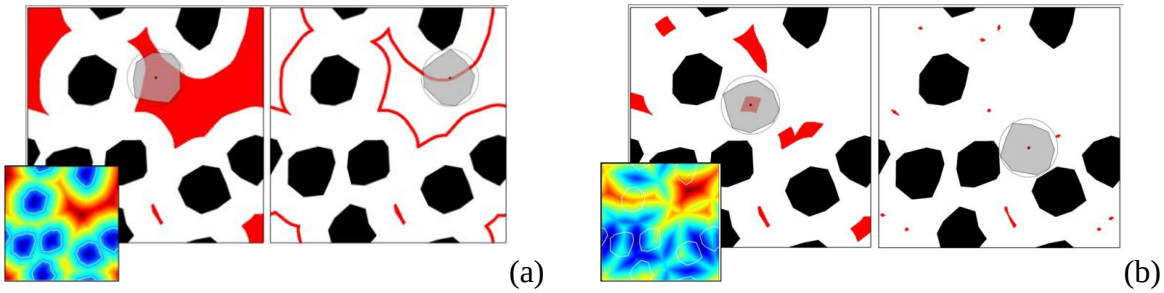

Fig 2. (a) Non-overlap and first neighbor distance criteria to restrict the random position of the new inclusion to be added (the function $LS_1(\vec{x})$ is represented in the insert), (b) First and second neighbor distance criteria to optimize spatial organization to obtain dense packing (the function $LS_2(\vec{x})$ is represented in the insert)

3.2 Inclusion morphing

Marginal corrections required to adjust the inclusion volume fraction or shapes and more substantial modifications allowing to produce polycrystalline or cellular microstructures motivate the development of a tool enabling the morphing of inclusions once their population is entirely generated by sequential addition. At this stage, the inclusions neighborhood is completely determined and can be used to modify their shape according to inter-inclusion distance rules. A complete expansion of inclusions until vanishing of the inter-grain joint thickness allows forming polycrystal-like microstructures.

The morphing technique is strongly based on level set functions. The $LS_1(\vec{x}_n)$ and $LS_2(\vec{x}_n)$ functions built during the sequential addition process are used to construct a function $O(\vec{x}_n)$ that can be contoured to extract updated shapes of the inclusions. The function

$$O(\vec{x}_n) = LS_1(\vec{x}_n) - LS_2(\vec{x}_n) \tag{6}$$

vanishes at points of equal distance between two nearest inclusions and is negative elsewhere. The zero level set of this function thus determines a Voronoï-like diagram, each cell enclosing an inclusion and points closer to it than to other inclusions. If the initial inclusion distribution is a dense arrangement of mono-sized spheres, the produced grains are convex and the result is exactly a Voronoï diagram (Fig. 3a). The use of multi-sized arbitrary shaped polyhedra leads to disordered microstructures (Fig. 3b). A joint between the grains with constant thickness w can be obtained by considering the function $O(\vec{x}_n) = LS_1(\vec{x}_n) - LS_2(\vec{x}_n) + w$.

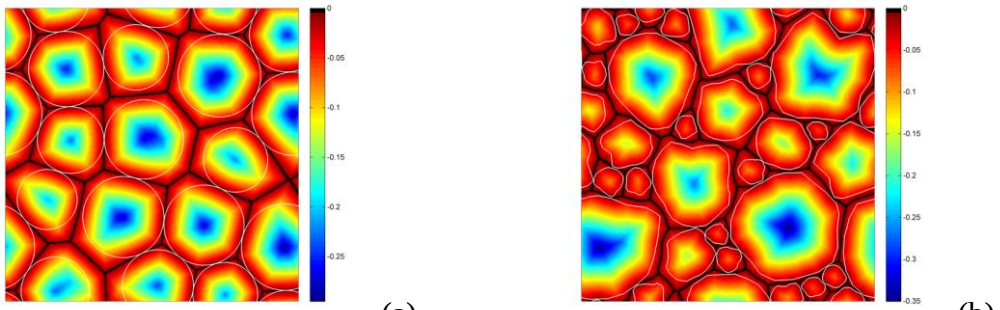

(a) (b)

Fig 3. (a) Convex Voronoï-like cells produced by a mono-sized spheres packing, (b) disordered cells produced by an arbitrary shaped multi-sized inclusion packing

3.3 Coating/bridging paste

The presented methodology also allows generating coatings and bridges around inclusions. It may reproduce, for instance, the clayey bridge between coarse particles of sand in clayey sand. Cement paste of concretes or precipitate coating in cemented rocks are others examples that can correspond to this coating paste.

On the one hand, a uniform coating of thickness w is trivially extracted with the w level set of $LS_1(\vec{x})$. On the other hand, bridges between two neighboring inclusions can be generated provided the inter-distance between two potentially bridged grains is small enough. The function $O(\vec{x}_n) = LS_1(\vec{x}_n) - LS_2(\vec{x}_n)$ (Fig.4) contains explicitly in each point n the distance between the two nearest point via n. The zero level set of $O(\vec{x}_n) = LS_1(\vec{x}_n) - LS_2(\vec{x}_n) - b$ give the geometry of bridges linking grains closer to each other than b.

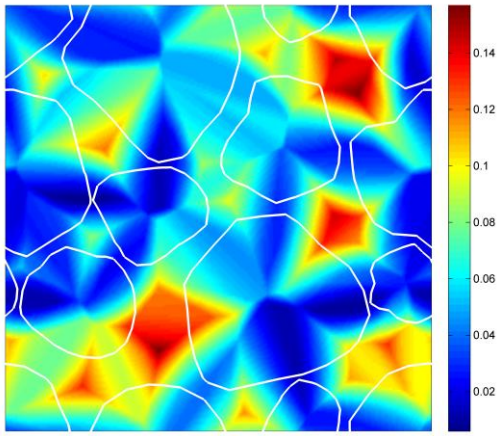

Fig 4. The function $O(\vec{x}_n) = LS_1(\vec{x}_n) - LS_2(\vec{x}_n)$ explicitly contains the information to create bridging past between inclusions.

4 MECHANICAL MODEL

4.1 X-FEM Computation

The complexity of generating finite element meshes for the generated RVEs motivates the use of an alternative discretization method. The eXtended Finite Element Method (Sukumar et al., 2001, Moës et al., 2003), that does not require meshes conforming to the material boundaries, is therefore used. In addition to be defined as an extension of the standard finite element scheme, this method uses the level set formalism to describe the RVE geometry, which allows its seamless integration with the RVE generator.

The principle of XFEM is to use a non-conforming regular mesh with additional degrees of freedom related to additional shape functions (denoted the enrichment) introducing the strain jumps induced by material heterogeneities. This treatment, concentrated on finite elements intersected by a material interface (e.g. inclusion/matrix boundary), uses signed distance functions to construct the enrichment and to subdivide elements by material at the stiffness integration stage. The interpolation of each displacement field components therefore reads

$$u_{XFEM}(x) = \sum_i N_i(x) d_i + \sum_i N_j(x) \Psi(x) a_j \tag{7}$$

where the first term represents the usual finite element polynomial interpolation containing the standard shape functions as a partition of unity. The second term introduces the XFEM enrichment with a_j the additional unknowns and $\Psi(x)$ the enrichment functions. For heterogeneous materials, the LS_1 level set (distance) function was shown to introduce the required strain jump at the material boundary. The XFEM methodology implemented in a 3D setting is coupled with periodic homogenization and fully compatible with the RVEs generated using the tools presented previously.

4.2 Elasto-plastic constitutive model

The elastic part of the deformation is considered through classical linear elasticity including constant values of the Young modulus and the Poisson ratio. The limit between the elastic and the plastic domain is represented by a Drucker-Prager yield surface:

$$f \equiv q - Mp - k = 0 \quad \text{with} \quad M = \frac{6\sin\phi}{3-\sin\phi} \quad \text{and} \quad k = \frac{6c\cos\phi}{3-\sin\phi} \tag{8}$$

where p and q are the mean stress and the deviatoric stress and c and ϕ are the cohesion and the friction angle, respectively. An associate flow rule is considered producing dilatancy upon plastic shearing (the dilatancy angle is equal to friction angle):

$$\dot{\varepsilon}_{ij}^{p} = \dot{\lambda}^{P} \frac{\partial f}{\partial \sigma_{ij}} \tag{9}$$

Progressive hardening is introduced through the evolution of the cohesive term with the deviatoric strain (corresponding to the plastic multiplier $\dot{\lambda}^{P}$):

$$k = k_0 + A\,\dot{\lambda}^{P} \tag{10}$$

5 RESULTS

5.1 Clayey sand

In this section, we deduce the macroscopic behaviour of a lime-treated clayey sand through the consideration of its mechanical behaviour at micro-scale. To achieve this, a representative microstructure was generated through the microstructure generation tool detailed in Section 3. Periodic conditions have been applied on the boundaries of the RVE. Then, the mechanical problem has been addressed through the XFEM scheme considering a linear elastic response of the sand grains and elasto-plastic behaviour of the clay matrix. Material parameters are reported in Table 1. The inclusion packing generates the inert grain (considered >2μm) in agreement with the grain size distribution of inert particles. A bridging paste is introduced to represent the clayey matrix corresponding to the soil particles <2μm. This distinct phase contains the clay particles, a certain quantity of lime from the treatment and micro-voids including water and air. This phase plays an important cohesive role, acting as a matrix, coating and bridging inert grains together.

This framework allows modeling, observing and understanding the basic mechanisms of plasticity propagation in the microstructure as well as studying the evolution of macroscopic elastic limit as a function of the morphology. A first application, assuming a 2D plane-strain problem, compares the macroscopic response of two specimens containing two different clay contents under oedometric compression (application of vertical loading while macroscopic radial displacements are constrained). Results are depicted in Figure 5. It is shown that even if the macroscopic stress state is mainly isotropic (with a low deviatoric component compared to the mean stress), the local microstructure contains many zones in which deviatoric strains occur. This is particularly the case in the clayey bridging zones where the distance between two sand particles is small. The specimen with the lower clay content exhibits the softer response and the lower elastic limit. This may seem counterintuitive because clay is the

compressible phase in the medium. However, this feature of behaviour has also been observed experimentally. Until a certain quantity, clay has a positive effect on the stiffness and strength of clayey sand. Clay reinforces the particles contacts, provides cohesion and avoids strain localization in the particle contacts.

The microstructure of a soil is highly three-dimensional and there is no trivial way to find a 2D mechanically equivalent description of a given 3D sample. Some morphological aspects concerning voids topology only emerge in 3D and the number of kinematically admissible mechanisms is also different. There is also no comparison possible in terms of volume fractions. Consequently, the clayey sand application is generalized in 3D with a clay content of 30 %. The same methodology is applied. However, up to now, due to computation time constraints, plasticity was not considered and a purely elastic computation is performed. Even if the behaviour of the clay matrix is not perfectly representative of real plastic clay, some general trends can be observed in terms of strain distribution in the microstructure (Figure 6). Strains are concentrated in the short clay bridges. The largest grains carry the main part of the stress. Chain forces are mainly developed across those large grains. Consequently, the largest strains occur mainly in the clayey bridges surrounding largest sand grains (see Figure 6, right).

Table 1. Material parameters used in the different mechanical computations

Materials	E [GPa]	υ [-]	c [MPa]	ϕ [°]	A [GPa]
Clayey sand 2D					
Sand particles	10	0.1	-	-	-
Treated clay matrix	0.5	0.2	0.5	23°	Perfectly plastic
Clayey sand 3D					
Sand particles	10	0.1	-	-	-
Treated clay matrix	0.5	0.2	-	-	-
Rock-type material					
Grains	60	0.1	-	-	-
Joints	30	0.3	40	17	1

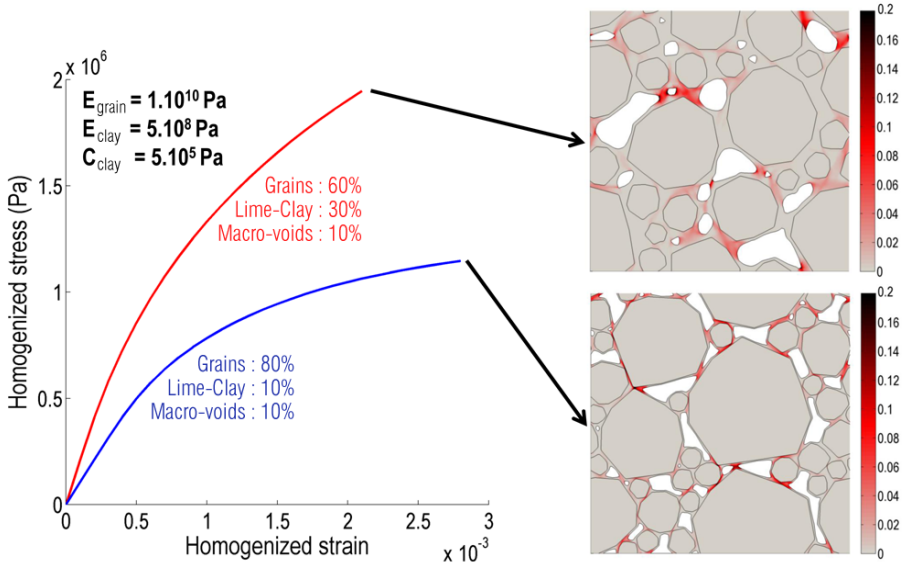

Fig 5. Macroscopic behaviour of lime-treated clayey sand upon oedometric compression interpreted from micro-scale computations. Focus on the effect of the clay content. The snapshots on the right represent the distribution of vertical strain in the microstructure. The size of RVE is 10 mm along each direction.

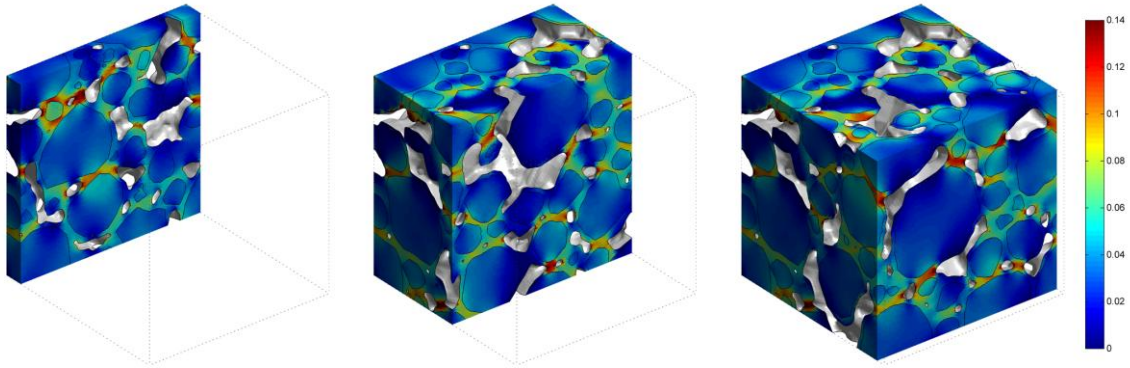

Fig 6. Vertical strain distribution obtained from 3D elastic computation of lime-treated clayey sand upon oedometric compression. The size of RVE is 10 mm along each direction.

5.2 Rock-type material

As opposed to soil-type materials, rock-type materials do not exhibit macro-voids and the material can be considered as a continuum medium, even at micro-scale. The existing voids are included in the rock matrix. A 3D microstructure made of grains and large joints with a grain volume fraction of 58% was generated with the LS-RSA tool (Figure 7) and subjected to triaxial loading. The grains do not present any preferential orientation. They are assumed purely elastic, whereas a plastic behaviour is assumed in the joints. The set of parameters used in the computations is defined in Table 1. The applied loading follows a typical triaxial test with a strong confinement. A confinement of 100 MPa is first applied in all directions, followed by an increase of the axial stress, the other stress components remaining fixed. This high confining stress is used to avoid any convergence problem in the mechanical problem, and to keep the local strain distribution consistent with a small strain description. The strain are still concentrated in the weakest phase (the joints) while the grains remain almost unstrained. The plastic dilatancy in the joints produces high dilatant volumetric strains. The macroscopic mechanical response of the RVE is depicted in Figure 8.

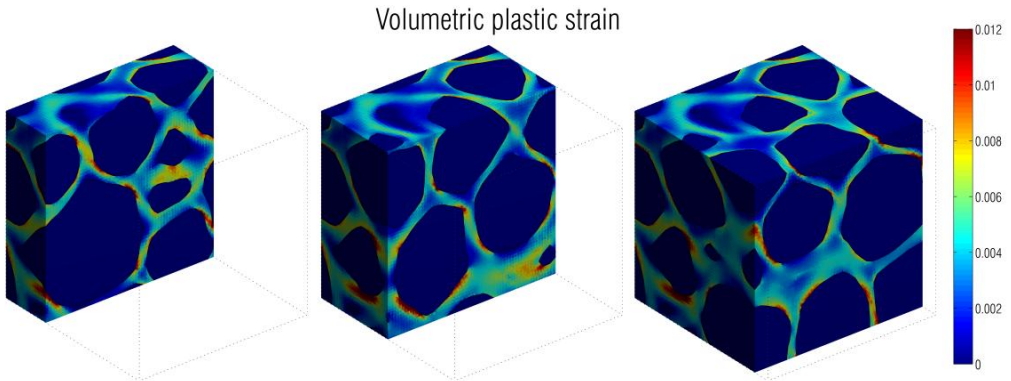

Fig 7. Volumetric strain distribution obtained in the rock-type material at 350 MPa of deviatoric stress. Strains occur in the joints. The size of RVE is 10 mm along each direction.

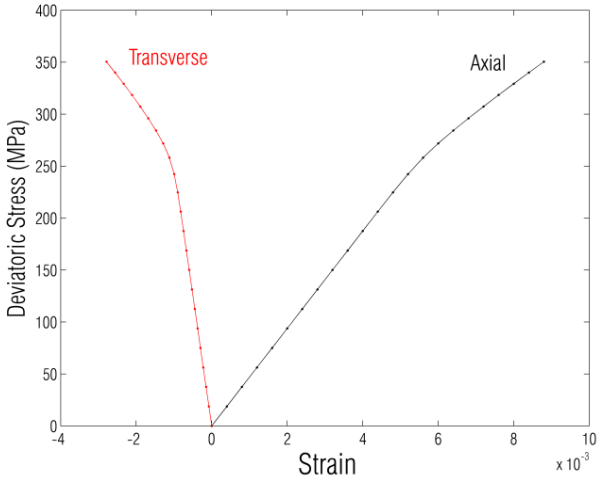

Fig 8. Homogenized response of the RVE. Mechanical response under triaxial conditions depicting the average deviatoric stress applied as a function of the axial and transverse strains.

6 CONCLUSIONS

An efficient methodology including microstructural RVE generation of porous media combined with a XFEM computational scheme has been proposed to investigate the mechanical properties of heterogeneous geomaterials at small scale. A periodic homogenization scheme allows the scale transition in order to deduce homogenized response of the material from a macroscopic point of view. This framework allows understanding the basic mechanisms of plasticity propagation which control the mechanical response at macroscopic (laboratory) scale. In companion works (Massart and Selvadurai, 2012, Sonon et al., 2013), the obtained local damage propagation from the mechanical computations is coupled with fluid transport modeling, which allows identifying microstructural features responsible for permeability evolution due to mechanical degradation.

ACKNOWLEDGEMENT

The first author gratefully acknowledges F.R.S-FNRS Belgium for funding through the FRIA grant 5.0.011.12.F.

REFERENCES

Cooper D.W. (1988). Random-sequential-packing simulations in three dimensions for spheres, Phys. Rev. A 38, 522–524.

Hashemi M.A., Khaddour G., François B., Massart T.J., Salager S. (2013). A tomographic imagery segmentation methodology for multi-phase granular materials based on simultaneous region growing. Submitted.

Kousnetsova V., Brekelmans W.A.M., Baaijens F.T.P. (2001). An approach to micro–macro modeling of heterogeneous materials, Comput. Mech. 27, 37–48.

Kouznetsova V., Geers M.G.D., Brekelmans W.A.M. (2002). Multi-scale constitutive modelling of heterogeneous materials with a gradient-enhanced computational homogenization scheme, Int. J. Numer. Methods Engrg. 54, 1235–1260.

Massart T.J., Selvadurai A.P.S. (2012). Stress-induced permeability evolution in a quasi-brittle geomaterial, J. Geophys. Res., 117 B07207.

Moes N., Cloirec M., Cartraud P., Remacle J.F. (2003). A computational approach to handle complex microstructure geometries, Comp. Meth. Appl. Mech. Engng. 192(28-30), 3163-3177.

Sethian J.A. (1999). Level Set Methods and Fast Marching Methods, Cambridge University Press, New York.

Sonon B., François B., Massart T.J. (2012). A unified level set based methodology for fast generation of complex microstructural multi-phase RVEs, Comp. Meth. Appl. Mech. Engng. 223-224, 103-122.

Sonon B., François B., Massart T.J. (2013). Generation of complex three-dimensional RVEs for computational homogenisation, In preparation.

Sonon B., François B., Selvadurai A.P.S., Massart T.J. (2013). XFEM modelling of degradation-permeability coupling in complex geomaterials. 13th International Conference on Fracture.

Sukumar N., Chopp D.L., Moës N., Belytschko T. (2001). Modeling holes and inclusions by level sets in the extended finite-element method. Comput. Methods Appl. Mech. Engrg. 190, 6183–6200.

THE INCORPORATION OF NEW ISOTROPIC AND KINEMATIC HARDENING RULES IN AN ANISOTROPIC CONSTITUTIVE MODEL

Panagiotis Sitarenios
School of Civil Engineering, National Technical University of Athens, Athens, Greece

Georgios Belokas
School of Civil Engineering, National Technical University of Athens, Athens, Greece

Michael Kavvadas
School of Civil Engineering, National Technical University of Athens, Athens, Greece

ABSTRACT: *The paper presents a new constitutive model to describe the mechanical behaviour of uncemented anisotropically consolidated clayey soils, by extending and improving previous models developed by the authors (Kavvadas 1982; Belokas & Kavvadas 2010) with respect to the anisotropic compression and the uniqueness of critical state. The model incorporates a rotated distorted ellipsoidal yield surface, a non-associated flow rule to reproduce zero total horizontal strains under K_0 conditions and a new mixed hardening rule consisting of an isotropic part to control the evolution of the size of the yield surface and a rotational - distortional part to describe the evolution of anisotropy. The model is capable of reproducing a) Intrinsic Compression Curves that depend on the degree of developed anisotropy and b) unique critical state conditions. The model capabilities are demonstrated through a series of numerical analyses.*

1 INTRODUCTION

The analysis of geotechnical boundary value problems using, either finite element or finite differences methods, requires the use of proper constitutive models, to provide the stress - strain relationship. Most of the models provided in the literature are formulated within the fundamental framework of Critical State Soil Mechanics (CSSM), based on the Modified Cam Clay (MCC). Within the same framework, quite a few models have been proposed to describe the behaviour of anisotropically consolidated soils (Kavvadas 1982; Dafalias 1986; Newson & Davies 1996; Kavvadas & Amorosi 2000; Wheeler et al. 2003; Taiebat & Dafalias 2013). The most common shortcomings of anisotropic models existing in the literature are: a) the inability to reproduce compression lines that depend on the level of induced anisotropy, b) the inability to reproduce unique critical state conditions, and finally c) the inability to simulate strain softening response usually observed under triaxial compression after K_0 consolidation.

In this paper a new constitutive model is proposed to describe the mechanical behaviour of uncemented anisotropically consolidated clayey soils, by extending and improving previous models developed by the authors (Kavvadas 1982; Belokas & Kavvadas 2010). The model incorporates new isotropic and kinematic hardening rules with an eye towards addressing the

aforementioned common modelling shortcomings. The proposed model can either be used independently to simulate the behaviour of anisotropically consolidated soils, or incorporated in advanced models for anisotropic structured - natural soils, to provide the behaviour of the Intrinsic Compression Envelope, where an initially structured soil should lie after substantial structure degradation (Belokas & Kavvadas 2010).

2 DESCRIPTION OF THE MODEL

The proposed model is formulated within the framework of incremental, rate - independent, theory of plasticity. All stresses are effective stress and the primes have been dropped for simplicity. The dots over symbols indicate an infinitesimal increment of the corresponding quantity, while bold - face symbols indicate tensors and : indicates tensorial product. The model equations are given in the multiaxial space.

2.1 Yield Surface

The model incorporates a single yield surface, that plays the role of a plastic yield envelope, differentiating between elastic and elastoplastic stress states. Any stress increment inside the yield surface is assumed to be elastic and results to fully reversible elastic strains, while, any elastoplastic stress increment leads to an updated position on the yield surface. The yield surface equation initially proposed by Kavvadas (1982) is used:

$$f(\sigma, \boldsymbol{s}, \alpha, \boldsymbol{b}) = \frac{1}{c^2}(\boldsymbol{s} - \sigma\boldsymbol{b}) : (\boldsymbol{s} - \sigma\boldsymbol{b}) - \sigma(2\alpha - \sigma) \tag{1}$$

where σ is the mean effective stress, $\boldsymbol{s}$ is the deviatoric stress tensor, α is the isotropic hardening variable controlling the size of the yield surface, $\boldsymbol{b}$ is the kinematic hardening variables tensor controlling the orientation of the yield surface in all deviatoric planes, and finally c a material constant defining the ratio of the axes of the yield surface.

As depicted in fig. 1, eq. 1 represents a distorted ellipsoid with its main axis along the direction $\boldsymbol{\beta} = \boldsymbol{b} + \boldsymbol{I}$, with $\boldsymbol{I}$ being the unit second order tensor. It is assumed from the beginning that any soil element that has been normally consolidated along a radial stress path with direction $\boldsymbol{\beta}$ lies on the tip of a distorted yield surface with its axis oriented along the same direction $\boldsymbol{\beta}$. It is evident that for any isotropically normally consolidated soil element the direction $\boldsymbol{\beta}$ coincides with the hydrostatic axis, meaning that the second order symmetrical tensor $\boldsymbol{\beta}$ vanishes, and thus eq. 1 reduces to the MCC yield surface.

2.2 Elasticity

To describe the behaviour inside the yield surface poro-elasticity is employed. The elastic component of the strain increment is assumed to be linearly related to the corresponding effective stress increment:

$$\dot{\sigma}^{\mathbf{e}} = K\dot{\epsilon}^{\mathbf{e}} \tag{2a}$$

$$\dot{\boldsymbol{s}}^{\mathbf{e}} = 2G\dot{\boldsymbol{e}}^{\mathbf{e}} \tag{2b}$$

The bulk modulus K comes from the CSSM swelling lines and takes the form:

$$K = \frac{\upsilon\sigma}{\kappa} \tag{3}$$

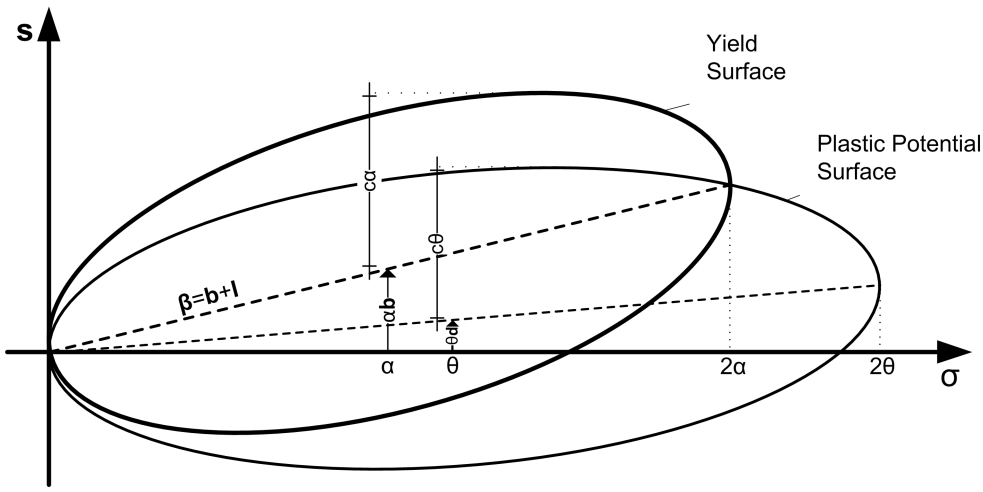

Fig. 1. The yield and the plastic potential surfaces of the proposed model.

where $v = 1 + e$ is the specific volume, κ the MCC compressibility parameter representing the slope of the swelling line in the $v - ln\sigma$ plane and finally σ the mean effective stress, resulting to a pressure dependant bulk modulus. The shear modulus is given according to isotropic linear elasticity, which leads to a relationship with the bulk modulus and the Poisson's ratio ν, according to eq. 4. This also results to a pressure dependant modulus.

$$G = \frac{3K(1-2\nu)}{2(1+\nu)} \tag{4}$$

2.3 Flow Rule

The flow rule determines the plastic strain increment $\dot{\boldsymbol{\epsilon}}^{\mathbf{p}}$ and generally, in incremental plasticity, takes the following form:

$$\dot{\boldsymbol{\epsilon}}^{\mathbf{p}} = \dot{\Lambda}\boldsymbol{P} \tag{5}$$

where $\dot{\Lambda} = \frac{1}{H}\left(\boldsymbol{Q} : \dot{\boldsymbol{\sigma}}\right)$ the plastic multiplier, H the plastic modulus defined in a later section, $\boldsymbol{P}$ the plastic potential tensor and $\boldsymbol{Q} = \left(Q, \boldsymbol{Q}^{\prime}\right) = (\frac{\partial f}{\partial \sigma}, \frac{\partial f}{\partial \boldsymbol{s}})$ the gradient of the yield surface:

$$\frac{\partial f}{\partial \sigma} = 2(\sigma - \alpha) - \frac{2}{c^2}\boldsymbol{b} : (\boldsymbol{s} - \sigma\boldsymbol{b}) \tag{6a}$$

$$\frac{\partial f}{\partial \boldsymbol{s}} = \frac{2}{c^2}(\boldsymbol{s} - \sigma\boldsymbol{b}) \tag{6b}$$

The $\dot{\Lambda}$ and $\boldsymbol{P}$ give the magnitude and the direction of plastic strain increment, respectively. The plastic potential tensor may either be directly assumed, using a proper mathematical nomenclature, or defined as the gradient of the plastic potential function. In the latter case, if the plastic potential function is assumed to coincide with the yield function, the selected flow rule is an associated flow rule, while in any other case, a non-associated flow rule is adopted.

Both options have been widely used in anisotropic constitutive models existing in the literature. Dafalias (1986), Kavvadas & Amorosi (2000) and Wheeler et al. (2003) incorporate associated flow rules. In contrast authors like Kavvadas (1982), Newson & Davies (1996), Dafalias et al. (2006) and Belokas & Kavvadas (2010) adopt a non-associated flow rule. The main idea behind whether selecting an associated or an non-associated flow rule lies on the orientation of

the yield surface. If the orientation of the yield surface during a radial consolidation stress path tends towards the slope of the imposed stress path then the plastic dilatancy predicted by an associated flow rule is unrealistic, especially under K_0 conditions. For that reason authors that use an associated flow rule (Dafalias 1986; Wheeler et al. 2003) incorporate hardening rules that bound the rotation of the yield surface to a slope smaller than the stress ratio imposed.

In the presented model a non-associated flow rule is selected, with the plastic potential tensor $\boldsymbol{P}$ being defined as the gradient $\boldsymbol{P} = \left(P, \boldsymbol{P}^{\prime}\right) = \left(\frac{\partial g}{\partial \sigma}, \frac{\partial g}{\partial \boldsymbol{s}}\right)$ of the following plastic potential function:

$$g(\sigma, \boldsymbol{s}, \theta, \boldsymbol{d}) = \frac{1}{c^2}(\boldsymbol{s} - \sigma \boldsymbol{d}) : (\boldsymbol{s} - \sigma \boldsymbol{d}) - \sigma(2\theta - \sigma) \tag{7}$$

where σ is the mean effective stress, $\boldsymbol{s}$ is the deviatoric stress tensor, θ is the size of the Plastic Potential Surface (PPS), $\boldsymbol{d}$ is the tensor controlling the orientation of the PPS in all deviatoric planes, and finally c the same material constant defining the ratio of the axes of the ellipsoid that was used for the yield surface. The plastic potential function assumed, has the same mathematical form with eq. 1 and thus, it also describes a rotated distorted ellipsoid (fig. 1), with a similar shape to the yield function. Differentiating eq. 7, the partial derivatives comprising the plastic tensor are:

$$\frac{\partial g}{\partial \sigma} = 2(\sigma - \theta) - \frac{2}{c^2}\boldsymbol{d} : (\boldsymbol{s} - \sigma \boldsymbol{d}) \tag{8a}$$

$$\frac{\partial g}{\partial \boldsymbol{s}} = \frac{2}{c^2}(\boldsymbol{s} - \sigma \boldsymbol{d}) \tag{8b}$$

The orientation tensor $\boldsymbol{d}$ is assumed to be analogous to its yield surface counterpart $\boldsymbol{b}$ according to eq. 9.

$$\boldsymbol{d} = \frac{1}{\chi}\boldsymbol{b} \tag{9}$$

Parameter χ that controls this analogy is defined through a calibration process, described in a following section, based on the requirement for zero horizontal total strains under a K_0 consolidation stress path. The size of the plastic potential function θ is calculated using eq. 10 based on the requirement that the PPS must pass through the current stress state.

$$\theta = \frac{1}{2}\left(\sigma + \frac{\frac{1}{c^2}(\boldsymbol{s} - \sigma \boldsymbol{d}) : (\boldsymbol{s} - \sigma \boldsymbol{d})}{\sigma}\right) \tag{10}$$

2.4 Hardening Rule

The proposed model incorporates a mixed hardening rule, comprising of an isotropic hardening component to describe the evolution of the hardening variable α and a kinematic (rotational - distortional) component to control the evolution of the anisotropy tensor $\boldsymbol{b}$.

Isotropic Hardening

Most of the anisotropic models proposed in the literature adopt the MCC isotropic hardening rule. In MCC the hardening rule controls the size of a non-rotating isotropic ellipse and thus, always corresponds to the isotropic compression curve of the material. Adopting exactly the same relationship to describe the evolution of the tip of a distorted yield surface, has the major shortcoming that under any radial stress path the same isotropic curve will be produced in the $v - \sigma$ plane, irrespective of the developed anisotropy. Although this is a major deficit of most of

the anisotropic constitutive models existing in the literature, it has drawn little attention. Newson & Davies (1996) proposed an equation to describe the difference on the position of the ICC depending on the developed degree of anisotropy, but didn't provide any further information on whether and how this equation has been incorporated to their model. Belokas & Kavvadas (2010) presented an anisotropic constitutive model for structured soils and introduced into their formulation an Intrinsic Compressibility Framework (ICF) (Belokas & Kavvadas 2011) to describe the behaviour of the structureless material and the dependence of the consolidation curve on the developed anisotropy.

According to the aforementioned framework a structureless material subjected to a radial consolidation stress path, moves along Intrinsic Compression Curves (ICC) which are assumed to be parallel straight lines in the $v - \ln\sigma$ plane (fig. 2), with slope described by the MCC compressibility parameter λ:

$$v = N_n - \lambda \ln\sigma \tag{11}$$

The relative location of the ICC lines is described by the parameter N_n which is assumed to

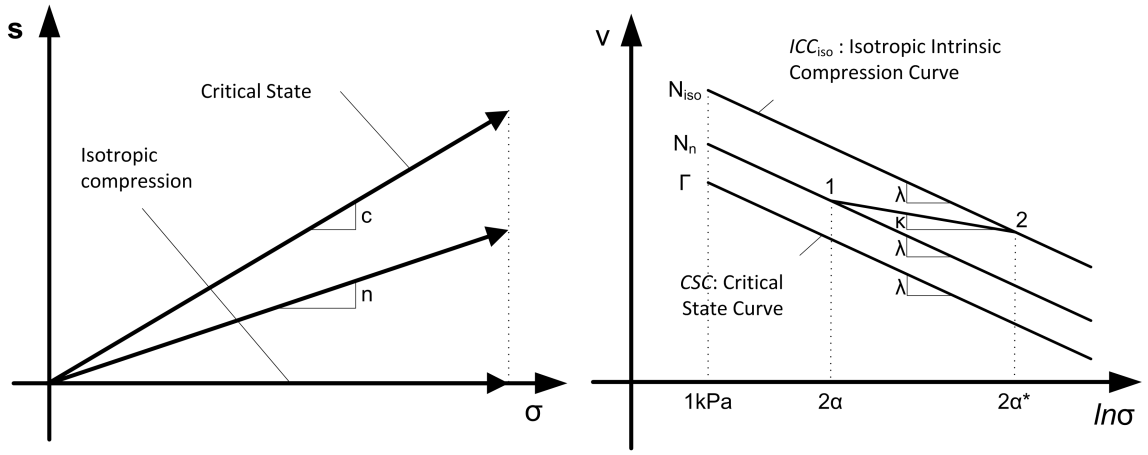

Fig. 2. Radial stress paths and their corresponding Intrinsic Compressibility Curves ICC_n in the $v - \ln\sigma$ plane.

depend on the consolidation stress ratio ($n = \sqrt{\boldsymbol{b} : \boldsymbol{b}}$):

$$N_n = \Gamma + (N_{iso} - \Gamma)\left(1 - \sqrt{\frac{\boldsymbol{b} : \boldsymbol{b}}{c^2}}\right)^r \tag{12}$$

where N_{iso}, Γ correspond to the N_n value of the isotropic ICC and the CSL respectivelly, while r is a material constant. Belokas & Kavvadas (2010) implemented the aforementioned ICF to their model in an rather approximate way, by assuming directly on the incremental form of their hardening rule. The major disadvantage of this approach is that the hardening rule adopted does not ensure that when anisotropy has stabilized, under a given radial stress path, the material state will lie exactly on the corresponding ICC. In an attempt to address this problem, in the proposed model a new isotropic hardening rule is derived starting from the desired behaviour in the $v - \ln\sigma$ plane, as was initially done in MCC.

Let's examine the case of a soil being radially consolidated under a stress path with slope ($n = \sqrt{\boldsymbol{b} : \boldsymbol{b}}$). After substantial plastic straining under stabilized anisotropy, the soil stress state will lie on the tip of the yield surface, where the mean effective stress has the value 2α. In the $v - \ln\sigma$ plane the material state should lie on the ICC that corresponds to the applied anisotropy

(eq. 12). Any material state on a given ICC (point 1 in fig. 2) can be projected on the Isotropic ICC using a proper swelling line of slope κ. This state is depicted as point 2 in fig. 2 and corresponds to a mean effective stress $2\alpha^*$. After some algebra it can be found that the connection between the two states is:

$$\alpha = \exp\left(\frac{N_{iso} - N_n}{\kappa - \lambda}\right)\alpha^* \tag{13}$$

Substituting N_n from eq. 12 and differentiating, the increment of the hardening variable α is defined by the following form:

$$\dot{a} = A\dot{a^*} + \dot{A}a^* \tag{14}$$

where:

$$A = exp\left(\frac{(\Gamma - N_{iso})\left(1 - \left(1 - \sqrt{\frac{\boldsymbol{b}:\boldsymbol{b}}{c^2}}\right)^r\right)}{\lambda - \kappa}\right) \tag{15a}$$

$$a^* = \frac{1}{2}exp\left(\frac{N_{iso} - v - \kappa \ln\sigma}{\lambda - \kappa}\right) \tag{15b}$$

$$\dot{a^*} = \frac{v}{\lambda - \kappa}a^*\dot{\Lambda}P \tag{15c}$$

$$\dot{A} = \frac{Ar(\Gamma - N_{iso})}{\lambda - \kappa}\left(1 - \sqrt{\frac{\boldsymbol{b}:\boldsymbol{b}}{c^2}}\right)^{r-1}\frac{1}{\sqrt{\frac{\boldsymbol{b}:\boldsymbol{b}}{c^2}}}\frac{\boldsymbol{b}:\dot{\boldsymbol{b}}}{c^2} \tag{15d}$$

As can be observed, the classical MCC isotropic hardening rule (eq. 15c) has also been incorporated in the proposed model, to describe the evolution of α^* that always lie on the Isotropic ICC, while the hardening variable α has a straight forward dependance on the developed level of anisotropy.

Kinematic Hardening

To control the evolution of anisotropy, a kinematic hardening rule is incorporated to describe the change in the oriantation of the yield surface. As observed in eq. 16 the proposed rule consists of two parts $\dot{\boldsymbol{b}_o}$ and $\dot{\boldsymbol{b}_d}$.

$$\dot{\boldsymbol{b}} = \dot{\boldsymbol{b}}_{\mathbf{o}} + \dot{\boldsymbol{b}}_{\mathbf{d}} \tag{16}$$

The first part $\dot{\boldsymbol{b}_o}$ is given by eq. 17 and is the rule initially proposed by Kavvadas (1982). This part of the hardening rule is responsible for rotating the yield surface towards the slope of the stress path imposed. The magnitude of anisotropy change is proportional to the plastic volumetric strain increment $\dot{\epsilon}^{\mathbf{p}}$, while the direction of the change is assumed parallel to the direction of $(\boldsymbol{s} - \sigma\boldsymbol{b})$. With the proposed kinematic rule anisotropy evolves always when a stress path different than radial is imposed, thus causing the yield surface to distort, and stops evolving only when a radial stress path is imposed and the yield surface has already get oriented towards the same direction.

$$\dot{\boldsymbol{b}}_{\mathbf{o}} = \frac{1}{a}\psi(\boldsymbol{s} - \sigma\boldsymbol{b})\dot{\epsilon}^{\mathbf{p}} \tag{17}$$

The second part $\dot{\boldsymbol{b}_d}$ is a new addition based in a novel idea proposed in the paper. As pointed out by Taiebat & Dafalias (2013) most of the rotational hardening rules proposed in the literature, for models that incorporate inclined yield surfaces, fail to reproduce unique critical state

in the $v - \ln\sigma$ plane. Moreover, Wheeler et al. (2003), state that the inclination of the yield curve at critical state should be solely dependent on stress conditions at the critical state and should be independent both of initial yield curve inclination and of the stress path taken to a critical state, in the sense that a critical state corresponds to a condition where fabric is being continuously destroyed and recreated. Extending the above idea we propose that a critical state should correspond to an isotropic yield surface like MCC, because a) isotropic corresponds to a random fabric and thus can describe the idea of continued destroyance and recreation of fabric, and b) according to CSSM an isotropic yield surface has been well established to describe the critical state of an initially isotropically consolidated material and thus should be also capable of describing the critical state of the same material initially anisotropically consolidated for the critical state to be independent of the initial degree of anisotropy and of the undertaken stress path. To mathematically implement this idea to the proposed model a new term $\dot{\boldsymbol{b}}_{\boldsymbol{d}}$ is introduced into the model's hardening rule and is assumed to have the following form:

$$\dot{\boldsymbol{b}}_{\mathbf{d}} = -\frac{1}{a^2}\boldsymbol{b}\left(\boldsymbol{s}-\sigma\boldsymbol{b}\right):\left(\boldsymbol{s}-\sigma\boldsymbol{b}\right)\left(\zeta_{\mathrm{v}}^{\mathrm{p}}\left|\dot{\epsilon}_{\mathrm{v}}^{\mathrm{p}}\right|+\zeta_{\mathrm{q}}^{\mathrm{p}}\left|\dot{\epsilon}_{\mathrm{q}}^{\mathrm{p}}\right|\right)\exp\left(-\left(\mathrm{n}_{\mathrm{v}}^{\mathrm{p}}\left|\epsilon_{\mathrm{v}}^{\mathrm{p}}\right|+\mathrm{n}_{\mathrm{q}}^{\mathrm{p}}\left|\epsilon_{\mathrm{q}}^{\mathrm{p}}\right|\right)\right) \tag{18}$$

where $\epsilon_{\mathrm{v}}^{\mathrm{p}}$ is the accumulated plastic volumetric strain, $\epsilon_{\mathrm{q}}^{\mathrm{p}} = \sqrt{\frac{2}{3}\left(\boldsymbol{e}_p:\boldsymbol{e}_p\right)}$ the magnitude of the accumulated plastic deviatoric strain, ($\zeta_{\mathrm{v}}^{\mathrm{p}}$, $n_{\mathrm{v}}^{\mathrm{p}}$) and ($\zeta_{\mathrm{q}}^{\mathrm{p}}$, $n_{\mathrm{q}}^{\mathrm{p}}$) are volumetric and deviatoric de-orientation parameters, respectively.

2.5 Plastic Modulus - Consistency Condition

The plastic modulus is derived from the consistency condition to ensure that any material state which initially lies on the yield surface will remain on the updated position of the yield surface during plastic loading. The plastic modulus is then calculated through the following equation:

$$H = -\left(\frac{\partial f}{\partial \alpha}\overline{\alpha} + \frac{\partial f}{\partial \boldsymbol{s}}:\overline{\boldsymbol{b}}\right) \tag{19}$$

The definition of $\overline{\alpha}$ and $\overline{\boldsymbol{b}}$ are given in Appendix 1.

3 MODEL PARAMETERS - CALIBRATION

The proposed model requires the following 11 parameters:

κ**:** poro-elasticity compressibility.
ν**:** poisson ratio.
λ**:** intrinsic compressibility.
c or c_i**:** projection of the critical state line in the stress space. Controls the shear strength in all deviatoric planes (if the different c_i values are used). In the simplest case it is proportional to the M parameter of the MCC: $c = \sqrt{(2/3)}M$.
N_{iso}**:** location of the ICC_{iso} in the $v - \ln\sigma$ plane.
r **:** controls the location of intermediate radial stress paths in the $v - \ln\sigma$ plane.
ψ**:** controls the evolution rate of induced anisotropy.
($\zeta_{\mathrm{v}}^{\mathrm{p}}$, $n_{\mathrm{v}}^{\mathrm{p}}$) and ($\zeta_{\mathrm{q}}^{\mathrm{p}}$, $n_{\mathrm{q}}^{\mathrm{p}}$): are volumetric and deviatoric anisotropy degradation parameters, that can be empirically estimated to match the response observed during probing or undrained tests.
Γ**:** the location of the CSL in the $v - \ln\sigma$ plane, comes directly from the position of the isotropic ICC: $\Gamma = N_{iso} - (\lambda - \kappa)\ln 2$, since in the proposed model critical state is represented by an isotropic ellipse, and thus is not considered an extra parameter.

Finally parameter χ that controls the relative orientation of the PPS with respect to the yield surface, can be estimated through a calibration process, under any given radial stress path (other that isotropic) where total dilatancy is known. Consider a radial (triaxial) stress path under a constant $b_q = n = q/p$. After substantial straining the yield surface will get oriented across this imposed stress ratio b_q and the PPS towards d_q according to eq. 9. Under stabilized conditions (see Belokas & Kavvadas (2011)) the model reproduces a total dilatancy $E_q = \epsilon_q/\epsilon_{vol} = \frac{\dot{\epsilon}^e_q + \dot{\epsilon}^p_q}{\dot{\epsilon}^e_{vol} + \dot{\epsilon}^p_{vol}}$. The plastic strains can be calculated through the flow rule (eq. 7), and the elastic law (eq. 2a and eq. 2b) can be used for the elastic strains. After considerable algebra the following second order equation is derived:

$$C d_q^2 + 2 d_q + \left\{ C \left(c^2 - b_q^2 \right) - 2 b_q \right\} = 0 \tag{20}$$

where:

$$C = E_q - E_q \frac{\kappa}{\lambda - \kappa} - \frac{1+\nu}{3(1-2\nu)} \frac{\kappa}{\lambda - \kappa} b_q \tag{21}$$

The real route of eq. 20 corresponds to the desired orientation d_q of the PPS, for total dilatancy to be E_q under a radial stress path with stress ratio b_q. The most common stress path to perform the aforementioned calibration process is a K_0 consolidation test. In such a test the stress ratio b_q is directly derived from the coefficient of earth pressure at rest K_0, $b_q^{K_0} = 3(1-K_0)/(1+2K_0)$, while simultaneously the total dilatancy reproduced shall be $E_q^{K_0} = 2/3$ for total horizontal stain to be zero. Finally parameter χ is calculated using eq 9.

4 MODEL SIMULATIONS

In order to demonstrate the capabilities of the proposed model a set of numerical analyses are performed and presented, namely: a) radial consolidation tests, b) K_0 tests (stress vs strain controlled) and finally c) drained and undrained shearing tests. The aforementioned analyses have been selected with a view towards highlighting the main features of the model. The simulation was performed using a single point algorithm, developed in Fortran, based on an implicit integration scheme to solve the constitutive equations. The main parameters used (table 1) are imaginary and have been selected to correspond to a medium plasticity clay .

Table 1. Values for the model parameters used in the analyses.

Parameter	Value	Parameter	Value
κ	0.05	χ	1.455[*2]
λ	0.15	ψ	40
ν	$1/3$	n_v	30
c	0.8165[*1]	n_q	60
N_{iso}	2.8	ζ_v	1.5
r	0.35	ζ_q	3.0

[*1] corresponds to $M = 1.0$.
[*2] for $K_0 = 0.5$ under 1D compression.

4.1 Radial Stress Paths

The first set of analyses correspond to radial consolidation tests. Three tests are presented under different stress ratios, namely: a) $n = 0$ corresponding to an isotropic compression, b) $n = 0.50$ and c) $n = 0.75$ that corresponds to a K_0 test with $K_0 = 0.5$. These analyses demonstrate the ability of the isotropic component of the hardening rule (eq. 14) to predict different ICC for different levels of anisotropy. The initial conditions correspond to a reconstituted soil that has been isotropically compressed to $p = 30kPa$ and then unloaded to $p = 10kPa$. The aforementioned initial state corresponds to an isotropic yield surface with a tip at $2\alpha = 30kPa$. For the tests under $n = 0.50$ and $n = 0.75$, before compression, the stress ratio is adjusted by increasing the deviatoric stress under constant mean stress to $q = 5kPa$ and $q = 7.5kPa$ respectively. Finally the material is compressed under constant stress ratio to $p = 1000kPa$. The results are presented in fig. 3. As observed in fig. 3b the tests performed at stress ratio of $n = 0.50$ and $n = 0.75$

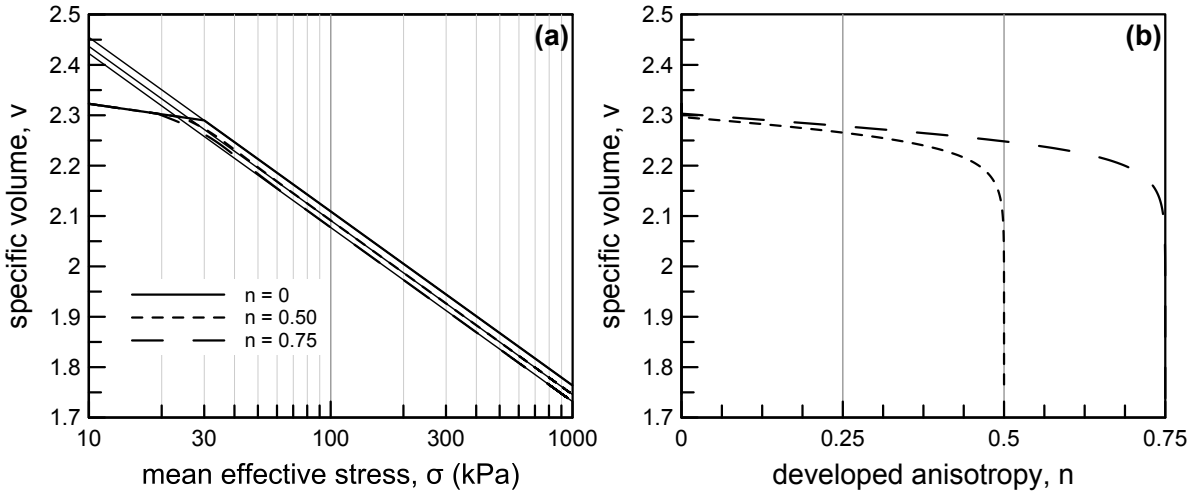

Fig. 3. Radial consolidation tests, under three different stress ratios ($n = 0$, $n = 0.5$ and $n = 0.75$), on an initially isotropically consolidated clay.

cause the anisotropy to evolve towards and finally stabilize at the stress ratio of the imposed stress path. Additionally in fig. 3a it can be seen that as anisotropy evolves, simultaneously the corresponding in the $v - \ln\sigma$ plane path, diviates from the isotropic ICC heading towards the corresponding ICC, as predicted by eq. 12.

4.2 K_0 Test

As already mentioned the radial consolidation test performed under a stress ratio of $n = 0.75$ corresponds to $K_0 = 0.5$. In this paragraph the aforementioned test is compared with its strain controlled counterpart, meaning a 1D consolidation test. Provided that the flow rule has been properly calibrated the two tests should lead to the same behaviour. Using the calibration process described in section 3 it comes that for $K_0 = 0.5$ parameter χ obtains the value $\chi = 1.455$ for $\dot{\epsilon}_q/\dot{\epsilon}_{vol} = 2/3$ corresponding to the required total dilatancy for zero total horizontal strains. The comparison is given in fig. 4.

It can be seen that from one hand the stress controlled radial compression test predicts the desired total dilatancy (fig. 4b), while on the other hand the strain controlled 1D compression test

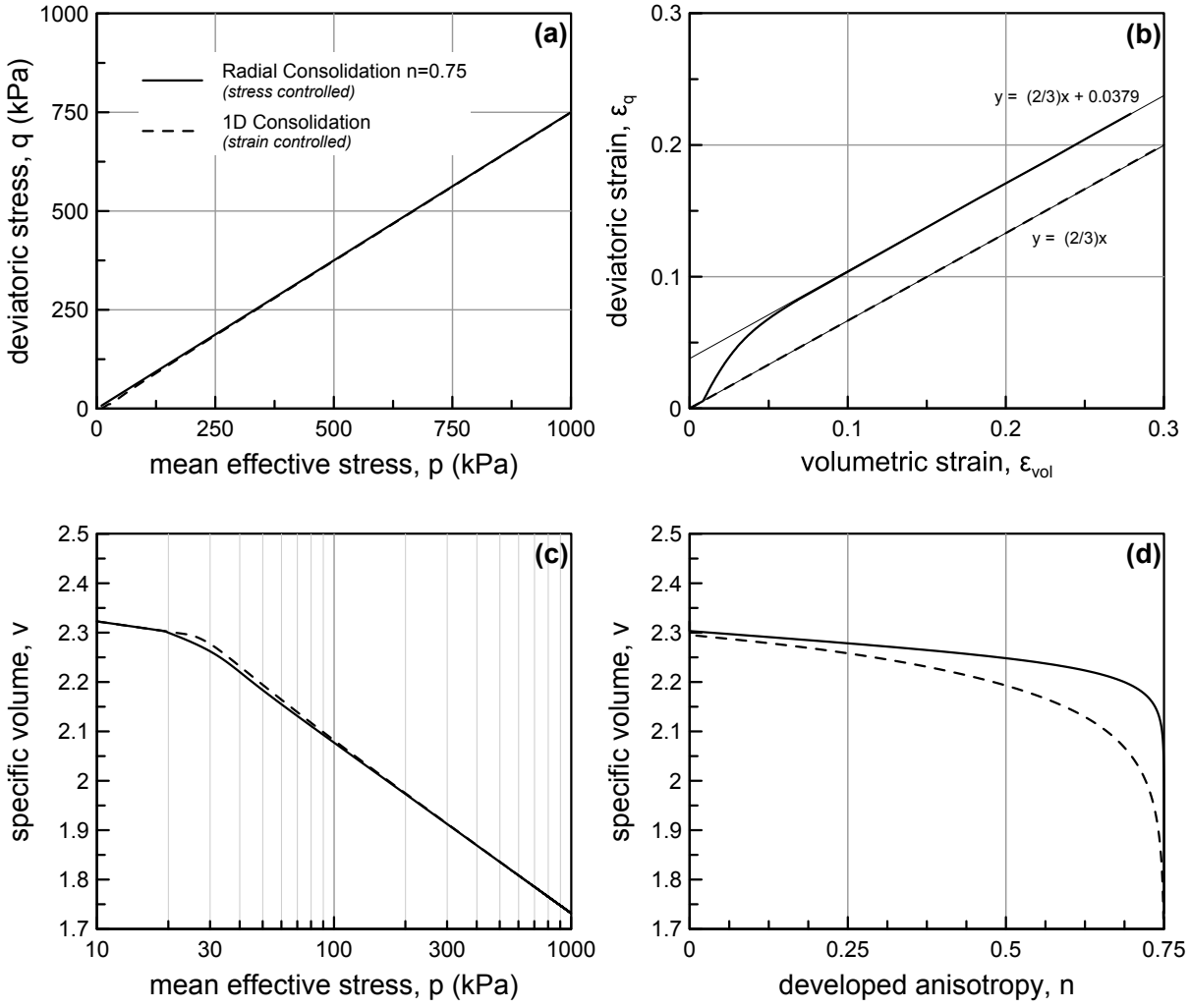

Fig. 4. Comparison between a stress controlled K_0 test and a strain controlled 1D compression test.

successfully predicts the desired stress path ratio, corresponding to the selected K_0. Additionally in fig. 4c it can be seen that both tests predict the same ICC, the one corresponding to the assumed K_0. The aforementioned comparison proves the ability of the adopted flow rule to predict the desired behaviour, when properly calibrated.

4.3 Undrained and Drained Shearing

Finally the material that has been consolidated under K_0 conditions is sheared under drained (fig. 5) and undrained (fig. 6) conditions, both in compression and extension. Initially the material state lies on the tip of a distorted yield surface with its main axis along the direction of the K_0 stress path. As can be observed, due to the effect of the de-orientation part of the kinematic hardening rule (eq. 18), anisotropy is gradually decreasing until the yield surface drops to the isotropic axis and remains there until the end of the test (fig. 5a and 6a), meaning that critical state will be reached under isotropic conditions, and thus correspond to unique conditions. The aforementioned behaviour can be observed in both drained and undrained triaxial tests where at the end of shearing, all stress paths lie on the same CSL in the $v - \ln\sigma$ plane. (fig. 5c and 6c). During extension tests a hook type behaviour can be observed in the $v - \ln\sigma$ or $\sigma - q$ plane for

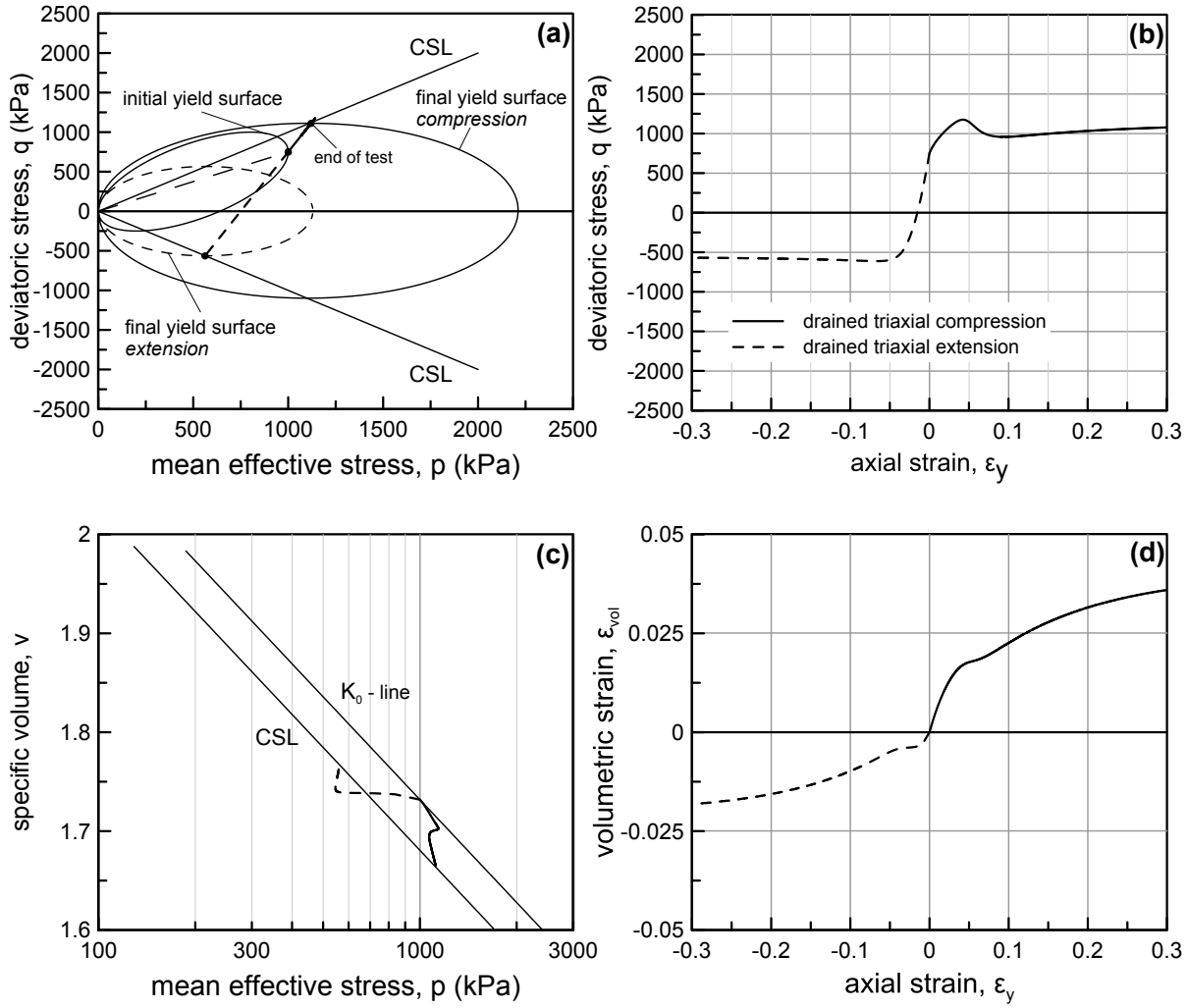

Fig. 5. Triaxial drained compression and extension tests of an initially K_0 normally consolidated soil.

the case of drained and undrained tests, respectively. It seems that this behaviour during triaxial extension cannot be avoided, and as pointed out by Taiebat & Dafalias (2013) this is the price one has to pay for unique critical state in both extension and compression.

5 CONCLUSIONS

A new model was presented within the framework of incremental theory of plasticity, based on the principles of CSSM, to simulate the behaviour of uncemented anisotropically consolidated clayey soils. The model incorporates a rotated - distorted yield surface, a non-associated flow rule derived from an also rotated - distorted plastic potential function, and finally a mixed hardening rule comprising of: a) an isotropic part based on an Intrinsic Compressibility Framework, and b) a kinematic hardening part based on the idea of reorientating an initially inclined yield surface towards the isotropic axes as critical state is approached.

Basic simulations presented in the paper show that the model is capable of reproducing: a) Intrinsic Compression Curves that depend on the level of applied anisotropy, b) unique critical state independent of the initial level of anisotropy and/or of the stress path followed, c) real-

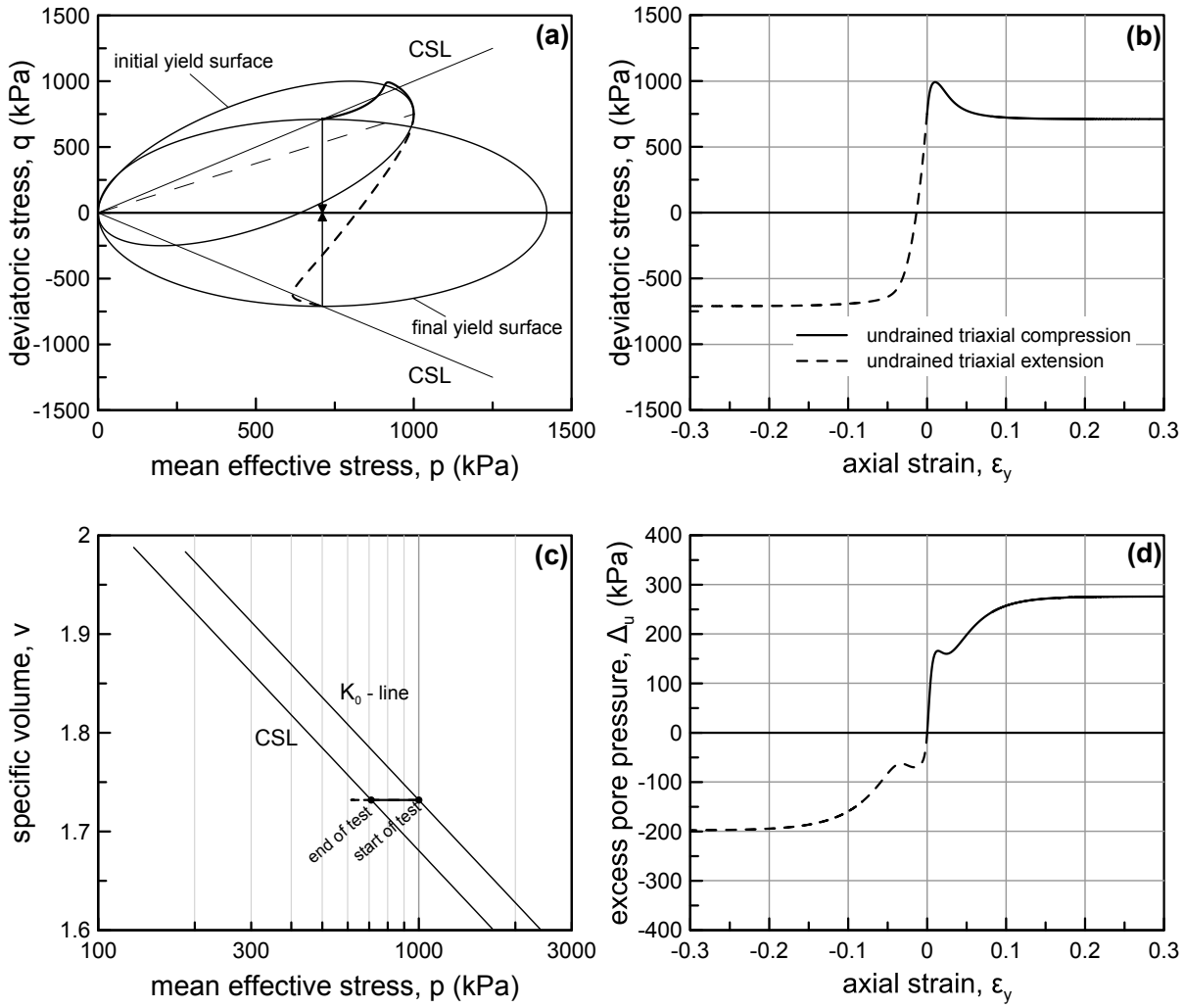

Fig. 6. Triaxial undrained compression and extension tests of an initially K_0 normally consolidated soil.

istic K_0 values and finally d) strain-softening behaviour for initially anisotropically normally consolidated soils that are triaxially compressed.

The model still needs to be evaluated towards experimental results and especially the behaviour reproduced by the de-orientational part of the proposed kinematic hardening rule. Also, in the future, a slightly modified formula for eq. 18 shall perhaps be incorporated to simulate a smoother anisotropy degradation in the transition towards critical state.

APPENDIX 1

The quantity $\overline{\alpha}$ in eq. 19 is given by:

$$\dot{a} = \dot{\Lambda}\overline{a} \tag{22}$$

where:

$$\overline{a} = A\overline{a^*} + \overline{A}a^* \tag{23a}$$

$$\overline{a^*} = \frac{v}{\lambda - \kappa} a^* P \tag{23b}$$

$$\overline{A} = \frac{Ar(\Gamma - N_{iso})}{\lambda - \kappa} \left(1 - \sqrt{\frac{\boldsymbol{b} : \boldsymbol{b}}{k^2}}\right)^{r-1} \frac{1}{\sqrt{\frac{\boldsymbol{b}:\boldsymbol{b}}{k^2}}} \frac{\boldsymbol{b} : \overline{\boldsymbol{b}}}{k^2} \tag{23c}$$

while quantity $\overline{\boldsymbol{b}}$ is:

$$\overline{\boldsymbol{b}} = \overline{\boldsymbol{b}}_{\mathbf{o}} + \overline{\boldsymbol{b}}_{\mathbf{d}} \tag{24}$$

where:

$$\overline{\boldsymbol{b}}_{\mathbf{o}} = \frac{1}{a}\psi(\boldsymbol{s} - \sigma\boldsymbol{b})\overline{P} \tag{25a}$$

$$\overline{\boldsymbol{b}}_{\mathbf{d}} = -\frac{1}{a^2}\boldsymbol{b}\,(\boldsymbol{s} - \sigma\boldsymbol{b}) : (\boldsymbol{s} - \sigma\boldsymbol{b}) \left(\zeta_{\mathrm{v}}^{\mathrm{p}} \left|\mathrm{P}\right| + \zeta_{\mathrm{q}}^{\mathrm{p}} \sqrt{\frac{2}{3}\boldsymbol{P}^{\cdot} : \boldsymbol{P}^{\cdot}}\right) \exp\left(-\mathrm{n}_{\mathrm{v}}^{\mathrm{p}} \left|\epsilon_{\mathrm{v}}^{\mathrm{p}}\right| - \mathrm{n}_{\mathrm{q}}^{\mathrm{p}} \sqrt{\frac{2}{3}\left(\boldsymbol{e}_p : \boldsymbol{e}_p\right)}\right) \tag{25b}$$

REFERENCES

Belokas, G. & Kavvadas, M. (2010). An anisotropic model for structured soils: Part i: Theory. *Computers and Geotechnics 37*(6), 737 – 747.

Belokas, G. & Kavvadas, M. (2011). An intrinsic compressibility framework for clayey soils. *Geotechnical and Geological Engineering 29*(5), 855–871.

Dafalias, Y. (1986). An anisotropic critical state soil plasticity model. *Mechanics Research Communications 13*(6), 341–347.

Dafalias, Y. F., Manzari, M. T., & Papadimitriou, A. G. (2006). Saniclay: simple anisotropic clay plasticity model. *International Journal for Numerical and Analytical Methods in Geomechanics 30*(12), 1231–1257.

Kavvadas, M. (1982). *Non - Linear Consolidation around driven piles in Clays*. Ph. D. thesis, Massachussets Institute of Technology (MIT), Cambridge, MA.

Kavvadas, M. & Amorosi, A. (2000). A constitutive model for structured soils. *Geotechnique 50*(3), 263–273.

Newson, T. & Davies, M. (1996). A rotational hardening constitutive model for anisotropically consolidated clay. *Soils and foundations 36*(3), 13–20.

Taiebat, M. & Dafalias, Y. F. (2013). Rotational hardening and uniqueness of critical state line in clay plasticity. In *Constitutive Modeling of Geomaterials*, pp. 223–230. Springer.

Wheeler, S., Ntnen, A., Karstunen, M., & Lojander, M. (2003). An anisotropic elastoplastic model for soft clays. *Canadian Geotechnical Journal 40*(2), 403–418.

UNIFIED DESCRIPTION OF TOYOURA SAND UNDER DIFFERENT LOADING AND DRAINAGE CONDITIONS

F. ZHANG
Department of Civil Engineering, Nagoya Institute of Technology, Nagoya, Japan

B. YE
Department of Geotechnical Engineering, Tongji University, Shanghai, China

G. L. YE
Department of Civil Engineering, Shanghai Jiaotong University, Shanghai, China

ABSTRACT: *In this paper, mechanical behavior of Toyoura sand is examined with a newly proposed elastoplastic model. The performance of the model is verified against the results of conventional triaxial tests for performed under different loading and drainage conditions. The model employs only eight parameters among which five are the same as those used in Cam-clay model. Once these parameters are determined from the conventional drained triaxial compression tests and undrained triaxial cyclic loading tests, their values are then fixed to uniquely describe the mechanical behavior of the Toyoura sand under various loading conditions. In the model, the concepts of subloading, superloading and stress-induced anisotropy are adopted. The most important feature of the model is that the correlation between the overconsolidation ratio, the inherent structure formed in depositary process and the stress-induced anisotropy is taken into account.*

1 INTRODUCTION

Mechanical behavior of sand has been investigated for years and so many reports on this topic can be found in literature that it is hard to list them completely within limited pages of references. The reason why so many researchers spend so much effort to learn it is that, the mechanical behavior of sand is dependent not only on the shape of particles, angular or round, but also on its density, the strain history, and even on the degree of structure formed in its deposition (Asaoka et al., 1998). Sand may behave quite differently under different loading and drainage condition. For instance, when subjected to undrained cyclic loading, loose sand will liquefy without transition from contractive to dilative state; for medium dense sand, liquefaction with cyclic mobility occurs while for dense sand, the liquefaction will never occur. Loose sand subjected to cyclic loading will liquefy under undrained condition but may be compacted to a denser state under drained condition (Asaoka, 2003).

The strain history, sometimes also called as the stress-induced anisotropy, has great influence on the behavior of sand. In the works by Ishihara and Okada (1982), the effect of pre-shearing on the cyclic behavior of sand was carefully investigated and it is concluded that the liquefaction resistance is dependent not only on the magnitude of the pre-shearing but also on its initial direction. Yamada et al. (2010) also conducted systematically a series of undrained triaxial conventional tests in which the samples before shearing have already subjected to undrained cyclic loading and had already experienced cyclic mobility process. In his research, a continuous and rapid change of the stress-induced anisotropy during

liquefaction has been confirmed, which again proves that the stress-induced anisotropy is a very important factor in modeling the mechanical behavior of sand.

Compared with undrained cyclic loading tests, drained cyclic loading tests are much fewer in literature. Hinokio et al. (2000) conducted the test on dense sand under constant mean stress, in which the confining pressure of on sand was kept constant and a maximum principal stress ratio (σ_1/σ_3) was cyclically loaded up to 4.0. It is found that dense sand subjected to relative large cyclic shearing will contract to some extent but will not contract further even if the cyclic shearing continues.

The mechanical behavior of sand is also stress-path dependent, in other words, the influence of intermediate stress should be considered properly. The research on this field can be referred to the works by Nakai and Mihara (1984) and Yao et al. (2008).

The research on constitutive modeling for sand has achieved very quick development recently. Some works are worth mentioning. The concept of subloading, proposed by Hashiguchi and Ueno (1977), makes it possible to describe the effect of overconsolidation or the density of soil. The concept of superloading, proposed by Asaoka et al. (1998), makes it possible not only to describe the effect of overconsolidation or density but also the effect of the soil structure formed in depositary process.

In this paper, the authors proposed a new constitutive model for sand in which apart from the concept of superloading (Asaoka et al., 1998) and the concept of subloading (Hashiguchi and Ueno, 1977), a new approach to describe the stress-induced anisotropy is proposed. As a matter of fact, the concept of stress-induced anisotropy was firstly modeled by Sekiguchi (1977). Since then many revisions have been made and can be found in literature. Unfortunately, the interrelation among the density effect, the structure and the stress-induced anisotropy were not considered in a systematic way. In this paper, the interrelation will be discussed and formulated in a rational way, by which the model is established trying to describe the overall mechanical behaviors of Toyoura sand, a typical clean sand, in a unified way. In other words, all the behavior of Toyoura sand, no matter what loading and drainage conditions may be, its mechanical behavior is described with a fixed set of material parameters. The most important thing that should be emphasized here is that the eight material parameters involved in the model, will be constant no matter what kind of loading or drainage conditions may be.

2 CYCLIC MOBILITY MODEL

The model proposed here is based on the concepts of subloading (Hashiguchi and Ueno, 1977) and superloading (Asaoka et al., 1998). Here a brief description of the yield surfaces shown in Fig.1 is given.

The similarity ratio of the superloading yield surface to normal yield surface R^* and the similarity ratio of the superloading yield surface to subloading yield surface R are the same as those in the work by Asaoka et al. (1998), namely,

$$R^* = \frac{\tilde{p}}{\overline{p}} = \frac{\tilde{q}}{\overline{q}}, \quad 0 < R^* \le 1, \quad R = \frac{p}{\overline{p}} = \frac{q}{\overline{q}}, \quad 0 < R \le 1, \quad \frac{\overline{q}}{\overline{p}} = \frac{\tilde{q}}{\tilde{p}} = \frac{q}{p} \tag{1}$$

where $(p, q), (\tilde{p}, \tilde{q})$ and $(\overline{p}, \overline{q})$ represent the present stress state, the corresponding normally consolidated stress state and the structured stress state at p-q stress space respectively, as shown in Fig.1(a). Throughout this paper, all the stressed discussed in the context are effective stressed. The normal yield surface is given in the following form as:

$$f = \ln\frac{\sigma_m}{\sigma^*_{m0}} + \ln\frac{\mathrm{M}^2 - \zeta^2 + \eta^{*2}}{\mathrm{M}^2 - \zeta^2} + \ln R^* - \ln R - \frac{\varepsilon_v^p}{C_p} = 0 \tag{2}$$

where, the variables involved in Eqs. (1), and (2) are defined as:

$$\eta^* = \sqrt{\frac{3}{2}\hat{\eta}_{ij}\hat{\eta}_{ij}},\ \hat{\eta}_{ij} = \eta_{ij} - \beta_{ij},\ \eta_{ij} = \frac{S_{ij}}{\sigma_m},\ \eta = \sqrt{\frac{3}{2}\eta_{ij}\eta_{ij}},\ \varsigma = \sqrt{\frac{3}{2}\beta_{ij}\beta_{ij}} \tag{3}$$

where, S_{ij} is the deviatoric stress tensor; β_{ij} is the anisotropic stress ratio tensor, and σ_{ij} is the stress tensor and is assumed to be positive in compression. In this model, the gradient of the *C.S.L.* is assumed to be constant. Fig.1(b) shows the yielding surfaces and its change in the flat ratio of the elliptical yield surface due to the anisotropy. It is assumed that the larger the stress-induced anisotropy ζ is, the larger the eccentric ratio of the ellipse will be.

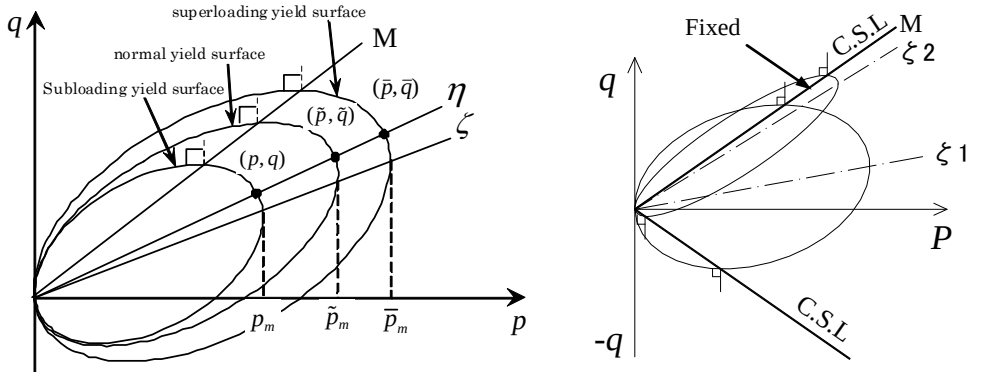

(a) Subloading, normal and superloading yield surfaces (b) Changes of subloading yielding surface at different ζ

Fig.1 Yield surfaces in *p*-*q* plane

An associated flow rule is employed in the present model, namely,

$$d\varepsilon_{ij}^p = \Lambda(\partial f / \partial \sigma_{ij}) \tag{4}$$

The consistency equation for the subloading yield surface can then be given as:

$$df = 0 \Rightarrow \frac{\partial f}{\partial \sigma_{ij}} d\sigma_{ij} + \frac{\partial f}{\partial \beta_{ij}} d\beta_{ij} + \frac{1}{R^*} dR^* - \frac{1}{R} dR - \frac{1}{C_p} d\varepsilon_v^p = 0, \quad C_p = \frac{\lambda - \kappa}{1 + e_0} \tag{5}$$

2.1 Evolution rule for stress-induced anisotropic stress tensor β_{ij}

The evolution rule for the anisotropic stress ratio tensor is defined as:

$$d\beta_{ij} = \frac{\mathrm{M}}{C_p} b_r (\mathrm{M} - \varsigma) d\varepsilon_d^p \frac{\hat{\eta}_{ij}}{\left\| \hat{\eta}_{ij} \right\|} = \sqrt{\frac{3}{2}} \frac{\mathrm{M}}{C_p} b_r (\mathrm{M} - \varsigma) d\varepsilon_d^p \frac{\hat{\eta}_{ij}}{\eta^*} \tag{6}$$

where it is assumed that the anisotropic stress ratio tensor β_{ij} will not exceed the stress ratio at critical state, the value of *M*. In other words, the stress ratio at the *C.S.L.* provides us with a natural physical limitation for its variation as ζ<*M*. The plastic component of the deviatoric strain tensor can be calculated as follow:

$$d\varepsilon_d^p = \sqrt{\frac{2}{3} de_{ij}^p de_{ij}^p} = \Lambda \sqrt{\frac{2}{3} \frac{df}{dS_{ij}} \frac{df}{dS_{ij}}} = \Lambda \frac{2\eta^*}{(\mathrm{M}^2 - \varsigma^2 + \eta^{*2})\sigma_m} \tag{7}$$

$$\frac{\partial f}{\partial \beta_{ij}} d\beta_{ij} = \Lambda \frac{\sqrt{6} M b_r (\mathrm{M} - \varsigma) \eta^{*2} (-2\mathrm{M}^2 + 3\eta_{ij}\beta_{ij})}{C_p (\mathrm{M}^2 - \varsigma^2 + \eta^{*2})^2 (\mathrm{M}^2 - \varsigma^2) \sigma_m} \tag{8}$$

*2.2 Evolution rule for degree of structure R**

The evolution rule for the degree of structure *R**, takes the same form as the one proposed by Asaoka et al. (2003):

$$dR^* = U^* d\varepsilon_d^p, \quad U^* = \frac{a\mathrm{M}}{C_p} R^* (1 - R^*) = \Lambda \frac{2a\mathrm{M} R^* (1 - R^*) \eta^*}{C_p (\mathrm{M}^2 - \varsigma^2 + \eta^{*2}) \sigma_m}, \quad (0 < R^* \le 1) \tag{9}$$

where *a* is a parameter that controls the collapsing rate of the structure during shearing.

2.3 Evolution rule for degree of overconsolidation R

In the present model, the changing rate of overconsolidation is assumed to be controlled by two factors, namely, the plastic component of the stretching and the incremental anisotropy as,

$$dR = U\left\|d\varepsilon_{ij}^{p}\right\| + R\frac{\eta}{\mathrm{M}}\frac{\partial f}{\partial \beta_{ij}}d\beta_{ij}, \quad \left\|d\varepsilon_{ij}^{p}\right\| = \sqrt{d\varepsilon_{ij}^{p}d\varepsilon_{ij}^{p}} = \Lambda\sqrt{\frac{\partial f}{\partial \sigma_{ij}}\frac{\partial f}{\partial \sigma_{ij}}} \tag{10}$$

by the definition of $d\beta_{ij}$ in Eq. (6), it is known that $d\beta_{ij}$ is proportional to the norm of the plastic strain tensor $\left\|d\varepsilon_{ij}^{p}\right\|$. U is given by the following relation as:

$$U = -\frac{m\mathrm{M}}{C_p}\left(\frac{(\sigma_m/\sigma_{m0})^2}{(\sigma_m/\sigma_{m0})^2+1}\right)\ln R \quad (p_0\text{=98.0 kPa, reference stress}) \tag{11}$$

$$dR = -\Lambda m\mathrm{M}\ln R\sqrt{6\eta^{*2}+\frac{1}{3}(\mathrm{M}^2-\eta^2)^2}\left[\frac{(\sigma_m/\sigma_{m0})^2}{(\sigma_m/\sigma_{m0})^2+1}\right]/\left[C_p(\mathrm{M}^2-\varsigma^2+\eta^{*2})\sigma_m\right]+R\frac{\eta}{\mathrm{M}}\frac{\partial f}{\partial \beta_{ij}}d\beta_{ij} \tag{12}$$

Meanwhile, the plastic volumetric strain rate can be evaluated as:

$$d\varepsilon_v^p = \Lambda\frac{\partial f}{\partial \sigma_m} = \Lambda\frac{\mathrm{M}^2-\eta^2}{(\mathrm{M}^2-\varsigma^2+\eta^{*2})\sigma_m} \tag{13}$$

Substituting Eqs.(8), (12) and (13) into Eq.(5), the positive valuable Λ can then be determined as:

$$\Lambda = \frac{\partial f}{\partial \sigma_{ij}}d\sigma_{ij}\Big/\left[\frac{1}{C_p(M^2-\varsigma^2+\eta^{*2})\sigma_m}(M_s^2-\eta^2)\right] \tag{14}$$

where

$$\begin{aligned} M_s^2 &= \mathrm{M}^2 - \frac{m\mathrm{M}\ln R}{R}\left[\frac{(\sigma_m/\sigma_{m0})^2}{(\sigma_m/\sigma_{m0})^2+1}\right]\sqrt{6\eta^{*2}+\frac{1}{3}(\mathrm{M}^2-\eta^2)^2} \\ &-2aM(1-R^*)\eta^* - (1-\frac{\eta}{\mathrm{M}})\frac{\sqrt{6}\mathrm{M}b_r(\mathrm{M}-\varsigma)\eta^{*2}(-2\mathrm{M}^2+3\eta_{ij}\beta_{ij})}{(\mathrm{M}^2-\varsigma^2+\eta^{*2})(\mathrm{M}^2-\varsigma^2)} \end{aligned} \tag{15}$$

If the incremental strain tensor is divided into elastic and plastic components, then the following relation can be obtained:

$$d\varepsilon_{kl} = d\varepsilon_{kl}^{e} + d\varepsilon_{kl}^{p}, \quad d\sigma_{ij} = E_{ijkl}d\varepsilon_{kl}^{e}, \quad d\sigma_{ij} = E_{ijkl}d\varepsilon_{kl} - \Lambda E_{ijkl}\frac{\partial f}{\partial \sigma_{kl}} \tag{16}$$

Substituting Eqs.(8), (12), (13), (15) and (16) into Eq.(5), it is possible to obtain another expression for the positive valuable Λ as follow,

$$\Lambda = \frac{\partial f}{\partial \sigma_{ij}}E_{ijkl}d\varepsilon_{kl}\Big/\left(h_p + \frac{\partial f}{\partial \sigma_{ij}}E_{ijkl}\frac{\partial f}{\partial \tilde{\sigma}_{kl}}\right), \; h_p = \frac{1}{C_p(\mathrm{M}^2-\varsigma^2+\eta^{*2})\sigma_m}[\mathrm{M}_s^2-\eta^2] \tag{17}$$

The loading criteria are given as:

$$\Lambda > 0 \Rightarrow loading;\ \Lambda = 0 \Rightarrow eutral;\ \Lambda < 0 \Rightarrow unloading \tag{18}$$

Eqs.(1)~(18) are discussed under the condition of conventional triaxial stress space (σ_2= σ_3). If the intermediate stress dependency is taken into consideration, then a TS concept proposed by Yao et al. (2008) is adopted. Because most of the equations are in the same form as those in the conventional triaxial stress space, the detailed description about formulation in TS space can be referred to the works by Yao et al. (2008) and Ye et al. (2012). In the following chapters, all the calculations are carried out in TS space.

Among the eight parameters involved in the model, five parameters, M, N, λ, κ, and ν are the same as those in Cam-clay model. The other three parameters, a: the parameter that controls the collapse rate of structure; m: the parameter that controls the losing rate of overconsolidation; and b_r: the parameter that controls the developing rate of stress-induced anisotropy; have clear physical meanings and can be determined by undrained triaxial cyclic loading tests and drained triaxial compression tests. Detailed description about the physical meaning and the way of determining these parameters can be referred to the work by Zhang et al. (2007).

3 PERFORMANCE OF THE PROPOSED MODEL

A set of sands with different densities that are prepared from a very loose sand using a numerical method by Asaoka (2003), are used to verify the density effect. In preparing the set of sand samples with different densities, the very loose sand whose material parameters are listed in Table 1 and initial state variable are listed in the first column of Table 2, marked with [0], is compacted by a small cyclic isotropic loading with the amplitude of 2.3kPa under a small confining pressure of 10kPa. After the compactions, these sands with different densities are isotropically consolidated to a prescribed confining pressure of 196 kPa, as shown in Fig.2. The state variables of these sands after they are isotropically consolidated to the confining pressure of 196 kPa, are also listed in Table 2 marked with [1]~[8]. Various kinds of triaxial tests under drained/undrained conditions subjected to monotonic and cyclic loading, are then calculated systematically in the following sections.

Table 1 Material parameters of Toyoura sand

Compression index λ	0.050
Swelling index κ	0.0064
Critical state parameter **M**	1.30
Void ratio **N** (p=98 kPa on *N.C.L.*)	0.87
Poisson's ratio ν	0.30
Evolution parameter overconsolidation m	0.01
Evolution parameter of structure a	0.50
Evolution parameter of anisotropy b_r	1.50

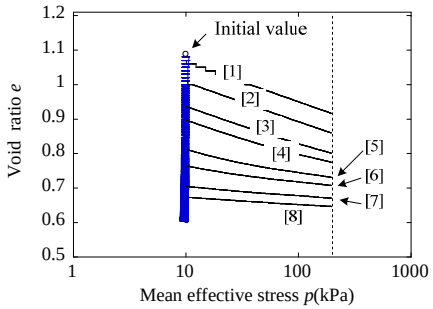

Fig.2 Set of sands with different densities

Table 2 State variables of sand samples after isotropic consolidation (p= 196 kPa)

State variables	[0]	[1]	[2]	[3]	[4]	[5]	[6]	[7]	[8]
e_0	1.19	0.916	0.860	0.801	0.775	0.731	0.707	0.671	0.646
p (kPa)	10.0	196.	196.	196.	196.	196.	196.	196.	196.
R_0^*	0.10	0.104	0.114	0.125	0.133	0.149	0.160	0.172	0.179
OCR ($1/R_0$)	1.0	1.49	5.03	17.5	30.1	73.4	118.	255.	426.
ζ_0	0.0	1.44E-5	1.47E-5	1.97E-5	3.42E-5	5.95E-4	3.73E-3	2.18E-2	3.79E-2

Fig.3 shows the stress paths and stress-strain relations of the sands with different densities in undrained triaxial cyclic loading tests. It is clear from the figures that very loose sands ([1] & [2]) generate a large failure strain along the path directly towards the zero stress state without transition from contractive state to dilative state. For relatively loose sands ([3] & [4]), they also generate large failure strain but the transition from contractive state to dilative state can be observed. For medium dense sands ([5] to [7]), however, cyclic mobility occurs and the strain increases gradually to a relatively larger scale. On the other hand, the dense sand ([8]) only generates a small amount of strain and never shows the cyclic mobility. Therefore, the mechanical behavior of sand subjected to undrained cyclic loading can be uniquely and properly described by the constitutive model under the condition that all the material parameters are kept constant.

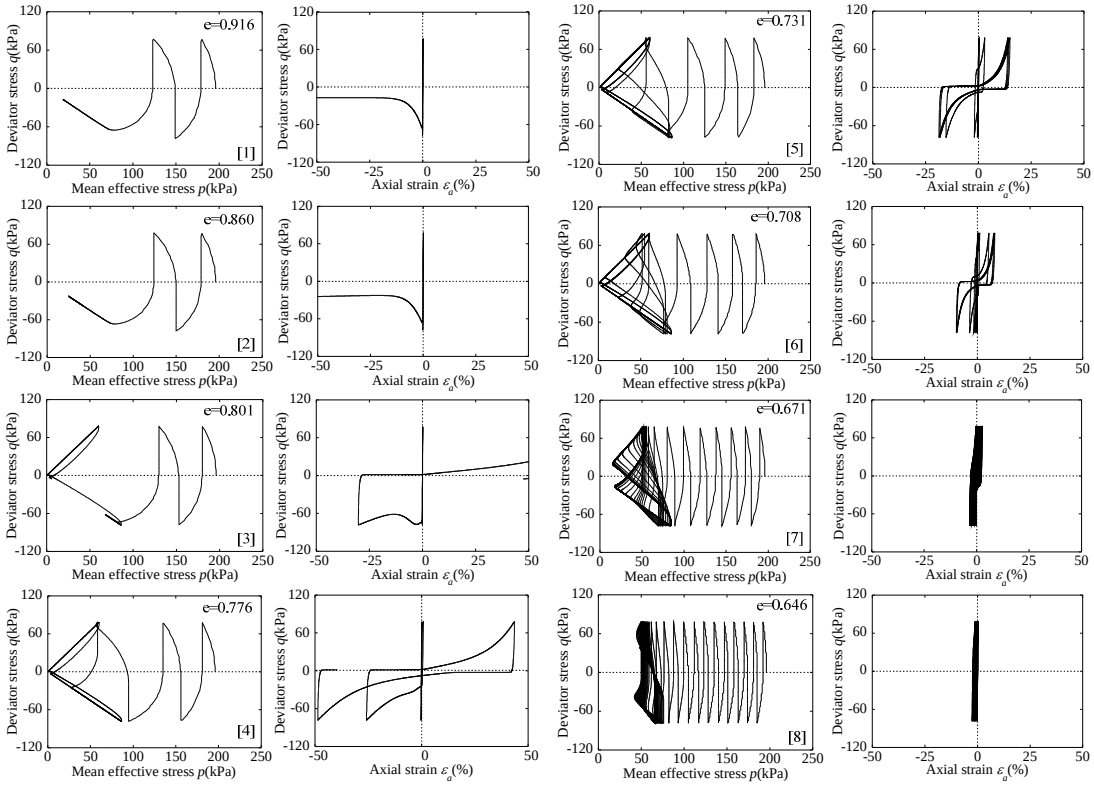

Fig.3 Stress paths, stress-strain relations of the sand specimens with different densities subjected to cyclic triaxial test under undrained condition

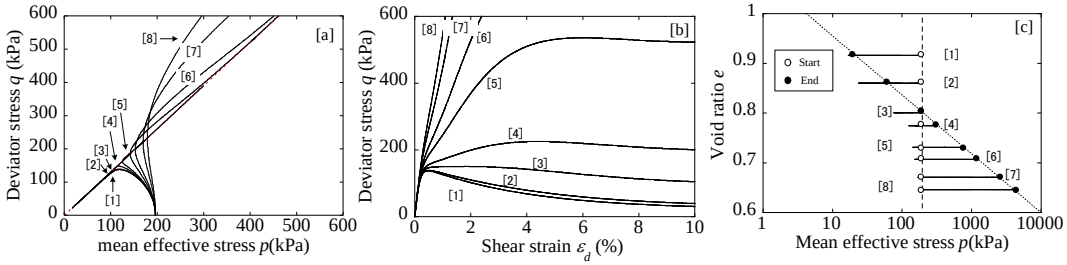

(a) Effective stress paths (b) Stress-strain relation (c) e-ln*p* relation

Fig.4 Simulation of undrained triaxial compression tests

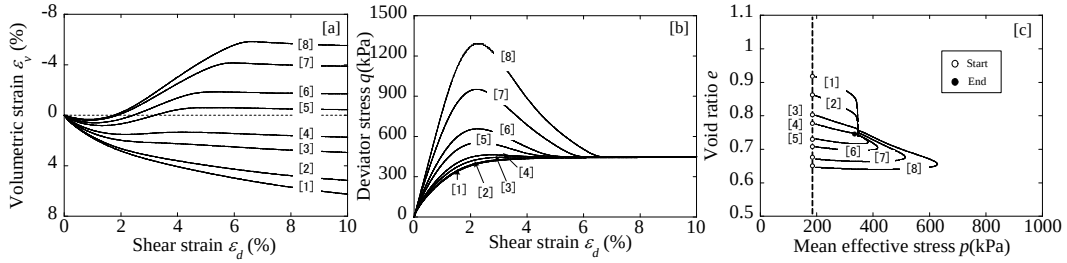

(a) Dilatancy (e) Stress-strain relation (c) e-*p* relation

Fig.5 Simulation of drained triaxial compression tests

Simulation of the Toyoura sand with different densities subjected to undrained/drained monotonic loading is shown in Figs.4 and 5. Under undrained conditions, loose sands ([1], [2]) reach its peak strength in small strain level and then collapse and flow rapidly toward the origin of the stress space. The stiffness of the medium dense sands ([3] to [6]) decreases

abruptly in certain strain level where a typical transition from contractive to dilative occurs. Dense sands [7] and [8], however, only show strain hardening, as shown in Fig.4.

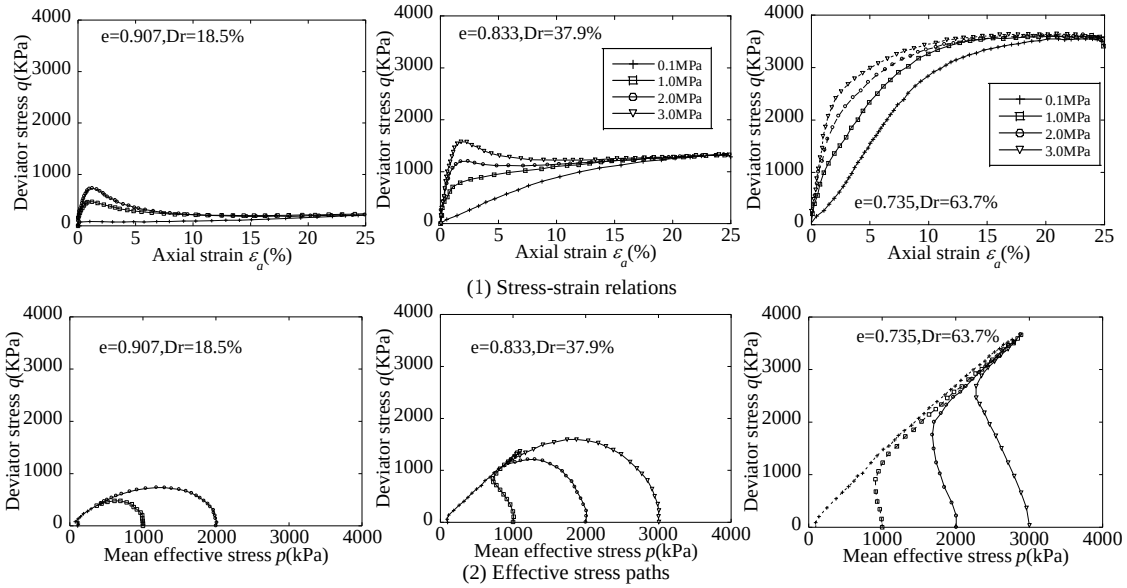

(1) Stress-strain relations

(2) Effective stress paths

Fig.6 Test results of stress paths and stress-strain relations of Toyoura Sand with the same void ratio but different confining stress in undrained triaxial compression test (Verdugo and Ishihara, 1996)

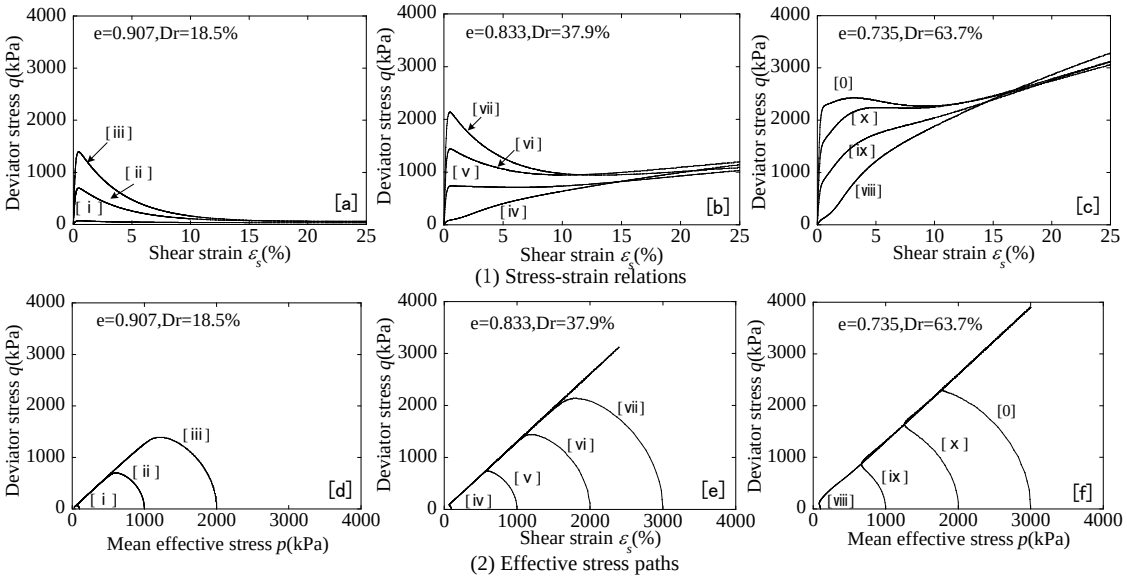

(1) Stress-strain relations

(2) Effective stress paths

Fig.7 Simulation of the test results in Fig.6

Fig.5 shows the simulated stress-strain-dilatancy relations of the sands in drained triaxial compression tests with constant confining stresses. It is known that the dense sands show a typical strain hardening-strain softening and the dilation due to shearing while the loose soils only show the strain hardening along with monotonic contraction. The transition from the contractive state to the dilative state is just dependent on the density of the sand.

Verdugo and Ishihara (1996) reported their test results of Toyoura sand, in which undrained triaxial compression tests on the sands with the same void ratio but different confining pressures were conducted under very high confining pressures (up to 3MPa). The test results in Fig.6 show that under the same void ratio, if a confining stress is large, the sand behaves like a loose sand, while if the confining stress is small; the sand behaves like a dense sand.

Such a phenomenon is called as “confining-stress dependency of sand”. In the tests, three groups of sands were considered, each of which has the same void ratio, while different group has different void ratio. Therefore, in the simulation it is necessary to adjust the density for all the sands before shearing. The initial values of the void ratios are set to be equal to 0.78, 0.70 and 0.65 respectively and are listed in Table 3. It is known from Fig.5 that the simulated results on the whole coincide well with the test results quantitatively and qualitatively.

Table 3 State variables of Toyoura sand samples used in the simulation shown in Fig.7

	p (MPa)	e_0	OCR ($1/R_0$)	R_0^*	ζ_0
[i]	0.10	0.89	1.5	0.50	0.00
[ii]	1.0	0.88	1.1	0.05	0.00
[iii]	2.0	0.89	1.0	0.02	0.00
[iv]	0.10	0.71	85.0	0.50	0.00
[V]	1.0	0.72	8.0	0.30	0.00
[vi]	2.0	0.71	5.0	0.24	0.00
[vii]	3.0	0.72	3.5	0.18	0.00
[viii]	0.10	0.65	280.0	0.50	0.00
[ix]	1.0	0.66	30.0	0.30	0.00
[x]	2.0	0.66	20.0	0.20	0.00
[xi]	3.0	0.66	12.0	0.20	0.00

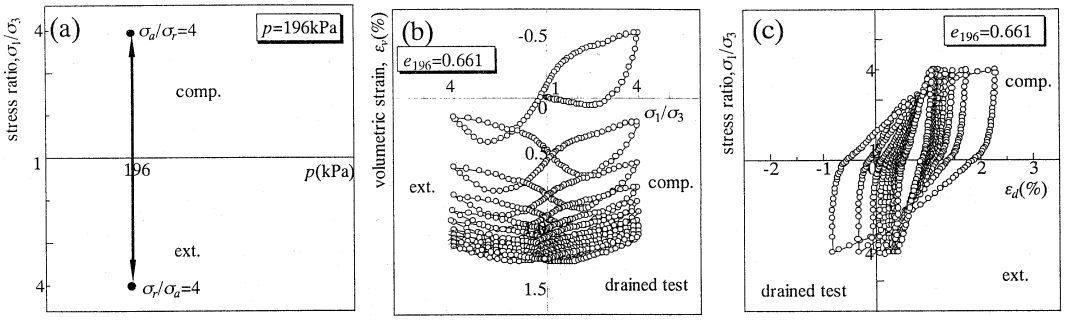

(a) Loading (b) Volumetric strain-stress ratio relation (c) Stress-strain relation

Fig.8 Test results of dense sand in drained cyclic loading tests (Hinokio, 2000)

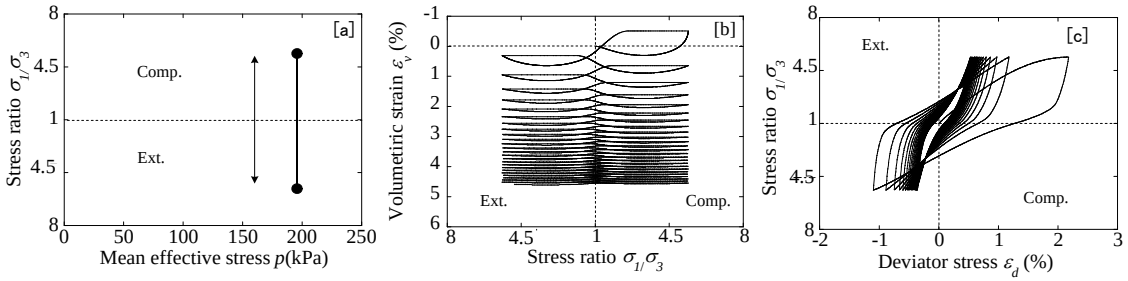

(a) Loading (b) Volumetric strain-stress ratio relation (c) Stress-strain relation

Fig.9 Simulation of the test results in Fig.8

Table 4 State variables of Toyoura sand sample in Figure 9

e_0	0.66
p (kPa)	196.
R_0^*	0.99
OCR ($1/R_0$)	53.6
ζ_0	0.0

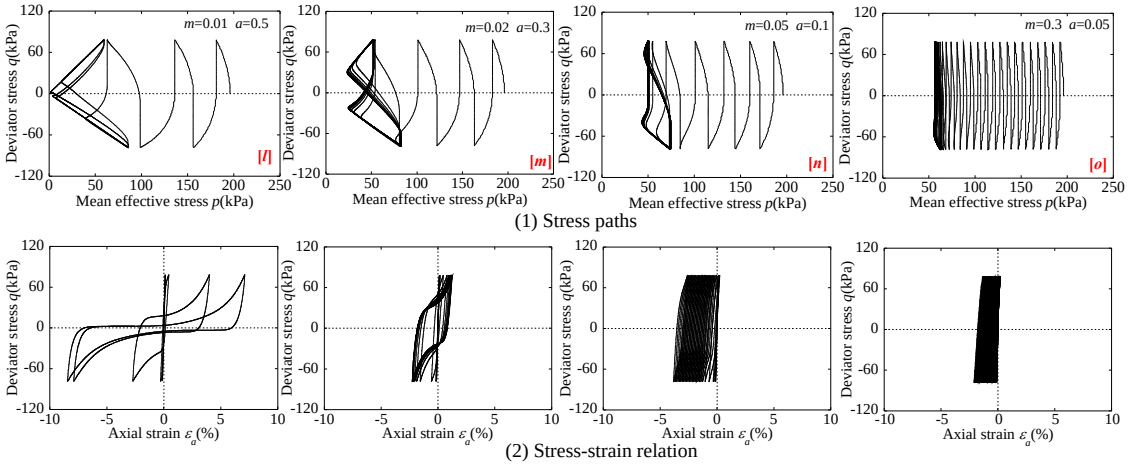

(1) Stress paths

(2) Stress-strain relation

Fig.10 Difference between clay and sand under undrained triaxial cyclic loading

Table 5 State variables and changed material parameters of samples in Figure 10

	[*l*]	[m]	[n]	[o]
e_0	0.69	0.69	0.69	0.69
p (kPa)	196.	196.	196.	196.
R_0^*	0.80	0.80	0.80	0.80
OCR ($1/R_0$)	35.0	35.0	35.0	35.0
ζ_0	0.0	0.0	0.0	0.0
m	0.01	0.02	0.05	0.30
a	0.50	0.30	0.10	0.05

The behaviors of dense sand subjected to drained cyclic loading under constant mean effective stress are also simulated. Fig. 15 shows the test results by Hinokio (2000). The cyclic loading condition is that the confining pressure of the sand is 196 kPa and the mean effective stress is kept constant while a shear stress with a maximum principal stress ratio of σ_1/σ_3=4 was loaded cyclically. At the beginning, the deviatoric stress-strain relation shows a relatively large loop, as the cyclic loading continues, however, the stiffness of the sand grows up and the stress-strain relation comes into an almost fixed loop as shown Fig.9(c). The volumetric strain shows dilatancy at the very beginning under cyclic loading but after then it turns to compression process until it reaches a steady state where the compression will not go further, as shown in Fig.9(b). In the simulation, the initial state valuables of the dense sand are listed in Table 4. As can be seen in Fig.10, the overall characteristics of the sand can be described quite well by the present model, for instance, the changes in dilatancy and stress-strain relations.

Figure 10 shows the different behavior of soils from sandy soil to clayey soil subjected to cyclic loading under undrained conditions. By changing the values of parameters a and m, as shown in Table 5, the difference between sandy soils and clayey soils can be easily and uniquely identified. For instance, in the case of sand [*l*], m=0.01 and a=0.50, which means that the loss of overconsolidation is very slow while the collapse of the structure is very fast, a typical cyclic mobility behavior is observed. In the case of clay [o], m=0.30 and a= 0.05, which means that the loss of overconsolidation is very fast while the collapse of the structure is very slow, a typical clayey soil behavior under cyclic loading is observed. The soils [*m*] and [*n*] just show the mechanical behavior of intermediate soils like silt.

4 CONCLUSIONS

In this paper, the overall behavior of Toyoura sand, a typical clean sand, is described in a unified way by the proposed model. For a given sand, the values of the material parameters

are fixed and can be easily determined by conventional drained triaxial compression tests and undrained triaxial cyclic loading tests. By using the uniquely determined material parameters, the mechanical behavior of the sand under different loadings and drainage conditions can be simulated in a unified way. The following detailed mechanical behavior of the sand with different densities is described in a satisfied way:

(1) Influence of the density effect
(2) Influence of the structure formed in depositary process
(3) Influence of the stress-induced anisotropy
(4) Mechanical behaviors of the sand subjected to cyclic loading under drained/undrained conditions
(5) Mechanical behaviors of the sand subjected to monotonic loading under drained/undrained conditions
(6) Confining-stress dependent behavior
(7) Difference of the mechanical behavior among sand, intermediate soils (sandy silty, silt, silty clay) and clay.

REFERENCES

Asaoka, A., Nakano, M. and Noda. T. (1998): Super loading yield surface concept for the saturated structured soils, Proc. of the Fourth European Conference on Numerical Methods in Geotechnical Engineering-NUMGE98, 232-242

Asaoka A. (2003): Consolidation of clay and compaction of sand, Keynote lecture, Proc. of the 12th Asian Regional Conference of Int. Society for Soil Mechanics and Geotechnical Engineering, Singapore, Leung et al. (eds), Vol.2

Hashiguchi, K. and Ueno, M. (1977): Elastoplastic constitutive laws of granular material, Constitutive Equations of Soils, Pro. 9th Int. Conf. Soil Mech. Found. Engrg., Spec. Ses. 9, Murayama, S. and Schofield, A. N. (eds.), Tokyo, JSSMFE, 73-82

Hinokio, M. (2000): Deformation characteristic of sand subjected to monotonic and cyclic loadings and its application to bearing capacity problem, Doctoral Thesis, Nagoya Institute of Technology, 141-144 (in Japanese)

Ishihara, K. and Okada, S. (1982): Effects of large preshearing on cyclic behavior of sand, Soils and Foundations, Vol.18, No.4, 31-45.

Nakai, T. and Mihara, Y. (1984): A new mechanical quantity for soils and its application to elastoplastic constitutive models, Soils and Foundations, Vol.24, No.2, 82-94

Sekiguchi, H. (1977): Rheological characteristics of clays, Proc. 9th Int. Conf. Soil Mech., Found. Eng., Tokyo, Vol.1, 289-292

Verdugo, R. and Ishihara, K. (1996): The steady state of sandy soils, Soils and Foundations, Vol.36, No.2, 81-91.

Yao, Y. P., Sun D. A. and Matsuoka, H. (2008): A unified constitutive model for both clay and sand with hardening parameter independent on stress path, Computers and Geotechnics, Vol.35, No.2, 210-222

Yamada, S., Takamori, T. and Sato, K. (2010): Effect on reliquefaction resistance produced by changes in anisotropy during liquefaction, Soils and Foundations, 50(1), 9-25.

Ye B., Ye G. L., Zhang F. (2012): Numerical modeling of changes in anisotropy during liquefaction using a generalized constitutive model, Computers and Geotechnics, 42, pp.62-72.

Zhang, F., Ye, B., Noda, T., Nakano, M. and Nakai, K. (2007): Explanation of cyclic mobility of soils: approach by stress-induced anisotropy, Soils and Foundations, 47(4), 635-648.

SIGNIFICANCE OF t_{ij} CONCEPT IN CONSTITUTIVE MODELING OF GEOMATRIALS

T. Nakai & H.M. Shahin
Department of Civil Engineering, Nagoya Institute of Technology, Nagoya, Japan

M. Hinokio
Department of Civil Engineering, Nagoya University, Nagoya, Japan

H. Kyokawa
Institute of Industrial Science, University of Tokyo, Tokyo, Japan

ABSTRACT: *Simple and unified method to describe stress-strain behavior in general three-dimensional stress condition, which has been called the t_{ij} concept, was presented by Nakai & Mihara (1984). Since this concept is based on the idea that the frictional law essentially governs soil behavior, its meaning is very clear. Using this concept, any kind of one-dimensional model and/or three-dimensional model formulated by using (p and q) can be easily extended to general three-dimensional conditions. Method for formulating the constitutive model using the t_{ij} concept and the meaning of the t_{ij} operator are reviewed. The validity of this concept is also checked by simulation of various types of shear tests in general three-dimensional conditions.*

1 INTRODUCTION

Figure 1 shows stress conditions in typical element tests of soils. Most of ordinary three-dimensional (3D) constitutive models have been formulated based on the test data under triaxial compression condition alone and using the Cam clay type stress invariants (p and q). However, such models cannot describe the stress-strain-strength of soils using unified material parameters in general 3D conditions as shown in Fig. 1. To describe the soil behavior under three different principal stresses, some material parameters in the models are given by a function of the magnitude of the intermediate principal stress. However, such method is not essential in rational modeling. Then, the concept of t_{ij} has been proposed to describe uniquely the stress-strain behavior in general three-dimensional stress condition (Nakai & Mihara, 1984). The details of this methodology were described in the previous papers (*e.g.*, Nakai & Hinokio, 2004; Nakai et al, 2011b) and the recent book (Nakai, 2012). Here, the procedure for incorporating this approach to ordinary elastoplastic models and the meaning of the concept are discussed.

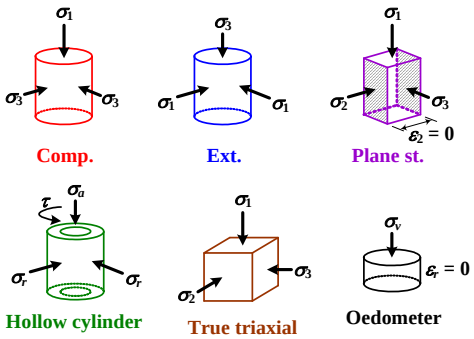

Fig. 1. Stress and strain conditions in typical element tests of soils

Before explanation of the concepts, let us review the well-known Mohr-Coulomb's failure criterion. Figure 2 shows Mohr's stress circle in τ-σ plane at failure, when major and minor principal stresses (σ_1 and σ_3) are applied to a soil without cohesion (c=0kPa). Since the influence of intermediate principal stress is not considered, Mohr-Coulomb's failure criterion is expressed as follows using the internal friction angle (ϕ):

$$\tan\phi = \frac{\tau}{\sigma_N} = \frac{\sigma_1 - \sigma_3}{2\sqrt{\sigma_1\sigma_3}} = \text{const.} \tag{1}$$

$$\sin\phi = \frac{\tau_{45^o}}{\sigma_{45^o}} = \frac{\sigma_1 - \sigma_3}{\sigma_1 + \sigma_3} = \text{const.} \tag{2}$$

Here, both expressions reduce to the condition of the stress ratio σ_1/σ_3=const. This criterion is based on the idea that the failure of granular materials such as soils is governed by the frictional law. As can be seen from Fig. 2, Eq. (1) represents the shear-normal ratio on $(\tau/\sigma)_{\max}$ plane, and Eq. (2) represents the shear-normal stress ratio on 45^o plane (or $\tau_{\max}$ plane), respectively. It is noticed that when the internal friction angle ϕ changes from 0^o to 90^o, the stress ratio τ/σ_N in Eq. (1) can take a value of 0 to infinite, but the value of stress ratio $\tau_{45^\circ}/\sigma_{45^\circ}$ should be between 0 and 1.

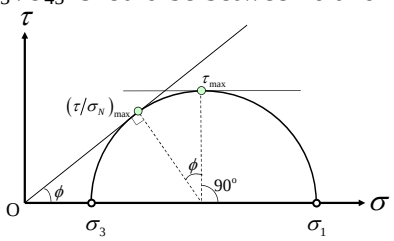

Fig. 2. Mohr's stress circle in τ-σ plane at failure

Murayama (1964) paid his attention to the $(\tau/\sigma)_{\max}$ plane not only at failure but also during shear deformation of soils, because it is considered appropriate that soil behavior during shear is governed by the frictional law and soil particles are most mobilized on this plane in two-dimensional condition. The following equation holds between ϕ_{mo} and (σ_1, σ_3):

$$\tan\left(45^o + \frac{\phi_{\text{mo}}}{2}\right) = \sqrt{\frac{1+\sin\phi_{\text{mo}}}{1-\sin\phi_{\text{mo}}}} = \sqrt{\frac{\sigma_1}{\sigma_3}} \tag{3}$$

Therefore, the mobilized plane is movable depending on the change of stress ratio. From Eq. (3), the stress invariants (normal and shear stresses on the mobilized plane) are expressed as follows using principal stresses:

$$\begin{cases} \sigma_N = \sigma_1 \cos^2\left(45° + \dfrac{\phi_{mo}}{2}\right) + \sigma_3 \sin^2\left(45° + \dfrac{\phi_{mo}}{2}\right) = \dfrac{2\sigma_1\sigma_3}{\sigma_1 + \sigma_3} \\ \tau = \left(\sigma_1 - \sigma_3\right)\cos\left(45° + \dfrac{\phi_{mo}}{2}\right)\sin\left(45° + \dfrac{\phi_{mo}}{2}\right) = \dfrac{\left(\sigma_1 - \sigma_3\right)\sqrt{\sigma_1\sigma_3}}{\sigma_1 + \sigma_3} \end{cases} \tag{4}$$

Now, as two-dimensional problems, it is also possible to formulate constitutive models for soil under plane strain or triaxial conditions using the following two stress invariants instead of Eq. (4):

$$\begin{cases} s = \dfrac{\sigma_1 + \sigma_3}{2} \\ t = \dfrac{\sigma_1 - \sigma_3}{2} \end{cases} \tag{5}$$

These invariants correspond to the shear and normal stress on 45^o plane in Fig. 2. However, the stress ratio t/s cannot take a value more than one as described before. Although it is possible to use both sets of the stress invariants (τ, σ_N) and (s, t) to describe two-dimensional behavior of soil, the stress (τ, σ_N) may be more essential and appropriate as the stress invariants used in modeling.

2 SPATIALLY MOBILIZED PLANE (SMP) AND OCTAHEDRAL PLANE

Since the mobilized plane is defined by only σ_1 and σ_3, the analytical soil deformation based on the concept of the mobilized plane is independent of σ_2. However, it is known that the soil behavior is influenced by the intermediate principal stress as well. In order to consider the influence of the intermediate principal stress, Matsuoka (1974) introduced not only the mobilized plane described above but also other two mobilized planes in which the shear-normal stress ratio is maximized between σ_1 and σ_2 and between σ_2 and σ_3, respectively (see Fig. 3). These three mobilized planes have been collectively called the compounded mobilized planes. In order to describe the soil behavior in general form, Matsuoka and Nakai (1974) paid attention to the plane ABC in Fig. 4, which is named the spatially mobilized plane. Here, three sides AC, AB and BC of plane ABC correspond to the three mobilized planes described above. As can be seen from this figure, the values of the coordinate axes intersected by the plane ABC (SMP) are proportional to the square root of the ratio between the corresponding principal stresses.

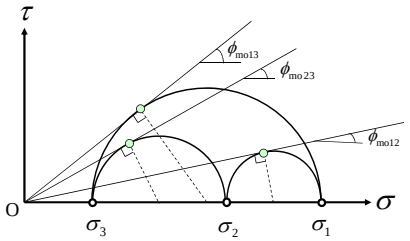

Fig. 3. Definition of three-mobilized planes

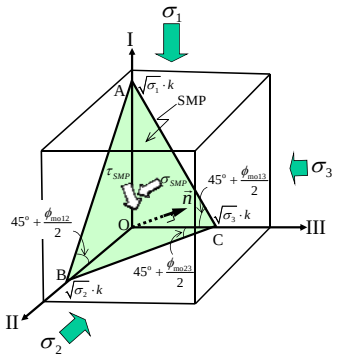

Fig. 4. Spatially mobilized plane in three-dimensional space

Therefore, the SMP coincides with the octahedral plane only under isotropic stress conditions and varies with possible changes of stress ratio. Then, the direction cosines (a_1, a_2 and a_3) of the normal to the SMP are expressed as follows using three-principal stresses:

$$a_1 = \sqrt{\frac{I_3}{I_2\sigma_1}}\ ,\ a_2 = \sqrt{\frac{I_3}{I_2\sigma_2}}\ ,\ a_3 = \sqrt{\frac{I_3}{I_2\sigma_3}}\quad (\text{where}\quad a_1^2 + a_2^2 + a_3^2 = 1) \tag{6}$$

where, I_1, I_2, and I_3 are the first, second and third stress invariants and expressed using three principal stresses as

$$\begin{cases} I_1 = \sigma_1 + \sigma_2 + \sigma_3 \\ I_2 = \sigma_1\sigma_2 + \sigma_2\sigma_3 + \sigma_3\sigma_1 \\ I_3 = \sigma_1\sigma_2\sigma_3 \end{cases} \tag{7}$$

The normal and shear stress on the SMP and the shear-normal stress ratio are expressed as

$$\begin{cases} \sigma_{SMP} = \sigma_1 a_1^2 + \sigma_2 a_2^2 + \sigma_3 a_3^2 \\ \tau_{SMP} = \sqrt{(\sigma_1 - \sigma_2)^2 a_1^2 a_2^2 + (\sigma_2 - \sigma_3)^2 a_2^2 a_3^2 + (\sigma_3 - \sigma_1)^2 a_3^2 a_1^2} \end{cases} \tag{8}$$

$$X = \frac{\tau_{SMP}}{\sigma_{SMP}} = \frac{2}{3}\sqrt{\frac{(\sigma_1-\sigma_2)^2}{4\sigma_1\sigma_2}+\frac{(\sigma_2-\sigma_3)^2}{4\sigma_2\sigma_3}+\frac{(\sigma_3-\sigma_1)^2}{4\sigma_3\sigma_1}}$$
$$= \frac{2}{3}\sqrt{\tan\phi_{mo12}{}^2+\tan\phi_{mo23}{}^2+\tan\phi_{mo13}{}^2} \quad (9)$$
$$= \sqrt{\frac{I_1I_2}{9I_3}-1}$$

As can be seen from Eq. (9), the shear-normal stress ratio is the quadratic mean of maximum shear-normal stress ratios ($\tan\phi_{mo12}$, $\tan\phi_{mo23}$ and $\tan\phi_{mo13}$) between two respective principal stresses. Also, the condition of the stress ratio τ_{SMP}/σ_{SMP}=const. gives the following criterion using the three stress invariants, which has been called the SMP criterion or Matsuoka & Nakai creiterion:

$$\frac{I_1I_2}{I_3} = \text{const.} \quad (10)$$

On the other hand, the octahedral plane is indicated as the plane ABC in Fig. 5 in three-dimensional space. The stress invariants (p and q) which are used in the ordinary models correspond to the normal and shear stresses on the octahedral plane as shown in Eq. (11).

$$\begin{cases} p = \sigma_{oct} = \frac{1}{3}(\sigma_1+\sigma_2+\sigma_3) \\ q = \frac{3}{\sqrt{2}}\tau_{oct} = \frac{1}{\sqrt{2}}\sqrt{(\sigma_1-\sigma_2)^2+(\sigma_2-\sigma_3)^2+(\sigma_3-\sigma_1)^2} \end{cases} \quad (11)$$

From Eq. (11), it can be seen that the stress invariant q (or the shear stress τ_{oct}) correspond to the quadratic mean of maximum shear stresses ($(\sigma_1-\sigma_2)/2$, $(\sigma_2-\sigma_3)/2$ and $(\sigma_1-\sigma_3)/2$) between two respective principal stresses.

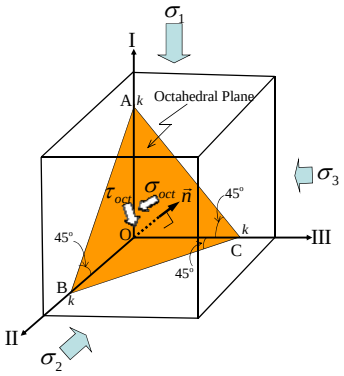

Fig. 5. Octahedral plane in three-dimensional space

3 DISCUSSION ON APPLICABILITY OF CAM CLAY TYPE MODELS

As shown in Fig. 6, the stress invariants (p and q) are also defined by the normal component ON and the in-plane component NP of the principal stress vector with respect to the octahedral plane, and expressed as follows using three principal stresses or stress tensor:

$$\begin{cases} p = \sqrt{\dfrac{1}{3}}\overline{\mathrm{ON}} = \dfrac{1}{3}(\sigma_1 + \sigma_2 + \sigma_3) = \dfrac{1}{3}\sigma_{ij}\delta_{ij} \\ q = \sqrt{\dfrac{3}{2}}\overline{\mathrm{NP}} = \dfrac{1}{\sqrt{2}}\sqrt{(\sigma_1 - \sigma_2)^2 + (\sigma_2 - \sigma_3)^2 + (\sigma_3 - \sigma_1)^2} = \sqrt{\dfrac{3}{2}(\sigma_{ij} - p\delta_{ij})(\sigma_{ij} - p\delta_{ij})} \end{cases} \tag{12}$$

The strain increment invariants ($d\varepsilon_v$ and $d\varepsilon_d$) used in formulation of ordinary models are also defined by the normal component O'N' and the in-plane component N'P' of the principal strain increment vector with respect to the octahedral plane (see Fig. 7), and expressed as follows:

$$\begin{cases} d\varepsilon_v = \sqrt{3}\overline{\mathrm{O'N'}} = d\varepsilon_1 + d\varepsilon_2 + d\varepsilon_3 = d\varepsilon_{ij}\delta_{ij} \\ d\varepsilon_d = \sqrt{\dfrac{2}{3}}\overline{\mathrm{N'P'}} = \dfrac{\sqrt{2}}{3}\sqrt{(d\varepsilon_1 - d\varepsilon_2)^2 + (d\varepsilon_2 - d\varepsilon_3)^2 + (d\varepsilon_3 - d\varepsilon_1)^2} \\ \qquad = \sqrt{\dfrac{2}{3}\left(d\varepsilon_{ij} - \dfrac{d\varepsilon_v}{3}\delta_{ij}\right)\left(d\varepsilon_{ij} - \dfrac{d\varepsilon_v}{3}\delta_{ij}\right)} \end{cases} \tag{13}$$

Most of three-dimensional ordinary Cam clay type models are formulated based on the idea that there are unique relations between the above stress invariants and the strain increment invariants.

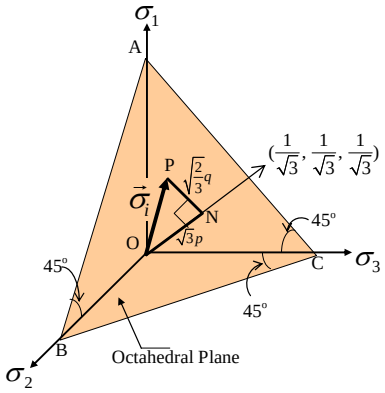

Fig. 6. Definitions of p and q

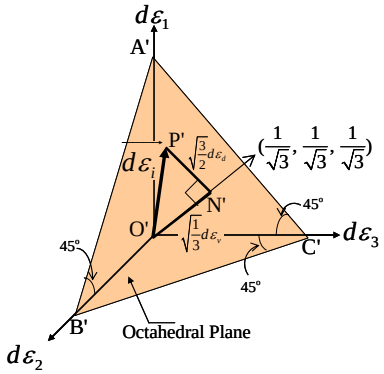

Fig. 7. Definitions of $d\varepsilon_v$ and $d\varepsilon_d$

Figures 8 and 9 show the observed results of drained triaxial compression ($\sigma_1>\sigma_2=\sigma_3$) and triaxial extension ($\sigma_1=\sigma_2>\sigma_3$) tests on normally consolidated Fujinomori clay and medium dense Toyoura sand under constant mean principal stress, in terms of stress ratio (q/p) versus deviatoric strain (ε_d) and volumetric strain (ε_v). It can be seen from these figures that the deformation and strength of soils in three-dimensional (3D) stress conditions cannot be described uniquely using these stress and strain invariants.

Figures 10 and 11 show the stress-dilatancy plots for Fujinomori clay and medium dense Toyoura sand respectively, where the strain increment ratio includes the elastic component. However, under shear loading, developed plastic strains are much larger than the elastic ones, and hence, the total plastic strain increment ratio is almost equal to the plastic strain increment ratio. It is found that there is no unique relation between $d\varepsilon_v/d\varepsilon_d$ and q/p, which means that the shape of yield surface on p-q plane is dependent on the relative magnitude of the intermediate principal stress

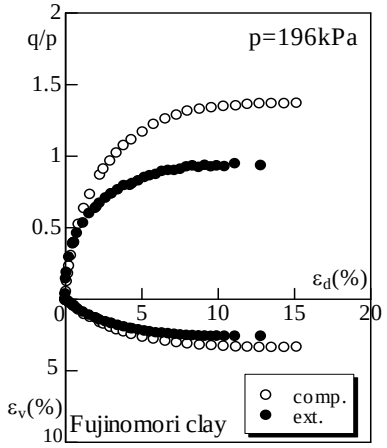

Fig. 8. Observed stress-strain relation in triaxial compression and extension tests on normally consolidated clay

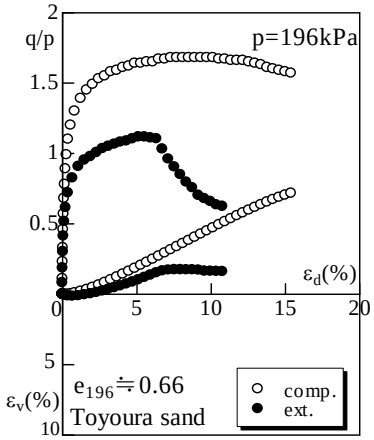

Fig. 9. Observed stress-strain relation in triaxial compression and extension tests on medium dense sand

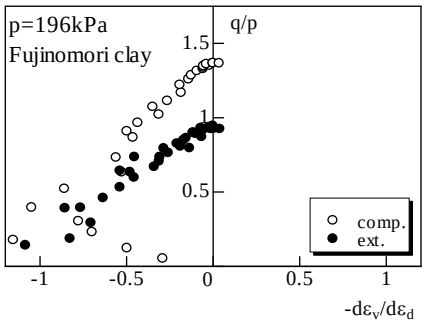

Fig. 10. Observed q/p - $d\varepsilon_v/d\varepsilon_d$ relation in triaxial compression and extension tests on normally consolidated clay

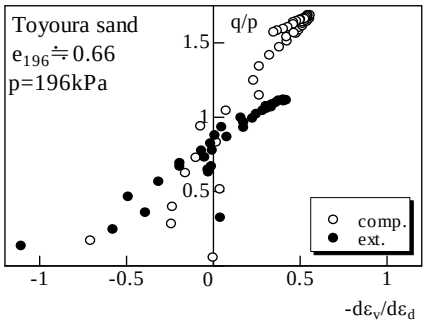

Fig. 11. Observed q/p - $d\varepsilon_v/d\varepsilon_d$ relation in triaxial compression and extension tests on normally consolidated clay

Figures 12 and 13 show the directions and the magnitudes of the observed shear strain increments represented by bold lines on the octahedral plane for true triaxial ($\sigma_1>\sigma_2>\sigma_3$) tests ($\theta$=15°, 30° and 45°). Here, the length of each bold line is proportional to the value of shear strain increment divided by the shear-normal stress ratio increment on the octahedral plane. In the figures, θ denotes the angle between σ_1-axis and the corresponding radial stress path on the octahedral plane, where θ=0° and 60° represent the stress path under triaxial compression and triaxial extension conditions, respectively. It can be seen that the direction of the observed shear strain increments deviates leftward from the direction of shear stress (radial direction) with the increase in stress ratio under three different principal stresses. On the other hand, since the plastic potential (yield surface) which is formulated using the stress invariants p and q is a circle on the octahedral plane as shown in Fig. 13, the calculated plastic strain increments are also radial in that plane. It goes without saying that the elastic strain increments as calculated by Hooke's law is radial just like the stress increment vector is in the octahedral plane.

It is noted that the direction of the strain increments in the octahedral plane has been traditionally less studied in the literature than the stress-dilatancy relation. For example, turning to Figs. 12 and 13, the directions of the strain increments at the 0^o and 60^o branches in the octahedral plane imply that the intermediate principal strain increment $d\varepsilon_2$ coincides with the minor principal strain increment $d\varepsilon_3$ and the major principal strain increment $d\varepsilon_1$, respectively. Hence, a small deviation of the directions of the strain increment on the

octahedral plane has much influence on the three-dimensional behaviors of soils. It is understood that the elastoplastic constitutive models whose yield functions are formulated using the invariants (p and q) are not capable of describing the influence of the intermediate principal stress on the deformation and strength characteristics of soils, even if the initial stress condition and the density of soils are the same.

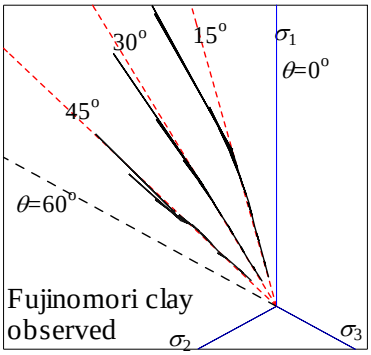

Fig. 12. Observed direction of $d\varepsilon_d$ on octahedral plane under three different principal stresses ($\sigma_1>\sigma_2>\sigma_3$) on normally consolidated clay

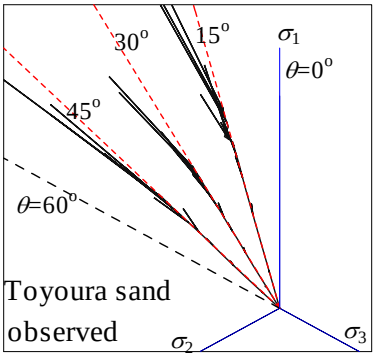

Fig. 13. Observed direction of $d\varepsilon_d$ on octahedral plane under three different principal stresses ($\sigma_1>\sigma_2>\sigma_3$) on medium dense sand

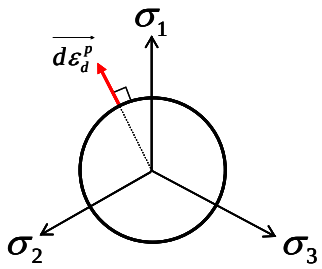

Fig. 14. Shape of yield surface of ordinary model such as Cam clay model on octahedral plane

4 FORMULATION OF CONSTITUTIVE MODEL BASED ON t_{ij} CONCEPT

From consideration of shear behavior under three-dimensional stresses, it was found out that there hold unique relations between the shear-normal stress ratio $X=\tau_{SMP}/\sigma_{SMP}$ and the strain increment invariants ($d\varepsilon_N^*$, $d\varepsilon_S^*$) which are defined by the normal and in-plane components (O'N' and N'T') of the principal strain increment vector with respect to the octahedral plane as shown in Fig. 14 (Nakai & Matsuoka, 1980, 1983). These new strain increments are expressed as

$$\begin{cases} d\varepsilon_N^* = d\varepsilon_1 a_1 + d\varepsilon_2 a_2 + d\varepsilon_3 a_3 \\ d\varepsilon_S^* = \sqrt{(d\varepsilon_1 a_2 - d\varepsilon_2 a_1)^2 + (d\varepsilon_2 a_3 - d\varepsilon_3 a_2)^2 + (d\varepsilon_3 a_1 - d\varepsilon_1 a_3)^2} \end{cases} \tag{14}$$

According to this idea which was named the SMP* concept, it is assumed that there are unique relations between the stress ratio τ_{SMP}/σ_{SMP} on the SMP and the strain increment invariants ($d\varepsilon_N^*$, $d\varepsilon_S^*$) based on the SMP, and the direction of the strain increment invariant (in-plane components of the principal strain increment to the SMP) $d\varepsilon_S^*$ coincides with that of the shear stress on the SMP τ_{SMP}. However, as can be seen from Eqs. (8) and (14), the transformation forms of stress invariants from the principal stresses and those of strain increment invariants from the principal strain increments are different. Then, it is difficult to apply this concept to the usual elastoplatic formulation as it is.

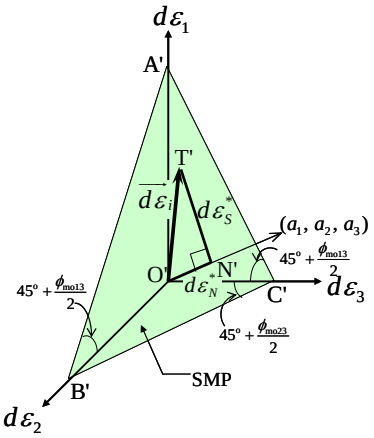

Fig. 14. Definitions of $d\varepsilon_N$* and $d\varepsilon_S$*

In order to generalize the concept of SMP*, the following principal values of the modified stress is defined using the direction cosines (a_1, a_2 and a_3) of the normal to the SMP in Eq. (6):

$$t_1 = a_1\sigma_1,\ t_2 = a_2\sigma_2,\ t_3 = a_3\sigma_3 \tag{15}$$

Using this modified stress, the stress invariants (normal and shear stresses on the SMP (σ_{SMP}, τ_{SMP}) in Eq. (8)) are expressed as the normal and in-plane components (t_N and t_S) of the principal modified stress vector (t_1, t_2, t_3) to the SMP as shown in Fig. 15 and the following equations:

$$\begin{cases} t_N = \sigma_{SMP} = t_1a_1 + t_2a_2 + t_3a_3 \\ t_S = \tau_{SMP} = \sqrt{(t_1a_2 - t_2a_1)^2 + (t_2a_3 - t_3a_2)^2 + (t_3a_1 - t_1a_3)^2} \end{cases} \tag{16}$$

It can be understood that the transformation form of the stress invariants from the modified stress in Eq. (16) is the same as that of the strain increment invariants in Eq.(14).

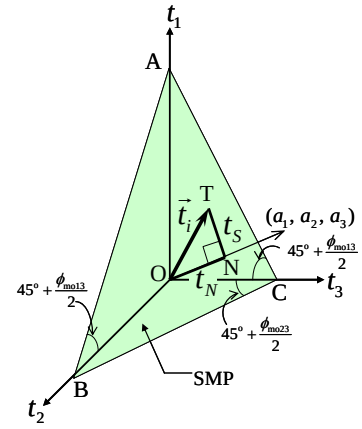

Fig. 15. Definitions of t_N and t_S

Now, in ordinary elastoplastic model such as the Cam clay model, the three-dimensional yield function is formulated using two stress invariants in Eq. (12), and the flow rule is assumed in stress space. This implies that the stress invariants *(p* and *q*) are related with the (plastic) strain increment invariants ($d\varepsilon_v$ and $d\varepsilon_d$) which transformation form should be the same as those of the stress invariants. In the t_{ij} concept which is considered to be the generalized concept of SMP*, since the transformation forms of the stress invariants in Eq. (16) and the strain increment invariants in Eq. (14) are the same, it is possible to describe three-dimensional behavior of soils using the two stress invariants (t_N and t_S) – i.e., formulate the yield function using t_N and t_S and assume the flow rule in the modified stress space.

Until now, explanation is done using the principal values of stress and strain increment for easy understanding. From now, the explanation will be done using general stress and strain increment to apply the t_{ij} concept to elastoplasticity. A symmetric unit tensor a_{ij} whose principal values are given by the direction cosines of the normal to the SMP in Eq. (6) can be defined as

$$a_{ij} = \sqrt{\frac{I_3}{I_2}} \cdot r_{ij}^{-1} = \sqrt{\frac{I_3}{I_2}} \cdot \left(\sigma_{ik} + I_{r2}\delta_{ik}\right)\left(I_{r1}\sigma_{kj} + I_{r3}\delta_{kj}\right)^{-1} \tag{17}$$

where δ_{ij} is the unit tensor, and I_1, I_2, and I_3 are the first, second and third invariants of σ_{ij} as mentioned before, and I_{r1}, I_{r2} and I_{r3} are the first, second and third invariants of r_{ij}, which is the square root of the stress tensor or $r_{ik}r_{kj}=\sigma_{ij}$. Therefore, the modified stress tensor t_{ij} is given by

$$t_{ij} = a_{ik}\sigma_{kj} \tag{18}$$

Here, t_{ij} is symmetric, and its principal axes coincide with those of σ_{ij}, because both a_{ik} and σ_{kj} are symmetric and coaxial. A comparison between the stress and strain increment tensors and their invariants used classically and those based on the t_{ij} concept is shown in Table 1. The definitions of some quantities related to stress in (a) the classical approach and (b) the t_{ij} concept are illustrated in Fig. 16 as well. It can be observed from Table 1 and Fig. 16 that by merely substituting the spatially mobilized plane (SMP) for the octahedral plane as the reference plane, the modified stress t_{ij} together with various scalars and tensors related to stress and strain increments can be analogically calculated (Nakai and Hinokio, 2004). For reference, tensor η_{ij} in Table 1 is the stress ratio tensor defined by Sekiguchi and Ohta (1977) to extend the ordinary isotropic models such as the Cam clay model to anisotropic ones. The corresponding stress ratio tensor based on the t_{ij} concept is given by x_{ij}.

	ordinary concept	t_{ij} concept
tensor normal to reference plane	δ_{ij} (unit tensor)	a_{ij} (tensor normal to SMP)
stress tensor	σ_{ij}	t_{ij}
mean stress	$p = \sigma_{ij}\delta_{ij}/3$	$t_N = t_{ij}a_{ij}$
deviatoric stress tensor	$s_{ij} = \sigma_{ij} - p\delta_{ij}$	$t'_{ij} = t_{ij} - t_N a_{ij}$
deviatoric stress	$q = \sqrt{(3/2)s_{ij}s_{ij}}$	$t_S = \sqrt{t'_{ij}t'_{ij}}$
stress ratio tensor	$\eta_{ij} = s_{ij}/p$	$x_{ij} = t'_{ij}/t_N$
stress ratio	$\eta = q/p$	$X = t_S/t_N$
strain increment normal to reference plane	$d\varepsilon_v = d\varepsilon_{ij}\delta_{ij}$	$d\varepsilon^*_N = d\varepsilon_{ij}a_{ij}$
deviatoric strain increment tensor	$de_{ij} = d\varepsilon_{ij} - d\varepsilon_v\delta_{ij}/3$	$d\varepsilon'_{ij} = d\varepsilon_{ij} - d\varepsilon^*_N a_{ij}$
strain increment parallel to reference plane	$d\varepsilon_d = \sqrt{(2/3)de_{ij}de_{ij}}$	$d\varepsilon^*_S = \sqrt{d\varepsilon'_{ij}d\varepsilon'_{ij}}$

Table 1. Comparison between tensors and scalars related to stress and strain increments in the ordinary concept and the t_{ij} concept

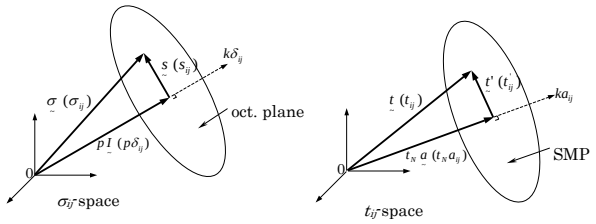

(a) ordinary concept (b) t_{ij} concept

Fig. 16. Definitions of t_N and t_S

The dots in Figs. 17 and 18 show the observed stress-dilatancy relation of the same tests in Figs. 10 and 11, arranged in terms of the relation between stress ratio t_S/t_N and strain increment ratio $d\varepsilon_N^*/d\varepsilon_S^*$ using the above stress and strain increment invariants based on the t_{ij} concept. It can be seen that though the relation between q/p and $d\varepsilon_v/d\varepsilon_d$ in Figs. 10 and 11 is very much influenced by the intermediate principal stress, the stress-dilatancy relation in Figs. 17 and 18 is independent of the intermediate principal stress.

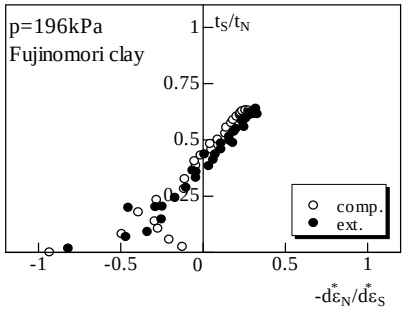

Fig. 17. Observed t_S/t_N - $d\varepsilon_N^*/d\varepsilon_S^*$ relation of triaxial compression and extension tests on normally consolidated clay

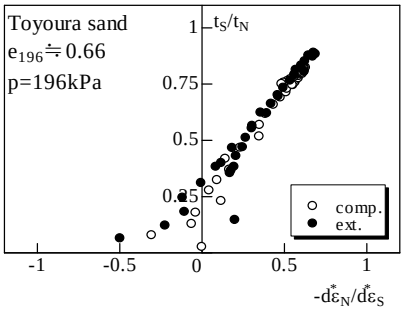

Fig. 18. Observed t_S/t_N - $d\varepsilon_N^*/d\varepsilon_S^*$ relation of triaxial compression and extension tests on medium dense sand

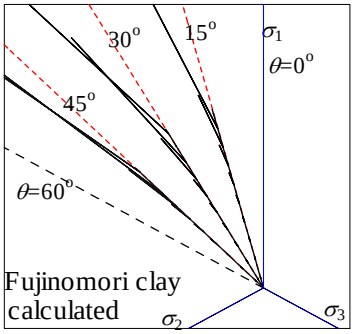

Fig. 19. Calculated directions of $d\varepsilon_d$ on the octahedral plane under three different principal stresses ($\sigma_1>\sigma_2>\sigma_3$) on normally consolidated Fujinomori clay

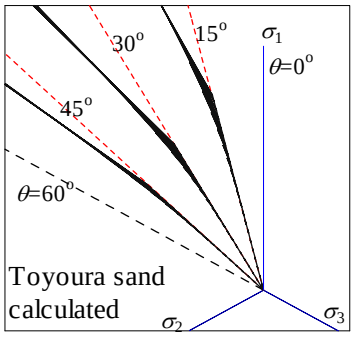

Fig. 20. Calculated directions of $d\varepsilon_d$ on the octahedral plane under three different principal stresses ($\sigma_1>\sigma_2>\sigma_3$) on Toyoura sand

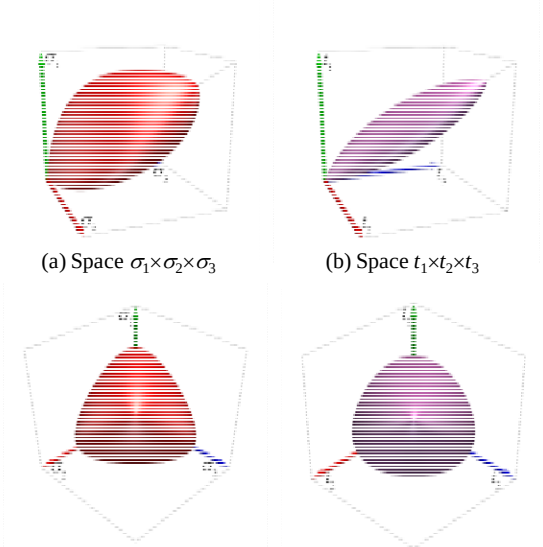

(a) Space $\sigma_1\times\sigma_2\times\sigma_3$ (b) Space $t_1\times t_2\times t_3$

(c) View from hydrostatic axis $\sigma_1=\sigma_2=\sigma_3$ (d) View from hydrostatic axis $t_1=t_2=t_3$

Fig. 21. Shape of yield surfaces in the principal spaces of σ_{ij} and t_{ij} (Pedroso *et al.*, 2005)

Figure 19 and 20 show the calculated directions of strain increments on the octahedral plane for true triaxial tests on clay corresponding to the observed results in Figs. 12 and 13. The calculated results describe well the observed directions of strain increments on the octahedral plane, including the leftward deviation from the radial direction with the increase of stress ratio. Figure 21 shows a view of the yield surface of model formulated using t_{ij} concept in the principal spaces of σ_{ij} and t_{ij} (Pedroso *et al.,* 2005). The shape of the yield surface on the octahedral plane in the σ_{ij} space is a rounded triangle and corresponds to that of the SMP criterion defined by Eq. (10) (Matsuoka and Nakai, 1974) (see diagram (c)). The shape of the yield surface in the t_{ij} space is also oval, though a little more rounded, but it is not a circle (see diagram (d)).

Now, let us show the meaning of the t_{ij} concept, focusing mostly on the microscopic point of view. Several researchers have shown that induced anisotropy of soils developed with the change of stresses is characterized by the frequency distribution of the inter-particle contact angles. It has then been shown from microscopic observation (e.g., Oda, 1972) and DEM simulation (e.g., Maeda et al, 2006) that, as the stress ratio increases, the average directions normal to the inter-particle contacts gradually concentrate in the same direction as the major principal stress (σ_1). Based on the these microscopic studies, Satake (1984) pointed out that the principal values (φ_1, φ_2) of the so-called fabric tensor φ_{ij}, which represents the relative distribution of the number of vectors normal to the inter-particle contacts, is approximately proportional to the square root of the corresponding principal stresses.

$$\frac{\varphi_1}{\varphi_2} \simeq \left(\frac{\sigma_1}{\sigma_2} \right)^{0.5} \tag{19}$$

Employing a fabric tensor, Satake (1982) also proposed the following modified stress tensor σ_{ij}^* for analyzing the behavior of granular materials:

$$\sigma_{ij}^* = \frac{1}{3} \varphi_{ik}^{-1} \sigma_{kj} \tag{20}$$

Figure 22 shows schematically the distribution of inter-particle contacts in 2D condition. Considering an equivalent continuum, such material exhibits anisotropy since the stiffness in the σ_1 direction should be larger than that in the σ_2 direction with the increase of stress ratio as shown in diagram (b). When adopting an elastoplastic theory, it is reasonable to treat the soil as an isotropic material by introducing the modified stress t_{ij} in which induced anisotropy is already taken into consideration. This is because the normality rule, for which the direction of plastic flow is normal to the yield surface (plastic potential), should hold in the isotropic space, like the transformed space used to analyze seepage problems in anisotropic ground and others. As shown in Eq. (6), the principal values of a_{ij} are inversely proportional to the square root of the respective principal stresses, therefore:

$$a_1 : a_2 = \frac{1}{\sqrt{\sigma_1}} : \frac{1}{\sqrt{\sigma_2}} \tag{21}$$

By comparison, it can be noted that a_{ij} corresponds to the inverse of the fabric tensor in Eq. (19), and t_{ij} defined by Eq. (18) corresponds to the modified stress introduced by Satake (1982) in Eq. (20). As shown in diagram (c) of Fig. 22, the stress ratio t_1/t_2 in the modified stress space is smaller than stress ratio σ_1/σ_2 in the ordinary stress space, because a_1 is smaller than a_2 as Eq. (21) shows. Then, it is reasonable to assume that the flow rule (normality condition) holds not in the σ_{ij} space but in the t_{ij} space, because the condition of

the anisotropic material under anisotropic stress ratio in diagram (b) can be considered to be the same as that of the isotropic material under lower stress ratio in diagram (c) in Fig. 22.

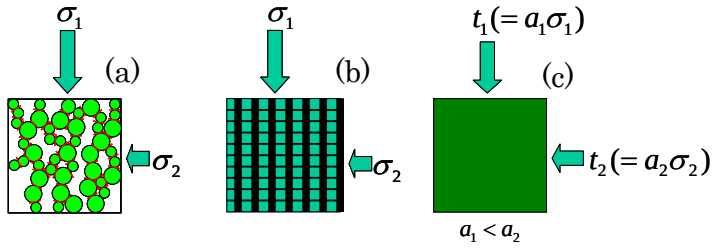

Fig. 22. Anisotropy and its expression

Next, it is described the reason why the stress and strain increment invariants used in the t_{ij} concept are defined as the normal and parallel components of the stress and strain increments with respect to the SMP instead of the octahedral plane. Irrecoverable behavior of materials such as metal is governed mostly by the deviatoric stress (or shear stress) alone, so that it is reasonable to consider the plane where shear stress is maximized (in 2D condition) and the averaged plane where shear stress between two principal stresses is maximized –. i.e., octahedral plane (in 3D condition). On the other hand, the irrecoverable behavior of geomaterials such as soil is governed by the frictional law between particles – i.e., shear-normal stress ratio. Therefore, attention should be paid to the plane where shear-normal stress ratio is maximized, i.e., the mobilized plane (in 2D condition), and the plane combined by the three planes where the shear-normal stress ratio between two respective principal stresses is maximized, i.e., the SMP (in 3D condition). In this sense, it is natural to formulate constitutive models using the normal and in-plane components of the stress and strain increments referred to the SMP. As a consequence, the influence of the intermediate principal stress on induced anisotropy and frictional resistance is introduced by adopting the t_{ij} concept.

5 USEFULNESS OF t_{ij} CONCEPT IN ELASTOPLASTIC MODELING

The yield function of ordinary elastoplastic models of soil such as the Cam clay model is expressed using the stress invariants (p and $\eta=q/p$) in the following form (e.g., Schofield and wroth, 1968; Roscoe and Burland, 1968):

$$f = F(p, \eta = q/p) - H = 0 \tag{22}$$

where H is the strain hardening parameter, which is given by strain-like variables. For example, in the Cam clay type models, F and H are given by

$$F = (\lambda - \kappa)\left\{\ln\frac{p}{p_0} + \zeta(\eta)\right\} = (\lambda - \kappa)\ln\frac{p_1}{p_0} \tag{23}$$

$$H = (-\Delta e)^p = (1 + e_0)\varepsilon_v^p \tag{24}$$

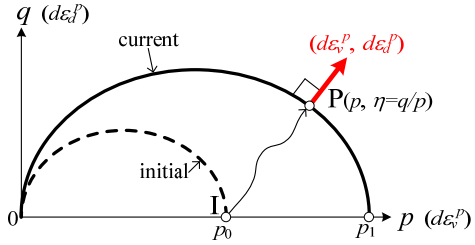

Fig. 23. Initial and current yield surfaces in the p – q plane and direction of plastic flow in an ordinary model such as Cam clay model

where λ and κ are the compression and swelling indices, $(-\Delta e)^p$ is the void ratio change from the initial state to the current state, and $\zeta(\eta)$ is an increasing function of η which satisfies $\zeta(\eta)=0$ (e.g., $\zeta(\eta)=\eta/M$ in the original Cam clay model). The solid curve in Fig. 23 shows the yield surface on $p-q$ plane represented by Eqs. (22) to (24). The broken curve shows the initial yield surface when $p=p_0$ and $\eta=0$. The yield function (yield surface) is convex in the stress space as illustrated in the figure. Here, p_0 and p_1 in Eq. (23) are the values of the mean stress on the p-axis for the initial yield surface (broken curve) and the current yield surface (solid curve) respectively, which determine the size of these surfaces. Then, since the direction of the plastic strain increment is normal to the yield surface in the Cauchy stress σ_{ij}, the plastic strain increment can be obtained as follows:

$$d\varepsilon_{ij}^{p}=\Lambda\frac{\partial F}{\partial\sigma_{ij}}=\Lambda\left(\frac{\partial F}{\partial p}\frac{\partial p}{\partial\sigma_{ij}}+\frac{\partial F}{\partial\eta}\frac{\partial\eta}{\partial\sigma_{ij}}\right) \tag{25}$$

Now, in three-dimensional modeling based on the t_{ij} concept, the yield function is given using the stress invariants (t_N and t_S) instead of (p and q):

$$f=F(t_N,\ X=t_S/t_N)-H=0 \tag{26}$$

$$F=(\lambda-\kappa)\left\{\ln\frac{t_N}{t_{N0}}+\zeta\left(X\right)\right\}=(\lambda-\kappa)\ln\frac{t_{N1}}{t_{N0}} \tag{27}$$

$$H=(-\Delta e)^p=(1+e_0)\varepsilon_v^p \tag{28}$$

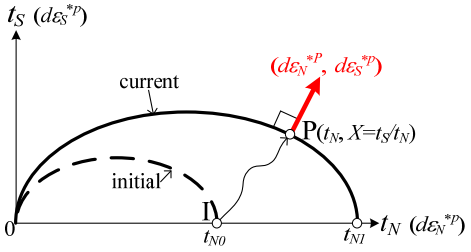

Fig. 24. Initial and current yield surfaces in the t_N–t_S plane and direction of plastic flow for the model based on the t_{ij} concept

where in the same way as the above expression of the ordinary modeling, $\zeta(X)$ is an increasing function of X which satisfies $\zeta(X)=0$, and t_{N0} and t_{N1} in Eq. (27) are the values of the mean stress on the t_N-axis for the initial yield surface (broken curve) and the current yield surface (solid curve) in Fig. 24. The plastic strain increment is calculated using an associated flow rule in t_{ij} space (see Fig. 24) as follows:

$$d\varepsilon_{ij}^{p}=\Lambda\frac{\partial F}{\partial t_{ij}}=\Lambda\left(\frac{\partial F}{\partial t_N}\frac{\partial t_N}{\partial t_{ij}}+\frac{\partial F}{\partial X}\frac{\partial X}{\partial t_{ij}}\right) \tag{29}$$

The model based on the t_{ij} concept can take into consideration simply and sophisticatedly the influence of the intermediate on the stress-strain-strength behavior of soil (e.g., Figs. 8 and 9). Since the t_{ij} concept is the generalized idea of the SMP* concept, the model can represent the uniqueness of stress-dilatancy relation in Figs. 17 and 18 and the deviation of the direction of deviatoric strain increment on the octahedral plane in Figs. 12 and 13 naturally (see Figs. 19 and 20).

In addition to the above, the t_{ij} concept has the following beneficial feature: Figure 25 shows the yield surface of the original Cam clay model in the p-q plane under triaxial compression (upper half) and triaxial extension (lower half) conditions. Figure 26 shows the yield surface of the t_{ij} model in (a) the t_N-t_S plane and (b) the p-q plane. It can be observed that the yield surface of the model based on the t_{ij} concept is symmetric with respect to the t_N-axis but not symmetric with respect to the p-axis. Also, it is noted that the yield surface of the

models is smooth over the whole domain, whereas the one in the original Cam clay model is not smooth at the tip on p-axis. Such smoothness of the yield surface ensures numerical stability in computations in the same way as the modified Cam clay model (Roscoe and Burland, 1968) does. Now, the lines for which the minor principal stress σ_3 is zero are indicated in every figure. It can be seen that models formulated using p and q such as the Cam clay model have tension zones (shaded area in Fig. 25) on and inside the yield surface. This means that the stress condition may enter the tension zone (σ_3<0) during elastic deformation in the numerical simulations of the ground behavior, because the yield surface is fixed during elastic deformation in conventional elastoplasticity. On the other hand, there is no tension zone in the yield surface formulated using t_N and t_S. This is because σ_3=0 condition is satisfied on the vertical axis (t_S axis) in Fig. 26(a). Hence, models based on the t_{ij} concept not only are capable of describing properly the influence of the intermediate principal stress but also have the above-mentioned benefit for numerical computations

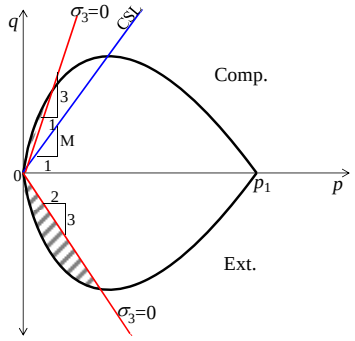

Fig. 25. Yield surface of the Cam clay model and tension zone on the p – q plane

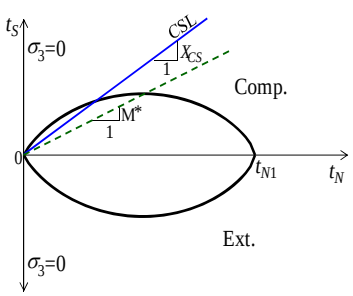

(a) Yield surface on t_N – t_S plane

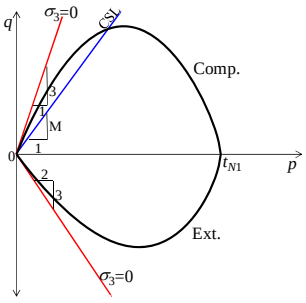

(b) Yield surface on p– q plane

Fig. 26. Yield surface of the Cam clay model and tension zone on the p – q plane

6 CONCLUSIONS

The concept of t_{ij} by which the influence of the intermediate principal stress can be automatically taken into account in three-dimensional modeling was explained, through its historical developments from the concept of the mobilized plane by Murayama. The physical meaning of the t_{ij} concept is discussed. Method to extend any Cam clay type models to ones valid in general three-dimensional conditions using the t_{ij} concept was presented. Another advantage of the t_{ij} concept in numerical computations was also presented, discussing the problem points in the ordinary Cam clay type models. Extension of one-dimensional models in which density, bonding, time-effect and other are considered (Nakai, et al., 2011a) to the three-dimensional ones using the t_{ij} concept presented here and its verification are described in other papers and book (Nakai, et al., 2011b; Nakai, 2012).

REFERENCES

Maeda, k., Hirabayashi, H. & Ohmura, A. (2006), "Micromechanical influence of grain properties on deformation – failure behaviors of granular media by DEM". Proceedings of Geomechnics and Geotechnics of Particulate Media, Yamaguchi, 173-179.

Matsuoka, H. (1974), "Stress-strain relationship of sand based on the mobilized plane", Soils and Foundations, Vol. 14(2), 47-61.

Matsuoka, H. & Nakai, T. (1974), "Stress-deformation and strength characteristics of soil under three different principal stresses". Proc. of JSCE, No. 232: 59-70.

Murayama, S. (1964), “A theoretical consideration on a behavior of sand”. Proceedings of IUTAM Symposium on Rheology and Soil Mechanics, Grenoble, 146-159.

Nakai, T. (2012), Constitutive Modeling of Geomaterials: Principles and Applications, CRC Press, Boca Raton London New York .

Nakai, T. & Hinokio, T. (2004), “A simple elastoplastic model for normally and over consolidated soils with unified material parameters”. Soils and Foundations, Vol. 44(2): 53-70.

Nakai, T. & Matsuoka, H. (1980), “A unified law for soil shear behavior under three-dimensional stress condition”. Proc. of JSCE, No. 303, 85-77 (in Japanese).

Nakai, T. & Matsuoka, H. (1983), “Shear behaviors of sand and clay under three-dimensional stress condition”. Soils and Foundations, Vol. 23(2), 26-42.

Nakai, T. & Mihara, Y. (1984), “A new mechanical quantity for soils and its application to elastoplastic constitutive models”. Soils and Foundations, Vol. 24(2), 82-94.

Nakai T., Shahin H.M., Kikumoto M., Kyokawa H., Zhang F. and Farias, M.M. (2011a), “A simple and unified one-dimensional model to describe various characteristics of soils”, Soils and Foundations, Vol. 51(6), 1129-1148.

Nakai T., Shahin H.M., Kikumoto M., Kyokawa H., Zhang F. and Farias, M.M. (2011b), “A simple and unified three-dimensional model to describe various characteristics of soils”. Soils and Foundations, Vol. 51(6), 1149-1168.

Oda, M. (1972), “The mechanism of fabric changes during compressional deformation of sand”. Soils and Foundations, Vol. 12(2), 1-18.

Pedoroso D.M., Farias M.M. and Nakai T. (2005), “An interpretation of subloading t_{ij} model in the context of conventional elastoplasticity theory”. Soils and Foundations, Vol. 45(4), 61-77.

Roscoe, K. H. & Burland, J. B. (1968), “On the generalized stress- strain behavior of wet clay”. Heyman and F. A. Leckie (eds.), Engineering Plasticity, Cambridge University Press, 535-609.

Satake, M. (1982), “Fabric tensor in granular materials”. Proceedings of IUTAM Conference on Deformation and Failure of Granular Materials, Delft, 63-68

Satake, M. (1984), “Anisotropy in ground and soil materials”. Tsuchi to Kiso, Vol. 32(11), 5-12 (in Japanese).

Schofield, A. N. and Wroth, C. P. (1968), Critical State Soil Mechanics, McGrow- Hill, London.

Sekiguchi, H. & Ohta, H. (1977), “Induced anisotropy and time dependency in clays”. Proceedongs of Specialty Session 9, 9th International Conf. on Soil Mech. and Foundation Eng., Tokyo, 229-238.

DESCRIPTION OF TORTUOSITY AND HYDRAULIC CONDUCTIVITY OF ANISOTROPIC POROUS MATERIALS

P. Guo
Department of Civil Engineering, McMaster University, Hamilton, ON, Canada

ABSTRACT: *Single-phase fluid flow in porous media is usually direction dependent owing to the tortuosity associated with the internal structures of materials that exhibit inherent anisotropy. This paper presents an approach to determine the tortuosity and permeability of porous materials using a structural measure quantifying the anisotropic distribution of pore voids. The approach uses a volume averaging method through which the macroscopic tortuosity tensor is related to both the average porosity and the directional distribution of pore spaces. Depending on the estimate for the drag on the fluid-solid interfaces, the upper and lower bounds of tortuosity are determined. The permeability tensor is derived from the macroscopic momentum balance equation of fluid in a porous medium and expressed as a function of the tortuosity tensor and the internal structure of the material. The analytical results generally agree with experimental data in the literature.*

1 INTRODUCTION

The internal structure of porous materials, including the geometry and connectivity of the pores, have direct influence on the flow of fluid in the medium and it should be taken into account when determining the permeability of such a material. One of the parameters that is often used is the tortuosity, which was first introduced to porous media studies by Carman (1937).

Despite the extensive use of the notion of tortuosity in describing flow in porous media, its definition or interpretations is not unique. The *geometrical tortuosity* (T_{Geo}) is the average path length per unit streamwise displacement of all fluid particle in a REV, disregarding the different velocities of particles moving along these path lines. It can be alternatively interpreted as the ratio between the shortest path of interconnected points in pore fluid space to the straight distance between these points (Bear, 1972). The *kinematic tortuosity* (T_{Kin}) is the average distance travelled per streamwise displacement in a time interval $[t, t+\delta t]$ by all fluid particles in the REV at time t (Clennell, 1997; Duda et al., 2011). The *dynamic tortuosity* (T_{Dyn}) is the average distance travelled per streamwise displacement in a time interval $[t, t+\delta t]$ by all fluid particles in the REV within the time interval $[t, t+\delta t]$ (Johnson et al., 1987; Bear, 1972 and Scheidegger, 1972). On the other hand, the hydraulic tortuosity factor τ_{KC} in the Kozeny-Carman equation (Carman 1937; Kozeny 1927) is the ratio of the effective hydraulic path length (L_e) to the straight line distance (L) in the direction of flow. Even though τ_{KC} may be very different from the geometric tortuosity (Clennell 1997),

$\tau_{KC} = L_e / L = 1/T_{Geo}$ is generally accepted for one dimensional streamwise flow. Nevertheless, the geometric tortuosity is important as it facilities determination of the average flow velocity streamwise (as discussed by Carman 1937). In this meaning, the geometric tortuosity can be related to both the kinematic and dynamic tortuosities.

According the capillaric model (Scheidegger 1972), for a porous medium having a series of parallel straight capillaries of arbitrary cross-section shape, based on Hagen-Poiseuille equation for laminar Newtonian flow, the permeability of the porous medium can be expressed as

$$k = \frac{\varphi D_h^2}{\psi} = \frac{\varphi D_\alpha^2}{C_0 \tau^2} \tag{1}$$

where D_α is the "average" hydraulic diameter, C_0 is a shape factor ($C_0 = 2$ for a circular pipe flow and 3 for flow between two parallel plates). The tortuosity factor τ is the same as the Kozeny-Carman hydraulic tortuosity factor τ_{KC}. The Kozeny theory yields a same expression for permeability (Kozeny 1927; Scheidegger 1972), with the hydraulic diameter being considered as that for a virtual stream tube. More specifically, D_α is considered as the average pore size on a plane perpendicular to the stream line and is determined as the ratio of the pore cross sections to the circumference of these pores.

By applying volume averaging techniques, Bear and Bachmat (1986, 1990) derived the tortuosity tensor and the permeability tensor for porous media. More specifically, the tortuosity tensor is in fact the static moment of oriented areal elements of fluid on the boundary of the REV per unit volume of the fluid phase within the REV. For some specific cases, Diedericks and Du Plessis (1995) modified the definition of tortuosity tensor by Bear and Bachmat (1986, 1990) by incorporating the differences between the macroscopic flow direction and streamwise direction at the local level. Unfortunately, the theoretically derived permeability tensor by Bear and Bachmat (1986, 1990) may not be applicable any more when using the definition by Diedericks and Du Plessis (1995).

Even though numerous studies have been performed on flow in porous media, the term tortuosity is still a source of misunderstanding and often causes confusions. The objective of this paper is to determine internal structural dependency of tortuosity and permeability as well as the connection between the tortuosity defined by Bear and Bachmat and the geometric tortuosity, the kinematic tortuosity and the hydraulic tortuosity factor in the Kozeny-Carman equation. To achieve this goal, the microscopic analysis of transport phenomena in porous media carried out by Bear and Bachmat (1986, 1990) is first revisited. A modification to the tensorial quantity α_{ij} and hence the permeability tensor is made to better take into account the characteristics of the fluid-solid interfaces. The results show intrinsic connection between different definitions of tortuosity and how the interaction between the fluid and solid phases have significant influence on the permeability tensor. The anisotropy of tortuosity and permeability is characterized using the directional distribution of pore voids. The lower bound and upper bound of the tortuosity and permeability are obtained from the analyses.

2 INCONSISTENCY IN TORTUOSITY COMPUTATION: SIMPLE CASE STUDIES

2.1 Two versions of Bear and Bachmat's momentum balance equation (1986, 1990)

In the original work of Bear and Bachmat (1986, 1990), the tortuosity tensor $T^*_{\alpha ij}$ is defined as

$$T^{*}_{\alpha ij} = \frac{1}{V_\alpha}\int_{S_{\alpha\alpha}} \mathring{x}_i \nu_{\alpha j} dS \tag{2}$$

with $x_i = \mathbf{r} - \mathbf{r}_0$, in which $\mathbf{r}$ and $\mathbf{r}_0$ are the position vectors of a point on $S_{\alpha\alpha}$ and the centre of the REV, respectively (as shown in Figure 1). Herein Phase-α and β are referred to as the fluid and solid phases respectively. The physical meaning of $S_{\alpha\alpha}$ and $\nu_{\alpha j}$ are defined in Figure 1a. $\mathbf{T}^{*}_{\alpha}$ expresses the total static moment of the oriented areal element comprising the $S_{\alpha\alpha}$-surface, with respect to planes passing through the centroid of the REV, per unit volume of the α-phase within V_0. According to Bear and Bachmat (1990), $T^{*}_{\alpha ij}$ transforms the local body force into the macroscopic one, and α_{ij} introduces "the effect of the configuration of the solid-fluid surface in the term that transforms part of the force resisting the flow at a point to an averaged resistance force at the fluid-solid interface".

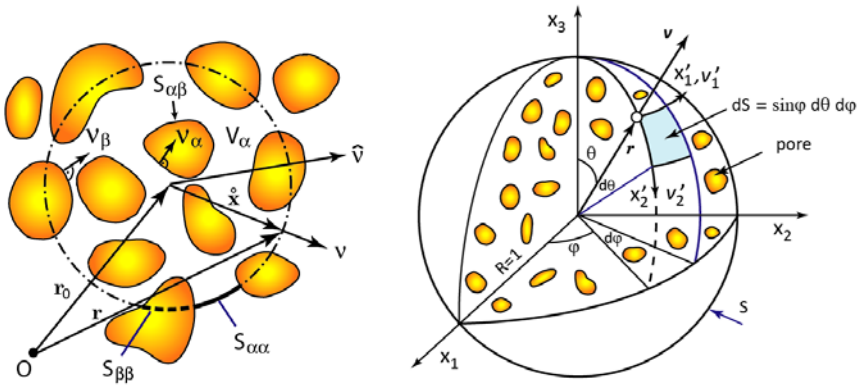

Figure 1. (a) REV of a porous medium and (b) a unit sphere

Based on the volume averaging, the macroscopic momentum balance equation of the fluid in a porous medium is expressed as

$$\overline{\rho}^{\alpha}_{\alpha}\frac{D_\alpha \overline{V^m_j}^{\alpha}}{Dt} = \overline{\left(\frac{\partial \tau_{\alpha ij}}{\partial x_i}\right)}^{\alpha} - \left(\frac{\partial \overline{p_\alpha}^{\alpha}}{\partial x_i} + \overline{\rho}^{\alpha}_{\alpha} g \frac{\partial z^{\alpha}}{\partial x_i}\right) T^{*}_{\alpha ij} \tag{3}$$

The first term of the r.h.s of Eq. (3) can be computed from

$$\varphi\overline{\left(\frac{\partial \tau_{\alpha ij}}{\partial x_i}\right)}^{\alpha} = \frac{\partial \varphi \overline{\tau_{\alpha ij}}^{\alpha}}{\partial x_i} + \frac{1}{V_0}\int_{S_{\alpha\beta}} \tau_{\alpha ij}\nu_{\alpha i} dS \tag{4}$$

The surface integral in the second term of the r.h.s. of Eq. (4) expresses "the viscous resistance, or viscous drag force exerted by the solid phase on the flow fluid at their contact surface within the REV, per unit volume of porous medium" (Bear and Bachmat, 1990). Bear and Bachmat proposed two methods to estimate the surface integral $\int_{S_{\alpha\beta}} \tau_{\alpha ij}\nu_{\alpha i} dS$ on the r.h.s of Eq. (4), which resulted in two versions of the macroscopic momentum balance equation (1986, 1990):

$$\bar{\mu}_\alpha^\alpha \alpha_{ij}^{\pm} C_\alpha \phi_0 \frac{\bar{V}_{\alpha j}^{\alpha} - \bar{V}_{\beta j}^{\beta}}{\Delta^2} = -\phi_0 T_{\alpha ij}^{*} \left(\frac{\partial \bar{p}^{\alpha}}{\partial x_j} + \bar{\rho}^{\alpha} g \frac{\partial z}{\partial x_j} \right) \tag{5}$$

α_{ij}^{+} and α_{ij}^{-} are second-rank tensors characterizing the geometry configuration of $S_{\alpha\beta}$ in terms of its unit normal vector and are defined as

$$\alpha_{ij}^{\pm} = \delta_{ij} \pm \widetilde{\nu_i \nu_j}^{\alpha\beta} = \delta_{ij} \pm \frac{1}{S_{\alpha\beta}} \int_{S_{\alpha\beta}} \nu_{\alpha i} \nu_{\alpha j} dS \tag{6}$$

where δ_{ij} is the Kronecker delta function, $\nu_{\alpha i}$ the unit normal vector of $S_{\alpha\beta}$ (as shown in Figure 1a). The permeability tensor is then obtained as

$$k_{ij} = \frac{\phi_\alpha \Delta_\alpha^2}{C_\alpha} G_{\alpha ij}^{*}; \quad G_{\alpha ij}^{*} = (\alpha_{il}^{\pm})^{-1} T_{\alpha lj}^{*} \tag{7}$$

where ϕ_0 is the porosity of the material defined as $\phi_0 = \phi_\alpha = V_\alpha / V_0$ for saturated porous media, μ_α is the dynamic viscosity of the fluid, C_α a shape factor related to pore sizes, while V_i, ρ and p are the velocity, density and pressure respectively, the hydraulic radius Δ_α is the ratio of fluid volume to the fluid-solid interface area (i.e., $\Delta_\alpha = V_\alpha / S_{\alpha\beta}$).

For an isotropic material, it is interesting to compare the above expression with Eq. (1). In this case, $\alpha_{ij}^{\pm}$ and $T_{\alpha ij}^{*}$ can be expressed as $\alpha_{ij}^{\pm} = a^{\pm} \delta_{ij}$ and $T_{\alpha ij}^{*} = T_0^{*} \delta_{ij}$. The equivalent hydraulic tortuosity factor τ is then $\tau = \sqrt{a^{\pm} / T^{*}}$ (Guo, 2012). It has been shown that under some conditions the resulting τ value may be smaller than unity (Ahmadi et al., 2011)

2.2 Two simple examples

Now let us examine a simple case when a flow line cross the boundary of a porous medium obliquely, as shown in Figure 2a & b. For the macroscopic flow in the horizontal direction, the different definitions of torotuosity give the same value of $T_{Geo} = T_{Kin} = T_{Dyn} = \cos\theta = L / L_e$ with L_e being the effective flow length. The correct Kozeny-Carman hydraulic tortuosity factor $\tau_{KC} = L_e / L = 1/\cos\theta$ is also obtained from the analysis for laminar Newtonian flow between two parallel plates based on Hagen-Poiseuille equation. From the definition for tortuosity by Bear and Bachmat in Eq. (2), the tortuosity component of flow for the cases in Figure 2a & b is $T_{Bear}^{*} = 1$. It is found that, except the tortuosities derived by Bear and Bachmat (1986, 1990), the three other definitions have the same value.

For the horizontal flow shown in Figure 2a & b, the corresponding component of α_{ij}^{-} is $\alpha^{\pm} = 1 \pm \sin^2\theta$. The Kozeny-Carman hydraulic tortuosity factor can be obtained from Eq. (7) by calculating k_{11}, which yields $\tau_{Bear} = \sqrt{\alpha^{-} / T_{Bear}^{*}} = \cos\theta$ based on Bear and Bachmat (1990). This result may be questionable since it implies that the effective length L_e is shorter than the length L of the porous medium. It can be shown that $\tau_{Bear} = \sqrt{\alpha^{+} / T_{Bear}^{*}} = \sqrt{1 + \sin^2\theta}$ based on Bear and Bachmat (1986).

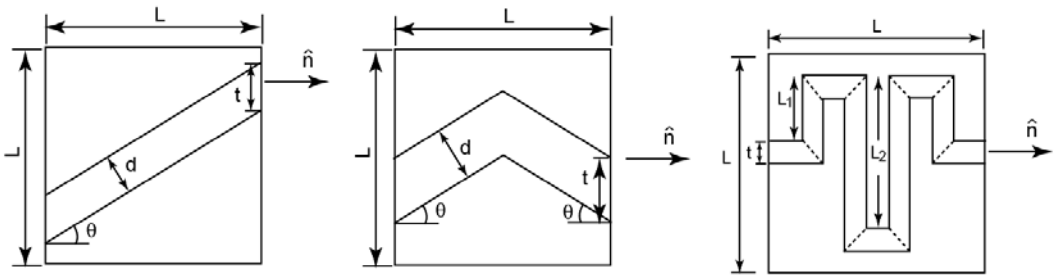

(a) (b) (c)

Figure 2. A porous medium with (a, b) a flow line cross the boundary obliquely, and (c) a U-shaped flow channel

The second example to examine is a porous medium with a U-shaped flow channel as shown in Figure 2c. Since the average interstitial flow velocity is the same at all cross-sections of the flow channel, the different definitions of torotuosity, including the definition by Bear and Bachmat, give the same value of $T = L / L_e$ with $L_e = 2\left(L_1 + L_2\right)$. When determining the coefficient of permeability using Eq. (7) and the Kozeny-Carman hydraulic tortuosity factor, one has

$$\alpha^{-} = \frac{L}{L_e} = \frac{L}{L + 2\left(L_1 + L_2\right)}; \quad \tau_{Bear} = \sqrt{\frac{\alpha^{-}}{T^{*}_{Bear}}} = 1 \tag{8}$$

Obviously, the equivalent hydraulic tortuosity factor from Bear and Bachmat's derivation is incorrect. In all three examples, τ_{Bear} values based on Bear and Bachmat (1991) are smaller than their correct values. It can be shown that the hydraulic tortuosity factors evaluated using α^{+}_{ij} are also different from the correct ones.

The above examples reveal inconsistency in the tortuosity *T* and the equivalent hydraulic tortuosity factor τ in Bear and Bachmat's derivations with other definitions or the Kozeny-Carman hydraulic tortuosity factor.

3 MODIFICATION TO BEAR-BACHMAT'S MOMENTUM BALANCE EQUATION

A review on the methods Bear and Bachmat (1986, 1990) used to estimate the surface integral on the r.h.s of Eq. (4) reveals that the stresses $\tau_{\alpha ij}$ in the fluid in the close vicinity of the $S_{\alpha\beta}$-surfaces are determined in different approaches. In Bear and Bachmat (1986), $\tau_{\alpha ij}$ is determined from the constitutive relation

$$\tau_{\alpha ij} = \mu_{\alpha}\left(\frac{\partial V^{m}_{i}}{\partial x_j} + \frac{\partial V^{m}_{j}}{\partial x_i}\right) \tag{9}$$

in which $\partial V^{m}_{i} / \partial s_{v}$ is the velocity gradient in the direction perpendicular to the $S_{\alpha\beta}$-surfaces. In Bear and Bachmat (1990), the following relation is actually adopted:

$$\tau_{\alpha ij} v_{\alpha j} = \mu_\alpha \frac{\partial V_i^m}{\partial s_v} \tag{10}$$

The velocity gradient $\partial V_i^m / \partial s_v$ in the direction perpendicular to the $S_{\alpha\beta}$-surfaces is also estimated in different approaches, which may not in agreement with the reality in some cases.

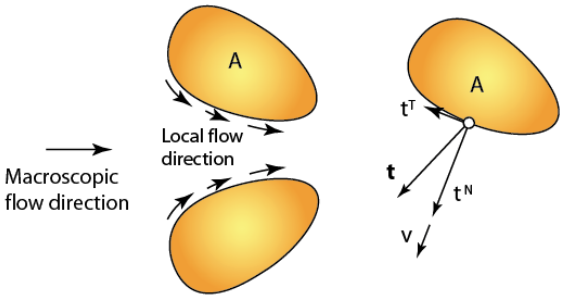

Figure 3. Surface traction on the fluid-solid interface $S_{\alpha\beta}$

A different approach is proposed herein to estimate the surface integral on the r.h.s of Eq. (4). Refer to Figure 3, let $\tau_{\alpha ij}$ = viscous stress tensor, $t_{\alpha j}$ = traction vector on the fluid-solid interface $S_{\alpha\beta}$, $t_{\alpha j}^T$ and $t_{\alpha j}^N$ = the normal and tangential components of $t_{\alpha j}$ relative to the local tangent plane of $S_{\alpha\beta}$, $v_{\alpha i}$ = unit vector representing the normal of $S_{\alpha\beta}$. When the local flow direction is different from the macroscopic flow direction, the interaction between the solid and fluid phases results in non-zero normal traction components $t_{\alpha j}^N$ on $S_{\alpha\beta}$. The traction vector $t_{\alpha j}$ and its components in the normal and tangential directions of $S_{\alpha\beta}$ are expressed as:

$$\tau_{\alpha i} = \tau_{\alpha ij} v_{\alpha j},\ \tau_{\alpha i}^T = \tilde{\alpha}_{ij} t_{\alpha j},\ \tau_{\alpha i}^N = (\delta_{ij} - \tilde{\alpha}_{ij}) t_{\alpha i} \tag{11}$$

in which $\tilde{\alpha}_{ij} = \delta_{ij} - v_{\alpha i} v_{\alpha j}$. It follows that

$$\tau_{\alpha i} = (\tilde{\alpha}_{ij})^{-1} \tau_{\alpha j}^T \tag{12}$$

The tangential traction $t_{\alpha j}^T$ on the $S_{\alpha\beta}-$surface is related to the tangential velocity gradient in the close vicinity of the $S_{\alpha\beta}-$surface by

$$t_{\alpha i}^T = \mu_\alpha \frac{\partial V_i^m}{\partial s_v} \tag{13}$$

Using this relation to estimate the surface integral on the r.h.s of Eq. (4) yields a modification to the macroscopic momentum balance equation in Eq. (5) as

$$\bar{\mu}_\alpha^\alpha (\alpha_{ij}^-)^{-1} C_\alpha \phi_0 \frac{\bar{V}_{\alpha j}^\alpha - \bar{V}_{\beta j}^\beta}{\Delta^2} = -\phi_0 T_{\alpha ij}^* \left(\frac{\partial \bar{p}^\alpha}{\partial x_j} + \bar{\rho}^\alpha g \frac{\partial z}{\partial x_j} \right) \tag{14}$$

and the same expression of permeability tensor as Eq. (7) with $G^*_{\alpha ij} = \alpha^-_{il} T^*_{\alpha lj}$. For isotropic porous materials or 1D macroscopic flow, the equivalent Kozeny-Carman hydraulic tortuosity factor based on the above modification is:

$$\tau_{KC} = \sqrt{\alpha^- T^*} \tag{15}$$

4 VERIFICATION OF MODIFIED BEAR-BACHMAT'S MOMENTUM BALANCE EQUATION

4.1 Streamwise channel flow

The validity of the modification to Bear-Bachmat's momentum balance equation and the resulting tortuosity are examined using the cases shown in Figure 2. It is found that Eq. (15) yields the correct τ_{KC} values for all cases.

4.2 Flow in isotropic porous media

For an isotropic porous medium with random distribution of solid particles, Guo (2012) and Ahmadi et al. (2011) derived the relation between $T^*_{\alpha ij}$ and α^-_{ij} as

$$\alpha^-_{ij} = \frac{1}{3}(2\delta_{ij} + T^*_{\alpha ij}) \tag{16}$$

Similarity, for the definitions in Bear and Bachmat (1986), one obtains $\alpha^+_{ij} = (4\delta_{ij} - T^*_{\alpha ij})/3$. For an isotropic medium, the above relations are simplified as $\alpha^\pm_{ij} = a^\pm \delta_{ij}$, $T^*_{\alpha ij} = T^*_{\alpha 0}\delta_{ij}$ with $T^*_{\alpha 0} = \phi_0$, $a^- = \left(2 + T^*_{\alpha 0}\right)/3$ and $a^+ = \left(4 - T^*_{\alpha 0}\right)/3$. As such, the hydraulic tortuosity factors obtained from different methods are

$$\tau_{Bear91} = \sqrt{\frac{a^-}{T^*_{\alpha 0}}} = \sqrt{\frac{2+\phi_0}{3\phi_0}};\ \tau_{Bear86} = \sqrt{\frac{a^+}{T^*_{\alpha 0}}} = \sqrt{\frac{4-\phi_0}{3\phi_0}};\ \tau_{cor} = \sqrt{\frac{1}{a^- T^*_{\alpha 0}}} = \sqrt{\frac{3}{(2+\phi_0)\phi_0}} \tag{17}$$

The variation of these hydraulic tortuosity factors with porosity is presented in Figure 4.

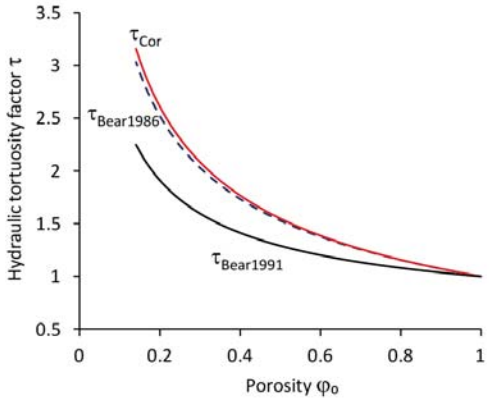

Figure 4. Estimated hydraulic tortuosity factor for an isotropic porous medium

It is interesting to note that the expressions of the hydraulic tortuosity factors in Eq. (17) define the range of tortuosity factors of porous materials with all connected, uniformly distributed pore voids in the form of $\tau = (\phi_0)^{-p}$ with p = 0.4 and 0.6, respectively. It seems that τ_{Bear91} and τ_{cor} are practically the lower and upper bounds of measured tortuosity factors in the literature.

5 ANISOTROPIC PERMEABILITY AND DIRECTIOANL DISTRIBUTION OF VOIDS MAJOR HEADINGS

The anisotropic nature of porous media is characterized using the spatial distribution of pore voids described by a probability density function (Pietruszczak and Krucinski 1989). Consider a test line of length $L = 2R$ in direction $\mathbf{v}$ and passing the centre of the unit sphere in Figure 1(b). Let $l(\mathbf{v}) = \Sigma l_i(\mathbf{v})$ be the total length of intersections of this test line with pores. The fraction of this test line occupied by pores is referred to the linear porosity $\phi(\mathbf{v}) = l(\mathbf{v}) / L$ in the direction of $\mathbf{v}$. $\phi(\mathbf{v})$ reflects the directional variation of the pore space and can be expressed

$$\phi(\mathbf{v}) = \phi_0(1 + \Omega_{ij}\nu_i\nu_j + \Omega_{ijkl}\nu_i\nu_j\nu_k\nu_l + \cdots) \tag{18}$$

in which ϕ_0 is the average volumetric porosity of the material, Ω_{ij} and Ω_{ijkl} are symmetric traceless tensors. When only the first two terms are used, the directional distribution of pore space is simplified as

$$\phi(\mathbf{v}) = \phi_0(\delta_{ij} + \Omega_{ij})\nu_i\nu_j \tag{19}$$

For this case, if the eigenvalues of Ω_{ij} are distinct, $\phi(\mathbf{v})$ can reflect smooth orthogonal anisotropy. The symmetry axes of the orthogonal anisotropy are coincident with the principle axes of Ω_{ij}. If two eigenvalues of Ω_{ij} are equal, then $\phi(\mathbf{v})$ describes the transverse isotropy (Pietruszczak and Krucinski 1989).

Using concept of linear porosity, Guo (2012) proved that $T^*_{\alpha ij}$ is a function of ϕ_0 and Ω_{ij}:

$$T^*_{\alpha ij} = \phi_0\left[\delta_{ij}\left(1 + \frac{1}{35}\Omega_{kl}\Omega_{kl}\right) + \frac{3}{7}\Omega_{ij} + \frac{4}{35}\Omega_{ik}\Omega_{kj}\right] \tag{20}$$

Substituting Eq. (20) into Eq. (7), the lower and upper bounds of the permeability tensor are determined as

$$k_{ij} = \frac{\phi_\alpha \Delta_\alpha^2}{C_\alpha} G^*_{\alpha ij}; \quad G^U_{\alpha ij} = (\alpha^-_{il})^{-1} T^*_{\alpha lj}; \quad G^L_{\alpha ij} = \alpha^-_{il} T^*_{\alpha lj} \tag{21}$$

in which (Guo, 2012)

$$\alpha^-_{ij} = \frac{1}{3}\left(2\delta_{ij} + T^*_{\alpha ij}\right) = b_1\delta_{ij} + b_2\Omega_{ij} + b_3\Omega_{ik}\Omega_{kj}; \quad (\alpha^-_{ij})^{-1} = \frac{1}{I_{\alpha 3}}\left(\alpha_{ik}\alpha_{kj} - I_{\alpha 1}\alpha_{ij} + I_{\alpha 2}\delta_{ij}\right)$$

$$I_{\alpha 1} = \alpha_1 + \alpha_2 + \alpha_3 = 3b_1 + b_3 I_{\Omega 2}$$

$$I_{\alpha 2} = \alpha_1\alpha_2 + \alpha_2\alpha_3 + \alpha_1\alpha_3 = 3b_1^2 + \left(b_2^2 - 4b_1b_3\right) I_{\Omega 2} + 2b_3 I_{\Omega 2}^2 - 3b_2 b_3 I_{\Omega 3}$$

$$I_{\alpha 3} = \alpha_1\alpha_2\alpha_3 = b_1^3 + b_1 b_2^2 I_{\Omega 2} + b_2^3 I_{\Omega 3} + b_3^2\left(b_1 I_{\Omega 2}^2 + b_2 I_{\Omega 2} I_{\Omega 3} + b_3 I_{\Omega 3}^2\right) - b_1 b_3\left(2b_1 I_{\Omega 2} + 3b_2 I_{\Omega 3}\right)$$

$$b_1 = \frac{1}{3}\left[2 + \phi_0\left(1 + \frac{1}{35}\Omega_{kl}\Omega_{kl}\right)\right],\ b_2 = \frac{\phi_0}{7},\ b_3 = \frac{4\phi_0}{105}$$

The hydraulic radius in Eq. (21) can be estimated as $\Delta_\alpha = \phi_\alpha / \Sigma_{\alpha\beta}$ with $\Sigma_{\alpha\beta} = S_{\alpha\beta} / V_0$ being the specific area based on the bulk volume of the REV.

6 CONCLUDING REMARKS

This paper presents a mathematical framework to determine the directional dependency of tortuosity and anisotropic permeability of porous media, using a structural measure describing the anisotropic distribution of pore voids. The key to successful implementation of this approach is the determination of directional variation of pores in porous media, which can be done through digital image analysis using different methods. The tortuosity tensor is derived based on a volume averaging approach and is related to the directional pore voids distribution. Depending on the estimate for the drag on the fluid-solid interfaces, the upper and lower bounds of tortuosity are determined. The permeability tensor is obtained from the macroscopic momentum balance equations of the fluid, which is related to the tortuosity tensor and eventually expressed as a function of the directional distribution of pore voids. When simplified to isotropic porous media, the theoretical analysis yields an explicit expression for the tortuosity as a function of porosity, which is in agreement with experimental data in the literature. A systematic experimental study is ongoing for the verification of the proposed approach.

ACKNOWLEDGEMENT

Funding provided by the Natural Sciences and Engineering Research Council of Canada is gratefully acknowledged.

REFERENCES

Ahmadi,M. M., Mohammadi,S. & Hayati, N. A. (2011), "Analytical derivation of tortuosity and permeability of monosized spheres: A volume averaging approach". Phys. Rev. E 83, 026312, 8p.

Bear, J. (1972), Dynamics of fluids in porous media. Elsevier, New York London.

Bear, J. and Bachmat, Y. (1986), "Microscopic modelling of transport phenomena in porous media. 2: Application to mass, momentum and energy transport". Transp. Porous Med. 1, 213-240.

Bear, J. & Bachmat, Y. (1990), Introduction to modeling of transport phenomena in porous media. Kluwer Academic, Dordrecht.

Carman, P.C. (1937), "Fluid flow through granular beds". Transactions, Institution of Chemical Engineers, 15, 150-166.

Clennell, M.B. (1997), "Tortuosity: a guide through the maze". In: Developments in Petrophysics (eds. Lovell, M.A. and Harvey, P.K). Geological Society of London, Special Publication 122, 299–344.

Diedericks, G.P.J. & Du Plessis, J. P. (1995), "On tortuosity and areosity tensors for porous media". Transp. in Porous Med. 20, 265–279.

Duda, A., Koza, Z. and Matyka, M. (2011), "Hydraulic tortuosity in arbitrary porous media flow". Phys. Rev. E 84, 036319, 8p

Dullien, F. A. L. (1992). Porous media: Fluid transport and pore structure. 2nd ed. Acad Press, New York.

Guo, P. (2012), "Dependency of tortuosity and permeability of porous media on directional distribution of pore voids". Transport in Porous Media, 95(2), 285-303.

Johnson, D. L., Koplik, J. and Dashen, R. (1987), "Theory of dynamic permeability and tortuosity in fluid-saturated porous media". J. Fluid Mech. 176, 379-402.

Kozeny, J. (1927), "Uber Kapillore Leintung des Wossers im Boden", Stizungsber. Akad. Wiss. Wien 136, 271-306.

Pietruszczak S. & Krucinski S. (1989). "Description of anisotropic response of clays using a tensorial measure of structural disorder". Mech. Mater. **8**, 237-249.

Scheidegger, A E. (1972), The physics of flow through porous media. University of Toronto Press.

COMPUTATION OF STRAIN DEPENDENT PERMEABILITY OF POROUS MEDIA USING AN ENHANCED PIPE NETWORK MODEL

Hyu-Soung Shin & Kwang-Yeom Kim
Geotechnical Engineering Research Division, Korea Institute of Construction Technology (KICT), GyeongGi-Do, South Korea

Gyan N. Pande
Civil and Computational Engineering Research Centre, Swansea University, Swansea, UK

ABSTRACT: *Determination of transport properties of geomaterials is an important issue in many fields of engineering analysis and design. Permeability is indirectly related to the porosity, pore-size distribution and pore-architecture of the porous media. These parameters evolve when a strain field is imposed on it. Physical measurement of permeability under a strain field in laboratory conditions is difficult, if not impossible, expensive and prone to a large number of uncertainties.*
In this paper, we propose an enhanced pore network model to compute permeability of a porous media under stress/strain. Data of pore-size distribution obtained from Mercury Intrusion Porosimetry (MIP) are used to compute permeability of samples of rock from various oil fields. It is shown that permeability can be predicted from the model with sufficient accuracy. A hypothesis for change in porosity, pore size distribution and pore architecture due to imposed mechanical strains is then proposed. Based on this permeability is computed again for the same samples of rocks as used before but now under uniaxial and biaxial compressive or tensile strain fields. It is shown that depending on the state of strain field imposed, permeability evolves in an anisotropic manner. Permeability under tensile strain fields increases dramatically compared to the reduction that takes place under compressive field of the same magnitude.

1 INTRODUCTION

Determination of porosity, pore-size distribution and permeability is crucial in many areas of engineering sciences. It is one of the most important parameters in relation to viability and performance of oil recovery wells, engineered barriers for nuclear waste disposal and sequestration of CO2 in underground facilities. For engineering analysis of these projects, a deeper understanding of variation of permeability with temperature, imposed stress and its degradation with time is required. Measuring permeability in physical experiments is expensive, time consuming and fraught with innumerable sources of error. Need for a rational computational model for parametric studies for various projects cannot therefore be over-emphasised. This paper proposes an enhanced 'pore network' model which when coupled with various hypotheses, relating to distribution of strain in the porous media, can be used to obtain estimates of anisotropic permeability tensor of a porous medium

2 PORE NETWORK MODEL

A three-dimensional, micro-mechanical pipe network model forming the shape of a cube has been adopted by a number of researchers in the past (Bryant & Blunt, 1992; Bakke & Øren, 1997; Pereira et. al., 1996). The pipes represent the inter-connected pore space and pore network in a sample of a material. The pore size distribution and porosity of a material as obtained from MIP or other means are statistically replicated in the computational model. Here we assume a log-normal probability density function for 'pore/pipe' diameters. Fluid pressure is applied to one face of the cube whilst four adjoining surfaces are sealed so as to force a one-dimensional flow. The face of the cube opposite to the one on which pressure is applied has prescribed zero pressure. The fluid is allowed to percolate through the network system progressively. These ideas are based on the well-known theory of percolation of statistical physics (Stauffer, 1985). Depending on the capillary pressure in a pipe, which may be positive or negative, the specific pipe may or may not be penetrated at a certain pressure head. If the fluid is unable to penetrate then a "dead-end" condition is reached along that particular flow path. Once equilibrium is reached and a constant one-dimensional flow through the system is achieved, Darcy's Law is used to compute the resultant 'effective' permeability.

The above model of flow, especially the simplicity of pore network, has been criticised by many researchers. Following this, attempts have been to simulate real pore network of rocks as revealed by microscopic or CT scanning methodologies. However, it has recently been proposed that a completely 'random' continuous distribution of pipes of statistically varying diameters can also be treated by a numerical integration scheme, cubic network of pipes representing the lowest order of integration (Pietruszczak & Pande, 2012).

In a cubic network model, six pipes meet at a 'node' in the interior of the cube. Thus co-ordination number (number of connection, $\alpha = 6$) for interior nodes is 6 whilst that for nodes on the surface, edge and corners of the cube is 5, 4 and 3 respectively (Fig. 1).

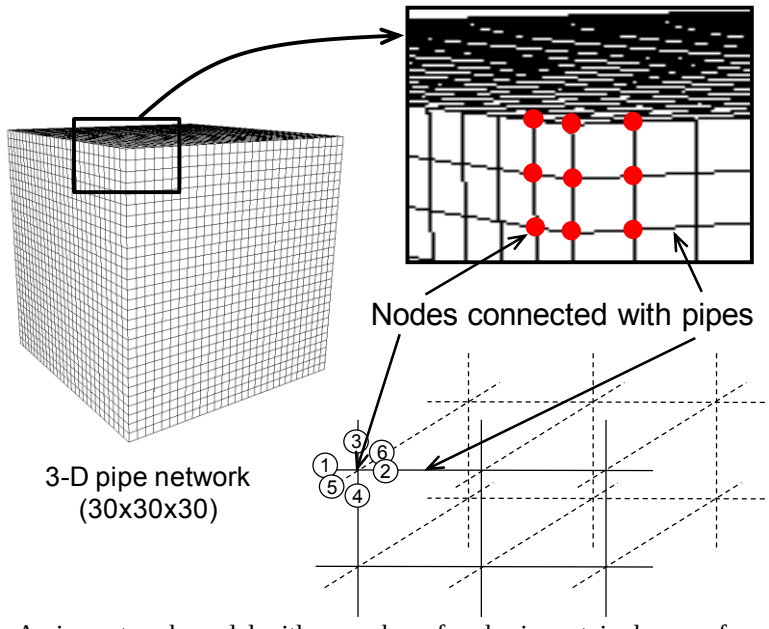

Fig. 1. A pipe network model with a number of nodes in certain degree of connectivity

Since the main theme of this paper is to investigate stress/strain dependence of permeability, which in general will be anisotropic, we need to introduce the concept of 'directional porosity', and 'directional pore-size distribution'. The former was introduced by Pietruszczak & Kruciniski (1989) & Inglis & Pietruszczak (2003) and the latter is an implicit consequence of the former. Here, we assume that permeability varies continuously with the

direction with reference to the principal axes of material anisotropy, if any. Generally, the 'virgin' material will be considered as initially isotropic but it is likely to be anisotropic with reference to strength as well as permeability on imposition of a strain/stress field (except in the case of a purely volumetric strain/hydrostatic stress). It is also postulated that the axes of anisotropy of permeability coincide with the directions of principal strain.

Once strains are imposed on a porous media, directional porosity evolves except in the case of 'volumetric strains' which lead to a change in porosity without directional bias. In general, a change in porosity is related to isotropic volumetric strains through Eq. (1) assuming solid part of the porous media is not compressible.

$$\Delta n = n' - n = \frac{(n-1)\varepsilon_v}{(1-\varepsilon_v)} \tag{1}$$

where *n* and *n*' are original and changed porosities by isotropic volumetric strain. Considering non-uniform strains imposed, the Eq. (1) can be generalised to:

$$\begin{aligned} n'_1 &= \frac{A'_v}{A'} = \sqrt[3]{n}\prod_j \frac{(\sqrt[3]{n}-\varepsilon_j)}{(1-\varepsilon_j)},\ j = 2, 3 \\ n'_2 &= \frac{A'_v}{A'} = \sqrt[3]{n}\prod_j \frac{(\sqrt[3]{n}-\varepsilon_j)}{(1-\varepsilon_j)},\ j = 1, 3 \\ n'_3 &= \frac{A'_v}{A'} = \sqrt[3]{n}\prod_j \frac{(\sqrt[3]{n}-\varepsilon_j)}{(1-\varepsilon_j)},\ j = 1, 2 \end{aligned} \tag{2}$$

where ε_1 ε_2 ε_3 are the principal strains, directions of which coincide with that of the pipe network. A and A_v indicate total area and pore area of the model's cross-section perpendicular to principal directions, respectively and apostrophe means the modified values by imposed strains. From the three principal areal porosities, the corresponding mean pore diameters (ρ_1, ρ_2, ρ_3) can be computed. The normal procedure of allocating pipe sizes according to a probability distribution function can be used to set up the pipe network model.

3 HYPOTHESES RELATING CHANGE IN PORE-SIZE DISTRIBUTION DUE TO STRAIN

It is well known that permeability of a porous media is highly dependent on pore-size distribution. Thus two media having the same porosity and the same average pore-size can have widely different permeabilities if their pore-size distributions are different. How does the pore-size distribution change under a certain strain influence permeability has not been studied in the past. However, the current and anticipated advances in X-ray CT technology (Shin et. al., 2012) should permit such studies in the future. For the purpose of this study two hypotheses have been investigated. These are:

Hypothesis 1: A principal compressive or tensile strain causes a uniform decrease or increase in the diameters of the pipes aligned normal to the direction of the principal strain (see Fig. 2). The overall change in directional porosity corresponds to the magnitude of imposed strain according to Eq. (2) above.

Hypothesis 2: A principal compressive or tensile strain causes a decrease or increase in the diameters of the pipes which is proportional to the original diameter, D (prior to imposition of strain). Again this applies to pipes aligned normal to the direction of the principal strain (see Fig. 2). The overall change in directional porosity here again to be such as to correspond to the magnitude of imposed strain according to Eq. (2) above.

Obviously only in the case of pure volumetric strain, isotropy of permeability will be retained which seems logical. In all other cases, porous media will have anisotropic permeability after imposition of a strain field.

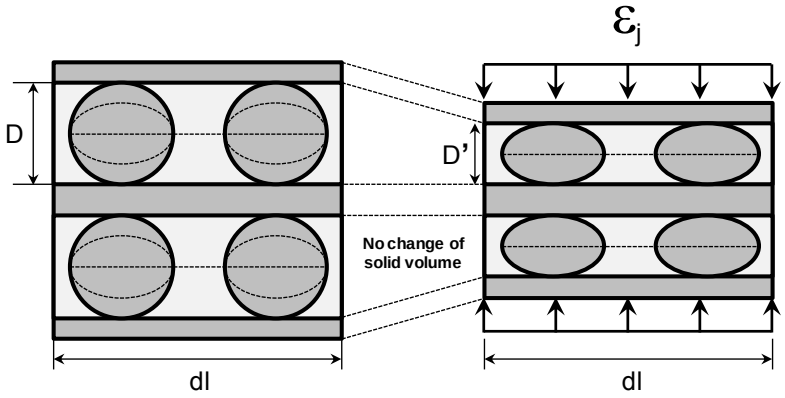

Fig. 2. A schematic diagram of change of the cross-sectional area and shape of pores due to strains imposed (a) Before imposition of uniaxial strain (b) After imposition of uniaxial strain

4 EXPERIMENTAL RESULTS ON POROSITY, PORE-SIZE DISTRIBUTION OF ROCKS AND VALIDATION OF THE NETWORK MODEL

For computation of permeability using pore network model requires a probability density distribution function for pore diameters. In petroleum engineering practice the pore diameter distribution are determined from MIP tests whereby mercury is injected into a specimen of rock at increasing pressures. The Washburn equation (Washburn, 1921) is also used for this purpose, to determine the pore size distribution. As the pressure is increased, smaller and smaller pores are penetrated by the mercury, the pore size being determined by the equation using the applied pressure as the capillary pressure.

From the data a probability density distribution is constructed such that the area under the curve is equal to 1. This is calculated by dividing the fractional volume change by the range in pore diameter. After considering different probability distribution functions for available data, it is noted that a log-normal distribution fits in reasonably well and has been adopted here. An arithmetic mean and standard deviation are calculated on this data range, ignoring any zero values of fractional volume (which corresponds to no further mercury penetration on an increase in pressure). A coefficient of variation is then calculated from these two values (mean value and standard deviation) and is used as input to the software.

In order to validate the network model proposed in this study, the experimental data mentioned above were used. The 17 samples from Heriot-Watt University are available Report (Lokemane et. al., 2001). Results of absolute permeability measurements on various types of sandstone were made available along with MIP data. The rock types used are mostly sandstone from various regions.

For these rock types the network model was run with pore characteristics determined by a log-normal approximation to the experimental data given. The modeling procedure was carried out to determine the mean pore size and coefficient of variation for each test which were then used as input parameters to the program. The results of the network modeling are provided below in Table 1 together with the measured permeability.

This information has also been plotted graphically as shown in Fig. 3. The 45° line represents a direct agreement. Points above the line are over-estimates by the computer program and points below the line are under-estimates. It is seen that relatively good agreement with a discrepancy about 15% has been obtained between the values measured in the laboratory and those predicted by the proposed network model. The computation results

for the samples of sandstone designated as DB show relatively wider discrepancy from the measured ones, which, however, seem to present well overall trend of measured permeabilities with respect to the mean pore size and pore size distribution as the correlation coefficient between measured and computed permeabilities was 0.97.

Table 1. Experimental data and calculated results from the network model

Sample	Mean diam. (μm)	Coeff. of Variation	Porosity (%)	Calculated Permeability (mD)	Measured Permeability (mD)	Error (%)
F1	49.24	1.582	21.68	719.56	800	10.06
F2	54.28	1.566	21.9	894.23	800	10.54
L3	36.92	1.532	24.49	491.64	550	10.61
L4	38.98	1.451	24.92	653.25	550	15.81
L5	35.56	1.471	24.66	515.13	550	6.34
LA1	34.154	1.561	19.09	314.38	350	10.18
LA2	34.462	1.451	19.61	391.18	350	10.53
SRA1	30.125	1.473	21.48	315.19	350	9.94
SRA2	31.14	1.533	20.74	293.04	350	16.28
SRA3	27.39	1.174	19.93	410.27	350	14.69
DB1	5.58	1.089	14.47	14.34	10	30.25
DB2	4.7	1.247	14.34	7.52	10	24.83
DB3	4.78	1.203	14.08	8.27	10	17.26
N1	27.36	1.222	19.06	366.21	350	4.43
N2	25.54	1.346	19.27	361.96	350	3.30
CL2	24.298	1.535	12.57	109.14	100	8.38
CL3	27.329	1.529	13.11	145.45	100	31.25

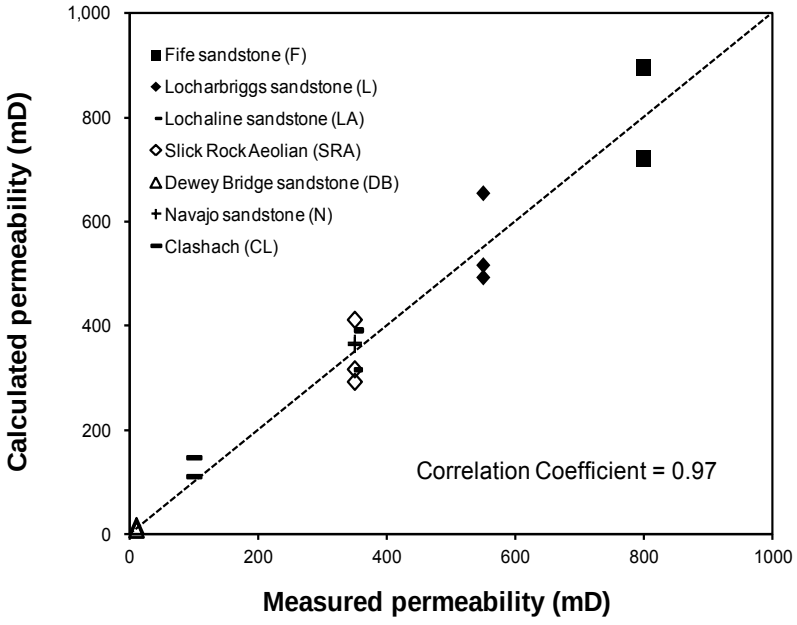

Fig 3. Comparison between the measure and computed permeability results

5 RESULTS

Stresses acting on a porous media cause strains depending on its constitutive behaviour. Stains can be split into a volumetric part and a deviatoric part. It is the volumetric stain which causes the change in porosity and consequently permeability. As stated in Section 2 the actual grains of soil or rock in a mass are assumed incompressible. All principal strain components are considered individually to induce change of diameter of the pipes in the relevant direction so that a non-uniform biaxial or trixial strain leads to a reduction or increase (depending on compressive or tensile nature of the imposed strain) cross-section of pipes representing pores as well as change in the shape from circular to elliptical. Effect of directional areal porosity induced by non-uniform strain impositions as mentioned in section 2 can be taken into account in computation of anisotropic permeability in each principal strain direction. It should be noted that the same strain field in different porous media may lead to the same change in permeability, but a completely different stress field depending on their constitutive properties. This is the reason that we have adopted strain and not stress as the basis for variation in permeability.

It is obvious that if the constitutive behaviour is nonlinear, which it invariably is, volumetric strains, compressive or dilational may arise from imposed changes in stress field. The permeabilities for any rock are therefore stress/strain path dependent. The method of permeability recalculation by a change in the pore size distribution is based on the hypotheses outlined in Section 3 and there is a need to verify them.

A series of numerical parametric studies was undertaken considering different strain fields. Defining the ratio of lateral strain (ε_h) to vertical strain (ε_v) as α ($\varepsilon_h/\varepsilon_v$), cases with α varying from 0 to 1 were studied. For this, all the basic material and pore characteristics of test L4 (Table 1) were adopted. A fixed random seed was used for generating the pipe network model, which has the dimension of 15 x 15 x 15. Single phase flow of water (surface tension, T= 72.0 x 10-3 N/m and contact angle, $\vartheta = 70°$) was taken into consideration. By choosing appropriate values of α, vertical and horizontal permeabilities under strain are calculated separately by allowing vertical and horizontal flow only through the pipe network, respectively.

It is obvious that vertical as well as horizontal permeabilities decrease with increasing compressive strains in the conditions of uniaxial as well as volumetric strain. As seen in Fig. 4, where permeabilities have been normalised with reference in strain free state, the rate of reduction of permeability increases in both vertical and horizontal direction at higher values of α. Obviously, the reduction of permeability in the direction perpendicular to major compressive principal strain direction appears to be much larger, which is a clear demonstration of the effects of directional areal porosities induced by a deviatoric strain field (Fig. 4(c)).

In contrast to compressive strains, dilational (tensile) strains induce an increase of permeability in all the principal direction. The rate of increase of permeability in tension is much higher (160%) compared to the decrease in compression case for the same magnitude of strains. Of course in this study, effect of cracking and propagation of cracks has been ignored and will be presented in a separate publication.

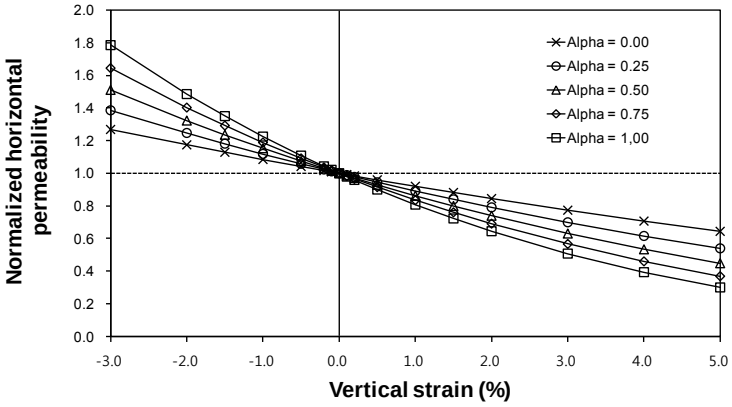

(a) Variation of horizontal permeability

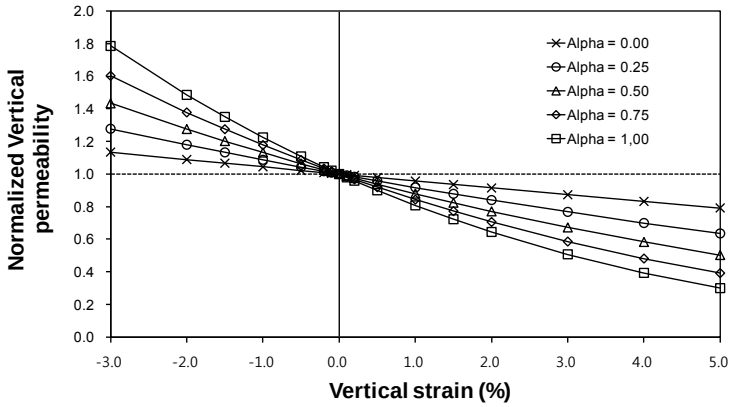

(b) Variation of vertical permeability

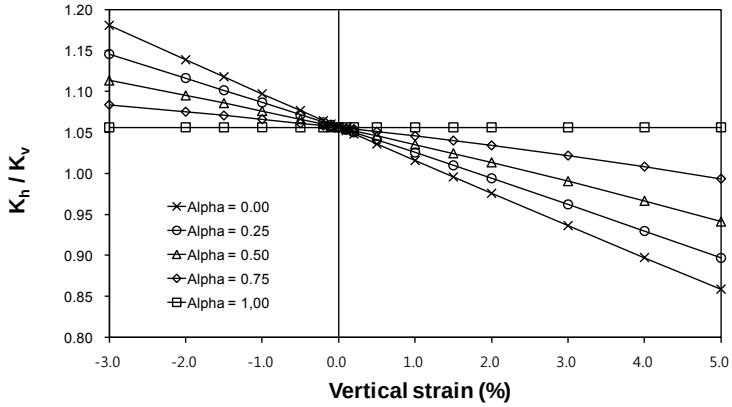

(c) Ratio variation of horizontal and vertical permeabilities

Fig. 4. Variation of permeability in variety of strain constraints

6 CONCLUSIONS

In this paper an advanced network model to compute permeability of a porous media under a field of strain has been proposed. It takes into account the influence of evolving porosity and changes in pore size distribution. Two hypotheses are proposed for computation of strain-dependent permeability: changes are in shape and size of pores in the direction of the principal strain imposed. The computational model as applied to strain free situation has been

validated using measured data available in literature from various oil fields. The results were shown to be in good agreement with a correlation coefficient of 0.97.

It can be concluded that strain imposition to an isotropic porous media can lead to directional areal porosity depending on magnitude and orientation of principal strains. It has been shown that increase in permeability due to a dilatational strain is much larger than the reduction in permeability due to a compressional strain of the same magnitude. Therefore, it can be concluded that strain imposition leads to changes of permeability in compression as well as dilation. The sensitivity is more pronounced in dilation mode. Furthermore, the ratio of principal strain components imposed also influence the evolution of anisotropic permeabilities.

REFERENCES

Bakke, S. & Øren, P.E. (1997), "3-D Pore-Scale Modelling of Sandstones and Flow Simulations in the Pore Networks", SPEJ, Vol. 2, 136.

Blunt, M.J., King, M. & Scher, H. (1992), "Simulation and Theory of Two-Phase Flow in Porous Media", Phys. Rev. A, Vol. 46, 7680.

Bryant, S. & Blunt, M.J. (1992), "Prediction of Relative Permeability in Simple Porous Media", Phys. Rev. A, Vol. 46, 2004.

Carmichael, R.S. (1989), "Practical Handbook of Physical Properties of Rocks and Minerals", CRC Press, Boston.

Inglis D. & Pietruszczak, S. (2003), "Characterization of anisotropy in porous media by means of linear intercept measurements", Intern. Journal of Solids & Structures, Vol. 40, 1243-1264.

Lokemane, S. B., Main, S.E.I., Ngwenya B., Hamilton, S., Jones, C., Smart, B. & Somerville, J. (2001), "Mussel Project - Final Report", Heriot-Watt University, Department of Petroleum Engineering, Rock Mechanics Research Group.

Pereira, G.G., Pinczewski, W.V, Chan, D.Y.C., Paterson, L. & Øren, P.E. (1996), "Pore-Scale Network Model for Drainage Dominated Three-Phase Flow in Porous Media", Transport in Porous Media, Vol. 24, 167.

Pietruszczak, S. & Krucinski, S. (1989), "Description of anisotropic response of clays using a tensorial measure of structural disorder", Mechanics of Materials, Vol. 8, 237-249.

Pietruszczak, S. & Pande, G.N. (2012), "Description of hydraulic and strength properties of anisotropic geomaterials", Studia Geomechanica, Vol. 34, 3-16.

Shin, H.S., Kim, K.Y. & Pande, G.N. (2012), "Porosity and pore-size distribution of geomaterials from X-ray CT scans", Springer Series in Geomechanics & Geoengineering (SSGG) on Advanced Multiphysical Testing of Soils and Shales (AMTSS), L. Laloui and A. Ferrari (Eds.), 177-186.

Stauffer, D. (1985), "Introduction to percolation theory", Taylor & Francis, London.

Washburn, E.W. (1921), "The dynamics of capillary flow", Physical Review, Vol.17(3), 273.

PERSISTENT SHEAR BAND IN VARIABLY SATURATED POROUS MATERIALS

Xiaoyu Song
Department of Civil Engineering and Environmental Engineering, Stanford University, Stanford, CA, 94305-4020 USA

Ronaldo I. Borja
Department of Civil Engineering and Environmental Engineering, Stanford University, Stanford, CA, 94305-4020 USA

ABSTRACT: *Geomaterials such as soils and rocks exhibit a certain degree of permeability that allows fluids to enter into the inter-particle and/or inter-aggregate pores, to mix with each other, and to interact with the surrounding solids. The processes governing the interaction among the solid, liquid, and gas phases are highly complex and may involve mechanical, chemical, and electrical processes. Failure occurs when the solid matrix cannot take any more loads. On a macroscopic scale, failure is accompanied by the formation of localized but intense deformation or failure zones in the solid matrix, called shear bands. In this paper, we demonstrate the impact of heterogeneity on the triggering of a persistent shear band in unsaturated soils. Heterogeneity is specified in the form of spatially varying density and degree of saturation. We show that both types of heterogeneity have a first-order effect on the triggering of a persistent shear band in unsaturated soils.*

1 INTRODUCTION

A class of problems that has attracted considerable attention in computational solid mechanics involves very large deformation occurring over a very narrow zone. Shear bands are narrow zones of intense shear, often accompanied by compaction or dilation; the displacement field is continuous but the strain field exhibits a discontinuity. Material and/or geometric imperfection is known to be a common trigger of deformation bands. In the past, arbitrary imperfections in the form of weak elements have been used in finite element simulations to trigger a persistent shear band because of the uncertainties in quantifying actual specimen imperfections. However, advances in nondestructive, noninvasive imaging techniques (Rechenmacher et al. 2011, Yoshimoto et al. 2011) have now allowed for more accurate quantification of the spatial variation of density and degree of saturation in a specimen of granular materials. It is well known that the strength and stiffness of a granular material correlate very well with density and degree of saturation, so knowing the spatial variation of these two continuum variables allows the spatial inhomogeneities within a specimen to be prescribed deterministically.

In this paper, we focus on spatially varying density and degree of saturation as triggers of a persistent shear band in unsaturated soils. We underscore the word ‘persistent’ since multiple shear bands in different places are always expected to form in a heterogeneous porous material. However, many of these shear bands will simply disappear, and only one or two will persist. In a typical simulation of such problem, it is important not to interfere with the solution, and thus,

we avoid enhancing the kinematics of a localizing element (Borja and Regueiro 2001; Liu and Borja 2008) until we fully resolve the persistent shear band. Resolution of the persistent shear band requires that conventional finite element solution be advanced a little beyond the bifurcation point, but not too far from it so as not to have to deal with mesh-sensitivity issues. In this paper, we use the Rudnicki and Rice (1975) criterion to identify the persistent shear band.

With the assumption that the pore air pressure is zero, the coupled hydromechanical equations simplify to two field equations, namely, the balance of momentum for the mixture and the balance of mass for the liquid phase. To capture the inception of a persistent shear band, we use an advanced critical-state constitutive model with a state parameter (Jefferies 1993) formulated by Borja et al. (2013b). For the numerical simulations, we use a mixed finite element formulation in two dimensions, along with stabilized low-order quadrilateral mixed elements (White and Borja 2008). Under homogeneous boundary condition, we demonstrate that heterogeneity in density and degree of saturation can have first-order effects on the ensuing persistent shear band.

2 HYDROMECHANICAL EQUATIONS

Following the classic mixture theory, let ϕ^{s}, ϕ^{w} and ϕ^{a} represent the volume fractions of solid, water, and air, respectively. The degree of saturation of the fluid is then obtained as

$$S_r = \frac{\phi^{\mathrm{w}}}{1-\phi^{\mathrm{s}}}\,. \tag{1}$$

Let $\boldsymbol{\sigma}$ and $\bar{\boldsymbol{\sigma}}$ denote the total and effective Cauchy stress tensors, respectively; and p and p_{a} the pore water and pore air pressures, respectively. The effective stress equation writes (Schrefler 1984, Borja 2006)

$$\boldsymbol{\sigma} = \bar{\boldsymbol{\sigma}} - B\bar{p}\mathbf{1}\,, \qquad \bar{p} = S_r p + (1-S_r)p_a, \tag{2}$$

where $\mathbf{1}$ is the second-order identity tensor, and B is the Biot coefficient. For soils, $B=1$ is typical. We can simplify the formulation by assuming that $p_{\mathrm{a}}=0$ (passive air pressure).

Consider a mixture of solid, water, and air in domain $\mathcal{B}$ with boundary $\partial\mathcal{B} = \overline{\partial\mathcal{B}_{\boldsymbol{u}} \cup \partial\mathcal{B}_{\boldsymbol{t}}}$, where $\partial\mathcal{B}_{\boldsymbol{u}}$ and $\partial\mathcal{B}_{\boldsymbol{t}}$ are non-overlapping boundaries where the displacement and tractions, respectively, are prescribed. The strong form of the boundary-value problem in the absence of inertia forces is as follows: Find the displacement field $\boldsymbol{u}$ and the pore water pressure field p such that

$$\boldsymbol{\nabla}\cdot(\bar{\boldsymbol{\sigma}} - S_r p\mathbf{1}) + \rho\boldsymbol{g} = \mathbf{0} \tag{3}$$

subject to boundary conditions

$$\boldsymbol{u} = \tilde{\boldsymbol{u}} \;\text{ on }\; \partial\mathcal{B}_{\boldsymbol{u}} \quad\text{and}\quad \boldsymbol{n}\cdot\boldsymbol{\sigma} = \tilde{\boldsymbol{t}} \;\text{ on }\; \partial\mathcal{B}_{\boldsymbol{t}} \tag{4}$$

where ρ is the total mass density of the mixture; $\boldsymbol{g}$ is the gravity acceleration vector; $\boldsymbol{n}$ is the outward unit normal vector to the boundary; and $\tilde{\boldsymbol{u}}$ and $\tilde{\boldsymbol{t}}$ are given displacement and traction boundary conditions, respectively.

Consider the same domain $\mathcal{B}$ with boundary $\partial\mathcal{B} = \overline{\partial\mathcal{B}_p \cup \partial\mathcal{B}_q}$, where $\partial\mathcal{B}_p$ and $\partial\mathcal{B}_q$ are non-overlapping boundaries where the pore water pressure and water flux, respectively, are prescribed. The mass conversation for water along with relevant flow boundary conditions can be stated as follows. Find $\boldsymbol{u}$ and p such that

$$(1-\phi^s)\dot{S}_r + \frac{\phi^{\mathrm{w}}}{K_{\mathrm{w}}}\dot{p} + S_r\boldsymbol{\nabla}\cdot\boldsymbol{v} = -\frac{1}{\rho_w}\boldsymbol{\nabla}\cdot\boldsymbol{w}, \tag{5}$$

subject to boundary conditions

$$p = \tilde{p} \ \text{ on } \ \partial\mathcal{B}_p \quad \text{and} \quad \boldsymbol{n} \cdot (\phi^{\text{w}} \tilde{\boldsymbol{v}}) = -\tilde{q} \ \text{ on } \ \partial\mathcal{B}_q, \tag{6}$$

where $\boldsymbol{v} = \dot{\boldsymbol{u}}$ is the velocity of the solid; $\boldsymbol{w}$ is the Eulerian relative water flow vector given by $\boldsymbol{w} = \rho_{\text{w}} \phi^{\text{w}} (\boldsymbol{v}_{\text{w}} - \boldsymbol{v})$, $\boldsymbol{v}_{\text{w}}$ is the water velocity, K_{w} is the bulk modulus of water, and the superposed dot denotes a material time derivative following the motion of the solid. In the following numerical simulations, we assume that water is incompressible. To complete the finite element formulation of the boundary value problem, we need three constitutive laws. The water retention curve relates the degree of saturation to the suction stress; Darcy's law relates Darcy's velocity $\bar{\boldsymbol{v}}$ to the pressure gradient $\boldsymbol{\nabla} p$; and an elastoplastic constitutive law relates the effective Cauchy stress tensor $\bar{\boldsymbol{\sigma}}$ to the infinitesimal strain rate tensor. $\boldsymbol{\nabla}^{\text{s}} \boldsymbol{v} = (\boldsymbol{\nabla} \boldsymbol{v} + \boldsymbol{v} \boldsymbol{\nabla})/2$.

The soil-water characteristic curve is described by the van Genuchten model (van Genuchten 1980) as follows,

$$S_r(p) = S_1 + (S_2 - S_1) \left[1 + (\frac{s}{s_a})^n \right]^{-m}, \tag{7}$$

where S_1, S_2, s_a, m and n are material parameters. Similarly, a relative permeability of the water phase is defined as

$$k_{\text{rw}}(\theta) = \theta^{1/2} \left[1 - (1 - \theta^{1/m})^m \right]^2, \ \ \theta = \frac{S_r(p) - S_1}{S_2 - S_1}. \tag{8}$$

Darcy's law for fluid saturated case is modified by this relative permeability to capture the effect of degree of saturation on the permeability of the fluid flow in partially saturated soils, i.e.,

$$\bar{v} = -k_{\text{rw}}(p) \boldsymbol{K}_{\text{sat}} \cdot \boldsymbol{\nabla} (\frac{p}{\rho_{\text{w}} g} + z) \tag{9}$$

Let $\boldsymbol{w}$ denote the vector of displacement variation such that $w_i \in H^1$ and $w_i = 0$ on $\partial\mathcal{B}_{u_i}$ and θ is the pressure variation such that $\theta \in H^1$ and $\theta = 0$ on $\partial\mathcal{B}_p$. The variational equations for linear momentum balance and fluid flow can be written as follows,

$$\int_{\mathcal{B}} \boldsymbol{\nabla}^s \boldsymbol{w} : (\bar{\sigma} - S_r p \mathbf{1}) \mathrm{d}V = \int_{\mathcal{B}} \boldsymbol{w} \cdot \rho \boldsymbol{g} \mathrm{d}V + \int_{\mathcal{B}_t} \boldsymbol{w} \cdot \hat{t} \mathrm{d}A, \tag{10}$$

$$\int_{\mathcal{B}} \theta S_r \boldsymbol{\nabla} \cdot \boldsymbol{v} \mathrm{d}V + \int_{\mathcal{B}} \theta (1 - \phi^{\text{s}}) \dot{S}_r \mathrm{d}V - \int_{\mathcal{B}} \boldsymbol{\nabla} \theta \cdot \bar{\boldsymbol{v}} \mathrm{d}V = \int_{\mathcal{B}_q} \theta \hat{q} \mathrm{d}V \tag{11}$$

We can integrate these equations in time domain to obtain the discrete evolutions of $\boldsymbol{u}$ and p.; please see Borja et al. (2013b) for detailed linearization and implementation through finite element method.

3 CONSTITUTIVE MODEL

Consider the following invariants of the effective Cauchy stress tensor

$$\bar{p} = \frac{1}{3} \text{tr}(\bar{\boldsymbol{\sigma}}), \qquad q = \sqrt{\frac{3}{2}} \left\| \bar{\boldsymbol{\sigma}} - \bar{p} \mathbf{1} \right\|, \qquad \cos 3\theta = \sqrt{6} \frac{\text{tr}(\bar{\boldsymbol{\sigma}} - \bar{p} \mathbf{1})^3}{\left[\text{tr}(\bar{\boldsymbol{\sigma}} - \bar{p} \mathbf{1})^2 \right]^{3/2}} \tag{12}$$

We use the $(\bar{p}, q, \theta)$ representation to formulate the three-invariant model for sand in the effective stress space. The ellipticity is defined as

$$\rho = q_{\text{ext}} / q_{\text{com}}, \quad 1/2 \leq \rho \leq 1, \tag{13}$$

where q_{com} and q_{ext} are the equivalent shear stress q on the compressive and extensional principal stress axis, respectively. The ellipticity ρ describes the deviation from roundness of the cross section of the yield surface on the deviatoric plane.

A three-invariant yield function for sand (Borja et al. 2013b) takes the form

$$F = \zeta q + \eta \bar{p} \tag{14}$$

where $\zeta(\rho, \theta)$ is a scaling function that captures the effect of ellipticity, and

$$\eta = \begin{cases} M\left[1 + \ln(\bar{p}_i/\bar{p})\right] & \text{if } N = 0; \\ (M/N)\left[1 - (1-N)(\bar{p}/\bar{p}_i)^{N/(1-N)}\right] & \text{if } N > 0. \end{cases} \tag{15}$$

The parameter M has the same meaning as in the modified Cam-Clay model, and $\bar{p}_i < 0$ takes the role of the plastic internal variable. The parameter N characterizes the curvature of the yield surface on the hydrostatic axis. If $\zeta = 1$, the yield surface degenerates into the original Cam-Clay yield surface (Borja et al. 2013b). At the Guass point level, this model is numerically implemented within the framework of the return-mapping algorithm presented in detail by Borja et al. (2013b).

4 NUMERICAL SIMULATION

We present a numerical simulation of a sand specimen under plane strain condition with initial heterogeneities in density and degree of saturation. The specimen is 137 mm tall, 39.5 mm wide, and 79.7 mm deep (out of plane). The specimen is discretized with 216 four-node quadrilateral mixed finite elements, which are stabilized to suppress pore pressure oscillation in the incompressible/nearly incompressible limit (White and Borja 2008). The boundary conditions are as follows: the top and bottom of the specimen are supported by vertical rollers that permit unconstrained shear band propagation; all boundaries are prescribed with zero flux to mimic a globally undrained condition. The material parameters are the same as the ones used in Borja et al. (2013b).

The initial density variation in the specimen is depicted by the contour of initial specific volume shown in Figure 1(a), which shows a relatively loose region in the lower part of the sample. This spatial density variation is prescribed at the Gauss integration points of each finite element. Figure 1(b) shows the initial heterogeneity in degree of saturation, which is prescribed at the pore pressure nodes of the mixed finite elements. Note that the initial degree of saturation shows no indication of a developing shear band.

The sample is compressed vertically at a rate of 0.002 cm/s until a persistent shear band develops. Figure 2(a) shows the fluid flow vectors superimposed with the degree of saturation in the specimen at a nominal axial strain of 3.0%, which corresponds to the compression at which a persistent shear band has fully developed. Note that a nearly saturated band forms in the sample. The flux vectors shows that the fluid is squeezed out of this band. The contour of the normalized localization function is presented in Figure 2(b). From Figure 2(b), we observe that the material loses stability within a region defined by a narrow band that cuts through the looser region of the sample, where the localization function switches from positive (stable) to negative (unstable) values.

The development of a band is corroborated by the contours of deviatoric and volumetric strains at the same nominal axial strain as shown in Figures 3(a) and (b), respectively. Specifically, Figure 3(a) shows that the band experiences significant compaction: the air voids are

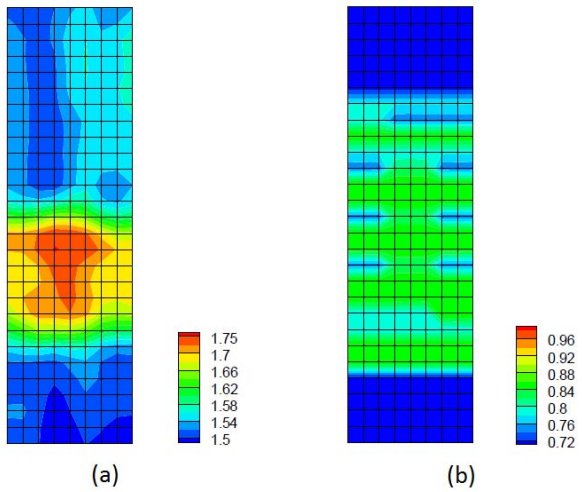

Fig. 1. Contours of: (a) initial specific volume; and (b) initial degree of saturation.

squeezed out, which explains why the degree of saturation increases even though the water is being expelled out of the band. Furthermore, Figure 3(b) shows the intense deviatoric strain developing inside the shear band. Because the loading history and boundary conditions favor the development of a homogeneous deformation, we can conclude that the ensuing inhomogeneous deformation is a result of the imposed heterogeneity in density and degree of saturation in the sample. We also remark that the deformation response depends on the rate of compression and the rate of fluid flow.

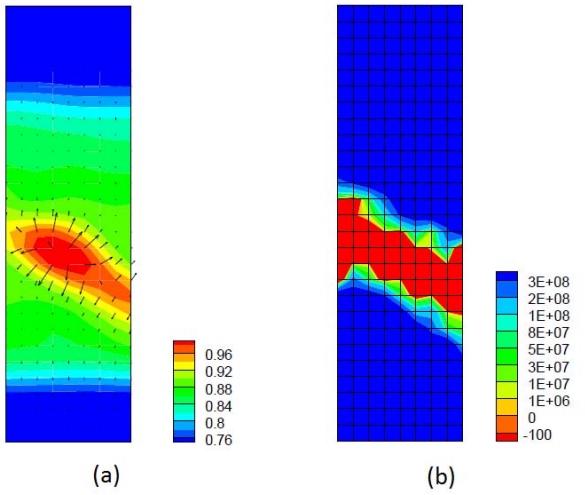

Fig. 2. Contours of: (a) fluid flow vectors superimposed with degree of saturation; and (b) localization function. Nominal axial strain = 3.0%.

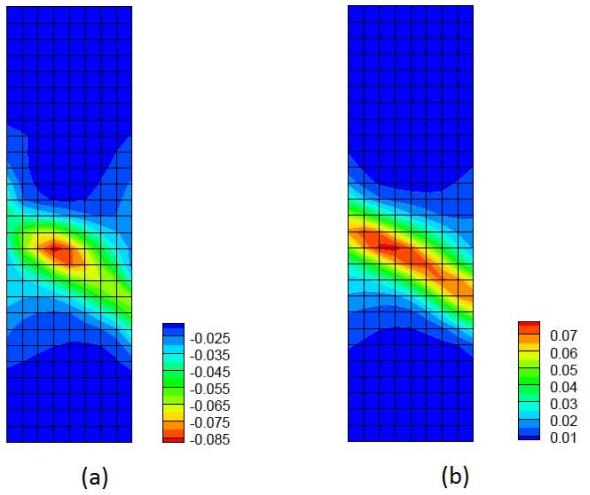

Fig. 3. Contours of: (a) volumetric strain; and (b) deviatoric strain. Nominal axial strain = 3.0%.

5 CLOSURE

Inspired by recent advances in high-resolution imaging that now allows non-destructive and non-invasive measurement of the spatial variations of density and degree of saturation, we have presented a mesoscopic approach to simulating the formation of a persistent shear band in unsaturated soils. We have shown that heterogeneities in density and degree of saturation have a first-order effect on the ensuing persistent shear band; thus, they also have a first-order effect on the triggering of failure in unsaturated porous materials. We should note that, very recently, the mechanical model presented in this paper has been validated experimentally through plane strain testing of dry sand with imposed heterogeneity in density (Borja et al. 2013a). Work is currently in progress to experimentally validate the hydromechanical model through similar laboratory testing of unsaturated soils with imposed heterogeneity in degree of saturation.

ACKNOWLEDGEMENTS

Support for this work was provided by the US National Science Foundation (NSF) under Contract Number CMMI-0936421 to Stanford University.

REFERENCES

Borja, R.I., (2006) “On the mechanical energy and effective stress in saturated and unsaturated porous continua.” *International Journal of Solids and Stuctures*, 43, 1764–1768.

Borja, R.I., Regueiro, R.A., (2001) “Strain localization of frictional materials exhibiting displacement jumps.” *Computer Methods in Applied Mechanics and Engineering*, 190, 2555–2580.

Borja, R.I., Song, X., Rechenmacher, A.L., Abedi, S., Wu, W. (2013a) “Shear band in sand with spatially varying density.” *Journal of the Mechanics and Physics of Solids*, 61, 219–234.

Borja, R.I., Song, X., Wu, W., (2013b) “Critical state plasticity, Part VII: Triggering a shear band in variably saturated porous media.” *Computer Methods in Applied Mechanics and Engineering*, http://dx.doi.org/10.1016/j.cma.2013.03.008.

Liu, F., Borja, R.I. (2008) "A contact algorithm for frictional crack propagation with the extended finite element method." *International Journal for Numerical Method in Engineering*, 76, 1489–1512.

Jefferies, M.G., (1993) "Nor-Sand: A simple critical state model for sand." *Géotechnique*, 35, 91–103.

Rechenmacher, A.L., Abedi, S., Chupin, O., Orlando, A.D., (2011) "Characterization of mesoscale instabilities in localized granular shear using Digital Image Correlation." *Acta Geotechnica*, 6, 205–217.

Rudnicki, J.W. and Rice, J.R., (1975) "Conditions for localization of deformation in pressure-sensitive dilatant materials." *Journal of the Mechanics and Physics of Solids*, 23, 371–394.

Schrefler, B.A., (1984) "The finite element method in soil consolidation (with application to surface subsidence)." *Ph.D. Thesis*, University College of Swansea, C/Ph/76/84.

van Genuchten, M.T., (1980) "A closed-form equation for predicting the hydraulic conductivity of unsaturated soils." *Soil Science Society of America Journal*, 44, 892–898.

White, J.A., and Borja, R.I. (2008) "Stabilized low-order finite elements for coupled solid-deformation/fluid-diffusion and their application to fault zone transients." *Computer Methods in Applied Mechanics and Engineering*, 197, 4353–4366.

Yoshimoto, N, Orense, R.P., Tanabe, F., Kikkawa, N., Hyodo, M., Nakata, Y. (2011)"Measurement of degree of saturation on model ground by digital image processing." *Soils and Foundations*, 51, 167–177.

DISCRETE ANALYSIS OF MICRO-STRUCTURAL EVENTS IN GRANULAR SHEAR ZONES

M. Nitka
Department of Civil and Environmental Engineering, Gdańsk University of Technology, Poland

J. Kozicki
Department of Civil and Environmental Engineering, Gdańsk University of Technology, Poland

J. Tejchman
Department of Civil and Environmental Engineering, Gdańsk University of Technology, Poland

ABSTRACT: *The evolution of shear zones in initially medium dense cohesionless sand in quasi-static earth pressure problems of a retaining wall was analyzed with a 3D discrete element method DEM using spheres with contact moments. The passive sand failure for a very rough retaining wall undergoing horizontal translation towards the backfill was discussed. Several characteristic micro-structural events occurring in shear zones in sand behind the wall at the grain-level such as: force chains, vortex structures, local void ratio fluctuations and strain non-uniformities were analyzed. The calculated geometry of shear zones was compared with experimental results of laboratory model tests using x-rays and a DIC technique DEM demonstrated its ability to investigate shear localization at grain level.*

1 INTRODUCTION

Earth pressure on retaining walls is one of the soil mechanics classical problems. In spite of an intense theoretical and experimental research over more than 200 years, there are still large discrepancies between theoretical solutions and experimental results due to the complexity of the deformation field in granular bodies near the wall caused by shear localization in the form of single or multiple narrow zones, which is a fundamental phenomenon of granular material behavior at large shear deformation (Gudehus & Nübel 2004, Tejchman 2008).

For granular materials, once a shear zone is formed, further deformation is mostly accommodated by the material within a shear zone. The peak and post-peak response of the material is thus controlled by localized shear zones. It is necessary to understand the underlying nature of granular material behaviour within shear zones to fully characterize the softening and critical state material response at the macro-level. The knowledge of both the distribution of shear zones and distribution of shear and volumetric strains within shear zones are important to explain the mechanism of granular deformation. The multiple patterns of shear zones are not usually taken into account in engineering calculations.

The objectives of the paper are numerical investigations of a quasi-static evolution of deformation structure within shear zone in initially medium dense cohesionless sand with the discrete element method (DEM). The DEM calculations were carried out under passive earth pressure conditions in sand behind a rigid vertical wall, which was moved towards the backfill. To simulate the behavior of sand, the three-dimensional discrete model YADE developed at University of Grenoble was used, allowing for introducing grain rolling resistance in order to take into account the grain roughness (Kozicki & Donze 2008). Particle

breakage was not considered because of the relatively low pressure level assumed in the simulations. Several characteristic micro-structural events occurring in shear zones at the grain-level such as force chains, vortex structures, local void ratio fluctuations, strain non-uniformities were analyzed. This paper is a continuation of our research works presented in the paper by Widuliński et al (2011) which showed a capability of DEM to describe out patterns of shear zones in sand placed behind a rigid and very rough retaining wall, undergoing passive and active movements: horizontal translation, rotation about the top and rotation about the toe. In this paper, micro-structure changes at the grain-level in shear zones were numerically studied during a complex boundary value problem with patterns of shear zones.

2 SHEAR ZONE PATTERN IN EXPERIMENTS

Figure 1 shows shear zones observed in experiments of passive mode with initially dense sand during wall translation by means of *x*-rays (Lucia (1966), Gudehus & Schwing (1986)), and the digital image correlation (DIC) technique (Niedostatkiewicz et al. (2011)). In the first case the retaining wall was 330 mm high and 190 mm wide. The sand used was rounded coarse quartz 'Leighton Buzzard' (grain size between 0.6-1.2 mm, mean grain diameter d_{50}=0.9 mm). In the second case, the specimen of 'Karlsruhe sand' (grain size between 0.08 mm-1.8 mm, d_{50}=0.50 mm) was 400 mm long, 200 mm high and wide. The wall was 0.175 m high. In the third case, the model tests were carried out in a metal strong box 360 mm long, 220 mm high and 20 mm wide with 'Borowiec sand' (grain size between 0.2-1.6 mm, d_{50}=0.8 mm). The wall height was 220 mm.

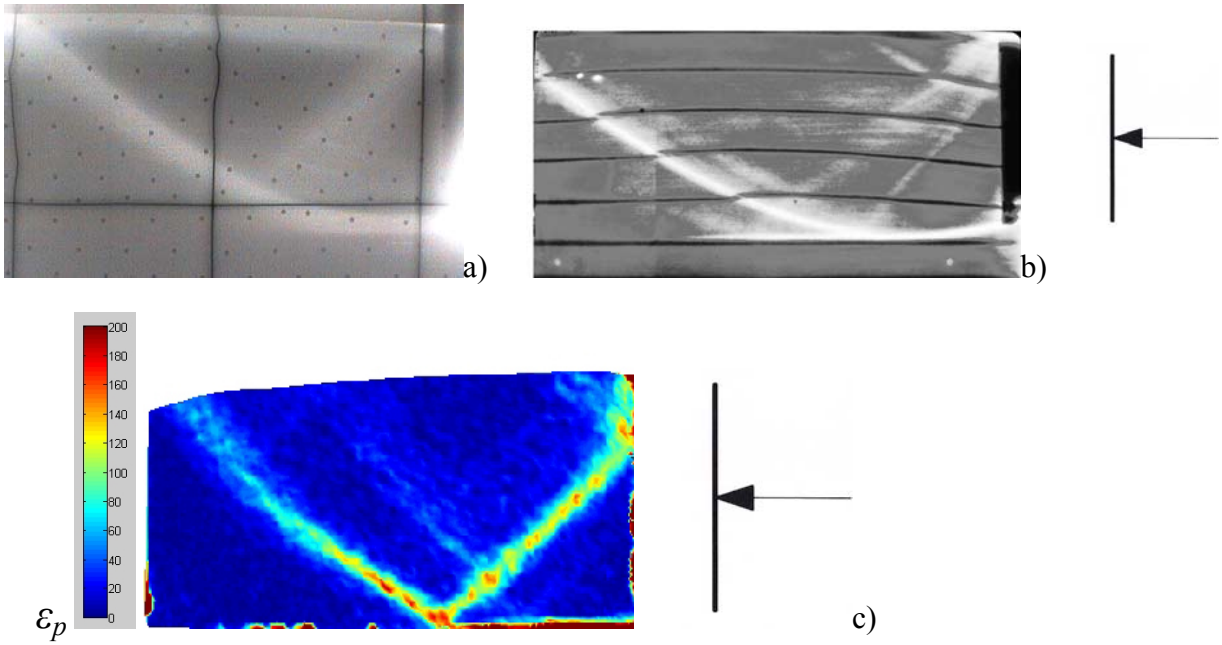

Fig. 1. Shear zone patterns observed in experiments of passive mode with initially dense sand during wall translation: a) x-ray radiograph (Lucia 1966), x-ray radiograph (Gudehus & Schwing 1986), B) DIC image (Niedostatkiewicz et al. 2011), ε_p - deviatoric strain)

In laboratory experiments (Figs.1a-1c), one distinct dilating curved shear zone started from the toe of the wall to the free boundary and accompanied by one (Fig.1a) or two (Fig.1b) weaker secondary radial shear zones propagating from the wall top were observed. In addition, two secondary (not fully developed) shear zones can be observed (Fig.1c); one

emerging slightly below the top of the wall in the right up corner of the sample and propagating to the free boundary, and the other one in the middle of the specimen, parallel to the main shear zone and propagating also to the free boundary (they appear slightly later as the first two shear zones).

3 DISCRETE ELEMENT METHOD

In numerical analyses using DEM, the mechanical response of geomaterials is governed by interactions at contacts between constituent particles and between particles and boundaries which are responsible for the emergent complexity of phenomena occurring in these materials. To simulate the behaviour of sand, a three-dimensional spherical discrete model YADE was developed at University of Grenoble (Kozicki and Donze 2008) by taking advantage of the so-called soft-particle approach (i.e. the model allows for particle deformation which is modelled as an overlap of particles). To simulate sand grain roughness, additional moments were introduced into a 3D model, which were transferred through contacts and resisted particle rotations (Kozicki and Donze 2008). In this way, grains were in contact with their neighbours through a certain contact surface (Iwashita and Oda 1998). Our discrete element model can simulate different grain shapes by using different symmetric and non-symmetric clusters of spheres (Kozicki et al. 2012). In our computational model we use exclusively spherical particles and we model the influence of contact flatness and thus the influence of the grain shape by assuming bending moments and bending stiffnesses at particle contacts. This approach has two main advantages: a) the computation time is significantly shortened (calculations with spheres and contact moments are 3-5 times faster than those using complex clumps (Kozicki et al. 2012) and b) the model is already one step closer to a micro-polar continuum model (Widulinski et al. 2011)). Pasternak and Mühlhaus (2005) demonstrated that the additional rotational degree of freedom of a micro-polar continuum arose naturally by mathematical homogenization of an originally discrete system of spherical grains with contact forces and moments. In addition, Ehlers et al. (2003) showed that a particle ensemble had the character of a micro-polar continuum and the couple stresses naturally result only from the eccentricities of the normal contact forces. Therefore, the choice of spheres with contact moments was in our discrete simulations intentional.

The material parameters were calibrated with the corresponding axisymmetric triaxial laboratory test results on Karlsruhe sand by Wu (1992). The index properties of 'Karlsruhe' sand are: mean grain diameter d_{50}=0.50 mm, grain size among 0.08 mm and 1.8 mm, uniformity coefficient U=2, maximum specific weight γ_d^{max}=17.4 kN/m^3, minimum void ratio e_{min}=0.53, minimum specific weight γ_d^{min}=14.6 kN/m^3 and maximum void ratio e_{max}=0.84. The sand grains are classified as sub-rounded/sub-angular. The triaxial compression tests were carried out with initially dense sand (initial void ratio e_o=0.53) and initially loose sand (e_o=0.80) in the confining pressure range σ_c=50-1000 MPa.

During calibration simulations, a cubical sand specimen of 10×10×10 cm^3 was used (Kozicki et al. 2012). A simplified linear grain distribution curve was assumed, namely, the grain range was among 2.5 mm and 7.5 mm with d_{50}=5.0 mm instead of d_{50}=0.5 mm for real Karlsruhe sand). The tests were modelled using confining smooth rigid wall elements (without inducing non-homogeneous deformation). The top and bottom boundaries moved vertically as loading platens under strain-controlled conditions to simulate the confining pressure p. Figure 2 shows the calculated evolution of the vertical normal stress σ_1 and volumetric strain ε_v versus vertical normal strain ε_1 for spheres with contact moments during triaxial compression with initially dense sand (e_o=0.53, d_{50}=5 mm) as compared to the laboratory experiments by Wu (1992) at confining pressure σ_c=200 kPa. The following

discrete material parameters were assumed: (E_c=0.3 GPa – modulus of elasticity of the grain contact, ν_c=0.3 - Poisson's ratio υ_c of the grain contact, μ=18^o - inter-particle friction angle, β=0.7 - rolling stiffness coefficient, η=0.4 - rolling limit coefficient, ρ=25.5 kN/m^3 – mass density, a=0.08 – damping parameter and d_{50}=5.0 mm – mean grain diameter).

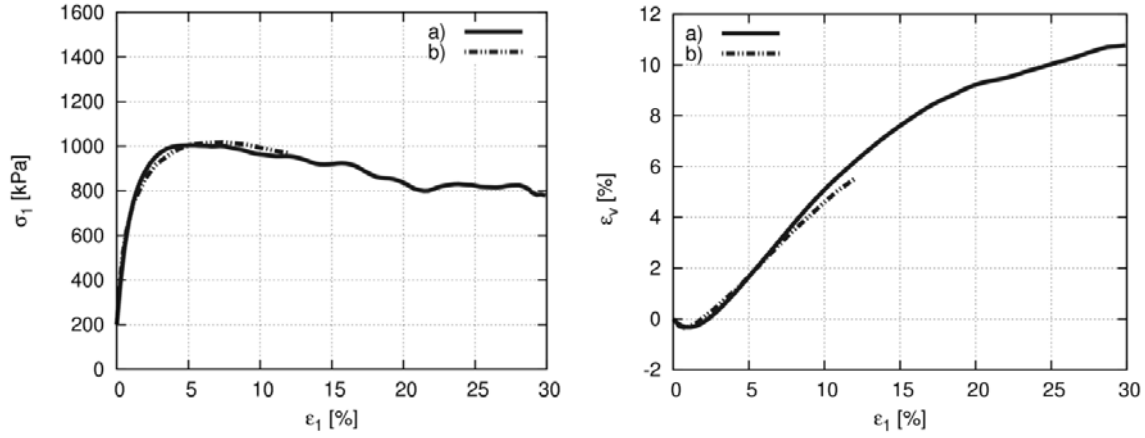

a) b)

Fig. 2. Vertical normal stress σ_1 versus vertical normal strain ε_1 and volumetric strain ε_v versus ε_1 during homogeneous triaxial compression test (initial void ratio e_o=0.53, confining pressure σ_c=200 kPa): a) discrete results with spheres and contact moments using linear contact model (E_c=0.3 GPa, ν_c=0.3, μ=18^o, β=0.7, η=0.4, d_{50}=5.0 mm), b) experimental results by Wu 1992 with d_{50}=0.5 mm

4 DEM RESULTS OF EARTH PRESSURE PROBLEM

The discrete calculations were performed with a sand body of a height of 200 mm and length of 400 mm to compare them directly experimental results (Fig.1b). The height of the retaining wall was h=200 mm. The vertical retaining wall and bottom of the granular specimen were assumed to be stiff and very rough. Since the effect of the specimen depth turned out to be almost negligible, discrete calculations were mainly performed with the specimen depth equal to the grain size (i.e. only one grain layer was simulated in the perpendicular plane) in order to significantly accelerate simulations.

The calculations were carried out with three different mean grain diameters of sand using a linear grain size range: d_{50}=5.0 mm (grain size range 2.5-7.5 mm, 2'600 spheres) d_{50}=2.0 mm (grain size range 1-3 mm, 15'600 spheres) and d_{50}=1.0 mm (grain size range 0.5-1.5 mm, 62'600 spheres). The initial void ratio of sand was e_o=0.63. The loading speed was slow enough to ensure that tests were conducted under quasi-static conditions. The calculations were carried out with the parameters determined in Section 3: E_c=0.3 GPa, ν_c=0.3, μ=18^o, β=0.7, η=0.4, ρ=25.5 kN/m^3 and a=0.08. The computation time CPU was ca. 14 days (d_{50}=2.0 mm) and 30 days (d_{50}=1.0 mm) using PC 3 GHz.

Figure 3 presents the calculated evolution of the resultant normalized horizontal earth pressure force $K=2E_h/(\gamma h^2)$ versus normalized horizontal wall displacement u/h by means of DEM for the different sphere size d_{50}=1 mm, 2 mm and 5 mm (E_h – horizontal wall force). The normalized horizontal earth pressure force has a typical evolution for initially dense granulates during biaxial compression, triaxial compression and shearing. The specimen exhibits initial strain hardening up to the peak (u/h=0.03-0.04), followed by softening before reaching approximately an asymptote. It strongly fluctuates after the peak that is attributed to

the build-up and collapse of force chains - the main carrier of stresses transferred within the granular assembly (Alonso-Marroquin et al. 2006), Fi.12. For larger spheres, the parameter K_{max} becomes higher.

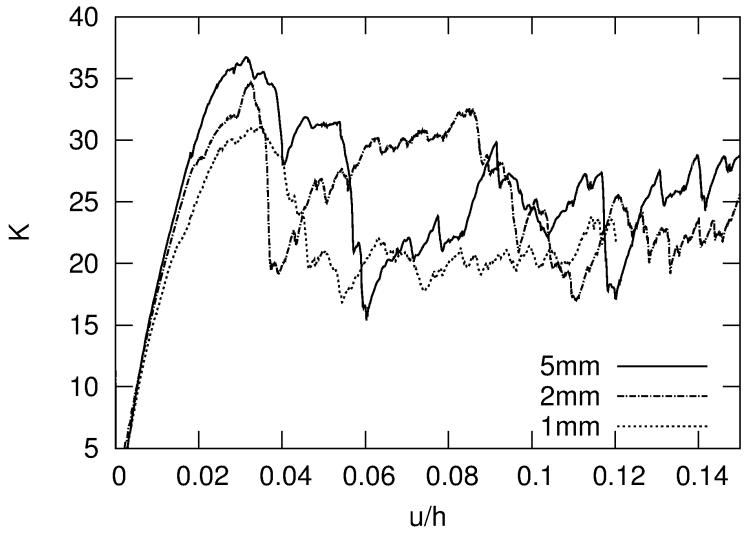

Fig. 3. DEM results (passive case, translating wall): evolution of resultant normalized horizontal earth pressure force $K=2E_h/(\gamma h^2)$ versus normalized horizontal wall displacement u/h (γ=16.75 kN/m^3, h=0.2 m, e_o=0.63)

The shear zones are clearly recognizable from the presence of the grain rotation ω and resultant grain rotations ω^c and an increase of void ratio e (Figs.4-8). The quantities ω^c and e were calculated from the area $5d_{50}\times5d_{50}$. First, a curved shear zone forms at the bottom of the moving wall and propagates up to the top boundary (Fig.4). Next, a radial shear zone appears at the wall top that propagates to the specimen bottom (d_{50}=1-2 mm) (Fig.4). Except of two main shear zones, there exist also other less visible localized zones. The geometry of shear zones is similar as in experiments (Fig.1). The thickness of the main curved shear zone increases with increasing d_{50}. At the residual state, it is 20 mm ($20\times d_{50}$) with d_{50}=1.0 mm based on the distribution of grain rotations. The inclination of the main curved shear zone to the horizontal is 50^o. In turn, the main radial shear zone is inclined to the vertical under 50^o. The distribution of the grain rotations ω and resultant grain rotations ω^c is non-uniform in a curved and radial shear zone along their length (Fig.5) and width (Fig.8a). The resultant rotation has its maximum in the mid-width of the shear zone. It is equal to 45^o-70^o (d_{50}=1-5 mm). The distribution of void ratio across the shear zone is strongly non-uniform (Figs.6 and 8b), alternating in a nearly periodic fashion (Fig.7) as in biaxial compression tests based on the DIC technique (Chupin et al. 2011). The specimen globally dilates in the shear zones, however, the local void ratio can also reduce (local contractancy zone is observed) (Fig.10b). The maximum value of e in the shear zone at the residual state is about 0.75 (Fig.7).

The evolution of the contact network in the sand specimen is demonstrated in Fig.9. The colour intensity represents the different compressive normal contact force between two particles. The distribution of internal contact forces is non-uniform and continuously changes (Tordesillas et al. 2010). Force chains of heavily loaded grain contacts bear and transmit the compressive load on the entire granular system and are the predominant structure of internal forces at micro-scale. They build up and collapse. The force chains are created mainly along the curved and radial shear zone and the region between the wall, radial and curved shear zone. Thus, the anisotropy of the numerical test is very strong due to obliquely oriented force chains.

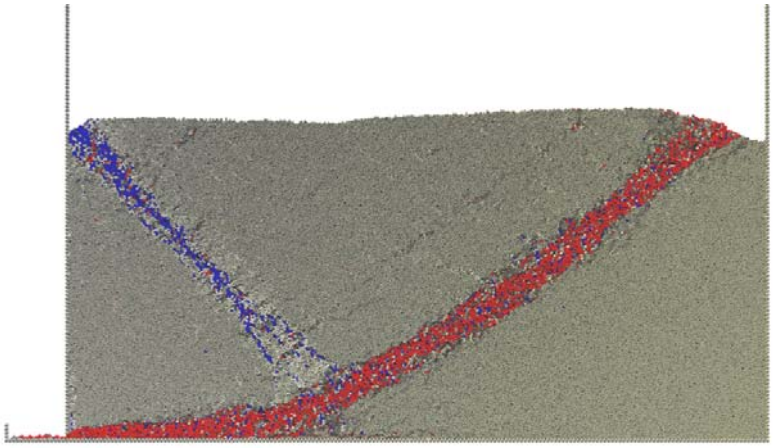

Fig. 4. Deformed granular body with distribution of grain rotation for initially medium dense sand at residual state of u/h=0.15 (d_{50}=1.0 mm)

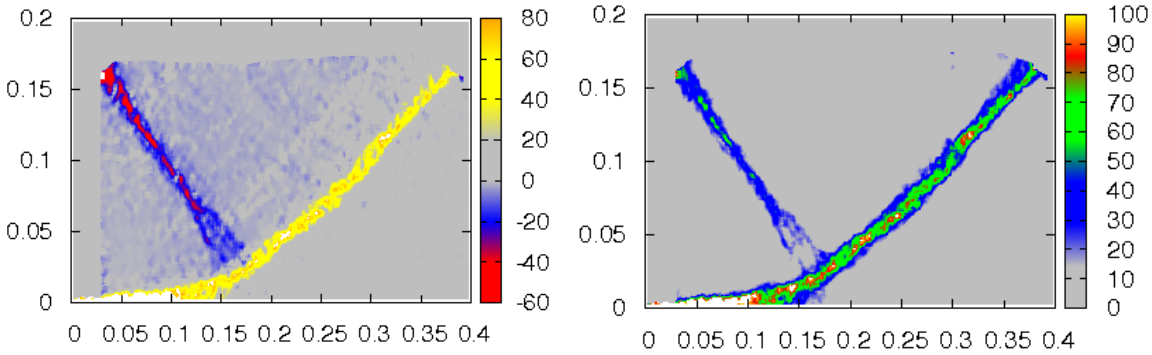

a) b)

Fig. 5: Distribution of resultant grain rotation ω^c (a) and $|\omega^c|$ (b) in initially medium dense sand (e_o=0.63) at residual state of u/h=0.15 (d_{50}=1 mm) (scale denotes rotation intensity in [°])

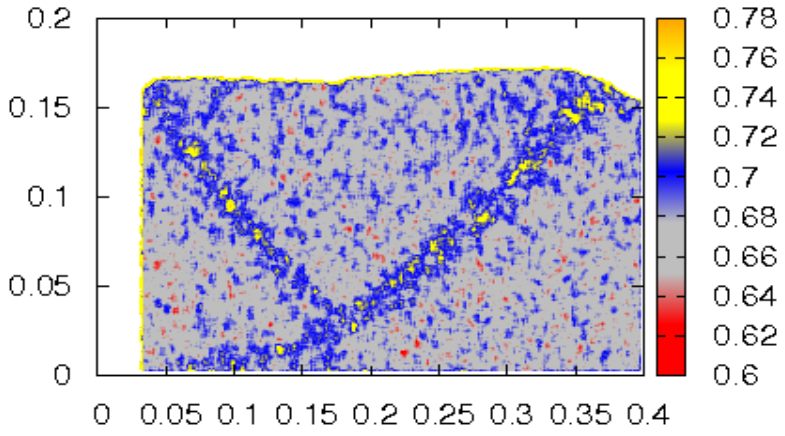

Fig. 6. Distribution of void ratio *e i*n initially medium dense sand (e_o=0.63) at residual state of u/h=0.15 (d_{50}=1.0 mm) (scale denotes void ratio intensity in [-])

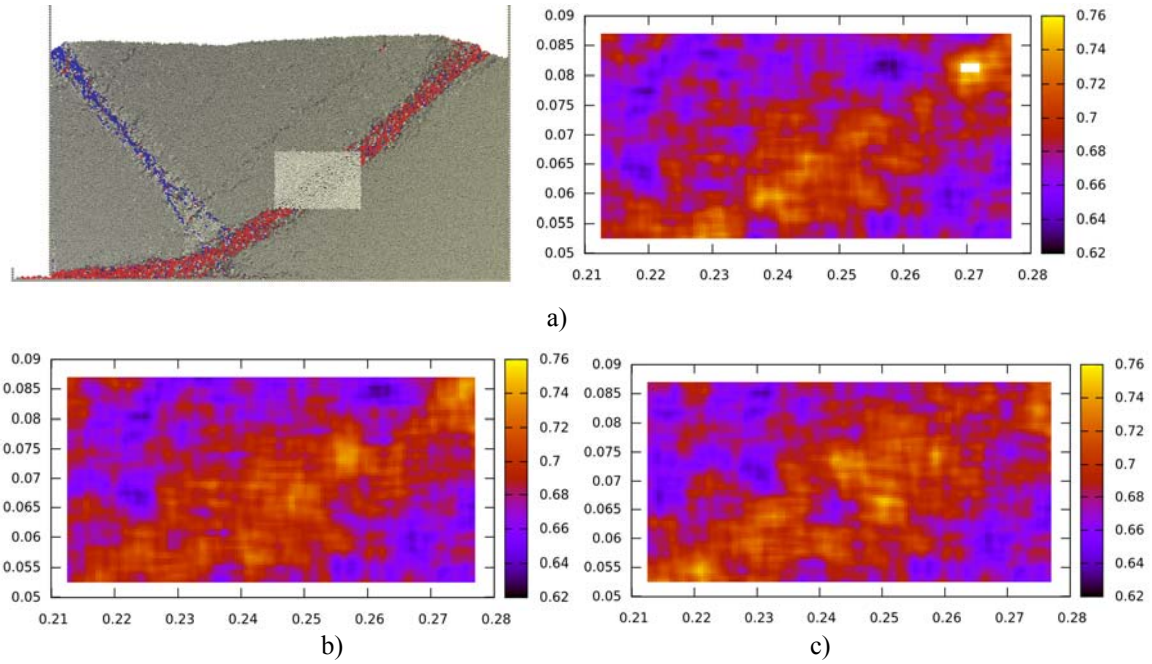

Fig. 7. Distribution of void ratio e in mid-part of curved shear zone (d_{50}=1 mm) for initially medium dense sand (e_o=0.63) (vertical left axis – vertical co-ordinate, vertical right axis – void ratio, horizontal axis – horizontal co-ordinate) for different horizontal wall displacement: a) u/h=0.065 b) u/h=0.10 and c) u/h=0.15

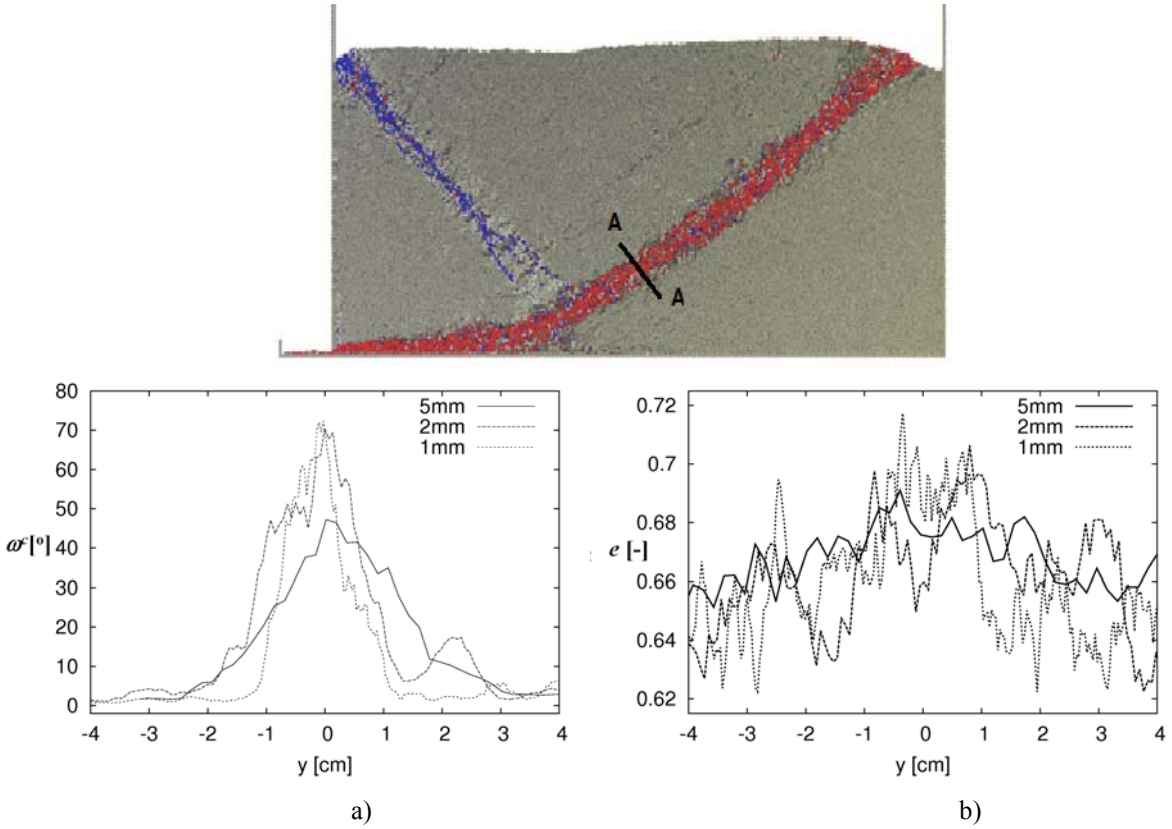

Fig. 8. Distribution of resultant grain rotation (a) and void ratio e (b) across shear zone (section A-A) in initially medium dense sand (e_o=0.63) at residual state with d_{50}=5 mm, d_{50}=2 mm and d_{50}=1 mm

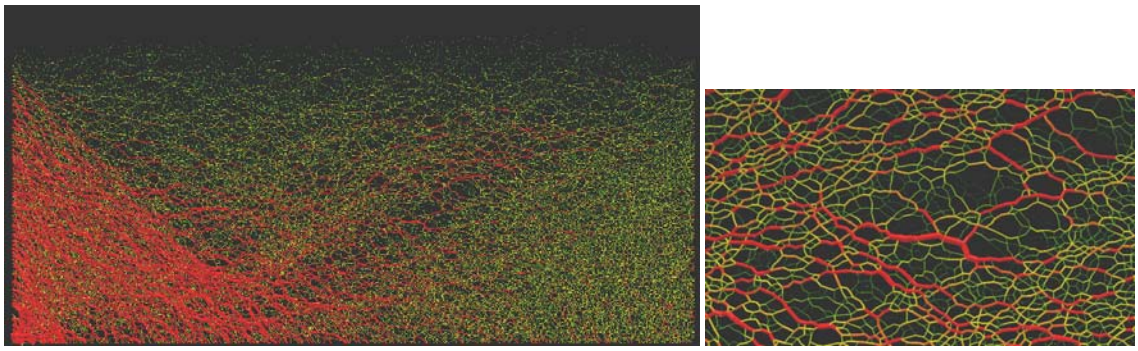

a) b)

Fig. 9. Distribution of contact normal forces between spheres at residual state of u/h=0.15 (d_{50}=1 mm) in entire granular specimen (a) and in fragment of curved shear zone (zoom) (b)

Figure 10 presents a spontaneous occurrence of displacement fluctuations in the granular specimen in the form of clusters of circulating cells (so-called vortex structures) observed both in real experiments (Abedi et al. 2012, Richefeu et al. 2012) and discrete simulations (Kuhn 1999, Alonso-Marroquin et al. 2006, Liu et al. 2012). The plots were obtained by drawing the displacement difference vector ($\vec{V}_i - \vec{V}_{avg}$) for each sphere with respect to the background translation corresponding to the homogeneous (affine) strain ($\vec{V}_i$ represents the sphere displacements during e.g. 100 iterations and $\vec{V}_{avg} = \frac{1}{n}\sum_i^n \vec{V}_i$ are the average displacements). The individual particle displacements are able to form large long-range deformation vortex structures, wherein cells rotate as a rigid body whereas the space between them is characterized by intense shear deformation. The vortex-like patterns are well recognized in particular at the residual state. Several vortices occur in the curved shear zone (Fig.10b) with the diameter of the shear zone thickness. They rotate counter clockwise. These fluctuation loops are connected closely with force chains and alternating changes of local void ratio and global macroscopic stress fluctuations. They are a direct manifestation of grain rearrangement.

A link between the force chain, vortex structure and porosity changes in a curved shear zone at the residual state during normalized displacement increment u/h=0.1 (from u/h=0.15 up to u/h=0.16) is shown in Fig.11. During the wall translation increment, one force chain disappears and a new one appears (Fig.11b). This new force chain blocks a movement of grains and a vortex vanishes. Small dilatancy occurs close to a broken force chain and small contractancy near a new force chain.

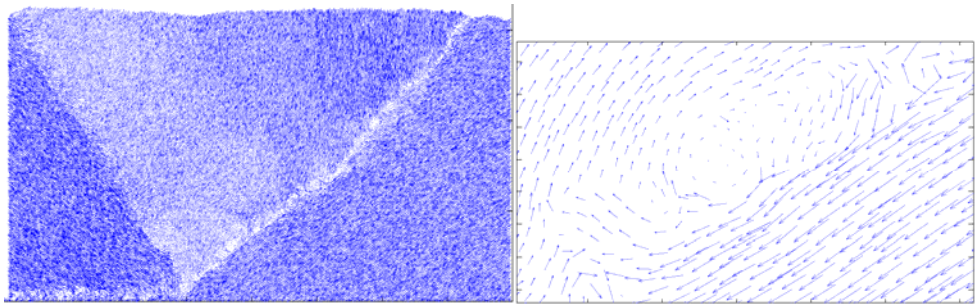

a) b)

Fig. 10. Displacement fluctuations (vortex structures) in entire granular specimen (a) and in fragment of curved shear zone (b) at residual state of u/h=0.15 (d_{50}=1 mm)

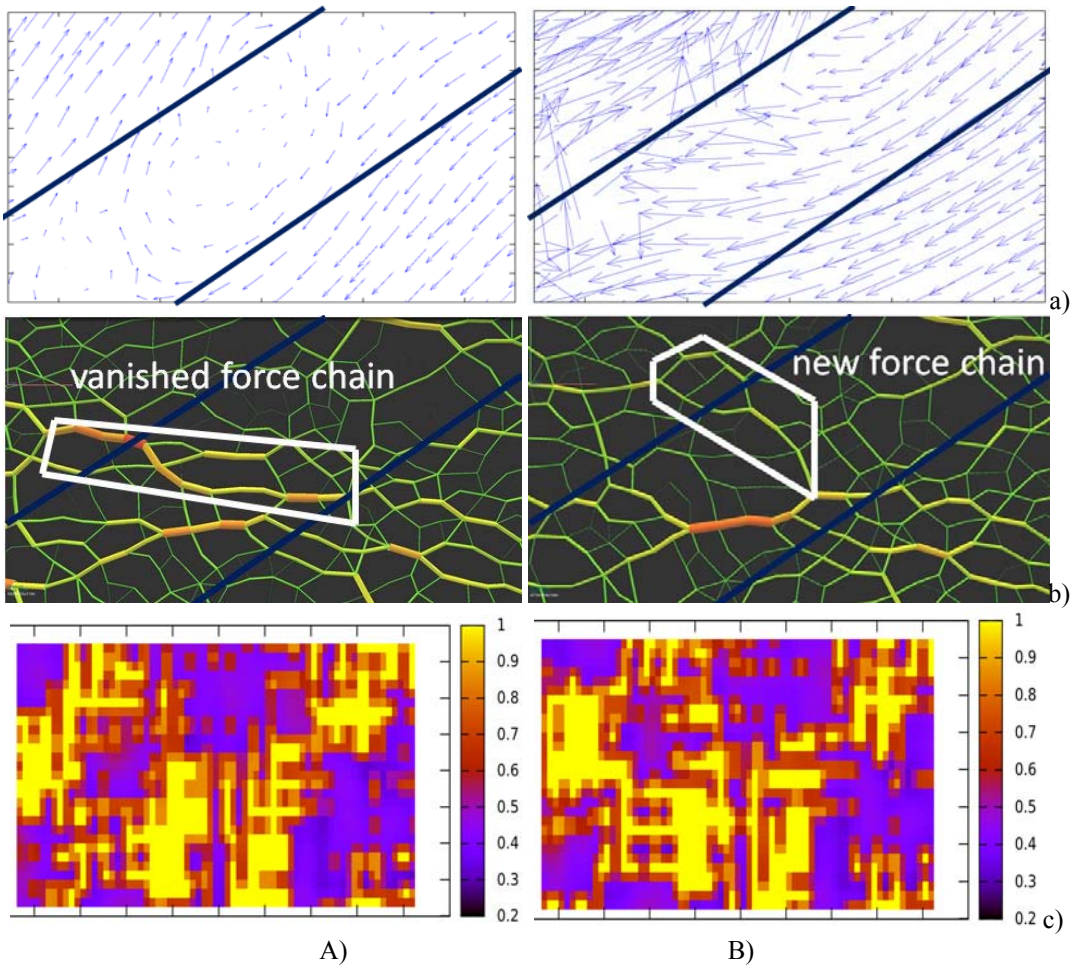

Fig. 11. Evolution of micro-structure in curved shear zone at *u/h*=0.15 (A) and *u/h*=0.16 (B): a) map of displacement fluctuation, b) distribution of force chains, c) map of void ratio

5 CONCLUSIONS

The following conclusions can be also drawn from our discrete simulations of earth pressures behind a retaining wall using DEM:

DEM realistically predicts the experimental results of a pattern of shear zones in the interior of initially medium dense sand. Grain rotations are noticeable only in shear zones. Dilatancy takes place in shear zones with small local contractancy regions. The global wall pressure increases with increasing mean grain size.

In the shear zone, vortex structures and local void ratio fluctuations systematically occur that seem to have a periodically organized structure. The distribution of internal contact forces is non-uniform and continuously changes. Deformation of force chains plays a key role in the formation of vortex structures.

REFERENCES

Abedi, S., Rechenmacher, A. L. and Orlando, A. D. (2012), "Vortex formation and dissolution in sheared sands". Granular Matter, Vol. 14, 6, 695-705.

Alonso-Marroquin, F., Vardoulakis, I., Herrmann, H., Weatherley, D. & Mora, P. (2006), "Effect of rolling on dissipation in fault gouges". Physical Review E 74, 031306, 1-10.

Chupin, O, Rechenmacher, A. L. & Abedi, S. (2011), "Finite strain analysis of non-uniform deformations inside shear bands in sands". International Journal for Numerical and Analytical Methods in Geomechanics, doi: 10.1002/nag.1071, 2011.

Ehlers, W., Ramm, E., Diebels, S. & D'Addetta, G.A. (2003), "From particle ensembles to Cosserat continua: homogenisation of contact forces towards stresses and couple stresses". Int. J. Solids and Structures, Vol. 40, 6681-6702.

Gudehus, G. & Schwing, E. (1986), „Standsicherheit historischer Stützwände". Internal Report of the Institute of Soil and Rock Mechanics, University Karlsruhe.

Gudehus, G. & Nübel, K. (2004), "Evolution of shear bands in sand". Geotechnique 113, Vol. 54(3), 187–201.

Iwashita, K. & Oda, M. (1998), "Rolling resistance at contacts in simulation of shear band development by DEM". ASCE J Eng Mech. Vol. 124(3), 285–92.

Kozicki, J. & Donze, F.V. (2008), "A new open-source software developed for numerical simulations using discrete modelling methods". Computer Methods in Applied Mechanics and Engineering Vol. 197, 4429-4443.

Kozicki, J., Tejchman, J. and Mróz, Z. (2012), "Effect of grain roughness on strength, volume changes, elastic and dissipated energies during quasi-static homogeneous triaxial compression using DEM". Granular Matter, Vol. 14(4), 457-468.

Kuhn, M. R. (1999), "Structured deformation in granular materials". Mechanics of Materials Vol. 31, 407-442.

Liu, X., Papon, A. & Mühlhaus, H.-B. (2012), "Numerical study of structural evolution in shear band". Philosophical Magazine, doi.org/10.1080/14786435.2012.715249.

Lucia, J.B.A. (1966), "Passive earth pressure and failure in sand". Research Report, University of Cambridge.

Niedostatkiewicz, M., Leśniewska, D. & Tejchman, J. (2011), "Experimental analysis of shear zone patterns in sand for earth pressure problems using Particle Image Velocimetry". Strain, Vol. 47, s2, 218-231.

Pasternak, E. & Mühlhaus, H.-B. (2006), "Generalised homogenisation procedures for granular materials". Journal of Engineering Mathematics Vol. 52(1), 199-229.

Richefeu, V., Combe, G. & Viggiani, G. (2012), "An experimental assessment of displacement fluctuations in a 2D granular material subjected to shear". Geotechnique Letters, Vol. 2, 113–118.

Tejchman, J. (2008), FE modeling of shear localization in granular bodies with micro-polar hypoplasticity. Springer Series in Geomechanics and Geoengineering (eds. W. Wu and R.I. Borja), Springer Verlag, Berlin-Heidelberg.

Tordesillas, A., Walker, D. M. & Qun Lin, Q. (2010), "Force cycles and force chains". Physical Review E 81, 011302.

Widulinski, L., Tejchman, J., Kozicki, J. and Leśniewska, D. (2011), "Discrete simulations of shear zone patterning in sand in earth pressure problems of a retaining wall". Int. J. Solids and Structures, Vol. 48(7-8), 1191-1209.

Wu, W. (1992). Hypoplastizität als mathematisches Modell zum mechanischen Verhalten granularer Stoffe. Heft 129, Institute for Soil- and Rock-Mechanics, University of Karlsruhe.

ON THE DESCRIPTION OF FRACTURE PROPAGATION IN BRITTLE MATERIALS

E. Haghighat & S. Pietruszczak
Department of Civil Engineering, McMaster University, Hamilton, Ont., Canada

ABSTRACT: *In this paper, the problem of damage propagation in brittle materials is investigated. Two conceptually different frameworks are discussed, viz. Extended FEM as well as the standard FEM approach, the latter incorporating a constitutive law formulated through volume averaging in the neighborhood of the embedded discontinuity. The onset and the propagation of cracks are described using the level set method for both these approaches. Some numerical examples are provided that involve a three-point bending test, as well as a shear test in which a notched specimen is subjected to both shear and tension. It is demonstrated that the volume averaging technique, enhanced by the level set method for tracking the crack evolution, gives nearly the same results as those based on Extended FEM.*

1 INTRODUCTION

Modeling of damage initiation and propagation has been one the most intensely researched topic over the last few decades. The existing analytical solutions are restricted to an elastic material and involve simple geometries and boundary conditions. Therefore, they are not directly relevant to practical engineering problems. The latter require, in general, a numerical analysis that typically involves the use of the finite element method. The early methodologies for capturing the progressive damage within the finite element framework were based on tracing the crack propagation on the element boundaries by introducing interface elements (Schellekens & de Borst, 1993). Alternative approaches that were developed involved the use of elements with embedded localization zones (Belytschko et al., 1988) as well as meshless approximations dealing with discontinuous fields (Belytschko et al., 1996; Fleming et al., 1997). More recently, after introduction of the partition of unity method (Melenk & Babuška, 1996), the so-called Extended Finite Element Method (XFEM) has been developed. XFEM was initially formulated for mesh-independent modeling of tensile crack propagation (Belytschko & Black, 1999; Moës et al., 1999). The first extension of the original framework incorporated the crack tip enrichment and the contact condition (Dolbow et al., 2000; Dolbow et al., 2001). Later, the framework was combined with the level set method for tracking the propagating crack in the solution domain (Stolarska et al., 2001). Since then, XFEM has been applied to a broad class of problems including modeling cohesive crack propagation (Wells & Sluys, 2001; Moës & Belytschko, 2002), modeling of fracture process in saturated porous media under both isothermal and non-isothermal conditions (Réthoré et al., 2007; Khoei et al., 2012), etc.

The primary difficulty in implementing XFEM is the need to deal with additional degrees of freedom. Although the approach itself is well suited for modeling the crack propagation,

the computational effort associated with the use of additional degrees of freedom is very significant. The latter has a two-fold implication. First, the computational time associated with solving the new system of equations increases by at least an order of 2. In addition, the computational effort is further increased by the need to invoke special techniques for integration within the enriched elements. These issues become even more protuberant when dealing with three-dimensional cases and/or problems involving more than one field variable, such as coupled problems in physics.

In parallel with advances in finite element techniques, methodologies have also been developed to describe discontinuous/localized deformation by enhancing the standard phenomenological constitutive laws. The first such approach (Pietruszczak & Mroz, 1981) advocated the use of volume averaging to estimate the properties of an initially homogeneous medium intercepted by a shear band/interface. The proposed constitutive relation incorporated the properties of constituents (viz. intact material and interface) as well as a characteristic dimension associated with the structural arrangement. This approach was later revised (Pietruszczak; 1995,1999) and applied to a broad range of practical engineering problems (e.g., Xu & Pietruszczak, 1997; Shieh-Beygi & Pietruszczak, 2008; Pietruszczak & Gdela, 2010). In addition, other continuum frameworks have been developed employing various regularizations techniques that included the use of micro-polar continua (Mühlhaus & Vardoulakis, 1987; Borst, 1991) non-local theories (Pijaudier-Cabot & Bažant, 1987), as well as gradient-dependent formulations (Aifantis, 1984; Mühlhaus & Alfantis, 1991; de Borst & Mühlhaus, 1992). The use of enhanced constitutive relations is computationally attractive as it can be employed within the standard FEM framework without the need to introduce additional degrees of freedom.

This paper is focused on modeling of multiple cohesive cracks propagation in a class of brittle materials, such as concrete, in the tensile stress regime. Both XFEM and the approach based on volume averaging in the neighborhood of the crack (Pietruszczak, 1999) are employed. The latter approach is enhanced by incorporating the level set method, similar to that used in XFEM, in order to capture a discrete nature of the crack propagation process. It is demonstrated that both methodologies, i.e. XFEM and EnVA (Enhanced Volume Averaging), yield virtually identical results for modeling of brittle fracture propagation. This gives the advantage to the averaging scheme as the latter requires significantly less computational effort.

2 FORMULATION OF THE PROBLEM

A discontinuous motion $\mathbf{v}(\mathbf{x},t)$ in the domain Ω that contains a discontinuity surface Γ_d can be defined as (Wells & Sluys, 2000)

$$\mathbf{v}(\mathbf{x},t) = \hat{\mathbf{v}}(\mathbf{x},t) + \mathcal{H}_{\Gamma_d}\tilde{\mathbf{v}}(\mathbf{x},t) \tag{1}$$

where, $\hat{\mathbf{v}}(\mathbf{x},t)$ and $\tilde{\mathbf{v}}(\mathbf{x},t)$ are continuous functions in the solution domain Ω and $\mathcal{H}_{\Gamma_d} = \mathcal{H}(\phi)$ is chosen as the symmetric form of the step function, i.e.,

$$\mathcal{H}(\phi) = \begin{cases} +1 & \phi > 0 \\ -1 & \phi < 0 \end{cases} \tag{2}$$

where $\phi = \phi(\mathbf{x})$ is the signed distance function from the discontinuity interface Γ_d, as defined in following sections. Denoting the jump of a function on the discontinuity interface by $[\![\bullet]\!]$, the velocity of crack opening, i.e. $\dot{\mathbf{g}}$, can be defined as

$$\dot{\mathbf{g}} = [\![\mathbf{v}]\!] = \left(\hat{\mathbf{v}} + \mathcal{H}_{\Gamma_d}\tilde{\mathbf{v}}\right)^{+} - \left(\hat{\mathbf{v}} + \mathcal{H}_{\Gamma_d}\tilde{\mathbf{v}}\right)^{-} = \hbar\,\tilde{\mathbf{v}} \quad ; \quad \hbar = [\![\mathcal{H}]\!] \tag{3}$$

where, for the symmetric step function, $\hbar = 2$ .Considering that $\nabla\mathcal{H}(\phi) = \mathcal{H}'\nabla\phi = \hbar\,\delta_{\Gamma_d}\nabla\phi$, the velocity gradient of the discontinuous motion (1) can be expressed as

$$\nabla^s\mathbf{v} = \nabla^s\hat{\mathbf{v}} + \mathcal{H}_{\Gamma_d}\nabla^s\tilde{\mathbf{v}} + \delta_{\Gamma_d}(\hbar\tilde{\mathbf{v}}\otimes\mathbf{n})^s \tag{4}$$

where $\mathbf{n} = \nabla\phi$ is the normal to the interface.

2.1 Space discretization for XFEM strategy

Within the XFEM strategy, a discontinuous field can be incorporated by introducing an enrichment function and additional degrees of freedoms. Thus, the discontinuous motion (1) can be approximated by

$$\mathbf{v}^h(\mathbf{x},t) = \hat{\mathbf{v}}^h(\mathbf{x},t) + \mathcal{H}_{\Gamma_d}\tilde{\mathbf{v}}^h(\mathbf{x},t) = \hat{\mathbf{N}}(\mathbf{x})\dot{\hat{\mathbf{d}}}(t) + \mathcal{H}_{\Gamma_d}\tilde{\mathbf{N}}(\mathbf{x})\dot{\tilde{\mathbf{d}}}(t) = \mathbf{N}(\mathbf{x})\dot{\bar{\mathbf{d}}}(t) \tag{5}$$

where, $\hat{\mathbf{N}}$ and $\tilde{\mathbf{N}}$ are standard finite element shape functions that may have different orders of approximation (Bordas & Legay, 2005) and $\hat{\mathbf{d}}$ and $\tilde{\mathbf{d}}$ are standard and enriched degrees of freedom, respectively. In order to obtain a better representation of the enriched approximation and to avoid the use of blending elements, a shifted form of approximation (5) can be introduced (Bordas & Legay, 2005)

$$\mathbf{v}^h(\mathbf{x},t) = \hat{\mathbf{N}}(\mathbf{x})\dot{\hat{\mathbf{d}}}(t) + \tilde{\mathbf{N}}(\mathbf{x})\boldsymbol{\Psi}(\mathbf{x})\dot{\tilde{\mathbf{d}}}(t) = \mathbf{N}(\mathbf{x})\dot{\bar{\mathbf{d}}}(t) \tag{6}$$

Here, $\boldsymbol{\Psi}(\mathbf{x})$ is the shifted form of the step function which is defined as

$$\boldsymbol{\Psi}(\mathbf{x}) = \begin{bmatrix} \mathcal{H}(\phi) - \mathcal{H}(\phi_1) & 0 & \dots & 0 \\ 0 & \mathcal{H}(\phi) - \mathcal{H}(\phi_2) & \dots & 0 \\ \vdots & \vdots & \ddots & \vdots \\ 0 & 0 & \dots & \mathcal{H}(\phi) - \mathcal{H}(\phi_n) \end{bmatrix} \tag{7}$$

and n is the number of interpolation functions. Note that the crack opening $\dot{\mathbf{g}}^h(\mathbf{x},t)$ can be expressed as

$$\dot{\mathbf{g}}^h(\mathbf{x},t) = [\![\mathbf{v}^h(\mathbf{x},t)]\!] = [\![\hat{\mathbf{N}}(\mathbf{x})]\!]\dot{\hat{\mathbf{d}}}(t) + [\![\tilde{\mathbf{N}}(\mathbf{x})\boldsymbol{\Psi}(\mathbf{x})]\!]\dot{\tilde{\mathbf{d}}}(t) = \hbar\,\tilde{\mathbf{N}}(\mathbf{x})\dot{\tilde{\mathbf{d}}}(t) \tag{8}$$

The latter representation makes use of the relation $[\![\boldsymbol{\Psi}(\mathbf{x})]\!] = (\mathcal{H}^{+} - \mathcal{H}^{-})\mathbf{I} = \hbar\,\mathbf{I}$, where $\mathbf{I}$ is the identity matrix.

2.2 The approach based on the volume averaging

Integrating the velocity gradient (4) over a representative elementary volume (REV), which includes the discontinuity interface, one obtains

$$\begin{aligned} \int_{\Delta v}\nabla^s\mathbf{v}\,dv &= \int_{\Delta v}\nabla^s\hat{\mathbf{v}}\,dv + \int_{\Delta v}\mathcal{H}_{\Gamma_d}\nabla^s\tilde{\mathbf{v}}\,dv + \int_{\Delta v}\delta_{\Gamma_d}(\hbar\tilde{\mathbf{v}}\otimes\mathbf{n})^s\,dv \\ &= \int_{\Delta v}\nabla^s\hat{\mathbf{v}}\,dv + \int_{\Delta v}\mathcal{H}_{\Gamma_d}\nabla^s\tilde{\mathbf{v}}\,dv + \int_{\Delta a}(\hbar\tilde{\mathbf{v}}\otimes\mathbf{n})^s\,da \end{aligned} \tag{9}$$

where Δv is the volume of REV and Δa is the area of the discontinuity inside the REV. Assuming that the variations of the integrands in (9) are small, one has

$$\Delta v\,\nabla^s\mathbf{v} = \Delta v\,\nabla^s\hat{\mathbf{v}} + (\Delta v^{+} - \Delta v^{-})\nabla^s\tilde{\mathbf{v}} + \Delta a(\hbar\tilde{\mathbf{v}}\otimes\mathbf{n})^s \tag{10}$$

Defining now $\chi = \Delta a / \Delta v$ and $\kappa = (\Delta v^{+} - \Delta v^{-}) / (\hbar \Delta v)$, as well as $\dot{\mathbf{g}} = \hbar \tilde{\mathbf{v}}$, one obtains

$$\dot{\boldsymbol{\varepsilon}} = \dot{\bar{\boldsymbol{\varepsilon}}} + \dot{\tilde{\boldsymbol{\varepsilon}}} \quad \text{where} \quad \begin{aligned} \dot{\boldsymbol{\varepsilon}} &= \nabla^s \mathbf{v} \\ \dot{\bar{\boldsymbol{\varepsilon}}} &= \nabla^s \hat{\mathbf{v}} + \kappa \nabla^s \dot{\mathbf{g}} \\ \dot{\tilde{\boldsymbol{\varepsilon}}} &= \chi (\dot{\mathbf{g}} \otimes \mathbf{n})^s \end{aligned} \tag{11}$$

which is identical to the strain decomposition introduced by Pietruszczak (1999). Note that the representation (11) may be simplified by assuming that the discontinuity divides the element into to approximately equal volumes, in which case there is $\kappa \to 0$. In (11), $\dot{\bar{\boldsymbol{\varepsilon}}}$ represents the deformation in the intact material while $\dot{\tilde{\boldsymbol{\varepsilon}}}$ is the strain rate due to deformation along the interface averaged over REV. In general, $\dot{\bar{\boldsymbol{\varepsilon}}}$ may include both elastic and plastic deformations in the intact material. Now, using the additivity postulate and following the standard plasticity procedure, the stress rate in the intact material $\dot{\boldsymbol{\sigma}}_{\Omega}$ can be defined as

$$\dot{\boldsymbol{\sigma}}_{\Omega} = \mathbb{D} : \dot{\bar{\boldsymbol{\varepsilon}}} = \mathbb{D} : (\dot{\boldsymbol{\varepsilon}} - \dot{\tilde{\boldsymbol{\varepsilon}}}) \tag{12}$$

where $\mathbb{D}$ is the fourth order stiffness operator. The stress vector in the intact material must be continuous along the interface, i.e. $\mathbf{n} \cdot \dot{\boldsymbol{\sigma}}_{\Omega} = \mathbf{n} \cdot \dot{\boldsymbol{\sigma}}_{\Gamma}$. Imposing this constraint and writing the constitutive relation for the interface as $\dot{\boldsymbol{\sigma}}_{\Gamma} \cdot \mathbf{n} = \dot{\mathbf{t}} = \mathbf{K} \cdot \dot{\mathbf{g}}$, one obtains

$$\mathbf{n} \cdot \mathbb{D} : \dot{\bar{\boldsymbol{\varepsilon}}} = \mathbf{K} \cdot \dot{\mathbf{g}} \qquad \text{where} \qquad \mathbf{K} = \mathbf{R} \cdot \mathbf{K}^{*} \cdot \mathbf{R}^{T} \tag{13}$$

In eq.(13), $\mathbf{K}$ is the stiffness operator for the interfacial material in the global coordinate system, while $\mathbf{K}^{*}$ defines the same operator relative to the local system along the interface. Using eq.(13), together with (11) and (12), one obtains

$$\dot{\mathbf{g}} = \mathbf{n} \cdot \mathbb{E} : \mathbb{D} : \dot{\boldsymbol{\varepsilon}} \quad \text{where} \quad \mathbb{E} = \mathbf{n} \otimes \left(\mathbf{K} + \chi \, \mathbf{n} \cdot \mathbb{D} \cdot \mathbf{n} \right)^{-1} \otimes \mathbf{n} \tag{14}$$

Now, substituting relation (14) into the constitutive equation (12), yields

$$\dot{\boldsymbol{\sigma}}_{\Omega} = \mathbb{D}_T : \dot{\boldsymbol{\varepsilon}} \qquad \text{where} \qquad \mathbb{D}_T = \mathbb{D} - \chi \; \mathbb{D} : \mathbb{E} : \mathbb{D} \tag{15}$$

Note that using the matrix notation, relations (11), (14) and (15) can be expressed as

$$\{\dot{\boldsymbol{\varepsilon}}\} = \{\dot{\bar{\boldsymbol{\varepsilon}}}\} + \{\dot{\tilde{\boldsymbol{\varepsilon}}}\} \quad \text{where} \quad \begin{aligned} \{\dot{\boldsymbol{\varepsilon}}\} &= [\mathbf{L}]\{\mathbf{v}\} \\ \{\dot{\bar{\boldsymbol{\varepsilon}}}\} &= [\mathbf{L}]\{\hat{\mathbf{v}} + \kappa \dot{\mathbf{g}}\} \\ \{\dot{\tilde{\boldsymbol{\varepsilon}}}\} &= \chi [\mathbf{N}]\{\dot{\mathbf{g}}\} \end{aligned}$$

$$\{\dot{\mathbf{g}}\} = [\bar{\mathbf{K}}]^{-1}[\mathbf{n}]^T[\mathbb{D}]\{\dot{\boldsymbol{\varepsilon}}\} \quad \text{where} \quad [\bar{\mathbf{K}}] = [\mathbf{K}] + \chi [\mathbf{n}]^T[\mathbb{D}][\mathbf{n}] \tag{16}$$

$$\{\dot{\boldsymbol{\sigma}}_{\Omega}\} = [\mathbb{D}_T]\{\dot{\boldsymbol{\varepsilon}}\} \quad \text{where} \quad \begin{aligned} [\mathbb{E}] &= [\mathbf{n}][\bar{\mathbf{K}}]^{-1}[\mathbf{n}]^T \\ [\mathbb{D}_T] &= [\mathbb{D}] - \chi [\mathbb{D}][\mathbb{E}][\mathbb{D}] \end{aligned}$$

where, $\left\{\nabla^s \bullet\right\} = \left[\mathbf{L}\right]\{\bullet\}$ and

$$[\mathbf{n}] = \begin{bmatrix} n_1 & 0 & 0 \\ 0 & n_2 & 0 \\ 0 & 0 & n_3 \\ n_2 & n_1 & 0 \\ n_3 & 0 & n_1 \\ 0 & n_3 & n_2 \end{bmatrix}; \qquad [\mathbf{L}] = \begin{bmatrix} \frac{\partial}{\partial x} & 0 & 0 \\ 0 & \frac{\partial}{\partial y} & 0 \\ 0 & 0 & \frac{\partial}{\partial z} \\ \frac{\partial}{\partial y} & \frac{\partial}{\partial x} & 0 \\ \frac{\partial}{\partial z} & 0 & \frac{\partial}{\partial x} \\ 0 & \frac{\partial}{\partial z} & \frac{\partial}{\partial y} \end{bmatrix} \tag{17}$$

The above defined constitutive relations are identical to those given in the article by Pietruszczak (1999).

2.3 Implicit integration of the constitutive relation

Using the formulation above, the residual form of the governing equations at time $t + \Delta t$ can be expressed as

$$\begin{aligned} \mathbf{r}^k &= \boldsymbol{\sigma}_\Omega^k - \left[\boldsymbol{\sigma}_\Omega^t + \mathbb{D} : \Delta\boldsymbol{\varepsilon} - \chi\, \mathbb{D} : \Delta\mathbf{g}^k \otimes \mathbf{n} \right] \\ \mathbf{s}^k &= \mathbf{n} \cdot \boldsymbol{\sigma}_\Omega^k - \mathbf{t}^k \end{aligned} \tag{18}$$

Expanding these residuals, using Taylor expansion, yields

$$\begin{aligned} \mathbf{r}^k + \frac{\partial \mathbf{r}^k}{\partial \boldsymbol{\sigma}_\Omega} : \delta\boldsymbol{\sigma}_\Omega^k + \frac{\partial \mathbf{r}^k}{\partial \mathbf{g}} \cdot \delta\mathbf{g}^k = 0 \\ \mathbf{s}^k + \frac{\partial \mathbf{s}^k}{\partial \boldsymbol{\sigma}_\Omega} : \delta\boldsymbol{\sigma}_\Omega^k + \frac{\partial \mathbf{s}^k}{\partial \mathbf{g}} \cdot \delta\mathbf{g}^k = 0 \end{aligned} \tag{19}$$

Equations (19) can also be expressed as

$$\begin{aligned} \mathbf{r}^k + \delta\boldsymbol{\sigma}_\Omega^k + \chi\, \mathbb{D} : \delta\mathbf{g}^k \otimes \mathbf{n} = 0 \\ \mathbf{s}^k + \mathbf{n} \cdot \delta\boldsymbol{\sigma}_\Omega^k - \mathbf{K}^k \cdot \delta\mathbf{g}^k = 0 \end{aligned} \tag{20}$$

Solving the above set for $\delta\boldsymbol{\sigma}_\Omega^k$ and $\delta\mathbf{g}^k$, one obtains

$$\begin{aligned} \delta\mathbf{g}^k &= \left(\mathbf{K}^k + \chi\, \mathbf{n} \cdot \mathbb{D} \cdot \mathbf{n} \right)^{-1} \cdot \left(\mathbf{s}^k - \mathbf{n} \cdot \mathbf{r}^k \right) \\ \delta\boldsymbol{\sigma}_\Omega^k &= -\left(\mathbf{r}^k + \chi\, \mathbb{D} : \delta\mathbf{g}^k \otimes \mathbf{n} \right) \end{aligned} \tag{21}$$

and

$$\begin{aligned} \Delta\mathbf{g}^{k+1} &= \Delta\mathbf{g}^k + \delta\mathbf{g}^k \\ \Delta\boldsymbol{\sigma}_\Omega^{k+1} &= \Delta\boldsymbol{\sigma}_\Omega^k + \delta\boldsymbol{\sigma}_\Omega^k \end{aligned} \tag{22}$$

Writing the constitutive relation in an incremental form, the tangential stiffness operator can be defined as

$$\Delta\boldsymbol{\sigma} = \mathbb{D}_T : \Delta\boldsymbol{\varepsilon}; \qquad \mathbb{D}_T = \mathbb{D} - \chi\, \mathbb{D} : \mathbb{E} : \mathbb{D} \tag{23}$$

The above representation completes the implicit integration scheme for the constitutive model as described in sub-section (*ii*).

3 DESCRIPTION OF CRACK INITIATION AND ITS PROPAGATION

The crack initiation is defined by a simple tensile strength criterion and the subsequent behavior incorporates strain softening. The propagating crack is traced by using the level set approach (see section *3.2*) for both methodologies, i.e. XFEM and EnVA.

3.1 The approach based on the volume averaging

In order to describe the mechanical characteristics of the interface, a simple damage model with strain-softening is employed. Within this framework, the maximum tensile strength of the material is defined as

$$\mathcal{F}_t(g_n) = \begin{cases} F_t & g_n \le \delta_c \\ F_t e^{\frac{-F_t}{G_f}(g_n - \delta_c)} & g_n > \delta_c \end{cases} \tag{24}$$

where, δ_c is the critical separation for imposing the contact condition in a penalty approach, F_t is the initial tensile strength of the material, and $\mathcal{F}_t(g_n)$ is the tensile strength at separation g_n. The failure function is written as

$$f(t_n, g_n) = t_n - \mathcal{F}_t(g_n) \tag{25}$$

For an active loading process involving $f(t_n, g_n) = 0$, the components of the traction vector can be expressed as

$$\begin{aligned} t_n &= F_t \exp\left(-\frac{F_t}{G_f}(g_n - \delta_c) \right) \\ t_{t_i} &= d\, K_t g_{t_i} = \frac{\mathcal{F}_t}{F_t} K_t g_{t_i} \end{aligned} \tag{26}$$

where $d = \mathcal{F}_t / F_t$ is the damage parameter and K_t is the shear stiffness of the interfacial material. In order to define the tangential stiffness operator, the incremental form of eq. (26) can be written as

$$\begin{aligned} \dot{t}_n &= k_{11}\dot{g}_n = \left\{ -\tfrac{F_t^2}{G_f} \exp\left(-\tfrac{F_t}{G_f}(g_n - \delta_c) \right) \right\} \dot{g}_n \\ \dot{t}_{t_i} &= k_{i1}\dot{g}_n + k_{i2}\dot{g}_{t_i} = \left\{ -\tfrac{F_t}{G_f} \exp\left(-\tfrac{F_t}{G_f}(g_n - \delta_c) \right) K_t g_{t_i} \right\} \dot{g}_n + \left\{ d\, K_t \right\} \dot{g}_{t_i}, \qquad i = 1, 2 \end{aligned} \tag{27}$$

Thus, the constitutive relation for the interfacial material, referred to the local coordinate system along the crack, can be expressed in the rate form

$$\dot{\mathbf{t}}^* = \mathbf{K}^* \cdot \dot{\mathbf{g}}^* \quad \text{where} \quad \mathbf{K}^* = \begin{bmatrix} k_{11} & 0 & 0 \\ k_{21} & k_{22} & 0 \\ k_{31} & 0 & k_{33} \end{bmatrix} \tag{28}$$

where $\mathbf{K}^*$ is the stiffness operator and its components are defined viz. eq. (27).

3.2 The strategy for tracing the crack propagation in both XFEM and EnVA approaches

As proposed in previous studies (cf. Stolarska et al., 2001; Sukumar et al., 2001)), the geometry of crack propagation is captured using a methodology known as the level set

method. Based on this approach, the moving interface $\Gamma_d(t)$ can be defined as the zero level set of a function $\phi(\mathbf{x},t)$, i.e.,

$$\begin{aligned} &\Gamma_d(t) = \{\mathbf{x} \mid \phi(\mathbf{x},t) = 0\} \\ &\phi(\mathbf{x},t) = \text{sign}\{\mathbf{n}_\Gamma \cdot (\mathbf{x} - \mathbf{x}_\Gamma)\} \ \min\|\mathbf{x} - \mathbf{x}_\Gamma\| \end{aligned} \tag{29}$$

where $\mathbf{n}_\Gamma$ is a normal to the direction of propagation, $\mathbf{x}$ is an arbitrary point in Ω, and $\mathbf{x}_\Gamma$ is the point located on the interface at the minimum distance from $\mathbf{x}$.

For two dimensional XFEM simulations, as performed in this study, the interface is defined as a one dimensional polygon of line segments passing through elements in which a crack has formed. Hence, for a node that is common for two adjacent enriched elements, the level set function can be defined as the minimum distance from this node to the respective line segments associated with these elements. For each element, the values of the level-set function at Gauss points can be determined from nodal values using FEM interpolation functions, i.e. $\phi = \sum N_i \bar{\phi}_i$.

In the case of volume averaging procedure, the same approach is used for tracing the propagating crack. By analogy to XFEM, the crack is introduced at the element level and the characteristic dimension χ is evaluated based on the geometry of the element and that of the propagating crack. Consequently, at all Gauss points associated with this element the constitutive relation employing the volume averaging is used. Given the similarity of this procedure to the general methodology for tracing the interface adopted in XFEM, the results obtained from these two approaches are very similar. Also, the strain-softening response is numerically very stable.

Based on the maximum tensile strength criterion, the direction of the propagation can be defined as being orthogonal to the direction of the maximum normal tensile stress. For the propagating crack, the information extracted from the tip element can be inaccurate, particularly when no tip enrichment is introduced. Although, this may not have a significant effect on the load-displacement response of the structure, it remains important in terms of local accuracy, i.e. tracing the direction of the propagating crack. In order to deal with this problem, the direction of the propagation is found based on defining an average direction associated with adjacent Gauss points at which the criterion for crack formation has been met. The search includes the so-called candidate elements that are in the neighborhood of the tip element, as illustrated in Fig.1

It should be noted that, compared to the enhanced volume averaging approach, modeling of crack propagation using XFEM faces some additional difficulties. Initially, the crack location and the propagation pattern are unknown. Thus, the location of the enriched elements is unknown and, as a result, the enrichments must be introduced *a priori* within the region where crack may potentially initiate and propagate. This increases the total number of DOFs and thus requires more computational effort. In addition, a special strategy is needed for performing integration within the enriched elements, such as sub-triangulation, which also affect the computational efficiency. An associated difficulty here involves the need for the data transfer (in terms of stress/strain and the state variables) between standard and partitioned elements. Finally, there is also an inherent difficulty in dealing with additional degrees of freedom in nodes that have not yet been activated.

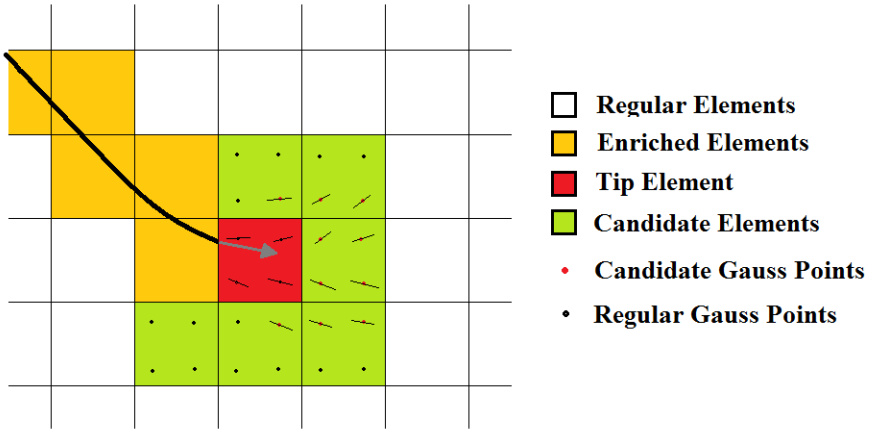

Figure 1. Tracing of the direction of crack propagation

4 NUMERICAL SIMULATIONS

In this section some numerical examples are provided that deal with both XFEM and EnVA methodologies for describing the initiation and propagation of damage in brittle materials. For both cases, the level set method is used for tracing the crack propagation.

The first example given here involves a simply supported concrete beam subjected to an increasing vertical displacement applied in the middle of the span, Fig.2. The geometry is taken from the paper of Moës & Belytschko (2002), and the material properties are assumed as follows

$$E=36.5\times10^{3}\ \text{MPa};\quad \nu=0.1;\quad F_t=3.19\,\text{MPa};\quad G_f=0.05\ \text{N/mm};\quad \delta_c=1\times10^{-4}\ \text{mm}$$

The key results of the analysis are presented in Fig.3. The figure on the left shows the damage pattern. The failure process involves development of tensile cracks near the middle of the span and subsequent propagation of a dominant vertical crack in the center of the beam. The load-displacement (δ) response becomes unstable after reaching the peak (see the figure on the right-hand side). It is evident that the solution based on XFEM is virtually identical to that obtained using the EnVA methodology. This applies to both, the progressive evolution of damage as well as the global deformation characteristics.

The second example involves a simulation of a shear-tension test of Nooru-Mohamed (1992). The geometry of the problem is provided in Fig.4. The loading process consisted of two different stages. First, a horizontal displacement of $\delta_x=0.005\,\text{mm}$ was applied on the vertical faces under $\delta_y=0$. At this stage, referred to as the shearing stage, no cracks were formed. Then, a vertical displacement δ_y was imposed along the horizontal faces, while the δ_x remained constant. This stage resulted in onset and propagation of tensile cracks. The analysis was carried out assuming the following material properties

$$E=29\times10^{3}\,\text{MPa};\quad \nu=0.15;\quad F_t=3.67\,\text{MPa};\quad G_f=0.05\,\text{N/mm};\quad \delta_c=1\times10^{-3}\,\text{mm}$$

The key results of the analysis are presented in Figs.5-7. Fig.5 shows the cracking pattern superimposed on the contours of horizontal (u) and vertical (v) displacements. In this case, two macrockraks form, at the notches, and propagate towards the center of the specimen. The fracture pattern is identical for both XFEM and EnVA approaches.

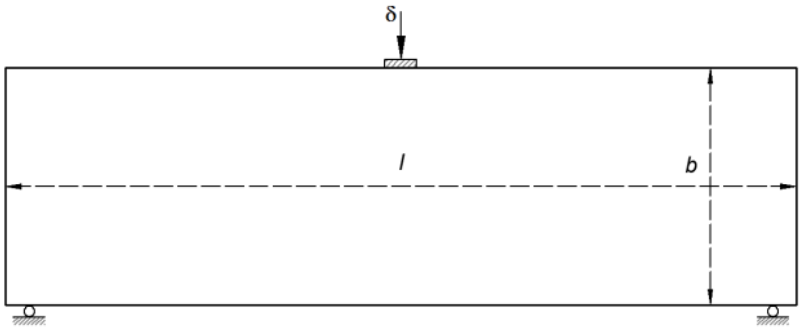

Figure 2. Three point bending test on a concrete beam, $l = 600\,\text{mm}$ & b=150 mm

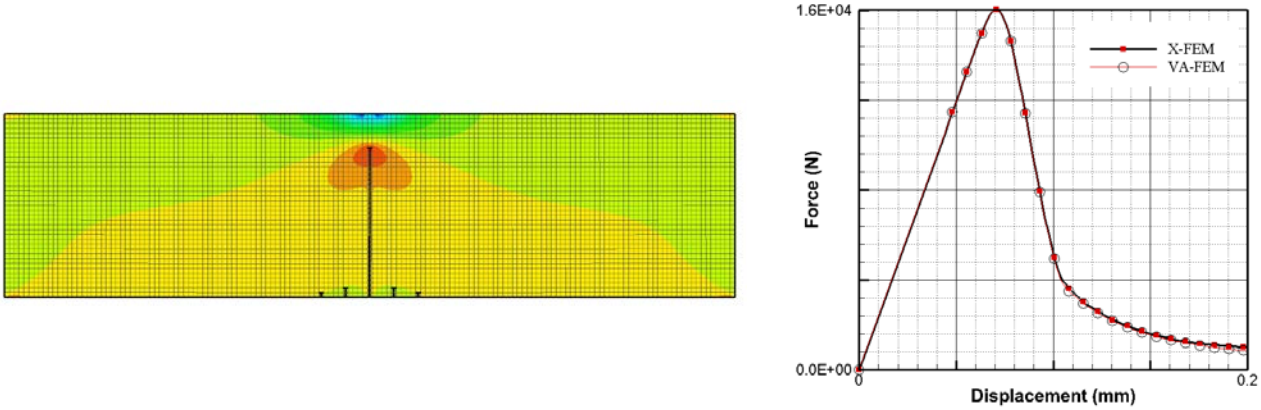

Figure 3. Left: Left: cracking pattern and the contours of the maximum normal tensile stress intensity; Right: resultant external force vs corresponding vertical displacement

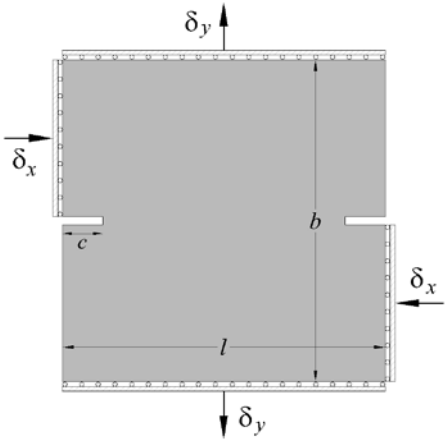

Figure 4. Mixed-mode test of Nooru-Mohamed ($l = b = 200\text{mm}, c = 25\text{mm}, t = 50\text{mm}$)

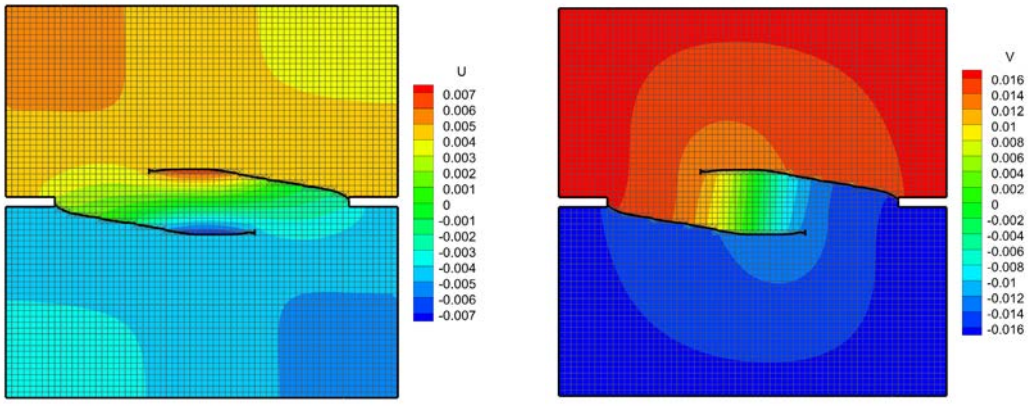

Figure 5. Cracking pattern superimposed on the contours of horizontal (u) and vertical (v) displacements (mm)

Figs.6-7 present the evolution of the components of the reaction force against imposed boundary displacements as well as the crack tip opening. Again, as the vertical displacement is imposed, the response becomes unstable. The global characteristics are very similar for both methodologies, i.e. XFEM and EnVA. This is particularly evident both prior to as well as at the early stages of the onset of global instability, which is of primary interest for practical engineering purposes. At very advanced stages of deformation, the enhanced volume averaging method predicts less crack opening than the XFEM.

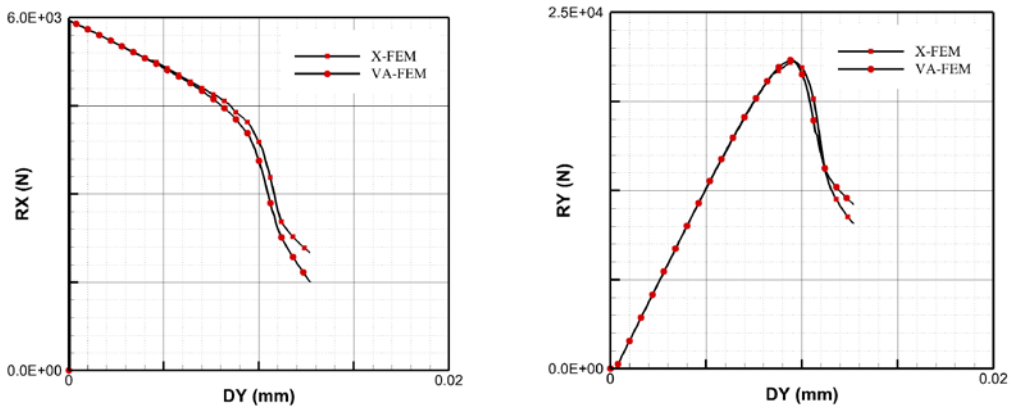

Figure 6. Reaction components (RX and RY) vs. vertical displacement (DY)

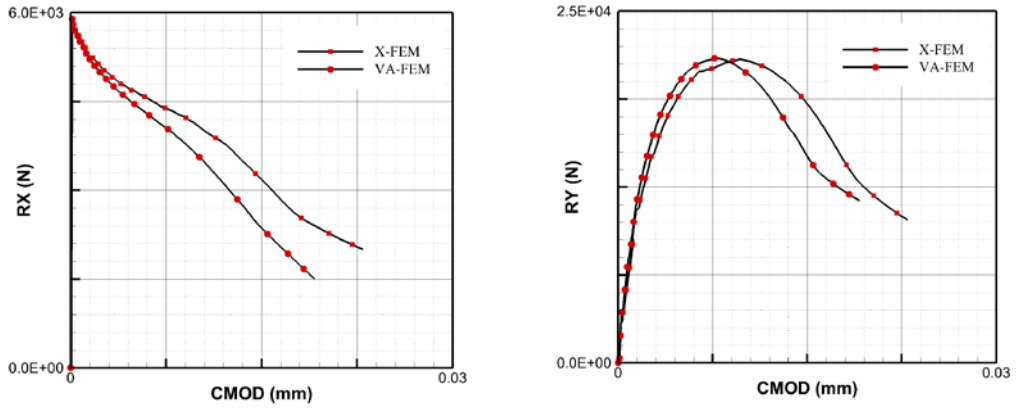

Figure 7. Reaction force vs. CMOD (crack mouth opening displacement)

5 FINAL REMARKS

In this paper, the problem of damage propagation in brittle materials was investigated using two conceptually different frameworks. The first one was based on Extended FEM approach that incorporates a discontinuous displacement field using the partition of unity property of the FE shape functions (Belytschko & Black, 1999). The second methodology involved standard FEM framework that incorporates a constitutive relation obtained through volume averaging in the neighborhood of the embedded discontinuity (Pietruszczak & Mroz, 1981). The latter approach has been enhanced by employing the level set method, similar to that used in XFEM, in order to capture a discrete nature of the crack propagation process. Two boundary value problems were examined that involved propagation of cohesive macrocracks leading to the loss of stability at the macroscale. It was demonstrated that the both methodologies, i.e. XFEM and EnVA (Enhanced Volume Averaging), yield virtually identical results for modeling of brittle fracture propagation. This gives the advantage to averaging scheme as it requires significantly less computational effort in the numerical implementation.

REFERENCES

Aifantis, E.C. (1984), "On the microstructural origin of certain inelastic models". Journ. Eng. Materials & Technology, 106(4), 326–330.

Belytschko, T. & Black, T. (1999), "Elastic crack growth in finite elements with minimal remeshing". Int. J. Numer. Meth. Eng., 45(5), 601–620.

Belytschko, T. et al. (1996), "Meshless methods: an overview and recent developments". Comp. Meth. Appl. Mech. & Eng., 139(1), 3–47.

Belytschko, T., Fish, J. & Engelmann, B.E. (1988), "A finite element with embedded localization zones". Comp. Meth. Appl. Mech. & Eng., 70(1), 59–89.

Bordas, S. & Legay, A. (2005), X-FEM Mini-Course, Ecole Polytehnique Federale de Lausanne.

Borst, R. de (1991), "Simulation of strain localization: a reappraisal of the cosserat continuum". Eng. Comp., 8(4), 317–332.

de Borst, R. & Mühlhaus, H.B. (1992), "Gradient-dependent plasticity: Formulation and algorithmic aspects". Int. J. Numer. Meth. Engng, 35(3), 521–539.

Dolbow, J., Moës, N. & Belytschko, T. (2001), "An extended finite element method for modeling crack growth with frictional contact". Comp. Meth. Appl. Mech. & Eng., 190(51), 6825–6846.

Dolbow, J., Moës, N. & Belytschko, T. (2000), "Discontinuous enrichment in finite elements with a partition of unity method". Finite Elements in Analysis and Design, 36(3), 235–260.

Fleming, M. et al. (1997), "Enriched element-free Galerkin methods for crack tip fields". Int. J. Numer. Meth. Engng, 40(8), 1483–1504.

Khoei, A.R., Moallemi, S. & Haghighat, E. (2012), "Thermo-hydro-mechanical modeling of impermeable discontinuity in saturated porous media with X–FEM technique". Eng. Fracture Mech., 96, 701-723.

Melenk, J.M. and Babuška, I. (1996), "The partition of unity finite element method: basic theory and applications". Comp. Meth. Appl. Mech. & Eng., 139(1), 289–314.

Moës, N. & Belytschko, T. (2002), "Extended finite element method for cohesive crack growth". Eng. Fracture Mech., 69(7), 813–833.

Moës, N., Dolbow, J. & Belytschko, T. (1999), "A finite element method for crack growth without remeshing". Int. J. Numer. Meth. Engng, 46(1), 131–150.

Mühlhaus, H.B. & Alfantis, E.C. (1991), "A variational principle for gradient plasticity". Int. J. Solids & Structures, 28(7), 845–857.

Mühlhaus, H.B. & Vardoulakis, I. (1987), "The thickness of shear bands in granular materials". Géotechnique, 37(3), 271–283.

Nooru-Mohamed, M.B. (1992), Mixed-mode fracture of concrete: an experimental approach. PhD thesis, Delft Univ. of Technology, Delft.

Pietruszczak, S. (1995), "Undrained response of granular soil involving localized deformation". Journ. Eng. Mech., 121(12), 1292–1297.

Pietruszczak, S. (1999), "On homogeneous and localized deformation in water-infiltrated soils". Int. J. Damage Mech., 8(3), 233–253.

Pietruszczak, S. & Gdela, K. (2010), "Inelastic analysis of fracture propagation in distal radius". Journ. Appl. Mech., 77(1), 1-11.

Pietruszczak, S. & Mroz, Z. (1981), "Finite element analysis of deformation of strain-softening materials". Int. J. Numer. Meth. Engng, 17(3), 327–334.

Pijaudier-Cabot, G. & Bažant, Z.P. (1987), "Nonlocal damage theory". Journ. Eng. Mech., 113(10), 1512–1533.

Réthoré, J., Borst, R. de & Abellan, M.-A. (2007), "A two-scale approach for fluid flow in fractured porous media". Int. J. Numer. Meth. Engng, 71(7), 780–800.

Schellekens, J. & de Borst, R. (1993), "On the numerical integration of interface elements". Int. J. Numer. Meth. Engng, 36(1), 43–66.

Shieh-Beygi, B. & Pietruszczak, S. (2008), "Numerical analysis of structural masonry: mesoscale approach". Computers & Structures, 86(21-22), 1958–1973.

Stolarska, M., Chopp, D.L., Moës, N. & Belytschko, T. (2001), "Modelling crack growth by level sets in the extended finite element method". Int. J. Numer. Meth. Engng, 51(8), 943–960.

Sukumar, N., Chopp, D.L., Moës, N. & Belytschko, T. (2001), "Modeling holes and inclusions by level sets in the extended finite-element method". Comp. Meth. Appl. Mech. & Eng., 190(46), 6183–6200.

Wells, G.N. & Sluys, L.J. (2001), "A new method for modelling cohesive cracks using finite elements". Int. J. Numer. Meth. Engng, 50(12), 2667–2682.

Wells, G.N. & Sluys, L.J. (2000), "Three-dimensional embedded discontinuity model for brittle fracture". Int. J. Solids & Structures, 38(5), 897–913.

Xu, G. & Pietruszczak, S. (1997), "Numerical analysis of concrete fracture based on a homogenization technique". Computers & Structures, 63(3), 497–509.

SHEAR BANDING IN CROSS-ANISOTROPIC SAND DEPOSITS LOADED THROUGH FLEXIBLE AND STIFF BOUNDARIES

P.V. Lade
Department of Civil Engineering, The Catholic University of America, Washington, D.C. 20064, USA

E. Van Dyck
Schnabel Services, Inc., Glen Ellen, VA 23059, USA

N.M. Rodriguez
Dept. of the Navy, Naval Sea Systems Command 05C, Washington Navy Yard, Washington, DC 20376, USA

ABSTRACT: *Torsion shear experiments were performed on large hollow cylinder specimens of Fine Nevada sand with principal stress directions relative to vertical, α, varying from 0° to 90° and with the intermediate principal stress, σ_2, varying from σ_3 to σ_1 as indicated by $b = (\sigma_2-\sigma_3)/(\sigma_1-\sigma_3)$. The Fine Nevada sand was deposited by dry pluviation producing a sand fabric with horizontal bedding planes and cross-anisotropic characteristics. The stress conditions were achieved by varying the pressures inside and outside the hollow cylinder specimen relative to the shear stress and the vertical deviator stress according to a pre-calculated pattern. All stresses and all strains were determined. The soil behavior was determined for a pattern of combinations of α varying with increments of 22.5° from 0° to 90° and b varying with increments of 0.25 from 0.0 to 1.0. The friction angles varied considerably with α and b, thus indicating the importance of the intermediate principal stress and the principal stress directions relative to the horizontal bedding planes. In addition to the conventional shear bands, "canyon" shear bands due to the cross-anisotropy were observed in the σ_1-direction at high b-values. The strength variation was influenced by the flexibility of the boundaries in certain regions.*

1 INTRODUCTION

Torsion shear tests performed on hollow cylinder specimens represents the better way of investigating the effects of principal stress directions on the behavior of the soil, because in these tests the bedding planes remain horizontal and the principal stresses are rotated relative to the bedding planes. In addition, there are only minor effects of imposed non-uniform stress conditions if the specimen is sufficiently tall (Lade 1981). In these experiments the direction of the major principal stress may be changed relative to the cross-anisotropic deposit created by dry pluviation. This allows studying the direction of shear banding relative to the direction of the major principal stress in cross-anisotropic sand deposits.

The details of the preparation of the hollow cylinder specimens, the experimental procedures and program and the strength results of these torsion shear tests on dense, Fine Nevada sand were presented by Lade et al. (2013), and the directions of shear banding are presented and analyzed here.

2. FRICTION ANGLES AND DILATION ANGLES

The strength results of the torsion shear tests on dense Fine Nevada sand were presented and discussed by Lade et al. (2013). All friction angles obtained from the torsion shear tests have been corrected to correspond to the target void ratio of $e = 0.53$ using the formula $e \cdot \tan\varphi = \text{const}$. The experiments were performed with the same mean normal stress and the friction angles are not sensitive to small variations in σ_m, so they can be taken to correspond to the same value of $I_1 = 3 \cdot \sigma_m = 300$ kPa. Fig. 1 shows the three-dimensional variation in friction angle for $0 \leq b \leq 1$ and for $0° \leq \alpha \leq 90°$. The surface presented in this diagram was modeled by a failure criterion for cross-anisotropic soils presented by Rodriguez and Lade (2013).

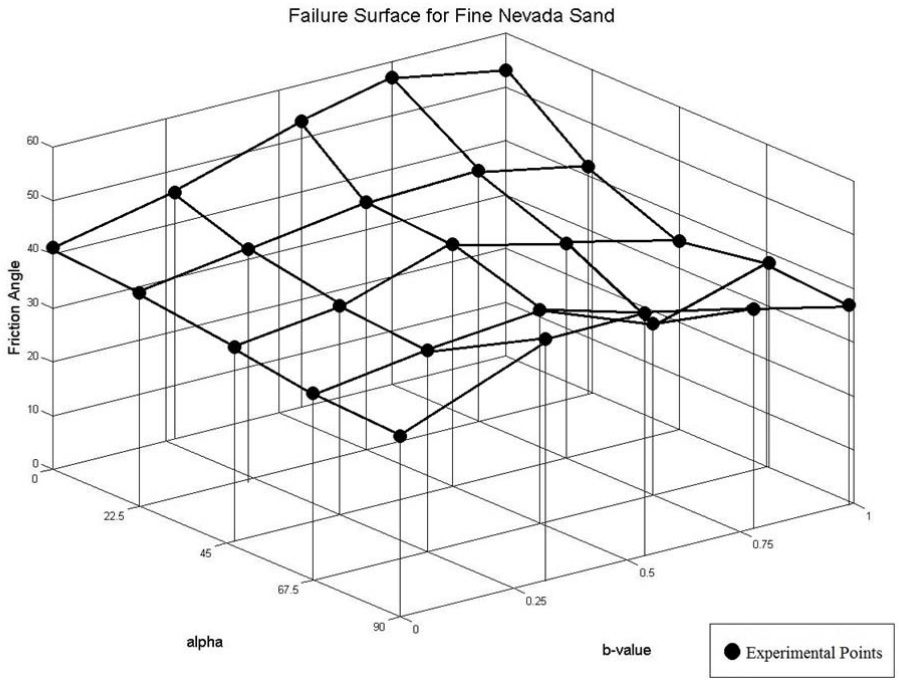

Fig. 1. Composite α-b-φ diagram of three-dimensional failure surface for dense Fine Nevada sand.

The angles of dilation, ψ, were determined for each experiment on the basis of the slope of the volume change relation at or near failure. Fig. 2 shows the variation of ψ with b and α. This variation is the basis for the cross-anisotropic soil behavior. It is seen that the angle of dilation is typically around 10° for most of the test conditions, and it is highest in the far corner ($\psi = 28°$) where $\alpha = 0°$ and $b = 1.0$. It then varies in a smooth fashion with α and b. Just like the variation of the friction angle, the lowest values of the dilation angle are exhibited at an inclination of the major principal stress of $\alpha = 67.5°$, which corresponds approximately to sliding in the direction of least resistance.

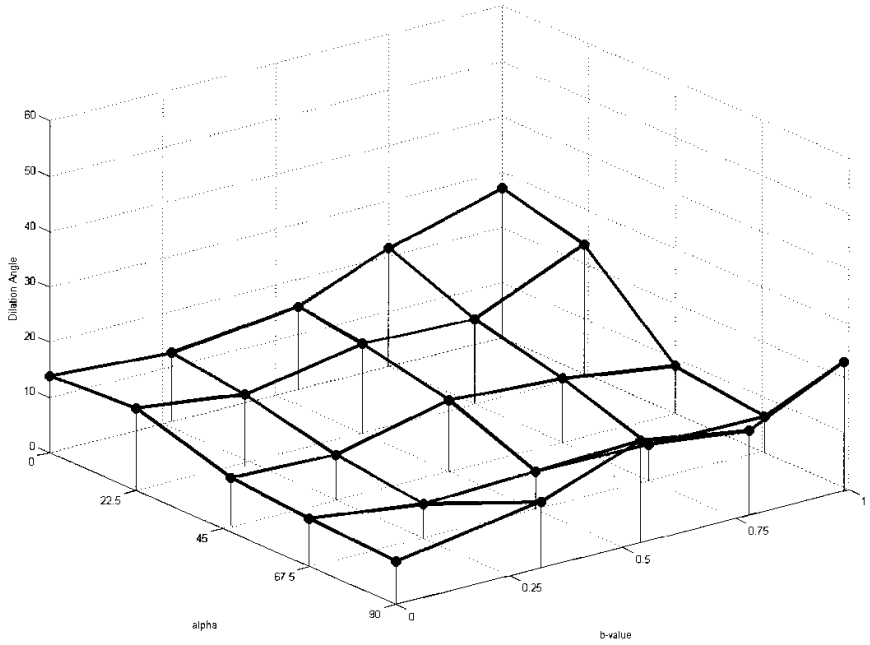

Fig. 2. Composite α-b-ψ diagram of three-dimensional failure surface for dense Fine Nevada sand.

3. SHEAR BANDS IN CROSS-ANISOTROPIC SAND

The shear band directions were measured at the end of each test while the specimen was held on a vacuum. The grid drawn on the surface of the specimens prior to shearing helped in measuring the angles of the shear bands correctly. Usually, the shear bands are oriented such that the normal to the shear band is contained in the wall (Lade et al. 2008), as indicated on the photographs in Fig. 3. All but the experiments at b = 0.0 have resulted in peak failure caused by development of shear bands. The experiments with b = 0.0 exhibited smooth peak failure with shear banding developing in the softening regime.

Fig. 3. Hollow cylinder specimens after failure under stress conditions with (a) b = 0.25 and α = 22.5°, (b) b = 0.25 and α = 90°, and (c) b = 0.59 and α = 90°.

Figs. 4-6 show comparisons of measured shear band directions, β, relative to the σ_1-directions with the theoretical directions calculated according to the classical equations for the torsion shear tests. The shear band inclinations typically vary within 5 to 10 degrees along its length around the hollow cylinder specimens due to small variations in void ratio. Thus, complete consistency between the experimental results and the theoretically predicted inclinations could not be expected. The large β-ranges of 14° shown for α = 67.5° and b=0.75

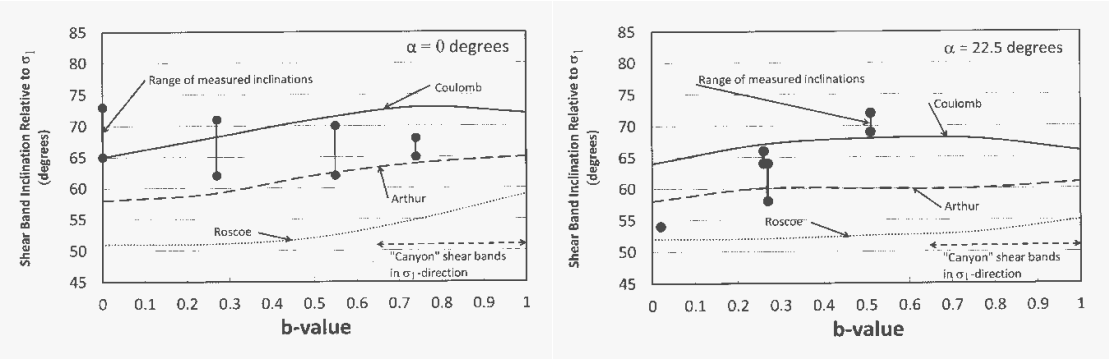

Fig. 4. Shear band inclination relative to σ_1-direction for torsion shear tests on Fine Nevada sand with α = 0° and α = 22.5°.

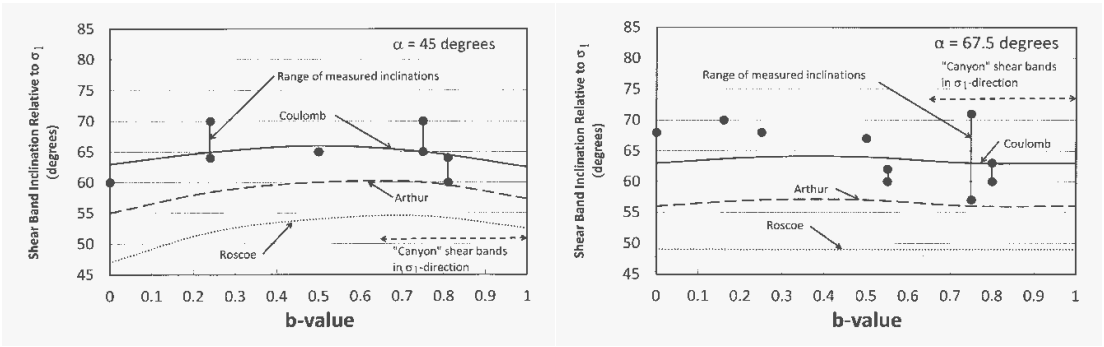

Fig. 5. Shear band inclination relative to σ_1-direction for torsion shear tests on Fine Nevada sand with α = 45° and α = 67.5°.

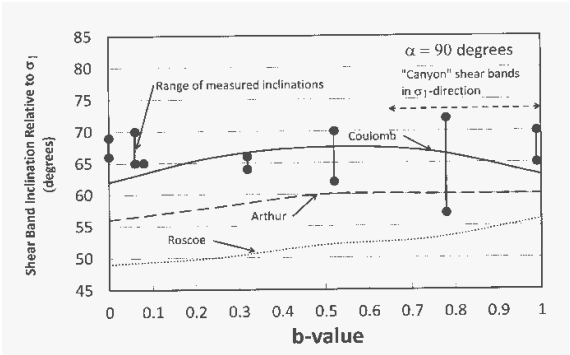

Fig. 6. Shear band inclination relative to σ_1-direction for torsion shear tests on Fine Nevada sand with α = 90°.

and 15° for $\alpha = 90°$ and $b = 0.78$ (in Figs. 5 and 6) each corresponds to measurements on two hollow cylinder specimens and thus includes the scatter from one to another specimen. Within this scatter, the diagrams in Figs. 4-6 show that the shear band inclination in the torsion shear tests appear to fit best with the variation proposed by the Coulomb direction, i.e. the shear bands tend to form angles of $\pm(45° - \varphi/2)$ with the direction of the major principal stress, σ_1, or $\beta = \pm(45° + \varphi/2)$ with the σ_1-plane, as shown in the diagrams. This is true for all α-angles and low to medium b-values. Examples are shown in Fig. 3.

However, for high b-values the hollow cylinder specimens showed more than one type of shear band pattern. This is due to the cross-anisotropic character of the sand deposit for which the shear strength is lower in the horizontal direction than in the vertical direction. Thus, shear failure would occur in the horizontal direction for high b-values, even though the intermediate principal stress, σ_2, was smaller than the major principal stress, σ_1. This has previously been observed in true triaxial tests on cross-anisotropic sand deposits (Abelev and Lade 2003). For b-values greater than 0.6-0.7, horizontal shear failures were observed in all the hollow cylinder specimens, independent of the inclination, α, of the major principal stress. For these higher b-values the Coulomb inclination of the shear bands were observed in all experiments, but additional shear banding occurred across the wall thickness of the specimen.

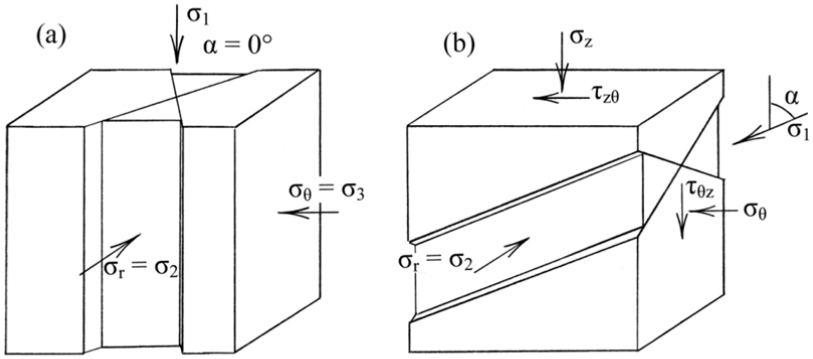

Fig. 7. Sketches of shear band pattern in torsion shear tests on cross-anisotropic sand deposits tested at high b-values.

Fig. 7 shows two sketches of the shear band pattern for high b-values. In both cases the shear bands appear to be inclined in the σ_1-direction, but this is because extension type conditions occur with the minor principal stress perpendicular to the indicated σ_1-directions. The shear bands therefore appear as wide "canyons" on the outside surface of the hollow cylinder specimen rather than as relatively thin shear bands of the type shown in Fig. 3. Calculation of the correct ε_2-strains in the area of the "canyon" is not possible (and they would not correspond to uniform strains), but once the shear banding initiates in the horizontal direction, the shear strength in the σ_1-direction is also affected and it begins to decline.

Examples of shear banding at high b-values are shown in Figs. 8 and 9. The photos correspond to α-values close to 0°, 22.5° and 45° (Fig. 8) and 67.5° and 90° (Fig. 9). The actual values of α and b at the time of shear banding are given in the legends of the photos. It is clear that the reason these shear bands occur is that the surrounding flexible rubber membrane allows non-uniform deformations to occur. If the membranes had been rigid rather than flexible, then shear banding would have been impeded or prevented until higher stresses could have been reached. This was discussed by Lade and Wang (2012 a and b).

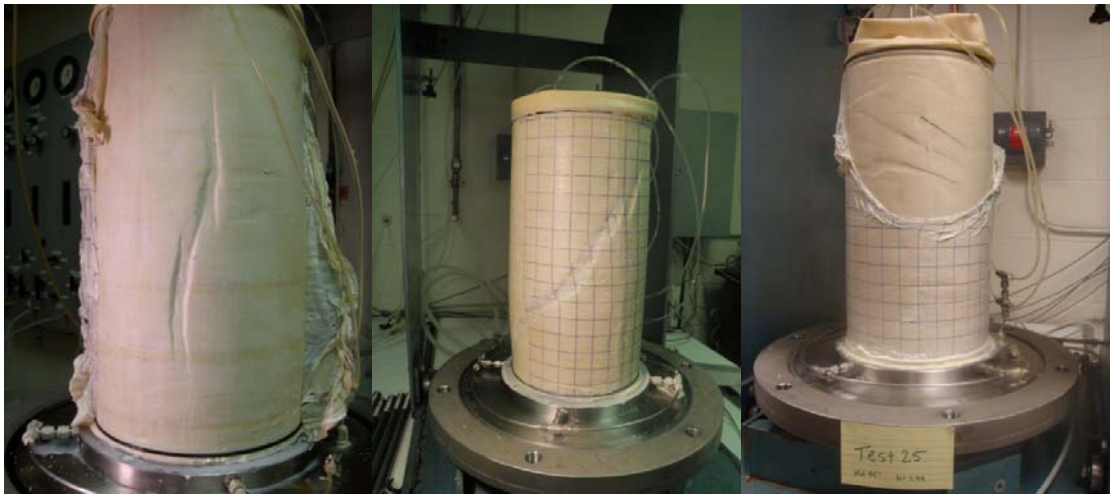

Fig. 8. Shear band pattern in hollow cylinder specimen with (a) $\alpha = 0°$ and $b = 0.79$, (b) $\alpha = 22.5°$ and $b = 0.76$, and (c) $\alpha = 45°$ and $b = 0.75$. In two cases, the outer layer of the membrane has been peeled off to clearly show the width and the sides of the "canyon" shear band oriented vertically in the direction of the major principal stress.

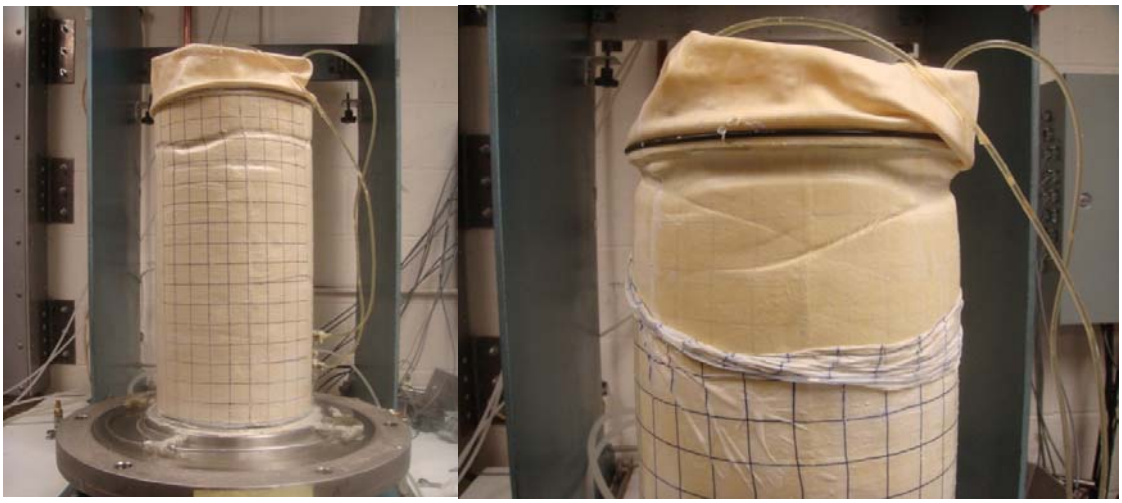

Fig. 9. Shear band pattern in hollow cylinder specimen with (a) $\alpha = 67.5°$ and $b = 1.0$ and (b) $\alpha = 90°$ and $b = 1.0$. In the latter case, the outer layer of the membrane has been peeled off to clearly show the width and the sides of the "canyon" shear band oriented horizontally in the direction of the major principal stress.

4. EFFECTS OF STIFF AND FLEXIBLE BOUNDARIES

It is clear from the observed cross-anisotropic behavior in torsion shear tests and the explanations given above that the stiffness of the boundaries surrounding the specimen is important for experiments with high *b*-values in which failure can occur in the direction of the intermediate principal stress. This is partly because the strength is lower in the horizontal directions than in the vertical direction, but additional effects are at play.

In triaxial extension tests (b = 1.0) performed on cross-anisotropic sand specimens with stiff and flexible boundaries, Lade and Wang (2012 a and b) found that in specimens with stiff boundaries the specimens showed greater moduli, even at very small strains, lower strain-to-failure and greater strengths than in specimens with flexible boundaries. While the flexible membranes allow development of non-uniform strains, shear bands and necking, this is not sufficient to account for the large differences in strengths obtained from the two types of boundaries. In comparison, the stiff, smooth boundaries impose uniform strains at the boundaries. The behavior of the granular material inside the specimen may be affected by the movement of the individual grains in the specimen, which in turn is affected by the boundary conditions: Lade and Wang (2012 a and b) speculated that force chains may be supported and become stronger under enforced uniform strains, while they may be allowed to buckle under flexible boundary conditions, thus producing a weaker response to similar external stresses. Such different behavior has been observed in DEM calculations of assemblies of spherical grains, as presented by Tordesillas et al. (2008, 2011), Peters and Walizer (2013) and Cooper (2011). Whether this ultimately explains the observed behavior is unknown at this time.

5. CONCLUSIONS

Research is being performed to contribute to establishment of more realistic modeling of soil behavior. Real soils, as they occur in-situ, clearly behave cross-anisotropically with a vertical axis of rotational symmetry. This real behavior is most often assumed to be isotropic, and a number of observed behavior patterns are therefore not predicted correctly. Torsion shear experiments have been performed on hollow cylinder specimens to determine the variation of the friction angle of dense, Fine Nevada sand deposited with cross-anisotropic fabric. Systematic variations of the intermediate princial stress and directions of the major principal stress have been employed in these experiments. For a constant value of $b = (\sigma_2 - \sigma_3)/(\sigma_1 - \sigma_3)$, the friction angle is found to vary by 4° at b = 0.0 to 16° at b = 0.75 as the σ_1-direction changes from vertical to horizontal. However, for a given void ratio and all b- and α-values, the friction angle varies by as much as 22°. Based on these results and previous knowledge it appears that six different factors play important roles in determining the friction angle for a given sand: (1) initial void ratio, (2) minor principal stress, (3) intermediate principal stress, (4) cross-anisotropic fabric, (5) orientation of the major principal stress relative to the bedding planes, and (6) occurrence of shear bands.

The effects of stiff and flexible boundaries on the behavior of the cross-anisotropic granular material is pronounced at high b-values, where shear banding can occur across the hollow cylinder wall because the strength is lower in the horizontal directions than in the vertical direction, but additional effects appear to be at play. Lade and Wang (2012 a and b) found that in true triaxial specimens with stiff boundaries the specimens showed greater moduli, even at very small strains, lower strain-to-failure and greater strengths than in specimens with flexible boundaries. These effects are likely to be present in the horizontal directions of the hollow cylinder specimens, where the flexible membranes allow non-uniform strains, early shear banding and lower strengths.

Acknowledgements
The research presented here was performed with support from the National Science Foundation under Grant No. CMMI-0757827. Grateful appreciation is expressed for this support.

REFERENCES

Abelev, A.V., and Lade, P.V. (2003): Effects of Cross-Anisotropy on Three Dimensional Behavior of Sand. I: Stress-Strain Behavior and Shear Banding, *Journal of Engineering Mechanics*, ASCE, 129(2), 160-166.

Cooper, W.L. (2011): Communication of Stresses by Chains of Grains in High-Speed Particulate Media Impacts, *SEM XI International Congress & Exposition on Experimental and Applied Mechanics*, Uncasville, CT, June 13-17.

Lade, P.V. (1981): Torsion Shear Apparatus for Soil Testing," *Laboratory Shear Strength of Soil, ASTM STP 740*, R.N. Yong and F.C. Townsend, Eds., ASTM, 145-163.

Lade, P.V., Nam, J. and Hong, W.P. (2008) Shear Banding and Cross-Anisotropic Behavior Observed in Laboratory Sand Tests with Stress Rotation, *Canadian Geotechnical Journal,* 45(1), 74-84.

Lade, P.V., Rodriguez, N.M., and Van Dyck, E.J. (2013): Effects of Principal Stress Directions on 3D Failure Conditions in Cross-Anisotropic Sand, *Journal of Geotechnical and Geoenvironmental Engineering*, ASCE (accepted).

Lade, P.V. and Wang, Q. (2012a): Method for Uniform Strain Extension Tests on Sand, *Geotechnical Testing Journal*, 35(4), 607-617.

Lade, P.V. and Wang, Q. (2012b): Effects of Stiff and Flexible Boundary Conditions in Triaxial Extension Tests on Cross-Anisotropic Sand Behavior, *Geotechnical Testing Journal*, ASTM, 35(5), 715-727.

Peters, J.F., and Walizer, L.E. (2013): Patterned Non-Affine Motion in Granular Media, *Journal of Engineering Mechanics*, ASCE. DOI 10.1061/(ASCE)EM.1943-7889.0000556

Rodriguez, N.M., and Lade, P.V. (2013): Effects of Principal Stress Directions and Mean Normal Stress on Failure Criterion for Cross-Anisotropic Sand, *Journal of Engineering Mechanics*, ASCE (accepted).

Tordesillas, A., Multhuswamy, M., and Walsh, S.D.C. (2008): Mesoscale Measures of Nonaffine Deformation in Dense Granular Assemblies, *Journal of Engineering Mechanics*, ASCE, 134(12), 1095-1113.

Tordesillas, A., Lin, Q., Zhang, J., Behringer, R.P., and Shi, J. (2011): Structural Stability and Jamming of Self-organized Cluster Conformations in Dense Granular Materials," *Journal of Mechanics and Physics of Solids*, 59, 265-296.

NUMERICAL MODELING OF STRAIN LOCALIZATION AND INTERFACE DAMAGE IN CEMENT BASED MATERIALS

C.F. Jin
Laboratory of Mechanics of Lille, University of Lille, Villeneuve d'Ascq, France

Q.Z. Zhu
Laboratory of Multiscale Modeling and Simulation, University of Paris East, Marne La Valle, France

S. Pietruszczak
Department of Civil Engineering, McMaster University, Hamilton, Ont., Canada

J.F. Shao
Laboratory of Mechanics of Lille, University of Lille, Villeneuve d'Ascq, France

ABSTRACT: *In this paper, the interface damage and strain localization within the matrix are modeled for a representative volume element (RVE) of concrete. The development of displacement discontinuities along interfaces is simulated using the Extended Finite Element Method (XFEM). A new cohesive interface damage model is proposed to describe the progressive debonding process. For modeling the strain localization (microcrack growth) in cement paste matrix, a homogenized elastic-crack model is used. The macroscopic behavior is controlled by the properties of the matrix and the plastic deformation along the crack. Various numerical simulations at the level of REV are performed. The obtained results clearly show that the failure in concrete is initiated by interface debonding and is followed by crack propagation (strain localization) inside the cement paste. The interface damage plays an important role in the macroscopic failure process of concrete. The failure mode depends on the spatial distribution and size of aggregates.*

1 INTRODUCTION

Mechanical behavior of cement-based materials is inherently related to the evolution of their microstructure. At the mesoscale, concrete can be viewed as a two-phase composite comprising the cement paste matrix and aggregates. The failure process in concrete is, in general, affected by two coupled phenomena, i.e. debonding along the matrix-aggregate interfaces and strain localization (microcrack initiation and propagation) inside the cement paste. A number of laboratory investigations have shown that the macroscopic properties of concrete, in particular the mechanical strength, are strongly affected by the size and distribution of aggregates under both mechanical loading and desiccation process (Bisschop and van Mier, 2002; Grassl et al., 2010; Rougelot et al., 2010; Szczesniak et al., 2013). At the same time, the strain localization associated with the initiation and propagation of microcracks within the cement paste is the precursor of macroscopic failure in concrete. In the classical approaches of continuum mechanics, the analysis of strain localization is generally based on the bifurcation theory or stability analysis (Rudnicki and Rice, 1975; Vardoulakis, 1981; de Borst, 1991). The strain localization leads to strain softening and spurious mesh dependency in the context of a numerical analysis. Various methods have been proposed in order to define a localization limiter and then regularize the ill-posed boundary value problems. Those include, for instance, non-local models (Pijaudier-Cabot and Bazant, 1987; Rodriguez-Ferran et al., 2004), higher order gradient approaches (de Borst and MuhIhaus, 1992), as well as the Cosserat continuum theory (de Borst and Sluys, 1991). However, in these models, the displacement discontinuity related to the inception of cracks is

not properly accounted for. For the strain localization analysis in brittle-plastic materials like concrete, a simple homogenization/volume averaging procedure has been developed in the article by Pietruszczak and Mroz (1981) and later modified in Pietruszczak (1999). Within this approach, the macroscopic response in the presence of localization is controlled by the local behaviour of the crack, perceived as an interface, and that of the continuum in the neighbourhood of the crack. This approach is adopted in the present work for the description of strain localization in the cement paste. For the purpose of modelling of interfaces between aggregates and cement paste, interface elements can be employed within the classical finite element method. It is generally necessary to use a suitable remeshing technique for modelling progressive debonding. Alternatively, the Extended Finite Element Method (XFEM) may be used as it provides an efficient way for modelling both the interfaces and the crack propagation without resorting to remeshing (Belystshko and Black, 1999; Möes et al., 1999; Zhu et al., 2011). In the present work, the XFEM methodology is applied for modelling the behaviour along interfaces between aggregates and cement paste. First, a damage model is proposed for describing the progressive interface debonding. Later, the results of numerical simulations are presented. These results clearly show that the failure process in concrete is initiated by interface debonding and followed by crack propagation (strain localization) inside the cement paste. The interface damage plays an important role in the macroscopic failure process of concrete. The failure mode depends on the spatial distribution and the size of aggregates.

2 ELASTIC DAMAGE MODEL FOR INTERFACE

The contact between aggregate and cement paste is considered as an elastic interface along which the displacements are discontinuous. Consider two solid bodies, Ω^+ and Ω^-, separated by a smooth interface S, with the unit normal vector $\mathbf{n}$ directed from Ω^- to Ω^+. The displacement jump across the interface is denoted by $[\![\boldsymbol{\xi}]\!]$ and the traction on the interface is $\mathbf{T}$. The elastic behavior along the interface is defined as

$$\mathbf{T} = \mathbf{C}_S \cdot [\![\boldsymbol{\xi}]\!] \tag{1}$$

where $\mathbf{C}_S$ is the second order elastic stiffness tensor, taken to be positive definite. For an isotropic and linearly elastic material, there is

$$\mathbf{C}_S = \lambda_s \mathbf{n} \otimes \mathbf{n} + \mu_s (1 - \mathbf{n} \otimes \mathbf{n}) \tag{2}$$

where λ_s and μ_s are the normal and tangential moduli of the interface.

Based on experimental investigations (Rougelot et al., 2010), the interfaces in concrete exhibit progressive damage and debonding under mechanical stresses and desiccation process. In order to describe this damage process, two scalar variables are introduced below and are expressed as functions of displacement discontinuities, i.e.

$$\omega_n = 1 - e^{-b_1 \varepsilon_n} \quad ; \quad \omega_t = 1 - e^{-b_2 \varepsilon_t} \tag{3}$$

$$\varepsilon_n = <[\![\boldsymbol{\xi}]\!]_n> / h \quad ; \quad \varepsilon_t = [\![\boldsymbol{\xi}]\!]_t / h \tag{4}$$

Here, b_1 and b_2 are material parameters controlling the damage kinetics in the normal and tangential direction, respectively, while h is a characteristic length representing the thickness

of interface. The elastic moduli of interface are affected by the damage process and are expressed as

$$\lambda_s(\omega_n,\omega_t)=\lambda_{s0}(1-\omega_n)\ ,\quad \mu_s(\omega_n,\omega_t)=\mu_{s0}(1-\omega_n-\omega_t) \tag{5}$$

where λ_{s0} and μ_{s0} are the normal and tangential moduli of the undamaged interface, respectively.

3 XFEM MODELING OF INTERFACE

Consider a representative element (RVE) of concrete occupying a volume Ω with an external boundary S. The RVE is perceived as a multiphase composite, comprising the cement paste (designated as the phase $r=0$) and spherical inclusions (phases $r=1,2,...,n$) as shown in Figure 1.

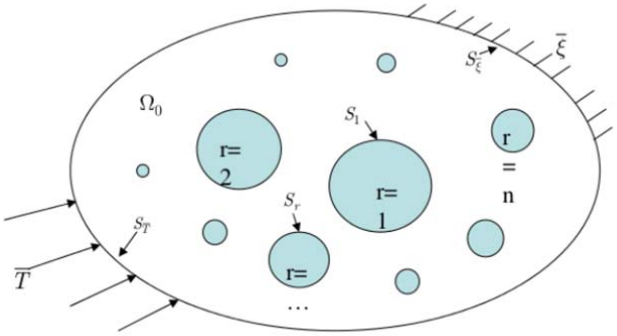

Figure 1: RVE of concrete with imperfect interfaces

Let Ω_r and f_r denote the volume and the volume fraction of each phase and let S_r be the interface between the matrix and the r^{th} type of inclusion. The boundary values problem is governed by the equilibrium equations, constitutive relations and boundary conditions. In the context of finite element modeling, the virtual work theorem is applied to the RVE that leads to the weak formulation of the problem

$$\sum_{r=0}^{n}\int_{\Omega_r}\Delta\boldsymbol{\varepsilon}^r:\mathbb{C}^r:\boldsymbol{\varepsilon}^r d\Omega_r+\sum_{r=1}^{n}\int_{S_r}\Delta[\![\boldsymbol{\xi}]\!]^r\cdot\mathbf{C}_s^r\cdot[\![\boldsymbol{\xi}]\!]^r dS_r=\int_{S_{\bar{T}}}\Delta\boldsymbol{\xi}\cdot\bar{\mathbf{T}}dS_{\bar{T}} \tag{6}$$

Here, $\boldsymbol{\varepsilon}^r$ and $\Delta\boldsymbol{\varepsilon}^r$ denote the strain field and its variation in the r^{th} phase and $\mathbb{C}^r$ is the corresponding tangential stiffness operator. Upon the geometrical discretization and taking into account the displacement discontinuities at the interfaces, the enriched displacement field inside an element Ω^e is given by

$$\tilde{\boldsymbol{\xi}}(\mathbf{x})=\sum_{i=1}^{n_e}N_i(\mathbf{x})\boldsymbol{\xi}_i(\mathbf{x})+\sum_{j=1}^{n_e}M_j(\mathbf{x})\psi_j(\mathbf{x})\mathbf{r}_j \tag{7}$$

where $\psi_j(\mathbf{x})$ are the enriched functions related to interface discontinuities. Over the last few years, various forms of these functions have been proposed. In the present work, we adopt the representation suggested by Zhu et al. (2011), viz.

$$\psi_j(x) = \frac{1}{2}\varphi(\phi_x)(1-\varphi(\phi_x)\varphi(\phi_j)) \tag{8}$$

In eq. (7), n_e is the number of nodes in the standard finite element framework; here, the number of enriched nodes in the relevant element is assumed to be the same as that in the standard finite element. Moreover, $\mathbf{r}_j$ are complementary unknowns associated with the j^{th} enriched node, ϕ_x is the value of the level set function at point $\mathbf{x}$, ϕ_j is the value of level set function at j^{th} node and φ is the commonly defined sign function.

In order to determine the macroscopic response of the RVE, the macroscopic strains are evaluated by taking into account the strain fields inside each constituent phase as well as the displacement discontinuities of interfaces, i.e.

$$\mathbf{E} = \sum_{r=0}^{n} f_r \overline{\boldsymbol{\varepsilon}}^r + \sum_{r=1}^{n} \int_{s_r} \frac{1}{2\Omega} (\llbracket \boldsymbol{\xi} \rrbracket^r \otimes \mathbf{n}^r + \mathbf{n}^r \otimes \llbracket \boldsymbol{\xi} \rrbracket^r) dS_r \tag{9}$$

with

$$\llbracket \boldsymbol{\xi} \rrbracket^r = \boldsymbol{\xi}^0 |_{S_r} - \boldsymbol{\xi}^r |_{S_r} \quad , \quad \overline{\boldsymbol{\varepsilon}}^r = \frac{1}{\Omega_r} \int_{\Omega_r} \boldsymbol{\varepsilon}^r d\Omega_r \tag{10}$$

Similarly, the average stresses for the RVE are given by

$$\boldsymbol{\Sigma} = \sum_{r=0}^{n} f_r \overline{\boldsymbol{\sigma}}^r \quad , \quad \overline{\boldsymbol{\sigma}}^r = \frac{1}{\Omega_r} \int_{\Omega_r} \boldsymbol{\sigma}^r d\Omega_r \tag{11}$$

4 ELASTOPLASTIC MODELING OF CEMENT PASTE

Before the onset of strain localization, the mechanical behavior of cement paste is described by the elastoplastic model proposed by Pietruszczak et al. (1988). Without going into details of the formulation, this model employs a quadratic function of basic stress invariants for defining the yield and failure surfaces, a non-associated flow rule that allows for the description of compaction-dilatancy transition and a hardening law governed by accumulated plastic distortion. In the present work, the strain localization inside the cement paste is checked by using the bifurcation criterion (Rudnicki and Rice, 1975). According to this criterion, the strain localization occurs when the acoustic tensor satisfies the following condition

$$\det(\mathbf{Q}) = 0 \quad , \quad \mathbf{Q} = \mathbf{n} \cdot \mathbb{L} \cdot \mathbf{n} \tag{12}$$

where $\mathbb{L}$ is the tangent elastoplastic stiffness operator and $\mathbf{n}$ denotes the orientation of the localized band.

After the strain localization, the cement paste is described as an elastic body intercepted by a localization band viewed as a volume-less interface (c.f. Shieh-Beygi and Pietruszczak, 2008). The mechanical behavior of interface is described by an elastoplastic model incorporating strain softening that is attributed to the evolution of the tangential component

of velocity discontinuity. The rate form of the elastoplastic constitutive law for the interface is given by

$$\dot{\mathbf{T}} = \mathbf{K}^{ep} \cdot \dot{\mathbf{g}} \tag{13}$$

where $\mathbf{K}^{ep}$ is the tangent stiffness tensor relating the traction rate $\dot{\mathbf{T}}$ to the velocity discontinuity rate $\dot{\mathbf{g}}$. The macroscopic constitutive behavior for the RVE, in the presence of localization, is determined by a simple volumetric averaging procedure (Pietruszczak, 1999). The constitutive relation takes the form

$$\dot{\boldsymbol{\sigma}} = \mathbb{C}^h : \dot{\boldsymbol{\varepsilon}} \quad , \quad \mathbb{C}^h = \mathbb{C} : (\mathbb{J} - \mu \mathbf{n} \otimes (\mathbf{E}^{-1} \otimes \mathbf{n} : \mathbb{C})) \tag{14}$$

$$\mathbf{E} = \mathbf{K}^{ep} + \mu \mathbf{n} \cdot \mathbb{C} \cdot \mathbf{n} \tag{15}$$

Here, $\mathbb{C}$ is the elastic stiffness tensor of the intact material, while $\mathbb{J}$ is a fourth order operator defined as $J_{pqkl} = \delta_{pk}\delta_{ql}$. The parameter μ defines the ratio of the surface area of the localization plane to the volume associated with the averaging domain. Thus, $1/\mu$ has the dimension of length and may be considered as a characteristic length parameter.

5 NUMERICAL SIMULATIONS

In this section, the results of some numerical simulations are presented for the representative volume of concrete.

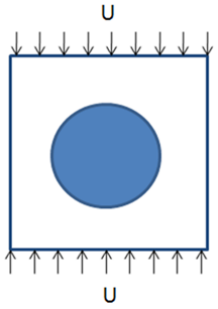

Figure 2: Uniaxial compression of the RVE with a single inclusion (volume fraction of 35%)

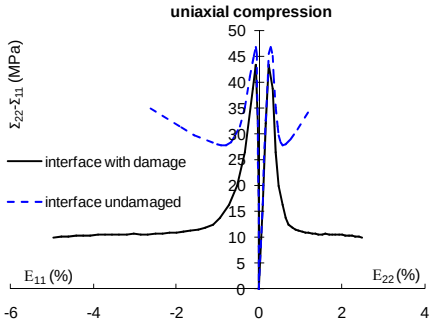

Figure 3: Typical stress-strain curves in uniaxial compression

The first example is concerned with the uniaxial compression of the RVE containing one spherical inclusion, as shown in Figure 2. Two sets of simulations have been carried out; namely, with and without modeling the damage process along the inclusion-matrix interface. Typical stress-strain curves are presented in Figure 3. For the considered loading conditions

(displacement-controlled), a brittle behavior is obtained. In the case without the interface damage, the unstable softening response in the post-peak regime is attributed to the strain localization inside the cement paste. With the interface damage, both the peak stress and residual strength are significantly reduced and the concrete behavior becomes more brittle. Therefore, it seems that the interface damage plays an important role in the mechanical response and failure process of concrete.

In order to study the influence of confining pressure, two other sets of simulations were performed that involved a uniaxial and triaxial compression of the RVE with 8.75% of inclusions. The obtained stress-strain curves are shown in Figure 4. It is evident that, as the confining pressure increases, the peak stress also increases and there is a transition from brittle to ductile behavior, which is consistent with the experimental evidence. Figure 5 shows the deformed meshes of the RVE for the two tests considered. The failure process starts with the interface debonding, which is followed by the strain localization in the cement paste. The failure pattern is influenced by the confining pressure. In the uniaxial compression, there is a single macroscopic crack in the cement paste. In the triaxial compression, one observes multiple cracks in various orientations. This is again in agreement with most of the experimental data.

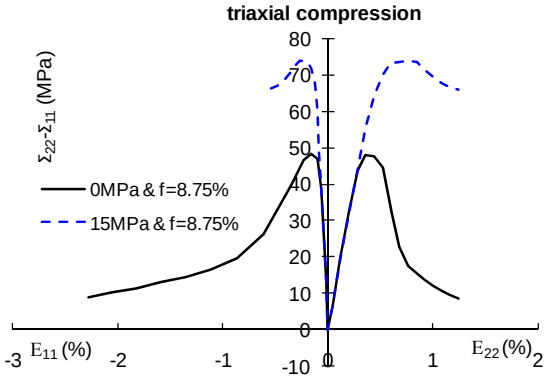

Figure 4: Stress-strain curves in uniaxial and triaxial compression

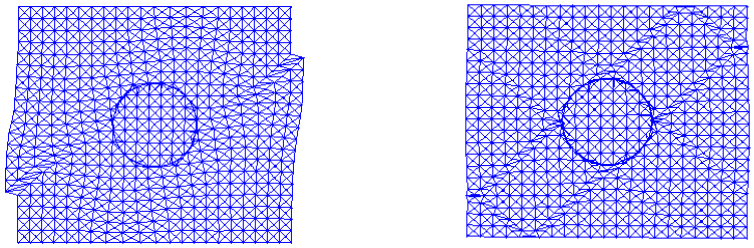

Figure 5: Deformed meshes in uniaxial compression (left) and triaxial compression (right), respectively

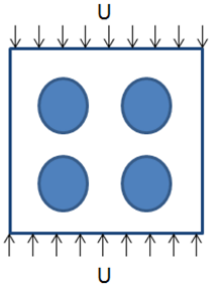

Figure 6: RVE of concrete with four inclusions

Finally, the last example deals with the RVE containing four inclusions, as shown in Figure 6. The volume fraction of inclusions is the same as that for the RVE with a single inclusion. Figure 7 provides a comparison between stress-strain curves obtained for the two RVE's. It can be seen that the macroscopic response of concrete is affected by the inclusion size. In general, the larger the inclusion the smaller the peak stress and the residual strength. This means that the interface damage and strain localization are both facilitated by the presence of large inclusions. Figure 8 shows the deformed mesh for the considered RVE.

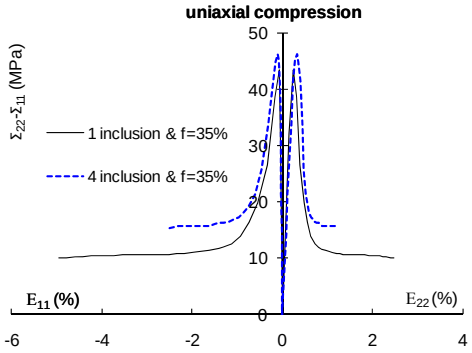

Figure 7: Comparisons of stress-strain curves for two RVE subjected to uniaxial compression

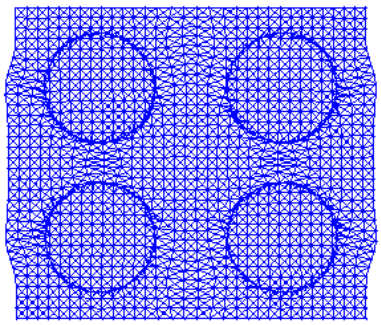

Figure 8: Deformed mesh for uniaxial compression of the RVE with four inclusions

6 FINAL REMARKS

In this work, a numerical analysis of failure process in a typical concrete material has been conducted by taking into account the interface debonding and strain localization in the cement paste. The Extended Finite Element method was used for the description of interface between aggregate and cement paste. A new damage model has been proposed for modeling the progressive debonding process. The onset of strain localization in the cement paste was assessed based on the classical bifurcation theory. A volume averaging in the vicinity of the crack was employed for the description of cement paste behavior in the post localization regime. Various numerical examples have been presented. It was shown that the failure process in concrete is inherently controlled by both the strain localization and interface debonding. The interface damage process may play an important role. The mechanical behavior of concrete is influenced by both the size and the distribution of aggregates. The failure pattern depends on the confining pressure and the microstructure of concrete.

ACKNOWLEDGEMENT

The present work was partially supported by ANDRA (French National Agency of Radioactive Waste Management), which is gratefully acknowledged.

REFERENCES

Belystshko T, Black T. Elastic crack growth in finite elements with minimal remeshing. Int. J. Num. Meth. Eng. 1999; 45(5):601-620

Bisschop J, van Mier JGM. Effect of aggregates on drying shrinkage microcracking in cement-based composites. Materials and Structures 2002:35(8); 453–461

de Borst R. and Sluys L.J. (1991). Localisation in a cosserat continuum under static and dynamic loading conditions. Computer Methods in Applied Mechanics and Enginerring, 805-827.

de Borst R., and MuhIhaus H.B. (1992). Gradient dependent plasticity formulation and algorithmics aspects. Int. J. Num. Meth. Eng, 35:521-539

Grassl P Wong HS, Buenfeld NR. Influence of aggregate size and volume fraction on shrinkage induced micro-cracking of concrete and mortar. Cement and Concrete Research 2010:40(1); 85-93

Möes N, Dolbow J, Belytschko T. Finite element method for crack growth without remeshing. Int. J. Num. Meth. Eng. 1999; 46(1):131-150

Pietruszczak S., Jiang J. and Mirza F.A. (1988). An elastoplastic constitutive model for concrete. Int. J. Solids Struct., 24(7):705-722.

Pietruszczak, S. and Mroz Z (1981). Finite element analysis of deformation of strain softening materials. Int. J. Num. Anal. Meth. Geomech, 17:791-805.

Pietruszczak S. (1999). On homogeneous and localized deformation in water-infiltrated soils. Journal of Damage Mechanics, 8(3):233-253.

Pijaudier-Cabot G. and Bazant Z.P. (1987). Nonlocal damage theory. Journal of Engineering Mechanics, 118(10):1512-1533.

Rodriguez-Ferran A, Morata I, Huerta A. Efficient and reliable non-local damage models. Comput. Methods Appl. Mech. Engng. 2004; 193:3431-3455

Rougelot T, Burlion N, Bernard D, Skoczylas F. About microcracking due to leaching in cementitious composites: X-ray microtomography description and numerical approach. Cement and Concrete Research 2010:40(2); 271-283

Rudnicki J.W. and Rice J.R. (1975). Conditions for the localization of the deformation in pressure sensitive dilatants materials. Journal of Mechanics and Physics of Solids, 23:371-394.

Shieh-Beygi, B, Pietruszczak S. (2008) Numerical analysis of structural masonry: mesoscale approach. Computers & Structures, 86:1958-1973.

Szczesniak M, Rougelot T., Burlion N., Shao J.F. (2012), Compressive strength of cement-based composites: Roles of aggregate diameter and water saturation degree, Cement & Concrete Composites 37 (2013) 249–258

Vardoulakis I. (1981). Bifurcation analysis of the plane rectilinear deformation on dry samples. Int. J. Solids Struct., 17:1085-1101.

Zhu Q.Z., Gu S.T., Yvonnet J., Shao J.F. and He Q.C. (2011) Three-dimensional numerical modeling by XFEM of spring-layer imperfect curved interfaces with applications to linearly elastic composite materials. Int. J. Num. Meth. Eng, 88(4):307-328

THE EFFECT OF RADIAL WALLS ON CPT IN A DEM-BASED VIRTUAL CALIBRATION CHAMBER

M. Arroyo, J. Butlanska & A. Gens
Department of Geotechnical Engineering and Geosciences, UPC, Barcelona, Spain

C. O'Sullivan
Department of Civil Engineering, Imperial College of Science and Technology, London, UK

ABSTRACT: *Radial walls are rigid frictionless boundaries used to diminish the computational cost of CPT simulation in DEM-based calibration chambers. They are introduced because the apparent symmetry of the problem dictates that their presence should have no bearing in the simulation results. It is shown here by means of a dedicated test series that this is not always the case and that, particularly for dense samples, a noticeable increase on cone penetration resistance results from the introduction of radial walls. Further model exploration reveals that close to the cone a larger radial stress is sustained in chambers with radial walls. Force network analysis shows that such stress increase can be traced to the stabilizing effect of radial walls on strong force chains.*

1 INTRODUCTION

Cone penetration tests are one of the basic tools of geotechnical soil characterization. They are particularly valuable for granular soils, where intact sample retrieval is very difficult. Interpretation of CPT test results in sands still relies largely on empirical correlations (Schnaid 2009). These correlations are often developed in calibration chambers (CC), where the soil state and properties can be carefully controlled (Huang & Hsu, 2004). Calibration chambers are relatively large pieces of equipment, and calibration chamber testing is expensive and time-consuming. The idea of complementing the physical tests with virtual equivalents (i.e. numerical models) is attractive. Boundary value problems involving large strain rigid-contact in dilatant materials are difficult to model with continuum-based approaches (Jassim et al. 2011; Bienen et al. 2011). It is therefore worth exploring the potential of alternative approaches such as the discrete element method.

Arroyo et al. (2011) showed that a CPT performed in a virtual calibration chamber (VCC) filled with a discrete analogue of Ticino sand resulted on steady state penetration values that were in close quantitative agreement with predictions based on correlations previously established in physical chambers. DEM-based VCC for CPT have been also presented later by Mc Dowell et al. (2012) and Lin & Wu (2012).

While the advantages of DEM-based VCC testing are clear, a number of areas require further exploration. One of these is the effect of radial walls in the simulation outcomes. Radial rigid walls are introduced in VCC as a simple means by which to exploit the problem cylindrical symmetry to reduce the model size. Radial rigid walls have been often used: Arroyo et al (2011) used full (360° section coverage) chambers, but also half and quarter chambers (180° and 90° section coverage, respectively); McDowell et al. (2012) used

chambers with 90° and 30° section coverage; Lin & Wu (2012) only a chamber with 45° section coverage.

The reasoning behind is that since the problem has an inherent cylindrical symmetry, displacements in the circumferential direction should be purely random and not relevant for the macroscopic outcome. However, it is not clear, for instance, to what extent there is a coupling between the fluctuations of particle motions in different coordinate directions. In fact, several investigators have warned about the effect of rigid wall boundary conditions on the macroscopic outcomes of DEM-based tests. Cui et al. (2007) studying triaxial compression tests noted that radial walls did influence the shear strength measured in the test as well as the shape of the localized failure mode. Marketos & Bolton (2010) showed how the apparent macroscopic stiffness of an oedometric test could be strongly affected by the details of the contact at the boundary top and bottom walls.

Butlanska et al (2009) did already study if the introduction of radial walls affected the homogeneity of the DEM VCC. However their analysis focused mostly on the initial states of the specimens and in the results of medium density samples. Their results are reanalyzed and extended in what follows.

2 NUMERICAL MODEL

2.1 Numerical approach

The DEM PFC3D code (Itasca 2005) was used to perform all numerical simulations in this paper. The model is composed of spherical particles that displace independently of one another and only interact at the contact point. The particles are assumed rigid. The contact law employed is lineal elasto-plastic. The normal and tangential stiffness (k_n and k_s) at any contact are calculated using following scaling rule:

$$\begin{aligned} k_n &= 2K_{eff}\,\frac{D_1 D_2}{D_1+D_2} \\ k_s &= \alpha k_n \end{aligned} \tag{1}$$

where α and K_{eff} are parameters to be calibrated. The interparticle friction (φ_μ) describes the plastic part of the contact law. To speed up model convergence non-viscous damping (δ) was also included.

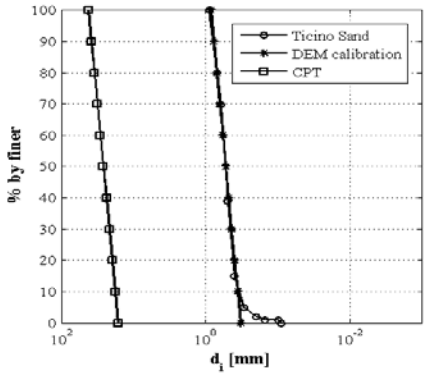

Fig. 1 Grain size curves of Ticino Sand and of the discrete materials used in the simulations.

2.2. Calibration

The discrete material was calibrated to represent the behaviour of Ticino sand. Because Ticino sand is very angular the DEM particles had rotation inhibited. Model parameter calibration was performed on a small sample with 8 mm side and filled with approximately 4700 particles with the grain distribution shown in Fig. 1 (DEM calibration). Material parameters (K_{eff}, α, φ_μ and δ) were determined by trial and error to provide a best fit to a single isotropically compressed drained triaxial test confined at 100 kPa and formed with D_R=75%. The best fit was found for: K_{eff}=300MN, α=0.25, tan(φ_μ)=0.35 and δ=0.05 (Butlanska et al. 2009). The calibrated material is then scaled-up by a factor of 50 (curve CPT in Fig 1) to reduce the number of particles in the calibration chamber models.

2.3. Calibration chamber models

Three different calibration chamber models are used here. A schematic view of the different models and the cone used in the simulation can be seen in Fig. 2. The reference or full chamber model is cylindrical with outer rigid, frictionless walls. The diameter and height of CC are 1.2 m and 0.7 m, respectively. This model was filled with approximately 60000 particles using the radius expansion method. The half and quarter chamber models have the same height and diameter, but their horizontal section is reduced by inserting two frictionless radial walls, aligned at 180° in the first case and 90° in the second. The number of particles is reduced roughly in the same proportion as the section. The cone diameter is 71.2 mm, the tip angle is 60° and both the tip and a friction shaft of 30 cm behind it are perfectly rough (i.e. a cone-particle contact has the same friction as a particle-particle contact).

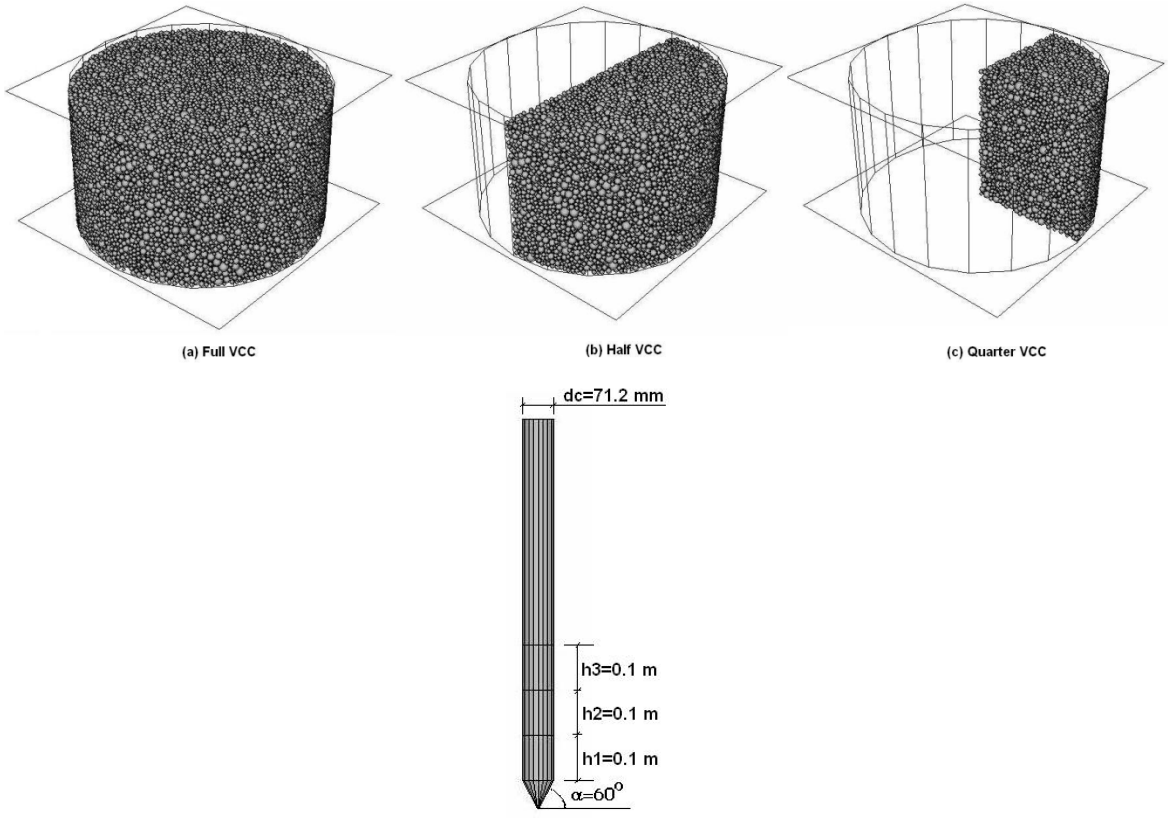

Fig. 2 Calibration chamber models (above) and cone (below)

2.4. Testing program

Six CPT tests are examined here, two for each calibration chamber model (full, half and quarter). Three of them were performed on specimens at a relative density close, but not identical, to 75%, whereas the other three were performed at a relative density close, but not identical, to 90%. All the tests were performed under an isotropic initial stress of 100 kPa. This value is computed at the boundary and maintained constant during the simulation by servo-controlling the displacement of the circumferential wall and the top horizontal boundary. This approach mimics the arrangement of a physical CC when operating under stress-controlled BC1 boundary conditions. The radial walls are immobile throughout the simulation. Details of the initial state of the tests are presented in Table 1. The area reduction factor indicated in the table is a numerical shorthand to designate the full, half and quarter chamber models.

Table 1 Test program

	Model (area reduction factor)	Target RD (%)	Achieved RD (%)
T34	0.25	75.0	72.8
T32	0.5	75.0	76
T16	1	75.0	75.2
T35	0.25	90.0	86.1
T33	0.5	90.0	90.7
T20	1	90.0	90.7

3 MACROSCOPIC RESULTS

As explained elsewhere (Arroyo et al. 2011) the raw penetration curves form the simulations are very noisy because of the large relative size of the scaled discrete material with respect to cone dimensions. However that noise can be filtered out simply by fitting the raw penetration curve with a curvilinear trend:

$$q_{c,trend}(h) = a[1-\exp(-bh)] \tag{2}$$

Where h represents the depth of the cone tip, and the adjustment parameter a can be identified with the cone point resistance. The fitted curves for the six test examined here are shown in Fig. 3. There is some trend, particularly for the test series performed at a higher density, towards higher cone resistances when chamber section is reduced. The effect, however, does not seem very strong. A better observation is achieved if the small but influential differences between the initial densities of the tests are accounted for.

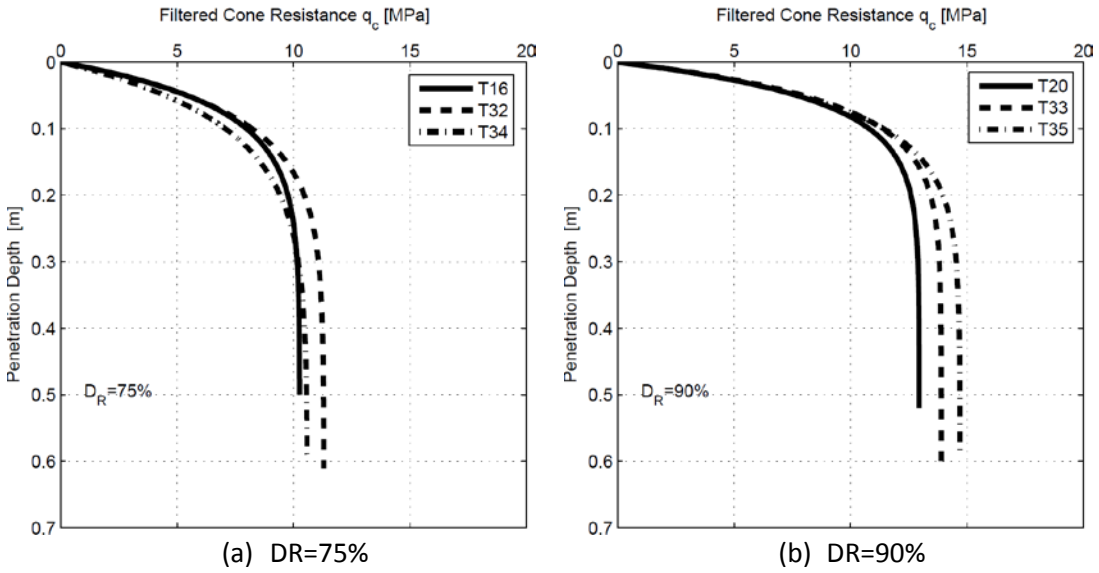

Fig. 3 Filtered penetration curves for all the tests

Indeed, as shown in Arroyo et al (2011) cone resistance measured in DEM simulations like those here analyzed is closely predicted by the following empirical expression by Jamiolkowski et al (2003)

$$q_c = 23.19 C_F \; p_a \left(\frac{p'}{p_a} \right)^{0.56} e^{2.97 D_R} \tag{3}$$

In the expression above p_a is the reference (atmospheric) pressure, C_F a size correction factor dependent on R_D -chamber diameter/cone diameter ratio-, p' the mean initial effective stress in the chamber and D_R the initial relative density.

In the test series analyzed here both R_D and p' are identical for all tests; however there were small variations – see Table 1- in the initially attained D_R. The exponential term in expression (3) is used to correct for these variations and obtain a cone resistance for each test at the initial target density; then all the results thus corrected are normalized by the value obtained for the full VCC. The final outcomes of this procedure are the results illustrated in Fig. 4. There the influence of the reduced section created by the radial rigid walls on the cone penetration value can be identified.

The trend towards increased penetration resistance when the model section is reduced is now clear. It is also more important for the denser specimens, attaining more than a 30% increase over the reference value for the smaller chamber (with 90° section coverage or, equivalently, 0.25 area reduction factor).

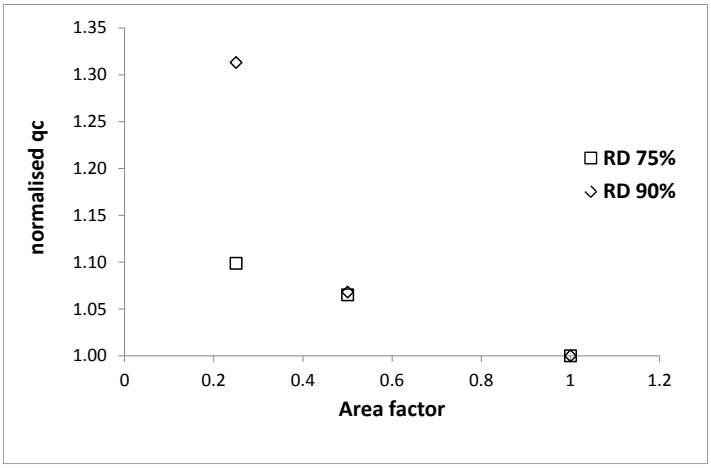

Fig. 4 Cone tip resistance corrected for relative density variation and referred to that of full chamber tests

4 INITIAL STATE

One possible explanation for the higher cone resistance attained in reduced section chambers might be the influence of the radial walls during the chamber filling process. That influence will appear as heterogeneity in the material. Butlanska et al (2009) explored in detail this aspect, using measurement spheres as averaging volumes. They found that there was a small but noticeable effect of the radial walls on the circumferential distribution of porosity in the chamber. Next to the radial walls the porosity was higher (Fig. 5a). This is in contrast with the effect of the outer circumferential wall; when initial porosity is plotted against a radial coordinate it decreases as the wall is approached: this effect is independent of the sectional area of the model (Fig. 5 b).

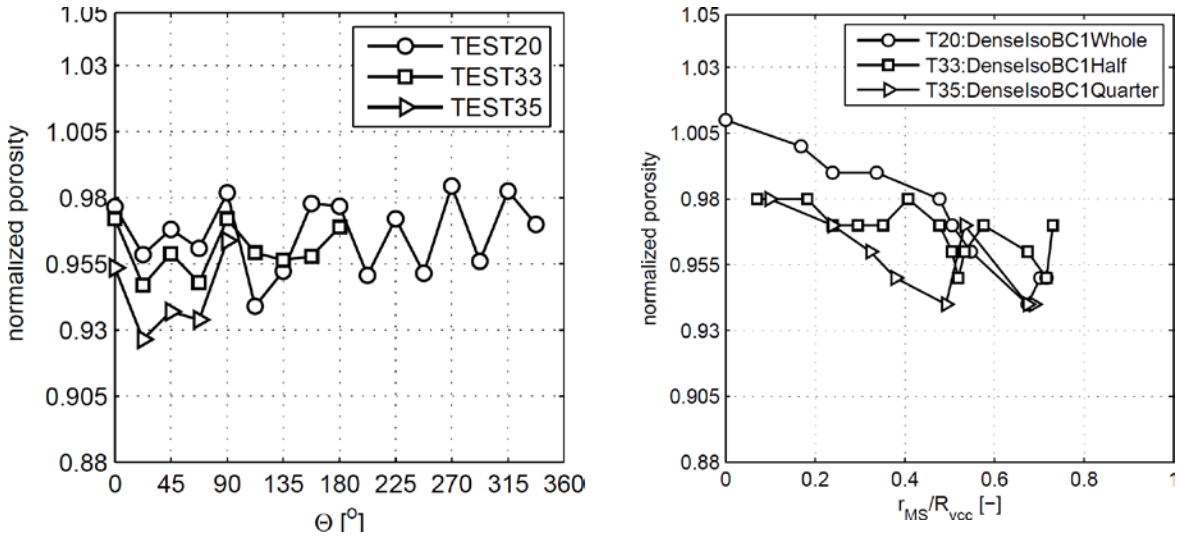

(a) Butlanska et al (2009) (b)

Fig. 5 Initial normalised porosity against (a) angular coordinate (b) normalised radial distance

The different influence of the radial and perimeter walls on the initial state might be due to their different nature. The radial walls are passive (fixed) during model construction, whereas the circumferential wall is active (servo controlled). Increased porosity close to walls passive during specimen formation was also observed by Marketos & Bolton (2010). However it is

difficult to envisage a mechanism by which this slightly larger porosity near to the wall in the smaller chamber would enhance cone resistance.

5 PENETRATION STAGE

In this section we examine detailed results from the chamber state during the penetration tests, when the cone tip was located at a depth of 5.4 cone diameters or 0.39 m, well into the steady-state zone of the tip resistance curve for all tests. The purpose of this examination is to identify the mesoscale signatures and microscale mechanisms that lead to the observed macroscopic effect of radial walls on the steady-state cone tip resistance.

5.1 Stress state near the cone

Calculation of stresses in DEM was here based on a well-established procedure (Potyondy and Cundall, 2004) in which representative or notional average grain stresses, σ_{ij}^{p}, are first computed and then these are averaged in a reference volume to obtain the representative volume stress.

Fig. 6 illustrates the variation in the different stress components with normalized depth, evaluated in a stack of cylindrical shells around the cone shaft with outer diameter equal to two cone diameters. In the figure the cone position serves as the origin of the vertical axis and the vertical distances (positive above the cone tip) are normalized by the cone diameter. Stresses are normalized by the initial confining stress of 100 kPa.

T16, and T34 at DR = 75%

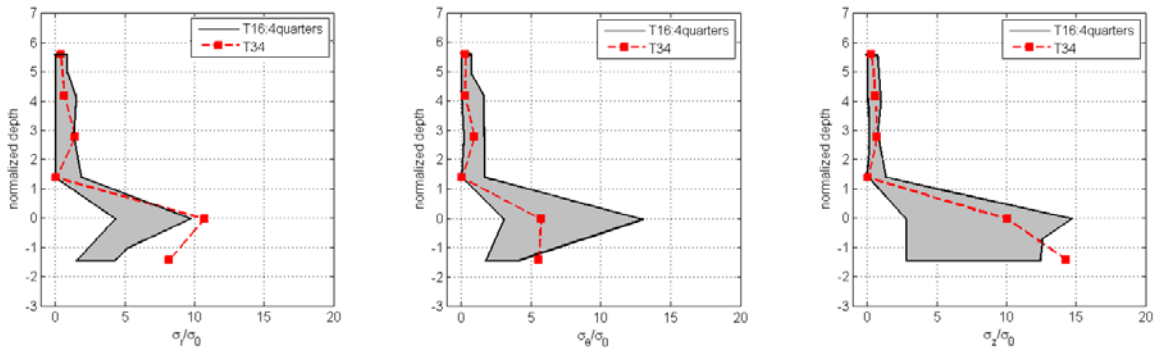

T20 and T35 at DR = 90%

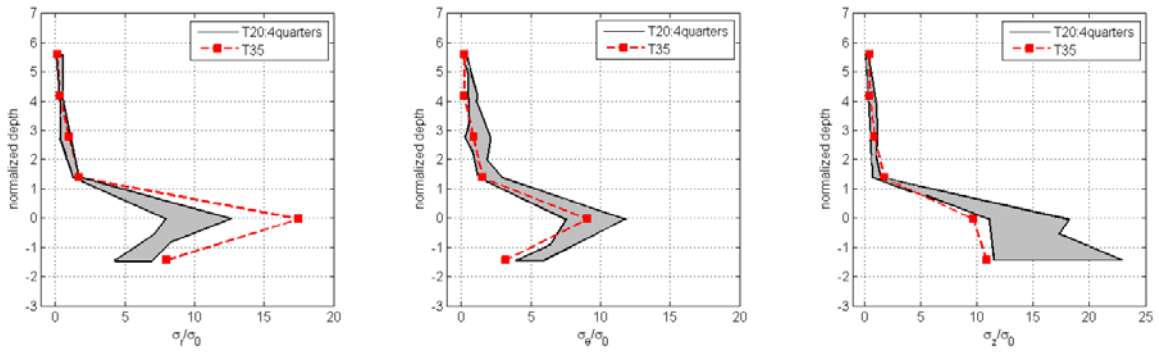

Fig. 6 Comparison of stresses at the chamber axis obtained on the 4 quarters of a full (360° section) VCC model (T16 and T20) and those measured in a quarter chamber VCC (T34 and T35). Only the range of stresses measured from 4 quarters of full VCC is shown

The figure examines to what extent the results from the quarter chamber represent a trend or can be attributed to the fluctuation inherent in DEM computations. To do so the full chamber model is treated as if it was formed by four juxtaposed ideal quarter models. We compute stresses in each of these ideal quarters and compare the values obtained with those computed in the rigid wall bounded quarter chamber. The strongest stress anomaly is apparent in the radial stress plots, where the rigid wall bounded quarter results plot above the range of the ideal quarters in the crucial near tip zone.

5.2 Contact forces

Plotting of contact force networks is a classical means of examining DEM results. The heterogeneity of the magnitude of contact forces in discrete media force networks is well known, relatively distinct strong force chains that carry a large proportion of the stress form in the material (Radjai et al. 1996). This is highlighted in Fig. 7 and Fig. 8, where contact forces are segregated in three distinct levels: extreme (5 standard deviations above the mean); large (above average but not extreme); small (below average). Fig. 7 corresponds to a full chamber case, whereas Fig. 8 corresponds to a reduced, quarter chamber.

The configurations of strong force chains appearing on the small chamber are more inherently unstable (i.e. longer and/or with more curvature) than those appearing in the full chamber. Specifically, the vertical section extreme forces in the quarter chamber arch from the cone tip side towards the chamber bottom, whereas they follow the cone axis on the full chamber. Also, in the horizontal section both extreme and large force chains appear to maintain more closely a radial orientation than their counterparts in the full chamber.

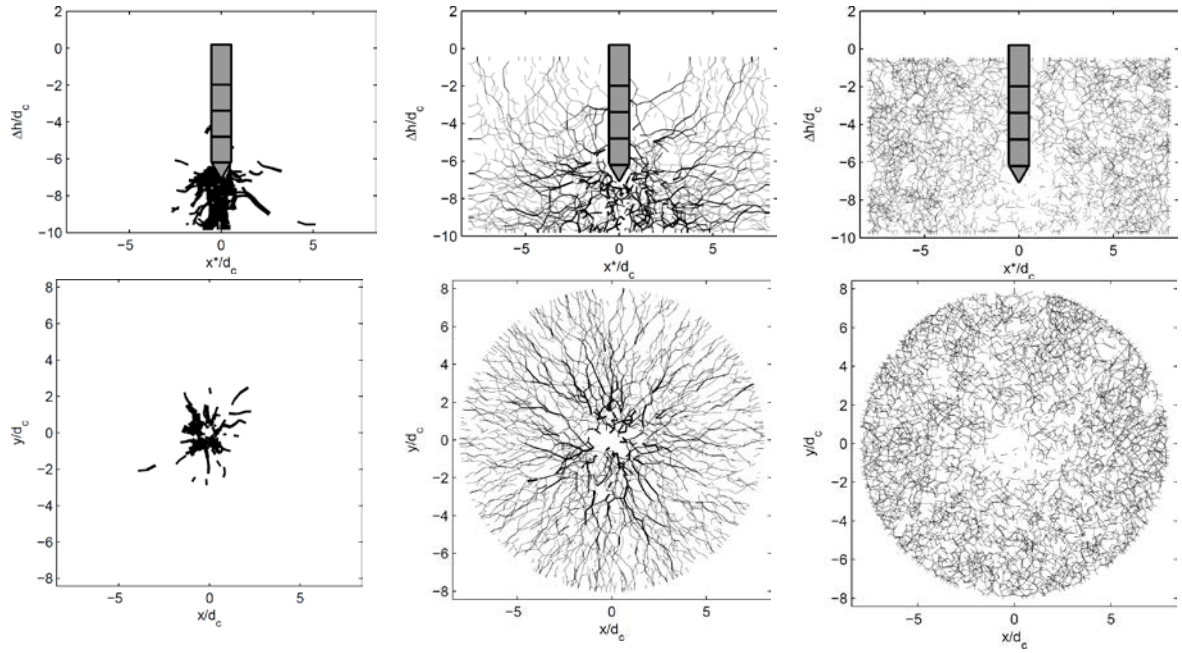

(a)$F_N > \langle F_N \rangle + 5\sigma$ (b) $\langle F_N \rangle < F_N < \langle F_N \rangle + 5\sigma$ (c) $F_N < \langle F_N \rangle$

Fig. 7 Force networks on vertical and horizontal sections separated according to magnitude. Results for test T20, DR = 90%, full chamber

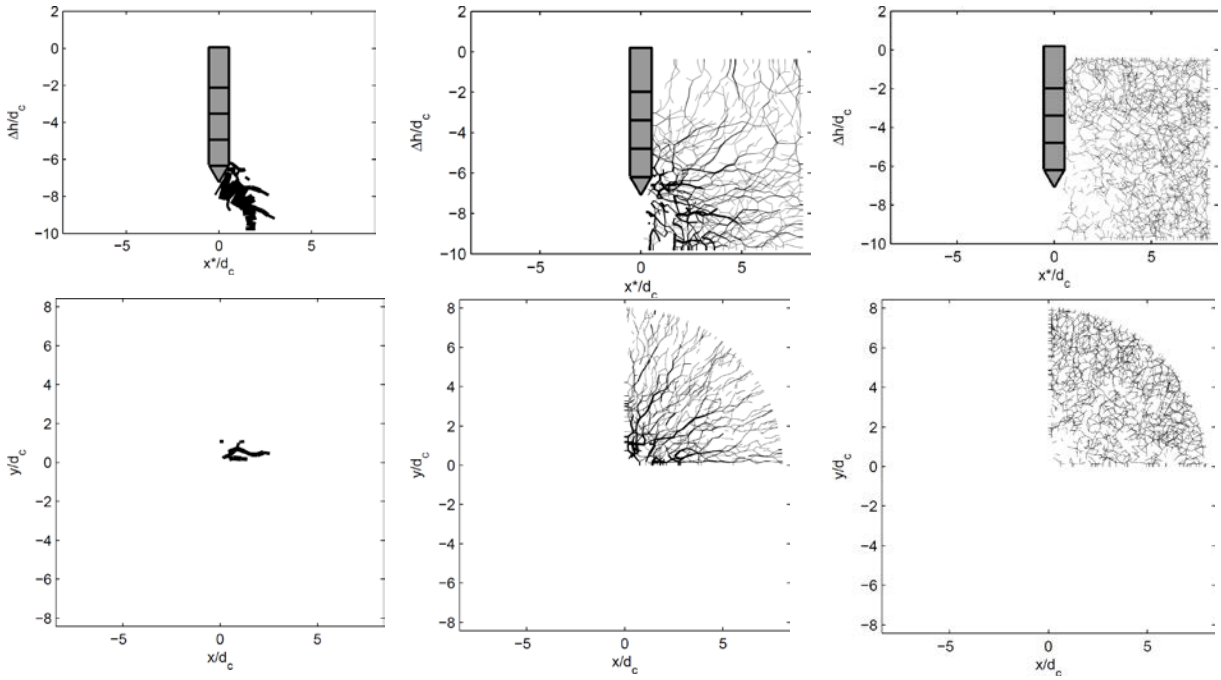

(a)$F_N > \langle F_N \rangle + 5\sigma$ (b) $\langle F_N \rangle < F_N < \langle F_N \rangle + 5\sigma$ (c) $F_N < \langle F_N \rangle$

Fig. 8 Force networks on vertical and horizontal sections separated according to magnitude. Results for test T35, DR = 90%, quarter chamber

6 CONCLUSION

The experiments examined revealed that the introduction of radial walls to limit model extent might introduce some bias towards higher cone resistances. That bias increased with density and with area reduction; note that the smallest section here investigated was that of the quarter chamber, smaller sections are likely to increase the bias. It is acknowledged that the nature and magnitude of such bias might also depend on other model characteristics, particularly those with a direct effect on force chain stability. For instance Cui et al (2007) noted that the introduction of frictionless radial walls reduced triaxial compression resistance in their models, by comparison with those using periodic boundaries, but that result was obtained with a monodisperse discrete material having freedom to rotate. Until a formal framework emerges that enables a systematic treatment of strong force chain constraints in DEM models it seems necessary to systematically check for biases when global symmetry is enforced at the micro level.

ACKNOWLEDGEMENT

The support of the Ministry of Education of Spain through research grants BIA2008-06537 and BIA2011-27217 is gratefully acknowledged.

REFERENCES

Arroyo, M., Butlanska, J., Gens, A., Calvetti, F. & Jamiolkowski, M. (2011) “Cone penetration tests in a virtual calibration chamber” Géotechnique, 51, 6, 525-531 doi: 10.1680/geot.9.P.067

Butlanska, J., Arroyo, M. & Gens, A. (2010a) “Size effects on a virtual calibration chamber”, Proc. 7th European Conference on Numerical Methods in Geotechnical Engineering, NUMGE 2010, Benz & Nordal, eds., Taylor & Francis pp 225-230

Butlanska, J., Arroyo, M. & Gens, A. (2010b) “Virtual Calibration Chamber CPT tests on Ticino sand”, Proc. 2nd International Symposium on Cone Penetration Testing, CPT'10, Huntington beach, California, Robertson & Mayne (eds.), Vol.2, 217-224

Butlanska, J., Arroyo, M. & Gens, A. (2009) “Homogeneity and symmetry in DEM models of cone penetration”, Powders & Grains 2009, Nakagawa & Luding (eds), AIP Conference Proceedings 1145, 425-429

Cui, L., O’Sullivan, C. & O’Neill, S. (2007). “An analysis of the triaxial apparatus using a mixed boundary three-dimensional discrete element model” Géotechnique 57, No. 10, 831–844

Huang, A.B. & Hsu, H.H. (2004) “Advanced calibration chambers for cone penetration testing in cohessionless soils” in Viana & Mayne, *ISC-2 Geotechnical and geophysical site characterization*, 147-166

Jamiolkowski, M., Lo Presti, D.C.F. & Manassero, M. (2003) “Evaluation of relative density and shear strength of sands from CPT and DMT”, in Germaine, Sheahan & Whitman, *Soil Behavior and soft ground construction, ASCE Geotechnical Special Publication 119*, 201-238

Jassim, I., Hamad, F. & Vermeer, P. (2011) “Dynamic material point method with applications in geomechanics”, *ComGeo II. 2nd International Symposium on Computational Geomechanics* 27 April – 29 April 2011, Cavtat-Dubrovnik, Croatia

Lin, J. and Wu,W. (2012) “Numerical study of miniature penetrometer in granular material by discrete element method”. Philosophical Magazine, 92(28-30):3474–3482, October 2012.

Marketos, G. & Bolton, M. D. (2010) “Flat boundaries and their effect on sand testing”, Int. J. Numer. Anal. Meth. Geomech.; 34:821–837

McDowell G. Falagush, O. & Yu, H.-S. (2012) “A particle refinement method for simulating DEM of cone penetration testing in granular materials”, Géotechnique Letters 2, 141–147, http://dx.doi.org/10.1680/geolett.12.00036

Radjai, F., M. Jean, J.-J. Moreau, and S. Roux (1996) “Force distributions in dense two-dimensional granular systems”. Physical review letters 77 (2), 274

Schnaid, F (2009) “In situ testing in geomechanics”, Taylor & Francis

AN ADAPTIVE RVM APPROACH FOR ASSESSMENT OF ELASTIC COMPRESSIBILITY OF SANDSTONE

Z.B. Liu
Laboratory of Mechanics of Lille, University of Lille 1-Science and Technology, 59655, Lille, France

J.F. Shao
Laboratory of Mechanics of Lille, University of Lille 1-Science and Technology, 59655, Lille, France

ABSTRACT: *This study is devoted to assessing elastic compressibility of sandstone with the adaptive relevance vector machine (ARVM) according to the mineral composition and microstructural characteristics. Based on the data collected, the relevance vector machine (RVM) is first trained adaptively with some samples to learn the relations between the elastic compressibility of sandstone and the mineral composition or the microstructural features. Then, the trained RVM is tested with the remaining samples to evaluate its performance in assessment of elastic compressibility of sandstone. During the assessment, an iterative strategy is adopted to optimize the hyper-parameters to improve the performance of the RVM. The results show that the width hyper-parameter has obvious effect on the RVM performance while the kernel type shows little influence. By comparison with other techniques such as the artificial neural network (ANN) and the support vector machine (SVM), the ARVM performs much better than the ANNs and its performance in assessment of elastic compressibility of sandstone is equivalent to the optimized SVMs. Therefore, it is feasible to apply the ARVM for assessing elastic compressibility of sandstone according to the mineral composition and the microstructural features.*

1 INTRODUCTION

Physical properties of porous materials are related to the mineral compositions and/or the microstructural characteristics. Sandstone is a typical porous material composed of solid particles and pore spaces. Solid particles form the skeleton and are surrounded by the pore space. Solid particles are comprised of various minerals such as the quartz, the feldspar and the detrital clay. The pore spaces can be classified into three types, i.e. the intergranular pores, the connective pores and the micro pores. Different composition of minerals and different geometry of the pore space result in diverse physical behavior of sandstone. Therefore, the physical properties of sandstone depend largely on the mineral composition and the microstructural features. In this way, the physical properties of sandstone can be correlated with the mineral composition and microstructural characteristics.

Elastic compressibility is one of the critical physical features of porous media. Recently, elastic compressibility of different materials has been studied by various kinds of techniques (Kimizuka et al. 2008; Poon et al. 2008; Xu et al. 2010; Cairns et al. 2013). Discussion on empirical relations between the compressibility of sandstone and the stress as well as the pore structure can be found in Zimmerman (1990). Also, quantitative prediction of the compressibility of sandstone is exploited in this work. Another study has been reported for the prediction of rock mechanical behavior using the Neural Networks (Zhang and Song 1992). Recently, some experiments have been conducted to measure the fractal characteristics of the pore structure of low permeability sandstone (Qin et al. 2012); also, a pore structure model was used to predict the elastic wave velocity in fluid-saturated sandstones (David and Zimmerman 2012). The elastic compressibility of sandstone has been

formerly tested in laboratory (Caruso et al. 1985) with many time-consuming experiments. The curves of elastic compressibility versus previous maximum pressure have been obtained assuming that elastic compressibility at any given pressure is a function of the stress history of a sample (Wissler and Simmons 1985). These results indicate that the physical characteristics of sandstone can be in essence depended on the pore and mineral compositions. However, no specific method has been proposed to interpret this dependency. An assessment of elastic compressibility is in fact unreasonable by considering the effect of external loads without influence of mineral compositions and microstructures. Unfortunately, not many models have been reported that account for the relation between the elastic compressibility of sandstone and the other related factors such as the mineral composition and the microstructural properties.

Therefore, in this study, we focus on assessment of the elastic compressibility of sandstone based on the mineral composition and the pore structures as well as the external loads using the ARVM. The RVM is a probabilistic approach for learning disciplines among data (Tipping 2000). The hyper-parameters influence the performance of RVMs (Tipping 2001). We present an iterative strategy to optimize the RVM hyper-parameters adaptively and then apply this approach to assess the elastic compressibility of sandstones. We aim to: (1) make assessment of elastic compressibility of sandstone according to the mineral compositions and pore structural features using the ARVM; (2) show the effects of hyper-parameters of RVM in the assessment of elastic compressibility of sandstones. Hence the specific effects of mineralogy or pore structure are not included in this study.

2 MATERIAL AND TARGET FUNCTION

Elastic compressibility of sandstone can be tested in laboratory by gauges. This testing process however is not easy to follow and takes too much time. It would be better if we can make assessment based on some physical propertes that are easy to be obtained. Therefore, this study aims to develop a model for assessment of elastic compressibility of sandstone based on a list of data samples. The dataset used in this study is obtained from the experimental results of physical properties of sandstones. Many properties of the sandstone samples like the mineralogy, the bulk density and the pore features are measured as well as the elastic compressibility values. The samples used in the experiment are mostly clean quartz arenites, subarkoses and argillaceous quartz arenites, in which kaolinite is the dominant pore-filling mineral. Three types of total porosity are summarized, i.e. the intergranular (equidimensional), the connective (tabular or tubular shaped), and the micro (less than a few microns in size) porosity on the basis of point counting SEM images(Caruso et al. 1985).

The statistical features of the dataset are given in Table 1. In the table, a_A, a_B and a_C are the elastic compressibility coefficients measured by gauges settled in three orthogonal directions. In all, 37 samples of sandstone are collected and each sample has 11 properties. In order to test the generalizaiton capability of the proposed ARVM strategy, 30 samples are used to train the models to obtain optimal model parameters. The left 7 samples are used as testing samples to validate the generalization ability of the model.

The RVM model is trained with the above strategy and then to give an assessment of the testing samples given in Table 2. The Gaussian kernel is used in the modeling. The absolute percentage error (APE) and the mean absolute percentage error (MAPE) is defined as the target function to evaluate model performance

$$APE = \sum_{i=1}^{n} \left| \frac{Y_i - Y_i^*}{Y_i} \right| \times 100\%; \tag{1}$$

$$MAPE = \frac{1}{n}\sum_{i=1}^{n}\left|\frac{Y_i - Y_i^*}{Y_i}\right| \times 100\% \quad (2)$$

Also, the coefficient of determination, denoted by R^2, is used to show how the estimated values of compressibility fit the measured values of the testing samples given in Table 2.

Meanwhile, in order to show the capability of ARVM, we compare the estimated results of ARVM to that of other techniques, like Artificial Neural Networks (ANNs) and Support Vector Machines (SVMs).

Table 1 Statistical features of data samples

Factors		NO.	Minimum	Maximum	Mean	Std. deviation
Mineralogy (%)	Quartz	37	65	98	86.1	9.9
	Feldspar	37	0	15	4.4	4.4
	Shard clay	37	1	28	6.9	7.5
	Others	37	0	7	2.6	2.6
Pore structure (%)	Pore among particles	37	24	76	60.8	15.0
	Pore wall	37	4	26	14.2	5.5
	Micro pore	37	10	63	25.0	14.5
Average particle size(μm)		37	65	350	131.2	65.7
Bulk density ($g \cdot cm^{-3}$)		37	1.78	2.96	2.109	0.216
Average void ratio (%)		37	8.5	30.5	20.45	5.55
Loading pressure (MPa)		37	10	100	41.6	32.4
Measured compressibility ($MPa^{-1} \times 10^6$)	a_A	37	14.1	86.0	37.00	14.71
	a_B	37	15.6	94.2	37.98	16.69
	a_C	37	15.8	105.0	41.15	20.02

Table 2 Testing samples of elastic compressibility of sandstone

NO.	Mineralogy [vol %]				Average particle size[μm]	Density [g·cm-3]	Average void ratio[%]	Pore distribution[%]			Pressure [MPa]	Compressibility coefficients $MPa^{-1} \times 10^6$		
	Quartz	Feldspar	Shard clay	Others				Among particle	Pore wall	Micro pore		a_A	a_B	a_C
1	94	0	1	5	120	2.41	17.8	72	13	15	50	26.0	24.9	27.0
2	95	0	5	0	130	2.03	21.7	76	10	14	50	31.0	26.4	27.3
3	80	9	4	7	80	2.21	15.6	57	26	17	10	34.4	48.6	82.9
4	96	1	2	1	115	1.94	24.1	70	14	16	10	47.8	50.5	50.4
5	90	4	6	0	145	2.01	23.4	69	11	20	100	29.0	24.3	27.0
6	90	4	6	0	145	2.01	23.4	69	11	20	50	30.5	27.4	30.9
7	75	9	15	1	85	2.96	25.9	40	16	44	30	58.1	57.0	55.1

3 METHODOLOGY: ADAPTIVE RELEVANCE VECTOR MACHINE FOR ASSESSMENT

The relevance vector machine (RVM) is firstly proposed in a Bayesian framework with probabilistic significance for learning in general models(Tipping 2000). It establishes a mapping between the target variables and the associated independent variables, i.e.

$$y = f(x\ ;\ w) = \sum_{i=1}^{N} w_i K(x,\ x_i) + w_0 = w^t \phi(x) \quad (3)$$

where, N is the total sample number; i is the i^{th} sample number; $y = f(x\ ;\ w)$ is the mapping; $x,\ x_i$ denote the associated independent variables; $K(x,\ x_i)$ is the kernel functions; $\phi(x) = [1,\ K(x,\ x_1),\ K(x,\ x_2),\ ....,\ K(x,\ x_n)]^t$; w_i is the weight of i^{th} sample, $w = [w_0\ ,\ w_1\ ,...,\ w_N]^t$.

In regression, the RVM employs Eq. (1) with an additive noise term to link the input x_n and scalar target variable t_n

$$t_n = f(x_n;\ w) + \in_n \tag{4}$$

where $\in_n$ is a zero-mean white noise process with variance σ^2, i.e., $p(\in_n|\ \sigma^2) = N(\in_n|\ 0,\ \sigma^2)$.

Posing $\beta = \sigma^2$, and assuming independence of the samples, the likelihood of training samples is

$$p(t \mid X,\ w,\ \beta) = (2\pi\beta^{-1})^{-N/2} \exp\left(-\frac{1}{2}\beta \left\| t - \phi w \right\|^2 \right) \tag{5}$$

where $t = [t_1,....,\ t_N]^t$, $X = [X_n]_{n=1}^N$. With more parameters $(N+1)$ than training data samples (N), direct maximum-likelihood estimation of w would lead to over-fitting. In the RVM Bayesian framework, zero-mean Gaussian shrinkage priors are imposed on every w_i and, assuming the independence of the parameters, we have

$$p(w_i|\ \alpha_i) = \mathrm{N}(w_i|0,\ \alpha_i^{-1}) \Rightarrow p(w|\alpha) = \prod_{i=0}^{N} N(w_i|0\ ,\ \alpha_i^{-1}) \tag{6}$$

with $\alpha = [\alpha_0,\ \alpha_1,\ ...,\ \alpha_N]^t$, a $N+1$ vector of hyper-parameters representing the precision on the parameters. Finally uniform hyper-priors are assumed for all the precision hyper-parameters, α and β. An interesting property of these hyper-priors is that when the evidence of the model is maximized with respect to the hyper-parameters the corresponding parameters to be zero. This is a type of "automatic relevance determination"(MacKay 1994) leading to a sparse set of parameters w. Using Bayes rule and the properties of Gaussian functions, the posterior distribution of the weight can also be described by a Gaussian:

$$p(w|X,t,\alpha,\beta) = N(w|m,\Sigma) \tag{7}$$

where the mean m and covariance Σ are given by

$$m = \beta\Sigma\Phi^t t;\qquad \Sigma = (A + \beta\Phi^t\Phi)^{-1} \tag{8}$$

with $A = diag(\alpha_0,\ ....,\ \alpha_N)$ a diagonal matrix of precisions.

In practice, the values of α and β are estimated by maximizing the marginal likelihood $p(t|X,\ \alpha,\ \beta)$, i.e., using a type-II maximum-likelihood method (Berger 1985). Only the most probable values are thus calculated, an approximation to estimating and using their full distribution. With this simplification, the marginal likelihood can be obtained by integrating out the weight parameters

$$p(t|X,\ \alpha,\ \beta) = \int p(t|X,\ w,\ \beta)p(w|\alpha)dw = N(t|0,\ \beta^{-1}I + \Phi A^{-1}\Phi^t) \tag{9}$$

Values of α and β that maximizes (the log of) Eq.(7) can then be obtained iteratively, using the following update rules

$$\alpha_i^{new} = \frac{1-\alpha_i \Sigma_{ii}}{m_i^2}; \quad (\beta^{new})^{-1} = \frac{\|t-\Phi m\|^2}{N-\sum_{i-1}^{N}(1-\alpha_i \Sigma_{ii})} \tag{10}$$

where m_i is the i^{th} element of the estimated posterior weight w and Σ_{ii} the i^{th} diagonal element of the posterior covariance matrix Σ from Eq.(8).

Once the iterative procedure has converged to the "most probable values α_{MP} and β_{MP}, the distribution of target value t_* for a new data point x_* is also Gaussian and estimated through

$$\begin{aligned} p(t_*|X, t, \alpha_{MP}, \beta_{MP}) &= \int p(t_*|X, w, \beta_{MP}) p(w|X, t, \alpha_{MP}, \beta_{MP}) dw \\ &= N(t_*|m^t \varphi(x_*), \sigma_*^2) \end{aligned} \tag{11}$$

$$\sigma_*^2 = \beta_{MP}^{-1} + \varphi(x_*)^t \Sigma \varphi(x_*) \tag{12}$$

where Σ is given by Eq.(8) with α and β set at their optimal value.

Unlike optimization of the weight w, the width hyper-parameter r^2 is user-defined before model training. In order to optimize the width value, the target function should be defined first. The adaption of the kernel parameter can be implemented as follows:

(a) Initialize the hyper-parameter r^2 in a proper range and specify the initial r_0^2 and an appropriate step for iteration;

(b) Specify one kernel function;

(c) Train the RVM model with the some samples to obtain an optimal value α_{MP} and the weight w;

(d) Compute the posterior distribution output $P(t|X, w)$;

(e) Calculate the TF value;

(f) Update the width parameter $r_{k+1}^2 = r_k^2 + step$, loop to (b) till $r^2 = \max(r^2)$;

(g) Find the maximum TF value for each kernel function and let the corresponding value of r^2 be the optimal width value.

After the above steps, the predicted outputs are obtained as well as the optimal r^2 value. Implementation of the assessment is shown in Figure 1.

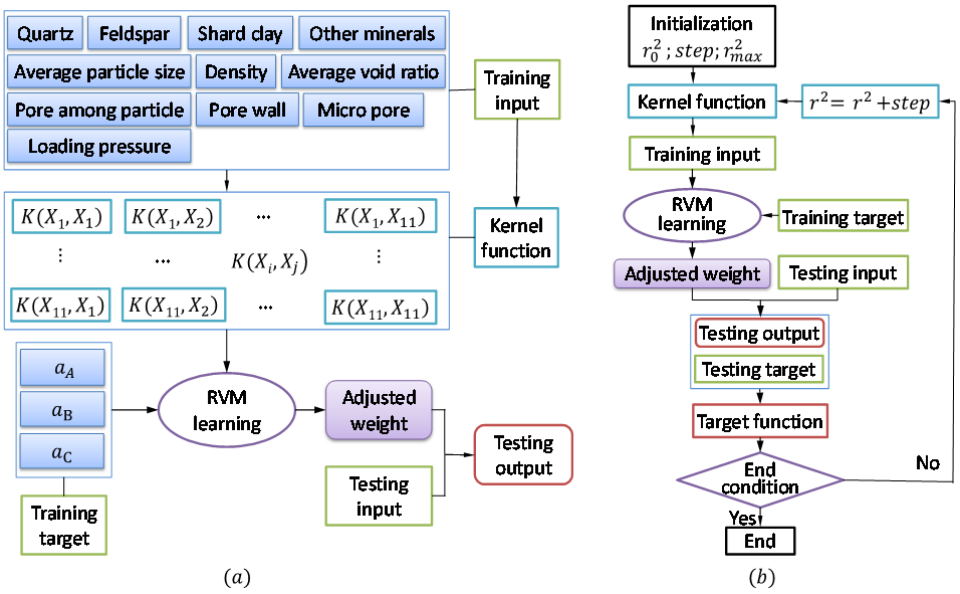

Figure 1 Assessment of elastic compressibility of sandstone

4 RESULTS AND DISCUSSION

4.1 Effect of hyper-parameter

The adapting process of hyper-parameters on RVM performance is given in Figure 2 and Figure 3, respectively, for predicted error and R^2 of the measured and the predicted value. It is shown apparently in Figure 2 and Figure 3 that the hyper-parameter values have evident effects on the mean absolute percentage errors and R^2 values. And the effects cannot be quantified by a definite function. Hence an iteration technique is utilized in this study.

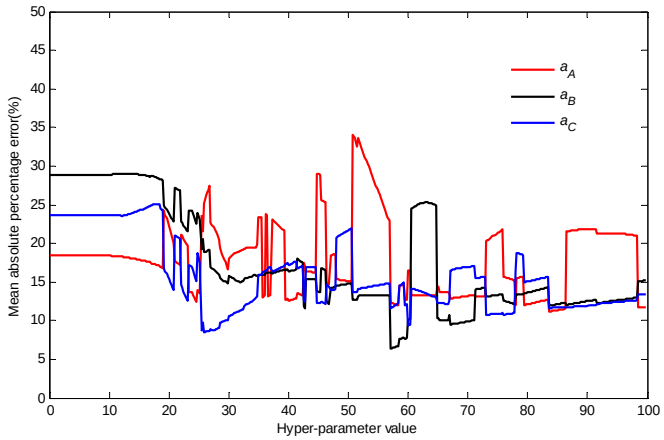

Figure 2 Adapted predicted error versus hyper-parameter value for testing samples

Our purpose is to find the optimal hyper-parameter value that can produce the minimum predicted errors and the maximum R^2 values. We can observe from Figure 2 that the MAPEs of a_A, a_B and a_C obtain the minimum values with different hyper-parameter values. The component of a_A arrives at the minimum 14.02 with hyper-parameter being 39.26. The component of a_B arrives at the minimum 6.06 with hyper-parameter being 59.61. The component of a_C arrives at the minimum 6.97 with hyper-parameter being 44.61. As shown in Figure 3, the R^2 values of a_A and a_C arrive at the maximum value 0.99 with hyper-parameter value near to 27.61 and that of a_B arrives at the maximum 0.99 with hyper-parameter being 60.41. Hence the hyper-parameter values can be optimized by the iteration computing technique.

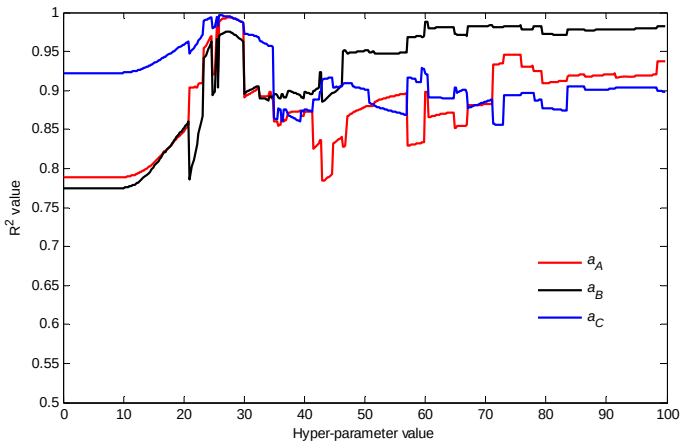

Figure 3 Adapted R^2 value versus hyper-parameter value for testing samples

4.2 Comparison with other techniques

The predicted results of the ARVM are given comparatively in Table 3 with that of the ANNs and the PSO-SVMs for the test samples. In the ARVM modeling, the optimal hyper-parameter is obtained to be 39.26, 59.61 and 44.61 for a_A, a_B and a_C, respectively. The corresponding APEs are shown in Figure 4.

Table 3 Predicted elastic compressibility of different approaches

NO.	Measured value ($(MPa^{-1}\times10^6)$)			ANN predicted ($MPa^{-1}\times10^6$)			PSO-SVM predicted ($MPa^{-1}\times10^6$)			ARVM predicted ($MPa^{-1}\times10^6$)		
	a_A	a_B	a_C	a_A	a_B	a_C	a_A	a_B	a_C	a_A	a_B	a_C
1	26.0	24.9	27.0	25.0	25.2	24.3	27.1	24.6	28.5	29.2	23.8	22.5
2	31.0	26.4	27.3	30.0	29.4	25.6	32.1	27.9	28.0	31.4	26.3	27.0
3	34.4	48.6	82.9	59.9	65.1	87.0	42.2	54.4	79.6	46.3	52.1	75.8
4	47.8	50.5	50.4	41.9	39.7	43.9	41.9	55.2	57.7	39.1	43.9	48.2
5	29.0	24.3	27.0	28.1	26.8	24.1	30.1	26.1	26.5	25.2	25.8	28.5
6	30.5	27.4	30.9	34.8	33.0	32.3	31.2	31.5	32.1	35.9	29.7	34.8
7	58.1	57.0	55.1	54.9	61.6	69.9	55.1	60.6	62.9	58.6	55.4	54.9

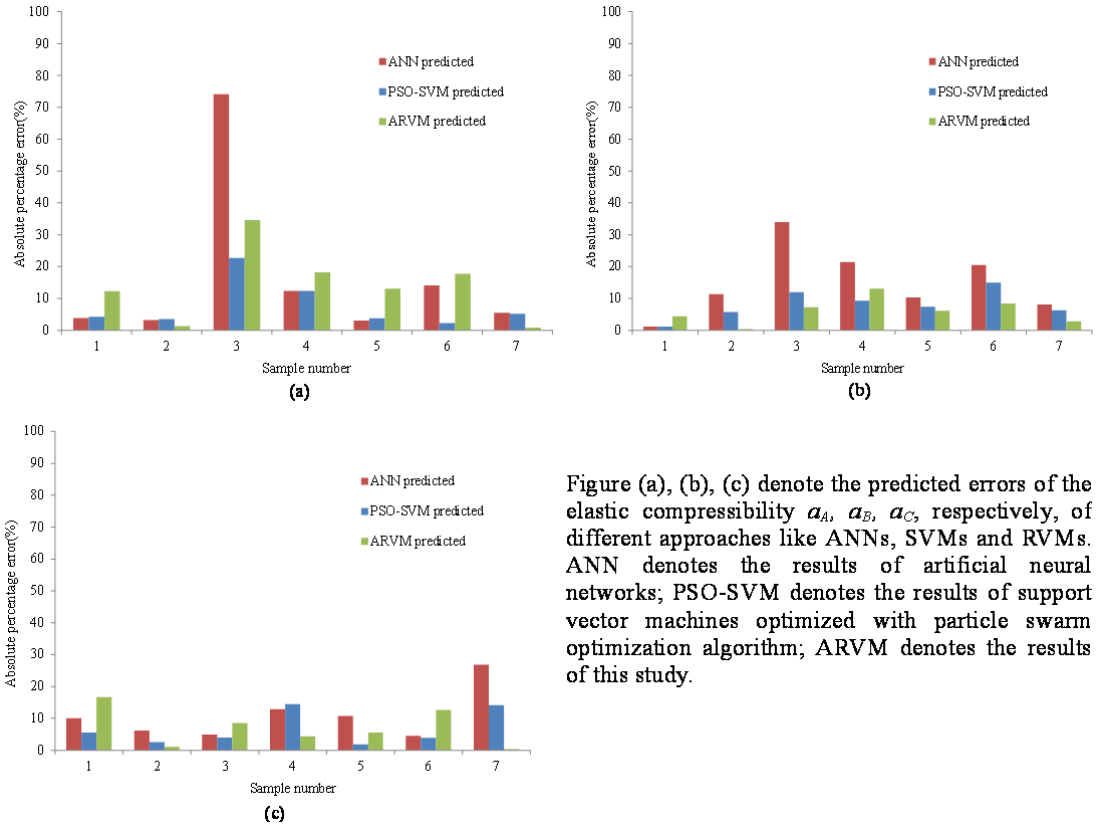

Figure (a), (b), (c) denote the predicted errors of the elastic compressibility a_A, a_B, a_C, respectively, of different approaches like ANNs, SVMs and RVMs. ANN denotes the results of artificial neural networks; PSO-SVM denotes the results of support vector machines optimized with particle swarm optimization algorithm; ARVM denotes the results of this study.

Figure 4 Predicted errors of different approaches for estimating elastic compressibility

The predicted errors of the three techniques are mostly less than 15% except for the sample NO.3. Hence these techniques can perform well in the assessment of the elastic compressibility of sandstones according to characteristics of mineralogy and microstructures. The MAPE of ARVM for assessment of a_A, a_B and a_C is 14.02, 6.06, 6.97, respectively.

Comparing the results in Figure 4, we find these techniques perform better in assessment of a_B and a_C than that of a_A.

We can observe from Figure 4-(a) that the predicted errors of ARVM in assessing a_A are less than that of the ANNs and bigger than that of the PSO-SVM. It is shown in Figure 4-(b) that the predicted errors of ARVM are much smaller than that of ANNs and SVMs except for the test sample NO.1 and NO.4. In Figure 4-(c), we can observe that the predicted errors of ARVM are mainly smaller than that of the ANNs and equivalent to that of the SVMs. Therefore, we conclude that the ARVM is capable and reliable for assessment of elastic compressibility of sandstones according the characteristics of mineralogy and microstructures.

5 CONCLUSIONS

It is costly to measure certain mechanical properties of rocks. The above work shows the possibility and feasibility of assessment of elastic compressibility of sandstone based on some easily measure properties. Based on the results obtained, conclusions can be made as follows:

(a) The ARVM technique is feasible and reliable for assessment of elastic compressibility of sandstones according to the mineralogy and other physical properties. Thus it can be used as an intellectual tool to assess the rock mechanical parameters that are costly to be identified by field or laboratory experiments.

(b) The width hyper-parameter in RVM influences its performance in the assessment. The presented iterative strategy is capable of optimizing the model parameters although it is time-consuming.

(c) The ARVM performs much better than the ANNs and can perform equivalently to the PSO optimized SVMs in the assessment of compressibility of sandstone. Further, the specific effects of mineral or micro structure on physical properties should be exploited in future.

ACKNOWLEGEMENTS

Financial support from China 973 Program for Key Basic Research Project (Grant No.2011CB013504) and China Natural Science Foundation (No.50911130366) is gratefully acknowledged. The authors are also grateful to people who help for improvement of the work.

REFERENCES

Berger JO (1985) Statistical Decision Theory and Bayesian Analysis. Second Edition. Springer-Verlag, New York

Cairns AB, Catafesta J, Levelut C, Rouquette J, van der Lee A, Peters L, Thompson AL, Dmitriev V, Haines J, Goodwin AL (2013) Giant negative linear compressibility in zinc dicyanoaurate. Natural Material advance online publication

Caruso L, Simmons G, R.Wilkens (1985) The physical properties of a set of sandstones—Part I. The samples. Int J Rock Mech Min Sci Geomech Abstr 22 (6):381-392

David EC, Zimmerman RW (2012) Pore structure model for elastic wave velocities in fluid-saturated sandstones. Journal of Geophysical Research: Solid Earth 117 (B7):n/a-n/a. doi:10.1029/2012JB009195

Kimizuka H, Ogata S, Li J (2008) Hydrostatic compression and high-pressure elastic constants of coesite silica. J Appl Phys 103 (5):053506

MacKay DJC (1994) Models of Neural Networks III: Bayesian Methods forBack propagation Networks.

Poon B, Rittel D, Ravichandran G (2008) An analysis of nanoindentation in linearly elastic solids. Int J Solids Struct 45:6018-6033

Qin SG, Wu HL, Tian MB, Wu JC, Yao SL (2012) Fractal Characteristics of the Pore Structure of Low Permeability Sandstone. Applied Mechanics and Materials 190:482-486

Tipping ME The Relevance Vector Machine. In: Solla SA, Leen TK, Müller KR (eds) Advances in Neural Information Processing Systems, MIT, 2000. MIT, pp 652-658

Tipping ME (2001) Sparse Bayesian learning and the relevance vector machine. J Mach Learn Res 1:211-244

Wissler TM, Simmons G (1985) The physical properties of a set of sandstones—Part II. Permanent and elastic strains during hydrostatic compression to 200 MPa. Int J Rock Mech Min Sci Geomech Abstr 22 (6):393-406

Xu H, Yusheng Zhao, Zhang J, Wang Y, Hickmott DD, Daemen Ll, Hartl MA, Wang L (2010) Anisotropic elasticity of jarosite: A high-P synchrotron XRD study. Am Mineral 95:19-23

Zhang Q, Song J (1992) Predicting mechanical behaviors of rock or rock engineering by neural network. Chin J Rock Mech Eng 11 (1):35-43

Zimmerman RW (1990) Compressibility of sandstones, vol 29. Elsevier Science,

MODELLING OF SHEAR MODULUS OF UNSATURATED FINE GRAINED SOILS AT VERY SMALL STRAIN

K. S. Wong
Department of Engineering Geology, Institute of Hydrogeology, Engineering Geology and Applied Geophysics, Faculty of Science, Charles University in Prague, Prague, Czech Republic

D. Masin
Department of Engineering Geology, Institute of Hydrogeology, Engineering Geology and Applied Geophysics, Faculty of Science, Charles University in Prague, Prague, Czech Republic

ABSTRACT: *Shear modulus at very small strain is an important parameter in the design of geotechnical structures. The existing and new models have been evaluated using measured shear modulus at very small strain for a low plasticity fine grained soil available in the literature. It is found that the new model can be used to predict shear modulus at very small strain due to increase and decrease of mean net stress at constant suction. Moreover, the new model is able to predict a trend consistent with the experimental data for wetting-induced collapsible soil while existing models predict a contradictory trend.*

1 INTRODUCTION

Shear modulus at very small strain (0.001% or less), G_o is a key parameter in the design of geotechnical structures subjected to static and cyclic loadings. Although numerous researches have been conducted on the measurement of shear modulus at very small strain and empirical formulations were proposed and verified for saturated and dry soils, only recently investigation on G_o for unsaturated soil have been performed.

A few models have been proposed to predict shear modulus at very small strain for unsaturated soil. Some of them are simple semi-empirical formulations (Biglari et al., 2011; Leong et al., 2006; Ng and Yung, 2008; Sawangsuriya et al., 2009) while others involve complex formulation with larger number of variables (Biglari et al., 2011; Vassallo et al., 2007). Most of the existing models can predict shear modulus at very small strain due to increase of mean net stress at constant suction or increase of suction at constant mean net stress. Some of the existing models also include effects of stress history. However, most of the models cannot predict the shear modulus for wetting-induced collapsible soil. Recently, Wong et al. (2013) proposed a new model, which is simple but captures the effects of stress and suction as well as collapse during wetting on shear modulus at very small strain. A low plasticity fine grained soil data available in the literature are used to evaluate the existing and new models.

2 EXISTING MODELS FOR SHEAR MODULUS AT VERY SMALL STRAIN

Existing models used to predict shear modulus at very small strain can be divided into two primary groups depending on the stress variables used in the model. The first primary group adopts the following form.

$$G_o = \alpha f(p - u_a) g_1(s) + \beta g_2(s) \tag{1}$$

where mean net stress, $(p - u_a)$ and matrix suction, $s = (u_a - u_w)$ are used in the formulation. p, u_a and u_w are total mean stress, pore air and pore water pressures respectively. The first primary group can further be sub-divided into two categories depending on whether $\beta = 0$ or $\beta > 0$. Ng & Yung (NY) model proposed by Ng and Yung (2008) is under category with $\beta = 0$. NY model has the following equation for shear modulus at very small strain,

$$G_o = A\rho e^m \left[\left(\frac{p - u_a}{p_r} \right)^n \right] \left[1 + \frac{s}{p_r} \right]^k \tag{2}$$

where bulk density, $\rho = (G_s + S_r e)/(1+e)$. G_s, S_r and e are respectively specific gravity, degree of saturation and void ratio of the unsaturated soil. ρ_w is density of water. Sawangsuriya, Edil & Bosscher first (SEB1) model by Sawangsuriya et al. (2009) are under category with $\beta > 0$. SEB1 model has the following equation for shear modulus at very small strain,

$$G_o = A f_2(e) (p - u_a)^n + C\Theta^k s \tag{3}$$

in which

$$f_2(e) = \frac{1}{0.3 + 0.7e^2} \tag{4}$$

where C is a dimensionless parameter and $\Theta^k = S_r$.

The second of the primary groups adopts the following form:-

$$G_o = \alpha f[(p - u_a), s] \tag{5}$$

BMDJS model proposed by Biglari et al. (2011) has the following formulation which is based on the framework suggested by Gallipoli et al. (2003).

$$G_o = A p_a^{1-n} f_1(e) OCR_{p'}^m (p')^n h(S_r) \tag{6}$$

in which isotropic average soil skeleton stress is

$$p' = (p - u_a) + \chi s \tag{7}$$

where $\chi = S_r$. Function

$$h(S_r) = 1 - a'[1 - \exp(b'\zeta)] \tag{8}$$

where a' and b' are dimensionless parameters and oversonsolidation ratio, $OCR_{p'} = \frac{p_o'(\zeta)}{p'}$.

Based on Gallipoli et al. (2003), $p_o'(\zeta)$ is obtained from

$$\ln p_o^{'}(\zeta)=\frac{\lambda-\kappa}{\frac{e}{e_s}(\zeta)\lambda-\kappa}\ln p_o^{'}(0)+\frac{\left(\frac{e}{e_s}(\zeta)-1\right)N}{\frac{e}{e_s}(\zeta)\lambda-\kappa} \tag{9}$$

in which

$$\frac{e}{e_s}(\zeta)=1-a\left[1-\exp(b\zeta)\right] \tag{10}$$

where $\zeta=1-S_r$ and $e_s=N-\lambda\ln p^{'}$. e_s is the saturated void ratio measured during virgin compression with respect to the same average soil skeleton stress corresponding to the unsaturated void ratio, e. N is the intercept of the saturated normal compression line, λ is the slope of the saturated normal compression line and κ the saturated swelling index. $p_o^{'}(0)$ is the isotropic average soil skeleton stress on the saturated normal compression line.

Wong et al. (2013) proposed a new model tackling the effects of stress and suction as well as collapse during wetting to shear modulus at very small strain. The formulation used in the new model is as follows,

$$G_o=\begin{Bmatrix} Ap_r^{1-n}e^m\left(p^{'}\right)^n & s\le s_e \\ Ap_r^{1-n}e^m\left(p^{'}\right)^n\left(\frac{s}{s_e}\right)^k & s>s_e \end{Bmatrix} \tag{11}$$

where the reference pressure, p_r is taken as 1 kPa. Following Khalili and Khabbaz (1998), the isotropic average soil skeleton stress can be represented by Equation 7, in which

$$\chi=\begin{Bmatrix} 1 & s\le s_e \\ \left(\frac{s_e}{s}\right)^\gamma & s>s_e \end{Bmatrix} \tag{12}$$

where γ is taken as 0.55 and s_e is the suction where the transition between saturated and unsaturated states occurs. For main drying path, $s_e = s_{en}$ while for main wetting path $s_e = s_{exp}$ in which s_{en} is air entry value and s_{exp} is air expulsion value. The effect of hydraulic hysteresis is considered in the formulation by normalising the suction with air entry value at main drying path or air expulsion value at main wetting path. At scanning curves in transition of drying to wetting or wetting to drying, the ratio at the main drying or wetting path is adopted.

3 MATERIAL AND MODEL CALIBRATION

In the following, we evaluate different models using experimental data on Zenoz kaolin by Biglari et al. (2012) and Biglari et al. (2011). Evaluations using other data sets can be found in Wong et al. (2013). Zenoz kaolin is an commercial Iranian kaolin. It is classified as CL according to the Unified Soil Classification System. Clay and silt fraction of Zenoz kaolin is

about 18% and 60% respectively. Some of the properties for Zenoz kaolin are summarised in Table 1.

Table 1. Index properties of Zenoz kaolin used in the evaluation of models

Parameter	Value
Maximum dry density: kN/m^3	17.4
Optimum water content: %	15.4
Percentage of sand: %	22
Percentage of silt: %	60
Percentage of clay: %	18
Specific gravity	2.65
Liquid limit: %	29
Plastic limit: %	17
Plasticity index: %	12
Classification(USCS)	CL

There are four models used in the evaluation, namely NY, SEB1, BMDJS and the new models. For NY, SEB1 and BMDJS models, the variables are mean net stress, matrix suction, void ratio and degree of saturation. For the new model, suction at air expulsion or air entry is required instead of degree of saturation. The effect of void ratio on the air entry or air expulsion value of suction is not considered. According to Biglari et al. (2011), suction at air expulsion is 5 kPa. The suction at air entry is assumed to be two times of suction at air expulsion. For low plasticity clay, it is observed that suction at air entry is about two times of the suction at air expulsion from the soil water characteristic curve (SWCC) reported by Ng et al. (2009).

The calibration procedures for the models used in the evaluation are described in this section. The parameters A, m, n of NY and the new models are calibrated by fitting the shear modulus at very small strain during an isotropic loading-unloading test for a saturated soil. Parameter k is obtained using shear modulus during an isotropic loading test at a suction of 50 kPa. For SEB1 model, parameter n is taken as 0.5 as adopted in Sawangsuriya et al. (2009) and parameter A are obtained by fitting the shear modulus at very small strain during isotropic loading for saturated soils. Parameter C of SEB1 model is obtained by fitting the shear modulus at very small strain during isotropic loading at a suction of 50 kPa. Parameters for BMDJS model are obtained from Biglari et al. (2011). Model parameters for NY, SEB1, BMDJS and the new models are summarised in Table 2.

4 EVALUATION OF MODELS

Shear modulus at very small strain for commercially available Zenoz kaolin reported by Biglari et al. (2012) is used to evaluate the existing and proposed models. The specimen was prepared using moist tamping method at a water content of about 11.9%, which is 3.5% dry of the optimum from standard Proctor compaction test. The adopted method was intended to prepare samples, which could be brought to a virgin state at relatively low stress. The after compaction suction was 240 kPa. Subsequently, the samples were brought up to net mean stress of 50 kPa.

Fig. 1 shows the shear modulus at very small strain during isotropic loading-unloading test for a saturated soil. As BMDJS, NY and the new models are fitted to shear modulus during loading-unloading, the corresponding predictions agree well with the experimental data. Due to SEB1 model is calibrated using shear modulus during loading, thus a satisfactory prediction is expected. During unloading, SEB1 model underestimates the shear modulus.

The predicted shear modulus during unloading is slightly larger than those during loading attributed to an increase in the value of void ratio function as the soil become denser after loading.

Table 2. Model parameter values used by models for Zenoz kaolin

Parameter	NY model	SEB1 model	BMDJS model	New model
A	1150.21	3000	134.32	2176.12
M	-2.81	-	0.345	-3.05
N	0.380	0.5	0.626	0.375
K	0.260	-	-	0.370
C	-	750	-	-
N	-	-	0.997	-
λ	-	-	0.0725	-
κ	-	-	0.02	-
A	-	-	0.104	-
B	-	-	2.91	-
a'	-	-	0.143	-
b'	-	-	2.355	-
s_{en} : kPa	-	-	-	10*
s_{exp}: kPa	-	-	-	5

* assumed value

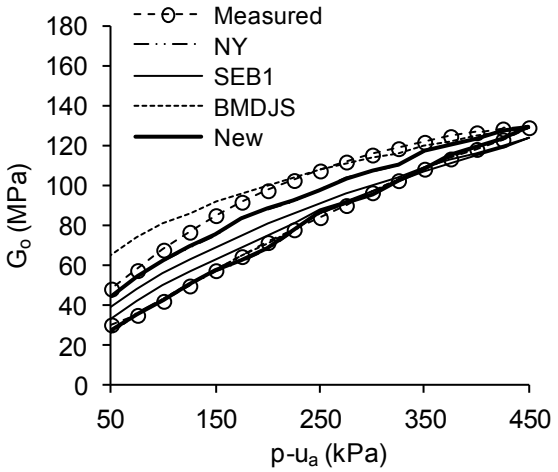

Fig. 1. Prediction of shear modulus at very small strain during isotropic loading-unloading cycle for saturated Zenoz kaolin

Fig. 2 compares the predicted and measured shear modulus at very small strain during an isotropic compression tests at matrix suction of 50 kPa. The specimen experiences plastic compression due to wetting-induced collapse when the after-compaction suction of 240 kPa is reduced to 50 kPa. As all the models are fitted to the measured shear modulus, the corresponding predictions agree well with the experimental data.

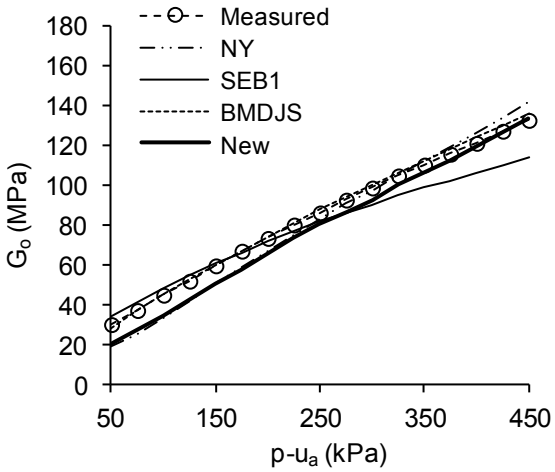

Fig. 2. Prediction of shear modulus at very small strain for unsaturated Zenoz kaolin during isotropic loading at suction of 50 kPa

Fig. 3 compares the predicted and measured shear modulus at very small strain during an isotropic loading-unloading test at matrix suction of 150 kPa. The specimen also experiences plastic compression due to wetting-induced collapse when the after-compaction suction of 240 kPa is reduced to 150 kPa. All the models predict an increasing trend with mean net stress consistent with experimental data. BMDJS and the new models give a good prediction on the shear modulus. NY model slightly underestimates but SEB1 model overestimates the shear modulus.

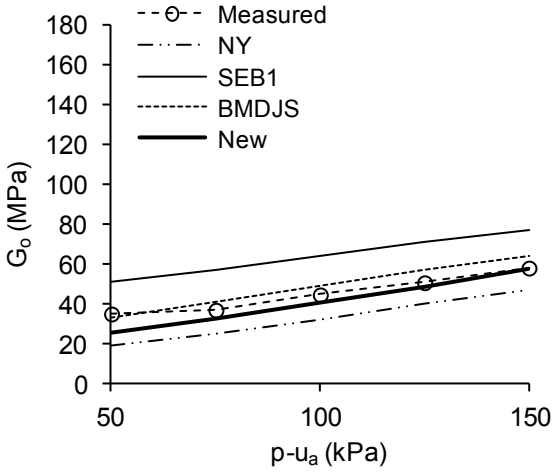

Fig. 3. Prediction of shear modulus at very small strain for unsaturated Zenoz kaolin during isotropic loading at suction of 150 kPa

Fig. 4 shows the variations of shear modulus at very small strain during loading-unloading cycle at suction of 300 kPa. All the models predict a trend and amount of hysteresis consistent with the experimental data. It is found that SEB1 model overestimates the shear modulus the most, while the other models are closer to the data. The difference in predictions is larger than those during isotropic loading test at suction of 150 kPa as suction of 300 kPa is further from the suctions used in the model calibrations.

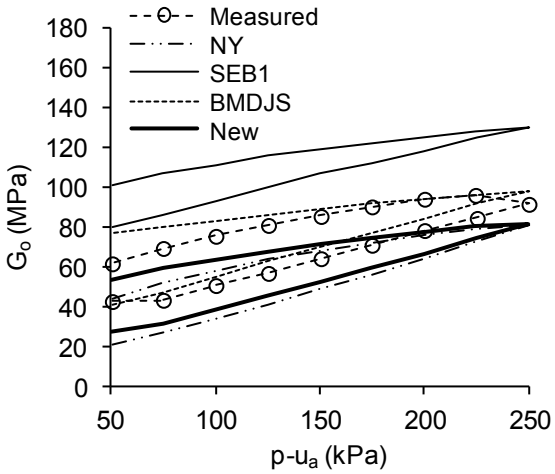

Fig. 4. Prediction of shear modulus at very small strain during isotropic loading-unloading cycle for unsaturated Zenoz kaolin at suction of 300 kPa

Fig. 5 compares the predicted and measured shear modulus at very small strain during wetting for a collapsible unsaturated soil. After equalization at mean net stress and matrix suction of 50 and 300 kPa respectively, the mean net stress is increased to 350 kPa. Under a constant mean net stress, the suction is reduced from 300 kPa to 50 kPa. NY, SEB1, BMDJS model predicts a decreasing trend when the suction was decreased from 300 to 50 kPa in contrast with the experimental data. For NY model, this suggests that the increase in shear modulus due to an increase in value of function ρe^m is unable to compensate the effect of suction reduction. For SEB1 model, this is because the increase in void ratio function does not compensate the reduction of shear modulus due to decreasing in function $S_r s$. For BMDJS models, this is because the increase in void ratio function does not compensate the reduction of shear modulus due to decreasing of average soil skeleton stress and function $h(S_r)$. The predicted shear modulus by the new model increases slightly as suction is reduced from 300 to 150 kPa. As the suction is further reduced to 50 kPa, there is a decreasing trend in the predicted shear modulus. The predicted trend is consistent with the experimental data. As the suction reduces from 300 kPa to 150 kPa, suction at air expulsion instead of air entry is adopted to normalise the suction and while the state lies at the scanning curve the ratio s/s_e is constant. The increase in predicted shear modulus attributed to the increase in void ratio function is more significant than the decrease due to a reduction of average skeleton stress. When the suction is further decreased to 50 kPa, there is a significant decrease in s/s_e value. This results in a decrease in the predicted shear modulus.

5 SUMMARY AND CONCLUSIONS

Several models from different categories, namely NY model proposed by Ng and Yung (2008), SEB1 model suggested by Sawangsuriya et al. (2009), BMDJS model presented by Biglari et al. (2011) and the new model proposed by Wong et al. (2013) have been evaluated. Shear modulus at very small strain for a low plasticity fine grained soils available in the literature are used in the evaluation. NY, BMDJS and new models can be used to predict shear modulus at very small strain in low plasticity fine grained soil due to increase and decrease of mean net stress at constant suction. It is found that NY, SEB1 and BMDJS models predict a contradictory trend with experimental data for wetting-induced collapsible unsaturated soil. Contrary, the new model is able to predict a trend consistent with the experimental data. The new model is evaluated in more detail in Wong et al. (2013).

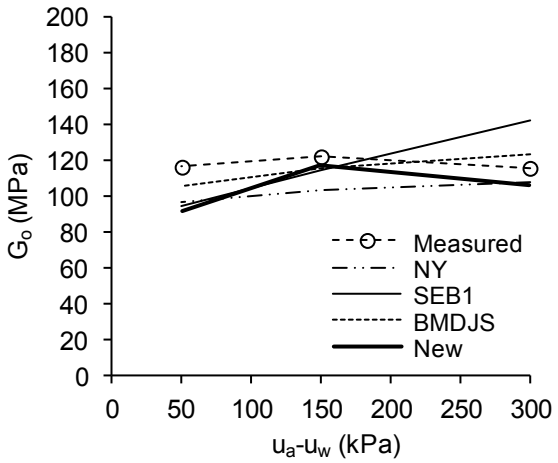

Fig. 5. Prediction of shear modulus at very small strain during wetting for normal consolidated unsaturated Zenoz kaolin

ACKNOWLEDGEMENT

The authors would like to acknowledge Prof. Charles Ng and the whole research group of Hong Kong University of Science and Technology for valuable discussions. Financial support by the research grant GACR P105/12/1705 is greatly appreciated. The first author is supported by a post-doc grant at Charles University in Prague.

REFERENCES

Biglari, M., d'Onofrio, A., Mancuso, C., Jafari, M. K., Shafiee, A., and Ashayeri, I. (2012). "Small-strain stiffness of Zenoz kaolin in unsaturated conditions." Canadian Geotechnical Journal, 49(3), 311-322.

Biglari, M., Mancuso, C., d'Onofrio, A., Jafari, M. K., and Shafiee, A. (2011). "Modelling the initial shear stiffness of unsaturated soils as a function of the coupled effects of the void ratio and the degree of saturation." Computers and Geotechnics, 38(5), 709-720.

Gallipoli, D., Gens, A., Sharma, R., and Vaunat, J. (2003). "An elasto-plastic model for unsaturated soil incorporating the effects of suction and degree of saturation on mechanical behaviour." Geotechnique, 53(1), 123-135.

Khalili, N., and Khabbaz, M. H. (1998). "A unique relationship for Ï‡ for the determination of the shear strength of unsaturated soils." Geotechnique, 48(5), 681-687.

Leong, E. C., Cahyadi, J., and Rahardjo, H. (2006) "Stiffness of a compacted residual soil." Geotechnical Special Publication, 1168-1180.

Ng, C. W. W., Xu, J., and Yung, S. Y. (2009). "Effects of wetting-drying and stress ratio on anisotropic stiffness of an unsaturated soil at very small strains." Canadian Geotechnical Journal, 46(9), 1062-1076.

Ng, C. W. W., and Yung, S. Y. (2008). "Determination of the anisotropic shear stiffness of an unsaturated decomposed soil." Geotechnique, 58(1), 23-35.

Sawangsuriya, A., Edil, T. B., and Bosscher, P. J. (2009). "Modulus-suction-moisture relationship for compacted soils in postcompaction state." Journal of Geotechnical and Geoenvironmental Engineering, 135(10), 1390-1403.

Vassallo, R., Mancuso, C., and Vinale, F. (2007). "Modelling the influence of stress-strain history on the initial shear stiffness of an unsaturated compacted silt." Canadian Geotechnical Journal, 44(4), 463-472.

Wong, K. S., Masin, D., and Ng, C. W. W. (2013). "Modelling of small strain stiffness of unsaturated fine grained soils." In preparation.

ON IMPROVING A SIMPLE ANISOTROPIC CLAY MODEL

A.G. Papadimitriou & G.I. Agapoulaki
Department of Civil Engineering, University of Thessaly, Volos, Greece

ABSTRACT: *The objective of this paper is to present an easy-to-implement constitutive alteration for enhancing the accuracy of the well-established SANICLAY model of Dafalias et al. (2006). The alteration consists of introducing distortional hardening of the yield surface, and thus better taking into account the consolidation history of the soil prior to shearing. Its importance lies firstly on the fact that the constitutive alteration introduces merely one extra model constant, which is easily calibrated (without trial-and-error runs). Hence, this alteration adds to the already favorable balance between accuracy and simplicity of the original model. In addition, the nature of the proposed alteration has generic value and may be easily introduced to a number of existing constitutive models that employ the same yield surface shape thus providing similarly enhanced accuracy*.

1 INTRODUCTION

State-of-the-art constitutive models for geomaterials are not being used in geotechnical practice, mainly because they have not been implemented in numerical codes. In our opinion, the reason for this is that code developers believe that even if they were provided to practitioners for use, these models would not eventually be used because of their complicated nature. On the contrary, simple, yet outdated, constitutive models (e.g. Modified Cam Clay, Burland 1965) that are readily available in numerical codes are continuously being used in geotechnical projects at the cost of accuracy, or equivalently at the cost of increased factors of safety in design.

In between these two extremes lie a number of constitutive models, which bridge the gap between accuracy and simplicity, and are now trying to find their way into numerical codes. One of these models is SANICLAY, proposed by Dafalias et al. (2006). It is a non-associative flow rule model, which is characterized by an isotropically and rotationally hardening yield surface. It builds on a modification of the associative flow rule isotropic MCC model, at the expense of merely three (3) extra constants, but to the benefit of significantly enhanced accuracy. The common ground of the two (2) models is the shape of the plastic potential surface, whose rotational hardening capability originates from Dafalias (1986) as the simplest possible energetic extension of the MCC model from isotropic to anisotropic response. Since its original proposal in 1986, the foregoing shape and hardening capability of the plastic potential surface (and of the yield surface in cases of associative flow rule) have acted as the constitutive link of a great number of (also relatively simple) models (e.g. Dafalias 1987, Korhonen and Lojander 1987, Thevanayagam and Chameau 1992, Newson and Davies 1996, Wheeler et al. 1999, Wheeler et al. 2003, Taiebat et al. 2010).

This paper focuses on the hardening rules of this surface, when it acts as the yield surface of simple models (as the ones mentioned above) for accurately simulating the consolidation history and its effects on the shearing that follows. For this purpose, it adds a distortional hardening capability to the yield surface of SANICLAY, always aiming at retaining its basic characteristic: simplicity. To do, section 2 presents briefly the equations of SANICLAY (which acts as a reference model herein), while section 3 presents the experimental motivation behind the proposed addition of a distortional hardening rule (which is the subject of section 4). Then, section 5 presents the calibration procedure, while the paper ends with section 6, where simulations exhibiting the enhanced accuracy are presented.

2 SANICLAY AS A REFERENCE MODEL

SANICLAY (Dafalias et al. 2006) is a simple anisotropic plasticity model, which provides quite satisfactory simulation of the rate-independent behavior of normally and slightly overconsolidated sensitive clays that do not exhibit destructuration during loading. Simulations become less accurate for high OCR values. It is characterized by a non associative flow rule, which is introduced by adopting a yield surface different than the plastic potential surface. Besides the isotropic hardening of the yield surface, both surfaces evolve according to a rotational hardening rule (which also introduces distortion to surfaces).

For simplicity, the formulation of SANICLAY is presented here in the triaxial space, in terms of effective stress quantities $p = (\sigma_a + 2\sigma_r)/3$, $q = (\sigma_a - \sigma_r)$ and strain quantities $\varepsilon_v = (\varepsilon_a + 2\varepsilon_r)$, $\varepsilon_q = 2(\varepsilon_a - \varepsilon_r)/3$, where subscripts a and r denote the axial and the radial directions, respectively.

2.1 Elastic strain rate

With the total strain rate components' additive decomposition into elastic (superscript e) and plastic (superscript p) parts, the elastic strain rate adopts the isotropic hypoelastic relations:

$$\dot{\varepsilon}_v^e = \frac{\dot{p}}{K} \quad ; \quad \dot{\varepsilon}_q^e = \frac{\dot{q}}{3G} \tag{1}$$

The elastic bulk modulus adopts its form from the MCC model, $K = p(1 + e_{in})/\kappa$, with e_{in} the initial values of the void ratio e and κ the slope of the rebound line in the $e - \ln p$ space. Concurrently, the elastic shear modulus G is expressed in terms of K and a constant Poisson's ratio v.

2.2 Flow rule and model surfaces

The corresponding equations for the volumetric and deviatoric plastic strain rates are given by the flow rule:

$$\dot{\varepsilon}_v^p = \langle L \rangle \frac{\partial g}{\partial p} \quad ; \quad \dot{\varepsilon}_q^p = \langle L \rangle \frac{\partial g}{\partial q} \tag{2}$$

where g is the plastic potential and L is the loading index (or plastic multiplier) to be specified in the sequel. L is enclosed in the Macauley brackets $< >$ in order to signal the events of plastic loading when $L > 0$ and $< L > = L$, and elastic unloading when $L \leq 0$ and $< L > = 0$.

For SANICLAY, the plastic potential surface has the shape of a rotated (and distorted) ellipse and is analytically described by (see Fig.1):

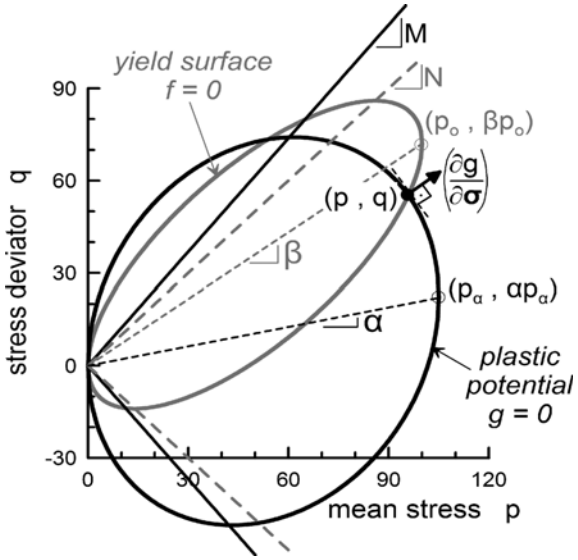

Figure 1: SANICLAY model surfaces in triaxial stress space (from Dafalias et al. 2006)

$$g = \left(q - pa\right)^2 - \left(M^2 - a^2\right) p \left(p_a - p\right) = 0 \tag{3}$$

where M is the critical stress ratio, α is a non-dimensional variable which introduces anisotropy in the plastic potential and p_α is the value of p at $q=p\alpha$, so that Eq. (3) is satisfied for (p, q) values at yield. Although a single M may be used for reasons of simplicity, for greater accuracy, $M = M_c$ when the deviatoric stress ratio $\eta = q/p > \alpha$, and $M = M_e$ when $\eta = q/p < \alpha$, where $M_c \geq M_e$ are SANICLAY constants (as shown in Fig.1). Clearly, one must have $|\alpha| < M$ for real-valued (p, q) in Eq. (3).

The SANICLAY yield surface is expressed similarly to the plastic potential by:

$$f = \left(q - p\beta\right)^2 - \left(N^2 - \beta^2\right) p \left(p_o - p\right) = 0 \tag{4}$$

where p_o, β and N respectively substitute for p_α, α and M of Eq. (3).

In particular, β is the rotational hardening variable of the yield surface that introduces anisotropy the same way that variable α does in the plastic potential. N is a SANICLAY constant similar in nature to M, but taken the same value in compression and extension for simplicity without loss of accuracy. Clearly one must have $|\beta| < N$ for real-valued (p, q) in Eq. (4). Observe in Fig.1 that q on f=0 at the deviatoric stress-ratio M is not the peak q stress, the latter occurring at deviatoric stress-ratio N. This is exactly the property that allows for the undrained softening in compression to take place after K_o consolidation, and the very reason for introducing an f different than g.

2.3 Rate evolution equations for the internal variables

For the p_o variable the classical evolution law of critical state soil mechanics is given by:

$$\dot{p}_o = \langle L \rangle \bar{p}_o = \langle L \rangle \left(\frac{1 + e_{in}}{\lambda - \kappa} \right) p_o \left(\frac{\partial g}{\partial p} \right) \tag{5}$$

where e_{in} is the initial value of the void ratio e and λ, κ are the slopes of the normal compression and rebound lines, respectively, in the e-ln$p$ space, while L is the loading index that is related to the partial derivatives of the $f = 0$ function in terms of p, q, p_o, and β, to the loading increments $\dot{p}$ and $\dot{q}$ and the forms of $\overline{p}_o$ (Eq. 5) and $\overline{\beta}$ (see below, in Eq. 7), based on standards methods on plasticity (see section 2.4).

The rate evolution equation for α is described as:

$$\dot{\alpha} = \langle L \rangle \overline{a} = \langle L \rangle \left(\frac{1+e_{in}}{\lambda - \kappa} \right) C \left(\frac{p}{p_o} \right)^2 \left| \frac{\partial g}{\partial p} \right| |\eta - x\alpha| \left(\alpha^b - \alpha \right) \tag{6}$$

$$\eta / x > \alpha \Rightarrow \alpha^b = M_c \;\; ; \;\; \eta / x < \alpha \Rightarrow \alpha^b = -M_e$$

where C is a SANICLAY constant, that also controls the rate evolution equation for the β variable (in Eq. 5):

$$\dot{\beta} = \langle L \rangle \overline{\beta} = \langle L \rangle \left(\frac{1+e_{in}}{\lambda - \kappa} \right) C \left(\frac{p}{p_o} \right)^2 \left| \frac{\partial g}{\partial p} \right| |\eta - \beta| \left(\beta^b - \beta \right) \tag{7}$$

$$\eta > \beta \Rightarrow \beta^b = N \;\; ; \;\; \eta < \beta \Rightarrow \beta^b = -N$$

Note that the $(\partial g / \partial p)$ term in Eqs (5) through (7) introduces the volumetric plastic strain rate and diminishes the evolution of all surfaces at the critical state. Furthermore, observe the operation of "*attractors*" α^b and β^b in Eqs (6) and (7), that enforce the aforementioned conditions of $|a| < M$ and $|\beta| < N$ for real valued (p, q) in Eqs (3) and (4), respectively.

2.4 Flow rule and model surfaces

For the completion of the model, the determination of the loading index L is obtained by standard methods of plasticity, whereby the consistency condition $\dot{f} = 0$ is applied to Eq. (4) and in conjunction with Eqs (5) and (7) yields:

$$L = \frac{1}{K_p} \left(\frac{\partial f}{\partial p} \dot{p} + \frac{\partial f}{\partial q} \dot{q} \right) \tag{8}$$

$$K_p = -\left(\frac{\partial f}{\partial p_o} \overline{p}_o + \frac{\partial f}{\partial \beta} \overline{\beta} \right) \tag{9}$$

with the values of $\overline{p}_o$ and $\overline{\beta}$ clearly defined in Eqs (5) and (7), respectively.

3 EXPERIMENTAL MOTIVATION

As presented in detail in Dafalias et al. (2006), SANICLAY leads to rather accurate simulations for low OCR values, but its simulations for high OCR values (3 and beyond) are qualitatively similar to those produced by the MCC model. In other words, for high OCR values, the SANICLAY leads to overprediction of yield stresses and hence stiffer overall response in the early stages of loading, something that is especially true when shearing initiates after isotropic consolidation.

A possible remedy for these shortcomings is a change in the form of the yield surface equation $f = 0$, which controls the undrained effective stress path to a large degree. Papadimitriou et al. (2010) offered alternative forms for the $f = 0$ function (i.e. alternative

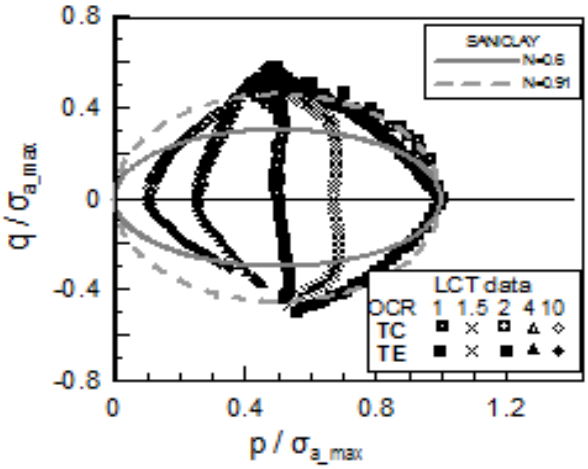

Figure 2: Comparison of SANICLAY yield surface shapes for $\beta = 0$ and $N = 0.6$ and 0.91 to effective stress paths from undrained triaxial tests after isotropic consolidation and OCR = 1 to 10 on LCT (data: Gens 1982).

forms for Eq. 4), aiming to provide increased accuracy to SANICLAY. Here, a similar but not identical approach is followed, i.e. the target is to control the undrained effective stress path by changing the shape of the yield surface, yet without changing the form of Eq. (4). The required possible changes may be envisioned by first solving Eq. (4) for real values of q, which yields:

$$q_{1,2} = p\beta \pm \sqrt{\left(N^2 - \beta^2\right) p\left(p_o - p\right)} \tag{10}$$

Observe in Eq. (10) that the term under the square root reduces to zero for $|\beta| = N$, thus reducing the yield surface to the $q = p\beta$ line. Hence, constant N is practically the maximum value that $|\beta|$ should be allowed to take, otherwise the yield surface ceases to "*exist*" as a convex surface. This limitation of Eq. (4) is taken into account in the model by the last term in parentheses of Eq. (7), as detailed in Dafalias et al. (2006) and is therefore not explained further herein. What is of interest here is that the term under the square root is larger for $\beta = 0$, than for any other value of β, negative or positive, where $N > |\beta| >> 0$. Qualitatively, this means that for a constant N, the yield surface for $\beta = 0$ is quite "*taller*" in the (p, q) space, as compared to what occurs for any other value of β. Hence, if constant N is calibrated for anisotropic consolidated specimens (e.g. $N = 0.91$ after 1D consolidation of Lower Cromer Till (LCT) clay; see Dafalias et al. 2006), the yield surface for $\beta = 0$ is quite "*tall*", and potentially "*taller*" than what it should be on the basis of experimental data. For example, Fig. 2 compares the form of Eq. (4) for $N = 0.91$ and $\beta = 0$, to the effective stress paths from undrained triaxial compression and extension tests on LCT clay (for OCR values ranging from 1 to 10), following isotropic consolidation (Gens 1982). Observe, that the large majority of the experimental data plot within the yield surface shape for $N = 0.91$. Yet, the shapes of the effective stress paths clearly denote yielding at q values much lower than what the yield surface for $N = 0.91$ implies (e.g. yielding for the triaxial compression and extension tests and OCR = 1.5, 2.0 may be located where the initially (almost) p = constant effective stress paths "*turn*" towards failure). From the point of view of modelling, employing $N = 0.91$ for simulating such tests would lead to an over-overestimation of the yield stresses and to an overall response that is stiffer than what the data show, at least in the initial stages of loading. Hence, based on this figure, a more appropriate yield surface shape for these isotropically

consolidated samples could potentially be obtained by employing Eq. (4) with a smaller N value, like $N = 0.6$ also depicted in Fig. 2.

Nevertheless, while this $N = 0.6$ seems appropriate for isotropically consolidated samples, it is considered too low for K_o-consolidated samples that require $N = 0.91$ (see Dafalias et al. 2006 for calibration process). In practice, using such a low value of N would set, via Eq. (7), a rather low maximum value of $|\beta| = N = 0.6$ (since $\beta^b = N$). Hence, at the end of anisotropic consolidation (i.e. consolidation with constant stress ratio $K = \sigma_r/\sigma_a < 1$), the β would not necessarily coincide with the constant deviatoric stress ratio at consolidation $\eta_K = 3(1-K)/(1+2K)$. This may occur if $\eta_K > N$, as for example for K_o-consolidation of LCT for which $K = K_o = 0.49$ and $\eta_K = \eta_{Ko} = 0.77 > 0.6$ (= N). In other words, the yield surface would not "*align*" along the applied constant η_K value during K_o-consolidation, and would be very "*thin*" due to the relatively low N value (see Eq. 10). More importantly, the fact that N (= 0.6) << M_c (= 1.18 for LCT clay) would lead to excessive post-peak softening response for triaxial compression tests following K_o-consolidation.

Hence, as is, the SANICLAY model is unable to provide similarly accurate predictions for shearing after both isotropic and anisotropic consolidation with a single set of model constants. In other words, given its simplicity, one should probably calibrate the model according to the consolidation history in the application at hand.

4 INTRODUCING DISTORTIONAL HARDENING OF THE YIELD SURFACE

In concept, the experimentally depicted shortcoming of SANICLAY simulations may be remedied if the N of Eq. (4) is not a model constant but a model variable. In particular, it is expected that model simulations would ameliorate if the N was lower when $\beta = 0$ (e.g. $N = 0.6$ for Lower Cromer Till; see Fig. 2) and if it increased when $|\beta|$ increased (e.g. $N = 0.91$ for the same material after K_o-consolidation; see Dafalias et al. 2006). In other words, one could devise a relation between N and $|\beta|$, as for example a simple linear relation:

$$N = N_I + \left|\frac{\beta}{\beta_K}\right|\left(N_K - N_I\right) \tag{11}$$

where N_I is the value of N for isotropically consolidated specimens (consolidation with stress-ratio $K = 1$ and/or $q = 0$) and N_K the value of N for anisotropically consolidated specimens (consolidation with constant $K < 1$ and/or constant $\eta_K = q/p > 0$). In order for Eq. (11) to yield the required results for N, the parameter β_K should be set equal to the applied (and constant) η_K of the anisotropic consolidation path. Setting $\beta_K = \eta_K$ implies also that the yield surface will be allowed to "*align*" along the applied η_K of the anisotropic consolidation path, as successfully proposed in the original SANICLAY model.

In order to show how Eq. (11) works, it may be applied for the LCT data of Gens (1982). In this case, the anisotropic consolidation is 1-D compression (or K_o-consolidation) and hence $K = K_o$ and $\beta_K = \eta_{Ko}$, which for LCT clay leads to $\beta_K = \eta_{Ko} = 0.77$ (due to $K_o = 0.49$; see Dafalias et al. 2006). Then, model constant $N_I = 0.6$, based on the calibration procedure of Fig. 2 on the basis of isotropically consolidated undrained triaxial test results, while model constant $N_K = 0.91$, based on the calibration procedure presented in Dafalias et al. (2006) on the basis of K_o-consolidated undrained triaxial tests. It should be underlined here that N_K and β_K should correspond to the same anisotropic consolidation path, yet only N_K is a model constant, since β_K is calibrated on the basis of K_o.

Based on the above, it is clear that $N_K \geq N_I$, with this inequality depicting a general trend for all clays. Thus, Eq. (11) describes a generally increasing linear function of N as a function of $|\beta|$, with a minimum value of $N = N_I$ (for $\beta = 0$).

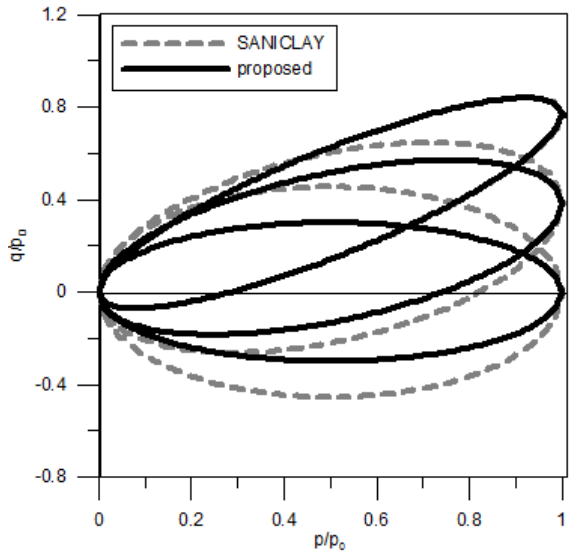

Figure 3: Effect of the linear N-$|\beta|$ relation on the yield surface shape for $\beta = 0$, 0.385 and 0.77 (for $N_I = 0.6$, $N_K = 0.91$, $\beta_K = 0.77$) and comparison to the yield surfaces of SANICLAY for the same β values and $N = 0.91$.

Figure 3 presents an example of the effect of the linear relation of Eq. (11) on the shape of the yield surface for three (3) distinct values of β, i.e. $\beta = 0$, $\beta = \beta_K/2 = 0.385$, $\beta = \beta_K = 0.77$. The depicted yield surfaces correspond to the values for LCT clay, i.e. $N_I = 0.6$, $N_K = 0.91$. For comparison purposes, the same figure includes the yield surface shapes of SANICLAY for the same β values and $N = N_K = 0.91$. Observe that for $\beta = 0.77$, the two yield surface shapes coincide, while the difference between the 2 yield surface shapes increase as β decreases to zero. In all cases, the yield surfaces of SANICLAY are generally "*taller*" than what procures by employing Eq. (11), at least for the usual values of $\beta \leq \beta_K$.

While Eq. (11) describes the desired shapes of the yield surface for various values of β, it cannot be used directly for changing the N value of the $f = 0$ equation (Eq. 4), since it would lead to a violation of the consistency condition. Therefore, in order to implement this linear relation between N and $|\beta|$ in the constitutive model, variable N must be considered an additional hardening parameter of the yield surface (on top of the isotropic and rotational parameters p_o and β, respectively). Given its effect on the yield surface shape, Fig. 2, the N may be considered as a distortional hardening parameter, with a rate equation given by:

$$\dot{N} = \langle L \rangle \bar{N} \tag{12}$$

In order to define this equation in a manner consistent with the linear variation of Eq. (11), one may consider that the clay has zero strength and stresses at slurry with $p = p_o = 0$, $q = 0$, $\beta = \alpha = 0$. Hence, at slurry, the (initial) value of N is $N = N_I$ (for zero stresses and $\beta = 0$). In comparison to β, which takes both positive and negative values, N is always positive, with a minimum value of $N = N_I$. Yet, its rate of evolution may be either positive (in cases that the $|\beta|$ increases) or negative (in cases that the |β| decreases). Given that $\dot{N}$ is thus related to the rate of $|\beta|$ and not the rate of β itself, its definition, in combination with Eq. (12), is given by:

$$\bar{N} = \begin{cases} \left| \dfrac{N_K - N_I}{\beta_K} \right| \left| \bar{\beta} \right| & , \quad if \;\; \beta\bar{\beta} \geq 0 \\ -\left| \dfrac{N_K - N_I}{\beta_K} \right| \left| \bar{\beta} \right| & , \quad if \;\; \beta\bar{\beta} < 0 \end{cases} \tag{13}$$

The need for the slightly complicated nature of Eq. (13) becomes clear if one considers the case of triaxial extension after K_o-consolidation. In particular, K_o-consolidation of a sample from slurry imposes an increase of β from zero to β_K, and thus an increase of N from N_I to N_K respectively, via the use of the upper part of Eq. (13). After the end of K_o-consolidation, application of triaxial extension loading leads to a decrease of the positive-valued β and thus to a respective decrease of N relative to its value N_K, via the use of the lower part of Eq.(13). This continues until $\beta = 0$, which brings N back to its initial value $N = N_I$. If triaxial extension loading continues, the β continues to decrease and may become negative. As a result, the $|\beta|$ starts increasing, thus leading to an increase of N again, which is materialized via the use of the upper part of Eq.(13).

All the above have made N a distortional hardening parameter of the model. Hence, its appearance in Eqs (8) and (9), via the yield surface derivatives with respect to p and p_o, as well as Eq. (7), via the value of "*attractor*" β^b, has no longer a fixed value defined as a model constant. More importantly, a new derivative should be estimated, i.e. $\partial f / \partial N$, for use in the consistency condition to provide an enhanced version of Eq. (9) for the plastic modulus K_p, namely:

$$K_p = -\left(\frac{\partial f}{\partial p_o} \overline{p}_o + \frac{\partial f}{\partial \beta} \overline{\beta} + \frac{\partial f}{\partial N} \overline{N} \right) \tag{14}$$

Other than the introduction of distortional hardening of the yield surface, the enhanced SANICLAY variant described herein retains the forms of Eqs (1) through (8), supplemented by Eqs (12) through (14). Nevertheless, it should be underlined that the enhanced version of SANICLAY degenerates to the original formulation by merely setting $N_K = N_I = N$.

5 MODEL CALIBRATION

The SANICLAY model (Dafalias et al. 2006) requires calibration of eight (8) constants, i.e. the five (5) constants of the MCC model (M_c, M_e, κ, λ, v) and three (3) extra constants (N, C, x). Based on its enhancement presented above, the N is no longer constant, and its variation is controlled by two (2) model constants, N_K and N_I, via Eq. (11), thus increasing the total number of constants to nine (9).

In general, the calibration of these constants is straightforward, since it requires data from well established laboratory tests, namely:

- One-dimensional (K_o) or preferably isotropic consolidation tests to stresses significantly larger than the preconsolidation pressure with at least one unload-reload cycle using an oedometer or a triaxial device (for constants κ, λ)
- Lateral stress measurements during one-dimensional (K_o) compression and swelling reaching stresses significantly larger than the preconsolidation pressure using either a computer controlled triaxial device or a lateral stress oedometer (for constants x, v)
- Undrained triaxial compression (CK_oUC) and extension (CK_oUE) tests on normally K_o-consolidated clay (for constants N_K, C), and similar triaxial tests (CIUC, CIUE) following isotropic consolidation, preferably for OCR > 1 (for constant N_I).
- All available shear tests can be used for estimation of critical state strength constants M_c and M_e.

The details of the calibration process for constants M_c, M_e, κ, λ, v and x is detailed in Dafalias et al. (2006) and will not be repeated here. The emphasis here will be set on the two (2) new model constants N_K and N_I, and on C, the only model constant that requires trial and error runs. In particular, their calibration is presented with reference to the tests on Lower

Cromer Till (LCT), based on the work of Gens (1982). LCT is classified as a low plasticity sandy silty-clay (CL, with liquid limit $w_L = 25\%$ and plasticity index $I_P = 13\%$), with the main clay minerals being calcite and illite. The tests on LCT were all performed on samples consolidated from a slurry with an initial water content $w = 31\%$. Table 1 summarizes the model constants and their values for LCT clay.

Table 1. Model Constants and their values for LCT clay

Constant	Description	Value
M_c	Value of η at critical state in compression	1.18
M_e	Value of η at critical state in extension	0.86
κ	Compressibility of clay with OCR > 1	0.009
λ	Compressibility of NC clay	0.063
ν	Elastic Poisson's ratio	0.2
x	Saturation limit of anisotropy (for η=constant paths)	1.56
N_I	Shape of yield surface for β=0	0.6
N_K	Shape of yield surface for high β values	0.91
C	Rate of evolution of anisotropy	36

The calibration of constant N_K is identical to that of constant N of SANICLAY. It requires the data from an undrained shearing test on a normally consolidated sample. In such a path, the total volumetric strain rate is zero, a condition that in conjunction with the assumption of a non-rotating yield surface yields the equation of the effective stress path in the p – η space by integration of the corresponding differential equation (see Dafalias 1986, Dafalias et al 2002). In particular, of interest for the calibration of N_K is not the whole effective stress path, but two pairs of (p, η) on it, the one at the end of consolidation (p_{in}, η_{in}) and the other at critical state (p_f, η_f). To be consistent with the assumption of a non-rotating yield surface (β = constant), one should require that the selected η_{in} is not far from the η_f (e.g. $2\eta_{in} > \eta_f$), so that from Eq. (7) the induced rate of β is not large, thus, satisfying approximately the foregoing assumption. Practically, given the available tests for calibration of the model constants it is the CK_oUC test on normally consolidated clay that is suitable for the purpose at hand. For this case, the (p_{in}, η_{in}) is given by:

$$\eta_{in} = \beta_{Ko} = \eta_{Ko} = 3\left(1 - K_o\right) / \left(1 + 2K_o\right) \qquad \text{and} \qquad p_{in} = p_{Ko} \tag{15}$$

This pair, along with the other (p_f, $\eta_f = M_c$) pair are inserted in the aforementioned equation of the undrained stress path (Dafalias 1986, Dafalias et al 2002), one has:

$$\frac{p_f}{p_{Ko}} = \left(\frac{N_K{}^2 - \eta_{Ko}{}^2}{N_K{}^2 - 2\eta_{Ko} M_c + M_c{}^2} \right)^{1 - \frac{\kappa}{\lambda}} \tag{16}$$

Hence, one merely needs to solve Eq. (16) for N_K, given data of a CK_oUC test on normally consolidated clay. As deduced by Eq. (16) the smaller the N_K compared to M_c the more softening SANICLAY and its enhanced version predict. Doing so for LCT clay, provided a value of $N_K = 0.91$ (given the values of model constants in Table 1).

The calibration of constant N_I may be performed by comparing effective stress path data of undrained tests in (preferably) over-consolidated samples (OCR > 1) to candidate yield surface shapes, by using Eq. (4), for $\beta = 0$ and various values of N. For example, Fig. 2 compares two (2) such yield surface shapes, for $\beta = 0$ and $N = 0.6$ and 0.91 to effective stress path data of undrained triaxial compression and extension tests for OCRs from 1 up to 10.

Based on this comparison, a value of $N = 0.6$ seems to be the most appropriate as the one delineating the elastic region (especially for OCR = 2), and this value is set to be the appropriate value for N_I. Higher values of N_I over-estimate the elastic region and lead to simulations of a stiffer overall response, while smaller values have the opposite effect.

Finally, the calibration of constant C requires the execution of trial-and-error runs, having all other constants calibrated in advance. Observe that C quantifies the rate of rotation of the plastic potential surface and the yield surface via Eqs (6) and (7), respectively. Hence, tests appropriate for its calibration are those that induce significant surface rotation, or in other words, tests for which the η_{in} is far from η_f of the effective stress path, and possibly of opposite sign. Practically, a CK_oUE test on normally consolidated clay is very suitable for the purpose at hand. As presented in detail by Dafalias et al (2006), the higher the value of C the higher the predicted undrained strength in triaxial extension in such tests. Performing such trial-and-error runs with the enhanced SANICLAY model, led to a value of $C = 36$. Note, that for the same clay, trial-and-error runs with the original SANICLAY model led to a value of $C = 16$. This need for increase in the value of C for the enhanced model originates from the fact that the enhanced model operates with a comparatively "*shorter*" yield surface during its rotation (see Fig. 3, their difference for $\beta = \beta_K / 2$ and $\beta = 0$). Hence, the enhanced model requires a comparatively higher value of C to attain a similarly high value of undrained strength in triaxial extension.

6 ENHANCED MODEL PERFORMANCE

Based on the above, the enhancement of SANICLAY proposed herein focuses on the yield surface, and introduces changes to its shape on the basis of the consolidation history (via the value of N which varies on the basis of β; see Eq. 11). Nevertheless, the large majority of constitutive equations of the enhanced model are identical to those of SANICLAY. Hence, the enhanced model is expected to provide simulations qualitatively similar to those of the original model.

Of interest here is to depict the quantitative differences that the proposed model enhancement provides. Given that the shape of the yield surface for shearing after K_o-consolidation is calibrated identically to what holds for SANICLAY ($N_K = 0.91$ = constant N), the enhanced model is not expected to show significantly different response in such tests. On the contrary, quantitative differences are to be expected for shearing after isotropic consolidation. Hence, due to length limitations, this paper presents comparison of simulations with the original and the enhanced SANICLAY model only for the latter type of tests.

In particular, Fig. 4 compares test data from undrained triaxial compression and extension tests after isotropic consolidation (CIU tests) and OCR = 1, 2 and 10 (different symbols), to pertinent simulations performed with the original (dashed lines) and the enhanced SANICLAY (solid lines) models. More specifically, Fig. 4a performs the comparison in terms of effective stress paths normalized over the maximum axial stress during consolidation σ_{a_max}, whereas Fig. 4b does the same in terms of the deviatoric stress-strain response. The comparison included in this figure shows that the original model overpredicts the undrained strength in both compression and extension, but simulations with the enhanced model are much closer to the data in practically all cases.

Similarly, Fig. 5 compares test data from drained triaxial compression tests after isotropic consolidation (CID tests) and OCR = 1 and 10 (different symbols), to pertinent simulations performed with the original (dashed lines) and the enhanced SANICLAY (solid lines) models.

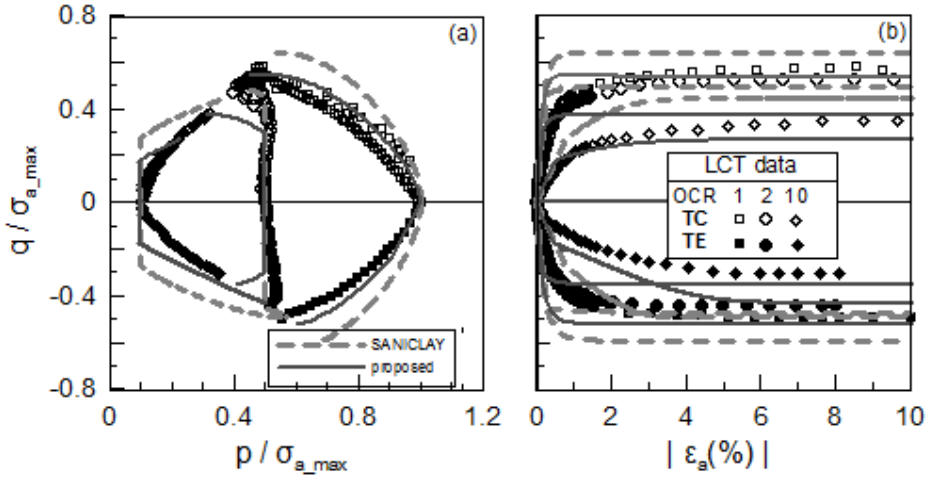

Figure 4: Comparison of data to simulations with the use of SANICLAY and its proposed enhanced version for CIU tests on LCT and various OCR values, in terms of: a) effective stress path, b) stress-strain response

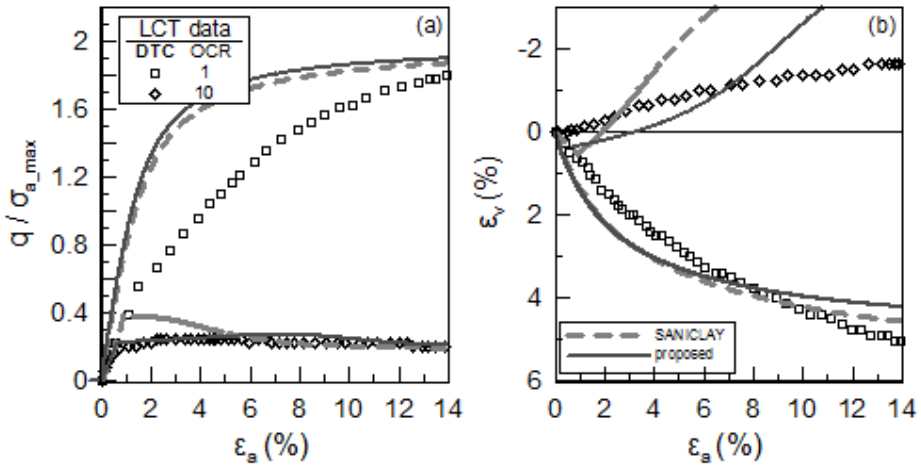

Figure 5: Comparison of data to simulations with the use of the SANICLAY and its proposed enhanced version for CID tests on LCT and various OCR values, in terms of: a) stress-strain response, b) relation between volumetric and deviatoric strains.

More specifically, Fig. 5a performs the comparison in terms of the deviatoric stress-strain response, whereas Fig. 5b does the same in terms of the relation between volumetric and deviatoric strains during loading. This comparison shows that for OCR = 10 the original model overpredicts the peak strength and the dilatancybut simulations with the enhanced model are much closer to the data. On the contrary, the simulations for OCR = 1 are almost identical, and hence there is no benefit from using the enhanced formulation.

7 CONCLUSIONS

The proposed change in constitutive equations (introduction of distortional hardening of the yield surface) is analytically simple. It comes at the cost of one extra model constant, which is directly measured and does not require trial-and-error runs. Moreover, appropriate calibration of this extra constant makes the new model variant degenerate to its original version. Hence, the proposed constitutive alteration does not alter the philosophy of the

original SANICLAY model, i.e. its emphasis on simplicity. More importantly, based on the proposed calibration procedure, the enhanced model provides improved accuracy in shearing following isotropic consolidation, while it is expected to retain the accuracy of the original formulation in shearing following anisotropic consolidation (e.g. K_o-consolidation).

In addition, the nature of the proposed constitutive alteration has generic value and may be easily introduced to a number of existing constitutive models that employ the same yield surface shape and rotational hardening capability thus providing similarly enhanced accuracy for clay response. Note, that the usability of such simple anisotropic models is even wider, if one takes into account that they may also be potentially used for simulating the cyclic/dynamic clay response (e.g. Taiebat et al 2011), but also of other geomaterials whose cyclic response may be considered as potentially reminiscent of clay response (e.g. sand stabilized with colloidal silica; see overview in Papadimitriou and Agapoulaki 2013).

ACKNOWLEDGEMENT

The authors would like to sincerely thank Professor Yannis F. Dafalias, University of California Davis & National Technical University of Athens, for his fruitful insights to this work. This research has been co-financed by the European Union (European Social Fund, ESF) and Greek national funds through the Operational Program "Education and Lifelong Learning" of the National Strategic Reference Framework (NSRF) - Research Funding Program: Thales. Investing in knowledge society through the European Social Fund.

REFERENCES

Dafalias YF. (1986), “An anisotropic critical state soil plasticity model”, Mechanics Research Communications, 13(6): 341–347

Dafalias YF. (1987), “An anisotropic critical state clay plasticity model”, Proceedings of 2nd IC on Constitutive Laws for Engineering Materials: Theory and Applications, New York, Desai CS et al. (eds). Elsevier: Amsterdam, 513–521.

Dafalias YF, Manzari MT, Akaishi M. (2002), “A simple anisotropic clay plasticity model”, Mechanics Research Communications, 29(6): 241–245

Dafalias YF, Manzari MT, Papadimitriou AG. (2006), “SANICLAY: simple anisotropic clay plasticity model”, International Journal for Numerical and Analytical Methods in Geomechanics, 30(12): 1231–1257.

Gens A. (1982), “Stress–strain and strength of a low plasticity clay”, Ph.D. Thesis, Imperial College, London University, p. 856

Korhonen KH, Lojander M. (1987), “Yielding of perno clay”, Proceedings of 2nd IC on Constitutive Laws for Engineering Materials: Theory and Applications, New York, Desai CS et al. (eds), vol. II. Elsevier: Amsterdam, 1249–1255.

Newson TA, Davies MCR. (1996), “A rotational hardening constitutive model for anisotropically consolidated clay”, Soils and Foundations, 36(3): 13–20.

Papadimitriou A. G., Agapoulaki K. I. (2013), “Mechanical response and simulation of sands stabilized with colloidal silica against liquefaction”, Proceedings, International Conference

on Earthquake Geotechnical Engineering: From Case History to Practice, Istanbul, June 17-19

Papadimitriou A. G., Vranna A., Dafalias Y. F., Manzari M. T. (2010), "Effect of yield surface shape on the simulated elasto-plastic response of cohesive soils", Proceedings, 7th European Conference on Numerical Methods in Geotechnical Engineering, Trondheim, Norway, June 2-4

Taiebat M., Dafalias YF., Peek R. (2010), "A destructuration theory and its application to SANICLAY model", International Journal for Numerical and Analytical Methods in Geomechanics; 34: 1009-1040

Taiebat M., Kaynia A., Dafalias YF. (2011), "Application of an anisotropic model for structured clay to seismic slope stability", Journal of Geotechnical and Geoenvironmental Engineering, ASCE, 137(5): 492-504

Thevanayagam S, Chameau JL. (1992), "Modelling anisotropy of clays at critical state", Journal of Engineering Mechanics (ASCE) 118(4): 786–806.

Wheeler SJ, Karstunen M, Naatanen A. (1999), "Anisotropic hardening model for normally consolidated soft clays", Proceedings of NUMOG VII on Numerical Models in Geomechanics, Pande GN, Pietruszczak S, Schweiger HF (eds), vol. II. Balkema: Rotterdam, 33–40.

Wheeler SJ, Naatanen A, Karstunen M, Lojander M. (2003), "An anisotropic elastoplastic model for soft clays", Canadian Geotechnical Journal, 40: 403–418

GEOMECHANICAL BEHAVIOUR OF ROCK SALT: ASSESSMENT OF EXISTING MODELS

Kavan Khaledi
Faculty of Civil and Environmental Engineering, Chair for Foundation Engineering, Soil and Rock Mechanics, Ruhr-Universität Bochum, Bochum, Germany

Maria Datcheva
Institute of Mechanics, Bulgarian Academy of Sciences, Sofia, Bulgaria

Tom Schanz
Faculty of Civil and Environmental Engineering, Chair for Foundation Engineering, Soil and Rock Mechanics, Ruhr-Universität Bochum, Bochum, Germany

ABSTRACT: *During the past couple of decades, salt caverns have gained attentions for underground storage of compressed air, natural gas, CO_2 and H_2. Design and stability analysis of a salt cavern require a specific constitutive law which can describe the material behaviour of the rock salt under different thermo–hydro–mechanical conditions at different time scales. Strain rate dependent behaviour, creep, dilatancy, damage, failure, post failure, permeability changes and the temperature effects are some of the most important features that a good constitutive law should be able to describe. This paper discusses four well known constitutive models for rock salt separated in two groups in regard to the structure level of modelling, namely the groups of "macro–structural" and "micro–structural" models. The macro–structural models considered in this paper use the continuum mechanics concepts i.e. visco–plasticity and damage mechanics while the micro–structural models employ micro–level phenomena like dislocation creep and recovery in order to model the material behaviour at the macro–level. The capability and weakness of each of the models are listed and a qualitative comparison is made between the referred models. Finally, the necessity of constitutive model enhancement for making reliable predictions in designing salt caverns is discussed and research work for the future is suggested.*

Keywords: *Visco–plasticity, Creep, Dilatancy, Micro structure, Dislocation creep, Dislocation Recovery*

1 INTRODUCTION

The low permeability and adequate thermal and mechanical properties of rock salt have made it a suitable choice for the underground storage of compressed air, natural gas, CO_2 and H_2 . Accurate design and stability analysis of underground openings in the rock salt will be possible only if a proper constitutive law is used to describe the salt material behaviour. In this paper, the main properties of four existing rock salt constitutive models are presented. These models were chosen because they are well accepted and approved within the German research community dealing with time–dependent behaviour of rock salt. The models are separated in two groups

regarding their modelling concept, i.e. the group of "macro–structural" models and the group of "micro–structural" models. The "macro–structural" model group consists of two models, namely the *Cristescu* and *Lux/Hou* models. These models describe the material behaviour using the continuum mechanical concepts like elasticity, visco–plasticity and continuum damage. Also we selected two "micro–structural" models for our study. These models are *Günther/Salzer* and the *Composite Dilatancy* models . The "micro–structural" models employ micro–level physical phenomena like dislocation creep and recovery of dislocations to obtain the constitutive equations at macro level.

2 MECHANICAL PROPERTIES OF ROCK SALT

It is well known that rock salt responses to loading by elastic and visco–plastic deformation (Günther & Salzer 2007). When a constant load is applied to the rock salt, a time–dependent ductile deformation without any visible macroscopic fracture is observed. This behaviour is called "creeping" and it is highly affected by the environmental factors like temperature and humidity. Creep in the rock salt is predominantly carried by dislocations (linear imperfections) in the salt crystal lattice. Dilatancy is understood as the volume increase during deformation due to micro–cracking and it is one of the main characteristics of the salt that should be considered in the applied constitutive law. Dilatation and damage cause a number of consequences: increasing permeability, accelerating creep and creep rupture, mechanical weakening (Hunsche & Hampel 1999).

3 MACRO–STRUCTURAL APPROACH

3.1 Cristescu's Model

Cristescu formulated an elastic/visco–plastic model in order to model the transient and the stationary creeps of rock salt considering the volumetric dilatation and compressibility (see (Cristescu 1993; Cristescu & Gioda 1994; Cristescu & Hunsche 1998)). Based on this model, the total strain rate is obtained using Eq. 1. $\dot{\boldsymbol{\varepsilon}}^{el}$, $\dot{\boldsymbol{\varepsilon}}^{tr}$ and $\dot{\boldsymbol{\varepsilon}}^{st}$ are the elastic, transient and stationary parts of the total strain rate, respectively. In the following, these quantities are explained in detail.

$$\dot{\boldsymbol{\varepsilon}}^{total} = \dot{\boldsymbol{\varepsilon}}^{el} + \dot{\boldsymbol{\varepsilon}}^{tr} + \dot{\boldsymbol{\varepsilon}}^{st} \tag{1}$$

Elasticity: Eq. 2 represents the elastic part of the total strain rate. Parameters K and G are the bulk and shear moduli, respectively, σ is the mean stress and $\mathbb{I}$ is the unit tensor. Elastic parameters may depend on stress and strain invariants. They may also depend on a damage parameter which describes the micro–cracking history evolution (Cristescu & Gioda 1994).

$$\dot{\boldsymbol{\varepsilon}}^{el} = \frac{\dot{\boldsymbol{\sigma}}}{2G} + \left(\frac{1}{3K} - \frac{1}{2G}\right)\dot{\sigma}\mathbb{I} \tag{2}$$

Transient Creep: Eq. 3 represents a non–associated visco–plastic law which describes the evolution of the irreversible transient part of the total strain. F and H are the visco–plastic potential and the yield function, respectively. Cristescu assumed that both functions depend on two stress invariants only: the mean stress (σ) and the octahedral shear stress (τ). The viscosity coefficient k_t may depend on stress and strain state and on a damage parameter. W is the irreversible work

per unit volume used as work hardening parameter. The brackets $\langle\rangle$ return 0 if the value of the function in it is negative and otherwise the positive part of the function.

$$\dot{\boldsymbol{\varepsilon}}^{tr} = k_t \left\langle 1 - \frac{W(t)}{H(\boldsymbol{\sigma})} \right\rangle \frac{\partial F(\boldsymbol{\sigma})}{\partial \boldsymbol{\sigma}} \tag{3}$$

Experiments performed by Cristescu proved that there exists a domain in the $\sigma - \tau$ stress plane whose boundary distinguishes the dilatancy from the compressibility response. Outside this domain, an irreversible volumetric dilatation of the rock salt takes place, while inside the domain salt is considered to be compressible. Fig. 1a shows the dilatancy–compressibility boundary. Another boundary curve which specifies the short term failure for the salt is also depicted in this figure. It should be noted that only stresses which are below the short term failure curve can be described by Eq. 1. The explanation about how to determine the dilatancy and the short term failure zones from experimental data has been provided in (Cristescu & Gioda 1994; Cristescu & Hunsche 1998). Function F has the key role in describing the volumetric deformation and also the failure. Eqs. 4 defines the evolution of the volumetric strain.

$$\dot{\varepsilon}_v^{tr} = k_t \left\langle 1 - \frac{W(t)}{H(\boldsymbol{\sigma})} \right\rangle \frac{\partial F(\boldsymbol{\sigma})}{\partial \boldsymbol{\sigma}} \mathbb{I} = k_t \left\langle 1 - \frac{W(t)}{H(\sigma,\tau)} \right\rangle \frac{\partial F(\sigma,\tau)}{\partial \sigma} \tag{4}$$

Considering the aforementioned assumptions and the fact that $\dfrac{\partial F(\sigma,\tau)}{\partial \sigma}$ goes to infinity at the short term failure boundary, the potential function F has been derived in (Cristescu 1993). Fig. 1b shows the contour plot of F and H. Two typical examples of applying the Cristescu's model for rock salt is shown in Fig. 2. In the first example, the transient creep of the rock salt was modelled. A constant hydrostatic load ($\sigma = 40$ MPa) was applied to the rock salt specimen while the deviatoric stress was increased in seven steps ($\tau = 5, 10, 15, 20, 25, 30, 32.5$ MPa). The duration of each step is 10-15 days. The change of strain has been calculated using the transient creep equation. Obtained results are in a good agreement with the experimental data reported in (Cristescu 1993). The second example describes the short– term strain–stress behaviour of the rock salt in triaxial test conditions. The hydrostatic part of stress was kept constant ($\sigma = 40$ MPa) and the deviatoric part was increased with a constant rate ($\dot{\tau} = 21.4$ MPa/min). As shown, the volume increase (dilatation) and the failure can be precisely described using this model.

Stationary Creep: The stationary creep rate is defined by the following equation:

$$\dot{\boldsymbol{\varepsilon}}^{st} = k_s \frac{\partial S}{\partial \boldsymbol{\sigma}} \tag{5}$$

where k_s is the viscosity coefficient and S is the stationary creep potential function. The function S has been obtained in (Cristescu & Gioda 1994; Cristescu & Hunsche 1998). The irreversible volumetric changes inside the compressibility zone has been assumed to be zero for stationary creep because the volume can not shrink to zero. The contour plot of function S is shown in Fig. 1a. Two typical creep curves are depicted in Fig. 4b which shows the transient and the stationary creep responses using the Cristescu's model.

Damage and Creep Failure: A scalar damage parameter D has been defined via Eq. 6 to determine the amount of energy released due to the micro–cracking.

$$D(t) = W_{vol}^{max} - W_{vol}(t) \tag{6}$$

$W_{vol}(t)$ denotes the volumetric visco–plastic work per unit volume and W_{vol}^{max} is its maximum value which is reached at the dilatancy boundary. The critical value of damage D_F for characterizing the creep failure is obtained empirically. Therefore, the long–term failure or creep

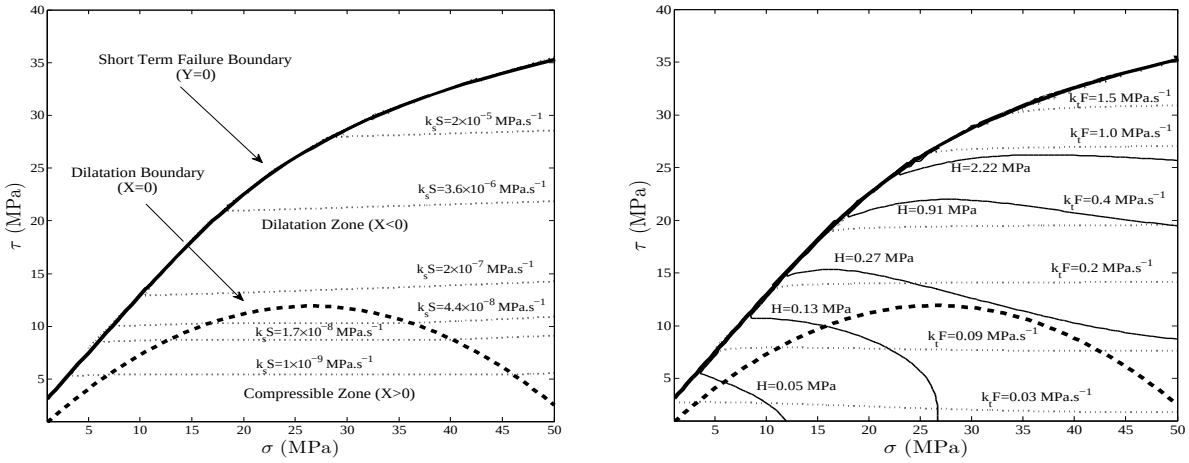

(a) Stationary creep

(b) Transient creep

Fig. 1: Description of the potential and yield functions in $\tau - -\sigma$ plane.

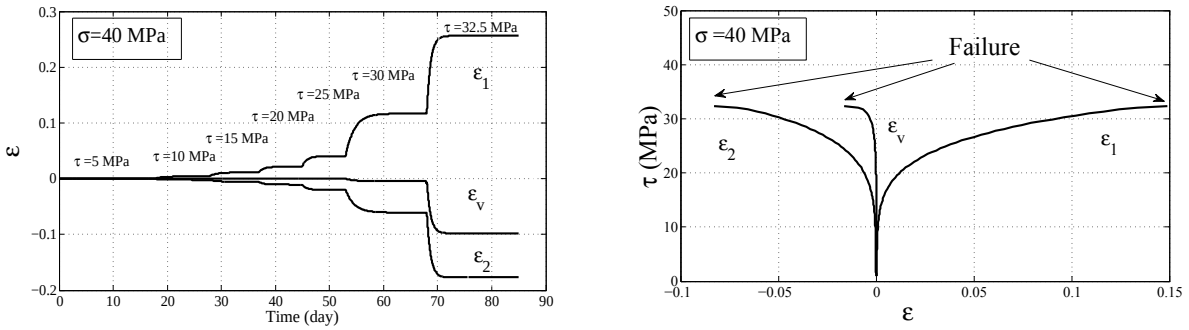

(a) Creep strain in a triaxial test

(b) Strain–stress curves in a triaxial test

Fig. 2: Creep and true triaxial test results for rock salt

rupture occurs when $D(t)$ is equal to its ultimate value D_F. For describing the tertiary creep the dependency of the viscosity coefficient k_s on the damage parameter has to be investigated.

3.2 Lux/Hou Model

The Hou/Lux model considers the strain rate as a sum of four parts, i.e. elastic part $\dot{\varepsilon}_{ij}^{el}$, visco–plastic part $\dot{\varepsilon}_{ij}^{vp}$, damage dilatancy $\dot{\varepsilon}_{ij}^{d}$ and damage healing $\dot{\varepsilon}_{ij}^{h}$.

$$\dot{\varepsilon}_{ij}^{total} = \dot{\varepsilon}_{ij}^{el} + \dot{\varepsilon}_{ij}^{vp} + \dot{\varepsilon}_{ij}^{d} + \dot{\varepsilon}_{ij}^{h} \tag{7}$$

Elastic strain: The elastic strain is obtained using the generalized Hooke's law. The equation below gives the elastic part of the total strain rate.

$$\dot{\varepsilon}_{ij}^{el} = \frac{1}{2G}\frac{\dot{s}_{ij}}{1-D} + \left(\frac{1}{9K} - \frac{1}{6G}\right)\frac{\dot{I}_1}{1-D}\delta_{ij} \tag{8}$$

where D is the damage parameter and s_{ij} and I_1 are the deviatoric stress and the first stress invariant, respectively, δ_{ij} is the Kronecker delta.

Visco–plastic strain: The visco–plastic strain is described via the Hou/Lux–ODS model which is an extension of the Lubby2 model (see (Heusermann, Rolfs, & Schmidt 2003)). The visco–plastic strain rate can be divided into two parts, namely transient (tr) and steady–state (ss) parts.

The following equations define the visco–plastic strain rate:

$$\begin{cases} \dot{\varepsilon}_{ij}^{vp} = \dot{\varepsilon}_{ij}^{tr} + \dot{\varepsilon}_{ij}^{ss} \\ \dot{\varepsilon}_{ij}^{tr} = \dfrac{3}{2}\dfrac{1}{\eta_k(\sigma_{vM}, D)}\left(1 - \dfrac{\epsilon^{tr}}{\epsilon_{\infty}^{tr}(\sigma_{vM}, D)}\right)\dfrac{s_{ij}}{1-D} \\ \dot{\varepsilon}_{ij}^{ss} = \dfrac{3}{2}\dfrac{1}{\eta_m(\sigma_{vM}, T, D)}\dfrac{s_{ij}}{1-D} \end{cases} \tag{9}$$

The damage parameter D has a direct influence on visco–plastic strain, i.e. the damage increases the effect of stress and the transient creep rate. The parameter ϵ_{∞}^{tr} is the equivalent strain value at which the transient creep will end. This strain limit depends on the von Mises stress σ_{vM} and the damage parameter D and it is determined from experimental results. The parameter ϵ_{∞}^{tr} has been defined by Lux and Hou in a way that it accounts for the differences between hardening after stress increase and recovery after a stress decrease (Hou 2003). η_k and η_m are viscosity parameters. Both values are nonlinear functions of the von Mises stress and the damage parameter. The parameter η_m which affects the steady–state creep rate is also dependent on the absolute temperature. The details about these variables can be found in (Hou 2003). The visco–plastic strain rate obtained from Eq. 9 does not change the volumetric strain. Volumetric changes (dilatancy and compressibility) are described in the following.

Damage dilatancy strain: This is the strain that is induced by damage. Like in Cristescu's model, Hou and Lux have defined a dilatancy zone in the $\sigma_{_{eff}} - \sigma_{_{min}}$ plane with $\sigma_{_{eff}} = \sigma_{vM}/(1 - D)$. In this zone, the volumetric dilatancy, micro–cracks and damage develop. Because of this reason, other relevant factors like permeability, creep rate and creep rupture have an upward trend. Figure 3 shows the dilatancy boundary and the failure boundary. The dilatancy damage strain rate $\dot{\varepsilon}_{ij}^{d}$ is composed of $\dot{\varepsilon}_{ij}^{ds}$ term, as a result of shear induced damage and the $\dot{\varepsilon}_{ij}^{dz}$ term which is the damage strain rate under a tensile stress. Both terms are expressed on the basis of the theory of plasticity (Schulze, Heemann, & Zetsche 2007). Equation 10 describes how the damage–induced strain rate is defined. Q^{ds} and Q^{dz} are plastic potential functions for the damage–induced strain under shear and tensile stresses, respectively. This equation also indicates that the flow functions F^{ds} and F^{dz} determine the magnitude of the strain rate due to the damage.

$$\dot{\varepsilon}_{ij}^{d} = \dot{\varepsilon}_{ij}^{ds} + \dot{\varepsilon}_{ij}^{dz} = a_3 \frac{\left\langle F^{ds}/F^{*} \right\rangle^{a_1}}{(1-D)^{a_2}} \frac{\partial Q^{ds}}{\partial \sigma_{ij}} + a_3 \frac{\left\langle F^{dz}/F^{*} \right\rangle^{a_1}}{(1-D)^{a_2}} \frac{\partial Q^{dz}}{\partial \sigma_{ij}} \tag{10}$$

where a_1, a_2, a_3 are material parameters. The mathematical expressions for Q^{ds}, Q^{dz}, F^{ds}, F^{dz} can be found in (Hou 2003).

Damage Healing Strain: The word healing is used for the overall process of the damage decreasing. Fig. 3 depicts the healing boundary identified by Hou and Lux in the $\sigma_{_{eff}} - \sigma_{_{min}}$ stress plane. Within the healing zone, the closing of micro–cracks takes place and the damage heals. There exists also a transient area between the healing and the dilatancy boundaries which is called *constant volume zone*. In this zone, the volumetric deformation and the damage remain constant. Similar to the dilatancy damage strain, the healing damage strain is expressed within the plasticity theory. Equation 11 describes how the healing damage strain rate is obtained. The mathematical expressions for the healing potential function Q^h and the flow function F^h can be found in (Hou 2003; Lux & Eberth 2007).

$$\dot{\varepsilon}_{ij}^{h} = -\frac{\left\langle F^{h}/F^{*} \right\rangle \left\langle -\varepsilon_{vol} \right\rangle}{a_{11} + a_{12}\exp(a_{13}\varepsilon_{vol})} \frac{\partial Q^{h}}{\partial \sigma_{ij}} \tag{11}$$

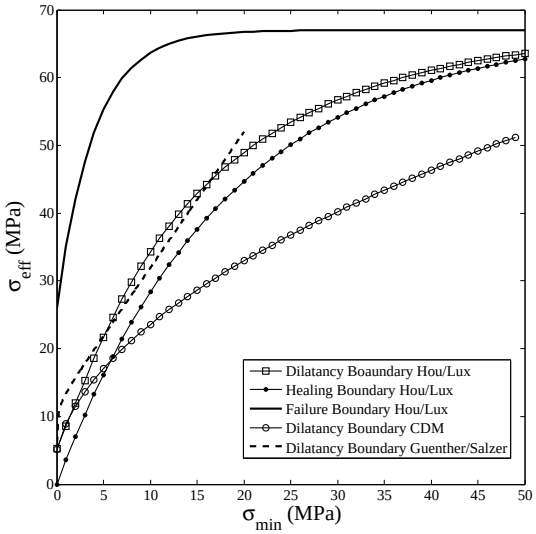

Fig. 3: Dilatancy and healing boundaries for the Hou/Lux–CDM and Günther/Salzer models.

Damage Evolution: As demonstrated in Fig. 3, only one of the three following cases is possible at any moment:

- Stress is above the dilatancy boundary ⇒ there is no healing process and damage develops as follows (a_{15}, a_{16} and a_{17} are model parameters):

$$\dot{D} = a_{15} \frac{\left[\left\langle F^{ds}/F^{*}\right\rangle + \left\langle F^{dz}/F^{*}\right\rangle\right]^{a_{16}}}{(1-D)^{a_{17}}} \tag{12}$$

- Stress state is below the healing boundary ⇒ there is no damage process and healing develops as follows (a_{11}, a_{12} and a_{13} are model parameters):

$$\dot{D} = -\frac{D\left\langle F^{h}/F^{*}\right\rangle}{a_{11} + a_{12}\exp(a_{13}\varepsilon_{vol})}$$

- Stress state is between the dilatancy and the healing boundaries ⇒ there is no damage and no healing process ⇒ $\dot{D} = 0$.

4 MICRO–STRUCTURAL APPROACH

4.1 Günther/Salzer Model

This constitutive model is based on the physical processes on macro and micro level which can describe all three creep phases in the scope of a single creep model. Based on this model, the total deformation rate consists of an elastic part and a creep part:

$$\begin{cases} \dot{\varepsilon}_{ij}^{total} = \dot{\varepsilon}_{ij}^{el} + \dot{\varepsilon}_{ij}^{cr} \\ \dot{\varepsilon}_{ij}^{el} = -\dfrac{\nu}{E}\dot{\sigma}_{kk}\delta_{ij} + \dfrac{1+\nu}{E}\dot{\sigma}_{ij} \\ \dot{\varepsilon}_{ij}^{cr} = 3/2\ \dot{\varepsilon}_{_{eff}}^{cr}\ s_{ij}/\sigma_{_{eff}} \end{cases} \tag{13}$$

where ε_{eff} and σ_{eff} are called effective strain and effective stress, respectively, whose values are defined as follows:

$$\begin{cases} \sigma_{eff} = \sqrt{\frac{3}{2}\, s_{ij} s_{ij}} \ , \quad s_{ij} = \sigma_{ij} - \frac{1}{3}\, \sigma_{kk} \delta_{ij} \\ \dot{\varepsilon}^{cr}_{eff} = A_p \frac{\sigma^{n_p}_{eff}}{(\varepsilon^{V,0}_{eff} + \varepsilon^{V}_{eff})^{\mu}} \end{cases} \tag{14}$$

where ε^{V}_{eff} is a state parameter which governs the hardening, recovery and damage behaviour. Initially, the deformation rate depends on the dislocations presented in the natural crystal of the rock salt which is shown as $\varepsilon^{V,0}_{eff}$. As deformation continues, new dislocations are generated and the density of dislocations increases. Therefore, the value of ε^{V}_{eff} goes up and this yields a reduction in the effective creep rate $\dot{\varepsilon}^{cr}_{eff}$. This step can be considered as the transient part of creep. With further deformation, some intra–crystalline processes cause the reduction of the existing dislocations. These process is called dislocation *recovery*. With the growing density of dislocations, or hardening, also the recovery rate increases. When the rate of the recovery and the generation of dislocations are equal, the value of ε^{V}_{eff} remains constant and the creep enters into its stationary phase. In the long–term creep tests, the increase of the local stress causes generation of micro–cracks and progressive damage (Günther & Salzer 2007). Because the damage counteracts the hardening, the rock salt becomes more and more ductile and the value of ε^{V}_{eff} decreases rapidly yielding the tertiary creep phase. Considering these micro level processes, Günther and Salzer proposed the following equation for the evolution of the effective strain hardening ε^{V}_{eff}:

$$\dot{\varepsilon}^{V}_{eff} = \dot{\varepsilon}^{cr}_{eff} - \dot{\varepsilon}^{E}_{eff} - \dot{\varepsilon}^{S}_{eff} \tag{15}$$

where $\dot{\varepsilon}^{E}_{eff}$ and $\dot{\varepsilon}^{S}_{eff}$ are the recovery creep and the damage evolution creep rate, respectively, that are defined through the following relations:

$$\dot{\varepsilon}^{E}_{eff} = \frac{\varepsilon^{V}_{eff}}{t_c \exp(Q/RT)} \tag{16}$$

$$\dot{\varepsilon}^{S}_{eff} = \dot{\varepsilon}_{vol} = f(\sigma_{min}, U_{Dil}) \tag{17}$$

The term $t_c \exp(Q/RT)$ defines the time at which the stationary creep starts to develop. The parameter t_c is determined experimentally. As equation 16 shows, the recovery creep is a function of temperature. Equation 17 demonstrates that the damage evolution rate is equal to the volumetric strain rate $\dot{\varepsilon}_{vol}$. Günther and Salzer developed a function for describing volumetric strain rate (see (Günther & Salzer 2007)). This function depends on U_{Dil} and σ_{min}, where U_{Dil} is the inelastic strain work performed above the dilatancy boundary and σ_{min} is the minimum principle stress. During the creep test, the effective hardening rate $\dot{\varepsilon}^{V}_{eff}$ is positive in the transient creep domain and converges to zero in case of stationary creep. If damage is considered, the effective hardening rate decreases and becomes negative. Therefore, the creep rate accelerates and the tertiary creep occurs. Figure 4a represents the typical creep response using the Günther/Salzer's model.

The Günther/Salzer's model can be used for modelling the triaxial short–term strength tests. In this case, the stress sensitivity parameter n_p is not a constant anymore. Instead, this parameter depends on the volumetric strain evolution. Therefore, we have:

$$n_p = \frac{n_0 + n_1 \exp(n_2\, \sigma_3)\ (1 - \exp(-n_3\, \varepsilon_{vol}))}{(1 - \varepsilon_{vol})^{n_4}}$$

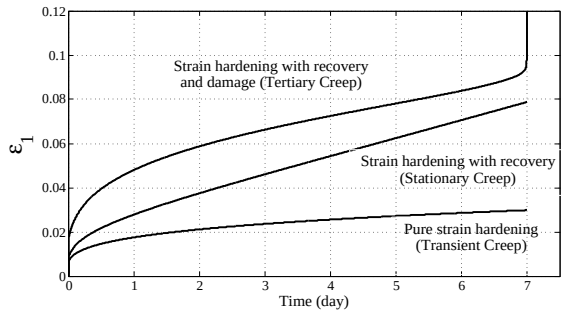

(a) Günther/Salzer's model (b) Cristescu's model

Fig. 4: Typical creep behaviour of the rock salt

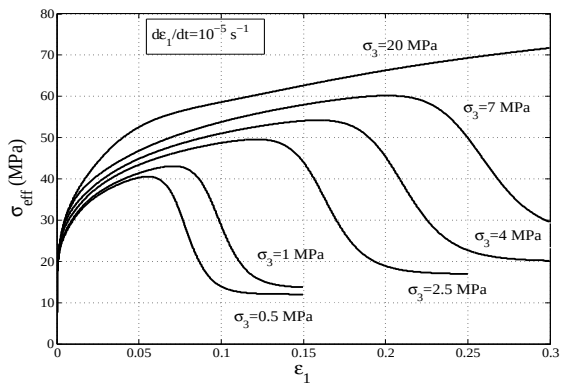

(a) Constant deformation rate (b) Constant confining pressure

Fig. 5: Triaxial short–term strength test modelled using Günther/Salzer's model

where n_0 denotes the stress exponent for the non damaged rock salt. σ_3 is the confining pressure and n_1,..., n_4 are the model parameters. Figure 5 represents two examples of triaxial test modeling using Günther/Salzer's model.

4.2 Composite Dilatancy Model

The Composite Dilatancy Model (CDM) describes the mechanical behaviour of the rock salt using the micro–physical deformation mechanisms. According to the careful microscopic observations, each crystal grain of salt is made of several smaller parts named *subgrain*. The subgrain structure consists of: 1) the subgrain boundaries which are formed by dislocations with high density; and 2) the subgrain interior with a much lower dislocation density. The interior part is more ductile than the boundaries and it shows a different deformation behaviour. This is quite similar to a composite material. Therefore, the model is named *composite model* (Hampel & Schulze 2007). As we explained before, during the transient creep, an increase of the free–dislocation density occurs and, at the same time, a rearrangement of the subgrain structure develops (recovery). When the balance between the dislocation generation and the dislocation recovery is achieved, the stationary creep will take place. Similar as for the Günther/Salzer model, the strain rate is defined using Eq. 13, but the equation for the effective creep rate reads:

$$\begin{cases} \dot{\varepsilon}^{cr}_{eff} = F_h(\Phi, \sigma_{min}, \tau)\, \delta_{dam}(D, \sigma_{min})\ P_F((\tau - \tau_{dil}), \sigma_{min}, (\varepsilon_{tot} - \varepsilon_F))\ \dot{\varepsilon}^{cr}_{non-dil} \\ \dot{\varepsilon}^{cr}_{non-dil} = \dfrac{b}{M}\rho v_0 \exp(-\dfrac{Q}{RT}) \sinh\left(\dfrac{b\ \Delta a(r)\ \sigma^*(w,r,a)}{MK_BT}\right) \end{cases} \tag{18}$$

where $\dot{\varepsilon}^{cr}_{non-dil}$ refers to the non–dilatant creep rate. This term is derived from Orwan's equation (see (Hampel & Schulze 2007; Hunsche & Hampel 1999) which describes the dislocation creep for the crystalline materials. Parameters b, M and K_B are Burger's vector, Teylor factor and Boltzmann constant, respectively and v_0 is a model parameter. The dependency of the creep rate on temperature has been expressed by an exponential term while the hyperbolic sine term describes the stress dependency of the creep. In the isothermal condition, only the terms ρ, Δa and σ^* change during the transient creep. $\rho = 1/r^2$ is the dislocation density with r as the mean distance between dislocations. Δa is the activation area which is also a function of r. The term σ^* is the effective internal stress acting inside the subgrains that drive the mobile dislocations and it is a function of r and two other micro–structural properties, namely the average diameter of subgrains (w) and the average width of subgrain's walls (a). The mathematical expressions for Δa and σ^* can be found in (Hampel & Schulze 2007; Hunsche & Hampel 1999; Cristescu & Hunsche 1998). The evolution equations for micro–structural parameters are defined using the following relations:

$$\begin{cases} \dot{r} = \dfrac{r_{st} - r}{k_r}\ \dot{\varepsilon}^{cr}_{non-dil} \\ \dot{a} = \dfrac{a_{st} - a}{k_a}\ \dot{\varepsilon}^{cr}_{non-dil} \\ \dot{w} = \dfrac{w_{st} - w}{k_w}\ \dot{\varepsilon}^{cr}_{non-dil} \end{cases} \tag{19}$$

where r_{st}, a_{st} and w_{st} are the stationary values of the micro–structural parameters and are determined from experiments. k_r, k_a and k_w are the model parameters and they affect the dislocation recovery time. The creep enters its stationary phase when the parameters r, a and w approach to their stationary values .

The functions F_h, δ_{dam} and P_F are correction factors for the effects of humidity, damage and post failure, respectively. As Eq. 18 shows, the effective creep rate $\dot{\varepsilon}^{cr}_{eff}$ will be obtained by multiplying these factors with the non–dilatant creep rate $\dot{\varepsilon}^{cr}_{non-dil}$. The function $F_h(\Phi, \sigma_{min}, \tau)$ describes the dependency on the relative humidity Φ of the dilated rock salt. σ_{min} and τ are the minimal principal stress and the octahedral shear stress, respectively. The function $\delta_{dam}(D, \sigma_{min})$ defines the dependence of the effective creep rate on the damage parameter D. This function causes weakening and at last failure. Similar to the previous models, the CDM model defines a dilatancy zone in the stress space. In the dilatancy zone, the damage parameter D increases with the volumetric deformation. The equation of damage evolution is defined as:

$$\dot{D} = \sigma_{mean}\, \dot{\varepsilon}_{vol} \tag{20}$$

where σ_{mean} and $\dot{\epsilon}_{vol}$ are the mean stress and the volumetric strain rate, respectively. The equation for the volumetric strain rate reads:

$$\dot{\varepsilon}_{vol} = r_v(\sigma_{mean}, \tau)\, \dot{\varepsilon}^{cr}_{non-dil} \tag{21}$$

The empirical function r_v which depends on the mean and the octahedral stresses is equal to zero beyond the dilatancy zone. That means there is no volumetric deformation below the dilatancy boundary. The last term that should be explained is the $P_F((\tau - \tau_{dil}), \sigma_{min}, (\varepsilon_{tot} - \varepsilon_F))$. This function describes the post failure behaviour, where τ_{dil} is the value of octahedral stress the at dilatancy boundary and the expression $(\varepsilon_{tot} - \varepsilon_F)$ is the strain in the post failure range. The strain at failure ε_F is determined empirically. All the dilatancy related terms i. e. F_h, δ_{dam} and P_F converge to unity in case of a creep deformation below the dilatancy boundary. Further details of the model can be found in (Hampel & Schulze 2007).

5 QUALITATIVE MODEL COMPARISON

In this section, a qualitative comparison is made between the aforementioned models. The criteria for the model assessment are listed below. By focusing on these items, we aimed to identify the capabilities and the weaknesses of each of the considered here models.

- *Transient creep*: All four models are able to describe the transient creep appropriately.
- *Stationary creep*: All four models can model the stationary creep. The Cristecu's and Hou/Lux models describe the transient and the stationary creep using separate equations, while CDM and Günther/Salzer's models have a single equation for both creep phases.
- *Tertiary creep or long–term failure*: The Günther/Salzer's, CDM and Hou/Lux models introduce equations which can predict the long–term failure. They can also model the accelerated creep. Commenting about the accuracy of their prediction will be possible if the results are compared with in–situ or laboratory test data. The Günther/Salzer's and CDM models describe the tertiary creep as a consequence of stationary creep phases. That means, they use one single equation for all three steps of creep. Regarding the Cristescu's model, the time of long–term failure is obtained when the damage parameter is equal to the critical value but still the relation between stationary creep viscosity coefficient k_s and damage parameter should be investigated in order to model the tertiary creep.
- *Failure in the triaxial short–term strength test*: All the models have the capability of describing the $\sigma - \varepsilon$ relation in the pre–failure regime. They can also predict the failure in the short–term strength test. It should be mentioned that these models have proposed different equations for shot–term failure boundary in the stress space. Therefore, different level of accuracy for the failure prediction is expected.
- *Post failure in the triaxial short–term strength test* : the Cristescu's model does not describe the post failure behaviour of the rock salt. Other models are able to fulfil this requirement.
- *Cyclic loading*: All four models are able to model either loading or unloading, however, there is no dependence on the number of cycles and therefore no ageing or fatigue may be simulated.
- *Dilatancy boundary*: The dilatancy boundaries used by the models do not match and this causes the difference in predictions of damage progress and volumetric strain evolution. The difference between dilatancy boundaries increases when the minimum principle stress exceeds 10 MPa (see Fig. 3).
- *Volumetric dilatancy*: In the Cristecu's and Hou/Lux models, the volumetric dilatancy can be easily calculated as $\varepsilon_{vol} = \varepsilon_1 + \varepsilon_2 + \varepsilon_3$. Günther/Salzer's and CDM models proposed specific equations for the volumetric dilatancy (see Eqs. 17 and 21).
- *Volumetric compressibility*: The CDM model does not consider any compressibility for the rock salt below the dilatancy boundary. The Cristescu's model does not take the compressibility into account only for the stationary creep. The Günther/Salzer's and Hou/Lux models describe compressibility and healing in the healing zone.
- *Damage evolution*: Damage evolution is formulated through the inelastic strain work performed in dilatancy zone or volumetric strain changes elsewhere. All the models except the Cristecu's model have considered the direct effect of damage on the total strain rate.
- *Effects of temperature*: The Cristescu's model introduced in this paper is valid for ambient temperature. The effect of temperature on the creep behaviour is taken into account by considering the viscosity coefficients and the dilatancy threshold as functions of temperature. The details about this dependency have been provided in (Cristescu & Gioda 1994). The effect of temperature has been formulated in the CDM and Hou/Lux models for both transient and stationary creeps while in the Günther/Salzer's model only the stationary creep is

affected by temperature. It should be mentioned that all four models have considered isothermal conditions.

- *Effects of humidity*: Humidity increases the creep rate above the dilatancy boundary. The humidity influence has been considered in the CDM model. however, the other models have no description about this important factor.
- *Effects of dilatancy on the elastic parameters*: The elastic parameters are not constant for the damaged rock salt. The effect of dilatancy and damage on the elastic parameters has been reported for the Cristescu's and Günther/Salzer's models (see (Matei & Cristescu 2000) and (Günther & Salzer 2007)).
- *Effects of the third stress invariant*: The third stress invariant plays no role in the Cristescu's, Günther/Salzer's and CDM models and the stress space is described by two invariants only while, in the Hou/Lux model, the Lode angle is considered as the third stress invariant.
- *Number of model parameters*:The Cristescu's model has totally 21 model parameters for the transient and the stationary creep equations. These parameters have been obtained from experimental data. The Hou/Lux, Günther/Salzer's and CDM models have 28, 20 and 18 parameters, respectively, to describe the transient, stationary and tertiary creep.
- *Numerical implementation*: Since the micro–structural models describe the different phases of the creep in one single equation then the numerical implementation of these equations seems to be easier. On the other hand, the existence of exponential and hyperbolic terms in the CDM model and a high exponent item in the Günther/Salzer model increases the instability of the equations. Because of this reason, using small time steps is suggested for numerical integration of these equations.

6 CONCLUSIONS

In this paper, four well accepted and approved constitutive models within the German rock salt modelling community were introduced, compared and critically discussed. The procedure of the material modelling was discussed for each method separately. In the following, a qualitative assessment about the capabilities of the models was made considering a number of criteria. In general, the properties of rock salt alter due to thermal, mechanical and hydraulic loading. Temperature and pore water pressure effects change the material properties as well as stress field in the rock salt. The expected variation of the temperature in a salt cavern is between 10 to 300 C° and the prospective pressure is up to 16 MPa (Olivella & Gens 2002). Therefore, accurate design and stability analysis of a salt cavern will be possible only if a coupled constitutive law for the thermal, hydraulic and mechanical forces is obtained. In conclusion, the following items are suggested for further investigations in this field of study.

- Extending the existing constitutive laws to the thermo–hydro–mechanical equations;
- Considering the pore fluid interaction;
- Developing equations for the large strains (geometrical non–linearity);
- Assess the influence of anisotropy including damage anisotropy;
- Improving the equation for the dilatancy boundary;
- Investigate the humidity effect on the creep rate;
- Evaluate the influence of the third stress invariant;
- Studying the effects of long–term complex cyclic loading on the rock salt behaviour;
- More in detail investigate the relation between dilatancy and permeability evolution.

Acknowledgement

This work was performed in the frame of the project ANGUS+ funded by the Federal Ministry of Education and Research (BMBF) under grant no. 03EK3022C. The authors are grateful for their support.

REFERENCES

Cristescu, N. (1993). A general constitutive equation for transient and stationary creep of rock salt. *Int. J. Rock Mech. Min. Sci. Geomech 30*(2), 125–139.

Cristescu, N. & Gioda, G. (1994). *Visco-Plastic Behaviour of Geomaterials*. Springer Verlag, Wien-New York.

Cristescu, N. & Hunsche, U. (1998). *Time Effects in Rock Mechanics*. Wiley, Chichester.

Günther, R. & Salzer, K. (2007). A model for rock salt, describing transient, stationary, and accelerated creep and dilatancy. In *Proceeding of the 6th Conference on The Mechanical Behavior of Salt- SALTMECH6, Hannover , Germany, 22-25 May 2007*.

Hampel, A. & Schulze, O. (2007). The composite dilatancy model: A constitutive model for the mechanical behavior of rock salt. In *Proceeding of the 6th Conference on The Mechanical Behavior of Salt- SALTMECH6, Hannover , Germany, 22-25 May 2007*.

Heusermann, S., Rolfs, O., & Schmidt, U. (2003). Nonlinear finite element analysis of solution mined storage caverns in rock salt using the LUBBY2 constitutive model. *Computers and Structures 81*, 629–638.

Hou, Z. (2003). Mechanical and hydraulic behavior of rock salt in the excavation disturbed zone around underground facilities. *Int. J. Rock Mech. Min. Sci 40*, 725–738.

Hunsche, U. & Hampel, A. (1999). Rock salt- the mechanical properties of the host rock material for radio active waste repository. *Engineering Geology 52*, 271–291.

Lux, K. H. & Eberth, S. (2007). Fundamental and first application of a new healing model for rock salt. In *Proceeding of the 6th Conference on The Mechanical Behavior of Salt- SALTMECH6, Hannover , Germany, 22-25 May 2007*.

Matei, A. & Cristescu, N. (2000). The effects of volumetric strain on elastic parameters for rock salt. *Mechanics of cohesive frictional materials 5*, 113–124.

Olivella, S. & Gens, A. (2002). A constitutive model for crushed salt. *International journal for numerical and analytical methods in geomechanics 26*, 719–746.

Schulze, O., Heemann, U., & Zetsche, F. (2007). Comparison of advanced constitutive models for the mechanical behavior of rock salt - results from a joint research project- i. modeling of deformation processes and benchmark calculation. In *Proceeding of the 6th Conference on The Mechanical Behavior of Salt- SALTMECH6, Hannover , Germany, 22-25 May 2007*.

EQUIVALENT MOHR-COULOMB STRENGTH PARAMETERS ACCOUNTING FOR THE INFLUENCE OF INTERMEDIATE PRINCIPAL STRESS

Y.-K. Lee
Department of Coastal Construction Engineering, Kunsan National University, Gunsan, Jeonbuk 573-701, South Korea

S. Jeon
Department of Energy Systems Engineering, Seoul National University, Seoul 151-742, South Korea

ABSTRACT: *In this paper, a convenient method to find an equivalent tangential friction angle and cohesion for any failure criterion expressed in terms of the stress invariants is proposed. The main idea is to find the Mohr-Coulomb failure surface making tangential contact with the targeting failure surface at the failure stress points in the principal stress space. Hence the proposed method provides a systematic way to find the equivalent tangential friction angle and cohesion for various criteria that are either independent of the intermediate principal stress (referred to here as 2-D criteria) or depend on it (3-D criteria). Illustrative implementations of the proposed method are carried out for two 3-D rock failure criteria, i.e. the Hoek-Brown & Willam-Warnke (HB-WW) criterion and the Mohr-Coulomb & Jiang-Pietruszczak (MC-JP) criterion, which are the 3-D versions of the original Hoek-Brown (H-B) criterion and the Mohr-Coulomb criterion, respectively (Lee et al., 2012). The influence of both the hydrostatic pressure and similarity angle on the instantaneous tangential friction angle and cohesion of the 3-D criteria is investigated. The predicted equivalent friction angle and cohesion for the 3-D failure criteria show a substantial dependency on* σ_2*, which does not occur for a 2-D failure criterion.*

1 INTRODUCTION

Establishing failure condition of rock has been one of the most attractive research topics in rock engineering. As a consequence of the experimental findings over the past decades, a number of rock failure criteria have been proposed. The criteria are linear if the strength is linearly dependent on the confining stress, otherwise they are non-linear. Furthermore, a rock failure criterion is recognized here as '3-D' if the influence of all three principal stresses on failure is considered, whereas it is referred to as '2-D' if the effect of the intermediate principal stress is ignored. For example, the Mohr-Coulomb (M-C) and the Hoek-Brown (H-B) (1980), which are the two most common criteria for rock failure, are referred to as 2-D linear and 2-D non-linear, respectively, while the modified Wiebols and Cook (Zhou, 1994) is a 3-D linear criterion. It is acknowledged that most of the criteria proposed so far have their advantages and limitations in view of the easiness of application and the mathematical robustness. Colmenares & Zoback (2002) and Benz & Schwab (2008) conducted comprehensive comparative studies on the most common failure criteria of rock by fitting those criteria to some typical true triaxial (also known as polyaxial) test data sets from the literature and showed that the overall fitting quality of 2-D criteria is much lower than those of 3-D criteria.

Despite its limitations that the strength nonlinearity and the effect of the intermediate principal stress on the failure are ignored, the M-C failure criterion is still widely used in rock engineering. This is maybe due to its simplicity in the selection of the associated strength parameters, i.e. the friction angle (ϕ) and cohesion (c), from the conventional triaxial tests on rock specimens. In addition, most rock engineering practitioners are familiar with the way of understanding the rock strength in terms of the friction angle and cohesion. These explain the fact that most commercial codes for the stability analysis of rock structures are equipped with the M-C criterion. In contrast, there are very few commercial codes that include non-linear or 3-D failure criteria for rock which could provide more improved strength predictions over the M-C.

Therefore, finding the equivalent friction angle and cohesion from other criteria has become an important issue for the implementation of the non-linear failure criterion in the context of the M-C criterion. Based on the Balmer (1952) theory, Hoek (1990) derived the formula giving the instantaneous tangential friction angle and cohesion of the H-B criterion at the appropriate value of normal stress. More recently, Hoek et al. (2002) suggested empirical relationships providing the average friction angle and cohesion of the generalized H-B criterion for given stress range of σ_3 by fitting the linear Mohr-Coulomb equation to the non-linear H-B envelope. However, lesser attention has been paid to the calculation of the equivalent Mohr-Coulomb parameters from the criteria other than the H-B.

In this paper, a new and convenient approach to find the instantaneous tangential friction angle and cohesion of rock failure criteria in 3-D stress regime is briefly introduced. The new method proposed by Lee and Bobet (2013) is quite general in that it is applicable to any non-linear and 3-D failure criteria provided that the criteria can be expressed in terms of stress invariants. In addition, illustrative implementation of the method with the 3-D linear criterion MC-JP and the 3-D non-linear criterion HB-WW (Lee et al. 2012) is carried out and the stress path dependency of the predicted instantaneous M-C parameters is discussed.

2 ROCK FAILURE CRITERIA IN TERMS OF STRESS INVARIANTS

2.1 Stress Invariants

If a failure criterion of rock is expressed in terms of stress invariants, the failure surface can be more conveniently displayed in 3-D principal stress space and at the same time the geometric interpretation of the criterion becomes straightforward. In this paper, the failure criteria are represented in terms of the Nayak & Zienkiewicz (1972)'s stress invariants ξ, ρ and θ defined as

$$\xi = I_1/\sqrt{3}; \quad \rho = \sqrt{2J_2}; \quad \theta = (1/3)\cos^{-1}\left(\left(3\sqrt{3}/2\right)\left(J_3/J_2^{3/2}\right)\right) \tag{1}$$

where $I_1 = \sigma_{ii}$ is the first invariant of the stress tensor σ_{ij}, while $J_2 = s_{ij}s_{ij}/2$ and $J_3 = s_{ij}s_{jk}s_{ki}/3$ are the second and third invariants of the deviatoric stress tensor $s_{ij} = \sigma_{ij} - \left(I_1/3\right)\delta_{ij}$. The geometric meaning of these invariants in the principal stress space is depicted in Fig. 1; ξ is the distance from the origin to the deviatoric plane containing the stress point $\mathbf{p}(\sigma_1, \sigma_2, \sigma_3)$, ρ is the radial distance from the hydrostatic axis to **p** in the deviatoric plane, and θ is the similarity angle measuring the direction of **p,** which is in the

range of $0 \le \theta \le \pi/3$ for $\sigma_1 \le \sigma_2 \le \sigma_3$. For triaxial compression ($\sigma_1 > \sigma_2 = \sigma_3$), $\theta = 0$, while for the stress condition of triaxial extension ($\sigma_1 = \sigma_2 > \sigma_3$), $\theta = \pi/3$.

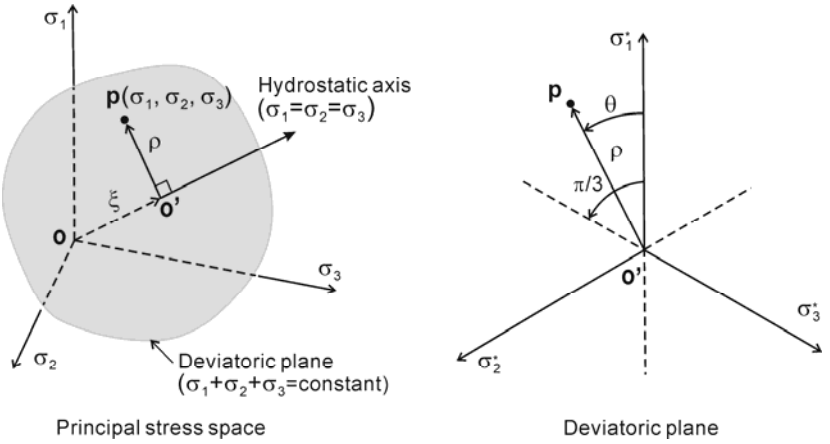

Fig. 1. Geometric representation of stress invariants

2.2 The M-C and H-B failure criteria in 3-D Stress Space.

In the M-C criterion, failure of rock is assumed when the relationship between the major principal stress (σ_1) and the minor principal stress (σ_3) satisfies

$$\sigma_1 = \sigma_3(1-\sin\phi)/(1+\sin\phi) + 2c\cos\phi/(1-\sin\phi) \tag{2}$$

whereas, in the H-B criterion, the relationship is non-linear and expressed as

$$\sigma_1 = \sigma_3 + \sqrt{m\sigma_c\sigma_3 + s\sigma_c^2} \tag{3}$$

where m and s are material constants and σ_c is the uniaxial compression strength of intact rock.

Considering the Nayak & Zienkiewicz's stress invariants, the alternative form of the M-C criterion is expressed as

$$\rho = g_{MC}(\theta)h_{MC}(\xi) = g_{MC}(\theta)\left(\frac{2\sqrt{2}\sin\phi}{3-\sin\phi}\xi + \frac{2\sqrt{6}c\cos\phi}{3-\sin\phi}\right) \tag{4}$$

where

$$g_{MC}(\theta) = \frac{3-\sin\phi}{(3-\sin\phi)\cos\theta + \sqrt{3}(1+\sin\phi)\sin\theta} \tag{5}$$

and, for the H-B criterion, it is

$$\rho = g_{HB}(\xi,\theta)h_{HB}(\xi) = g_{HB}(\xi,\theta)\left(\frac{-m\sigma_c + \sqrt{m^2\sigma_c^2 + 12\sqrt{3}m\sigma_c\xi + 36s\sigma_c^2}}{3\sqrt{6}}\right) \tag{6}$$

with

$$g_{HB}(\theta,\xi) = \frac{3m\sigma_c\cos\left(\theta+\frac{2\pi}{3}\right) + 3\sqrt{m^2\sigma_c^2\cos^2\left(\theta+\frac{2\pi}{3}\right) + \left(12s\sigma_c^2 + 4\sqrt{3}m\sigma_c\xi\right)\sin^2\left(\theta+\frac{\pi}{3}\right)}}{\left(-2m\sigma_c + 2\sqrt{m^2\sigma_c^2 + 36s\sigma_c^2 + 12\sqrt{3}m\sigma_c\xi}\right)\sin^2\left(\theta+\frac{\pi}{3}\right)} \tag{7}$$

Here, $\rho = h_{MC}(\xi)$ and $\rho = h_{HB}(\xi)$ represent the failure conditions in the meridional sections associated with triaxial compression, i.e. $\theta = 0$. $g_{MC}(\theta)$ in Eq.(4) is the function defining the shape of the deviatoric section of the M-C criterion and satisfies

$$g_{MC}(0) = 1; \qquad g_{MC}(\pi/3) = k = (1-\sin\phi)/(1+\sin\phi) \tag{8}$$

For $0 \le \theta \le \pi/3$, the trajectory of $g_{MC}(\theta)$ in the deviatoric plane is a straight line, which results in the irregular hexagonal deviatoric section. Independence of $g_{MC}(\theta)$ on ξ implies that the shape of the deviatoric section along the hydrostatic axis is not altered. Similarly, the function $g_{HB}(\xi,\theta)$ specifies the deviatoric shape of the H-B criterion. However, in contrast to the M-C, the trajectory of $g_{HB}(\xi,\theta)$ is slightly curved and dependent on ξ, so that the deviatoric section of the H-B criterion is pseudo-hexagonal and the shape of it evolves with the variation of hydrostatic pressure.

2.3 3-D failure surfaces criteria smoothly approximating the 2-D criteria

Besides ignoring the effect of the intermediate principal stress σ_2, singular corners implied both in the M-C and H-B criteria pose mathematical difficulty in their numerical implementation because the gradient is not defined along these corners. However, the singularity can be avoided if the deviatoric shape functions g_{MC} in Eq. (4) and g_{HB} in Eq. (6) are replaced by other appropriate smooth functions. For example, the shape function proposed by Jiang & Pietruszczak (1988) takes the form

$$g_{JP}(\theta) = \frac{\left(\sqrt{1+\lambda} - \sqrt{1-\lambda}\right)k}{k\sqrt{1+\lambda} - \sqrt{1-\lambda} + (1-k)\sqrt{1-\lambda\cos 3\theta}} \tag{9}$$

where $\lambda \to 1$ is a constant. With the definition of k in Eq. (8) and the assumption of $\lambda = 0.999$, it can be shown that g_{JP} is also convex for $0 \le \phi \le 57.8^\circ$. For most rocks, ϕ is within this range.

Another well known smooth deviatoric shape was proposed by Willam & Warnke (1974) as

$$g_{WW}(\theta) = \frac{2(1-k^2)\cos\left(\theta-\pi/3\right) + (2k-1)\sqrt{4(1-k^2)\cos^2\left(\theta-\pi/3\right) + 5k^2 - 4k}}{4(1-k^2)\cos^2\left(\theta-\pi/3\right) + (2k-1)^2} \tag{10}$$

which is derived from the elliptic approximation, so that it is convex in the entire physical range of $0.5 \le k \le 1$.

Combining the shape function g_{JP} with Eq. (4) results in the following 3-D linear failure criterion MC-JP (Lee et al., 2012)

$$\rho = g_{MC-JP}(\theta) h_{MC}(\xi) = g_{MC-JP}(\theta) \left(\frac{2\sqrt{2}\sin\phi}{3-\sin\phi} \xi + \frac{2\sqrt{6}c\cos\phi}{3-\sin\phi} \right) \tag{11}$$

which represents the smooth surface contacting the original M-C failure surface at the corners if k in Eq. (9) is assumed as in Eq. (8).

On the other hand, the replacement of g_{HB} in Eq. (6) with g_{WW} yields the following 3-D non-linear failure criterion HB-WW (Lee et al., 2012)

$$\rho = g_{WW}(\xi,\theta) h_{HB}(\xi) = g_{WW}(\xi,\theta) \left(\frac{-m\sigma_c + \sqrt{m^2\sigma_c^2 + 12\sqrt{3}m\sigma_c\xi + 36s\sigma_c^2}}{3\sqrt{6}} \right) \tag{12}$$

With the assumption of k in Eq. (10) as

$$k(\xi) = \frac{-2m\sigma_c + 2\sqrt{m^2\sigma_c^2 + 3\sqrt{3}m\sigma_c\xi + 9s\sigma_c^2}}{-m\sigma_c + \sqrt{m^2\sigma_c^2 + 12\sqrt{3}m\sigma_c\xi + 36s\sigma_c^2}} \tag{13}$$

Eq. (12), in the principal stress space, depicts the smooth and convex surface wrapping the original H-B criterion with making the contacts along the corners.

Fig. 2 shows the three dimensional plots of the MC-JP and HB-WW criteria along with their corresponding 2-D criteria for the strength parameters given in the figure. It is evident that each 3-D criterion is identical to its 2-D version for the triaxial compression ($\theta = 0$) and triaxial extension ($\theta = \pi/3$) stress regimes.

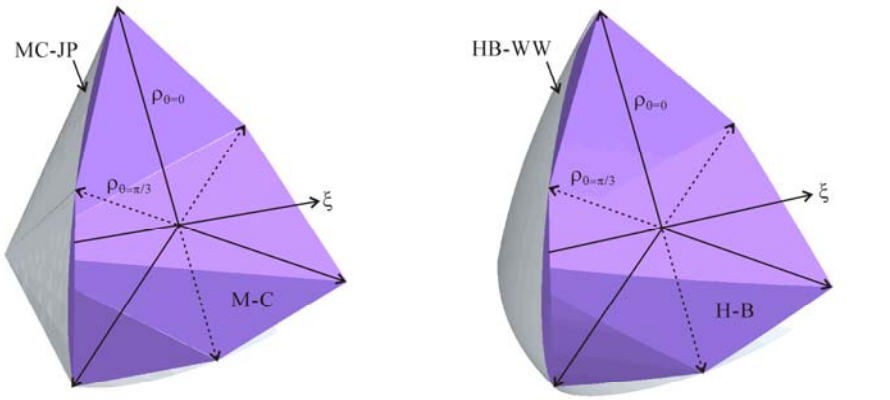

a) M-C & MC-JP ($\phi = 45^\circ$, $c = 21$ MPa) b) H-B & HB-WW ($m = 12$, $s = 1$, σ_c=100 MPa)

Fig. 2. Failure surface plotted in the principal stress space

3 TANGENTIAL EQUIVALENT MOHR-COULOMB PARAMETERS

The instantaneous friction angle ϕ_i and cohesion c_i of non-linear criterion can be calculated by imposing the condition of tangential contact between two failure surfaces at a given stress invariants (ξ, ρ, θ) at failure, which are

$$\frac{\partial \rho_{MC}}{\partial \xi} = \frac{\partial \rho_{\alpha}}{\partial \xi} \tag{14}$$

$$\rho_{MC} = \rho_{\alpha} \tag{15}$$

where the subscript α implies any failure criterion of interest such as H-B, MC-JP, and HB-WW. Recalling Eq. (4), Eq. (14) results in the expression for the instantaneous tangential friction angle as

$$\phi_i = \sin^{-1}\left(\frac{(\partial \rho_{\alpha} / \partial \xi)(\sqrt{3}\sin\theta + 3\cos\theta)}{2\sqrt{2} - (\partial \rho_{\alpha} / \partial \xi)(\sqrt{3}\sin\theta - \cos\theta)} \right) \tag{16}$$

and then the corresponding instantaneous tangential cohesion is obtained from Eq. (15) as

$$c_i = \frac{3 - \sin\phi_i}{2\sqrt{6}\cos\phi_i} \frac{\rho_{\alpha}}{\overline{g}_{MC}(\theta)} - \frac{\tan\phi_i}{\sqrt{3}} \xi \tag{17}$$

where

$$\overline{g}_{MC}(\theta) = \frac{3 - \sin\phi_i}{(3 - \sin\phi_i)\cos\theta + \sqrt{3}(1 + \sin\phi_i)\sin\theta} \tag{18}$$

It should be noted that the new method employing Eq. (16) and Eq. (18) is quite general since it can be applied to any failure criterion if the criterion is expressed in terms of stress invariants. Moreover, in the new method, the equivalent M-C parameters are calculated directly from the components of the stress tensor, which is a favorable feature for the numerical analysis since the calculation of the principal stresses as required in the Balmer (1952)'s approach is not necessary.

4 ILLUSTRATIVE IMPLEMENTATIONS

The influence of σ_2 on the strength predictions in the 2-D and 3-D criteria are demonstrated in Fig.3, where $\phi = 45^{\circ}$ and $c = 21\text{MPa}$ are assumed for the M-C and MC-JP criteria, while $m = 12$, $\sigma_c = 100\text{MPa}$, and $s = 1$ (i.e., intact rock) are assumed for the H-B and HB-WW criteria. The figure clearly shows that, contrary to the M-C and H-B criteria in which the effect of σ_2 are neglected, the MC-JP and HB-WW predict the strengthening effect with increasing σ_2, viz. σ_1 rises from the lowest value at the triaxial compression to the peak followed by a decrease to the lowest value at the triaxial extension.

The tangential instantaneous friction angle ϕ_i and cohesion c_i calculated from Eq. (16) and Eq. (17), respectively, are shown in Fig. 4 and Fig.5. As expected, σ_2 has no impact on the

equivalent M-C parameters of the 2-D H-B criterion, whereas the effect of σ_2 in the MC-JP and HB-WW is obvious. The computed values of the equivalent M-C parameters for the two 3-D criteria show similar behavior to the strength prediction, viz. initial increase followed by descending after the peak as σ_2 moves from σ_3 to σ_1. Regardless of σ_3, each curve of ϕ_i and c_i from the linear MC-JP criterion is bounded in the exactly same range of the associated strength parameter values, i.e. $45^\circ \le \phi_i \le 48.37^\circ$ and $21\text{MPa} \le c_i \le 23.63\text{MPa}$ in this example, which is not the case for the non-linear HB-WW criterion.

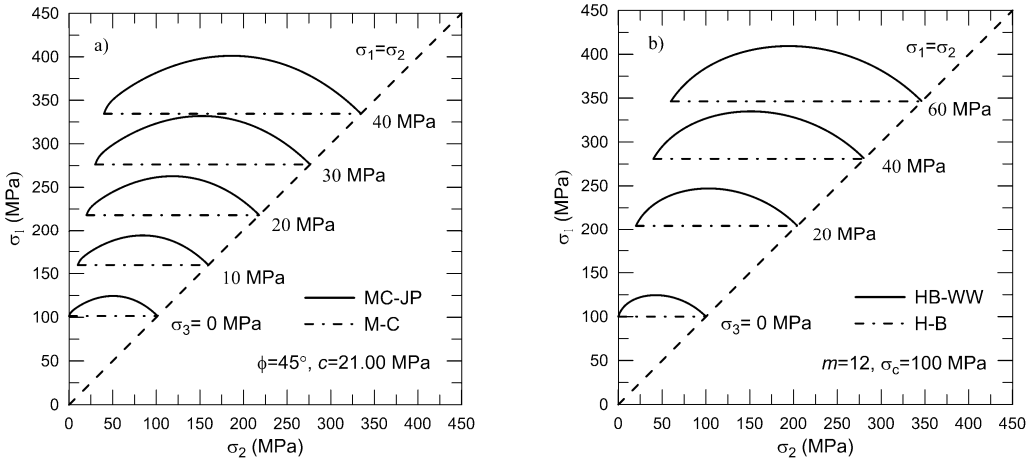

Fig. 3. Effect of intermediate principal stress σ_2 on the stress σ_1 at failure

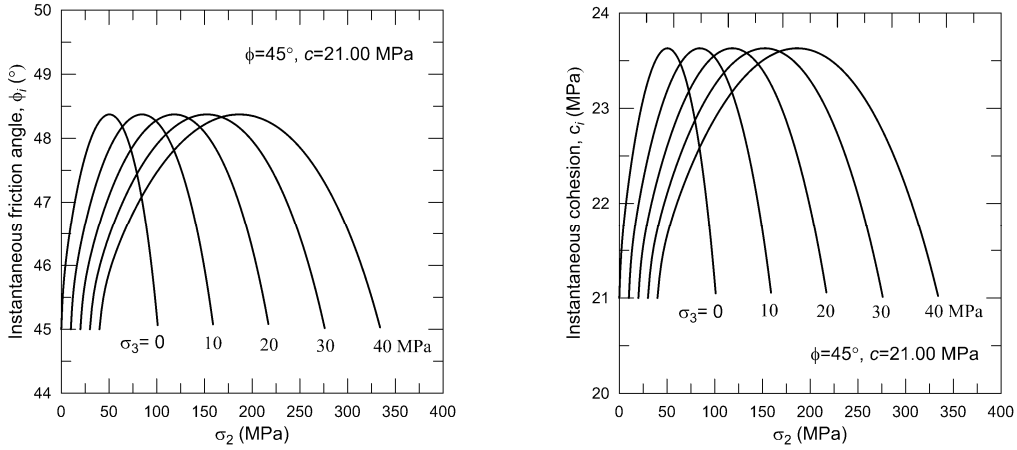

Fig. 4. Effect of σ_2 on the tangential instantaneous M-C parameter of the MC-JP criterion

Fig.6 shows the meridional variation of ϕ_i and c_i calculated for the HB-WW criterion. ϕ_i tends to decrease exponentially from 90° associated with the apex of the failure surface to the lower value as the hydrostatic stress (i.e. $\xi/\sqrt{3}$) increases. The steepest decrease occurs in meridional section of $\theta = 0$, whereas the gentlest decrease takes place in the meridional section related to the θ value of approximately 30°. This implies that the variation of ϕ_i with θ in the deviatoric section is not monotonic. Theoretically large value of c_i is expected at

the stress point near the apex of the non-linear failure surface, from which c_i decreases rapidly to the lowest value, which corresponds to the shear stress intercept in the normal stress – shear stress space. After reaching the lowest values, c_i begins to increase with the increasing hydrostatic stress. Fig. 6 confirms that the HB-WW criterion also manifests this typical meridional behavior of c_i expected from the non-linear failure criterion. The value of ξ giving the least c_i is different in each deviatoric section because the variation of the curvature nearby the origin is very complicated. Finally, it should be mentioned that ϕ_i and c_i of the MC-JP remain constant in a meridional section due to its linear feature although they may varies with θ in the deviatoric section.

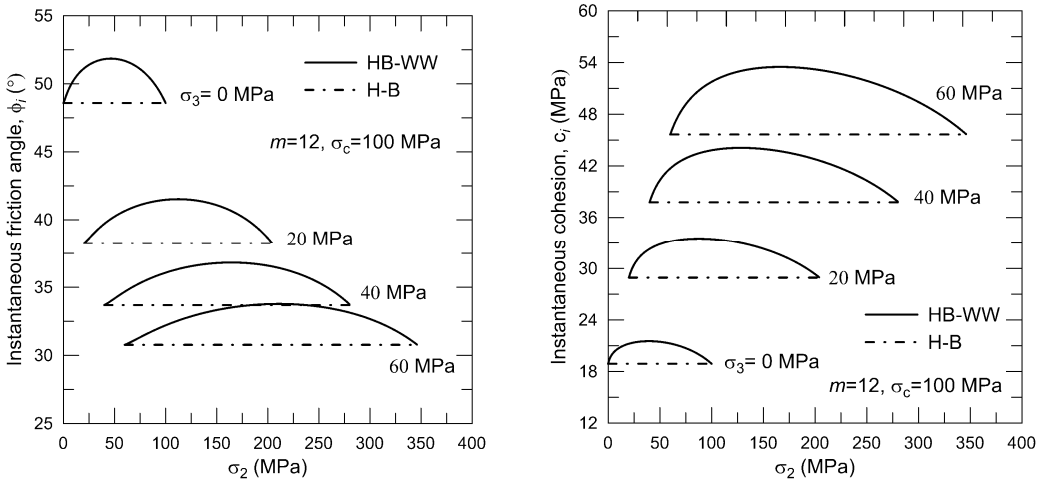

Fig. 5. Effect of σ_2 on the tangential instantaneous M-C parameter of the HB-WW criterion

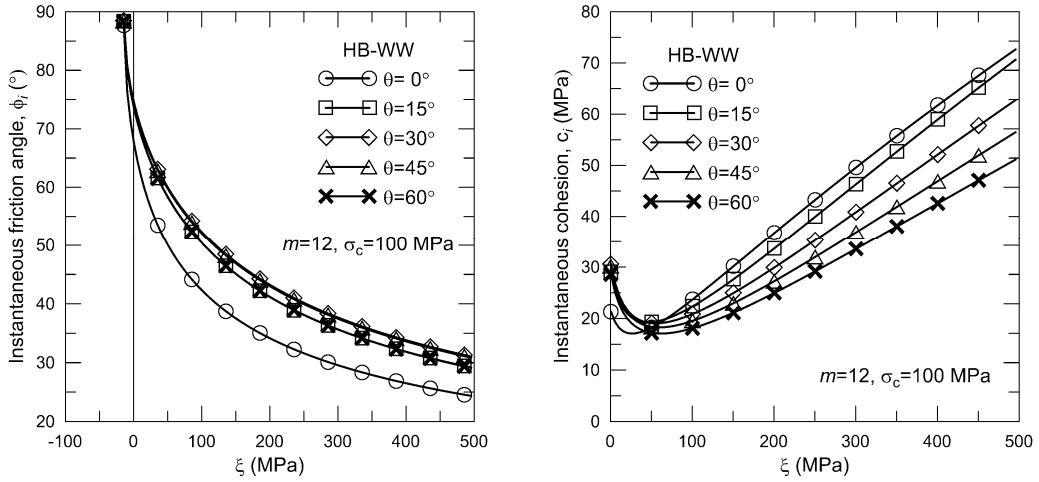

Fig. 6. Meridional variation of ϕ_i and c_i in the HB-WW criterion

5 CONCLUSIONS

The M-C and H-B criteria are two most widely accepted linear and non-linear failure conditions in rock engineering, respectively. They are called 2-D criteria since the effect of the intermediate principal stress σ_2 on the failure is neglected in their formulation. Recently, to accommodate the experimental evidence collected from the true triaxial test on various rock samples, many efforts have been devoted to the development of the 3-D rock failure criterion which can consider the influence of σ_2 on the failure of rock. Along with these efforts, Lee et al. (2012) suggested the 3-D failure criteria MC-JP and HB-WW, which are the extensions of the original M-C and H-B criteria to their 3-D version, respectively.

Although the use of the M-C criterion could result in too simplified approximation of real strength characteristics of rock in some cases, it is still commonly acknowledged in many rock mechanics calculations. Probably, this is due to the fact that most practitioners are familiar with the way of understanding the rock strength in terms of the friction angle and cohesion. Moreover, most of commercial numerical codes are equipped with the M-C failure criterion, but few of them provide more accurate 2-D non-linear or 3-D failure criteria. Therefore, finding the equivalent M-C parameters from 2-D non-linear and 3-D failure criteria is very important for the implementation of these more advanced criteria in the framework of the M-C criterion.

In this paper, a general method to calculate the instantaneous tangential friction angle and cohesion of 2-D non-linear and 3-D failure criteria is proposed. The formulation is carried out in terms of Nayak & Zienkiewicz's stress invariants. Therefore, the method can be applied to any failure criterion provided that it is expressed in terms of stress invariants. Furthermore, the equivalent M-C parameters are directly calculated from the tensor components, which precludes the redundant calculation steps for the principal stresses in the numerical analysis.

The illustrative implementation of the new method for the MC-JP and HB-WW criteria shows that the method is very useful in investigating the behavior of the tangential friction angle and cohesion of these criteria in both the meridional and deviatoric sections.

ACKNOWLEDGEMENT

This research was supported in part by the fund provided by the Korea Institute of Geoscience and Mineral Resources (KIGAM, 2012-2013).

REFERENCES

Balmer, G. (1952), "A general analytical solution for Mohr's envelope". American Society of Testing and Materials, Vol. 52, 1260-1271.

Benz, T. & Schwab, R. (2008), "A quantitative comparison of six rock failure criteria". Int. J. Rock. Mech. Min. Sci., Vol. 45, 1176-1186.

Colmenares, L.B. & Zoback, M.D. (2002), "A statistical evaluation of intact rock failure criteria constrained by polyaxial test data for five different rocks". Int. J. Rock Mech. Min. Sci., Vol. 39, 695-729.

Hoek, E. & Brown, E.T. (1980), Underground excavations in rock. Institution of Mining and Metallurgy, London.

Hoek, E. (1990), "Estimating Mohr-Coulomb friction and cohesion values from the Hoek-Brown failure criterion". Int. J. Rock Mech. Min. Sci., Vol. 27(3), 227-229.

Hoek, E., Carranza-Torres, C. & Corkum, B. (2002), "Hoek-Brown criterion – 2002 edition". Proceedings of NARMS-TAC Conference, Toronto, Vol. 1, 267-273.

Jiang, J. & Pietruszczak, S. (1988), “Convexity of yield loci for pressure sensitive materials”. Comput. Geotech. Vol. 5, 51-63.

Lee, Y.-K. & Bobet, A. (2013), “Instantaneous friction angle and cohesion of 2-D and 3-D Hoek-Brown failure criteria in terms of stress invariants”. Rock Mech. Rock Eng., DOI: 10.1007/s00603-013-0423-6.

Lee, Y.-K., Pietruszczak, S. & Choi, B.-H. (2012), “Failure criteria for rocks based on smooth approximations to Mohr-Coulomb and Hoek-Brown failure functions”. Int. J. Rock Mech. Min. Sci., Vol. 56, 146-160.

Willam, K.J. & Warnke, E.P. (1974) “Constitutive model for triaxial behavior of concrete”. Colloquium on Concrete Structures Subjected to Triaxial Stresses, ISMES Bergamo, IABSE Report .

Zhou, S. (1994), “A program to model the initial shape and extent of borehole breakout”. Comput. Geosci. Vol. 20, 1143-60.

GROUND PENETRATING RADAR SYSTEM FOR DETECTION OF DESICCATION CRACKS IN SOILS

P.C. Prat, A. Ledesma, A. Cuadrado and H. Levatti
Dept. of Geotechnical Engineering and Geosciences, UPC-BARCELONATECH, Barcelona, Spain

ABSTRACT: *In this paper we explore a relatively simple, non-destructive, indirect technique using a ground penetrating radar (GPR) system to detect cracks that form and propagate inside a soil specimen during desiccation. Although GPR devices have been used for multiple applications, their use in the detection of small cracks (few millimeters wide), has not been demonstrated yet. The experiments and the methodology used to test the accuracy of a small commercial GPR device for crack identification are described. The main objective was to identify what type of signals and what crack width can be detected using the GPR device. The results indicate that cracks of one or two millimeters wide can be detected depending on its position and shape. On the other hand, sub-millimeter cracks are undetectable with the currently existing devices in the market. In spite of the limitations the GPR method can be useful to find time-related bounds of when the cracks appear, and to point at their location. Because the GPR systems are in constant evolution this technique could become a very versatile and convenient method to scan soils under different kinds of processes both in the laboratory and in the field.*

1 INTRODUCTION

Clayey soils tend to shrink and crack when subject to desiccation. This phenomenon is quite common in nature and there are many published works on the subject (Chertkov, 2002, Hu, et al., 2008, Kodikara, et al., 2000, Kodikara, et al., 2004, Lakshmikantha, et al., 2007, Lakshmikantha, et al., 2009, 2012, Morris, et al., 1992, Péron, et al., 2009, Vogel, et al., 2005). However, until the development of unsaturated soil mechanics the problem has not been analyzed considering the parameters that govern the behavior of soil in the unsaturated state, primarily suction. Tensile strength (suction dependent) and fracture toughness are shown as the most relevant parameters (Ávila, et al., 2002, Lakshmikantha, et al., 2012), but a definite model explaining that process is yet to be formulated.

In laboratory tests many cracks appear on the top boundary of soil specimens but there are others than are not visible. Various experiments have shown that cracks may start at any point within the specimen (Cuadrado, 2013, Lakshmikantha, 2009, Lakshmikantha, et al., 2013). To detect the cracks that start at the bottom boundary or within the sample one would need sophisticated techniques such as X-ray, magnetic resonance or electrical resistivity tomography (Hassan and Toll, 2013, Mukunoki, et al., 2010, Otani and Obara, 2004, Samoulian, et al., 2003), usually very expensive and involving very complicated setups. However, detection of those non-visible cracks is important because cracking due to drying in soils is a very

complex three-dimensional process and the study cannot limit itself to the outer visible cracks.

In this paper we explore a relatively simple, non-destructive, indirect technique using a ground penetrating radar (GPR) system to detect cracks that form and propagate within the specimen during desiccation. While surface cracking allows following the evolution of the external cracking pattern with time, the GPR technique may be helpful to detect the cracks within the soil. Only complete monitoring of those inner cracks will help in explaining the phenomenon with greater accuracy. However, although GPR devices have been used for multiple applications, their use in the detection of small cracks (few millimeters wide), has not been demonstrated yet. Because the ground is formed by three distinct phases (water, gas and solid) during the drying process, and the changes in time of each phase modify the soil's electromagnetic properties, there is added difficulty to the interpretation of the results of this method.

The experiments and the methodology used to test the accuracy of a small commercial GPR device for crack identification are described. The main objective was to identify what type of signals and what crack width can be detected using the GPR device. The results indicate that cracks of one or two millimeters wide can be detected depending on its position and shape. On the other hand, sub-millimeter cracks are undetectable with the currently existing devices in the market.

In spite of these limitations the GPR method can be useful to find time-related bounds of when the cracks appear, and to point at their location.

2 GPR FUNDAMENTALS

The GPR is a nondestructive technique that uses electromagnetic pulses to detect reflecting surfaces inside the soil allowing imaging buried objects, stratigraphy and other soil features at shallow depths, providing continuous, real-time profiles of the subsurface. Normally the equipment consists of a computerized control system connected to antennas which are moved slowly along the ground surface to produce a continuous subsurface profile. One antenna emits the electromagnetic pulses and a second one records the reflected signal from the objects, discontinuities or other features inside the soil.

The reflected wave originates from changes in the electromagnetic properties of the soil that may be caused by variations in water content, density changes due to the presence of stratigraphic surfaces and discontinuities, or voids existing in the path of the pulse. Therefore the success of the technique relies to great extent on a sufficient dielectric contrast at the crack location to produce a clear reflected signal. The penetration depth of the pulses, and data resolution, depend on the wavelength and the soil's dielectric constant. These parameters are mainly controlled by the soil's moisture content. The depth and resolution are inversely proportional magnitudes: increasing the antenna's frequency a better resolution is obtained but the depth is smaller.

The theoretical background of the method is the theory of electromagnetic fields, described by Maxwell's equations (1), and the constitutive equations (2):

$$\nabla \boldsymbol{D} = \rho_f; \quad \nabla \boldsymbol{B} = 0; \quad \nabla \times \boldsymbol{E} = -\frac{\partial \boldsymbol{B}}{\partial t} + \boldsymbol{M}; \quad \nabla \times \boldsymbol{H} = -\frac{\partial \boldsymbol{D}}{\partial t} + \boldsymbol{J} \tag{1}$$

$$\boldsymbol{D} = \varepsilon \boldsymbol{E}; \quad \boldsymbol{H} = \frac{\boldsymbol{B}}{\mu}; \quad \boldsymbol{J} = \sigma \boldsymbol{E} \tag{2}$$

Fig. 1. StructureScan Mini®

Fig.2. Soil specimen and methacrylate plate with scanning grid

where $\boldsymbol{E}$ = electric field, $\boldsymbol{H}$ = magnetic field, $\boldsymbol{D}$ = electric displacement field, $\boldsymbol{B}$ = magnetic induction, $\boldsymbol{J}$ = free current density, $\boldsymbol{M}$ = magnetization field and ρ_f = free charge density. The parameters that appear in Eqs. (2) describe the electromagnetic properties of the medium and are: ε (dielectric permittivity), μ (magnetic permeability) and σ (electric conductivity).

The use of the GPR is based on the dielectric permittivity ε, which represents the permittivity of an electromagnetic pulse through the medium, compared to the void permittivity. It is a non-dimensional parameter that depends on the electric conductivity and the thickness of the layer. For most of the materials in the ground this parameter has a value between 1 (air) and 81 (water). The GPR produces results by detecting wave reflections produced while the wave crosses the boundary between two materials with different dielectric constants.

Soils are often mixtures of different types of materials. Separately, each element has its own electromagnetic properties. Together, they form a medium where the dielectric permittivity, magnetic permeability, and electric conductivity depend on the properties of each material and its percentage in the mixture. There are several models that characterize these mixtures, which can also be used when considering a medium consisting of a single solid material, plus water and air (Pérez, 2001).

Electromagnetic waves propagate in water at very low speed and with high attenuation. The dielectric permittivity of water is large (around 80 but variable with temperature and mineral composition) and the high permittivity contrast with the other materials that make up the soil makes water a key element in the average propagation speed of electromagnetic waves in soils. Studies have shown (Knoll and Knight, 1994) that with the usual frequencies used for GPR the dielectric permittivity as well as the electric conductivity of the soil increases with the degree of saturation.

In addition to the degree of saturation, other properties such as particle size and porosity have also an impact in the average value of those parameters.

3 GPR DEVICE AND EXPERIMENTAL PROGRAM

The GPR device used in the present work is a small compact unit, model StructureScan Mini® manufactured by Geophysical Survey Systems Inc. (Fig. 1). The antenna's nominal frequency is 1600 MHz allowing a depth penetration up to about 40 cm, although for soils those values may change considerably depending on the clay's mineral composition and water content.

Fig. 3. Block test: (a) mold with strips inserted; (b) after pouring slurry; (c) surface cracks at 30 days

The device is a self-contained unit where both emitting and receiving antennas are located. It has four wheels that allow easy displacement and provides reading the distance traveled during the exploration. The path is guided by three laser beams, one to the front and two to the sides. Unfortunately many of the parameters that might be helpful to adjust for soils cannot be modified by the user during recording, and their impact must be introduced during post-processing using the accompanying dedicated software RADAN® (GSSI, 2009), which is designed to process, view, and document 2D and 3D data sets collected with the StructureScan Mini®. The software allows customizing the size and colors of targets, use of multiple transform options, background removal filtering, data migration, gain control, and adjusting the parameters to suit the soil's characteristics.

The soil used in the experiments is a well-known Barcelona silty clay (Barrera, 2002). It is a fine-grain soil, with 60% passing the #200 sieve and unit weight of particles γ_s = 27 kN/m^3, liquid limit w_L= 32, and plastic limit w_P= 16. Two types of tests have been conducted: with cylindrical and rectangular block specimens.

For the first type of tests the specimen was a soil cylinder of 80 cm in diameter and 10 cm thick. The clay, initially slurry, was poured in the mold and was left to dry in a controlled laboratory environment (24^{o}C and 60% relative humidity) for 36 days. The specimen was scanned periodically using the GPR device in order to detect developing cracks within the sample. Attempts were made to calibrate as much as possible the available device parameters to accommodate the evolving soil's characteristics. To allow the displacement of the GPR, a 1 cm-thick methacrylate plate was placed on top of the specimen during scanning. The scanning area consisted of a 30 cm × 30 cm grid, with a 5 cm separation between lines, providing 7 lanes in two orthogonal directions. Figure 2 shows the soil specimen immediately after been poured in the mold and the methacrylate plate with the scanning grid.

The second type of tests was conducted on specimens made using a rectangular planter pot, of the type commonly found in garden stores. The purpose was to determine the minimum crack opening that the GPR device can detect. The specimen shape allowed the use of less amount of soil for the required specimen depth. Several artificial cracks were induced in the specimen, both horizontal and vertical, by means of rectangular wood or metal strips of several thicknesses (between 2 and 6 mm). After the strips were inserted in the mold (Fig. 3a), the slurry was poured and left to dry in an open-air environment (Fig. 3b). After one month of drying some cracks had appeared on the surface (Fig. 3c) and the consistency of the specimen was hard enough to perform the GPR scan. This was conducted in the direction parallel to the longest side of the specimen (from right to left in the figure).

4 RESULTS AND DISCUSSION

The purpose of the experiments was two-fold: with the cylindrical specimen the objective was to determine the ability of the GPR to detect internal cracks and how they are shown as a result of the GPR scan, while with the rectangular block specimen the objective was to determine the range of crack width that can be detected with the method.

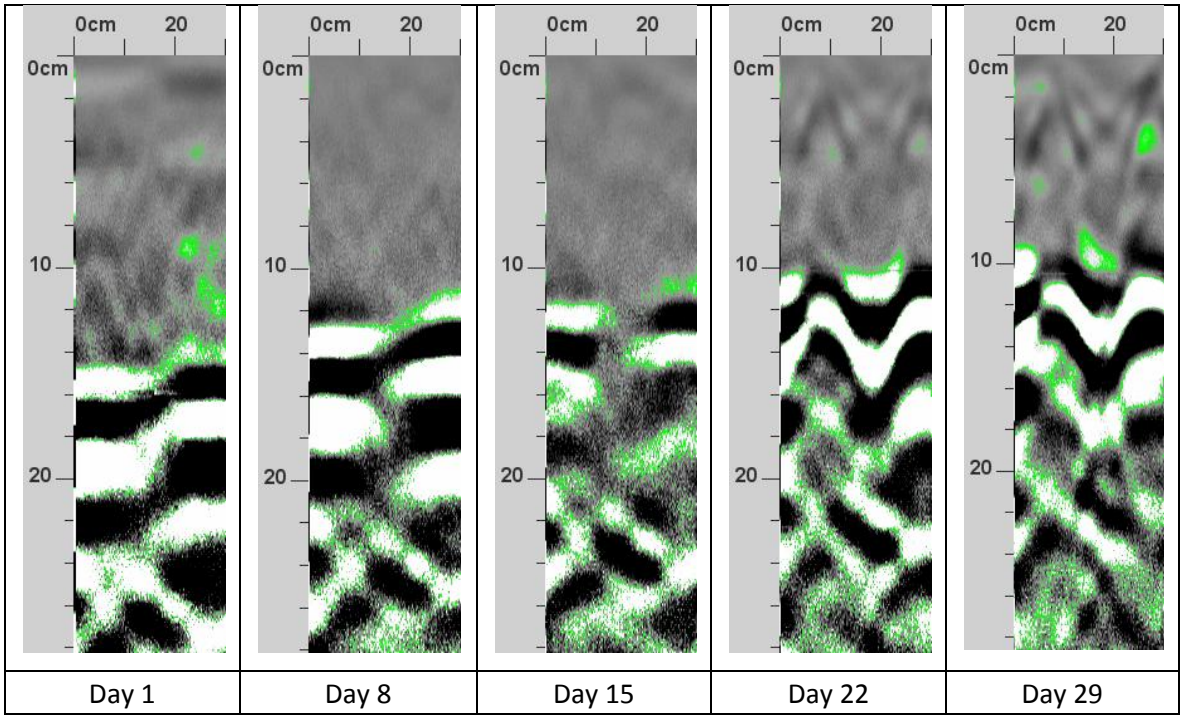

Fig. 4. Time evolution of the GPR profiles along lane 1 of the recording grid

4.1 Cylindrical specimen test

With the cylindrical specimen the GPR has been used to systematically search and track non-visible cracks. The device is capable of detecting cracks a few millimeters thick. It is also able to determine the separation between cracks when the distances are 5 cm or more. Cracks closer together create interferences that prevent a correct interpretation of the data. This test has shown that the crack signal is identified as a hyperbolic shape indicating the presence of reflectors or more or less abrupt changes in the dielectric constant of the medium.

Figure 4 shows the evolution of the GPR readings at 1, 8, 15, 22 and 29 days from the start of the test along lane 1 of the grid shown in Figure 2. The figure shows the progressive shrinkage of the sample (shown in light gray color) due to drying. The GPR images corresponding to days 8 and 15 show a fairly homogeneous grayscale profile which suggests that there are no major cracks or internal heterogeneities along the lane. The images for days 22 and 29 show the characteristic hyperbolic pattern near the surface, coinciding with major cracks visible on the external surface along lane 1.

A key issue is to establish how to recognize a crack in the ground from a GPR profile. Figure 5 shows the GPR profile along lane 1 (in red) corresponding to day 21, compared with the visible surface crack pattern. The figure shows that the crack crossing the sample results in a darker shade in the upper right corner of the GPR profile. The thinner crack almost perpendicular to lane 1 is not detected. However, on day 22 this crack has propagated towards the center of the specimen and it is wider. The GPR profile in this case easily captures the crack as shown by the hyperbolic pattern near the upper left corner (Figure 6).

Figure 7 shows the GPR profile on the same day 22, but along lane 3, where the cracks are closer. Cracks can be recognized in the GPR profile, and the distance between them measured and checked with the visible surface pattern. Therefore, the method allows not only to detect invisible cracks, but also to calculate the distance between them by measuring the distance between the tips of the hyperbolic patterns in the GPR profile. This has a limit when the cracks are very close: figure 8 shows the GPR profile along lane 4 where only one hyperbolic pattern can be seen, whereas there are two cracks along the path.

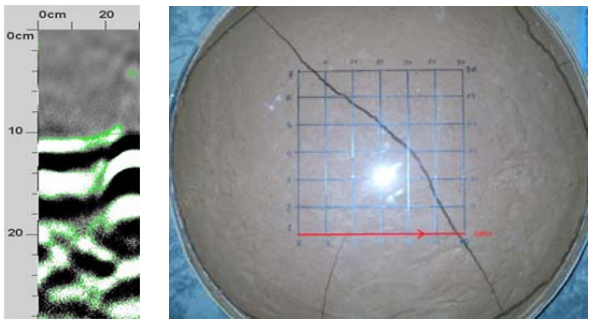

Fig. 5. GPR profile (lane 1) and cracks at day 21

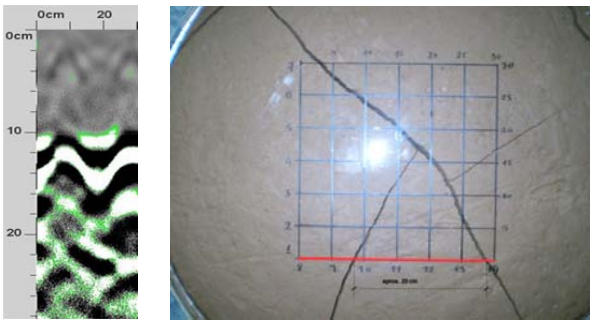

Fig. 6. GPR profile (lane 1) and cracks at day 22

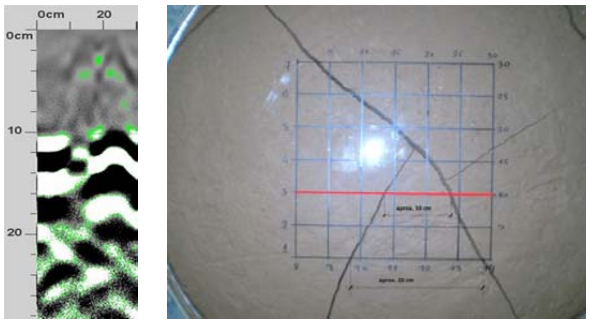

Fig. 7. GPR profile (lane 3) and cracks at day 22

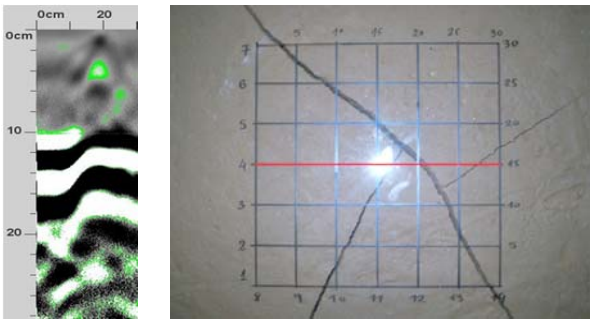

Fig. 8. GPR profile (lane 4) and cracks at day 22

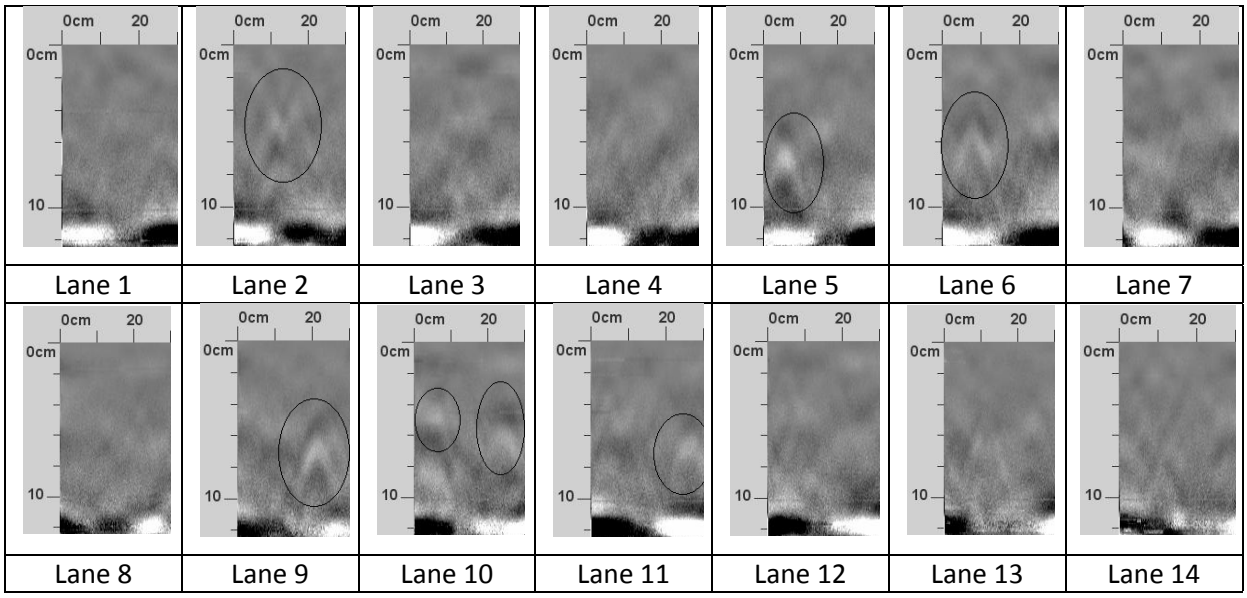

Fig. 9. GPR profiles along the 14 lanes at day 20, before the formation of surface (visible) cracks

The ability of the GPR method to detect cracks that start inside the specimen and that may or may not propagate towards the surface has also been proved. Figure 9 shows the GPR profiles along the 14 lanes obtained on day 20, before any surface crack was visible. The figure also shows the suspected patterns that might correspond to internal cracks. The data is then plotted on the surface image of the specimen (Fig. 10a), to check coincidence between horizontal and vertical lanes which happens only at three locations. Two of those locations correspond to cracks that will become visible on the surface image of day 22 (Fig. 10b). The other one does not appear to correspond to any visible crack on that day. However, on day 28 a crack has appeared nearby (Fig. 11a) which further propagates to become a large surface crack on day 36 (Fig. 11b).

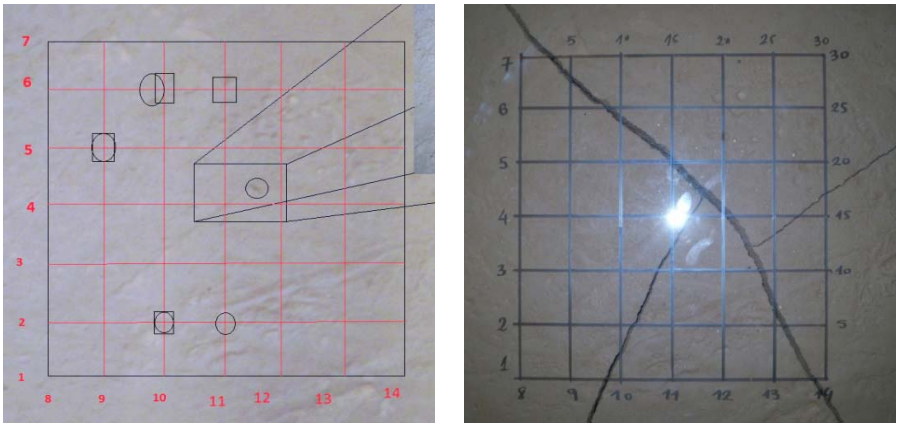

Fig. 10. Comparison of (a) forecasted crack locations from GPR profiles at day 20, left, and (b) actual cracks formed at day 22, right

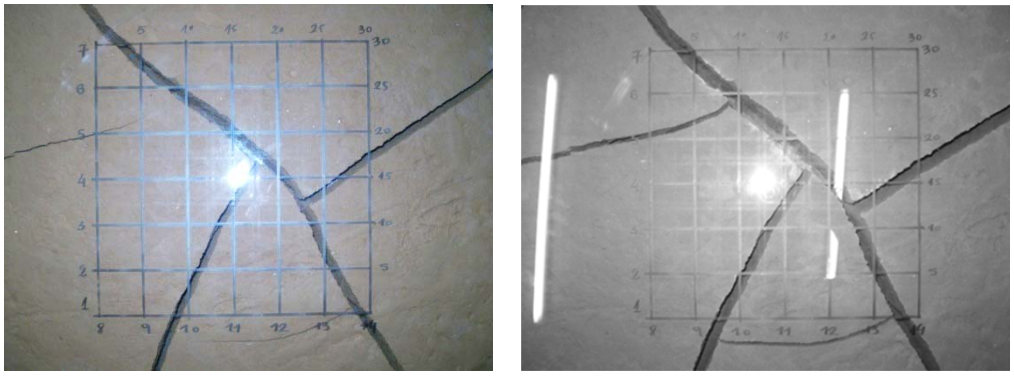

Fig. 11. Actual cracks formed (a) at day 28, left, and (b) at day 36, right

Further post-processing with the RADAN® software (GSSI, 2009) allows a quasi-3D visualization of the cracks. As an example, the main crack showing on the surface at day 22 can be tracked as shown in Figure 12, where each image corresponds to the points indicated in the surface image.

4.2 Rectangular block specimen test

The results of this test indicate that 1-2 mm wide cracks can be detected depending on the position and shape and on the moisture content of the specimen. Higher moisture content and more superficial cracks result in easier detection and interpretation of the received signal. Cracks less than 5 mm wide and at depths of 8 cm or more are difficult to distinguish from the signal's background noise. Hairline or sub-millimeter cracks cannot be identified with the current GPR technology.

In this test five strips of different thickness and material were inserted into the soil (Fig. 3a), three vertical (A, metal, 6 mm; B, metal, 4 mm; and C, metal, 2 mm) and two horizontal (D, metal, 2mm; and E, wood, 5 mm). Figure 13 shows the GPR profile obtained shortly after the surface cracks became visible and before the strips were removed. The figure has a yellow box showing two hyperbolic patterns that indicate the position of the two surface cracks. Below is a red box showing the location of the vertical strips (A, B, C) with three consecutive hyperbolic patterns located approximately at the same depth. In the same figure an ellipse indicates the position of strips D and E. It is not clear whether the corresponding hyperbolic patterns have been really detected by the GPR or they are actually an overlap effect of the tail of the hyperbolas corresponding to strips C, B and A. The lower horizontal line delimits approximately the depth of the specimen.

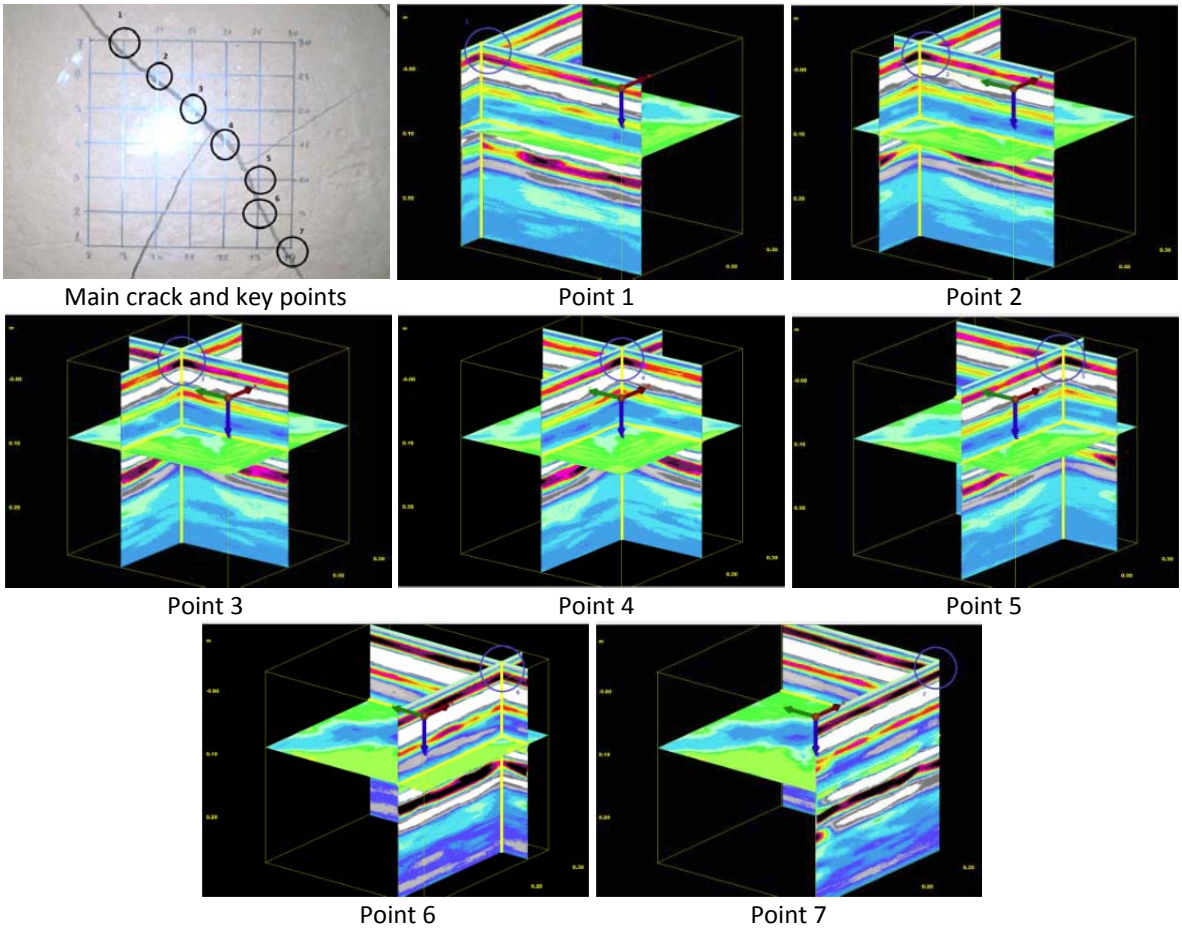

Fig. 12. 3D visualization of the main crack using RADAN®

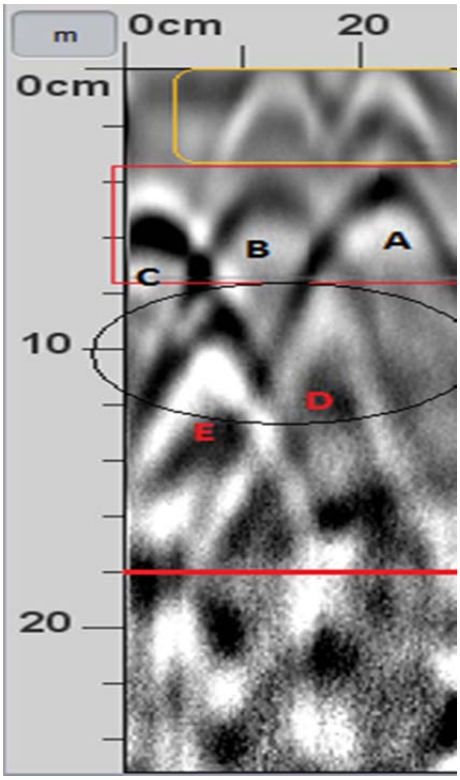

Fig. 13. GPR profile of the rectangular block specimen test with strips inserted shortly after the first cracks were visible on the external surface

5 CONCLUSIONS

A relatively simple non-destructive indirect technique using a ground penetrating radar (GPR) for detecting crack formation and propagation within soil specimens during drying has been developed and discussed in this paper. While surface cracks allow tracking the evolution of the external cracking pattern over time, the GPR technique can be used to explain the phenomenon of cracking more accurately by allowing a more comprehensive monitoring of the internal cracks. This is a novel technique in the case of soil cracking, although GPR devices have been used for many applications previously. For soils, the interpretation of the results obtained by this technique is complex because during the drying process its electromagnetic properties do not remain constant over time due to the changes that occur in each of the material's phases.

Two types of tests have been conducted. The first was performed on a cylindrical specimen of 80 cm in diameter and 10 cm thick, which was monitored using the GPR to identify non-visible internal cracks. The GPR is capable of detecting cracks a few millimeters thick, as well as to determine the separation between cracks when the distance is approximately more than 5 cm. Closer cracks create interferences that prevent the correct interpretation of the data. This test has shown that the crack signal is identified with a hyperbolic pattern in the GPR profiles indicating the presence of reflectors or abrupt changes in the dielectric constant of the medium.

A second type of test has been conducted to characterize the minimum crack thickness that the GPR is capable to detect. This test was carried on a rectangular block specimen where strips of different materials and thickness were inserted to create artificial cracks. The results indicate that the cracks of one or two millimeters in width can be detected depending on its position and shape and on the moisture content of the specimen. For now, hairline or sub-millimeter cracks cannot be identified with the technique and equipment used.

Despite the drawbacks and that it is not possible to clearly identify the origin of a crack, the technique does allow to establish an upper-bound of the instant when the crack occurs, once it has reached sufficient thickness to be detected. This allows for a better understanding on the relationship between the soil's parameters and crack formation.

The GPR technique that has been developed shows good promise but still has some limitations with current technology. However, by combining the capabilities of the GPR with traditional systems for testing drying soils, the prediction and understanding of the reasons and the ways in which the soil shrinks and then cracks initiate and propagate can be greatly improved. A key advantage of the GPR system is its low cost compared to other systems such as X-rays, CT scans and MRIs. Its portability and ease of use and continuous evolution makes it a good choice to work in the field and in the laboratory.

ACKNOWLEDGEMENT

Financial support from research grants BIA2009-08341, awarded by the former Spanish Ministry of Science and Innovation, and BIA2012-36498, awarded by the Spanish Ministry of Economy and Competitiveness, is gratefully acknowledged.

REFERENCES

Ávila, G., Ledesma, A., and Lloret, A. (2002). Measurement of fracture mechanics parameters for the analysis of cracking in soils. *Proc., 3rd International Conference on Unsaturated Soils - UNSAT 2002*, Swets & Zeitlinger, 547-552.

Barrera, M. (2002). *Estudio experimental del comportamiento hidro-mecánico de suelos colapsables.* Ph.D. Thesis, UPC-BarcelonaTech.

Chertkov, V. Y. (2002). Modelling cracking stages of saturated soils as they dry and shrink. *European Journal of Soil Science*, 53, 105-118.

Cuadrado, A. (2013). *Detección de grietas por desecación en arcillas mediante GPR.* Master Thesis, UPC-BarcelonaTech.

GSSI (2009). RADAN® Manual. Geophysical Survey Systems, Inc., Salem, NH, USA.

Hassan, A., and Toll, D. G. (2013). Electrical resistivity tomography for characterizing cracking of soils. *Proc., GeoCongress 2013 - Stability and Performance of Slopes and Embankments III*, American Society of Civil Engineers, 818-827.

Hu, L. B., Hueckel, T., Péron, H., and Laloui, L. (2008). Modeling Evaporation, Shrinkage and Cracking of Desiccating Soils. *Proc., IACMAG 12*, IIT Mumbai, 1083-1090.

Knoll, M. D., and Knight, R. (1994). Relationships between dielectric and hydrogeologic properties of sand-clay mixtures. *Proc., Fifth International Conference on Ground Penetrating Radar*, Waterloo Centre for Groundwater Research, 45-61.

Kodikara, J., Barbour, S. L., and Fredlund, D. G. (2000). Desiccation cracking of soil layers. *Proc., Unsaturated Soils for Asia*, Balkema, 693-698.

Kodikara, J. K., Nahlawi, H., and Bouazza, A. (2004). Modelling of curling in desiccation clay. *Canadian Geotechnical Journal*, 41, 560-566.

Lakshmikantha, M. R. (2009). *Experimental and theoretical analysis of cracking in drying soils.* Ph.D. Thesis, UPC-BarcelonaTech.

Lakshmikantha, M. R., Prat, P. C., and Ledesma, A. (2007). Characterization of crack networks in desiccating soils using image analysis techniques. *Proc., Numerical Models in Geomechanics X*, Balkema, London, 167-176.

Lakshmikantha, M. R., Prat, P. C., and Ledesma, A. (2009). Image analysis for the quantification of a developing crack network on a drying soil. *Geotech. Test. J.*, 32(6), 505-515.

Lakshmikantha, M. R., Prat, P. C., and Ledesma, A. (2012). Experimental evidences of size-effect in soil cracking. *Canadian Geotechnical Journal*, 49(3), 264-284.

Lakshmikantha, M. R., Reig, R., Prat, P. C., and Ledesma, A. (2013). Origin and mechanism of cracks seen at the bottom of a desiccating soil specimen. *Proc., GeoCongress 2013 - Stability and Performance of Slopes and Embankments III*, American Society of Civil Engineers, 790-799.

Morris, P. H., Graham, J., and Williams, D. J. (1992). Cracking in drying soils. *Canadian Geotechnical Journal*, 29, 263-277.

Mukunoki, T., Otani, J., Maekawa, A., Camp, S., and Gourc, J. P. (2010). Investigation of crack behavior on cover soils at landfill using X-ray CT. *Advances in X-ray Tomography for Geomaterials*, J. Desrues, G. Viggiani, and P. Bésuelle, eds., John Wiley & Sons, 213-219.

Otani, J., and Obara, Y. (2004). X-ray CT for geomaterials: Soils, Concrete, Rocks. Swets & Zeitlinger.

Pérez, V. (2001). *Radar de subsuelo. Evaluación para aplicaciones en arqueología y en patrimonio histórico-artístico.* Ph.D. Thesis, UPC-BarcelonaTech.

Péron, H., Hueckel, T., Laloui, L., and Hu, L. B. (2009). Fundamentals of desiccation cracking of fine-grained soils: experimental characterisation and mechanisms identification. *Canadian Geotechnical Journal*, 46(10), 1177-1201.

Samoulian, A., Cousin, I., Richard, G., Bruand, A., and Tabbagh, A. (2003). Electrical resistivity imaging for detecting soil cracking at the centimetric scale. *Soil Science Society of America Journal*, 67(5), 1319-1326.

Vogel, H. J., Hoffmann, H., and Roth, K. (2005). Studies of crack dynamics in clay soil. I: Experimental methods, results and morphological quantification. *Geoderma*, 125(3-4), 203-211.

DYNAMIC LINEARIZATION OF NONLINEAR YIELD ENVELOPES FOR LIMIT ANALYSIS APPLICATIONS

A.V. Lyamin
Centre of Excellence for Geotechnical Science and Engineering, University of Newcastle, Australia

K. Krabbenhøft
Centre of Excellence for Geotechnical Science and Engineering, University of Newcastle, Australia

J. Huang
Centre of Excellence for Geotechnical Science and Engineering, University of Newcastle, Australia

ABSTRACT: *Computational limit analysis provides a fast and convenient means of evaluating the stability or bearing capacity of geostructures. It is based on numerical optimization techniques and the latest trend is to use robust conic programming algorithms. The shortcoming, however, is that the types of problems covered by conic programming are not very general. In practice, this means that only criteria containing linear and quadratic terms (such as Drucker-Prager) or those that involve linear terms in the principal stresses (such as Mohr-Coulomb) can be considered. In the present paper this shortcoming is addressed. The idea is to maintain an efficient and robust conic programming algorithm as the main solution engine. Nonlinear criteria are then handled by a dynamic linearization procedure that involves a sequence of standard conic programming solutions in an iterative scheme that turns out to converge relatively rapidly*.

1 INTRODUCTION

Computational limit analysis provides a fast and convenient means of evaluating the stability or bearing capacity of geostructures. In contrast to conventional displacement based finite element analysis which requires that the full load-displacement response is traced, computational limit analysis requires the solution of a single nonlinear optimization problem. The solution of this optimization problem – whose size is proportional to the number of nodes in the mesh and thus may be very large – is the most critical part of any limit analysis procedure.

The development of solution algorithms applied to computational limit analysis problems have to a large extent followed the developments in general numerical optimization (where typical applications include scheduling, portfolio optimization, utility maximization and similar problems in economics and management science). The latest trend, starting with the work of Ciria (2004), has been to use conic programming algorithms. The types of problems covered by conic programming are more general than those of linear programming but less general than those of nonlinear programming. Indeed, the major limitation is that the constraints must be conic. In practice, this means that only criteria containing linear and quadratic terms (such as Drucker-Prager) or those that involve linear terms in the principal stresses (such as Mohr-Coulomb) can be considered (Krabbenhoft et al. 2007, 2008). While the efficiency and robustness of state-of-the-art conic programming algorithms are superior to that of general nonlinear programming algorithms, it is somewhat of a shortcoming that only rather simple yield criteria can be handled. In particular, criteria that involve a nonlinear failure envelope in $\sigma_1 - \sigma_3$ space are outside the scope of conic programming.

In the present paper this shortcoming is addressed. The idea is to maintain an efficient and robust conic programming algorithm as the main solution engine. Nonlinear criteria are then handled by a dynamic linearization procedure that involves a sequence of standard conic programming solutions in an iterative scheme that turns out to converge relatively rapidly. This is demonstrated with respect to the Hoek-Brown and a number of other nonlinear criteria.

2 LIMIT ANALYSIS USING SOCP

Regardless of particular dicretization employed the finite element limit analysis formulation leads to a convex mathematical program, which (considering the dual form of kinematic formulations) can be cast as follows

$$\begin{aligned} &\text{maximize} \quad \lambda \\ &\text{subject to} \quad \mathbf{B}^{\mathrm{T}}\boldsymbol{\sigma} = \mathbf{p}_0 + \lambda \mathbf{p} \\ &\qquad\qquad f_i(\boldsymbol{\sigma}) \le 0, \quad i = \{1, \ldots, N_\sigma\} \end{aligned} \tag{1}$$

where λ is a load multiplier, $\boldsymbol{\sigma}$ is a vector of stress variables, $\mathbf{B}^{\mathrm{T}}$ is global equilibrium matrix, $\mathbf{p}_0$ and $\mathbf{p}$ are vectors of prescribed and optimizable forces, respectively, f_i is the yield function for stress set i and N_σ is the number of stress nodes. The solution to problem (1) can be found efficiently by using general Interior-Point methods (IPM) or specialized conic optimization solvers (SOCP). In last case the optimization problem to solve becomes

$$\begin{aligned} &\text{minimize} \quad \mathbf{c}^{\mathrm{T}}\mathbf{x} \\ &\text{subject to} \quad \mathbf{A}\mathbf{x} = \mathbf{b} \\ &\qquad\qquad \mathbf{x} \in K \end{aligned} \tag{2}$$

where $\mathbf{c}$ is an objective function vector, $\mathbf{x}$ is a vector of problem variables, $\mathbf{A}$ is a matrix of equality constraint coefficients, $\mathbf{b}$ is a rhs vector and K is a global cone composed of N_σ number of sub-cones. The stress-conic transformations required to convert (1) into (2) can be found e.g. in Krabbenhoft et al. (2007). In the case of multi-surface plasticity (which is used here for dynamic linearization) the number of cones involved in (2) will be multiplied by the number of basic surfaces representing each multi-surface yield locus.

3 LINEARIZATION PROCEDURE

Proposed linearization scheme covers both internal and external type of yield envelope approximation. Internal linearization guarantees rigorous lower bound estimates on collapse load when used with static discretization of problem at hand. And external linearization reinforces, respectively, rigorous upper bound solutions when employed with kinematic formulation of limit analysis.

Only plain strain conditions are considered in this study, however the approach adopted seems to be general to work also for plain stress and three-dimensional problems. Basic idea is based on the fact that any yield function with curved envelope in hydrostatic plan, which has the same cross-section in deviatoric plan as Mohr-Coulomb (MC) or Drucker-Prager (DP) criteria, can be approximated locally (at current level of hydrostatic stress) with required accuracy by a series of MC or DP surfaces (which are also called *basic* surfaces in the rest). The major challenge, however, is to guarantee at minimal cost the robust convergence of linearized problem to a solution which is close to that of original problem. Therefore this

study aims to develop such a linearization scheme which will work efficiently regardless of the particular shape of nonlinear yield envelope involved and the geometry and the loading conditions of the problem considered.

3.1 Local Linearization

For the purpose of comparison and performance judgment the linearization is implemented in the way that the number of basic surfaces, N_b, and the approximation accuracy, ε, can be specified. Given these two parameters the sequence of basic surfaces is constructed as depicted in Figure 1. First the curvature, κ, of original yield envelope is estimated at current

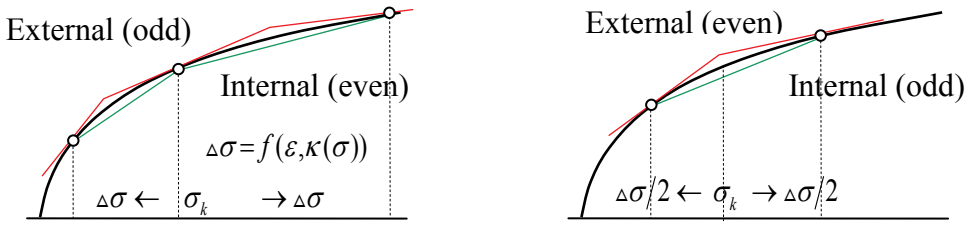

Figure 1. Local linearization schemes for curved yield envelopes.

stress level, σ_k. This gives then the radius of referencing circle which in combination with specified accuracy allows to estimate the distance, $\Delta\sigma$ between intersections of two consecutive basic surfaces as shown in Figure 1. Next, the sequence of N_b +1 points for internal *even* (or external *odd*) linearization and N_b points for external *even* (or internal *odd*) linearization is generated by stepping symmetrically forward and backward from current stress point σ_k. If stepping backward finds the apex of yield envelope being passed, the apex is taken as the first point in sequence and all remaining backward steps are transferred to be the extra forward steps. This results in that the required number of basic surfaces being maintained throughout all approximations. Finally all basic surfaces are constructed by cutting the original yield envelope through two consecutive points in the case of internal linearization. While the external approximation proceeds by constructing tangential planes at each point.

3.2 Global Linearization

Though theoretically nothing prevents local linearization to be as accurate as required and, consequently, to have as many basic surfaces as needed to provide the required accuracy on some interval around current stress point, in practice it appears (as will be demonstrated later in the paper) that such naive approach is not robust. Either the number of basic surfaces which warrants the convergence makes computations too expensive when required accuracy increases, either (if to keep number of basic surfaces constant) the convergence becomes a problem. Therefore, what is proposed here is to construct accurate internal linearization by using only two basic surfaces and then extend it by another two surfaces to accomplish global linearization covering entire region of definition for considered yield function, as shown in Figure 2. This approach is naturally suitable for lower bound limit analysis discretization, but it can be argued that it can be applied also for upper bound discretizations as well, providing

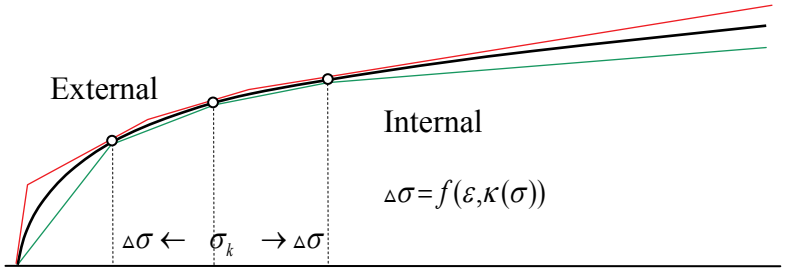

Figure 2. Global linearization for curved yield envelopes.

that convergence check includes also verification that none (or very limited amount) of stress points actually come out of accurate linearization region. The obtained solutions than will not be rigorous upper bounds, but very close ones (denoted by UB* in results sections) and with controlled accuracy. Otherwise it is suggested that global external linearization can be also employed as depicted by red line in Figure 2. However, as will be shown later, in this case some extra care needs to be taken to have a steady convergence.

3.3 Convergence Check

As soon as the limit analysis optimization problem is solved using generated set of basic yield functions, the obtained stresses are used to produce new linearization. This is repeated till convergence is reached. The convergence check verifies first that two consecutive load multipliers differ not more than by specified tolerance. Next it is checked that no stress point is located beyond the original yield envelope (with two different tolerances, tol_{int} and tol_{ext}, are normally employed for internal and external linearizations). And finally it is checked that none of the stress points is going outside the linearization interval given by the first and the last linearization points. It should be mentioned here that this last check is particularly important in the case of global internal linearization when it is employed together with kinematic discretization. It is reinforced then that the obtained solution is close to the rigorous upper bound with specified accuracy. With all these vefifications in place it can be argued that for practical purposes the internal global linearization is a reasonable choice regardless of any particular finite element discretization (as will be demonstrated in Numerical Examples section).

4 NONLINEAR YIELD CRITERIA

Various strength functions have been proposed to represent nonlinear strength envelopes for geotechnical materials e.g., bilinear functions (Lefebvre, 1981), trilinear functions (de Mello, 1977). Several publications (e.g., Charles & Watts, 1980; Charles & Soares, 1984; Collins et al., 1988; Maksimovic, 1989; Perry,1994) employed a simple power law relation of the form $f(\sigma) = A\sigma^n$, where A and n are constants. More general envelopes were suggested e.g. by DiMaggio & Sandler (1971), Desai et al. (1981) and recently by Krabbenhoft et al. (2012). The others to mention include famous Lade's double parameter model (Lade, 1977) and Hoek-Brown 2002-edition yield criterion for intact rock mass (Hoek et al., 2002).

In this study three of the above mentioned nonlinear yield envelopes have been used for testing purposes, namely Hoek-Brown (2002), Desai's modified cap model (1981) and Krabbenhoft et al. (2012). These set was chosen to have yield functions specified both in principle stresses and stress invariants spaces. The particular form of these criteria is briefly described below.

4.1 Hoek-Brown Criterion

The Hoek-Brown criterion was first proposed in 1980 and updated several times. The latest version (Hoek et al., 2002) used in this study is given by the following equation

$$\sigma_1 = \sigma_3 + \sigma_{ci}\left(m_b \frac{\sigma_3}{\sigma_{ci}} + s\right)^{\alpha} \tag{3}$$

where

$$m_b = m_i \exp\left(\frac{GSI-100}{28-14D}\right)$$
$$s = \exp\left(\frac{GSI-100}{9-3D}\right) \tag{4}$$
$$\alpha = \frac{1}{2} + \frac{1}{6}\left(e^{\frac{-GSI}{15}} - e^{\frac{-20}{3}}\right)$$

The geotechnical strength index, GSI, ranges from about 10, for extremely poor rock masses, to 100 for intact rock. The parameter D is a factor that depends on the degree of disturbance. For the analyses presented in this paper the following values of Hoek-Brown parameters have been employed: GSI=80, σ_{ci} =50, m_i=1, D=0, with corresponding envelope illustrated in Figure 3.

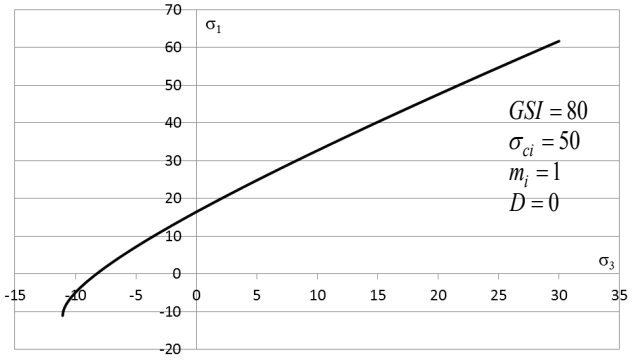

Figure 3. Typical envelope of Hoek-Brown yield criterion.

The uniaxial compressive strength and the tensile strength are given, respectively, by

$$\sigma_c = \sigma_{ci}\, s^{\alpha} \quad \text{and} \quad \sigma_t = -\frac{s\,\sigma_{ci}}{m_b} \tag{5}$$

The linearization scheme proposed requires estimation of slope and curvature of nonlinear envelope at current stress level. Therefore the expressions of the first and the second derivatives are given for each of criteria used in this paper. For Hoek-Brown criterion they are expressed as

$$\frac{\partial\sigma_1}{\partial\sigma_3} = 1 + am_b\left(m_b\frac{\sigma_3}{\sigma_{ci}} + s\right)^{\alpha-1}; \quad \frac{\partial^2\sigma_1}{\partial\sigma_3{}^2} = \frac{a(a-1)m_b{}^2}{\sigma_{ci}}\left(m_b\frac{\sigma_3}{\sigma_{ci}} + s\right)^{\alpha-2} \tag{6}$$

which exhibit the following asymptotic trends

$$\frac{\partial\sigma_1}{\partial\sigma_3} \to \infty \text{ with } \sigma_3 \to \sigma_t; \qquad \frac{\partial\sigma_1}{\partial\sigma_3} \to 1 \text{ with } \sigma_3 \to \infty \tag{7}$$

4.2 Desai's Model

In contrast to Hoek-Brown criterion, which is given in principle stresses, the one proposed by Desai et al. (1981) is expressed originally in stress invariants (Figure 4). The present work employs Desai's criterion in the form

$$J_2 = A + \beta I_1 - C\exp\left(-BI_1\right) \tag{8}$$

where I_1 and J_2 are first stress and second deviatotic stress invariants, respectively; and A, B, C and β are material strength parameters found from conventional triaxial tests. For numerical examples of Section 5 we used A=15, B=0.02, C=10, β=0.1.

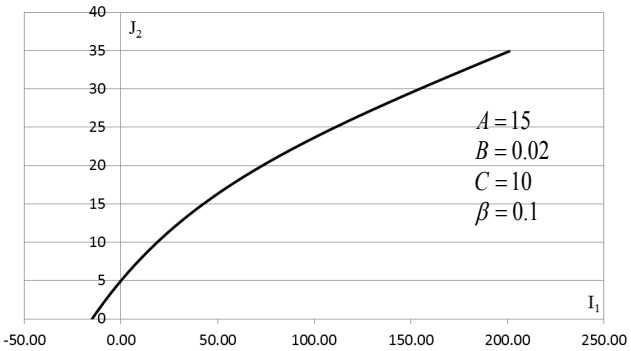

Figure 4. Typical envelope of Desai's yield criterion.

The intersection of the yield envelop with the axes, and the first and the second derivatives for Desai's criterion are given by

$$\begin{aligned} &J_{2c} = A - C \quad \text{and} \quad I_{1t} : A + \beta I_1 - C\exp\left(-BI_1\right) = 0 \\ &\frac{\partial J_2}{\partial I_1} = \beta + CB\exp\left(-BI_1\right); \qquad \frac{\partial^2 J_2}{\partial {I_1}^2} = -CB^2\exp\left(-BI_1\right) \end{aligned} \tag{9}$$

with the following asymptotic behavior

$$\frac{\partial J_2}{\partial I_1} \to \beta \quad \text{with } I_1 \to \infty \tag{10}$$

4.3 Krabbenhoft et al. Criterion

Another practical nonlinear yield criterion was recently proposed by Krabbenhoft et al. (2012) aiming to take into account the dependency of soil friction angle on the confining pressure, particularly at lower stress levels. This criterion is mostly applicable to sands and was given in the form

$$\sigma_1 = k\sigma_3 + s_c\left(1 - \exp\left(-a\frac{\sigma_3}{s_c}\right)\right) \tag{11}$$

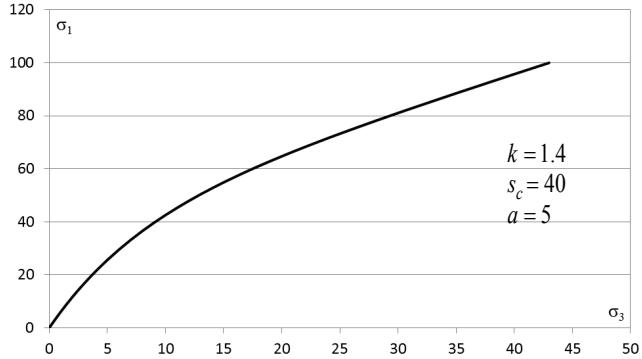

Figure 5. Typical envelope of Krabbenhoft criterion.

which is a curved envelope (Figure 5) that passes through the origin and tends toward the asymptote:

$$\sigma_1 = k\sigma_3 + s_c \quad \text{when} \quad \sigma_3 \to \infty \tag{12}$$

The parameters k and s_c define the asymptote slope and intersection with σ_1 axis, respectively, and a defines the curvature (values used in numerical examples are: k=1.4, s_c =40, a=5).

Thus, the uniaxial compressive strength, and function derivatives for Krabbenhoft criterion are given by

$$\sigma_c = s_c$$
$$\frac{\partial \sigma_1}{\partial \sigma_3} = k + a \exp\left(-a\frac{\sigma_3}{s_c}\right); \quad \frac{\partial^2 \sigma_1}{\partial {\sigma_3}^2} = -\frac{a^2}{s_c}\exp\left(-a\frac{\sigma_3}{s_c}\right) \tag{13}$$

with

$$\frac{\partial \sigma_1}{\partial \sigma_3} \to k+a \quad \text{when } \sigma_3 \to 0; \qquad \frac{\partial \sigma_1}{\partial \sigma_3} \to k \quad \text{when } \sigma_3 \to \infty \tag{14}$$

5 NUMERICAL EXAMPLES

To be able to judge objectively about the performance of dynamic linearization schemes, it is important to consider the examples where the stress field developed due to loading would be far away from being uniform or covering only a small interval. Especially important is to test the cases where the stress points will be present as at the vicinity of the apex of yield envelope (tensile stress) as well as being located at high compressive stress levels. This will test the robustness of convergence procedure, as the oscillation of stresses at high curvature area (close to the apex of yield envelope) in subsequent linearization iterates is the main factor posing the challenge to dynamic linearization procedure as it is done accurately only locally (around current stress point).

With above considerations in mind the following sequence of text examples have been selected. First, the cantilever beam was considered with linearized Hoek-Brown criterion to check robustness of local and global linearization schemes when both compressive and tensile stresses are induced by loading. Next, the classical strip footing and passive earth pressure problems have been tested for all three of described earlier yield criteria.

5.1 Cantilever Beam

The cantilever beam is very simple, but nevertheless quite effective test problem for linearization procedure. The problem geometry, loading and boundary conditions, as well as finite element mesh used in computations are shown in Figure 6.

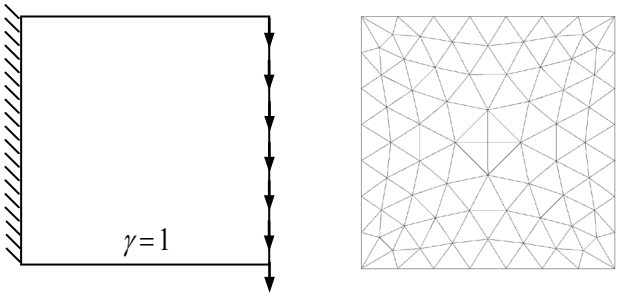

Figure 6. Cantilever beam loaded by shear force.

First, the local linearization was tested with the accuracy parameter ε set to 0.01, 0.001 and 0.0001. The results presented in Table 1-Table 4 for lower bound analyses demonstrate that very good convergence is achieved in all cases even with $N_b = 1$. In the tables below $\Delta\sigma_k$ denotes the maximum difference (among all nodes) between stresses obtained in two subsequent linearization iterations for some particular node in the mesh. Whereas $\Delta\sigma_R$ shows how much stress point at current iteration is outside the linearization interval established on previous iteration. It is clearly seen from Table 1-Table 4 that $\Delta\sigma_k$ reduces to a small value towards the last convergence iteration, while $\Delta\sigma_R$ goes into negative range, meaning that point σ_{k+1} stays close to σ_k and inside the linearization interval formed around point σ_k (Figure 1).

Table 1. Cantilever beam, local internal linearization, Hoek-Brown, LB, ε = 0.01.

Itr	$N_b = 1$				$N_b = 2$			
	Load	Yield	$\Delta\sigma_k$	$\Delta\sigma_R$	Load	Yield	$\Delta\sigma$	$\Delta\sigma_R$
1	1.934	-1.2e+0	23.03	-1.22	1.825	-1.9e-1	22.54	-3.59
2	2.031	-6.5e-1	6.975	3.50	2.146	-2.2e-9	7.291	-2.66
3	2.029	-6.5e-1	2.928	-1.78	2.213	-2.1e-8	7.947	-1.88
4	2.027	-6.4e-1	1.094	-1.78	2.230	-4.7e-9	3.107	-0.95
6	2.026	-6.5e-1	0.390	-1.79	2.237	-1.4e-7	1.558	-0.81
8	2.025	-6.5e-1	0.247	-1.79	2.238	-3.6e-7	0.843	-0.92

Table 2. Cantilever beam, local internal linearization, Hoek-Brown, LB, ε = 0.001.

Itr	$N_b = 1$				$N_b = 2$			
	Load	Yield	$\Delta\sigma$	$\Delta\sigma_R$	Load	Yield	$\Delta\sigma$	$\Delta\sigma_R$
1	2.448	5.4e+0	27.29	7.65	2.322	2.3e+0	26.31	3.75
2	2.264	1.6e+0	10.30	5.38	2.248	6.6e-2	3.258	0.51
3	2.235	7.7e-3	8.595	6.22	2.250	-7.6e-9	0.289	-0.85
4	2.235	-4.7e-2	0.378	-0.42	2.250	-1.4e-8	0.041	-0.87

Table 3. Cantilever beam, local internal linearization, Hoek-Brown, LB, ε = 0.0001.

Itr	$N_b = 1$				$N_b = 2$			
	Load	Yield	$\Delta\sigma$	$\Delta\sigma_R$	Load	Yield	$\Delta\sigma$	$\Delta\sigma_R$
1	2.484	6.3e+0	27.64	9.92	2.446	4.9e+0	27.39	8.68
2	2.283	1.2e+0	10.42	6.58	2.269	1.3e+0	9.608	4.70
3	2.249	7.3e-2	10.21	7.03	2.250	3.9e-3	8.310	5.18
4	2.249	-4.4e-3	0.382	-0.10	2.250	-5.9e-8	0.189	-0.26

Table 4. Cantilever beam, local external linearization, Hoek-Brown, LB.

Itr	ε = 0.001				ε = 0.0001			
	$N_b = 1$		$N_b = 2$		$N_b = 1$		$N_b = 2$	
	Load	Yield	Load	Yield	Load	Yield	Load	Yield
1	2.488	6.4e+0	2.377	6.9e-1	2.488	6.4e+0	2.450	5.0e+0
2	2.285	1.3e+0	2.260	2.8e-1	2.285	1.3e-1	2.270	1.2e+0
3	2.251	8.2e-2	2.263	2.8e-1	2.251	8.2e-2	2.252	1.8e-2
4	2.250	2.9e-4	2.262	2.8e-1	2.250	2.9e-4	2.252	2.0e-2
5	2.250	1.1e-6	2.261	2.7e-1	2.250	1.1e-6	2.252	1.8e-2

Unfortunately, this is not the case for upper bound discretization, as can be concluded looking at Table 5 & Table 6. The high the accuracy of linearization (external is used for upper bound here), the more basic surfaces are required to provide more or less sensible convergence rates ($N_{b,min} = 10$ for $\varepsilon = 0.0001$)!

Table 5. Cantilever beam, local external linearization, Hoek-Brown, UB, ε = 0.01.

Itr	$N_b = 1$				$N_b = 4$			
	Load	Yield	$\Delta\sigma$	$\Delta\sigma_R$	Load	Yield	$\Delta\sigma$	$\Delta\sigma_R$
1	2.773	6.6e+0	39.43	14.15	2.642	2.9e+0	41.27	-6.0e-9
2	2.784	3.7e+3	3733	12.10	2.565	2.5e+0	20.03	1.3e+0
3	2.819	9.3e+1	3638	16.19	2.561	3.9e+0	14.08	5.9e-1
4	2.793	2.2e+3	2140	10.13	2.572	2.6e+0	15.13	-6.7e-2
5	2.676	5.7e+3	5662	11.74	2.558	3.3e+0	14.60	-1.6e-9
6	2.658	1.9e+1	5645	9.33	2.567	2.7e+0	13.43	-6.7e-2
7	2.589	4.8e+3	4811	8.97	2.560	3.8e+0	14.06	-1.2e-8
8	2.642	6.7e+1	4782	11.87	2.572	2.6e+0	15.10	-6.7e-2
9	2.632	1.1e+1	65.82	10.33	2.558	3.3e+0	14.45	-2.7e-9
10	2.663	1.8e+2	175.0	10.31	2.568	2.6e+0	13.40	-6.7e-2

Table 6. Cantilever beam, local external linearization, Hoek-Brown, UB.

Itr	ε = 0.001, $N_b = 4$				ε = 0.0001, $N_b = 10$			
	Load	Yield	$\Delta\sigma$	$\Delta\sigma_R$	Load	Yield	$\Delta\sigma$	$\Delta\sigma_R$
1	2.518	9.1e-1	38.13	4.0e+0	2.487	2.0e+0	37.04	4.4e+0
2	2.492	7.8e+0	11.26	8.0e-1	2.483	1.1e+1	12.97	5.6e-1
3	2.486	4.3e-1	11.45	5.2e-1	2.476	3.3e-2	12.64	4.8e-2
4	2.487	2.7e-1	4.67	-4.1e-2	2.476	3.3e-2	0.966	-1.0e-1
5	2.487	2.6e-1	4.62	-1.3e-1	2.476	3.3e-2	0.266	-1.7e-1

And this trend is obviously common for both internal and external local linearizations as shown in Table 7.

Table 7. Cantilever beam, local internal vrs external linearization, Hoek-Brown, UB.

Itr	ε = 0.001				ε = 0.0001			
	Internal, $N_b = 4$		External, $N_b = 5$		Internal, $N_b = 10$		External, $N_b = 11$	
	Load	Yield	Load	Yield	Load	Yield	Load	Yield
1	2.354	2.3e-2	2.532	5.4e+0	2.474	1.3e+0	2.482	3.0e-1
2	2.466	6.4e-9	2.539	2.0e+1	2.481	1.1e+1	2.482	1.1e+1
3	2.473	-2.8e-8	2.478	4.5e-1	2.474	-9.8e-8	2.475	4.2e-1
4	2.473	-7.2e-8	2.475	6.5e-2	2.474	-6.3e-7	2.474	4.6e-2

In search for the remedy, the damping was introduced on $\Delta\sigma_k$. This addition has improved situation substantially in terms of minimum number of basic surfaces, $N_{b,\ min}$, required to achieve convergence. However the convergence rate observed for UB computations (Table 8) was nevertheless noticeably below the level observed for LB computations.

Table 8. Cantilever beam, local external linearization, damping, Hoek-Brown, UB.

Itr	$\varepsilon = 0.01$, $N_b = 3$		$\varepsilon = 0.001$, $N_b = 3$		$\varepsilon = 0.0001$, $N_b = 5$	
	Load	Yield	Load	Yield	Load	Yield
1	2.740	8.2e+0	2.538	4.6e+0	2.606	4.0e+0
2	2.525	1.4e+1	2.530	3.0e+1	2.632	4.0e+1
3	2.487	2.2e+0	2.483	5.9e+0	2.506	1.9e+1
4	2.482	3.4e-1	2.476	4.9e+0	2.479	1.5e+1
5	2.477	6.0e-1	2.482	1.1e+1	2.485	1.4e+1
6	2.476	2.3e-1	2.476	1.2e-1	2.475	1.7e+1
7	2.476	3.0e+0	2.475	2.6e-1	2.474	1.6e-1
8	2.475	2.8e+0	2.475	1.1e-1	2.474	1.1e-1

In contrast, looking at results given in Table 9 & Table 10 it appears that global linearization approach described in Subsection 3.2 proves to be robust regardless of any particular accuracy chosen. And this can be stated for both internal and external (with damping) types of linearization (Table 11). It should be mentioned here also that, as pointed out in Section 3.3, the difference in results obtained with internal and external linearization is quite moderate (comparing results in Table 10 and Table 11), which allows to consider the internal linearization to be used alone for practical computations (when used with internal linearization the upper bound is denote by UB*).

Table 9. Cantilever beam, global internal linearization, Hoek-Brown, LB.

Itr	$\varepsilon = 0.01$			$\varepsilon = 0.001$			$\varepsilon = 0.0001$		
	Load	Yield	$\Delta\sigma$	Load	Yield	$\Delta\sigma$	Load	Yield	$\Delta\sigma$
1	1.825	-1.9e-1	22.43	2.121	-1.2e-7	26.02	1.920	-5.6e-3	23.24
2	2.146	-1.0e-9	7.344	2.242	-1.0e-6	5.136	2.209	-8.5e-9	11.89
3	2.213	-1.4e-8	8.191	2.249	-4.7e-7	1.691	2.249	-9.9e-6	9.387
4	2.230	-8.4e-9	3.077	2.250	-3.8e-7	1.202	2.250	-1.7e-7	0.420
5	2.235	-6.4e-8	1.830	2.250	-3.7e-7	0.595	2.250	-2.3e-7	0.041
6	2.237	-2.6e-7	1.468	2.250	-3.1e-7	0.246	2.250	-2.6e-7	0.027

Table 10. Cantilever beam, global internal linearization, Hoek-Brown, UB*.

Itr	$\varepsilon = 0.01$			$\varepsilon = 0.001$			$\varepsilon = 0.0001$		
	Load	Yield	$\Delta\sigma$	Load	Yield	$\Delta\sigma$	Load	Yield	$\Delta\sigma$
1	2.040	-4.3e-9	32.55	2.351	-2.2e-8	35.57	2.128	-2.4e-9	31.32
2	2.363	-2.2e-9	7.245	2.466	-7.9e-8	4.713	2.435	-1.1e-9	8.374
3	2.433	-1.8e-9	2.372	2.473	-2.3e-9	1.247	2.471	-3.6e-8	5.251
4	2.447	-2.4e-8	4.901	2.473	-1.5e-7	0.284	2.474	-3.4e-8	1.913
5	2.451	-2.7e-8	0.911	2.473	-4.0e-7	0.026	2.474	-1.5e-7	0.815
6	2.452	-2.1e-8	0.490	2.473	-8.6e-8	0.100	2.474	-2.6e-7	0.678

Table 11. Cantilever beam, global external linearization, Hoek-Brown, UB.

Itr	$\varepsilon = 0.01$		$\varepsilon = 0.001$		$\varepsilon = 0.0001$	
	Regular	Damping	Regular	Damping	Regular	Damping
1	2.740	2.740	2.533	2.533	2.664	2.664
2	2.506	2.506	2.545	2.545	2.585	2.585
3	2.485	2.481	2.481	2.480	2.526	2.525
4	2.485	2.478	2.482	2.476	2.607	2.484
5	2.479	2.476	2.477	2.480	2.569	2.488
6	2.482	2.475	2.483	2.475	2.655	2.477
7	2.480	2.475	2.478	2.475	2.541	2.476
8	2.483	2.475	2.483	2.475	2.527	2.476
9	2.478	2.475	2.478	2.474	2.543	2.475
10	2.483	2.475	2.483	2.474	2.534	2.475

5.2 Strip Footing

All three yield criteria described in Section 4 are employed in this example to check the robustness of dynamic linearization. Though local linearization was already ruled out from being used as a general choice for practical calculations it is still tested in this example (only with Hoek-Brown criterion) for comparison purposes. The strip footing problem description is given in Figure 7 together with adopted discretization.

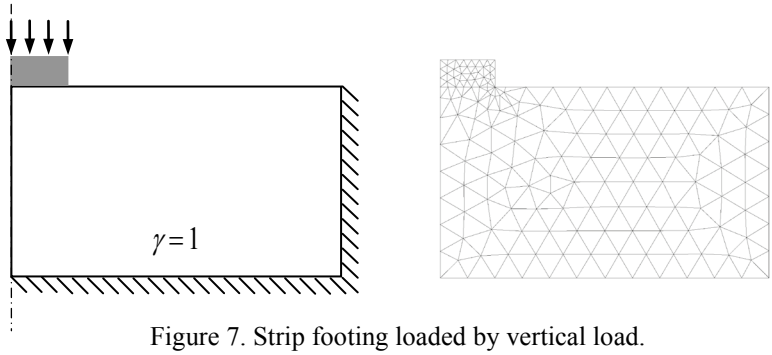

Figure 7. Strip footing loaded by vertical load.

Obtained results are tabulated in Table 12 - Table 15 in similar fashion as was done for cantilever beam problem. Straight to notice that local linearization scheme works quite well for this example, as can be judged from Table 12. The explanation to this fact is that all (or majority) of stress points are located in compressive range, where the curvature of yield envelope is quite moderate.

Table 12. Strip footing, local internal with $N_b = 2$ for LB and local external with $N_b = 1$ for UB, Hoek-Brown.

Itr	ε = 0.01		ε = 0.001		ε = 0.0001	
	LB	UB	LB	UB	LB	UB
1	61.77	87.70	66.67	87.70	69.26	87.70
2	60.98	72.67	60.83	72.67	61.01	72.67
3	61.04	72.56	61.04	72.56	61.08	72.56
4	61.04	72.55	61.05	72.55	61.08	72.55
5	61.05	72.55	61.05	72.55		72.55

Table 13. Strip footing, global internal linearization, Hoek-Brown.

Itr	ε = 0.01		ε = 0.001		ε = 0.0001	
	LB	UB*	LB	UB*	LB	UB*
1	60.08	71.04	55.29	64.87	52.99	61.97
2	60.97	72.23	60.96	72.32	61.02	72.44
3	61.06	72.36	61.07	72.51	61.08	72.54
4	61.07	72.38	61.07	72.51	61.08	72.54

Table 14. Strip footing, global internal linearization, Krabbenhoft.

Itr	ε = 0.01		ε = 0.001		ε = 0.0001	
	LB	UB*	LB	UB*	LB	UB*
1	5.847	13.46	9.54	22.38	10.90	20.91
2	9.868	21.74	10.99	24.62	11.16	24.90
3	10.94	24.15	11.16	24.96	11.17	25.02
4	11.12	24.73	11.17	25.01	11.17	25.03
5	11.15	24.86	11.17	25.01		
6	11.15	24.88				

Table 15. Strip footing, global, internal, Desai.

Itr	ε = 0.01		ε = 0.001		ε = 0.0001	
	LB	UB*	LB	UB*	LB	UB*
1	43.87	52.60	52.53	63.36	46.12	53.76
2	54.21	65.01	55.63	66.75	55.64	66.53
3	55.83	66.94	56.08	67.24	56.18	67.34
4	56.06	67.23	56.13	67.31	56.20	67.38
5	56.09	67.27	56.14	67.32	56.21	67.39
6	56.09	67.27	56.14	67.32		

The main conclusion (which supports the one derived in the previous example) though is drawn from results given in Table 13 - Table 15. Namely, internal global linearization with four basic surfaces is robust and moderately priced scheme suitable for both lower and upper bound discretizations. Normally it requires 3 fold of CPU time per iteration comparing to a single surface analysis and 3-4 convergence iterations to reach the steady solution. All together proposed dynamic linearization requires usually 10-12 times of CPU effort comparing to a single Mohr-Coulomb criterion. But, the benefits are much more valuable. First, by using SOCP programming the reliable convergence is guaranteed for each linearization iteration. Normally SOCP convergence is achieved in 20-40 iterations. Multiplied by 3-4 linearization iterations the total effort requires 100-150 iterations. Comparing to general purpose IPM procedure, which in authors experience can take up to 300-400 iterations, the above figure looks quite positive. But much more important benefit from dynamic linearization implemented under SOCP umbrella is the ability to use reliable SOCP solver in the case when different materials (including those which cannot be transformed directly to second order or rotated quadratic cones) are present in the problem domain.

5.3 Passive Earth Pressure

This is the last example selected and the same set of computations as for the strip footing was performed here. Figure 8 illustrates the geometry, boundary and loading conditions involved.

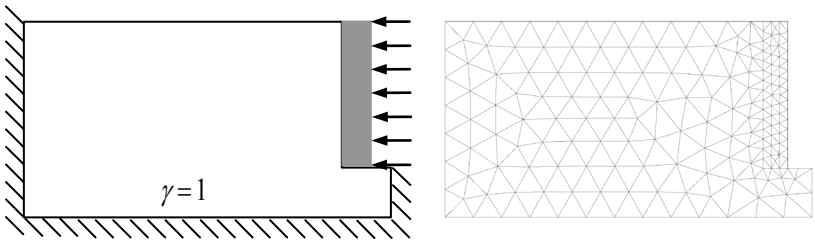

Figure 8. Passive earth pressure problem.

Results obtained are summarized in Table 16 - Table 19. From Table 16 it follows that again local linearization is struggling to produce robust convergence for upper bound limit analysis due to significant number of stress points being involved in oscillation in the area of high curvature of stress envelope. On the other hand Table 17 - Table 19 demonstrate that global internal dynamic linearization works well for all nonlinear yield criteria employed in this study.

Table 16. Passive earth pressure, local external linearization ($N_b = 2$ for LB), Hoek-Brown.

Itr	ε = 0.01		ε = 0.001		ε = 0.0001	
	LB	UB ($N_b = 3$)	LB	UB ($N_b = 5$)	LB	UB ($N_b = 11$)
1	21.88	26.33	22.75	26.08	23.07	26.23
2	22.43	25.99	22.63	25.98	22.75	25.98
3	22.50	25.98	22.54	25.98	22.58	25.99
4	22.52	25.98	22.54	25.98	22.54	25.98
5	22.53	25.98	22.54	25.98	22.54	25.99

Table 17. Passive earth pressure, global internal linearization, Hoek-Brown.

Itr	ε = 0.01		ε = 0.001		ε = 0.0001	
	LB	UB*	LB	UB*	LB	UB*
1	21.88	25.30	22.28	25.47	21.79	24.71
2	22.43	25.83	22.53	25.92	22.48	25.95
3	22.50	25.87	22.54	25.95	22.53	25.97
4	22.52	25.88	22.54	25.95	22.54	25.97
5	22.53	25.88	22.54	25.95	22.54	25.97

Table 18. Passive earth pressure, global internal linearization, Krabbenhoft.

Itr	ε = 0.01		ε = 0.001		ε = 0.0001	
	LB	UB*	LB	UB*	LB	UB*
1	3.984	5.461	4.722	6.641	4.972	6.927
2	4.977	6.809	5.007	7.010	5.011	7.029
3	5.007	6.974	5.011	7.030	5.011	7.034
4	5.009	6.999	5.011	7.032		7.034
5	5.009	7.003		7.032		
6		7.004				

Table 19. Passive earth pressure, global internal linearization, Desai.

Itr	ε = 0.01		ε = 0.001		ε = 0.0001	
	LB	UB*	LB	UB*	LB	UB*
1	17.69	20.67	19.04	22.60	20.03	23.06
2	20.08	23.70	20.31	24.02	20.41	24.06
3	20.35	24.06	20.40	24.12	20.42	24.15
4	20.38	24.10	20.40	24.13	20.42	24.15
5	20.38	24.11	20.40	24.14		24.15
6	20.38	24.11				

6 CONCLUSIONS

Based on results of tests performed with three different yield criteria employed it can be concluded that linearization scheme suggested in this study works quite well. Normally it requires only 3-5 iterations for procedure to converge to a steady solution. This can be considered as moderate price to pay for robustness and generality of proposed scheme, which allows a wide range of nonlinear yield criteria to be treated in a context of efficient second order conic programming framework.

REFERENCES

Charles, J.A., and Watts, K.S. 1980. The influence of confining pressure on the shear strength of compacted rockfill. *Geotechnique*, 30(4), 353–367.

Charles, J.A., and Soares, M.M. 1984. Stability of compacted rockfill slopes. *Geotechnique*, 34(1), 61–70.

Ciria Suarez, H. 2004. Computation of upper and lower bounds in limit analysis using second-order cone programming and mesh adaptivity, PhD Thesis, Massachusetts Institute of Technology.

Collins, I.F., Gunn, C.I.M., Pender, M.J., and Wang, Y. 1988. Slope stability analyses for materials with a nonlinear failure envelope. *Int. J. Numer. Analyt. Meth. Geomech*., 12(5), 533–550.

Desai, C.S., Phan, H.V. and Sture, S.C. 1981. Procedure, selection and application of plasticity models for soil. *Int. J. Numer. Anal. Meth. Geomech*. 5(3), 295-311.

DiMaggio, F.L. and Sandler I.S. 1971. Material model for granular soil, *J. Engng. Mech. Div.*, Proc. Am. Soc. Civ. *Eng*.197(3).

Hoek, E. and Brown, E.T. 1980. Empirical strength criterion for rock masses. *J. Geotech. Eng. Div. ASCE,* 106(9):1013–1035.

Hoek, E., Carranza-Torres, C.T., Corkum, B. 2002. "Hoek-Brown failure criterion-2002 edition". *Proceedings of the fifth North American rock mechanics symposium,* 1:267–273.

Krabbenhøft, K., Lyamin, A.V. and Sloan, S.W. 2007. Formulation and solution of some plasticity problems as conic programs. *International Journal of Solids and Structures,* 44(5), 1533-1549.

Krabbenhoft, K., Lyamin, A.V., Sloan, S.W. 2008. Three-dimensional Mohr-Columb limit analysis using semidefinite programming, *Communications in Numerical Methods in Engineering*, 24, 1107-1119.

Krabbenhoft, S., Clausen, J. and Damkilde, L. 2012. The Bearing Capacity of Circular Footings in Sand: Comparison between Model Tests and Numerical Simulations Based on a Nonlinear Mohr Failure Envelope. *Advances in Civil Engineering*, Volume 2012, Article ID 947276, doi:10.1155/2012/947276

Lade P.V. 1977. Elasto-plastic stress-strain theory for cohesionless soil with curved yield surfaces. *Int. J. Solids Struct*. 13(11), 1019-1035.

Lefebvre, G. 1981.Strength and slope stability in Canadian soft clay deposits. *Can. Geotech. J.*, 18(3), 420–442.

Maksimovic, M. 1989. Nonlinear failure envelope for soils. *J. Geotech. Eng*., 115(4), 581–586.

de Mello, V.B.F. 1977. Reflections on design decisions of practical significance to embankment dams -17th Rankine lecture.'' *Geotechnique*, 27(3), 281–354.

Merifield, R.S., Lyamin, A.V., Sloan, S.W. 2006. Limit analysis solutions for the bearing capacity of rock masses using the generalised Hoek-Brown criterion, *International Journal of Rock Mechanics and mining sciences*, 43 (6), 920-937.

Perry, J. 1994. A technique for defining non-linear shear strength envelopes and their incorporation in a slope stability method of analysis. Q. J. Eng. Geol., 27(3), 231–241.

DOMAIN REDUCTION METHOD FOR SINGLE AND TWO-PHASE DYNAMIC SOIL-STRUCTURE INTERACTION PROBLEMS

Andrzej Truty
Department of Environmental Engineering, Cracow University of Technology, Cracow,Poland

Thomas Zimmermann
Zace services Ltd, Lausanne, Switzerland

ABSTRACT: *Transient dynamic soil-structure time history analyses for single or two-phase fully or partially saturated media require appropriate techniques for correct representation of boundary conditions and inclusion of the free field motion into the model. Size of the computational model is frequently a serious limitation in practical applications. One of the approaches that allows to reduce computational effort is the domain reduction method (DRM) formulated first by Bielak et.al. (Bielak, Loukakis, Hisada, & Youshimura 2003),(Youshimura, Bielak, Hisada, & Fernandez 2003), for single phase, later on extended to the two-phase fully saturated media by Kantoe et al. (Kantoe 2006). In this paper an implicit DRM method is proposed for two-phase fully or partially saturated media, extending the theory given by Aubry and Ozanam (Aubry & Ozanam 1988) (for static consolidation), using a stabilized (through pressure Laplacian) u-p formulation (Truty & Zimmermann 2006) worked out for low order 2D/3D BBAR and EAS elements. Numerical results for twin shallow tunnels subject to the Loma Prieta earthquake show robustness of the method.*

1 INTRODUCTION

Nonlinear dynamic time history analyses using FE models put certain restrictions on size of elements, time step and size of the domain adjacent to the structure. Spurious wave reflections usually result from the truncation of the FE model, even if special viscous boundaries are used. Also when the source of the excitation is far from the structure or is nonuniform the computational model may become extremely large and therefore computationally inefficient. To overcome this difficulty Bielak et.al. (Bielak, Loukakis, Hisada, & Youshimura 2003),(Youshimura, Bielak, Hisada, & Fernandez 2003) proposed a two step procedure called domain reduction method (DRM), for single-phase media, which allows to move source of the excitation to a smaller domain relatively close to the structure and thus to reduce the size of the computational model. In 2006 Kantoe (Kantoe 2006), and later Kantoe et al.(Kantoe, Zdravkovic, & Potts 2008) published an implicit DRM formulation for dynamic consolidation of fully saturated media. Although full saturation is the most interesting case for engineering practice, we still have to deal, in many cases, with media that are partially saturated (earth dams etc..). In this paper we will briefly describe the set of equations governing dynamic consolidation of two-phase partially saturated media and present major steps to derive the corresponding DRM formulation. Contrary to the work by Kantoe the DRM model is derived in a semi-discrete form that allows to apply any suitable time integration scheme to the momentum and fluid mass balance equations. Efficiency of

the method is tested on the problem of twin tunnels subjected to a scaled Loma Prieta earthquake acceleration record.

2 GOVERNING EQUATIONS FOR TWO-PHASE DYNAMIC CONSOLIDATION

Based on static formulation by Aubry and Ozanam (Aubry & Ozanam 1988) the two-phase dynamic consolidation of fully or partially saturated media, designed for the $u-p$ format, can be written as the following set of differential equations and corresponding boundary and initial conditions.

- overall equilibrium equation for the solid and fluid phases written in terms of the total stress

$$\sigma_{ij,j}^{\text{tot}} + \rho\, g\, b_i = \rho\, \ddot{u}_i \tag{1}$$

$$\rho = \rho_{\text{dry}} + n\, S\, \gamma^{\text{F}} \tag{2}$$

  where total stress is denoted by σ_{ij}^{tot}, earth acceleration by g, solid skeleton bulk density by ρ_{dry}, water specific weight by γ^F, porosity by n and current saturation ratio by S
- extended effective stress principle after Bishop

$$\sigma_{ij}^{\text{tot}} = \sigma_{ij} + \delta_{ij}\ S\ p \tag{3}$$

  where Kronecker's symbol is denoted by δ_{ij}, effective stresses by σ_{ij} and pore pressure by p
- fluid flow continuity equation including the effect of compressibility of the fluid and partial saturation

$$S\,\dot{\varepsilon}_{kk} + \ v_{k,k}^{\text{F}} = \left(n\frac{S}{K^F} + n\,\frac{\partial S}{\partial p}\right)\ \dot{p} \tag{4}$$

  where $k-$th component of Darcy velocity vector is denoted by v_k^F, while fluid bulk modulus by K^F
- linearized strain-displacement relations

$$\varepsilon_{ij} = \frac{1}{2}\left(u_{i,j} + u_{j,i}\right) \tag{5}$$

  where engineering strain is denoted by ε_{ij} and $i-$th component of displacement vector is denoted by u_i
- nonlinear elasto-plastic constitutive relation

$$\dot{\sigma}_{ij} = D_{ijkl}^{\text{e}}\left(\dot{\varepsilon}_{kl} - \dot{\varepsilon}_{kl}^{\text{p}}\right) \tag{6}$$

  where D_{ijkl} denotes $ijkl$ component of fourth-order current elasticity tensor and $\dot{\varepsilon}_{kl}$, $\dot{\varepsilon}_{kl}^{\text{p}}$ denote rates of total and plastic strains respectively.
- extended Darcy's law (including optionally the inertial term)

$$v_i^F = k_{ij}k_r(S)\left(\frac{1}{\gamma^F}p_{,j} + b_j - \frac{1}{g}\ddot{u}_j\right) \tag{7}$$

- simplified constitutive equations for saturation ratio S, after van Genuchten (Genuchten 1980), and relative permeability coefficient $k_r(S)$ after Irmay (Irmay 1956)

$$S = S(p) = \left\{\begin{array}{ll} S_r + \dfrac{1-S_r}{\left[1+\left(\alpha\dfrac{p}{\gamma_{\text{F}}}\right)^2\right]^{1/2}} & \text{if } p > 0 \\ 1 & \text{if } p \le 0 \end{array}\right\} \tag{8}$$

$$k_r\left(S\right) = \left(\frac{S - S_r}{1 - S_r}\right)^3 \tag{9}$$

where the residual saturation ratio is denoted by S_r, and α is a material parameter responsible for a decrease of a saturation ratio with an increase of a pressure suction

- near field boundary conditions to be satisfied at any time $t \in [0, T]$

$$\sigma_{ij}^{\text{tot}} n_j = \overline{t_i} \text{ on } \Gamma_{\text{t}} \quad ; v_i^{\text{F}} n_i = \overline{q} \text{ on } \Gamma_{\text{q}} \quad ; u_i = \overline{u}_i \text{ on } \Gamma_{\text{u}} \quad ; p = \overline{p} \text{ on } \Gamma_{\text{p}} \tag{10}$$

Γ_{t}, Γ_{q}, Γ_{u}, Γ_{p} are parts of the boundary where the total stresses, fluid fluxes, displacements and pore pressures are prescribed.
A special treatment is required for so-called *seepage surface* where the free surface intersects with domain boundary, see (Aubry & Ozanam 1988) for details.

- farfield boundary conditions
To analyze truncated FE models, a zeroth-order paraxial absorbing boundary formulation (coherent with the u-p format), proposed by Modaressi and Bonzenati (Modaressi & Benzenati 1994), is extended here to handle partial saturation in a simplified manner. The total viscous stress and fluid flux, on the absorbing boundary, are defined as follows

$$\sigma_i^s = -\left\{\rho \frac{c_p^2}{V_{p1}} \left(\lambda_s + 2\mu_s\right) n_i n_j + \rho\, c_s \left(t_{1i} t_{1j} - t_{2i} t_{2j}\right)\right\} v_j^s + n_i \left(S\, p - S_o\, p_o\right) \tag{11}$$

$$\Phi = k \left[\rho \left(1 - \frac{c_p^2}{V_{p1}^2} - \rho^F\right)\right] n_k a_k^s \tag{12}$$

The corresponding shear and dilatational wave velocities, for solid phase, are defined through the expressions

$$c_s = \sqrt{\frac{G}{\rho}} \qquad c_p = \sqrt{\frac{\lambda + 2\, G}{\rho}} \tag{13}$$

while the approximate first dilatational wave velocity for medium filled by a compressible fluid is defined as

$$V_{p1}^2 = c_p^2 \left(1 + \frac{Q}{\lambda + 2\, G}\right) \tag{14}$$

and

$$\frac{1}{Q} = n \frac{S}{K^F} + n \frac{dS}{dp} \tag{15}$$

Components of solid velocity and acceleration vectors are denoted by v_i^s and a_i^s. Normalized components of normal and tangential vectors are denoted by n_i and t_{1i}, t_{2i} respectively. In the expression for the total viscous stress the $S_o\, p_o$ term is added to cancel the initial saturation/pressure prior to running dynamic time history analysis. The $\dfrac{dS}{dp}$ term is computed using van Genuchten's law while k is the permeability value along the normal direction. It has to be mentioned that this formulation is only approximate and hence spurious reflections are not fully eliminated. For single-phase media expressions given above correspond to well known Lysmer viscous dashpots.

- initial conditions

$$u_i(t = t_o) = u_{io} \quad ; \quad p(t = t_o) = p_o \tag{16}$$

2.1 Semi-discrete form of balance equations

In the following derivations the HHT$_\alpha$ implicit schemes are used fulfilling unconditional stability. The HHT$_\alpha$ scheme nicely damps high frequencies without disturbing low ones.

The following expressions (Zienkiewicz, Chan, Pastor, Schrefler, & Shiomi 1999), (Hilber, Hughes, & Taylor 1977) are used to integrate solid displacements, velocities and pore pressures in time

$$\mathbf{u}_{n+1} = \mathbf{u}_n + \dot{\mathbf{u}}_n \Delta t + \frac{\Delta t^2}{2}\left[(1-2\beta)\,\ddot{\mathbf{u}}_n + 2\beta \ddot{\mathbf{u}}_{n+1}\right] \tag{17}$$

$$\dot{\mathbf{u}}_{n+1} = \dot{\mathbf{u}}_n + \Delta t\left[(1-\gamma)\,\ddot{\mathbf{u}}_n + \gamma \ddot{\mathbf{u}}_{n+1}\right] \tag{18}$$

$$p_{n+1} = p_n + (1-\theta)\,\dot{p}_n \Delta t + \theta \Delta t \dot{p}_{n+1} \tag{19}$$

with

$$-\frac{1}{3} \leq \alpha < 0, \;\; \gamma = \frac{(1-2\alpha)}{2}, \;\; \beta = \frac{(1-\alpha)^2}{4}, \;\; \theta \geq \frac{1}{2} \tag{20}$$

The resulting semi-discrete matrix form of the overall equilibrium in the HHT scheme can be written as follows

$$\mathbf{M}\ddot{\mathbf{u}}_{n+1} + \mathbf{C}\dot{\mathbf{u}}_{n+\alpha} + \mathbf{F}'_{\text{int}}(\mathbf{u}_{n+\alpha}) + \mathbf{C}^F \mathbf{p}_{n+\alpha} = \mathbf{F}_{\text{ext}n+\alpha} \tag{21}$$

To preserve symmetry of the resulting matrix form (if we neglect the inertial term in the Darcy law) the semi-discrete matrix form of balance of the mass for the fluid phase is written at $t_{n+\alpha}$

$$\left(\mathbf{C}^F\right)^{\mathrm{T}} \dot{\mathbf{u}}_{n+\alpha} - \mathbf{H}^F\, \mathbf{p}_{n+\alpha} + \mathbf{R}^F \ddot{u}_{n+\alpha} - \mathbf{h}^F - \mathbf{M}^F \dot{\mathbf{p}}_{n+\alpha} + \mathbf{Q}^F = \mathbf{0} \tag{22}$$

where

$$\mathbf{F}'_{int}(\mathbf{u}_{n+\alpha}) = \int_\Omega \mathbf{B}^{\mathrm{T}} \boldsymbol{\sigma}(\mathbf{u}_{n+\alpha}) \mathrm{d}\Omega \tag{23}$$

$$\mathbf{C}^F = \int_\Omega \mathbf{N}^{\mathrm{T}} S_{n+\alpha} \mathbf{1}^{\mathrm{T}} \mathrm{d}\Omega \tag{24}$$

$$\mathbf{H}^F = \frac{1}{\gamma^F} \int_\Omega \nabla \mathbf{N}^{\mathrm{T}} \mathbf{k} \nabla \mathbf{N} \mathrm{d}\Omega \tag{25}$$

$$\mathbf{M}^F = \int_\Omega \mathbf{N}^{\mathrm{T}} c_{n+\alpha} \mathbf{N} \mathrm{d}\Omega \tag{26}$$

$$\mathbf{R}^F = \int_\Omega \nabla \mathbf{N}^{\mathrm{T}} \mathbf{k} \frac{1}{g} \mathbf{N} \mathrm{d}\Omega \tag{27}$$

$$\mathbf{h}^F = \int_\Omega \nabla \mathbf{N}^{\mathrm{T}} \mathbf{k} \mathbf{b} \mathrm{d}\Omega \tag{28}$$

$$\mathbf{Q}^F = \int_{\Gamma_q} \mathbf{N}^{\mathrm{T}} \overline{q} \mathrm{d}\Omega \tag{29}$$

In the above expressions matrices of the standard shape functions are denoted by **N**, strain-displacement operator by **B**, normalized gravity direction vector by **b**, current permeability matrix by **k**, storage coefficient $c_{n+\alpha} = c(p_{n+\alpha}) = n\left(\frac{S_{n+\alpha}}{K^F} + \frac{dS_{n+\alpha}}{dp}\right)$, g is an earth acceleration

(g=9.81 m/s^2), and imposed fluid flux at boundary Γ_q is denoted by $\overline{q}$. In order to reduce computational complexity we assume that all matrices in fluid mass balance equation are treated in an explicit manner. It has to be mentioned that within ZSOIL code (Elmepress and Zace Services Limited 2013) low order elements (BBAR or EAS) are exclusively used, hence equal interpolation order for displacement and pressure degrees of freedom is the only choice. This setting may yield spurious spatial pressure oscillations in the incompressibility limit, and for that reason a special stabilization procedure, based on pressure Laplacian, is used to circumvent this deficiency (the same as for the standard static consolidation problems) (Truty & Zimmermann 2006).

3 DRM METHOD FOR SINGLE AND TWO-PHASE PARTIALLY SATURATED MEDIA

The goal of DRM method is to reduce the size of the the computational model to the structure and only a small adjacent part of the subsoil. Let us consider a domain that includes a fault, source of the excitation forces $\mathbf{P}_e(t)$, and a structure (see Fig.1(a)). At this point we may analyze two computational models. The first one, called "background model" (see Fig.1(b)), includes subsoil and source of the load $\mathbf{P}_e(t)$, while the second one, called "reduced model" (see Fig.1(c)), includes the structure and a small part of the subsoil. Zone between Γ and Γ^+ consists of a single row of finite elements while $\tilde{\Omega}^+$ is only a part of the exterior domain Ω^+ placed outside of Γ.

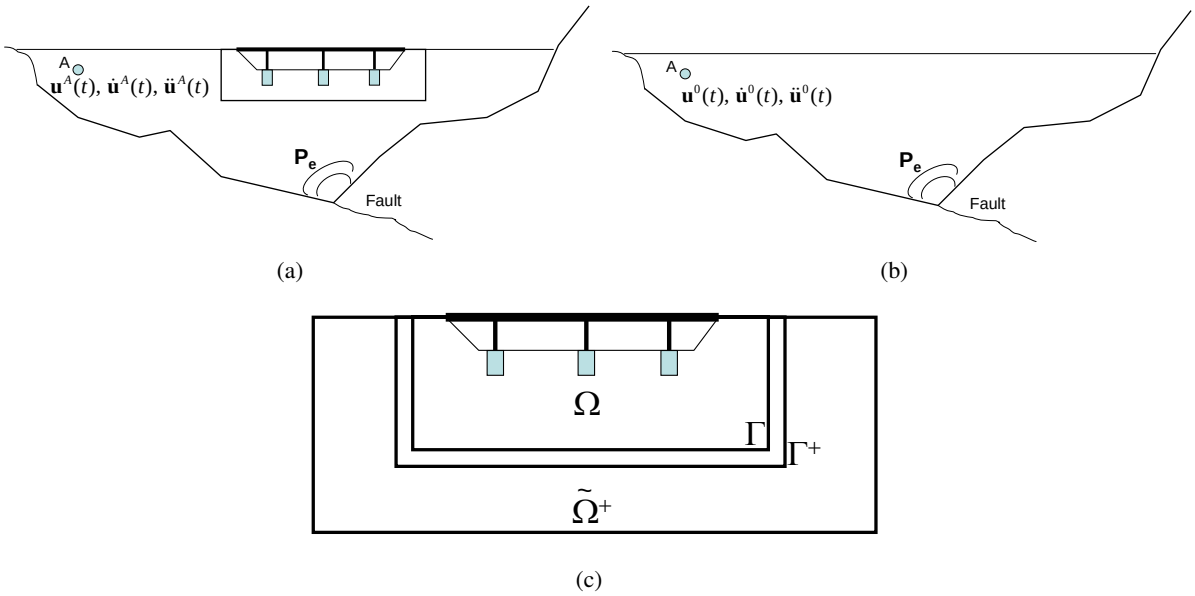

Fig. 1. General idea of DRM method. (a) Full model of subsoil, structure, and source of the loading $\mathbf{P}_e(t)$. (b) Background model. (c) Reduced model.

By solving the background model one may compute the free field motion induced by $\mathbf{P}_e(t)$. Resulting free field displacements, velocities, accelerations, pore pressures and pore pressure rates are denoted by $u^0(t)$, $\dot{u}^0(t)$, $\ddot{u}^0(t)$, $p^0(t)$, $\dot{p}^0(t)$ respectively. The background model is partitioned into interior domain Ω and the exterior one Ω^+. The Γ boundary separates interior and exterior domains. The free field quantities at any point in the interior domain are denoted using index $()_i$, at the boundary Γ with index $()_b$ and in the exterior domain using index $()_e$. Nodal points that belong to the boundary Γ are labeled as *b*, nodes that are in the Ω^+ domain and do not

belong to the boundary Γ are labeled as *e*, and the remaining ones as *i*. For the sake of simplicity damping (in overall equilibrium) and stabilization term (in the fluid mass balance) are neglected here (adding these terms is straightforward).

After partitioning the domain into Ω and Ω^+ one may write equations of overall equilibrium (eq.30), (eq.31) and fluid mass balance (eq.32), (eq.33) in Ω and Ω^+ respectively ($\mathbf{P}_b$, $\mathbf{Q}_b$ represent boundary forces/fluxes along Γ while $\mathbf{P}_e$, $\mathbf{Q}_e$ excitation forces/fluxes).

- Overall equilibrium in Ω

$$\begin{bmatrix} \mathbf{M}_{ii}^{\Omega} & \mathbf{M}_{ib}^{\Omega} \\ \mathbf{M}_{bi}^{\Omega} & \mathbf{M}_{bb}^{\Omega} \end{bmatrix} \begin{Bmatrix} \ddot{\mathbf{u}}_i \\ \ddot{\mathbf{u}}_b \end{Bmatrix} + \begin{Bmatrix} \mathbf{F}'_{int_i} \\ \mathbf{F}'_{int_b} \end{Bmatrix} + \begin{bmatrix} \mathbf{C}^{\mathbf{F}\Omega}_{ii} & \mathbf{C}^{\mathbf{F}\Omega}_{ib} \\ \mathbf{C}^{\mathbf{F}\Omega}_{bi} & \mathbf{C}^{\mathbf{F}\Omega}_{bb} \end{bmatrix} \begin{Bmatrix} \mathbf{p}_i \\ \mathbf{p}_b \end{Bmatrix} = \begin{Bmatrix} \mathbf{0} \\ \mathbf{P_b} \end{Bmatrix} \tag{30}$$

- Overall equilibrium in Ω^+

$$\begin{bmatrix} \mathbf{M}_{bb}^{\Omega^+} & \mathbf{M}_{be}^{\Omega^+} \\ \mathbf{M}_{eb}^{\Omega^+} & \mathbf{M}_{ee}^{\Omega^+} \end{bmatrix} \begin{Bmatrix} \ddot{\mathbf{u}}_b \\ \ddot{\mathbf{u}}_e \end{Bmatrix} + \begin{Bmatrix} \mathbf{F}'_{int_b} \\ \mathbf{F}'_{int_e} \end{Bmatrix} + \begin{bmatrix} \mathbf{C}^{\mathbf{F}\Omega^+}_{bb} & \mathbf{C}^{\mathbf{F}\Omega^+}_{be} \\ \mathbf{C}^{\mathbf{F}\Omega^+}_{eb} & \mathbf{C}^{\mathbf{F}\Omega^+}_{ee} \end{bmatrix} \begin{Bmatrix} \mathbf{p}_b \\ \mathbf{p}_e \end{Bmatrix} = \begin{Bmatrix} -\mathbf{P}_b \\ \mathbf{P}_e \end{Bmatrix} \tag{31}$$

- Fluid mass balance in Ω

$$\begin{bmatrix} \mathbf{R}^{\mathbf{F}\Omega}_{ii} & \mathbf{R}^{\mathbf{F}\Omega}_{ib} \\ \mathbf{R}^{\mathbf{F}\Omega}_{bi} & \mathbf{R}^{\mathbf{F}\Omega}_{bb} \end{bmatrix} \begin{Bmatrix} \ddot{\mathbf{u}}_i \\ \ddot{\mathbf{u}}_b \end{Bmatrix} + \begin{bmatrix} \left(\mathbf{C}^{\mathbf{F}\Omega}_{ii}\right)^{\mathrm{T}} & \left(\mathbf{C}^{\mathbf{F}\Omega}_{ib}\right)^{\mathrm{T}} \\ \left(\mathbf{C}^{\mathbf{F}\Omega}_{bi}\right)^{\mathrm{T}} & \left(\mathbf{C}^{\mathbf{F}\Omega}_{bb}\right)^{\mathrm{T}} \end{bmatrix} \begin{Bmatrix} \dot{\mathbf{u}}_i \\ \dot{\mathbf{u}}_b \end{Bmatrix} - \begin{bmatrix} \mathbf{H}^{\mathbf{F}\Omega}_{ii} & \mathbf{H}^{\mathbf{F}\Omega}_{ib} \\ \mathbf{H}^{\mathbf{F}\Omega}_{bi} & \mathbf{H}^{\mathbf{F}\Omega}_{bb} \end{bmatrix} \begin{Bmatrix} \mathbf{p}_i \\ \mathbf{p}_b \end{Bmatrix} - \\ - \begin{bmatrix} \mathbf{M}^{\mathbf{F}\Omega}_{ii} & \mathbf{M}^{\mathbf{F}\Omega}_{ib} \\ \mathbf{M}^{\mathbf{F}\Omega}_{bi} & \mathbf{M}^{\mathbf{F}\Omega}_{bb} \end{bmatrix} \begin{Bmatrix} \dot{\mathbf{p}}_i \\ \dot{\mathbf{p}}_b \end{Bmatrix} = \begin{Bmatrix} -\mathbf{Q}^{\mathbf{F}}{}_i + \mathbf{h}^{\mathbf{F}}{}_i \\ -\mathbf{Q}^{\mathbf{F}}{}_b + \mathbf{h}^{\mathbf{F}\Omega}_b \end{Bmatrix} \tag{32}$$

- Fluid mass balance in Ω^+

$$\begin{bmatrix} \mathbf{R}^{\mathbf{F}\Omega^+}_{bb} & \mathbf{R}^{\mathbf{F}\Omega^+}_{be} \\ \mathbf{R}^{\mathbf{F}\Omega^+}_{eb} & \mathbf{R}^{\mathbf{F}\Omega^+}_{ee} \end{bmatrix} \begin{Bmatrix} \ddot{\mathbf{u}}_b \\ \ddot{\mathbf{u}}_e \end{Bmatrix} + \begin{bmatrix} \left(\mathbf{C}^{\mathbf{F}\Omega^+}_{bb}\right)^{\mathrm{T}} & \left(\mathbf{C}^{\mathbf{F}\Omega^+}_{be}\right)^{\mathrm{T}} \\ \left(\mathbf{C}^{\mathbf{F}\Omega^+}_{eb}\right)^{\mathrm{T}} & \left(\mathbf{C}^{\mathbf{F}\Omega^+}_{ee}\right)^{\mathrm{T}} \end{bmatrix} \begin{Bmatrix} \dot{\mathbf{u}}_b \\ \dot{\mathbf{u}}_e \end{Bmatrix} - \begin{bmatrix} \mathbf{H}^{\mathbf{F}\Omega^+}_{bb} & \mathbf{H}^{\mathbf{F}\Omega^+}_{be} \\ \mathbf{H}^{\mathbf{F}\Omega^+}_{eb} & \mathbf{H}^{\mathbf{F}\Omega^+}_{ee} \end{bmatrix} \begin{Bmatrix} \mathbf{p}_b \\ \mathbf{p}_e \end{Bmatrix} - \\ - \begin{bmatrix} \mathbf{M}^{\mathbf{F}\Omega^+}_{bb} & \mathbf{M}^{\mathbf{F}\Omega^+}_{be} \\ \mathbf{M}^{\mathbf{F}\Omega^+}_{eb} & \mathbf{M}^{\mathbf{F}\Omega^+}_{ee} \end{bmatrix} \begin{Bmatrix} \dot{\mathbf{p}}_b \\ \dot{\mathbf{p}}_e \end{Bmatrix} = \begin{Bmatrix} \mathbf{Q}^{\mathbf{F}}{}_b + \mathbf{h}^{\mathbf{F}\Omega+}_b \\ -\mathbf{Q}^{\mathbf{F}}{}_e + \mathbf{h}^{\mathbf{F}}{}_e \end{Bmatrix} \tag{33}$$

The above equations must be linear in Ω^+ but can be nonlinear in Ω. To fulfill this condition any nonlinear constitutive model associated with the finite element in the exterior domain must work in the linear elastic mode, using stiffness parameters frozen at the initial state. The same requirement applies to flow properties $S(p)$, $c(p)$ that must also be frozen at the initial state. At this point one may assemble coresponding balance equations in the Ω and Ω^+ domains and apply the following decomposition of primary variables (and their time derivatives) in the exterior domain

$$\mathbf{u}_e(t) = \mathbf{u}^o(t) + \hat{\mathbf{u}} \tag{34}$$

$$\mathbf{p}_e(t) = \underbrace{\mathbf{p}^0(t) - \mathbf{p}_e^{init}}_{\mathbf{p}^{0*}(t)} + \underbrace{\mathbf{p}_e^{init} + \tilde{\mathbf{p}}}_{\hat{\mathbf{p}}} \tag{35}$$

The $\hat{\mathbf{u}}$ and $\tilde{\mathbf{p}}$ are understood as vectors of relative values with respect to the free field. Decomposition of the pressure field in the proposed form simplifies the implementation procedure, especially if the dynamic driver is preceeded by other computational drivers (like excavation/construction etc..) generating the initial conditions. By assembling balance equations boundary forces/fluxes will disappear from the system and primary variables at nodes in the exterior domain will be replaced by $\hat{\mathbf{u}}$ and $\hat{\mathbf{p}}$

$$\begin{bmatrix} \mathbf{M}^{\Omega}_{ii} & \mathbf{M}^{\Omega}_{ib} & \mathbf{0} \\ \mathbf{M}^{\Omega}_{bi} & \mathbf{M}^{\Omega}_{bb}+\mathbf{M}^{\Omega^+}_{bb} & \mathbf{M}^{\Omega^+}_{be} \\ \mathbf{0} & \mathbf{M}^{\Omega^+}_{eb} & \mathbf{M}^{\Omega^+}_{ee} \end{bmatrix} \begin{Bmatrix} \ddot{\mathbf{u}}_i \\ \ddot{\mathbf{u}}_b \\ \ddot{\hat{\mathbf{u}}}_e \end{Bmatrix} + \begin{Bmatrix} \mathbf{F}'_{int_i} \\ \mathbf{F}'_{int_b} \\ \mathbf{0} \end{Bmatrix} + \begin{bmatrix} \mathbf{0} & \mathbf{0} & \mathbf{0} \\ \mathbf{0} & \mathbf{K}^{\Omega^+}_{bb} & \mathbf{K}^{\Omega^+}_{be} \\ \mathbf{0} & \mathbf{K}^{\Omega^+}_{eb} & \mathbf{K}^{\Omega^+}_{ee} \end{bmatrix} \begin{Bmatrix} \mathbf{u}_i \\ \mathbf{u}_b \\ \hat{\mathbf{u}}_e \end{Bmatrix} +$$
$$+ \begin{bmatrix} \mathbf{C}^{\mathbf{F}\Omega}_{ii} & \mathbf{C}^{\mathbf{F}\Omega}_{ib} & \mathbf{0} \\ \mathbf{C}^{\mathbf{F}\Omega}_{bi} & \mathbf{C}^{\mathbf{F}\Omega}_{bb}+\mathbf{C}^{\mathbf{F}\Omega^+}_{bb} & \mathbf{C}^{\mathbf{F}\Omega^+}_{be} \\ \mathbf{0} & \mathbf{C}^{\mathbf{F}\Omega^+}_{eb} & \mathbf{C}^{\mathbf{F}\Omega^+}_{ee} \end{bmatrix} \begin{Bmatrix} \mathbf{p}_i \\ \mathbf{p}_b \\ \hat{\mathbf{p}}_e \end{Bmatrix} = \begin{Bmatrix} \mathbf{0} \\ -\mathbf{M}^{\Omega^+}_{be}\,\ddot{\mathbf{u}}^0_e - \mathbf{K}^{\Omega^+}_{be}\,\mathbf{u}^0_e - \mathbf{C}^{\Omega^+}_{be}\,\dot{\mathbf{u}}^0_e - \mathbf{C}^{\mathbf{F}\Omega^+}_{be}\,\mathbf{p}^{0*}_e \\ \mathbf{P_e} - \mathbf{M}^{\Omega^+}_{ee}\,\ddot{\mathbf{u}}^0_e - \mathbf{K}^{\Omega^+}_{ee}\,\mathbf{u}^0_e - \mathbf{C}^{\Omega^+}_{ee}\,\dot{\mathbf{u}}^0_e - \mathbf{C}^{\mathbf{F}\Omega^+}_{ee}\,\mathbf{p}^{0*} \end{Bmatrix} \tag{36}$$

$$\begin{bmatrix} \mathbf{R}^{\mathbf{F}\Omega}_{ii} & \mathbf{R}^{\mathbf{F}\Omega}_{ib} & \mathbf{0} \\ \mathbf{R}^{\mathbf{F}\Omega}_{bi} & \mathbf{R}^{\mathbf{F}\Omega}_{bb}+\mathbf{R}^{\mathbf{F}\Omega^+}_{bb} & \mathbf{R}^{\mathbf{F}\Omega^+}_{be} \\ \mathbf{0} & \mathbf{R}^{\mathbf{F}\Omega^+}_{eb} & \mathbf{R}^{\mathbf{F}\Omega^+}_{ee} \end{bmatrix} \begin{Bmatrix} \ddot{\mathbf{u}}_i \\ \ddot{\mathbf{u}}_b \\ \ddot{\hat{\mathbf{u}}}_e \end{Bmatrix} + \begin{bmatrix} \left(\mathbf{C}^{\mathbf{F}\Omega}_{ii}\right)^{\mathrm{T}} & \left(\mathbf{C}^{\mathbf{F}\Omega}_{ib}\right)^{\mathrm{T}} & \mathbf{0} \\ \left(\mathbf{C}^{\mathbf{F}\Omega}_{bi}\right)^{\mathrm{T}} & \left(\mathbf{C}^{\mathbf{F}\Omega}_{bb}\right)^{\mathrm{T}}+\left(\mathbf{C}^{\mathbf{F}\Omega^+}_{bb}\right)^{\mathrm{T}} & \left(\mathbf{C}^{\mathbf{F}\Omega^+}_{be}\right)^{\mathrm{T}} \\ \mathbf{0} & \left(\mathbf{C}^{\mathbf{F}\Omega^+}_{eb}\right)^{\mathrm{T}} & \left(\mathbf{C}^{\mathbf{F}\Omega^+}_{ee}\right)^{\mathrm{T}} \end{bmatrix} \begin{Bmatrix} \dot{\mathbf{u}}_i \\ \dot{\mathbf{u}}_b \\ \dot{\hat{\mathbf{u}}}_e \end{Bmatrix} -$$
$$\begin{bmatrix} \mathbf{H}^{\mathbf{F}\Omega}_{ii} & \mathbf{H}^{\mathbf{F}\Omega}_{ib} & \mathbf{0} \\ \mathbf{H}^{\mathbf{F}\Omega}_{bi} & \mathbf{H}^{\mathbf{F}\Omega}_{bb}+\mathbf{H}^{\mathbf{F}\Omega^+}_{bb} & \mathbf{H}^{\mathbf{F}\Omega^+}_{be} \\ \mathbf{0} & \mathbf{H}^{\mathbf{F}\Omega^+}_{eb} & \mathbf{H}^{\mathbf{F}\Omega^+}_{ee} \end{bmatrix} \begin{Bmatrix} \mathbf{p}_i \\ \mathbf{p}_b \\ \hat{\mathbf{p}}_e \end{Bmatrix} - \begin{bmatrix} \mathbf{M}^{\mathbf{F}\Omega}_{ii} & \mathbf{M}^{\mathbf{F}\Omega}_{ib} & \mathbf{0} \\ \mathbf{M}^{\mathbf{F}\Omega}_{bi} & \mathbf{M}^{\mathbf{F}\Omega}_{bb}+\mathbf{M}^{\mathbf{F}\Omega^+}_{bb} & \mathbf{M}^{\mathbf{F}\Omega^+}_{be} \\ \mathbf{0} & \mathbf{M}^{\mathbf{F}\Omega^+}_{eb} & \mathbf{M}^{\mathbf{F}\Omega^+}_{ee} \end{bmatrix} \begin{Bmatrix} \dot{\mathbf{p}}_i \\ \dot{\mathbf{p}}_b \\ \dot{\hat{\mathbf{p}}}_e \end{Bmatrix} =$$
$$\begin{Bmatrix} -\mathbf{Q}^{\mathbf{F}}{}_i + \mathbf{h}^{\mathbf{F}}{}_i \\ \mathbf{h}^{\mathbf{F}\Omega}_b + \mathbf{h}^{\mathbf{F}\Omega+}_b \\ \mathbf{h}^{\mathbf{F}}{}_e \end{Bmatrix} + \begin{Bmatrix} \mathbf{0} \\ -\mathbf{R}^{\mathbf{F}\Omega^+}_{be}\,\ddot{\mathbf{u}}^0_e - \left(\mathbf{C}^{\mathbf{F}\Omega^+}_{be}\right)^{\mathrm{T}}\,\dot{\mathbf{u}}^0_e + \mathbf{H}^{\mathbf{F}\Omega^+}_{be}\,\mathbf{p}^{0*} + \mathbf{M}^{\mathbf{F}\Omega^+}_{be}\,\dot{\mathbf{p}}^{0*} \\ -\mathbf{Q}^{\mathbf{F}}{}_e - \mathbf{R}^{\mathbf{F}\Omega^+}_{ee}\,\ddot{\mathbf{u}}^0_e - \left(\mathbf{C}^{\mathbf{F}\Omega^+}_{ee}\right)^{\mathrm{T}}\,\dot{\mathbf{u}}^0_e + \mathbf{H}^{\mathbf{F}\Omega^+}_{ee}\,\mathbf{p}^{0*} + \mathbf{M}^{\mathbf{F}\Omega^+}_{ee}\,\dot{\mathbf{p}}^{0*} \end{Bmatrix} \tag{37}$$

The $\mathbf{P}_e$ and $\mathbf{Q}_e$ terms can now be derived from eq.(31), and eq.(33) respectively, assuming that these are solved for a simpler problem that does not include the structure

$$\mathbf{P}_e = \mathbf{M}^{\Omega^+}_{eb}\ddot{\mathbf{u}}^0_b + \mathbf{M}^{\Omega^+}_{ee}\ddot{\mathbf{u}}^0_e + \mathbf{K}^{\Omega^+}_{eb}\mathbf{u}^0_b + \mathbf{K}^{\Omega^+}_{ee}\mathbf{u}^0_e + \mathbf{C}^{\mathbf{F}\Omega^+}_{eb}\mathbf{p}^{0*}_b + \mathbf{C}^{\mathbf{F}\Omega^+}_{ee}\mathbf{p}^{0*}_e \tag{38}$$

$$-\mathbf{Q}_e = -\mathbf{h}^{\mathbf{F}}{}_e + \mathbf{R}^{\mathbf{F}\Omega^+}_{eb}\ddot{\mathbf{u}}^0_b + \mathbf{R}^{\mathbf{F}\Omega^+}_{ee}\ddot{\mathbf{u}}^0_e + \left(\mathbf{C}^{\mathbf{F}\Omega^+}_{eb}\right)^{\mathrm{T}}\dot{\mathbf{u}}^0_b + \left(\mathbf{C}^{\mathbf{F}\Omega^+}_{ee}\right)^{\mathrm{T}}\dot{\mathbf{u}}^0_e - \mathbf{H}^{\mathbf{F}\Omega^+}_{eb}\mathbf{p}^{0*}_b - \mathbf{H}^{\mathbf{F}\Omega^+}_{ee}\mathbf{p}^{0*}_e - \mathbf{M}^{\mathbf{F}\Omega^+}_{eb}\dot{\mathbf{p}}^{0*}_b - \mathbf{M}^{\mathbf{F}\Omega^+}_{ee}\dot{\mathbf{p}}^{0*}_e \tag{39}$$

As the method is implemented in the finite element framework we need to select at least a single row of finite elements, in the reduced model, that is treated as a boundary layer separating the interior and exterior domains. One may easily notice that these extra terms on the right hand side are computed only within the layer of elements in boundary domain. Starting from the above equations one may linearize them and apply any time integration scheme (Newmark, HHT or any other). The method was implemented within the ZSOIL code (Elmepress and Zace Services Limited 2013) starting with version ZSOIL.PC 2013.

4 NUMERICAL EXAMPLE

To verify DRM method an example of twin tunnels (see Fig.(2(a))) subject to the scaled (by factor 0.2) Loma Prieta (see Fig. 2(b)) acceleration record (record shown in the figure is not scaled), is analyzed. In this example two dynamic models are considered, a rigid base (run in relative displacements) and compliant base one (run in the absolute). For the rigid base model bedrock is assumed to be infinitely stiff and hence depth of the model is 30m while for the compliant base model a 15m layer of a bedrock is added. In the latter model, at the bottom, boundary viscous dashpots are added and excitation is transfered through the viscous tractions computed based on velocities integrated via Newmark scheme from given acceleration record (Mejia & Dawson 2006). The free field motions for both dynamic models are computed for a simple shear layer assuming that subsoil is fully saturated while bedrock is an impermeable material (in compliant base model). The shear layer model is discretized using Q4-BBAR elements assuming periodic boundary conditions for displacements and pore pressures (only one element along the L_1 dimension is used) (see Fig.3(a), Fig.3(c)). In both reduced models (see Fig.3(b), Fig.3(d)), at external edges of the exterior domain, viscous dashpots are added. In both dynamic models the scaled acceleration record is assumed to be given at the base of the model (in case of compliant base model no deconvolution procedure was carried out to transfer the signal from top layer of the bedrock to the base). In the implementation we assume that mesh in the reduced model must be fully overlapped by the mesh of the background model (shear layer mesh in considered cases). To study the accuracy of the method with respect to the size of the reduced model dimension L_2 three computations were run, for $L_2 = 280$ m, $L_2 = 160$ m and $L_2 = 100$ m, for both dynamic models. Subsoil is modeled as nonlinear elastic-plastic Mohr-Coulomb model in which stiffness Young modulus at low strains is a power function of current mean effective stress p' according to the formula $E = E_o \left(\dfrac{p'}{\sigma_{ref}} \right)^m$. Material properties for subsoil are as follows: $E_o = 300000$ MPa, $\nu = 0.2$, $m = 0.5$, $\phi = 27^o$, $c = 5$ kPa, $k = 10^{-7}$ m/s, $S_r = 0.0$, $\alpha = 0.1$ m^{-1}, $\gamma_{dry} = 17$ kN/m^3, $e_o = 0.559$. Low frequency damping is activated for subsoil using Rayleigh mass proportional damping with factor $\alpha_o = 1.257$ that corresponds to the 5% damping at frequency 2Hz. Tunnel lining is modeled as an elastic beam with section depth of 30 cm and elastic parameters $E = 30000000$ kPa, $\nu = 0.2$, with zero damping. Bedrock in the compliant base model is assumed to be an elastic material characterized by $E = 1000000$, kPa, $\nu = 0.3$, $\gamma = 23$ kN/m^3 with zero damping. The averaged Q4-BBAR element size is 1.2m while the applied time step $\Delta t = 0.01$ s. The HHT scheme was used in all cases ($\alpha = -0.3$). All dynamic time history analyses for reduced models (models that include the structure) were preceeded by static two-phase uncoupled analyses consisting of the initial state (assuming $K_o^{insitu} = 0.7$) and then the excavation/construction step during which tunnel lining was installed. This requires special procedures to handle adding/removing boundary conditions and ability to preserve remaining reactions. This option is standard in the ZSOIL code.

Horizontal displacement time history at point A for rigid base model is shown in Fig.4(a). One may notice that for $L_1 = 280$m and $L_1 = 160$m during first 5s of shaking quite a good agreement is achieved. Later on certain deviation is observed. Additional computations, carried out for a rigid base model with larger value of damping parameter $\alpha_o = 2.512$, show much beter agreement for cases $L_1 = 280$m and $L_1 = 160$m while for $L_1 = 100$ m still some deviations are observed. These observed deviations are caused by the assumption of a rigid base that causes lot of reflections if damping is too low, but also by the fact that paraxial viscous dashpots cannot fully absorb incoming waves. This spurious effects are well visible at end of shaking when

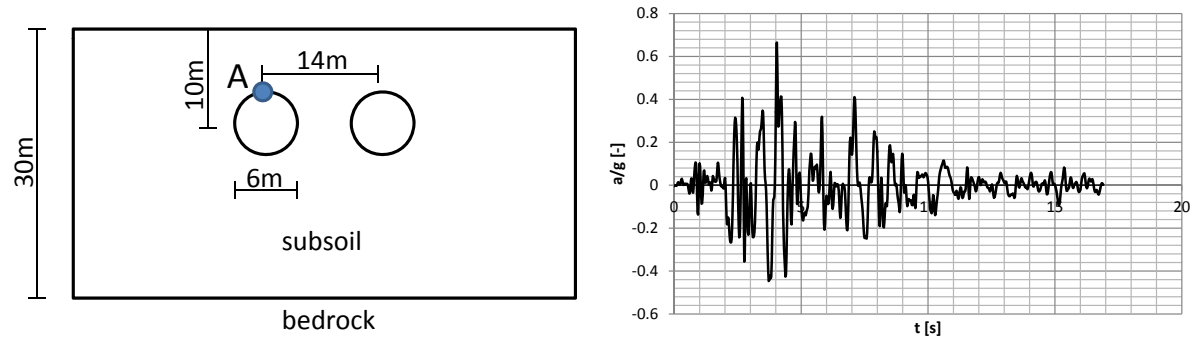

(a) (b)

Fig. 2. Data setup. (a) Geometry of the problem. (b) Baseline corrected and filtered (10 Hz low pass Butterworth filter) original Loma Prieta acceleration record (18.10.1989 Corralitos station)).

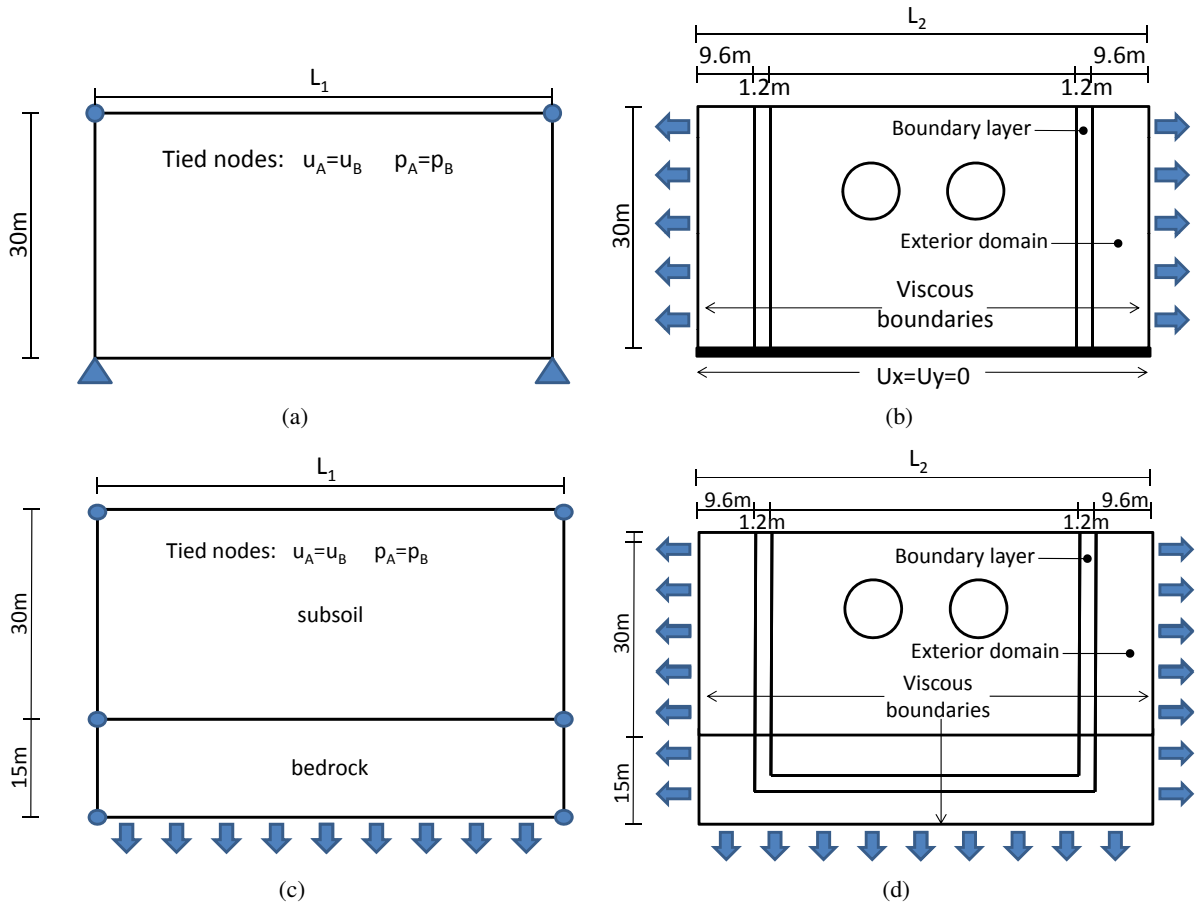

(a) (b) (c) (d)

Fig. 3. Data setup. (a) Free field model for rigid base assumption. (b) Reduced model for rigid base assumption. (c) Free field model for compliant base assumption. (d) Reduced model for compliant base assumption.

displacement amplitudes are still large. Computations carried out for compliant base model show an excellent agreement for all three reduced models (see Fig.4(a)).

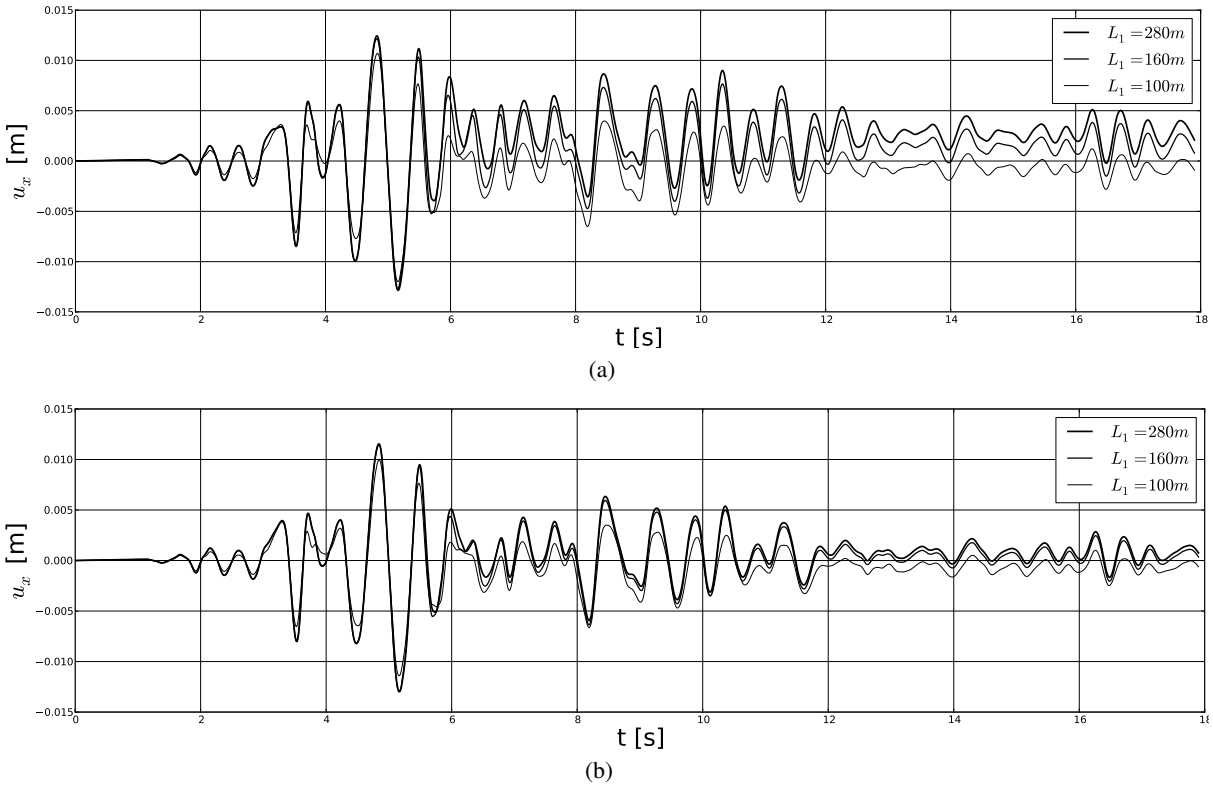

Fig. 4. u_x time histories at point A for rigid base model. (a) Damping parameter $\alpha_o = 1.256$. (b) Damping parameter $\alpha_o = 2.512$.

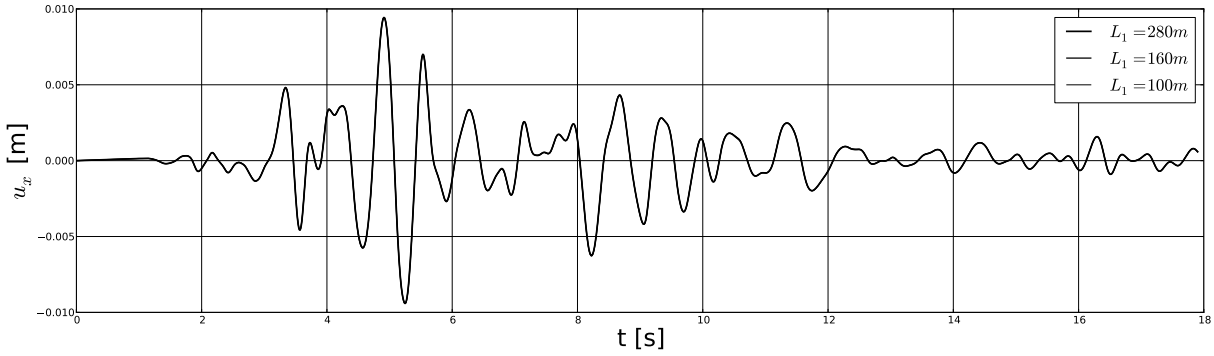

Fig. 5. u_x time histories at point A for compliant base model (damping parameter $\alpha_o = 1.256$).

5 CONCLUSIONS

Although DRM method is applicable to linear and nonlinear problems, the free field motion must be analyzed as a linear one. The benefit of the method is such that only a relatively small part of the subsoil, adjacent to the structure, needs to be included in the analysis. Moreover, the spatial dimension of a free field motion problem can be lower than the one of the reduced model (structure plus small adjacent subsoil zone). Typically, one may find the free field motion

from a 1D shear layer model and then analyze the 2D/3D soil-structure interaction based on this simple free field solution. Proper selection of the size of the reduced model, dimensions of the exterior domain for complex soil models in mixed saturated/partially saturated conditions is still an open issue and requires more research. The compliant base model shows much better behavior compared to the rigid base model that causes lots of spurious wave reflections from rigid boundary. This model combined with the DRM method proves to be a robust tool for solving nonlinear soil-structure interaction problems.

REFERENCES

Aubry, D. & Ozanam, O. (1988). Free-surface tracking through non-saturated models. In Swoboda (Ed.), *Numerical Methods in Geomechanics*, Innsbruck, pp. 757–763. Balkema.

Bielak, J., Loukakis, K., Hisada, Y., & Youshimura, C. (2003). Domain reduction method for three-dimensional earthquake modeling in localized regions. part i: Theory. *Bulletin of the seismological Society of America 93*, 817–824.

Elmepress and Zace Services Limited (1985-2013). *Z_SOIL manual*. Lausanne, Switzerland: Elmepress and Zace Services Limited.

Genuchten, V. (1980). A closed form equation for predicting the hydraulic conductivity of unsaturated soils. *Soil Sciences Am. Soc. 44*, 892–898.

Hilber, H. M., Hughes, T. J. R., & Taylor, R. L. (1977). Improved numerical dissipation for time integration algorithms in structural dynamics. *Earthquake Engineering & Structural Dynamics 5*, 283–292.

Irmay, S. (1956). On the hydraulic conductivity of unsaturated soils. *Trans. Am. Geophys. Union 35*, 463–468.

Kantoe, S. (2006, May). *Development of time integration schemes and advanced boundary conditions for dynamic analysis*. Ph. D. thesis, Department of Civil and Environmental Engineering, Imperial College of Science, Technology and Medicine, London, SW7 2BU.

Kantoe, S., Zdravkovic, L., & Potts, D. (2008). The domain reduction method for dynamic coupled consolidation problems in geotechnical engineering. *International Journal for Numerical and Analytical Methods in Geomechanics 32*, 659–680.

Mejia, L. & Dawson, E. (2006). Earthquake deconvolution for FLAC. paper 04-10. In *4th International FLAC Symposium on Numerical Modeling in Geomechanics*, Minneapolis, pp. 2–9.

Modaressi, H. & Benzenati, I. (1994). Paraxial approximation for poroelastic media. *Soil Dynamics and Earthquake Engineering 13*, 117–129.

Truty, A. & Zimmermann, T. (2006). Stabilized mixed finite element formulations for materially nonlinear partially saturated two-phase media. *Computer Methods in Applied Mechanics and Engineering 195*, 1517–1546.

Youshimura, C., Bielak, J., Hisada, Y., & Fernandez, A. (2003). Domain reduction method for three-dimensional earthquake modeling in localized regions. part ii: Verification and applications. *Bulletin of the seismological Society of America 93*, 825–840.

Zienkiewicz, O., Chan, A., Pastor, M., Schrefler, B., & Shiomi, T. (1999). *Computational Geomechanics with Special Reference to Earthquake Engineering*. John Wiley & Sons Ltd.

ON THE APPLICATION OF HIGH-ORDER ELEMENTS IN LARGE DEFORMATION PROBLEMS OF GEOMECHANICS

M. Nazem, M. Kardani, J.P. Carter and S.W. Sloan

Australian Research Council Centre of Excellence for Geotechnical Science and Engineering, The University of Newcastle, NSW, Australia

ABSTRACT: *This paper addresses the application of 15-noded triangular elements for large deformation analysis of geotechnical problems using the Arbitrary Lagrangian-Eulerian method. Important aspects of the formulation, including the nodal recovery process and the remapping of state variables, are discussed. The efficiency of these elements is represented by investigating the undrained response of a soil layer under a strip footing subjected to large deformations, and comparing the analysis results with results obtained using quadratic triangular elements. The results indicate that the 15-noded elements not only decrease the computational time, but increase the accuracy of the numerical results.*

1 INTRODUCTION

The finite element method (FEM) is the most popular computational tool for analysing the behaviour of a wide range of complex engineering problems. The Updated-Lagrangian (UL) method is a common strategy to model large deformations. In this method all quantities are measured at the last equilibrium configuration, and the nodal coordinates are updated according to the incremental displacements at the end of each time step. In problems with relatively large deformations, updating the nodal coordinates often leads to mesh distortion and entanglement of the elements, which are the severe drawbacks of the UL method for geotechnical applications. Mesh distortion is usually followed by loss of accuracy or spontaneous termination of the analysis. Adaptive finite element methods provide a means to overcome the mesh distortion issue, and are divided into two main groups, viz., the h-adaptive and the r-adaptive methods. In computational geomechanics, significant research has been devoted to the application of linear and quadratic elements within an adaptive framework. High-order elements, on the other hand, have attracted less attention in adaptivity, mainly due to the complexities arising in mesh generation and its optimisation, the nodal recovery process, and remapping of state variables. Since their application in predicting the collapse load of soil under footings, first presented by Sloan and Randolph (1982), high-order elements have rarely been used for solving geotechnical problems involving large deformations, particularly within an r-adaptive finite element framework.

In this paper we address the application, as well as the advantages, of high-order elements for solving large deformations problems in geomechanics by the Arbitrary Lagrangian-Eulerian (ALE) method based on the operator split technique. Specifically, we draw attention to 15-noded triangular elements with quartic interpolation functions. By studying the soil behavior under a strip footing subjected to large deformations, it is shown that these

elements not only improve the accuracy of the numerical results, but also significantly reduce the computational time.

2 ARBITRARY LAGRANGIAN-EULERIAN METHOD

The ALE method is based on the idea of separating the material and mesh displacements to eliminate mesh distortion in the UL method. This separation introduces unknown mesh displacements into the governing global system of equations, in addition to the unknown material displacements. In the so-called coupled ALE method, a supplementary set of equations in terms of the material and mesh displacements is established through a mesh motion scheme, and the two sets of unknown displacements are then solved simultaneously. On the other hand, the decoupled ALE method, or the operator-split technique, first solves the material displacements via the equilibrium equation and then computes the mesh displacements through a mesh refinement technique. In this method, the analysis is performed in two steps: an UL step followed by an Eulerian step. In the UL step, we solve the governing equations to fulfill equilibrium and obtain the material displacements. The mesh at the end of the UL step may be distorted. In the Eulerian step, the distorted mesh is refined to obtain the mesh displacements. All state variables are then transferred from the old mesh to the new mesh. The ALE method used in this study is based on the mesh optimization technique developed by Nazem et al. (2006) and is summarized in following algorithm.

ALE algorithm (for each increment) based on the Newton-Raphson iterative method:

1. Form the external force vector, $\mathbf{F}_{ext}$.
2. For the i^{th} iteration, assemble the tangential stiffness matrix, $\mathbf{K}_T$ and solve the equilibrium equation to find the incremental displacements, $\Delta\mathbf{u}$, according to

$$\begin{aligned} \mathbf{K}_{T(i-1)} \cdot \Delta\mathbf{u}_{(i)} &= \mathbf{F}_{ext} - \mathbf{F}_{int(i-1)} \\ \mathbf{u}_{(i)} &= \mathbf{u}_{(i-1)} + \Delta\mathbf{u}_{(i)} \end{aligned} \tag{1}$$

   where $\mathbf{F}_{int}$ represents the internal force vector and $\mathbf{u}$ is the total displacement vector.
3. Compute the strain increments and integrate the constitutive equations to update the stresses and the internal forces.
4. Repeat Steps (2) and (3) until the unbalanced forces are smaller than a prescribed tolerance.
5. Update the spatial coordinates of the material points according to the incremental displacements.
6. Refine the mesh to eliminate mesh distortion and find the new mesh displacements.
7. Remap the state variables from the old mesh to the new mesh.
8. Update the total displacement vector according to the new mesh displacements and the previous material displacements.
9. Set the material coordinates equal to the mesh coordinates.
10. Recalculate the internal forces to form the unbalanced force vector for the next increment.

The mesh refinement procedure in Step (6) of the ALE algorithm is based on the use of a simple elastic analysis, presented by Nazem et al. (2006) and improved by Nazem et al. (2008). In this method the mesh displacements are obtained by re-discretising all the boundaries of the problem, which include the boundaries of each discrete body, the material interfaces and the loading boundaries, resulting in prescribed values of the mesh displacements for the nodes on these boundaries. Each boundary node is then relocated along the boundary as necessary. With the known total displacements of these nodes on the

boundaries, an elastic analysis is then performed using the prescribed boundary displacements to obtain the mesh displacements for all the internal nodes and hence the optimal new mesh. An important advantage of this mesh optimisation method is its independence of the element topology, element type, and problem dimensions. After the mesh refinement, all variables need to be mapped from the old mesh to the new mesh. Due to its importance, this procedure is explained in more detail as follows.

3 REMAPPIG OF STATE VARIABLES

In this section the remapping of state variables from the old mesh to the new mesh is presented. Generally speaking, all state variables at Gauss points, such as components of stress and hardening parameters (if any), must be considered for remapping. In the ALE method based on the operator split technique, remapping is usually performed using the convection equation according to (Hughes et al. 1981)

$$\dot{f}^r = \dot{f} + \left(v_i^r - v_i\right) \times \frac{\P f}{\P x_i} \tag{2}$$

where $\dot{f}^r$ and $\dot{f}$ denote the time derivatives of an arbitrary function f with respect to the mesh and material coordinates respectively, v_i is the material velocity, and v_i^r represents the mesh velocity. The procedure for remapping is explained here for Cauchy stresses only. However, it can be generalised to other state variables. Multiplying Equation (2) by the time increment and substituting the stresses for the function *f* provides

$$\sigma_{ij}^r = \sigma_{ij} + (u_k^r - u_k) \cdot \frac{\partial \sigma_{ij}}{\partial x_k} \tag{3}$$

where σ_{ij}^r are the stress components at the Gauss points of the new mesh and σ_{ij} are the stresses at the Gauss points of the old mesh. For two-dimensional elements, the gradients of the stresses in Equation (3) are expressed in terms of the derivative of the stresses with respect to the normalised coordinates ζ and η according to

$$\frac{\partial \sigma_{ij}}{\partial x_1} = \frac{\partial \sigma_{ij}}{\partial \xi} \cdot \frac{\partial \xi}{\partial x_1} + \frac{\partial \sigma_{ij}}{\partial \eta} \cdot \frac{\partial \eta}{\partial x_1} \qquad \frac{\partial \sigma_{ij}}{\partial x_2} = \frac{\partial \sigma_{ij}}{\partial \xi} \cdot \frac{\partial \xi}{\partial x_2} + \frac{\partial \sigma_{ij}}{\partial \eta} \cdot \frac{\partial \eta}{\partial x_2} \tag{4}$$

The local derivatives of the stresses can be computed using the nodal shape functions

$$\frac{\partial \sigma_{ij}}{\partial \xi} = \sum_{k=1}^{n} \frac{\partial N_k}{\partial \xi} \cdot \sigma_{ij}^k \qquad \frac{\partial \sigma_{ij}}{\partial \eta} = \sum_{k=1}^{n} \frac{\partial N_k}{\partial \eta} \cdot \sigma_{ij}^k \tag{5}$$

where *n* is the number of nodes per element and σ_{ij}^k are the components of the nodal stresses. To compute the nodal stresses, the super convergent patch recovery technique developed by Zienkiewicz and Zhu (1992) is used. In this method, it is assumed that the stress values in a patch of elements are computed using a polynomial of the same order as the basic shape functions. Thus, for two-dimensional quartic elements, the stresses may be written as

$$\boldsymbol{\sigma} = \mathbf{P.a} = \left[1, x, y, x^2, xy, y^2, x^3, x^2y, xy^2, y^3, x^4, x^3y, x^2y^2, xy^3, y^4\right] \cdot \left[a_1, a_2, a_3, ..., a_{15}\right]^{\mathbf{T}} \tag{6}$$

Zienkiewicz et al. (1993) proposed the use of normalised coordinates in Equation (6) instead of global coordinates to avoid ill-conditioning of equations, particularly for higher order elements. The normalised coordinates in a two-dimensional patch, $\bar{x}$ and $\bar{y}$, can be written as

$$\bar{x}_i = -1 + 2\frac{x_i - x_{\min}}{x_{\max} - x_{\min}} \qquad \bar{y}_i = -1 + 2\frac{y_i - y_{\min}}{y_{\max} - y_{\min}} \tag{7}$$

where x_{min} and x_{max} represent the minimum and maximum values of the x-coordinates in the patch, respectively, and y_{min} and y_{max} are defined similarly for the y-coordinates. A least squares minimisation is then used to find the unknown values of **a**, which provides

$$\mathbf{a} = \left[\sum_{i=1}^{m} \mathbf{P}^{\mathbf{T}}\left(\bar{x}_i, \bar{y}_i\right)\mathbf{P}\left(\bar{x}_i, \bar{y}_i\right)\right]^{-1}\left[\sum_{i=1}^{m} \mathbf{P}^{\mathbf{T}}\left(\bar{x}_i, \bar{y}_i\right)\sigma\left(\bar{x}_i, \bar{y}_i\right)\right] \tag{8}$$

where $\sigma\left(\bar{x}_i, \bar{y}_i\right)$ represents the stress values at the Gauss points and m is the number of Gauss points in a patch. The stresses at any node in the patch can now be obtained by substituting its normalised coordinates in Equation (6).

4 NUMERICAL EXAMPLE

To investigate the efficiency of 15-noded elements, we consider the classical geomechanics problem of an undrained layer of soil under a rigid rough strip footing subjected to a vertical prescribed settlement. The problem domain, boundary conditions, and soil properties are represented in Fig. 1. The soil layer is assumed to be weightless and its nonlinear behaviour is simulated by the Tresca material model. Due to symmetry, only the right-hand half of the problem is considered in the analysis, and four different triangular grids have been used to subdivide the domain into finite elements. These four base grids are depicted in Fig. 2. Each grid is discretised by triangular elements considering three groups A, B, and C. In group A every triangle of the grid is replaced by a 6-noded triangular element, whereas in group B each triangle is substituted by a quartic 15-noded element. In group C, every triangle is subdivided into four 6-noded elements. The number of elements, number of degrees of freedom, number of Gauss points in each finite element mesh, and the size of the elements under the footing are summarised in Table 1. For each grid, the number of elements in groups A and B, and number of nodal points (and consequently the number of degrees of freedom) in groups B and C are identical. In all finite element analyses the footing was subjected to a prescribed overall vertical displacement equal

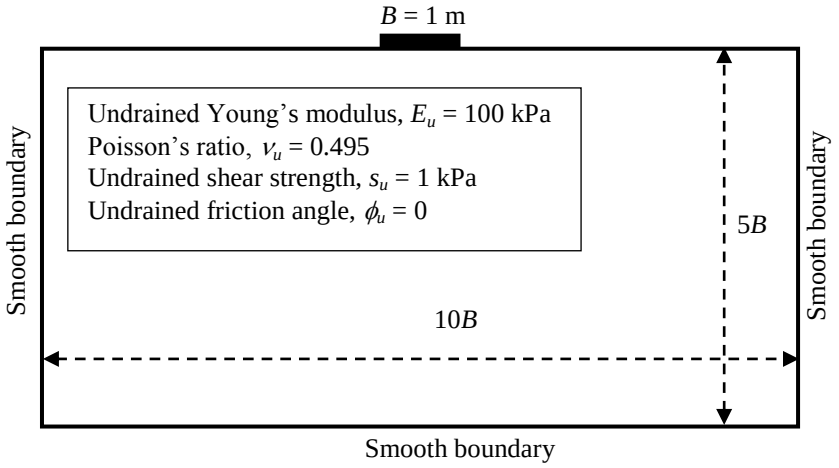

Fig. 1. Rough and rigid strip footing on an undrained layer of clay

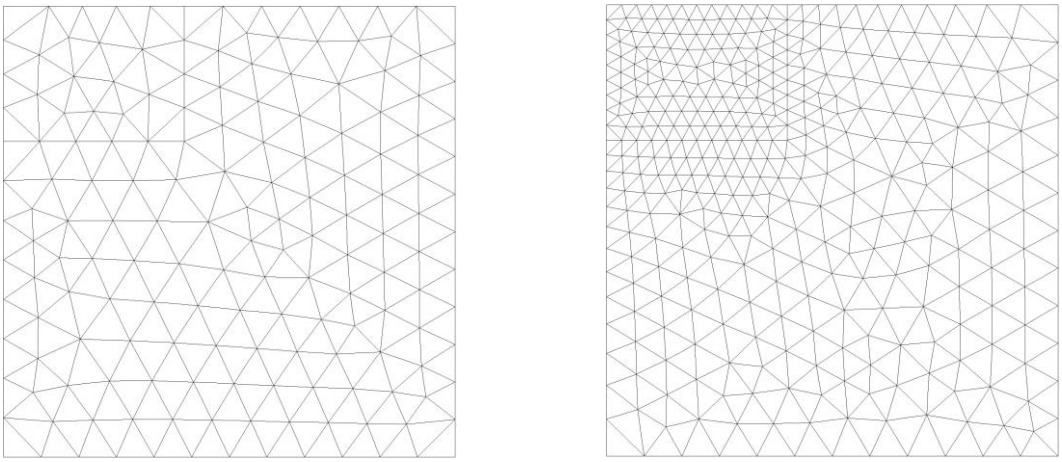

a. Grid 1 b. Grid 2

c. Grid 3 d. Grid 4

Fig. 2. Finite element grids

to its total width. The soil behaviour was predicted assuming small deformation as well as large deformation. Each analysis was conducted using 1000 equal load steps.

Table 1. Finite element meshes

Grid - Group	Number of elements	Nodes per element	Degrees of Freedom	Gauss points	Element size under footing
1 – A	286	6	1167	1716	0.5*B*
2 – A	669	6	2717	4014	0.17*B*
3 – A	1735	6	7005	10414	0.08*B*
4 – A	5831	6	23433	34986	0.04*B*
1 – B	286	15	4621	3432	0.5*B*
2 – B	669	15	10785	8028	0.17*B*
3 – B	1735	15	27889	20820	0.08*B*
4 – B	5831	15	93513	69972	0.04*B*
1 – C	1144	6	4621	6864	0.25*B*
2 – C	2676	6	10785	16056	0.08*B*
3 – C	6940	6	27889	41640	0.04*B*
4 – C	23324	6	93513	139944	0.02*B*

4.1 Results of small strain analyses

Firstly, we investigate the precision of all finite element meshes using small strain analyses. According to Prandtl's plasticity solution the undrained bearing capacity of a weightless layer of soil under a rigid strip footing, q_u, is given by

$$q_u = N_c s_u \tag{9}$$

where N_c represents the capacity factor and is equal to $2+\pi \approx 5.14$. Table 2 shows the capacity factor predicted by each finite element mesh, the error in calculating the capacity factor, the CPU time normalised by the CPU time of the fastest analysis, and the total number of iterations to achieve a converged solution. Based on the topology information provided in Table 1 and analysis results summarised in Table 2, the following conclusions are drawn.

- Although being the slowest, mesh 4-B provides the most accurate capacity factor. The largest overestimation of capacity factor is obtained by mesh 1-A.
- The numbers of equilibrium iterations in all analyses are more or less the same. The average number of iterations per increment is 2.
- Comparing the accuracy of the finite element meshes in group B with the accuracy of their counterparts in group C reveals that subdividing a 15-noded element into four 6-noded elements, which increases the number of integration points while maintaining the number of nodal points, increases the error in the predicted capacity factors by up to 7%. Apparently, such a subdivision decreases the computational time, but this statement may not apply in all cases since the band width of the stiffness matrix normally changes after subdivision.
- In the bearing capacity problem considered here, the quartic elements clearly outperform the quadratic elements. This can be verified by comparing (a) the performances of meshes 2-B and 4-A, and (b) the performances of meshes 3-B and 4-C. Mesh 2-B includes 669 15-noded elements, 10785 degrees of freedom, and 8028 integration points while mesh 4-A has 5831 6-noded elements, 23433 degrees of freedom, and 34986 integration points. However, the bearing capacity predicted by mesh 2-B is more accurate than the capacity computed by mesh 4-A, and mesh 2-B is ~4.5 times faster than mesh 4-A. Similarly, the number of elements and degrees of freedom in mesh 3-B are significantly less than the number of elements and degrees of freedom in mesh 4-A. Nonetheless, mesh 3-B predicted a more accurate capacity factor in a shorter analysis time.

Table 2. Numerical results

Grid - Group	Small strain analysis				ALE analysis			
	N_c	Error in N_c (%)	Normalised CPU time	Total iterations	Maximum soil resistance / s_u	Error in soil resistance (%)	Normalised CPU time	Total iterations
1–A	6.29	22.4	1.0	2000	11.35	66.9	1.0	2968
2–A	5.70	10.9	3.7	2002	9.46	39.1	11.5	3205
3–A	5.44	5.8	14.8	2002	8.44	24.1	23.8	3931
4–A	5.30	3.1	270.0	2001	-----	-----	-----	-----
1–B	5.45	6.0	9.2	2002	8.07	18.7	9.7	4592
2–B	5.27	2.5	60.4	2008	7.00	2.9	43.7	4969
3–B	5.21	1.3	304.4	2018	6.99	2.8	201.5	6413
4–B	5.17	0.5	3874.9	2020	6.80	0.0	5944.0	10127
1–C	5.81	13.0	6.72	2001	10.2	50	5.5	3734
2–C	5.45	6.0	26.2	2001	8.65	27.2	36.7	4206
3–C	5.31	3.3	96.1	2006	8.04	18.23	135.9	4219
4–C	5.23	1.75	2506.7	2006	7.40	8.8	4579.0	5780

4.2 Results of large deformation (ALE) analyses

A closed-form analytical solution for the bearing capacity of soil under a strip footing subjected to large deformations does not exist in the literature. Under such conditions the soil resistance usually tends to increase due to changes in geometry. For this particular problem, a transition should take place from the bearing capacity of a surface strip footing, i.e., $2 + \pi$, at small footing displacements, to something close to the ultimate capacity of a strip footing located at the bottom of a deep vertical-sided trench, i.e., $2 + 2\pi$. The latter should be mobilised at quite large footing displacements, of the order of several footing widths, as the footing buries itself into the layer of soil. An early stage of this transition is shown graphically in Fig. 3 by plotting the soil resistance, normalised by its shear strength, versus the settlement of footing, normalised by its width. Only mesh 4-A could not complete the analysis due to mesh distortion, which occurred at prescribed displacement of 0.64*B*. Although the soil behaviour could have been investigated further by applying a larger value of prescribed displacement, Fig. 3 shows that the applied displacement is large enough to reflect the effect of nonlinearity due to large deformations and geometry changes. It is notable that the UL method was not able to successfully analyse this problem in many cases due to mesh distortion, and thus the UL results are not discussed here for brevity.

According to Fig. 3, the maximum soil resistance achieved at a settlement of 1*B* is significantly higher than $5.14s_u$. The plots in Fig. 3 also indicate that the overestimation of the soil resistance increases as the density of the finite element mesh, or the degree of polynomial shape functions, decreases. The exact value of soil resistance at a settlement of 1*B* cannot be calculated analytically, but small strain analyses indicated that mesh 4-B provided the most accurate results. Based on this fact, and considering that the most accurate finite element mesh would probably have predicted the lowest soil resistance, it is reasonable to suggest that the best estimation for soil resistance at a settlement of 1B is given by mesh 4-B, i.e., $6.80s_u$. Therefore, the accuracy of the other finite element meshes can be studied by comparing their results with the result predicted by mesh 4-B. For the finite element meshes considered in this study, Table 2 shows the maximum soil resistance normalised by its shear strength, the error in estimating the soil resistance, the CPU time normalised by the CPU time of the fastest analysis, and the total number of iterations to achieve the solution. Important outcomes from the comparative study are summarised in Tables 1 and 2 are briefly explained

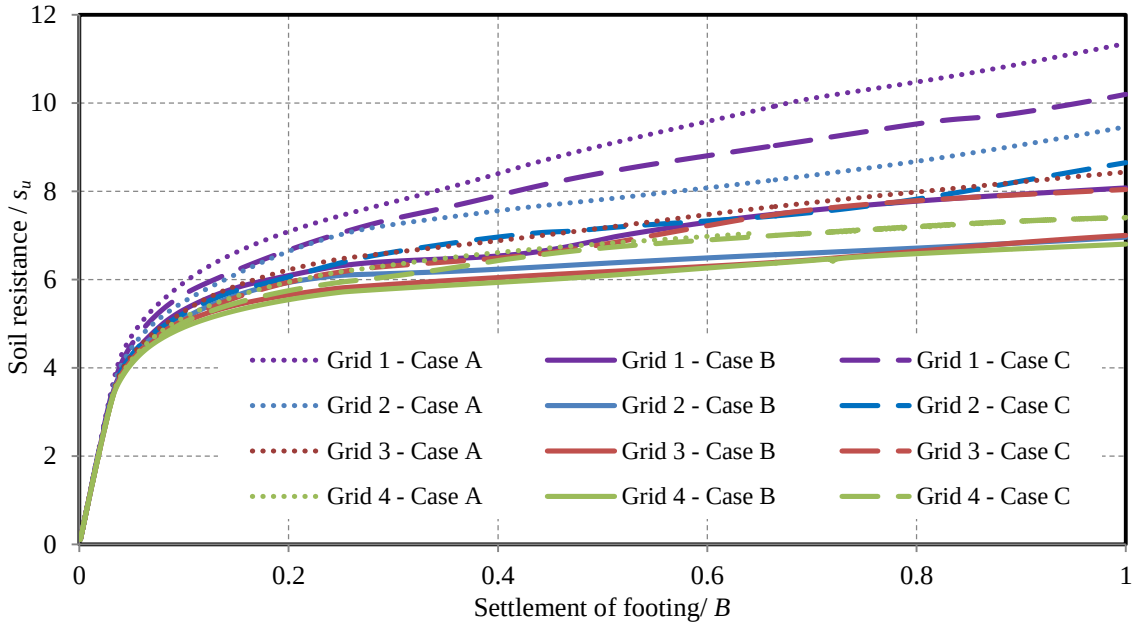

Fig 3. Normalised soil resistance versus normalised settlement of footing predicted by the ALE method.

in the following.

- Unlike small deformation analyses, the number of iterations to satisfy equilibrium by the ALE method increases as the density of the mesh increases. This is mainly due to the fact that the remapping of state variables may cause violation of equilibrium or violation of the consistency relations of plasticity. In the ALE method, if a previously yielded material point is located outside the yield surface (in new mesh) after remapping it will be shifted back to the yield surface. Then, the unbalanced forces due to the difference between the external forces and the internal forces are calculated and transferred to the subsequent increment. This correction is necessary to satisfy the yield criterion and it usually increases the number of equilibrium iterations in future increments, depending on the number of integration points. An alternative strategy is to conduct further iterations at the end of the increment.
- For the large deformation analysis of a footing, Table 2 clearly shows the superior performance of 15-noded elements in comparison with the 6-noded elements. For instance, the soil resistance predicted by mesh 2-B, which comprises 669 15-node elements, is more accurate than the resistance obtained by meshes 3-C and 4-C, which have 6940 and 23324 6-node elements, respectively. A similar advantage can be seen by comparing the performance of mesh 2-B with the performance of mesh 3-A.
- Similar to the results of the small strain analyses, the ALE results indicate that subdividing a 15-noded element into 4 6-noded triangular elements decreases the efficiency of the finite element method.

5 CONCLUSIONS

In this paper, a computational procedure for large deformation analysis of geomechanics problems by the Arbitrary Lagrangian-Eulerian method using high-order 15-noded elements was presented. For the footing problem considered in this study, the results obtained by small strain analyses, as well as large deformation analyses, indicate that 15-noded elements not only increase the accuracy of the analysis, but also significantly reduce the computational time. Compared to finite element meshes discretized by 6-noded elements, the meshes comprised of 15-noded elements deliver more accurate results with fewer elements, degrees of freedom, and integration points.

REFERENCES

Hughes, T.J.R., Liu, W.K. & Zimmermann, T.K. (1981), "Lagrangian-Eulerian finite element formulation for incompressible viscous flow". Comp Meth in App Mech Eng, Vol. 29(3), 329-349.

Nazem, M., Sheng, D. & Carter, J.P. (2006), "Stress integration and mesh refinement for large deformation in geomechanics". Int. J. Num. Meth. Eng., Vol. 65, 1002-1027.

Nazem, M., Sheng, D., Carter, J.P. & Sloan, S.W. (2008), "Arbitrary-Lagrangian-Eulerian method for large-deformation consolidation problems in geomechanics". Int. J. Num. Anal. Meth. Geomech., Vol. 32, 1023-1050.

Sloan, S.W. & Randolph, M.F. (1982), "Numerical Prediction of collapse loads using the finite element methods". Int. J. Num. Anal. Meth. Geomech., Vol. 6(1), 47-76.

Zienkiewicz, O.C. & Zhu, J.Z. (1992), "The superconvergent patch recovery and a posteriori error estimates. Part 1:The recovery technique". Int. J. Num. Meth. Eng., 33, 1331-1364.

Zienkiewicz, O.C., Zhu, J.Z. & Wu, J. (1993), "Superconvergent patch techniques – some further tests". Comm Numer Meth Eng, 9, 251-258.

VALIDATING GEOTECHNICAL FINITE ELEMENT MODELS

R.B.J. Brinkgreve
Department of Civil Engineering & Geosciences, Delft University of Technology, Delft, Netherlands

ABSTRACT: *There is a need for guidelines on validation of geotechnical finite element calculations. In Europe, different initiatives have started to work on this subject, among which the NAFEMS geotechnical committee. The author is a member of this committee and author of a reference publication on validation of numerical modelling in geotechnical engineering (Brinkgreve, 2013).This paper presents the main ideas of that publication. In addition to the reasoning behind validation of finite element calculations and a definition of related terms, it highlights the most important sources of discrepancies between a real project and its corresponding numerical model. The second part of the paper is devoted to the various methods of validation. The process of validation involves a validation of the model as a whole, as well as a validation of the various model components, but it starts with a verification of the methods and models implemented in the software. The last chapter describes some non-technical issues related with decisions, responsibilities and organizational issues to control the quality of numerical modelling as part of the geotechnical design process.*

1 INTRODUCTION

In the past decennia the Finite Element Method (FEM) has been used increasingly for the analysis of stress, deformation, structural forces, bearing capacity, stability and groundwater flow in geotechnical engineering applications. The role of the FEM has evolved from a research tool into a daily engineering tool. This has been possible because of the increase of computer power, available for every engineer, and the development of robust and user-friendly software packages. The finite element method has obtained a position next to conventional design methods, and offers significant advantages in complex situations, such as the design of tunnels and deep excavations in suburban areas. However, as with every other method, the FEM also has its limitations. These limitations are not always recognised by users of finite element software, which can lead to unreliable designs.

Despite the development of easy-to-use finite element programs, it is difficult to create a good model that enables a realistic analysis of the physical processes involved in a real project and that provides a realistic prediction of design quantities (i.e. displacements, stresses, pore pressures, structural forces, bearing capacity, safety factor, drainage capacity, pumping capacity, etc.). This is particularly true for geotechnical applications, because the highly non-linear and heterogeneous character of the soil material is difficult to capture in numerical models. The complexity of soil behaviour is caused by various phenomena on the soil particle level and leads to macroscopic observations such as stress-, stress path and

strain-dependency of stiffness, critical state behaviour and failure, compaction and dilatancy, strain localisation, creep and relaxation, anisotropy, hysteresis, variability of properties, and several more. When using the finite element method, soil is modelled by means of a constitutive model (stress-strain relationship) which is formulated in a continuum framework. The choice of the constitutive model and the corresponding set of model parameters are the most important items to consider when creating a finite element model for a geotechnical project. It forms the main limitation in the numerical modelling process, since the constitutive model, no matter how complex, will always be a simplification of the real soil behaviour.

Considering the use of geotechnical finite element software, it is often the younger generation of engineers who perform the numerical modelling and produce colourful results; sometimes without fully understanding the backgrounds and limitations of the constitutive models and the numerical methods used in the software. Supervisors, i.e. project managers or senior engineers, often find it difficult to validate the outcome, especially when these do not match with what they would expect based on their experience. This leads to the conclusion that there is a need for guidelines on validation of geotechnical finite element calculations, which is the main motivation for this paper.

This paper is based on a recent NAFEMS publication on Validating numerical models in Geotechnical Engineering (Brinkgreve, 2013). After defining the terms Validation and Verification (Chapter 2), the paper summarizes the main sources of discrepancies (Chapter 3), the various methods of validation (Chapter 4) and some non-technical issues (Chapter 5). More details about these subjects as well as a checklist of discrepancy sources and questions to be asked in the validation process can be found in the original NAFEMS publication.

2 WHAT IS VALIDATION AND VERIFICATION?

The terms Validation and Verification are often used in relation to the process to control the quality of results obtained with numerical modelling software. In fact, there is a clear distinction between the two terms.

Verification is the process of determining that a computational model accurately represents the underlying mathematical model and is capable of reproducing its theoretical solution. Moreover, the process to verify that a model or method has been properly implemented in a computer program is also called verification. The aim of the verification process is to answer questions like:

- Does the computer reproduce the results that are to be expected for the implemented model or method?
- Considering some of the processes which are relevant for the practical problem and for which a solution exists, does the computer model give an answer that is acceptably close to this solution, and can any difference be explained?

A term that is often used in relation to the verification process is *benchmark*. Strictly speaking, a benchmark is an example used to compare and evaluate the performance of an entity against other entities. In the framework of the verification process, the entity is a computer model and the benchmark is generally a well-defined example problem for which a reference solution exists. The performance is the accuracy at which the reference solution is reproduced by a computer model. Schweiger (1998, 2002, 2006) uses the term *benchmarking* for a process to evaluate the variation in results from different modellers or different software packages for a well-defined example problem. Hence, he clearly includes the role of the 'user' in his definition of benchmarking.

Validation is the process of determining the degree to which a model (including the parameters selected for that model) is an accurate representation of the real world from the perspective of the intended uses of the model (NAFEMS & ASME, 2009). In other words: Validation is the process to make plausible that a computer model includes the essential features for a real situation to be analysed and the results obtained with the model are representative for the situation in reality. The aim of the validation process is to answer questions like:

- Regarding the analysis and design quantities to be considered for the real project, does the model and the selected model parameters provide an accurate representation of reality?

Both verification and validation are important to consider for developers of numerical modelling software as well as users and other persons with responsibilities to use the modelling results for the analysis and design of real projects. However, the balance in applying these two methods may be different amongst them. In general, verification is mostly (but not entirely) a task for software developers, whereas validation is mostly (but not entirely) a task for users. In any case, it is essential for users of advanced numerical tools to understand the possibilities and limitations of the models and methods they are using.

3 SOURCES OF DISCREPANCIES

Since a numerical model involves several components that may introduce approximations and errors, it is necessary to identify each of these components and their role in and contribution to the discrepancy as a whole. Identifying possible individual discrepancies gives insight and may result in an improvement of the model and a possible reduction of the overall modelling error. It may also enable a quantification of the variation of design quantities by considering parameter uncertainties and their possible value ranges. A summary of the main sources of discrepancies between reality and its numerical model is given below.

3.1 Simplifications

Finite element models are, in various ways, a simplification of reality. These simplifications should be regarded in the framework of the validation process. The following simplifications can be identified:

- Geometrical simplifications: Reality is always three-dimensional (3D), but most geotechnical models are still 2D (plane strain or axisymmetric). Other geometrical simplifications are generally made in the extent at which details are taken into account regarding the modelling of the ground surface, soil layers, structures, model boundaries, etc.
- Simplifications in material behaviour: Among all materials in the world, soil is probably one of the most complex ones. Considering the numerical modelling of geotechnical deformation problems, soil behaviour is formulated by means of a stress-strain relationship (constitutive model). In general, the more complex a model, the more model parameters it has, which all need to be determined from soil investigation data (field or lab tests). A model should at least capture the features of soil behaviour that are relevant for the engineering problem to be solved. It is important to realise that even the most complex model is still a simplification of real soil behaviour.
- Simplifications in the construction process: Geotechnical projects often involve several construction stages with different load conditions, including those that involve changes in water conditions. In principle, they all need to be considered in the

numerical analysis, since the most critical stresses, deformations or stability situation may occur in intermediate construction stages. However, the construction and loading history is generally simplified, which may lead to discrepancies between the model and reality.

3.2 Modelling errors

In addition to the aforementioned simplifications there is a variety of other sources of modelling errors. Some of these can be reduced when they are recognised; some can even be completely avoided. The process of validation can help to identify and quantify such modelling errors.

- Input errors: A finite element model requires large amounts of data to be entered in the software package. The chance that some of these data are wrong is significant. Fortunately, it is possible to avoid this source of modelling errors. The validation process can help to identify input errors. Therefore, a check on the consistency of the input data is a necessary part of the validation process. Adequate input and output features (such as tables showing an overview of crucial parameters) as well as warnings and error messages in the software package can simplify the validation process.
- Discretisation errors: The numerical modelling of a practical situation involves a division of the soil and structures into a calculation grid (mesh) with cells (elements) that contain the properties of the material. The spatial discretisation (mesh coarseness and interpolation order of the elements) defines the accuracy at which the solution is approximated. Upon mesh refinement, the numerical solution tends to converge towards the theoretical solution, but the 'true' solution is generally approached from the unsafe side (under-estimation of displacements; over-estimation of stability and bearing capacity). Apart from the spatial discretisation, a discretisation of the loading process is applied by taking finite load steps (or time steps) during the calculation. The larger the steps, the more the discretised loading procedure may deviate from the physical loading process, which is continuous in reality. In particular in transient processes (dynamics, groundwater flow), the time stepping is essential.
- Limitations in methods: Numerical methods have their possibilities and limitations. The use of a method beyond its limitations will lead to modelling errors. For example, in order to model membrane effects in a geogrid reinforcement, it is necessary that the geometry is at least updated according to the calculated displacements. Membrane effects are only obtained when large deformation effects are taken into account, for example when using the Updated Lagrange method.

3.3 Constitutive models

In addition to what is mentioned before on constitutive models, there are some particular aspects to take into account regarding the modelling of soil behaviour:

- Pseudo-elastic behaviour: Even though soil behaviour is far from elastic, the basis of a constitutive model is often elasticity theory. A true elastic model is based on an elastic potential or (complementary) strain energy function. In the case that such an elastic potential cannot be formulated, the model is a pseudo-elastic model, and may lead to energy dissipation or generation(!). The latter may lead to unreliable results. The most well-known example of a true elastic model is Hooke's law of isotropic linear elasticity. It is tempting to reformulate the stiffness in Hooke's law as a simple stress-

dependent power law, but this leads to a pseudo-elastic model that may suffer from inconsistencies. Fortunately, elastic formulations are never used in isolation, but they may still dominate the model behaviour, especially under unloading or reloading conditions.

- Non-associated plasticity: Plasticity theory is used to formulate the Mohr-Coulomb failure criterion into a set of yield functions to identify whether plastic strains will occur. The actual calculation of plastic strains is based on a plastic potential function, which usually has a similar shape as the yield function. A difference between both functions is denoted as non-associated plasticity. For models based on non-associated plasticity the uniqueness of the solution cannot be proven. As a result, numerical models may suffer from changing mechanisms and non-unique failure loads which are influenced by the numerical discretisation (mesh, time step). Considering the simple Mohr-Coulomb model with a dilatancy angle less than the friction angle, it should be realised that this situation may lead to the issues related to non-associated plasticity.
- Strain-softening: Regarding the use of softening models in boundary value problems, several researchers have demonstrated that the numerical results may show severe mesh-dependency. As soon as plastic strains develop, the material will locally soften, whilst material outside the plastic zone will retain its strength. The finer the mesh, the smaller the plastic zone and the larger the plastic strains, which will lead to more severe softening behaviour. This will not only affect post-peak behaviour, but also failure loads and bearing capacities in practical applications may suffer from severe mesh-dependence.
- Undrained behaviour: Modelling undrained behaviour in an effective stress approach can be very sensitive. The modelling of undrained behaviour can be simply done by adding a large bulk stiffness for the pore water, such that the soil as a whole becomes nearly incompressible. Apart from the possibly inaccurate pore pressure calculated in this way (it requires at least high-order elements), it should be realized that the actual pore pressure strongly depends on the constitutive model being used, and may be wrong for the particular type of soil being modelled. If the pore pressure is wrong, the effective stress will also be wrong and, considering effective strength properties, the resulting undrained shear strength will be wrong as well.

3.4 Uncertainties

There are many aspects in a real project that are not completely known (yet) or which cannot be measured accurately in the field. In other words, there are uncertainties as to what we need to model precisely to reflect the real construction process and the conditions that are applied to the real structure during its lifetime. Examples of uncertainties are the precise location of soil layers and the spatial variation of soil properties in the ground. All such uncertainties can lead to discrepancies between the behaviour of a model and the behaviour of a structure as observed in reality. There are various ways to deal with uncertainties in the design process. Some methods are described below:

- Global safety factor approach: Considering the calculation of geotechnical safety factors in advanced numerical models the following expression is generally used:

  Safety factor=(Available resistance)/(Minimum resistance required for equilibrium)

  In the numerical algorithm that deals with this safety factor approach, the available resistance is reduced until geotechnical failure is observed. The safety factor obtained

in this way is perceived to be similar to the classical geotechnical definition of a safety factor. However, reducing the resistance of the soil material by reducing the strength properties may change the characteristics of the model behaviour, such that the model does not represent the actual material anymore. Moreover, it can be questioned what to do with other model parameters (for example the stiffness or the dilatancy angle). Finally, considering undrained materials, should the safety factor be calculated for drained or undrained conditions?

- Partial factor approach: In order to deal with differences in uncertainties, one may consider using partial factors for different parameters. The use of partial factors, such as in Eurocode 7, is based on a more elaborate probabilistic approach in which a minimum reliability level is defined for the structure as a whole. There is still no common sense on how to deal with Eurocode 7 in the finite element method. Different design approaches and calculation schemes can lead to different results. Nevertheless, it is possible to perform finite element calculations according to the various design approaches in Eurocode 7. When doing so, similar remarks as mentioned above for the global safety factor approach should be taken into account.
- Parametric analysis: To analyse the influence of uncertainties in loads, model parameters and even geometric variations, a parametric analysis may be performed. In a parametric analysis the key uncertain parameters of the numerical model are identified and their variation is characterised by means of an upper and lower bound value. From the combinations of upper and lower bound values, maximum and minimum values of various output quantities can be assembled which gives an impression of the variation (range) of results that can be expected. Although parametric analysis does not remove any of the discrepancies as mentioned in the previous sections (simplifications, modelling errors, limitations in constitutive models), some uncertainties in model parameters can at least be analysed.

3.5 Misinterpretation of results

If the modelling process has been successfully completed such that the model is an actual representation of the physical problem, it is not a guarantee that the calculation will run smoothly. Numerical 'tricks', tolerances and compromises may be necessary to come to a solution. It should be validated that tolerances and compromises will not lead to an unrealistic approximation of the original model. If the calculation has successfully finished and results have been obtained it is not the end of the story. It should be realised that the computer model does not directly provide the answer to the engineering problem. Therefore, a translation needs to be made from the results of the computer model towards the engineering and design issues. The translation and (mis)interpretation of results may also lead to discrepancies between the real situation and the computer model.

An example where misinterpretation might occur is in the evaluation of a safety factor from a strength reduction analysis. First of all it should be verified whether a realistic failure mechanism has developed. Absolute values of total displacements do not have a physical meaning in this case; the mechanism can best be viewed on the basis of the plastic strains or incremental displacements at failure. The safety factor itself is defined in the step where the mechanism has fully developed. When the calculation stops too early, the safety factor may be interpreted wrong (too low). Conversely, locking (depending on the type of elements used) may cause that the strength reduction process continues after a full mechanism has developed, which may lead to an overestimation of the safety factor. Special attention is needed when the model includes structural elements, which behaviour is generally assumed to be elastic. However, during the strength reduction procedure there is a transfer of loads

from the soil to the structures. This requires careful inspection that the structural forces are still acceptable for the resulting safety factor.

It should also be realised that the model may not include all phenomena that are relevant for the real situation. Again, the constitutive model plays an important role in this respect, but also local mechanisms such as piping will not be found in general, since such mechanisms cannot be obtained with a standard continuum approach.

4 METHODS OF VALIDATION

In the previous chapter some sources of discrepancies between a real project and its numerical model have been identified. In order for a particular project to manage the uncertainties and reduce the discrepancies, the numerical model must be validated. Validation of the model as a whole will not be enough to make plausible that the results that are obtained from the model are representative for the real situation. In fact, discrepancies in individual components may accidentally cancel each other out if they are not validated individually. The validation process should therefore comprise the individual modelling components in addition to a validation of the integral model.

4.1 Verification

Before considering validation of a computer model for a practical situation, it is relevant to verify that the models and methods implemented in a software package are reliable. In the first place this is a responsibility of the software developers, but also users of finite element software should consider performing a verification of models and methods that are relevant for the solution of their engineering problem. Verification is done by comparing the results of computer models for typical situations with known solutions. Arbitrary practical situations are unlikely to have known solutions. However, some particular aspects or phenomena that the practical situation involves may be simplified to situations for which a known solution exists or for which a solution can be derived. In the framework of numerical modelling of geotechnical applications the following solutions can be used for verification:

- Elasticity solutions for soil continua and structures (e.g. Settlement and stress distribution below a strip footing on elastic soil; bending of beams, plates and shells subjected to different loads, considering different types of supports).
- Elastoplastic solutions (e.g. Cylindrical cavity expansion for small and large deformations)
- Bearing capacity solutions (e.g. Failure of a vertical cut in cohesive soil; bearing capacity of a rigid circular or strip footing on cohesive or frictional soil)
- Elasto-dynamic solutions (e.g. one-dimensional wave propagation; pulse load on an elastic half space (known as Lamb's problem))
- Solutions of flow or coupled problems (e.g. Darcy's solution for confined flow; Unconfined flow through a homogeneous medium with vertical faces (known as Muskat's problem); One-dimensional consolidation)

4.2 Upper and lower bound solutions (Limit Analysis)

For engineering problems involving the analysis of bearing capacity or stability and for which no analytical solution is available (which is by far for most practical situations), solutions based on upper and lower bound theorems (limit analysis) may be used to encapsulate the solution. The lower bound solution for an external failure load on a continuum is based on finding an equilibrium solution for the stress distribution in the full continuum that balances the external load and that does not violate a given failure criterion

for the stress state. The upper bound solution for an external load on a continuum is based on the evaluation of all forces acting on an assumed kinematically admissible failure mechanism where the internal forces are limited by the given failure criterion for the stress state. If a solution for the external load can be found in which both the upper bound and lower bound conditions are met, the solution is considered to be the true failure load (uniqueness theorem). However, this will rarely be the case for practical situations, but it can be useful to determine an upper and lower bound solution which are sufficiently close to each other, such that they can be used to validate the numerical solution.

Much work on upper and lower bound solutions has been done by Sloan and co-workers (e.g. Lyamin & Sloan 2002a/b). Over the last decade, they developed a numerical framework based on finite elements and linear programming, which can be used for several types of geotechnical applications, including slopes, embankments, foundations and excavations. Although the method may seem to resemble the finite element method, it is based on different principles and can be used to validate stability or bearing capacity solutions obtained from true finite element models. It should be noted that the upper bound solutions are based on associated plasticity, which may introduce a difference compared to the finite element model to be validated. Nevertheless, limit analysis can be very useful to validate stability and bearing capacity solutions obtained from finite element analysis.

4.3 Validation of constitutive models and parameters

The selection of a constitutive model should be based on an evaluation of the capabilities (and limitations) that it has to describe the essential features of soil behaviour for the situation at hand. In that respect, the constitutive model provides the qualitative description of soil behaviour, whereas the parameters in the model are used to quantify the behaviour. The composition of the model plus parameters can be regarded as the 'artificial soil' that is used in the numerical model, which should be representative for the real soil behaviour in the application. Before considering the numerical model in full detail, it makes sense to evaluate the behaviour of the artificial soil (= model + parameters) separately in single stress point simulations of soil lab tests (e.g. drained and undrained triaxial tests, oedometer test, DSS test, CRS test). The results of the lab test simulations can be compared with real test data. This provides insight in the possibilities and limitations of the model to describe particular features of soil behaviour and the accuracy at which it does so. Moreover, parameters can be optimised to make a 'best fit' to the test data.

It should be noted that the stress paths, stress levels and strain levels in the real application can be significantly different than those in the soil lab tests. Hence, a good fit between the results of a simulated test and the real test data is not a guarantee that the artificial soil is a good representation of the real soil in the practical application. Nevertheless, the numerical simulation of soil lab tests is relevant to qualitatively understand the behaviour of the model and should therefore be considered in the validation process.

In contrast to soil lab tests, in-situ tests cannot be simplified to a single stress point model. However, some in-situ tests, such as a pressuremeter test, can still be modelled as a boundary value problem using a finite element model. This modelling can be useful to optimise the in-situ stiffness and strength properties.

As part of the validation of model parameters for the engineering application it might also be considered to perform a preliminary analysis on a semi one-dimensional soil column representing the ground profile at the project location. In the case that the project involves mainly vertical loading, the soil column analysis can be used to check if the calculated settlements match the expected settlements (based on engineering judgement or conventional settlement calculations). Moreover, if time-dependent behaviour (consolidation or creep) is involved, the initial soil column analysis may be used to validate the model parameters and

initial conditions leading to a particular settlement rate at the start of the project. This settlement rate can be compared with measurements from the past or with what is supposed to be realistic for that location.

4.4 Validation of the mesh and model boundaries

Model boundaries are introduced to limit the extent of the numerical model. It has to be validated whether the outcome of the finite element model is not influenced by the choice of the model boundaries. This can crudely be done by redoing the numerical analysis with model boundaries taken further away and comparing the results, but that may be a time-consuming way of working. It should at least be verified after any numerical analysis that changes in stress and strain near the model boundaries are relatively small. This is not required near (vertical) symmetry boundaries, but there it should be validated that the symmetry conditions are properly applied. In the case of groundwater flow or coupled analysis, for example, there should be no flow across the symmetry boundary.

For a dynamic analysis, it should be checked that there are no spurious reflections at the model boundaries. The best way to check this is by creating an animation of the velocities in the model.

The discretisation of the model (division into elements, i.e. the mesh), in relation to the type of elements used, determines the accuracy at which the numerical solution is approximated. In general, a finer mesh gives a more accurate solution. Refinement is particularly needed in parts of the model where stress or strain concentrations will occur. This is usually the case around loads and structural elements in the mesh. Local mesh refinement (as opposed to global refinement) is a useful way to create accurate and, at the same time, efficient meshes.

In addition to the accuracy of the mesh, it needs to be validated that the quality of the elements themselves is acceptable. Very slender elements must be avoided. At least a visual inspection is needed. The 'slenderness' is usually expressed as the element aspect ratio, being the ratio of the radius of the maximum inner circle over the radius of the minimum outer circle, normalised at unity for the optimum element (equilateral triangle or square quadrilateral). These values are available in most commercial finite element software nowadays and should be checked.

4.5 Validation of initial conditions

It is necessary to initialise the stress in the model and validate that this stress state is in correspondence with the situation in reality. The initial situation may involve total or effective stress components, pore water pressures, pre-consolidation stress, void ratio and other state parameters, depending on the constitutive model(s) being used.

A simplified procedure to generate the initial stresses is to integrate the weight of the soil column above each stress point to calculate the vertical total stress, then subtract the pore pressure to calculate the vertical effective stress and then multiply by a given K_0-value to calculate the lateral effective stress, and assuming all shear stress components to be zero. This 'K_0-method' has the disadvantage that equilibrium is not guaranteed. Therefore, when such a method is used, it has to be validated that the resulting stress state is in equilibrium and that it is realistic to assume that the initial shear stresses are zero.

Alternatively, initial stresses can be calculated by loading the model with the gravitational forces associated with the self-weight of the materials. Although this 'Gravity method' will result in an equilibrium state at the end of the calculation, it may not properly resemble the initial stress state of the situation in reality, since the full loading history of the environment is not taken into account. Therefore, in addition to the standard gravity method, it may be

necessary to perform a number of subsequent calculations to simulate the relevant loading conditions in the past that are of influence on the stress state at the start of the engineering application considered. Note that undrained soils may need to be modelled temporarily as drained soils during the initial stress calculations in order to avoid the generation of unrealistic excess pore pressures.

In an effective stress analysis, it is essential to create a realistic distribution of initial pore water pressures. Simple hydrostatic pore pressure distributions may be generated on the basis of a phreatic level, whereas more complicated situations may require a separate groundwater flow calculation to be performed. In the latter case, realistic hydraulic conductivities (permeabilities) are required, which are often difficult to obtain from soil investigation data. That is why modellers often 'abuse' the phreatic level tool to create more complicated pore pressure distributions based on non-horizontal level sections. Care has to be taken with such an approach, since in reality non-horizontal levels imply groundwater flow and possibly non-hydrostatic pore pressure distributions. A 'jump' in the phreatic level should definitely be avoided, since this would cause a similar jump in pore pressure all the way down in the model, which is highly unrealistic.

4.6 Other methods of validation

In addition to a validation of model components, there are various ways validate the integral model by comparing the results obtained from the numerical simulation with other sources.

- Measurements: Measurements taken from monitoring during the execution of a project (displacements, pore pressures, structural forces, etc.) can not only be used to validate the results of a numerical model, but also to update the parameters being used, provided the measurements are sufficiently accurate and reliable. The updated model can be used to make a better prediction of construction phases that are yet to come.
- Design charts: In the past, researchers have published various diagrams of particular engineering and design aspects in geotechnical engineering, such as settlements, stability and wall deflections. Most design charts were published in the time that computer modelling was not so common in the geotechnical engineering practice, but they are still relevant. Although design charts are quite general and may not be very precise, they can be of great help to validate numerical models in the sense that they give an indication of the order of magnitude that should be expected in certain situations.
- Other software: Other software tools, ranging from spreadsheets with simple design rules or analytical methods via conventional geotechnical analysis software to other advanced 2D or 3D numerical modelling software (other than used for the model to be validated) may be used to obtain independent solutions for comparison.

4.7 Benchmarks

A benchmark, in the framework of validation and verification, is a well-defined example problem for which a reference solution exists, whereas the term benchmarking has been defined as the process to evaluate the variation in results from different modellers or different computer software for a well-defined example problem. Most benchmarks are simplified practical problems for which no analytical solution exists; only a (numerical) reference solution. Modellers can use a benchmark to check if they obtain a similar solution. Since the solution is obtained using numerical methods, a small deviation (few percent) from the reference solution is likely to occur and is quite acceptable. Larger deviations may still be

acceptable, depending on the type of problem and the level of detail that is provided with the benchmark. Published benchmarks have shown that quite large differences can occur, which underlines the need for validation of numerical models. A number of benchmark examples for geotechnical engineering have been defined and published. More details can be found in the NAFEMS publication (Brinkgreve, 2013).

In addition to published benchmarks, researchers in the past have set up instrumented full-scale tests with the purpose to investigate particular aspects of soil behaviour. Thereby, they have organised competitions for engineers to predict particular test results for which measurements would become available. The purpose of such a prediction competition is to evaluate the performance of numerical models and the modelling capabilities of engineers in general (rather than individual performances). In contrast to benchmark examples, no reference solution is available, but the reference is the measurement data that becomes available after the test has been performed. A number of such prediction competitions and their results have been documented. Similarly as for the benchmark examples, the prediction competitions show large variations in results as well as deviations from the measurements. These deviations can be reduced by knowledge and experience of the modelling engineer as well as a proper validation of the numerical model. It also underlines the importance of using an appropriate constitutive model to describe the soil behaviour.

5 NON-TECHNICAL ISSUES

In addition to the 'technical' issues related to the validation of numerical models for geotechnical applications, there are non-technical issues involved with the validation process.

The first issue is the availability or lack of data; in particular soil data. In practice, there is often a lack of soil investigation data. It is important to convince clients or project owners of the need of sufficient and good quality soil investigation. It does not only reduce the uncertainties in ground conditions, but it will also facilitate the validation of model parameters, thereby reducing the risk that the design is inadequate because it is based on insufficient or wrong geotechnical data.

Another non-technical issue is the distribution of responsibilities among the persons and organisations involved in the various aspects of numerical modelling. First, it is the responsibility of the *engineer* (user of finite element software) to create a computer model and to determine the required parameters such that the model accurately represents the real project and captures the phenomena that lead to the quantities that need to be determined or interpreted from the model (deformations, stresses, structural forces, flow, etc.). This responsibility includes a proper validation of the model and its components.

Second, it is the responsibility of the *supervisor* (manager) of the modelling engineer or the project manager to control that the model created and used by the project engineer is a reliable model on the basis of which the project can be properly analysed and/or designed with the required safety level. This responsibility involves a check on how and to what extent the model has been validated by asking the right questions. The responsibility of the supervisor also involves taking care of mentoring, coaching and training of the younger engineers such that they can develop the necessary skills to become experts in numerical modelling in addition to their geotechnical skills in general.

Third, it is the responsibility of the *organisation* in which numerical models are being used to create an environment in which the importance and complexity of numerical modelling is being realised on all levels. If numerical modelling is part of their activities, it should be included in their quality procedures. The organisation should be structured such that there is sufficient knowledge and room, not only to create numerical models but also to validate models and to control the process from the early stage of numerical modelling to the

interpretation of the results towards the geotechnical design. Ideally, this knowledge should beshared within the organization.

Finally, it is the responsibility of the *software developer* to produce software that has been sufficiently verified and that is (ideally) free of programming errors. It is also the responsibility of the software developer to properly document the models and methods that are implemented in the software and make this documentation available to the user.

6 CONCLUSIONS

In this paper a summary is given of a recent NAFEMS publication on validating numerical models for geotechnical engineering applications. Validation, in this respect, is the process to make plausible that a numerical model includes the essential features for a real situation to be analysed and its results are representative for the situation in reality.

The first part of the paper describes the sources of discrepancies between a real project and its numerical model. Insight in the discrepancies is essential for a proper validation of the model and to reduce modelling errors. A significant part of modelling inaccuracy and uncertainty is related to the modelling of soil behaviour. A thorough understanding of the possibilities and limitations of constitutive models and underlying theories is needed to decide which model is best considering the main features of soil behaviour that are relevant for the real situation. Good soil investigation data provide the essential basis of soil modelling, parameter determination, creating initial conditions, and the validation thereof.

The second part of the paper is devoted to the various methods of validation. The process of validation involves a validation of the model as a whole, as well as a validation of the various model components, but it starts with a verification of the methods and models implemented in the software. Particular model components that need to be validated are the geometry, the model boundaries, the material behaviour, the finite element mesh, the initial conditions and the calculation phases.

In view of the validation process, it is useful to learn from situations that have been analysed in the past. In this respect the paper refers to benchmarks and prediction competitions that can be found in more detail in literature. The benchmarks and prediction competitions clearly demonstrate the need for a proper validation of numerical models, since the results from different modelling groups show significant differences.

The last chapter describes some non-technical issues related with decisions, responsibilities and organizational issues to control the quality of numerical modelling as part of the geotechnical design process.

ACKNOWLEDGEMENT

The author would like to thank the NAFEMS Geotechnical Committee for their feedback on the original document and for their consent to publish this summarizing paper.

REFERENCES

Brinkgreve R.B.J. (2013), Validating Numerical Modelling in Geotechnical Engineering, NAFEMS, UK.

Carter J.P., Desai C.S., Potts D.M., Schweiger H.F., Sloan S.W. (2000). Computing and computer modelling in geotechnical engineering. Proc. GeoEng 2000, Int. Conf. on Geotechnical and Geological Engineering, Melbourne. Technomic, 1157-1252.

Lyamin A.V., Sloan S.W. (2002). Upper Bound Limit Analysis Using Linear Finite Elements And Non-Linear Programming. International Journal For Numerical And Analytical Methods In Geomechanics, Vol. 26, 181-216.

Lyamin A.V., Sloan S.W. (2002). Lower Bound Limit Analysis Using Non-Linear Programming, International Journal For Numerical Methods In Engineering, Vol. 55, 573-611.

NAFEMS i.c.w. ASME (2009). What is Verification and Validation? Leaflet. NAFEMS, UK. www.nafems.org.

Potts D.M., Zdravkovic L. (1999). Finite element analysis in geotechnical engineering: Theory. London, Thomas Telford.

Potts D.M., Zdravkovic L. (2001). Finite element analysis in geotechnical engineering: Application. London, Thomas Telford.

Schweiger H.F. (1998), Results from two geotechnical benchmark problems. Proc. 4th European Conf. Numerical Methods in Geotechnical Engineering (ed. A. Cividini), Springer, 645–654.

Schweiger H.F. (2002), Results from numerical benchmark exercises in geotechnics. Proc. 5th European Conf. Numerical Methods in Geotechnical Engineering (ed. P. Mestat), Presses Ponts et chaussees, Paris, 305–314.

Schweiger H.F. (2006), Results from the ERTC7 benchmark exercise, Proceedings NUMGE 2006 (ed. H.F. Schweiger), Taylor & Francis, London, 3-8.

IMPLEMENTATION OF A QUASI-STATIC MATERIAL POINT METHOD FOR GEOTECHNICAL APPLICATIONS

B. Wang, P.J. Vardon & M.A. Hicks
Department of Geoscience and Engineering, Delft University of Technology, Delft, The Netherlands

ABSTRACT: *The Material Point Method (MPM), introduced originally in fluid mechanics, shows improved computational characteristics compared to the conventional Finite Element Method (FEM), when used for large deformation problems. It does this by avoiding extreme mesh distortion, by utilising a background mesh (the computational grid) with material points that can move through the mesh. The development and implementation of a MPM code is presented within the framework of a quasi-static arbitrary Lagrangian-Eulerian description. The analysis can be split into three main phases: (i) the initialisation phase, where the locations of the material points are prescribed; (ii) the solution of the equation of motion, using the updated Lagrangian method; and (iii) the convective phase, where the material points are moved in accordance with the displacements of the computational grid. Three benchmark problems are presented to verify and validate the model, comprising column compression (1-D), cantilever beam (2-D) and slope stability (including elasto-plasticity). The results show good agreement with published results.*

1 INTRODUCTION

In computational problems involving large-strain with the Finite Element Method (FEM), the mesh can become extremely distorted. Due to this disadvantage, Sulsky et al. (1994, 1995) adapted the Material Point Method (MPM), first used in fluid mechanics, for solid mechanics problems. MPM uses two spatial discretisations, the first in which state variables are traced on a set of material points representing the body of the continuum, while the equation of motion is solved on the second discretisation (a computational mesh). The computational mesh is maintained in its original position, or is adjusted in an appropriate way to avoid mesh distortion after each loading step, thereby removing the disadvantage from FEM of extreme mesh distortion.

MPM has been utilised for a limited number of engineering problems, e.g. silo discharge (Wieckowski, 1999) and plastic forming (Wieckowski, 2004), and adopted more recently for geotechnical analysis, including the modelling of anchor pull-out (Coetzee et al., 2005). Most of the MPM implementations are for dynamic problems that require explicit time integration and therefore very small time steps. However, limited implementations have been undertaken for quasi-static problems (Beuth et al., 2007, 2008, 2011). Therefore, this paper focuses on the development and implementation of a quasi-static MPM model designed to address a variety of geotechnical problems. The formulation of the implemented MPM method is first described, and then three benchmark problems are analyzed and compared with analytical results.

2 QUASI-STATIC MPM FORMULATION

Initially a fixed background grid is generated, which is estimated to bound the ensuing material point motion. This mesh is therefore an *a priori* prediction of the domain covering the trajectory of the material points. If the behaviour is difficult to predict, dynamic mesh generation may be employed, thereby reducing the need for mesh prediction and certain computational issues that occur with empty computational grid cells (Shin et al., 2010); this approach has been adopted for the third validation example in this paper. The background mesh is only used for the computation and therefore no state variables are stored with reference to the nodes.

A set of material points are then created over the domain, representing the material within the domain, and are assigned the properties, constitutive models and other state information. The initial location of the points in relation to the computational grid is not restricted, but in this case the Gaussian point positions are chosen in the first instance for convenience. These material points are then able to move through the computational grid as the simulation progresses.

A typical computational cycle is shown in Fig. 1, depicting the roles of both the material points and background computational mesh. This cycle is repeated at each load step of the simulation. The phases are described in detail below.

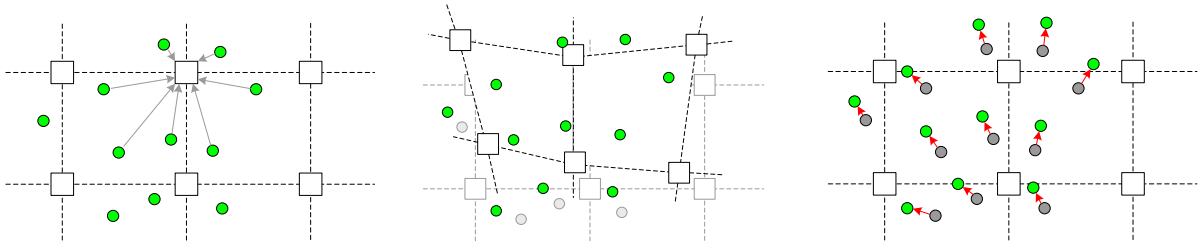

(a) Initialisation phase (b) Updated- Lagrangian phase (c) Convection phase

Fig. 1. Computational cycle of MPM (after Sulsky & Schreyer, 1996)

2.1 Initialisation Phase

The information stored in conjunction with the material points is gathered on the nodes using the method of weighted averages as described in equation (1). In this case the shape functions from the computational grid are used and these are the same shape functions as for FEM.

$$m_i = \sum_{p=1}^{N_p} H_i(X_p) m_p \tag{1}$$

where m is a description of the state variable, $H(X)$ is the shape function at location X, N_p is the number of material points in a computational grid cell and the subscripts i and p refer to node and material point numbering respectively.

Where the computational grid elements are not fully filled with material points, an ill-conditioned stiffness matrix may be formed, which could lead to numerical instability. This effect is especially significant when only one material point exists within an element, in particular when it is in or near a corner. Therefore, an additional material stiffness, of an insignificant magnitude relative to the real material stiffness, is assigned to each node.

To achieve a spatially converged solution, i.e. not dependent upon the mesh or initial material point positions, a greater number of material points than the Gaussian points is often required. This is due to the changing position of the material points and the non-uniform distribution throughout the computational grid. If this is the case a subdivision algorithm is

used to initialise the locations of the material points. This subdivides the initial element into smaller cells and the material points are then put on the local Gaussian point positions. In this case 16, 36, or 64 material points are adopted for quadratic 8-noded quadrilateral elements.

Finally, a direct integration over the computational grid cells is undertaken to form the FEM equivalent matrices using information stored in conjunction with the material points, e.g. the material stiffness, current stress conditions and density. This method is presented in equation (2) for an elastic stiffness matrix:

$$\mathbf{K} = \sum_{p=1}^{N_p} (\mathbf{B}^T(X_p)\mathbf{D}_p\mathbf{B}(X_p))v_p \tag{2}$$

where **K** is the stiffness matrix, **B** is the matrix of shape function spatial differentials, **D** is the elasticity matrix and v_p is the volume of material associated with the material point *p*.

2.2 Updated-Lagrangian Phase

The Updated-Lagrangian phase is where the governing equation is solved, using the current configuration of the body to formulate the equations of motion. This phase is the same as an Updated-Lagrangian FEM (UL-FEM) analysis.

2.2.1 Virtual Work Expressions

Applying the virtual work principle, followed by Galerkin's variational principle and then by the use of the divergence theorem, the equilibrium equation expressed in the weak form is shown in equation (3):

$$\int \sigma_{ij} \cdot \frac{\partial \delta u_i}{\partial x_i} dV = \int_V \gamma_i \cdot \delta u_i dV + \int_S \tau_i \cdot \delta u_i dS \tag{3}$$

where δu_i represents the components of virtual displacement, σ_{ij} are the Cartesian components of the Cauchy stress tensor, x_i are the Cartesian coordinates, γ_i represents the body force, τ_i denotes the prescribed part of the traction on the surface S and the volume of the body is represented by *V*.

For large deformation formulations, the Cauchy stress is usually calculated either from the second Piola-Kirchhoff stress and Green-Lagrange strain tensors (see Bathe, 1996), or, as in this paper, via a rate dependant formulation using the Jaumann stress rate and velocity strain tensors (Bathe, 1996). Equation (4) presents the Jaumann stress rate:

$$^{t}\overset{\nabla}{\sigma}_{ij} = {}_{t}C_{ijrs}\,{}^{t}\dot{\varepsilon}_{rs} \tag{4}$$

where $^{t}\overset{\nabla}{\sigma}_{ij}$ is the Jaumann stress rate at time *t*, ${}_{t}C_{ijrs}$ is the incremental stress-strain tensor referring to the configuration at time *t*, and $\dot{\varepsilon}_{rs}$ is the strain rate. The Cauchy stress rate can be written as equation (5):

$$^{t}\dot{\sigma}_{ij} = {}^{t}\overset{\nabla}{\sigma}_{ij} - {}^{t}\sigma_{ip}\,{}^{t}\dot{\omega}_{pj} - {}^{t}\sigma_{jp}\,{}^{t}\dot{\omega}_{pi} \tag{5}$$

where $^{t}\dot{\omega}_{rs}$ is the spin tensor (also called vorticity tensor) rate at time *t*.

The relationship shows that the rate of change of the Cauchy stress with respect to time, $\dot{\sigma}_{ij}$, is equal to the Jaumann stress rate, which gives the rate of change in Cauchy stress due to material straining, plus the effect of the rate of rigid body rotation of the material; that is, the rate of rotation of stress (Bathe,1996). The incremental strains, $\Delta\varepsilon_{ij}$, and rotations, $\Delta\omega_{ij}$, are given by:

$$\Delta\varepsilon_{ij} = \frac{1}{2}\left(\frac{\partial \Delta u_i}{\partial x_j} + \frac{\partial \Delta u_j}{\partial x_i} \right) \tag{6}$$

$$\Delta\omega_{ij} = \frac{1}{2}\left(\frac{\partial \Delta u_j}{\partial x_i} - \frac{\partial \Delta u_i}{\partial x_j} \right) \tag{7}$$

Equations (4) and (5) are inserted into equation (3), using the substitutions of equations (6) and (7), so that the virtual work principle stated in equation (3) can be re-written in the incremental form:

$$\int \left(C_{ijkl}\Delta\varepsilon_{kl}\delta\varepsilon_{ij} + \sigma_{ij}\Delta u_{k,i}\delta u_{k,j} - 2\sigma_{ik}\Delta\varepsilon_{kj}\delta\varepsilon_{ij} \right) dV = \text{Right Hand Side} \tag{8}$$

2.2.2 Spatial Discretisation

Equation (8) is solved by discretising in space by finite elements. Due to the fact that the configuration of the body changes continuously in a large deformation analysis, the last calculated configuration is referred to for all static and kinematic variables in the solution scheme in the updated Lagrangian (UL) formulation.

The displacement field can be expressed over the whole domain, using the shape functions, as a function of the nodal values, i.e.

$$\Delta\mathbf{u}(r,s) = \mathbf{H}\Delta\hat{\mathbf{u}} \tag{9}$$

where $\hat{\mathbf{u}}$ is the nodal displacement vector, $\mathbf{H}$ is the matrix of shape functions and *r, s* are the local coordinates. The strains at any point, $\Delta\boldsymbol{\varepsilon}$, can then be determined from the nodal displacements via the relationship:

$$\Delta\boldsymbol{\varepsilon} = \mathbf{B}\Delta\hat{\mathbf{u}} \tag{10}$$

Taking the discretised form, the equilibrium equation can then be formulated as:

$$({}_t^t\mathbf{K}_L + {}_t^t\mathbf{K}_{NL})\mathbf{U} = {}_t^{t+\Delta t}\mathbf{R} - {}_t^t\mathbf{F} \tag{11}$$

where $\mathbf{U}$ is the vector of increments in the nodal displacements; ${}_t^{t+\Delta t}\mathbf{R}$ are the externally applied nodal loads at time $t+\Delta t$, the upper left superscript indicating that the external force occurs at time $t+\Delta t$, but is calculated using the configuration at time *t* as indicated by the lower left subscript; ${}_t^t\mathbf{F}$ are nodal forces equivalent to the element stresses at time *t*; ${}_t^t\mathbf{K}_L = \int_{{}^tV} {}_t^t\mathbf{B}_L^T\, {}_t\mathbf{D}_t^t\mathbf{B}_L\, d\,{}^tV$ is the small strain linear elastic stiffness matrix; and ${}_t^t\mathbf{K}_{NL}$ is the nonlinear stiffness matrix accounting for the geometry change due to large deformation:

$$ {}^{t}_{t}\mathbf{K}_{NL} = \int_{{}^{t}_{t}V} (\mathbf{B}_{NL}^{T}\boldsymbol{\sigma}\mathbf{B}_{NL} - 2\mathbf{B}_{L}{}^{T}\tilde{\boldsymbol{\sigma}}\mathbf{B}_{L}) d\,{}^{t}_{t}V \tag{12} $$

where the nonlinear strain-displacement transformation matrix is expressed as:

$$ \mathbf{B}_{NL} = \begin{bmatrix} {}_{t}h_{1,1} & 0 & {}_{t}h_{2,1} & 0 & \dots & {}_{t}h_{N,1} & 0 \\ {}_{t}h_{1,2} & 0 & {}_{t}h_{2,2} & 0 & \dots & {}_{t}h_{N,2} & 0 \\ 0 & {}_{t}h_{1,1} & 0 & {}_{t}h_{2,1} & \dots & 0 & {}_{t}h_{N,1} \\ 0 & {}_{t}h_{1,2} & 0 & {}_{t}h_{2,2} & \dots & 0 & {}_{t}h_{N,2} \end{bmatrix} \tag{13} $$

where ${}_{t}h_{k,j} = \dfrac{\partial h_k}{\partial_t x_j}$ are the shape function differentials with respect to the Cartesian coordinates, *x*, for the configuration at time *t*. $\boldsymbol{\sigma}$ is the Cauchy stress matrix, while the matrix $\tilde{\boldsymbol{\sigma}}$ used in the second term of the integrand of $\mathbf{K}_{NL}$ is defined as follows (in 2D):

$$ \tilde{\boldsymbol{\sigma}} = \begin{bmatrix} \sigma_{11} & 0 & \sigma_{12} \\ 0 & \sigma_{22} & \sigma_{12} \\ \sigma_{12} & \sigma_{12} & \sigma_{11}+\sigma_{22} \end{bmatrix} \tag{14} $$

Note that the component ${}^{t}_{t}\mathbf{K}_{NL}$ becomes highly significant when the stresses are of the same order as the material stiffness moduli.

In FE analysis, Gaussian or Newton-Cotes integration schemes are commonly used to provide integration of polynomial shape functions, with the number of integration points determined by the order of the polynomial to be integrated. However, as previously discussed, numerical integration over the computation domain in MPM is approximated by direct summation over the material points, and so the accuracy of the integration will be largely dependent on the number of material points within an element. In this formulation, direct integration over the material points as demonstrated in equation (2) has been implemented for computational efficiency. Other approaches include utilising an intermediate mapping algorithm, where the material point information is first mapped to the Gaussian points (Beuth et al., 2011).

After the solution of the nodal displacements, the stresses, displacements and other state variables are recovered at the material points in the same manner as in FEM, using the inverse of equation (1).

2.3 Convection Phase

In this stage the material points remain in their deformed locations whereas the computational grid is 'reset'. Material points will keep their global positions, properties and state variables, with the information at the nodes discarded. A house-keeping algorithm is used to trace the material points, and to determine in which computational grid cell the material points are located. The deformation gradient can then be calculated to update the material point volume, as shown in equation (15):

$$ \Omega_{p}^{t+\Delta t} = J_{t}^{t+\Delta t} \cdot \Omega_{p}^{t} \tag{15} $$

where Ω_p^t and $\Omega_p^{t+\Delta t}$ are the volumes calculated for times t and $t+\Delta t$, respectively, and $J_t^{t+\Delta t}$ denotes the Jacobian determinant of the deformation gradient calculated for time $t+\Delta t$ and related to the configuration at time t.

An advantage of this approach is that the computational grid can be chosen for convenience. After this phase the original computational grid can be reused, altered or refined.

3 BENCHMARK PROBLEMS

3.1 Column Compression

The first verification model is for 1-D compression. A 10m high column is discretised into a computational grid consisting of ten 8-noded square elements. Within each element 4 material points are initially located at the Gaussian point positions, as shown in Fig. 2(a). Both sides of the domain are constrained in the horizontal direction, and the bottom of the mesh is fully fixed.

An increasing stress is applied at the top from 0 to 10 MPa, in 40 equal load steps. A plane strain condition is assumed and a linear elastic model employed. The Young's modulus and Poisson's ratio are 10 MPa and 0.3, respectively. After loading, the column is less than half of the original height, as indicated by the closely grouped material points in Fig. 2(b).

The stress-strain curve for the one-dimensional compression problem is plotted in Fig. 3, alongside UL-FEM results for the same problem. As can be seen from the figure, the MPM results correspond well with the UL-FEM solution, but a gradually increasing deviation occurs at larger deformation. This is due to the relatively small number of material points located within each element. As each material point (which is also one of the integration points in the calculation of the stiffness matrix) moves, no matter where it is, the same weighting coefficients are used for the numerical integration which leads to some inaccuracies in the solution. This problem can be alleviated by increasing the number of material points within each element, as in section 3.2.

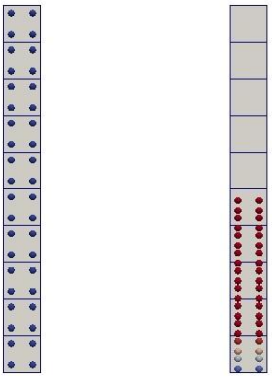

(a) Before loading (b) After loading

Fig. 2. 1-D Column compression

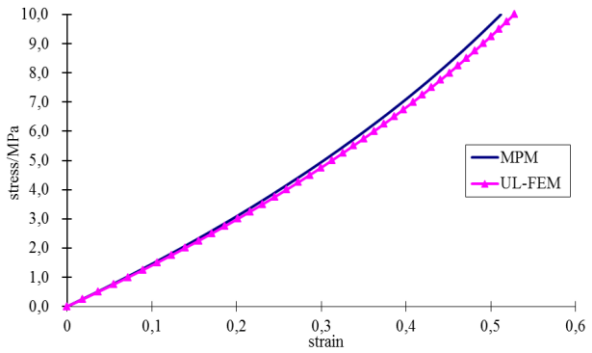

Fig. 3. Stress-strain curve for 1-D compression

3.2 Cantilever Beam

The same 2-D linear elastic cantilever beam as considered by Beuth et al.(2011) has been analysed using MPM and UL-FEM. The beam is subjected to gravity loading, and its initial configuration is shown in grey in Fig. 4(a). The beam is fixed along its left edge, and has a length of 1m and a depth of 0.3m. A plane strain condition is assumed in the analysis, with a Young's modulus of 100 kPa and a Poisson's ratio of 0. The computational grid covers the whole area of the expected beam deformation. The self-weight is increased from 0 kN/m^3 up to 4 kN/m^3, with each applied increment equal to 0.2 kN/m^3. The final configuration of the

beam is also shown in Fig. 4(a), in which the colouration represents the longitudinal stress along the beam, with blue representing compression and red representing tension. The computational grid consists of 40 8-node quadrilateral elements, where, within each element representing the initial beam geometry, 64 material points are initially assigned.

Fig. 4(b) shows the relationship between the self-weight and the tip vertical displacement. Numerical results from a UL-FEM analysis are also presented for comparison, showing excellent agreement.

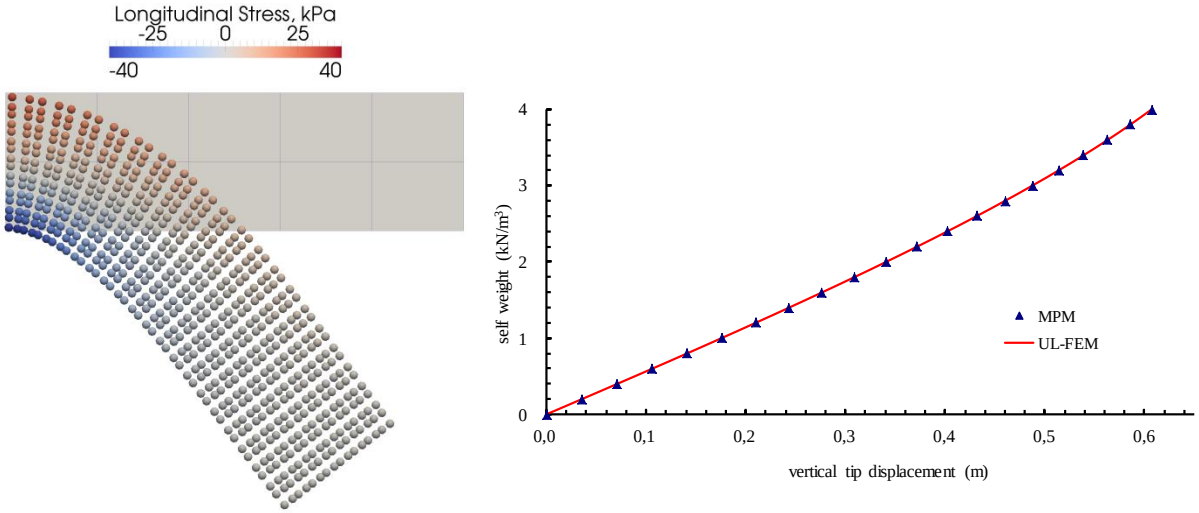

(a) Initial and final deformed configurations (b) Load-displacement curves using MPM and FEM

Fig. 4. Linear elastic cantilever beam example

3.3 Slope Stability

A simple slope stability problem has been analysed using an elastic perfectly-plastic soil model employing the von Mises failure criterion. Slope failure is triggered by gradually increasing the self-weight of the soil, with the strength parameters held constant. Soil flow dynamics has not been included in this example.

The geometry of the slope is depicted in Fig. 5: the height of the slope is 1m and the slope angle is 60°. The Young's modulus and Poisson's ratio of the soil are E=100kPa and υ=0.33, respectively, and the cohesion is c=1.0kPa. The self-weight is incrementally increased to $\gamma = 10\,\text{kN/m}^3$. The problem is plane strain, and the boundary conditions are rollers on the left boundary allowing only vertical movement and full fixity at the base. The computational grid is made up of 8-noded quadrilateral elements that are dynamically created and destroyed in each computational step, depending on whether any material point is located in an element. Initially there are 136 elements, with 36 material points inserted into each. The original material point locations are shown in the figure as grey crosses.

The slope configuration modelled by MPM is depicted in Fig. 5, along with the final (deformed) computational grid, with the colouration of the material points depicting shear stress level. A comparative analysis undertaken with UL-FEM is presented in Fig. 6, for 400 8-noded elements. It is seen that, when the self-weight reaches around 5.4 kN/m^3, the bottom of the mesh starts to experience excessive distortions near the slope toe in the UL-FEM analysis, causing the solution not to converge. This example demonstrates that MPM can describe large strains in a soil in a more reasonable way than FEM, without undue computational instability.

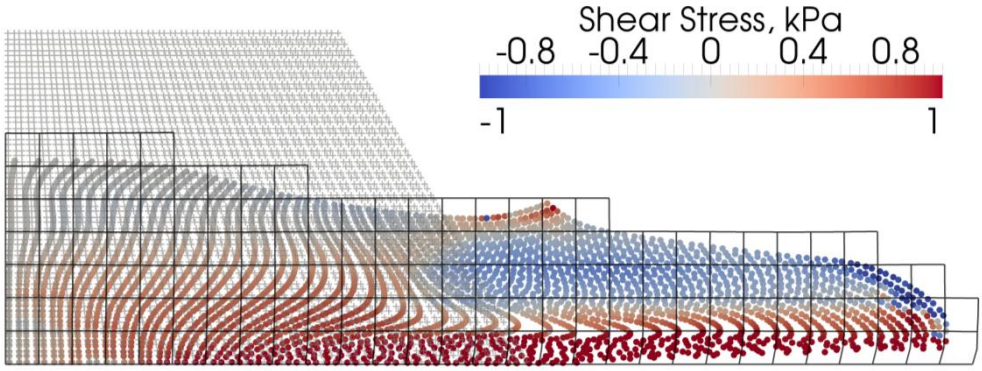

Fig. 5. Initial and final configurations of the collapsed slope

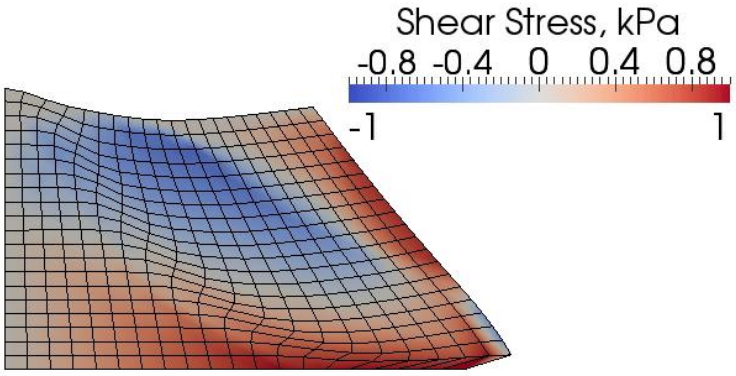

Fig. 6. Excessive mesh distortions exist in the UL-FEM calculation

4 CONCLUSION

A quasi-static MPM framework has been developed and implemented. The approach is verified by two elastic benchmark examples, with a third example presented to highlight the improved computational characteristics in solving large-deformation elastoplastic problems compared to the Finite Element Method.

ACKNOWLEDGEMENT

This work is funded by the China Scholarship Council (CSC) and by the Section of Geo-Engineering, Delft University of Technology.

REFERENCES

Bathe, K.J. (1996), Finite Element Procedures (2nd edn), Prentice-Hall, NJ.

Beuth, L., Benz, T., Vermeer, P.A., Coetzee, C.J., Bonnier, P., Van Den Berg, P. (2007), "Formulation and validation of a quasi-static material point method", Proceedings of 10th International Symposium on Numerical Methods in Geomechanics, Rhodes, Greece, Vol. 10, 189-195.

Beuth, L., Benz, T., Vermeer, P.A., Wieckowski, Z. (2008), "Large deformation analysis using a quasi-static Material Point Method", J. Theoret. Appl. Mech., Vol. 38, 45–60.

Beuth, L., Wieckowski, Z., Vermeer, P.A. (2011), "Solution of quasi-static large-strain problems by the material point method', Int. J. Numer. Anal. Meth., Vol. 35, 1451–1465.

Coetzee, C.J., Vermeer, P.A., Basson, A.H. (2005), "The modeling of anchors using the material point method", Int. J. Numer. Anal. Meth., Vol. 29, 879–895.

Shin, W.-K., Miller, G.R., Arduino, P., Peter, M.H. (2010), “Dynamic meshing for Material Point Method computations”, Int. J. Comput. Math., Vol. 68, 84-92.
Sulsky, D., Chen, Z., Schreyer, H.L. (1994), “A particle method for history-dependent materials”, Comput. Method. Appl. Mech. Engrg., Vol. 118, 179–196.
Sulsky, D., Zhou, S.J., Schreyer, H.L. (1995), “Application of a particle-in-cell method to solid mechanics”, Comput. Phys. Commun., Vol. 87, 236–252.
Sulsky, D., Schreyer, H.L. (1996), “Axisymmetric form of the material point method with applications to upsetting and Taylor impact problems”, Comput. Method. Appl. Mech. Engrg., Vol. 139, 409–429.
Wieckowski, Z. (1999), “A particle-in-cell solution to the silo discharging problem”, Int. J. Numer. Meth. Eng., Vol. 45, 1203–1225.
Wieckowski, Z. (2004), “The Material Point Method in large strain engineering problems”, Comput. Meth. Appl. Mech. Engrg., Vol. 193, 4417-4438.

A Comparison of the Local Discontinuous and Continuous Galerkin Methods in Simulating Unsaturated Flow

A. Ghavam-Nasiri
School of Civil Engineering, University of Sydney, NSW 2006, Australia

A.H. El-Zein
School of Civil Engineering, University of Sydney, NSW 2006, Australia

ABSTRACT: *Simulating flow in unsaturated soils is essential for solving a range of geomechanics and geo-environmental problems. Water retention curves (WRC) is one of the most important constitutive relationships governing the transport of water in partially saturated soils and, consequently, impacting their hydraulic, mechanical and chemical behaviour. Sudden drops in the values of water content in WRCs have been observed empirically and are known to cause numerical difficulties in coupled flow simulations. The Local Discontinuous Galerkin (LDG) method is an alternative to the more conventional continuous Galerkin (CG) finite element formulation and is more suited to problems with discontinuities as well as p- and h-adaptive finite element schemes. While the LDG has been applied to the Richards equation, no systematic comparison of the performances of the LDG and the CG methods in the presence of sharp drops in the WRC has been made in the literature. Little guidance, therefore, exists as to whether the LDG is better suited for this type of problems.*

In this paper, we investigate whether the LDG is more computationally efficient than the CG in simulating flow in unsaturated soils in the presence of sharp drops in the WRC. We base our analyses on the 1D, steady-state version of the Richards equation. We conduct performance comparisons using error norms for state and flux variables, discretizations with linear elements, and different WRC equations with different parameters, including cases of weak and strong non-linearity. We find that the LDG method provides better computational economy (CPU cost for required level of accuracy) than the CG method and the advantage is even more pronounced for flux variables. In addition, the LDG method is stable when dealing with highly nonlinear van Genuchten WRCs, while the CG method stops converging for higher mesh densities.

1 INTRODUCTION

The discontinuous Galerkin (DG) methods fall into the general category of weighted residual techniques for the numerical solution of partial differential equations (PDEs). The same space function is used in both the continuous Galerkin method and the discontinuous Galerkin methods, the latter providing relaxed continuity at inter-element boundaries. In the discontinuous methods, discontinuity of either field variables or their derivatives, usually both, can be simulated while the continuity of the computational domain is maintained. As a result, the DG can deal with elements independently of each other or, in other words, at a local level. In addition, since the method does not require elements to be conforming at their

interfaces, the DG is highly suitable for h-, p- and hp-adaptive methods, because neighboring elements can have different orders of approximation.

The DG methods have been studied widely over the last two decades (Cockburn et al., 2000, Zienkiewicz et al., 2003). They have been found to integrate features of both the finite element method and finite difference (finite volume) method. For example, the DG methods resolve into the traditional finite difference method if a constant element is chosen. Alternatively, imposing a continuous function and enforcing cross-boundary continuity leads to the continuous finite element method. The local nature of the DG methods is uniquely useful for reducing demand for computational resources, and their main advantage is their extremely high parallelisability and their high-order accuracy (Cockburn and Shu, 1998).

A number of DG methods have now been proposed in the literature. All of these methods duplicate the degrees of freedom (DOF) at the element interfaces to allow for the discontinuity. However, what distinguishes between these methods is the way the relationship between duplicate DOFs is built. The local discontinuous Galerkin (LDG) method was introduced by Cockburn and Shu (1998), as a generalized extension of the approach proposed by Bassi and Rebay (1997). The basic idea of the LDG method is to suitably rewrite the original system of equations in order to achieve stability even without slope limiters. The LDG method uses discontinuous discretisation in both time and space. Cockburn and Shu (1998) proved the stability and derived error estimates of the LDG method.

The LDG method offers many advantages over conventional finite element solutions of unsaturated flow, transport, and mechanics problems in soils; namely, more accurate simulation of sharp fronts, easier representation of domain discontinuities, algorithms that are more suited to h- and p-adaptivities, and better mass balances between elements. However, it is more complex to formulate and implement and typically uses four, eight, and sixteen times more degrees of freedom than the same finite element mesh in the CG method (linear elements) for 1, 2, and 3 dimension problems, respectively. This rate decreases for higher-order interpolation functions, because some DOFs appear inside the elements and require no DOF duplication. The LDG has been applied to a large number of problems in soils, saturated and unsaturated, including the Richards' equation (Li et al., 2007), advection-diffusion equation and elastic and non-elastic mechanics. When it has been used to solve problems such as poro-elasticity (e.g., Stelzer and Hofstetter, 2005; and Phillips and Wheeler, 2008) and thermo-elasticity (Zheng et al., 2010), it has been found to be computationally efficient. However, no systematic comparison of the performances of the LDG and the CG methods in the presence of sharp drops in the WRC has been made in the literature. Little guidance, therefore, exists as to whether the LDG is better suited for this type of problems.

In this paper, we investigate whether the LDG is more computationally efficient than the CG in simulating flow in unsaturated soils in the presence of sharp drops in the WRC. We base our analyses on the one-dimensional, steady-state version of the Richards equation. We establish the CPU time and storage required to achieve a given level of accuracy for both methods, i.e. the computational economies.

We conduct these comparisons using error norms for state and flux variables, with linear and quadratic elements, and different WRC equations, including cases of strong non-linearity.

2 GOVERNING EQUATIONS

Flow in porous media can be described by Darcy's equation. This equation has been extended to unsaturated media by Richards (Richards, 1931). Combined with a mass conservation statement, it leads to the pressure head form of Richards' equation for steady state, without source/sink, and horizontal, non-gravity flow is:

$$\nabla(k(h)\nabla h) = 0 \tag{1}$$

where h is the pressure head and $k(h)$ is the hydraulic conductivity of the soil layer. The hydraulic conductivity for saturated soil is independent of the pressure head. For unsaturated soils, Gardner's exponential relation (Gardner, 1958) is as follows:

$$k(h) = k_s.k_r(h) \tag{2a}$$

$$k_r(h) = e^{ah} \tag{2b}$$

where k_s is hydraulic conductivity in saturated condition, k_r is relative hydraulic conductivity, and α is an experimentally-determined parameter. Tracy (2006) states that some soils can be modeled by Irmay's experimental equation as follows:

$$k_r = \left(\frac{\theta - \theta_r}{\theta_s - \theta_r}\right)^m \tag{3}$$

where θ is the volumetric moisture content, θ_r is the residual volumetric moisture content, θ_s is the saturated volumetric moisture content and m is an experimentally-determined parameter. Substituting Eq. (2) in (3) gives an exponential form of moisture content:

$$\theta = \theta_r + (\theta_s - \theta_r)e^{\alpha h/m} \tag{4}$$

A more widely-used water content profile is van Genuchten's equation (Van Genuchten, 1980):

$$\theta = \theta_r + \frac{\theta_s - \theta_r}{[1 + (-\xi h)^n]^m} \tag{5}$$

where ξ and n are parameters and $m = 1 - 1/n$. In addition, Van Genuchten (1980) derived the relative hydraulic conductivity based on Mualem's theory (Mualem, 1976) as follows:

$$k_r(h) = \frac{\{[1 - (-\xi h)^{n-1}][1 + (-\xi h)^n]^{-m}\}^2}{[1 + (-\xi h)^n]^{m/2}} \tag{6}$$

Figure 1 shows water content variations as a function of hydraulic pressure head for the Gardner exponential WRC for a three sets of parameters, designated as problems 1, 2, and 3. WRC values for these problems are presented in Table 1.

Table 1. Gardner WRC values for problems 1, 2, and 3.

	θ_s	θ_r	α	m
Problem 1	0.75	0.05	0.30	1.00
Problem 2	0.75	0.05	0.45	1.00
Problem 3	0.75	0.05	0.60	1.00

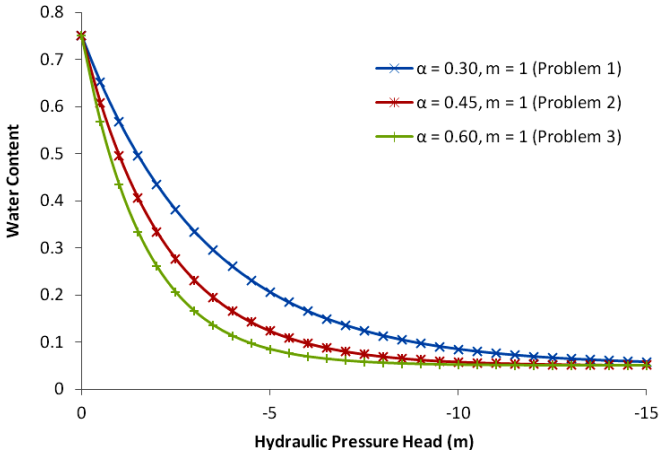

Fig. 1. Water content for Gardner WRC: Problems 1, 2, and 3.

The more complex van Genuchten WRC yields more non-linearity and sharper jumps in water content profiles that are reported to be in excellent agreement with observed data (Van Genuchten, 1980). These sharp jumps cause instabilities in numerical simulation of unsaturated flow, and a variety of techniques have been implemented to overcome these numerical difficulties (e.g., see van Genuchten, 1982; Allen and Murphy, 1985; and Rathfelder and Abriola, 1994). In this paper, the effect of non-linearity is studied for 3 different problems designated as problems 4 to 6 for van Genuchten WRC. Figure 2. illustrates water content vs. hydraulic pressure head and WRC values for these problems are presented in Table 2.

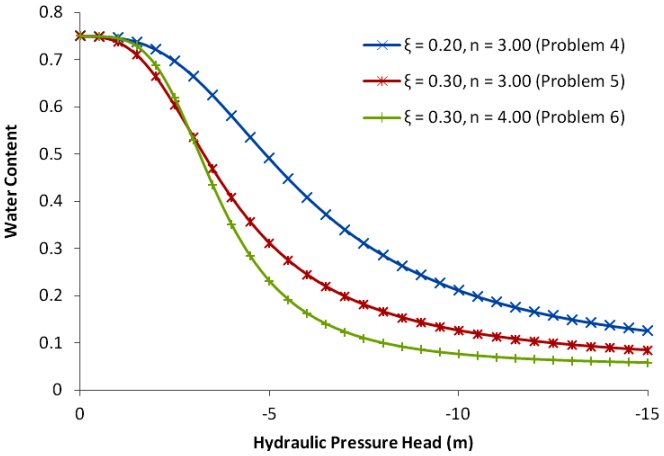

Fig. 2. Water content for van Genuchten WRC: Problems 4, 5, and 6.

Table 2. van Genuchten WRC values for problems 4, 5, and 6.

	θ_s	θ_r	ξ	n
Problem 4	0.75	0.05	0.20	3.00
Problem 5	0.75	0.05	0.30	3.00
Problem 6	0.75	0.05	0.30	4.00

3 ANALYTICAL SOLUTION

In order to validate the numerical results and estimate error norms, we consider analytical solutions for the problem of unsaturated flow for a one-layered Gardner soil. The horizontal flow through a homogenous Gardner soil can be described by (Gardner, 1958; Warrick et al., 2008):

$$h \approx h_1 + \frac{1}{\alpha}\ln\left\{1 - \frac{x}{L} + \exp\left[\alpha\left(h_2 - h_1\right)\right]\frac{x}{L}\right\} \tag{7}$$

where h is hydraulic pressure head, h_1 and h_2 are the specified hydraulic pressure heads at the boundaries, x is the horizontal coordinate, and L is the domain length. The flow Darcy velocity v is constant for 1D problems without hydraulic source/sinks, and the solution is described by Warrick et al. (2008):

$$v = -k(h)\frac{dh}{dx} \tag{8}$$

by substituting Equations (2) and (7) into Equation (8):

$$v = k_s \frac{e^{\alpha h_1} - e^{\alpha h_2}}{L\alpha} \tag{9}$$

4 THE LOCAL DISCONTINUOUS METHOD

We present here an LDG formulation for the steady state unsaturated flow. The LDG formulation has been presented for transient Richards' equation by Li et al. (2007). Equation 1 is elliptic. We can rewrite it as a system of first-order differential equations for a one-dimensional domain Ω where $0 < x < L$:

$$v = -k(h)\frac{dh}{dx}; \quad \frac{dv}{dx} = 0 \qquad \in \Omega \tag{10}$$

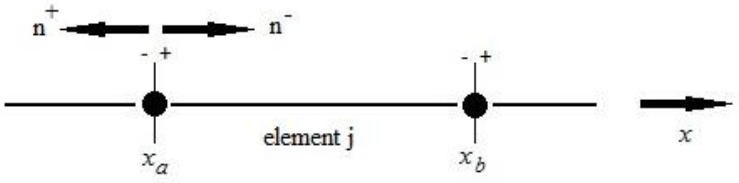

Fig. 3. Illustration of element j quantities (modified from Li (2006))

The mixed weak formulation considering Eq. 10 over a typical element gives

$$\int_{\Omega_e} \varphi v\,dx - \int_{\Omega_e} \frac{d}{dx}(\varphi k(h))h\,dx + \left[\varphi k(\hat{h})\hat{h}\right]_{xa}^{xb} = 0 \tag{11a}$$

$$\int_{\Omega e} \frac{d\psi}{dx} v\,dx - \left[\psi\hat{v}\right]_{xa}^{xb} = 0 \tag{11b}$$

where φ and ψ are test functions. LDG numerical field and flux variables can be derived from Cockburn and Shu (1998) as follows:

$$\hat{h} = \underline{\{h\}} + C_{12}\underline{[h]} \tag{12a}$$

$$\hat{v} = \underline{\{v\}} - C_{11}\underline{[h]} - C_{12}\underline{[v]} \tag{12b}$$

where C_{11} and C_{22} are LDG coefficients with

$$\underline{\{h\}} = 0.5\left(h^+ + h^-\right); \quad \underline{[h]} = h^+.n^+ + h^-.n^- \tag{13a}$$

$$\underline{\{v\}} = 0.5\left(v^+ + v^-\right); \quad \underline{[v]} = v^+.n^+ + v^-.n^- \tag{13b}$$

We assume that h and v vary over an element, according to the space shape functions:

$$h = \sum_{j=1}^{Ne} \varphi_j h_j = \phi^T \underline{h}; \quad v = \sum_{j=1}^{Ne} \varphi_j v_j = \phi^T \underline{v} \tag{14}$$

Other quantities used in the formulation are defined in Figure 3. The choice of numerical fluxes in the discontinuous Galerkin method is critical, and it is discussed for diffusion problems by Kirby and Karniadakis (2005). Substitution of Eq. 12 into 11 yields a matrix formulation and a discrete algebraic system of equations. Li (2006) presents the equations for a steady state heat transfer problem in 2D. We extend it here to unsaturated flow in 1D as follows:

$$\begin{bmatrix} E_f & H_f \\ J_f & 0 \end{bmatrix}\begin{pmatrix} \underline{v} \\ \underline{h} \end{pmatrix} + \sum_{i=1}^{2}\begin{bmatrix} 0 & H_{f,i} \\ J_{f,i} & G_{f,i} \end{bmatrix}\begin{pmatrix} \underline{v} \\ \underline{h} \end{pmatrix} - \sum_{i=1}^{2}\begin{bmatrix} 0 & H_{f,B,i} \\ J_{f,B,i} & G_{f,B,i} \end{bmatrix}\begin{pmatrix} \underline{v} \\ \underline{h} \end{pmatrix}_{(NB,i)} = 0 \tag{15}$$

5 NUMERICAL IMPLEMENTATION

Dealing with nonlinear differential equations requires an iterative scheme. We use a well-known procedure called the Picard iteration method of successive substitution (direct iteration procedure) for both CG and LDG methods in order to solve the nonlinear Richards' equation (Eq. 1).

The iterative scheme is also useful in handling linear equations. Introducing the scheme to the CG method for a linear problem is straightforward, and one cycle of iterations is sufficient. On the other hand, two possible approaches can be followed for the DG methods: (1) assembling all the element equations and constructing the global matrices in the same way as for the CG method; or (2) starting from boundaries and solving the equations, element by element. A major disadvantage of the first approach is the loss of the localised nature of the DG method and the considerable memory requirements, in comparison with the CG method, that arise from this. In the present study we follow the second approach. For more details on iterative schemes, the reader is referred to Barrett et al. (1994), Reddy (2004), and Li (2006).

Error measurement or estimation is required for the evaluation of results from numerical simulations, and establishing a convergence criterion in iterative and adaptive schemes.

We use the following error norm for the Continuous Galerkin method:

$$\| error_{CG} \| = \left(\frac{\sum_{i=1}^{n} (u_i - \hat{u}_i)^2}{\sum_{i=1}^{n} \hat{u}_i^{\,2}} \right)^{1/2} \tag{16}$$

where n is the number of nodes, and u_i and $\hat{u}_i$ are exact and predicted primary variables (i.e. pressure head), respectively. On the other hand, a mixed FEM formulation is used for the discontinuous Galerkin method; therefore, the gradient variable (i.e. flow velocity) participates in the system of equations as well as the error norms, as follows:

$$\| error_{LDG} \| = \left(\frac{\sum_{i=1}^{n} (\sum_{k=1}^{m} (u_i^{\,k} - \hat{u}_i^{\,k})^2 + \sum_{k=1}^{m} (q_i^{\,k} - \hat{q}_i^{\,k})^2)}{\sum_{i=1}^{n} (\sum_{k=1}^{m} (\hat{u}_i^{\,k})^2 + \sum_{k=1}^{m} (\hat{q}_i^{\,k})^2)} \right)^{1/2} \tag{17}$$

where m is the order of the approximation polynomial and q represents gradient variable.

6 RESULTS

We assess and compare the computational economies of the CG and LDG methods, i.e. the computational resources (CPU and memory) required to achieve a given level of accuracy. We base our simulations on three test problems for Gardner WRCs (problems 1, 2, and 3) and another three for van Genuchten WRCs (problems 4, 5, and 6). The domain and boundary conditions for these problems are illustrated in Fig. 4 and soil properties have been presented earlier in Tables 1 and 2. Given the tiny analysis execution time of 1D problems, the processing time is defined here as the average time after running each problem 100 times. This is to ensure the CPU measurements are not overly affected by variable factors related to other jobs the computer may be performing.

In this study, we use a uniform discretisation. For Gardner WRC, we calculate the true error for each mesh resolution using the analytical error norms. However, for van Genuchten, we assume a high resolution mesh (1280 elements) to be the exact solution, since no analytical solution is available for this problem.

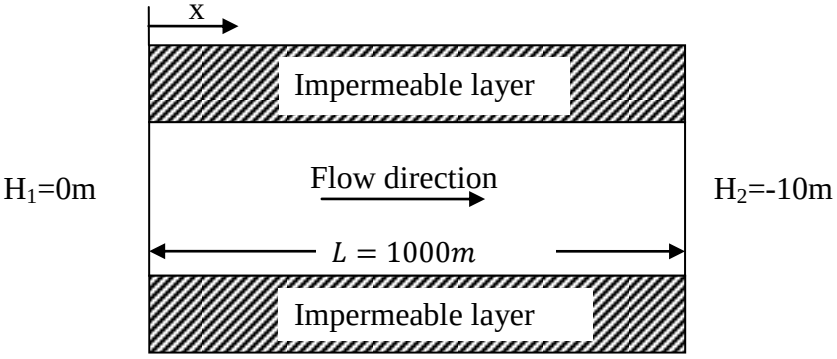

Fig. 4. Test problem domain and boundary conditions

Gardner WRC

The exponential Gardner WRC is a relatively simple model, mostly used for testing numerical procedures (e.g. Tracy, 2010). The effect of the number of elements on the error norm is presented in Fig. 5 for hydraulic pressure head and flow velocity. Predictably, as the WRC becomes more nonlinear, the error norm increases and solution accuracy declines. It is

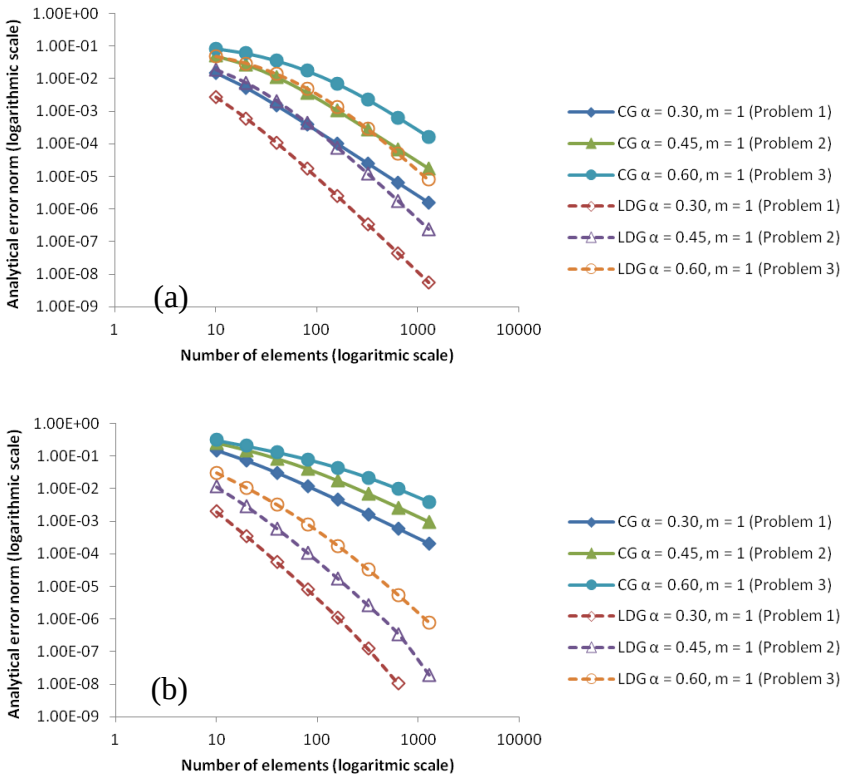

Fig. 5. Accuracy vs. number of elements for Gardner WRC: a) Pressure head, b) Flow Velocity

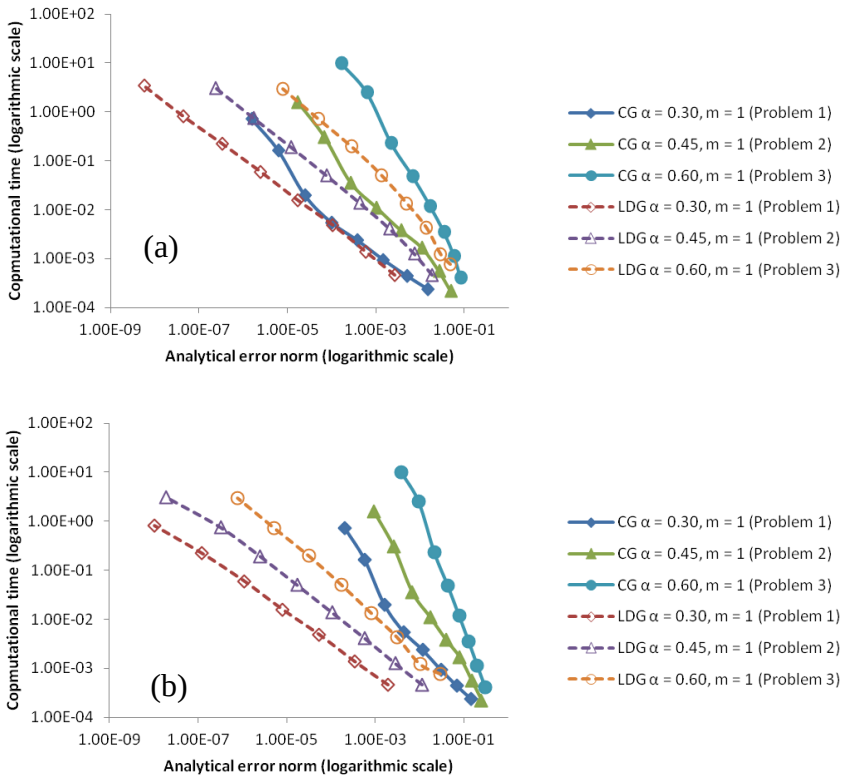

Fig. 6. Accuracy vs. computational time for Gardner WRC: a) Pressure head, b) Flow Velocity

clear from Fig. 5 that the LDG method yields more accurate predictions than the CG for both state (hydraulic pressure head) and gradient (flow velocity) variables. This is in agreement with a number of studies on the order of accuracy of discontinuous Galerkin methods and especially with the LDG method (Cockburn and Shu, 1998). However, since the LDG uses a large number of degrees of freedom than the CG for the same mesh, higher accuracy does not necessarily translate into better computational economy, i.e. faster execution time in reaching a set error norm target.

Computational economies of the two methods are compared in Fig, 6. We note here that the calculated time is the required time for solving both state and gradient variables. The LDG method clearly converges faster for all investigated problems and mesh densities, especially when higher accuracy is required. The effect is even more pronounced for the gradient variable (flow velocity). This is because, in the CG, calculating gradient variables is conducted through numerical differentiation which leads to loss of accuracy, whereas in the LDG, gradient variables are primary degrees of freedom on a par with potential variables (pressure head).

van Genuchten WRC

We choose the van Genuchten WRC to investigate flow through unsaturated porous media because this model shows excellent agreement with the experimental data (Van Genuchten, 1980). Problems 4, 5 and 6 have been chosen to reflect increasing level of non-linearity in the van Genuchten WRC. The results for van Genuchten WRC generally confirm our findings for the simpler Gardner WRCs, with three exceptions. The concordant findings are:

1. higher accuracy of LDG's predictions compared to CG's predictions of pressure head under the same mesh density (Fig. 7a), with the discrepancy becoming even more pronounced for predictions of flow velocity (Fig. 7b);
2. better computational economy (in terms of CPU time) of LDG's predictions of flow velocity compared to CG's predictions (Fig. 8b);

The three exceptions are as follows. First, the change in accuracy with mesh density in Fig. 7 and of computational time with accuracy in Fig. 8 no longer follow smoothly declining curves, as they do in Fig. 5 and Fig. 6. Clearly, the stronger non-linearity of van Genuchten WRCs is behind this behavior, since the effect of a particular mesh refinement will depend on the extent of to which it leads to refinement around the quasi-discontinuity. In this investigation, we used equidistant elements and did not target refinement to the area of sudden jump in the variables.

Second, the CG, under the strong non-linearity of van Genuchten WRC, stops converging beyond a given mesh density and cannot therefore achieve high accuracy. In contrast, the LDG method remains stable even for much higher mesh densities (e.g., 2500 elements) while, the CG stops converging beyond about 100 and 50 elements for problems 5 and 6, respectively. This is in agreement with Li et al. (2007) who reported numerical difficulties encountered in finite element simulations of flow under strongly non-linear WRCs. In practice, the LDG method shows no limitation, except high computational time, for higher resolutions. It must be noted here that using enrichment concepts such as eXtended finite element (XFM) method would very likely improve the performance of the CG method and it would be useful in the future to conduct these comparisons with the enriched CG.

Third, unlike the case of Gardner's WRC, the computational economy of the CG for hydraulic pressure (when the method converges and has comparable accuracy to LDG) is actually better than the LDG's (see Fig. 8a). This is due to the fact that, when it converges,

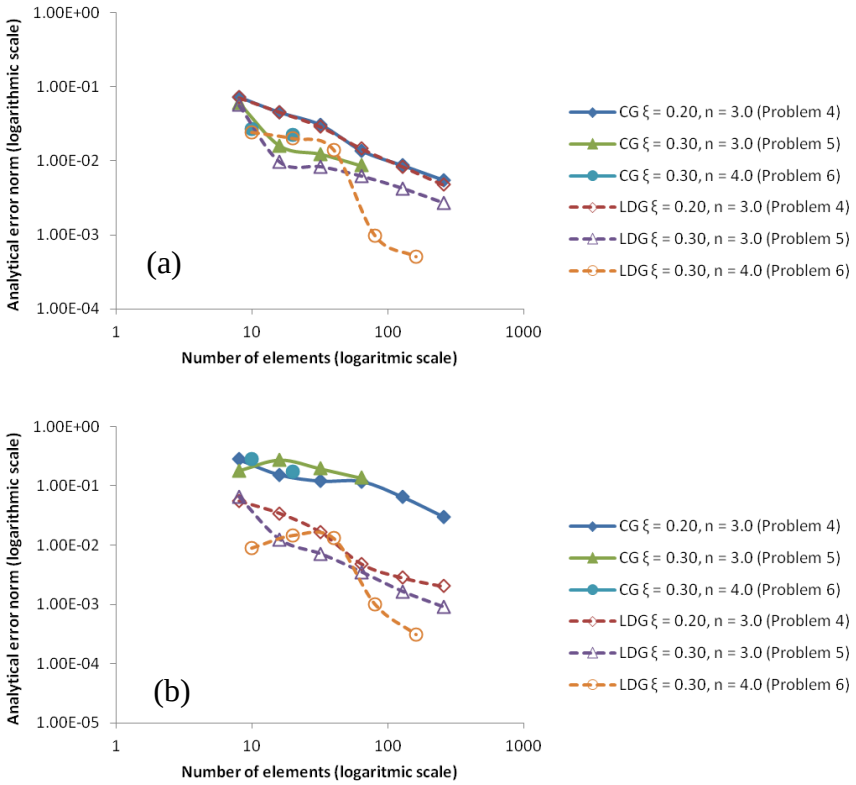

Fig. 7. Accuracy vs. number of elements for van Genuchten WRC: a) Pressure head, b) Flow Velocity (CG stops converging beyond 100 and 50 elements in problems 5 and 6)

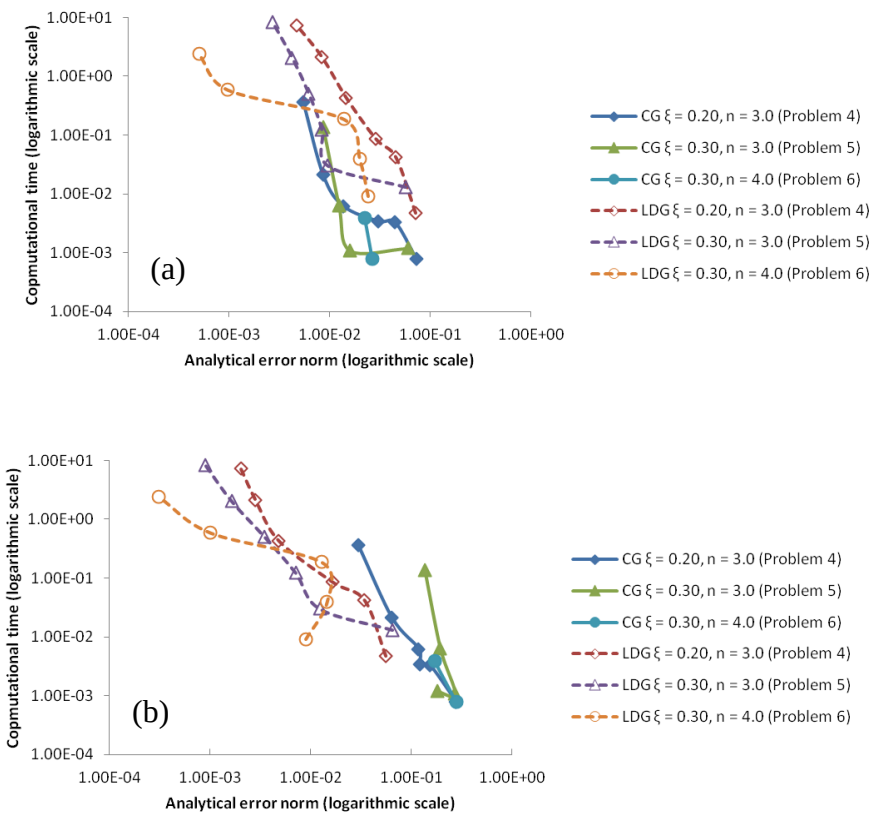

Fig. 8 Accuracy vs. computational time for van Genuchten WRC: a) Pressure head, b) Flow Velocity

the CG requires a relatively small number of iterations to reach a given precision. However, as mentioned above, the LDG's computational economy is superior for flow velocity predictions, and the CG cannot achieve the higher levels of accuracy that LDG is capable of, even for state variables.

7 CONCLUSIONS

We have investigated the ability of the LDG method to model the sharp fronts in WRCs for flow through unsaturated porous media. When a relatively high level of accuracy (high mesh densities) is required for hydraulic pressure head, we found that the computational economy (CPU cost for a given level of accuracy) of the LDG method is superior to that of the CG method, using both Gardner and van Genuchten WRCs. Furthermore, when it comes to flux variable (i.e. flow velocity), the LDG method is considerably faster than the CG method with all tested mesh densities. However, when a relatively low level of accuracy is required and only hydraulic pressure (rather than flow velocity) is of interest, the CG performs better than the LDG.

All in all, the LDG method seems to be a computationally efficient and stable procedure for dealing with sharp fronts for highly nonlinear constitutive models such as van Genuchten, and the computation time required for this method to reach a certain level of accuracy is usually less than for the CG method. This is particularly true for high mesh densities since the CG method either shows an exponential growth in computational time or does not converge at all, whereas the required time for the LDG increases quadratically and this method is much more stable than the CG method.

It is important to keep in mind that our findings are limited, at this moment in time, to steady-state, 1D flow problems, for one simplified type of problems. Clearly, a useful extension of this work is to investigate whether our findings hold for higher order elements, enriched CG methods, problems in 2D and 3D dimensions, more complex domain shapes and boundary conditions and, most importantly, coupled thermal, hydrological, mechanical and chemical problems. It would also be useful to include memory requirements in our assessment of computational economy.

ACKNOWLEDGEMENT

This project is supported by Australian Research Council (ARC) Discovery Project grant DP130100203.

REFERENCES

ALLEN, M. B. & MURPHY, C. 1985. A finite element collocation method for variably saturated flows in porous media. *Numerical Methods for Partial Differential Equations,* 1**,** 229-239.

BARRETT, R., BERRY, M., CHAN TONY, F., DEMMEL, J., DONATO, J., DONGARRA, J., EIJKHOUT, V., POZO, R., ROMINE, C. & VAN DER VORST, H. 1994. *Templates for the Solution of Linear Systems: Building Blocks for Iterative Methods,* Society for Industrial and Applied Mathematics.

BASSI, F. & REBAY, S. 1997. A High-Order Accurate Discontinuous Finite Element Method for the Numerical Solution of the Compressible Navier–Stokes Equations. *Journal of Computational Physics,* 131**,** 267-279.

COCKBURN, B., KARNIADAKIS, G. E. & SHU, C.-W. 2000. Discontinuous Galerkin Methods: Theory, Computation and Applications. *Lecture Notes in Computational Science and Engineering*. Berlin Springer-Verlag and Heidelberg GmbH & Co. K.

COCKBURN, B. & SHU, C.-W. 1998. Local discontinuous Galerkin method for time-dependent convection-diffusion systems. *SIAM Journal on Numerical Analysis,* 35**,** 2440-2463.

GARDNER, W. R. 1958. Some Steady-State Solutions of the Unsaturated Moisture Flow Equation With Application to Evaporation From A Water Table. *Soil Science,* 85**,** 228-232.

KIRBY, R. M. & KARNIADAKIS, G. E. 2005. Selecting the Numerical Flux in Discontinuous Galerkin Methods for Diffusion Problems. *Journal of Scientific Computing,* 22-23**,** 385-411.

LI, B. Q. 2006. *Discontinuous finite elements in fluid dynamics and heat transfer,* London, Springer.

LI, H., FARTHING, M. W., DAWSON, C. N. & MILLER, C. T. 2007. Local discontinuous Galerkin approximations to Richards' equation. *Advances in Water Resources,* 30**,** 555-575.

MUALEM, Y. 1976. A new model for predicting the hydraulic conductivity of unsaturated porous media. *Water Resour. Res.,* 12**,** 513-522.

PHILLIPS, P. & WHEELER, M. 2008. A coupling of mixed and discontinuous Galerkin finite-element methods for poroelasticity. *Computational Geosciences,* 12**,** 417-435.

RATHFELDER, K. & ABRIOLA, L. M. 1994. Mass conservative numerical solutions of the head-based Richards equation. *Water Resour. Res.,* 30**,** 2579-2586.

REDDY, J. N. 2004. *An Introduction to Nonlinear Finite Element Analysis,* USA, Oxford University Press.

RICHARDS, L. A. 1931. Capillary Conduction Of Liquids Through Porous Mediums. *Physics,* 1**,** 318-333.

STELZER, R. & HOFSTETTER, G. 2005. Adaptive finite element analysis of multi-phase problems in geotechnics. *Computers and Geotechnics,* 32**,** 458-481.

TRACY, F. T. 2006. Clean two- and three-dimensional analytical solutions of Richards' equation for testing numerical solvers. *Water Resour. Res.,* 42**,** W08503.

TRACY, F. T. 2010. Testing Computational Algorithms for Unsaturated Flow. *Open Hydrology Journal,* 4**,** 227-235.

VAN GENUCHTEN, M. T. 1980. A closed-form equation for predicting the hydraulic conductivity of unsaturated soils. *Sci. Soc. Am. J.,* 892-898.

VAN GENUCHTEN, M. T. 1982. A comparison of numerical solutions of the one-dimensional unsaturated-saturated flow and mass transport equations. *Advances in Water Resources,* 5**,** 47-55.

WARRICK, A. W., HINNELL, A. C., FERRÉ, T. P. A. & KNIGHT, J. H. 2008. Steady state lateral water flow through unsaturated soil layers. *Water Resour. Res.,* 44**,** W08438.

ZHENG, L., SAMPER, J., MONTENEGRO, L. & FERNÁNDEZ, A. M. 2010. A coupled THMC model of a heating and hydration laboratory experiment in unsaturated compacted FEBEX bentonite. *Journal of Hydrology,* 386**,** 80-94.

ZIENKIEWICZ, O. C., TAYLOR, R. L., SHERWIN, S. J. & PEIRO, J. 2003. On discontinuous Galerkin methods. *International Journal for Numerical Methods in Engineering,* 58**,** 1119-1148.

HYDROMECHANICAL ANALYSIS OF A VOLCANIC ASH SLOPE SUBJECTED TO WETTING AND DRYING CYCLES

L. Laloui, A. Ferrari, J. Eichenberger, J. Fern
Ecole Polytechnique Fédérale de Lausanne (EPFL), Laboratory for Soil Mechanics (LMS), Lausanne, Switzerland; email: lyesse.laloui@epfl.ch

ABSTRACT: *The paper presents the work carried out for the analysis of the hydro-mechanical behaviour of a volcanic ash in unsaturated conditions for the establishment of a landslide early warning system (EWS) in a Costa Rican quarry. Rapid mass movements involving ash material occurred in the greater quarry area during heavy rainfall events. Laboratory testing and numerical analyses were combined to provide a better understanding of the triggering mechanism and to provide guidelines for the EWS. Along with conventional laboratory analyses, the experimental program involved tests carried out under suction control to assess the volumetric response in unsaturated conditions of the material and to highlight potential collapse-upon-wetting phenomena. The behaviour of the material was analysed in a modern framework for soils in unsaturated conditions developed at the EPFL. Numerical simulations were performed with a coupled hydro-mechanical finite elements code in which the mentioned constitutive model is implemented. The analyses allowed a better understanding of the landslide triggering mechanism and provided pore water pressure values which are associated with the failure mechanism and can be used as threshold values for the EWS.*

1 INTRODUCTION

The paper deals with the analysis of an ash deposit covering a pozzolana core body located on the South-West slope of the Irazú Volcano in Costa Rica. The area around the quarry is covered with air-fall volcanic ashes which were deposited by successive explosive eruptions. Landslides involving the ashes have been reported in the greater area and have been associated with intense rainfall events. Landslides in the mining area were first reported in 1996 and then again in 2005. No comprehensive geotechnical investigation was carried out in order to analyse the failure mechanisms. It is believed that the failures occurred in unsaturated conditions as the hill slopes are too steep to host any permanent groundwater table. Moreover, due to their poorly consolidated state, volcanic ashes can undergo collapse-upon-wetting phenomena when they are subjected to an increase of the degree of saturation. Those phenomena are connected with the progressive disappearance of capillarity menisci within the solid skeleton when the soil voids are progressively filled by water. Collapse-upon-wetting can be responsible for landslide triggering before a rise of the groundwater table due to a decrease in the available shear strength associated to suction reduction. A literature research showed that other countries throughout world with similar topography and geology have also experienced such failures (among others, Olivares and Picarelli, 2003; Bilotta et al., 2005; Amaral et al. 2009).

The presented work combines a laboratory testing program and numerical simulations in order to provide an insight on the possible failure mechanisms for the ash deposit and to give some indications for an early warning system (EWS) to be installed in the quarry.

2 LABORATORY TESTING

The laboratory program was carried out on a volcanic ash from the mountainside of the Irazú Volcano in Costa Rica. The material was sampled by Shelby tubes at a depth of about 1.5 m. The tested soil has a liquid limit $w_l = 0.26$ and a plastic limit $w_l = 0.20$. Natural water content for the delivered samples was in the range 0.22 – 0.24. The hygroscopic water content is about 0.02 at the laboratory relative humidity (approximately 50%). The specific gravity is $G_s = 2.61$ and the unit weight is in the range 11.6 – 12.5 kN/m^3. The grain-size distribution presents a sand-size fraction of 48% and a silt-size fraction of 50%.

Specimens were prepared by moist tamping at a water content of 0.24 and at a dry unit weight of 9.9 kN/m^3 (average initial void ratio of 1.58), in order to reproduce the average characteristics of the delivered samples. Matric suction of the compacted specimens was measured by contact filter paper and resulted in the range 20 - 40 kPa, corresponding to an initial degree of saturation of about 40%.

The experimental program was designed in order to better understand the coupled hydro-mechanical response of the material when it is subjected to changes in suction as a consequence of the rainfall infiltration. To this regard, controlled-suction tests were planned and executed in order to obtain the retention properties of the material, the dependency of the permeability on the degree of saturation, the volumetric response of the material under different stress paths. In addition, the tests were used to derive the parameters of the constitutive model described in the following section.

The water retention curve was obtained by a controlled-suction pressure plate apparatus. The specimens were prepared at the different initial void ratios in confining rings (35 mm diameter and 4 mm height). Axis translation technique was then applied to control matric suction (*s*) at a zero vertical stress. At the end of each suction step, specimens were weighted and their volumes measured. Solid weights were measured at the end of the test and water content and degree of saturation back calculated for each specimen. Volumetric deformations during complete drying paths were limited. Sorbino and Foresta (2002) observed a similar behavior during suction increments at low vertical stresses on volcanic ashes from the Vesuvian area.

The relationship between matric suction and degree of saturation is depicted in Figure 1. Experimental points obtained in main drying and wetting paths are represented. The point corresponding to the hygroscopic water content is also represented (suction ~ 80 MPa). Considered void ratios are in the range 1.45 – 1.55. No significant dependency of the retention properties in this range was observed. Also, at this stage of the work, no significant hysteretical effects were registered.

The following expression (van Genuchten, 1980) was used to fit the experimental points:

$$S_r = S_{r,res} + \frac{1 - S_{r,res}}{\left[1 + (\alpha s)^n\right]^m} \tag{1}$$

where $S_{r,res}$ is the residual degree of saturation (equal to 0.03), α is a parameter related to the inverse of the air entry value, n and m are two fitting parameters. The fitting provided the values $\alpha = 0.91$ (m^{-1}), $n = 2.19$ and $m = 0.42$. The air entry value was found to be around 2 kPa.

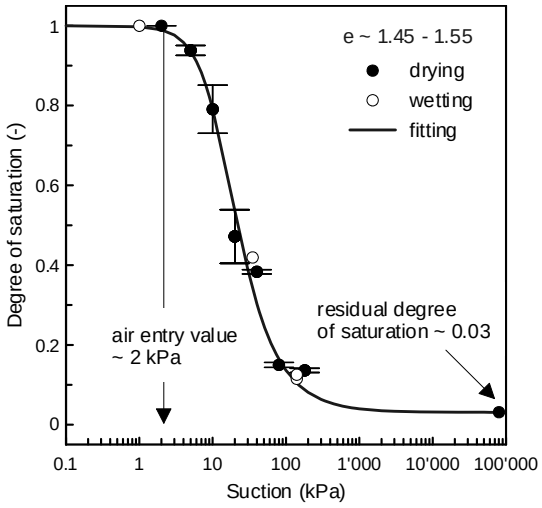

Figure 1. Water retention curve obtained in drying and wetting paths

A series of oedometric tests in controlled suction conditions was carried out. Loading/unloading cycles at constant suctions were performed to assess the evolution of the preconsolidation pressure and stiffness with suction. Suction reduction tests at constant vertical net stress were carried out to verify the position of the loading collapse yield limit of the material. Tests were carried out in a controlled-suction oedometer using the axis translation technique, keeping a constant air pressure and varying the applied water pressure through a pressure/volume controller. After the reference air pressure translation, all tested specimens were allowed to equalise at the initial suction (20 or 40 kPa), applying a very low vertical net stress (5 - 7 kPa) in order to ensure contact between the loading ram and the specimen. The different stress paths followed in the test programme are depicted in the vertical net stress, suction plane in Figure 2.

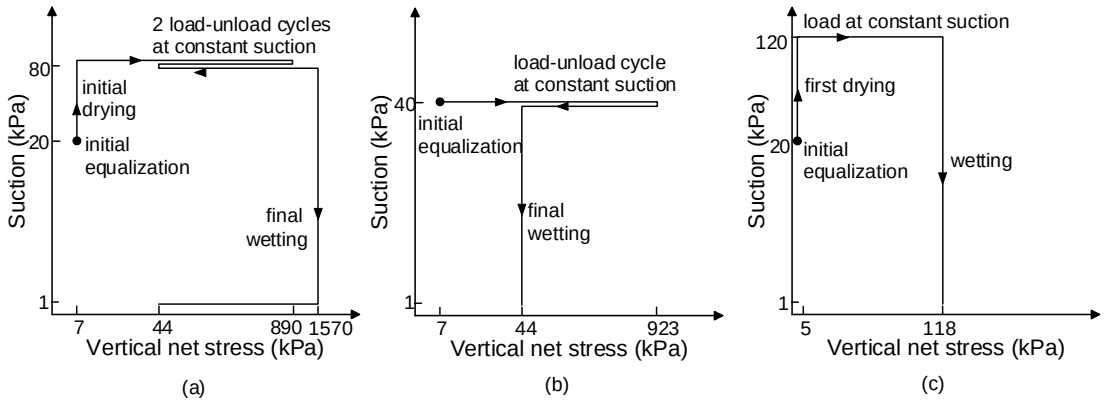

Figure 2. Stress paths applied in the controlled-suction oedometric tests

In the loading and unloading oedometer tests applied suction was maintained at 80 kPa and 40 kPa, respectively (Figure 2.a and 2.b). Starting from the initial value, the vertical net stress (σ_v^{net}) was increased and reduced in steps, allowing for each step the consolidation process, induced by the load variation, to extinguish. A third test (Figure 2.c) was carried on a specimen dried at 120

kPa of suction, then loaded at 118 kPa of vertical net stress and finally wetted in steps up to a suction value of 1 kPa.

Results of constant suction loading-unloading oedometer tests (stress paths *a* and *b* in Figure 2) are plotted in the volumetric deformation, vertical net stress plane (Figure 3) and compared with a conventional oedometric test in saturated conditions (s = 0). As expected, the preconsolidation vertical stress increases significantly as applied suction increases. On the contrary, no significant changes in stiffness are registered when suction increases. The results allow to define the loading collapse yield locus LC of the material in terms of effective preconsolidation vertical stress versus suction, where the vertical effective stress (σ'_v) is defined as: $\sigma'_v = \sigma_v^{net} + sS_r$ (see next section for a detailed description of the effective stress concept and the LC shape used in this work).

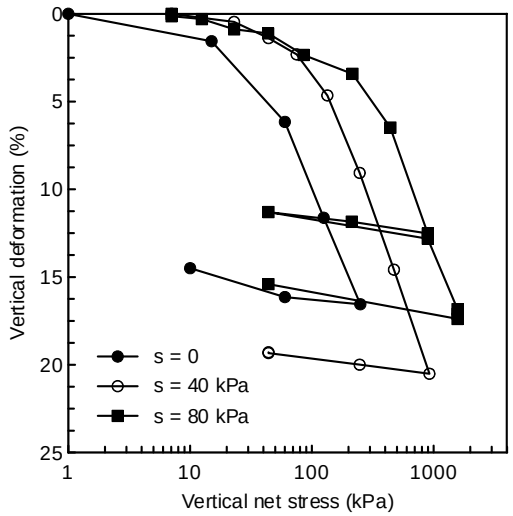

Figure 3. Result of the controlled-suction loading-unloading tests

Figure 4.a depicts the obtained LC along with the stress path of test *c* (Figure 2.c) represented in terms of vertical effective stress and suction. Figure 4.b shows that a significant volumetric strain was registered when the wetting path meets the initial LC position (step DE). This experimental result confirms that the initial position of the LC, obtained by the loading-unloading cycles at constant suction, can be used to assess the collapsibility of the material upon wetting. The volumetric deformation registered during this wetting step is essentially plastic and it is referred as a collapse-upon-wetting phenomenon. The hardening of the material during the wetting implies a movement of the LC.

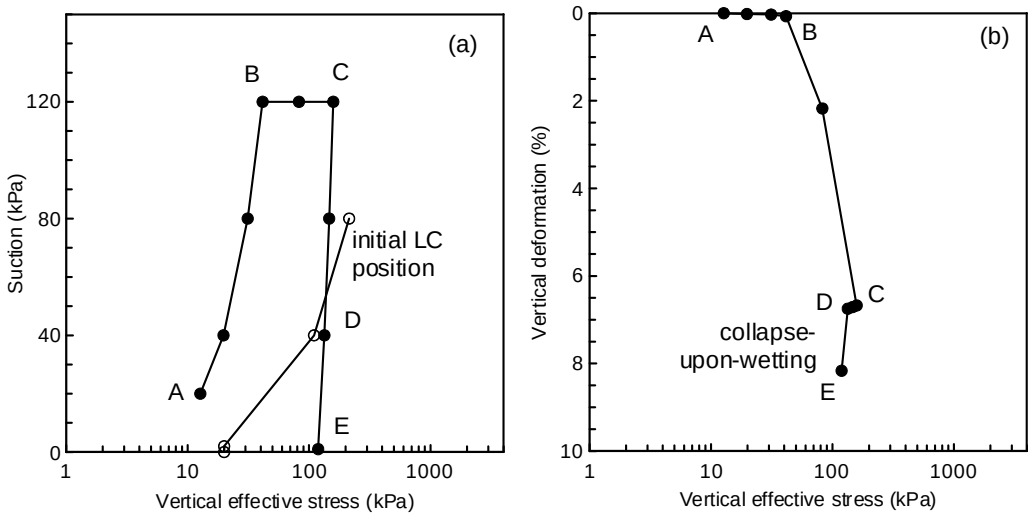

Figure 4. Interpretation of the oedometric test c in terms of vertical effective stress.

3 CONSTITUTIVE MODELLING

This section reviews the main concepts of the ACMEG-s (Advanced Constitutive Model for Environmental Geomechanics) elasto-plastic constitutive model developed at the EPFL (Nuth and Laloui 2007; Nuth and Laloui 2008). The model is used in the present work for the modelling of the onset of landslides in partially saturated ash slopes due to rainfall infiltration. The model is based on the effective stress concept extended to partially saturated conditions. It takes into account fundamental aspects for the mechanical response of the material in unsaturated condition such as the effects of the degree of saturation, the hystertical features and the void ratio dependency of the water retention curves, the effects of the overconsolidation on the stiffness and on the shear strength, and the dependency of the compressibility on the confining pressure.

The model is a Cam-Clay-type elasto-plastic model and is based on the so-called initial Hujeux's model (Hujeux 1979). The increment of strain $d\varepsilon_{ij}$ is decomposed into:

$$d\varepsilon_{ij} = d\varepsilon_{ij}^{e} + d\varepsilon_{ij}^{p} \tag{2}$$

where $d\varepsilon_{ij}^{e}$ is the elastic strain increment and $d\varepsilon_{ij}^{p}$ the plastic strain increment.

The elastic deformation can be expressed as:

$$d\varepsilon_{ij}^{e} = C_{ijkl} d\sigma'_{kl} \tag{3}$$

The tensor C_{ijkl} is the mechanical elastic tensor and is composed of non-linear elastic moduli. The elastic strain increment $d\varepsilon_{ij}^{e}$ can be decomposed in volumetric and deviatoric increments which are related to mean effective, respectively deviatoric stress by means of spherical stress-dependent elastic moduli. σ'_{kl} in equation is the effective stress for unsaturated soils:

$$\sigma'_{kl} = \left(\sigma_{kl} - u_a \delta_{kl}\right) + S_r \left(u_a - u_w\right) \delta_{kl} \tag{4}$$

where σ_{kl} is the total stress, u_a is the air pressure, u_w is the water pressure, S_r is the degree of saturation and δ_{kl} is the Kronecker's delta $\left(\delta_{kl} = 1 \text{ if } k = l, 0 \text{ else}\right)$. As mentioned, the difference between the total stress σ_{kl} and the air pressure u_a is called the net stress $\sigma_{kl\,net}$. The difference between u_a and u_w is defined as the matric suction s.

The critical state line is defined in the plane of deviatoric stress q versus mean effective stress p', with a slope M. The slope of the critical state line in the plane volumetric plastic strain vs. mean effective stress $\left(\varepsilon_v^p - \ln p'\right)$ is β, p'_{CR0} being the initial critical state pressure:

$$\ln \frac{p'_{CR}}{p'_{CR0}} = \beta \varepsilon_v^p \tag{5}$$

In the ACMEG-s model, the plastic irreversible strain increment $d\varepsilon_{ij}^p$ is induced by two coupled dissipative processes: an isotropic and a deviatoric plastic mechanism. The yield limits of each mechanism, bounding the elastic domain in the effective stress space, can be written as:

$$\tilde{f}_{iso}(p', \varepsilon_v^p, r_{iso}) = p' - r_{iso}.d.p'_{CR}, \quad \tilde{f}_{dev}(p', q, r_{dev}, \varepsilon_v^p, \varepsilon_d^p) = q - Mp'\left(1 - b \ln \frac{p'}{p'_{CR}}\right) r_{dev} \tag{6}$$

where p'_{CR} is the critical state pressure. d, b, r_{iso} and r_{dev} are material parameters. ε_v^p and ε_d^p are respectively the volumetric plastic strain and the deviatoric plastic strain. The critical state pressure can be related to the preconsolidation pressure $p_c^{'}$ using the material parameter d, that represents the distance in the volumetric plane between the normally consolidated line and the critical state line:

$$p'_c = d.p'_{CR} \tag{7}$$

Using the space of triaxial stress variables q and p', the elastic domain is enclosed by an ellipsoidal surface which is cut by the isotropic yield limit (see Figure 5). Adding the suction s as a third axis of the space, Figure 5 shows that the elastic domain gets larger with suction. This accounts for the fact that a dryer material will have higher strength and stiffness. The following equation gives the mathematical formulation of the contribution of the capillary effects to the mechanical behaviour. The principle is to introduce a dependency of the preconsolidation pressure p'_c on the level of suction s and using a material parameter γ_s:

$$p'_c = \begin{cases} p'_{c0} & \text{if } s \le s_e \\ p'_{c0}\left[1 + \gamma_s \log\left(s / s_e\right)\right] & \text{if } s \ge s_e \end{cases} \tag{8}$$

p'_{c0} is the initial preconsolidation pressure at zero suction and s_e is the air entry value. The expression is the equivalent of the LC curve presented in terms of the vertical effective stress in the previous section when the triaxial stress variables are considered.

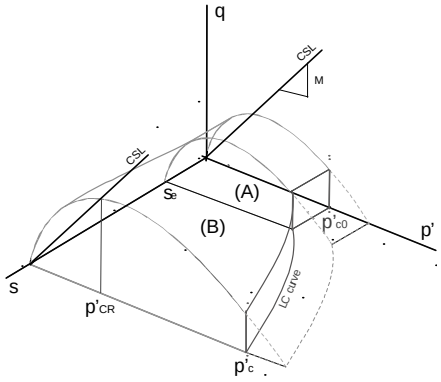

Figure 5. Yield surface shape and critical state line (CSL) in a (p', q, s) space.

In the present work, the evolution of the degree of saturation S_r with respect to suction s is taken into account by the curve depicted in Figure 1. For the flow problem, the generalized Darcy's law is used to describe the relative velocity of the fluid with respect to the solid skeleton. The permeability tensor $\mathbf{K}_w$ depends in general on the degree of saturation S_r. Assuming hydraulic isotropic conditions, the water relative permeability coefficient k_{rw} is defined according to the following relationship:

$$k_{rw} = k_{sat} S_r^{\lambda} \tag{9}$$

where k_{sat} is the coefficient of permeability in saturated conditions and λ is a material parameter. Constant head permeability tests provided $k_{sat} = 5.5 \cdot 10^{-5}$ m/s. The permeability dependency on the degree of saturation was determined by the back analysis of the transient water exchange registered in the controlled-suction tests. The analysis provided λ = 12.3.

The constitutive model presented above is implemented into the finite element code called LAGAMINE (Charlier 1987; Collin 2003). The code features hydro-mechanically coupled finite elements.

4 NUMERICAL SIMULATIONS

The hydro-mechanical response of the ashes were analysed using an ash-filled column FEM model and a two dimensional cross section FEM model. One example of one dimensional analysis is presented in this section. Data provided by the quarry owner showed that the ash thickness is 2 m on average. A 6 m column was used and divided into two sections – the upper with a thickness of 2 m for the ash cover and the lower with a thickness of 4 m for the substratum. The initial suction was set at 20 kPa as this was the lower value measured by the laboratory. The constitutive model ACMEG-s was used for the ash material while an elastic constitutive law with high stiffness was used for the substratum. The constitutive parameters used for the ash were obtained from the back-analysis of the experimental data and are reported

in Table 1. The ash is initially normal-consolidated. Precipitation registered in the wet season 2005 for the area of the mine was applied as boundary condition to the top of the ash column (Figure 6.a). The month of August is the time window for initial conditions. Early September the first rash of rain is applied. Figure 6.b shows the evolution of the pore water pressure for depth of 0.5 m, 1 m, 1.5 m and 2 m. Suction at surface decreases immediately while almost 20 days are needed to register a suction reduction at 2 m depth.

Table 1. Parameters for the elasto-plastic ACMEG-s and water retention model

		Symbol	*Description*	*Value*
Stress-strain model	Elastic parameters	K_{ref}	Bulk modulus	$2*10^5$ kPa
		G_{ref}	Shear modulus	$1.4*10^5$ kPa
		n^e	Elastic exponent	0.5
	Plastic parameters	φ´	Friction angle	35.5°
		β_0	Compressibility coefficient	-9
		*α	Dilatancy coefficient	1.3
		*a		0.02
		b	see equation	0.1
		*c		0.08
		d	see equation	2
	Limits of elastic domain	r^e_{dev}	Initialisation of deviatoric mechanism	0.32
		r^e_{iso}	Initialisation of isotropic mechanism	0.3
Capillary effects		γ_s	Coefficient of LC curve	1.6
		*Ω	Coef. var. compressibility	0
		s_e	Air entry value	2 kPa

*see Nuth & Laloui (2007) for a complete explanation of parameters.

As the soil increases its degree of saturation, the delay of the suction changes propagation for the deep layers reduces to a few days. This tendency is related to the increase in permeability of the ash as the degree of saturation increases. In general a few dry days allows the suction to increase at the surface but this rapidly decreases with a second rush of rain.

The factor of safety is computed for the ash column assuming an infinite slope condition and a slope of 50°. A Mohr-Coulomb envelope is assumed with the contribution of suction to the shear strength equal to $s \cdot S_r \cdot \tan(\varphi')$. The unit weight of the ash is computed taking into account the degree of saturation. The evolution of the factor of safety is depicted in Figure 6.c. The figure shows that the factor of safety is close to 1 for the deepest layer and that failure can occur before positive pore water pressures are generated. At 2 m depth, a suction value in the range 12-13 kPa would be associated to a failure. Figure 6.d depicts the accumulation of the plastic volumetric strain at the considered depths. Volumetric plastic strain accumulates at depths greater than 0.5 m when the soil is wetted for the first time; interestingly, the highest accumulation is observed at a depth of 1.5 m, indicating that the most severe collapse-upon-wetting phenomena may occur at that depth.

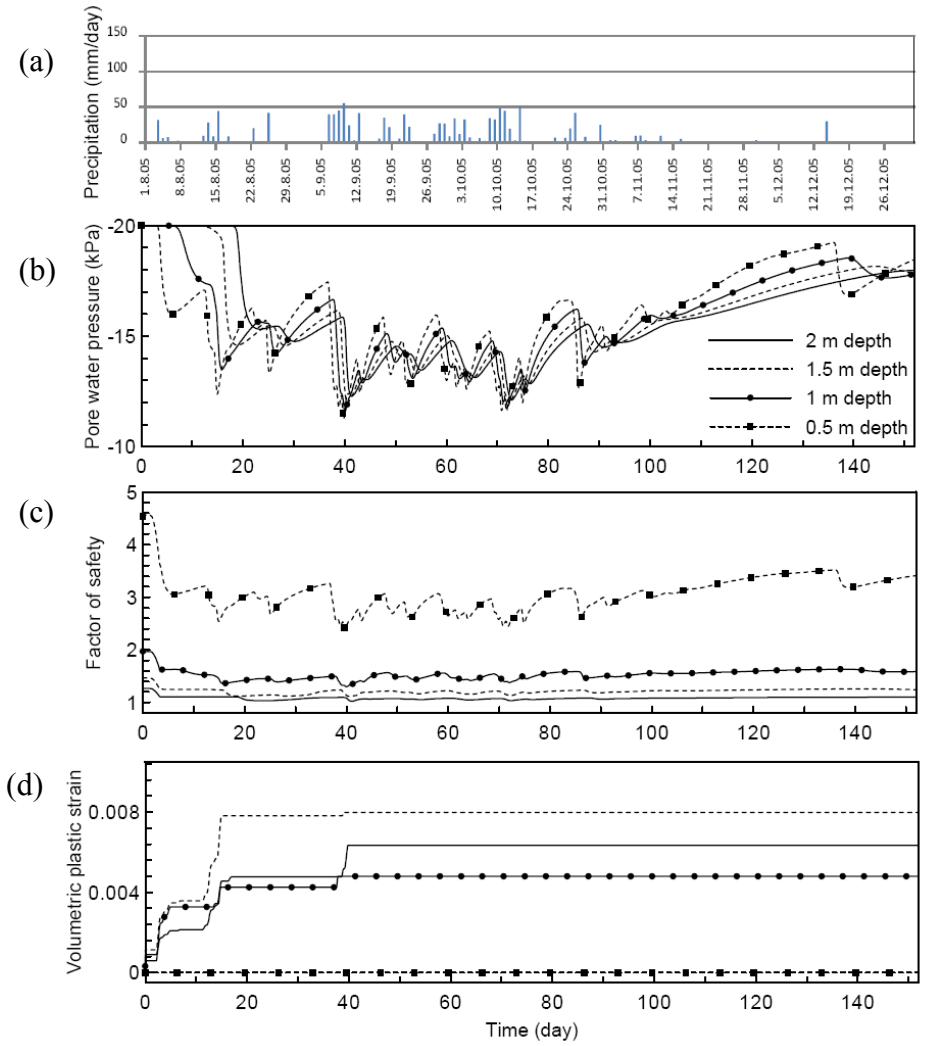

Figure 6. FEM numerical simulation of rainfall infiltration in an ash column

5 DISCUSSION AND CONCLUSIONS

A comprehensive experimental program was carried out in order to characterize the hydro-mechanical response of an ash cover during rainfall infiltration. The obtained results highlighted the yield limit of the material related to the collapsibility upon wetting and allowed to calibrate an advanced constitutive model based on the effective stress concept extended to partially saturated conditions. Numerical simulations were carried out with a coupled hydro-mechanical finite elements code in which the mentioned constitutive model is implemented. The analyses allowed to better understand the landslide triggering mechanism and to obtain values for the pore water pressure which are associated to the failure mechanism. In particular it is expected that failure may take place at a depth between 1.5 m and 2 m. The predicted failure mechanism is associated to a suction reduction and it may be triggered before positive pore water pressure develops. In this sense, matric suction is proposed as a variable to be monitored in-situ and linked to the EWS (Eichenberger et al. 2013). The analysis provided useful indications on the positioning of the sensors: suction should be monitored with particular attention between 1.5 m

and 2 m depth, where the failure mechanism may develop and be enhanced by collapse-upon-wetting phenomena.

ACKNOWLEDGMENTS

The work described in this paper was supported by the project SafeLand, ‘‘Living with landslide risk in Europe: Assessment, effects of global change, and risk management strategies,’’ under Grant Agreement No. 226479 and by the project Wandland, ‘‘Effects of wetting and drying cycles on landslide activity,’’ under Grant Agreement No. PERG06-GA-2009-256426 in the 7th Framework Programme of the European Commission. Support was also provided by Swiss Competence Center Environment and Sustainability, TRAMM 2 Project. This support is gratefully acknowledged.

REFERENCES

Amaral, P., Marques, R., Queiroz, G., Zêzere, J.L. and Marques, F. (2009). Distributed transient modelling of rainfall-triggered shallow landslide for susceptibility assessment in Ribeira Quente valley, Landslide Processes, from geomorphologic mapping to dynamic modelling: pp.89-94

Bilotta, E., Cascini, L., Foresta V. and Sorbino G. (2005). Geotechnical characterisation of pyroclastic soils involved in huge flowslides, Geotechnical and Geological Engineering 23: pp. 365-402.

Charlier, R. (1987). Approche unifiée de quelques problèmes non linéaires de mécanique des milieux continus par la méthode des éléments finis. PhD thesis, Université de Liège.

Collin, F. (2003). Couplages thermo-hydro-mécaniques dans les sols et les roches tendres partiellement saturés. PhD thesis, Université de Liège.

Eichenberger, J., Ferrari, A. and Laloui, L. (2013). Early warning thresholds for partially saturated slopes in volcanic ashes, in Computers and Geotechnics(49): 79-89, 2013.

Hujeux, J. (1985). Une loi de comportement pour le chargement cyclique des sols. Génie Parasismique. Paris, Les éditions de l'E.N.P.C.: 287-353.

Nuth, M. and Laloui, L. (2007). New insight into the unified hydro-mechanical constitutive modelling of unsaturated soils. Unsat Asia 2007, Nanjing, p. 109-125.

Nuth, M. and Laloui, L. (2008). Effective stress concept in unsaturated soils: Clarification and validation of a unified framework. International journal for numerical and analytical methods in Geomechanics 32, 2008, p. 771-801.

Olivares, L. and Picarelli, L. (2003). Shallow flowslides triggered by intense rainfalls on natural slopes covered by loose unsaturated pyroclastic soils, Géotechnique 53(2).

Sorbino, G. and Foresta, V. (2002). Unsaturated hydraulic characteristics of pyroclastic soils. Proc. 3rd International Conference on Unsaturated Soils; 10-13 March, Recife, Brasil, vol. 1, pp. 405-410.

van Genuchten, M.T. (1980). A closed form equation for predicting the hydraulic conductivity of unsaturated soils. Soil Sci. Soc. Am. J. 44:892–898.

THM PROCESSES IN A FRACTURED FORMATION

A.P.S. Selvadurai and A.P. Suvorov
Department of Civil Engineering and Applied Mechanics, McGill University, Montréal, QC, Canada

P.A. Selvadurai
Department of Civil and Environmental Engineering, University of California, Berkeley, CA, USA

ABSTRACT: *The paper uses a computational approach to examine the THM processes that are initiated in a fractured fluid-saturated formation when glacial loads are applied by an advancing glacier. The constitutive modelling takes into account Biot poroelasticity of the intact material and the presence of a sparse distribution of sessile but hydraulically interacting fracture systems. The modelling considers coupled thermo-hydro-mechanical effects in both the intact rock and fractures. The computational modelling addresses pore fluid generation within the fractured formation due to an advancing glacier that exerts both a normal stress and a fluid pressure at the base of the glacier. Computational modelling provides an assessment of the role of fractures in moderating the pore pressure generation within the fractured rock mass.*

1 INTRODUCTION

The fully coupled hydro-mechanical problem for a fully saturated geological material was first presented by Biot (1941) and reformulated by several others including Rice and Cleary (1976), Norris (1992) and references to further studies are given by Selvadurai (1996, 2007). The solutions for coupled THM problems in geological materials have been obtained by many researchers and a comprehensive review is given by Selvadurai and Suvorov (2012). The behaviour of rocks containing fractures has been analyzed in papers by Noorishad et al. (1984), Selvadurai and Nguyen (1995), Nguyen and Selvadurai (1998), Rutqvist et al. (2002), Chan et al. (2005). The methods used to study the behaviour of a fractured rock mass containing multiple fractures can be divided into three categories: a fractured continuum approach, a discrete fracture network approach and the hybrid approach. In the fractured continuum models there are single porosity models (Long et al. 1985; Carrera et al. 1990; Sitharam et al. 2001) and dual porosity models (Barenblatt et al. 1960; Pruess and Narasimhan 1985; Khalili and Selvadurai, 2003). In these approaches, the location of individual fractures is not specified and the influence of fractures is introduced phenomenologically. In the discrete network models, the fractured rock mass is treated as a discontinuous medium by assuming that the rock mass consists of block regions separated by fractures. The regions are generally assumed to be impermeable, and therefore, groundwater will flow only along the fractures. Furthermore, 3D flow models of discrete fracture networks have been proposed (Long and Witherspoon 1985; Long and Billaux 1987; Nguyen and Selvadurai, 1998; Pearce and Pande, 2007; Zhang et al. 2009; Massart and Selvadurai, 2012). These models can simulate each fracture but when the rock mass consists of a large number of fractures the system becomes very complex and makes the computational modelling non-

routine. To simplify the models, orthogonal fracture systems and parallel fracture systems have been considered (Dershowitz et al., 1991; Tsang, et al. 1996). Such discrete network models can also serve as tools for estimating the permeability of a rock mass. Based on a representative unit containing a sufficient number of fractures, numerical analysis can be carried out to determine the effective permeability of the unit (Oda, 1985; Hsieh et al 1985; Cacas, et al. 1990). When the distribution of permeability is inhomogeneous, as would be the case involving narrow fractures in a relatively permeable rock matrix, the effect of such inhomogeneities can be accounted for through the introduction of an effective isotropic permeability measure. A recent advance that proposes the use of the geometric mean of the spatial permeability variation, which displays a lognormal distribution, has recently been discussed by Selvadurai and Selvadurai (2010). Other effective media representations for porous media with fracture-type inclusions have also been discussed by Suvorov and Selvadurai (2010). In the hybrid or discrete-continuum approach, the dominant fractures are modeled as 2D or 3D bodies that are embedded in a 3D porous medium (Carrera and Lurdes 2000). The rock mass is assumed to consist of a dominant fracture network and a fractured rock matrix (dual fracture model). The dominant fractures are modeled as relatively large fractures, as in the discrete approach, whereas the hydraulic properties of the fractured rock matrix are modified to take into account the minor fractures, as in the continuum approach. The dominant fractures are categorized into three groups: pipe-shaped, plane and belt-shaped fractures. They are modeled by 1D elements, 2D plane elements and 3D solid elements, respectively. This paper presents typical results for the fluid velocity, pressure, temperature, and displacements in the entire rock mass consisting of the intact rock and individual fractures.

In the present study each dominant fracture has the shape of a prism or prismatoid and is modelled individually using 3D solid elements. The surrounding rock matrix is assumed to contain minor fractures, pores and voids and, therefore, its permeability is taken to be non-zero. We will refer to the dominant fractures as fracture zones and the surrounding rock matrix is referred to as the intact rock. A rock mass containing an intact part and a relatively small volume fraction of fracture zones, only 0.29%, is examined in detail. Such a small volume fraction of fracture zones can be explained, in part, by the small thickness of each fracture zone, equal to 10 m, and the large dimensions of the rock mass, e.g., a height of 1700 m. The fractures have orientations with angles of inclination ranging from 0^o to $\pm 90^o$. The fractures that have a zero-degree angle of inclination are vertical, and $\pm 90^o$ are horizontal. This paper contains illustrations that show the fluid velocity, pressure, temperature, and the effective stresses averaged over the volume of individual fracture zones. The values of these dependent variables averaged over the entire body of the rock mass are also given.

2 CONSTITUTIVE AND GOVERNING EQUATIONS

For the linear elastic isotropic rock, the strain stress constitutive equation is given by

$$\sigma_{ij} = 2G_D\varepsilon_{ij} + (K_D - \frac{2}{3}G_D)\varepsilon_V\delta_{ij} - 3K_D\alpha_s T\delta_{ij} - \alpha p\delta_{ij} \quad (1)$$

Here K_D, G_D denote the bulk and shear modulus of the drained rock, respectively, α_s is the thermal expansion coefficient of the solid phase of the rock, and α is the Biot coefficient defined as $\alpha = 1 - K_D / K_s$, where K_s is the bulk modulus of the solid phase.

The effective stress is defined by

$$\sigma'_{ij} = \sigma_{ij} + \alpha p\delta_{ij} = 2G_D\varepsilon_{ij} + (K_D - \frac{2}{3}G_D)\varepsilon_V\delta_{ij} - 3K_D\alpha_s T\delta_{ij} \quad (2)$$

For an isotropic fluid-saturated porous medium Darcy's law can be written as

$$v_i = -\frac{k}{\mu}(p_{,i} + \rho_f g \delta_{i3}) \tag{3}$$

where v_i is the spatially averaged flow velocity, k is the permeability of the rock and μ is the dynamic viscosity. Also, ρ_f denotes the fluid density, g is the gravitational acceleration and here it is assumed that the gravitational acceleration vector is pointing in the negative direction of the vertical z-axis. We assume that the heat transfer in the system is through conduction and the fluid flow velocities in both the pore space in the intact rock and through the fractures are slow enough such that the convective heat transfer terms can be neglected. Therefore heat transfer in the isotropic body is described by Fourier's law of heat conduction

$$h_i = -k_c T_{,i} \tag{4}$$

where k_i is the equivalent heat conductivity of the rock and h_i are the components of the heat flux vector.

Equilibrium equations written in terms of the displacements are

$$(K_D + \frac{4}{3}G_D)u_{k,ki} + G_D u_{i,kk} - 3K_D \alpha_s T_{,i} - \alpha p_{,i} - (n\rho_f g + (1-n)\rho_s g)\delta_{i3} = 0 \tag{5}$$

where ρ_s is the density of the solid phase. The fluid flow equation can be written as

$$(\frac{n}{K_f} + \frac{\alpha - n}{K_s})\frac{\partial p}{\partial t} - \frac{k}{\mu} p_{,ii} + \alpha \frac{\partial u_{i,i}}{\partial t} = n3\alpha_f \frac{\partial T}{\partial t} + (\alpha - n)3\alpha_s \frac{\partial T}{\partial t} \tag{6}$$

where α_f is the thermal expansion coefficient of the fluid phase and K_f is the bulk modulus of the fluid phase.The heat conduction equation is given by

$$c_p \frac{\partial T}{\partial t} - k_c T_{,ii} = 0 \tag{7}$$

where c_p is the equivalent specific heat of the rock. Each of these equations is valid inside a domain with spatially uniform material properties, i.e., inside the fractures and the intact part of the rock.

The initial and boundary conditions that correspond to glacial loading are now considered. Assume that the glacier of nonuniform thickness moves along the upper surface of the rock. The thickness of the glacier is denoted by $l = l(x, y, t)$ where (x, y) are the inplane coordinates. Therefore, on the upper surface the fluid pressure can be written as

$$p(x, y, z^{top}, t) = \rho_f g l(x, y, t) \tag{8}$$

where z^{top} is the z-coordinate of the upper surface. Since the densities of the glacier constituents are almost equal, the normal stress acting on the upper surface is given by

$$\sigma_z(x, y, z^{top}, t) = -\rho_f g l(x, y, t) \tag{9}$$

Therefore, the effective stress on the upper surface can be evaluated from (2) as

$$\sigma'_z(x, y, z^{top}, t) = -\rho_f g l(1 - \alpha) \tag{10}$$

In addition, the temperature change caused by the presence of the glacier is prescribed on the upper surface

$$T(x, y, z^{top}, t) = T_u(x, y, t) \tag{11}$$

On the lower surface, $z = z^{bot}$, we can prescribe zero vertical displacement u_3, fluid velocity and heat flux, i.e.

$$u_3(x, y, z^{bot}, t) = 0\,;\ \left(\frac{\partial p}{\partial z}\right)_{z=z^{bot}} = 0\ ;\ \left(\frac{\partial T}{\partial z}\right)_{z=z^{bot}} = 0 \tag{12}$$

On the perimeter contour C we impose zero displacement, fluid velocity, and heat flux in the direction of the normal to the surface

$$u_n = 0 \quad ; \quad \frac{\partial p}{\partial n} = 0 \quad ; \quad \frac{\partial T}{\partial n} = 0 \tag{13}$$

where $\partial / \partial n = \mathbf{n}\nabla$ is the normal derivative to the surface. If the elastic deformation of the rock mass is neglected, (5) can be written as

$$(\frac{n}{K_f} + \frac{\alpha - n}{K_s})\frac{\partial p}{\partial t} - \frac{k}{\mu} p_{,ii} = n3\alpha_f \frac{\partial T}{\partial t} + (\alpha - n)3\alpha_s \frac{\partial T}{\partial t} \tag{14}$$

The computational modelling of the coupled THM problem is described in greater detail in Selvadurai and Suvorov (2010) and Selvadurai et al. (2011, 2013) and will not be repeated here.

3 COMPUTATIONAL MODELLING AND NUMERICAL RESULTS

The rock mass is a heterogeneous geomaterial on a macroscale in the sense that the fracture zones have properties different from those of the intact rock. In the particular problem being examined, the permeability of the fracture zones is about six orders of magnitude greater than the permeability of the intact rock, and the Young's modulus is approximately 10 times smaller. The material of the solid grains of the rock, or the solid phase, was assumed to be compressible both in the intact rock and fracture zones (this is achieved by setting the Biot coefficient equal to 0.7, $K_D / K_s = 0.3$). The fluid was also assumed to be compressible both in the fracture zones and in the intact rock mass (the temperature-independent fluid bulk modulus is set equal to 2.2 GPa). For the rock associated with the scenario being examined, the porosity is assumed to be 0.05 both for the fracture zones and the intact rock. The DECOVALEX report (Chan and Stanchell, 2008) gives the value of the porosity as 0.1 for the fracture zones, and 0.002 for the intact rock.

The primary emphasis of this work was to analyze the behaviour of the rock mass when it is subjected to advancing glacial loads. Glacial loads arise due to the accumulation of ice and water, i.e., glacier, on the upper surface of the rock mass. In this study we have assumed that accumulation of this mixture of ice and water can be taken into account by prescribing the fluid pressure, the compressive stress and the temperature change on regions of the upper surface of the rock mass. The magnitude of the prescribed fluid pressure and the compressive stress naturally depends on the thickness of the frozen mixture and is thus dependent on both on time and spatial coordinates. (The magnitude of the effective stress applied on the upper surface also depends on the value of the Biot coefficient. (see (9)) A spatially non-uniform time-dependent glacial load is considered.

The finite element model of the intact rock mass is created by vertical extrusion of the in-plane geometry of the rock simplified to a quadrilateral shape. Each fracture surface was drawn in the corresponding work plane, whose position and angle of inclination was defined with respect to the global coordinate system. Each fracture surface was then extruded and embedded into the rock mass. Finally, the shape of the fractures was modified to ensure alignment of the perimetral edges of a fracture with respect to the upper and/or lower surface of the rock mass. The geometry of the rockmass, the locations of the fracture system and the finite element discretization of the rockmass and the fracture system are shown in Figure 1.

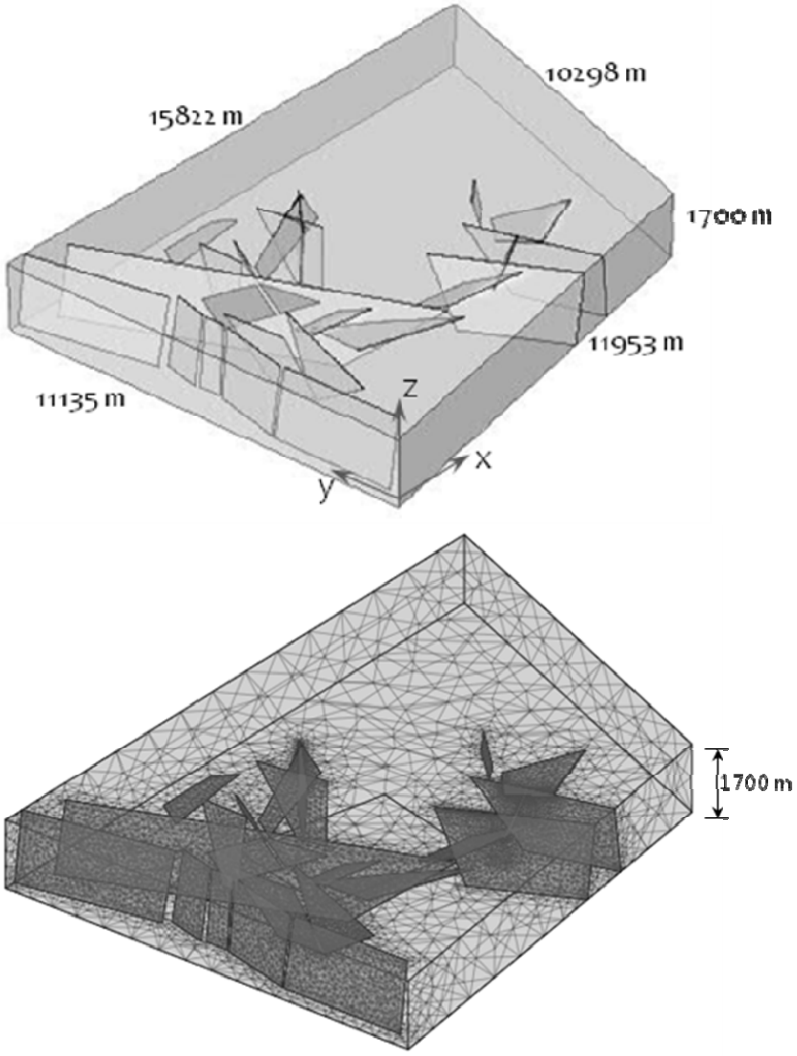

Figure 1. The dimensions of the sparsely fractured rockmass, locations of the fractures and the finite element discretization

The effect of the moving glacier on the response of the rock is simulated by applying a spatially non-uniform and time-dependent loading to the upper surface of the fractured rock. The dependence of the applied loading on the position and time is given by

$$p(x,y,z^{top},t) = p_{\max}F; \quad \sigma'_{zz}(x,y,z^{top},t) = \sigma'_{\max}F; \quad T(x,y,z^{top},t) = T_{\max}F \qquad (12)$$

where

$$F(x,t) = \frac{1}{2} + \frac{1}{\pi}\arctan\{\frac{1}{100}(-x - 3000[m] + 4.03E\{-8t[\sec]\})\} \qquad (13)$$

and $p_{\max}, \sigma'_{\max}$, and $T_{\max}$ are the maximum values of the fluid pressure, effective stress σ'_{zz} and the temperature change, respectively, applied to the upper surface $z = z^{top}$. The function F changes from 1 for small x to zero for large x resembling the smooth transition zone function (Fig.2). The loading front can be defined as the surface that separates the region under the glacier from the region outside the glacier. The position of the loading front can be found by solving the equation $F(x,t) = 1/2$, the middle value, for each time. This gives $x_{front} = -3000[m] + 4.03E\{-8t[\sec]\}$. At time $t = 5900$ *years*, the position of the loading

front is given by $x \approx 4500$ m. The velocity of the loading front is given by $dx_{front}/dt = 1.27$ m/year. From (7), the applied fluid pressure, the normal effective stress σ'_{zz} and the temperature change are approximately equal to zero outside the glacier on the upper surface. Under the glacier on the upper surface, the maximum fluid pressure $p_{\max}$ is set equal to 1 MPa, the maximum effective stress $\sigma'_{\max}$ is -0.3 MPa, and the maximum temperature change $T_{\max}$ is -10 C (Fig.2). We consider two loading cases. In the first case the rock is subjected to only the fluid pressure p and vertical compressive stress σ'_{zz} applied to the upper surface. In the second case the cooling (negative temperarure change) T is applied to the upper surface together with the fluid pressure and compressive stress. The properties of the rock are shown in Table 1.

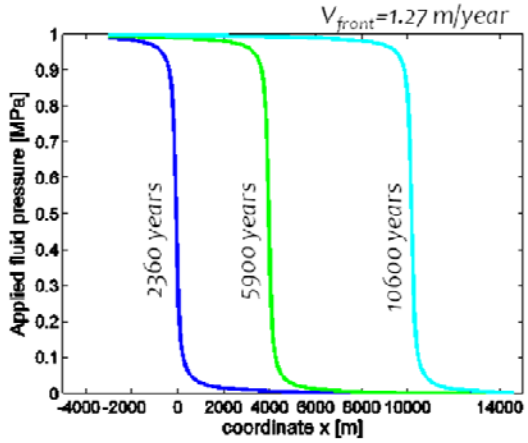

Figure 2. The profile of the glacial loading (fluid pressure) advancing along the *x*-axis

Figure 3 illustrates the temperature within the rock 5900 years after the start of the motion of the glacier. The initial temperature change is set equal to zero. The maximum temperature change prescribed on the upper surface is -10 C under the glacier, and zero outside the glacier. We observe that after 5900 years steady-state was not reached because at the lower surface of the rock the temperature is still warmer than -10 C.

Figure 4 illustrates the fluid pressure within the fractured rock at time 5900 years. (The figure on the left shows the fluid pressure within the rock subjected only to the fluid pressure and compressive stress. The figure on the right shows the response of the rock subjected to cooling in addition to the surface fluid pressures and normal stress. The initial pressure is taken equal to zero which corresponds to a fully drained condition; the in situ fluid pressures are excluded in these presentations). In the fractures beneath the glacier the fluid pressure quickly becomes uniform and equal to the maximum value of 1 MPa due to their large permeability. In the intact part of the rock near the lower surface, the pressure remains smaller than 1 MPa. We observe that the cooling does not change the fluid pressure near the upper surface of the rock, where the pressure is prescribed, but makes the fluid pressure smaller near the lower surface. This reduction will increase the vertical pressure gradient and, consequently, lead to the development of a faster fluid flow.

Figure 5 shows the vertical displacement or deflection in the fractured rock at time 5900 years. The displacement is negative which is indicative of the contraction of the rock. It is seen that the cooling increases the magnitude of the vertical displacement. In these figures the displacement of the deformed surface was magnified by 10000 times to highlight the various

effects of the poroelastic behaviour of the fractured rock mass, but the deformations are still small and can be described by the small strain theory.

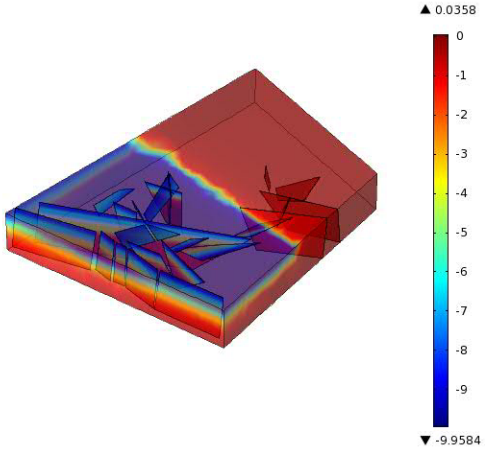

Figure 3. Temperature change distribution [^{o}C] within the rock mass 5900 years after the motion of glacier

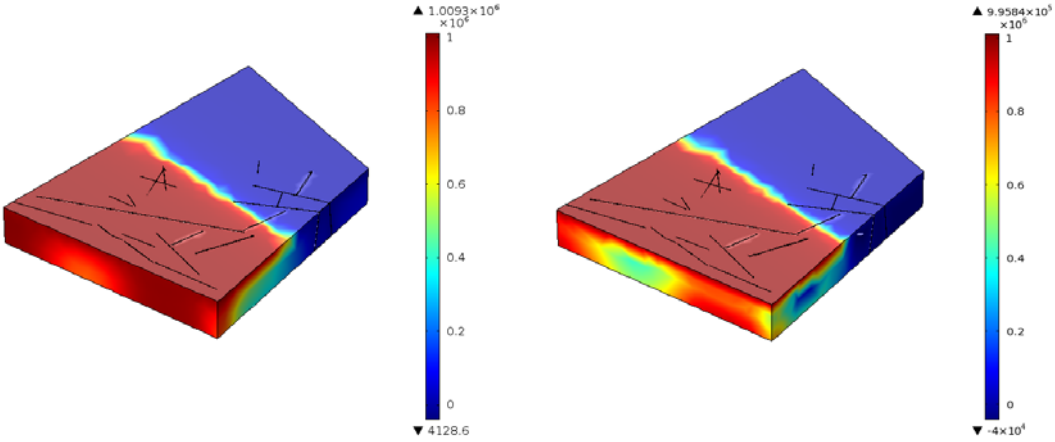

Figure 4. Distribution of fluid pressure [Pa] within the rock at 5900 years. The rock is subjected to the spatially non-uniform fluid pressure and compressive stress (left) and to glacial cooling, fluid pressure and compressive stress (right).

Figure 6 illustrates the vertical fluid velocity in the intact part of the fractured rock at time 5900 years. The vertical fluid velocity can be both positive and negative. Positive velocity implies that the fluid flows out of the rock, i.e., upwards, and negative velocity means that the fluid flows into the rock, i.e., downwards. It can be seen that the magnitude of the negative velocity is much larger than the positive velocity, which is consistent wth the direction of the pressure gradient vector. Under the glacier near the loading front the fluid flows into the rock with the maximum velocity. Upon application of the cooling of -10 C, this velocity increases almost by a factor of two from -6 E-13 m/s to -1.4 E-12 m/s. This can be explained by the reduction of the fluid pressure near the lower surface of the rock and thus increase of the vertical pressure gradient.

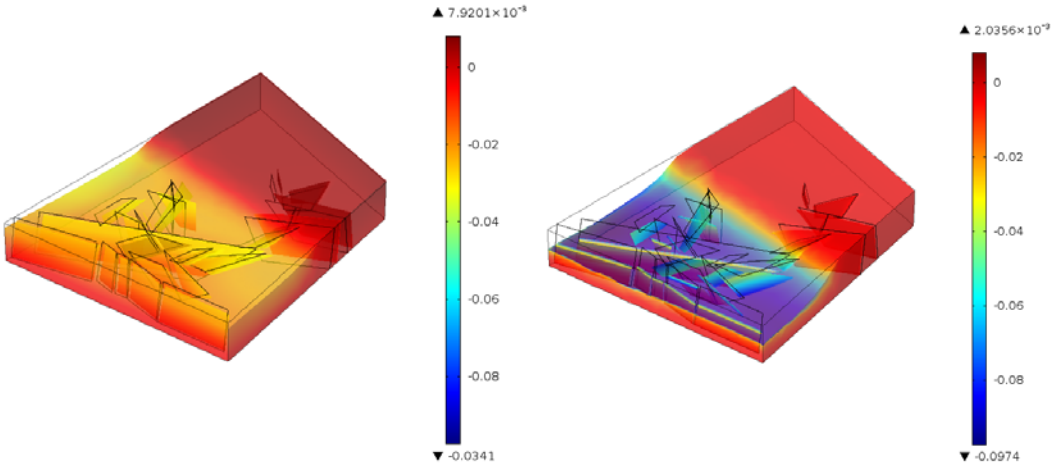

Figure 5. Distribution of the vertical displacement [m] inside the rock at time 5900 years. The rock is subjected to the spatially non-uniform fluid pressure, compressive stress (left) and to cooling, fluid pressure and compressive stress (right).

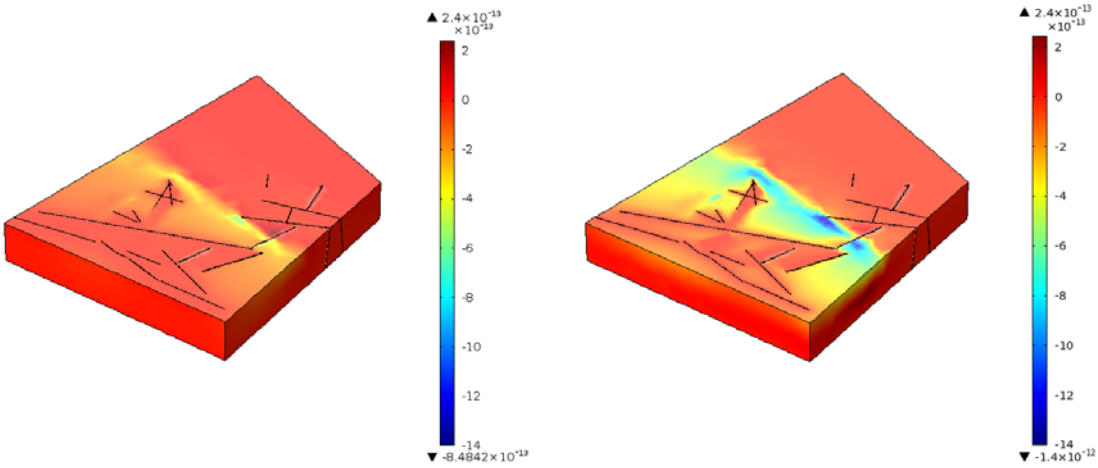

Figure 6. Distribution of the vertical fluid velocity [m/s] within the intact part of the rock at time 5900 years. The rock is subjected to the spatially non-uniform fluid pressure, compressive stress (left) and to the cooling, fluid pressure and compressive stress (right).

Figure 7 illustrates the vertical fluid velocity within the fractures of the rock at time 5900 years. It can be seen that in the fractures oriented vertically, the fluid velocity is much larger than in the intact part of the rock (compare with Figure 6). This can be explained by the large permeability of fractures compared to that of the intact rock. We observe that within the vertical fractures the fluid can flow in the positive and negative directions, but the fluid velocity in the negative direction (i.e. towards the lower surface of the rock, is larger). In the fractures having horizontal orientation the vertical fluid velocity is smaller than in the vertical fractures.

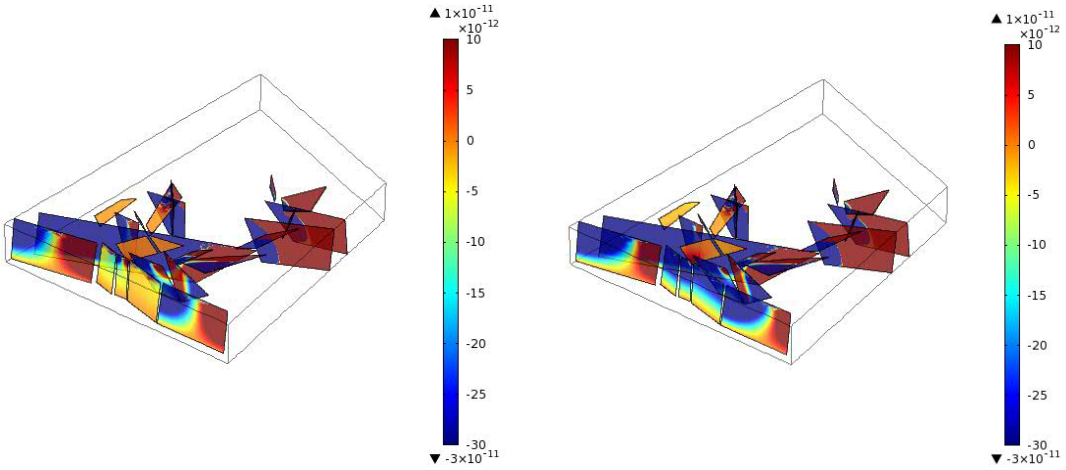

Figure 7. Distribution of the vertical fluid velocity [m/s] within the rock fractures at time 5900 years. The rock is subjected to the spatially non-uniform fluid pressure and compressive stress (left), and to glacier-induced cooling, fluid pressure and compressive stress (right).

Table 1. Properties of intact rock mass and fracture zones

Property	Intact rock mass	Fracture zone
Porosity n	0.05	0.05
Biot coefficient α	0.7	0.7
Young's modulus E_D	30 GPa	3 GPa
Poisson's ratio ν_D	0.25	0.25
Permeability k	1.55e-19 m^2 (deep rock)	3e-13 m^2
Dynamic viscosity γ	0.001 Pa·s	0.001 Pa·s
Fluid bulk modulus K_f	2.2 GPa	2.2 GPa
Thermal expansion coefficient of solid phase	8.3e-6 1/^{o}C	8.3e-6 1/^{o}C
Thermal expansion coefficient of fluid phase	69e-6 1/^{o}C	69e-6 1/^{o}C
Equivalent specific heat c_p^*	1830500 N/(m^2 K)	1830500 N/(m^2 K)
Equivalent conductivity k_c^*	3.66 W/(m K)	3.66 W/(m K)

4 CONCLUDING REMARKS

The influence of an advancing glacier on the thermo-hydro-mechanical response of the fractured rock was studied in detail. The motion of the glacier is simulated by applying non-zero fluid pressure, compressive stress and temperature change to a portion of the upper surface of the rock covered by the glacier. Outside the glacier the loads are set to zero. The glacier causes contraction of the rock, i.e., negative strain in the direction of the rock thickness. This deflection increases when the cooling is applied together with the fluid pressure and compressive stress. The fluid pressure in the fractured rock subjected to the glaciation loading is mainly positive. This fluid pressure increases with time as the glacier

advances to occupy a larger portion of the rock surface. The fluid pressure at the lower surface becomes smaller when the cooling is taken into account which results in the increase of the pressure gradient. The net vertical fluid velocity in the rock is primarily negative which suggests that the fluid mainly flows into the rock towards the lower surface of the rock. The fluid velocity in the fractures of the rock is about 1000 times larger than the velocity in the intact part of the rock. The velocity nearly doubles when the cooling is taken into account. The direction of the fluid velocity in the fractures is mainly negative but large velocities in the positive direction, i.e., towards the upper surface of the rock mass, also occur. It is believed that the direction of the fluid velocity vector depends on the fracture location and its angle of inclination.

The glaciation loading gives rise to the compressive and tensile mean effective stresses in the fractured rock. The tensile stresses can result in the formation of new fractures. When the cooling is not present, the dominant stress in the rock must be compressive and the mean effective stress averaged over the volume of the rock is compressive. The tensile stresses however may still occur beneath the glacier and exterior to the glacier. When the cooling is taken into account, the magnitude of tensile stresses may significantly increase and the average mean effective stress may become tensile.

It is of interest to study further the influence of the fractures on the response of the rock. For this purpose, the response of the fractured rock can be compared with that of the homogeneous rock, i.e., without fractures. Both rocks could be subjected to the same loading simulating the motion of the glacier, i.e. the fluid pressure and compressive stress applied to the top surface. As was mentioned before, the fluid velocity in the fractures is much larger than in the homogeneous rock. However, the fluid velocity in the intact part of the fractured rock, more precisely its average value, may be smaller, in absolute value, than the velocity in the homogeneous rock.

The magnitude of the mean effective stress can also be compared for fractured and homogeneous rocks. Since the loading is spatially non-uniform, the mean stress can be tensile near the upper surface of the homogeneous rock, especially near the loading front. This can be a potential site for creation of new fractures in the homogeneous rock. In the fractured rock the tensile mean stress in general may increase, and in addition, the mean stress can change the sign and become tensile in the location in which it was compressive in the homogeneous rock.

The response of the fractured rock subjected to the geostatic loading can also be examined. It is known that the geostatic loading causes contraction of the rock, i.e., the displacement towards the lower surface. The fluid pressure changes linearly from zero value on the upper surface to its maximum value on the lower surface. The mean effective stress in the fractured rock must be mostly compressive, but near the upper surface the mean stress may become tensile. It appears that the tensile stress may be caused by the presence of the fractures since in the homogeneous rock subjected to the same geostatic loading the mean stress must be compressive throughout. Therefore, in the fractured rock the geostatic loading can also lead to creation of new fractures originating at the upper surface.

ACKNOWLEDGEMENT

The work described in this paper was initiated through research support provided by the Nuclear Waste Management Organization, Ontario and through a Discovery Research Grant awarded by the Natural Sciences and Engineering Research Council of Canada.

REFERENCES

Barenblatt, G.I., Zeheltsov, I.P., Kochina, I.F. (1960) Basic concepts in the theory of seepage of homogeneous liquids in fissured rocks. *Journal of Applied Mathematics and Mechanics*, 24(5), p. 1286-1303.

Biot, M.A. (1941) General theory of three-dimensional consolidation. *Journal of Applied Physics*, 12, p. 155-164.

Cacas, M.C., Ledoux, E., Demarsily, G., Tillie, B., Barbreau, A., Durand, E., Feuga, F., Peaudecerf, P. (1990) Modeling fracture flow with a stochastic discrete fracture network – calibration and validation, 1. The flow model. *Water Resources Research*, 26(3), p. 479-489.

Carrera, J., Heredia, S., Vomvoris, S., and Hufschmied, P. (1990) Modelling of flow with a small fractured monzonitic gneiss block. In Hydrogeology of low permeability environments, *International Association of Hydrogeologist, Hydrogeology: Selected Papers*, 2. Edited by S.P. Neuman and I. Neretnieks. Heise, Hanover, Germany, p. 115-167.

Carrera, J.J., Lurdes, M.L. (2000) Mixed discrete-continuum models: a summary of experiences in test interpretation and model prediction. In: *Dynamics of Fluid in Fractured Rock. Geophysical Monograph* 122, American Geophysical Union, Washington, D.C., p. 251-266.

Chan, T., Christiansson, R., Boulton, G.S., Ericsson, L.O., Hartikainen, J., Jensen, M.R., Mas Ivars, D., Stanchcell, F.W., Vistrand, P., Wallroth, T. (2005) DECOVALEX III BMT 3/BENCHPAR WP4: The thermo-hydro-mechanical responses to a glacial cycle and their potential implications for deep geological disposal of nuclear fuel waste in a fractured crystalline rock mass, *International Journal of Rock Mechanics & Mining Sciences*, 42, p. 805-827.

Chan, T., Stanchell, F.W. (2008) *DECOVALEX THMC TASK E – Implications of Glaciation and Coupled Thermohydromechanical Processes on Shield Flow System Evolution and Performance Assessment*. HWMO TR-2008-03.

Dershowitz, W.S., Wallmann, P., Geier, J.E., Lee, G. (1991) Discrete fractured network modeling of tracer migration experiments at the SCV site. SKB Report 91-23. Swedish Nuclear Power and Management Co., Stockholm, Sweden.

Hsieh, P.A., Neuman, S.P., Stiles, G.K., Simpson, E.S. (1985) Field determination of the three-dimensional hydraulic conductivity tensor of anisotropic media, 2. Methodology and application to fractured rocks. *Water Resources Research*, 21(11), p. 1667-1676.

Khalili, N., Selvadurai, A.P.S. (2003) A Fully Coupled Constitutive Model for Thermo-Hydro-Mechanical Analysis in Elastic Media with Double Porosity. *Geophysical Research Letters* 30(24), p. SDE 7-1, 7-5.

Long, J.C.S., Billaux, D.M. (1987) From field data to fracture network modelling: an example incorporating spatial structure. *Water Resources Research*, 23(7), p. 1201-1216.

Long, J.C.S., Witherspoon, P.A. (1985) The relationship of the degree of interconnection to permeability in fracture networks. *Journal of Geophysical Research*, 90(B4), p. 3087-3098.

Long J.C.S., Gilmour, P., Witherspoon, P.A. (1985) A model for steady fluid flow in random three-dimensional networks of disc-shaped fractures. *Water Resources Research*, 21(8), p. 1105-1115.

Massart, T.J., Selvadurai, A.P.S. (2012) Computational homogenization based evaluation of damage-induced permeability evolution in quasi-brittle geomaterials. *Journal of Geophysical Research* (*Solid Earth*), doi:10.1029/2012JB009251

Noorishad, J., Tsang, C.F., Witherspoon, P.A. (1984) Coupled thermo-hydraulic-mechanical phenomena in saturated fractured porous rocks: Numerical approach. *Journal of Geophysical Research* 89, p. 10365-10373.

Norris A. (1992) On the correspondence between poroelasticity and thermoelasticity, *Journal of Applied Physics* 71(3), p. 1138-41.

Nguyen, T.S., Selvadurai, A.P.S. (1998) A model for coupled mechanical and hydraulic behaviour of a rock joint. *International Journal for Numerical and Analytical Methods in Geomechanics*, 22, p. 29-48.

Oda, M. (1985) Permeability tensor for discontinuous rock masses. *Geotechnique*, 35(4), p. 483-495.

Pearce, A., Pande, G. N.(2007) *SDPCAL: Stress Dependant Permeability Calculations*, Technical Report, Schlumberger Geomechanics Centre of Excellence, Bracknell, England.

Pruess, K., Narasimhan, T.N. (1985) A practical method for modeling fluid and heat flow in fractured porous media. *Society of Petroleum Engineers Journal*, 25(1), p. 14-16.

Rice, J. R., Cleary, M.P. (1976) Some basic stress-diffusion solutions for fluid saturated elastic porous media with compressible constituents. *Reviews of Geophysics and Space Physics* 14: p. 227-241.

Rutqvist, J., Wu, Y.-S., Tsang, C.-F., Bodvarsson, G. (2002) A modeling approach for analysis of coupled multiphase fluid flow, heat transfer, and deformation in fractured porous rock. *International Journal of Rock Mechanics and Mining Science*, 39, p. 429-442.

Selvadurai, A.P.S. (Ed.) (1996) *Mechanics of Poroelastic Media*, Kluwer Academic Publishers, Dordrecht.

Selvadurai, A.P.S. (2007) The analytical method in geomechanics. *Applied Mechanics Reviews*, Vol. 60, p. 87-106.

Selvadurai, A.P.S., Nguyen, T.S. (1995) Computational modeling of isothermal consolidation of fractured porous media. *Computers and Geotechnics*, 17, p. 39-73.

Selvadurai, A.P.S., Selvadurai, P.A. (2010) Surface permeability tests: experiments and modelling for estimating effective permeability. *Proceedings of the Royal Society Mathematical and Physical Sciences Series*, 466, p. 2819-2846.

Selvadurai, A.P.S. and Suvorov, A. (2010) *Application of the COMSOL Multiphysics Code for Coupled Thermo-Hydro-Mechanical Modelling Relevant to Deep Geologic Repositories*, Nuclear Waste Management Office Report NWMO TGS-509, ON, Canada.

Selvadurai, A.P.S., Suvorov, A.P. (2012) Boundary heating of poro-elastic and poro-elasto-plastic spheres. *Proceedings of the Royal Society, Series A*, doi: 10.1098/rspa.2012.0035

Selvadurai, A.P.S., Suvorov, A.P., Selvadurai, P.A (2011) *Application of the COMSOL Multiphysics Code for Coupled Thermo-Hydro-Mechanical Modeling of Fractured Rock Mass Subjected to Glaciation Loads* , Nuclear Waste Management Office Report NWMO TGS-510, ON, Canada

Selvadurai, A.P.S., Suvorov, A.P., Selvadurai, P.A. (2013) Thermo-hydro-mechanical behaviour of a fractured rock mass during a glacial advance (*in preparation*)

Sitharam, T.G., Sridevi., J., Shimizu, N. (2001) Practical equivalent continuum characterization of jointed rock masses. *International Journal of Rock Mechanics & Mining Sciences*, 38(3), p. 437-448.

Suvorov, A.P., Selvadurai, A.P.S. (2011) Geomaterial properties of porous materials with randomly oriented ellipsoidal pores estimated via effective medium methods and a computational approach. *Computers and Geotechnics*, 38, p. 721-730.

Tsang, Y.W., Tsang, C.F., Hale, F.V. (1996) Tracer transport in a stochastic continuum model of fractured media. *Water Resources Research*, 32(10), p. 3077-3092.

Zhang, Xi, Jeffrey, R.G., Thiercelin, M. (2009) Mechanics of fluid driven fracture growth in naturally fractured reservoirs with simple network geometries. *Journal of Geophysical Research*, 114, B12406.

MODELLING SWELLING BEHAVIOR OF ANHYDRITIC CLAYEY ROCKS

A. Ramon
Department of Geotechnical Engineering and Geosciences. Universitat Politècnica de Catalunya, Barcelona, Spain

International Center for Numerical Methods in Engineering (CIMNE). Barcelona.

E.E. Alonso
Department of Geotechnical Engineering and Geosciences. Universitat Politècnica de Catalunya, Barcelona, Spain

ABSTRACT: *The swelling behavior observed in anhydritic rocks is explained by the precipitation of gypsum crystals in open discontinuities. Gypsum crystals growing in discontinuities contribute to open them and induce deformations or pressures (if the displacements are restrained). A model has been formulated to reproduce the expansive behavior in sulphated rocks. The formulation describes the kinetics of dissolution and precipitation of sulphated minerals and transforms the mass of precipitated gypsum to imposed swelling strains due to gypsum crystal growth. The model also keeps track of the solute transport and takes into account the effect of the existing load on crystal growth. A simulation of the heave observed in Pont de Candí Bridge is performed. The calculations reproduce the long term vertical displacements measured at the ground surface and the distribution of vertical strains measured in depth. A sensitivity analysis is also reported.*

1 INTRODUCTION

Anhydritic and gypsiferous clay rocks often experience the development of significant expansion. Several cases of swelling behavior observed in tunnels excavated through sulphated clay rocks in Central Europe and Spain have been described in the literature (Wittke and Pierau, 1979; Kovari et al, 1988; Alonso et al., 2007). The development of expansion in tunnels concentrates in an active expanding layer under the tunnel floor and typically evolves in time without apparent stabilization.

The development of swelling strains in sulphated clayey rocks has also been observed below foundations at significant depths. This is the case of Pont de Candí railway bridge which has experienced a sustained heave at high rates ranging from 5 to 10 mm/month (Alonso and Ramon (2012) and Ramon and Alonso (2012)) The bridge crosses a valley which was subjected to intense tectonic activity, which resulted in faults and folded strata. Sediments belong to old Tertiary formations. Each pillar of the bridge is founded on an Eocene hard red claystone, having variable contents of anhydrite and gypsum, by means of a massive foundation consisting of a group of 3x3 bored piles, 1.65 m in diameter and 20 m long in average, capped by a rigid slab as shown in Figure 1. Long sliding micrometers, up to 60 m long, were installed near the four central pillars of the bridge. They recorded the development of increasing upward vertical displacements at depth, in an active layer 9-15 m thick. This active layer was located below the tip of the piles, within an anhydritic gypsiferous claystone. Repeated measurements of vertical displacements recorded in depth indicated a concentration of increasing deformations in the active layer without significant movements at shallower or deeper positions. Another characteristic of the records of all the

extensometers was that the measured vertical displacements in each extensometer evolve in time following the same pattern in depth over time (Figure 2). The maximum values of vertical strain were always measured at the same depths. The expansion phenomenon resulted not only in the heave of piles and the viaduct itself, but also in a ground heave which could be measured by a network of surface topographic marks that covered an area 200 meters wide centered along the axis of the viaduct. To remediate the heave of the structure an embankment was built partially filling the valley of Pont de Candí viaduct. This remedial measure was inspired by the belief that applying vertical stress on the active layer would reduce the rate of heave and eventually would be able to eliminate it. The rate of measured heave on the structure after the construction of the embankment decreased. Figure 2 shows the measurements of vertical strains in depth before and after the construction of the embankment. Compressive strains were also measured in the layers above the active layer some time after the application of embankment loading (Figure 2). Sliding micrometers measured a decreasing rate of vertical strains in the active layer after the construction of the embankment (Figure 3).

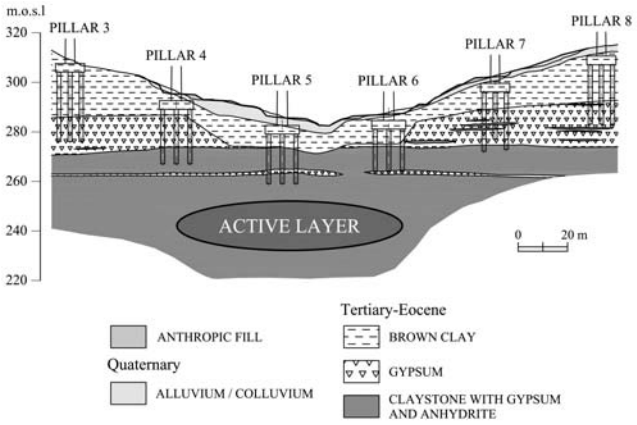

Figure 1. Location of the active layer and geological profile along the axis of Pont de Candí Bridge

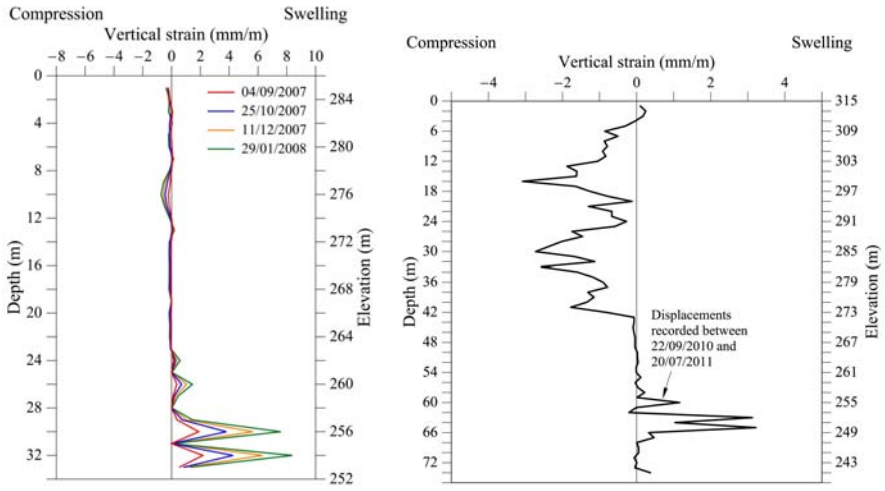

Figure 2. Vertical strains measured near Pillar P5 a) before the construction of the embankment. Reference measurement from July 12, 2007; b) after the construction of the embankment

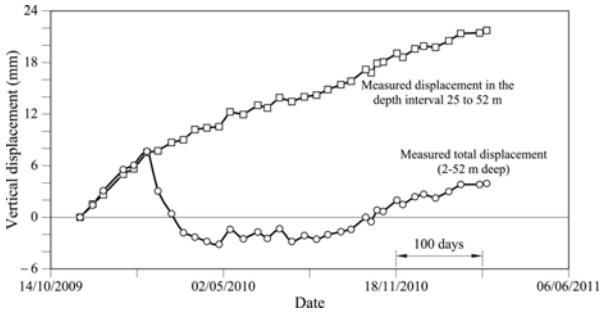

Figure 3. Evolution of the integral of vertical strains measured between pillars P6 and P7 by a sliding micrometer.

2 SWELLING PHENOMENA

Swelling phenomena in sulphated clayey rocks are explained by the precipitation of gypsum crystals in open discontinuities. The presence of anhydrite plays a central role in the phenomenon. Figure 4 shows the solubility of gypsum and anhydrite for different temperatures. Since the solubility of anhydrite is higher than the solubility of gypsum below 56ºC water in contact with the anhydritic gypsiferous clayey rock will tend to dissolve anhydrite (CaSO4) until the concentration of calcium sulphate in water reaches the solubility of anhydrite. This sulphate concentration implies supersaturation conditions with respect to gypsum (CaSO4·H2O). Therefore the excess of calcium sulphate dissolved (with respect to the solubility of gypsum) will tend to precipitate as gypsum crystals. Precipitation of crystals occurs more easily if some "open" space is available. Pores of claystones provide an extremely reduced space and water flow is essentially restrained through them. But joints provide a more favourable environment for crystal growth: the "open" space increases dramatically, as well as the permeability.

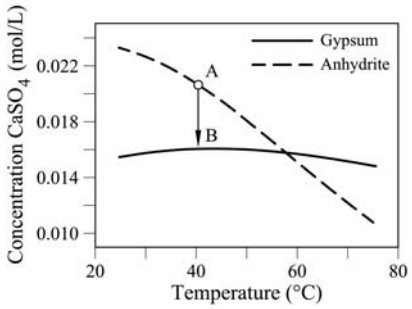

Figure 4. Solubility of anhydrite and gypsum for different temperatures

A conceptual representation of this interpretation is sketched in Figure 5. The figure represents a fracture in the clayey rock with gypsum and anhydrite crystals on the surface of the faces of the fracture and also the flow of water through it. When pure water circulates through the fracture water dissolves anhydrite and the concentration of solute increases. Dissolution of anhydrite will proceed until the equilibrium concentration with respect to anhydrite is reached. The precipitation of calcium sulphate in gypsum crystals will occur when saturated water with respect to anhydrite enters in contact with gypsum crystals. Later on, water will reach again the solubility of anhydrite and the process will continue.

Swelling will be controlled not only by the total mass of the precipitated gypsum (which may occur at a distance from the source of anhydrite dissolution) but also by the geometry of

precipitated crystals and its interaction with the surrounding soil/rock. The process of precipitation of gypsum in discontinuities is thought to act as a local jacking effect pushing apart the rock mass, opening discontinuities and inducing swelling strains.

Hydraulic cross-hole tests performed in the area of Pont de Candí viaduct revealed the existence of horizontal hydraulically connected fractures in the active layer which provided the necessary open space for gypsum crystals to grow and also confirmed the presence of circulating water. Above and below the active layer a sharp decrease of the permeability was found.

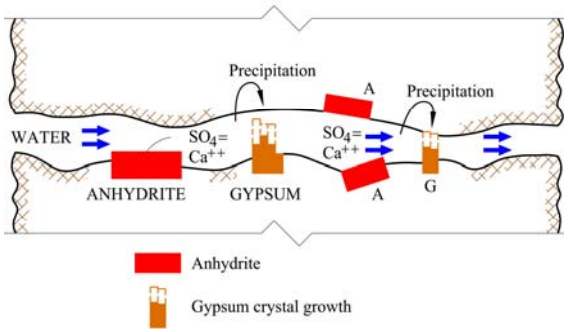

Figure 5. Conceptual representation of the mechanism of swelling due to gypsum precipitation in a fracture

3 MODEL FORMULATION

Figure 6 shows a representative volume of the active layer under the existing total stresses. The precipitation of gypsum in discontinuities will tend to open the discontinuities and will result in the development of deformations whose direction and intensity will be controlled by the geometry of fracture families (Figure 6a and Figure 6b).

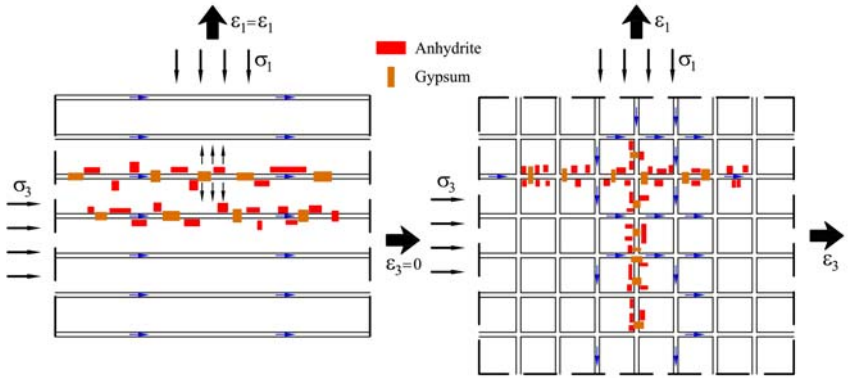

Figure 6. A "representative element" of sulphated rock for (a): swellling in vertical direction, (b): swelling in two directions

The phenomenon has been formulated within a general framework of hydromechanical analysis for saturated and unsaturated porous media. The material involved in the swelling mechanism is not a standard material. The solid skeleton of the rock (Figure 7) is made up of an insoluble clay matrix and two soluble minerals, gypsum and anhydrite, which may dissolve and precipitate. This structure determines the formulation of mass balance of solid phase. The model should describe the processes of dissolution and precipitation of minerals, the effect of dissolution or precipitation of gypsum in the water sink/source term of the

equation of the mass balance of water and the mechanical effects (swelling strains and pressures). The formulation also needs to keep track of the solute transport.

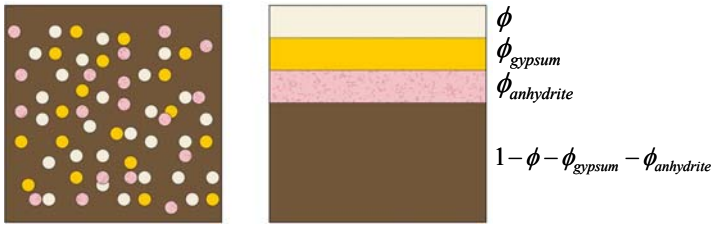

Figure 7. Phase diagram of porous sulphated rock

The three mass balance equations for the insoluble clay minerals, soluble gypsum and soluble anhydrite are:

$$\frac{\partial}{\partial t}\left(\rho_s\left(1-\phi-\phi_{anh}-\phi_{gyp}\right)\right)+\nabla\cdot\left[\left(\rho_s\left(1-\phi-\phi_{anh}-\phi_{gyp}\right)\right)\frac{d\mathbf{u}}{dt}\right]=0 \tag{1}$$

$$\frac{\partial\left(\rho_{gyp}\phi_{gyp}\right)}{\partial t}+\nabla\cdot\left[\left(\rho_{gyp}\phi_{gyp}\right)\frac{d\mathbf{u}}{dt}\right]=\frac{dm_{gyp}}{dt} \tag{2}$$

$$\frac{\partial\left(\rho_{anh}\phi_{anh}\right)}{\partial t}+\nabla\cdot\left[\left(\rho_{anh}\phi_{anh}\right)\frac{d\mathbf{u}}{dt}\right]=\frac{dm_{anh}}{dt} \tag{3}$$

In these equations ρ_s, ρ_{gyp} and ρ_{anh} are the densities of the insoluble minerals, gypsum and anhydrite, and **u** is the displacement vector, which is accepted as a unique field for the porous medium. ϕ_{gyp} and ϕ_{anh} describe the volume fractions of gypsum and anhydrite. The rates of precipitated or dissolved mass of gypsum and anhydrite (*dm/dt*) are introduced as source/sink terms in the mass balances of the soluble solid phases (Equations 2 and 3).
Using the material derivative

$$\frac{D_s(\bullet)}{Dt}=\frac{\partial(\bullet)}{\partial t}+\frac{d\mathbf{u}}{dt}\cdot\nabla(\bullet) \tag{4}$$

equations (1), (2) and (3) become

$$\frac{D_s\phi}{Dt}+\frac{D_s\phi_{anhydrite}}{Dt}+\frac{D_s\phi_{gypsum}}{Dt}=\frac{\left(1-\phi-\phi_{anhydrite}-\phi_{gypsum}\right)}{\rho_s}\frac{D_s\rho_s}{D_t}+ \\ +\left(1-\phi-\phi_{anhydrite}-\phi_{gypsum}\right)\nabla\cdot\frac{d\mathbf{u}}{dt} \tag{5}$$

$$\frac{D_s\phi_{gypsum}}{Dt}=-\frac{\phi_{gypsum}}{\rho_{gypsum}}\frac{D_s\rho_{gypsum}}{Dt}-\phi_{gypsum}\nabla\cdot\frac{d\mathbf{u}}{dt}+\frac{1}{\rho_{gypsum}}\frac{dm_{gypsum}}{dt} \tag{6}$$

$$\frac{D_s\phi_{anhydrite}}{Dt}=-\frac{\phi_{anhydrite}}{\rho_{anhydrite}}\frac{D_s\rho_{anhydrite}}{Dt}-\phi_{anhydrite}\nabla\cdot\frac{d\mathbf{u}}{dt}+\frac{1}{\rho_{anhydrite}}\frac{dm_{anhydrite}}{dt} \tag{7}$$

Combining Equations (5), (6) and (7) the mass balance equation of solid phase is obtained:

$$\frac{D_s\phi}{Dt}=\left[\frac{\left(1-\phi-\phi_{anh}-\phi_{gyp}\right)}{\rho_s}\frac{D_s\rho_s}{Dt}+\frac{\phi_{anh}}{\rho_{anh}}\frac{D_s\rho_{anh}}{Dt}+\frac{\phi_{gyp}}{\rho_{gyp}}\frac{D_s\rho_{gyp}}{Dt}\right]+ \\ +\left(1-\phi\right)\nabla\cdot\frac{d\mathbf{u}}{dt}-\frac{1}{\rho_{gyp}}\frac{dm_{gyp}}{dt}-\frac{1}{\rho_{anh}}\frac{dm_{anh}}{dt} \tag{8}$$

Accepting that densities ρ_s, ρ_{gyp} and ρ_{anh} are constant, the variation of porosity in time becomes,

$$\frac{D_s\phi}{Dt}=\left(1-\phi\right)\nabla\cdot\left(\frac{d\mathbf{u}}{dt}\right)-\frac{1}{\rho_{gyp}}\frac{dm_{gyp}}{dt}-\frac{1}{\rho_{anh}}\frac{dm_{anh}}{dt} \tag{9}$$

Eq. 9 indicates that the variation in porosity in time has two components, the volumetric strain rate induced by solid displacements and the volumetric strain rate induced by the precipitation or dissolution of crystals.

The kinetics of precipitation/dissolution of gypsum and anhydrite are described by means of two mass rate equations, which have been formulated following the structure suggested by Lasaga (1984)

$$\frac{dm_{gyp}}{dt}=\sigma_c\kappa\xi_{gyp}\phi_{gyp}\left(\left|\left(\frac{\omega_l^m}{\omega_{l_{sat,gyp}}^m\left(T,p\right)}\right)^\theta-1\right|\right)^\eta \tag{10a}$$

$$\frac{dm_{anh}}{dt}=\sigma_c\kappa\xi_{anh}\phi_{anh}\left(\left|\left(\frac{\omega_l^m}{\omega_{l_{sat,anh}}^m\left(T,p\right)}\right)^\theta-1\right|\right)^\eta \tag{10b}$$

where:

$$\xi_{gyp}=\frac{\omega_l^m-\omega_{l_{sat,gyp}}^m}{\left|\omega_l^m-\omega_{l_{sat,gyp}}^m\right|} \tag{11a}$$

$$\xi_{anh}=\frac{\omega_l^m-\omega_{l_{sat,anh}}^m}{\left|\omega_l^m-\omega_{l_{sat,anh}}^m\right|} \tag{11b}$$

where, ω_l^m is the mass fraction of dissolved sulphate in water. The precipitated or dissolved mass of mineral in time depends on: the "degree" of superasaturation or undersaturation, the volumetric fraction of mineral crystals, ϕ_{anh} and ϕ_{gyp}, the specific surface of crystals, σ_c (m^2 of crystal surface/m^3 of crystal) and a rate constant κ (kg/(s·m^2)).

The equilibrium mass fractions of calcium sulphate in water at saturation conditions with respect to gypsum ($\omega_{l_{sat,gyp}}^m$) and with respect to anhydrite ($\omega_{l_{sat,anh}}^m$) depend on temperature, T, and on the prevailing pressure acting on crystals, p, as described by Scherer (1999):

$$\omega_{l_{sat}}^m=\omega_{0l_{sat}}^m\,exp\left(\frac{pv_c}{R_gT}\right) \tag{12}$$

where, v_c is the molar volume of the crystal; R_g is the ideal gas constant, and T is the absolute temperature. Temperature was constant in the case analyzed. This was probably the situation in the active region below the pile's tip.

Gypsum precipitation incorporates molecules of water in its crystalline structure. This process is taken into account in the source/sink term of the mass balance of water equation. The mass balance equation for the water can be written as:

$$\phi \frac{D_s \rho_l}{Dt} + \rho_l \frac{D_s \phi}{Dt} + \rho_l \phi \nabla \cdot \left(\frac{d\mathbf{u}}{dt} \right) + \nabla \cdot (\rho_l \mathbf{q}_l) = f^w \tag{13}$$

where, ρ_l is the density of the water; $\boldsymbol{q}_l$ is the flow rate of water, and f^w any sink or source of water. One kg of gypsum captures 0.21 kg of water when it precipitates. However, the f^w term is negligible in the open system analyzed here.

Equilibrium equation in terms of total stresses reads

$$\nabla \cdot \boldsymbol{\sigma} + \mathbf{b} = 0 \tag{14}$$

where $\boldsymbol{\sigma}$ is the stress tensor and $\mathbf{b}$ is the vector of body forces. The strains induced by precipitation of gypsum are calculated from the amount of precipitated volume of gypsum and the prevailing stress acting on crystals and are considered as imposed deformations.

$$\frac{d\varepsilon_i}{dt} = \frac{\gamma_i}{\rho_{gyp}} \frac{dm_{gyp}}{dt} \quad , \quad i = 1,\ 2,\ 3 \ ; \tag{15}$$

1=Vertical (z) ; 2, 3= Horizontal (h)

The parameter γ_i is a coefficient that takes into account the effect of the stress applied on crystals on the strains induced by precipitation. It will be assumed to be controlled by stress,

$$\gamma_i = \gamma_{max} e^{-b\sigma_i'} \text{ for } \sigma_i' > 0 \text{, i=1, 2, 3} \tag{16a}$$

$$\gamma_i = \gamma_{max} \text{ for } \sigma_i' = 0 \text{, i=1, 2, 3} \tag{16b}$$

(a given volume of precipitated crystals is expected to induce higher swelling strains under a lower confining stress).

The model needs to keep track of the minerals dissolved in water. Dissolution of both anhydrite and gypsum results in calcium sulphate solute ($CaSO_4$). Then, one equation for the mass conservation of solute is formulated for calcium sulphate solute transport:

$$\begin{aligned} &\rho_l \omega_l^m \nabla \cdot \left(\frac{du}{dt} \right) + \phi \frac{D_s \left(\rho_l \omega_l^m \right)}{Dt} + \nabla \cdot \left(\rho_l \omega_l^m q_l - \boldsymbol{D} \nabla \cdot \omega_l^m \right) = \\ &= -\frac{dm_{gyp}}{dt} \left(1 - \frac{\rho_l \omega_l^m}{\rho_{gyp}} \right) - \frac{dm_{anh}}{dt} \left(1 - \frac{\rho_l \omega_l^m}{\rho_{anh}} \right) \end{aligned} \tag{17}$$

In this equation the product $\rho_l \omega_l^m$ is the concentration of sulphate in water in units of mass/volume. The term $\boldsymbol{D} \nabla \cdot \omega_l^m$ accounts for the diffusive rate of flow following a Fick's law.

$\boldsymbol{D}$ is the diffusion coefficient. The precipitation and dissolution of sulphated minerals are treated as a source or sink of calcium sulphate solute.

This formulation was included in the Finite Element program for coupled thermo-hydro-mechanical analysis in porous media CODE BRIGHT (DETCG, 2010 and DIT-UPC 2002)

4 SIMULATION OF SWELLING BEHAVIOR IN PONT DE CANDÍ BRIDGE

A column 15 m wide and 55 m long of the foundation material at the central pillar of the bridge (P5) has been modelled under plane strain conditions. Figure 8 shows the geometry of the model. The active layer, 15 m thick, was included at the position estimated by the sliding micrometers. Below and above the active layer the soil is non expansive. The column of foundation material was assumed to be confined laterally. An inert porous material was used at both sides of the column to facilitate the definition of the flow boundary conditions. The horizontal flow conditions in the active layer were reproduced. A phreatic level was defined above the active layer and a horizontal flux of water was imposed in the active zone. The fractured and highly permeable sulphated claystone was modelled as a porous material.

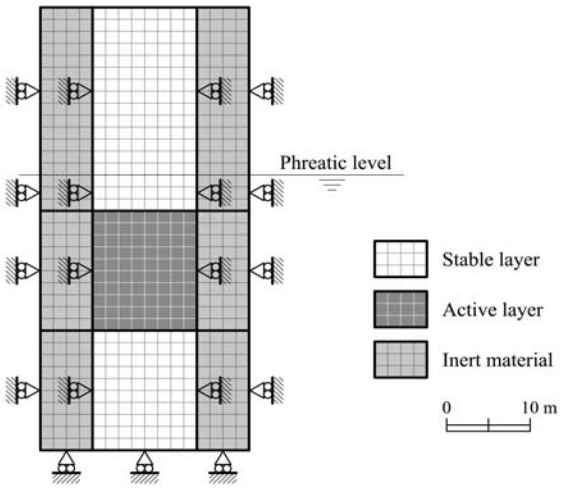

Figure 8. Geometry of finite element model.

The initial mineral porosities were approximated from observations in recovered cores and were considered homogeneous in the active layer. The compound kinetic coefficient, $\sigma_c \cdot \kappa$, was back calculated by matching the swelling records with the calculated heave. The hydraulic characteristics of the material were defined by the initial open porosity and the intrinsic permeability. The initial open porosity (0.09) was higher than rock matrix porosity to account for fissures. An intrinsic permeability of $2 \cdot 10^{13}$ m^2, found in the cross-hole hydraulic tests, was adopted for the active layer. An isotropic linear elastic behaviour was considered for the material of the column. The initial state of stress was given by an at rest earth pressure coefficient K_0=2.

An attempt to reproduce the distribution of swelling strains measured in the active layer has been performed. Gypsum precipitation occurs in open fractures. Measured vertical swelling strains accumulate over time in thin bands inside the active layer (Figure 2) probably as a result of a relative higher presence of fractures at those depths. These bands, having a higher intensity of fractures, will have more anhydrite in contact with water. The distribution in depth of the initial anhydrite content at depths corresponding to the active layer has been

chosen according to the pattern of swelling strains measured near the central pillar P5 (Figure 2). The values of initial anhydrite content at different depths have been varied to adjust the calculated vertical displacements to the measured heave in the field (Figure 9). Figure 10 shows the calculated vertical strains within the active layer. The simulation reproduces the swelling strains measured before the construction of the embankment (Figure 10 and Figure 2a).

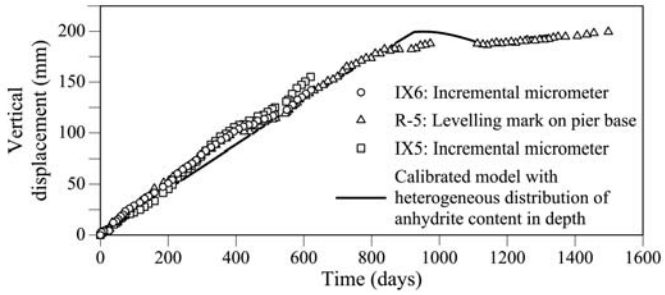

Figure 9. Surface heave measured in the field and calculated with the non homogeneous distribution of anhydrite.

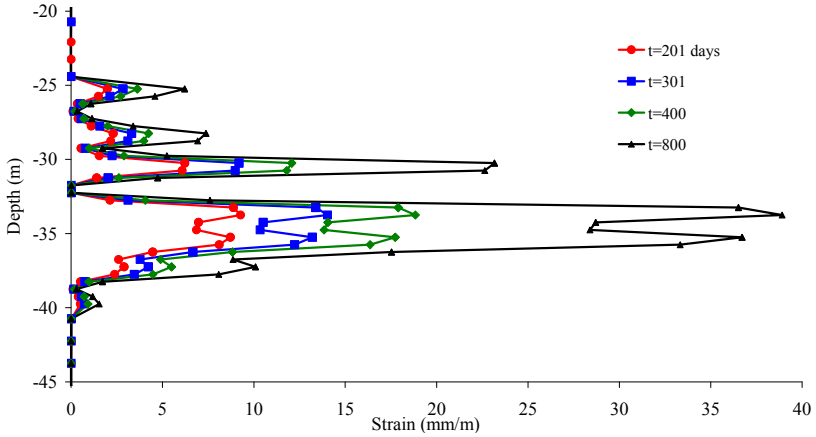

Figure 10. Calculated vertical strains in the active layer at different times

The comparison between the calculated heave at the surface of the column and the evolution of the heave measured by topographic levelling at the ground surface level is given in Figure 9. The vertical strains due to crystal growth only occur in the active layer and the material located above the active layer is pushed upwards. The calculated vertical displacements reproduce the field heave records in a four year period of observations. The construction of the embankment was simulated by applying a loading at the upper boundary of the column. The model reacts to embankment construction and the calculated vertical displacement reproduce the field measurements recorded after the "construction" of the embankment (t=924 days in Figure 9).

A sensitivity analysis was performed to study the relevance of the model parameters. The model described was considered as a base case. For the study of the effect of each parameter only the value of the parameter analyzed was changed, and the other parameters maintained the value they had in the base case. It was found that the initial mineral content has an important effect on the development of heave because it controls the rates of dissolution and precipitation (Eq. 10). Gypsum content has a small effect. However, anhydrite volumetric

fraction has a very significant effect on calculated swelling. The value of equilibrium concentration at saturation with respect to gypsum and anhydrite, which depends on temperature, has also a significant effect on vertical strains. In contrast, the initial porosity, the permeability and the induced gradient have minor effect on the calculated heave. Stress effects are substantial in the model developed. Several cases characterized by different embankment heights have been calculated to examine the effect of the increment of load applied at the surface on the vertical strains calculated (Figure 11). The rates of the calculated vertical displacements after the simulation of the construction of the embankment for different load increments are summarized in Figure 12a. Actual observations of heave rate (figure 12b) compare reasonably well with calculations.

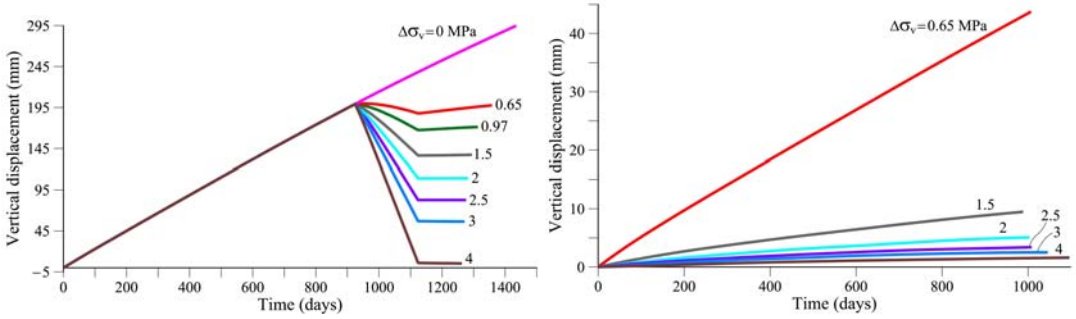

Figure 11. Calculated vertical displacements at the natural ground surface.

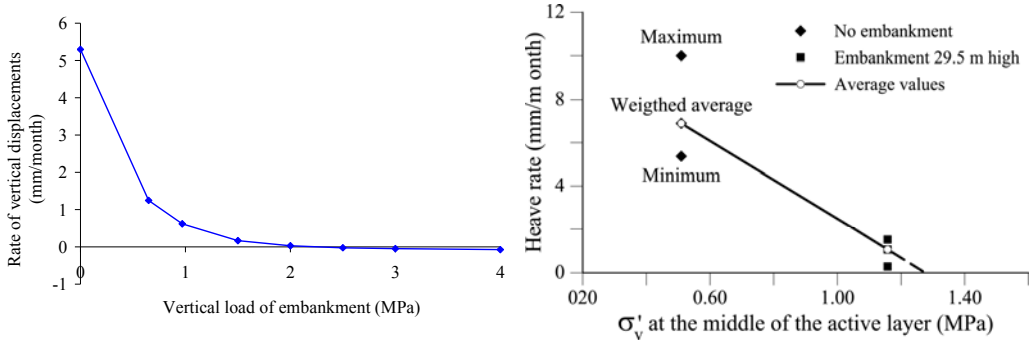

Figure 12. a) Calculated rates of vertical displacements after 70 days of application of vertical load; b) Effect of vertical confining stress on the heaving rate measured in the bottom part of pier 5

5 CONCLUSIONS

Pont de Candí is a unique case of heave induced by gypsum crystal growth. The process was probably activated by the construction of the foundation piles and reconnaissance borings. In this way water was transferred from the upper aquifer to the underlying fissured level of anhydritic claystone. Gypsum crystals precipitate whenever supersaturated sulphate conditions are found. The presence of anhydrite guarantees supersaturation. The process has been simulated by formulating the balance equations of a porous media having insoluble as well as soluble minerals. Rate equations for dissolution/precipitation are based on past accumulated research on this topic. Displacements and stresses are a consequence of the volume of precipitated mass. Direct observations indicate that crystal grows in discontinuities, a phenomenon controlled by stresses. Finally the concentration of sulphate

has to be determined by means of a transport equation. Parameter identification required the back analysis of field heave records. Once calibrated, the model is able to predict the long term performance of bridge foundations and in particular, the effects of adding weight to counteract the foundation heave.

6 ACKNOWLEDGEMENTS

The support and funding provided by the Spanish National Agency for Railway Infrastructure (ADIF) is highly appreciated.

7 REFERENCES

Alonso, E. E., Berdugo, I. R., Tarrago, D. & Ramon, A. (2007). Tunnelling in sulphate claystones. Invited lecture. Proc. 14th Eur. Conf. Soil Mech. Geotech. Engng, Madrid 1, 103–122.

Alonso, E. y Ramon, A. (2012) Massive attack to cement-treated railway embankments. Géotechnique ahead of print. [http://dx.doi.org/10.1680/geot.SIP13.P.023]

Alonso, E.E., Berdugo, I.R. and Ramon, A. (2012). Extreme expansive phenomena in anhydritic-gypsiferous claystones: the case of Lilla tunnel. Géotechnique, accepted for publication.

DETCG (2010). CODE_BRIGHT User's Guide. Available on-line: https://www.etcg.upc.edu/recerca/code_bright.

DIT-UPC (2002). CODE_BRIGHT, a 3-D program for thermo-hydro-mechanical analysis in geological media: User's guide, CIMNE, Barcelona.

Kovári, K., Amstad, C. & Anagnostou, G. (1988). Tunnelling in swelling rocks. Proc. 29th U.S. Symp. Rock Mech. Balkema, Cundall et al (eds): 17-32.

Lasaga, A. C. (1984). Chemical kinetics of water–rock interactions. J. Geophys. Res. 89, No. B6, 4009–4025.

Ramon, A & Alonso, E. (2012). Heave of a railway bridge modelling of gypsum crystal growth. Géotechnique ahead of print. http://dx.doi.org/10.1680/geot.12.P.035

Scherer, G. (1999). Crystallization in pores. Cement and Concrete Research, 29, 1347-1358.

Wittke, W. & Pierau, B. (1979). Fundamentals for the design and construction of tunnels in swelling rocks. Proc. Int. Congr. on Rock Mechanics, Montreux, Vol 2: 719-729.

HYDROSTATICS AND RELATIVE MOTION OF PORE FLUID

R. R. de Jager & F. A. J. M. Mathijssen
Royal Boskalis Westminster, Papendrecht, & Faculty of Civil Engineering and Geosciences, Delft University of Technology, The Netherlands

F. Molenkamp
Faculty of Civil Engineering and Geosciences, Delft University of Technology, The Netherlands

ABSTRACT: *In numerical analysis of saturated heterogeneous geomechanics both hydrostatics and relative pore fluid motion are accounted for simultaneously, often neglecting the linear momentum and internal energy related to the transient heterogeneous hydrostatic force.*
The aim of the presented analysis is to demonstrate the applicability of the decomposition of all macroscopic quantities into two modes, namely one due to transient heterogeneous hydrostatics and the other due to the relative motion of the pore fluid.
Special attention is given to the roles of the transient linear momentum and internal energy due to the transient heterogeneous hydrostatic force term $p(\nabla n)$ *per unit of volume of the saturated bulk, in which* p *is the macroscopic pore fluid stress and* ∇n *is the gradient of the porosity. These characteristics of heterogeneous hydrostatics are quantified for the simple 1-dimensional case of a porous saturated hydrostatic column composed of elastic grains forming together a heterogeneous porous skeleton*.

1 INTRODUCTION

In this paper the physics of spatially variable, saturated geomaterials is considered, which has been a popular topic in research for many years. The physical framework expressed in terms of balance equations and constitutive models forms the basis of most models used in these fields.

At the early development of a coherent physical and constitutive framework two branches of approach have been recognized (de Boer, 2000). The first, often termed 'phenomenological' approach (Terzaghi, 1925, 1943) has been widely applied in soil mechanics. The description of (hydro)statics formed its starting point. The second, more generic approach (Fillunger, 1936, Truesdell, Toupin, 1960) has been indicated as 'mixture theory'. It is attracting increasing attention as a scientific method for modelling at the scale of continuum mechanics, while being strengthened further by combining with micromechanical observations and modelling, a.o. involving volume averaging and homogenization (e.g. Berryman, 2005). The extensive comparison between and combination of different approaches has led to consensus on the formulation of the balance equations at the scale of continuum mechanics, at least for uniform conditions. However, many porous media, such as soils, are non-uniform as a result of their (geological) origin.

Nonetheless, for the mixture theory approach the description of the natural phenomenon of hydrostatics seems to require further attention (e.g. El Tani, 2007). Under hydrostatic

conditions, the stresses in a saturated porous medium with an open, interconnected pore network do not depend on the volume fraction of the pore fluid or solid particles. This apparent hydrostatic paradox has been observed and studied for centuries (e.g. Pascal, 1663). On the contrary, the dependence on volume fraction of the conserved quantities is one of the starting points of mixture theory (Truesdell, 1969).

In this paper we apply the conservation equations for combined hydrostatics and relative motion of the pore fluid for spatially variable, saturated geomaterials. A novel methodology is employed, using superposition of hydrostatic and flow related terms.

The aim of the presented analysis is to demonstrate the applicability of this superposition of two modes, namely one due to transient heterogeneous hydrostatics and the other due to the relative motion of the pore fluid. In particular the transient linear momentum and energy due to the transient heterogeneous hydrostatic force term $p(\nabla n)$ per unit of volume of the saturated bulk are quantified, in which the macroscopic pore fluid stress p and the gradient ∇n of the porosity n occur.

For this research aim it suffices to consider the deformable solid skeleton to be composed of elastically deformable particles, while for convenience the deformation of the solid skeleton due to interparticle displacements is described by equivalent isotropic linear elasticity. For the pore fluid elastic volumetric deformability and linear viscosity are accounted for. In the description of inertial effects the kinetic and mechanical power balances of linear momentum conservation are taken into account, while including the effect of tortuosity of the porous network (Biot, 1956[b,c], Coussy, 1995, 2004).

2 GENERALIZATION OF SUPERPOSITION

The physical phenomena of transient hydrostatics, Darcy's viscous pore fluid flow and saturated poro-dynamics are superposed. The motion of the solid skeleton is described by displacement field $\boldsymbol{u}$. The relative velocity of the visco-elastic pore fluid with respect to the solid skeleton is described by relative velocity field $\boldsymbol{v}$, implying the absolute macroscopic velocity field $\boldsymbol{v}_f$ of the pore fluid to be described by

$$\boldsymbol{v}_f = \dot{\boldsymbol{u}} + \boldsymbol{v} \tag{1}$$

These macroscopic mean velocities in the representative elementary volume REV of the solid skeleton $\dot{\boldsymbol{u}}$ and the pore fluid $\dot{\boldsymbol{u}} + \boldsymbol{v}$ are illustrated in figure 1.

The acceleration $\dot{\boldsymbol{v}}_f$ of the pore fluid is expressed by the application of the material (co-moving) time derivative of the pore fluid, thus

$$\dot{\boldsymbol{v}}_f = \ddot{\boldsymbol{u}} + \dot{\boldsymbol{v}}\big|_{\dot{\boldsymbol{u}}} \tag{2}$$

in which $\dot{\boldsymbol{v}}\big|_{\dot{\boldsymbol{u}}} = \dot{\boldsymbol{v}}_f - \ddot{\boldsymbol{u}}$ indicates the relative acceleration of the pore fluid with respect to the solid skeleton.

To arrive at a consistent macroscopic framework for saturated heterogeneous geomechanics the quantities in the macroscopic balance equations are decomposed for cases without and with relative motion of the pore fluid by considering the following two superposed modes of deformation and flow, namely:

mode $[h]$ without relative motion of the pore fluid with respect to the solid skeleton, involving the effects of gravity, transient pore fluid stress and transient density.

mode $[v]$ with relative motion of the pore fluid with respect to the solid skeleton, involving viscous and inertial motion.

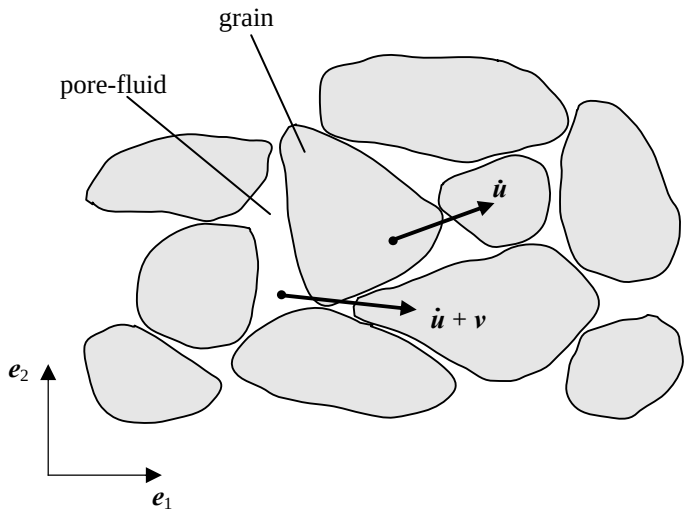

Figure 1. Cross-section of saturated granular skeleton at current spatial state. The macroscopic mean velocities in REV for the skeleton and pore fluid are indicated by $\dot{\boldsymbol{u}}$ and $\dot{\boldsymbol{u}} + \boldsymbol{v}$ respectively.

To derive superposable balance expressions for both superposed modes, all spatial gradients and material rates of all material quantities are subdivided into two superposed parts, using superscripts $[h]$ and $[v]$.

As material time derivatives first the macroscopic velocity and acceleration vectors $\dot{\boldsymbol{u}}$ and $\ddot{\boldsymbol{u}}$ of the solid skeleton and the relative velocity and acceleration vectors $\boldsymbol{v}$ and $\dot{\boldsymbol{v}}|_{\dot{\boldsymbol{u}}}$ of the pore fluid with respect to the solid skeleton are decomposed as follows

$$\dot{\boldsymbol{u}} = \dot{\boldsymbol{u}}^{[h]} + \dot{\boldsymbol{u}}^{[v]}; \qquad \ddot{\boldsymbol{u}} = \ddot{\boldsymbol{u}}^{[h]} + \ddot{\boldsymbol{u}}^{[v]}; \qquad \boldsymbol{v} = \boldsymbol{v}^{[h]} + \boldsymbol{v}^{[v]}; \qquad \dot{\boldsymbol{v}}|_{\dot{\boldsymbol{u}}} = \dot{\boldsymbol{v}}|_{\dot{\boldsymbol{u}}}^{[h]} + \dot{\boldsymbol{v}}|_{\dot{\boldsymbol{u}}}^{[v]} \tag{3}$$

while defining the relative pore fluid velocity $\boldsymbol{v}^{[h]}$ and acceleration $\dot{\boldsymbol{v}}|_{\dot{\boldsymbol{u}}}^{[h]}$ due to the transient mode $[h]$, thus without relative motion of the pore fluid with respect to the solid skeleton, to be zero, thus

$$\boldsymbol{v}^{[h]} = \boldsymbol{0} \quad \Rightarrow \quad \boldsymbol{v} = \boldsymbol{v}^{[v]}; \qquad \dot{\boldsymbol{v}}|_{\dot{\boldsymbol{u}}}^{[h]} = \boldsymbol{0} \quad \Rightarrow \quad \dot{\boldsymbol{v}}|_{\dot{\boldsymbol{u}}} = \dot{\boldsymbol{v}}|_{\dot{\boldsymbol{u}}}^{[v]} \tag{4}$$

The corresponding spatial gradients read, while also substituting Eq. (4)

$$\begin{aligned} &\boldsymbol{\nabla} \otimes \dot{\boldsymbol{u}} = \boldsymbol{\nabla} \otimes \dot{\boldsymbol{u}}^{[h]} + \boldsymbol{\nabla} \otimes \dot{\boldsymbol{u}}^{[v]}; \qquad \boldsymbol{\nabla} \otimes \ddot{\boldsymbol{u}} = \boldsymbol{\nabla} \otimes \ddot{\boldsymbol{u}}^{[h]} + \boldsymbol{\nabla} \otimes \ddot{\boldsymbol{u}}^{[v]} \\ &\boldsymbol{\nabla} \otimes \boldsymbol{v} = \boldsymbol{\nabla} \otimes \boldsymbol{v}^{[v]}; \qquad\qquad \boldsymbol{\nabla} \otimes \dot{\boldsymbol{v}}|_{\dot{\boldsymbol{u}}} = \boldsymbol{\nabla} \otimes \dot{\boldsymbol{v}}|_{\dot{\boldsymbol{u}}}^{[v]} \end{aligned} \tag{5}$$

3 EXPRESSIONS FOR SATURATED HETEROGENEOUS GEOMECHANICS

The balance equations of saturated heterogeneous geomechanics according to the mixture and poro-dynamic theories (e.g. Bowen, 1976, 1982, Nigmatulin, 1991, Ehlers, 2002, Coussy, 1995, 2004) are applied, involving the conservation of mass, linear momentum and energy of both phases. These equations are first decomposed for both transient superposed modes $[h]$ without and $[v]$ with relative motion of the pore fluid and subsequently recomposed. Then the resulting expressions of the conservation of mass, linear momentum and energy of both the pore fluid and solid skeleton read:

Conservation of mass of pore fluid

$$\overset{\cdot}{\overline{n\rho_f}} + \rho_f \boldsymbol{v} \bullet \left(\boldsymbol{\nabla} n\right) + n\rho_f \boldsymbol{\nabla} \bullet \left(\dot{\boldsymbol{u}} + \boldsymbol{v}\right) + J^{fs} = 0 \tag{6}$$

Conservation of mass of solid skeleton

$$\dot{\overline{(1-n)\rho_s}} + (1-n)\rho_s(\boldsymbol{\nabla}\bullet\dot{\boldsymbol{u}}) - J^{fs} = 0 \tag{7}$$

Conservation of linear momentum of pore fluid

$$n\rho_f\left(\ddot{\boldsymbol{u}} + \dot{\boldsymbol{v}}\big|_{\dot{\boldsymbol{u}}}\right) - n(\boldsymbol{\nabla} p) - n\rho_f\boldsymbol{b} + \boldsymbol{R}^{fs[v]} + \boldsymbol{R}^{fs[tor]} - J^{fs}(\dot{\boldsymbol{u}} + \boldsymbol{v}) = \boldsymbol{0} \tag{8}$$

Conservation of linear momentum of solid skeleton

$$(1-n)\rho_s\ddot{\boldsymbol{u}} - (\boldsymbol{\nabla}\bullet\boldsymbol{\sigma}^*) - (1-n)(\boldsymbol{\nabla} p) - (1-n)\rho_s\boldsymbol{b} - \boldsymbol{R}^{fs[v]} - \boldsymbol{R}^{fs[tor]} + J^{fs}\dot{\boldsymbol{u}} = \boldsymbol{0} \tag{9}$$

Conservation of energy of pore fluid

$$n\rho_f\dot{e}_f - n\,p\boldsymbol{\nabla}\bullet(\dot{\boldsymbol{u}} + \boldsymbol{v}) + \boldsymbol{\nabla}\bullet(n\boldsymbol{q}_f) - n\rho_f h_f + E_Q^{fs} - J^{fs}\eta_f T_f = 0 \tag{10}$$

Conservation of energy of solid skeleton

$$\begin{aligned}(1-n)\rho_s\dot{e}_s - \boldsymbol{\sigma}^* : (\boldsymbol{\nabla}\otimes\dot{\boldsymbol{u}}) - (1-n)\,p(\boldsymbol{\nabla}\bullet\dot{\boldsymbol{u}}) + \boldsymbol{\nabla}\bullet\left[(1-n)\boldsymbol{q}_s\right] - (1-n)\rho_s h_s + ... \\ ... - \boldsymbol{R}^{fs[v]}\bullet\boldsymbol{v}^{[v]} - E_Q^{fs} + J^{fs}\left(e_s - e_f + \eta_f T_f + \boldsymbol{v}^{[v]}\bullet\dot{\boldsymbol{u}}^{[v]} + a\,\boldsymbol{v}^{[v]}\bullet\boldsymbol{v}^{[v]}/2\right) = 0\end{aligned} \tag{11}$$

The complexity increases gradually from the mass to the energy equations, with each equation adding new quantities, all being defined in terms of the sign convention of continuum mechanics with tension and stretching positive. For intrinsic quantities of the pore fluid and solid skeleton the subscripts $\square_f$ and $\square_s$ are used respectively, while for the volume-averaged quantities per unit of volume of the mixture in REV the corresponding superscripts $\square^f$ and $\square^s$ are applied.

The additional quantities in the expressions Eqs. (6) and (7) of the conservation of mass are the mass density ρ of both phases and the exchange of mass J^{fs} from the pore fluid to the solid skeleton per unit of volume of the mixture in REV.

The quantities in the linear momentum equations Eqs. (8) and (9) concern the intergranular stress tensor $\boldsymbol{\sigma}^*$ of the solid skeleton per unit of volume of mixture in REV, the body force vector $\boldsymbol{b}$ per unit of mass of both phases and the exchange of linear momentum $\boldsymbol{R}^{fs}$ from the pore fluid to the solid skeleton per unit of volume of mixture in REV.

The conservation of energy according to Eqs. (10) and (11) adds the following quantities, namely the internal energy e per unit of mass of each phase, the heat flux vector $\boldsymbol{q}$ per unit of volume of each phase, h the rate of internal energy supply by radiation per unit of mass of each phase and E_Q^{fs} the rate of thermal energy exchange from the pore fluid to the solid skeleton per unit of volume of the mixture in REV.

The summation convention for repeated indices in the index notation leads for the expression of the volumetric strain rate of the solid skeleton to $\boldsymbol{\nabla}\bullet\dot{\boldsymbol{u}} = \partial\dot{u}_k/\partial x_k = \dot{\varepsilon}_{vol}$ and of the pore fluid to $\boldsymbol{\nabla}\bullet(\dot{\boldsymbol{u}} + \boldsymbol{v}) = \partial(\dot{u}_k + v_k)/\partial x_k = \dot{\varepsilon}_{f\_vol}$ respectively and for the divergence vector of the intergranular stress tensor $\boldsymbol{\sigma}^*$ per unit of volume of the mixture in REV to $\boldsymbol{\nabla}\bullet\boldsymbol{\sigma}^* = \partial\sigma_{ik}^*/\partial x_k\,\boldsymbol{e}_i$, in which $\boldsymbol{e}_i$ $(i = 1,2,3)$ represents the Cartesian triad of unit base vectors.

The interaction vector of momentum exchange $\boldsymbol{R}^{fs}$ as exerted by the pore fluid on the solid skeleton is expressed by:

$$\boldsymbol{R}^{fs} = \boldsymbol{R}^{fs[h]} + \boldsymbol{R}^{fs[v]} + \boldsymbol{R}^{s[tor]} = p(\boldsymbol{\nabla} n) + n^2\mu\boldsymbol{\kappa}^{-1}\bullet\boldsymbol{v} + (a-1)n\rho_f\,\dot{\boldsymbol{v}}\big|_{\dot{\boldsymbol{u}}} \tag{12}$$

involving the combined heterogeneous interaction force (e.g. de Boer, 2000, Coussy, 2004), accounting for the following three effects, namely:

- the interaction force of the pore fluid stress resulting from the heterogeneity of the porous network

$$\boldsymbol{R}^{fs[h]} = p(\boldsymbol{\nabla} n) \tag{13}$$

- the interaction force of viscous pore fluid flow (Darcy, 1856, see also e.g. Gray, Millar, 2004, Straughan, 2012,), involving viscosity μ and intrinsic permeability tensor $\boldsymbol{\kappa}$

$$\boldsymbol{R}^{fs[v]} = n^2 \mu \boldsymbol{\kappa}^{-1} \bullet \boldsymbol{v} \tag{14}$$

- the hydrodynamic interaction force due to the tortuosity of the porous network as encountered by the pore fluid flow as a consequence of the geometrical structure of the solid skeleton (Plona, 1980, Johnson, Plona, Scala, Pasierb, Kojima, 1982, Coussy 1995, 2004), involving tortuosity parameter a, namely

$$\boldsymbol{R}^{s[tor]} = (a-1) n \rho_f \dot{\boldsymbol{v}}\big|_{\ddot{\boldsymbol{u}}} \tag{15}$$

In the following applications the exchange of mass remains zero, thus $J^{fs} = 0$, and the exchange of thermal energy E_Q^{fs} remains unspecified. In fact in the application in this paper only the simple case of constant temperature will be elaborated.

The recomposed balance expressions Eqs. (6)~(11) demonstrate, that the transient heterogeneous hydrostatic force term $p(\nabla n)$ per unit of volume of the saturated bulk has been eliminated completely from the governing equations by the counteracting interaction force $\boldsymbol{R}^{fs[h]}$ of the pore fluid stress resulting from the heterogeneity of the porous network, as expressed by Eq. (13). The remaining interactions of linear momentum exchange only concern the interaction force $\boldsymbol{R}^{fs[v]}$ of viscous pore fluid flow Eq. (14) and the hydrodynamic interaction force $\boldsymbol{R}^{s[tor]}$ due to the tortuosity of the porous network Eq. (15), both concerning mode $[v]$ with relative pore fluid motion. It is noted that the related power of mechanical energy exchange by the heterogeneous hydrostatic interaction is expressed by $\boldsymbol{R}^{fs[h]} \bullet \dot{\boldsymbol{u}}^{[h]}$, involving also the velocity vector $\dot{\boldsymbol{u}}^{[h]}$ of the solid skeleton due to mode $[h]$.

Consequently these recomposed governing equations are valid for saturated heterogeneous geomaterials even though both the heterogeneous force $p(\nabla n)$ and the counteracting interaction force $\boldsymbol{R}^{fs[h]}$ Eq. (13) do not occur. It is concluded that for taking account of the heterogeneity it suffices to apply the heterogeneous porosity field $n(\boldsymbol{x})$ in Eqs. (6)~(11) without requiring any spatial differentials.

4 SIMPLE ELASTIC GEO-MODEL FOR CONSTANT TEMPERATURE

To demonstrate the decomposition of the behaviour of saturated heterogeneous geomaterials into the two modes, thus without and with relative pore fluid motion, it suffices to consider for convenience a heterogeneous equivalent elastic solid skeleton, composed of elastic particles with frictional interparticle interactions, and a visco-elastic pore fluid.

For the pore fluid an elastic volumetric strain rate $\dot{\varepsilon}^e_{f\_vol}$ is considered, expressed by

$$\dot{\varepsilon}^e_{f\_vol} = \nabla \bullet (\dot{\boldsymbol{u}} + \boldsymbol{v}) = -\frac{\dot{\rho}_f}{\rho_f} = \frac{\dot{p}}{K_f} \tag{16}$$

which for constant temperature is described by the third and fourth terms, in which K_f represents the elastic bulk modulus of the pore fluid at that constant temperature. In addition the viscous pore fluid flow at the background of Darcy's law involves the following relation between the deviatoric rates of strain $\dot{\boldsymbol{\varepsilon}}^d_f$ and stress $\dot{\boldsymbol{\sigma}}^d_f$ of the pore fluid, namely

$$\dot{\boldsymbol{\varepsilon}}^d_f = \frac{\nabla \otimes (\dot{\boldsymbol{u}} + \boldsymbol{v}) + (\dot{\boldsymbol{u}} + \boldsymbol{v}) \otimes \nabla}{2} - \frac{\nabla \bullet (\dot{\boldsymbol{u}} + \boldsymbol{v})}{3} \boldsymbol{I} = \frac{\dot{\boldsymbol{\sigma}}^d_f}{2\mu} \tag{17}$$

The deformation rate of the solid skeleton is considered to be due to both the material rates of the isotropic part $p\boldsymbol{I}$ of the pore fluid stress tensor and the intergranular stress tensor $\boldsymbol{\sigma}^*$. The elastic volumetric strain rate $\dot{\varepsilon}_{vol}^{m-e}$ of the solid skeleton due to a changing mineral density ρ_s of the grains, illustrated on the left side of figure 2, is affected by both the isotropic part $p\boldsymbol{I}$ of the pore fluid stress tensor and the intergranular stress tensor $\boldsymbol{\sigma}^*$ and is expressed by

$$\dot{\varepsilon}_{vol}^{m-e} = -\frac{\dot{\rho}_s}{\rho_s} = -\frac{\dot{\rho}_s\big|_{\dot{\boldsymbol{\sigma}}^*=\boldsymbol{0}}}{\rho_s} - \frac{\dot{\rho}_s\big|_{\dot{p}=0}}{\rho_s} = \dot{\varepsilon}_{vol}^{m-e}\Big|_{\dot{\boldsymbol{\sigma}}^*=\boldsymbol{0}} + \dot{\varepsilon}_{vol}^{m-e}\Big|_{\dot{p}=0} = \frac{\dot{p}}{K_{sf}} + \frac{\dot{\boldsymbol{\sigma}}^* : \boldsymbol{I}}{(1-n)3K_{sf}} \tag{18}$$

in which two complementary parts are distinguished, namely the part $\dot{\varepsilon}_{vol}^{m-e}\big|_{\dot{\boldsymbol{\sigma}}^*=\boldsymbol{0}}$, exclusively due to the material rate $\dot{p}$ of the pore fluid stress and the part $\dot{\varepsilon}_{vol}^{m-e}\big|_{\dot{p}=0}$, exclusively due to the material rate of the isotropic part of the intergranular stress $\left(\dot{\boldsymbol{\sigma}}^* : \boldsymbol{I}\right)/3$ as induced in the particles. In the last two terms of Eq. (18) the elastic bulk modulus K_{sf} of the mineral composing the particles occurs.

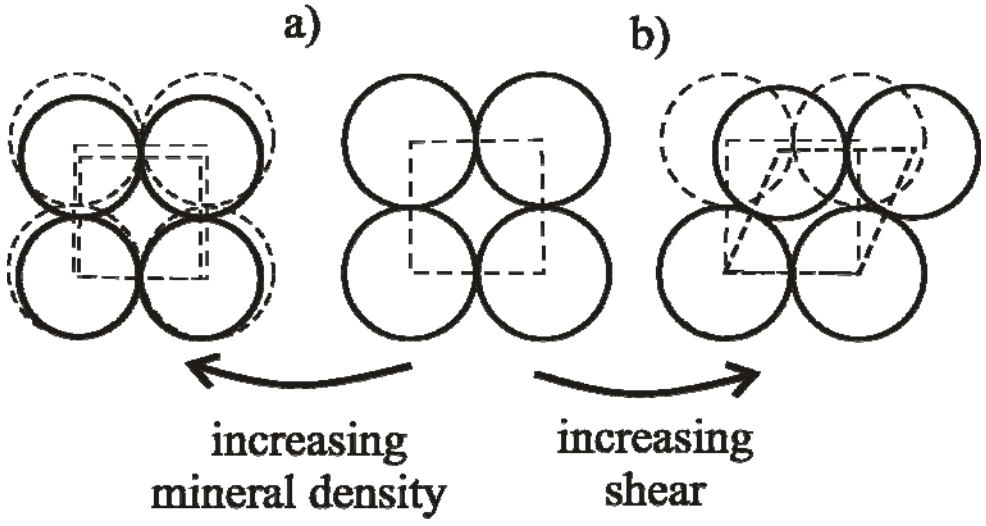

Figure 2. Illustration of two superposed micromechanical deformation mechanisms of the solid skeleton, namely: a) deformation mechanism, involving a change of the mineral density, b) deformation mechanism, involving a change of the intergranular structure.

For later convenience the elastic volumetric strain rate $\dot{\varepsilon}_{vol}^{m-e}\big|_{\dot{\boldsymbol{\sigma}}^*=\boldsymbol{0}}$ of the mineral particles due to the material rate $\dot{p}$ of the pore fluid stress, occurring in Eq. (18), and the corresponding partial velocity field $\dot{\boldsymbol{u}}^{m-e}\big|_{\dot{\boldsymbol{\sigma}}^*=\boldsymbol{0}}$ of the solid skeleton, to be recalled in Eq. (22), will be replaced by the following shorthand quantities, adding an over-tilde, namely

$$\tilde{\dot{\varepsilon}}_{vol}^{m-e} = \dot{\varepsilon}_{vol}^{m-e}\Big|_{\dot{\boldsymbol{\sigma}}^*=\boldsymbol{0}}; \qquad \tilde{\dot{\boldsymbol{u}}}^{m-e} = \dot{\boldsymbol{u}}^{m-e}\Big|_{\dot{\boldsymbol{\sigma}}^*=\boldsymbol{0}} \tag{19}$$

Additionally, the material rate of the intergranular stress $\boldsymbol{\sigma}^*$ affects the microscopic intergranular structure (or fabric) of the solid skeleton, involving interparticle slippage and rolling and as such inducing the strain rate tensor $\dot{\boldsymbol{\varepsilon}}^{gs}$ of the granular structure, as illustrated on the right side of figure 2. For constant temperature the combined strain rate $\dot{\boldsymbol{\varepsilon}}^*$ of the solid skeleton as affected by the intergranular stress $\boldsymbol{\sigma}^*$ is expressed by

$$\dot{\boldsymbol{\varepsilon}}^* = \boldsymbol{D}^{-1} : \dot{\boldsymbol{\sigma}}^{J*} \tag{20}$$

which involves the inverse fourth order tangent stiffness tensor $\boldsymbol{D}^{-1}$ and the objective (Jaumann) intergranular stress rate tensor $\dot{\boldsymbol{\sigma}}^{J^*}$. However, recalling also Eq. (18) it should be recognized that combined strain rate $\dot{\boldsymbol{\varepsilon}}^*$ as induced by the intergranular stress must also include the effect of the elastic volumetric strain rate $\dot{\varepsilon}_{vol}^{m\_e}\big|_{\dot{p}_f=0}$, representing the effect on the mineral density ρ_s by the intergranular stress $\boldsymbol{\sigma}^*$. Consequently the combined strain rate $\dot{\boldsymbol{\varepsilon}}^*$ of the solid skeleton as affected by the intergranular stress $\boldsymbol{\sigma}^*$ is of the form

$$\dot{\boldsymbol{\varepsilon}}^* = \boldsymbol{D}^{-1} : \dot{\boldsymbol{\sigma}}^{J^*} = \frac{\dot{\varepsilon}_{vol}^{m\_e}\big|_{\dot{p}_f=0}}{3}\boldsymbol{I} + \dot{\boldsymbol{\varepsilon}}^{gs} \tag{21}$$

This expression clarifies the role of the inverse tangent stiffness tensor $\boldsymbol{D}^{-1}$, indicating that for constant temperature the combined strain rate $\dot{\boldsymbol{\varepsilon}}^*$ of the solid skeleton is due to both the changes of the mineral density and the intergranular structure. For the aim of this paper it suffices to approximate this tangent stiffness tensor by equivalent isotropic linear elasticity.

Consequently the velocity gradient $\boldsymbol{\nabla} \otimes \dot{\boldsymbol{u}}$ of the solid skeleton can be expressed in terms of the decomposed velocity gradients for the different deformation mechanisms of the solid skeleton and the combined superposed modes $[h]$ and $[v]$ as follows

$$\boldsymbol{\nabla} \otimes \dot{\boldsymbol{u}} = \boldsymbol{\nabla} \otimes \left(\dot{\boldsymbol{u}}^{*\_[h]} + \dot{\boldsymbol{u}}^{*\_[v]} + \dot{\tilde{\boldsymbol{u}}}^{m\_e[h]} + \dot{\tilde{\boldsymbol{u}}}^{m\_e[v]} \right) \tag{22}$$

in which for both superposed modes the velocity gradients are expressed by:

$\boldsymbol{\nabla} \otimes \dot{\boldsymbol{u}}^*$ - velocity gradient of the solid skeleton due to the change of the intergranular stress $\boldsymbol{\sigma}^*$, which changes the intergranular structure (or fabric) of the solid skeleton mainly due to interparticle slippage and rolling and marginally due to the change of the density of the minerals composing the grains. Nevertheless, considering the aim of the paper, also for this part simple equivalent elasticity is applied.

$\boldsymbol{\nabla} \otimes \dot{\tilde{\boldsymbol{u}}}^{m\_e}$ - *elastic* velocity gradient of the solid skeleton by the material rate of the pore fluid stress $p\boldsymbol{I}$ acting on the solid skeleton due to the change of the density ρ_s of the minerals composing the grains, in which the short-hand definition according to Eq. (19) has been applied for the first time.

Then the corresponding strain rates tensors can be described as follows:

- the strain rate tensor of the solid skeleton due to change of the intergranular stress tensor $\boldsymbol{\sigma}^*$, which changes both the structure (or fabric) and the density of the minerals composing the grains.

$$\dot{\boldsymbol{\varepsilon}}^* = \left(\boldsymbol{\nabla} \otimes \dot{\boldsymbol{u}}^* + \dot{\boldsymbol{u}}^* \otimes \boldsymbol{\nabla} \right) / 2 \tag{23}$$

- the *elastic* strain rate tensor of the solid skeleton due to change of the material density ρ_s of the minerals composing the grains by a changing pore fluid stress p.

$$\dot{\tilde{\boldsymbol{\varepsilon}}}^{m\_e} = \left(\boldsymbol{\nabla} \otimes \dot{\tilde{\boldsymbol{u}}}^{m\_e} + \dot{\tilde{\boldsymbol{u}}}^{m\_e} \otimes \boldsymbol{\nabla} \right) / 2 = \frac{\boldsymbol{I}\,\dot{p}}{3K_{sf}} \tag{24}$$

Finally adding the strain rates according to Eqs. (20) and (24) leads for the strain rate of the solid skeleton for the case of constant temperature to (e.g. Verruijt, 1982a/b)

$$\dot{\boldsymbol{\varepsilon}} = \dot{\boldsymbol{\varepsilon}}^* + \dot{\tilde{\boldsymbol{\varepsilon}}}^{m\_e} = \boldsymbol{D}^{-1} : \dot{\boldsymbol{\sigma}}^{J^*} + \frac{\boldsymbol{I}\,\dot{\tilde{\varepsilon}}_{vol}^{m\_e}}{3} = \boldsymbol{D}^{-1} : \dot{\boldsymbol{\sigma}}^{J^*} + \frac{\boldsymbol{I}\,\dot{p}}{3K_{sf}} \tag{25}$$

5 CHARACTERISTICS OF TRANSIENT HYDROSTATICS

For the transient hydrostatic case of mode $[h]$ the linear momentum conservation of the pore fluid (8) and the solid skeleton Eq. (9) reduce to respectively

$$\boldsymbol{\nabla} p + \rho_f \boldsymbol{b} = \boldsymbol{0}; \quad \boldsymbol{\nabla} \bullet \boldsymbol{\sigma}^* + (1-n)\left(\rho_s - \rho_f\right)\boldsymbol{b} = \boldsymbol{0} \tag{26}$$

while for constant temperature the energy conservation of the pore fluid Eq. (10) and the solid skeleton Eq. (11) decrease to respectively

$$\rho_f \, \dot{e}_f = p \, \dot{\varepsilon}_{f\_vol}; \quad (1-n)\rho_s \, \dot{e}_s = \boldsymbol{\sigma}^* : \dot{\boldsymbol{\varepsilon}} + (1-n)\, p \, \dot{\varepsilon}_{vol} \tag{27}$$

in which the volumetric strain rate of the pore fluid $\dot{\varepsilon}_{f\_vol}$ can be calculated by applying (16) and the strain rate tensor $\dot{\boldsymbol{\varepsilon}}$ of the solid skeleton follows from the application of Eq. (25).

To quantify the order of magnitude of the deformation of a porous skeleton due to changes of the pore fluid stress, consider the 1-dimensional loading case of a submerged saturated soil column. The level of the water surface is subjected to a slow upward rate of hydrostatic motion $\dot{z}$. This transient hydrostatic motion induces locally the following rate of hydrostatic pore fluid stress $\dot{p}^{[h]}$, inducing an equal rate of the vertical total normal stress component $\dot{\sigma}_{33}^{[h]}$, where the upward vertical direction is indicated by unit base vector $\boldsymbol{e}_3$, namely

$$\dot{p}^{[h]} = \dot{\sigma}_{33}^{[h]} = -\rho_f \, g \, \dot{z} \tag{28}$$

Then from (28) for the rate of the vertical intergranular stress component $\dot{\sigma}_{33}^{*[h]}$ follows that

$$\dot{\sigma}_{33}^{*[h]} = \dot{\sigma}_{33}^{[h]} - \dot{p}^{[h]} = 0 \tag{29}$$

It is noted that in this 1-dimensional hydrostatic case the vertical intergranular stress component $\dot{\sigma}_{33}^{*[h]}$ remains constant. The corresponding horizontal normal strain rates are taken zero, thus

$$\dot{\boldsymbol{\varepsilon}}_{11}^{[h]} = \dot{\boldsymbol{\varepsilon}}_{22}^{[h]} = 0 \tag{30}$$

Assuming equal properties in any horizontal direction, the resulting rates of the horizontal normal intergranular stress components will be equal, thus

$$\dot{\sigma}_{11}^{*[h]} = \dot{\sigma}_{22}^{*[h]} \tag{31}$$

Application of Eq. (25) and substitution of Eq. (30) enables to express the vertical and horizontal normal strain rates of the solid skeleton by

$$\begin{aligned} \dot{\boldsymbol{\varepsilon}}_{11}^{[h]} = \dot{\boldsymbol{\varepsilon}}_{22}^{[h]} &= 2\,\mathrm{D}_{1111}^{-1}\,\dot{\sigma}_{11}^{*[\mathrm{h}]} + \mathrm{D}_{1133}^{-1}\,\dot{\sigma}_{33}^{*[\mathrm{h}]} + \frac{\dot{p}^{[h]}}{3K_{sf}} = 0 \\ \dot{\boldsymbol{\varepsilon}}_{33}^{[h]} &= 2\,\mathrm{D}_{3311}^{-1}\,\dot{\sigma}_{11}^{*[\mathrm{h}]} + \mathrm{D}_{3333}^{-1}\,\dot{\sigma}_{33}^{*[\mathrm{h}]} + \frac{\dot{p}^{[h]}}{3K_{sf}} \end{aligned} \tag{32}$$

Substituting Eqs. (29) and (31) in Eq. (32) gives for the horizontal and vertical normal strain rates respectively

$$\dot{\boldsymbol{\varepsilon}}_{11}^{[h]} = 2\,\mathrm{D}_{1111}^{-1}\,\dot{\sigma}_{11}^{*[\mathrm{h}]} + \frac{\dot{p}^{[h]}}{3K_{sf}} = 0; \qquad \dot{\boldsymbol{\varepsilon}}_{33}^{[h]} = 2\,\mathrm{D}_{3311}^{-1}\,\dot{\sigma}_{11}^{*[\mathrm{h}]} + \frac{\dot{p}^{[h]}}{3K_{sf}} \tag{33}$$

Solving the first and second expressions of Eq. (33) for the rate of the horizontal normal intergranular stress component $\dot{\sigma}_{11}^{*[\mathrm{h}]}$ and the vertical strain rate $\dot{\boldsymbol{\varepsilon}}_{33}^{[h]}$ for transient hydrostatics leads to respectively

$$\dot{\sigma}_{11}^{*[\mathrm{h}]} = -\frac{1}{2\,\mathrm{D}_{1111}^{-1}}\frac{\dot{p}^{[h]}}{3K_{sf}}; \qquad \dot{\boldsymbol{\varepsilon}}_{33}^{[h]} = \left\{1 - \frac{\mathrm{D}_{3311}^{-1}}{\mathrm{D}_{1111}^{-1}}\right\}\frac{\dot{p}^{[h]}}{3K_{sf}} \tag{34}$$

To quantify the order of magnitude of the vertical strain increment $\Delta\boldsymbol{\varepsilon}_{33}^{[h]}$ due to an increment of the hydrostatic upward movement of the water level of $\Delta z = 1$ metre first both quantities in Eq. (34) are estimated in terms of equivalent isotropic linear elastic tangent stiffness parameters, expressed by

$$\mathrm{D}_{1111}^{-1} \approx \frac{1}{2G(1+\nu)}; \qquad \mathrm{D}_{3311}^{-1} \approx -\frac{\nu}{2G(1+\nu)} \tag{35}$$

thus expressed in terms of the equivalent tangent shear modulus G and Poisson's ratio ν of the solid skeleton. Substituting Eq. (35) in both expressions of Eq. (34) leads respectively to

$$\dot{\sigma}_{11}^{*[\mathrm{h}]} = -\frac{G(1+\nu)}{3K_{sf}}\dot{p}^{[h]}; \qquad \dot{\boldsymbol{\varepsilon}}_{33}^{[h]} = \frac{(1+\nu)}{3K_{sf}}\dot{p}^{[h]} \tag{36}$$

Substituting Eqs. (16) and (36) in the first and second expression of Eq. (27) gives for the rates of the internal energy of the pore fluid and solid skeleton respectively

$$\dot{e}_f = \frac{p\,\dot{p}^{[h]}}{\rho_f K_f}; \qquad \dot{e}_s = \left\{\frac{\sigma_{33}^*}{(1-n)\rho_s} + \frac{p}{\rho_s}\right\}\dot{\boldsymbol{\varepsilon}}_{33}^{[h]} \approx \left\{\frac{\sigma_{33}^*}{(1-n)\rho_s} + \frac{p}{\rho_s}\right\}\frac{(1+\nu)}{3K_{sf}}\dot{p}^{[h]} \tag{37}$$

For this transient hydrostatic column the vertical interaction force $R_3^{fs[h]}$ per unit of volume of the mixture in REV resulting from the vertical heterogeneity follows from Eq. (13) and reads

$$R_3^{fs[h]} = p\,n_{,3} \tag{38}$$

which is just the product of the instantaneous pore fluid stress and the vertical gradient of the porosity n.

The corresponding mechanical power $E_M^{fs[h]}$ per unit of volume in REV by the work of this heterogeneous hydrostatic interaction force $R_3^{fs[h]}$ is expressed by the product of this instantaneous force $R_3^{fs[h]}$ and the vertical velocity $\dot{u}_3^{[h]}$ of the solid skeleton, resulting from the vertical strain rate $\dot{\boldsymbol{\varepsilon}}_{33}^{[h]}$ by transient hydrostatics as distributed over the height h of the column, thus $\dot{u}_3^{[h]} = \int_0^h \dot{\boldsymbol{\varepsilon}}_{33}^{[h]} dh$, leading to

$$E_M^{fs[h]} = R_3^{fs[h]}\dot{u}_3^{[h]} \tag{39}$$

It may be noted that although both heterogeneous hydrostatic characteristics according to Eqs. (38) and (39) can be properly quantified, they do not occur in the recomposed balance equations Eqs. (6)~(11) anymore. Forces with such characteristics are known as "equilibrated forces" (e.g. Passman, Nunziato, Walsh, 1984).

To quantify the order of deformation due to transient hydrostatics consider a solid skeleton composed of quartz particles and with a porosity n in the range $0.3 < n < 0.6$. The bulk stiffness K_{sf} of the mineral is about: $40 < K_{sf} < 70$ [GPa] and the equivalent tangent shear modulus G remains in the range: $0.02 < G < 2$ [GPa], while for the range of the equivalent Poisson's ratio is assumed: $0.1 < \nu < 0.4$. Then substituting these estimated ranges in the second expression of Eq. (36), while noting the corresponding increment of the pore fluid stress $\Delta p^{[h]} = 10^4$ [N/m^2], gives for the corresponding range of the vertical strain increment of the solid skeleton roughly

$$5\times10^{-8} < \left\|\Delta\boldsymbol{\varepsilon}_{33}^{[h]}\right\| < 12\times10^{-8} \tag{40}$$

This strain range remains marginal compared to the engineering strains, which for serviceability are usually in the following range: $10^{-4} < \|\Delta\boldsymbol{\varepsilon}\| < 10^{-2}$. For the corresponding range of the ratio $\dot{\sigma}_{11}^{*[\mathrm{h}]} / \dot{p}^{[h]}$ of the stress rates in Eq. (36) follows roughly

$$10^{-4} < -\dot{\sigma}_{11}^{*[h]} \big/ \dot{p}^{[h]} < 10^{-2} \tag{41}$$

indicating that for a column composed of quartz particles the rate of change of the horizontal intergranular stress remains negligible.

However, for much softer soils like peat, with a decomposing organic substance as solid skeleton, the hydrostatic deformation may become larger and possibly even of practical relevance in geotechnical engineering. Recent experimental research on peat with reversible loading gave a bulk stiffness K_{sf} of the solid substance as defined by Eq. (25) of $K_{sf} \approx 0.14 \ [\text{GPa}]$, thus 2 to 3 decades more flexible than quartz. On that basis from (36) follows for the vertical strain increment of the solid skeleton composed of peat

$$\dot{\varepsilon}_{33}^{[h]} = \frac{(1+\nu)}{3K_{sf}} \dot{p}^{[h]} \approx \frac{1.3\times10^{4}}{3\times0.14\times10^{9}} \approx 3\times10^{-5} \tag{42}$$

which is still small compared to the above-mentioned range of relevant engineering strains. However, the writers hypothesize that for virgin loading of peat this flexibility will be substantially larger, which should be investigated for engineering relevance.

6 GENERAL OBSERVATIONS AND CONCLUSIONS

In numerical analysis of saturated heterogeneous geomechanics both hydrostatics and relative pore fluid motion are accounted for simultaneously, often neglecting the linear momentum and internal energy related to the transient heterogeneous hydrostatic force $p(\nabla n)$ per unit of volume of the saturated bulk, in which p is the macroscopic pore fluid stress and ∇n is the gradient of the porosity.

To distinguish between transient heterogeneous hydrostatics and deformation modes with relative motion of the pore fluid, first all macroscopic quantities and governing equations have been decomposed into two modes, namely one without and the other with relative pore fluid motion. Subsequently recomposing these balance equations has shown to lead to balance equations in which the heterogeneous hydrostatic force term $p(\nabla n)$ does not occur anymore, because it is locally fully balanced by a counteracting heterogeneous hydrostatic interaction force $\boldsymbol{R}^{fs[h]}$ per unit of volume. The same is true for the corresponding mechanical power. It can be concluded that for taking account of heterogeneity it suffices to apply the heterogeneous porosity field $n(\boldsymbol{x})$ in the recomposed balance equations without requiring any spatial differentials.

These characteristics of heterogeneous hydrostatics are quantified for the simple 1-dimensional case of a submerged porous saturated hydrostatic column composed of elastic grains forming together a heterogeneous porous skeleton. The engineering relevance of hydrostatics is shown to remain negligible for solid granular skeletons composed of minerals like quartz. However, this relevance will increase with the flexibility of the “particles” composing the solid skeleton.

ACKNOWLEDGEMENT

This research is supported by the Dutch Technology Foundation STW, applied science division of the Dutch Organisation of Scientific Research (NWO), and the Technology Program of the Ministry of Economic Affairs.

REFERENCES

Berryman J G, (1980). “Confirmation of Biot theory”. Appl. Phys. Lett., Vol. 37, 382-384.

Berryman J G, (2005). “Comparison of upscaling methods in poroelasticity and its generalizations”. J. Engng. Mech., Vol. 131(9), 928-936.

Biot M A, (1956[a]). “Theory of propagation of of elastic waves in a fluid-saturated porous solid. I. Low-frequency range”, J. Acoustic Society of America, Vol. 28(2), 168-178.

Biot M A, (1956[b]). “Theory of propagation of of elastic waves in a fluid-saturated porous solid. II. Higher frequency range”, J. Acoustic Society of America, Vol. 28(2), 179-191.

Bowen, R.M. (1976), “Theory of mixtures”, in Continuum Physics, Vol. III, edited by A.C. Eringen, Academic Press, New York, 1-127.

Bowen R M, (1982). “Compressible porous media models by use of the theory of mixtures”, Int. J. Engng. Sci., Vol. 20(6), 679-735.

Coussy O, (1995). “Mechanics of porous continua”, Wiley, Chichester.

Coussy O, (2004). “Poromechanics”, Wiley, Chichester.

De Boer R, (2000). “Theory of porous media”, Springer, Heidelberg.

Darcy H, (1856). “Les fontaines publiques de la ville Dijon”, Dalmont, Paris (in French).

Ehlers W, (2002). “Foundations of multiphasic and porous media”, In: Porous Media, Theory, Experiments and Numerical applications, Ehlers and Bluhm (eds.), Springer, 3-86.

El Tani M, (2007). “Hydrostatic paradox of saturated media”, Géotechnique, Vol. 57(9), 773-777. Discussions: El Tani M, Kolymbas D, Verruijt A, (2008). Géotechnique 58, 835-837.

Fillunger P, (1936). “Erdbaumechanik”, Selbstverlag des Verfassers, Wien (in German).

Gray W G, Millar C T, (2004). “Examination of Darcy’s law for flow in porous media with variable porosity”, Environ. Sci. Technology, Vol. 38(22), 5895-5901.

Johnson D L, Plona T J, Scala C, Pasierb F, Kojima H, (1982). “Tortuosity and acoustic slow waves”, Phys. Review Letters, The American Physical Society, Vol. 49(25), 1840-1844.

Nigmatulin R I, (1991). “Dynamics of multiphase media”, Revised and augmented edition, Hemisphere Publishing Corporation (Taylor and Francis Group), Vol. 1: Multiphase flow, Vol. 2: Fluid dynamics. Nigmatulin R I: Moscow State University, Originally published in Russian by Nauka Moscow, English edition editor: J C Friedly: University of Rochester, New York, Translator: M A Piterman: University of Rochester, New York.

Pascal B, (1663). “Traitez de l’equilibre des liqueurs, et de la pesanteur de la masse de l’air: contenant l’explication des causes de divers effets de la nature qui n’avoient point esté bien connus jusques-icy, & particulierement de ceux que l’on avoit attribuez à l’horreur du Vuide”, Chez Guillaume Desprez, Paris. (In French).

Passman S L, Nunziato J W, Walsh E K, (1984). “A theory of multiphase mixtures”, Rational Thermodynamics, Appendix 5C, 286-325.

Plona T J, (1980). “Observation of a second bulk compressional wave in a porous medium at ultrasonic frequencies”, Appl. Phys. Lett., Vol. 36(4), 259-261.

Straughan B, (2012). “Structure of the dependence of Darcy and Forchheimer coefficients on porosity”. Int. J. Engrg. Sci. , Vol. 48, 1610-1621.

Terzaghi, K. (1925), “Erdbaumechanik auf bodenphysikalischer Grundlage”, Leipzig-Wien, Franz Deuticke (In German).

Terzaghi K, (1943). “Theoretical soil mechanics”, J. Wiley & Sons.

Truesdell C, Toupin R A, (1960). “The classical field theories”, Encyclopedia of Physics, Vol. 3(1), Flügge S. (Ed.), Springer-Verlag.

Truesdell C, (1969). ”Rational thermodynamics”, McGraw-Hill, New York.

Verruijt A, (1982/a), “The theory of consolidation”, Proc. of the NATO advanced study institute on mechanics of fluids in porous media, Newark, Delaware, USA, July 18-27, Series E, Applied Sciences, No. 82, also published in: Fundamentals of transport phenomena in porous media, J. Bear and M.Y. Corapcioglu (eds.), Martinus Nijhoff, Dordrecht, 1984, 351-368.

Verruijt A, (1982/b), “Some remarks on the principle of effective stress”, in: IUTAM Conference on deformation and failure of granular materials, Delft, eds. P. A. Vermeer, H. J. Luger, A. A. Balkema, Rotterdam, 167-170.

SOIL SUCTION AND CRACKING FROM THE ONSET TO THE END OF DESATURATION: MICRO-SCALE EVIDENCE AND MODEL

T. Hueckel
Department of Civil and Environmental Engineering, Duke University, Durham, NC, USA

B. Mielniczuk and M.S. El Youssoufi
MIST Laboratory, IRSN, CNRS UMR 5508, Montpellier, France
LMGC UMR UM2-CNRS 5508, Université Montpellier 2, 34095 Montpellier Cedex 5, France

L.B. Hu
Department of Civil and Environmental Engineering, University of Toledo, Ohio, USA

L. Laloui
EPFL, Lausanne, Switzerland

ABSTRACT: *A multi-scale, multi-physics sequence of processes is discussed as developing during drying of non-clayey soils. Two variables are believed to be central in drying: suction resulting from the evaporation and effective stress associated with external constraints imposed on drying shrinkage. These two variables are tracked across the scales, both in experiments and simulations. The effective stress is critical as leading eventually to soil drying-cracking. Cracking is a most unwanted development in soil undergoing dewatering. Drying cracks often arise in the apparent absence of external forces. Hence, a tensile eigen-stress pattern resulting from stiff inclusions, or tensile stress produced by reaction forces at the boundary constraints need to be contemplated to reach cracking criteria. An earlier tubular micro-scale model of porous drying medium indicates that transport of water toward evaporating surface during saturation phase induces a high suction. A critical suction value is reached at which water body boundary is penetrated in an unstable manner by air. At the meso-scale such air penetration constitutes a surface imperfection, inducing a total stress concentration near its tip, and in the presence of significant pore suction, a rapid increase in local tensile effective stress and crack propagation. Recent experimental results from a configuration of a cluster of grains provide geometrical data suggesting that an imperfection resulting from of air entry penetrates deep into the granular medium over 4 - 8 radii of the typical pore. Further evolution entails separation of grain clusters by funicular bridge instabilities, and in the last stage formation of two-grain pendular capillary bridges. The final phase is associated with a gradual decrease of the micro-scale suction within these elementary bridges, which eventually evolve into a positive pressure before the bridge rupture.*

1 INTRODUCTION

Suction developing in drying soils and related drying cracking criteria have been intriguing points in unsaturated soil mechanics for some times. The issue starts with often very high values of suction observed from so called soil – water characteristic curves, which taken at face value should generate grain crushing, and culminates with a drying cracking criterion paradox that the tensile drying cracks seem to occur at a compressive effective stress state. The purpose of this paper is to bring together recent micro-scale measurements of capillary forces in model granular systems, numerical simulations of drying at a meso-scale, and provide an approach that disentangles the paradox.

Cracking is almost inevitable in soil structures subject to drying. Desiccation cracking arises in the apparent absence of external forces. Hence, a stress resulting from the reaction

forces generated at the external or internal constraints in response to suction, should be contemplated to arrive at a cracking criterion. Also an internal, self-equilibrated stress pattern due to kinematic incompatibilities, or a non-uniform moisture local content can generate throughtout the drying body (Peron et al., 2009). We apply our recent meso-scale model (Hu et al., 2013a, b, and c) of the shrinkage of drying tubular pores. We hence assess the generated stress in the vicinity of an imperfection, and a stress concentration near its tip, in the presence of significant pore suction. This approach allows us to use the effective stress analysis, which otherwise, away from the stress concentration usually yields compressive effective stress and hence a paradoxical criterion of tensile crack in a compressed body (Scherer, 1990; Hueckel et al., 2011). Experimental results from a hypothetical microstructure of a cluster of grains provide data concerning the evolution of capillary forces during drying and suggesting that events of air entry occur via local pore water surface instability penetrating deep into the granular medium over 4-8 internal radii of the typical pore (Mielniczuk et al., 2013; Hueckel et al., 2013). We postulate that such penetration generates an imperfection in the soil body, to cause a sufficient tensile stress concentration and even in the presence of large suction, the propagation of the drying macro-crack.

2 SCENARIO OF PROCESSES INVOLVED IN DRYING OF POROUS MEDIA

Drying of a porous body is envisioned as a sequence of multi-physics processes that are to be considered at different scales. We start with the observation that the system of pores detected via mercury porosimetry evolves in a particular way during drying (e.g. in Bioley silt, Peron et al., 2009). At different stages of drying, i.e. at the onset at liquid limit, LL, then near shrinkage limit, SL, and at the nearly complete desaturation, D, two classes of pores are seen to evolve in a distinctly different way. These classes, referred to as Large Pores (LP) of around 1.5 μm in diameter and Small Pores (SP) of 0.5 μm do not form any particularly distinct modes originally, but their evolution makes them distinct. As material dries from LL to SL, the Large Pores fraction is reduced to one third and less of the original fraction and altogether disappear at the end of drying (i.e. at w = 0.8%), whereas the volume fraction of the initial SP increases visibly compared to the initial state.

To reproduce this evolution, the medium is idealized as consisting of bunches of parallel cylindrical deformable vessels with two initial diameters, corresponding to LP and SP. There are twelve SPs per one LP in a representative volume, their external wall radius being 3.6 μm, shown in Fig. 1a and b. While we discuss only 1-D shrinkage, in a more general case the elementary volumes, the pore-vessels can be arranged as in Fig. 1b with 2-D intercalating layers of tubes oriented orthogonally ones to the others. As a result all quantities are appropriately weighed averages of the values pertaining to individual tubes. The vapor flux applied at the pore-vessel end imposes the Poiseuille flow of water throughout the vessel, associated with the shrinkage of tubes, commensurate with the volume of water removed.

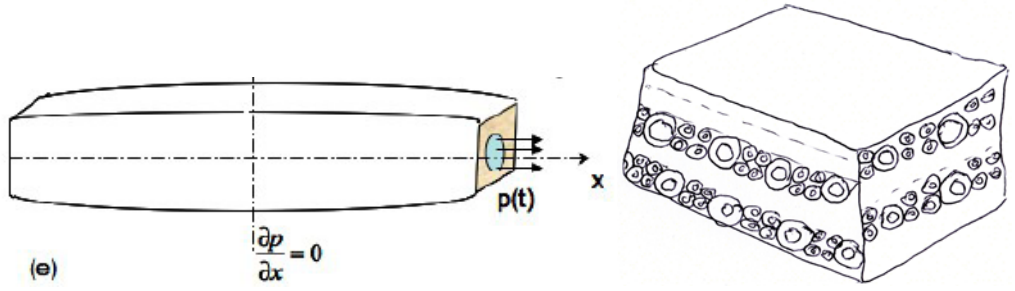

Fig. 1 (a) Model of a deformable pore-vessel subject to evaporation flux; (b) 2-D model of pore-vessels arranged in layers of perpendicular tubes

The water (negative) pressure increases until it reaches a critical value at the vessel exit, at which air penetrates the external boundary of the soil body. Two known criteria, of meniscus plunging and of water cavitation (tensile stress rupture) yield numerically the same criterion. The air entry event starts the second phase of soil desiccation during which the saturation degree actually decreases. In the next phase the evaporating flux is applied at a moving inter-phase interface within the vessel, leading to an increasing presence of the gas phase with the soil body.

The main result from the simulation is the evolution of the (negative) pressure o suction of water. Fig. 2 shows the evolution of pressure in a Large Pore-vessel shortly after it was invaded by air. As seen, the process after the air entry leads to a rapid demise of the pore water pressure, and hence the flow of water. Following the phase of water flow, the next phase consists in an incremental depletion of water via localized phase transition at the moving interface, until all water is gone. In that phase there is no change in pore pressure, hence there is no further volume change of the vessel. Hu et al., 2013b performed simulations of the entire process and the results for the Bioley silt are shown in Fig. 2 in terms of the pore volume change versus water volume loss. Specific instants: of the air entry into LPs, complete cessation of flow in LP, completion of the water removal from all LPs, the air entry into SP, and similar stages in the SP's can be clearly identified. At the meso scale of the assembly of pore-vessels the water pressure is seen to grow only during the flow phase, as a function of the flow dominant pore-vessel diameter, the smallest vessels requiring the highest suctions to activate the flow.

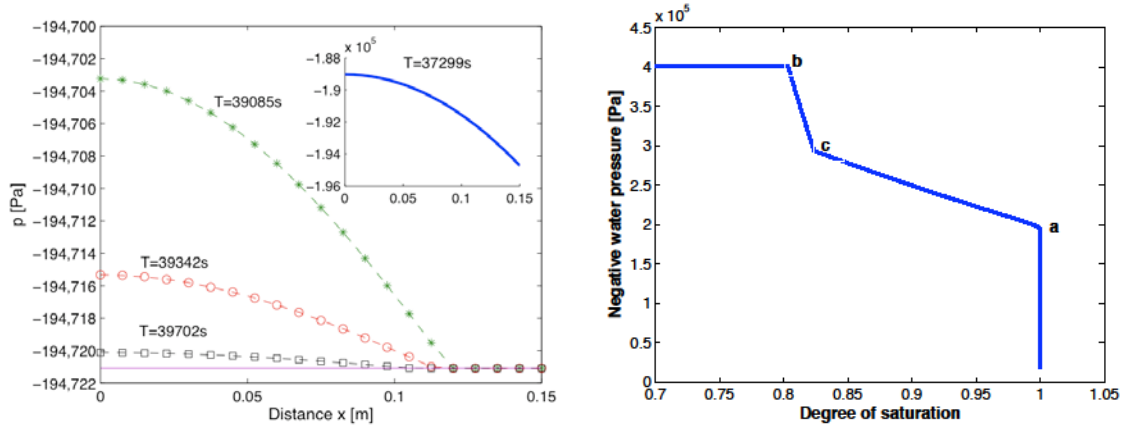

Fig. 2 Evolution of water pressure in pore vessel during drying after air entry into the vessel between *x=0.15* and 0.12 m from the tube center. Shown are three instances 3 minutes one after another, demonstrating a rapid decrease in pressure gradient

Fig. 3 Simulated soil-water characteristic curve obtained via pressure weighing procedure for the systems of the two modes of vessels vs Degree of Saturation

Nevertheless, as seen in Fig. 3, which simulates the soil – water characteristic curve, in this model, the highest suction of the individual smallest pores acts over a decreasing population of pores, and hence does not reach excessively high values per representative volume.

3 AIR ENTRY

The above numerical meso-scale studies calibrated against the experimental results of Peron et al., 2009 yield the value of suction corresponding to the air entry. A numerical criterion for the air entry is generally accepted in soil mechanics (Terzaghi, 1927, see also Lu and Likos, 2003) and expressed via critical pressure difference that of the fluid, p, and atmosphere, p_a, (eq. 1) at a point when a decreasing meniscus radius becomes smaller that the largest pore throat radius. In our case, the radius of meniscus, r, becomes equal to the entrance of the

pore-vessel tube $r = a(t)$, and with τ_s being water surface tension, and θ the wetting angle, the critical pressure reads

$$p - p_a = -\frac{2\tau_s \cos\theta}{r}; r = a|_{x=L} \tag{1}$$

The main point to be stressed is that the change of pore size during drying is substantial, and hence the value of the critical pore size needs to be accordingly adjusted. The resulting values of the critical pore pressure are 194 kPa for the class of large pores of the order of the original 1.5 μm that shrunk to 0.78 μm and 280 kPa for the class of small pores of the order of the original 0.5 μm that shrunk to 0.42 μm (Hu et al., 2013b).

The air entry phenomenon, despite that it occurs at the scale of a single pore, is considered a macroscopic property of soil, mainly based on the assumption of the equality of the fluid pressure at both scales.

A suggestive air entry mechanism in a 2D granular system has been envisioned by Childs (1969) in terms of a succession of stages during drying and re-wetting (Fig. 4).

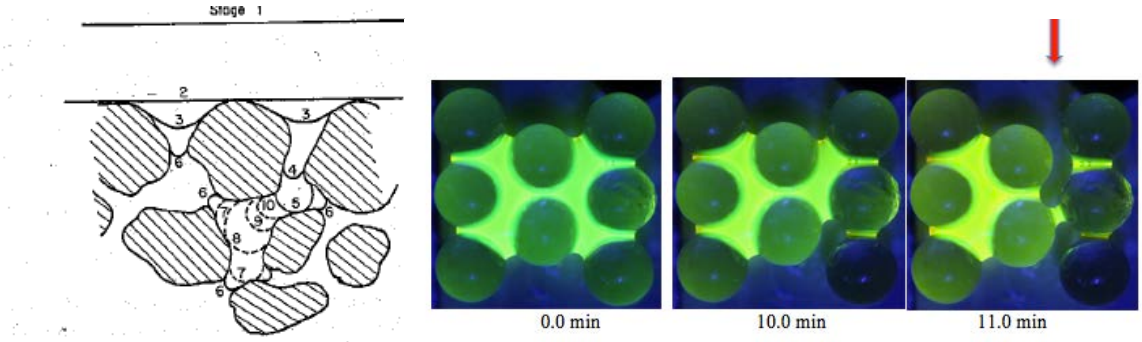

Fig. 4. Succession of meniscus evolution during suction dewatering and rewetting, by Childs (1969)
Fig. 5. Evolution of model grain assembly during drying. The arrow points to air entry sites

However, recent experiments at a meso-scale with drying of model clusters of smooth glass grains (Mielniczuk et al., 2013) with the funicular water bound between them reveal that there are more than a single air entry mode. The most characteristic two modes identified in experimental systems tested of 3, 4, 5, 6 and 8 silica grains in distilled water were two classes corresponding to a negative or positive local Gaussian curvature (which is a product of the two principal curvatures) of the surface of the local meniscus. Most typically, for a negative Gaussian curvature (or concave/convex meniscus) a non-symmetric mode of the unstable evolution of the water body constitutes a most common air entry mechanism into the body of the saturated soil. While the circumstances and numerical criterion for the event are still an open question, it clearly is an unstable and localized displacement of the gas/liquid interface in form of a finger, occurring at a several orders of magnitude higher rate than the preceding process manifested among others by a slow evolution of the liquid/gas interface. Fig. 5 shows three of a series of images of a 2D saturated cluster of 8 grains (Mielniczuk et al., 2013) shot every 90 seconds during natural isothermal drying (using Canon EOS 500D camera). Grains were 3.5 mm in diameter ultrafine silica (glass) spheres, while the liquid is ultra-pure deionized water. As indicated, it took 10 minutes from the initial configuration to reach the intermediate one, and less than 90 additional seconds to develop the final configuration with the gas penetration. The depth of the penetration of the gas finger is about 4 times the average size (diameter) of the pore. For smaller configurations a fast camera

imaging revealed that the unstable process takes about 1/2000-th of a second to develop a new configuration.

An alternative, symmetric entry mode takes place at a point with a positive Gaussian curvature (concave/concave meniscus) between the spheres and consists of a multi- step process: starting with a convergence of two gas/liquid interfaces situated opposite one another (at the front and back of the picture), followed by formation of a suspended thin film of liquid, followed by a further thinning of the film, leading to coalescence of the two surfaces, undergoing what seems like a 2-D water cavitation, which subsequently propagates symmetrically with a circular projection until its boundary reaches the solid walls of the sphere. This is shown in Fig. 6 for a six-sphere cluster. Notably, the non-symmetrical scenario occurs for systems with higher separations between grains, while for lower separations a symmetrical scenario takes place. The unstable part of the process starts at the point when the thin film of water bifurcates. The bifurcations of thin films and thin sheets have been known for sometime (see e.g. Taylor, 1959), but for capillary bridges have been observed only recently by Maeda and Israelachvili (2012) with a mixture of water and vapor molecules, of an intermediate density.

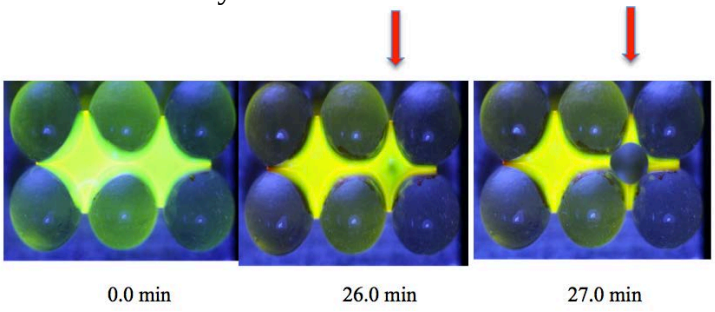

Fig. 6. Evolution of the water body between 6 silica (glass) spheres subjected to evaporation at constant temperature, constant ambient vapor pressure. The red arrow indicates a localized symmetric unstable mode of the interface evolution (air entry via thin film instability)

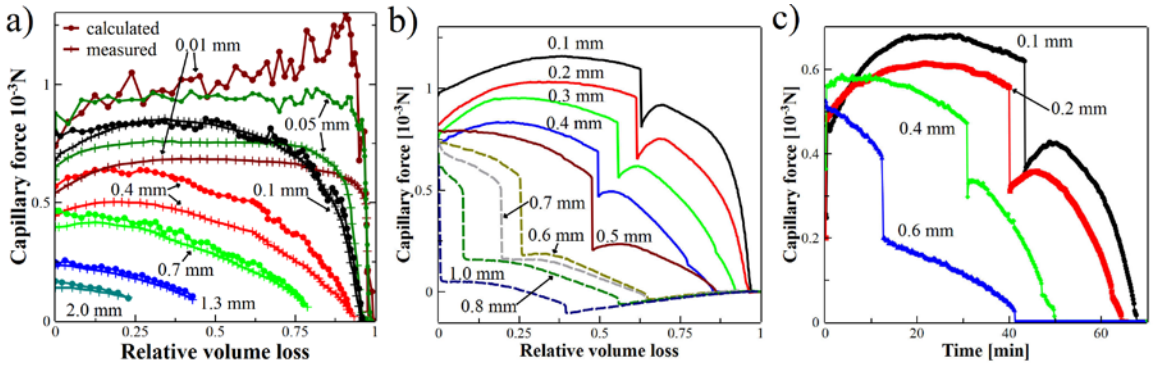

Fig. 7. Evolution of the total resultant capillary force between two spheres during evaporation, calculated from the radii of curvature and measured directly in the experiment (a); measured for 3, (b); and 4 spheres (c).

Interestingly, the symmetric mode of air entry shown above is a prime example of a transformation of a funicular bridge into three pendular ones, which in turn, depending on the inter-granular distance, may undergo a rupture. In general it is seen that the inter-granular force undergoes during evaporation a modest growth above the initial value (up to 20%), to be followed by a steady decline, most commonly to zero. Both events: the air entry and water body rupture, are invariably associated with a substantial discontinuity of the inter-granular force. Fig. 7 shows the evolution of the inter-granular force of systems of 2, 3 and 4 grains

with coplanar positions of their spheres. As seen, the jump of the force reaches up to 70% of the maximum force.

Capillary theory (see e.g. Willett et al., 2000) states that the total inter-granular capillary force, F_C is a sum of two components, resulting respectively from suction in water of capillary bridge acting over the liquid/solid contact and surface tension acting over the perimeter line of solid/liquid/air contact. Both components are proportional to the surface tension coefficient, τ_s, and depend on the radii of curvature of the bridge at the mid height, horizontal, r_g and vertical one, $r_{ext.}$

$$F_C = \tau_s [2\pi r_g + \pi r_g^2 (r_g^{-1} - r_{ext}^{-1})] \qquad (2)$$

The two components for a pendular bridge of 4μm between two silica (glass) grains obtained experimentally for different (constant separations) are shown in Fig. 8. At the beginning of the evaporation, suction force stays more or less steady and the total force is dominated by the surface tension force component. The latter decreases all the time while for smaller separations it accelerates toward the end (last ¼ of the initial water volume) of the process. Notably, at the end of drying both components decrease to zero. It is common in unsaturated soil mechanics to emphasize the role of suction component in suction hardening, while ignoring the surface tension component.

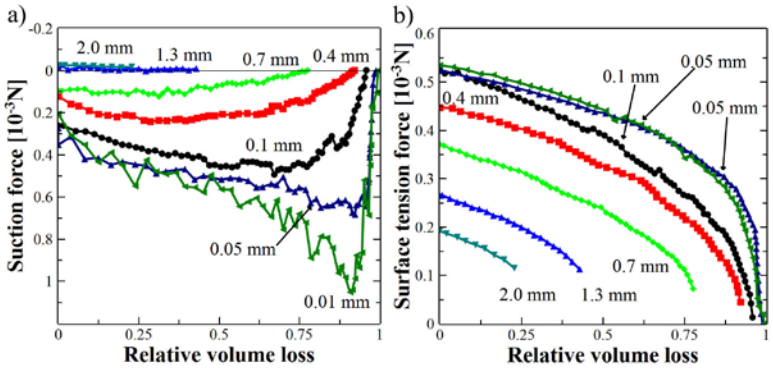

Fig. 8. Evolution of suction force and surface tension force during dryin of two-sphere water bridge

Interestingly, suction in itself, whitch by virtue of Laplace-Young law depends on the sum of the two normal curvatures at the mid height of the pendular bridge, is not neccessarily always positive. For larger separations (> 1mm) it is indeed negative (hence a repulsive pressure, indeed), whereas for the small (including very small) separations it evolves during drying from the initial attractive (suction) to repulsive (pressure) at the small water volumes remaining (Fig. 9). Notably, in a series of parallel experiments of extension of capillary bridges, at various constant values of bridge liquid volume the initial suction transforms into considerable pressure (hence repulsive force).

As seen from Laplace-Young equation (2) this occurs as a direct result of the evolution of the curvatures of the gorge and external (or side) curvature of the neck. The gorge curvature imparts positive pressures, whereas the external curvature induces always suction. The gorge curvature is from the onset larger than the external curvature for 2 and 1.3 mm separations. But for smaller separations, < 0.7 mm, the gorge curvature is initially nearly half or less than the external one, and external curvature is dominant, and practically independent of separation, resulting in a higher suction.

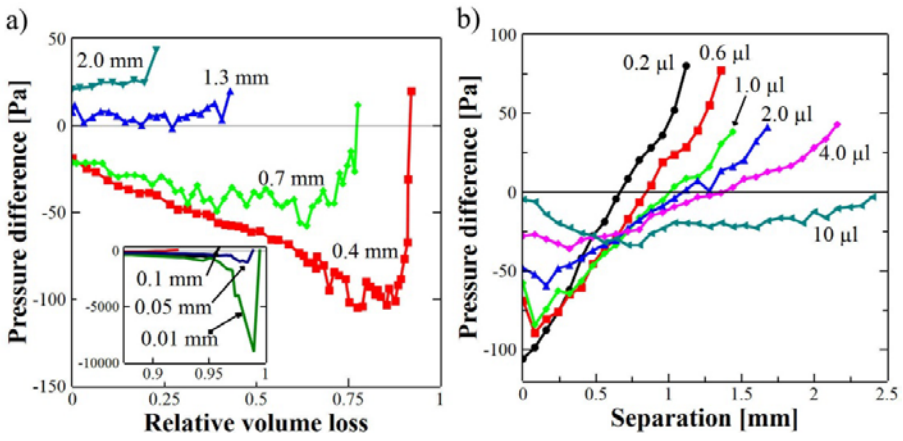

Fig. 9. Evolution of pressure difference (negative means suction) in the capillary bridge between two-grains: (a) during evaporation; (b) during extension

The maximum of suction is the matter of the competing rates of evolution of the two curvatures. Nevertheless, near 90% of water gone, the gorge becomes so tiny, and its curvature very high, resulting hence in a positive pressure. It should be realized that the phenomena described immediately above refer to the very terminal phases of drying of the granular medium. Yet, they indicate quite a complex dynamics of development of suction in capilary bridges, much more than it is usually presented in macro-scopic models of unsaturated soils.

4 DRYING CRACKING

Most of soil systems, either natural or engineered exposed to drying do crack at some point, unless drying occurs in idealized conditions of no kinematic constraints whatsoever. The occurrence of cracking, which takes place at a surprisingly narrow range of water content, changes substantially both the dynamics of further evaporation and the configuration, and hence the mechanical boundary conditions of the unsaturated soils. Those two aspects are widely ignored in the unsaturated soil mechanics.

As mentioned earlier, criteria of desiccation cracking via macroscopic approach suffer from a major handicap. A consideration of a 1D drying of a constrained saturated granular body easily shows that a modest total stress is generated in reaction to the constraints and that it is tensile, whereas the values of suction induced by the evaporation flux is significant. Consequently, the resulting effective stress appears to be compressive. This is counterintuitive, as drying failure evidently occurs through tensile cracking.

Scherer (1992) postulated a scenario, suggesting that desiccation cracking is necessarily triggered through crack propagation from a tip of a pre-existing structural flaw in the soil body, at which a substantial total stress concentration occurs. Consequently, the remote total stress is augmented locally through a stress concentration and becomes larger in absolute terms than the elevated suction. As a result the local effective stress becomes tensile, and hence prone to reach the tensile strength of the material, and thus prompting the crack propagation evolving from the material flaw.

We postulate that a non-symmetric finger of air entry as described above, constitutes a sufficient imperfection (flaw) in the drying granular body to produce enough of a concentration of total stress induced by the kinematic restraints to the drying shrinkage around the tip of the flaw, to generate crack propagation, as proposed by Péron et al., 2010, and Hu et al., 2011.

Within the above framework we consider an air finger (flaw) with depth c and curvature radius at the finger tip of r_c at the soil surface, which is surrounded by the micro-tubes pore system as shown in Fig.10. The network of hollow cylinder pore-vessels of micro-tubes representing at the meso-scale the pore system is adapted from the model of Hu et al., 2013a to simulate the shrinkage mechanism for silty soil due to water evaporation. The external radius (R_{ext}) of the tubes equal to $3.6\mu m$ is calculated from the measured macroscopic porosity and the initial and current internal radius (R_{int}) are equal to 1.5 and 0.75 μm, respectively. These radii are identified as representative of Large Pores based on the mercury intrusion porosimetry data on Bioley silt and calibrated simulation (Hu et al., 2013 a, b). Using the principles of linear fracture mechanics, the stress at the external boundary of the tubes, which are placed near the flaw tip can be calculated as the far-field (macro-scale) stress at crack initiation as (stress is positive in tension)

$$\sigma_x = \frac{K_{I\,crit} + \frac{1}{2} p\sqrt{\pi r_c}}{B\sqrt{\pi c}} \tag{3}$$

where $K_{I\,crit}$ is the critical stress intensity factor, B is a constant equal to 1.12 and p is the fluid pressure inside of the pore (Scherer, 1992).

The depth of a flaw (c) can be estimated from Fig. 4b as 2-4 times the diameter of the original biggest pore, assessed for Bioley silt as d=1.5 μm (hence c =7.5 μm for that silt). Hu et al., 2013a. The flaw tip curvature radius r_c is found to be of the same order as the internal radius of the biggest pore (d/2=0.375 μm). A desiccation crack is generally initiated when the soil suction reaches the suction value at the air entry moment. Considering the biggest current pore size of $0.75\mu m$, the suction value at air entry for Bioley silt has been calculated as 194 kPa (Hu et al., 2013b). Adopting a value of 0.16 kN/m$^{3/2}$ for the critical stress intensity factor as measured by Chertkov (1995) for a sandy silt soil, a value of σ_x = 39kPa is obtained for the macro scale total stress from Eq. 3. This value is close enough to the one obtained experimentally by Péron (2008) in simulations of the drying experiments on constrained slabs of Bioley silt (25 kPa). The local total stress at the flaw tip is hence estimated as

$$\sigma_c^{\max} = 2B\sigma_x\sqrt{\frac{c}{r_c}} \tag{4}$$

which yields a value of 295 kPa (tension), which translates into about 101 kPa of the local effective tensile stress at the crack tip. That is equivalent to compressive 235 kPa of effective macro-scale stress at cracking.

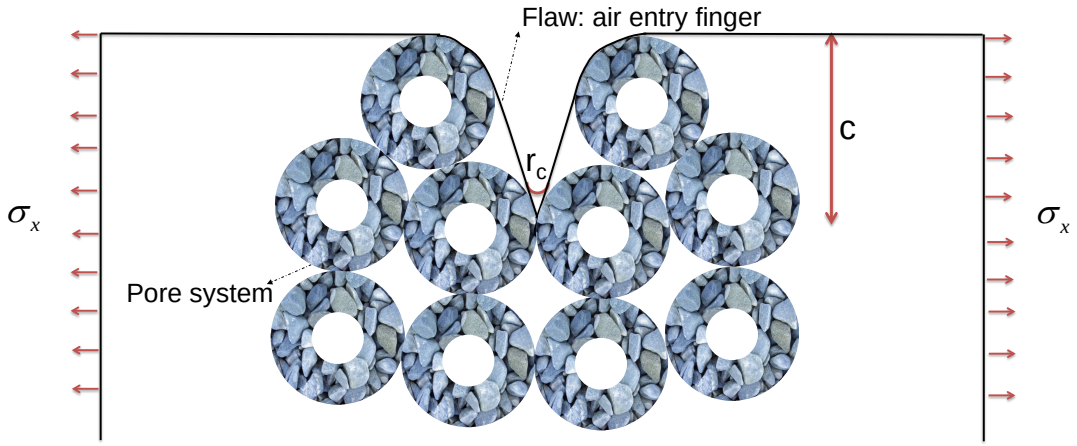

Fig. 10. An idealized meso-scale pore network in the vicinity of an air finger

5. CONCLUSIONS

A multi-scale scenario of evolution of suction, effective stress, air entry and cracking during drying of non-clayey soils is discussed in view of macro-, meso- and micro- scale experiments. While the picture emerging is far from being complete, some findings are consistent with, and some different, from the current thinking in unsaturated soil mechanics. The evolution of resultant inter-granular forces during drying needs to be considered, rather than that of suction alone. Indeed, the effect of surface tension during drying may become dominant in inter-granular interactions toward end of drying. Suction per se undergoes evolution from positive to negative, hence exerting repulsion across the liquid bridge. In no investigated case any dramatic increase of suction toward the end of drying was seen.

The air entry was observed on granular models as an unstable evolution of the liquid body surface in a variety of forms. One of the forms is penetration of an air pocket with depth of 3-8 radii of the typical largest pore. The penetration is seen to be associated with a sudden decrease by half of inter-granular force. No particular condition for the instability producing the air entry has been identified, as yet.

The air entry has been postulated to for a material imperfection, giving rise to the total stress concentration near its tip. The stress arises in response to constraining drying shrinkage at the substrate or reaction points. Such stress concentration, is shown in a linear elasticity fracture mechanics parametric study to produce a sufficiently high hike in the local tensile effective stress value to promote the growth of tensile crack, despite high suction and hence a compressive effective stress at a macro-scale. As the air entry constitutes a common and ubiquitous occurrence, and most of drying bodies are constrained in their shrinkage, the above postulate appears to yield a reasonable criterion for drying cracking.

ACKNOWLEDGEMENT

Portion of the work has been funded by the US NSF, grant No. 0324543 of CMMI Division, Geomechanics and Geomaterials Program (T. Hueckel) and support of CNRS, MIST laboratory and the Languedoc-Roussillon region (B. Mielniczuk, M. S. El Youssoufi, T. Hueckel).

REFERENCES

Childs E.C. (*1969*) An introduction to the physical basis of *soil* water phenomena. London: Wiley, Interscience.

Chertkov, V.Y., (1995), Evaluation for soil of crack net connectedness and critical stress intensity factor, Int. Agrophysics, 9, 189 -195

Hu, L.B. H. Peron, L. Laloui and T. Hueckel, A multi-scale multi-physics model of soil drying, Geofrontiers, 2011,

Hu, L. B., H. Péron, T. Hueckel, L. Laloui, (2013a) Desiccation shrinkage of non-clayey soils: multi-physics mechanisms and a microstructural model, Int. J. Numer. Anal. Meth. Geomech, DOI: 10.1002/nag.2108.

Hu, L. B., H. Péron, T. Hueckel, L. Laloui, (2013b) Desiccation shrinkage of non-clayey soils: a numerical study, Int. J. Numer. Anal. Meth. Geomech., DOI: 10.1002/nag.2107

Hu, L. B., H. Péron, T. Hueckel, L. Laloui, (2013c) Mechanisms and critical properties in drying shrinkage of soils: experimental and numerical parametric studies, Can. G. J., in print

Hu, L. B., M. Monfared, B. Mielniczuk, L. Laloui, T. Hueckel, M. S. El Youssoufi, 2013, Multi-scale approach to cracking criteria for drying soils, GeoCongress, ASCE 2013, 838 -845

Kodikara J., Barbour S.L., Fredlund D.G., 1999, Changes in clay structure and behaviour due to wetting and drying. in Proceedings of the eighth Australia-New Zealand Conference on Geomechanics, Vitharana ND, Colman R (eds). Hobart, Australia, 1999; 179–185.

Lu, N. and Likos, W., 2003,

Maeda, N; Israelashvili, JN; Kohonen, MM, 2003, Evaporation and instabilities of microscopic capillary bridges, Proc. National Academy of Sciences: 100, 3: 803-808

Mielniczuk, B., T. Hueckel, M. S. El Youssoufi (2013) Micro-scale study of rupture in desiccating granular media, GEO-CONGRESS 2013,

Pellenq RJM, Coasne B, Denoyel RO, Coussy O. 2009, Simple phenomenological model for phase transitions in confined geometry. 2. Capillary condensation/evaporation in cylindrical mesopores. Langmuir 25(3):1393–1402.

Péron, H.,T. Hueckel, L. Laloui, L.B. Hu (2009), Fundamentals of desiccation cracking of fine-grained soils: experimental characterization and mechanism identification, Canadian Geotechnical J., 46, 1177-1201

Péron, H., L. Laloui, L.B. Hu, and T. Hueckel (2010), Desiccation of drying soils, in Mechanics of Unsaturated Geomaterials, p. 55-86, edited by L. Laloui, J. Wiley, Hoboken, NJ,

Péron, H. (2008) Desiccation cracking of soils, PhD thesis, EPFL, Lausanne

Scherer G.W., 1992, Crack-tip stress in gels, *J. Non-Cryst. Solids*, vol. 144, 210-216

Taylor, G.I., 1959, The dynamics of thin sheets of fluid. III. Disintegration of fluid sheets, Proc. R. Soc. London, Ser. A 253, 313 ~1959

Terzaghi K., 1927, Concrete roads - A problem in foundation engineering. Journal of the Boston Society of Civil Engineers 1927; 14:265–282.

Willett, Ch. D., Adams, M. J., Johnson, S. A., Seville, J. P. K. (2000). Capillary bridges between two spherical bodies, *Langmuir* 16: 93-96.

HIGH PRESSURE GAS TRANSPORT UNDER COUPLED THERMAL, HYDRAULIC, CHEMICAL AND MECHANICAL BEHAVIOUR

L.J. Hosking
Geoenvironmental Research Centre, Cardiff School of Engineering, Cardiff University, Cardiff, UK

M. Sedighi
Geoenvironmental Research Centre, Cardiff School of Engineering, Cardiff University, Cardiff, UK

H.R. Thomas
Geoenvironmental Research Centre, Cardiff School of Engineering, Cardiff University, Cardiff, UK

ABSTRACT: *This paper presents the development of a theoretical framework to study high pressure reactive gas transport in geo-materials. The development is based on a coupled thermo-hydro-chemo-mechanical (THCM) formulation. Theoretical features related to gas transport and solid-gas interactions are included in the coupled THCM formulation. Particular focus has been placed upon the accurate description of gas mixture behaviour under supercritical conditions. An application of the model is presented which demonstrates the key processes involved as the in situ gas of a geological formation is replaced by another gas injected at high pressure. The work is of relevance to applications such as the geological sequestration of carbon dioxide in coal and enhanced coalbed methane recovery.*

1 INTRODUCTION

The reactive transport behaviour of multicomponent gas at high pressure is considered in this paper. This is achieved via the development of an existing theoretical formulation of reactive gas transport within a coupled thermal, hydraulic, chemical and mechanical (THCM) model. This provides further capabilities to study processes related to high pressure gas flow in geoenergy applications such as carbon dioxide sequestration and coalbed methane recovery.

The basis of the work is a coupled THCM formulation, developed by Thomas and co-workers at the Geoenvironmental Research Centre, Cardiff University (e.g. Thomas and He, 1998; Thomas et al., 2012). The chemical behaviour is considered therein via a combination of theoretical advances in multicomponent chemical transport and geochemistry under coupled THCM behavior (Thomas et al., 2012; Sedighi et al., 2012). The work has recently been extended to include the reactive transport of ideal gas mixtures (Masum, 2012).

Multiphase flow models consider some level of integration between thermal, hydraulic and mechanical behaviour. The behaviour of dissolved and gas chemical components have been included in some models, considering mainly ideal gas behaviour (e.g. Xu and Pruess, 2001; Masum, 2012). In this paper further integration of non-ideal reactive transport of multicomponent gas in coupled THCM modelling is described.

The background theoretical and numerical formulation of the coupled THCM model is first provided in a summarized form. The description of the theoretical formulation for non-ideal multicomponent reactive gas transport is presented in greater detail, including the features specific to high pressure gas flow in reactive porous media. An example application of the model simulating the processes involved in carbon dioxide sequestration in coal is provided.

2 BACKGROUND OF THE COUPLED THCM FORMULATION

A mechanistic approach is employed and the laws of energy conservation, mass conservation and stress equilibrium are applied to derive the governing equations for heat transfer, moisture and chemical transport and mechanical behavior, respectively. The governing equations are presented in terms of the primary variables, namely, temperature (T), pore water pressure (u_l), pore air/gas pressure (u_g), concentrations of dissolved and gas chemicals (c_α^i, $\alpha = l, g$), and displacements (**u**). In terms of chemical transport, the governing equations describe chemical components in the liquid and gas phases, including a sink/source term for chemical reactions with the solid phase, expressed as:

$$\frac{\partial \theta_l c_l^i}{\partial t} + \frac{\partial R_{c_l}^i}{\partial t} = -\nabla \cdot \left(q_{c_l}^i \right) \tag{1}$$

$$\frac{\partial \theta_g c_g^i}{\partial t} + \frac{\partial R_{c_g}^i}{\partial t} = -\nabla \cdot \left(q_{c_g}^i \right) \tag{2}$$

where t is time and ∇ is the gradient operator. The terms θ_l and θ_g represent the volumetric liquid water and gas contents, respectively. The terms $q_{c_l}^i$ and $q_{c_g}^i$ represent the chemical flux of the i^{th} component in the liquid and gas phases, respectively. Finally, the terms $R_{c_l}^i$ and $R_{c_g}^i$ represent various sinks/sources due to phase transformations and geochemical reactions for the i^{th} component in the liquid and gas phases, respectively.

The expanded governing equations for each flow process are expressed in the following general form:

$$\begin{aligned} &\mathbf{C}_{\Psi l} \frac{\partial u_l}{\partial t} + \mathbf{C}_{\Psi T} \frac{\partial T}{\partial t} + \sum_{j=1}^{N} \mathbf{C}_{\Psi c_\alpha} \frac{\partial c_\alpha^j}{\partial t} + \mathbf{C}_{\Psi \mathbf{u}} \frac{\partial \mathbf{u}}{\partial t} \\ &= \nabla \left[\mathbf{K}_{\Psi l} \nabla \cdot u_l \right] + \nabla \left[\mathbf{K}_{\Psi T} \nabla \cdot T \right] + \nabla \cdot \sum_{j=1}^{N} \left[\mathbf{K}_{\Psi c_\alpha} \nabla \cdot c_\alpha^i \right] + J_\Psi \end{aligned} \tag{3}$$

where N represents the number of chemical components in the respective phase, and **C** and **K** matrices are the storage and flux terms, respectively. Binary subscripts have been assigned to illustrate how each primary variable ψ may be influenced in the coupled system. The term J_ψ is used to represent the gravitational flux.

The finite element method is employed to spatially discretise the equations, and a finite difference algorithm is employed to achieve temporal discretisation. This has been found to provide a suitable solution for the current problem (Thomas and He, 1998). Further details of the numerical solutions can be found in Thomas and He (1998). The numerical equations can be expressed in matrix form as:

$$\mathbf{A}\phi + \mathbf{B}\frac{\partial \phi}{\partial t} + \mathbf{C} = \{0\} \tag{4}$$

where **A**, **B** and **C** are the matrices of coefficients and ϕ represents the vector of primary variables.

Further details of the theoretical and numerical solutions can be found in Thomas and He (1998) and Thomas et al. (2012). Detailed developments in the formulation of the gas chemical module of the model are presented in the following sections.

3 GAS CHEMICAL TRANSPORT FORMULATION

The development of the multicomponent gas chemical transport equation in Eq. (2) is presented in detail in this section. The gas chemical flux is considered as the sum of flux components due to advection and diffusion (Bird et al., 1960). The advective flux is driven by bulk gas pressure gradients and is expressed using Darcy's law, which for the i^{th} component yields:

$$q_{ad}^{i} = X_{g}^{i}\left(c_{g}^{T}\mathbf{v}_{\mathbf{g}}\right) = -c_{g}^{i}k_{g}\nabla\cdot u_{g} \tag{5}$$

where q_{ad}^{i} and X_{g}^{i} represent the advective flux and mole fraction of the i^{th} component, respectively. The terms c_{g}^{T}, $\mathbf{v}_{\mathrm{g}}$ and k_g represent the total gas concentration, Darcy velocity and gas conductivity, respectively.

Bulk gas properties are dependent on pressure, temperature and composition (Kee et al., 2003). In order to include the effects of composition on gas transport properties such as compressibility, viscosity and diffusivity, the present formulation treats the bulk gas as a mixture of gas chemicals. The bulk gas phase pressure u_g is calculated using the real gas law (Hagoort, 1988):

$$u_{g} = ZRT\sum_{i=1}^{N_g} c_{g}^{i} \tag{6}$$

where Z is the compressibility factor, R is the universal gas constant and N_g is the number of gas components in the mixture.

From Eq. (5) and Eq. (6) the advective flux for the i^{th} gas component can be expressed in an expanded form as:

$$q_{ad}^{i} = -c_{g}^{i}k_{g}ZRT\sum_{j=1}^{N_g}\nabla\cdot c_{g}^{j} - c_{g}^{i}k_{g}ZR\sum_{j=1}^{N_g}c_{g}^{j}\nabla\cdot T \tag{7}$$

A molecular diffusion flux exists in the presence of a concentration gradient, and is described using Fick's law of diffusion considering effective diffusion coefficients D_{i}^{e} (Bird et al., 1960). The molecular diffusion flux for the i^{th} gas component is then given by:

$$q_{diff}^{i} = D_{i}^{e}\nabla\cdot c_{g}^{i} \tag{8}$$

The sink/source term for the i^{th} gas chemical in Eq. (2) is expressed as the temporal derivative of R_{g}^{i}. An adsorption isotherm model is used to describe the absolute amount of gas adsorbed at a given pressure and temperature. The extended Langmuir isotherm (ELI) is applied for multicomponent gas systems and has been shown to provide an accurate fit to experimental data for a range of gas species and their mixtures at high pressure (e.g. Chaback et al., 1996). According to the ELI approach, the adsorbed concentration of each component *i*

in equilibrium with the free gas concentrations of components k is expressed as (Ruthven, 1984):

$$c_s^i = \frac{V_L^i b_L^i ZRT c_g^i}{1 + ZRT \sum_{k=1}^{N_g} b_L^k c_g^k} \tag{9}$$

where c_s^i represents the adsorbed concentration, V_L^i represents the saturation capacity of the porous medium and b_L^i is the reciprocal of the Langmuir pressure.

Eq. (9) allows the sink/source term in Eq. (2) to be recast in the following form for multicomponent gas adsorption:

$$\frac{\partial R_g^i}{\partial t} = \sum_{j=1}^{N_g} (1-n) \frac{S_g \partial c_s^i}{\partial c_g^j} \frac{\partial c_g^j}{\partial t} = \sum_{j=1}^{ng} \left[\frac{(1-n) S_g V_L^i b_L^i ZRT \left(1 - b_L^j ZRT c_g^i + ZRT \sum_{k=1}^{ng} b_L^k c_g^k\right)}{\left(1 + ZRT \sum_{k=1}^{ng} b_L^k c_g^k\right)^2} \right] \frac{\partial c_g^j}{\partial t} \tag{10}$$

where n represents the porosity.

The advective and diffusive fluxes defined in Eq. (7) and Eq. (8), and the sink/source term in Eq. (10) may then be substituted into the mass balance equation given in Eq. (2). Expansion of the first term in Eq. (2) in terms of the primary variables then gives the governing equation for the transport of the i^{th} gas chemical component:

$$\begin{aligned} &\left(n c_g^i \frac{\partial S_l}{\partial s} \right) \frac{\partial u_l}{\partial t} + \left(n c_g^i \frac{\partial S_l}{\partial s} \frac{\partial s}{\partial T} \right) \frac{\partial T}{\partial t} + \sum_{j=1}^{N_g} \left(\delta_{ij} n S_g - n c_g^i ZRT \frac{\partial S_l}{\partial s} + (1-n) S_g \frac{\partial c_s^i}{\partial c_g^j} \right) \frac{\partial c_g^j}{\partial t} \\ &+ \left(c_g^i S_g \mathbf{m}^T \mathbf{P} \right) \frac{\partial \mathbf{u}}{\partial t} = \nabla \left[- c_g^i k_g ZR \sum_{j=1}^{N_g} c_g^j \nabla \cdot T \right] + \nabla \cdot \sum_{j=1}^{N_g} \left[\left(c_g^i k_g ZRT + \delta_{ij} D_i^e \right) \nabla \cdot c_g^j \right] \end{aligned} \tag{11}$$

where S_l and S_g represent the degrees of liquid water and gas saturation, respectively. The terms s, $\mathbf{m}$ and $\mathbf{P}$ represent suction, a differential operator and the strain matrix, respectively. Finally, the term δ_{ij} is the Kronecker delta.

4 BEHAVIOUR OF GAS MIXTURES AT HIGH PRESSURE

The major properties of gas species and their mixtures are highly dependent on pressure, temperature and composition. For example, the phase change of species such as carbon dioxide to supercritical state at high pressure has a significant impact on its behaviour. The key gas properties based on the formulation described are i) non-ideal bulk gas compressibility, ii) bulk gas viscosity, and iii) component diffusivities. Appropriate relationships to describe the above properties as a function of pressure, temperature and composition have been adopted in the model.

In this work non-ideal compressibility behaviour is considered using an equation of state (EoS) approach, which provides a relationship between pressure, volume and temperature (Dake, 1978). Deviations of real gases from ideal gas behaviour are expressed by the compressibility factor Z, which is the ratio between the actual molar volume $V_{m,real}$ and the ideal molar volume $V_{m,ideal}$. The EoS proposed by Peng and Robinson (1976) is used because it is widely applied, accurate and yet requires little input data (Wei and Sadus, 2000). The

Peng and Robinson EoS is expanded to multicomponent form using the van der Waals mixing rules, and expresses the bulk gas pressure as:

$$u_g = \frac{RT}{V_{m,ideal} - b_{mix}} - \frac{a_{mix}}{V_{m,ideal}^{\ 2} + 2b_{mix}V_{m,ideal} - b_{mix}^{\ 2}} \tag{12}$$

where b_{mix} represents the effective volume of the molecules contained in one mole of bulk gas, and a_{mix} is a coefficient accounting for intermolecular interactions in the mixture.

Real gas behaviour may approach the conceptual model of an ideal gas at low pressures and high temperatures. For an ideal gas the factors a_{mix} and b_{mix} become zero and Eq. (12) reduces to the ideal gas law. However, the ideal gas law does not accurately describe the pressure-volume-temperature characteristics of gas under the majority of conditions (Dake, 1983). The factors a_{mix} and b_{mix} are therefore used to form the coefficients of a cubic equation in terms of Z, which is solved accordingly.

Fig. 1 shows the variation of the Z factor for pure carbon dioxide (CO_2) and a series of binary gas mixtures with gas pressure as predicted by the implemented EoS. Results are presented for gas at a temperature of 318 K.

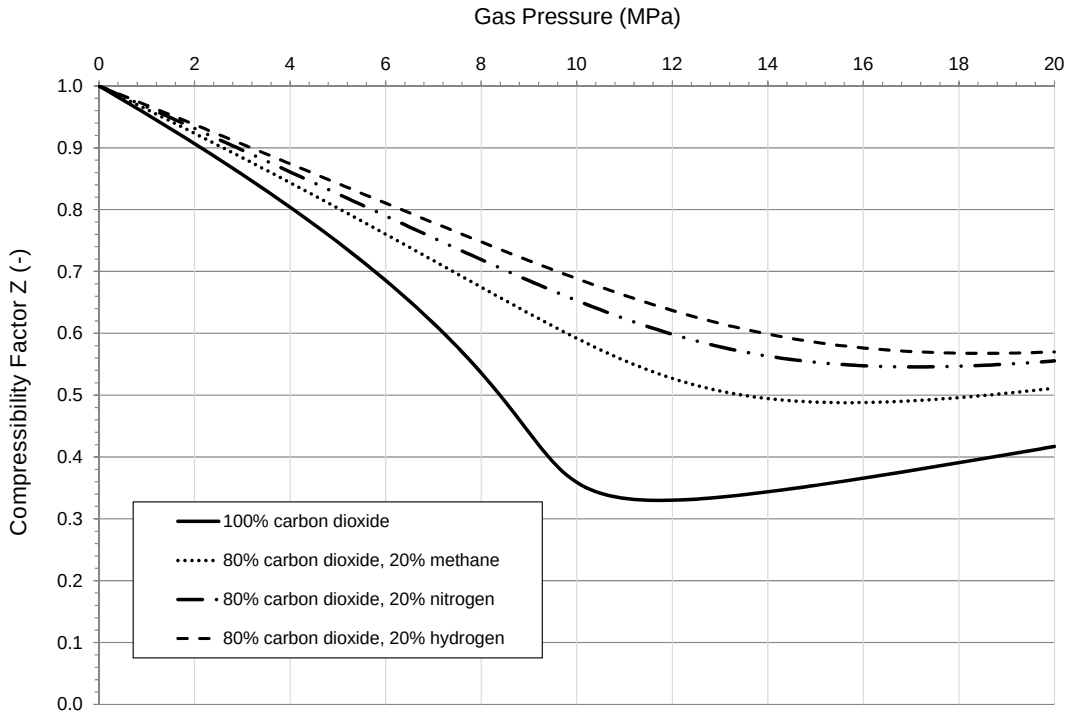

Fig. 1. Influence of gas composition on the compressibility factor at 318K.

It can be seen from Fig. 1 that the addition of methane (CH_4), nitrogen (N_2) or hydrogen (H_2) each at 0.2 mole fraction affects the extent to which the gas deviates from ideal gas behaviour.

Gas mixture viscosity has been included using the model proposed by Chung et al. (1988). This model was selected because the authors reported absolute deviations of around 9% for non-polar gas mixtures at high pressures, which is suitably accurate for the present formulation. To the knowledge of the author, experimental data for gas diffusivity at high

pressure is fairly limited. The correction of gas diffusion coefficients for high pressure is therefore achieved using a simple empirical model described by Poling et al (2001), which considers an inverse relationship between the diffusion coefficients and density.

5 REACTIVE FLOW OF MULTIPLE GASES

This section presents an example application of the model to study the advective/diffusive reactive transport of multicomponent gas at high pressure. Simulation conditions consider the replacement of in situ coalbed CH_4 by gas injected at high pressure. Simulations involving the injection of pure CO_2 and a mixture of 80% CO_2 and 20% N_2 are presented to illustrate the role of gas composition on the replacement of CH_4. In both cases gas is injected at 8 MPa at x = 0 m into a coalbed of 100 m length with unit cross sectional area. The coal is initially saturated with CH_4 at 3 MPa, and gas is abstracted at 0.101 MPa at x = 100 m.

The specified problems have been analyzed using 500 equally sized quadratic elements representing the coalbed. An initial time step of 10 seconds has been chosen, which is allowed to vary depending on the convergence rate. The simulation time considered is 16 days. Material properties have been selected based on those reported by Pini et al. (2011). Accordingly, the initial permeability and porosity are 9.9×10^{-15} m^2 and 0.08, respectively. Adsorption saturation capacities V_L^i of CO_2, N_2 and CH_4 are 3378 mol m^{-3}, 2062 mol.m^{-3} and 2116 mol.m^{-3}, respectively, with corresponding Langmuir pressures of 0.8 MPa, 7.14 MPa and 1.60 MPa. These values show that although the saturation capacities of N_2 and CH_4 are similar, CH_4 reaches its adsorption saturation capacity at a much lower pressure than N_2.

Coal is a highly reactive medium that exhibits matrix swelling in response to gas adsorption. This process may affect the flow of gas by reducing the major flow pathway for gas. An implicit geomechanical model is applied that describes the evolution of porosity and permeability during coal-matrix deformation. For the present application the matrix deformation was included using a similar model presented by Gilman and Beckie (2000). In this model, sorption induced swelling is described by a Langmuir type strain curve.

Fig. 2 and 3 shows the gas composition profiles at the end of the simulation period for the injection of pure CO_2 and the binary CO_2:N_2 mixture, respectively.

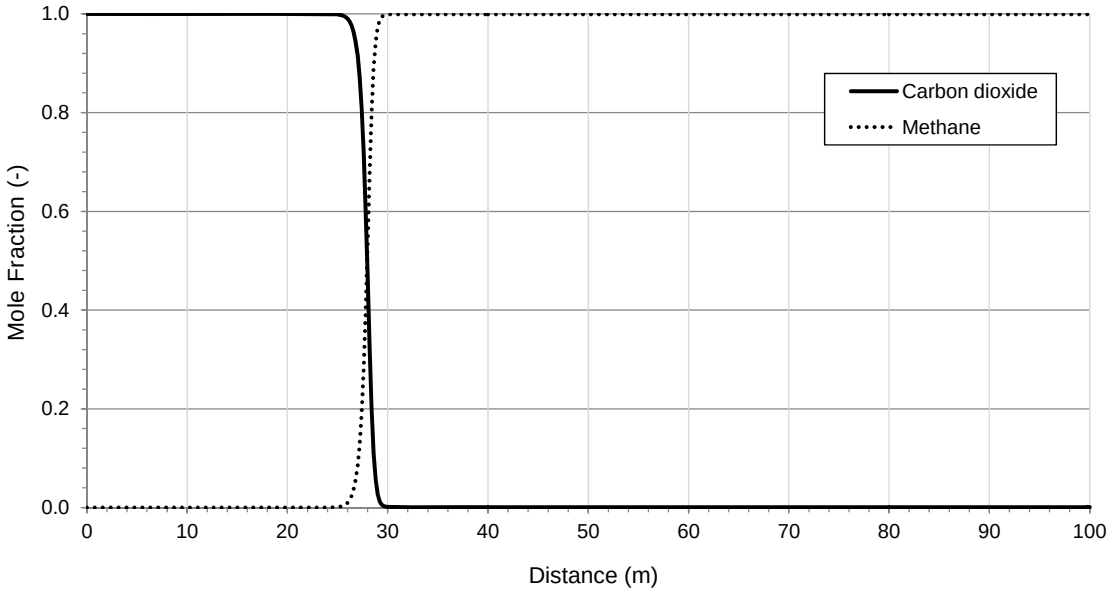

Fig. 2. Composition profiles after 16 days of simulation for the replacement of CH_4 with a pure CO_2.

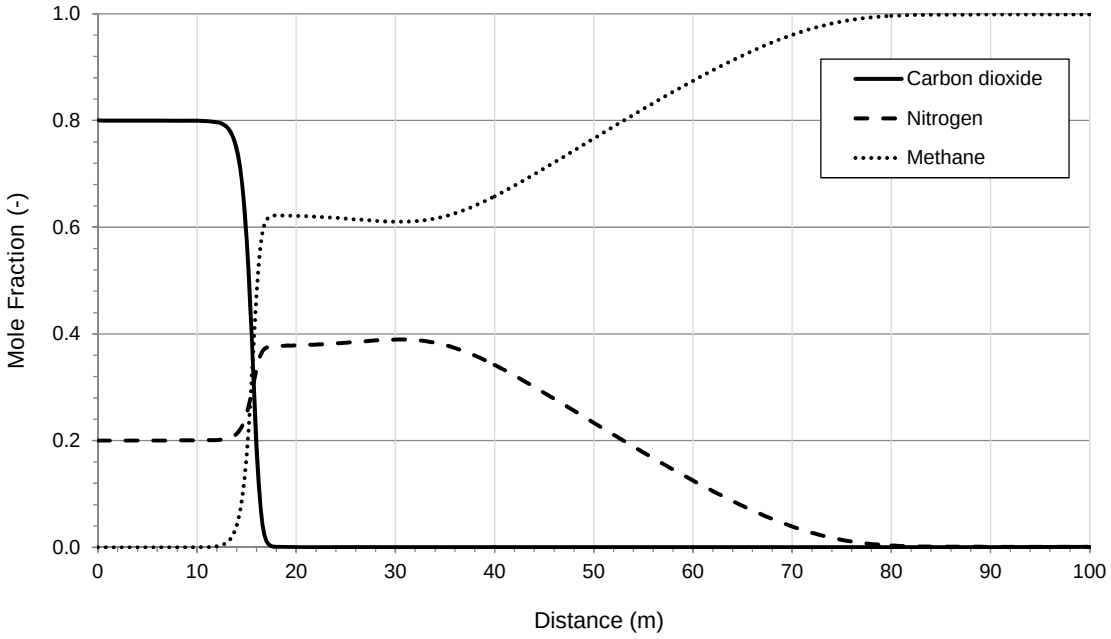

Fig. 3. Composition profiles after 16 days of simulation for the replacement of CH_4 with a gas mixture consisting of 80% CO_2 and 20% N_2.

Due to higher greater preference of coal for adsorption of carbon dioxide, pure CO_2 completely displaces the CH_4. The composition profile in Fig. 2 retains the characteristics of a system dominated by advective transport. The results presented in Fig. 3 demonstrate that the addition of N_2 to the injected gas has a significant impact on the behaviour. A CO_2 injection front is again evident, but N_2 has advanced more rapidly and mixed with CH_4 along a second, smoother injection front. This can be attributed to the fact that coal has a lower preference for the adsorption of N_2 than both CO_2 and CH_4. As a result, N_2 does not displace the adsorbed CH_4 in the same manner as CO_2. Instead N_2 advances beyond the CO_2 injection front and displace the adsorbed CH_4 along a smooth injection front, as observed in Fig. 3.

6 CONCLUSIONS

Theoretical features related to high pressure gas transport and solid-gas interactions have been presented in this paper, within the context of the coupled THCM behaviour of geo-materials. Development has been undertaken to describe the behaviour of multicomponent gas at high pressure in terms of the following properties: i) non-ideal bulk gas compressibility, ii) bulk gas viscosity, iii) gas component diffusivity, and iv) multiple gas adsorption/desorption.

Example applications considering the transport of multicomponent gas at high pressure have been presented. The nature of in situ gas replacement by gas injected at high pressure is strongly affected by the adsorption/desorption characteristics of the components involved. More strongly adsorbing components fully displace in situ gas with a sharp injection front and little mixing. Less strongly adsorbing components produce a smoother injection front with significant mixing.

The developments presented here provide advanced capabilities to simulate processes related to emerging deep geoenergy applications, such as carbon dioxide sequestration and coalbed methane recovery.

ACKNOWLEDGEMENT

The work described in this paper has been carried out as part of the first author's PhD studies. The financial support, provided by the Welsh European Funding Office (WEFO) via the GRC's (Geoenvironmental Research Centre) Seren project, is gratefully acknowledged.

REFERENCES

Bird, R.B., Stewart, W.E. & Lightfoot, E.N. (1960), Transport phenomena, John Wiley & Sons, New York.

Chaback, J.J., Morgan, W.D. & Yee, D. (1996), "Sorption of nitrogen, methane, carbon dioxide and their mixtures on bituminous coals at in-situ conditions". Fluid Phase Equilibria, Vol. 117, 289-296.

Chung, T.H., Ajlan, M., Lee, L.L. & Starling, K.E. (1988), "Generalized multiparameter correlation for nonpolar and polar fluid transport properties". Ind. Eng. Chem. Res., Vol. 27(4), 671-679.

Dake, L.P. (1978), Fundamentals of reservoir engineering, Elsevier, Amsterdam, The Netherlands.

Gilman, A. & Beckie, R. (2000), "Flow of coal-bed methane to a gallery". Transport in Porous Media, Vol. 41(1), 1-16.

Hagoort, J. (1988), Fundamentals of gas reservoir engineering, Elsevier, Amsterdam, The Netherlands.

Kee, R.J., Coltrin, M.E. & Glarborg, P. (2003), Chemically reacting flow: Theory and practice, John Wiley & Sons, Hoboken, New Jersey.

Masum, S. (2012), "Modelling of reactive gas transport in unsaturated soil – a coupled thermo-hydro-chemical-mechanical approach". Ph.D. Thesis, Cardiff University, UK.

Peng D.Y. & Robinson D.B. (1976), "A new two-constant equation of state". Ind. Eng. Chem. Fund., Vol. 15(1), 59-64.

Pini, R., Storti, G. & Mazzotti, M. (2011), "A model for enhanced coal bed methane recovery aimed at carbon dioxide storage". Adsorption, Vol. 17(5), 889-900.

Poling, B.E., Prausnitz, J.M. & O'Connell, J.P. (2001), The properties of gases and liquids, McGraw-Hill, New York.

Ruthven, D.M. (1984), Principles of adsorption and adsorption processes, Wiley, New York.

Sedighi, M., Thomas, H.R., & Vardon, P.J. (2012), "On the Reactive Transport of Chemicals in Unsaturated Expansive Soils", The 4th International Conference on Problematic Soils, Wuhan, China, 211-218.

Thomas, H.R. & He, Y. (1998), "Modelling the behaviour of unsaturated soil using an elastoplastic constitutive relationship". Géotechnique, Vol. 48(5), 589-603.

Thomas, H.R., Sedighi, M. & Vardon, P.J. (2012), "Diffusive reactive transport of multicomponent chemicals under coupled thermal, hydraulic, chemical and mechanical conditions". Journal of Geotechnical and Geological Engineering, Vol. 30(4), 841-857.

Wei, Y.S. & Sadus, R.J. (2000), "Equations of state for the calculation of fluid-phase equilibria". American Institute of Chemical Engineers Journal, Vol. 46(1), 169-196.

Xu, T. & Pruess, K. (2001), "Modeling multiphase non-isothermal fluid flow and reactive geochemical transport in variably saturated fractured rocks: 1. Methodology". American Journal of Science, Vol. 301, 16-33.

A HYDROMECHANICAL SOLUTION FOR CO2 INJECTION PROCESS IN DEEP AQUIFERS

Chao LI
Laboratory of soil mechanics - Chair "Gaz naturel" Petrosvibri, Swiss Federal Institute of Technology, EPFL, Lausanne, Switzerland

Paul BARES
Laboratory of soil mechanics - Chair "Gaz naturel" Petrosvibri, Swiss Federal Institute of Technology, EPFL, Lausanne, Switzerland

Lyesse LALOUI
Laboratory of soil mechanics - Chair "Gaz naturel" Petrosvibri, Swiss Federal Institute of Technology, EPFL, Lausanne, Switzerland
King Abdulaziz University, Jeddah, Saudi Arabia

ABSTRACT: *This study focuses on a specific problem related to the surface uplift induced by the injection of CO2 at depth. The adopted methodology includes the development of a mathematical model that incorporates the deformable behaviour of storage media and the flow of two immiscible fluids (CO2 and water) within the aquifers while the surface rock or caprock layer is modelled as a thin plate. Governing equations are solved for the axisymmetric flexural deflection due to a constant rate of injection of CO2. Comparison of the results with the surface uplift measurements (In Salah project), show good agreement. The results show that this semi-analytical solution is capable of capturing the pressure build-up during the very early stage of injection, resulting in a high rate of surface uplift. Compared to a FEM simulation, the calculation time required using the semi-analytical solution is very short; it can be employed as a preliminary design tool for risk assessment using parameters such as the injection rate, porosity, rock properties and geological structures. This semi-analytical solution provides a convenient way to estimate the influence of high injection rates of CO2 on the surface uplift. The methodology in this development can easily incorporate other pressure distributions; thus advances in hydrology researches can also benefit this approach.*

1 INTRODUCTION

Geological sequestration of CO2 is considered as a mitigation technology to reduce carbon dioxide from entering the atmosphere by capturing and storing the CO2 from industrial emissions. It can help limit the amount of CO2 entering the atmosphere and the greenhouse effect and thus allow for the continued use of fossil fuels. Deep saline aquifers are considered to be suitable geological formations for CO2 storage because of their large capacity to trap the intended volume of CO2 (Bachu, 2000). However, there are some aspects that need to be considered, such as the case of the In Salah CO2 storage site in central Algeria; here CO2 has been injected into a deep seated aquifer since 2004 and surface heave has been detected at a rate of up to 7mm/year around each of the three injection wells (Onuma and Ohkawa, 2009).

Numerical investigations of this observation have been conducted by Rutqvist et al. (2010). The results indicate that the observed uplift at In Salah can be explained by pressure-induced poro-elastic expansion of the injection zone, which includes deformations within the sealing caprock layer just above the aquifer. In addition, the vertical displacement has a similar distribution trend as the fluid overpressure during injection, which reaches a maximum around injection well and decreases gradually with distance from the injection well (Vilarrasa et al., 2010b). Injection of CO2 into deep aquifers is considered as a

hydromechanical coupled process (Rutqvist, 2012). High rates (>1Mt/year) of injection of CO2 into an aquifer could result in an abrupt fluid pressure build-up within the injection area (Rohmer and Seyedi, 2010). This increase in fluid pressure leads to deformation of the aquifer and the sealing caprock. Induced strain may propagate to the surface and can also cause variations in the porosity resulting in alterations in the hydraulic properties such as permeability. As a consequence, the state of fluid overpressure changes further. Employing a hydromechanical coupling technique can help estimate the surface or caprock deformation more accurately.

Selvadurai (2009a) and (2009b) has derived a convenient mathematical model for determining the surface uplift and caprock vertical deformation respectively. By taking in account bending effects, the axisymmetric flexural deflections of the surface layer and caprock layer have been deduced analytically. Nevertheless a flat overpressure within the injection zone is assumed in the study, which could be refined. Two analytical solutions proposed by Nordbotten et al. (2005) and Dentz and Tartakovsky (2009a) predict more realistic distributions of fluid overpressure which has the same order of magnitude as numerical simulations (Vilarrasa et al., 2010a).

The goal of this paper is to assess the surface uplift and caprock deformation by deriving a semi-analytical solution, which takes a more realistic evolution of overpressures into account. First, a mathematical analysis of the pressurization-induced displacement is given. This is followed by the incorporation of the real distribution of overpressure. After proposing several numerical simulations using the semi-analytical analysis, the solution is employed to estimate the surface uplift observed at the In Salah project as an illustrative example.

2 CAPROCK DEFORMATION DUE TO PRESSURIZATION

2.1 Embedded plate approach

Selvadurai (2009b) has proposed a straightforward analytical approximation to estimate the primary caprock deformation due to constant injection-induced uniformly distributed overpressures over a circular region located under the caprock layer. The proposed system consists of an overburden region and a storage unit with a primary caprock in between. CO2 is injected into an *m*-metre-thick injection zone within a storage unit with a distance l to the primary caprock (Fig. 1). The injection zone can be situated just below the primary caprock (*l*=*m*/2). Injection of fluids at a constant rate through a vertical injection well causes radial pressurization in the injection zone, the so-called disc-shaped pressurized zone. The approach assumes that (i) the caprock is oriented horizontally and embedded between an overburden region and a storage region, (ii) the caprock layer is considered as a thin plate and (iii) it behaves elastically. The assumption of a thin plate applied here is justified by its thickness in relation to the dimension (radius) of the pressurized zone (Selvadurai, 2000). Both overburden and storage regions are modelled as half-space regions and an isotropic elastic model is applied to these regions.

The embedded caprock layer exhibits flexural behaviour that is governed by the Germain-Poisson-Kirchhoff thin plate theory (Selvadurai, 2000). The governing equation is written in polar coordinates with the Laplace operator $\tilde{\nabla}^2 = \frac{d^2}{dr^2} + \frac{1}{r}\frac{d}{dr}$:

$$D\tilde{\nabla}^2\tilde{\nabla}^2 w(r) + q^{(s)}(r) - q^{(o)}(r) = 0 \tag{1}$$

where the deflection $w(r)$ is constrained by contact stresses $q^{(s)}(r)$ and $q^{(o)}(r)$,which are applied on the contact faces between the caprock and respective regions. The flexural rigidity of the embedded caprock layer is expressed by $D\left(=G_c h^3/6(1-\nu_c)\right)$ with the thickness h of

the caprock layer, shear modulus G_c and Poisson's ratio of the caprock ν_c. The pressurization of intensity Δp [Pa/m3] is within a disc-shaped pressurized region with a radius of influence R and thickness m located at a distance l from the interface between the caprock and the storage region as shown in Fig. 1. The interactions between the caprock and the adjacent regions are induced by the pressurization that can be considered as an injection pressure over the hydrostatic pressure presented in the storage region. The caprock layer is then assumed to be in bonded contact with the storage and overburden regions, of which the relevant kinematic interface conditions are:

$$w(r, z=0) = u_z^{(s)q}(r,0) + u_z^{(s)p}(r,0) = u_z^{(o)q}(r,0) \tag{2}$$

$$u_r^{(s)}(r, z=0) = u_r^{(s)p}(r,0) = u_r^{(o)}(r,0) = 0 \tag{3}$$

where u_r and u_z are, respectively, the radial and axial displacement vector in the polar coordinates, u^p is the displacement due to overpressure Δp and u^q is the displacement constrained by the contact stress q.

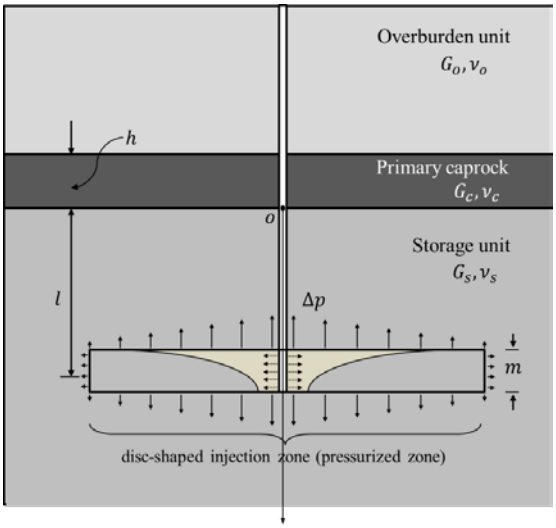

Fig.1 The idealized configuration of an embedded caprock layer.

2.2 Pressurization-induced deflection

According to Segall et al. (1994), the surface displacement of the storage region induced by a distribution of axisymmetric overpressure can be written as:

$$u_z^{(s)p}(r,0) = \frac{\alpha_s}{G_s} \int_0^\infty \int_0^\infty \Delta p(\rho) \cdot g_z(r, z=0; \rho, d)\, \mathrm{d}\rho\, \mathrm{d}d \tag{4}$$

An approximation for operating the integral is given by:

$$g_z(r, z=0; \rho, d) = -(1-2\nu_s)\rho \int_0^\infty \xi J_0(\xi r) J_0(\xi\rho) e^{-\xi d}\, \mathrm{d}\xi \tag{5}$$

is the Green's function, which corresponds to a ring of dilatation at radius $\rho \in [0, \infty]$ and depth $d \in \left[l - m/2, l + m/2\right]$.

The integral (4) can therefore be expressed as follows:

$$u_z^{(s)p}(r,0) = -\frac{(1-2\nu_s)\alpha_s m}{G_s}\int_0^\infty \xi J_0(\xi r)e^{-\xi l}\int_0^\infty \rho\Delta p(\rho) J_0(\xi\rho)\mathrm{d}\rho\,\mathrm{d}\xi \tag{6}$$

Eq.(6) shows a linear relationship between the displacement and the material properties (i.e., $1/G_s$ and ν_s). The displacement induced by pressurization depends strongly on the Bessel integral of the overpressure function $\Delta p(\rho)$. Operating $u_z^{(s)p}(r,0)$ with the zeroth-order Hankel transform gives:

$$\overline{u}_z^{(s)p}(\xi) = -\frac{(1-2\nu_s)\alpha_s m}{G_s}\overline{\Delta p}(\xi)e^{-\xi l} \tag{7}$$

where $\overline{\Delta p}$ is the zeroth-order Hankel transform of Δp.

Selvadurai (2009b) stated that the displacement was constrained by the contact stresses:

$$\overline{u}_z^{(s)q}(r,0) = \frac{(3-4\nu_s)}{4G_s(1-\nu_s)}\frac{1}{\xi}\overline{q}^s(\xi) \tag{8}$$

$$\overline{u}_z^{(o)q}(r,0) = \frac{(3-4\nu_o)}{4G_o(1-\nu_o)}\frac{1}{\xi}\overline{q}^o(\xi) \tag{9}$$

Combing the kinematic constrain Eq.(2) to which the storage region is subjected, the displacement induced by the pressurization Eq.(7) and restricted deflection by contact stress Eq.(8), one can obtain the following equation after the zeroth-order Hankel transform:

$$w(r) = \frac{\Omega m}{h^2}\int_0^\infty \frac{\xi}{1+\Phi\xi^3}\overline{\Delta p}\left(\frac{\xi}{h}\right)e^{-\frac{\xi l}{h}}J_0\left(\frac{\xi r}{h}\right)d\xi \tag{10}$$

where Ω and Φ are constants dependant on the properties of the medium:

$$\Omega = \frac{\alpha_s(1-\nu_s)(1-2\nu_s)(3-4\nu_o)}{G_s(1-\nu_s)(3-4\nu_o)+G_o(1-\nu_o)(3-4\nu_s)} \tag{11}$$

$$\Phi = \frac{(3-4\nu_s)(3-4\nu_o)G_c}{24(1-\nu_c)\left[G_s(1-\nu_s)(3-4\nu_o)+G_o(1-\nu_o)(3-4\nu_s)\right]} \tag{12}$$

3 OVERPRESSURE INDUCED BY CO2 INJECTION

To find the deflection w(r) according to Eq. (10), the overpressure distribution $\overline{\Delta p}$ must be incorporated. Selvadurai (2009a, b) considers a constant overpressure distributed within the pressurization zone. However, CO2 injection will result in a high concentration of overpressure around the injection well and this overpressure vanishes with the distance to the well (Vilarrasa et al., 2010b); such an overpressure pattern is necessary to estimate the magnitude of the deformation more accurately. This can be derived from two analytical solutions proposed by Nordbotten et al. (2005) and Dentz and Tartakovsky (2009a), which describe the advancing interface between the injected CO2 and host water. Both solutions consider that an abrupt interface separates the two fluids, which are assumed to be immiscible (Bear, 1972). As shown in Fig. 2, the problem formulation is divided into three regions: (1) around the injection well, only injected CO2 exists ($r \le r_b$); (2) the intermediate region where two fluids coexist but separated by a sharp interface ($r_b \le r \le r_0$); (3) the outer region where only host water exists ($r_0 \le r \le R$). The governing equation for the interface position can be derived as (Bear, 1972):

$$\frac{1}{r}\frac{\partial}{\partial r}\left[\zeta\frac{Q_0-2\pi r\left(\rho_w-\rho_c\right)g\left(k/\mu_c\right)\left(m-\zeta\right)\partial\zeta/\partial r}{\zeta+\left(m-\zeta\right)\mu_w/\mu_c}\right]+2\pi\phi\frac{\partial\zeta}{\partial t}=0, \tag{13}$$

where Q_0 is the volumetric flux rate of injected CO2 and ζ denotes the vertical position of the interface between two fluids. Both solutions (Dentz and Tartakovsky, 2009a; Nordbotten et al., 2005) are approximations to the exact solution of Eq.(13). The properties and development of both solutions are not detailed in this paper; the reader is referred to the original works of Nordbotten et al. (2005) and Dentz and Tartakovsky (2009a) for their approaches. In addition, the validity of both solutions has been discussed in (Dentz and Tartakovsky, 2009b; Lu et al., 2009).

The interface equations derived by Nordbotten et al. (2005), denoted by NB and Dentz and Tartakovsky (2009a), denoted by DZ, are written respectively as:

$$\zeta_{NB}\left(r,t\right)=m\left[1-\frac{\mu_c}{\mu_w-\mu_c}\left(\sqrt{\frac{\mu_w Q_0 t}{\mu_c\phi\pi m r^2}}-1\right)\right] \tag{14}$$

where $r_b(t)$ the radius at which the interface intersects the lower domain boundary and is determined by the volume conservation (Dentz and Tartakovsky, 2009a):

$$\zeta_{DZ}(r,t)=\frac{Q_0}{2\pi kmg}\frac{\mu_w-\mu_c}{\rho_w-\rho_c}\ln\left(\frac{r}{r_{b,DZ}(t)}\right) \tag{15}$$

Plugging the interface equations Eq.(14) and Eq.(15) into the integration of Darcy's law, the overpressure expressions from the two analytical solutions are derived by Vilarrasa et al.(2010a).

Taking the overpressure equations Eq.(17) (corresponding to the solution of NB) and Eq.(19) (corresponding to the solution of DZ)) from (Vilarrasa et al., 2010a), we can derive expressions for the vertically averaged overpressure for the two analytical solutions using the zeroth–order Hankel transform:

$$\begin{aligned}\overline{\Delta p}_{NT}(\xi)=&\frac{A}{\xi^2}\left[y\ln\left(\frac{y}{\xi R}\right)J_1(y)+J_0(y)\right]_{\xi R}^{\xi r_0}+A\left[\ln\left(\frac{R}{r_0}\right)+Br_0\right]\frac{r_0J_1\left(\xi r_0\right)-r_bJ_1\left(\xi r_b\right)}{\xi}\\&-AB\int_{r_b}^{r_0}r^2J_0(\xi r)dr+A\left[\ln\left(\frac{R}{r_0}\right)+B\left(r_0-r_b\right)\right]\frac{r_bJ_1\left(\xi r_b\right)-r_wJ_1\left(\xi r_w\right)}{\xi}\\&+\frac{AC}{\xi^2}\left[y\ln\left(\frac{y}{\xi r_b}\right)J_1(y)+J_0(y)\right]_{\xi r_b}^{\xi r_w}\end{aligned} \tag{16}$$

with parameters $A=\frac{Q_0\mu_w}{2\pi kd};B=\sqrt{\frac{\mu_c\phi\pi d}{\mu_w V(t)}};C=\frac{\mu_c}{\mu_w}$ and $R=\sqrt{\frac{2.25k\rho_w gt}{\mu_w S_s}}$.

$$\begin{aligned}\overline{\Delta p}_{DT}(\xi)=&\frac{A}{\xi^2}\left[y\ln(\frac{y}{R\xi})J_1(y)+J_0(y)\right]_{\xi R}^{\xi r_0}\\&+\frac{A}{\mu_w}\left(\hat{B}\frac{r_0J_1(\xi r_0)-r_wJ_1(\xi r_w)}{\xi}+\frac{\mu_c}{\xi^2}\left[y\ln(\frac{y}{r_b\xi})J_1(y)+J_0(y)\right]_{\xi r_0}^{\xi r_w}+\hat{C}\int_{r_b}^{r_0}r\ln(\frac{r}{r_b})\ln(\frac{r_b}{r})J_0(\xi r)dr\right)\end{aligned} \tag{17}$$

and parameters $\hat{B}=\mu_w\ln(\frac{R}{r_b})-\frac{\mu_w-\mu_c}{2\gamma};\hat{C}=\frac{(\mu_w-\mu_c)\gamma}{2}$ and $\gamma=\frac{Q_0\left(\mu_w-\mu_c\right)}{2\pi km^2g\left(\rho_w-\rho_c\right)}$.

Introducing Eqs.(16) and (17) into Eq.(10), we can obtain the CO2 injection-induced caprock deflection, taking into consideration the real distribution of overpressure in the aquifer that has a moving interface associated with the hydrodynamic displacement of immiscible fluids.

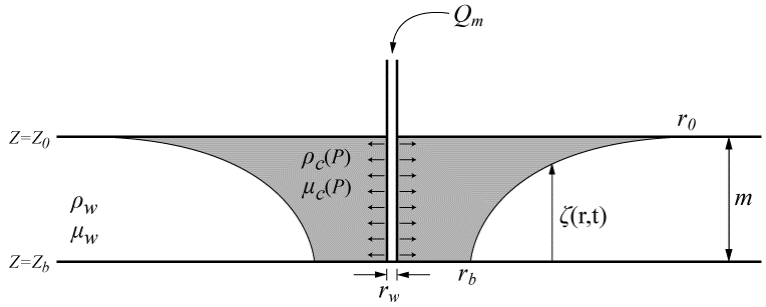

Fig.2 Injection of CO2 into a homogeneous horizontal aquifer (Vilarrasa et al., 2010b)

4 NUMERICAL APPLICATION

4.1 Case studies

The infinite integration of Eq.(10) shows an oscillatory and decaying nature, which can be achieved with a suitable quadrature. To ensure the convergence of the integration, an appropriate number of intervals is chosen to perform the numerical calculation using Matlab®.

We considered an example of a 100m thick caprock layer which is 1km underground. Through a vertical well with a radius $r_w = 0.15\text{m}$, CO2 is injected at a constant rate of 100kg/s into an *m*=100m thick aquifer which located at a certain depth from the caprock. Material parameters are listed in the Table 1.

Table 1. Parameter values used in numerical experiments

Parameter	Symbol	Unit	Overburden unit	Storage unit	Caprock layer
Shear modulus	*Go, Gs, Gc*	GPa	1	10	5
Poisson's ratio	ν_o, ν_s, ν_c	-	0.25	0.25	0.25
Porosity in the injection zone	ϕ	-		0.15	-
Permeability in the injection zone	k	m^2		1.0e-13	-
Thickness of the caprock	*m*	m		100	
Distance from the caprock to the middle of the injection zone	*l*	m		50	
Well radius	r_w	m		0.15	
Injection rate	Q_m	kg/s		100	

The spatial distribution of overpressure is displayed in the Fig. 3. As stated in (Vilarrasa et al., 2010a), the overpressure decreases with distance logarithmically in the DZ solution while it decreases linearly with the solution of NB over the region where the two fluids coexist. As expected, the overpressure calculated using the DZ solution is higher than the one using NB. The pressurization-induced deflection has the same trend as the overpressure (Fig. 4). The curvature of the deflected shape is smoother in the case of NB around the injection well than that with the solution of DZ, which will further influence the stress development.

Temporal evolution of the caprock deflection is shown in Fig. 5 with various permeabilities. With a constant rate of injection, the fluid pressure increases dramatically at the very beginning of the injection period. As a consequence of the elastic model, the

deflection reflects the effect of overpressure and shows the same behaviour. The deflection increases gradually after one year of injection and reaches a maximum. The deflection is almost proportional to the inverse of the permeability (see Eq.(16) and Eq.(17)). Thus the permeability can be considered as an important factor to limit the overpressure build-up and subsequent deflections.

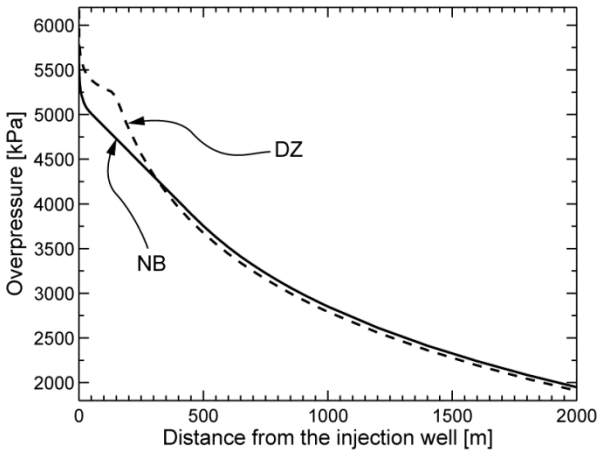

Fig. 3. Spatial distribution of vertically averaged overpressure after 100 days of injection the reference parameters

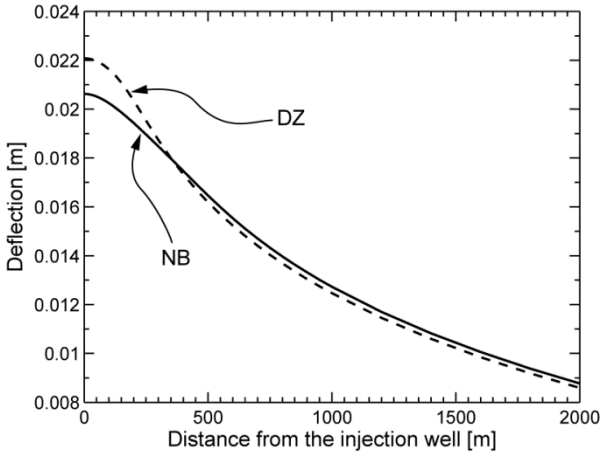

Fig. 4. Spatial distribution of the deflection of the caprock after 100 days of injection with the reference parameters

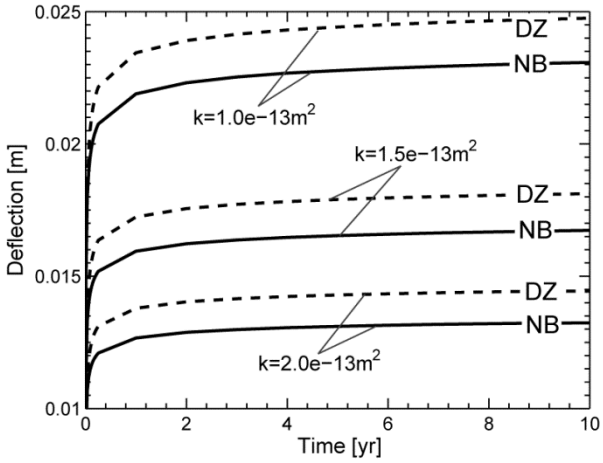

Fig. 5. Deflection at the injection well with time with the variation in permeability

4.2 Application to the case of the In Salah project

The injection of CO2 into the deep aquifer at the In Salah project lead to more than 1500 micro-seismic events throughout 2009 and 2010 (Oye et al., 2012), which are believed to be generated from the cracking or fracturing of the reservoir when the injection pressure exceeds the formation fracture pressure (Bohloli et al., 2012). Surface deformation around the CO2 injection wells at In Salah was analysed by satellite-borne SAR data (Onuma and Ohkawa, 2009). Surface heave was detected around all three injection wells. Hence it is clear that this is an issue that must be handled seriously. Surface uplift at In Salah has been investigated using semi-analytical solutions (Vasco et al., 2008). Rutqvist et al. (2009, 2010) investigated the surface uplift around one specific injection well at In Salah using a 3D finite element model. The results are comparable to the field measurements. Here we apply the proposed semi-analytical approach in order to assess the surface uplift around the same injection well as in (Rutqvist et al., 2009, 2010) and compared the results to both the measured data and numerical simulations. Since the semi-analytical solution is for the purpose of a preliminary estimation, the objective here is to focus on a simple geometry case and to capture the overall behaviour of the surface deformation around the injection well.

Through the injection well KB501 (see Fig. 6), the CO2 is injected into a 20m thick water-saturated layer at a rate of about 8kg/s (Rutqvist et al., 2009).The injection zone is situated at 1800m underground (Rutqvist et al., 2009). Fig. 6a clearly shows that a surface heave, at a rate of 5mm, has been detected. More specifically, the surface uplift reaches 10mm during the first year (Fig. 6b).

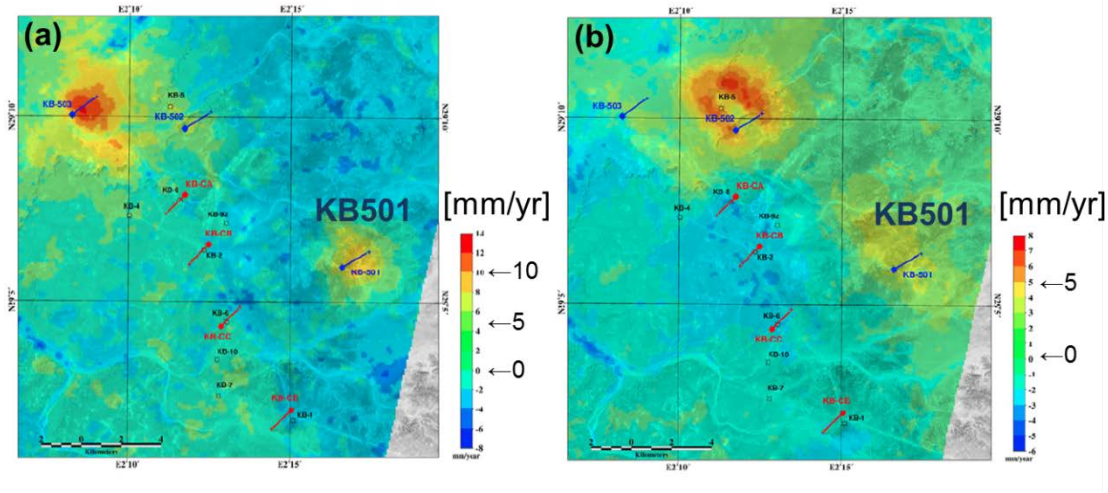

Fig. 6. Vertical displacement rate of the term from (a) 2004/7/31 to 2008/5/31 and (b) 2004/7/31 to 2005/9/24 at the In Salah detected by DInSAR stacking. KB-501 is CO2 injection well (Onuma and Ohkawa, 2009).

To evaluate the surface uplift, the geometry shown in Fig. 7 is used. The system includes a 10m thick thin surface layer and an injection zone that is within a storage unit. The injection zone is located 1800m below the surface rock layer. The overburden unit is actually eliminated. The problem is therefore to assess the interaction between a bonded surface rock layer and a deep storage unit, while CO2 is injected at a certain depth within the storage unit.

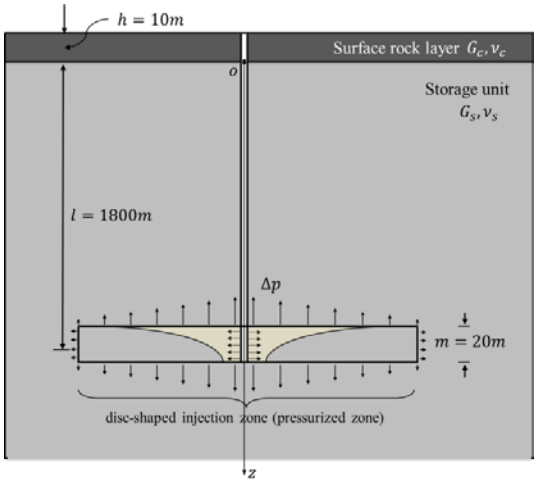

Fig. 7. Geometry of the model to simulate the surface uplift around the injection well KB501 at In Salah

Material properties of the injection zone are directly taken from (Rutqvist et al., 2009) (Table 2) and the mechanical properties of the storage unit also correspond to the mean value of material sets in (Rutqvist et al., 2009).

Table 2. Material parameters used in the simulation of In Salah uplift

Parameter	Unit	Storage unit	Surface layer
Shear modulus	GPa	3	0.5
Poisson's ratio	-	0.2	0.2
Porosity in the injection zone	-	0.17	-
Permeability in the injection zone	m^2	1.3e-14	-

Fig. 8 shows good agreement of the results between the semi-analytical solution and the actual measurements. The model reproduces about an 11mm surface uplift in the first year while the detected surface uplift was around 10mm (Fig. 6b). After 3 years of injection, the maximum calculated uplift is 16mm, which is similar to the measured uplift (15mm) (Fig. 6b). Using the 3D finite element model, Rutqvist et al. (2009) also found a surface uplift of 12mm, which is in the same order of magnitude as that found with the semi-analytical solution.

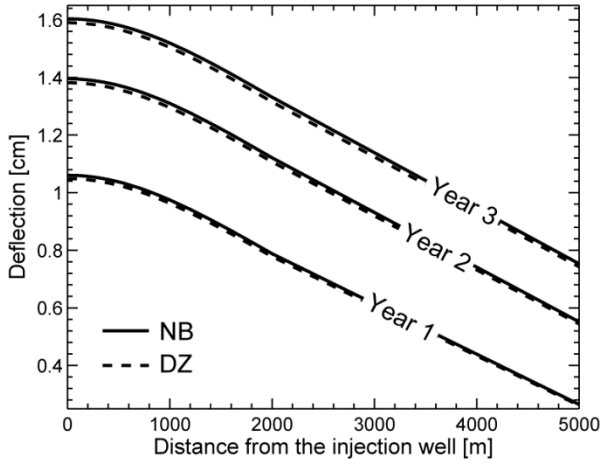

Fig. 8. Surface uplift calculated by the semi-analytical solution

5 CONCLUSIONS

This paper presents a semi-analytical approach to estimate the caprock deflection due to CO2 injection. The model examines the interaction between a primary caprock and adjacent regions with elastic material properties, which is induced by the pressurization within the injection zone. Using the embedded plate approach, the primary caprock is modelled as a thin-plate layer and adjacent regions are modelled as semi-infinite half-space regions. For the fluid part, two analytical solutions have been introduced into this approach. The expressions have been derived in order to develop a compact analytical solution. This approach can take into account a moving front of immiscible fluids and a more realistic fluid pressure distribution. Several numerical experiments have been undertaken to illustrate the influence of factors such as geometry, overpressure magnitude and material properties on the caprock deflection. Finally we employ this approach to assess the surface uplift observed at In Salah. A good agreement in the temporal evolution and the magnitude has been found between the measurements and calculated results. Compared to finite element calculations, this approach can be considered as an alternative preliminary calculation tool for assessing the impact of various factors during CO2 injection.

The development within this paper is straightforward. One can incorporate other analytical solutions in relation to the fluid dynamics into the mechanical approach. Thus, advances in hydrology research can also be of benefit to this approach.

ACKNOWLEDGEMENT

The authors gratefully acknowledge Petrosvibri S.A. for funding of the Chair “Gaz Naturel” and supporting this research.

REFERENCES

Bachu, S., 2000. Sequestration of CO2 in geological media: criteria and approach for site selection in response to climate change. Energy Conversion and Management 41, 953-970

Bear, J., 1972. Dynamics of Flow in Porous Media. Elsevier, New York

Bohloli, B., Aker, E., Cuisiat, F., Oye, V., Khn, D., 2012. Analysis of pressure versus flow regime of CO2 to assess matrix and fracture injection at In Salah, Algeria.

Dentz, M., Tartakovsky, D.M., 2009a. Abrupt-interface solution for carbon dioxide injection into porous media. Transport in Porous Media 79, 15-27

Dentz, M., Tartakovsky, D.M., 2009b. Response to “Comments on Abrupt-Interface Solution for Carbon Dioxide Injection into Porous Media by Dentz and Tartakovsky (2008)” by Lu et al. Transport in Porous Media 79, 39-41

Fjaer, E., 2008. Petroleum Related Rock Mechanics. Elsevier Science.

Geertsma, J., 1973. Land subsidence above compacting oil and gas reservoirs. Journal of Petroleum Technology 25, 734-744

Lu, C., Lee, S.Y., Han, W.S., McPherson, B.J., Lichtner, P.C., 2009. Comments on “abrupt-interface solution for carbon dioxide injection into porous media” by M. Dentz and D. Tartakovsky. Transport in Porous Media 79, 29-37

Nordbotten, J.M., Celia, M.A., Bachu, S., 2005. Injection and storage of CO2 in deep saline aquifers: Analytical solution for CO2 plume evolution during injection. Transport in Porous Media 58, 339-360

Onuma, T., Ohkawa, S., 2009. Detection of surface deformation related with CO2 injection by DInSAR at In Salah, Algeria. Energy Procedia 1, 2177-2184

Oye, V., Zhao, P., Khn, D., Iranpour, K., Aker, E., Bohloli, B., 2012. Monitoring of the In Salah CO2 storage site (Krechba) using microseismic data analysis.

Rohmer, J., Seyedi, D.M., 2010. Coupled large scale hydromechanical modelling for caprock failure risk assessment of CO2 storage in deep saline aquifers. Analyse hydromècanique á grande èchelle pour l'èvaluation du risque de fracturation de la couverture de stockage du CO2 dans les aquifères profonds 65, 503-517, doi:10.2516/ogst/2009049.

Rutqvist, J., 2012. The geomechanics of CO2 storage in deep sedimentary formations. Geotech Geol Eng 30, 525-551, doi:10.1007/s10706-011-9491-0.

Rutqvist, J., Vasco, D.W., Myer, L., 2009. Coupled reservoir-geomechanical analysis of CO2 injection at In Salah, Algeria. Energy Procedia 1, 1847-1854, doi:10.1016/j.egypro.2009.01.241.

Rutqvist, J., Vasco, D.W., Myer, L., 2010. Coupled reservoir-geomechanical analysis of CO2 injection and ground deformations at In Salah, Algeria. International Journal of Greenhouse Gas Control 4, 225-230

Segall, P., Grasso, J.-R., Mossop, A., 1994. Poroelastic stressing and induced seismicity near the Lacq gas field, southwestern France. Journal of Geophysical Research: Solid Earth 99, 15423-15438, doi:10.1029/94jb00989.

Selvadurai, A.P.S., 2000. Partial Differential Equations in Mechanics 2: The Biharmonic Equation, Poisson's Equation. Springer.

Selvadurai, A.P.S., 2009a. Heave of a surficial rock layer due to pressures generated by injected fluids. Geophysical Research Letters 36, L14302, doi:10.1029/2009GL038187.

Selvadurai, A.P.S., 2009b. Mechanics of an embedded caprock layer during pressurization of a CO2 storage reservoir. Int. Centre for Comp. Eng., 466-475

Vilarrasa, V., Bolster, D., Dentz, M., Olivella, S., Carrera, J., 2010a. Effects of CO2 compressibility on CO2 storage in deep saline aquifers. Transport in Porous Media 85, 619-639, doi:10.1007/s11242-010-9582-z.

Vilarrasa, V., Bolster, D., Olivella, S., Carrera, J., 2010b. Coupled hydromechanical modeling of CO2 sequestration in deep saline aquifers. International Journal of Greenhouse Gas Control 4, 910-919, doi:10.1016/j.ijggc.2010.06.006.

A DISCRETE ELEMENT APPROACH TO MODELLING ENHANCED DISSOLUTION AND DEFORMATION OF GEOMATERIALS

S. Panthi, L.B. Hu
Department of Civil Engineering, University of Toledo, Toledo, OH 43606, USA

ABSTRACT: *The evolution of mechanical and transport properties of geomaterials may be strongly influenced by the interaction of chemical and mechanical processes in various environmental circumstances. Such interaction often occurs at the intergranular contact scale but its consequences are manifested at the different scales, contributing to critical mechanisms in many natural and engineering geomechanical processes. This paper is focused on a numerical approach for the interaction of mechanical processes and intrinsic or externally controlled chemical processes. Discrete element modelling (DEM) is employed. The effect of the mineral dissolution on the mechanical response at the grain contact is incorporated into a modified linear contact model. Two kinetic rate formulations to account for mechanical enhanced dissolution are examined, both allowing the evolving local mechanical response (contact force or displacement) to be considered in the description of the enhanced dissolution process at each grain contact. DEM simulations are performed to examine the overall mechanical response of quartz and calcite particle assembles subject to mineral dissolution. The results demonstrate the important role of the kinetic rate characteristics of the dissolution process. The presented analysis is a feasibility study of the use of DEM to model coupled chemo-mechanical phenomena.*

1 INTRODUCTION

Geochemical changes resulting from various environmental circumstances often induce earthen materials to respond through a series of mechanisms of mechanical deformation and chemical reactions. The interaction of chemical and mechanical processes may play a significant role in the evolution of mechanical and transport properties of geomaterials. Such interaction often occurs at the intergranular contact scale but its consequences are typically manifested at the upper scales, contributing to critical mechanisms in many natural geomechanical processes such as sediment subsidence, rock weathering and landsliding. Geochemical reactions and their effects on the mechanical behavior of geomaterials are also of great concern in a number of engineering applications, including petroleum or gas extraction and geological CO2 storage. Chemically mediated compaction resulting from mechanically enhanced dissolution and simultaneous mechanical weakening can lead to the enhanced evolution of porosity and permeability. This is of primary relevance to long-term effects of CO2 storage in deep sedimentary formations (Rutqvist, 2012), where the presence of high CO2 pressure may induce accelerated stressed granular dissolution and subsequent enhanced deformation (e.g. Le Guen et al., 2007; Spiers et al., 2010).

Mechanisms of coupled chemo-geomechanical processes are investigated for the natural process of normal consolidation of sediments in Hu & Hueckel (2007a) that proposed and numerically examined a series of scenarios of the coupled processes spanning over multiple scales. The interactive characteristics of multi-scale mechanisms were also examined from the perspective of self-organization (Hu & Hueckel, 2009). The major challenges at hand lie in the characterization of critical processes at each scale and the homogenization across scales. The present study focuses on a specific multi-scale numerical tool, discrete element modelling (DEM), employed to investigate the behavior of particulate assemblies where chemically affected contact mechanisms play an important role.

We are especially interested in the linkage between the mineral dissolution occurring at grain contact and the overall response of a granular assembly. A basic DEM contact model is modified to describe the local contact force-displacement, taking into consideration the mineral dissolution. The kinetic rate laws of the enhanced mineral dissolution are formulated as affected by the mechanical response at the grain contact. DEM simulations are carried out for both calcite and silica assemblies to assess the role of the chemo-mechanical coupling.

2 MODELLING MICRO-SCALE GRANULAR CONTACT

The mechanisms involved in the enhanced mineral dissolution and subsequent evolution of mechanical and hydraulic properties are believed to be linked to the processes occurring at different scales. Fig. 1a presents three scales needed to be considered. At the micro-scale level of granular contacts, the key element is the intensified chemo-mechanical coupling between mechanical damage and mass dissolution. The processes involved are: deformation of sediment grains, including plastic deformation, especially near contact between grain asperities and corresponding locally smooth surface of another grain; dilatant damage induced by the plastic yielding; infiltration of the dilatant zone by pore water; activation of damage (microcracking) related internal interfaces between pore liquid and solid; dissolution of minerals at these interfaces; diffusion of the dissolved species within the grain away from the reaction sites. At the meso-scale, intergrain diffusion of the dissolved minerals occurs in the pore water and subsequently the dissolved minerals precipitate on the free surface of adjacent or remote grains. These results in a reduction of pore space and eventually a stiffness increase and a permeability decrease at the macro-scale.

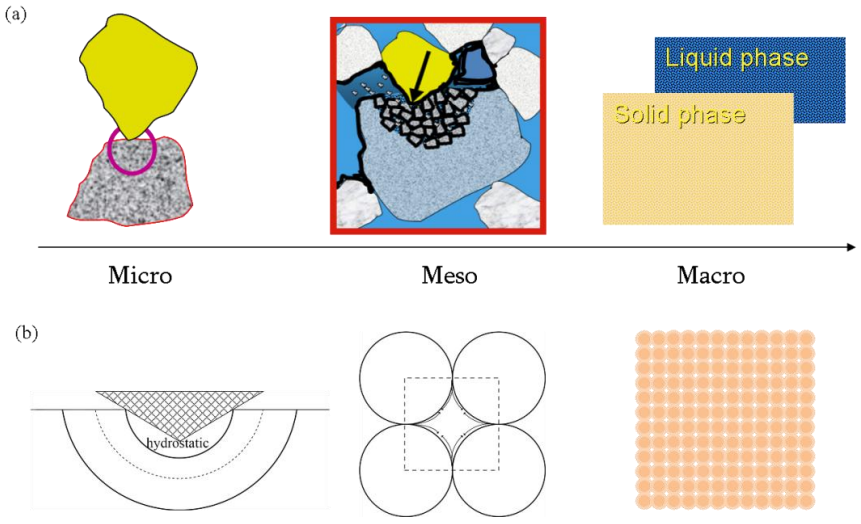

Fig. 1: (a) Multi-scale considerations for predominantly stressed dissolution mechanisms in granular materials. (b) Schematics of geometry of mathematical model established at each scale in Hu **&** Hueckel, 2007; Hu et al., 2013.

A sequence of three-scale models discussed above was developed by Hu & Hueckel (2007a) who simulated soil aging, and later identified leading feedbacks and feedforwards of inter-scale coupling to evaluate the evolution of stiffness (Hueckel & Hu, 2009) and eventually permeability (Hu et al., 2013). Quantities at the macro-scale are derived through cross-scale transfer functions (e.g., volume averaging). Indeed, the macroscopic representative elementary volume (REV) considered in the above mentioned work is of prototype topology (e.g., a regular periodic assembly of grains in Fig. 1b), mainly due to computational demands. This naturally leads to the consideration of employing an effective computational tool such as DEM, which has attracted great interests across a variety of research communities since its introduction in the seminal work by Cundall & Strack (1979).

Obviously, the basic discrete element contact models at the fundamental (micro-) scale are not capable of dealing with coupling effects. In DEM analysis particles are often assumed to rigid but can overlap with each other. The overlap is analogous to the deformation that occurs between real particles (O'Sullivan, 2011). It can be described by a contact-force formulation. Typical contact models, e.g., linear model or Hertz contact model are used to describe the linear or nonlinear displacement response to the contact force at the contacts. In the present study a linear contact model is used. The relationship describing the contact interaction is characterized by the normal contact stiffness k_n and the shear contact stiffness k_s.

$$\mathrm{F}_n = \begin{cases} \mathrm{k}_n \mathrm{U}_n, & \text{if } \mathrm{U}_n \leq 0 \\ 0, & \text{if } \mathrm{U}_n > 0 \end{cases} \tag{1}$$

U_n is the relative normal displacement and F_n is the normal contact force. The (tangential) shear stiffness k_s relates the incremental shear force to the incremental relative shear displacement.

$$\mathrm{dF}_s = -\mathrm{k}_s \mathrm{dU}_s \tag{2}$$

The shear and normal forces must also satisfy a non-slip condition: $|\mathrm{F}_s| \leq \mu |\mathrm{F}_n|$, where μ is the Coulomb friction coefficient.

The simplicity of its contact models at the particle level is also among its main strengths, making this numerical tool computationally affordable. Compromises have to be made to allow adequate representation of characterization of critical mechanisms of micro-mechanical responses and at the same time meet computational demands arising from analysis of large quantities of particles.

The present study explores a degradation based contact model to address the chemical dissolution effect on the material weakening, which affects the local (grain scale) mechanical response in terms of force or stress, and displacement or strain, and in turn the chemical dissolution rate. The physics basis for the altered contact mechanism is closely associated with the chemical dissolution mechanisms between two stressed grains. The involved processes may be explained via several mechanisms, which are either sequential or parallel. It is also possible that different scenarios are more pertinent for different minerals, and that some of their elements occur simultaneously with different intensities.

Mechanisms proposed for the elementary process of pressure solution are particularly pertinent, such as the water film diffusion and free-face pressure solution. The former assumes that dissolution takes place at the grain contact area with solutes diffusing along an adsorbed water film layer (e.g., Weyl, 1959; Rutter, 1976). Alternatively, a so-called "island–channel" structure etched chemically in the mineral may provide access to dissolution sites as well as a preferential path of transport of solute (e.g., Raj & Chyung, 1981; Spiers & Schutjens, 1990). As shown in Fig. 2a, the enhanced dissolution and diffusion processes are

often considered at only the contact surface area. Numerical analyses have shown that the enhanced deformation based on pressure solution theory is only appreciable after prolonged periods of time, usually in geological scales. However, a number of soil aging tests suggest that the time scale of the underlying physico-chemical processes can be of days, weeks or months (e.g., Hueckel et al., 2001). This observation motivated Hu & Hueckel (2007a) to investigate the effect of the near-contact damage and irreversible deformation at intergranular contact and developed a coupled indentation-transport model to simulate the relevant chemo-mechanical processes, as shown in Fig. 2b.

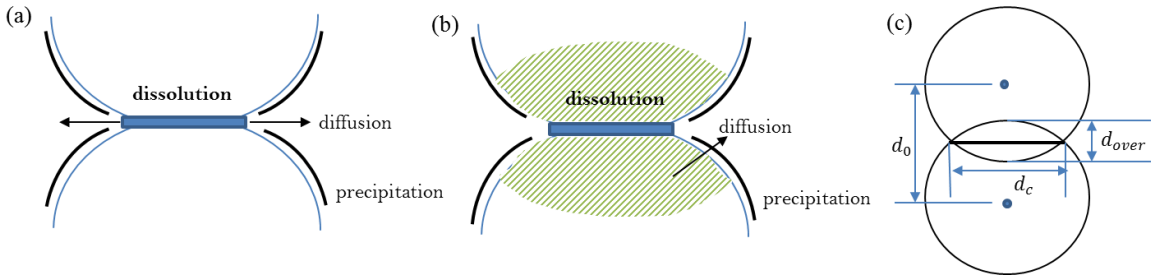

Fig. 2. (a) Schematics of enhanced dissolution mechanisms focused on the contact area, commonly adopted in pressure solution theory (e.g. Yasuhara et al., 2003, Zhang & Spiers, 2005). (b) Schematics of enhanced dissolution mechanisms taking into consideration the near-contact localized deformation and damage (Hu & Hueckel, 2007a). (c) DEM configuration of particle contact with geometry parameters indicated for subsequent modelling considerations.

Clearly, employing a DEM scheme imposes certain restrictions on the flexibility of possible coupled formulations. The contact model needs to maintain its simplicity while adequately represent the critical interactive chemo-mechanical mechanism. The present study is restricted to the analysis of enhanced contact dissolution and does not take into account the diffusion and precipitation processes. We introduce to the linear contact model as presented in eqs. (1) and (2) a degradation effect to account for the chemical effects on the granular contact responses.

$$\mathrm{k}_n = \mathrm{k}_{n0}(1-\Phi) \tag{3a}$$
$$\mathrm{k}_s = \mathrm{k}_{s0}(1-\Phi) \tag{3b}$$

Thus the contact model is modified to account for the chemical effects on the granular contact responses. For simplicity both normal and shear modulus are modified in the same way. The degradation parameter, Φ, introduced in eq. (3) is formulated as a function of the solid mass removal parameter from the system, ξ, by adopting an exponential function form used by Lydzba et al. (2007).

$$\Phi = 1 - \alpha e^{-\xi/\beta_1} - (1-\alpha)\, e^{-\xi/\beta_2} \tag{4}$$

As such, Φ is constrained by the following inequality: $0 \leq \Phi \leq 1$, which imposes a rational range for mechanical degradation. An advantage of such formulation is that, even though conceptually a reaction progress variable can be proposed, e.g., the mass removal ratio, to be confined between 0 and 1, because the conventional chemical reaction kinetic laws do not necessarily impose bounds for the involved mass quantities, there is no control over the range of values it can reach. The adopted formulation will bound the degradation parameter in a sensible range, while the numerical values of mass removal can be determined via typical kinetic rate laws.

3 GEOCHEMISTRY CONSIDERATIONS IN CONTACT MODELS

The chemical variable ξ is defined to relate to the mass dissolution, for example, as the relative mass removal being the ratio of the dissolved mass (or mol) of mineral to the original mass (or mol) of mineral, $d\xi = dM_{\text{diss}}/M_0$. The dissolved amount of solid mineral is largely described by a specific reaction rate law. But under the influence of (high) intergranular contact stress or irreversible deformation/damage, the dissolution rate formulation can take various forms. In the presented study, we investigated two types of dissolution rate formulations, including one based on theories for pressure solution processes and the other on a damage-enhanced kinetic rate law.

The first type of formulation indicates that the dissolution rate is strongly affected by the contact stress. The following equation is proposed by Yasuhara et al. (2003).

$$\frac{\mathrm{dM_{diss}}}{dt} = \frac{3\pi v_m^2 k_+ \rho_g d_c^2}{4RT}\sigma_{\text{eff}} \tag{5}$$

υ_{m} is the molar volume of the solid, k_+ is the dissolution rate constant, ρ_{g} is the grain density, R is the ideal gas constant, T is the absolute temperature, d_{c} is the diameter of the grain-to-grain contacts, hence $\pi/4d_c^2$ is the contact area, A_{con}, indicated in Fig. 2c. The effective stress σ_{eff} can be simply replaced with the average contact stress $\sigma_{\text{con}}=F_{\text{n}}/A_{\text{con}}$, if stress localization effect is ignored and an eventual chemical equilibrium state is excluded from consideration.

Hence, the rate of ξ can be expressed as

$$\dot{\xi} = \frac{\mathrm{dM_{diss}}}{dt}\cdot\frac{1}{M_0} = \frac{3v_m^2 k_+ \rho_g}{RT}F_{\text{n}}\cdot\frac{1}{\rho_g}\cdot\frac{1}{\frac{1}{6}\pi\bar{d}^3} = \frac{18v_m^2 k_+}{\pi RT\bar{d}^3}F_{\text{n}} \tag{6}$$

whereas the average diameter of the two grains in contact, $\bar{d} = 0.5(d_1 + d_2)$, is used for the grain volume calculation. As such, the dissolution rate is computed and the dissolution updated at each time step, dependent on the contact normal force, whereas the displacement response evolves as affected by the degradation degree as a function of mass dissolution.

The second type of formulation considers the near-contact damage as the dominant factor. For a specific mineral-water reaction, e.g., silica-water reaction, a rate equation was proposed in Hu & Hueckel (2007a), which incorporated the irreversible plastic strain into the specific surface area in the kinetic rate law established by Rimstidt & Barnes (1980) for silica interaction with water. Adopting DEM approach, we simply use the overlap distance between the two grains, d_{over}, to describe the progress of strain development. In addition, in order to use the same value of the rate constant (in mol/(m^{2}s)) as in eq. (6), we modify the rate law in Hu & Hueckel (2007a) to yield a relative dissolution removal quantity with respect to the mole of the original mineral.

$$\dot{\xi} = \widetilde{\mathrm{A}}k_+ \mathrm{a}_{SiO_2}a_{H_2O}^2, \quad \widetilde{\mathrm{A}} = \Gamma\frac{d_{\text{over}}}{d_0} \tag{7}$$

where d_0 describes the initial distance of the two grains just in contact, i.e., $d_0 = d_1 + d_2$. The function $\widetilde{\mathrm{A}}$ represents the relationship between the dissolution reaction rate and the accumulated local deformation, characterized via a parameter, Γ, which entails the opening of the micro-cracks around the near contact for specific surface area where dissolution occurs, $\Gamma = \varphi V^0/(A^0\upsilon_m V_g)$, where $V^0 = 1\ \mathrm{m}^3$, $A^0 = 1\ \mathrm{m}^2$, V_g is the grain volume using the average diameter of the two grains in contact as discussed in eq. (6), and φ is a proportionality

constant that relates the opening of surface area due to micro-cracking (Hu & Hueckel, 2007a).

4 ASSESSMENT OF THE RESPONSES OF QUARTZ AND CALCITE MINERALS

The influence of the possible chemo-mechanical processes as discussed in the preceding sections can be examined in a series of soil aging tests conducted in oedometer tests. The primary purpose of this experimental study is to use the laboratory aging simulation technique discussed in Hueckel et al. (2001) to investigate the role of the geochemical kinetic rate characteristics of silica-water and calcium carbonate-water interaction. Two types of soil samples were prepared, a clean sand consisting of primarily quartz, and a sandy silt with significant amount of calcite (approximately 8~10%). They were tested for secondary compression in LoadTrac II (GeoComp, MA). The preliminary results were limited to short-period aging under constant loads and they indicate that such aging tests for much longer periods are needed.

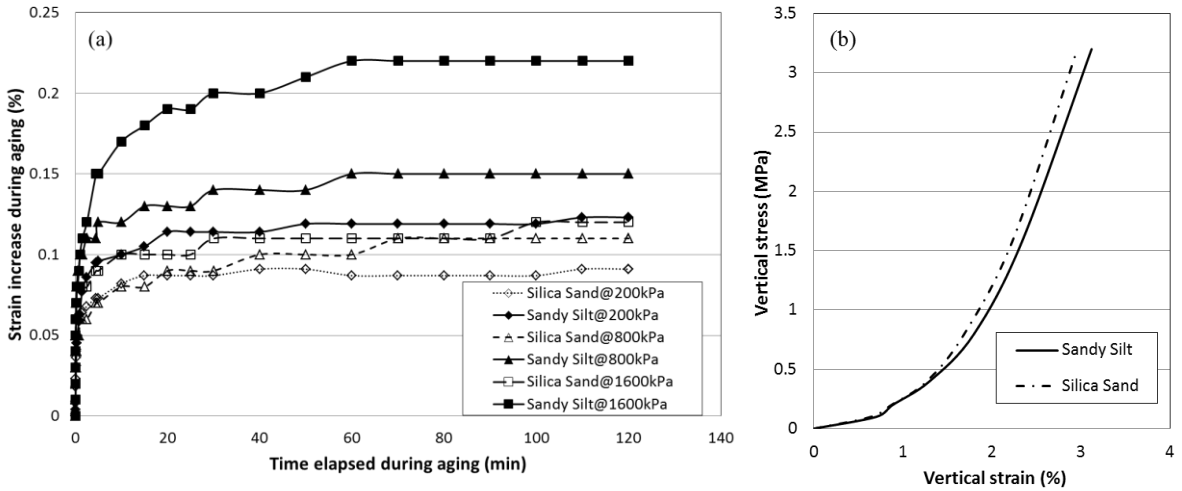

Fig. 3. (a) Experimental results of aging strain developed under different axial stress levels for a sand and a silt with a significant fraction of calcite. (b) Axial (vertical) strain response during the entire testing period.

Fig. 3a shows the development of the secondary compression strain at different stress levels. We removed the strain due to consolidation by identifying the intersection point of the last two linear segments of the settlement-log(t) curve as the end of the consolidation. If we can attribute this strain development to the interaction of mineral and water, it appears that the calcite dissolution in general leads to more significant deformation. Higher stress also seems to result in larger strain development. It is also interesting to note that the overall strain response during the entire loading period as shown in Fig. 1b seems to indicate that the calcite containing soil is at least slightly softer, which may be influenced by the chemo-mechanical interaction processes.

5 NUMERICAL INVESTIGATIONS

In this section we present a DEM numerical study of enhanced deformation affected by grain contact dissolution of two different minerals, quartz and calcite. It was not designed to simulate the behavior of actual soil specimens presented in the preceding section: each particle is considered to consist of a single mineral species subject to dissolution. The analysis presented in what follows is primarily focused on dissolution enhanced mechanical degradation, simulations of creep or aging strain under constant stress state is not discussed.

DEM simulations of such phenomena based on viscous mechanisms can be found in Kuhn & Mitchell (1993); Wang et al. (2008) and Kwok & Bolton (2010), and a macroscopic model for creep as a chemically enhanced intrinsic rate dependent damage process was developed in Hu & Hueckel (2007b).

The calcite dissolution kinetics and in general, the reaction rate equations between carbonate minerals and water are especially complicated, often involving multiple simultaneous or sequential chemical reactions. For simplicity, the same forms of kinetic rate formulation discussed in Section 3 for quartz-water reaction are used to describe the calcite dissolution, with one rate constant acting as the dominant controlling parameter. Table 1 includes the key parameters used for the DEM simulation. Numerous sources (e.g., Sjoberg, 1976; Rimstidt & Barnes, 1980; Palandri & Kharaka, 2004) were consulted on the ranges of rate constants at room temperature (T=298.15K), because the kinetic rate typically depends on the specific surface area available for reaction, conversions and calibrations are often needed to compare the results from different sources.

Table 1. List of values of key parameters used in the simulations.

Parameters	Value	
Initial contact normal stiffness (K_{no})	1×10^{9} (N/m)	
Initial contact shear stiffness (K_{so})	1×10^{9} (N/m)	
Friction coefficient (μ)	0.25	
Material constant (α)	0.250	
Material constant (β_1)	0.252	
Material constant (β_2)	1.020	
	quartz	calcite
Molar volume (V_m)	22.7 (cm^3/mol)	31.2 (cm^3/mol)
Density (ρ_g)	2650 (kg/m^3)	2710 (kg/m^3)
Dissolution rate constant (k_+)	3.98×10^{-14} ($mol/m^2/s$)	1.55×10^{-6} ($mol/m^2/s$)

The simulation was implemented in PFC2D (Itasca, 2008) using its FISHBANK programming language. An assembly of 986 particles (disks) was confined in a rectangular box formed by four walls. The lateral walls were fixed and the axial load was applied as the top wall was moving downward in a strain controlled loading process. Fig. 4 shows the overall axial stress-strain response at a very high loading rate of 6.7×10^{-3} /s. It illustrates the effect of the rate-dependent grain dissolution process coupled with mechanical degradation. Both the stress (dictated by contact force) controlled dissolution rate as described by eq. (6) and the "deformation" (contact displacement) controlled dissolution rate as described by eq. (7) were examined, as this rate is needed to compute the chemical variable, ξ, and hence the degradation variable, Φ, at each contact. Both formulations result in roughly the same strain development for quartz and it almost coincides with the curve corresponding to the simulation without the consideration of dissolution and degradation, as the dissolution rate of quartz is so small and its effect is barely appreciable unless for a significantly prolonged period of time. Interestingly a portion of the stress-strain curve without degradation is below those undergoing degradation, although the difference is small, this can be attributed to the manner the stress and strain are averaged in PFC2D and the random nature of particle generation that influences the subsequent simulation.

Much faster calcite dissolution leads to a softer response. The difference between these two rates is of 8 orders of magnitude, and as a consequence, the effect of the degradation for calcite is readily appreciable after 1% strain development. The likely source for the apparently substantially fast calcite dissolution includes the very high contact force (see eq.(6)), due to the high contact stiffness employed in the simulations.

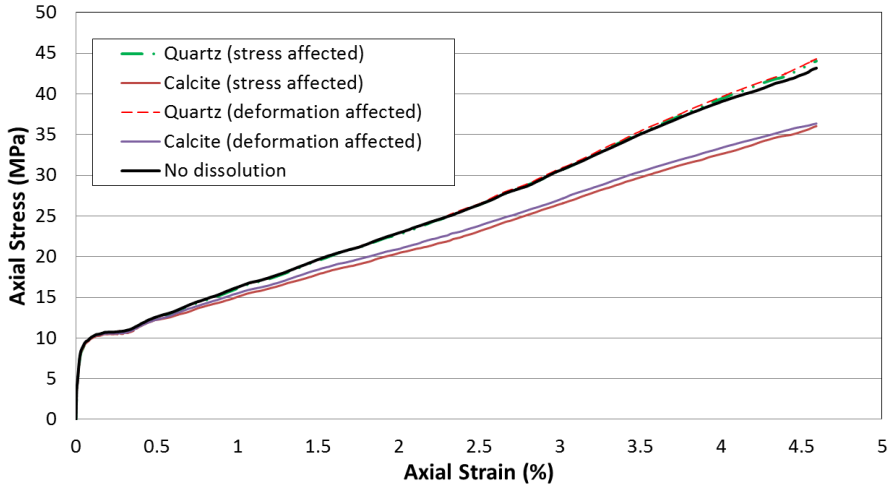

Fig. 4. Simulation of the responses of quartz and calcite assemblies subject to dissolution.

The evolving grain contact characteristics may entail also stiffening and/or hardening effect due to the localized near-contact strain hardening and simply the increase in contact area (Hu & Hueckel, 2007a). Nonlinear models such as Hertz contact model readily provide the nonlinear relationship between the contact force and the contact displacement. For the sake of simplicity and consistency with the formulation proposed in the preceding sections, we introduce a stiffening term, Λ, which is proportional to the square root of the contact surface area, A_{con}.

$$\mathrm{k}_n \;=\; \mathrm{k}_{n0}(1-\Phi+\Lambda), \quad \Lambda = \lambda\left(\frac{A_{\mathrm{con}}}{A_0}\right)^{1/2} \tag{8}$$

A_0 is the average area of the two particles (disks) in contact, $A_0 = 0.5(\pi d_1^2/4 + \pi d_2^2/4)$. λ is a constant. Fig. 5 presents the simulation results subjected to both degradation and stiffening effects. The value of λ is set to be high so that the overall response obtained from each simulation is in the stiffening side. Again, the influence of quartz dissolution is very little and not appreciable after a short period of time. The interplay between stiffening and degradation mechanisms is illustrated.

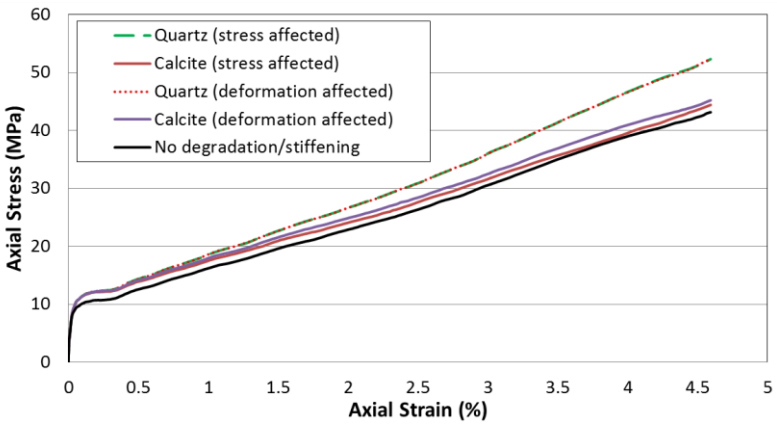

Fig. 5. Simulation of the responses of quartz and calcite assemblies subject to dissolution degradation and stiffening.

Clearly the presented results should be regarded as a numerical exercise rather than predictions of material response. It demonstrates the feasibility of DEM approach for linking

coupled processes and generating overall material response as affected micro-scale mechanisms at the grain contact.

6 CONCLUSIONS

The presented study explores a DEM approach to modelling coupled phenomena in which the interaction of mechanical processes and intrinsic, spontaneous chemical processes plays a critical role. Analyzed in this study is a prime example of multi-scale interaction of mineral dissolution and enhanced mechanical deformation. The primary motivation for the use of DEM is that it allows one to relate the coupled grain contact mechanisms to the overall response of a particle assembly. The implementation of the chemo-mechanical coupling into the contact model has to be accomplished with necessary simplifications to allow the use of only conventional contact parameters. Obviously, more complex and sophisticated contact models can be developed to account for the influence of additional localized properties on the coupled processes. It is to the analyst's discretion to maintain a reasonable balance between the computational cost and the adequate representation of the complexity of the mathematical model.

The presented analysis examines a modified linear contact model that describes the degradation effect caused by mineral dissolution, which evolves with time with its rate being affected by the local grain contact force or contact displacement. Both force and displacement controlled formulations are used to describe the kinetic rate laws for enhanced dissolution. Simulations of quartz and calcite minerals, characterized by different rate constants and physical properties, indicate different softened stress-strain responses. The implementation is focused on the evolving contact stiffness, whereas the possibilities of modifying or developing hardening/softening based force-displacement models to describe adequate contact force-displacement deserve future investigation. Only dissolution is considered in the presented analysis and continuing development of modelling the diffusion and precipitation processes at and near the grain contact is much needed.

ACKNOWLEDGEMENT

The authors wish to acknowledge the financial support provided by the University of Toledo through a Faculty Summer Research Fellowship.

REFERENCES

Cundall, P.A. & Strack, O.D.L. (1979), "A discrete numerical model for granular assemblies". Geotechnique, Vol. 29(1), 47–65.

Hu, L.B. & Hueckel, T. (2007a), "Coupled chemo-mechanics of intergranular contact: toward a three-scale model". Comput. Geotech., Vol. 34(4), 306-327.

Hu, L.B. & Hueckel, T. (2007b), "Creep of saturated materials as a chemically enhanced rate dependent damage process". Int. J. Num. Anal. Meth. Geomech., Vol. 31(14), 1537-1565.

Hu, L.B., Panthi, S. & Hueckel, T. (2013), "Multi-scale characterization of coupling mechanisms for evolving permeability in oil/gas bearing sediments compaction". Geotech. Geol. Eng., accepted.

Hueckel, T., Cassiani, G., Fan, T., Pellegrino, A., & Fioravante, V. (2001), "Effect of aging on compressibility of oil/gas bearing sediments and their subsidence". J. Geotech. Geoenv. Eng., ASCE, Vol. 127(11), 926-938.

Hueckel, T., & Hu, L.B. (2009), "Feedback mechanisms in chemo-mechanical multi-scale modeling of soil and sediment compaction". Comput. Geotech., Vol. 36(6), 934-943.

Itasca. (2008), PFC2D User's Guide. Itasca Consulting Group Inc, Minneapolis, USA.
O'Sullivan, C. (2011), Particulate Discrete Element Modelling: A Geomechanics Perspective. Spon Press, New York, USA.
Kuhn, M. & Mitchell, J.K. (1993), "New perspectives on soil creep". J. Geotech. Eng., Vol. 119(3), 507-524.
Kwok, C.Y. & Bolton, M.D. (2010), "DEM simulations of thermally activated creep in soils". Geotechnique, Vol. 60(6), 425-433.
Le Guen, Y., Renard ,F., Hellmann, R., Brosse, E., Collombet, M., Tisserand, D. & Gratier, J.-P. (2007), "Enhanced deformation of limestone and sandstone in the presence of high Pco2 fluids". J. Geophys. Res., Vol. 112, B05421.
Lydzba, D., Pietruszczak, S. & Shao, J.F. (2007), "Intergranual pressure solution in chalk: a multiscale approach".Comput. Geotech., Vol. 34(4), 291-305.
Palandri, J. L. & Kharaka, Y. K. (2004), "A compilation of rate parameters of water-mineral interaction kinetics for application to geochemical modeling", USGS open file report
Raj, R. & Chyung, C.K. (1981). "Solution-precipitation creep in glass ceramics". Acta. Metall., Vol. 29(1), 159-66.
Revil, A. (1999), "Pervasive pressure-solution transfer : A poro-visco-plastic model". Geophys. Res. Lett., Vol. 26(2), 255-258.
Rimstidt, J.D. & Barnes, D.L. (1980), "The kinetics of silica water reaction". Geochim. Cosmoch. Acta, Vol. 44(11), 1683-1699.
Rutter, E.H. (1976). "The kinetics of rock deformation by pressure solution". Philos. Trans. R. Soc. A., Vol. 283(1312), 203-219.
Rutqvist, J. (2012), "The geomechanics of CO2 storage in deep sedimentary formations". Geotech. Geol. Eng., Vol. 30(3), 525-551.
Sjoberg, E. L. (1976), "A fundamental equation for calcite dissolution kinetics". Geochim. Cosmoch. Acta, Vol. 40(4), 441-447.
Spiers, C.J. & Schutjens, P.M.T.M. (1990). "Densification of crystalline aggregates by fluid phase diffusional creep. In Meridith, P.G. & Barber, D. (eds.), Deformation Processes in Minerals, Ceramics and Rock. Unwin Hyman, London, 334–353.
Wang, Y.H., Xu, D. & Tsui, K.Y. (2008), "Discrete element modeling of contact creep and aging in sand". J. Geotech. Geoenv. Eng., Vol. 134(9), 1407-1411.
Weyl, P.K. (1959), "Pressure solution and the force of crystallization - a phenomenological theory". J. Geophys. Res., Vol. 64(11), 2001-2025.
Yasuhara, H., Elsworth, D. & Polak, A. (2003), "A mechanistic model for compaction of granular aggregates moderated by pressure solution". J. Geophys. Res. Vol. 108(B11), 2530, doi:10.1029/2003JB002536.
Zhang, X. & Spiers, C.J. (2005), "Compaction of granular calcite by pressure solution at room temperature and effects of pore fluid chemistry". Int. J. Rock Mech. Min. Sci., Vol. 42(7-8), 950-960.

TWO-PHASE NUMERICAL MODEL FOR SOIL–FLUID INTERACTION PROBLEMS

Zdzisław Więckowski
Department of Mechanics of Materials, Łódź University of Technology, Łódź, Poland

ABSTRACT: *An extension of the material point method is proposed in order to solve large deformation problems of geo-mechanics including possible state change of the soil from the saturated solid to the fluidized one and phenomenon of transport of a soil by a fluid. The material point method can be interpreted as an arbitrary Lagrangian–Eulerian approach to the finite element method and allows for analysis of problems with very large strains as the computational element mesh is defined in an Eulerian format and does not suffer from element distortions. This method can also be interpreted as a meshless method because the material points carrying the information on state variables are defined independently of the mesh. In the proposed approach, both media, the soil and fluid, are represented by two sets of material points the motion of which is controlled by two kinematically independent vectors of degrees of freedom defined on the computational element mesh. The soil–fluid interaction forces are modelled by Ergun's law. The problem of erosion is studied in the paper.*

1 INTRODUCTION

Several ways of modelling transition processes like solid fluidization or sedimentation have been applied so far. The discrete and continuum approaches formulated in Eulerian or Lagrangian formats have been implemented. Also, some combinations of these approaches have been utilized which lead to some mixed methods. The soil fluidization phenomenon leading to erosion have been modelled mostly by tracking the work (related to friction) of the shear stress component acting on a bed surface and switching soil particles to a "fluid mode" (or fluidized mode) after reaching some threshould value by this work. Another method is treating the solid–fluid mixture as a two-phase material which can change its behaviour during the physical process and allows to modell state transitions like changing the saturated soil into a fluidized soil or a fluid with flowing silo grains as well as changing the state of a fluid with suspended soil grains into a saturated soil. An attempt to model such phenomena as sedimentation, separation and fluidization has been done by Andrews & O'Rourke (1996) by the use of multiphase particle-in-cell method (MP-PIC), see also (Harlow 1964). Solid–gas interaction problems have been analyzed in this work. One-dimensional problems have been solved by modelling the gas by the particle-in-cell method and treating the solid as discrete particles.

An approach which makes use of the frictional work criterion is the idea by Oñate et al. (2006) and Oñate et al. (2008) where the particle finite element method (PFEM) has been utilized. In this method, the soil particles change their mode to the fluid one after detaching from a bed surface.

El Shamy & Aydin (2007) considered an erosion problem for a horizontal bed. The discrete element method has been used to trace the motion of soil particles while the problem of motion of fluid—described by the averaged Navier–Stokes equations—has been solved using the finite volume method formulated in the Eulerian format. The Ergun law (Ergun 1952) has been utilized in this paper to describe the interaction between the soil and fluid. El Shamy et al. (2012) have used another mixed approach where the averaged Navier–Stokes equations have been solved by the finite element method.

A two-phase material model is used by Nguyen et al. (2012) to simulate the dredged sediment transport. Both the media, the fluid and solid, are treated as viscous fluids. The Navier–Stokes equations are solved by the finite volume method formulated in the Eulerian format.

A multiphase model of solid–fluid mixture has been applied by Shakibaeinia & Jin (2010) to simulate a sand discharge into water. The—so called—moving particle semi-implicit method (MPS) has been used by these authors. The method can be classified as a kernel point-based method; it shows strong similarity to the smoothed particle hydrodynamics method (SPH).

A single phase erosion model is studied by Stefanova et al. (2012) by the use of the smoothed particle hydrodynamics method (SPH).

A two-phase solid–fluid model has been implemented in the material point method by Jassim et al. (2012) and applied to some small deformation problems. The motion of a liquid in pores is traced with the help of separate velocity field for the liquid and is governed by Darcy's law. As only one type of material points is defined in this model, it does not allow for solving the transition problems.

In the present work, the solid–fluid mixture is described by a two-phase material model and the dynamic evolution equations for the mixture are stated. The approximate solution of these equations are found by the use of the material point method. The behaviour of the soil is described by elastic-viscoplastic constitutive relations while the fluid is represented by the compressible viscous liquid. So far, the material point method has been successfully applied to large deformation problems of granular flow (Więckowski, Youn, & Yeon 1999; Więckowski 2004) and geomechanics (Beuth, Więckowski, & Vermeer 2011).

2 DESCRIPTION OF THE PROBLEM

In the present work, a soil–fluid mixture is considered to be able to change its state from that observed for a solid granular body—with a fluid in pores—to the liquefied state with soil grains flowing in the fluid. The reverse change, sedimentation, can also occur when the floating grains get into contact and start to interact with each other directly by contact forces. Both the states are illustrated in Figure 1. In this section, the terms, *low porosity* and *high porosity*, will be used. The terms are related to the two states shown on the left and right sides of the figure, respectively. The two limit states, the dry soil and pure liquid states, can be treated as a special cases of these two states. The partially saturated solid can be treated as the case of *low porosity*.

The well known equations describing the mechanical behaviour of a porous saturated medium, introduced by Biot (1941) in the static case and in the dynamic case (Biot 1956a; Biot 1956b) govern the motion of both constituents: the soil and the fluid. The equations can also be found in the book by Verruijt (2010) and paper by Zienkiewicz & Shiomi (1984) where an early finite element analyses of consolidation problems can be found.

Let the tensor of the effective stress be defined as follows:

$$\sigma'_{ij} = \sigma_{ij} + \alpha\, p\, \delta_{ij} \tag{1}$$

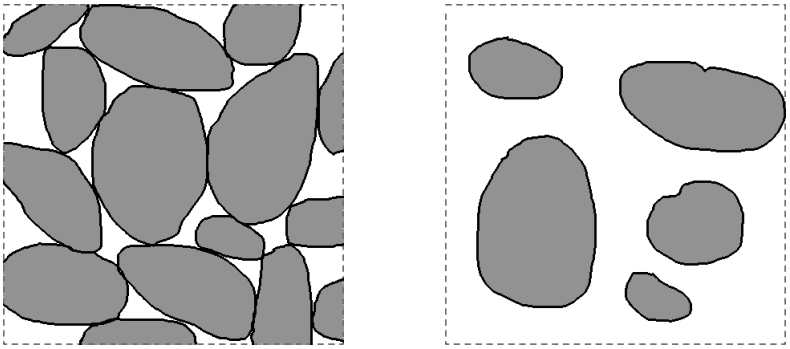

Fig. 1. Solid–liquid mixture with low (left) and high (right) porosity

where σ_{ij} is the total stress tensor, p the pore pressure in the fluid, δ_{ij} the Kronecker delta-symbol while α is the Biot coefficient which is considered here as equal to 1.

Using the definition of the effective stress (Eq. 1), the two states of the solid–fluid mixture shown in Figure 1 can also be identified by means of this notion: the low porosity case is related to stress state $\sigma'_{ij} \neq 0$ while the high porosity state means that the effective stresses vanish, $\sigma'_{ij} = 0$.

Let v_i and w_i be the velocity vectors for the solid and fluid, respectively, and let symbol n denote the porosity of the soil. The equations of motion for both the media can be stated as follows:

$$(1-n)\,\varrho_{\mathrm{s}}\,\dot{v}_i = \sigma'_{ij,j} - (1-n)\,p_{,i} + f_{\mathrm{d}\,i} + (1-n)\,\varrho_{\mathrm{s}}\,g_i, \tag{2}$$

$$n\,\varrho_{\mathrm{f}}\,\dot{w}_i = -n\,p_{,i} + n\,s_{ij,j} - f_{\mathrm{d}\,i} + n\,\varrho_{\mathrm{f}}\,g_i \tag{3}$$

where ϱ_{s} and ϱ_{f} denote the mass density of the solid skeleton and the fluid, respectively, s_{ij} is the deviatoric part of the stress tensor, g_i is the vector of acceleration of gravity, $f_{\mathrm{d}\,i}$ is the vector of the force which the fluid acts on the unit volume of the solid. Symbols v_i and w_i in Eqs. (2) and (3) represent the actual velocities for the solid and fluid, respectively. The tortuosity of the fluid flow path is not taken into account in Eqs. (2) and (3).

The law of mass conservation can be expressed in the form of the following equations, e.g. (Verruijt 2010):

$$n\,\dot{\varepsilon}_{\mathrm{f}}^{\mathrm{vol}} = (1-n)\,v_{i,i} + n\,w_{i,i}, \tag{4}$$

$$\dot{n} + n\,\dot{\varepsilon}_{\mathrm{f}}^{\mathrm{vol}} = -(n\,w_i)_{,i} \tag{5}$$

where $\dot{\varepsilon}_{\mathrm{f}}^{\mathrm{vol}} = d_{\mathrm{f}\,ii}$ is the rate of the volumetric strain for the fluid, d_{ij} denotes the rate-of-deformation tensor. Eqs. (4) and (5) are derived under the assumptions that the product of the fluid velocity vector and pressure gradient is disregarded, and that the compressibility of solid grains is very small. It should be noted that Eq. (5) is not used in the numerical analysis in this work—the current field of porosity is evaluated on the base of current position of the material points representing the solid.

The constitutive relations are the next group of governing equations in the problem of the considered two-phase medium. In the case of the solid phase, the elastic–viscoplastic material model with the Drucker–Prager yield condition and a non-associative flow rule is used. The model has been described in details in (Więckowski 2004), and is represented briefly below in a symbolic way,

$$\overset{\nabla}{\sigma}{}'_{ij} = f_{ij}(\sigma_{pr}, d_{rs}) \qquad \text{in the case of low porosity,} \tag{6}$$

$$\sigma'_{ij} = 0 \qquad \text{in the case of high porosity.} \tag{7}$$

When the solid–fluid mixture is changing from the saturated soil state to the liquefied soil (the fluid with flowing soil grains) the first invariant of the effective stress tensor tends to zero through the negative values and porosity is increasing

$$\sigma'_{kk} \to 0^- \quad \& \quad \dot{n} > 0.$$

Reaching the zero value by σ'_{kk} means that the material is liquefied. The inverse process (sedimentation) in the case of decreasing porosity, $\dot{n} < 0$, cannot be controlled by tracking the value of the first stress invariant, σ'_{kk}, and a threshould value for porosity, n_0, is introduced for which the onset of contact of soil grains appears and the relation (6) becomes applicable.

In the case of fluid, the fluid fraction is traced in order to detect possibility of voids that can appear—for example—when the fluid splashes. This means that in the case when the fluid is a cloud of separate drops (there are some voids in the volume occupied by the fluid) the pressure and other stress components vanish,

$$p = 0 \quad \& \quad s_{ij} = 0.$$

When the voids in the fluid disappear and the mass concentration for the fluid grows, the following constitutive relations become applicable:

$$\dot{p} = -K_{\mathrm{f}}\, \dot{\varepsilon}^{\mathrm{vol}}_{\mathrm{f}} \tag{8}$$

$$s_{ij} = 2\mu_{\mathrm{e}}\, d_{ij} \tag{9}$$

where K_{f} denotes the bulk modulus for the fluid and μ_{e} the fluid effective viscosity. Obviously, the same equations are valid in the state when no voids exist in the fluid and the pressure is positive. The effective viscosity occuring in Eq. (9) is assumed in the form (e.g. Batchelor & Green 1972)

$$\mu_{\mathrm{e}} = \mu \left(1 + \tfrac{5}{2}\,\phi + 5.2\,\phi^2\right) \tag{10}$$

where ϕ denotes the volume fraction of the particles suspended in the fluid. This formula is derived for the fluid with spherical particles suspended in it.

The interaction between the soil and fluid is described by the use of Ergun's law (Ergun 1952):

$$f_{\mathrm{d}\,i} = n^2 \left[\frac{\mu}{\kappa}\,(w_i - v_i) + n\,\varrho_{\mathrm{f}}\,\frac{F}{\sqrt{\kappa}}\,|\boldsymbol{w} - \boldsymbol{v}|\,(w_i - v_i)\right] \tag{11}$$

where $f_{\mathrm{d}\,i}$ denotes the vector of the drag force, κ permeability of the soil and F Forchheimer's coefficient. The latter two quantities are related with porosity as follows:

$$\kappa = \frac{n^3\, d_p^2}{a\,(1-n)^2}, \quad F = \frac{b}{\sqrt{a}\, n^{3/2}}$$

where d_p denotes the average particle size of the soil, $a = 150$, $b = 1.75$. Eq. (11) gives very accurate results in the wide range of porosity value (up to 0.8). It should be noted that by constituting the interaction between the soil and fluid by Ergun's equation, the influences of local rotations of the soil on the fluid motion and local rotations of the fluid on the soil motion are neglected.

The equations of motion, Eqs. (2) and (3), the mass conservation equations, Eqs. (4) and (5), the constitutive equations for the soil and fluid, and the Ergun constitutive relation, Eqs. (11) has to be satisfied for any internal point of the regions occupied by the corresponding medium, the soil and the fluid. To complete the formulation of the considered initial–boundary problem, the appropriate boundary and initial conditions has to be defined.

3 SOLUTION OF THE PROBLEM

To solve the problem by the material point method, the principle of virtual work is employed. If $\boldsymbol{v} \in V^{\mathrm{s}}$ and $\boldsymbol{w} \in V^{\mathrm{f}}$ are kinematically admissible velocity fields for the solid and fluid phases, respectively, while σ'_{ij} is the effective stress tensor for the solid and σ_{ij} denote the stress tensor for the fluid, the principle of virtual work takes the form of two equations

$$\int_{\Omega^{\mathrm{s}}} \bar{\varrho}_{\mathrm{s}}\, \dot{v}_i\, \delta v_i \,\mathrm{d}x = \int_{\Omega^{\mathrm{s}}} \left((-\sigma'_{ij} + n_{\mathrm{s}}\, p\, \delta_{ij})\, \delta v_{i,j} + (p\, n_{\mathrm{s},i} + f_{\mathrm{d}\,i} + \bar{\varrho}_{\mathrm{s}}\, g_i)\, \delta v_i \right) \mathrm{d}x + \int_{\Gamma_t^{\mathrm{s}}} t'_i\, \delta v_i \,\mathrm{d}s - \int_{\Gamma_t^{\mathrm{f}}} n_{\mathrm{s}}\, p\, \delta v_i\, n_i \,\mathrm{d}s \quad \forall \delta \boldsymbol{v} \in V_0^{\mathrm{s}}, \tag{12}$$

$$\int_{\Omega^{\mathrm{f}}} \bar{\varrho}_{\mathrm{f}}\, \dot{w}_i\, \delta w_i \,\mathrm{d}x = \int_{\Omega^{\mathrm{f}}} (-n_{\mathrm{f}}\, \sigma_{ij}\, \delta w_{i,j} + (-\sigma_{ij}\, n_{\mathrm{f},j} - f_{\mathrm{d}\,i} + \bar{\varrho}_{\mathrm{f}}\, g_i)\, \delta w_i) \,\mathrm{d}x - \int_{\Gamma_t^{\mathrm{f}}} n_{\mathrm{f}}\, t_i\, \delta w_i \,\mathrm{d}s \quad \forall \delta \boldsymbol{w} \in V_0^{\mathrm{f}} \tag{13}$$

where V_0^{s} and V_0^{f} denote the spaces of kinematically admissible displacements for the solid and fluid media, respectively, defined as follows:

$$V_0^{\mathrm{s}} = \left\{ \boldsymbol{u} : u_i = 0 \text{ on } \Gamma_u^{\mathrm{s}} \right\},$$
$$V_0^{\mathrm{f}} = \left\{ \boldsymbol{u} : u_i = 0 \text{ on } \Gamma_u^{\mathrm{f}} \right\}.$$

In Eqs. (12) and (13), symbols $\bar{\varrho}_{\mathrm{s}}$ and $\bar{\varrho}_{\mathrm{f}}$ denote the mass concentration fields for both the phases while n_{s} and n_{f} are the volume fraction for the solid and fluid phases, respectively. In the case of fully saturated material, the latter two symbols have simple relations with porosity, $n_{\mathrm{s}} = n$, $n_{\mathrm{f}} = 1 - n$.

The occurrence of terms related to the porosity gradient on the right-hand-sides of Eqs. (12) and (13) is worth noting.

Let a region initially occupied by each phase be divided into a set of subregions. Let each subregion be represented by one its points, called a material point. We assume that the mass concentration fields are represented by the masses and the position of the material points,

$$\bar{\varrho}_{\mathrm{s}} = \sum_{i=1}^{N_{\mathrm{s}}} M_{\mathrm{s}i}\, \delta(\boldsymbol{x} - \boldsymbol{X}_{\mathrm{s}i}),$$
$$\bar{\varrho}_{\mathrm{f}} = \sum_{i=1}^{N_{\mathrm{f}}} M_{\mathrm{f}i}\, \delta(\boldsymbol{x} - \boldsymbol{X}_{\mathrm{f}i})$$

where M_i and $\boldsymbol{X}_i$ denote the mass and the position of the i-th material point, $\delta(\boldsymbol{x})$ is the Dirac δ-function. Indices "s" and "f" relates to the solid and fluid phases, respectively, in the above equations. Beside this space discretization (of Lagrangian type), another one—an Eulerian finite element mesh, called a computational mesh, covering the virtual position of the analyzed body—is also used. This mesh can be changed arbitrarily during calculations or remain constant. Both the kinds of the space discretisation used in the material point method are shown in Figure 2.

The main unknown in the considered problem, velocity fields $\boldsymbol{v}$ and $\boldsymbol{w}$ are approximated by the use of interpolation functions defined on the computational mesh $\mathbf{N}$ and nodal degrees of freedom defined independently for the solid, $\mathbf{v}$, and the fluid, $\mathbf{w}$,

$$\boldsymbol{v} = \mathbf{N}\, \mathbf{v}, \tag{14}$$
$$\boldsymbol{w} = \mathbf{N}\, \mathbf{w}. \tag{15}$$

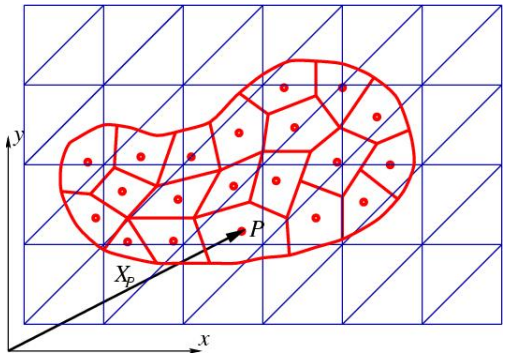

Fig. 2. Space discretisation in the material point method

After substitution of Eqs. (14) and (15) into the equations of virtual work (12) and (13), the following system of ordinary differential equations is obtained:

$$\mathbf{M}_{\mathrm{s}}\,\dot{\mathbf{v}} = \mathbf{F}_{\mathrm{s}} + \mathbf{F}_{\mathrm{d}} + \mathbf{F}_{sn} - \mathbf{R}_{\mathrm{s}}, \tag{16}$$

$$\mathbf{M}_{\mathrm{f}}\,\dot{\mathbf{w}} = \mathbf{F}_{\mathrm{f}} - \mathbf{F}_{\mathrm{d}} + \mathbf{F}_{\mathrm{f}n} - \mathbf{R}_{\mathrm{f}} \tag{17}$$

where $\mathbf{M}_{\mathrm{s}}$ and $\mathbf{M}_{\mathrm{f}}$ are mass matrices, $\mathbf{F}_{\mathrm{s}}$ and $\mathbf{F}_{\mathrm{f}}$ the vectors of nodal external forces, $\mathbf{R}_{\mathrm{s}}$ and $\mathbf{R}_{\mathrm{f}}$ the vectors of nodal internal forces, $\mathbf{F}_{\mathrm{d}}$ is the vector of nodal drag forces related to Ergun's law, $\mathbf{F}_{sn}$ and $\mathbf{F}_{\mathrm{f}n}$ are the vectors of nodal solid–fluid interaction forces related to inhomogeneity of the porosity field. System (16)–(17) is solved by the use of the explicit time integration algorithm with the diagonalized mass matrices. The main difference between the finite element (FEM) and material point (MPM) methods is based on the fact that the state variables are traced at the material points, defined independently of the computational mesh in MPM, and at integration points connected with elements in FEM. The details of MPM computations can be found in (Więckowski 2004).

4 EXAMPLE

A problem of erosion of a slope attacked by water is analyzed. The geometry of the problem is illustrated in Figure 3. The slope shown on the left side of the figure is subjected to an attack of water stored in a reservoir. The water attack starts after opening a gate located in a lower part of the left reservoir wall. The dimensions in the figure are shown in metres. The non-slip and symmetry boundary conditions are considered for the solid and fluid phases, respectively, on the bottom edge of the analyzed region. The symmetry boundary conditions are considered on the left vertical edge of the slope and the vertical wall of the reservoir.

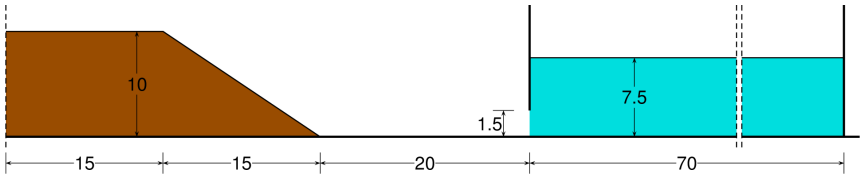

Fig. 3. Slope erosion—initial configuration

It is assumed that the soil is dry sand being modelled by the elastic–viscoplastic constitutive relations with the following material data: mass density of the skeleton $\varrho_s = 2850\,\mathrm{kg/m^3}$, initial mass concentration $\bar{\varrho}_s = 1500\,\mathrm{kg/m^3}$, Young's modulus $E = 10\,\mathrm{MPa}$, Poisson's ratio $\nu = 0.3$,

internal friction angle $\varphi = 30^\circ$, parameters in the viscous law: $\gamma = 1{\cdot}10^{-3}\,\mathrm{s}^{-1}$ and $N = 1$, grain diameter $d_p = 1$ mm. Calculations have been made with the following threshould value for porosity: $n_0 = 0.5$.

The material parameters for the fluid are set as follows: mass density $\varrho_f = 1000\,\mathrm{kg/m}^3$, viscosity $\mu = 8.905{\cdot}10^{-4}$ Pa·s and bulk modulus $K = 2.128{\cdot}10^7$ Pa. The last parameter is set 100 times smaller than the actual value for water to reduce the computation time by increasing the time increment value used in the explicit procedure of integration of the dynamic equations.

The initial stress field for the solid has been found from an analysis of the quasi-static problem. The finite element method has been employed to find the stress field related to gravity forces applied in 5 equal load increments. The initial stress field for the fluid is related to the hydrostatic state.

The applied regular structured mesh has 6266 nodes and 12000 elements; 70460 material points are introduced: 19920 for the solid phase and 50540 for the fluid one. Calculations have been made with the time increment equal to $2.5{\cdot}10^{-5}$ s.

The history of the process is shown in Figures 4 and 5 where a middle part of the problem is shown. Three different matter states, dry sand, pure water and soil–water mixture, are represented by different colours in the figures. The processes of transport of the soil by water and water flow through the porous material are illustrated in the figures. The part of the slope surrounding its bottom tip is displaced from the initial position and transported by the fluid at the beginning of the flow process (Figure 4). It can be observed in Figure 5 that some part of the soil comes to the reservoir due to reverse motion of the fluid. After 100 s of the process, the surface of the fluid becomes almost flat.

The computation time was about 1.76 hours for one second of the analysis time; a PC computer equipped with Intel Core i7 970 processor (3.20 GHz) was utilized.

CONCLUSIONS

Two phase solid–fluid model has been built into the material point method. It is shown in the paper that this approach allows for modelling very challenging tasks like state transition problems for the solid–fluid mixture like erosion. In the included example, the erosion process for a slope attacked by water is analysed, and the phenomenon of transport of the solid by the fluid is modelled.

Other analyses, not shown in this paper, have proved the ability of the method to handle such problems as breaching, being of interest of the dredging technology, and seepage flow. The described approach allows to solve soil–fluid interaction problems with large deformation and predict outcomes of related phenomena.

ACKNOWLEDGEMENTS

The financial support from the European Community's Seventh Framework Programme (Marie Skłodowska-Curie Intra European Fellowship) through grant PIEF-GA-2010-274335 is gratefully acknowledged (project title: Enhancement of the Material Point Method for Fluid–Structure Interaction and Erosion, GEO FLUID). The research was carried out at Deltares, Stieltjesweg 2, 2628 CK Delft, The Netherlands.

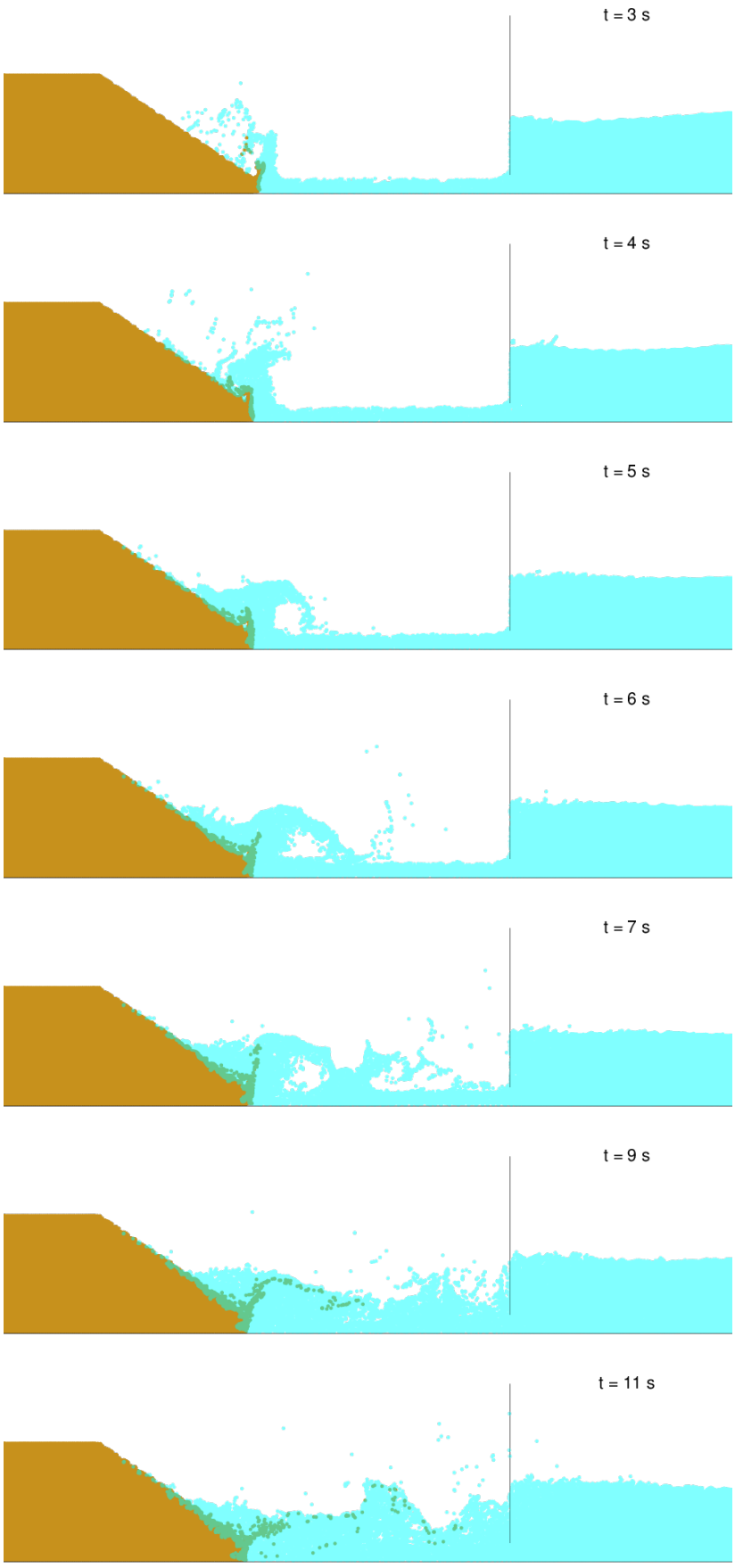

Fig. 4. Slope erosion process

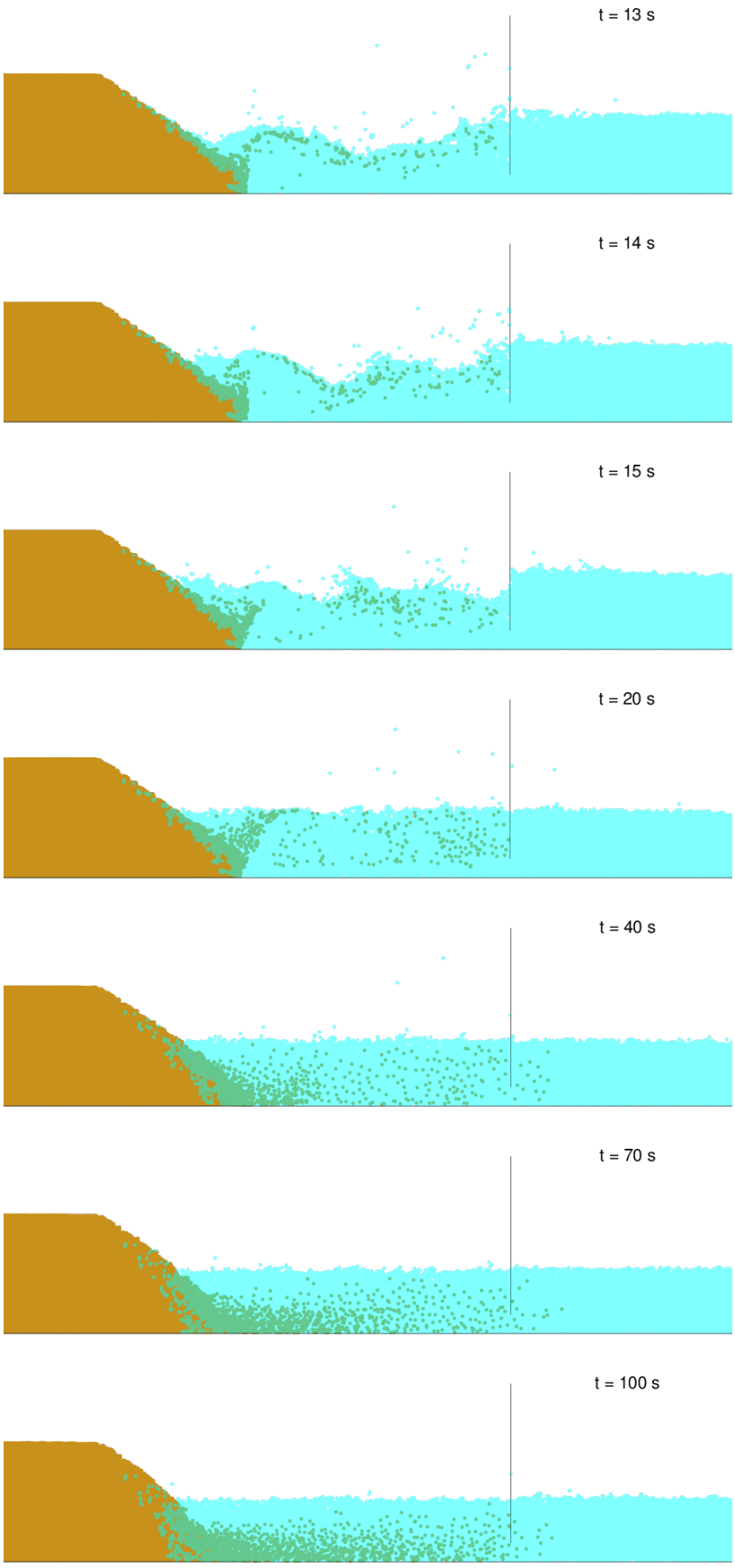

Fig. 5. Slope erosion process—continued

REFERENCES

Andrews, M. & O'Rourke, P. (1996). The multiphase particle-in-cell (MP-PIC) method for dense particulate flows. *Int. J. Multiphase Flow 22*, 379–402.

Batchelor, G. & Green, J. (1972). The determination of the bulk stress in a suspension of spherical particles to order c^2. *J. Fluid Mech. 56*, 401–427.

Beuth, L., Więckowski, Z., & Vermeer, P. (2011). Solution of quasi-static large-strain problems by the material point method. *Int. J. Num. Anal. Meth. Geomech. 35*, 1451–1465.

Biot, M. (1941). General theory of three-dimensional consolidation. *Journal of Applied Physics 2*, 155–164.

Biot, M. (1956a). Theory of propagation of elastic waves in a fluid-saturated porous solid. I. Low-frequency range. *Journal of Acoustical Society of America 28*, 168–178.

Biot, M. (1956b). Theory of propagation of elastic waves in a fluid-saturated porous solid. II. Higher-frequency range. *Journal of Acoustical Society of America 28*, 179–191.

El Shamy, U., Abdelhamid, Y., Krueger, P., & An, Z. (2012). A particle-based model of flow-induced scour. In *Proc. 6th International Conference on Scour and Erosion (ICSE6)*, Paris, August 27–31.

El Shamy, U. & Aydin, F. (2007). A micro-scale model for the analysis of flood-induced piping in river levees. In F. Silva-Tulla & P. Nicholson (Eds.), *Proc. GeoDenver 2007 Embankments, Dams, and Slopes*, Denver, Colorado.

Ergun, S. (1952). Fluid flow through packed column. *Chemical Engineering Progress 48*, 89–94.

Harlow, F. (1964). The particle-in-cell computing method for fluid dynamics. In B. Adler, S. Fernbach, & M. Rotenberg (Eds.), *Methods for Computational Physics, Vol. 3*. Academic Press, New York.

Jassim, I., Stolle, D., & Vermeer, P. (2012). Two-phase dynamic analysis by material point method. *Int. J. Numer. Anal. Meth. Geomech.* Published online in Wiley Online Library.

Nguyen, D., Levy, F., Van Bang, D., Guillou, S., Nguyen, K., & Chauchat, J. (2012). Simulation of dredged sediment releases into homogeneous water using a two-phase model. *Advances in Water Resources 48*, 102–112.

Oñate, E., Celigueta, M., & Idelsohn, S. (2006). Modeling bed erosion in free surface flows by the particle finite element method. *Acta Geotechnica 1*, 237–252.

Oñate, E., Idelsohn, S., Celigueta, M., & Rossi, R. (2008). Advances in the particle finite element method for the analysis of fluid multibody interaction and bed erosion in free surface flows. *CMAME 197*, 1777–1800.

Shakibaeinia, A. & Jin, Y.-C. (2010). A weakly compressible MPS method for modeling of open-boundary free-surface flow. *Int. J. Numer. Meth. Fluids 63*, 1208–1232.

Stefanova, B., Seitz, K., Bubel, J., & Grabe, J. (2012). Water-soil interaction simulation using smoothed particle hydrodynamics. In *Proc. 6th International Conference on Scour and Erosion (ICSE6)*, Paris, August 27–31.

Verruijt, A. (2010). *An Introduction to Soil Dynamics, Vol. 24: Theory and Applications of Transport in Porous Media*. Springer Verlag, Berlin.

Więckowski, Z. (2004). The material point method in large strain engineering problems. *Comp. Meth. Appl. Mech. Engng. 193*, 4417–4438.

Więckowski, Z., Youn, S., & Yeon, J. (1999). A particle-in-cell solution to the silo discharging problem. *Int. J. Num. Meth. Engng. 45*, 1203–1225.

Zienkiewicz, O. & Shiomi, T. (1984). Dynamic behaviour of saturated porous media; the generalized biot formulation and its numerical solution. *Int. J. Num. Meth. Engng. 8*, 71–96.

A DOUBLE SCALE MODELLING APPROACH FOR HYDRO-MECHANICAL COUPLING

B. van den Eijnden[1,2,3]
[1] *Andra, 1-7 Rue Jean Monnet, Chatenay-Malabry, France*

F. Collin[2], P. Bésuelle[3], R. Chambon[3]
[2] *Argenco, Liège, Belgium*

[3] *Lab. 3SR, Grenoble, France*

ABSTRACT: *An approach is investigated for the modelling of the hydro-mechanical coupled behaviour of Callovo-Oxfordian claystone, a potential host rock for radioactive waste repositories in France. This approach is a double-scale finite element method, distinguishing a micro and a macro scale. At the micro level a representative elementary volume (REV) is used to model the material behaviour. The global response of this REV serves as an implicit constitutive law for the macro scale. On the macro scale, a poro-mechanical continuum is defined with fully coupled hydro-mechanical behaviour, the micro scale contains a model that takes into account the material micro structure to provide the material response to deformation and the associated stiffness matrices. Computational homogenization is used to retrieve the macro tangent stiffness from the micro level. This double scale approach is applied in the simulation of biaxial deformation tests, demonstrating the possibility of using the double scale modelling approach with the presented model at the micro level. The response at the macro level is compared with the micro-mechanical behaviour.*

1 INTRODUCTION

The principle of deep geological repositories for the storage of radioactive waste relies among others on the low permeability of the host rock. As the permeability is influenced by mechanical alteration of the material, the coupling between hydraulic and mechanical behaviour of the host rock is of importance in the study of radioactive waste storage. In this context we develop a fully-coupled hydromechanical model based on micro-mechanical considerations. Therefore two scales are defined; a macro scale at engineering level and a micro scale at the material level. On the macro level, field equations are solved using a finite element method. In the integration points of the macro level the constitutive behaviour is modelled using a representative elementary volume (REV) with micro structure. A wide range of approaches for the modelling of this REV is described in literature. No review will be given here; we focus on the finite element square (FE^2) method using a periodic REV with finite element discretization to model the constitutive behaviour for the macro level.
In hydromechanical coupled FE^2 computations a deformation and a pore pressure gradient prescribed by the macro level lead to a boundary value problem on the REV on the micro level. Once this micro problem is solved, the averaged response and its variational relation to the prescribed deformation in the form of tangent stiffness terms can be derived by homogenization to

serve as feedback for the macro level.
For the homogenization of the tangent stiffness matrices, different approaches can be considered. In the research preceding this work (Frey et al. (2012), Marinelli (2013)) a numerical approach by perturbation of the prescribed deformation variables is followed. This implies solving the micro problem multiple times for small perturbations of the enforced boundary values in order to give a finite difference approximation of the tangent stiffness matrix of the problem. Although the method is straightforward and widely applicable, the computational expense of solving the micro problem several times is a major drawback. A more efficient homogenization scheme like computational homogenization can significantly reduce the computation time of the multi scale computation.
Computational homogenization has been used for deriving the response and tangent stiffness matrices from periodic REVs for mechanical problems, see for example Miehe & Koch (2002) and Kouznetsova et al. (2004), the latter of which used static condensation of the FE rigidity matrix to derive the tangent stiffness matrix. This method has been extended to diffusive problems of thermomechanical coupling by Ozdemir et al. (2008) and is used for the homogenization of hydro-mechanical properties by Massart & Selvadurai (2012) under the assumption of steady-state flow at the micro scale. A fully transient approach to computational homogenization for hydro-mechanically coupled problems is given by Su et al. (2011). In this work, computational homogenization with static condensation is applied on coupled behaviour of periodic REVs taking into account the hydro-mechanical couplings.
This paper is structured as follows: first the micro-mechanical model is summarized, after which the averaging definitions for upscaling to the macro level are given. Next, the problem statement at the macro level is given, leading to the tangent terms needed to solve the problem on the macro scale. An example of an FE^2 computation of a purely mechanical problem is given. Section 6 gives the computational homogenization approach for deriving the tangent stiffness matrices for HM coupling. A final section is used for the application of the derived tangents in a double-scale biaxial deformation experiment to test the performance of the homogenized tangents. Conclusions are made on the obtained results and the paper closes with some final remarks.

2 MICRO SCALE MODEL

On the micro scale, a model for hydromechanical coupling (Frey et al. (2012)) is used. This model assumes the material to be composed of elastic solids separated by evolving interfaces. A linear-elastic constitutive law is used for the solids, thereby concentrating possible degradation in the interfaces. Cohesive forces between the solid grains act normally and tangentially to the interface orientation as a function of the history of respectively the normal and tangential relative displacement of the opposite interface boundaries. Two separate damage laws are used to describe these forces (Figure 1). In addition to the cohesive forces which are part of the mechanical system, the interfaces form a pore channel network that is fully saturated. Fluid transport is controlled by the conductivity of the channels formed by the interface openings and the fluid pressure distribution. Fluid pressure and pressure gradient within the interfaces lead to fluid normal forces $\boldsymbol{f}_p$ and fluid drag forces $\boldsymbol{f}_D$ acting on the solids. In this way, the hydromechanical coupling is controlled by the interface openings. Fluid compressibility is taken into account by defining the constitutive law of the fluid as:

$$\dot{\rho}^w = \frac{\rho^w}{k^w}\dot{p} \qquad\qquad \rho^w = \rho_0^w \exp\left(\frac{1}{k^w}\left(p - p_0\right)\right) \tag{1}$$

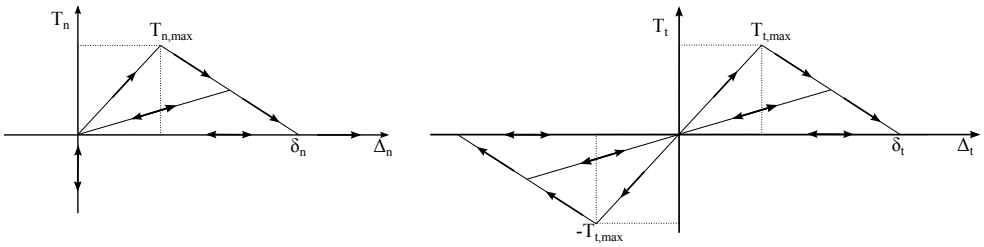

Fig. 1. Damage law for interface cohesive forces. Normal cohesive forces T_n and tangential cohesive forces T_t are a function of respectively relative normal displacement Δ_n and relative tangential displacement Δ_t of the opposite interface boundaries. δ_t and δ_n are the critical interface openings at which the point of complete decohesion is reached.

Integration of the Stokes equation for flow in the channel gives a volume flux $\frac{\bar{\omega}}{\rho}$ as function of the pressure gradient:

$$\frac{\bar{\omega}}{\rho^w} = -\kappa(s)\frac{dp}{ds} \qquad\qquad \kappa(s) = \kappa\left(\Delta_n(s)\right) \tag{2}$$

with κ a hydraulic conductivity term as an arbitrary function of the normal opening Δ_n and the shape and flow assumptions of the channel at location s. After substitution by Equation 1, integration over a channel j between points A^j and B^j gives the constant mass flux $\bar{\omega}^j$ in the interface element:

$$\bar{\omega}^j = \frac{k^w \rho_0}{\exp\left(\frac{p_0}{k^w}\right) \int\limits_{A^j}^{B^j} \frac{1}{\kappa(s)} ds} \left(\exp\left(\frac{p(B^j)}{k^w}\right) - \exp\left(\frac{p(A^j)}{k^w}\right)\right) \tag{3}$$

In the following, we will summarize this equation for the mass flux in channel j between points A^j and B^j as

$$\bar{\omega}^j = \phi^j(\lambda^{B^j} - \lambda^{A^j}) \tag{4}$$

A mass balance equation can be written for all channel connection points as a sum of the fluxes in the connected channels j:

$$\sum_j \bar{\omega}^j = 0 \tag{5}$$

Periodic boundary conditions for pressure difference over the REV $\left(\Delta p_i = \frac{\partial p^M}{\partial x_i}\left(x_i^{(+)} - x_i^{(-)}\right)\right)$ are enforced by

$$\Delta p_i = p_i^+ - p_i^- \qquad\qquad \lambda_i^+ - \lambda^{\Delta p_i}\lambda_i^- = 0 \tag{6}$$

with superscript $+$ and $-$ indicating the dependent and independent boundaries of the REV (Figure 2) and λ the exponential pressure terms as used above; $\lambda^{\Delta p_i} = \exp(\Delta p_i / k^w)$. Using Equation (6) to prescribe the dependent pressure at the channel connections on the top and right boundaries and the mass balance equations (Equation 4) for all other channel connections, system of equations (Equation 7) is built to solve the fluid problem. $[.]$ is used for matrices and $\{.\}$ for column vectors of any size.

$$[\Phi]\{\lambda\} = \{0\} \tag{7}$$

This system of equations is singular and an additional equation is needed. This additional expression is given by penalizing the pressure at one of the internal nodes, hereby implicitly imposing

the average pressure $\bar{p}$ in the REV. Once the fluid problem is solved, the fluid effort on the mechanical system is calculated and the mechanical system is solved, leading to new configuration with new channel conductivities. In this way the coupled problem is solved in an iterative way, while solving the hydraulic and mechanical systems independently. Details on the micro model and a full development of the numerical procedures is given by Frey (2010).

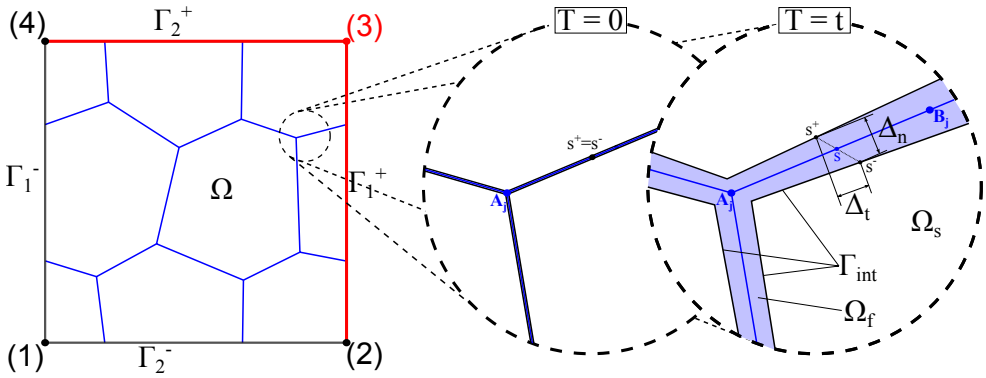

Fig. 2. REV with corner node numbering (1)-(4), domain Ω and external boundary Γ^{ext} definitions; $\Gamma^{ext} = \Gamma_2^- \cup \Gamma_1^+ \cup \Gamma_2^+ \cup \Gamma_1^-$. The internal boundaries Γ^{int} are defined on the opposite sides of the interfaces; they coincide in the initial configuration ($T = 0$). The fluid domain Ω_f is the domain in the interfaces and assumed to be small with respect to Ω^s; $\Omega \approx \Omega^s$.

3 MICRO-MACRO COUPLING BY HOMOGENIZATION

Considering a balanced REV with periodic boundary conditions (Figure 2) the macro responses σ_{ij}^M (Cauchy stress), M (fluid mass per unit volume) and m_i^M (fluid mass flux) are found by homogenization :

$$\sigma_{ij}^M = \frac{1}{V_\Omega}\int_\Omega \sigma_{ij} dV = \frac{1}{V_\Omega}\int_{\Gamma^{ext}} f_i^{ext} x_j dS + \int_{\Gamma^{int}} f_i^{int} x_j dS \tag{8}$$

$$M_i^M = \frac{1}{V_\Omega}\int_{\Omega_f} \rho_f dV \tag{9}$$

$$m_i^M = \frac{1}{V_\Omega}\int_\Omega m_i dV = \frac{1}{V_\Omega}\int_{\Gamma^{ext}} \bar{q} x_i dS \tag{10}$$

The external boundary forces f_i^{ext} in Equation (8) are all the forces acting on the external boundary Γ^{ext} to enforce the boundary conditions. The internal boundary forces f_i^{int} are the forces acting on the internal interface boundaries Γ^{int}, they comprise the cohesive forces, fluid normal forces and the fluid drag forces. Because the cohesive forces and fluid normal forces are anti-symmetric by definition, they cancel out in the integration under small strain assumption. The only force giving a non-zero term in the integration is the fluid drag force $\boldsymbol{f}_D$. Moreover, the macro pressure p^M is linked to the average micro pressure $\bar{p}$ by:

$$p^M = \bar{p} = \frac{1}{V_f}\int_{\Omega_f} p dV \tag{11}$$

4 MACRO SCALE BALANCE EQUATIONS

On the macro level, we define a poromechanical continuum under quasi-static assumption, for which the classical balance equations can be written using the principle of virtual work by any two kinematically admissible fields $u^\star$ and $p^\star$:

$$\int_\Omega \left(\sigma_{ij}^M \frac{\partial u_i^\star}{\partial x_j} - \rho g_i u_i^\star \right) dV - \int_\Gamma \bar{t}_i^M u_i^\star dS = 0 \tag{12}$$

$$\int_\Omega \left(m_j^M \frac{\partial p^\star}{\partial x_j} - \dot{M} p^\star \right) dV - \int_\Gamma \bar{q}^M p^\star d\Gamma = 0 \tag{13}$$

with σ_{ij}^M the Cauchy total stress at the macro level, ρ the density, g_i the gravitational acceleration, $\bar{t}$ the boundary traction, $\dot{M}$ the time derivative of the fluid mass per unit volume, m_i^M the fluid mass flux and $\bar{q} = m_i n_i$ the fluid over a boundary with outward normal vector n_i. In the following, the influence of gravitational acceleration will not be considered; the development including gravitational effects follows the same approach including mass density ρ in the response variables.

The field Equations (12-13) are solved by finite element discretization using a Newton-Raphson iterative scheme. In this iteration scheme a linearization of the field equations is needed to give an estimate of the next test solution. Elaborating on the linearization of these field equations and spatial discretization for solving the problem is beyond the scope of this paper, details can be found in Frey (2010). We only mention here that, regardless the framework that is used, increments $\delta\sigma_{ij}^M$, $\delta\dot{M}$ and δm_i^M are needed for obtaining equilibrium. Linearization of the constitutive equations gives these increments as:

$$\delta\sigma_{ij}^M = C_{ijkl} \frac{\partial \delta u_k}{\partial x_l} + A_{ij} \delta p + B_{ijl} \frac{\partial \delta p}{\partial x_l} \tag{14}$$

$$\delta\dot{M} = D_{kl} \frac{\partial \delta u_k}{\partial x_l} + E \delta p + G_l \frac{\partial \delta p}{\partial x_l} \tag{15}$$

$$\delta m_i^M = I_{ikl} \frac{\partial \delta u_k}{\partial x_l} + J_i \delta p + L_{il} \frac{\partial \delta p}{\partial x_l} \tag{16}$$

The terms C_{ijkl}, A_{ij}, B_{ijl}, H_{kl}, E, G_l, I_{ikl}, J_i and L_{il} are the tangent stiffness matrices. Since constitutive equations are not defined on the macro scale, these tangents need to be derived from the micro scale in a consistent way to the homogenization of σ_{ij}, $\dot{M}$ and m_i. A straightforward but computationally expensive way to derive the tangent stiffness matrices, is to solve the micro problem eight times; once for the boundary value problem and seven times with a perturbation of each of the boundary condition variables. In this way a finite difference approximation of the tangent stiffness matrices is found. In the following, a computational homogenization method is proposed as an alternative to the numerical perturbation approach. Using this method, the problem at the micro level only needs to be solved once, after which the tangent stiffness matrices can be derived from the information of the micro level that is available when the micro problem has reached equilibrium. Homogenization by numerical perturbation will be used to validate the results that are to be obtained by the proposed method.

5 FE^2 COMPUTATION

To demonstrate the possibilities of FE^2 computations, a purely mechanical biaxial compression test is modelled. Boundary conditions are given in figure 3, strain-controlled loading is applied

up to a vertical compression of 2.0 %. A large strain finite element method with local second gradient model developed by Chambon et al. (2001, 2002) is used to solve the field equations at the macro level. The use of the local second gradient model allows the use of any classical model; in this case the micro scale computations. The introduction of the second gradient model leads to an additional term to the field equation to be solved;

$$\int_{\Omega} \left(\sigma_{ij} \frac{\partial u_i^*}{\partial x_j} + \Sigma_{ijk} \frac{\partial u_i^*}{\partial x_j \partial x_k} \right) d\Omega - \int_{\Omega} \left(\bar{t}_i u_i^* + \bar{T}_i \frac{\partial u_i^*}{\partial x_k} n_k \right) d\Gamma \tag{17}$$

with Σ_{ijk} the double stress tensor, $\bar{T}_i$ the external double traction and n_k the normal to the boundary. To avoid difficulties in the displacement field functions, constraints on the the second gradient displacement field are enforced by a field of Lagrange multipliers. The variational relation between stress σ_{ij}^M and strain $\partial u_k / \partial x_l$ comes from the consistent tangent stiffness matrix C_{ijkl} in Equation 8. Computational homogenization (Kouznetsova et al. 2001) is used to derive the consistent tangent stiffness from the global system of equations at the micro level. The second gradient part has a similar type of relation between double stress and double strain involving a sixth-order tensor (or 8×8 matrix). A general isotropic linear relation containing six individual parameters is derived by Mindlin (1964) of which a specific case depending on a single parameter D (Matsushima et al. 2002) is used here. The parameter D implicitly governs the internal length.

Spatial discretization of field Equation (17) over the domain of the specimen is done by means of 4800 nine-node quadrilateral elements with four integration points (Matsushima et al. 2002). This means that 19,200 REV boundary value problems are solved by means of a finite element computation at the micro level during each iteration of each loading step at the macro level.

A 1×1 mm REV with a micro structure of four solids separated by cohesive interfaces (Figure 3b) is used. Young's modulus of the solids is 1 GPa with Poisson's ratio of 0.25. The cohesion of the interfaces has an initial stiffness of 2 GPa/m with a maximum cohesive traction of 5 MPa. The critical interface openings δ_n and δ_t (Figure 1) are 0.125 mm. The second gradient stiffness on the macro scale is $D = 20$ kN.

Figure 3a shows the result of the biaxial computation. The strain localization in a shear band during the softening part of the global response (Figure 3c) at the macro level can be traced back to the damage and decohesion of the interfaces at the micro level as shown in Figure 3b

Computation time for the above given loading path in 120 loading steps containing a total of 480 iterations is approximately 14h (CPU-time). 94% of this time is used to solve the REV-boundary value problem at the micro level. This means that for this mechanical case, the FE^2 model is approximately 16 times slower than a classical finite element problem with the same mesh for the macro scale. A more complex micro structure with a finer mesh however, will quickly lead to less efficiency.

6 COMPUTATIONAL HOMOGENIZATION OF THE TANGENT STIFFNESS MATRICES

The objective is to extend the FE^2 approach described above for the modelling of HM-coupled problems using a finite element method proposed by Collin et al. (2005). The second gradient part of this method is similar to the mechanical example above, meaning that the hydromechanical coupling only concerns the classical part of the macro model. In addition, the second gradient

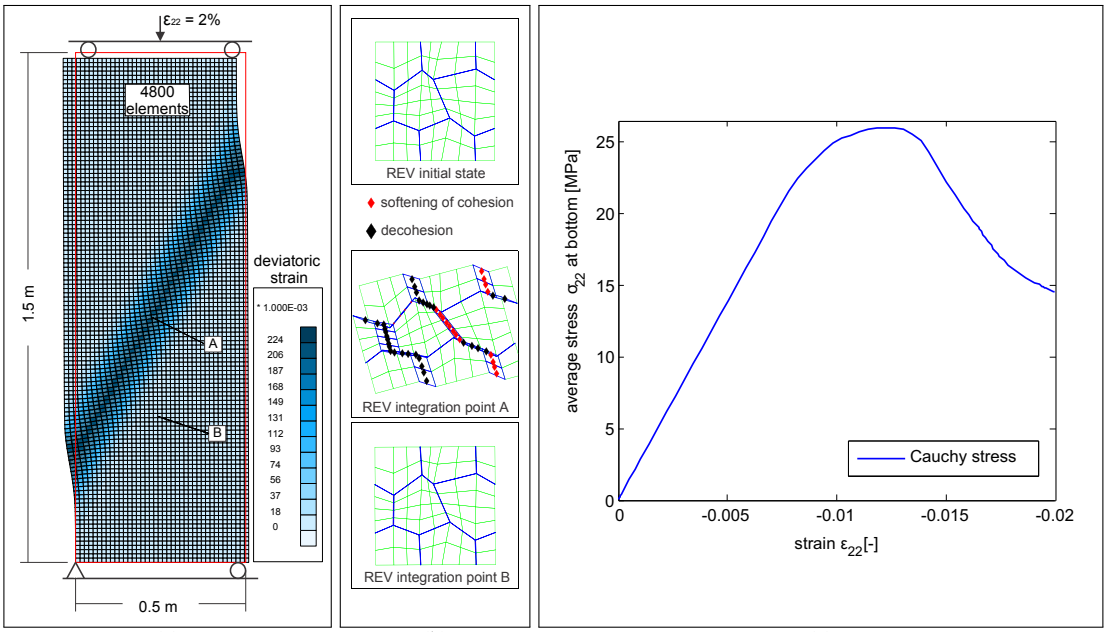

(a) (b) (c)

Fig. 3. (a) Deformed mesh with color scale for deviatoric (Von-Mises equivalent) strain at 2% vertical compression. In red the initial specimen boundaries. (b) The initial REV, the deformed REV in an integration point in the shear band and a deformed REV outside the shearband. (c) The global stress response at the bottom of the specimen.

part of the model is local. This allows the use of the hydromechanical model used in this paper. Next to the tangent stiffness C_{ijkl} the hydromechanical coupling asks for the other tangent stiffness terms in Equations (14-16). The following part of this paper will focus on the computational homogenization for deriving these HM-coupled tangent terms.

The HM-coupled tangent terms for the macro scale need to be computed based on the balanced equations of the micro level. Because the iterative approach is used on the micro level between the hydraulic and mechanical systems, no fully coupled global system of equations is available at the end of the micro loading step. Only a mechanical system, linear in variation of displacement $\{\delta u\}$ and a fluid system linear in fluid pressure exponential terms $\{\lambda\}$ were used to solve the micro problem. For the purpose of homogenization, a new coupled system of equations is built after equilibrium is obtained at the end of the loading step at the micro level. The combination of the mechanical system of equations, the linearization and discretization of Equation (9) and (10) and the linearization of the expression for fluid normal and drag forces leads to;

$$\left[K\right]\left\{\delta U\right\} = \left\{\delta F\right\}, \qquad \left\{\delta U\right\} = \begin{Bmatrix}\delta u \\ \delta p\end{Bmatrix}, \left\{\delta F\right\} = \begin{Bmatrix}\delta f \\ \delta M \\ \delta m_i\end{Bmatrix} \tag{18}$$

with $\{\delta f\}$ the nodal residual forces.

6.1 ELIMINATION OF PRESSURE DEGREES OF FREEDOM

The variation of nodal pressure degrees of freedom $\{\delta p\}$ can be eliminated from Equation (18) using a matrix $[T_p]$. This matrix relates the variation of nodal pressure to the variation of nodal displacement $\{\delta u\}$, average pressure $\delta\bar{p}$ and pressure difference between opposite REV boundaries $\delta\Delta\bar{p}_i$. This matrix is derived from the fluid system of Equations (7) and the definition of average fluid pressure (11) by discretization and linearization with respect to the degrees of

freedom $\{u\}$ and $\{p\}$ and $\Delta\bar{p}_i$:

$$\left[\frac{\partial(\Phi\cdot\lambda)}{\partial u} \;\; \frac{\partial(\Phi\cdot\lambda)}{\partial p} \;\; \frac{\partial(\Phi\cdot\lambda)}{\partial \Delta\bar{p}}\right] \begin{Bmatrix} \delta u \\ \delta p \\ \delta\Delta\bar{p} \end{Bmatrix} = \{0\} \tag{19}$$

$$\left[\frac{\partial\bar{p}}{\partial u} \;\; \frac{\partial\bar{p}}{\partial p}\right] \begin{Bmatrix} \delta u \\ \delta p \end{Bmatrix} = \delta\bar{p} \tag{20}$$

The system of Equations (19) is still singular, but combining Equation (20) with one of the equations for mass conservation in Equation (19) gives the well-posed system

$$\left[\Lambda_u \;\; \Lambda_p \;\; \Lambda_{\Delta\bar{p}}\right] \begin{Bmatrix} \delta u \\ \delta p \\ \delta\Delta\bar{p} \end{Bmatrix} = \begin{Bmatrix} 0 \\ \vdots \\ \delta\bar{p} \\ \vdots \\ 0 \end{Bmatrix} \tag{21}$$

from which it is found that

$$\{\delta p\} = [T_p] \begin{Bmatrix} \delta u \\ \delta\bar{p} \\ \delta\Delta\bar{p} \end{Bmatrix}, \qquad [T_p] = [\Lambda_p]^{-1} \left[\Lambda_u \;\; \Lambda_I \;\; \Lambda_{\Delta\bar{p}}\right] \tag{22}$$

$\{\Lambda_I\}$ is a column vector with value 1 on the position at which the average pressure was added to the fluid system of equations and a zero at all other positions. When $[T_p]$ is used for eliminating δp from δU in Equation (18), this is reduced to

$$\left[H\right] \begin{Bmatrix} \delta u \\ \delta\bar{p} \\ \delta\Delta\bar{p} \end{Bmatrix} = \begin{Bmatrix} \delta f \\ \delta M \\ \delta m_i \end{Bmatrix}, \qquad \left[H\right] = \left[K\right]\left[T_P\right] \tag{23}$$

Note that the condensation of the fluid terms is now replaced by the elimination by matrix $[T_p]$. Matrix $[H]$ can be condensed on the prescribed corner nodes (1), (2) and (4) and pressure terms $\delta\bar{p}$ and $\delta\Delta\bar{p}_i$ using the approach described by Kouznetsova et al. (2001). The condensation on the corner nodes implies first the elimination of the dependent degrees of freedom using the periodic boundary conditions. This results in the reduced system $[K^\star]$ that can be partitioned in prescribed $(^{\mathrm{p}})$ and free $(^{\mathrm{f}})$ degrees of freedom:

$$\begin{bmatrix} K^{\star\mathrm{pp}} & K^{\star\mathrm{pf}} \\ K^{\star\mathrm{fp}} & K^{\star\mathrm{ff}} \end{bmatrix} \begin{Bmatrix} \delta U^{\mathrm{p}} \\ \delta u^{\mathrm{f}} \end{Bmatrix} = \begin{Bmatrix} \delta F^{\star\mathrm{p}} \\ 0 \end{Bmatrix}. \tag{24}$$

Here $\delta\bar{p}$ and $\{\delta\Delta\bar{p}\}$ and corner node displacement $\{\delta u^C\}$ are now part of $\{\delta U^{\mathrm{p}}\}$, giving 9 prescribed variables. The same goes for δM, $\{\delta m\}$ and $\{\delta f^{\star C}\}$ with respect to $\{\delta F^{\star\mathrm{p}}\}$. This system can now be condensed on the controlling degrees of freedom (displacement of the three corner nodes and the average pressure and pressure gradient) as

$$[S]\left\{\delta U^{\mathrm{p}}\right\} = \left\{\delta F^{\star\mathrm{p}}\right\} \qquad \text{with:} [S] = [K^{\star\mathrm{pp}}] - [K^{\star\mathrm{pf}}][K^{\star\mathrm{ff}}]^{-1}[K^{\star\mathrm{fp}}] \tag{25}$$

Notice that $\{\delta f^{\star C}\}$, part of $\{\delta F^{\star\mathrm{p}}\}$, is the column vector of condensed forces on the corner nodes, the same forces as f^{ext} in Equation (8). Furthermore, the variation of the corner node displacements $\{\delta u^C\}$ is fully prescribed by the variation of strain enforced on the REV. The next step is to determine the variation of internal drag forces that form the internal forces f_i^{int} in Equation (8).

6.2 HOMOGENIZATION OF FLUID DRAG FORCES INFLUENCE

The fluid drag forces $\boldsymbol{f}_D$ due to the fluid flow acting on the solid boundaries along the channel interfaces are a function of the interface opening and the pressure gradient in the channel:

$$\boldsymbol{f}_D = \boldsymbol{f}_D(\{u\}, \{p\}) \tag{26}$$

Linearization of this expression gives the variation of the fluid drag forces and in discretized form this can be written as

$$\begin{bmatrix} K_D^M & K_D^H \end{bmatrix} \begin{Bmatrix} \delta u \\ \delta p \end{Bmatrix} = \{\delta f_D\} \tag{27}$$

Following the same procedure as described above, substitution of the pressure terms using $[T_p]$ (Equation (22)) and eliminating the dependent displacements from $\{\delta u\}$ gives

$$\begin{bmatrix} K_D^{\star \mathrm{p}} & K_D^{\star \mathrm{f}} \end{bmatrix} \begin{Bmatrix} \delta U^{\mathrm{p}} \\ \delta u^{\mathrm{f}} \end{Bmatrix} = \{\delta f_D\} \tag{28}$$

with $\{\delta U^{\mathrm{p}}\}$ the variation of the 9 prescribed terms $\{u^C\}$, $\bar{p}$ and $\Delta\bar{p}_i$. Again, using relation $\{\delta u^{\mathrm{f}}\} = [K^{\star \mathrm{ff}}]^{-1}[K^{\star \mathrm{fp}}]\{\delta U^{\mathrm{p}}\}$ derived from Equation (24), the variations of unknown displacement can be eliminated to get

$$[S_D]\{\delta U^{\mathrm{p}}\} = \{\delta f_D\} \tag{29}$$

6.3 DERIVING THE TANGENT STIFFNESS MATRICES

From the macro level, the boundary conditions for the REV are enforced by

$$\delta u_k^{(c)} = \left(\frac{\partial \delta u_k}{\partial x_l}\right)^M x_l^{(c)} \tag{30}$$

$$\delta \Delta p_k = \left(\frac{\partial \delta p}{\partial x_k}\right)^M \delta_{kl}(x_l^{(+)} - x_l^{(-)}) \tag{31}$$

$$\tag{32}$$

where superscript M is added to stress that these are the boundary conditions prescribed by the macro level. With this in mind, Equation (25) and can be rewritten as:

$$\sum_{c=1,2,4} S^{C}_{jk}{}^{(b)(c)} \delta u_k^{(c)} + S^{A}_{j}{}^{(b)} \delta \bar{p} + S^{B}_{jk}{}^{(b)} \delta \Delta \bar{p}_k = \delta f_j^{\star (b)} \tag{33a}$$

$$\sum_{c=1,2,4} S_k^{D(c)} \delta u_k^{(c)} + S^E \delta \bar{p} + S_k^G \delta \Delta \bar{p}_k = \delta M \tag{33b}$$

$$\sum_{c=1,2,4} S^{I}_{ik}{}^{(c)} \delta u_k^{(c)} + S_i^J \delta \bar{p} + S_{ik}^L \delta \Delta \bar{p}_k = \delta m_i \tag{33c}$$

The superscripts ^{A}-^{L} correspond to the tangent terms in Equation 14-14. In the same way, Equation (29) becomes

$$\sum_{c=1,2,4} S_{Djk}^{C(a)(c)} \delta u_k^{(c)} + S_{Dj}^{A(a)} \delta \bar{p} + S_{Djk}^{B(a)} \delta \Delta \bar{p}_k = \delta f_{D_j}^{(a)} \tag{34}$$

where (c) and (a) are used for the prescribed corner node numbering and (b) is used for all nodes on the interfaces that are involved in the drag forces (boundary Γ^{int}). The forces $f_{D_j}^{(b)}$ and

$f_j^{\star(a)}$ represent the internal forces f_j^{int} and external forces f_j^{ext} from Equation (8). For the time derivative of fluid mass $\dot{M}$, a finite difference approximation is made, from which follows that

$$\dot{M}^{t+\Delta t} = \frac{M^{t+\Delta t} - M^t}{\Delta t} \qquad\qquad \delta\dot{M}^{t+\Delta t} = \frac{\delta M^{t+\Delta t}}{\Delta t}. \tag{35}$$

Using Equations (30-35) for substitution, the hydromechanically coupled consistent tangent stiffness matrix are found:

$$C_{ijkl} = \frac{1}{V^\Omega} \sum_{c=1,2,4} \left(\sum_{b=1,2,4} x_i^{(b)} S^{C\,(b)(c)}_{jk} x_l^{(c)} + \sum_{a\in\Gamma^{int}} x_i^{(a)} S^{C\,(a)(c)}_{Djk} x_l^{(c)} \right) \tag{36}$$

$$A_{ij} = \frac{1}{V^\Omega} \sum_{b=1,2,4} x_i^{(b)} S_j^{A(b)} + \sum_{a\in\Gamma^{int}} x_i^{(a)} S_{Dj}^{A(a)} \tag{37}$$

$$B_{ijl} = \frac{1}{V^\Omega} \left(\sum_{b=1,2,4} x_i^{(b)} S_{jl}^{B(b)} + \sum_{a\in\Gamma_I} x_i^{(a)} S_{Djl}^{B(a)} \right) \left(x_l^{(+)} - x_l^{(-)} \right) \tag{38}$$

$$\vdots \tag{39}$$

$$L_{il} = \frac{1}{V^\Omega} S_{il}^L \left(x_l^{(+)} - x_l^{(-)} \right) \tag{40}$$

7 DOUBLE SCALE EXPERIMENT WITH HYDROMECHANICAL COUPLING

A unit cell experiment is performed to test the tangent stiffness matrices that are derived by computational homogenization. The response of this (dimensionless) unit cell is homogeneous and directly provided by the homogenized result of a single REV. To control the boundary conditions a nonlinear system of equations is solved following a Newton-Raphson iteration scheme that uses the homogenized tangent matrices as the linearization of the problem. This gives an experiment to test the quality of the tangent stiffness matrices while avoiding additional complexity of the discretization at the macro scale. Because steady-state assumption is used on the micro level (see section 2), this unit cell experiment is consequently in steady-state. A dimensionless variable α will therefore be used to define loading rates. A square REV of 1.0 mm containing 16 irregularly shaped solids is used (see Figure 5). Young's modulus for the solids is 1.0 GPa with a Poisson's ratio $\nu = 0.25$. The initial elasticity modulus of the cohesive forces is 1.0 GPa/m with a maximum cohesion of $T_{max} = 5.0$ MPa. The opening for total decohesion is $\delta_{t,n} = 0.05$ mm. The fluid constitutive parameters are: $\rho_0 = 1.0 \times 10^3$ kg/m^3, $\mu = 1.0 \times 10^{-9}$ Pa.s and $k^w = 2.2$ GPa. The experiment is performed in two stages; first a confining stress of 2.0 MPa is applied together with an average fluid pressure of 1.0 MPa and a pressure gradient of 100 MPa/m, the latter resulting in a pressure difference of 0.1 MPa between opposite REV boundaries. This preloading stage gives an initial state of deformation with an initial fluid mass flux and an initial fluid mass per volume M^0. The second stage consists of a compression in vertical direction corresponding to a strain of $\varepsilon_{22}^M = (\partial u_2/\partial x_2)^M = 0.02\alpha$. At the same time fluid mass is added to the REV to maintain a fluid mass per unit volume $M(\alpha) = M^0 + 50\alpha$ kg/m^3 while the initial mass flux m_i over the REV boundaries and confining stress σ_{11} are kept constant. A variation of strains $\partial\Delta u_1/\partial x_i$, average fluid pressure Δp^M and pressure gradient $\Delta(\partial p/\partial x_i)^M$ are needed to obtain equilibrium. The nonlinear problem to find these variations is solved following a Newton-Raphson scheme that uses the tangent stiffness.

The stress and fluid pressure response are given in Figure 4. Since it is not the purpose of this

experiment to represent the behaviour of any realistic material, nor to model a realistic test, the actual results are not discussed in detail. It should be sufficient to notice that different zone can be distinguished; from linear-elastic loading in the beginning of the experiment to a zone in which complete decohesion of either the normal or the tangential component occurs (see Figure 5) , leading to a softening response at the macro level. The convergence of the problem is evaluated in these different stages of loading.

The experiment is performed twice, once using numerical perturbation for homogenization and

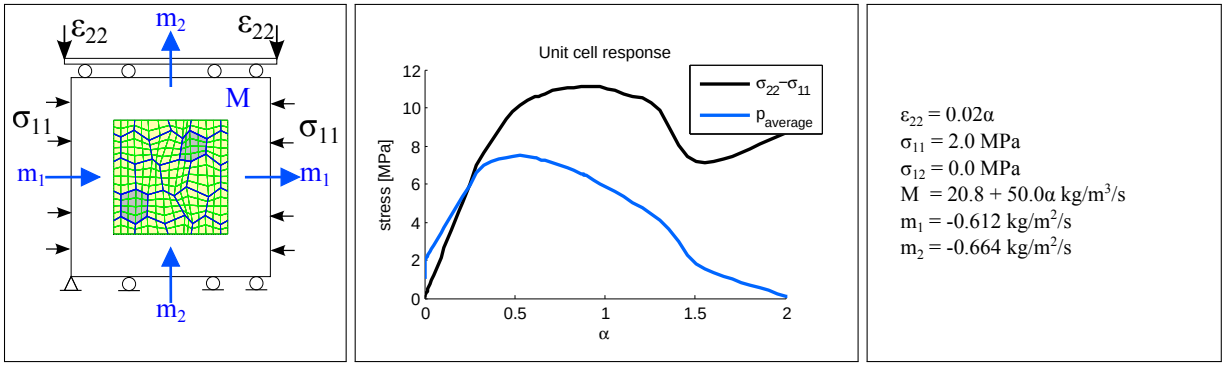

(a) (b) (c)

Fig. 4. Biaxial experiment results. (a) The the unit cell with the REV and enforced boundary conditions. (b) The stress response. The apparent hardening in the final phase can be related to enforced drainage $M = M(\alpha)$. (c) The enforced loading terms.

once using the computational approach presented in this paper. The same sequence of loading steps is used for both experiments and the convergence for characteristic stages are compared. The convergence norm to determine convergence at the macro scale in the second phase of the experiment is defined in Equation 41, where $\Delta\hat{a}^i$ is the error in the test solution $\hat{a}^i$ for variable a in iteration i defined as $\Delta\hat{a}^i = \hat{a}^i - a$. Convergence is reached when R^i is smaller than a certain convergence criterium ϵ.

$$R^i = \frac{1}{3}\left(\sqrt{\frac{\left(\Delta\hat{\sigma}_{11}^{M,i}\right)^2 + \left(\Delta\hat{\sigma}_{12}^{Mi}\right)^2}{\left(\sigma_{11}^{M}\right)^2 + \left(\sigma_{12}^{M}\right)^2}} + \sqrt{\frac{\left(\Delta\hat{M}^i\right)^2}{M^2}} + \sqrt{\frac{(\Delta\hat{m_1}^i)^2 + (\Delta\hat{m_2}^i)^2}{(m_1)^2 + (m_2)^2}} \right) \tag{41}$$

Plots of the convergence graphs are given in Figure 5. In all stages of the deformation, the convergence obtained by the two methods is of the same quality, which demonstrates that the computational homogenization gives tangent stiffness matrices with the same order of consistency as obtained by numerical perturbation.

8 CONCLUSIONS AND REMARKS

A computational homogenization approach for the FE^2 modelling of fully coupled hydromechanical behaviour is presented. The developments of this approach have been done for the specific micro mechanical model of solids with hydromechanical cohesive interfaces. The homogenization approach is applied in a double-scale biaxial experiment to test the consistency of the derived tangent stiffness matrices. This experiment has demonstrated that the obtained convergence is of the same order of effectiveness as the convergence obtained with homogenization by numerical perturbation. It can be concluded that the proposed approach of computational homogenization can be applied to derive the consistent tangent stiffness matrix that is needed for

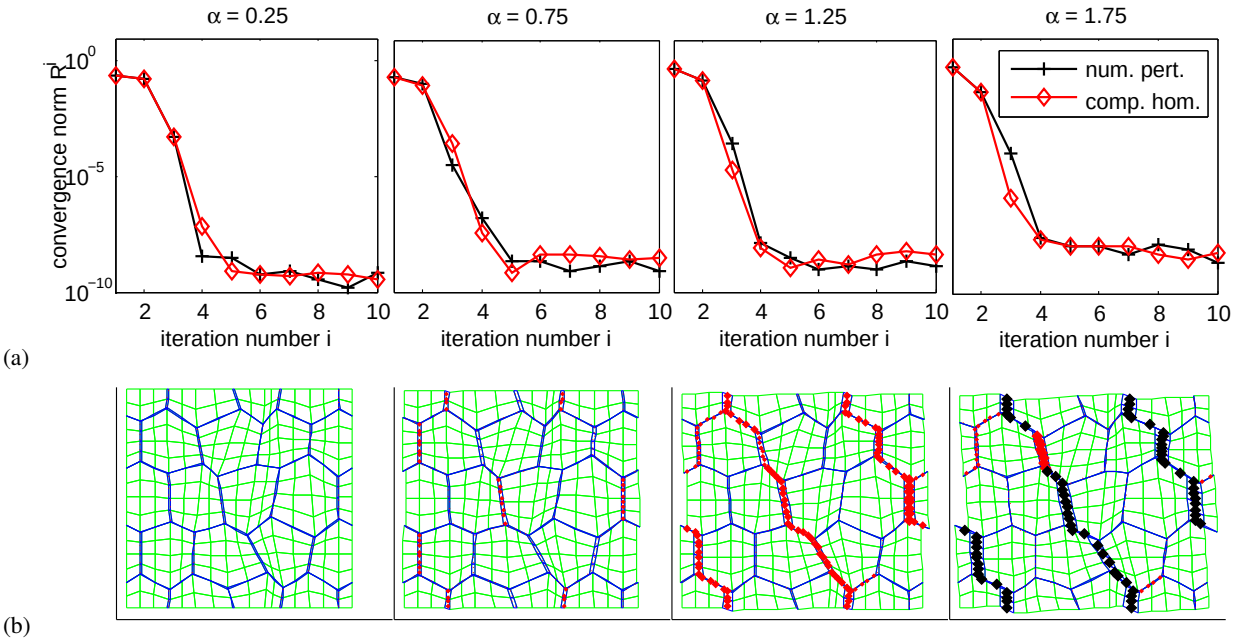

Fig. 5. Loading step results. (a) Curves of the convergence norms obtained by numerical perturbation (black) and computational homogenization (red). (b) Deformed meshes of the REV with softening (red diamond) and total decohesion (black diamond) occurring in the interfaces.

solving the finite element problem on the macro scale, hereby providing a FE^2 multi scale model for fully-coupled problems using computational homogenization.

The HM-coupled biaxial experiment presented here is in steady-state, since the micro scale model is in steady-state by definition of the fluid problem. The use of this approach in FE^2 methods is not necessarily restricted to steady-state problems and transient response on the macro level can be modelled under the condition that the REV is small enough with respect to the macro problem to justify the assumption of the 'quasi-steady-state' conditions at the micro scale.

A REV with a simple, theoretical micro structure is used here just to show the possibility of using the homogenization approach. The development of more appropriate constitutive laws on the micro level and a more realistic meshing of the micro structure will allow more realistic modelling of the behaviour of the claystone.

ACKNOWLEDGEMENT

The authors express their acknowledgement to the French national agency for radioactive waste management ANDRA for their financial support.

REFERENCES

Chambon, R., Caillerie, D., & Matsushima, T. (2001). Plastic continuum with microstructure, local second gradient theories for geomaterials: localization studies. *Int. J. of Solids and Structures 38*, 8503–8527.

Collin, F., Chambon, R., & Charlier, R. (2005). A finite element method for poro mechanical modelling of geotechnical problems using local second gradient models. *Int. J. Num. Meth. Engng. 65*, 1749–1772.

Frey, J. (2010). *Modélisation multi-échelle de l'endommagement hydroméchanique des roches argileuses*. Ph. D. thesis, Université de Grenoble.

Frey, J., Dascalu, C., & Chambon, R. (2012). A two-scale poromechanical model for cohesive rocks. *Acta Geotechnica 7*, 1–18.

Kouznetsova, V., Brekelmans, W., & Baaijens, F. (2001). An approach to micro-macro modeling of heterogeneous materials. *Computational Mechanics 27*, 37–48.

Kouznetsova, V., Geers, M., & Brekelmans, W. (2004). Multi-scale second-order computational homogenization of multi-phase materials: a nested finite element strategy. *Comp. Meth. Appl. Mech. Engng. 193*, 5525–5550.

Marinelli, F. (2013). *Comportement couplé des géomatériaux: deux approches de modélisation numérique*. Ph. D. thesis, Université de Grenoble.

Massart, T. & Selvadurai, A. (2012). Stress-induced permeability evolution in a quasi-brittle geomaterial. *Journal of Geophysical Research 117*, 1–15.

Matsushima, T., Chambon, R., & Caillerie, D. (2002). Large strain finite element analysis of a local second gradient model: application to localization. *Int. J. Num. Meth. Engng. 54*, 499–521.

Miehe, C. & Koch, A. (2002). Computational micro-to-macro transitions of discretized microstructures undergoing small strain. *Archive of Applied Mechanics 72*, 300–317.

Mindlin, R. (1964). Micro-structure in linear elasticity. *Archive for Rational Mechnaics and Analysis 16*, 51–78.

Ozdemir, I., Brekelmans, W., & Geers, M. (2008). FE^2 computational homogenization for the thermo-mechanical analysis of heterogeneous solids. *Comp. Meth. Appl. Mech. Engng. 198*, 602–613.

Su, F., Larsson, F., & Runesson, K. (2011). Computational homogenization of coupled consolidation problems in micro-heterogeneous porous media. *Int. J. Num. Meth. Engng. 88*, 1198–1218.

A STUDY ON THE COUPLED THERMO-HYDRO-MECHANICAL BEHAVIOR OF ROCK MASS USING BOUNDARY ELEMENT METHOD

Myung Kyu, Song
Department of Civil Engineering, Nottingham University Malaysia Campus, Malaysia

ABSTRACT: *A study on the boundary element method is performed for the analysis of coupled thermo-hydro-mechanical behavior of rock mass. Series of constitutive equations are derived from the equation of free energy of closed system and fully coupled governing equations are derived on the basis of the constitutive equations and the conditions of moment equilibrium, continuity and energy conservation. The governing equations are solved in the Laplace transformed domain and the fundamental solutions are inversed to the real time domain. A special care is given to the integration process of the fundamental solutions because of its singularity. Also, the reciprocal equations are derived, which are the basic ingredients of the boundary element. With the fundamental solutions and the reciprocal equations, boundary element codes are developed in this study. To verify the boundary element code, comparisons are performed between the analytic and numerical solutions. The results show a good agreement in the transient state.*

1 INTRODUCTION

Thermally, hydraulically and mechanically coupled problems are required to be solved for many engineering projects such as nuc1ear waste disposal, geothermal energy extraction and non-isothermal consolidation. Moreover, such engineering fields require practical techniques to simplify the complex interaction between thermal, hydraulic and mechanical behavior. The first work on the coupled behavior of soil and water was done by Terzaghi. This was further extended to poroelasticity for multi-dimensional consolidation by Biot. Moreover, it was extended to thermoporoelasticity, which is the basis of the study for thermo-hydro-mechanical behavior of mass, by taking into account non-isothermal conditions (McTigue, 1986). For example, widely accepted disposal method of nuclear waste is to excavate deep underground space and put waste at deep underground to isolate it from the biosphere; For a long time after disposal, nuclear waste may generate heat and alter the hydro-geological conditions of the ground, while whose behaviour might not be correctly understood and anticipated.

The purpose of this study is to develop a numerical method for the evaluation of the behavior of fully saturated and heated rock mass using boundary element technique. The scope of this study is establishing the coupled governing equations, deriving fundamental solution of these equations, deriving reciprocal equations and building boundary element codes. The constitutive equations for the coupled behavior of rock mass are carefully investigated and the governing equations derived using the constitutive equations. Finally, verification is carried out with analytical solution and result of similar projects.

2 GOVERNING EQUATIONS

In this section, the governing equations for thermoporoelasticity are derived from the concept of free energy of closed system. Thermal, hydraulic and mechanical constitutive equations are then derived by linearization of free energy with respect to temperature, fluid pressure and stress of solid mass. Also, energy conservation law, Fourier's law, continuity equation, Darcy's law, modified Hooke's law and Navier's equation are used.

2.1 Constitutive equations

The free energy of close system(Φ) can be expressed as below.

$$\mathrm{d}\Phi = -\varepsilon_{ij}\mathrm{d}\sigma_{ij} - \Delta\nu\mathrm{d}P - S\mathrm{d}T \tag{1}$$

where σ_{ij} is stress, ε_{ij} is strain, P is fluid pressure, ν is fluid volume, T is temperature and S is entropy. Moreover, free energy has following characteristics.

$$\varepsilon_{ij} = -\left(\frac{\partial\Phi}{\partial\sigma_{ij}}\right)_{T,P},\ \Delta\nu = -\left(\frac{\partial\Phi}{\partial P}\right)_{\sigma_{ij},T},\ \Delta S = -\left(\frac{\partial\Phi}{\partial T}\right)_{\sigma_{ij},P} \tag{2}$$

Equation (2) means that stress-strain relation, fluid pressure-fluid volume relation, entropy-temperature relation behave linearly (e.g. elastically for mechanics). With first order Taylor's series expansion one can get the following equation.

$$\varepsilon_{ij} = L_{ijkl}\sigma_{kl} - M_{ij}P - N_{ij}\theta,\ \Delta\nu = -M_{kl}\sigma_{kl} + DP + \eta\theta,\ \Delta S = -N_{kl}\sigma_{kl} + \eta P + \omega\theta \tag{3}$$

where L_{ijkl} is constitutive tensor related to stress and strain tensor, M_{ij} is coupling constitute tensor related to hydraulic pressure and strain tensor, N_{ij} is coupling constitutive tensor related to temperature variation and strain tensor, D is constitutive coefficient related to fluid pressure and fluid volume fraction, and ω is constitutive coefficient related to temperature and entropy.

2.2 Derivation of governing equations

The equilibrium equation of a body is written in differential form as

$$\sigma_{ij} + b_i = 0 \tag{4}$$

where b_i is body force per unit volume. The stress-strain relationship, which is modified with thermo-mechanical and hydro-mechanical constitutive equations, can be expressed as

$$\sigma_{ij} = (\lambda + 2\mu)\varepsilon_{kk}\delta_{ij} + 2\mu\varepsilon_{ij} + (3\lambda + 2\mu)\beta_T^s\delta_{ij}\theta + \alpha\delta_{ij}P \tag{5}$$

where θ is temperature variation, μ is shear modulus, λ is Lame's elastic constant.
Combining the equilibrium, strain-displacement and stress-strain leads to the Navier equation with a generalization to include the additional temperature effects:

$$(\lambda + \mu)u_{j,ij} + \mu u_{i,ij} + (3\lambda + 2\mu)\beta_T^s\delta_{ij}\theta_{,j} + \alpha\delta_{ij}P_{,j} + b_i = 0 \tag{6}$$

By combining the conservation of energy equation and Fourier's law, following coupled thermal diffusion equation is derived to evaluated temperature field while exchanging energy between mechanical and hydraulic behaviour of rock mass.

$$k\theta_{,jj} + \Psi_T = C_p\dot{\theta} + \eta T_0\dot{P} - (3\lambda + 2\mu)T_0\beta_T^s\dot{u}_{j,j} \tag{7}$$

Finally, by utilizing the continuity equation and Darcy's law following hydraulic diffusion equation is derived similarly with equation (7):

$$\kappa P_{,jj} + \Psi_P = \frac{\alpha}{KB}\dot{P} - 3KM\dot{u}_{j,j} + \eta\dot{\theta} \tag{8}$$

3 BOUNDARY ELEMENT METHOD

In this section, fundamental solutions are derived, which are used as weight functions, and reciprocal equations, which are the basic ingredients of BEM, are obtained from the governing equations. Finally, reciprocal equations are discretized numerically using shape functions.

3.1 Derivation of fundamental solution

As all other weighted residual methods, BEM also requires weight functions, Green function solution. To obtain Green function, matrix form of governing equations may be useful for further derivation in such a way of separating variables from the differential operators.

$$\mathbf{B}(\partial\mathbf{x}, s) = [B_{mn}(\partial\mathbf{x}, s)]_{4\times4} \tag{9}$$

where each terms are

$$\begin{aligned}
&B_{ij}(\partial\mathbf{x}, s) = (\lambda+\mu)\frac{\partial^2}{\partial x_i \partial x_j} + \delta_{ij}\mu\nabla^2,\ B_{33}(\partial\mathbf{x}, s) = k\nabla^2 - C_p s = k(\nabla^2 - \lambda_3^2),\\
&B_{44}(\partial\mathbf{x}, s) = \kappa\nabla^2 - \left(\frac{\alpha}{KB}\right)s = \kappa(\nabla^2 - \lambda_4^2),\ B_{i3}(\partial\mathbf{x}, s) = (3\lambda+2\mu)\beta_T^s \frac{\partial}{\partial x_i} = \alpha_T \frac{\partial}{\partial x_i},\\
&B_{i4}(\partial\mathbf{x}, s) = \alpha\frac{\partial}{\partial x_i},\ B_{3j}(\partial\mathbf{x}, s) = (3\lambda+2\mu)\beta_T^s T_0 s\frac{\partial}{\partial x_j} = \alpha_T T_0 s\frac{\partial}{\partial x_j},\ B_{4j}(\partial\mathbf{x}, s) = \alpha s\frac{\partial}{\partial x_j},\\
&B_{34}(\partial\mathbf{x}, s) = -\eta T_0 s,\ B_{43}(\partial\mathbf{x}, s) = -\eta s
\end{aligned} \tag{10}$$

Using the above differential operator, the governing equations can be expressed in matrix form.

$$\mathbf{B}(\partial\mathbf{x}, s)\widetilde{\mathbf{U}} + \widetilde{\mathbf{F}} = 0 \tag{11}$$

Moreover, using a cofactor, the above equation can be expressed for the single scalar solution, which is subject to delta function.

$$\mathbf{B}(\partial\mathbf{x}, s)\mathbf{B}^*(\partial\mathbf{x}, s)\varphi + \frac{1}{s}\mathbf{I}\delta(\mathbf{x}) = 0 \tag{12}$$

The scalar solution can be obtained through several mathematical operations as follows.

$$\varphi = \frac{1}{2\pi(\lambda+2\mu)\mu k\kappa s}\left[\frac{1}{\lambda_1^2 - \lambda_2^2}\left(\frac{K_0(\lambda_1 r)}{\lambda_1^4} - \frac{K_0(\lambda_2 r)}{\lambda_2^4}\right) - \frac{r^2\ln r}{4\lambda_1^2\lambda_2^2} - \frac{(\lambda_1^2+\lambda_2^2)\ln r}{\lambda_1^2\lambda_2^2}\right] \tag{13}$$

Thus Green function solutions can be obtained using the following equation,

$$\mathbf{G} = \mathbf{B}^*(\partial\mathbf{x}, s)\varphi \tag{14}$$

The term $\widetilde{G}_{i3}$, for example, is shown in equation (15).

$$2\pi(\lambda+\mu)k\kappa s\widetilde{G}_{i3} = 2\pi(\lambda+\mu)k\kappa s B_{3i}^{*}\cdot\varphi(r,s)$$

$$= \left[\alpha_T \frac{\partial}{\partial x_i}\nabla^2\{\nabla^2-\lambda_4^2\}\kappa + \eta\alpha s\nabla^2\frac{\partial}{\partial x_i}\right]\cdot\left[\frac{1}{\lambda_1^2-\lambda_2^2}\left(\frac{K_0(\lambda_1 r)}{\lambda_1^4}-\frac{K_0(\lambda_2 r)}{\lambda_2^4}\right)-\frac{(\lambda_1^2+\lambda_2^2)\ln r}{4\lambda_1^2\lambda_2^2}\right] \quad (15)$$

$$= \left[\frac{K_1(\lambda_1 r)\{\eta\alpha s+\alpha_T\kappa(\lambda_1^2-\lambda_2^2)\}}{(\lambda_1^2-\lambda_2^2)\lambda_1} - \frac{K_1(\lambda_2 r)\{\eta\alpha s+\alpha_T\kappa(\lambda_2^2-\lambda_2^2)\}}{(\lambda_1^2-\lambda_2^2)\lambda_{21}} - \frac{\{\eta\alpha s-\alpha_T\kappa\lambda_4^2\}}{(\lambda_1^2-\lambda_2^2)r}\right]$$

Fortunately, the Laplace domain solution can be inversed to a time domain solution without any numerical approximation, i.e. the inversion is carried out purely analytically. The characteristics of solutions are different, as they represent the behavior for 3 different sources: Instant mechanical, thermal and hydraulic excitations. For the example, shown in figure 1, the characteristic of G_{41} is related to mechanical-hydraulic coupling: decaying of pressure after mechanical excitation.

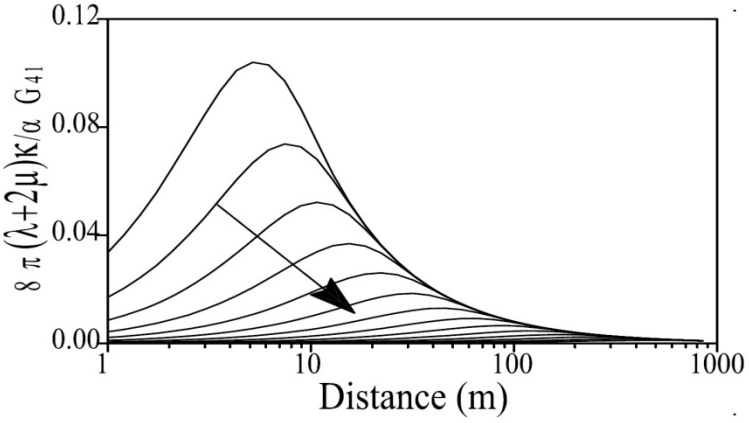

Fig. 1. Variation of mechanical-hydro coupling function

3.2 Reciprocal theorem

In the case of uncoupled single variable problem, integration formulation is derived from double integration by parts of the governing equation. However, for the coupled problem, integration formulation should be derived from the appropriate reciprocal theorem. Reciprocal theorem for themoporoelasticity starts with extended Hooke's law.

$$\dot{\sigma}_{ij} = \lambda\dot{\varepsilon}_{kk}\delta_{ij} + 2\mu\dot{\varepsilon}_{ij} + N_{ij}\dot{\theta} + M_{ij}\dot{P} \quad (16)$$

Using constitutive equations, e.g. Darcy's equation, reciprocal formulation for the initial value problem is derived in equation (17). Superscript (1) and (2) in equation (17) represent the two different states, while subscript 0 means that it is an initial value. Applying the appropriate source functions and fundamental solutions to the equation (17), one can derive the integral formulation for the primary variable of domain inside. However, for the boundary point, integration should be performed around semicirc1e to omit the singular point.

Another singularity problem arises when the second variable, such as internal stress, at internal points is calculated. For example, the calculation of internal stress requires the derivative of the singular integral of initial value. Song(2001) has proved that derivatives of fundamental solutions, which have order of 1/r singularity, can be integrated. The free term of hydraulic and thermal fundamental solution vanishing, the reciprocal formulation gets somewhat simplified by considering mechanical component only.

$$
\begin{aligned}
& s\int_S \dot{t}_i^{(1)} * u_i^{(2)} - t_i^{(2)} * \dot{u}_i^{(1)} \mathrm{d}S + \int_V \dot{b}_i^{(1)} * u_i^{(2)} - b_i^{(2)} * \dot{u}_i^{(1)} \mathrm{d}V \\
& + \frac{1}{T_0}\int_S \theta^{(1)} * q_T^{(2)} - \theta^{(2)} * q_T^{(1)} \mathrm{d}S + \int_V \theta^{(1)} * \Psi_T^{(2)} - \theta^{(2)} * \Psi_T^{(1)} \mathrm{d}V \\
& + \int_S P^{(1)} * q_P^{(2)} - P^{(2)} * q_P^{(1)} \mathrm{d}S + \int_V P^{(1)} * \Psi_P^{(2)} - P^{(2)} * \Psi_P^{(1)} \mathrm{d}V \\
& - \int_V \varepsilon_{ij}^{(1)} * (\sigma_{ij}^{0(2)} - M_{ij} P^{0(2)} - N_{ij}\theta^{0(2)}) - \varepsilon_{ij}^{(2)} * (\sigma_{ij}^{0(1)} - M_{ij} P^{0(1)} - N_{ij}\theta^{0(1)}) dV \\
& + \int_V P^{(1)} * (\frac{\alpha}{KB} P^{0(2)} - M_{ij}\varepsilon^{0(2)} + \eta\theta^{0(2)}) - P^{(2)} * (\frac{\alpha}{KB} P^{0(1)} - M_{ij}\varepsilon^{0(1)} + \eta\theta^{0(1)}) dV \\
& + \int_V \theta^{(1)} * (\frac{C_P}{T_0}\theta^{0(2)} - N_{ij}\varepsilon^{0(2)} + \eta P^{0(2)}) - \theta^{(2)} * (\frac{C_P}{T_0}\theta^{0(1)} - N_{ij}\varepsilon^{0(1)} + \eta P^{0(1)}) dV = 0
\end{aligned}
\tag{17}
$$

3.3 Discretization of reciprocal theorem

As most other numerical methods, Boundary Element Method (BEM) also requires discretization procedure. The discretization process enables numerical method applicable to bodies of arbitrary shape. That is, in contrast to analytic method, which always has an assumption of simple geometry, numerical method, like Finite Element Method (FEM), can analyze any arbitrary shaped model. One has to define the shape using mathematical function such as line or cubic curve so that can express the model boundary with given mathematical function. This is a shape function, with which some points represent the whole boundary shape.

However, there are some differences between FEM and BEM with respect to use of shape function. FEM assume that the shape function is used as an interpolation function (weight function) of primary variable. That is, distribution of values can be calculated from the values of discrete points. On the other hand, BEM use shape function only describe the boundary shape, and use Green function as weight function.

$$
\mathbf{x} = \mathbf{\Psi}^T \mathbf{x}^m, \mathbf{u} = \mathbf{\Phi}^T \mathbf{u}^m, \mathbf{t} = \mathbf{\Phi}^T \mathbf{t}^m \tag{18}
$$

where **x** is coordinate variable, **Ψ** is shape function, **u** is primary variable, **t** is secondary variable and **Φ** is weight function. The reciprocal equation is expressed with proper source function and fundamental solution as follows.

$$
\mathbf{cu} + \int_S \mathbf{F} * \mathbf{u} \mathrm{d}S = \int_S \mathbf{G} * \mathbf{t} \mathrm{d}S + \int_V \mathbf{B} \mathrm{d}V \tag{19}
$$

where **F** is secondary fundamental solution, **G** is primary fundamental solution, and **B** is source vector. Moreover, the above equation can be expressed in matrix form as follows.

$$
\mathbf{HU} = \mathbf{MT} + \mathbf{B} \tag{20}
$$

4 NUMERICAL RESULTS

A new-coupled boundary element code is developed for this study. To verify the program developed , comparison is performed with continuous heat source solution for the partially coupled governing equation (Berchenko, 1998).

4.1 Analytic solution

The analytic solutions, which are derived by Berchenco (1998) based on the use of singular solutions, are partially coupled, while fully coupled two-dimensional singular solution is derived and used In this study. He focused on the pore pressure and stress induced by heat generated by radioactive waste. So, thermal diffusion is assumed to be uncoupled, hydraulic diffusion affected only by temperature variation. However, Navier equation has both thermally and hydraulically coupled terms. The followings are the expressions for temperature, pore pressure and displacement respectively (Berchenco, 1998).

$$\theta = \frac{\Lambda}{4\pi k} E_1(\eta_3^2) \tag{21}$$

$$P = \frac{\Lambda}{4\pi k} \frac{\gamma}{1-\omega^2} [E_1(\eta_3^2) - E_1(\eta_4^2)] \tag{22}$$

$$u_i = \frac{\Lambda}{8\pi\mu} \frac{\gamma}{k} \frac{\eta x_i}{1-\omega^2} [\lambda U(\eta_3^2) - U(\eta_4^2)] \tag{23}$$

where

$$U(\eta^2) = \frac{1}{\eta^2}(1 - e^{-\eta^2}) + E_1(\eta^2) \tag{24}$$

4.2 Comparisons with numerical solution

For comparison, an example of 10m x 10m rectangular rock mass, which is fixed in two directions with plane strain condition as shown in Fig 2, has been used. Hydraulic pressure and temperature are maintained at 0 at the boundary. As an excitation, constant heat source is located at the center of the mass.

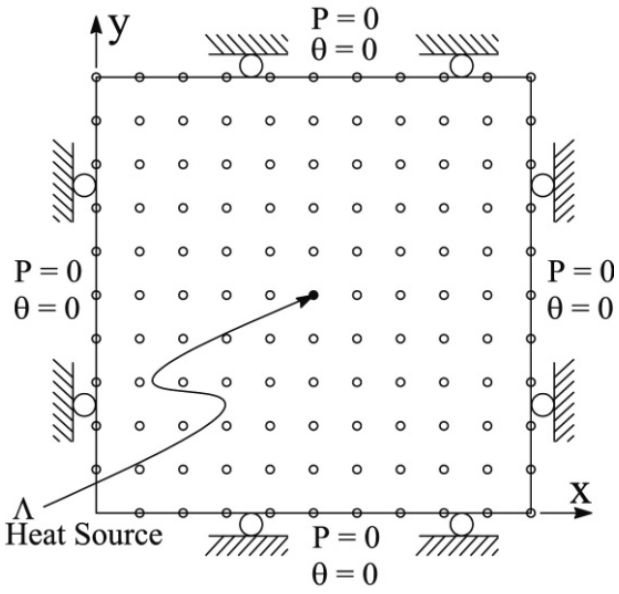

Fig. 2. Model for the comparison between the analytical and numerical solutions

Figure 3, 4 and 5 are the graphs for the comparison between the numerical and analytical solutions. In figure 3, within about 10 seconds of 100 seconds, numerical and analytical solutions are perfectly matched. However, due to the characteristics of constant heat source applied in the

interior of an infinite medium, the temperature of analytic solution increases continuously. On the other hand, that of numerical solution deviates from that of analytic solution as time goes. Moreover, as the point locates more distanced away from the center, the sooner does the deviation begins. Because the numerical solution is affected by boundary, whereas analytic solution isn't. Similar trend for the hydraulic pressure is seen in figure 4, but the divergence starts at earlier time than that of temperature. This is because the timing of deviation of solutions is related to the diffusion coefficient and generally diffusion of pressure is quicker than diffusion of temperature.

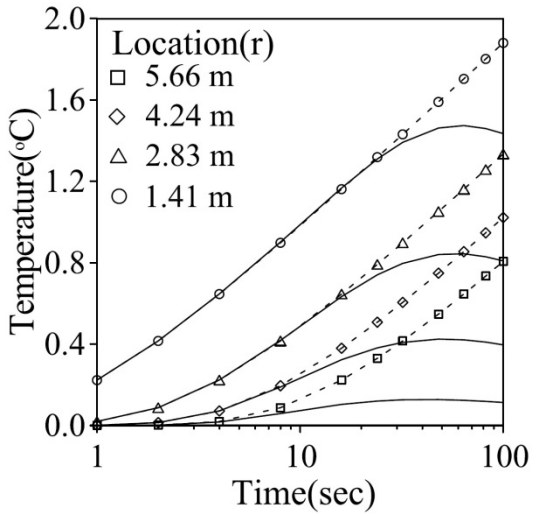

Fig. 3. Comparison between numerical and analytical results of temperature

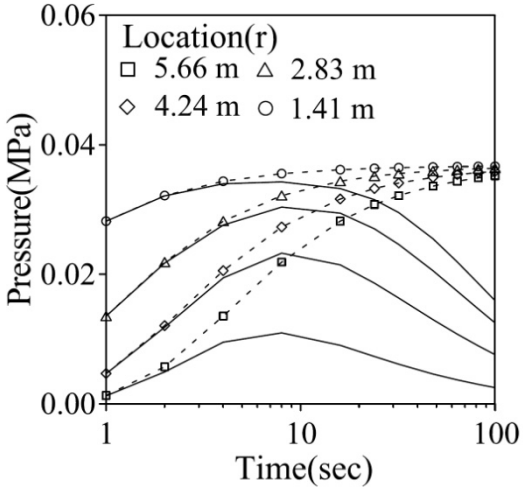

Fig. 4. Comparison between numerical and analytical results of pressure

However, the displacement shown in figure 5 shows a different trend compared to that in figure 3 and 4. This can be interpreted, as displacement is so quickly converged at a speed of seismic velocity of the medium, that the boundary effect is appeared from the beginning. Constant heat source being located at the center, the temperature rise propagates radially from the center.

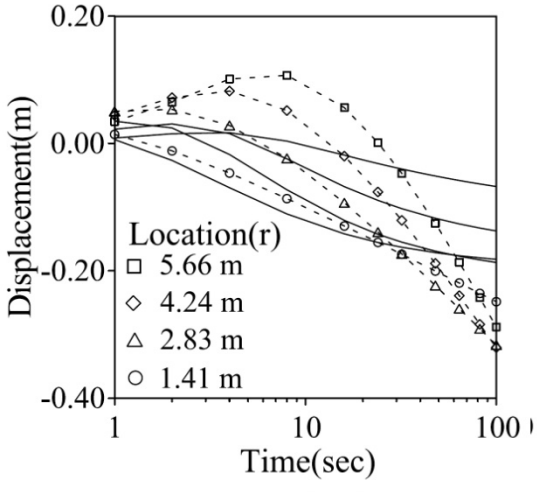

Fig. 5. Comparison between numerical and analytical results of displacement

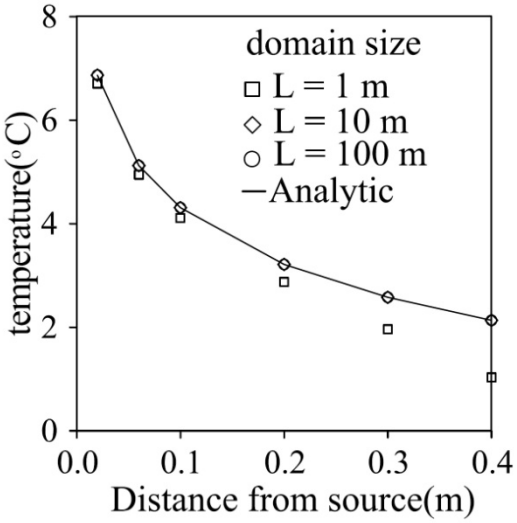

Fig. 6. Difference of temperature between analytical and numerical results for 3 different domain sizes

Due to coupling effect, pressure and displacement excited by the variation of temperature propagating toward the boundary. Thus it can be concluded that numerical and analytical solutions are identical in transient state, but due to difference of boundary condition, they diverge as a steady state is approached.

To identify the boundary effect, similar numerical tests are performed with 3 different domain sizes, and compared with analytical solution. The domain sizes are 1m x 1m, 10m x 10m, 100m x 100m. Figure 6 show that the analytical solution is well matched with numerical solution of L= 10m and L= 100m within 1 % error, but smallest domain size(L=1m) shows higher discrepancies between analytical and numerical solutions.

Figure 7 and 8 also show the similar trend that the analytical solution is well matched with numerical solution of L=10m and L=100m within 5% error, but smallest domain size (L=1m) shows significant discrepancy between analytical and numerical solution. So, if the boundary is far enough, numerical analysis will match analytical solution.

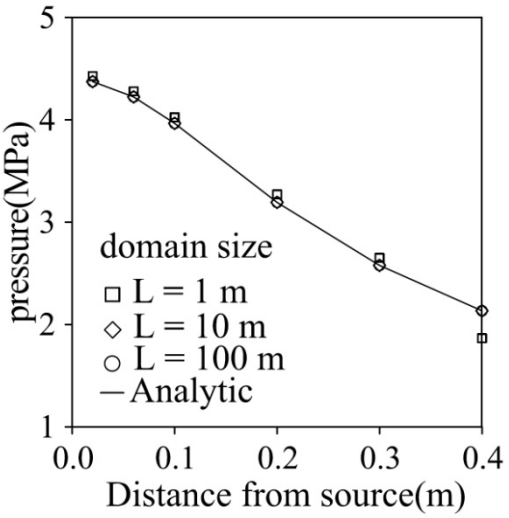

Fig. 7. Difference of pressure between analytical and numerical results for 3 different domain sizes

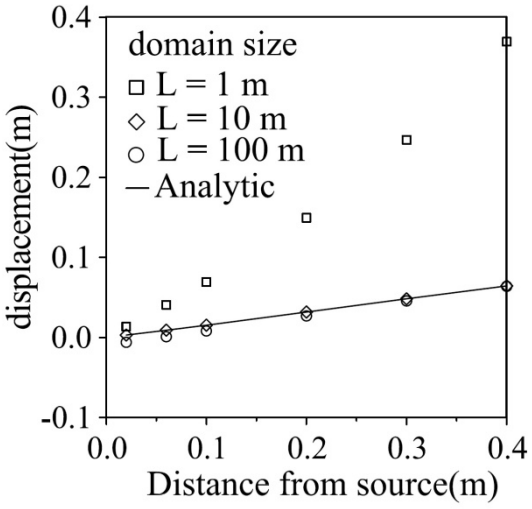

Fig. 8. Difference of displacement between analytical and numerical results for 3 different domain sizes

5 CONCLUSIONS

The boundary element method for the thermo-hydro-mechanical coupled behavior of porous media is investigated. A, numerical code has been developed and verified by comparing with analytic solution. The first step has been done is derivation of governing equations for the coupled thermal, hydraulic, and mechanical behavior of rock mass. Moreover, Green functions of these governing equations are derived as fundamental solutions for the boundary element method. Reciprocal theorem, another important ingredient for the BEM, is also derived. To verify developed code, analytical solutions, which are derived by Berchenko, are used. The results show a good agreement in the transient state.

REFERENCES

Banerjee, P. K., 1994, Boundary element methods in engineering, *McGraw-Hill Book Company*, London

Berchenko, I., 1998, Thermal loading of a saturated rock mass: Field experiment and modeling using thermoporoelastic singular solution, Ph.D. thesis, University of Minesota

Brebbia, C. A., J. Dominguez, 1989, Boundary elements – an introductory course, McGraw Hill Book Company, New York

Cleary, M. P., 1977, Fundamental solutions for a fluid-saturated porous solid, *Int. J. Solids Struct.*, 13:785-806

Dargush, G. F. and P. K. Banerjee, 1989, A time domain boundary element method for poroelasticity, *Int. J. Numer. Methods Eng.*, 28:2423-2449

Fung, Y. C., 1965, Foundations of solid mechanics, Prentice-Hall, Englewood Cliffs, New Jersey

Lewis, R. W. and B. S. Schrefler, 1987, The finite element method in the deformation and consolidation of porous media, *John Wiley & Sons*, Chichester

McTigue, D., 1986, Thermoelastic response of fluid-saturated porous rock, *J. Geophys, Res.*, 91:9533-9542

Moon, H. K., M. K. Song and S. I. Choi, 1997, Preliminary analysis of a conceptual radwaste repository, Proc. of Environmental and Safety Concerns in Underground Construction, 13-18

Song, M. K., 2001, A study on the thermo-hydro-mechanical behaviour of porous rock mass using boundary element method, PhD thesis, Hanyang University.

ACOUSTIC VELOCITY IN LAYERED ROCK MASSES WITH PERIODIC FRACTURES

A. Bacigalupo
Department of Civil, Chemical and Environmental Engineering, University of Genova, Genova Italy

L. Gambarotta
Department of Civil, Chemical and Environmental Engineering, University of Genova, Genova,Italy

ABSTRACT: *Fractures and layering in rock masses have a large impact on both the mechanical and hydraulic properties of the rock mass. When considering seismic elastic waves, fractures can also trap and guide waves and the behavior of such waves may prove useful for probing the geometrical and mechanical properties of the fractures. In the long-wavelength limit, when the size of the seismic wavelength is much larger than the layer and/or fracture spacing, the propagation velocity is obtained by the effective medium theory. However, when the wavelength becomes smaller, a dispersive behavior is obtained that may be significantly affected by the layer and fracture spacing.*
In the proposed paper a dynamic homogenization technique proposed by the Authors to analyze dispersive waves in periodic elastic materials (Bacigalupo & Gambarotta, 2012) is revised and extended to the analysis of dispersive waves in periodically layered fractured rock masses. The obtained results for some material meso-structures by means of the proposed approach are compared to those ones by the rigorous Floquet-Bloch theory. Finally, some examples representative of rock masses are presented and discussed.

1 INTRODUCTION

Fractures and layering in rock masses have a large impact on both the mechanical and hydraulic properties of the rock mass whose behavior depends not only on the properties of the intact rock but also on the joints behavior and distribution (i.e. their spacing, length, condition, orientation, continuity and the number of joint sets) and on the layer morphology (see for references Sayers & Kachanov, 1995, Monsen, 2001 and Guéguen & Sarout, 2011). When considering seismic elastic waves, fractures can also trap and guide waves and the behavior of such waves may prove useful for probing the geometrical and mechanical properties of the fractures (Boadu, 1997).

In the long-wavelength limit, when the size of the seismic wavelength is much larger than the layer and/or fracture spacing, the propagation velocity is obtained by the effective medium theory. However, when the wavelength becomes smaller, a dispersive behavior may be obtained that may be significantly affected by the layer and fracture spacing. Although it is well known that in fractured and porous reservoirs the effect of saturating fluid on wave propagation may be significant (see Lambert et al, 2006), because the fluid may cause significant frequency dependent attenuation and dispersion, these effects also occur in drained conditions in case of layered or fractured rocks (Nakagawa et al. 2002). If rock masses with stratification and periodic cracking are considered, the analysis of the propagation of dispersive waves can be performed through the classical approach of Floquet-

Bloch at the periodic cell level. However, in the more general case of wave propagation in bounded domains the analysis of the heterogeneous model would be very labor intensive so that multi-scale approaches based on non-local homogenization techniques are preferred (see Capdeville & Marigo, 2007, Capdeville et al, 2010, Bacigalupo & Gambarotta, 2012a).

In the present paper a dynamic homogenization procedure of layered rock systems is addressed, which is an enhancement of previous approaches already proposed by the Authors (Bacigalupo and Gambarotta, 2012a,b). In this contribution the overall second order elastic moduli and inertia terms are obtained as the result of a variational-asymptotic homogenization based on a proper down-scaling law, in which the fluctuation field at the micro-scale is assumed in a proper form that satisfies the continuity at the interface of adjacent cells.

To evaluate the accuracy of the dynamic model defined in the equivalent homogeneous continuum a periodic stratified rocky system is considered. The dispersion curves of shear and compressional waves along and transversely to the direction of the layers obtained by this model are compared with those by the rigorous approach by Floquet-Bloch. Therefore, in order to catch the influence of cracks on the dynamic response, the case of stratified rocks with periodic fissuring of rigid layers in agreement with Gross et al, 1995, and Bai & Pollard, 2000, is considered, assuming different fracture spacings. Also in this case, the dispersion functions obtained by the Floquet-Bloch approach are compared with those ones from the homogeneous model also to obtain the validity limits of the proposed model.

2 A MODEL OF PERIODIC LAYERED ROCK MASSES

Let us consider a layered rock mass having periodic meso-structure as shown in Figure 1.a and undergoing to small strains; its constituent elements are modelled as an elastic Cauchy continuum (non-linear constitutive equations may be considered if incremental approaches are adopted). In the periodic layers a periodic horizontal distribution of vertical cracks is considered. The material point is identified by vector $\mathbf{x}=\{x_1 \;\; x_2\}^T$ and the periodic materials is fully characterized by the periodic cell $\mathscr{A}=[0,\varepsilon]\times[0,\delta\varepsilon]$ with characteristic size ε shown in Figure 1.b, which is is spanned by the two independent orthogonal vectors $\mathbf{v}_1=d_1\mathbf{e}_1=\varepsilon\mathbf{e}_1$, $\mathbf{v}_2=d_2\mathbf{e}_2=\delta\varepsilon\mathbf{e}_2$. Accordingly, the elasticity tensor $\mathbb{C}^{m,\varepsilon}(\mathbf{x})$ and the mass density $\rho^{\varepsilon}(\mathbf{x})$ are $\mathscr{A}$-periodic, i.e. $\mathbb{C}^{m,\varepsilon}(\mathbf{x}+\mathbf{v}_i)=\mathbb{C}^{m,\varepsilon}(\mathbf{x})$, $\rho^{\varepsilon}(\mathbf{x}+\mathbf{v}_i)=\rho^{\varepsilon}(\mathbf{x})$, i=1,2, $\forall\mathbf{x}\in\mathscr{A}$. This suggest to consider a unit cell $Q=[0,1]\times[0,\delta]$ that reproduces the periodic microstructure by rescaling with the small parameter ε so that the two distinct scales are represented by the macroscopic (slow) variables $\mathbf{x}\in\mathscr{A}$ and the microscopic (fast) variable $\boldsymbol{\xi}=\mathbf{x}/\varepsilon\in Q$. The mapping of both the elasticity tensor and of the mass density may be defined on Q as follows: $\mathbb{C}^{m,\varepsilon}(\mathbf{x})=\mathbb{C}^{m}(\boldsymbol{\xi}=\mathbf{x}/\varepsilon)$, $\rho^{\varepsilon}(\mathbf{x})=\rho(\boldsymbol{\xi}=\mathbf{x}/\varepsilon)$, respectively.

The (micro)displacement $\mathbf{u}(\mathbf{x},t)$ at time t of a material point $\mathbf{x}$ is considered together with the corresponding (micro)strain tensor $\boldsymbol{\varepsilon}(\mathbf{x},t)=sym\nabla\mathbf{u}(\mathbf{x},t)$ and the (micro)stress tensor $\boldsymbol{\sigma}(\mathbf{x},t)=\mathbb{C}^{m}\left(\frac{\mathbf{x}}{\varepsilon}\right)\boldsymbol{\varepsilon}(\mathbf{x},t)$ which has to satisfy the local equation of motion $div\boldsymbol{\sigma}(\mathbf{x},t)=\rho\left(\frac{\mathbf{x}}{\varepsilon}\right)\ddot{\mathbf{u}}(\mathbf{x},t)-\mathbf{f}(\mathbf{x},t)$ where $\mathbf{f}(\mathbf{x},t)$ is the body force depending on the slow variable. The resulting set of partial differential equations is written in the form

$$div\left(\mathbb{C}^m\left(\frac{\mathbf{x}}{\varepsilon}\right)\nabla\mathbf{u}\left(\mathbf{x},t\right)\right)=\rho\left(\frac{\mathbf{x}}{\varepsilon}\right)\ddot{\mathbf{u}}\left(\mathbf{x},t\right)-\mathbf{f}\left(\mathbf{x},t\right)\ , \tag{1}$$

and then the displacement may be seen in the classical form $\mathbf{u}\left(\mathbf{x},\boldsymbol{\xi}=\frac{\mathbf{x}}{\varepsilon},t\right)$ as a function of both the slow and the fast variable (the elasticity tensor has the property $\mathbb{C}^m\mathbf{Z}=\mathbb{C}^m sym\mathbf{Z},\ \forall\mathbf{Z}$).

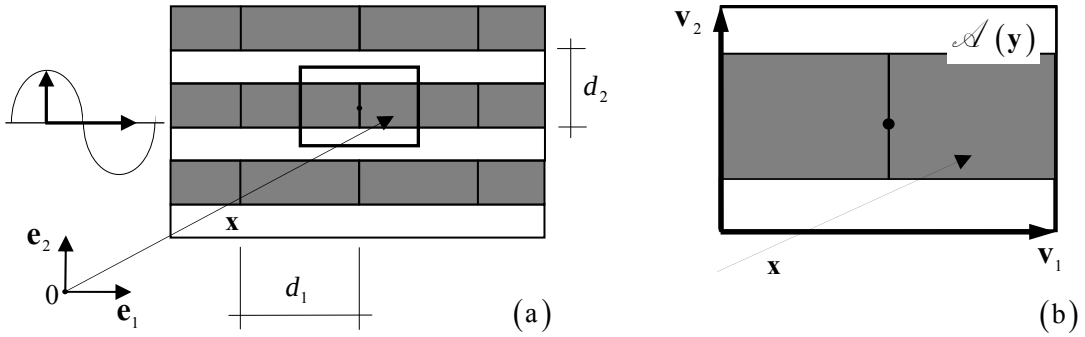

Fig. 1. (a) Fissured layered rock mass with periodic structure; (b) Unit cell and periodicity vectors.

3 SECOND ORDER DYNAMIC HOMOGENIZATION

The micro-displacement field is represented in the classical form $\mathbf{u}\left(\mathbf{x},t\right)=\mathbf{u}\left(\mathbf{x},\boldsymbol{\xi}=\frac{\mathbf{x}}{\varepsilon},t\right)$ considered in asymptotic homogenization, where $\mathbf{x}$ and $\boldsymbol{\xi}$ play the role of slow (macro) and fast (micro) coordinates. In the following the micro-displacement is considered to be $\mathscr{L}$-periodic, being $\mathscr{L}=\left[0,L\right]\times\left[0,\delta L\right]$ with L fixed such that L/ε is a large integer number. This condition is fulfilled in the case of $\mathscr{L}$-periodic body force for the static problem, and in the case of steady-state waves along the two orthotropy directions having wave-length L and δL.

According to Bacigalupo & Gambarotta (2012a), the displacement may be approximated by the truncated second order asymptotic series as follows

$$\mathbf{u}\left(\mathbf{x},\boldsymbol{\xi}=\frac{\mathbf{x}}{\varepsilon},t\right)\approx\mathbf{u}^{II}\left(\mathbf{x},\boldsymbol{\xi}=\frac{\mathbf{x}}{\varepsilon},t\right)=\mathbf{U}\left(\mathbf{x},t\right)+\varepsilon\mathbf{N}^1\left(\boldsymbol{\xi}\right):\mathbf{H}\left(\mathbf{x},t\right)+\varepsilon^2\mathbf{N}^2\left(\boldsymbol{\xi}\right)\vdots\boldsymbol{\kappa}\left(\mathbf{x},t\right), \tag{2}$$

that is the superposition of the macro-displacement $\mathbf{U}\left(\mathbf{x},t\right)$, assumed $\mathscr{L}$-periodic, and a complementary displacement field representing the micro-fluctuation due to the material heterogeneities. The latter one depends on the first and second gradient of the macro-displacement field $\mathbf{H}\left(\mathbf{x}\right)=\nabla\mathbf{U}\left(\mathbf{x}\right)$, $\boldsymbol{\kappa}\left(\mathbf{x}\right)=\nabla\otimes\nabla\mathbf{U}\left(\mathbf{x}\right)$, respectively, through the micro-fluctuation functions $\mathbf{N}^1\left(\boldsymbol{\xi}\right)$ and $\mathbf{N}^2\left(\boldsymbol{\xi}\right)$ (with components $N^1_{ikl}\left(\boldsymbol{\xi}\right)$ and $N^2_{iklp}\left(\boldsymbol{\xi}\right)$). These functions are the solution of the so called *cell problem*, depend on the fast coordinates and are Q-periodic with zero mean over Q, namely $\left\langle N^1_{ikl}\left(\boldsymbol{\xi}\right)\right\rangle=0$ and $\left\langle N^2_{iklp}\left(\boldsymbol{\xi}\right)\right\rangle=0$, $\left\langle\bullet\right\rangle$ being the averaging operator over Q.

Accordingly, the second order homogenized equations are derived via a combination of variational and asymptotic techniques to obtain a weak form of equation (1). By applying the

Hamilton's principle and by considering the $\mathscr{L}$ -periodicity of the micro-displacement and the $\mathscr{L}$-antiperiodicity of the traction on the boundary of $\mathscr{L}$, the variational problem corresponding to equation (1) is obtained by the Hamilton's principle

$$\min_{\mathbf{u}(\mathbf{x},t)} \int_{t_0}^{t_1} \mathcal{L}(\mathbf{u})\, dt = \min_{\mathbf{u}(\mathbf{x},t)} \int_{t_0}^{t_1} \left(\mathrm{T}(\mathbf{u}) - \Pi(\mathbf{u})\right) dt = \min_{\mathbf{u}(\mathbf{x},t)} \int_{t_0}^{t_1} \int_{\mathscr{L}} \left(\frac{1}{2}\rho \dot{u}_i \dot{u}_i - \frac{1}{2} \frac{\partial u_i}{\partial x_j} C^m_{ijhk} \frac{\partial u_h}{\partial x_k} + f_i u_i \right) d\mathbf{x} dt \,, \quad (3)$$

where $\mathcal{L}$ is the Lagrangian functional, T is the kinetic and Π the potential energy functional, respectively. By averaging the Lagrangian functional with respect to the parameter $\boldsymbol{\zeta} \in Q$, based on the argument that the precise "phase" of the microstructure with respect to the body force is generally unknown and a family of translated microstructures should therefore be considered, the second order homogenization problem may be now formulated by applying the Hamilton's principle with the averaged Lagrangian functional. If the displacement is restricted to the class of functions $\mathbf{u}^{II}$ having the form (2), the averaged functional depends on the macro-displacement $\mathbf{U}(\mathbf{x},t)$ and the minimization problem is written in the form

$$\min_{\mathbf{U}(\mathbf{x},t)} \int_{t_0}^{t_1} \bar{\mathcal{L}}\left(\mathbf{u}^{II}(\mathbf{U})\right) dt = \min_{\mathbf{U}(\mathbf{x},t)} \int_{t_0}^{t_1} \int_{\mathscr{L}} \left\langle \frac{1}{2}\rho \dot{u}_i^{II} \dot{u}_i^{II} - \frac{1}{2} \frac{\partial u_i^{II}}{\partial x_j} C^m_{ijhk} \frac{\partial \dot{u}_h^{II}}{\partial x_k} + f_i u_i^{II} \right\rangle d\mathbf{x} dt \,. \quad (4)$$

The Euler-Lagrangian equation, associated to the variational problem (4), is truncated at the third order in the static part and to the fifth order in the inertial part as assumed by Bacigalupo & Gambarotta (2012b). Accordingly, in the present approach the inertial terms are extended to those resulting from the micro-accelerations associated with the second-order strain $\boldsymbol{\kappa}(\mathbf{x},t)$. The resulting Euler-Lagrangian takes the form

$$\begin{aligned} \varepsilon^2 h_{ijkpqr} U_{i,jkqr} + \frac{\varepsilon}{2}\left(h_{ijpqr} - h_{pqijr}\right) U_{i,jqr} - h_{ijpq} U_{i,jq} = f_p(\mathbf{x},t) - \rho_M \ddot{U}_p + \varepsilon \rho_M I_{ipj} \ddot{U}_{i,j} + \\ + \varepsilon^2 \rho_M I_{iqpj} \ddot{U}_{i,qj} + \varepsilon^3 \rho_M I_{iqpjs} \ddot{U}_{i,qjs} - \varepsilon^4 \rho_M I_{iqjpsr} \ddot{U}_{i,qjsr} \,, \end{aligned} \quad (5)$$

where $h_{ijpq} = C_{ijpq}$, $h_{ijpqr} = \varepsilon^{-1} Y_{ijpqr}$, $h_{ijkpqr} = \varepsilon^{-2} S_{ijkpqr}$ and ρ_M, I_{ipj}, I_{iqpj}, I_{iqpjs}, I_{iqjpsr} are the effective elastic moduli and the effective inertia parameters of the second-order continuum, respectively. The first ones are obtained according to Bacigalupo (2013) in the form

$$C_{pqrs} = \left\langle C^m_{ijkl} B^H_{ijpq} B^H_{klrs} \right\rangle, \quad \frac{Y_{pqrst}}{\varepsilon} = \left\langle C^m_{ijkl} B^H_{ijpq} B^\kappa_{klrst} \right\rangle, \quad \frac{S_{pqhrst}}{\varepsilon^2} = \left\langle C^m_{ijkl} B^\kappa_{klrst} B^\kappa_{ijpqh} \right\rangle - \frac{\left\langle A^{H\_\kappa}_{pqhrst} \right\rangle}{12}, \quad (6)$$

where the localization tensors B^H_{ijpq}, B^κ_{ijpqr} and $A^{H\_\kappa}_{pqrjkh}$ are

$$B^{H}_{ijpq}\left(\xi=\frac{\mathbf{x}}{\varepsilon}\right)=\frac{1}{4}\left(\delta_{ip}\delta_{jq}+N^{1}_{ipq,j}+\delta_{jp}\delta_{iq}+N^{1}_{jpq,i}+\delta_{iq}\delta_{jp}+N^{1}_{iqp,j}+\delta_{jq}\delta_{ip}+N^{1}_{jqp,i}\right),$$

$$B^{\kappa}_{ijpqr}\left(\xi=\frac{\mathbf{x}}{\varepsilon}\right)=\frac{1}{4}\left(N^{1}_{ipq}\delta_{jr}+N^{1}_{ipr}\delta_{qj}+2N^{2}_{ipqr,j}+N^{1}_{jpq}\delta_{ir}+N^{1}_{jpr}\delta_{qi}+2N^{2}_{jpqr,i}\right),$$

$$\begin{aligned}A^{H\_\kappa}_{pqrjhk}\left(\xi=\frac{\mathbf{x}}{\varepsilon}\right)&=\left(C^{m}_{jkih}N^{2}_{ipqr}+C^{m}_{jkir}N^{2}_{ipqh}+C^{m}_{jkiq}N^{2}_{iprh}+C^{m}_{jhik}N^{2}_{ipqr}++C^{m}_{jhir}N^{2}_{ipqk}+C^{m}_{jhiq}N^{2}_{iprk}+\right.\\&+C^{m}_{pqir}N^{2}_{ijkh}+C^{m}_{pqih}N^{2}_{ijkr}+C^{m}_{pqik}N^{2}_{ijhr}+C^{m}_{priq}N^{2}_{ijkh}+C^{m}_{prih}N^{2}_{ijkq}+C^{m}_{prik}N^{2}_{ijhq}\left.\right)+\\&+\frac{1}{2}\left(C^{m}_{stir}N^{2}_{ijkh}N^{1}_{spq,t}+C^{m}_{srit}N^{2}_{sjkh}N^{1}_{ipq,t}++C^{m}_{shit}N^{2}_{sjkr}N^{1}_{ipq,t}+C^{m}_{stik}N^{2}_{ijhr}N^{1}_{spq,t}+C^{m}_{skit}N^{2}_{sjhr}N^{1}_{ipq,t}+\right.\\&+C^{m}_{stiq}N^{2}_{ijkh}N^{1}_{spr,t}+C^{m}_{sqit}N^{2}_{sjkh}N^{1}_{ipr,t}+C^{m}_{stih}N^{2}_{ijkq}N^{1}_{spr,t}+C^{m}_{shit}N^{2}_{sjkq}N^{1}_{ipr,t}+C^{m}_{stik}N^{2}_{ijhq}N^{1}_{spr,t}+\\&+C^{m}_{skit}N^{2}_{sjhq}N^{1}_{ipr,t}+C^{m}_{stih}N^{2}_{ipqr}N^{1}_{sjk,t}+C^{m}_{shit}N^{2}_{spqr}N^{1}_{ijk,t}+C^{m}_{stir}N^{2}_{ipqh}N^{1}_{sjk,t}+C^{m}_{srit}N^{2}_{spqh}N^{1}_{ijk,t}\\&+C^{m}_{stiq}N^{2}_{iprh}N^{1}_{sjk,t}+C^{m}_{sqit}N^{2}_{sprh}N^{1}_{ijk,t}+C^{m}_{stik}N^{2}_{ipqr}N^{1}_{sjh,t}+C^{m}_{skit}N^{2}_{spqr}N^{1}_{ijh,t}+C^{m}_{stir}N^{2}_{ipqk}N^{1}_{sjh,t}\\&\left.+C^{m}_{srit}N^{2}_{spqk}N^{1}_{ijh,t}+C^{m}_{stiq}N^{2}_{iprk}N^{1}_{sjh,t}+C^{m}_{sqit}N^{2}_{sprk}N^{1}_{ijh,t}+C^{m}_{stih}N^{2}_{ijkr}N^{1}_{spq,t}\right).\end{aligned}\tag{7}$$

Moreover, the effective inertia parameters in equation (5) have the form

$$\begin{aligned}&\rho_{M}=\langle\rho\rangle,\ I_{ipj}=\frac{\left\langle\rho\left(N^{1}_{ipj}-N^{1}_{pij}\right)\right\rangle}{\rho_{M}},\ I_{iqpj}=\frac{\left\langle\rho\left(\frac{1}{2}\left(N^{1}_{rpj}N^{1}_{riq}+N^{1}_{rij}N^{1}_{rpq}\right)-N^{2}_{ipqj}-N^{2}_{piqj}\right)\right\rangle}{\rho_{M}},\\&I_{iqpjs}=\frac{\left\langle\rho\left(N^{1}_{kip}N^{2}_{kqjs}-N^{1}_{kqp}N^{2}_{kijs}+2N^{1}_{kij}N^{2}_{kqps}-2N^{1}_{kqj}N^{2}_{kips}+N^{1}_{kis}N^{2}_{kqjp}-N^{1}_{kqs}N^{2}_{kijp}\right)\right\rangle}{4\rho_{M}},\\&I_{ijqpsr}=\left\langle\rho\left(N^{2}_{kijq}N^{2}_{kpsr}+N^{2}_{kpjq}N^{2}_{kisr}+N^{2}_{kisq}N^{2}_{kpjr}+N^{2}_{kpsq}N^{2}_{kijr}+N^{2}_{kijs}N^{2}_{kpqr}\right.\right.\\&\qquad\left.\left.+N^{2}_{kpjs}N^{2}_{kiqr}+N^{2}_{kijr}N^{2}_{kpsq}+N^{2}_{kirs}N^{2}_{kpjq}\right)\right\rangle\Big/8\rho_{M}\,.\end{aligned}\tag{8}$$

In case of centro-symmetric periodic cell one obtains $I_{ipj}=0$, $I_{iqpjs}=0$. If the density is homogeneous in the unit cell, the inertial terms take the form

$$\begin{aligned}&\rho_{M}=\rho,\quad I_{iqpj}=\frac{1}{2}\left\langle N^{1}_{rpj}N^{1}_{riq}+N^{1}_{rij}N^{1}_{rpq}\right\rangle,\\&I_{iqjpsr}=\frac{1}{8}\left\langle N^{2}_{kipq}N^{2}_{kjsr}+N^{2}_{kjpq}N^{2}_{kisr}+N^{2}_{kisq}N^{2}_{kjpr}+N^{2}_{kjsq}N^{2}_{kipr}+N^{2}_{kips}N^{2}_{kjqr}+\right.\\&\qquad\left.+N^{2}_{kjps}N^{2}_{kiqr}+N^{2}_{kipr}N^{2}_{kjsq}+N^{2}_{kirs}N^{2}_{kjpq}\right\rangle.\end{aligned}\tag{9}$$

If the third and fourth order inertial terms are neglected the equation of motion (5) takes the form of a second-order continuum (see Bacigalupo & Gambarotta, 2012a, Mindlin, 1965). Finally, if the material is homogeneous in the periodic cell, i.e. the microstructure disappears, the functions $N^{1}_{ikl}(\xi)$ and $N^{2}_{iklp}(\xi)$ are zero and both the elastic moduli and the inertial parameters defined by equations (6), (7), (8), (9) vanish and the equation of motion of the classical continuum is obtained.

Considering the rather common case of centro-symmetric periodic cell having orthotropic material phases (see for example Figure 1), the elastic wave propagation along the orthotropy

direction $\mathbf{e}_\beta$ ($\beta = 1,2$) is described by the non zero components of the macro-displacement vector $U_\alpha\left(x_\beta, t\right)$ ($\alpha = 1,2$) which are solution of the PDE

$$C_{\beta\alpha\beta\alpha}U_{\alpha,\beta\beta} - S_{\alpha\beta\beta\alpha\beta\beta}U_{\alpha,\beta\beta\beta\beta} = \rho_M \ddot{U}_\alpha - J_{\alpha\beta\alpha\beta}\ddot{U}_{\alpha,\beta\beta} + J_{\alpha\beta\beta\alpha\beta\beta}\ddot{U}_{\alpha,\beta\beta\beta\beta}, \tag{10}$$

indices α, β not summed. With $\hat{c}_\beta^\alpha = \sqrt{C_{\beta\alpha\beta\alpha}/\rho_M}$ denoting the velocity of the compressional $(\alpha = \beta)$ and shear $(\alpha \neq \beta)$ waves along direction $\mathbf{e}_\beta$ in the classical equivalent continuum ($S_{\alpha\beta\beta\alpha\beta\beta} = J_{\alpha\alpha\beta\beta} = 0$ in equation (10)), $\lambda_\beta^\alpha = \sqrt{S_{\alpha\beta\beta\alpha\beta\beta}/C_{\beta\alpha\beta\alpha}}$ the extensional $(\alpha = \beta)$ and shearing $(\alpha \neq \beta)$ characteristic lengths of the heterogeneous material, $J_{\alpha\beta\alpha\beta} = I_{\alpha\beta\alpha\beta}\rho_M\varepsilon^2$ the second-order inertia tensor ($I_{\alpha\alpha\beta\beta}$ being fourth-order tensor depending on the geometrical and mechanical properties of the cell) and $J_{\alpha\beta\beta\alpha\beta\beta} = I_{\alpha\beta\beta\alpha\beta\beta}\rho_M\varepsilon^4$ the fourth -order inertia tensor ($I_{\alpha\beta\beta\alpha\beta\beta}$ being sixth-order tensor depending on the geometrical and mechanical properties of the cell), the displacement equation of motion may be written in the form

$$\left(\lambda_\beta^\alpha \hat{c}_\beta^\alpha\right)^2 U_{\alpha,\beta\beta\beta\beta} - \hat{c}_\beta^{\alpha 2} U_{\alpha,\beta\beta} = \ddot{U}_\alpha - I_{\alpha\beta\alpha\beta}\varepsilon^2\ddot{U}_{\alpha,\beta\beta} + I_{\alpha\beta\beta\alpha\beta\beta}\varepsilon^4\ddot{U}_{\alpha,\beta\beta\beta\beta}. \tag{11}$$

To obtain the dispersion functions, let us seek solutions to equation (11) of the form $U_\alpha\left(x_\beta, t\right) = A\exp\left[i\left(kx_\beta - \omega t\right)\right]$, where $i^2 = -1$, k is the wave number and ω is the angular frequency. The wavelength and the phase velocity of the in-plane waves along direction $\mathbf{e}_\beta$ are $\lambda = 2\pi/k$ and $c_\beta^\alpha = \omega/k$, respectively. The dispersion function corresponding to both the longitudinal $(\alpha = \beta)$ and the transverse $(\alpha \neq \beta)$ oscillatory motion of the derived equivalent continuum take the following form

$$\omega = k\hat{c}_\beta^\alpha \sqrt{\frac{1 + \left(k\lambda_\beta^\alpha\right)^2}{1 + I_{\alpha\beta\alpha\beta}\left(k\varepsilon\right)^2 + I_{\alpha\beta\beta\alpha\beta\beta}\left(k\varepsilon\right)^4}} = k\hat{c}_\beta^\alpha \sqrt{\frac{1 + 4\pi^2\left(\lambda_\beta^\alpha/\lambda\right)^2}{1 + 4\pi^2 I_{\alpha\beta\alpha\beta}\left(\varepsilon/\lambda\right)^2 + 16\pi^4 I_{\alpha\beta\beta\alpha\beta\beta}\left(\varepsilon/\lambda\right)^4}}. \tag{12}$$

From equation (12) it results that for large wavelengths $(\lambda \to \infty)$ the angular frequency tends to the value related to the classical continuum, i.e $\omega \to k\hat{c}_\beta^\alpha$. If the third and fourth order inertial terms of are neglected in (5), the dispersion relation (12) takes the form in (Bacigalupo & Gambarotta, 2012a).

4 LAYERED ROCK MASS: THE INFLUENCE OF DISCONTINUITY PLANES

Let us consider a periodically layered fractured rock masses with equal layer thickness $\varepsilon/2 = 0.5$ m. The jointed rock mass is assumed in plane strain condition and the Young's moduli and Poisson ratios are assumed $E_1 = 56000$ MPa, $\nu_1 = 0.3$, $E_2 = 5600$ MPa, $\nu_2 = 0.3$, respectively. The mass density for both the components is $\rho_1 = \rho_2 = 2800$ kg/m^3. The periodic cell is considered having characteristic size $\varepsilon = 1$ m and is represented in Figure 2. In order to evaluate the influence of periodic joint in the stiffer layer of the rock mass on the characteristic lengths, on the overall inertial terms and on the phase velocities of

dispersive waves two different values of the fracture periodicity $\delta\varepsilon = 1$ m and $\delta\varepsilon = 2$ m are analyzed. The characteristic lengths $\lambda_\beta^\alpha = \sqrt{S_{\alpha\beta\alpha\beta}/C_{\beta\alpha\beta\alpha}}$ and the waves velocities $\hat{c}_\beta^\alpha = \sqrt{C_{\beta\alpha\beta\alpha}/\rho_M}$ in the first-order homogeneous continuum are shown in Table 1 and Table 2, respectively. The overall mass density is $\rho_M = 2800$ kg/m^3 and the non-vanishing components $I_{\alpha\beta\alpha\beta}$ the micro-inertia tensors needed to represent the compressional and shear waves along the orthotropy axes are given in Table 3.

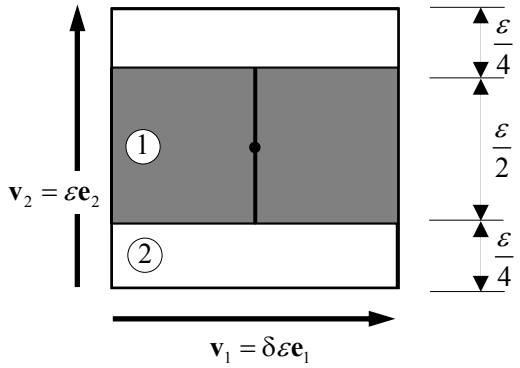

Figure 2. Periodic cell for the periodically jointed rock mass.

Tab.1 Characteristic lengths λ_β^α (mm) for $\delta\varepsilon = 1$ m and $\delta\varepsilon = 2$ m.

	$\lambda_{Sh-1} = \lambda_1^2$	$\lambda_{Ext-1} = \lambda_1^1$	$\lambda_{Sh-2} = \lambda_2^1$	$\lambda_{Ext-2} = \lambda_2^2$
$\delta\varepsilon = 1$ m	244.50	14.76	83.78	0.87
$\delta\varepsilon = 2$ m	451.15	41.29	104.80	6.83

Tab.2 Waves velocity $\hat{c}_\beta^\alpha$ (m/s) for $\delta\varepsilon = 1$ m and $\delta\varepsilon = 2$ m.

	$\hat{c}_1^2 = \hat{c}_2^1$	$\hat{c}_1^1$	$\hat{c}_2^2$
$\delta\varepsilon = 1$ m	1093.99	1731.38	2192.10
$\delta\varepsilon = 2$ m	1137.31	2187.66	2197.30

Tab.3 The non-vanishing components $I_{\alpha\beta\alpha\beta}$ for $\delta\varepsilon = 1$ m and $\delta\varepsilon = 2$ m.

	$I_{2121} = I_{1212}$	I_{1111}	I_{2222}
$\delta\varepsilon = 1$ m	1.046×10^{-2}	3.346×10^{-2}	1.302×10^{-2}
$\delta\varepsilon = 2$ m	1.396×10^{-2}	9.700×10^{-2}	1.380×10^{-2}

To evaluate the reliability and the validity limits of the non-local dynamic homogenization here proposed (see also Bacigalupo & Gambarotta, 2012a,b) the dispersion functions are compared with those obtained by the Floquet-Bloch approach. The latter are obtained by solving the Fourier transform in the time variable t of the microscopic motion equation (1) (by FEM procedure) in the periodic cell $\mathscr{A} = [0,\varepsilon]\times[0,\delta\varepsilon]$ (Figure 2) with the Floquet-Bloch boundary conditions

$$u_j\left(\mathbf{x}+\mathbf{v}_p\right)=e^{i\left(\mathbf{k}\cdot\mathbf{v}_p\right)}u_j\left(\mathbf{x}\right),$$
$$\sigma_{jq}\left(\mathbf{x}+\mathbf{v}_p\right)n_q=e^{i\left(\mathbf{k}\cdot\mathbf{v}_p\right)}\sigma_{jq}\left(\mathbf{x}\right)n_q, \tag{13}$$

where n_q is component of the outward normal unit vector of the periodic cell boundary $\partial\mathscr{A}$ and the vector $\mathbf{x}\in\partial\mathscr{A}$.

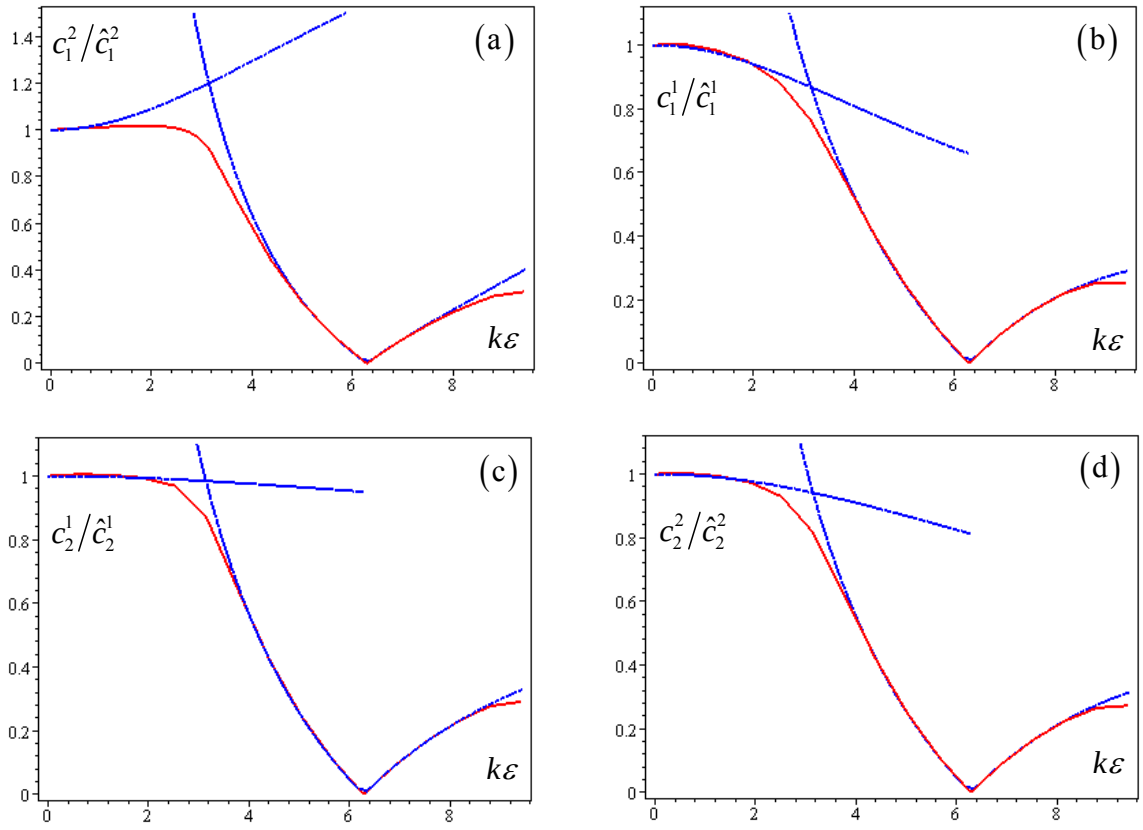

Figure 3: Shear and compressional waves: non-dimensional phase velocities versus non-dimensional wavenumber. Red line: heterogeneous material - Floquet-Bloch approach ; Blue line: second-order continuum. (a) S. waves in $\mathbf{e}_1$ direction; (b) C. waves in $\mathbf{e}_1$ direction; (c) S. waves in $\mathbf{e}_2$ direction; (d) C. waves in $\mathbf{e}_2$ direction.

The dimensionless phase velocity $c_\beta^\alpha/\hat{c}_\beta^\alpha$ of both shear and compressional waves for the distance between fractures $\delta\varepsilon=1$ m are shown in the diagrams of Figure 3 in terms of the dimensionless wavenumber $k\varepsilon$. The dispersion relations associated with shear and compressional waves along the directions of the layers and normal to the layers obtained of dynamic homogenization procedure (blue line: second-order continuum) are in good agreement with those obtained by Floquet-Bloch theorem for heterogeneous materials (red line). In particular, it is noted that for values of dimensionless wavenumber $k\varepsilon>\pi$ a better approximation of the dispersion curves may be obtained if the solution of the macroscopic motion equation (10) is assumed in the form $U_\alpha\left(x_\beta,t\right)=A\exp\left[i\left(\left(k-2\pi n/\varepsilon\right)x_\beta-\omega t\right)\right]$ (with $n\in\mathbb{Z}$) that gives the dispersion function

$$\omega = k\hat{c}_\beta^\alpha \left|1 - \frac{2\pi n}{k\varepsilon}\right| \sqrt{\frac{1+\left(k\varepsilon - 2\pi n\right)^2 \left(\lambda_\beta^\alpha / \varepsilon\right)^2}{1 + I_{\alpha\beta\alpha\beta}\left(k\varepsilon - 2\pi n\right)^2 + I_{\alpha\beta\beta\alpha\beta}\left(k\varepsilon - 2\pi n\right)^4}} \,. \tag{14}$$

This function is in good agreement with those obtained through the Floquet-Bloch theorem for $\pi\left(2n-1\right) < k\varepsilon < \pi\left(2n+1\right) \quad \forall n \in \mathbb{Z}$. In Figure 3 are shown the dispersion functions associated to $n = 0$ and $n = 1$.

The dimensionless phase velocity $c_\beta^\alpha / \hat{c}_\beta^\alpha$ of both shear and compressional waves for fracture spacings $\delta\varepsilon = 1$ m (Blue line) and $\delta\varepsilon = 2$ m (Green line) are shown in the diagrams of Figure 4 in terms of the dimensionless wavenumber $k\varepsilon$. From the diagrams of Figure 4 it emerges that the difference between the velocity of dispersive waves along the direction of layers (Figures 4.a and 4.b) and the corresponding one in the classical continuum is much higher compared to the corresponding results referred to the propagation along the direction orthogonal to the layers (Figures 4.c and 4.d). The phase velocity of the shear dispersive waves along the layers in the periodically fractured rock masses characterized by a distance between fractures $\delta\varepsilon = 1$ m is greater than that obtained for $\delta\varepsilon = 2$ m. An opposite behavior is found for the compressional waves along the layers. Furthermore, the phase velocity of the dispersive waves along the direction orthogonal to the layers does not differ much from the velocity obtained by considering the classical continuum.

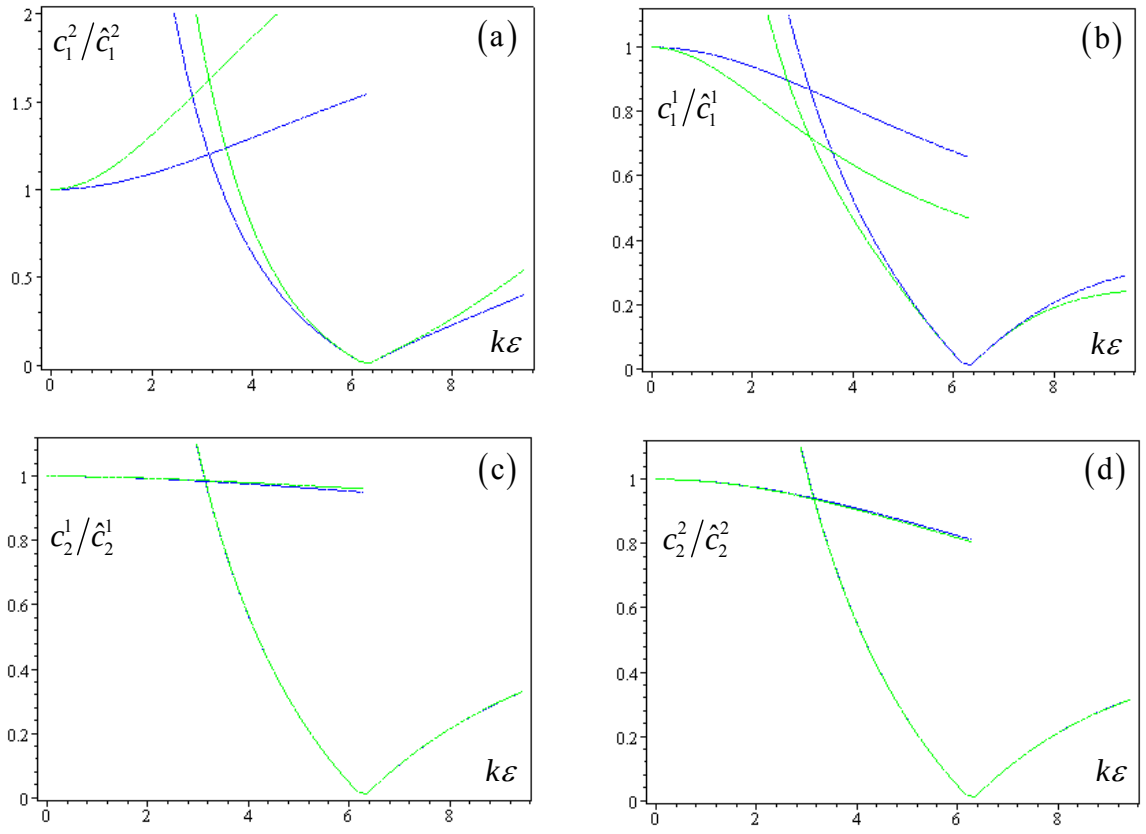

Figure 4: Shear and compressional waves: non-dimensional phase velocities obtained by second-order continuum versus non-dimensional wavenumber. blue line: $\delta\varepsilon = 1$ m ; green line: $\delta\varepsilon = 2$ m . (a) S. waves in $\mathbf{e}_1$ direction; (b) C. waves in $\mathbf{e}_1$ direction; (c) S. waves in $\mathbf{e}_2$ direction; (d) C. waves in $\mathbf{e}_2$ direction.

ACKNOWLEDGEMENT

The authors acknowledge financial support of the (MURST) Italian Department for University and Scientific and Technological Research in the framework of the research MIUR Prin09 project XWLFKW, *Multi-scale modeling of materials and structures*, coordinated by prof. A. Corigliano.

REFERENCES

Bacigalupo A. (2013) "Computational two-scale homogenization of periodic masonry: characteristic lengths and dispersive waves", submitted to Meccanica.

Bacigalupo A., Gambarotta L. (2012a) "Computational two-scale homogenization of periodic masonry: characteristic lengths and dispersive waves", Computer Methods in Applied Mechanics and Engineering, Vol. 213–216, 16–28.

Bacigalupo A. , Gambarotta L. (2012b): "A high-continuity multi-scale static and dynamic modelling of periodic materials", *Proceedings of the 6th European Congress on Computational Methods in Applied Sciences and Engineering (ECCOMAS 2012)*, Vienna, ISBN: 978-3-9502481-9-7.

Bai T. Pollard D.D. (2000) "Fracture spacing in layered rocks: a new explanation based on the stress transition", Journal of Structural Geology, Vol. 22, 43-57.

Boadu F.K. (1997) "Fractured rock mass characterization parameters and seismic properties: Analytical studies", Journ, Applied Geophysics, Vol. 36, 1-19.

Capdeville Y., Guillot L., Marigo J.-J.(2010) "1-D non-periodic homogenization for the seismic wave equation", Geophysical Journal International, Vol. 181, 897-910.

Capdeville Y., Marigo J.-J.(2007) "Second order homogenization of the elastic wave equation for non-periodic layered media", Geophysical Journal International, Vol. 170, 823-838.

Gross M.R., Fischer M.P., Engelder T., Greenfield R.J. (1995) "Factors controlling joint spacing in interbedded sedimentary rocks: integrating numerical models with field observation from the Monterey Formation, USA" , Geological Society Special Publication, No. 92, 215-233.

Guéguan Y., Sarout J. (2011), "Characteristic of anisotropy and dispersion in cracked medium", Tectonophysics, Vol. 503, 165-172.

Lambert G., Gurevich B., Brajanovski M. (2006) "Attenuation and dispersion of P-waves in porous rocks with planar fractures: Comparison of theory and numerical simulations", Geophysics, Vol. 71, N41-45.

Mindlin R.D. (1965), "Micro-structure in linear elasticity", Arch. Ration. Mech. Anal., Vol. 16, 51–78.

Monsen K. (2001) "Acoustic velocity in fractured rocks", J. of Geophysical Research, Vol. 106, 261-267.

Nakagawa S., Nihei K.T., Myer L.R. (2002) "Elastic wave propagation along a set of parallel fractures", Geophysical Research Letters, Vol. 29, 31-1-4.

Sayers C.M., Kachanov M. (1995) "Microcrack-induced elastic wave anisotropy of brittle rocks", J. of Geophysical Research, Vol. 100, (83), 4149-4156.

Stefanou I., Sulem J., Vardoulakis I., (2008) "Three-dimensional Cosserat homogenization of masonry structures: elasticity", Acta Geotecnica, Vol. 3, (1), 71-83.

ON THE DYNAMIC ANALYSIS OF TWO-PHASE SOILS

A. Cividini
Department of Architecture, Built Environment and Construction Engineering, Politecnico di Milano, Milan, Italy

G. Gioda
Department of Architecture, Built Environment and Construction Engineering, Politecnico di Milano, Milan, Italy

ABSTRACT: *The studies on the dynamic analysis of saturated soils led to various numerical approaches that involve different assumptions, different governing equations and also different sets of free variables. The relatively complex mathematical structure of the problem does not permit a straightforward evaluation of the consequences of these assumptions and, hence, makes the choice of the most appropriate numerical approach somewhat controversial. Here the complete formulation of dynamic two-phase problems is first summarized, under assumptions which seem acceptable in the geotechnical engineering context. Then, two finite element approaches are derived on this basis, the latter of which permits reducing the number of free nodal variables with respect to the first one. Finally, the results obtained in the solution of two benchmark problems are presented and commented upon.*

1 INTRODUCTION

The solution of geotechnical problems involving saturated two phase-soils requires the simultaneous analyses of the seepage flow and of the effective stress distribution within the soil skeleton. In quasi static conditions, under an acceleration field constant with time (i.e. the gravity field), the literature provides exhaustive theoretical bases and broadly accepted methods for the numerical analysis of seepage and of the coupled effective stress-flow problem, e.g. Desai (1976), Sandhu & Wilson (1969), Zaman et al. (2000).

In dynamic conditions however, e.g. during earthquakes, the analysis of seepage becomes less straightforward since recourse cannot be made anymore to the usual concept of hydraulic head (Bear, 1988; Bird et al., 2007). This led to various numerical approaches for dynamic coupled problems that involve different assumptions, different governing equations and different sets of free variables (Zienkiewicz & Shiomi 1984; Cividini & Pergalani, 1994; Zienkiewicz et al., 1999).

The relatively complex mathematical structure of the problem does not permit a straightforward evaluation of the consequences of these assumptions and, hence, makes the choice of the most appropriate numerical approach somewhat controversial. This suggested undertaking a study on the coupled dynamic analysis of saturated granular deposits. Its initial part, limited to dynamic seepage flows, was presented in Stucchi et al. (2010). Here the complete formulation of dynamic two-phase problems is derived, observing some difference in the final finite element equations with respect to those of other formulations presented in the literature. Then a simplified formulation is worked out in order to reduce the number of

the free nodal variables. The details of derivations are rather lengthy. They are omitted here for sake of briefness and will be presented in a parallel paper (Cividini & Gioda, 2013).

Two test problems are considered. The first one concerns the dynamic effects on a vertical rigid wall confining a water reservoir. The results obtained with the first formulation are compared with the closed form solution proposed by Westergaard (1933) and with the numerical results derived from the "reduced mixed formulation" for porous media with compressible fluid (Zienkiewicz & Shiomi, 1984).

Then, the two formulations proposed here are applied to the solution of a second illustrative problem concerning the dynamic behaviour of a shallow foundation. The comparison of their results permits drawing some preliminary conclusions on the accuracy of the simplified approach with respect to the "complete" one.

2 GOVERNING EQUATIONS

The equations necessary to describe the behavior of the liquid phase, which is denoted by subscript index *L*, are recalled first. They hold under the following assumptions that seem acceptable in the geotechnical context: a Newtonian pore liquid (water) is considered with constant deviatoric viscosity and no volumetric viscosity; the liquid has a constant density and its volumetric deformation linearly depends on the pore pressure; the influence of temperature is neglected; the fluid flow is laminar.

1) Equation of compatibility, relating the strain rate vector $\dot{\boldsymbol{\varepsilon}}_L$ to the relative (with respect to the skeleton) discharge velocity $\boldsymbol{w}$ and to the skeleton velocity $\dot{\boldsymbol{u}}$,

$$\dot{\boldsymbol{\varepsilon}}_L = \boldsymbol{B}\boldsymbol{w} + \boldsymbol{B}\dot{\boldsymbol{u}} \tag{1}$$

where $\boldsymbol{B}$ is the same 6x3 differential operator that governs the strain-displacement relationship for solids.

2) Constitutive relationship, expressing the stresses $\boldsymbol{\sigma}_L$ acting on the liquid phase,

$$\boldsymbol{\sigma}_L = \mu_L \boldsymbol{I}_1 \dot{\boldsymbol{\varepsilon}}_L + \boldsymbol{m}p = \mu_L \boldsymbol{I}_1 (\boldsymbol{B}\boldsymbol{w} + \boldsymbol{B}\dot{\boldsymbol{u}}) + \boldsymbol{m}p \tag{2}$$

where p is the pore pressure; μ_L is the shear viscosity; $\boldsymbol{I}_1$ is a 6x6 matrix of coefficients and $\boldsymbol{m}$ is a 6 component vector the entries of which are equal to 1 if they correspond to normal stresses, otherwise they vanish.

3) Equation of continuity, enforcing the conservation of the liquid mass,

$$\boldsymbol{m}^T (\boldsymbol{B}\dot{\boldsymbol{u}}) + \boldsymbol{m}^T (\boldsymbol{B}\boldsymbol{w}) - \frac{1}{B_U} \dot{p} = 0 \tag{3}$$

where the bulk modulus B_U depends on the compressibility of water and grains.

4) Equation of motion of the fluid phase, enforcing the momentum balance of the mass of water contained within a fixed unit volume of the porous medium,

$$\rho_L \dot{\boldsymbol{w}} + \rho_L (\ddot{\boldsymbol{u}} - \bar{\boldsymbol{g}}) - \mu_L \boldsymbol{B}^T [\boldsymbol{I}_1 \boldsymbol{B}(\boldsymbol{w})] - \mu_L \boldsymbol{B}^T [\boldsymbol{I}_1 \boldsymbol{B}(\dot{\boldsymbol{u}})] - \boldsymbol{B}^T (\boldsymbol{m}p) + \mu_L (\boldsymbol{K}')^{-1} \boldsymbol{w} = \boldsymbol{0} \tag{4}$$

where ρ_L is the density of the liquid phase; vectors $\dot{\boldsymbol{w}}$, $\ddot{\boldsymbol{u}}$, $\bar{\boldsymbol{g}}$ collect, respectively, the components of the relative discharge acceleration; of the skeleton acceleration and of the acceleration of gravity; $\boldsymbol{K}'$ is the intrinsic permeability matrix. Note that the quadratic

discharge velocity term has been neglected because its contribution is marginal in seepage problems.

5) The equation of motion of the two-phase medium can be written in the following form,

$$\rho_{Sat}(\ddot{\boldsymbol{u}} - \bar{\boldsymbol{g}}) + \rho_L \dot{\boldsymbol{w}} - \boldsymbol{B}^T[\boldsymbol{D}_S \boldsymbol{B}(\boldsymbol{u})] - \boldsymbol{B}^T[\boldsymbol{V}_{SL} \boldsymbol{B}(\dot{\boldsymbol{u}})] - \mu_L \boldsymbol{B}^T[\boldsymbol{I}_1 \boldsymbol{B}(\boldsymbol{w})] - \boldsymbol{B}^T(\boldsymbol{m}p) = \boldsymbol{0} \tag{5}$$

where $\boldsymbol{D}_S$ is the constitutive matrix of the solid phase and $\boldsymbol{V}_{SL}$ is the global constitutive viscosity matrix of the coupled solid and liquid phases.

The dynamic two-phase problem is governed by the system of three differential Eqs. (3), (4) and (5), which involve as unknown functions the relative discharge velocity $\boldsymbol{w}$, the skeleton displacements $\boldsymbol{u}$ and the pore pressure p.

3 BOUNDARY CONDITIONS

With reference to confined seepage flows, consider a saturated porous domain having surface Γ and volume Ω. The surface Γ is subdivided into its impervious part, Γ_w where the relative discharge velocity component normal to it $\bar{w}_n$ vanishes, and its pervious part Γ_p where the pore pressure $\bar{p}$ is known. These boundary conditions can be expressed as follows,

$$\boldsymbol{w}^T \boldsymbol{T}_1 \boldsymbol{m} = \boldsymbol{m}^T \boldsymbol{T}_1^T \boldsymbol{w} = \bar{w}_n = 0 \quad \text{on } \Gamma_w \tag{6a}$$

$$p = \bar{p} \quad \text{and} \quad \boldsymbol{\tau}_L = \boldsymbol{0} \quad \text{on } \Gamma_p \tag{6b,c}$$

where $\boldsymbol{T}_1$ is the 3x6 matrix of the direction cosines of the outward vector normal to Γ_w.

The surface Γ can be also subdivided into Γ_u, where the displacements $\bar{\boldsymbol{u}}$ are known, and Γ_σ where the three components of the total surface tractions $\bar{\boldsymbol{t}}$ are imposed,

$$\boldsymbol{T}_2 \boldsymbol{u} = \bar{\boldsymbol{u}} \quad \text{on } \Gamma_u \tag{6d}$$

$$\boldsymbol{T}_2 \boldsymbol{T}_1 \boldsymbol{\sigma} = \bar{\boldsymbol{t}} \quad \text{on } \Gamma_\sigma \tag{6e}$$

where $\boldsymbol{T}_2$ is the 3x3 matrix containing the direction cosines of the local reference system axes along which the boundary displacements and tractions are imposed.

4 FINITE ELEMENT FORMULATION

Let denote with n_w^e and n_u^e the number of nodes of the *e*-th element where relative discharge velocities $\boldsymbol{w}^e$ and displacements $\boldsymbol{u}^e$ are defined. The pore pressure p^e is seen here as an element variable and is defined at the element integration points.

The distributions of relative discharge velocities $\boldsymbol{w}$ and displacements $\boldsymbol{u}$ within the element depend on the interpolation function matrices $\boldsymbol{S}_w^e$ and $\boldsymbol{S}_u^e$.

$$\boldsymbol{w} = \boldsymbol{S}_w^e \boldsymbol{w}^e \quad ; \quad \boldsymbol{u} = \boldsymbol{S}_u^e \boldsymbol{u}^e \tag{7a,b}$$

Let also define the following matrices, $\boldsymbol{B}_w^e$ and $\boldsymbol{B}_u^e$, containing the space derivatives of the interpolation functions.

$$\boldsymbol{B}_w^e = \boldsymbol{B}\boldsymbol{S}_w^e \quad ; \quad \boldsymbol{B}_u^e = \boldsymbol{B}\boldsymbol{S}_u^e \tag{8a,b}$$

The first finite element formulation does not introduce further simplifying assumptions with respect to those already adopted for deriving the governing Eqs. (3), (4) and (5). The finite element form of Eqs. (4) and (5) is obtained by writing them and the corresponding boundary conditions in weak form; multiplying them, respectively, by a virtual variation $\delta \boldsymbol{w}$ of the relative discharge velocities and of the displacements $\delta \boldsymbol{u}$ and integrating over the volume Ω and over the relevant part of the surface Γ of an element of the porous medium. This leads to the following set of matrix equations

$$\begin{bmatrix} \boldsymbol{K}_S^e & \boldsymbol{0} \\ \boldsymbol{0} & \boldsymbol{0} \end{bmatrix} \begin{Bmatrix} \boldsymbol{u}^e \\ \boldsymbol{0} \end{Bmatrix} + \begin{bmatrix} \boldsymbol{V}_{Sat}^e & (\boldsymbol{V}_{Lwu}^e)^T \\ \boldsymbol{V}_{Lwu}^e & \boldsymbol{V}_{Lww}^e \end{bmatrix} \begin{Bmatrix} \dot{\boldsymbol{u}}^e \\ \boldsymbol{w}^e \end{Bmatrix} + \begin{bmatrix} \boldsymbol{M}_{Sat}^e & (\boldsymbol{M}_{Lwu}^e)^T \\ \boldsymbol{M}_{Lwu}^e & \boldsymbol{M}_{Lww}^e \end{bmatrix} \begin{Bmatrix} \ddot{\boldsymbol{u}}^e \\ \dot{\boldsymbol{w}}^e \end{Bmatrix} = = \begin{Bmatrix} -\boldsymbol{f}_{up}^e \\ \boldsymbol{f}_{Lp}^e \end{Bmatrix} + \begin{Bmatrix} \overline{\boldsymbol{f}}_{gSat}^e + \overline{\boldsymbol{f}}_t^e \\ \overline{\boldsymbol{f}}_{Lp}^e + \overline{\boldsymbol{f}}_{Lg}^e \end{Bmatrix} \tag{9}$$

where

$$\boldsymbol{K}_S^e = \int_{\Omega^e} (\boldsymbol{B}_u^e)^T \boldsymbol{D}_S \boldsymbol{B}_u^e d\Omega \quad ; \quad \boldsymbol{V}_{Sat}^e = \int_{\Omega^e} (\boldsymbol{B}_u^e)^T \boldsymbol{V}_{SL} \boldsymbol{B}_u^e d\Omega \tag{10a,b}$$

$$\boldsymbol{M}_{Sat}^e = \rho_{Sat} \int_{\Omega^e} (\boldsymbol{S}_u^e)^T \boldsymbol{S}_u^e d\Omega \quad ; \quad \boldsymbol{f}_{up}^e = \int_{\Omega^e} (\boldsymbol{B}_u^e)^T \boldsymbol{m} p^e d\Omega \tag{10c,d}$$

$$\overline{\boldsymbol{f}}_{gSat}^e = \rho_{Sat} \int_{\Omega^e} (\boldsymbol{S}_u^e)^T \overline{\boldsymbol{g}} d\Omega \quad ; \quad \overline{\boldsymbol{f}}_t^e = \int_{\Omega^e} (\boldsymbol{S}_u^e) \boldsymbol{T}_2^T \overline{\boldsymbol{t}}^e d\Omega \tag{10e,f}$$

$$\boldsymbol{M}_{Lww}^e = \rho_L \int_{\Omega^e} (\boldsymbol{S}_w^e)^T \boldsymbol{S}_w^e d\Omega \quad ; \quad \boldsymbol{M}_{Lwu}^e = \rho_L \int_{\Omega^e} (\boldsymbol{S}_w^e)^T \boldsymbol{S}_u^e d\Omega \tag{10g,h}$$

$$\boldsymbol{V}_{Lww}^e = \mu_L \int_{\Omega^e} (\boldsymbol{B}_w^e)^T \boldsymbol{I}_1 \boldsymbol{B}_w^e d\Omega + \mu_L \int_{\Omega^e} (\boldsymbol{S}_w^e)^T (\boldsymbol{K}')^{-1} \boldsymbol{S}_w^e d\Omega \tag{10i}$$

$$\boldsymbol{V}_{Lwu}^e = \mu_L \int_{\Omega^e} (\boldsymbol{B}_w^e)^T \boldsymbol{I}_1 \boldsymbol{B}_u^e d\Omega \quad ; \quad \boldsymbol{f}_{Lp}^e = \int_{\Omega^e} (\boldsymbol{B}_w^e)^T \boldsymbol{m} p^e d\Omega \tag{10j,k}$$

$$\overline{\boldsymbol{f}}_{Lp}^e = \int_{\Gamma_p^e} (\boldsymbol{S}_w^e)^T \boldsymbol{T}_1 \boldsymbol{m} \overline{p}^e d\Gamma \quad ; \quad \overline{\boldsymbol{f}}_{Lg}^e = \rho_L \int_{\Omega^e} (\boldsymbol{S}_w^e)^T \overline{\boldsymbol{g}} d\Omega \tag{10l,m}$$

Note that vectors $\boldsymbol{f}_{Lp}^e$ and $\boldsymbol{f}_{up}^e$ depend on the unknown pore pressure distribution within the element. Consequently, also the following equation that represents the finite element form of Eq.(3) is necessary for solution

$$\dot{p}^e = B_U (\boldsymbol{m}^T \boldsymbol{B}_u^e \dot{\boldsymbol{u}}^e + \boldsymbol{m}^T \boldsymbol{B}_w^e \boldsymbol{w}^e) \tag{11}$$

This “complete” formulation is referred to in the following as ***u-w*** approach.

A simplified formulation (referred to as ***u*** approach) is obtained taking into account that some terms of Eqs. (4) and (5) could be disregarded since their contribution is likely to be marginal (Zienkiewicz et al., 1999). These are the terms that contain the relative discharge acceleration and the second space derivatives of the discharge velocity and of the velocity of the solid phase. Based on these additional assumptions, Eq. (9) reduces to the following form that does not involve the discharge velocity as a free variable

$$\boldsymbol{K}_S^e \boldsymbol{u}^e + \boldsymbol{V}_{Sat}^e \dot{\boldsymbol{u}}^e + \boldsymbol{M}_{Sat}^e \ddot{\boldsymbol{u}}^e = -\boldsymbol{f}_{up}^e + \overline{\boldsymbol{f}}_{gSat}^e + \overline{\boldsymbol{f}}_t^e \tag{12}$$

Also in this case Eq. (11) is necessary to evaluate the pore pressure.

5 TIME INTEGRATION PROCEDURE

Let write Eqs. (9) and (12) in the same compact form expressed by Eq. (13), with obvious meanings of symbols. Note that vector $\boldsymbol{b}$ depends on the pore pressure, while $\bar{\boldsymbol{b}}$ is known and depends solely on time *t*.

$$\boldsymbol{Z}_1\boldsymbol{x}(t) + \boldsymbol{Z}_2\dot{\boldsymbol{x}}(t) + \boldsymbol{Z}_3\ddot{\boldsymbol{x}}(t) = \boldsymbol{b}(p,t) + \bar{\boldsymbol{b}}(t) \tag{13}$$

In order to integrate Eq. (13) in time, assume that the variation of $\ddot{\boldsymbol{x}}(t)$ within a time increment Δt_i is governed by an a priory chosen interpolation function (Newmark, 1959; Katona & Zienkiewicz, 1985). This leads to the following recursive forms, where $\Delta\ddot{\boldsymbol{x}}_i$ represents the increment of the second derivative at the end of the step and the coefficients β_0 and β_1 depend on the interpolation function adopted for $\ddot{\boldsymbol{x}}(t)$.

$$\boldsymbol{x}_i = \left[\boldsymbol{x}_{i-1} + \Delta t_i\dot{\boldsymbol{x}}_{i-1} + \frac{\Delta t_i^2}{2}\ddot{\boldsymbol{x}}_{i-1}\right] + \beta_0\frac{\Delta t_i^2}{2}\Delta\ddot{\boldsymbol{x}}_i \tag{14a}$$

$$\dot{\boldsymbol{x}}_i = \left[\dot{\boldsymbol{x}}_{i-1} + \Delta t_i\ddot{\boldsymbol{x}}_{i-1}\right] + \beta_1\Delta t_i\Delta\ddot{\boldsymbol{x}}_i \tag{14b}$$

$$\ddot{\boldsymbol{x}}_i = \ddot{\boldsymbol{x}}_{i-1} + \Delta\ddot{\boldsymbol{x}}_i \tag{14c}$$

Substitution of Eqs. (14) into Eq. (13) leads to.

$$\left[\beta_0\frac{\Delta t_i^2}{2}\boldsymbol{Z}_1 + \beta_1\Delta t_i\boldsymbol{Z}_2 + \boldsymbol{Z}_3\right]\Delta\ddot{\boldsymbol{x}}_i = -\boldsymbol{Z}_1\left[\boldsymbol{x}_{i-1} + \Delta t_i\dot{\boldsymbol{x}}_{i-1} + \frac{\Delta t_i^2}{2}\ddot{\boldsymbol{x}}_{i-1}\right] - \boldsymbol{Z}_2\left[\dot{\boldsymbol{x}}_{i-1} + \Delta t_i\ddot{\boldsymbol{x}}_{i-1}\right] + \\ - \boldsymbol{Z}_3\ddot{\boldsymbol{x}}_{i-1} + \boldsymbol{b}(p_i,t_i) + \bar{\boldsymbol{b}}(t_i) \tag{15}$$

Knowing the free variables $\boldsymbol{x}_{i-1}$, their derivatives and the pore pressure at time t_{i-1}, an iterative process is necessary to evaluate them at time t_i:

- Vector $\boldsymbol{b}(p_i,t_i)$ is approximated adopting the values of the pore pressure at time t_i obtained by the previous iteration.
- Vector $\Delta\ddot{\boldsymbol{x}}_i$ is determined by Eq. (15), then $\boldsymbol{x}_i$, $\dot{\boldsymbol{x}}_i$, $\ddot{\boldsymbol{x}}_i$ are updated through Eqs. (14).
- The pore pressure rate $\dot{p}_i$ is evaluated at the integration points of each element by means of Eq. (11) and p_i is determined through Eqs. (14).
- Vector $\boldsymbol{b}(p_i,t_i)$ is updated and the next iteration is carried out.
- The process ends when vector $\boldsymbol{x}(t_i)$ and the pore pressure p_i stabilize.

Considering the small value of the time steps adopted in most dynamic analyses, the iterative process could be avoided in linear analyses by adopting a time marching scheme in which vector $\boldsymbol{b}$ at time t_i is calculated on the basis of the element pore pressure at time t_{i-1}.

6 ILLUSTRATIVE EXAMPLES

Two test examples have been solved through the previously described ***u-w*** "complete" approach. To validate the numerical results, the first example was also solved with the "reduced mixed formulation", or ***u-U*** approach, proposed by Zienkiewicz and Shiomi (1984). The second example is used for investigating the accuracy of the simplified ***u*** approach the results of which are compared with those of the ***u-w*** formulation.

The first example concerns the evaluation of the water pressure distribution on a vertical rigid wall due to a dynamic excitation in the horizontal direction. This problem was first investigated by Westergaard (1933) who provided solutions frequently employed for estimating the effects of earthquakes on dams and on retaining structures in saturated granular soils.

Considering that the period of free vibrations T_0 of most dams is appreciably lower than the period of earthquakes T, it can be reasonably assumed that during time all points of the dam have the same horizontal acceleration, which coincides with the one of its base. Westergaard worked out two closed form solutions in plane. The first one neglects the vertical displacement of water, while the second solution takes it into account. The latter one is here adopted for evaluating the dynamic excess water pressure against the wall, i.e. the dynamic water pressure increment with respect to the hydrostatic condition.

The numerical analysis was based on a mesh consisting of 100 four node, quadrilateral isoparametric elements and of 126 nodes (6 of which belong to the vertical wall) where the fluid velocity components represent the nodal variables.

The numerical results are compared in Fig. 1 with Westergaard solution. Fig. 1a and 1b show, respectively, the maximum dynamic excess pressure distribution along the vertical coordinate and the variation with time of the excess pressure at the wall base. In these figures H is the height of the wall, p_{max} is the maximum excess pressure at the base from the closed form solution and T is the period of the sinusoidal excitation.

The ***u-w*** results are also compared with those obtained using the ***u-U*** formulation (Zienkiewicz & Shiomi, 1984). It can be observed that the ***u-w*** approach provides an acceptable approximation of the closed form solution, with an accuracy slightly higher than that of the ***u-U*** formulation.

The second example concerns a rigid strip footing on a homogeneous soil layer overlaying the bedrock. No relative movements are allowed between the foundation base and the soil. The mesh, consisting of 84 elements and 106 nodes, is shown in Fig. 2. The nodal variables are the displacements of the solid phase and the relative velocities of the liquid phase.

First the vertical dead load q is applied in a time interval Tq. Subsequently, a dynamic excitation is imposed to the bedrock which derives from the north-south component of El Centro 1940 earthquake. The excitation, lasting 5 seconds, is corrected so that at the end of it the velocity at the mesh bottom vanishes.

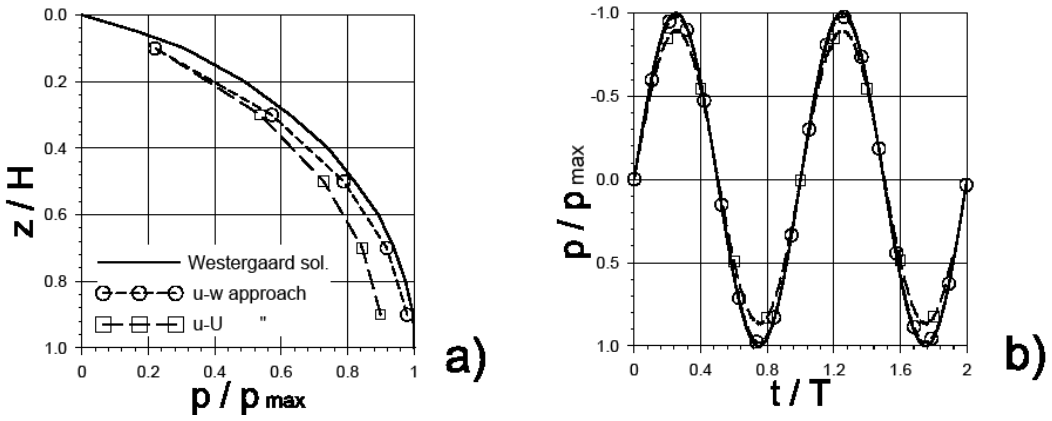

Fig. 1. Maximum dynamic excess pressure distribution along the vertical wall (a) and variations with time of the dynamic excess pressure at the wall base (b): comparison between the ***u-w*** results, Westergaard solution and the results of the ***u-U*** approach

Zienkiewicz & Bettess (1982) showed that, depending on the geometrical and material characteristics of the problem at hand, a fully coupled Biot dynamic analysis can be mandatory. The problem depicted in Fig. 2 falls in this category.

Figs. 3, 4 and 5 show the evolution in time of nodal displacements and of the average pore pressures obtained adopting the ***u-w*** approach. The displacements refer to points A and F, at the ground surface, and G, underneath the foundation corner. In Figs. 3 and 4, $u_{y\,fond}$ is the absolute value of the long term settlement of the foundation. The black dots in Figs. 3d and 4 represent the long term displacements due to the dead load in static conditions. Consequently, the difference between static and dynamic horizontal displacements in Fig. 3d is due to the permanent displacement induced by the earthquake motion.

The diagrams in Fig. 5 report the variation with time of the average pore pressure within elements 1, 2 and 3 in Fig. 2. It can be observed that, in this illustrative example, the base motion has appreciable effects on the horizontal displacements while it has a limited influence on the pore pressure.

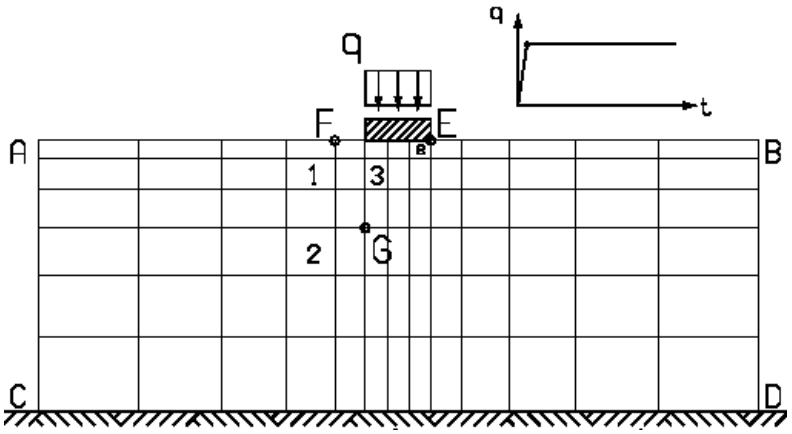

Fig. 2. Finite element scheme and loading conditions

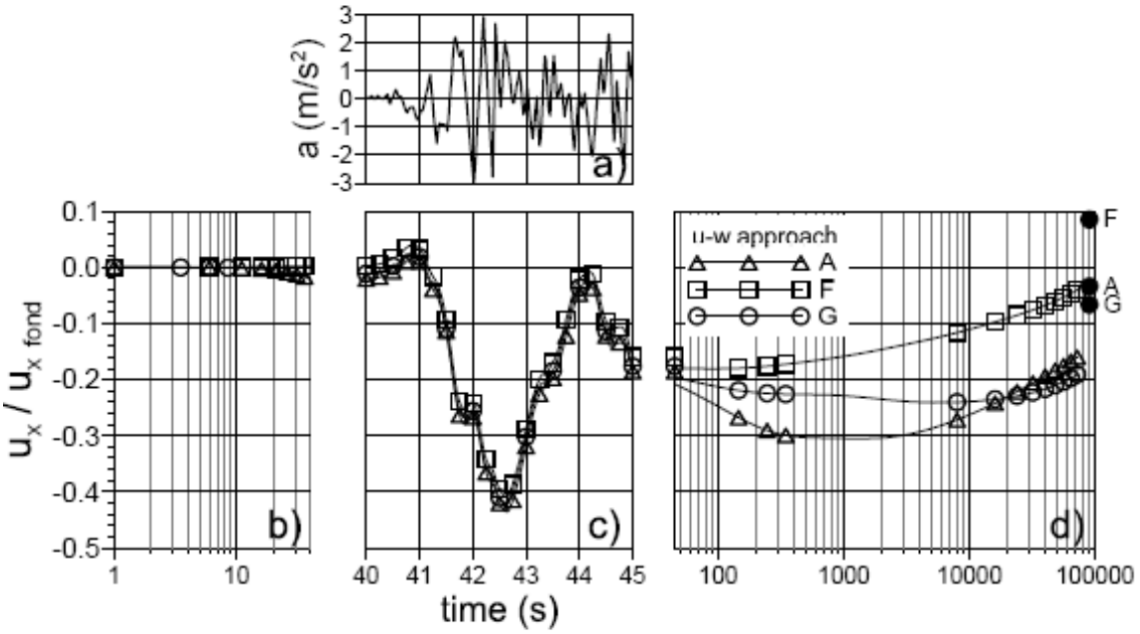

Fig. 3. Variation with time of: bedrock acceleration (a); horizontal displacements of nodes A, F and G (see Fig. 2) during the load application (b), the earthquake motion (c) and after it (d).

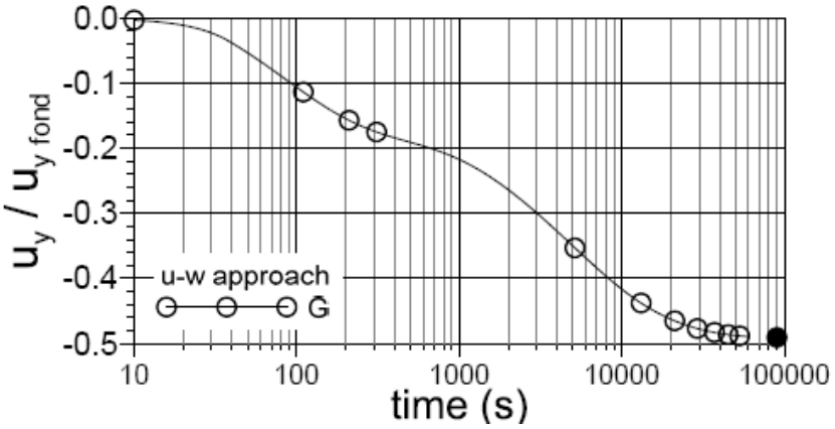

Fig. 4. Vertical displacement vs. time of point G (cf. Fig. 2)

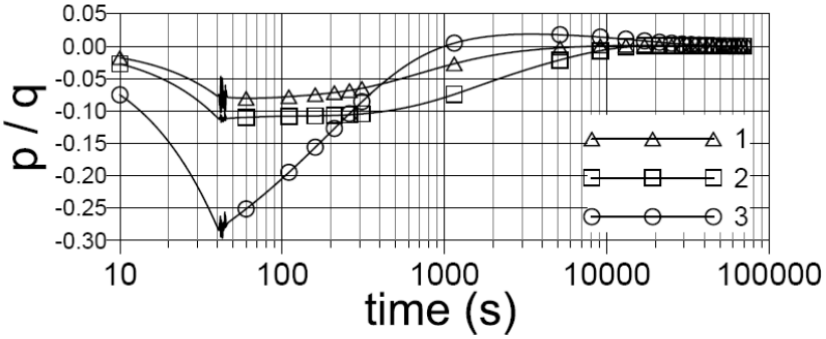

Fig. 5. Average pore pressure *p* vs. time in elements 1, 2 and 3 (cf. Fig. 2)

The analysis was then repeated adopting the simplified ***u*** approach. The difference between the results of ***u-w*** and ***u*** analyses are presented, in non-dimensional form, in Figs. 6 and 7. These diagrams show the variation in time of the difference between the horizontal displacement u_x of the foundation edge *E* (Fig. 6) and the average pore pressure *p* in element *e* located below the foundation edge (Fig. 7).

The displacement and pressure from the ***u*** approach are always lower than those from the ***u-w*** approach. The difference between the quantities evaluated with the two formulations increases during the loading stage, during the earthquake motion and also during the early stage of the post-earthquake consolidation process, then tends to decrease.

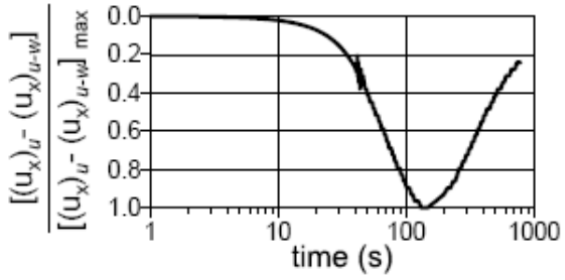

Fig. 6. Horizontal displacement u_x of node *E* (cf. Fig. 2): variation in time of the difference between the results of ***u*** and ***u-w*** approaches

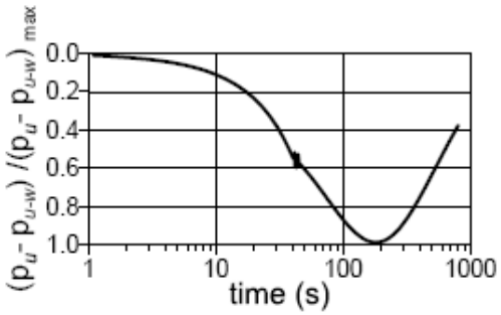

Fig. 7. Average pore pressure *p* in element *e* (cf. Fig. 2): variation in time of the difference between the results of ***u*** and ***u-w*** approaches

7 CONCLUDING REMARKS

The complete formulation of dynamic two-phase problems has been summarized introducing assumptions which seem acceptable in the geotechnical engineering context.

Two finite element approaches were derived on this basis. They are referred to as the "complete" ***u-w*** and the "simplified" ***u*** formulations. The latter of them, in fact, permits reducing the number of nodal variables with respect to the first one with a consequent reduction of the computational burden.

The results obtained in the solution of a first bench mark problem, involving solely the liquid phase, showed an acceptable agreement with the corresponding analytical solution.

A second text example was then solved which concerns the seismic response of a shallow foundation. A discrepancy was observed in this case between the results of the two approaches. In particular, the simplified ***u*** approach provides pore pressure and displacement values which are somewhat smaller than those obtained with the complete ***u-w*** formulation.

The analysis of the causes of this discrepancy, and of its relevance in engineering terms, requires some further investigation that will be part of the prosecution of this study.

ACKNOWLEDGEMENT

The CNR2012 and PRIN2008 financial support of the Ministry of University and Research of the Italian Government is gratefully acknowledged.

REFERENCES

Bear, J. (1988), Dynamics of Fluids in Porous Media, Dover Publications, NewYork, USA.

Bird, R.B., Stewart, W.E. & Lightfoot, E.N. (2007), Transport Phenomena, John Wiley & Sons, NewYork, USA.

Cividini, A. & Gioda, G. (2013), "On the finite element formulation of dynamic two-phase coupled problems". (in preparation).

Cividini, A. & Pergalani, F. (1994), "Alcuni aspetti della modellazione numerica di mezzi plurifase", Atti del Convegno CNR - Gruppo nazionale di coordinamento per gli studi di ingegneria geotecnica. Il ruolo dei fluidi nei problemi di ingegneria geotecnica, Mondovi" (Cuneo), 6-7 settembre, 1, II/61-II/75.

Desai, C.S. (1976), "Finite element residual schemes for unconfined flow". International Journal for Numerical Methods in Engineering, 10, 1415-1418.

Katona M.G. & Zienkiewicz, O.C. (1985), "A unified set of single step algorithms - Part 3: the beta-m method, a generalization of the Newmark scheme". International Journal for Numerical Methods in Engineering, 21, 1345-1359.

Newmark, N.M. (1959), “A method of computation for structural dynamics”, ASCE Journal of the Engineering Mechanics Division, 85(EM3), 67-94.

Sandhu, R.S. &Wilson, E.L. (1969), "Finite Element Analysis of Seepage in Elastic Media". ASCE Journal of the Engineering Mechanics Division, 95(EM3), 641-652.

Stucchi, R., Cividini, A. & Gioda, G. (2010), "Finite element approaches for the dynamic analysis of seepage", Ingegneria Sismica (Seismic Engineering), 27(1), 53-61.

Westergaard, H.M. (1933), "Water pressures on dams during earthquake". Transaction of American Society of Civil Engineers, 98, 418-434.

Zaman, M., Gioda, G. & Booker, J. (eds.) (2000), Modeling in Geomechanics, John Wiley & Sons, Chichester, UK.

Zienkiewicz, O.C. & Bettess, P. (1982), "Soil and saturated media under transient, dynamic conditions; general formulation and the validity of various simplifying assumption". In Soil Mechanics - Transient and Cyclic Loads: Constitutive Relations and Numerical Treatments (Pande, G.N., Zienkiewicz, O.C., Eds.), Wiley Series in Numerical Methods in Engineering.

Zienkiewicz, O.C. & Shiomi, T. (1984), "Dynamic behaviour of saturated porous media; the generalized Biot formulation and its numerical solution". International Journal for Numerical and Analytical Methods in Geomechanics, 8, 71-96.

Zienkiewicz, O.C., Chan, A.H.C., Pastor, M., Schrefler, B.A. & Shiomi, T. (1999), Computational Geomechanics, John Wiley & Sons, Chichester, UK.

DECOMPOSITION OF MEASURED GROUND VIBRATIONS INTO BASIC SOIL WAVES

D. Macijauskas
Department of Science & Technology, University of Luxembourg, Luxembourg

S. Van Baars
Department of Science & Technology, University of Luxembourg, Luxembourg

ABSTRACT: *Man-made vibrations from different types of sources are usually measured on the surface of the ground or building. The measured signal is always the superposition of all travelling basic waves. For a homogeneous half space there are three basic waves – the Compressional (P-wave), Shear (S-wave) and Rayleigh wave (R-wave). Depending on the measuring equipment, only the accelerations or velocities in time of the superposed wave can be measured, but not the distribution of the individual basic waves.*

Additional problems are that each of the basic waves has its own velocity, besides the body and surface waves have different attenuation laws. By using the rules of superposition of harmonic waves and also the propagation laws of the P-, S- and R-waves, it should be theoretically possible to split the measured superposed signal into the basic waves, because mathematically a system of equations can be assembled which describes the displacements at multiple measuring points in time.

In this paper this problem has been solved for a homogenous, elastic and isotropic soil, which is disturbed by a harmonically oscillating disc on the surface. A numerical simulation was performed using a finite element method. The displacements in time were recorded in 10 points on the surface and a system of superposed equations was assembled and solved.

The findings prove that each of the three basic waves has its own phase shift with the source, something which was not known before.

1 INTRODUCTION

In urban areas where the infrastructure is dense and construction of new structures is near existing ones, the vibrations caused by human activities frequently occur. Generated waves in the soil may adversely affect surrounding buildings. The most known sources of the human induced vibrations are traffic (trains, buses, trucks) and civil construction activity (installation of piles, sheet piles, tunnelling, demolishing of structures, etc.). Because of environmental requirements the level of the vibrations should not exceed certain threshold values in order to protect people from discomfort, the existing structures from damage and technological processes from disturbance. This means that the level of vibration must be predicted. According to a research by Hölscher and Waarts (2003) the reliability of prediction methods is disappointingly low, so it is evident that the soil models for vibrations should be improved first in order to get more accurate predictions.

According to theory, the vibrations in a homogeneous half space are complex superposed waves, made up of body and surface waves, which are the following three basic waves – the Compressional (P-wave), Shear (S-wave) and Rayleigh wave (R-wave). These three basic

waves have different attenuation, different propagation laws (wave speed) and different damping laws. The attenuation and propagation laws have been solved already, but the damping laws are still subject of study.

Bolton & Wilson (1990) concluded from cyclic tests on sand that the stress-strain behaviour of the soil is hysteretic and its corresponding damping parameters are strain dependent, though they are independent of the frequency up to 100 Hz. Van Baars (2011) noticed that man-made vibrations result in shear deformations with an amplitude no greater than $\hat{\gamma} = 0.01$. Van Baars used results from other researchers (Okur & Ansal, 2007, for instance) to demonstrate that fortunately the damping ratio is nearly constant up to this magnitude. Hysteretic damping is in fact a damping resulting from frictional shear deformation. Isotropic compression causes probably little or no damping.

In P -waves there is a deformation due to mostly isotropic compression but also some shear deformation, in S-waves there is only pure shear deformation and in R-waves there is a combination of mostly shear deformation but also deformation due to isotropic compression. Therefore the energy in the basic waves will not only attenuate differently and propagate differently, but also damp differently.

So, in order to have a better insight into the propagation of vibrations in a soil medium, the measured signal has to be decomposed into the basic waves and analysed separately. A main problem in the field is that, not independent waves are measured, but only superposed velocities or accelerations. So in order to study the measurements, a way to decompose the superposed waves into basic waves, should be found first.

2 DECOMPOSITION OF WAVES

In this paper this problem has been solved for a homogenous, elastic and isotropic soil, which is disturbed by a harmonically oscillating disc on the surface, see Figure 1.

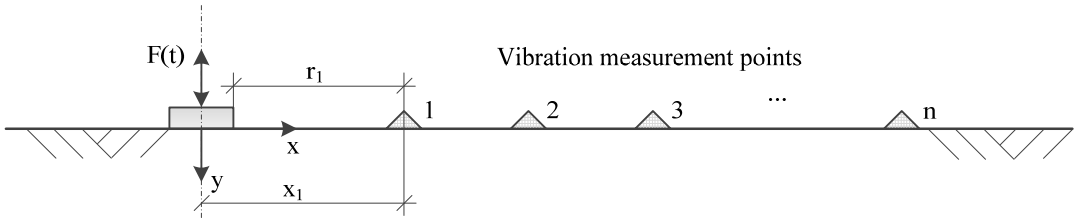

Fig. 1. Sketch of an oscillating plate and measurement points

The displacement of each point on the soil surface in direction *i* can be described as a superposition of the displacements of the three basic waves in that point:

$$u_i(r,t) = u_{p,i}(r,t) + u_{s,i}(r,t) + u_{r,i}(r,t) \tag{1}$$

where $u_{p,i}$, $u_{s,i}$, $u_{r,i}$, are the displacements of the P-, S- and R-wave respectively.

By taking into account the propagation laws of the general waves, Equation (1) can be rewritten for any measurement point as follows:

$$\begin{aligned} u_x(r,t) &= \hat{u}_{p,x}\sin\left(\omega t - k_p r - \Delta\phi_p\right) + \hat{u}_{s,x}\sin\left(\omega t - k_s r - \Delta\phi_s\right) - \hat{u}_{r,x}\cos\left(\omega t - k_r r - \Delta\phi_r\right) \\ u_y(r,t) &= \hat{u}_{p,y}\sin\left(\omega t - k_p r - \Delta\phi_p\right) + \hat{u}_{s,y}\sin\left(\omega t - k_s r - \Delta\phi_s\right) + \hat{u}_{r,y}\sin\left(\omega t - k_r r - \Delta\phi_r\right) \end{aligned} \tag{2}$$

where $\hat{u}_{j,i}$ is the amplitude of the j wave in the i direction, ω is the angular frequency of the harmonic wave, k_j is the j wave's number, $\Delta\phi_j$ is the phase shift of a the j wave.

In order to relate the measured vibrations of the different points with different distances, the attenuation laws of the basic waves will be used. The amplitudes of the body waves (P- and S-waves) attenuate proportional to x^{-1} and the surface wave (R-wave) attenuates proportional to $x^{-1/2}$, where x is the distance from the axis of symmetry, which is the middle of the disc (Fig. 1). For relatively small discs follows $x = r$. Now vibrations in any measurement point $i = 1 \ldots n$ can be expressed as functions of amplitudes in any other point, for example the 1st point:

$$\begin{aligned} u_{x,i}(r,t) &= \hat{u}_{p,x,1}\sin\left(\omega t - k_p r_i - \Delta\phi_p\right)\frac{x_1}{x_i} + \hat{u}_{s,x,1}\sin\left(\omega t - k_s r_i - \Delta\phi_s\right)\frac{x_1}{x_i} \\ &\quad -\hat{u}_{r,x,1}\cos\left(\omega t - k_r r_i - \Delta\phi_r\right)\sqrt{\frac{x_1}{x_i}} \\ u_{y,i}(r,t) &= \hat{u}_{p,y,1}\sin\left(\omega t - k_p r_i - \Delta\phi_p\right)\frac{x_1}{x_i} + \hat{u}_{s,y,1}\sin\left(\omega t - k_s r_i - \Delta\phi_s\right)\frac{x_1}{x_i} \\ &\quad +\hat{u}_{r,y,1}\sin\left(\omega t - k_r r_i - \Delta\phi_r\right)\sqrt{\frac{x_1}{x_i}} \end{aligned} \tag{3}$$

The back-calculated superposed signal can be used as a check, as well as the theoretical ratio of the R-wave's amplitudes on the surface $\hat{u}_{r,x,i} / \hat{u}_{r,y,i}$.

3 NUMERICAL SIMULATION

In order to check this technique, a 2-dimensional, axial symmetrical numerical simulation was performed with the Finite Element Method software Plaxis. The advantage of a numerical simulation is that the material damping can be put to zero. The general force-displacement matrix in Plaxis is based on the following equation:

$$[M]\{\ddot{u}\} + [C]\{\dot{u}\} + [K]\{u\} = \{F\} \tag{4}$$

where $[M]$ is the mass matrix, $\{u\}$ is the displacement vector, $[C]$ is the damping matrix, $[K]$ is the stiffness matrix and $\{F\}$ is the load vector. First and second derivatives of displacement vector are velocity and acceleration vectors respectively.

The damping matrix $[C]$ represents the material damping. In Plaxis 2D, Rayleigh damping is used, where $[C]$ is a function of the mass and stiffness matrices, according:

$$[C] = \alpha[M] + \beta[K] \tag{5}$$

where α and β are coefficients, which are kept zero in this simulation, to avoid any type of material damping.

The used geometry and mesh of the model can be found in Figure 2. The model is 50 m in length and width. The 10 measurement points for displacement recording were placed from 15 m to 24 m, at 1 m distance from each other. The soil is modelled with 15-node elements having a Young's modulus E = 51.02 MPa and a Poisson's ratio ν = 0.25. The oscillating

disc has a radius of 0.2 m, which is modelled with a plate element with stiffness $EI = 24$ MNm^2/m. First the disc is loaded with a static load of 20 kPa and later a harmonic load of ±10 kPa at 10 Hz is introduced.

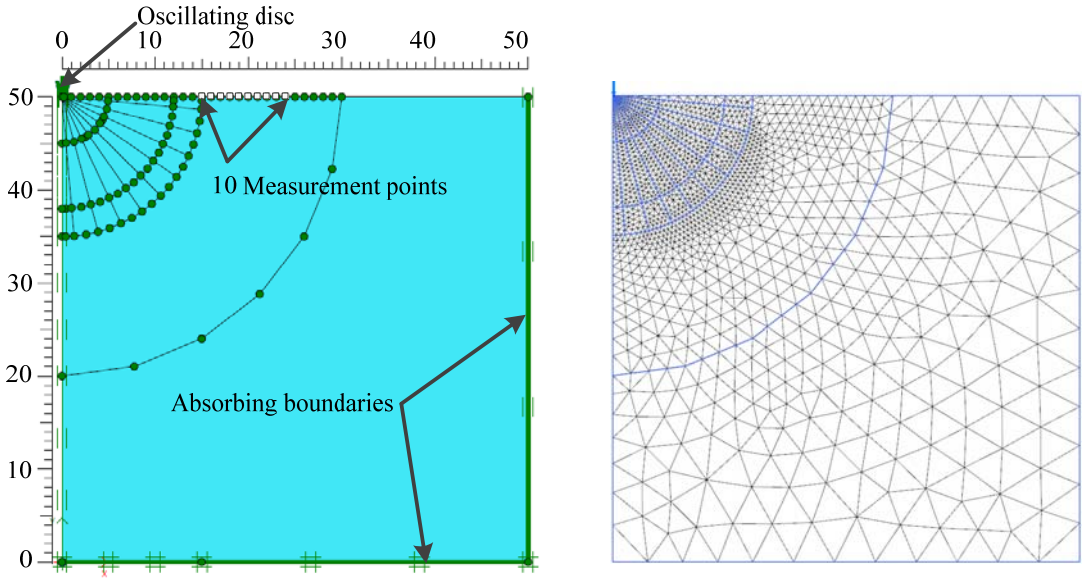

Fig. 2. Geometry and mesh of the FEM model

4 RESULTS

The displacements were first used after about 3 cycles, so that the starting up effect of the harmonic load has vanished. The time window for the measurement was also selected such that are no reflections yet from the absorbing boundaries, since they do not absorb perfectly.

4.1 First attempt

The idea of the first attempt was to use only the displacements which were measured at a selected time when the displacement reached a peak. It was assumed that the three basic waves were in phase with the original/superposed wave, similar as in the analytical solution of Miller and Pursey (1955).

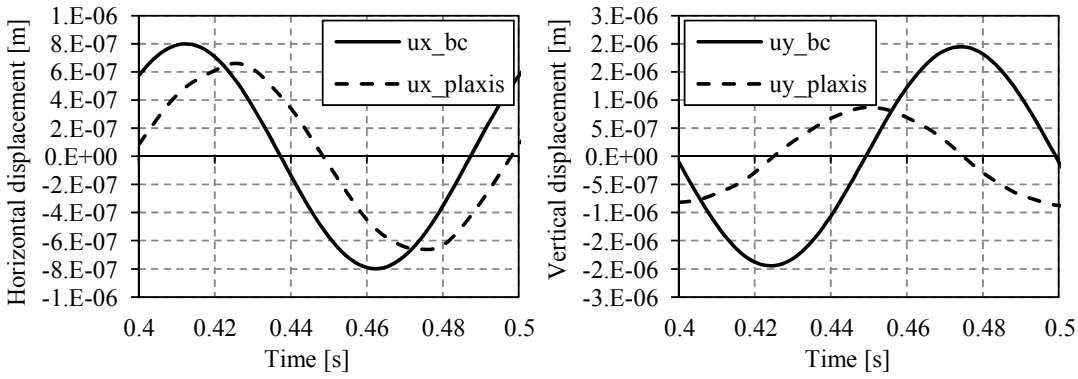

Fig. 3. First attempt: back-calculated results vs. Plaxis

The correlation factors are very low. The factor of the vertical component even becomes negative, which means there is no good solution. Also the ratio of the R-wave's amplitudes $\hat{u}_{r,x,i} / \hat{u}_{r,y,i}$ = 3.73 which is much greater than the theoretical $\hat{u}_{r,x,i} / \hat{u}_{r,y,i}$ = 0.682.

Only for the selected time (the peak of the dashed line) the solution almost fitted, but clearly not for the rest of the wave.

4.2 Attempt with phase shifts

A new attempt was done, but this time with allowing the basic waves to have different phases as the original/superposed wave. This leads to nine unknowns (six amplitudes and three phase shifts). Since the phases of the basic waves are now unknowns, the system of equations is not linear anymore, so the solution had to be found by using the least square method in an iterative way. In this attempt not only the peak values of the time-displacement graph, but all values of one cycle were used. One cycle $T = 0.1$ s. The calculations were performed with time steps of $\Delta t = 0.001$ s, which gives 100 time steps or points in a time-displacement graph. Since there are 10 measurement points with each 2 equations (horizontal and vertical); there is a system of 2000 equations. The horizontal and vertical displacements of the basic waves were solved and are shown in Figure 4.

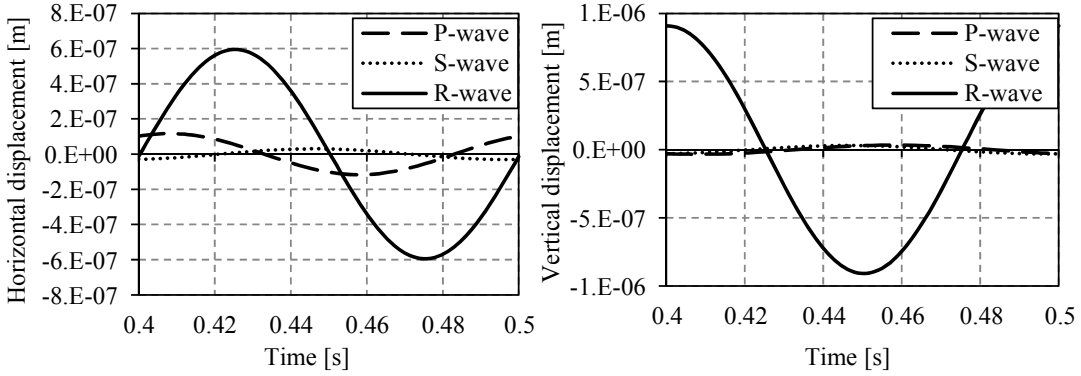

Fig. 4. Phase shifts: horizontal and vertical displacements of the basic waves

This time a perfect fit of the wave displacements was found for the back calculated wave with the recorded wave of Plaxis. The correlation factor R^2 is equal to 0.9986 for the combined displacements.

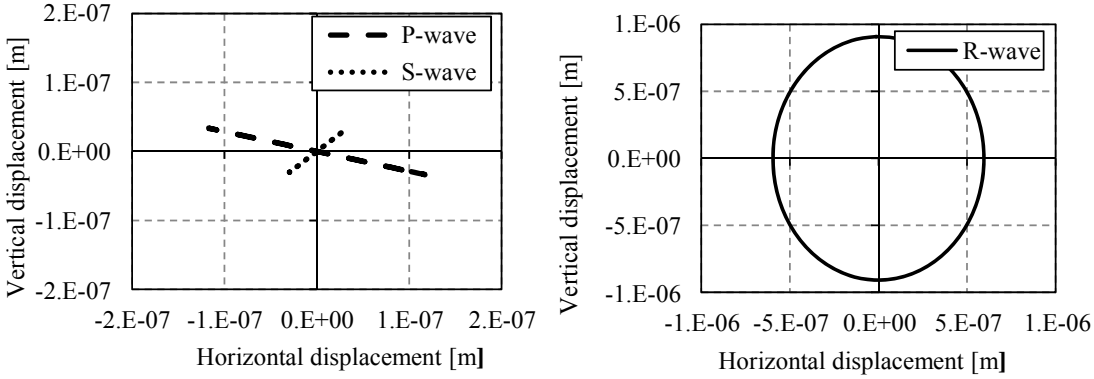

Fig. 5. Phase shifts: displacements on the surface of one cycle of the three basic waves

Figure 5 shows the displacements on the surface of one cycle of the three basic waves in point 1. Interesting is to note that both the P-wave and the S-wave do not act completely flat (horizontal for the P-wave and vertical for the S-wave). Also interesting is the ratio of the R-wave's amplitudes is found to be $\hat{u}_{r,x,i} / \hat{u}_{r,y,i} = 0.655$, which is in a quite good agreement with the theoretical $\hat{u}_{r,x,i} / \hat{u}_{r,y,i} = 0.682$.

4.3 Attempt with flat waves

The same attempt was done, but this time with the assumption that the body waves are flat, so the horizontal amplitude of the S-wave and the vertical amplitude of the P-wave are zero. Also the ratio of the theoretical R-wave's amplitudes was used, so $\hat{u}_{r,x,i} / \hat{u}_{r,y,i} = 0.682$. This reduces the amount of unknowns back to six (three amplitudes + three phase shifts).

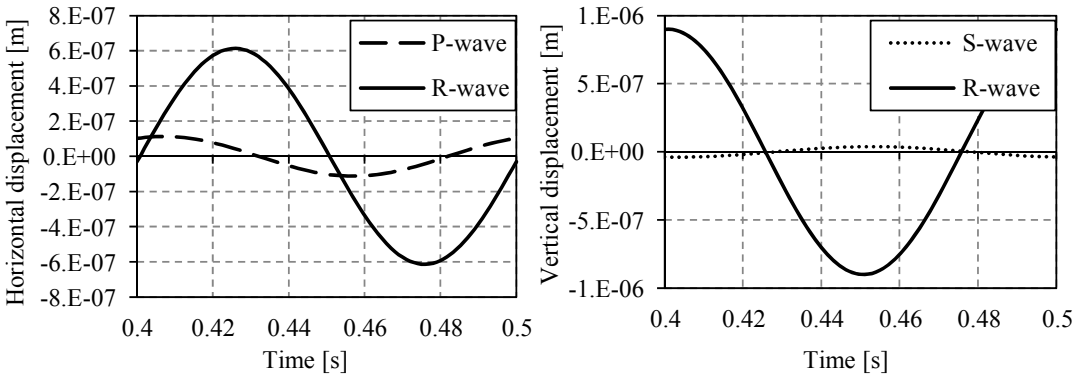

Fig. 6. Flat waves: horizontal and vertical displacements of the basic waves

Figure 6 shows the displacements on the surface of one cycle of the three basic waves in point 1.

Table 1. Effect of the reduction of unknowns

Wave	Direction	Unknown	9 unknowns	6 unknowns	Units
P	h	A_{px}	0.117	0.113	[m · 10^{-6}]
S	v	A_{sy}	0.031	0.039	[m · 10^{-6}]
R	h	A_{rx}	0.595	0.614	[m · 10^{-6}]
P	v	A_{py}	-0.034	-	[m · 10^{-6}]
S	h	A_{sx}	0.030	-	[m · 10^{-6}]
R	v	A_{ry}	0.908	from ratio	[m · 10^{-6}]
P	-	$\Delta\varphi_p$	-8.7	-12.1	[deg]
S	-	$\Delta\varphi_s$	-96.1	-71.1	[deg]
R	-	$\Delta\varphi_r$	51.9	53.5	[deg]
Ratio of the R-wave amplitudes					
		A_{rx} / A_{ry}	0.655	0.682	[-]
		mean(R^2)	0.9986	0.9982	

Forcing the body waves to be flat and the ratio of R-wave's amplitudes to be as the theoretical one, did not change the correlation factor very much. The combined mean

correlation factor for the horizontal and vertical displacements is still very high $R^2 = 0.9982$. The amplitudes and phase shifts are shown in Table 1. For most of them the difference is rather small, except for the S-wave's phase shift, which was found to have a difference of 25°.

The basic waves are shown in Figure 7 for one cycle when the soil body oscillates harmonically. As can be seen, the P- and S-waves are prior to the disc loading, but the R-wave is delayed. The values of the phase shifts shown in Figure 7 are the ones of Table 1.

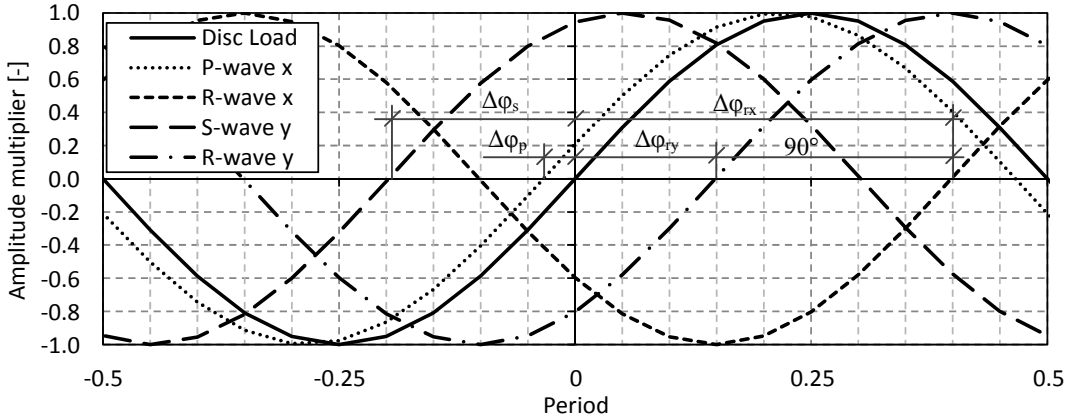

Fig. 7. Phase shifts of the basic waves

5 ENERGY BALANCE

Since the wave is now decomposed, the energy balance can be checked. Since there is no material damping, the emitted energy from the oscillating disc on the surface and the energy carried by the basic waves should be in balance (principle of energy conservation).

5.1 Total Energy

First of all the energy emitted from the source was calculated. For displacement recordings one point on the disc was selected. One point is sufficient, because the disc is stiff enough, so its own deformations are negligible.

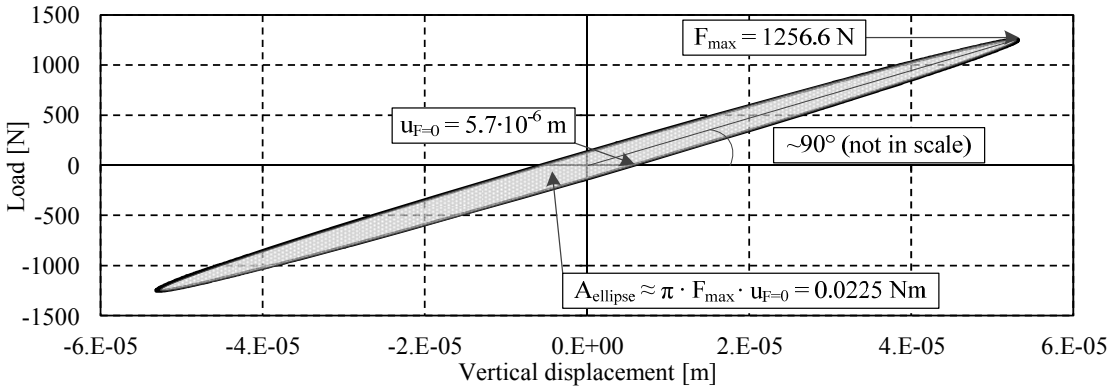

Fig. 8. Total emitted energy per cycle

The emitted energy per cycle from the oscillating disc was calculated from the load-displacement ellipse, which represents the work per cycle (Fig. 8). The total emitted energy was found to be 0.0225 Nm per cycle.

5.2 Energy in the basic waves

The energy in the R-wave was calculated by using the analytical solution of the R-wave's amplitudes in depth. These functions can be found in books of soil dynamics, like Kramer (1996), for instance. In order to estimate the total energy in the R-wave per cycle $E_{tot,r}$, the functions of the squared amplitudes (energy is proportional to the squared of the amplitudes) are integrated over depth for one wave length:

$$E_{tot,r} = \frac{1}{2}\rho\omega^2\left(2\pi r\lambda_r\right)\int_{y=0}^{y=\infty}\left(\hat{u}_x^2 + \hat{u}_y^2\right)dy \tag{6}$$

where ρ is the density of the medium, ω is the angular frequency of the harmonic wave, $\hat{u}_x$, $\hat{u}_y$ are the amplitudes of the R-wave in x and y direction respectively, r is the radius, λ_r is the length of the R-wave.

Unfortunately the analytical amplitude functions of the P- and S-waves, used by Miller and Pursey (1955), exist only for a very large radius, where the amplitudes are equal to zero on the surface. This is clearly not the case here. Therefore first the amplitude functions of the P- and S-waves have to be constructed.

Therefore the displacements were recorded in 19 additional points, placed in the soil volume (see Fig. 9 on the left). By using the amplitudes of the R-wave at the surface and the theoretical amplitude functions in depth, the displacements of the R-wave were calculated for the same 19 points. These displacements in time of the R-wave were subtracted from the recorded total displacements. The residual displacements in x and y directions were projected onto the x' and y' axis (see Fig. 9 on the right), which are the directions of the motion of an individual particle of the P- and S-waves, respectively. In this way, for the P- and S-waves, the amplitudes of the displacements in x' and y' axes were calculated.

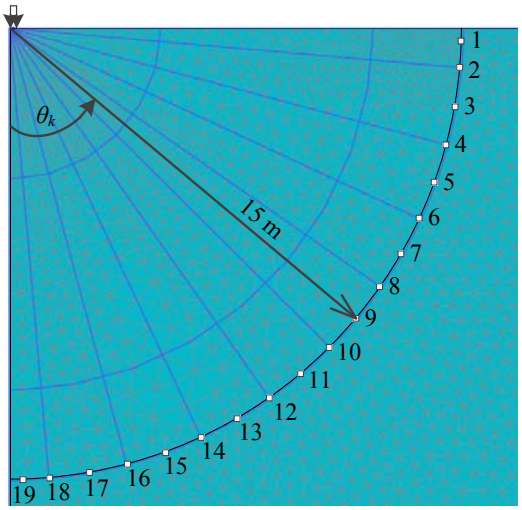

Coordinate system x'-y' at any point *k*

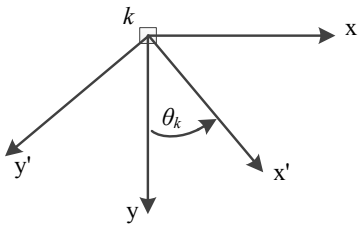

Displacements in u-v coordinate system

$$u_{x',k}(r,t) = u_{x,k}(r,t)\cdot\sin(\Theta_k) + u_{y,k}(r,t)\cdot\cos(\Theta_k)$$

$$u_{y',k}(r,t) = -u_{x,k}(r,t)\cdot\cos(\Theta_k) + u_{y,k}(r,t)\cdot\sin(\Theta_k)$$

Fig. 9. Additional points for the amplitudes of S- and P-waves

The total energy in the P- (or S-wave) per cycle $E_{tot,p(s)}$ can be calculated by integrating the squared functions of the amplitudes (energy is proportional to the squared of the amplitudes) over a surface of a half ball for one wave length:

$$E_{tot,p(s)} = \frac{1}{2}\rho\omega^2\left(2\pi r\lambda_{p(s)}\right)\int_{\Theta=0}^{\Theta=\pi/2}\left(\hat{u}_{p(s)}^2\cdot\sin\Theta\cdot r\right)d\Theta \tag{7}$$

where $\lambda_{p(s)}$ is the P- (or S-wave's) wave length, $\hat{u}_{p(s)}$ is the amplitude of the P- (or S-wave), Θ is the polar angle.

The total amount of energy carried by the basic waves was summed and found to be 0.0224 Nm per cycle, which is almost the same as the total emitted energy of 0.0225 Nm per cycle.

5.3 Distribution of Energy in Waves

Also the distribution of the total energy in the basic waves was checked. This problem was solved analytically by Miller and Pursey (1955), for a soil with Poisson's ratio v = 0.25, but this has never been checked numerically. The percentages of the total energy distribution in the basic waves can be found in Table 2.

Table 2. Distribution of the total energy in the basic waves

Solution	P-wave [%]	S-wave [%]	R-wave [%]
Analytical	6.9	25.8	67.4
FEM	10.8	28.5	60.7

As can be seen from this table, the distribution of the energy based on the analytical solution of Miller and Pursey fits reasonably well to the numerical solution, despite the fact that Miller and Pursey were not aware of the phase shifts of the basic waves. The small differences could be explained by different initial conditions between the solutions. First, in the analytical solution no phase shifts were considered. Second, a very small and flexible disc with infinite small radius was used, while in the numerical simulation a rigid disc was used. Third, numerical methods always have residual errors.

6 CONCLUSIONS

The example in this article discusses a harmonically oscillating disc on a homogeneous half space. The recorded superposed soil wave can be decomposed into its basic waves when multiple geophones are used. From the recorded data a system of non-linear equations can be assembled with six unknown parameters (three amplitudes and three phase shifts). These six parameters can be solved by using an iterative way of the least square method. This leads to a decomposition into the three basic waves, with each its own amplitude and phase shift. The superposition of only these basic waves describes very accurately the recorded superposed soil wave, proofing the existence of only three basic waves. The findings proof also that all three basic waves have phase shifts and these phase shifts are all different from each other. Both facts were not known before. Although it is important to notice the existing of the individual phase shifts, it is still not clear what causes them.

An energy balance showed that the amount of emitted energy by the load on the disc is the same as of the sum of energies of the basic waves. This is another type of evidence that only

three basic waves exist. The distribution of the energy over the three basic waves based on the analytical solution of Miller and Pursey (1955) fits reasonably well to the numerical solution shown in this article, despite the fact that Miller and Pursey were not aware of the phase shifts of the basic waves. The major part of the energy (more than 60 %) from a vertically oscillating disc on the surface goes into the R-wave.

REFERENCES

Journal

Okur, D.V. & Ansal A. (2007), "Stiffness degradation of natural fine grained soils during cyclic loading", Soil Dynamics and Earthquake Engineering, Vol. 27(9), 843-854.

Book

Kramer, S.L. (1996), Geotechnical Earthquake Engineering. Prentice Hall, New Jersey.

Proceedings

Bolton M.D. & Wilson J.M.R. (1990), "Soil stiffness and damping", Proceedings of The International Conference on Structural Dynamics, Eurodyn '90, University of Bochum, 1, 209-216,

Miller, G.F. & Pursey, H. (1955), "On the Partition of Energy between Elastic Waves in a Semi-Infinite Solid", Proceedings of the Royal Society of London. Series A, Mathematical and Physical Sciences, Vol. 233(1192), 55-69.

Van Baars, S. (2011), "Modelling of frictional soil damping in finite element analysis", Proceedings of The Second International Symposium on Computational Geomechanics, Croatia, ISBN 978-960-98750-1-1, April 2011.

Other

Hölscher, P. & Waarts, P. H. (2003), "Reliability of vibration prediction and reducing measures", Final Report. Delft Cluster, Delft.

EVALUATION OF BEARING CAPACITY OF SHALLOW STRIP FOUNDATION USING THE RANDOM FINITE ELEMENT METHOD

J. M. Pieczynska & W. Pula
Wroclaw University of Technology, Institute of Geotechnics and Hydrotechnics, Wroclaw, Poland

ABSTRACT: The *Random Finite Element Method (RFEM) was used to study the problem of strip footing embedded into cohesive and cohesionless soil. In the paper a single foundation was considered and discussed according to estimated bearing capacity statistics. For the first time in the analysis of the bearing capacity of spatially variable soil by means of RFEM , the effect of embedding has been taken into account. Analysis consisted of two types of soil. The first was blue clay from Taranto in Italy and the second was sand with a small residual cohesion. The soil parameters of blue clay were well stochastically defined, which allowed modeling cohesion and a friction angle as random fields. The authors have focused on the anisotropic case of the random field. The results clearly show that the introduction of anisotropy into random fields is more realistic, and makes RFEM predictions more effective for design purposes.*

1 INTRODUCTION

Reliability based design is one possible design approach suggested by building codes, such as Eurocodes. According to this approach the design of shallow footing can be devised into two groups of problems. The first is the influence of the random load and the second is the random character of soil properties. From a geotechnical point of view the second problem more heavily influences the randomness of bearing capacity estimation, on which shallow footing design is often based.

In the traditional approach of bearing capacity the Terzaghi formula (Terzaghi, 1943) is taken into account:

$$q_f = c'N_c + qN_q + 0.5\gamma BN_\gamma \tag{1}$$

where: q_f is the ultimate bearing stress, c' is the effective cohesion, q is the overburden load due to foundation embedment, γ is the soil unit weight, B is the footing width, and N_c, N_q and N_γ are the bearing capacity factors (the detailed equations can be found in literature, e.g. Bowels, 1996). In this paper, the authors have focused on the first two terms in the equation presented above. Thus, the ultimate bearing stress is defined as:

$$q_f = c'N_c + qN_q \tag{2}$$

Note that in this work, the estimates of the bearing capacity are obtained using the classical finite element method, and equation (2) is utilized solely for comparison of mean values.

The random character of the physical and mechanical soil parameters can be seen as fact, but the problem is how to effectively model such a problem. One of the methods is random field (Vanmarcke, 1983), which takes into account the mean value, standard deviation, distribution and correlation length of geotechnical parameters. The connection between random field theory and the deterministic finite element method leads to the random finite element method (RFEM). This method allows the estimation of the mean value and standard deviation of the bearing capacity by using Monte Carlo simulation. The numerical methodology of RFEM was first introduced by Griffiths and Fenton (1993) and applied in many geotechnical problems through the years (Griffiths & Fenton 2008).

Fenton and Griffiths (2001,2003) created a numerical algorithm for RFEM analysis of ultimate bearing stress. They focused only on the random character of soil strength parameters, neglecting the contributions of both the soil weight and the footing embedment. In the paper by Pieczyńska et al (2011) the soil weight problem was analyzed for two types of soil: clay (cohesion) and sand (cohesionless). This paper is a presentation of the influence of footing embedment on the bearing capacity. One more time, two types of soils were taken into account. The first is grey-blue clay from Taranto in Italy and the second is sand with small cohesion c = 1 kPa

Fenton and Griffiths (2003) only analyzed the isotropic case of the soil assuming that the spatial correlation is the same in both vertical and horizontal directions. Analyses have shown that the horizontal correlation length is much greater than the vertical one (Cherubini, 1997; Khemissa, 2011). In papers (Cherubini et al, 2009; Pieczynska et al, 2011) the anisotropic problem was presented and results clearly showed that the introduction of anisotropy into random fields is more realistic. Therefore the anisotropic case is analyzed within this study.

2 THE RANDOM FIELD MODEL FOR SOIL PROPERTIES

In this paper two random fields are taken into account, one for friction angle (ϕ) and one for cohesion (c), and both are not correlated. The algorithm used to generate such fields was Local Average Subdivision (LAS) (Fenton & Vanmarcke, 1990). The method generates normal random fields very effectively, with prescribed correlation structure.

The cohesion random field is assumed to be lognormaly distributed with mean μ_c, standard deviation σ_c and spatial correlation length θ_c. In order to generate the random field using the LAS method, a normally distributed random field (G_{lnc} (x)) should first be generated with zero mean value, unit variance and spatial correlation length. The equation below should then be used:

$$c(\mathbf{x}) = \exp\left\{\mu_{\ln c} + \sigma_{\ln c} G_{\ln c}(\mathbf{x})\right\} \tag{3}$$

where **x** is spatial position at which c is calculated and μ_{lnc} and σ_{lnc} are mean and standard deviation values of the underlying Gaussian field. They are related that are related to μ_c and σ_c by the following equations:

$$\sigma^2_{\ln c} = \ln\left(1 + \frac{\sigma_c^2}{\mu_c^2}\right) \tag{4}$$

$$\mu_{\ln c} = \ln \mu_c - \frac{1}{2}\sigma^2_{\ln c} \tag{5}$$

The second random field studied in this paper is the friction angle, which has a value directly related to the cohesion. It changes within a bounded interval. Fenton and Griffiths (2003) suggested to that field a bounded distribution – bounded of "tanh" distributed fields transformed as cohesion from the normal random field (G_ϕ(x)), according to:

$$\phi(\mathbf{x}) = \phi_{\min} + \frac{1}{2}(\phi_{\max} - \phi_{\min})\left\{1 + \tanh\left(\frac{sG_\phi(\mathbf{x})}{2\pi}\right)\right\} \tag{6}$$

where ϕ_{min} and ϕ_{max} are the limit values of the friction angle interval. Parameter s in the Eq. 6 is the scale factor depending on standard deviation. There is no analytic form of relationship between the standard deviation and the scale parameters. It can be obtained by numerical integration or by Taylor's expansion. The first order approximation leads to:

$$\sigma_\phi = \frac{1}{2}(\phi_{\max} - \phi_{\min})\frac{2s}{\pi\left(\exp(2\mu_\phi) + \exp(-2\mu_\phi) + 2\right)} \tag{8}$$

where μ_ϕ is the mean value of the friction angle which coincides with the value in the middle of the interval. The correlation structure of both fields is the same and expressed by the correlation function. In this paper the correlation function is assumed to be:

$$\rho = \exp\left\{-\sqrt{\left(\frac{2\tau_2}{\theta_x}\right)^2 + \left(\frac{2\tau_1}{\theta_y}\right)^2}\right\} \tag{9}$$

where $\tau_1=y_2-y_1$ and $\tau_2=x_2-x_1$ define the absolute distance between the two points in 2D space. Correlation lengths, θ_x and θ_y, can be specified from in situ tests, for example CPT tests (Cherubini et al, 2007; Vanmarcke, 1984).

3 SOIL PARAMETERS

The method of evaluating the bearing capacity of strip footing based on the finite element method incorporates five basic parameters: Young's modulus (E), Poisson's ratio (ν), dilation angle (ψ), cohesion (c), and friction angle (ϕ). Although the deformation parameters do not affect the bearing capacity they govern the initial elastic response of the soil. In the present study E, ν and ψ are held constant while c and ϕ are randomized. Plastic stress redistribution is accomplished using a viscoplastic algorithm merge with an elastic perfectly plastic (Coulomb – Mohr) failure criterion.

The study is considered on parameters of blue clay, which were well stochastically defined as a result of soil investigation (Cherubini et al, 2007). This kind of clay appears near Taranto in the South East of Italy. According to (Griffiths & Fenton, 2008) strength soil characteristics were defined as probability distributions and its parameters. All the values of the clay are shown in Table 1. The lower limit of the bounded distributed friction angle is ϕ_{min}=5˚, upper limit ϕ_{max}=35˚ and scale parameter s=2.27.

Table 1. Random characteristics of Taranto blue clay

	Mean value,	Standard deviation,	Distribution,
Cohesion (c)	36 kPa	20 kPa	lognormal
Friction angle (ϕ)	20°	4.8°	bounded
Young's modulus (E)	36 MPa		deterministic
Poisson's ratio (ν)	0.29		deterministic
Dilation angle (ψ)	20°		deterministic
Surcharge ($q=\gamma D$)	19 kPa		deterministic

The second soil was sand with small residual cohesion, c = 1kPa. The cohesion was used in the study to eliminate the problem of continuity of stress in the Coulomb – Mohr failure model. The probabilistic characteristics of sand are given in Table 2. The lower limit of the bounded distributed friction angle is $\phi_{min}=31^o$, upper limit $\phi_{max}=36^o$ and scale parameter s=2.41. Fig. 1 shows the comparison of friction angle probability density functions of clay and sand.

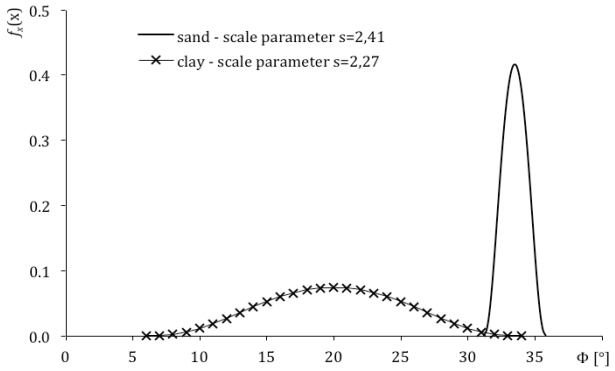

Fig. 1. Shapes of friction angle probability density function (bounded type).

Table 2. Random characteristics of sand

	Mean value,	Standard deviation,	Distribution,
Cohesion (c)	1 kPa	0.2 kPa	lognormal
Friction angle (ϕ)	33°	0.7°	bounded
Young's modulus (E)	100 MPa		deterministic
Poisson's ratio (ν)	0.25		deterministic
Dilation angle (ψ)	33°		deterministic
Surcharge ($q=\gamma D$)	19 kPa		deterministic

Setting the dilation angle equal to the friction angle means a presence of plastic dilation when yielding the soil.

4 FINITE ELEMENT METHOD

The bearing capacity analysis carried out in this paper uses 8 node quadrilateral elements. The theoretical basis of the method is described in detail in a book written by Smith and Griffiths (2004). In the first step the authors check the mesh influence on the bearing capacity

deterministic value. Fig.2 shows how the deterministic value of the bearing capacity changes according to changes in mesh size. There are two curves for each soil. Y=20 is a graphic interpretation for 20 elements in y-direction (vertical) and Y=30 for 30 elements.

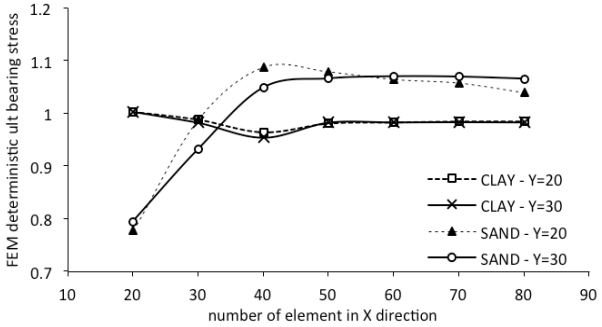

Fig. 2. Deterministic bearing capacity versus number of elements in x-direction (all standardized on analytical value)

According to the results presented in Fig. 2 for further investigations the authors decided to use a mesh with a size of 50 elements in x – direction and 20 elements in y – direction (Fig. 3). Each element is square with a side length of 0.1 m and the strip footing occupies 10 elements, thus giving a width of B=1 m. The additional mesh model is shown in Fig. 3 and contains an overburden load due to foundation embedment.

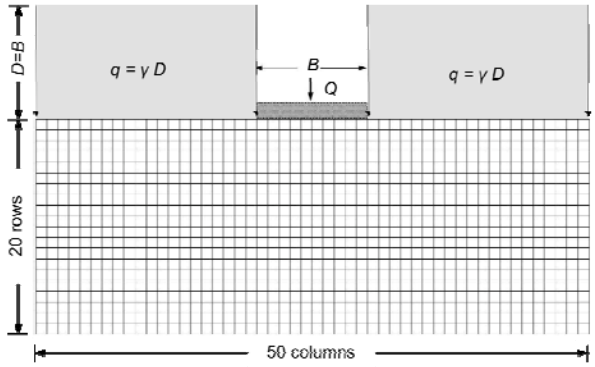

Fig. 3. Mesh used in analyses.

The idea of the random finite element method consists of merging the random field theory and finite element method. Every random field is discretized to finite mesh using the Local Averaging Method (Vanmarcke, 1983). Important parameters are correlation lengths θ_x and θ_y . The difference between isotropy and anisotropy in random fields is illustrated in Fig.4.

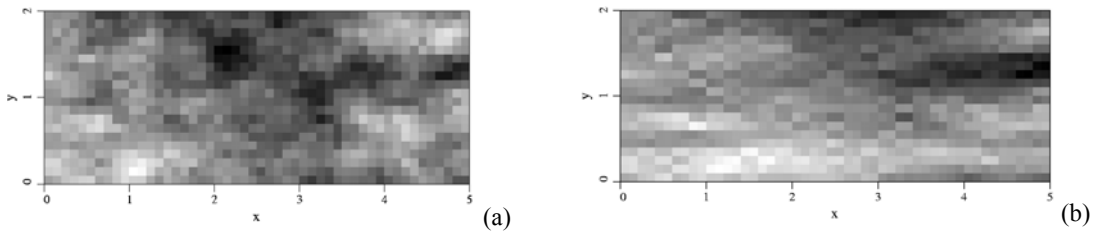

Fig. 4. Analyzed mesh of (a) isotropic soil with $\theta_x=0.5$, $\theta_y=0.5$; (b) anisotropic case with $\theta x=5.0$, $\theta_y=0.5$. The darker regions indicate weaker soil.

After many repetitions of numerical simulation, the estimation of the first two moments is possible. This is done through the use of Monte Caro simulation. In order to check the speed of convergence in the simulation process, computations were carried out for different numbers of realizations. In previous papers authors experience allowed 300 realizations as the minimal number. Results for Taranto blue clay were made according to that assumption, but for sand the authors used 500 realizations as the standard.

5 RESULTS

The problem analyzed in the present paper concerns the influence of footing embedment on bearing capacity. Computations within this study have been carried out for anisotropic random fields. It means that the horizontal correlation length differs from the vertical one. In the vertical direction only one correlation length θ_y has been considered – 1m. The parameter of study was the influence of the horizontal correlation length θ_x on bearing capacity parameters. In the present paper θ_x is equal to 0.2; 0.5; 0.7; 1; 5; 10; 50m. The correlation lengths for cohesion and friction angles are the same.

5.1 Taranto blue clay

Table 3 contains bearing capacity deterministic values of surface and embedded footing. The values show that FEM and analytical results are in good agreement. Fig. 5 shows the results of random ultimate bearing capacity mean value versus horizontal correlation length. Each curve express the quotient of expected value received from RFEM computations to the deterministic value calculated by FEM (second column of the Table 3). On the horizontal axis the fluctuation scale θ_x is standardized by the foundation width (B=1m). One curve shows the mean value of the surface footing, and the second curve shows the embedded footing.

Table 3. Deterministic value for clay

	FEM deterministic value	Analytic value
Surface foundation	528.491 kPa	538.50 kPa
Embedded footing	657.998 kPa	660.09 kPa

Both curves have the same progress. The average bearing capacity is greater for embedded footing than for surface one, which is compatible with the analytic situation (Table 3). There is almost no difference in progress between the curves, which may be due to the effect of the low sensitivity of bearing capacity random character on Both curves have local minimum in θ=1m.

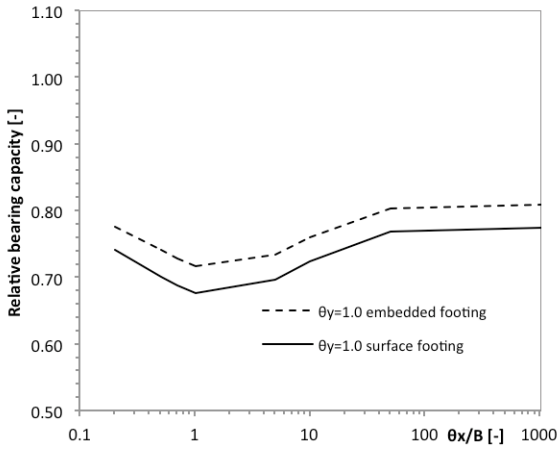

Fig. 5. Relative bearing capacity versus horizontal correlation length for Taranto blue clay.

Fig. 6 shows the standard deviation of bearing capacity as a function of the horizontal correlation length. Both curves have similar shapes, characterized by a constant increase when increasing the correlation length. For large values of horizontal correlation length (θ_x>10) the deviation is stabilizing.

A detail worth mentioning is the slight difference of the standard deviation with significant variations in the average (about 120 kPa). In the effect in Fig.7 – bearing capacity coefficient of variation versus horizontal correlation length – the attenuation of coefficient is visible, as a result of the foundation embedment.

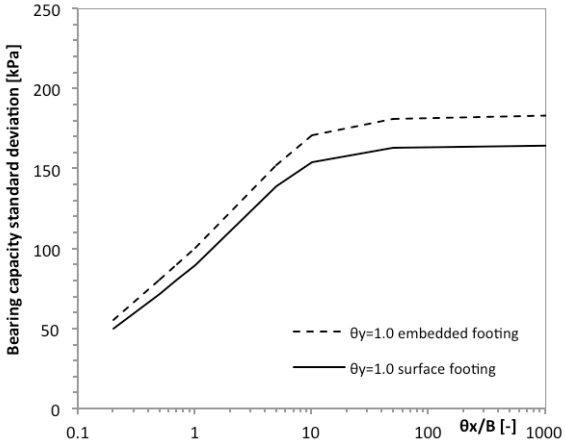

Fig. 6. Bearing capacity standard deviation versus horizontal correlation length for Taranto blue clay.

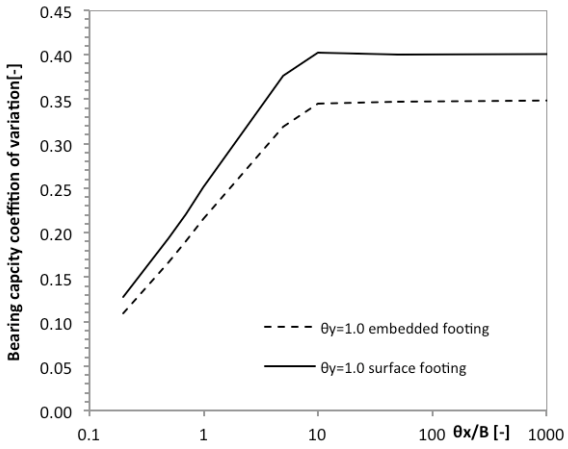

Fig. 7. Bearing capacity coefficient of variation versus horizontal correlation length for Taranto blue clay.

The coefficient of variation as well as the standard deviation of the bearing capacity are stable at a value higher than θ_x=10m.

In the paper (Fenton & Griffiths, 2003) the probability distribution of the shallow foundation based on weightless cohesive soil has been estimated. It has been shown that the bearing capacity obtained for random fields of cohesion and friction angles fits well to the lognormal distribution. In this paper the histogram of the results obtained for embedded footing on weightless cohesive soil is compared with the lognormal distribution function. For this purpose the numerical simulation on a sample of 2000 realizations has been computed. The results are shown in Fig.8.

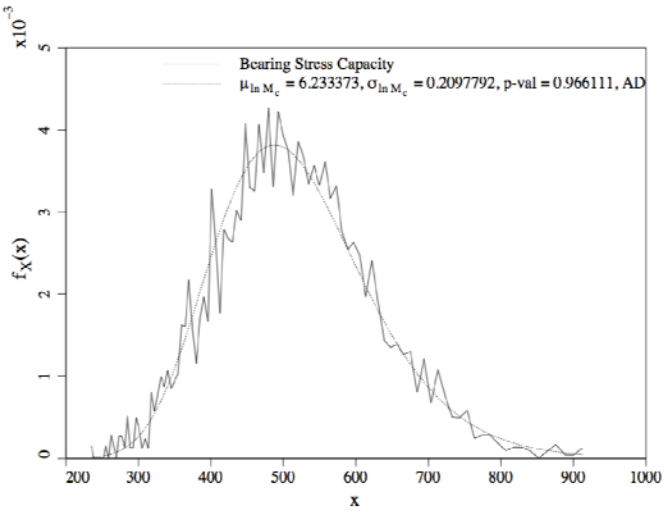

Fig. 8. The estimation theoretical density function of lognormal distribution to the empirical histogram of the bearing capacity (sample of 2000 realizations)

The dashed line, in Fig.8, shows the theoretical probability density function. In addition, hypothesis of lognormality has been tested Chi - square and Anderson – Darling test. Both of them show that there was no reason for rejecting the hypothesis.

5.2 Sand

The second soil analyzed in this paper is sand with small residual cohesion. Table 3 shows the results for deterministic FEM and analytic computations. FEM and analytical results are

closed one to another. In Fig. 9 the relative bearing capacities (define as in section 5.1) have been presented. There are two curves presented, one for shallow foundation, and the second one for embedment footing.

Table 3. Deterministic value for sand

	FEM deterministic value	Analytic value
Surface foundation	41.69 kPa	38.64 kPa
Embedded footing	534.85 kPa	534.39 kPa

The curves shown in Fig. 9 have similar character to the curves relating to the cohesive soil (Fig.5). It should be noted that in the case of cohesionless soil the curves are not parallel. In addition, the curve for the surface foundation has a local minimum for the horizontal correlation length θ_x=1m. It can be observed that both curves in Fig. 9 have higher standardized average bearing capacity than the curves in Fig. 5. It seems to be caused by the cohesion being less variable.

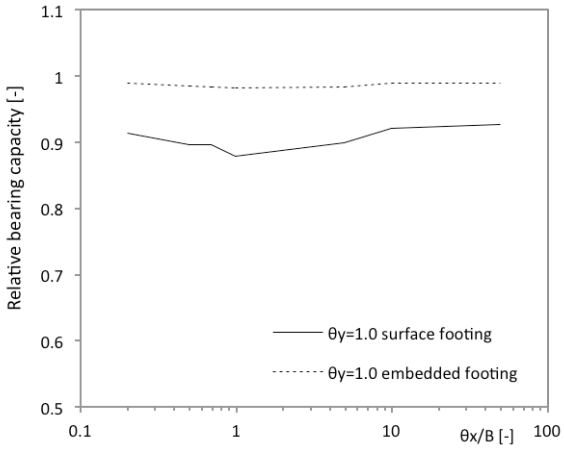

Fig. 9. Relative bearing capacity versus horizontal correlation length for sand.

Fig. 10 shows the result of standard deviation for sand. It is increasing as the horizontal correlation length increases. However the surface footing curve increase much more than the second one.

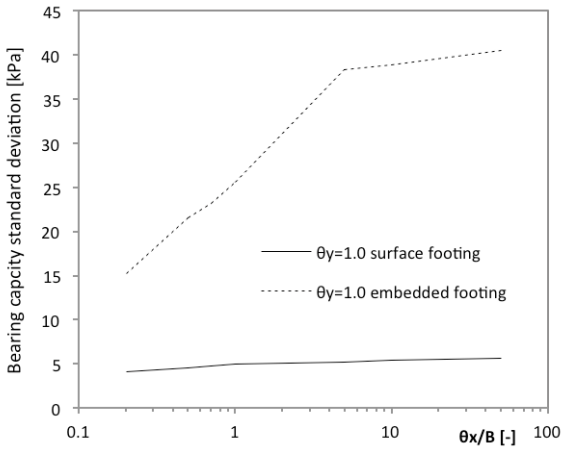

Fig. 10. Bearing capacity standard deviation versus horizontal correlation length for sand.

Coefficients of variation for cases with or without the overburden load q are shown in Fig. 11. It seems to be not very sensitive to an increase in the horizontal scale value compared to curves shown in Fig. 7. On the other hand the bearing capacity coefficient of variation stabilizes with respect to horizontal correlation length. Although the coefficient is suppressed when the surcharge next to the footing is taken into account.

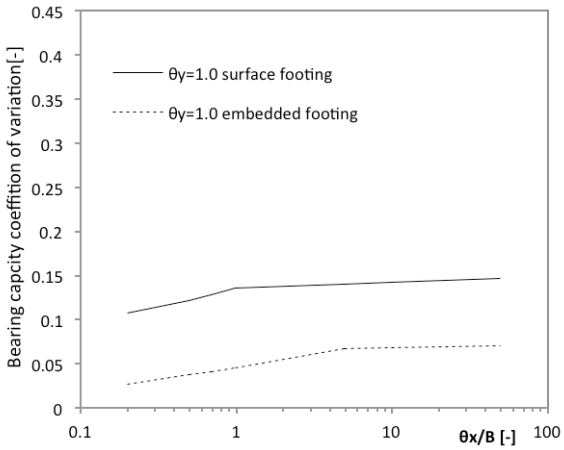

Fig. 11. Bearing capacity coefficient of variation versus horizontal correlation length for sand.

Another shape of distributions has been obtained for the bearing capacity of the sand. In Fig. 12 the surface footing histogram is compared with the lognormal distribution function. The comparison to the lognormal distribution is not perfect but from hypotheses, which have been examined by statistical goodness-of-fit test – Chi-square, lognormal gave the best evaluation.

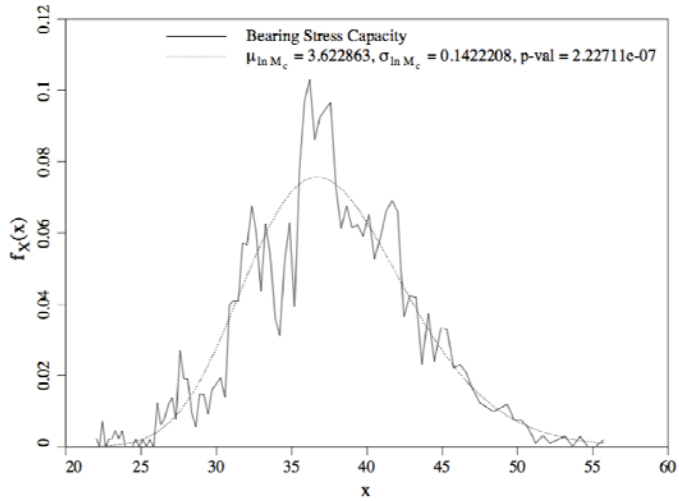

Fig. 12. The estimation theoretical density function of lognormal distribution to the empirical histogram of the bearing capacity (sample of 2000 realizations) for a shallow foundation on sand.

Lognormal distributions seem to be satisfactory for both cases obtained for sand. As in the previous case statistical goodness-of-fit testing has been carried out. In the case of embedded footing the results of fitting to the lognormal distribution are better than for the surface one.

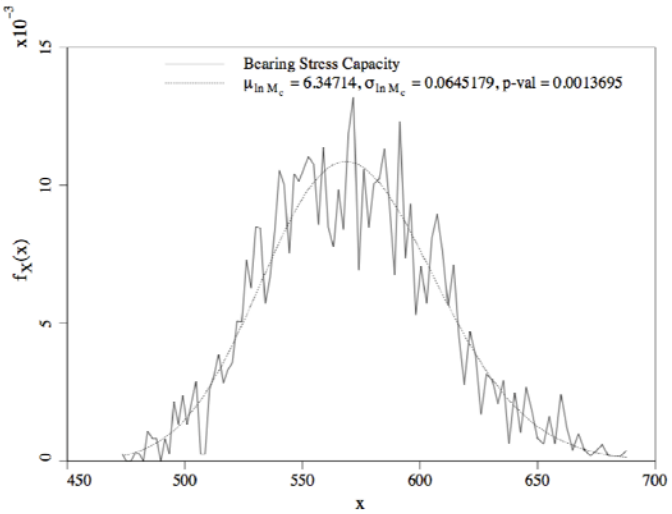

Fig. 13. The estimation theoretical density function of lognormal distribution to the empirical histogram of the bearing capacity (sample of 2000 realizations), for an embedded foundation on sand.

6 CONCLUDING REMARKS

In this paper the Random Finite Element Method has been implemented in the investigation of probability characteristics of bearing capacity. The analyzed problem consists of two types of soil: cohesive clay and sand with small residual cohesion. On the other hand two cases of foundation have been mentioned: a surface foundation and an embedded one. To each case a different horizontal correlation length has been taken into account. Results clearly show that the introduction of surcharge next to the footing suppresses the variability of the bearing capacity. The cohesive soil has demonstrated far greater bearing capacity fluctuations in comparison to the cohesionless one. It has been demonstrated that a lognormal distribution stands for reasonable evaluation of bearing capacity probability distribution.

ACKNOWLEDGMENT

This article, as a research project, was supported by Polish Government funds for science from 2010-2013.

REFERENCES

Bowles, J.E. (1996), Foundation Analysis and Design, (5th Ed.), New York: McGraw Hill.

Cherubini, C. (1997), "Data and consideration on the variability of geotechnical properties of soils", Proceedings of the ESREL Conf., Lisbon, 1538-1591.

Cherubini, C. and Vessia, G. & Pula, W. (2007), "Statistical soil characterization of Italian sites for reliability analysis", Proceedings., Characterization and Engineering properties of natural soils, Tan, Phoon, Hight and Lerouell (eds.), Singapore: 2681-2706.

Cherubini, C. Vessia, G. Pieczynska, J. & Puła, W. (2009), **"**Application of random finite element method to bearing capacity design of strip footing" Journal of GeoEngineering, Vol. 4 (3), 103-112.

Fenton, G.A. & Griffiths, D.V. (2008), Risk Assessment in Geotechnical Engineering, John Wiley & Sons, New York.

Fenton, G.A & Griffiths, D.V. (2003), "Bearing capacity prediction of spatially random c-φ soils". Canadian Geotechnical Journal, 40(1), 54–65.

Fenton, G.A & Vanmarcke, E.H. (1990), "Simulation of random fields via local average subdivision". ASCE Journal of Geotechnical Engineering, 116(8), 1733-1749.
Griffiths, D.V. & Fenton, G.A. (2001), "Bearing capacity of spatially random soil: the undrained clay Prandtl problem revisited". Geotechnique, 54(4), 351–359.
Griffiths, D.V. & Fenton, G.A. (1993), "Seepage beneath water retaining structures founded on spatially random soil". Géotechnique, 43(6), 577-587.
Khemissa, M. (2011), "Characterization of the anisotropy of a normally consolidated soft clay". Studia Geotechnica et Mechanica, 33(2), 41-65
Smith, I.M. & Griffiths, D.V. (2004), Programming the Finite Element Method, 4th Edition New York, NY John Wiley & Sons.
Pieczynska, J.M. Puła W. Griffiths D.V. Fenton, G.A. (2011), "Probabilistic characteristics of strip footing bearing capacity evaluated by random finite element method". in Proc. of ICASP 2011, Paper No. 10321 (CD-ROM), Zurich, Switzerland, August, 2011.
Terzaghi, K. (1943), Theoretical Soil Mechanics, New York: John Wiley & Sons.
Vanmarcke, E. (1983), Random Fields: Analysis and Synthesis, Cambridge MA: MIT Press.

AN OPTIMIZATION METHOD FOR APPROXIMATING THE MACROSCOPIC STRENGTH CRITERION OF STONE COLUMN REINFORCED SOILS

Maxime Gueguin, Ghazi Hassen, Jérémy Bleyer and Patrick de Buhan
Université Paris-Est, Laboratoire Navier (UMR 8205), CNRS, ENPC, IFSTTAR, Marne-La-Vallée, France

ABSTRACT: *In this contribution, the yield design homogenization method is applied to the evaluation of the ultimate bearing capacity of a purely cohesive soil reinforced by a periodic array of columnar inclusions, made of a purely frictional material (stone column technique). The method is implemented following a three-step procedure. a) First, the numerical determination of the macroscopic strength criterion is performed using the kinematic approach of yield design. b) Second, an easier to handle formulation of the criterion is obtained as the sum of a few ellipsoids in the stress space. c) Finally, the so-obtained approximation is incorporated into a numerical code, leading to the determination of an optimized upper bound for the ultimate load bearing capacity of a reinforced soil foundation, which is compared with previously obtained estimates for the same problem.*

1 INTRODUCTION

The growing need of constructions on poor quality soils has fostered the development of various soil improvement methods, among which the so-called ”stone column” reinforcement technique concerned by this contribution. This technique generally consists in incorporating into a purely cohesive native soil, a periodic distribution of cylindrical inclusions made of a highly frictional material (Priebe 1995). One of the main objectives of such a reinforcement technique is to increase the ultimate bearing capacity of a foundation soil subject to vertical loading. A key ingredient to such a calculation is the prior determination of the macroscopic strength criterion of the reinforced soil regarded as a homogenized material.

Using a homemade limit analysis code, this contribution presents a numerical upper bound estimate for the criterion in the stress space, for a given reinforcement volume fraction, soil cohesion and reinforcement friction angle (section 2). In view of being able to analyze the stability of a stone column-reinforced structure, a numerical optimization procedure is proposed based on the use of convex ellipsoidal sets defined by few parameters, which are combined in such a way as to obtain a fairly accurate approximation to the criterion (section 3). In section 4, the whole procedure is illustrated on producing an upper bound kinematic estimate for the ultimate bearing capacity of a stone column reinforced foundation.

2 AN IMPROVED UPPER BOUND FOR THE MACROSCOPIC STRENGTH CRITERION OF REINFORCED SOIL

2.1 Problem statement

A stone column reinforced soil may be seen as a periodic composite material, made of a regular array of cylindrical columnar inclusions embedded into the soil mass (see Figure 1). The reinforcement layout may be entirely described by a unit cell $\mathcal{C}$ of side s (spacing between two neighboring columns) containing one single reinforcing column of radius ρ. The reinforcement volume fraction η, which is the ratio between the volume occupied by the column and the volume of the unit cell, is then defined as:

$$\eta = \frac{\pi \rho^2}{s^2} \tag{1}$$

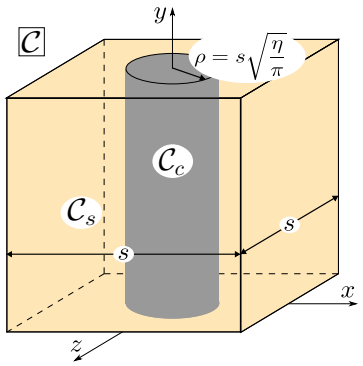

Fig. 1. Representative unit cell for a stone column reinforced soil.

The native soil is taken here as a purely cohesive soft clay, its strength capacities being described by a von Mises yield condition of the form:

$$f^s(\underline{\underline{\sigma}}) = \sqrt{\frac{1}{2}\underline{\underline{s}} : \underline{\underline{s}}} - k \leq 0 \tag{2}$$

where $\underline{\underline{s}}$ is the deviatoric stress and k the yield strength under pure shear conditions.

The column constituent material is a purely frictional granular soil obeying a Drucker-Prager strength criterion of the form:

$$f^c(\underline{\underline{\sigma}}) = \sqrt{\frac{1}{2}\underline{\underline{s}} : \underline{\underline{s}}} + a(\varphi)\mathrm{tr}\underline{\underline{\sigma}} \leq 0 \tag{3}$$

where φ denotes the friction angle. The expression of a is chosen as a function of φ in such a way that, under plane strain conditions, the Drucker-Prager criterion coincides with the classical Mohr-Coulomb criterion associated with the same friction angle. Calculations will be carried out with a perfect bonding condition at the soil-column interface.

2.2 Macroscopic strength criterion

Referring to this yield design (or limit analysis) theory, the macroscopic strength domain $\mathbf{G}^{hom}$ and the related strength criterion F of the reinforced soil are defined as follows:

$$\underline{\underline{\Sigma}} \in \mathbf{G}^{hom} \Leftrightarrow F\left(\underline{\underline{\Sigma}}\right) \leq 0 \Leftrightarrow \begin{cases} \forall \underline{\underline{\sigma}} \text{ statically admissible with } \underline{\underline{\Sigma}} \\ \forall \underline{\xi} \in \mathcal{C}_\alpha,\ f^\alpha\left(\underline{\underline{\sigma}}^\alpha\left(\underline{\xi}\right)\right) \leq 0, \quad \alpha = s, c \end{cases} \tag{4}$$

where $\mathcal{C}_\alpha$ is the unit cell sub-domain occupied by constituent α (c for column or s for soil) and $f^\alpha(.)$ its yield strength function given by either (2) or (3). A stress field $\underline{\underline{\sigma}}$ is statically admissible with a macroscopic stress $\underline{\underline{\Sigma}}$ if it complies with the following conditions:

- $\underline{\underline{\sigma}}$ is in equilibrium with no body forces:

$$\mathrm{div}\underline{\underline{\sigma}} = 0 \tag{5}$$

- the stress vector remains continuous across any possible discontinuity surfaces of the stress field:

$$\left[\underline{\underline{\sigma}}\right] \cdot \underline{n} = 0 \tag{6}$$

  where $\left[\underline{\underline{\sigma}}\right]$ denotes the jump of $\underline{\underline{\sigma}}$ across such a surface following its unit normal $\underline{n}$.
- $\underline{\underline{\sigma}} \cdot \underline{n}$ is *anti-periodic*, which means that it takes opposite values at any couples of points located on the opposite sides of the unit cell.
- $\underline{\underline{\Sigma}}$ is equal to the volume average of $\underline{\underline{\sigma}}$ over the unit cell:

$$\underline{\underline{\Sigma}} = \frac{1}{|\mathcal{C}|}\int_{\mathcal{C}} \underline{\underline{\sigma}}\, \mathrm{d}\mathcal{C} = \left\langle \underline{\underline{\sigma}} \right\rangle \tag{7}$$

2.3 Kinematic definition

According to the periodic homogenization method, a velocity field kinematically admissible with a macroscopic strain rate tensor $\underline{\underline{D}}$ is given, up to a rigid body motion, by:

$$\forall \underline{\xi} \in \mathcal{C},\ \underline{U}\left(\underline{\xi}\right) = \underline{\underline{D}} \cdot \underline{\xi} + \underline{\nu}\left(\underline{\xi}\right) \tag{8}$$

where $\underline{\nu}\left(\underline{\xi}\right)$ is a *periodic* fluctuation. The dualisation of the equilibrium equations by means of the *virtual work principle* with strength conditions (2) and (3), leads to the following kinematic definition of the macroscopic strength domain (Suquet 1985; de Buhan 1986):

$$\mathbf{G}^{hom} = \bigcap_{\underline{\underline{D}} \in \mathbb{R}^6} \left\{ \underline{\underline{\Sigma}} \,|\, \underline{\underline{\Sigma}} : \underline{\underline{D}} \leq \pi^{hom}\left(\underline{\underline{D}}\right) \right\} \tag{9}$$

with

$$\pi^{hom}\left(\underline{\underline{D}}\right) = \min_{\underline{U} \text{ ka } \underline{\underline{D}}} \left\{ \left\langle \pi\left(\underline{\underline{d}}\right) \right\rangle = \frac{1}{|\mathcal{C}|}\sum_\alpha \int_{\mathcal{C}_\alpha} \pi^\alpha\left(\underline{\underline{d}}\right)\, \mathrm{d}\mathcal{C}_\alpha \right\} \tag{10}$$

where $\underline{\underline{d}}$ denotes the microscopic strain rate tensor field associated to the velocity field $\underline{U}$, which is assumed to remain continuous, and $\pi^\alpha\left(\underline{\underline{d}}\right)$ is the support function of constituent α, given by:

$$\pi^s\left(\underline{\underline{d}}\right) = \begin{cases} k\sqrt{2\underline{\underline{d}} : \underline{\underline{d}}} & \text{if } \mathrm{tr}\underline{\underline{d}} = 0 \\ +\infty & \text{otherwise} \end{cases} \tag{11}$$

for the purely cohesive soil, and

$$\pi^c\left(\underline{\underline{d}}\right) = \begin{cases} 0 & \text{if } \mathrm{tr}\underline{\underline{d}} \geq 3\sqrt{2}a\sqrt{\underline{\underline{d}} : \underline{\underline{d}} - \frac{1}{3}\left(\mathrm{tr}\underline{\underline{d}}\right)^2} \\ +\infty & \text{otherwise} \end{cases} \tag{12}$$

for the purely frictional column material.

2.4 *Numerical simulation and results*

An upper bound estimate to the previously defined macroscopic strength domain is carried out by a homemade limit analysis code (similar to that developed by Makrodimopoulos & Martin (2007) or Pastor et al. (2011)) and using the second-order cone programming solver MOSEK (2008). Calculations are performed on the reinforced soil unit cell $\mathcal{C}$ leading to the evaluation of limit loads under plane strain conditions in the (x, y)-plane. This means that the unit cell is subject to a macroscopic strain rate tensor of the form:

$$\underline{\underline{D}} = \underline{\underline{\Delta}}(\gamma, \delta) = \begin{pmatrix} \cos\gamma\cos\delta & \frac{1}{2}\sin\delta & 0 \\ \frac{1}{2}\sin\delta & \sin\gamma\cos\delta & 0 \\ 0 & 0 & 0 \end{pmatrix} \tag{13}$$

where angles γ and δ specify the orientation of the loading in the space of plane strains in the Oxy-plane (see Figure 2(a)).

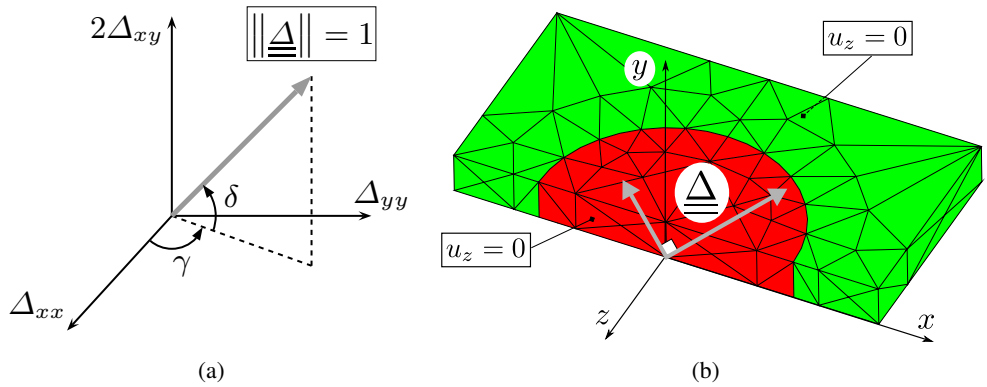

(a) (b)

Fig. 2. Plane strain loading of the unit cell: (a) angular parametrization, (b) mesh adopted for the numerical optimization.

As described by Hassen et al. (2013), thanks to the geometrical, material and loading symmetries, calculations may be performed on one half of the unit cell with a smooth contact condition on the sides parallel to the Oxy-plane. It can be also proved that the analysis can be restricted to a "slice" in the direction y. The mesh chosen to modelize the problem is given in Figure 2(b) with ten noded tetrahedric elements. Here the maximal resisting work of the unit cell will be minimized using, in each element, a velocity field chosen as a quadratic function of the coordinates, so that the strain field will be linear.

The loading is prescribed by applying *periodicity* conditions to the sides normal to the Ox-axis as well as to the sides normal to the Oy-axis according to equation (8). For each couple of angles (γ, δ), the numerical evaluation of the support function (denoted by $\pi^{num}(\underline{\underline{\Delta}})$) is stored verifying:

$$\pi^{hom}(\underline{\underline{\Delta}}) \leq \pi^{num}(\underline{\underline{\Delta}}),\ \forall \underline{\underline{\Delta}} \tag{14}$$

As an illustrative example, the so-obtained macroscopic strength criterion has been drawn in the space of non-dimensional macroscopic stresses $(\frac{\Sigma_{xx}}{k}, \frac{\Sigma_{yy}}{k}, \frac{\Sigma_{xy}}{k})$ for the following typical values:

$$\eta = 28\%, \quad \varphi = 35^\circ \tag{15}$$

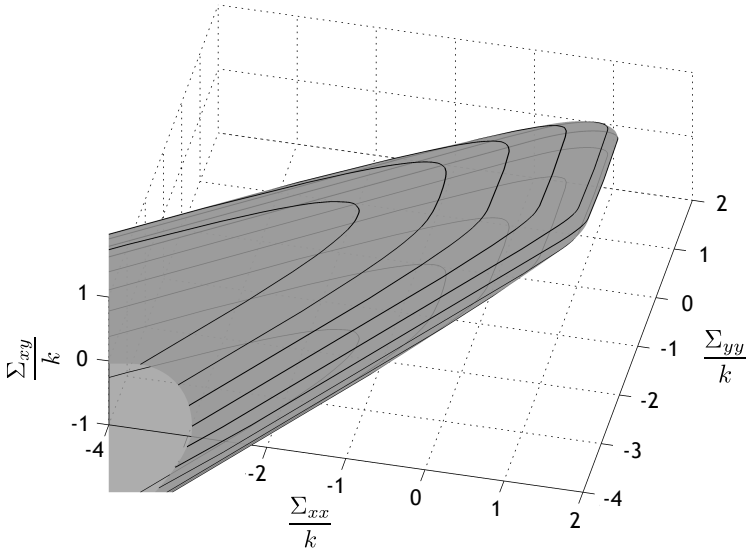

Fig. 3. Macroscopic strength domain in the $(\frac{\Sigma_{xx}}{k}, \frac{\Sigma_{yy}}{k}, \frac{\Sigma_{xy}}{k})$-space.

Figure 3 depicts the macroscopic yield surface and figure 4 displays its cross section by the zero shear stress plane, as well as those corresponding to the soil and the column materials. The latter figure clearly shows an improvement of the soil strength for high compressive stress states, due to the column reinforcement.

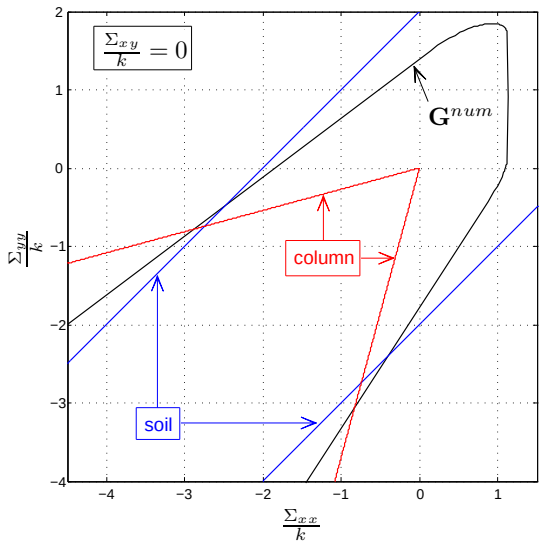

Fig. 4. Representations in the $(\frac{\Sigma_{xx}}{k}, \frac{\Sigma_{yy}}{k})$-plane of the native soil, reinforcement and reinforced soil strength domains.

It is worth noting that for many couples (γ, δ), there is no limit loads, so that the support value becomes infinite. The set of macroscopic strains directions generating a limit load is a cone denoted by $\left\{\underline{\underline{\Delta}}\right\}^{num}$. Moreover, despite the fact that the column is cohesionless, the reinforced material has a significant strength in the region of tensile stresses, the soil embedding the column.

3 APPROXIMATION USING CONVEX ELLIPSOIDAL SETS

3.1 Theoretical principle

As it will be shown in the next section, using the so-obtained strength criterion for computing limit loads of reinforced soil structures proves to be highly complex. In order to approximate the criterion with the fewest parameters as possible, it has been decided to use sums of convex ellipsoidal sets, in the sense of Minkowski summation. This means for instance that, for two sets A and B, the Minkowski sum (symbolised by $\oplus$) is defined as:

$$A \oplus B = \{a + b \,|\, a \in A, b \in B\} \tag{16}$$

which is sketched in figure 5, where A and B are a triangle and a circle, respectively.

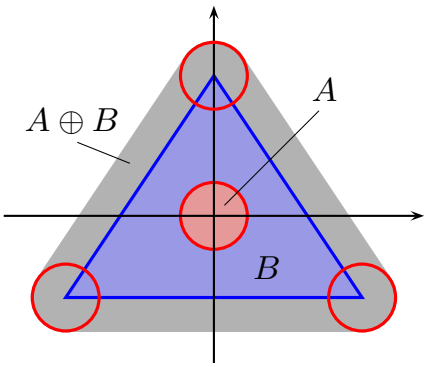

Fig. 5. Minkowski sum (shaded area) of two sets (triangle and circle).

Since, the macroscopic strength criterion is numerically defined as a polytope in the space of non-dimensional macroscopic stresses $(\frac{\Sigma_{xx}}{k}, \frac{\Sigma_{yy}}{k}, \frac{\Sigma_{xy}}{k})$, it is well-founded to try to approximate this polytope by a Minkowski sum of convex sets. It has been decided to use ellipsoidal sets, the support function of which is defined as (Bleyer & de Buhan 2013):

$$\pi_{ell}(\underline{\underline{\Delta}}) = \sup_{f_{ell}(\underline{\underline{\Sigma}}) \leq 0} \underline{\underline{\Sigma}} : \underline{\underline{\Delta}} = \sqrt{{}^t\underline{\underline{\Delta}} : \mathbb{A} : \underline{\underline{\Delta}}} - {}^t\underline{\underline{c}} : \underline{\underline{\Delta}} \tag{17}$$

where $\mathbb{A}$ is a fourth order tensor which specifies the orientation and dimensions of the ellipsoid in the stress space, $\underline{\underline{c}}$ the coordinates of its center and $f_{ell}(.)$ the yield function of the ellipsoid. For a sum of N ellipsoidal sets, the support function writes:

$$\pi_{Nell}(\underline{\underline{\Delta}}) = \sum_k \sqrt{{}^t\underline{\underline{\Delta}} : \mathbb{A}_k : \underline{\underline{\Delta}}} - {}^t\underline{\underline{c}} : \underline{\underline{\Delta}} \tag{18}$$

where $\mathbb{A}_k$ is the fourth order tensor defining ellipsoid number k and $\underline{\underline{c}}$ defines the center of one of them.

To approximate the strength domain, the standard deviation of the difference between π^{num} and π_{Nell} is minimized along all the macroscopic strains located in the cone $\left\{\underline{\underline{\Delta}}\right\}^{num}$. In order to obtain an upper bound for $\mathbf{G}^{hom}$, the support function of the approximation must remain larger

than the numerical one for all strain directions of $\left\{\underline{\underline{\Delta}}\right\}^{num}$. The minimization problem may therefore be written as follows:

$$\min_{\underline{x}\in\mathbb{R}^{6N+3}} \sum_{\underline{\underline{\Delta}}\in\left\{\underline{\underline{\Delta}}\right\}^{num}} \left(\pi^{num}(\underline{\underline{\Delta}}) - \pi_{Nell}(\underline{x},\underline{\underline{\Delta}})\right)^2 \tag{19}$$

under the condition

$$\pi^{num}(\underline{\underline{\Delta}}) \leq \pi_{Nell}(\underline{x},\underline{\underline{\Delta}}), \quad \forall \underline{\underline{\Delta}} \in \left\{\underline{\underline{\Delta}}\right\}^{num} \tag{20}$$

where vector $\underline{x}$ contains the $6N$ components associated to the tensors $\mathbb{A}_k$ $(k = 1, \ldots, N)$ as well as the three components of $\underline{\underline{c}}$.

3.2 Application to the macroscopic strength criterion

The approximation is made here using a sum of 3 and 8 ellipsoids. It is possible to evaluate the relative error due to the approximation for all strain directions of $\left\{\underline{\underline{\Delta}}\right\}^{num}$. For the stone column reinforced soil, the cone of outer normals to the strength domain is:

$$\underline{\underline{\Delta}} \in \left\{\underline{\underline{\Delta}}\right\}^{num} \Leftrightarrow \underline{\underline{\Delta}} = \sum_i \beta_i \underline{\underline{\Delta}}_i^{lim}, \; \forall \beta_i \geq 0 \tag{21}$$

where $\underline{\underline{\Delta}}_i^{lim}$ are the extremal strain directions normal to the strength domain, which can be detected numerically.

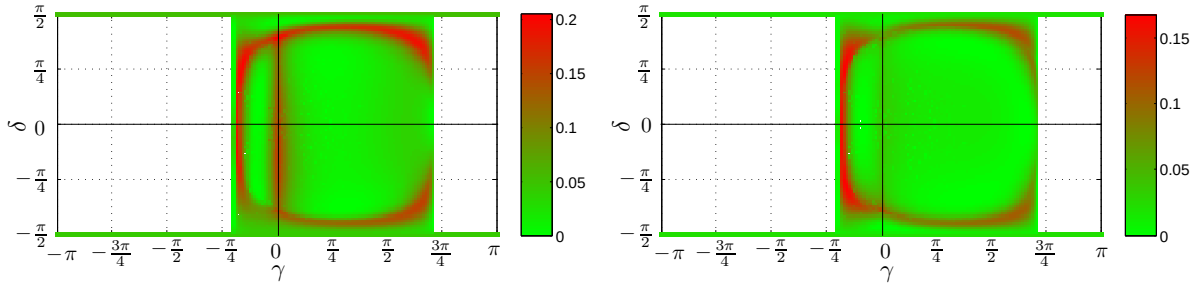

(a) (b)

Fig. 6. Approximation error (colorbar) depending on the strain orientation (γ, δ): (a) sum of 3 ellipsoids, (b) sum of 8 ellipsoids.

Figure 6 displays this error for both approximations as function of the strain orientation (γ, δ). In the case considered here, the maximum value of this relative error reaches here 20.4% for the approximation by a sum of 3 ellipsoids, decreasing to 16.8% for 8 ellipsoids.

The so-obtained approximations are also represented in the $(\frac{\Sigma_{xx}}{k}, \frac{\Sigma_{yy}}{k})$-plane in Figure 7 for the two extreme values of $\frac{\Sigma_{xy}}{k} = 0$ and 1. As expected both approximations are upper bounds for the macroscopic strength criterion. The average value of the relative error is reduced from 4.96% for 3 ellipsoids to 2.86% for 8 ellipsoids.

4 APPLICATION TO THE DETERMINATION OF THE LOAD BEARING CAPACITY OF A STONE COLUMN REINFORCED FOUNDATION

In order to apply the previously described procedure to a design example, the case of a strip footing acting upon a semi-infinite purely cohesive soil reinforced by purely frictional stone

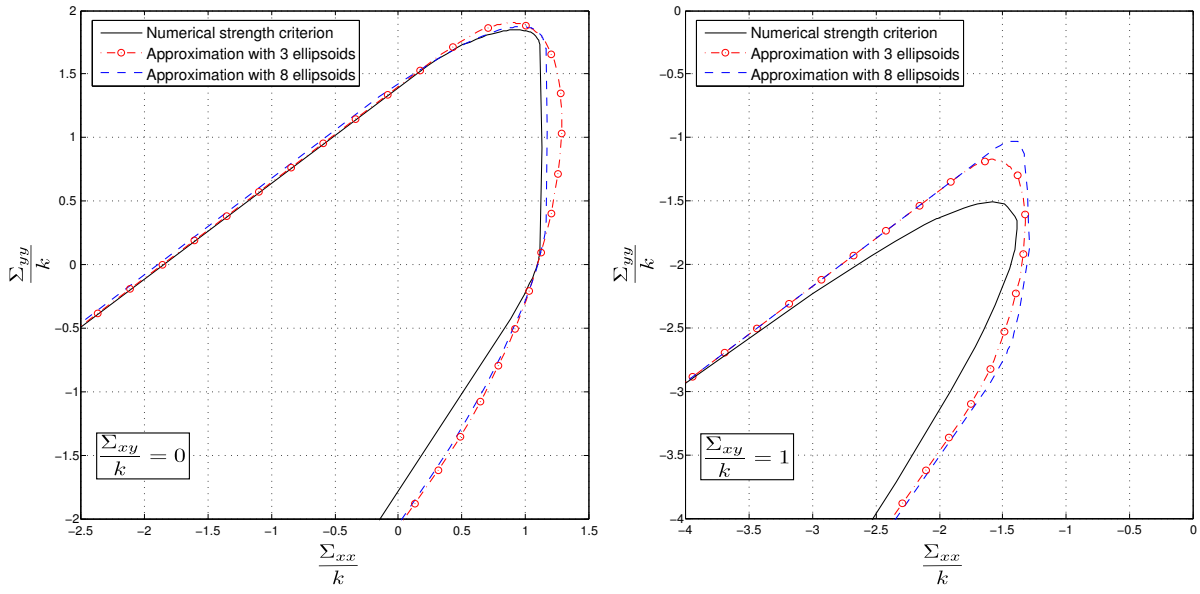

Fig. 7. Representations of strength criterion and approximations: (a) $\frac{\Sigma_{xy}}{k} = 0$, (b) $\frac{\Sigma_{xy}}{k} = 1$.

columns is considered (see Figure 8). The characteristics for the reinforcement are given by (15) and the specific weight will first not be taken into account, then set equal to the same value $\gamma = \gamma^s = \gamma^c = 18$ kN/m^3. The ultimate bearing capacity denoted by Q^+ will be estimated by considering that the whole soil layer has been reinforced.

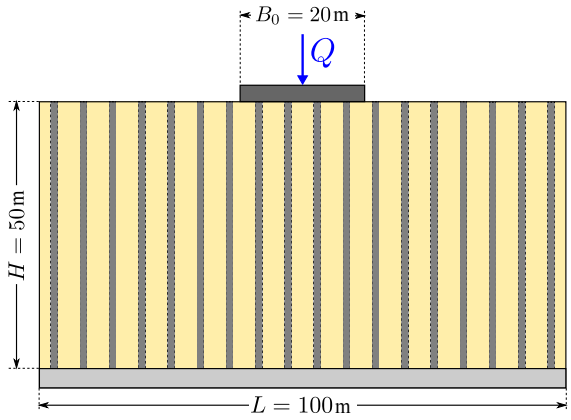

Fig. 8. Ultimate bearing capacity analysis of a stone column reinforced foundation.

4.1 A simple failure mechanism

The first upper bound estimate is searched by using a failure mechanism made of two rectangular triangular blocks, involving three velocity discontinuity lines. The two blocks are characterized by an angle α_i with a velocity $\underline{U}_i$ inducing a velocity inclined at β_i where i is the number of the block. The velocity jump between the two blocks is noted $[\underline{U}]_1^2$ and is inclined at an angle β_1^2 as sketched in Figure 9.

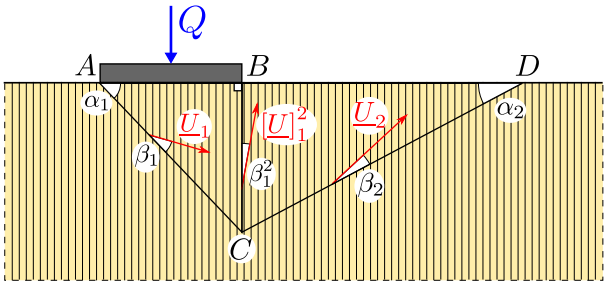

Fig. 9. Rigid block failure mechanism used for a first upper bound estimate.

It can be proved that the virtual work of external forces in such a failure mechanism may be written as:

$$W_e = QU_1 \sin(\alpha_1 - \beta_1) + \gamma \left(U_1 \frac{\tan \alpha_1}{2} - U_2 \frac{\tan^2 \alpha_1}{2 \tan \alpha_2} \frac{\sin(\alpha_2 + \beta_2)}{\sin(\alpha_1 - \beta_1)} \right) \tag{22}$$

where U_i denote the norm of the velocities. Since only velocity discontinuities are involved in the mechanism, the maximum resisting work is expressed as:

$$W_{mr} = \int_{AC} \pi^{num}(\underline{n}_{AC}, \underline{U}_1)\, \mathrm{d}s + \int_{BC} \pi^{num}(\underline{n}_{BC}, [\underline{U}]_1^2)\, \mathrm{d}s + \int_{CD} \pi^{num}(\underline{n}_{CD}, \underline{U}_2)\, \mathrm{d}s \tag{23}$$

with $\underline{n}$ is the normal unit vector to each discontinuity line and $\pi^{num}(\underline{n}, \underline{U})$ is the support function of the velocity jump accross this line. The value of $\pi^{num}(\underline{n}, \underline{U})$ is obtained from $\pi^{num}(\underline{\underline{\Delta}})$ by a reasoning explained in details by Hassen et al. (2013).

The application of the kinematic approach of yield design leads to the following inequations:

$$Q \leq Q^+ \;\Rightarrow\; \forall \underline{U},\, W_e(\underline{U}) \leq W_{rm}(\underline{U}) \tag{24}$$

which, using (22) and (23), allows to express the upper bound estimate $Q^{ub}_{2blocks}$ for this failure mechanism. The minimization is made by varying the angular parameters α_i and β_i numerically. The results are reported in Table 1 for the weightless problem and for $\gamma = 18$ kN/m^3.

4.2 Numerical application of the approximation of the macroscopic strength criterion

The approximations of the macroscopic strength criterion, introduced in section 3.2, will be now used for treating the same problem. This problem can be solved considering one half of the structure, with smooth contact boundary conditions for the lateral sides of the model as well as for the bottom side. The optimization of the problem is carried out by a homemade limit analysis code using the conic problem optimizer MOSEK. The mesh used for these calculations is displayed in Figure 10 with six noded elements.

For both approximations of the macroscopic strength criterion, the upper bound estimate (noted Q^{ub}_{Nell}) and the associated failure mechanism are obtained. All results are given in Table 1 and Figure 11 represents the failure mechanism with an approximation using 8 ellipsoids taken into account the gravity or not. The influence of gravity is reflected in the fact that the extension of the mechanism is larger when the specific weight is not taken into account.

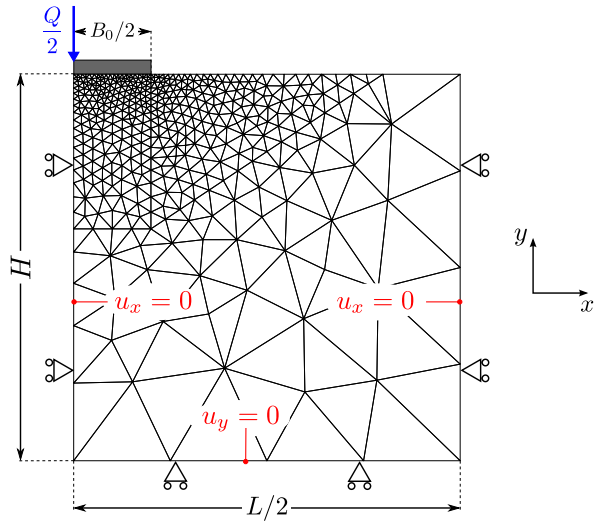

Fig. 10. Adopted finite element mesh for upper bound estimate with ellipsoidal set approximation.

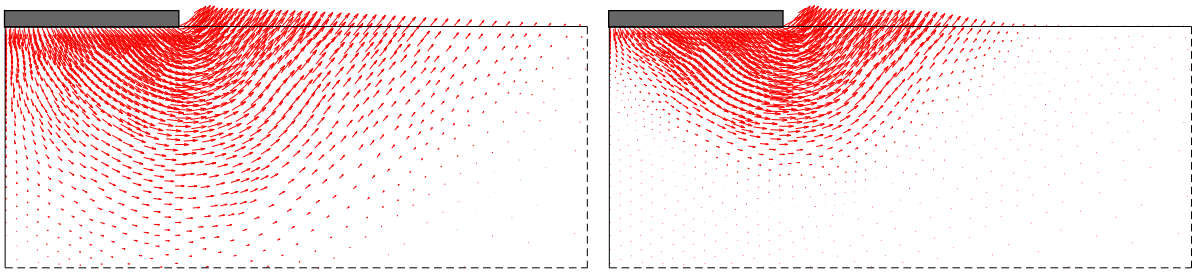

(a) (b)

Fig. 11. Failure mechanism using the 8 ellipsoids approximation: (a) Without gravity, (b) Gravity loaded.

Finally, different upper bound estimates previously obtained are summed up in Table 1. These values are compared to a lower bound estimate of Q^+ obtained from elastoplastic calculations by Hassen et al. (2010) and denoted here by $Q^{lb}_{el.pl.}$. The different percentages reported in this table represent the relative difference between each of these bounds and the well-known exact value for a non-reinforced purely cohesive soil $Q^+_{nr}/kB_0 = \pi + 2 \simeq 5.14$.

Table 1. Upper and lower bounds estimates for the bearing capacity of stone columns reinforced soils.

Case	without gravity (gap %)	gravity loaded (gap %)
$\frac{Q^{lb}_{el.pl}}{kB_0}$	5.95 (15.72)	6.30 (22.53)
$\frac{Q^{ub}_{2blocks}}{kB_0}$	7.36 (43.15)	7.79 (51.51)
$\frac{Q^{ub}_{3ell}}{kB_0}$	6.66 (29.53)	7.30 (41.98)
$\frac{Q^{ub}_{8ell}}{kB_0}$	6.63 (28.95)	7.27 (41.40)

As expected, the upper bounds obtained by ellipsoid-based approximations are closer to the lower bounds than the result of the kinematic approach using blocks failure mechanisms. The

potential loss of accuracy induced by the approximation is completely offset by the possibility of using more complicated failure mechanisms. Thanks to the present method, the difference between bounds of the non-dimensionnal load value $\frac{Q^+}{kB_0}$, is equal to 0.68 without gravity (1.41 with two blocks failure mechanism) and 0.97 when gravity is accounted for (1.39 with two blocks failure mechanism).

5 CONCLUDING REMARKS

The present contribution makes use a numerical code to evaluate the macroscopic strength criterion of a stone-column reinforced soil. Owing to the kinematic approach of yield design, this evaluation is a rigorous upper bound, depending on the material and geometrical characteristics. An analytical approximation of the macroscopic criterion as a sum of ellipsoids is then developed, aimed at performing calculations on reinforced geotechnical structures. The performance of such an approximation is then proved on a classical geotechnical design problem. This represents a fully original approach for treating geotechnical engineering problems, with acceptable computation times and could be developed as an alternative to finite element calculation with elastoplastic procedure.

The reinforcement by columnar inclusions provides, as expected, a gain in terms of bearing capacity, comparatively to the native soil. This improvement magnified when gravity is taken into account, due to the strength provided by the frictional material for highly compressive stresses. The efficiency of such a reinforcement technique is confirmed and could be measured for other typical geotechnical problems, as stability analysis of an embankment resting upon a reinforced soil or a buried foundation.

REFERENCES

Bleyer, J. & de Buhan, P. (2013). Yield surface approximation for lower and upper bound yield design of 3d composite frame structures. *Comput. Struct.*, Submitted to publication.

de Buhan, P. (1986). A fundamental approach to the yield design of reinforced soil structures (in french). Thèse d'Etat, Paris VI.

Hassen, G., de Buhan, P., & Abdelkrim, M. (2010). Finite element implementation of a homogenized constitutive law for stone column-reinforced foundation soils, with application to the design of structure. *Comput. Geotech. 37*, 40–49.

Hassen, G., Gueguin, M., & de Buhan, P. (2013). A homogenization approach for assessing the yield strength properties of stone column reinforced soils. *European J. of Mechanics, A/Solids 37*, 266–280.

Makrodimopoulos, A. & Martin, C. (2007). Upper bound limit analysis using simplex strain elements and second-order cone programming. *Int. J. Num. Anal. Meth. Geomech. 31*, 835–865.

MOSEK (2008). The mosek optimization tools for matlab manual. Available from: http://www.mosek.com.

Pastor, F., Kondo, D., & Pastor, J. (2011). Numerical limit analysis bounds for ductile porous media with oblate voids. *Mech. Research Comm. 38*, 350–354.

Priebe, H. (1995). The design of vibroreplacement. *Ground Eng.*, 31–37. December.

Suquet, P. (1985). Elements of homogenization for inelastic solid mechanics. In *CISM Lecture Notes*, pp. 193–278. Springer-Verlag.

STONE COLUMNS FOUNDATION ANALYSIS WITH CONCENTRIC RING APPROACH

S.A. Tan
Department of Civil & Environmental Engineering, University of Singapore, Singapore

K.S. Ng
Faculty of Civil Engineering, Universiti Teknologi MARA, Shah Alam, Malaysia

ABSTRACT: *In geotechnical engineering, the analysis of small footing founded on limited number of stone columns is normally treated as 3D problem. However, the 3D analysis requires extensive computational effort and time compared to 2D analysis. Therefore, in this study, a series of numerical analyses are performed to investigate the reliability of the 2D axisymmetric concentric ring model to be used in problems where stone columns are adopted as ground improvement method to support a small foundation. In this approach, a group of stone columns was modeled as a series of concentric rings of the same area replacement ratio as actual columns. The results of the 3D finite element model for stone column reinforced foundation provide the basis for this numerical comparison. End bearing column system was tested first followed by floating column system. The deformation characteristic of the footing under different geometry configuration and area ratio demonstrate the feasibility of the concentric ring approach in modeling stone column reinforced foundation. In addition, the validity of the concentric model has been proven in this study under short term and long term loading conditions and is able to display a realistic stress distribution between the column and the surrounding soil.*

1 INTRODUCTION

Small group of stone columns either fully or partially penetrating supported load applied at the surface, usually through a spread or mat foundation. The load is then transferred to the composite ground by a complex mechanism of load sharing and strain compatibility. The intricacy of this load transfer mechanism is less understood than the behavior of single stone column or columns under infinite column grid where unit cell concept prevails. Unlike piles with very large contrast of relative stiffness, stone columns and native soil have typical stiffness contrast of 10 – 40 times only, which makes the column very flexible compared to piles. In addition, the nonlinearity of stress-strain response and the drainage ability of the soil and column's aggregate further complicate the design of foundations resting on small group of stone columns. Small model tests (Wood et al, 2000; McKelvey et al., 2004; Shahu & Reddy, 2011) and numerical models results (Wehr, 2006; Killeen & B. McCabe, 2010) have, however, provided some qualitative insight into the likely behavior of stone columns group.

Numerical analyses of stone column reinforced ground can be modeled in different approaches: (1) axisymmetric unit cell, (2) axisymmetric concentric ring, (3) plane strain trench wall, (4) homogenization technique, and (5) three dimensional (3D) model. The first four approaches are considered as simpler two dimensional (2D) analyses. In geotechnical engineering, the analyses of small footing founded on limited number of stone columns is

normally treated as a 3D problem making the approaches in 1, 3, and 4 less suitable for use. However, the 3D analysis is time consuming and requires more expertise from the users than the corresponding 2D analysis. Therefore, 2D concentric ring model is probably more suitable for small foundation supported on stone columns, but more investigations into the application of this approach is needed. It is first adopted by Mitchell & Huber (1985) for large columns group. The properties in the ring element resemble the stone column material and the radius remains same as the spacing from the center column while the thickness is calculated so that the area ratio between column and the tributary soil remain the same.

The aim of this study is to investigate the reliability of the axisymmetric concentric ring model to be used in problems where stone column is adopted as ground improvement method to support small shallow foundations. The results of the 3D model for stone column reinforced foundation provide the basis for the numerical assessment of this approach. The deformation characteristic of the footing for different geometry configuration and different type of analysis is used to demonstrate the effectiveness and feasibility of the concentric ring approach in modeling stone column reinforced foundation. Both end bearing columns and floating columns systems are examined.

2 NUMERICAL MODEL

Elshazly et al. (2008) improved the model of Mitchell & Huber (1985). In their approach, the thickness and the radius of the ring are adjusted to give the correct equivalent area of the stone columns as shown in Fig.1. This approach is adopted in this study. The 2D analyses were executed using the finite element program PLAXIS 2D Ver. 9 with 15-noded triangular (quartic) elements. On the other hand, 3D analyses were performed using PLAXIS 3D foundation Ver. 2 with quadratic tetrahedral 10-noded (quadratic) elements.

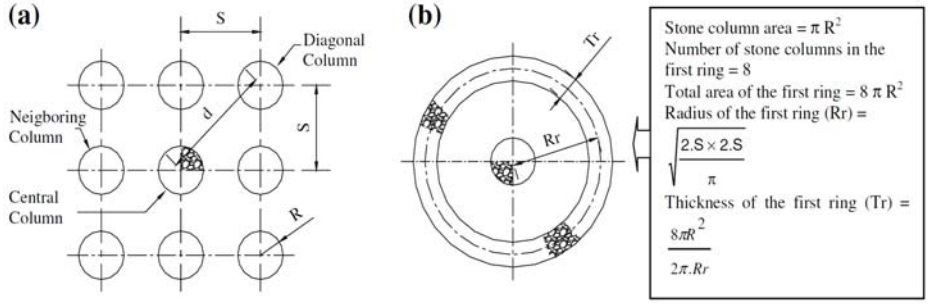

Fig.1. Concentric ring model (Elshazly et al., 2008)

In the numerical model, the soft soil was assumed 15.0 m thick and the stone columns were 1.0 in diameter. The water table was assumed to be at the ground surface. Hardening soil (HS) model was used for both the soft clay and column material, to replicate their non-linear responses, and the appropriate properties are tabulated in Table 1. The HS model is an extension of the well-known hyperbolic model developed by Duncan & Chang (1970). However, HS model supersedes the Duncan-Chang model by adopting plasticity theory rather than elasticity theory, including the dilatancy, and introducing the yield cap (Schanz et al., 1999).

Stone columns were typically used to support spread footings in soft clay ground. The footing was placed on the ground surface and was modeled as rigid plate having normal stiffness of $1x10^7$ kN/m and flexural rigidity of $1x10^5$ kNm^2/m. In this study, a 5 columns group was tested first. Subsequently the analyses on 9, 25, and 49 columns were also carried

out. Drained analyses which assumes very slow rate of loading were conducted followed by undrained analyses and consolidation analyses subsequently.

Table 1. Material properties

ID	Name	γ_{sat} (kN/m^3)	E_{50}^{ref} (kN/m^2)	E_{oed}^{ref} (kN/m^2)	E_{ur}^{ref} (kN/m^2)	c' (kN/m^2)	ϕ' (°)	ν_{ur} [-]	p^{ref} (kN/m^2)	m [-]
1	SC	20	10000	10000	30000	1	45	0.2	100	0.5
2	Clay	16	3000	2500	10000	1	25	0.2	100	1

3 NUMERICAL ANALYSES, RESULTS AND DISCUSSION

The feasibility of the concentric ring model used in 2D analysis to model individual columns needs to be tested under different kinds of conditions. These conditions includes end bearing columns, floating columns, drained analysis, undrained analysis and consolidations analysis. Only the important results pertinent to the deformation characteristics were discussed.

3.1 End bearing columns

First, the 5 individual columns in 3D model were set up. To reduce the computation effort, one fourth of the full model was adopted due to symmetry. The footing radius was 2.0 m while the spacing of column, *s* offset from horizontal distance of inner column was fixed at 1.0 m. The footprint replacement ratio $A_F = A_c / A_f$ is 0.31 where A_f is the area of the footing and A_c is the total area of stone columns. The concentric ring was then built into a 2D axisymmetric model. The calculated ring radius and thickness were 1.128 m and 0.443 m respectively. These models are shown in Fig. 2.

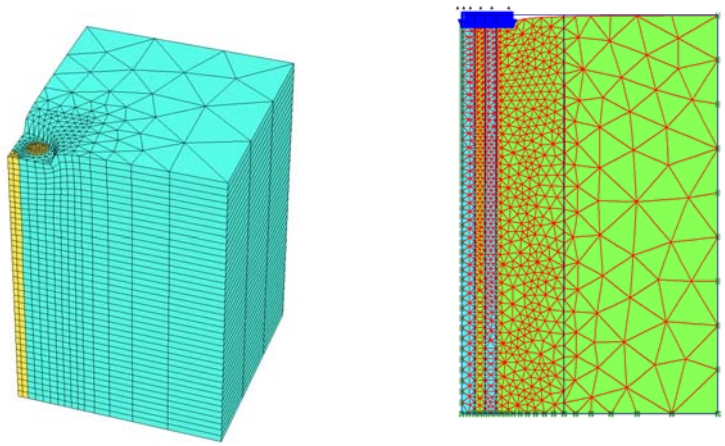

(a) (b)

Fig.2. Five columns models (a) 3D individual column, and (b) 2D concentric ring model

Both initial stress of the ground in 3D and 2D were simulated by gravity loading approach. Stone columns were modeled as “wish-in-place”. Vertical load acting on the circular footing was set at 50 kPa for this 5 columns group case. In the 5 columns group foundation analyses, square footing with equivalent footing size as circular footing was also used to make proper comparison. Sensitivity studies have been carried out on the sensitivity of mesh sizes and the boundary effects before the appropriate mesh and domain size were adopted in current models. The drained analyses results are shown in Fig. 3. The 2D concentric ring model

curve matches the 3D models very well. In addition, the results obtained by both 3D footings with square and circular shapes are also identical. The settlements for case without stone columns under 50 kPa is calculated to be 553 mm while it reduces to about 300 mm if the stone columns are used. A reduction of 56% in settlement or the settlement improvement factor, *n* of 1.8 is obtained with the inclusion of stone columns under the foundation.

For stone columns group, the interaction among the composite system under the load is very complex (column-column, column-footing, column-soil, soil-footing). The defomation for 5 columns are illustrated in Fig. 4. For 3D analysis, only the circular footing with indiviudal columns is discussed here due to the similar results obtained by 3D square footing case. In 3D analysis, shear band develops at the edge of the footing and inclined toward the center of the footing, forming a shear cone. The shear band developed at $45°+\phi_s'/2$ where $\phi_s'$is the friction angle of soft soil. At the same time, some bending outward of the outer column towards the unconfined side is also observed. Some bulging of section along the inner column are also noticed which indicates stable ductile deformation. This also suggests transfering of loadings to a greater depth. Whereas in 2D analysis, multiple shear bands develop across the outer column but the most obvious shear zone are similar to that in 3D model. Only minor bulging is seen at the upper part of inner column for 2D. Generally, 2D and 3D analyses display the same deformation mode of failure despite some discrepancy in detail. The physical testing of groups columns by Hu (1995) also produced similar deformation patterns.

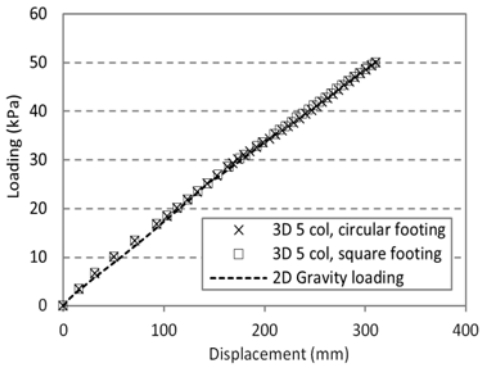

Fig.3. Numerical results for 5 columns group

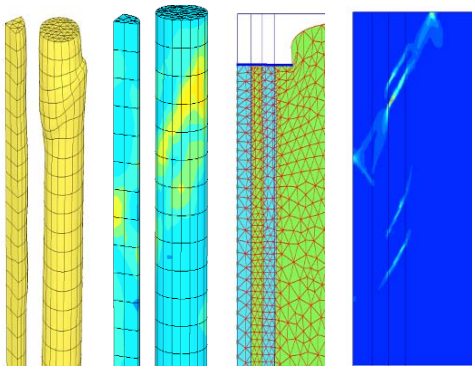

(a) (b) (c) (d)

Fig.4. (a) 3D deformation mode, (b) 3D incremental shear strain, (c) 2D failure mode, and (d) 2D incremental shear strain

Plastic points developed under the footing as shown in Fig.5. Yielding of the columns and soil are concentrated at upper zone. Columns material are subjected to high straining and reach the Mohr-Coulomb failure criterion especially for edge columns which has less restraint. Soil around the column underwent compaction hardening until they reach the cap type yield surface. The limit of this yield zone is about 2.3 times the footing radius measured from the centre axis. The agreement between 2D and 3D model is actually quite remarkable considering the difference in geometry for both models.

To futher investigate the validity of the concentric ring method, the stresses acting on the columns are examined in detail. It is found that in 3D, the stress conentration ratio, n_s (total stress acting on column over stress on surrounding soil) for inner column and outer column is approximately 4.5 and 3.7 respectively, measured right under the footing base. The same results are obtained for 2D analyis as well (Fig.6). The average values are taken from the stress points for each column and soil cluster where the extreme interface values are obmitted (due to high shear stress concentrations between column and soil interface). The

phenomenon where the outer columns are less loaded may probably be due to the existence of shear failure zones which reduce the sustained vertical stress. Another possible explanation is at the edge of footing, the columns is not reinforced by neighbouring columns resulting in lower limiting load.

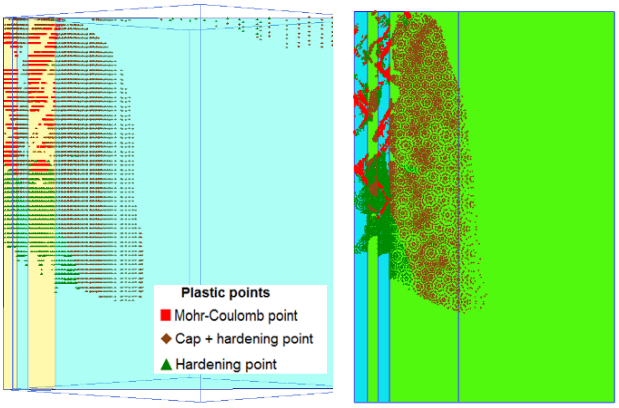

(a) (b)

Fig.5. Plastic points (a) 3D model (diagonal view), (b) 2D ring model.

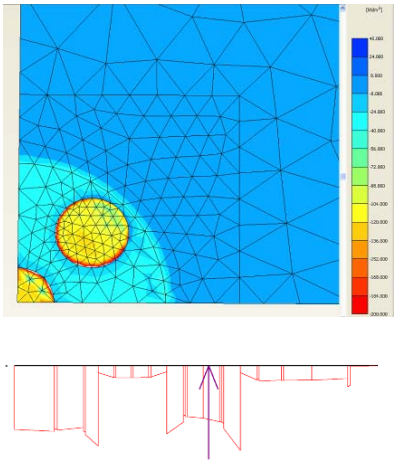

Fig.6. Stress concentrations between stone columns and surrounding soil for 3D (top) and 2D (bottom) analyses

Subsequently, the feasibility of concentric ring odel was tested for larger columns groups, namely 9 columns group, 25 columns group and 49 columns group. Footings and columns geometry for these groups are shown in Table 2. Lines used to connect a series of columns in the stone column configuration figures indicate series of rings used in 2D analyses. The radius and thickness for the outermost ring are denoted by r and T respectively. Present study used square footing (in 3D model) and the radius of footing for the 2D model was calculated for its equivalent area. The spacing of 1.5 m was used for all the cases here. In 2D analyses, the radius and thickness for the first ring (innermost) in 49 columns group is similar to the radius and thickness for the outermost ring in 9-column case while second ring is similar to the 25 columns group. Likewise, the inner ring's radius and thickness for 25 columns group is the same as 9 columns group outermost ring. The footprint replacement ratio for all these cases ranged from 0.28 to 0.32.

Load-displacement curves for cases of 9, 25 and 49 columns are shown in Fig.7. All 2D curves show good matches with 3D curves. Some 2D curves display minor oscillations especially when greater loading were applied. This phenomenon is due to convergence issues in finite element. However the overall shape of the load-displacement curves seems to remain realistic even with these small "stair-like" oscillations. It is worth noting that all three cases of different columns group yielded almost same displacement under every step of loading, for example, about 550 mm vertical displacement is observed for 80 kPa loading. One possible explanation is that the footprint replacement ratios for these three cases are about the same, A_F = 0.28, 0.31 and 0.32 for columns group of 9, 25 and 49 respectively. Another reason could be the insensitivity of size of footing to the overall performance, but this needed to be further investigated.

In all cases, the major deformation mode is of wedge shear band similar to the case of 5 columns although more distinct shear planes are shown in 3D models. Deformations modes for 25 columns group are shown in Fig. 8. Similar patterns of deformation are observed where shear band extends from the edge of footing and cut through the inner columns. Bending is also observed for outer columns where the edge columns have rather limited

lateral restraint. The stress state of soil and columns in both models are comparable judging from the plastic points distributions as shown in Fig. 9.

Table 2. Footings and columns geometry

No. of columns	Stone columns arrangement	Footing size (B x B)	Spacing, s (m)	2D configurations
9	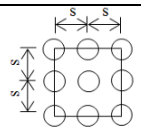	5 m x 5 m A_F =0.28	1.5 m	R = 2.821 m r = 1.693 m T = 0.591
25	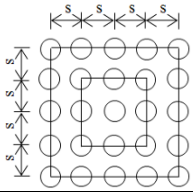	8 m x 8 m A_F =0.31	1.5 m	R = 4.514 m r = 3.385 m T = 0.591 m
49	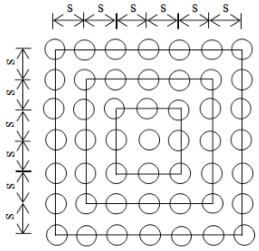	11 m x 11 m A_F =0.32	1.5 m	R = 6.206 m r = 5.078 m T = 0.591 m
R = Equivalent radius for 2D foundation r = concentric ring radius for the outermost columns T = thickness of the outermost concentric ring				

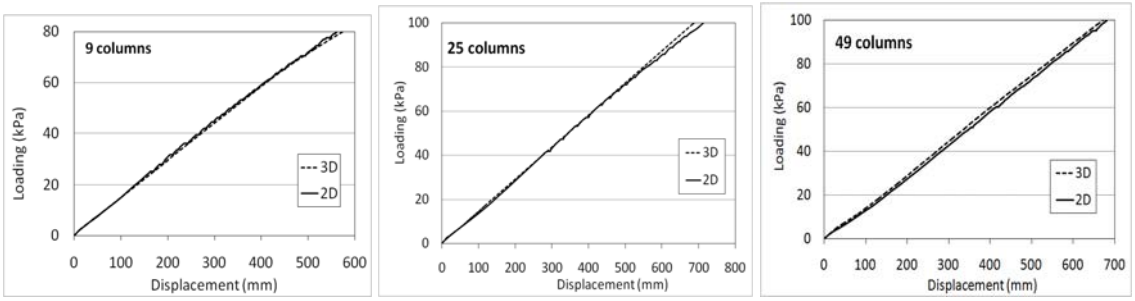

Fig.7. Load- displacement curves for 9, 25, and 49 columns

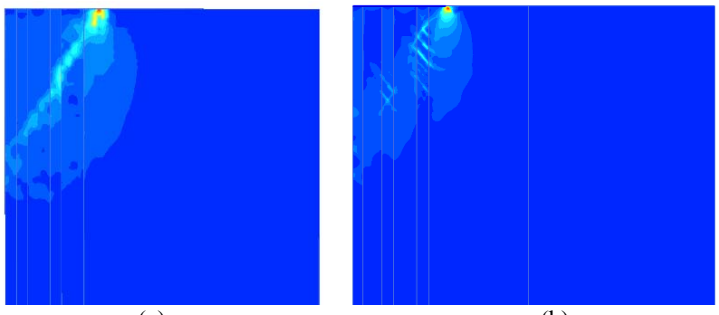

(a) (b)

Fig. 8. Shear planes for 25 columns footing (a) 3D model, and (b) 2D ring model.

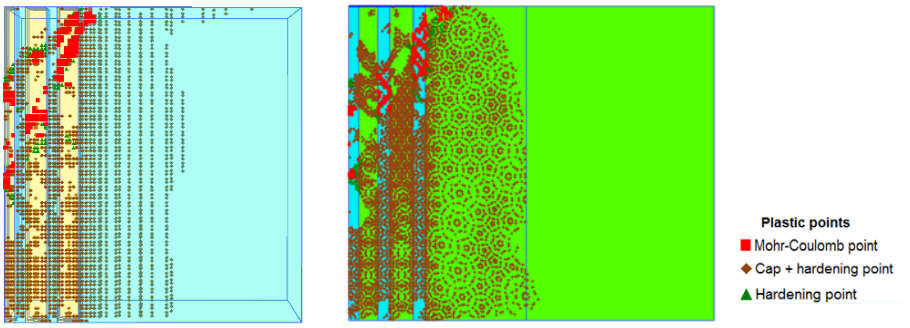

(a) (b)

Fig.9. Plastic points for 25 columns footing (a) 3D model, and (b) 2D ring model

The stress concentration ratios for 49 columns are shown in Fig.10. The innermost column has the highest stress concentration ratio of about n_s = 4.0 while outermost column has the lowest stress concentration ratio (as low as n_s = 2.5 for columns near the diagonal edge of footing in 49 columns case). The severity of shearing and bulging in the columns suggests that the stress sharing between column and clay is correlated to the deformation behaviors of both materials. Direct comparisons of the degree of deformation mode in 3D and 2D ring models are improper since each ring of column consist of a few individual columns in 3D model. Nevertheless the 2D ring models still gave reasonable stress concentration ratios where the values was not far different compared to 3D models. These values are within typical ranges of stress concentrations commonly found in the literature. Wood et al. (2000) experimental results however showed slighly dissimilar patterns of stress distribution. In their physical model test, the stress at the center of footing is lower than mid-radius and again lower for the columns at the edge. Deduced from similar numerical study, they further claimed that the centre column was less heavily loaded than the off-centre columns, but no explanation were given by the authors.

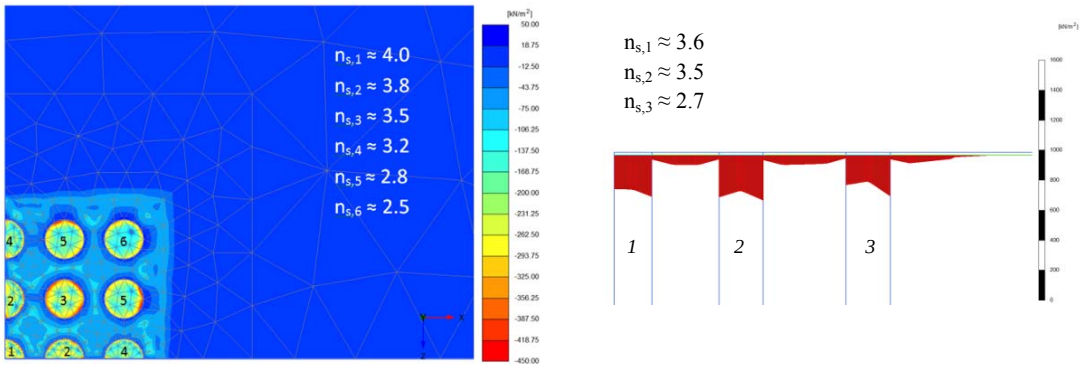

(a) (b)

Fig.10. Stress distributions for 25 columns group (a) 3D model, and (b) 2D model.

3.2 Floating columns

Similarly, the concentric ring method can also predict the behavior of floating columns well. It is demonstrated that the toe movements of floating stone columns in the 2D models agree very well with the 3D models as presented in Fig.11. The thickness of the soft layer, *d* is fixed at 15 m and the columns length, *L* was varied at 3.0m, 5.0m, and 10.0m. All the cases were loaded at 100 kPa except 5 columns case with 50 kPa loading. As expected, the results

indicated the punching behavior of floating stone column where toe movement is greater for shorter column. Besides, the larger the loaded area e.g. 49 columns, the more loads are transferred to the column toe resulting in larger toe movement which behavior is similar to the large pile groups.

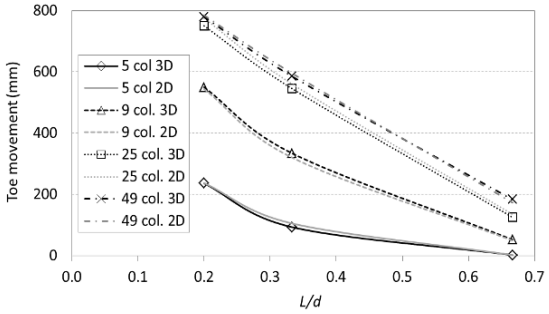

Fig.11. Toe movement for floating columns

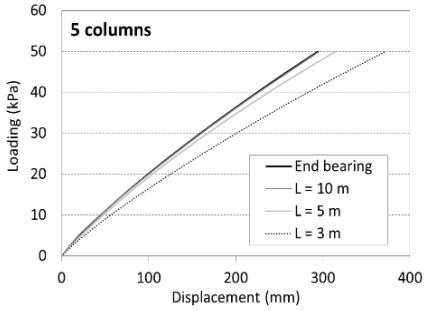

Fig.12. Load-displacement curve for 5 columns

The curves of 10.0m length for 5 columns group footing (i.e. L/d = 0.67) coincide with the result of end bearing column as shown in Fig. 12. Therefore, there exists an optimum length (between 5.0m to 10.0m) in which further increase of column length would not improve the deformation characteristic. The same result is also obtained by 9 columns group. However, 10.0m length is not the optimum length for 25 and 49 columns group. The reason lies in the larger size of footings in both of these groups where loaded area zone is deeper than 5 and 9 columns group. In other words, the optimum length for larger columns group has to be longer than the case of small columns group. The existence of optimum length in small foundation has also been recognized by Wood et al (2000). However, the relationship between the optimum length and the footing size need to be established through further investigations.

3.3 Undrained and Consolidation Analysis

Undrained analyses and coupled consolidation analyses for end bearing columns were executed first. The coefficient of permeability, k of columns and surrounding soil were determined as 1.0 m/day and 0.001 m/day respectively with isotropic condition applies. The model geometry and columns configurations are similar to drained analyses. All columns are fully penetrating. Model boundaries were set to be impermeable, and the pore pressure was only allowed to dissipate through the ground surface. The undrained analyses (i.e. instantaneous loading) results for 25 columns and 49 columns are shown in Fig.13. Again, the 2D concentric ring model is able to produce identical results as in 3D model.

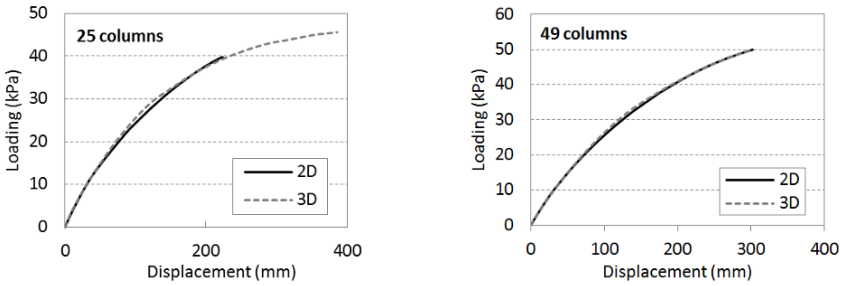

Fig. 13. Load-displacement curve for 25 and 49 columns (undrained analyses)

The results for consolidation analyses are shown in Fig.14. The loading period, T was varied to examine the different responses of improved ground. Surprisingly, the 2D results match 3D results very well. In other words, no adjustments are required for the 2D permeability parameters. For the same displacement value, the undrained capacity of the reinforced foundation is lower than the drained capacity which is expected for normally consolidated soils. The result of consolidation analyses with different loading period suggested that the faster the loading applied, the larger the settlement occurred. The analysis for loading period of 256 days is approaching the results of drained analyses.

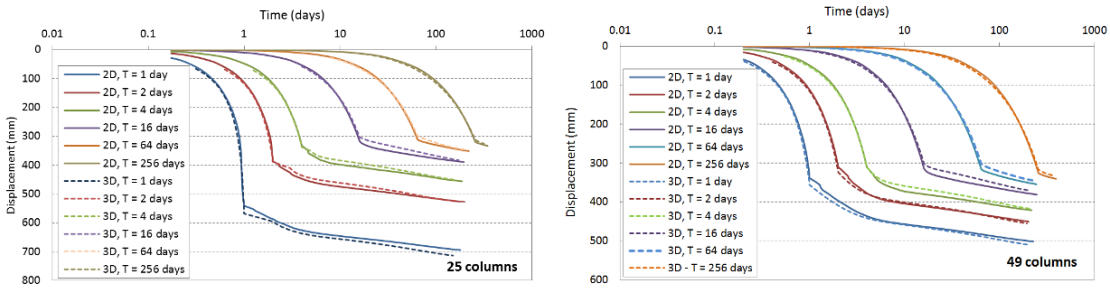

Fig.14. Consolidation analyses for 25 columns and 49 columns

The major deformation modes for undrained analyses is quite similar to the drained analyses where distinct shear plane begin from the edge of footing and propagates into the inner column along conical surface of about 45° (but less than 45° + ϕ_s'/2 as in drained analyses) with associated severe bending for outermost columns. Fig.15 illustrates the deformation pattern and shear plane for 2D and 3D models respectively. The bulging in the innermost column in 2D is less visible compare to 3D model. On top of the above-mentioned failure modes, footing subjected to undrained loading is also experiencing substantial heaving. Similarly to drained analysis, outer columns are less loaded than inner column therefore less vertical displacement is induced. Stress concentration ratios ranged from approximately 3.3 to 5.2 obtained from 3D's 25 columns group model. Despite similar deformation modes, the magnitude of shear volume changes for undrained analyses is greater than in drained analyses while the consolidation analyses results lie between them. This is expected since drained shear strength is higher than undrained shear strength.

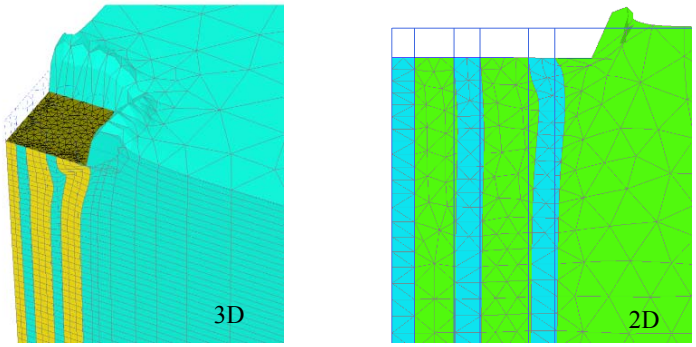

Fig. 15. Deformation mode for 2D and 3D models for undrained loading

For floating columns, the column length is fixed at 10.0m, the undrained and consolidation results are obtained for 49 columns (Fig. 16 & 17). The loading period in coupled consolidation analysis was set at 4 days. The 3D results agrees very well with the 2D concentric ring approach.

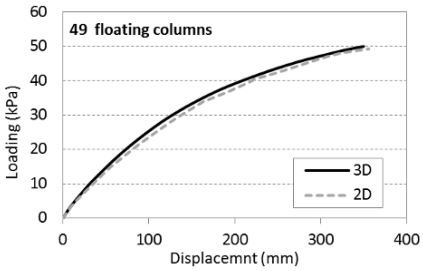

Fig. 16. Undrained analyses for 49 floating columns with L = 10 m.

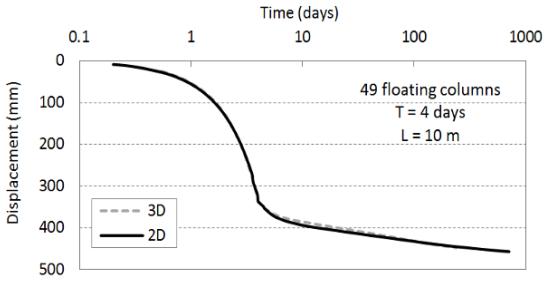

Fig. 17. Consolidation analyses for 49 floating columns with L= 10 m and 50 kPa loading for 4 days.

4 CONCLUSION

Deformation characteristics of stone columns within a group is a function of many factors e.g. area ratio, columns length, foundation size, foundation stiffness, and soil stratigraphy. Investigating the behavior of small column groups using 3D FEM model considering all influencing factors is numerically time consuming and can be quite expensive. Therefore, concentric ring model can serve as a more efficient approach compare to 3D model since less computation time and effort are required for 2D analyses. The validity of the concentric ring model has been proven in this study under short term and long term loading conditions for different numbers of columns in a group and is capable of having good reproduction of the stress distribution between columns and surrounding soil.

Unlike infinite grid condition, columns group possesses multiple deformation modes. Shearing planes are developed from the footing edge and cut across the outer columns into the inner columns. Concurrently, bending of outer columns occurred toward unconfined side due to low lateral resistance from the surrounding soil. Besides, some bulging is observed for the innermost column. Floating columns demonstrate additional punching mode and shorter columns experienced more toe movement compared to longer columns. The 2D concentric ring models had reproduced the deformation characteristic and the stress distribution around the columns and soil quite well compared to 3D models. This validates the 2D approach and makes it a practical and useful tool for design and analysis of small stone columns group.

REFERENCES

Elshazly, H. A., Hafez, D. H., & Mossaad, M. E. (2008), "Reliability of Conventional Settlement Evaluation for Circular Foundations on Stone Columns". *Geotechnical and Geological Engineering*, Vol. 26(3), 323–334.

Killeen, M. M., & McCabe, B. (2010), "A numerical study of factors affecting the performance of stone columns supporting rigid footings on soft clay". *Civil Research Session*.

McKelvey, D., Sivakumar, V., Bell, A., & Graham, J. (2004), "Modelling vibrated stone columns in soft clay", *Proceedings of the ICE - Geotechnical Engineering*, Vol. *157*(3), 137–149.

Mitchell, J. K., & Huber, T. R. (1985), " Performance of a stone column foundation". *Journal of Geotechnical Engineering*, Vol. 111(2), 205–223.

Shahu, J., & Reddy, Y. (2011), "Clayey soil reinforced with stone column group: Model Tests and Analyses". *J. Geotech. Geoenviron. Eng.*, *137*(12), 1265–1274.

Wehr, J. (2006), "The undrained cohesion of the soil as criterion for the column installation with a depth vibrator". *TRANSVIB*. Paris.

Wood, D. M., Hu, W., & Nash, D. F. T. (2000), "Group effects in stone column foundations: model tests". *Geotechnique*, Vol. *50*(6), 689–698.

ASSESSING THE LIQUEFACTION RISK REDUCTION OF REINFORCED SOILS: A HOMOGENIZATION APPROACH

Maxime Gueguin, Ghazi Hassen and Patrick de Buhan
Université Paris-Est, Laboratoire Navier (UMR 8205), CNRS, ENPC, IFSTTAR, Marne-La-Vallée, France

ABSTRACT: *In this contribution, an evaluation is given for the reduction of the liquefaction risk, which can be expected from reinforcing the soil by a periodic array of inclusions. Following a definition of the liquefaction risk reduction factor, the link is then established with the increase of longitudinal shear stiffness of the reinforced soil. Based on the homogenization theory for elastic periodic media, different geometries of the reinforcing inclusions are examined, with a particular focus on circular cylindrical (columnar) inclusions on the one hand, two mutually orthogonal arrays of trenches (cross trench configuration) on the other hand. A variational method based on minimum energy principles allows the derivation of theoretical lower and upper bounds for the reinforced soil longitudinal shear modulus. A comparison with results obtained from numerical simulations performed with a standard finite element code is then presented.*

1 INTRODUCTION

Soils reinforced by inclusions may be considered as composite materials and studied using homogenization methods. These methods are applicable considering the fact that the spacing between two neighboring columns is small in comparison with the overall dimensions of the structure. The validity of the homogenization method has been demonstrated as concerned the evaluation of the macroscopic elastic behaviour of fibre composite materials (Hashin & Rosen 1964; Hashin 1983) as well as, at a much larger scale, for soils strengthened by columnar inclusions (Balaam & Booker 1981; Canetta & Nova 1989; Abdelkrim & de Buhan 2007). Yet, the applications to geotechnical problems have been so far restricted to the evaluation of the settlement of the reinforced foundation under vertical loading and the pure shear loading problem has been rarely the subject of studies, even if it plays a major role in the response of reinforced ground subject to earthquake loading.

The present contribution intends to evaluate the liquefaction risk for a reinforced soil under a seismic solicitation, both constituents being considered as isotropic linear elastic materials with perfect bonding at their interface. First of all, a liquefaction risk reduction factor is defined, based on the analysis of the behaviour of a reinforced soil subject to a seismic wave, involving its macroscopic longitudinal shear stiffness (section 2). Two configurations will be more specifically studied. First, section 3 derives the analytical bounds for the longitudinal shear stiffness of a column-reinforced soil and the associated liquefaction risk reduction factor. Then section 4 develops the same evaluation for a cross trench reinforced soil and a comparison with the previous configuration is carried out, exhibiting a much greater efficiency in terms of liquefaction risk reduction for the cross trench configuration than for the columnar configuration.

2 SOIL REINFORCEMENT AS A LIQUEFACTION MITIGATION TECHNIQUE

2.1 Problem statement

Earthquakes induce major troubles on civil engineering structures, which may lead to major disasters. From a geotechnical point of view, one of the biggest threats is the so-called soil liquefaction phenomenon. Indeed a seismic solicitation involves a cyclic shear strain of the ground, which generates an excess pore water pressure in the different water-satured materials (sands or silts), leading to a liquefaction phenomenon, that is a collapse of their resistance. This may considerably reduce the bearing capacity of the soil.

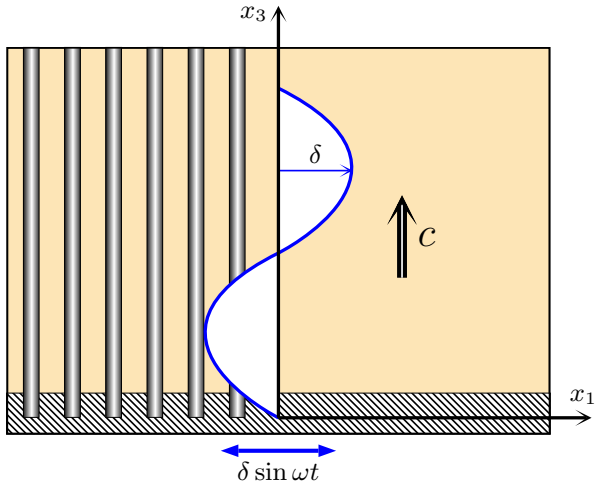

Fig. 1. Vertical propagation of a seismic shear wave in a soil layer.

The loading induced by a seismic loading can be schematized by a harmonic shear wave (see Figure 1) defined as:

$$\underline{\xi}\left(\underline{x},t\right) = \delta \sin\left[\omega\left(t - \frac{x_3}{c}\right)\right]\underline{e}_1 \tag{1}$$

where δ is the horizontal displacement amplitude and ω the angular frequency which characterize the seismic loading.

The shear wave velocity c is a characteristic of the soil and can be linked to the soil mass density ρ and the *longitudinal shear stiffness* G_L by the following classical relationship:

$$c = \sqrt{\frac{G_L}{\rho}} \tag{2}$$

where G_L is the component of the elastic stiffness tensor of the soil relating the shear stress and strain in the $(\underline{e}_1, \underline{e}_3)$ plane. For an isotropic elastic material, G_L reduces to the classical shear modulus (Lamé constant).

The cyclic strain field associated with the displacement field given by (1) is then:

$$\underline{\underline{\varepsilon}}\left(\underline{x},t\right) = -\delta\frac{\omega}{2c}\cos\left[\omega\left(t - \frac{x_3}{c}\right)\right]\left(\underline{e}_1 \otimes \underline{e}_3 + \underline{e}_3 \otimes \underline{e}_1\right) \tag{3}$$

corresponding to a pure shear strain amplitude γ equal to:

$$\gamma = \delta \frac{\omega}{2c} = \frac{\delta\omega}{2}\sqrt{\frac{\rho}{G_L}} \tag{4}$$

The accumulation of excess pore pressure, and thus the risk of liquefaction, is directly connected to this cyclic shear strain amplitude.

2.2 Shear strain amplitude localization in reinforced soils

In order to avoid any risk of liquefaction a possible solution is to strengthen the soil by the incorporation of inclusions (example of stone or vibro-concrete columns: Baez & Martin (1993) and Adalier et al. (2003)). The volume fraction occupied by the inclusion is denoted by η. One should distinguish the macroscopic shear strain amplitude γ^{hom} of the reinforced soil, seen as a homogenized material, and the average of the amplitude $\langle\gamma\rangle_s$ in the original soil in the presence of reinforcement.

An isotropic non-reinforced soil with a shear stiffness denoted by G_s is first compared to a reinforced soil, the macroscopic longitudinal shear stiffness of which is denoted by G_L. The ratio between the shear strain amplitude of these two materials subject to the same shear wave (1) (γ_s and γ^{hom} respectively) is deduced from (4):

$$\frac{\gamma^{hom}}{\gamma_s} = \sqrt{\frac{G_s}{G_L}} \tag{5}$$

with the simplifying assumption that the original soil mass density ρ_s is almost equal to the reinforced soil mass density $\langle\rho\rangle = (1-\eta)\rho_s + \eta\rho_r$. It is clear that this ratio is less than or equal to one, since the reinforcement strengthens the original soil. The amplitude of the homogenized soil shear strain is then smaller than that of the original soil (see Fig. 2).

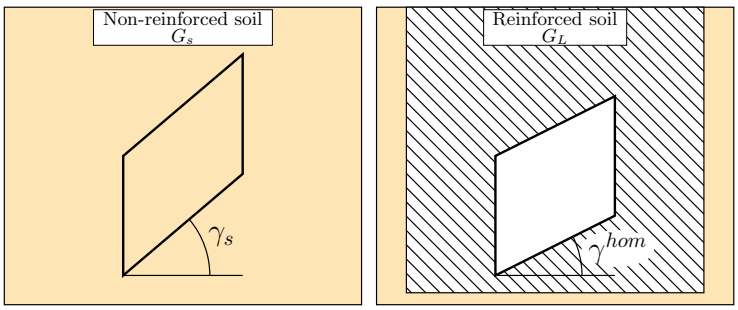

Fig. 2. Shear strain amplitude: (a) case of non-reinforced soil, (b) case of reinforced soil.

In fact, the relevant comparison is to be made between γ_s and the average value of the shear strain $\langle\gamma\rangle_s$ in the soil in the presence of reinforcement (see Figure 3), defined as:

$$\underline{\underline{\epsilon}} = \gamma^{hom}\left(\underline{e}_1 \otimes \underline{e}_3 + \underline{e}_3 \otimes \underline{e}_1\right) \;\rightarrow\; \langle\gamma\rangle_s = \frac{1}{\mathcal{C}_s}\int_{\mathcal{C}_s} \varepsilon_{13}\, dV = \lambda\gamma^{hom} \tag{6}$$

where $\mathcal{C}_s$ denotes the domain occupied by the soil and λ is defined as a *localization factor*. Its value depends on the geometry of the inclusions as it will be seen in the following sections, but will be greater than unity, the original soil having a smaller stiffness G_s than reinforcement material denoted by G_r.

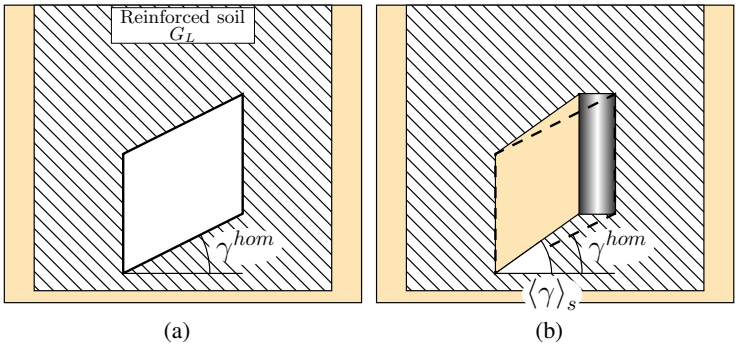

Fig. 3. Shear strain amplitude: (a) case of reinforced soil see as a homogenized material, (b) decomposition in both constituants.

The reduction of potential risk of soil liquefaction to be expected from the stiffening of the reinforcement by inclusions, which will conventionally be called *risk reduction factor* R, is defined as:

$$R = \frac{\langle\gamma\rangle_s}{\gamma_s} = \lambda\sqrt{\frac{G_s}{G_L}} \tag{7}$$

This factor, to be compared to unity, expresses the competition between the strenghtening effect and the localization in the soil. An evaluation of R will be now performed for different geometries of reinforcement.

3 LONGITUDINAL SHEAR MODULUS AND RISK REDUCTION FACTOR OF COLUMN-REINFORCED SOIL

The first case investigated is a group of circular cylindrical columnar inclusions introduced in a soil with a volume fraction $\eta = \pi\rho^2$, where ρ is the radius of a column, assuming that the side of the unit cell is taken equal to unity (Figure 4).

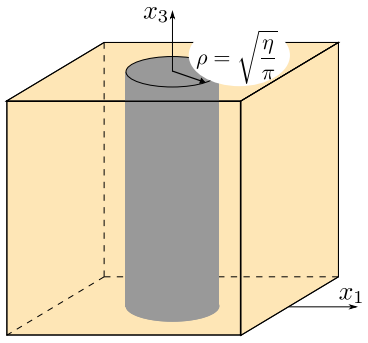

Fig. 4. Unit cell for a column configuration of reinforcement.

3.1 Upper bound estimate for G_L

It can proved (Gueguin et al. 2013) that, for any macroscopic strain $\underline{\underline{\epsilon}}$ and any displacement field $\underline{\xi}'$ kinematically admissible with $\underline{\underline{\epsilon}}$, the *minimum principle of the potential energy* gives the following inequality:

$$\forall \underline{\underline{\epsilon}},\ \forall \underline{\xi}' \text{ k.a. with } \underline{\underline{\epsilon}}, \quad \frac{1}{2}\underline{\underline{\epsilon}} : \mathbf{c}^{hom} : \underline{\underline{\epsilon}} \leq \left\langle \frac{1}{2}\underline{\underline{\varepsilon}}'(\underline{x}) : \mathbf{c}(\underline{x}) : \underline{\underline{\varepsilon}}'(\underline{x}) \right\rangle \tag{8}$$

where $\mathbf{c}(\underline{x})$ denotes the fourth order tensor of elastic moduli at point $\underline{x}$ of the unit cell and $\mathbf{c}^{hom}$ represents the macroscopic elastic stiffness tensor.

The prescribed macroscopic strain $\underline{\underline{\epsilon}}$ being of the form:

$$\underline{\underline{\epsilon}} = \Gamma\left(\underline{e}_1 \otimes \underline{e}_3 + \underline{e}_3 \otimes \underline{e}_1\right) \tag{9}$$

it follows that for this particular shear strain the left member of (8) simplifies to:

$$\frac{1}{2}\underline{\underline{\epsilon}} : \mathbf{c}^{hom} : \underline{\underline{\epsilon}} = 2G_L\Gamma^2 \tag{10}$$

so that we obtain an upper bound value for the macroscopic longitudinal shear modulus:

$$\forall \underline{\xi}' \text{ k.a. with } \underline{\underline{\epsilon}} = \Gamma\left(\underline{e}_1 \otimes \underline{e}_3 + \underline{e}_3 \otimes \underline{e}_1\right), \quad G_L \leq \frac{\left\langle \underline{\underline{\varepsilon}}'(\underline{x}) : \mathbf{c}(\underline{x}) : \underline{\underline{\varepsilon}}'(\underline{x}) \right\rangle}{4\Gamma^2} \tag{11}$$

For an adequate displacement field $\underline{\xi}'$, it can be proved that the upper bound is expressed as:

$$G_L \leq G_{L,col}^{ub} = G_s\left[1 + \frac{2\eta\left(G_r - G_s\right)}{\left(G_r + G_s\right) - \frac{4\eta}{\pi}\left(G_r - G_s\right)}\right] \tag{12}$$

3.2 Lower bound estimate for G_L

Using the *minimum principle of the complementary energy* with a macroscopic stress $\underline{\underline{\Sigma}}$ as loading parameter, a lower bound can be found for the same problem. For any stress field $\underline{\underline{\sigma}}'$ statically admissible with $\underline{\underline{\Sigma}}$, this principle may be written as:

$$\forall \underline{\underline{\Sigma}},\ \forall \underline{\underline{\sigma}}' \text{ s.a. with } \underline{\underline{\Sigma}}, \quad \frac{1}{2}\underline{\underline{\Sigma}} : \mathbf{s}^{hom} : \underline{\underline{\Sigma}} \leq \left\langle \frac{1}{2}\underline{\underline{\sigma}}'(\underline{x}) : \mathbf{s}(\underline{x}) : \underline{\underline{\sigma}}'(\underline{x}) \right\rangle \tag{13}$$

where $\mathbf{s}^{hom} = \left(\mathbf{c}^{hom}\right)^{-1}$ and $\mathbf{s}(\underline{x}) = \left(\mathbf{c}(\underline{x})\right)^{-1}$ are the macroscopic and local elastic compliance tensors, respectively.

For a macroscopic pure shear stress $\underline{\underline{\Sigma}}$ of the form:

$$\underline{\underline{\Sigma}} = T\left(\underline{e}_1 \otimes \underline{e}_3 + \underline{e}_3 \otimes \underline{e}_1\right) \tag{14}$$

the inequality (13) gives:

$$\forall \underline{\underline{\sigma}}' \text{ s.a. with } \underline{\underline{\Sigma}} = T\left(\underline{e}_1 \otimes \underline{e}_3 + \underline{e}_3 \otimes \underline{e}_1\right), \quad \frac{T^2}{2G_L} \leq \left\langle \frac{1}{2}\underline{\underline{\sigma}}'(\underline{x}) : \mathbf{s}(\underline{x}) : \underline{\underline{\sigma}}'(\underline{x}) \right\rangle \tag{15}$$

As a result, for an appropriately selected stress field (Gueguin et al. 2013), a lower bound for the longitudinal shear modulus of a column reinforced soil may be written as:

$$G_L \geq G_{L,col}^{lb} = G_s \left[1 - \frac{2\eta \left(G_r - G_s \right)}{\left(G_r + G_s \right) + \frac{4\eta}{\pi} \left(G_r - G_s \right)} \right]^{-1} \tag{16}$$

3.3 Comparison with numerical results for R

Two different estimates R_{col}^{+} and R_{col}^{-} of the risk reduction factor can be obtained from the displacement and stress fields previously used for deriving the bounds of G_L. Both are represented in Figure 6 as functions of the reinforcement volume fraction. After calculations, the first risk reduction factor estimate obtained from the displacement field is:

$$R_{col}^{+} = \lambda_{col}^{+} \sqrt{\frac{G_s}{G_{L,col}^{ub}}} \tag{17}$$

with

$$\lambda_{col}^{+} = \frac{1}{1-\eta} \left(1 - \frac{2\eta}{\left(1 + \frac{G_r}{G_s} \right) + \frac{4\eta}{\pi} \left(1 - \frac{G_r}{G_s} \right)} \right) \tag{18}$$

The second risk reduction factor estimate derives from the stress field used for deriving the lower bound of G_L and can be expressed as:

$$R_{col}^{-} = \lambda_{col}^{-} \sqrt{\frac{G_s}{G_{L,col}^{lb}}} \tag{19}$$

where

$$\lambda_{col}^{-} = \frac{G_{L,col}^{lb}}{G_s} \frac{1}{1-\eta} \left(1 - \frac{2\eta \frac{G_r}{G_s}}{\left(1 + \frac{G_r}{G_s} \right) - \frac{4\eta}{\pi} \left(1 - \frac{G_r}{G_s} \right)} \right) \tag{20}$$

R_{col}^{+} and R_{col}^{-} can also be compared with numerical simulations performed with the standard finite element code Cast3M (2003). Owing to the symmetries of geometry and loading, it can be proved that calculations may be done on a "slice" of the half unit cell. For this comparison, typical values of material parameters are adopted, namely a shear stiffness ratio between the column and the soil $\frac{G_r}{G_s}$ equal to 10 and a reinforcement volume fraction varying from $\eta = 0\%$ to $\eta = 40\%$. An exaggerated deformed configuration of the reinforced soil is sketched in Figure 5 (with $\eta = 12.6\%$) and an evaluation of R is numerically performed under shear loading.

It can be seen from Figure 6 that the two estimates R_{col}^{+} (plain curve) and R_{col}^{-} (dashed curve) bracket the numerical values (square symbols) even though they cannot be rigorously interpreted as bounds on R. It is worth noting that their average value (dashdotted curve) is a very accurate estimate for the reduction factor, numerical and analytical estimates show that column reinforcement technique is almost useless in terms of risk liquefaction reduction. Indeed the different

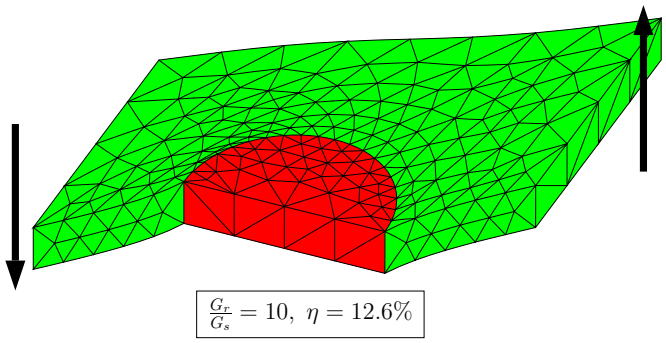

Fig. 5. Deformed configuration of a column reinforced soil under longitudinal shear loading (f.e.m calculation).

estimates of R being greater than unity, a slight increase in risk may be even observed for a column reinforced soil.

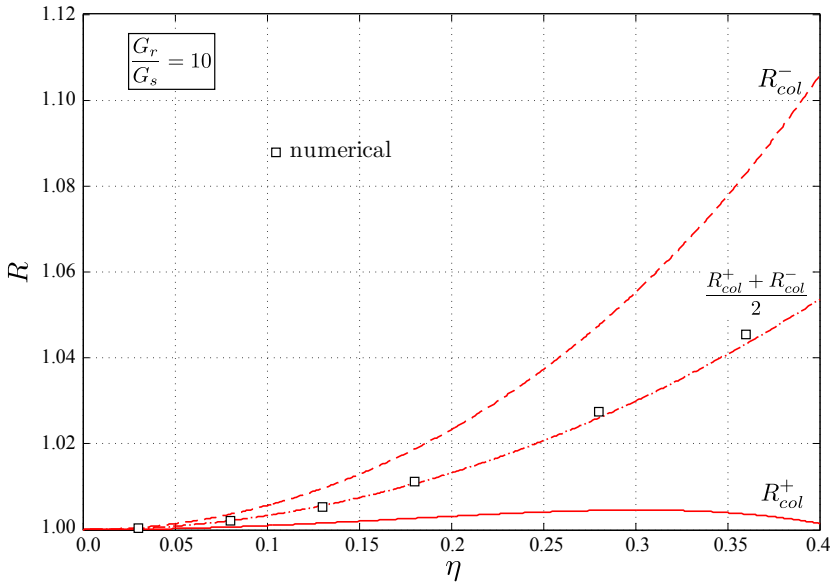

Fig. 6. Evaluations of the liquefaction risk reduction factor for a column reinforced soil.

4 THE CASE OF CROSS TRENCH CONFIGURATION

Performance of the most frequently used configuration of reinforcement by columnar inclusions being poor, a potentially innovative reinforcement technique (which is beginning to develop in practice) consists in improving the soil by a network of two perpendicular arrays of trenches, forming a ”honeycomb structure” embedded in the soil. This geometry is sketched in Figure 7 and will be called *cross trench* configuration. The thickness of a trench is noted t and the side of the unit cell is taken equal to unity so that the reinforcement volume fraction is $\eta = t(2 - t)$.

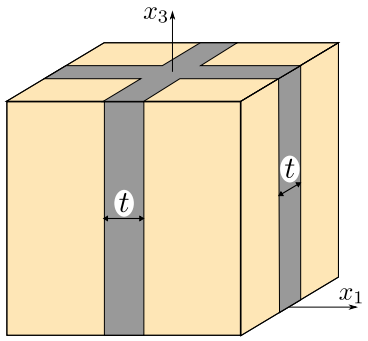

Fig. 7. Unit cell for a cross trench configuration of reinforcement.

4.1 Bounds and numerical estimates

Both variationnal methods already used for the column reinforced soil are implemented for the cross trench reinforcement configuration. On the basis of analytical calculations developed by Gueguin et al. (2013), it can be established that a first estimate of the risk reduction factor deduced from (8) is:

$$R_{ct}^{+} = \lambda_{ct}^{+}\sqrt{\frac{G_s}{G_{L,ct}^{ub}}} \tag{21}$$

with

$$G_{L,ct}^{ub} = G_r\left[\frac{\sqrt{1-\eta}+\frac{G_r}{G_s}\left(1-\sqrt{1-\eta}\right)}{\left(\eta-1+\sqrt{1-\eta}\right)+\frac{G_r}{G_s}\left(2-\eta-\sqrt{1-\eta}\right)}\right] \tag{22}$$

and

$$\lambda_{ct}^{+} = \left(2-\eta-\sqrt{1-\eta}+\frac{G_s}{G_r}\left(\eta-1+\sqrt{1-\eta}\right)\right)^{-1} \tag{23}$$

Using (13) with an appropriate stress field, a second estimate of the risk reduction factor of a cross trench reinforced soil can be written as:

$$R_{ct}^{-} = \lambda_{ct}^{-}\sqrt{\frac{G_s}{G_{L,ct}^{lb}}} \tag{24}$$

with

$$G_{L,ct}^{lb} = G_s\left[\frac{1-\eta}{(1-\eta)+\frac{G_s}{G_r}\left(\sqrt{1-\eta}-(1-\eta)\right)}+\frac{G_r}{G_s}\left(1-\sqrt{1-\eta}\right)\right] \tag{25}$$

and

$$\lambda_{ct}^{-} = \left(\sqrt{1-\eta}+\frac{G_s}{G_r}\left(1-\sqrt{1-\eta}\right)\right)^{-1} \tag{26}$$

A numerical simulation can also be made for this configuration and results are compared to both previous estimates of R. Figure 8 illustrates the fact that the reinforcing trench placed in the loading plane fully contributes to the reinforced shear stiffness, while the other trench perpendicular to the loading plane undergoes much less deformation. The cross trench reinforcement

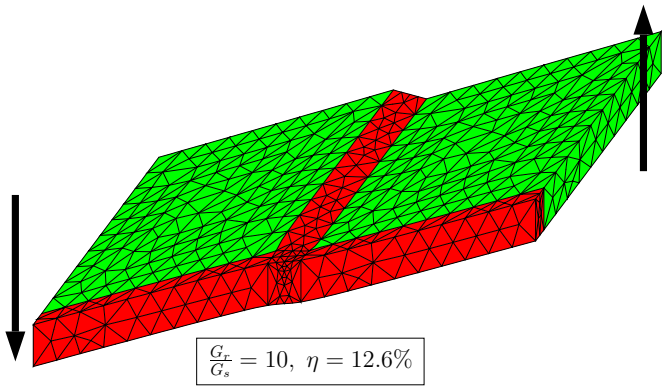

Fig. 8. Deformed configuration of a cross trench reinforced soil under longitudinal shear loading.

provides a kind of "bracing effect" to the shear loading.

Figure 9 displays the comparison between these estimates of R for a cross trench reinforced soil. A first remark is that the average value of R_{ct}^{+} and R_{ct}^{-} provides an excellent evaluation of this risk reduction factor. It is also worth noting that R is decreasing when η increases and is always less than unity. The efficience of the cross trench reinforcement is highlighted here, the risk being reduced by 24% for $\eta = 20\%$.

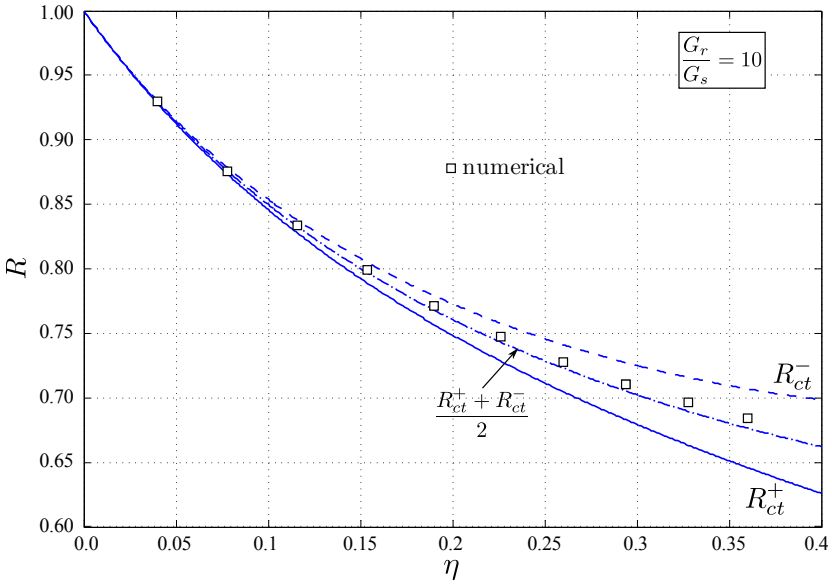

Fig. 9. Evaluations of the liquefaction risk reduction factor for a cross trench reinforced soil.

4.2 Parametric study for the risk reduction factor

The shear stiffness ratio $\frac{G_r}{G_s}$ and the reinforcement volume fraction η mainly influence the performance of the reinforcement technique in terms of liquefaction risk. For the cross trench configuration, a study has been made, choosing some fixed values of one parameter and expressing R as function of the other (see Figures 10 and 11). For the sake of clarity, only the average value

of the two estimates of this risk reduction factor are represented.

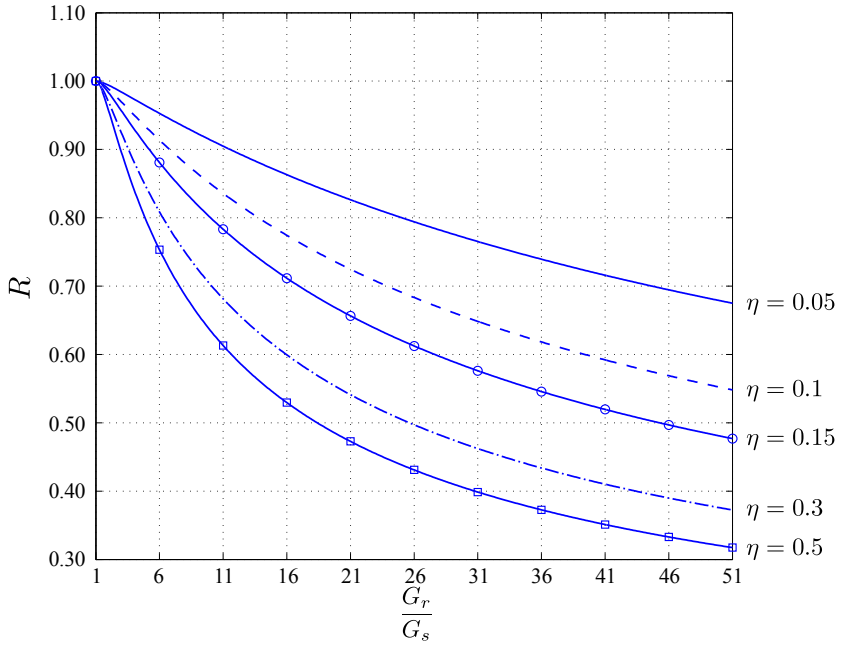

Fig. 10. Risk reduction factor of cross trench configuration as function of shear stiffness ratio $\frac{G_r}{G_s}$ for fixed values of η.

For different fixed values of η, the beneficial effect of the reinforcement is highlighted in Figure 10. However, it is worth noting that, for a shear stiffness ratio equal to 50, the risk reduction factor decreases from 0.68 to 0.48 when η goes from 5% to 15% while its decreases from 0.48 to 0.32 when η goes from 15% to 50%. This suggests that there is no need to increase the thickness of the trenches indefinitely, since the gain in terms of liquefaction risk being alternated.

In the same way, for different fixed values of $\frac{G_r}{G_s}$, the need to increase η is more obvious for small shear stiffness ratio. Indeed, for $\frac{G_r}{G_s} = 50$, the risk reduction factor rapidly decreases for small volume reinforcement fraction, then much more smoothly for higher volume fractions (Fig. 11).

5 CONCLUSIONS

Using the homogenization method for elastic periodic media, it has been possible to produce different estimates for the liquefaction risk reduction factor for a column reinforced soil as well as for a cross trench configuration. Analytical calculations allow to bracket the longitudinal shear stiffness for both techniques of reinforcement. An interesting result is that the reinforcement by columnar inclusions doesn't reduce the liquefaction risk, whereas the cross trench configuration provides an accurate reduction of this risk.

A short parametric study has been developed here for the cross trench reinforced soil depending on the two material and geometrical key parameters, namely the reinforcement volume fraction and the shear modulus ratio. All estimates being given by analytical formulas, charts may be easily drawn for different values of those characteristics which could be highly usefull

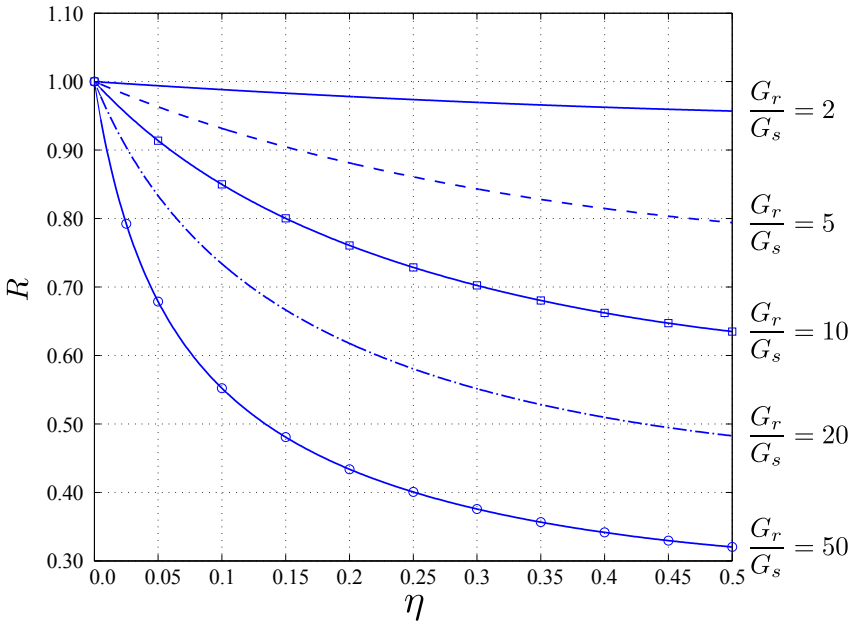

Fig. 11. Risk reduction factor of cross trench configuration as function of η for fixed values of $\frac{G_r}{G_s}$.

from an engineering design viewpoint. These results provide a strong theoretical background to the development of the cross trench reinforcement technique.

REFERENCES

Abdelkrim, M. & de Buhan, P. (2007). An elastoplastic homogenization procedure for predicting the settlement of a foundation reinforced by columns. *European J. of Mechanics, A/Solids 26*, 736–757.

Adalier, K., Elgamal, A., Meneses, J., & Baez, J. (2003). Stone columns as liquefaction countermeasure in non plastic silty soils. *Soil Dyn. Earthquake Eng. 23*, 571–584.

Baez, J. & Martin, G. (1993). Advances in the design of vibro systems for the improvement of liquefaction resistance. In *Proc. Symp. Ground improvement*, Canada, pp. 1–16. Vancouver Geotechnical Society.

Balaam, N. & Booker, J. (1981). Analysis of rigid rafts supported by granular piles. *Int. J. Num. Anal. Meth. Geomech. 5*, 379–403.

Canetta, G. & Nova, R. (1989). A numerical method for the analysis of ground improved by columnar inclusions. *Comput. Geotech. 7*, 99–114.

Cast3M (2003). http://www-cast3m.cea.fr.

Gueguin, M., de Buhan, P., & Hassen, G. (2013). A homogenization approach for evaluationg the longitudinal shear stiffness of reinforced soils: columns *vs*. cross trench configuration. *Int. J. Num. Anal. Meth. Geomech.*, Accepted for publication.

Hashin, Z. (1983). Analysis of composite materials-a survey. *J. Appl. Mech. 50*, 481–505.

Hashin, Z. & Rosen, B. (1964). The elastic moduli of fiber-reinforced materials. *J. Appl. Mech. 21*, 233–242.

A SIMPLIFIED COMPUTATIONAL MODEL FOR A PERIODIC SYSTEM OF HORIZONTALLY LOADED PILES

A. Urbański
Department of Environmental Engineering, Cracow University of Technology, Cracow, Poland

ABSTRACT: *A method of numerical simulations of the behaviour of a periodic system of piles loaded horizontally (example: an excavation supported by a soldier pile wall), named "2D/3D", is presented. It is indented as a tool allowing practising engineer-designer to omit the necessity of costly 3D analysis, but giving practically the same response. In the 2D/3D method, basic analysis of the geotechnical system is conducted in 2D FE model adopting assumption of plane strain (PS), but is enriched with results of subsidiary 3D tasks by the concept of elasto-plastic 1D connectors.*

1 MOTIVATION

Periodic systems of piles loaded horizontally are common in engineering. Examples include a so called "soldiers pile wall" (see Fig. 1), palisades or pile foundations of a sound barrier, etc. The common feature of these geo-structural systems is that a drilled pile is loaded horizontally, and this kind of load action governs the design with respect to both ultimate and serviceability limit states. The problem of piles submitted to lateral loads was analyzed by numerous researchers, starting from classical work of Broms (1964) up to recent works devoted mainly to 3D FE elasto-plastic analyses of pile-soil systems, to mention only two representative and latest papers of Sawant & Shukla (2012), Mardfekri et al. (2013).

The method presented here will be useful when a periodic system of piles is a part of some greater geo-structural system, as shown in the Fig. 2. In these circumstances 2D FE analysis (plane strain (PS) model) would be chosen by the majority of engineers, mainly because of the effectiveness of a design process.

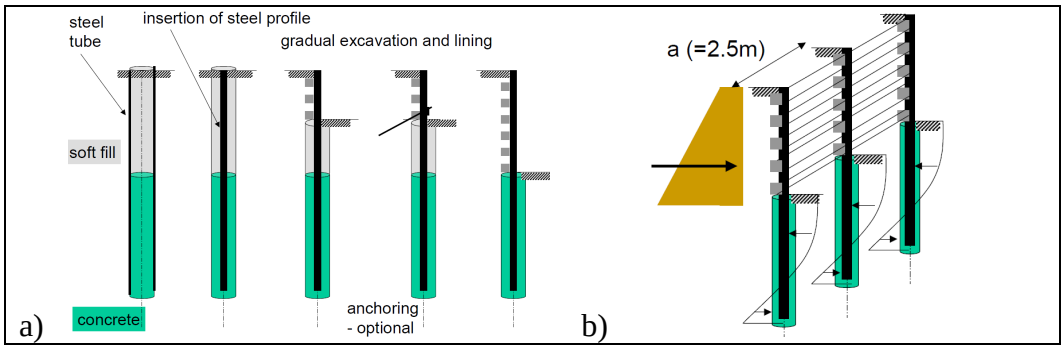

Fig. 1. Soldier wall („Berlin" type). a) Phases of construction. b) Load action.

The difficulty however appears because all fields (displacements **u**, strains **ε** and stresses **σ**) are 3D in their nature and drastically violate assumptions of the plane strain model in the ground surrounding the pile. Moreover, these local 3D periodic fields decide on a bearing capacity of the pile against horizontal forces, which, in turn, may strongly influence stability of the whole system. For example, treatment by the designer of the soldier pile wall system as continuous and constant in the "z" direction was the main reason of overestimation of the stability and in consequence in reaching of the ultimate state (marked as GEO in EC7) by the geo-structure shown in the Fig.2. N.B, the author's interest in the subject started from the analysis of this break-down case, where the method described below was first applied, yielding results (displacement, stability assessment) very close to the ones measured and observed in the field, see Urbanski & Grodecki (2013).

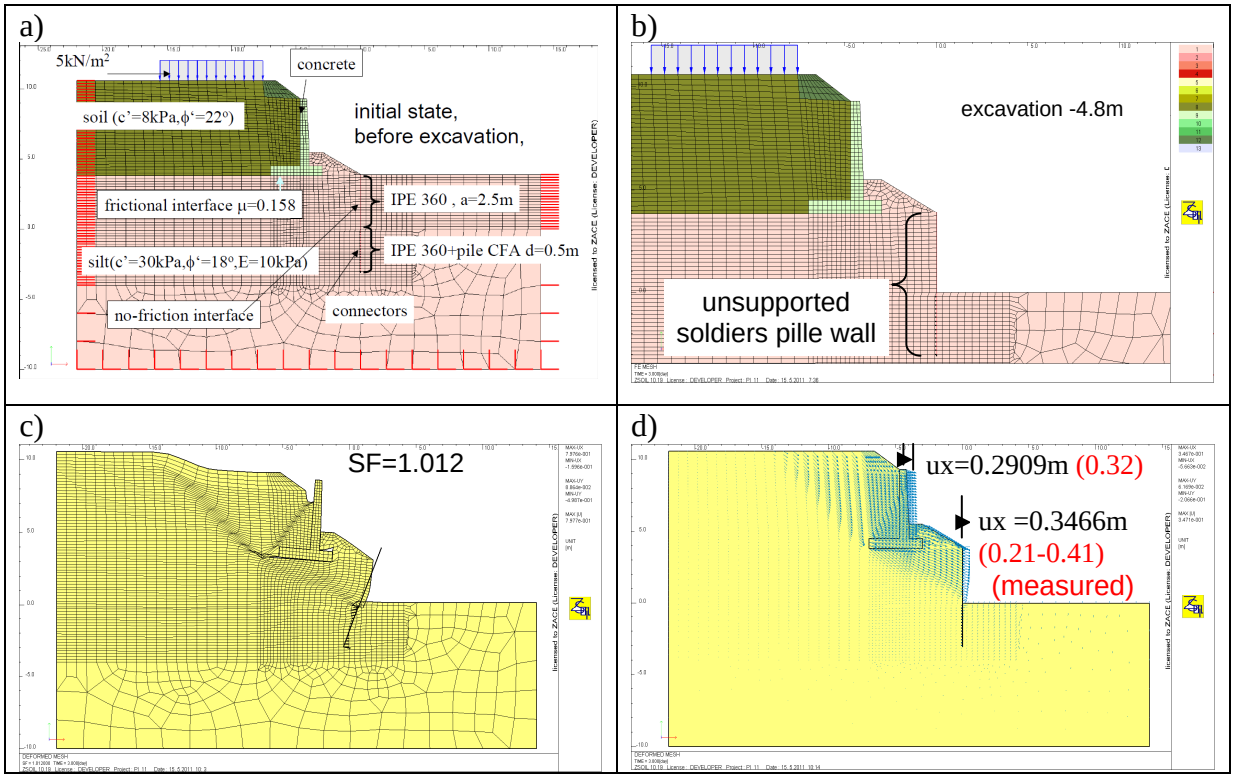

Fig. 2.Break-down of soldier wall and results of 2D/3D analysis a) initial situation, b) after excavation, c) simulated loss of stability by c-ϕ reduction method, d) simulated and observed displacements.

Full 3D FE analysis, however widely available nowadays (for example in ZSoil.PC package) is rejected by many practising engineers because of many reasons, such as lack of appropriate software, difficult and time consuming modeling, and generally much higher cost of 3D FE. They will accept a simpler method, basing on 2D analysis, even of lesser accuracy, if only its result would be reliable, particularly for the assessment of the ultimate limit state. The willingness of creating such a computational method being the compromise between the 3D and 2D analysis, and its base and introductory verification is the goal of the work.

2 A METHOD 2D/3D FOR ANALYSIS OF A PILE SYSTEM

In the method, called 2D/3D, the whole system resulting from geotechnical data for a given section is analyzed in 2D with the assumption of a plane strains model. The method is open for application of any constitutive model of soil media, here standard elasto-plastic Mohr-

Coulomb is used. The pile is modeled by beam elements but in the part below the ground surface they are connected to 2D continuum elements via fictitious connectors, i.e. elasto-plastic truss elements placed horizontally. Presence of these connectors is crucial in reproducing differences between 2D and 3D modeling. The idea of 2D/3D method is shown in the Fig. 3.

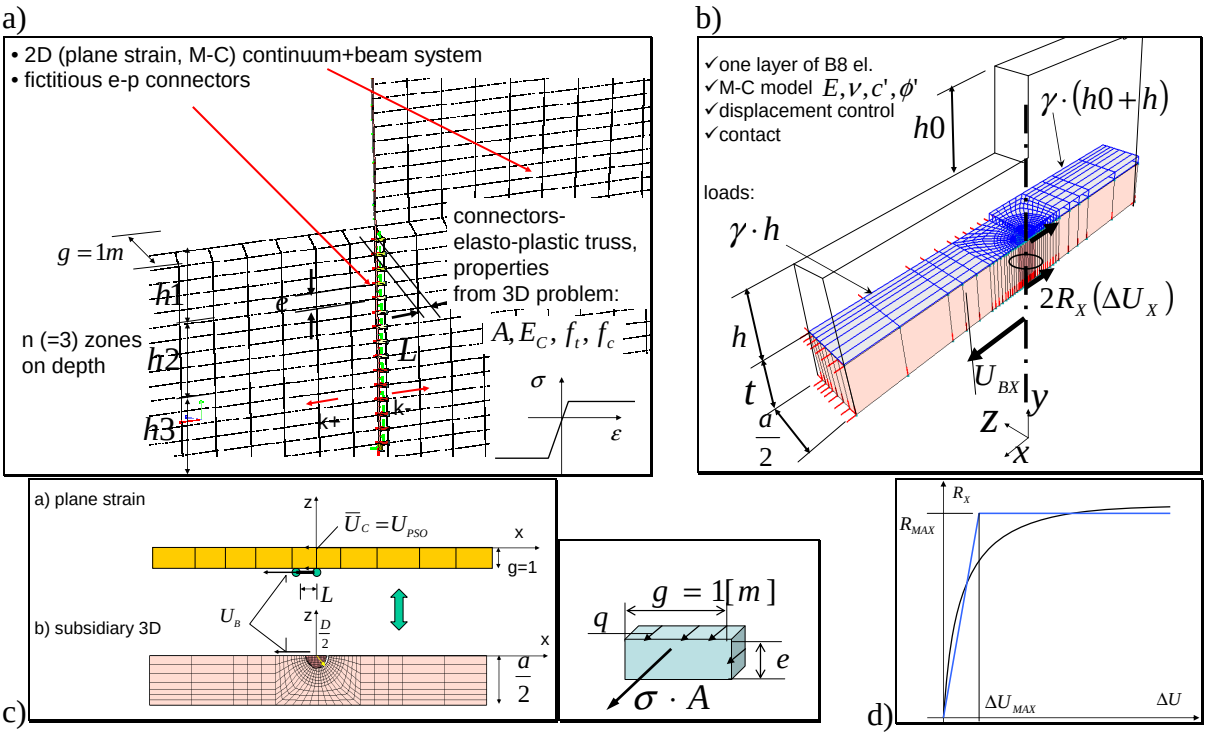

Fig. 3. Idea of FE modeling in 2D/3D method a) plane strain model with a pile and connectors b) subsidiary 3D problem, c) equivalency of the both models d) resulting relation $R_X(\Delta U)$

The identification of stiffness and strength properties of the connectors will be performed on the basis of a function relating the reaction force and the imposed displacement of a pile, obtained from the subsidiary 3D tasks for the layer of arbitrary small thickness *t*. Only 1/2 of the length *a* of one segment of periodic structure is taken due to symmetry. The loads acting on the layer are:

- vertical load due to soil weight (p_Y=-γh for the part beneath the excavated area, p_Y=-$\gamma(h_0+h)$ for the rest),
- horizontal displacements U_{XB}, imposed at the central node of the pile.

The kinematic boundary conditions are as follows (Fig. 3b):

- XY planes: (from symmetry and periodicity of the system) $U_Z(x,y,z=½a) = U_Z(x,y,z=0)=0$;
- XZ plane: (on the bottom of the model) $U_Y(x,y=0,z)=0$;
- YZ planes: (in the sufficient distance *l* from the centre) $U_X(x=\pm l,y,z)=0$.

The subsidiary problem is set also as an elasto-plastic one, with Mohr-Coulomb condition. In this FE model of a soil layer, considering vertical load and resulting compressive stresses $\sigma_{YY} = p_Y$ is crucial, because these stresses, when only introduced to the yield condition (in full 3D form), have a great influence on the plastic state and response of the media, particularly when soil posses low cohesion $C \approx 0$. In ZSoil it can be achieved by building a 3D FE model

with one layer of brick elements B8. Between the pile and the soil interface elements are introduced assuming frictionless unilateral contact (with constant topology of elements).

The output is a sum of 2 reaction forces (at the bottom and top node) as a function of the difference ΔU between displacement U_B and averaged mean displacement of soil $\overline{U}_C$, for $x=0$:

$$\overline{U}_C = \frac{2}{a-D}\int_{D/2}^{a/2} U_{3D}(0,0,z)dz \approx U_{3D}(0,0,a/2) \tag{1}$$

In practice, it can be replaced by the displacement taken at (*0,0,a/2*) as the discrepancy versus averaged value is meaningless for most of cases. Note however, that taking the difference ΔU but not the displacement U_B alone as an output is a must, because in this kinematic condition (i.e. periodic in *z* dir.), the force response on the applied displacement is strongly sensitive to the length of the model in the *x*-direction (is linearly dependent) while the difference ΔU is not. The difference ΔU taken for the 3D model represents the elongation of the connector,

$$\Delta U = U_B - \overline{U_C} \Rightarrow \varepsilon = \frac{\Delta U}{L} \tag{2}$$

because in 2D model U_B is the displacement of the pile while $\overline{U}_C$ is the displacement of the 2D plane strain continuum at the location of the pile, as shown in Fig. 3c. Fig 3d shows reaction R_X as a function of ΔU, and its approximation by a bilinear function.
Having given reaction forces $R_X = R_X(\Delta U)$, lateral resisting stresses q[kN/m^2], averaged on surface $t \cdot ½a$, can easily be obtained

$$q(\Delta U) = \frac{2 \cdot 2 \cdot R_X(\Delta U)}{t \cdot a} \tag{3}$$

Assuming that in the 2D model the connectors have an area *A*, are equally distributed in distance *e* and their length is *L*, while g=1 is the unit thickness of the plane strain model, taking into account the static equivalency between the forces in the connectors $F_C = \sigma \cdot A$ and force resulting from lateral resisting stresses q at $e \cdot g$ area in the form

$$\sigma \cdot A = q \cdot e \cdot g \tag{4}$$

the function between the stress and strain for the connector is

$$\sigma(\varepsilon) = \frac{q \cdot e \cdot g}{A} = \frac{4e \cdot g}{t \cdot a \cdot A} R_X(\varepsilon \cdot L) \tag{5}$$

Elasto-plastic properties of the connector (or rather its bilinear approximate model) are Young modulus of a fictitious 1D truss type element

$$E_C = \frac{4 \cdot}{t \cdot a} \frac{R_{MAX} \cdot e \cdot g \cdot L}{A \cdot \Delta U_{MAX}} \tag{6}$$

and the strength of its material in tension (f^+) and compression (f^-), separately:

$$\left.\begin{matrix} f^+ \\ f^- \end{matrix}\right\} = \frac{4 \cdot}{t \cdot a} \frac{R^{\pm}_{MAX} \cdot e \cdot g}{A} \tag{7}$$

These characteristics are dependent on the constitutive properties of the soil, the depth on which the considered layer is located, and on the direction of the considered movement marked +/- with respect to the *x*-axis, see Fig 3a. Introduction of the elasto-plastic connectors to the 2D plane strain model is the simplest (but approximate) way to reproduce such a feature of the pile system as a limited ability to sustain horizontal force. The verification of the correctness of the method by comparing its result with 3D analysis will be the subject of the next point.

3 A COMPARISON OF THE METHOD 2D/3D AND 3D FE ANALYSIS OF A SOLDIERS PILE SYSTEM

In order to verify the 2D/3D method, the two FE models, i.e. 3D and 2D, concerning the same system of piles corresponding to a soldier pile wall are analyzed. Both models were created and analyzed in ZSoil.PC v12.19 software. The analyzed system is a simplified one, in the way enabling comparison of the behavior of the immersed parts of piles. The loads are the horizontal force and the moment from active ground pressure as well as the vertical load due to the remaining ground from one side of the piles, on height 5m approximately. The overview of the example, with all necessary data is given in the Fig. 4. Note, that the density of the meshing as well as the extent of both models are similar. In the 2D model, the connectors (distance e=0.25m, length L=0.1m, area A=1.0m^2), are located at the midpoints of the continuum Q4 elements side.

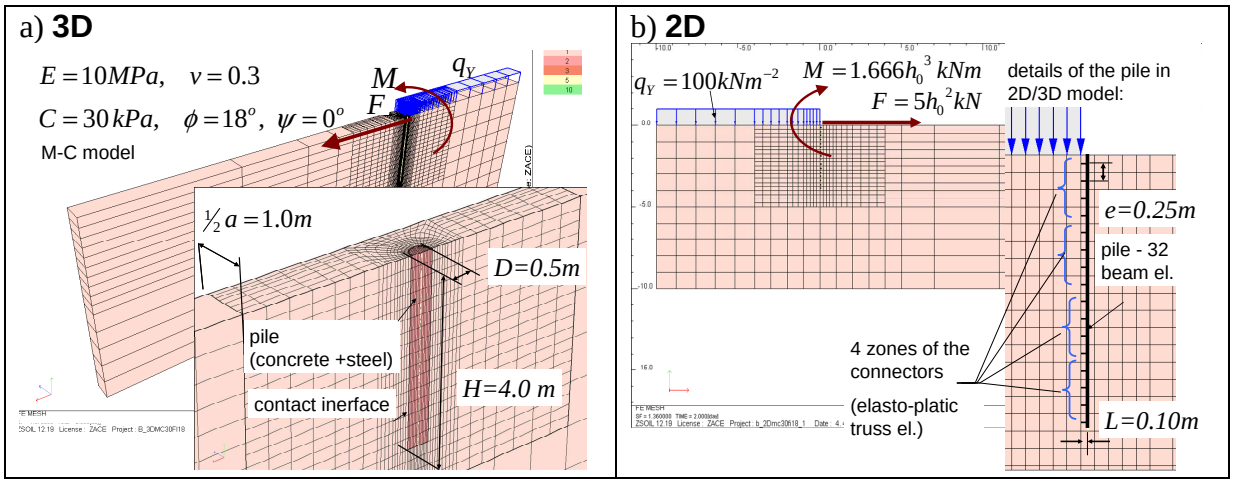

Fig. 4. FE models of simplified periodic pile system (soldier pile wall - only immerse part) in a) 3D b) 2D

3.1 Analysis of subsidiary 3D problem

The analysis by 2D/3D method firstly requires setting properties of the connectors. As these properties (mainly strength of a connector) depend strongly on the depth, in the example, to a 4m long pile, four zones (each of 1.0m) were assumed corresponding to the varying depth.

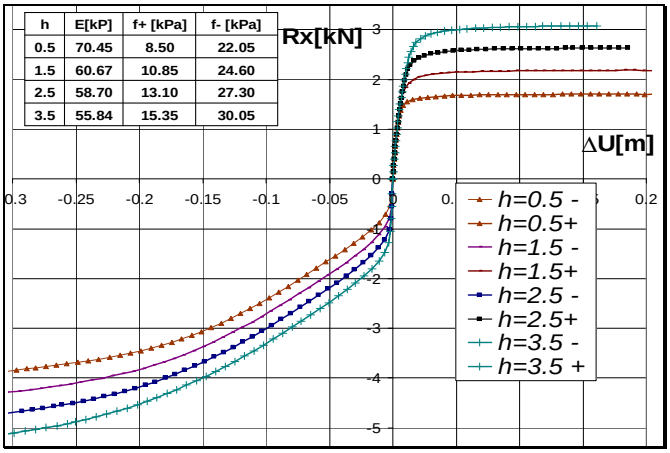

Fig. 5. Reaction forces as a function of displacements for the layers at different depth and properties of connectors

Fig 5. shows results for the subsidiary 3D problem for the reaction forces as a function of displacements for the layers at these depths, (thickness t=0.1m). Moreover, in the graph, a table containing elasto-plastic properties of connectors based on Eqs. (6),(7), is given.

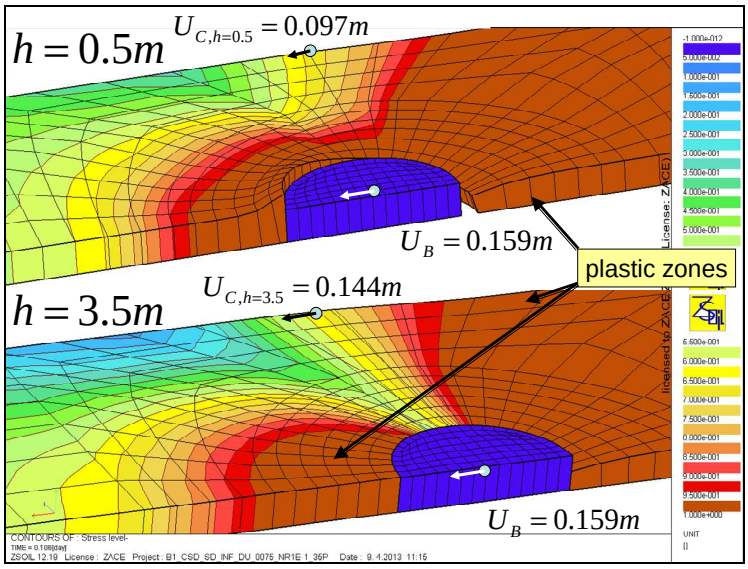

Fig. 6. Stress level maps (=1.0 plastic) and deformation of the layers at different depth

Fig. 6 shows the deformed mesh shape and stress level maps ($0 \le SL \le 1$, SL=1 for the plastic state), for the layers located at two depths h=0.5 m and h=3.5m, and for the same displacement imposed at the pile centre U_B=0.159m. Note however, that displacement U_C and the resulting elongation of the fictitious connector ΔU being an argument of its characteristic $R_X(\Delta U)$ differ substantially for these two cases: $U_{C,\ h=3.5}$=0.144m ($\Delta U_{\ h=3.5}$=0.015m, $R_{X,h=3.5}$=2.60kN) while $U_{C,\ h=0.5}$=0.097m, $\Delta U_{\ h=0.5}$=0.0615m, $R_{X,h=0.5}$=1.70kN. For the depth h=0.5m the reaction force R_X reaches ultimate value $R_{MAXh=0.5}$ in the bilinear model, while for the deeper one, it remains within "linear" range of the connector model (2.6/3.10*100%=83% of $R_{MAXh=3.5}$).

3.2 Comparative study of two models (2D/3D and 3D) of a soldier pile wall

The simulation of both model (2D/3D and 3D) has a following scenario: at first system is loaded with the weight of the resting ground q_Y=100 kN/m^2 from one side of a pile; the assumed horizontal pressure of this at the top of the model is $p=K_a \cdot \gamma \cdot a/2 \cdot h_0=0.5 \cdot 20 \cdot 1 \cdot h_0$ [kN/m], it gives the resultant force $F=1/2 \cdot p \cdot h_0=5 \cdot h_0^2$ kN (for a pressure with a triangular distribution along the height h_0) and moment $M=1/3 \cdot F \cdot h_0=1.666 \cdot h_0^3$ kNm acting at the top of the pile. Loads with values being a function of height h_0, $F(h_0)$ and $M(h_0)$, are then incrementally applied with the step Δh_0=0.05m, until the moment of reaching the critical height $h_{0MAX}+\Delta h_0$, causing failure. The displacement at the top U_{XB} and the pile rotation angle $\Delta U/H$ as a function of height h_0 in the stability range are shown on Fig. 7. For the 2D/3D model ($h_{0MAX,\ 2D}$=3.30m) while for the 3D one $h_{0MAX,3D}$=4.00m. This means, that in analyzed case, the 2D/3D model slightly (i.e. 17.5%=(4.00*3.30)/4.00*100%) underestimates bearing capacity of the system. This effect may be related to the simplified, stepwise distribution of vertical stresses σ_{YY} assumed in the subsidiary 3D model, which varies (particularly for the greater depth of) from the one, observed in the referential 3D model. For the lower height h_0 displacement results coincide.

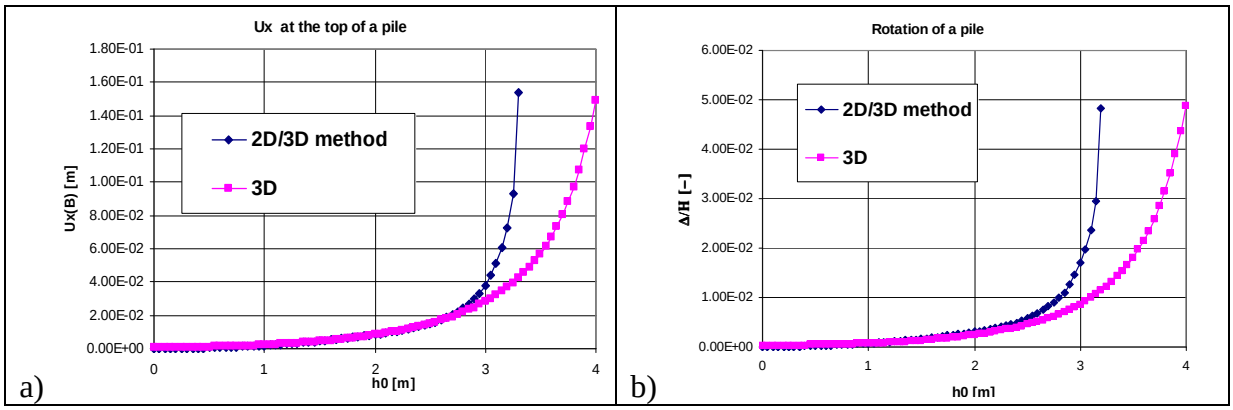

Fig. 7. Comparison of displacement/height relation for a soldiers pile wall

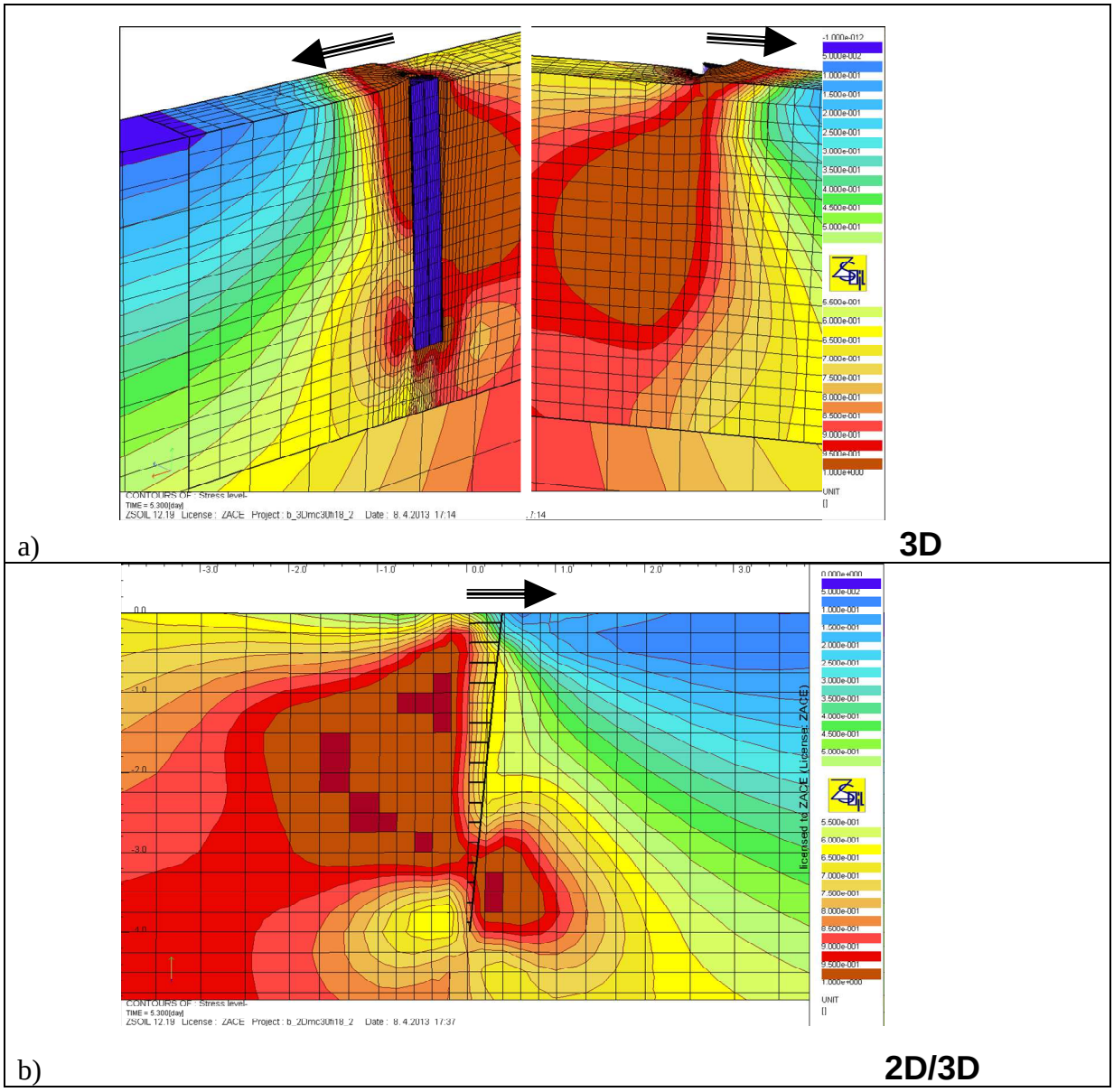

Fig. 8. Maps of stress level and the deformation for the two model
a) 3D (a view for both sides b) 2D/3D

In Fig. 8 maps of the stress level are shown for both models (for the case of height $h_0=h_{0MAX,2D}$=3.30m). Note, that for the upper zone in front of the pile in the 3D model, a zone of plastic yielding of the soil due to the pile pressing on it appears, while in the 2D model the connectors became plastic in that zone, instead.

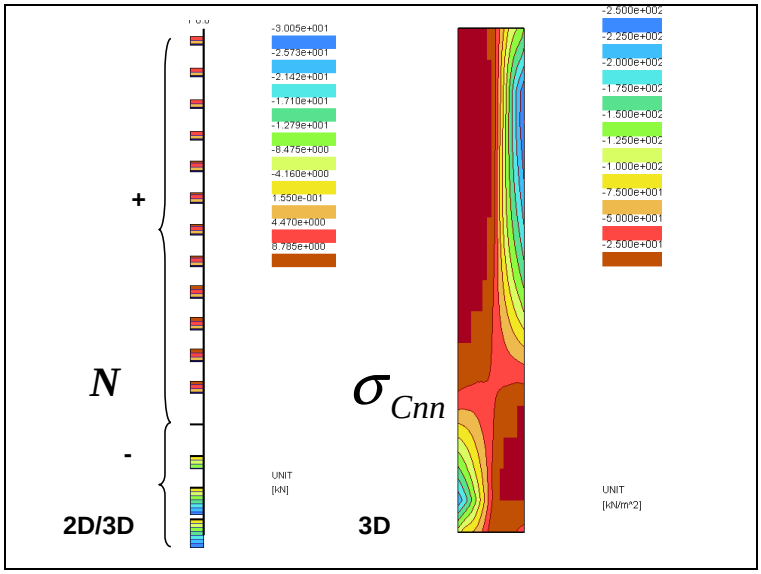

Fig. 9. Interaction pile-soil for both models

In Fig. 9 interaction between the pile and the surrounding soil is shown in a different manners, which are specific for both models. In 2D as forces N in all connectors (tensile (+) at the upper zone - i.e. pressing in the direction of force F, compressive (-) at the lower zone - i.e. pressing in the direction opposite to the force F). In 3D normal stresses σ_{Cnn} from the contact interface elements are mapped, at the whole pile circumference. Qualitatively, decomposition of both, along the pile, agrees.

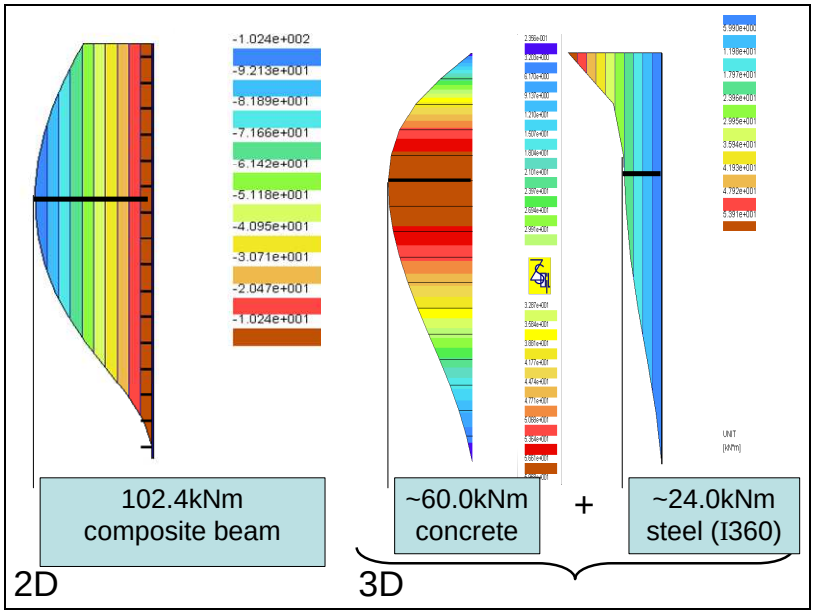

Fig. 10. Moment graphs in the pile for both models

Fig. 10. compares bending moments M obtained from both models, again for $h_0=h_{0MAX,2D}$=3.30m, i.e. F= 54.45kN, M=59.89kNm acting at the top of the pile. In 2D one chain of beam elements ($EI=EI_{Stell}+EI_{Concrete}$) is used, yielding $M_{MAX,2D}$=102.4kNm. In 3D a chain of beams element is used for the steel core inserted (I360), exclusively. Concrete is modelled by continuum elements (B8). Specialized post-processing option in ZSoil allows to calculate moments for such a group of continuum elements creating a beam, yielding $M_{MAX,3D}=(M_{Concrete}+M_{Steel})(h=2.75)$=60.0+24.0=84.0kNm. Relative difference between them equals δM=(102.4-84.0)/102.4*100%=17.9%.

4 CONCLUSIONS

In this paper only a basic and introductory verification of the 2D/3D method for the analysis of a periodic pile system loaded horizontally has been performed. The selected case was characterized by the geometry, load and soil constitutive data being "in the middle" of commonly encountered range. Moreover, this research study was close to a practical case, which was recently described by Urbanski & Grodecki (2013). In author's opinion, general and qualitative agreement between 3D FEM analysis, being the reference, and the proposed 2D/3D method was achieved. As for the quantitative results, observed discrepancy in bearing capacity (17.5% underestimation in 2D/3D) is explainable, due to too rough simplification of vertical stresses adopted in recent work. Also internal forces in the pile are evaluated with similar level of differences (17.9%). The issue of their minimization will be the subject of future research.

The key idea of 2D/3D method is to introduce fictitious connectors with properties identified during analysis of subsidiary 3D problem. This part of work is, at the current moment, in its initial phase. Finally, a numerical experiment is planned, covering a wide range of different geometrical, load, and constitutive data and elaboration of formula allowing user to create stiffness and strength parameters of connectors by hand calculation. The 2D/3D method presented in the paper, creates hope for a simple computational tool of these geo-structural system. It would be particularly useful in practical cases when a pile system is part of a larger geo-structure which has to be analyzed by 2D FEM. It allows to take into account local 3D phenomena in the soil surrounding pile, and its consequences on deformation and stability of the whole system.

REFERENCES

Broms, B. (1964) "The lateral resistance of piles in cohesive soils," J. Soil Mech. Found. Div., ASCE, Vol. 90, pp. 27-63.

Sawant, V. & Shukla, S. (2012) "Finite element analysis for laterally loaded piles in sloping ground" Coupled Systems Mechanics, Vol. 1, No. 1 (2012) 59-78.

Mardfekri, M., Gardoni, P. & Roesset, J., (2013) "Modeling laterally loaded single piles accounting for nonlinear soil-pile interactions", Journal of Engineering, Volume 2013, Article ID 243179, 7 pages

Urbański, A. & Grodecki, M. (2013), "Analysis of a breakdown of a deep excavation supported by soldier pile wall" (in polish). Technical Transactions (Czasopismo Techniczne). Cracow University of Technology Press (to appear).

NUMERICAL ANALYSIS OF THE LONG TERM SETTLEMENT OF ENERGY PILES

A. Di Donna
Swiss Federal Institute of Technology, EPFL, Station 18, CH 1015 Lausanne, Switzerland

F. Dupray
Swiss Federal Institute of Technology, EPFL, Station 18, CH 1015 Lausanne, Switzerland

L. Laloui
Swiss Federal Institute of Technology, EPFL, Station 18, CH 1015 Lausanne, Switzerland; King Abdulaziz University, Jeddah, Saudi Arabia

ABSTRACT: *Energy geostructures represent a renewable and clean source of energy which can be used for heating and cooling of buildings and de-icing of infrastructures. This technology couples the structural role of geostructures with the energy supply, using the principle of shallow geothermal energy. Heat is extracted from the ground during winter and injected into the ground during summer. This represents an additional thermal loading, seasonally cyclic, which is imposed to the soil and the structure itself. It is known that normally consolidated clays show thermoplastic deformation during heating. Thus, in this paper, the influence of temperature on the displacements of an energy pile foundation installed in normally consolidated clay is studied numerically. This represents one of the main issues involved, according to the Eurocode 7, in the geotechnical design of deep foundations. The results show that the thermal load induces additional movements of the foundation which are acceptable in normal working conditions but deserve to be considered in the design practice.*

1. INTRODUCTION

The energy geostructures are spreading rapidly in Europe and all around the world. This technology couples the structural role of geostructures with the energy supply, using the principle of shallow geothermal energy. This system allows extracting heat from the ground during winter to satisfy the heating needs of the buildings and injecting heat in the ground during summer, to satisfy the conditioning needs. As the energy geostructures represent a new engineering technology and they are becoming more and more common, an improved scientific knowledge of their behaviour is necessary. In the recent years, several efforts have been devoted to investigate and optimize the energy performance of such structures (Pahud, 2002). With regards to their mechanical behaviour and geotechnical design, efforts have been devoted to the in-situ characterization (Laloui et al., 2003; Bourne-Webb et al., 2009; Amatya et al., 2011), numerical analysis (Laloui et al., 2006, Dupray et al., 2013) and development of design tools (Knellwolf et al., 2011). An up to date state of the art on the subject can be found in Laloui and Di Donna (2011). The goal of this paper is to investigate numerically the long term response of an energy pile foundation to a seasonally cyclic thermal loading in terms of displacements.

2. MATHEMATICAL FORMULATION

The considered problem is represented by a concrete pile foundation subjected to a mechanical vertical load and able to exchange heat with the surrounding ground. Both the concrete and the soil are considered as porous materials composed by a solid and a liquid phase. The whole medium is considered to be fully saturated of water. The concrete behaviour is reproduced by a thermo-elastic model, while the soil behaves accordingly to a thermoelastic-thermoplastic constitutive model. Hence, three main aspects are involved in the problem, which are the mechanical, the thermal and the hydraulic ones. A coupled Thermo-Hydro-Mechanical (THM) formulation for saturated porous media is needed to correctly analyse the problem. The software used for this work is called LAGAMINE and the coupled THM formulation, implemented by Charlier (1987) and Collin (2003), is summarised in the following.

2.1 Governing equations

The equilibrium and balance equations, as well as the water and heat diffusions, are expressed in the moving current configuration through a Lagrangian-updated formulation. Assuming the Terzaghi formulation for effective stress, the equilibrium equation reads:

$$\mathrm{div}\left(\mathbf{D^{ep}}:(\boldsymbol{\varepsilon}-\boldsymbol{\varepsilon}^{\mathbf{Te}})\right)-\mathbf{grad}\,p_w+\rho\mathbf{g}=0 \tag{1}$$

where 'div' denotes the divergence, the symbol ":" the tensorial product, **grad** the gradient, $\mathbf{D^{ep}}$ the elasto-plastic constitutive tensor, $\boldsymbol{\varepsilon}$ the strain tensor, $\boldsymbol{\varepsilon}^{\mathbf{Te}}$ the thermo-elastic strain tensor, p_w the pore water pressure, **g** the gravity and ρ the total density of the material (including water ρ_w and solid ρ_s components). The mass conservation equation reads:

$$\partial_t p_w\left(n\frac{1}{K_w}+(1-n)\frac{1}{K_s}\right)+\partial_t T\left[n\beta'_w+(1-n)\beta'_s\right]+\mathrm{div}(\partial_t\mathbf{u_{rw}})=0 \tag{2}$$

where ∂_t represents the time derivative, n the porosity, $\frac{1}{K_w}$ and $\frac{1}{K_s}$ the water and solid skeleton compressibility, T the temperature, β'_w and β'_s the volumetric thermal expansion coefficients of water and solid skeleton and $\mathbf{u_{rw}}$ the relative velocity of water with respect to the solid. This latter can be expressed by the Darcy's law, as:

$$\partial_t\mathbf{u_{rw}}=-\frac{\mathbf{K}}{\rho_w\mathbf{g}}\cdot\left[\mathbf{grad}(p_w)+\rho_w\mathbf{g}\cdot\mathbf{grad}(z)\right] \tag{3}$$

where **K** is the hydraulic permeability tensor (measured in m/s) and z the vertical coordinate. The energy conservation equation reads:

$$\rho\hat{c}\,\partial_t T-\mathrm{div}(\Gamma\cdot\mathbf{grad}T)+\rho_w c_{p,w}\,\partial_t\mathbf{u_{rw}}\mathbf{grad}T=0 \tag{4}$$

where $\hat{c}$ is the soil specific heat (including water $c_{p,w}$ and solid $c_{p,s}$ components) and Γ the soil thermal conductivity (including water λ_w and solid λ_s components).

2.2 Constitutive models

The piles and the slab are made with concrete and behave thermo-elastically (with elastic modulus E_p and Poisson's ratio ν). The soil behaviour is simulated by a thermoelastic-

thermoplastic constitutive model called Advanced Constitutive Model for Environmental Geomechanics with Thermal aspects (ACMEG-T). It belongs to the Cam-Clay family and is based on the critical state theory. The isothermal part is based on the works of Hujeux (1979). Various successive improvements were made to extend it to the non-isothermal conditions: Laloui (1993), Modaressi and Laloui (1997), Laloui and Cekerevac (2008), Laloui and François (2009). Accordingly to the elasto-plasticity theory, the tensor of the total strain increment $\mathbf{d\varepsilon}$ is decomposed into elastic $\mathbf{d\varepsilon^e}$ and plastic $\mathbf{d\varepsilon^p}$ components, so that:

$$\mathbf{d\varepsilon} = \mathbf{d\varepsilon^e} + \mathbf{d\varepsilon^p} \tag{5}$$

The increment of total deformation can be split into volumetric $d\varepsilon_v$ and deviatoric $d\varepsilon_d$ deformation, so that:

$$\mathbf{d\varepsilon} = \frac{d\varepsilon_v}{3}\mathbf{I} + \mathbf{de} \quad \text{with} \quad d\varepsilon_v = \mathrm{tr}(\mathbf{d\varepsilon}) \quad \text{and} \quad d\varepsilon_d = \frac{\sqrt{6}}{3}\sqrt{\mathrm{tr}(\mathbf{de})^2} \tag{6}$$

where $\mathbf{de}$ represents the deviatoric strain tensor, $\mathbf{I}$ the unit tensor and 'tr' the trace of the tensor. Also the effective stress tensor $\mathbf{d\sigma'}$ can be split into the mean effective stress dp' and the deviatoric stress dq, as:

$$\mathbf{d\sigma'} = dp'\mathbf{I} + \mathbf{ds} \quad \text{with} \quad dp' = \frac{1}{3}\mathrm{tr}(\mathbf{d\sigma'}) \quad \text{and} \quad dq = \sqrt{\frac{3}{2}}\sqrt{\mathrm{tr}(\mathbf{ds})^2} \tag{7}$$

where $\mathbf{ds}$ represents the deviatoric stress tensor. In the elastic non-isothermal domain, the increments of volumetric and deviatoric deformation are respectively equal to:

$$d\varepsilon_v^e = \frac{dp'}{K_s} - \beta'_s dT \qquad \text{and} \qquad d\varepsilon_d^e = \frac{dq}{3G_s} \tag{8}$$

where G_s is the shear modulus. The non-linear elastic response is obtained through the following equations:

$$K_s = K_{ref}\left(\frac{p'}{p'_{ref}}\right)^{n_e} \quad \text{and} \quad G_s = G_{ref}\left(\frac{p'}{p'_{ref}}\right)^{n_e} \tag{9}$$

where K_{ref} and G_{ref} are the two modula at the reference mean effective stress p'_{ref} and n^e a material parameter. The plastic response is described by two-mechanisms, one isotropic and one deviatoric, which are coupled together. A pure isotropic loading causes only volumetric plastic deformation, while a pure deviatoric loading causes both deviatoric and volumetric plastic deformation. The two yield surfaces are temperature dependent, so that when a thermo-mechanical load leads the stress point on one of these two surfaces thermal plastic deformation (contraction) is developed. The isotropic yield limit reads:

$$f_{iso} = p' - p'_c r_{iso} = 0 \tag{10}$$

where p'_c is the pre-consolidation pressure and r_{iso} the degree of mobilization of plasticity of the isotropic mechanism (bounding surface theory, Dafalias and Herrmann, 1980). It is evolves with the volumetric plastic deformation, as:

$$r_{iso} = r_{iso}^{e} + \frac{\varepsilon_v^{p,iso}}{c + \varepsilon_v^{p,iso}} \tag{11}$$

where r_{iso}^{e} is the initial value of the degree of mobilization of plasticity, c a material parameter and $\varepsilon_v^{p,iso}$ the volumetric plastic deformation induced by the isotropic mechanism. In this model, the dependence of the pre-consolidation pressure on the temperature and its evolution with the development of volumetric plastic deformation is introduced accordingly to the equation proposed by Laloui and Cekerevac (2003), as:

$$p'_c = p'_{c0} e^{\beta \varepsilon_v^p} \left[1 - \gamma_T \cdot \ln\left(\frac{T}{T_0}\right)\right] \tag{12}$$

where p'_{c0} is the initial preconsolidation pressure (at initial temperature T_0), β the plastic coefficient and γ_T a material parameter which defines the shape of the isotropic yield function with respect to temperature. The deviatoric yield limit reads:

$$f_{dev} = q - Mp' \left(1 - b \cdot \ln\left(\frac{d \cdot p'}{p'_c}\right)\right) r_{dev} = 0 \tag{13}$$

where M is the slope of the critical state line (CSL) in the p'-q plane, b and d two material parameters and r_{dev} the degree of mobilization of plasticity for the deviatoric mechanism. This latter parameter has the same role than r_{iso} and reads:

$$r_{dev} = r_{dev}^{e} + \frac{\varepsilon_d^p}{a + \varepsilon_d^p} \tag{14}$$

where a is a material parameter, r_{dev}^{e} the initial value of the degree of mobilization of plasticity and ε_d^p the deviatoric plastic deformation. The parameter d represents the ratio between the pre-consolidation and the critical pressure. The coefficient M depends on the friction angles in compression and expansion, φ'_c and φ'_e, and on the Lode angle ϑ in order to take into account the effect of the stress path direction in the π plane, perpendicular to the principal stress space diagonal (Potts and Zdravković, 1999), accordingly to the formulation proposed by Van Eekelen (1980). The flow rule is associated for the isotropic mechanism, but not associated for the deviatoric one. This means that, calling the isotropic and deviatoric plastic potentials respectively g_{iso} and g_{dev}, $g_{iso}=f_{iso}$ but $g_{dev} \neq f_{dev}$ and (Nova and Wood, 1979):

$$g_{dev} = q - \frac{\alpha}{\alpha - 1} Mp' \left[1 - \frac{1}{\alpha}\left(\frac{d \cdot p'}{p'_c}\right)^{\alpha - 1}\right] = 0 \tag{15}$$

where α is a material parameter which expresses the dilatancy rule, as:

$$\frac{d\varepsilon_v^p}{d\varepsilon_d^p} = \alpha \left(M - \frac{q}{p'}\right) \tag{16}$$

In order to take into account the cyclic effects, the degree of plastification for the isotropic yield mechanism r_{iso} evolves during thermal cycles. In particular, it decreases during cooling, even if the response is perfectly elastic, as:

$$r_{iso} = \frac{p'_{cyc}}{p'_c} \tag{17}$$

where p'_{cyc} is the mean effective stress at the last change of loading direction. Therefore, starting from the second cycle, it reads:

$$r_{iso} = \frac{p'_{cyc}}{p'_c} + \frac{\varepsilon_v^{p,iso,cyc}}{c + \varepsilon_v^{p,iso,cyc}} \tag{18}$$

where $\varepsilon_v^{p,iso,cyc}$ is the volumetric plastic deformation induced by the isotropic mechanism starting from the last re-heating. After a certain number of cycles, no more thermo-plastic deformation is added, unless the maximum temperature imposed during the previous cycles is exceeded. Hence the model reproduces the cyclic thermal accommodation phenomenon shown by soils (Campanella and Mitchell, 1968).

3. NUMERICAL MODEL

The modelled foundation is composed of a slab with 150 piles (in a 7 x 15 grid), each with a diameter D of 80.0 cm, a length H of 20.0 m and spaced 7.0 m apart in both directions. The slab is 0.5 m thick and 110 m long. For the sake of simplicity and thanks to the symmetry of the case studied, the numerical model is limited to only 4 piles in 2D plane strain conditions. This latter assumption involves the fundamental simplification of considering a circular pile as an infinite wall, in the plane perpendicular to the one of the simulation. From a mechanical point of view, as the response of vertically loaded piles is controlled mainly by their axial stiffness, this transition from 3D to 2D plane strain conditions is taken into account by considering, for the piles, an equivalent Young's modulus E_{eq}, computed, as suggested by Prakoso and Kulhawi (2002) and Dupray et al. (2013), as:

$$E_{eq} = \frac{n_{p,row} A_p E_p}{L_r D} \tag{19}$$

where $n_{p,row}$ is the number of piles in a row in the third direction (15 in this case), A_p the pile base area, L_r the length of the slab in the third direction (110 m in this case). For the other parameters, such as the porosity, the permeability and the thermal conductivity and capacity, a weighted average over the soil and concrete properties is assumed for the piles. Finally, as the deformation in the third direction is prevented, the correspondent thermal deformation is redistributed along the two other directions. Thus, to take into account this aspect, an equivalent thermal expansion coefficient is considered. The geometry and boundary conditions of the considered model are represented in Figure 1. The initial temperature of the soil and the piles is 11 °C and the initial pore water pressure is assumed to be hydrostatic with the water table at the surface level. The temperature of the slab is fixed at 15 °C throughout the computation, in order to take into account the regulated temperature of the over building. The parameters used for the heat and water flow problem are collected in Table 1. The ACMEG-T parameters used to simulate the soil are collected in Table 2. The mechanical properties used for the concrete are summarized in Table 3. The soil is initially

normally consolidated. The interface between the pile and the soil is modelled with a thin layer of elements that behaves accordingly to the ACMEG-T model, with the same parameters as the soil but friction angles in compression and extension equal to 18° and 15° respectively.

4. RESULTS AND DISCUSSION

The first step of the calculation is represented by the application of a mechanical load of 1700 kN on each pile. The average displacement induced at the slab level in this phase is 2.5 cm, with a differential displacement between the centre of the foundation and the external pile of about 0.5 cm, which is in accordance with the limits imposed by the Eurocode 7 (BSI 2004, 2007). The second and main part of the simulation is represented by the application of a seasonally cyclic thermal loading. The results presented hereafter are obtained imposing a cyclic thermal loading, with a maximum injected and extracted power of 150 W/m, equal to each other. The main purpose is to investigate the effects of temperature variations on the displacements of such a foundation at the Serviceability Limit State (S.L.S.). Accordingly to the Eurocode 7, this represents one of the main issues when dealing with the design of deep foundations.

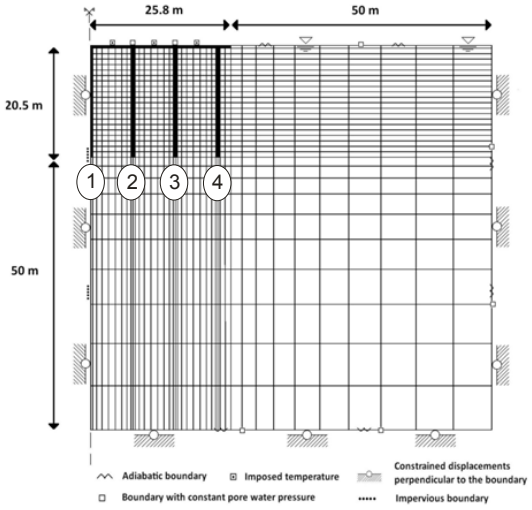

Figure 1: Geometry and boundary conditions of the model.

Table 1: Parameters for heat and water flow.

	Soil	Concrete
K [m/s]	10^{-8}	10^{-10}
n [-]	0.39	0.12
λ_w [W/mK]	0.6	0.6
$c_{p,w}$ [J/KgK]	4186	4186
λ_s [W/mK]	2.4	1.7
$c_{p,s}$ [J/KgK]	930	930

Table 2: Mechanical Properties for the soil.

Elastic Parameters		Plastic	
K_{ref} [MPa]	83.3	φ'_c [°]	26.0
G_{ref} [MPa]	38.5	φ'_e [°]	23.0
p'_{ref} [MPa]	1.0	β [-]	10.0
n^e [-]	1.0	α [-]	1.0
β'_s [K^{-1}]	$2.0 \cdot 10^{-5}$	a [-]	0.003
ρ_s [kN/m^3]	2700	b [-]	0.8
		c [-]	0.02
		d [-]	2.0
		r_{iso} [-]	0.3
		r_{dev} [-]	0.3
		γ_T [-]	0.15

Table 3: Mechanical Properties for piles and slab.

	Concrete
E_p [GPa]	35.0
ν [-]	0.25
ρ_s [kg/m^3]	2180
β'_s [$°C^{-1}$]	$3.6 \cdot 10^{-5}$

4.1 Temperature field

After about 5 years (stabilization), the temperature in the soil between the piles oscillates among a maximum value of 18 °C during summer and a minimum value of 10 °C during winter (Figure 2(a)). The temperature variations become negligible starting from about 35 m depth. Figure 2(b) shows the temperature inside one of the piles after the heating and cooling phases of the 1st, 5th and 7th years. It is possible to notice that the temperature is almost uniform along the pile, except at the extremes, where it must satisfy the equilibrium with the soil below and the slab above.

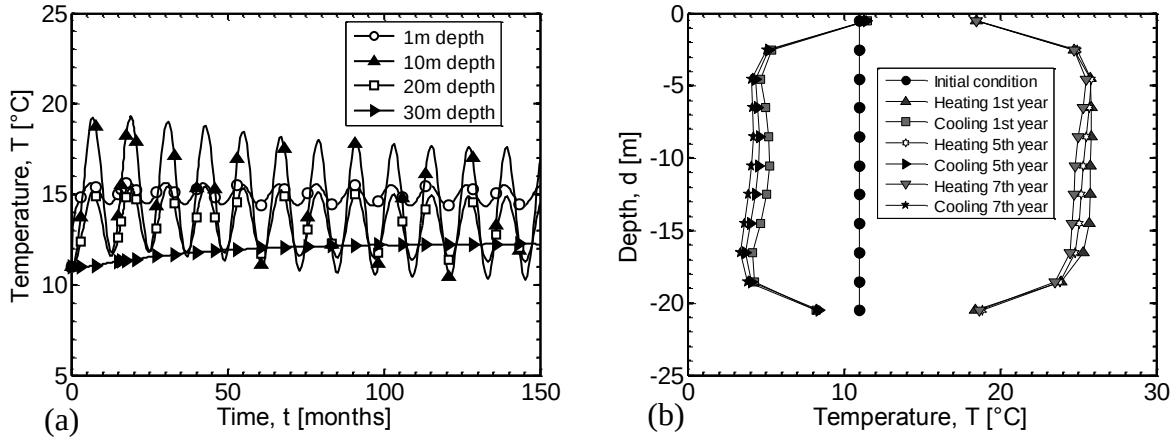

Figure 2: Evolution of temperature (a) in the soil and (b) in pile 2.

4.2 Soil strain and foundation displacements

Accordingly to the ACMEG-T model, the response of the soil is thermoelastic thermoplastic. This means that its thermal deformation has an elastic component (reversible), which is dilative during heating and contracting during cooling, and a plastic component, which is contracting during heating and irreversible. The entity of each component depends on soil's stress history, i.e. on its over-consolidation ratio (OCR), and on its properties (Table 2). Figure 3(a) represents the evolution with time of the volumetric plastic deformation of the soil between the second and the third pile at different depths. As expected due to the initial normally consolidated conditions, the soil contracts plastically during heating and does not show any irreversible deformation during cooling (contraction is positive).

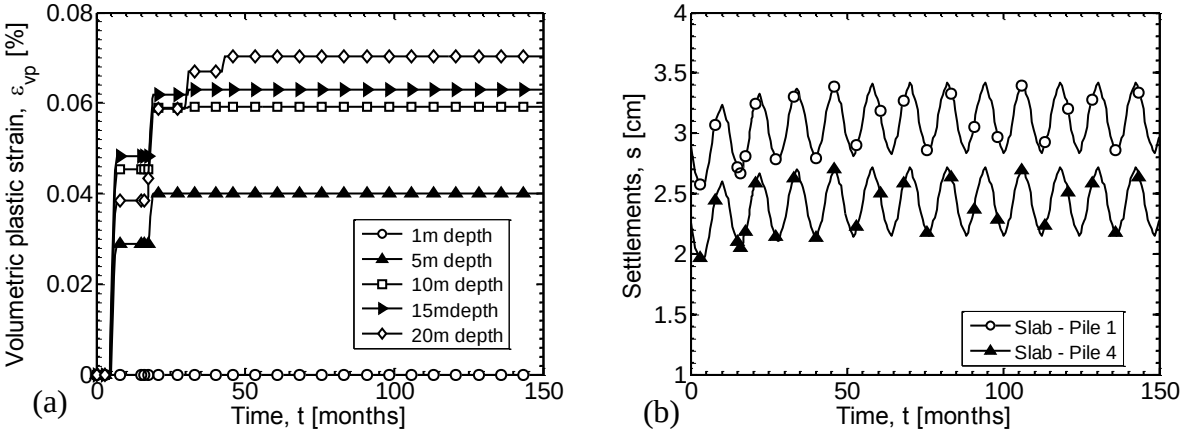

Figure 3: (a) Development of thermo-plastic deformation in the soil and (b) consequent thermal induced displacement of the foundation.

The thermal deformation of the soil results in additional displacements of the foundation, which include an irreversible component (additional settlement at the long time) and a reversible component, which makes the foundation moving upward during heating and downward during cooling. Figure 3(b) shows the displacement of the slab at the head of the central and external piles (respectively piles 1 and 4 in Figure 1). The additional irreversible displacement induced by the cyclic thermal loading is about 0.3 cm and almost completely developed during the first five years. The reversible oscillation is about 0.6 cm.

4. CONCLUSIONS

The main goal of this paper is to investigate the displacements induced by the thermal cyclic loading applied by energy piles on the surrounding soil (S.L.S.) at the long term. Several years of seasonally cyclic thermal loading were studied numerically and the results discussed. The soil is normally consolidated and its behaviour is reproduced with a thermoelastic thermoplastic model. As a consequence during heating its deformation has an elastic (dilative and reversible during cooling) and a plastic (contracting and irreversible during cooling) component. The former induces seasonally cyclic vertical displacements of the foundation while the latter induces an irreversible settlement of the structure itself. Moreover, the model is able to consider also the cyclic accommodative thermal aspect on the soil behaviour, so that plastic deformation is not only developed during the first thermal cycle but also during a certain number of cycles after the first one. In the case considered the additional irreversible settlement induced by the thermal loading is about 0.3 cm (12% of the one induced by the mechanical load) while the amplitude of the elastic cyclic displacement of the piles is about 0.6 cm.

ACKNOWLEDGEMENTS

This research project was funded by the Swiss Federal Office of Energy (contract Nb. 154’426). The authors would like to also acknowledge Dr. Fabrice Dupray for the scientific discussions and his help with the numerical issues.

REFERENCE

Amatya B.L., Soga K., Bourne-Webb P.J. and Laloui L. (2011). Review of observed thermo-mechanical performance of energy piles.

Barnichon J.D. (1998). Finite Element modeling in structural and petroleum geology. PhD thesis, Université de Liège.

Bourne-Webb P.J, Amatya B., Soga K., Amis T., Davidson C., and Payne P. (2009). Energy pile test at Lambeth College, London: geotechnical and thermodynamic aspects of pile response to heat cycles. Geotechnique 59(3), 237-248.

BSI (2004). BS EN 1997-1. Eurocode 7: part 1, section 7. British Standards Institution, London.

BSI (2007). BS EN 1997-2. Eurocode 7: part 2. British Standards Institution, London.

Campanella R.G. and Mitchell J.K. (1968). Influence of temperature variations on soil behavior. Journal of the Soil Mechanics and Foundation Division, ASCE, 94: 709-734.

Charlier, R. (1987). Approche unifiée de quelques problèmes non linéaires de mécanique des milieux continus par la méthode des éléments finis. PhD thesis, Université de Liège.

Collin, F. (2003). Couplages thermo-hydro-mécaniques dans les sols et les roches tendres partiellement saturés. PhD thesis, Université de Liège.

Dafalias Y., and Herrmann L., (1980). A bounding surface soil plasticity model. International Symposium on soils under cyclic and transient loading, Swansea: 335-345.

Dupray F., Laloui L. and Kazabgba A. (2013). Understanding the thermo-hydro-mechanical behaviour of seasonal heat storage in an energy pile foundation. Computers & Geotechnics, under review

Hujeux, J.C. (1979). Calcul numérique de problèmes de consolidation élastoplastique. PhD Thesis, Ecole Centrale, Paris.

Knellwolf C., Peron H. and Laloui L. (2011) Geotechnical analysis of heat exchanger piles. Journal of Geotechnical and Geoenvironmental Engineering, doi:10.1061/(ASCE)GT.1943-5606.0000513, 2011.
Laloui L. (1993). Modélisation du comportement thermo-hydro-mécanique des milieux poreux anélastique. PhD Thesis, Ecole Centrale de Paris.
Laloui, L., and Cekerevac, C. (2003). Thermo-plasticity of clays: an isotropic yield mechanism. Computers and Geotechnics, 30, No. 8, 649-660.
Laloui L. and Cekerevac C. (2008). Non-isothermal plasticity model for cyclic behaviour of soils. International Journal for Numerical and Analytical Methods in Geomechanics, 32(5): 437-460.
Laloui, L., and Di Donna, A. (2011). Understanding the Thermo-Mechanical Behaviour of Energy Piles. Proceedings of ICE - Civil Engineering 164, 184-191.
Laloui, L., and François, B. (2009). ACMEG-T : soil thermoplasticity model. Journal of Engineering Mechanics, ASCE, doi:10.1061/_ASCE_EM.1943-7889.0000011.
Laloui L., Moreni M. and Vulliet L. (2003). Comportement d'un pieu bi-fonction, fondation et échangeur de chaleur. Canadian Geotechnical Journal, 40, 388-402.
Laloui L., Nuth M. and Vulliet L. (2006). Experimental and numerical investigation of the behaviour of a heat exchanger pile. International Journal for Numerical and Analytical Methods in Geomechanics, 30(8):763-781.
Modaressi H. and Laloui L. (1997). A thermo-viscoplastic constitutive model for clays. International Journal for Numerical and Analytical Methods in Geomechanics, 21(5): 313–315.
Nova R. and Wood D.M. (1979). A constitutive model for sand in triaxial compression. International Journal for Numerical and Analytical Methods in Geomechanics, 3: 255–278.
Pahud D., (2002). Geothermal energy and heat storage. SUPSI-DCT-LEEE, Laboratorio di Energia, Ecologia ad Economia.
Potts D. M and Zdravković L. (1999). Finite element analysis in geotechnical engineering: theory. Thomas Telford Limited.
Prakoso, W. A., and Kulhawy, F. H. (2002). Contribution to piled raft foundation design. J. Geotech. and Geoenvir. Engrg. Volume 128 (8), pp. 709-709.
Van Eekelen H.A.M. (1980). Isotropic yield surfaces in three dimensions for use in soil mechanics. International Journal for Numerical and Analytical Methods in Geomechanics, 4, 98-101, 1980.

IMPLEMENTATION OF A 6–DOF HYPOPLASTIC MACROELEMENT IN A FINITE ELEMENT CODE

Claudio Tamagnini, Diana Salciarini, Raffaele Ragni
Department of Civil and Environmental Engineering, University of Perugia, Italy

ABSTRACT: *The macroelement concept, introduced for the first time by Nova & Montrasio (1991) is particularly well suited for complex soil–foundation–superstructure interaction (SFSI) problems of special structures such as tall bridge piers, towers or wind turbines under severe loading conditions. The capability of some of the models proposed in the literature to simulate the foundation response under six-dimensional loading paths (Bienen et al. 2006; Salciarini et al. 2011) is of great importance in the analysis of offshore structures such as mobile jack-up drilling units. In this work, the numerical implementation of the 6–dof hypoplastic macroelement proposed by Salciarini et al. (2011) in the Finite Element code Abaqus is presented. Particular attention has been paid to the development of a robust, accurate and efficient algorithm for the integration of the inelastic and incrementally non–linear constitutive equations of the macroelement. In this respect, an explicit adaptive integration algorithm with error control, based on the application of two embedded Runge–Kutta schemes of 2nd and 3rd order has been considered the most suitable candidate. The macroelement implementation has then be used to analyze the response to wind loading of a wind turbine. The results obtained from a series of cyclic and monotonic simulations demonstrate the computational efficiency of the proposed approach and the importance of the coupling effects between the different degrees of freedom of the foundation.*

1 INTRODUCTION

In the numerical modeling of soil–foundation–superstructure–interaction (SFSI) problems of structures resting on isolated, shallow footing with the FE method, a possible approach is to model the soil as a continuous medium, and adopting a suitable constitutive equation to reproduce the inelastic, non–linear and (possibly) hysteretic behavior of the soil. The main drawback of such an approach lies in the significant difference between the characteristic dimensions of the structural elements and of the soil volume interacting with the foundations. This leads to spatially discretized numerical models characterized by a very large number of degrees of freedom, and thus to a significant computational demand, particularly for strongly non–linear soil models and for cyclic/dynamic loading conditions.

A more efficient strategy, usually pursued in design practice, consists in lumping the soil–foundation system in a small number of deformable elements (typically elastic springs and viscous dashpots) that act on the superstructure as uncoupled deformable constraints located at the foundation. However, this approach has the limitation of being too oversimplified, if the deformable element response is compared to the typical observed behavior of actual shallow footing. In particular, even if non–linear force–displacement laws are assumed for the deformable

elements, it might still be impossible to reproduce irreversible and hysteretic response under cyclic loads. Moreover, the response of such elements is always uncoupled, *i.e.*, the variation of a certain component of the applied force has effects only on the corresponding, work–conjugated, displacement component. This contradicts a large number of experimental observations, such as those of Nova & Montrasio (1991) and Bienen et al. (2006), which clearly show how vertical displacements can occur even at constant vertical load, and how vertical load can change significantly under displacement paths performed at fixed vertical displacement (swipe tests).

An effective and efficient balance between computational and accuracy demands in the modeling of shallow foundations response in SFSI problems has been achieved by the introduction of the so-called "macroelement" approach by Nova & Montrasio (1991), which describes the global behavior of the foundation–soil system using a single, non–linear and inelastic, constitutive equation in rate–form. Recently, several macroelement models have been developed in the framework of the theory of plasticity (see, *e.g.*, Byrne & Houlsby 2003; di Prisco et al. 2006; Grange et al. 2009) or hypoplasticity (Salciarini & Tamagnini 2009; Salciarini et al. 2011). Recent applications of macroelement models in the analysis of seismic SFSI problems have been reported, *e.g.*, in Grange et al. (2009), Grange et al. (2010), Grange et al. (2011), di Prisco & Pisanò (2011).

In this work, the numerical implementation of the 6–dof hypoplastic macroelement proposed by Salciarini et al. (2011) in the Finite Element code ABAQUS is presented. In the development of the UEL routine to extend the code element library, particular attention has been paid to the development of a robust, accurate and efficient algorithm for the integration of the inelastic and incrementally non–linear constitutive equations of the macroelement. In this respect, an explicit adaptive integration algorithm with error control, based on the application of two embedded Runge–Kutta schemes of 2$^{\text{nd}}$ and 3$^{\text{rd}}$ order previously used, among others, by Tamagnini et al. (2000) for the integration of a hypoplastic constitutive model for sands, has been considered the most suitable candidate. A summary of the main features of the hypoplastic macroelement of Salciarini et al. (2011) is given in Sect. 2. The details of the integration algorithm are provided in Sect. 3.

The macroelement implementation has then be used to analyze the response to wind loading of a wind turbine. The FE model and the loading program adopted in the simulations are simplified, but sufficent for the task of testing the implementation of the macroelement and explore the accuracy and efficiency properties of the integration algorithm. Sect. 4 provides a summary of the main results obtained from a series of cyclic and monotonic simulations. Some concluding remarks and suggestion for further studies are finally given in Sect. 5.

2 THE HYPOPLASTIC MACROELEMENT OF SALCIARINI ET AL. (2011)

In Salciarini et al. (2011) macroelement, the mechanical response of the footing under general 6–dimensional loading conditions is provided by the following (dimensionless) constitutive equation in rate form:

$$\dot{\boldsymbol{t}} = \boldsymbol{\mathcal{D}}_t \dot{\boldsymbol{u}} \qquad \dot{v}_f = \boldsymbol{h}_v \cdot \dot{\boldsymbol{u}} \qquad \dot{\boldsymbol{d}} = \boldsymbol{\mathcal{H}}_d \dot{\boldsymbol{u}} \tag{1}$$

where (see Fig. 1):

$$\boldsymbol{t} := \boldsymbol{T}/V_{f0} \qquad \boldsymbol{T} := \left\{V \, , \, H_x \, , \, M_y/\ell \, , \, H_y \, , \, M_x/\ell \, , \, Q/\ell\right\}^T \tag{2}$$

$$\boldsymbol{u} := \boldsymbol{U}/\ell \qquad \boldsymbol{U} := \left\{U_z \, , \, U_x \, , \, \Theta_y \ell \, , \, U_y \, , \, \Theta_x \ell \, , \, \Omega \ell\right\}^T \tag{3}$$

and:

$$v_f = V_f/V_{f0} \qquad \boldsymbol{d} := \boldsymbol{\delta}/\ell \qquad \boldsymbol{\delta} := \left\{\delta_{zz}\ ,\ \delta_{xx}\ ,\ \delta_{yz}\ ,\ \delta_{yy}\ ,\ \delta_{xz}\ ,\ \delta_{xy}\right\}^T \tag{4}$$

In eq. (1) to (4), $\boldsymbol{T}$ and $\boldsymbol{U}$ are the generalized force and displacement vectors, respectively; V_f is the bearing capacity of the foundation under centered vertical loading; $\boldsymbol{\delta}$ the *internal displacement* vector, used as a directional internal variable to reproduce more accurately the evolution of the stiffness with loading direction in cyclic loading conditions; $\boldsymbol{\mathcal{D}}_t$ is the dimensionless tangent stiffness matrix of the system; $\boldsymbol{h}_v$ and $\boldsymbol{\mathcal{H}}_d$ are hardening functions providing the evolution laws for the internal variables; the scaling factor for forces, V_{f0}, is the initial bearing capacity of the foundation under centered vertical loading conditions; the scaling factor for displacements, ℓ is a characteristic dimension of the footing (*e.g.*, its diameter D).

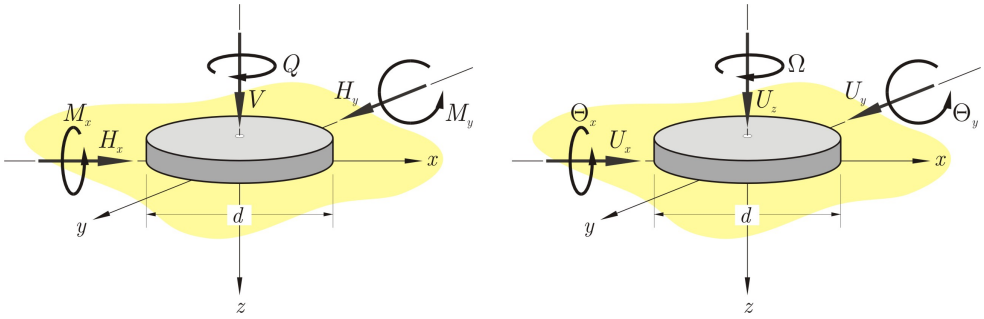

Fig. 1. Reference frame and notation adopted for generalized forces and displacements.

The tangent stiffness matrix $\boldsymbol{\mathcal{D}}_t$ assumes the following general format:

$$\boldsymbol{\mathcal{D}}_t := A_1(\rho)\boldsymbol{\mathcal{L}}(\boldsymbol{T},\boldsymbol{q}) + \boldsymbol{\mathcal{N}}(\boldsymbol{T},\boldsymbol{q},\boldsymbol{d}) \tag{5}$$

where:

$$\boldsymbol{\mathcal{N}}(\boldsymbol{t},v_f,\boldsymbol{d}) := \begin{cases} A_2(\rho)\boldsymbol{\mathcal{L}}\boldsymbol{\eta}_\delta\boldsymbol{\eta}_\delta^T + A_3(\rho)Y(\boldsymbol{t},v_f)\boldsymbol{m}(\boldsymbol{t},v_f)\boldsymbol{\eta}_\delta^T & (\boldsymbol{\eta}_\delta\cdot\dot{\boldsymbol{u}} > 0) \\ A_4(\rho)\boldsymbol{\mathcal{L}}\boldsymbol{\eta}_\delta\boldsymbol{\eta}_\delta^T & (\boldsymbol{\eta}_\delta\cdot\dot{\boldsymbol{u}} \le 0) \end{cases} \tag{6}$$

In the above equations, the matrix $\boldsymbol{\mathcal{L}}$ is related to the tangent stiffness $\boldsymbol{\mathcal{D}}^e$ of the system upon full displacement reversal (pseudo–elastic stiffness) by the relation $\boldsymbol{\mathcal{L}} = (1/m_R)\boldsymbol{\mathcal{D}}^e$, with m_R a material constant; the $A_k(\rho)$ (with $k = 1,\ldots,4$) are scalar functions of a suitably scaled norm ρ of $\boldsymbol{d}$ (see Salciarini et al. 2011 for details); the unit vector $\boldsymbol{m}$ provides the velocity direction $\boldsymbol{\eta}$ under collapse conditions; the loading function Y is a dimensionless measure of the distance of the current loading state from the failure locus (FL), and the unit vector $\boldsymbol{\eta}_\delta := \boldsymbol{d}/\|\boldsymbol{d}\|$ is the internal displacement direction. A complete description of the model can be found in Salciarini et al. (2011). Here only a few details are given on the constitutive functions defining: the failure locus of the footing; the loading function Y and the flow direction vector $\boldsymbol{m}$.

The scalar function which defines the FL in the 6–dimensional loading space is a slightly simplified version of the function adopted by Martin (1994):

$$f(\boldsymbol{t},v_f) = \left(\frac{t_2}{h_0 v_f}\right)^2 + \left(\frac{t_3}{m_0 v_f}\right)^2 + \left(\frac{t_4}{h_0 v_f}\right)^2 + \left(\frac{t_5}{m_0 v_f}\right)^2 + \left(\frac{t_6}{q_0 v_f}\right)^2 - 2a\left(\frac{t_4 t_5 - t_2 t_3}{h_0 m_0 v_f^2}\right) - \left(\frac{t_1}{v_f}\right)^{2\beta_1}\left(1 - \frac{t_1}{v_f}\right)^{2\beta_2} = 0 \tag{7}$$

where h_0, m_0, q_0, β_1 and β_2 model constants (see Martin 1994 or Bienen et al. 2006, for the details on their physical meaning). For each admissible load vector $\boldsymbol{t}$ a corresponding *image state* on the FL, defined as:

$$\bar{\boldsymbol{t}} := \xi \boldsymbol{t} \qquad \text{such that:} \qquad f(\bar{\boldsymbol{t}}, v_f) = f(\xi \boldsymbol{t}, v_f) = 0 \tag{8}$$

The scalar $\xi \geq 1$, which can be determined by solving $(8)_2$, provides a suitable measure of the distance of the current state from the FL. Thus, the loading function Y can be defined as:

$$Y(\boldsymbol{t}, v_f) = \left\{ \frac{1}{\xi(\boldsymbol{t}, v_f)} \right\}^{\kappa} \tag{9}$$

where κ is a model constant.

As in Salciarini & Tamagnini (2009), the flow direction vector $\boldsymbol{m}$ can be obtained as the normalized gradient of a scalar function g, for which a slightly simplified version of the plastic potential of Bienen et al. (2006) is adopted:

$$g(\boldsymbol{t}) = \left(\frac{t_2}{\alpha_h h_0 v_g} \right)^2 + \left(\frac{t_3}{\alpha_m m_0 v_g} \right)^2 + \left(\frac{t_4}{\alpha_h h_0 v_g} \right)^2 + \left(\frac{t_5}{\alpha_m m_0 v_g} \right)^2 + \left(\frac{t_6}{\alpha_q q_0 v_g} \right)^2 - 2a \left(\frac{t_4 t_5 - t_2 t_3}{\alpha_h \alpha_m h_0 m_0 v_g^2} \right) - \left(\frac{t_1}{v_g} \right)^{2\beta_3} \left(1 - \frac{t_1}{v_g} \right)^{2\beta_4} = 0 \tag{10}$$

In the above equation, α_h, α_m, α_q, β_3 and β_4 are model constants, and $v_g(\boldsymbol{t})$ is a dummy parameter to be determined from the condition $g(\boldsymbol{t}, v_g) = 0$.

3 INTEGRATION ALGORITHM

The integration algorithm selected for the implementation of the hypoplastic macroelement in the FE code Abaqus is an explicit, adaptive Runge–Kutta scheme of the 3rd order with error control, successfully applied by Tamagnini et al. (2000) for the integration of a hypoplastic constitutive model for sands.

Let $[t_n, t_{n+1}]$ be the time interval corresponding to a generic time step, and let $\Delta \boldsymbol{u}_{n+1}$ be the prescribed displacement increment obtained from the solution of the global equilibrium equations at a given iteration. Due to the rate–independent character of the constitutive equations, it is convenient to restate the evolution problem in terms of a non–dimensional time measure:

$$T = \frac{t - t_n}{t_{n+1} - t_n} = \frac{t - t_n}{\Delta t_{n+1}} \qquad \text{so that:} \qquad \frac{d}{dt}(\cdot) = \frac{1}{\Delta t_{n+1}} \frac{d}{dT}(\cdot)$$

As the velocity $\dot{\boldsymbol{u}}$ is assumed constant during the time step, the evolution equations (1) can be recast in the following standard format:

$$\frac{d\boldsymbol{x}}{dT} = \boldsymbol{F}(\boldsymbol{x}) \qquad \text{where} \qquad \boldsymbol{y} := \begin{Bmatrix} \boldsymbol{t} \\ v_f \\ \boldsymbol{d} \end{Bmatrix} \qquad \text{and} \qquad \boldsymbol{F} := \begin{Bmatrix} \boldsymbol{\mathcal{D}}_t \Delta \boldsymbol{u}_{n+1} \\ \boldsymbol{h}_f \cdot \Delta \boldsymbol{u}_{n+1} \\ \boldsymbol{\mathcal{H}}_d \Delta \boldsymbol{u}_{n+1} \end{Bmatrix} \tag{11}$$

The integration of the ODE $(11)_1$ is performed using an adaptive substepping strategy in which the normalized time step $[0, 1]$ is split into substeps $\Delta T_{k+1} = T_{k+1} - T_k$ such that $\sum \Delta T_k = 1$. Using the Runge–Kutta–Fehlberg approach, the size of each substep is selected by comparing

the solutions obtained for the same substep by two Runge–Kutta explicit algorithms of order 2 and 3, respectively:

$$\tilde{\boldsymbol{x}}_{k+1} = \boldsymbol{x}_k + \Delta T_{k+1} \sum_{i=1}^{2} \tilde{c}_i \, \boldsymbol{F}_i(\boldsymbol{x}_k, \Delta T_{k+1}) \tag{12}$$

$$\hat{\boldsymbol{x}}_{k+1} = \boldsymbol{x}_k + \Delta T_{k+1} \sum_{i=1}^{3} \hat{c}_i \, \boldsymbol{F}_i(\boldsymbol{x}_k, \Delta T_{k+1}) \tag{13}$$

where:

$$\boldsymbol{F}_i := \boldsymbol{F}(\boldsymbol{x}_i) \qquad \boldsymbol{x}_i := \Delta T_{k+1} \sum_{j=1}^{p-1} \beta_{ij} \boldsymbol{F}_j \qquad (\text{with } p = 2 \text{ or } 3)$$

and the coefficients $\tilde{c}_i$, $\hat{c}_i$ and β_{ij} are determined imposing that the method in eqs. (12) and (13) are of order 2 and 3, respectively, see Stoer & Bulirsch (1993) for details.

Let $R_{k+1} := \|\boldsymbol{R}_{k+1}\| / \|\hat{\boldsymbol{x}}_{k+1}\|$, with:

$$\boldsymbol{R}_{k+1} := \hat{\boldsymbol{x}}_{k+1} - \tilde{\boldsymbol{x}}_{k+1}$$

be a measure of the relative difference between the two solutions. This quantity can be compared with a prescribed error tolerance TOL, to check if $R_{k+1} < \text{TOL}$. In the affirmative case, the solutions obtained meet the required accuracy level and thus $\boldsymbol{x}_{k+1} = \hat{\boldsymbol{x}}_{k+1}$ and we can proceed with the next substep. In this case, the substep size can be increased according to the following extrapolation formula:

$$\Delta T_{k+2} = \min \left\{ 0.9 \, \Delta T_{k+1} \left(\frac{\text{TOL}}{R_{k+1}} \right)^{1/3} ; \; 4 \, \Delta T_{k+1} \right\} \tag{14}$$

If, on the contrary, $R_{k+1} \geq \text{TOL}$ the substep is rejected and a new, smaller substep size is computed according to the same extrapolation formula (14):

$$\Delta T_{k+2} = \max \left\{ 0.9 \, \Delta T_{k+1} \left(\frac{\text{TOL}}{R_{k+1}} \right)^{1/3} ; \; \frac{1}{4} \, \Delta T_{k+1} \right\} \tag{15}$$

From eqs. (14) and (15) is apparent that the extrapolation to bigger substep sizes after an accepted substep is limited to four times the initial value, while the reduction of substep size after a rejected substep is limited to 25% of the initial value.

4 APPLICATION: SSI ANALYSIS OF A WIND TURBINE

4.1 Details of the FE model and macroelement calibration

In order to demonstrate the characteristics of the proposed integration algorithm, a series of FE analysis have been performed to model the soil–foundation interaction processes due to wind loading of a medium size (850 kW) wind turbine funded on a circular raft (Fig. 2). This problem, already analyzed by Buscarnera et al. (2010) using an elastoplastic, anisotropic hardening macroelement model, has been choosen as a simple, but realistic test case for the hypoplastic macroelement implementation.

Fig. 2. A typical medium–sized wind turbine.

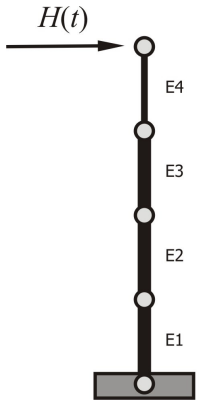

Fig. 3. FE model of the wind turbine.

The wind turbine, mounted on a 30 m high, conical hollow steel tower, has total weight of 320 kN, including the three–blade rotor. The diameter of the tower varies from a maximum of 3.5 m at the base to a minimum of 2.0 m at the top, and its total weight is 406 kN. The turbine foundation is a circular r.c. raft, with diameter D = 12 m and thickness H = 1.2 m. The total weight of the foundation raft is 3393 kN, and is much larger than the entire weight of the structure.

The simplified FE model adopted to simulate the behavior of the structure is shown in Fig. 3. The variable section steel tower is modeled with 4 sections (E1 to E4) of different bending stiffness. Each section is discretized with 3 linear interpolation beam elements. The geometrical, physical and mechanical properties of each section are reported in Tab. 1.

Table 1. Area, moment of inertia and apparent density of the four sections of the tower.

Section #	A (m^2)	J (m^4)	ρ_{app} (t/m^3)
E1	0.350	0.4657	1.60
E2	0.306	0.3131	7.85
E3	0.263	0.1981	7.85
E4	10.000	20.8330	7.85

The foundation is assumed to rest on a homogeneous coarse–grained dense soil layer of very large thickness, with a friction angle ϕ = 40°, an average shear modulus G = 40 MPa and Poisson's ratio ν = 0.3. From the data on soil shear strength, the bearing capacity V_{f0} for a centered vertical load has been estimated equal to 356.46 MN. Due to the relatively high stiffness of the soil and the relatively low vertical loads applied, this value has been assumed constant and independent of the foundation displacement history.

The macroelement properties have been selected in order to match the aforementioned properties of the foundation soil (Tab. 2). In particular: the model small–strain stiffness coefficients k_v, k_h, k_m and k_c have been computed according to the elasticity solution for a rigid circular plate on a linear elastic half space; the constant h_0 has been calibrated based on the assumed friction angle at the foundation–soil interface; the constant m_0 has been chosen according to the maximum amount of relative eccentricity (e/D) allowed at low vertical loads; the constants β_k (with $k = 1, \ldots, 4$) have been selected in order to match the failure locus assumed by Buscarn-

era et al. (2010). The flow direction parameters α_h and α_m have been calibrated based on the corresponding constants μ and ψ of Buscarnera et al. (2010) model; the hardening constant k_1 has been set equal to zero to keep V_f constant, and, finally, the stiffness degradation coefficient κ and the internal displacement–related constants m_R, m_T, R, β_r and χ have been selected after a series of preliminary simulations, in order to obtain a realistic behavior of the foundation under cyclic loading.

Table 2. Model constants adopted in the numerical simulations.

k_v (–)	k_h (–)	k_m (–)	$k_q^\dagger$ (–)	k_c (–)	G (MPa)	h_0 (–)	m_0 (–)	$q_0^\dagger$ (–)	a (–)	β_1 (–)	β_2 (–)	α_h (–)	α_m (–)	$\alpha_q^\dagger$ (–)
2.857	2.353	0.476	0.918	0.0	40.0	0.6	0.3	0.6	0.0	1.0	0.95	1.25	3.467	2.30
β_3 (–)	β_4 (–)	k_1 (–)	w_1 (–)	w_2 (–)	c_1 (–)	c_2 (–)	c_3 (–)	κ (–)	m_R (–)	m_T (kPa)	R (m)	β_r (–)	χ (–)	
1.0	0.95	0.0	1.0	1.0	0.0	0.0	0.0	1.4	3.0	1.5	0.03	1.00	1.50	

† This constant has no effect on model predictions for the problem examined.

4.2 FE simulations program

For the simple problem at hand, and following Buscarnera et al. (2010), the wind turbine has been subjected to the actions of self weight, responsible for the vertical component V of the foundation load, and of the wind pressure on the rotor (the wind action of the tower being assumed negligible). The wind action on the rotor has been assumed equivalent to an horizontal load $H(t)$, varying cyclically from 0 to 400 kN, applied on the turbine axis. As the load H varies, the foundation is subjected to a horizontal load $H_x(t) = H(t)$ and to an overturning moment $M_y(t) = \ell H(t)$, where ℓ is the rotor height with respect to the foundation base.

Table 3. FE simulations program.

Simulation #	V (kN)	$H_{\min}$ (kN)	$H_{\max}$ (kN)	number of cycles	number of steps	TOL (–)
r01	4367	0	400	20	100	1.0e-5
r02	4367	0	400	1	50	1.0e-5
r03	4367	0	400	1	20	1.0e-5
r04	4367	0	400	1	10	1.0e-5
r05	4367	0	400	1	5	1.0e-5
r06	4367	0	400	1	5	1.0e-4
r07	4367	0	400	1	5	1.0e-3
r08	4367	0	400	1	5	1.0e-2

The different loading programs considered in this study are summarized in Tab. 3. The first simulation (r01) is performed to illustrate the cyclic behavior of the macroelement model under a typical combined loading program. For this reason, 20 cycles of loading–unloading have been considered in this case. Then, a first group of parametric simulations (r02 to r05, with constant error tolerance of 1.0e-5) have been performed to assess the algorithm efficiency as a function of the step size. In these simulations, where only the first loading branch is considered, the step size is varied from 4 kN (n = 100 step) to 80 kN (n = 5 steps). As the prescribed tolerance is the

same, the accuracy of the different solutions is comparable; the efficiency of the computational procedure is evaluated in terms of the total number of substeps (including rejected ones) required to meet the prescribed error tolerance. Finally, a second group of parametric simulations (r05 to r08, with a constant step size of 80 kN) have been performed to evaluate the algorithm accuracy as a function of the prescribed tolerance, which ranges from 1.0e-5 to 1.0e-2.

According to Buscarnera et al. (2010) the range of frequencies which can be considered typical of wind load excitations (1-60 Hz) is relatively far from the characteristic frequencies of the system for the particular case examined and, therefore, the response of the structure is almost frequency–independent. For this reason, all the simulations reported in Tab. 3 have been performed under quasi–static conditions.

4.3 Results of the FE simulations

The response of the foundation to the applied cyclic loading in simulation r01 is displayed in Fig. 4 to 6. Fig. 4 shows the horizontal load H_x *vs*. horizontal displacement U_x curve; Fig. 5 the rocking moment M_y *vs*. rotation Θ_y curve, and Fig. 6 the vertical displacement U_z *vs*. the horizontal displacement U_x curve.

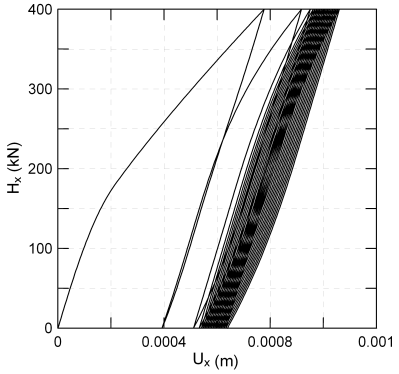

Fig. 4. Cyclic response of the tower foundation: horizontal load H_x *vs*. horizontal displacement U_x.

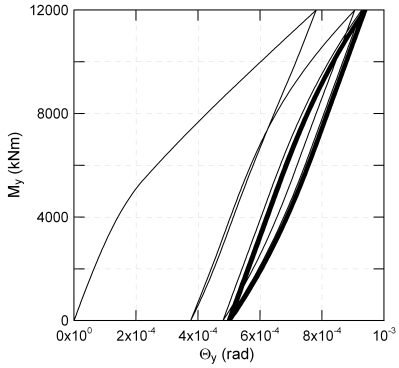

Fig. 5. Cyclic response of the tower foundation: rocking moment M_y *vs*. rotation Θ_y.

In the two load(moment)–displacement(rotation) curves of Figs. 4 and 5, the macroelement displays a clearly non–linear behavior, with strong irreversible displacements (rotations) accumulated in the first 3 cycles. During the following cycles, the loading–unloading response of the macroelement displays a hysteretic behavior, with a limited amount of horizontal displacement accumulation, and almost stable moment–rotation cycles. The fully coupled character of the macroelement response is demonstrated by the displacement path of Fig. 6. The application of a cyclic eccentric horizontal load at constant vertical load gives rise to a progressive accumulation of irreversible vertical settlements, most of which occur during the first 3 cycles. From a qualitative point of view, the predicted behavior of the footing under cyclic loading is fully consistent with the one obtained by Buscarnera et al. (2010), although with a kinematic hardening elastoplastic macroelement model.

Figs. 7 and 8 show the comparison between the solutions obtained for the first loading branch with different step sizes (simulations r01 to r05), in terms of horizontal force *vs*. displacement and rocking moment *vs*. rotation curves, respectively. As expected, since the error tolerance used in all the simulations of this group is the same, the different solutions are practically identical,

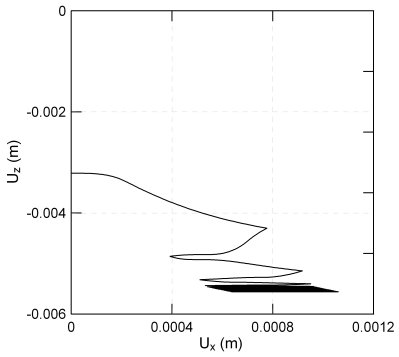

Fig. 6. Cyclic response of the tower foundation: vertical displacement U_z *vs.* horizontal displacement U_x.

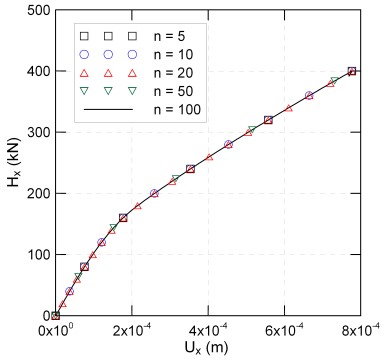

Fig. 7. Comparison of the solutions obtained with different step sizes (first loading branch only): H_x *vs.* U_x.

regardless of the step size. However, as the step size increases, more substeps are needed to meet the accuracy requirements, so the 5 simulations differ in terms of efficiency.

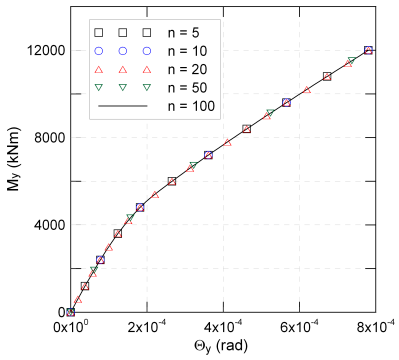

Fig. 8. Comparison of the solutions obtained with different step sizes (first loading branch only): M_y *vs.* Θ_y.

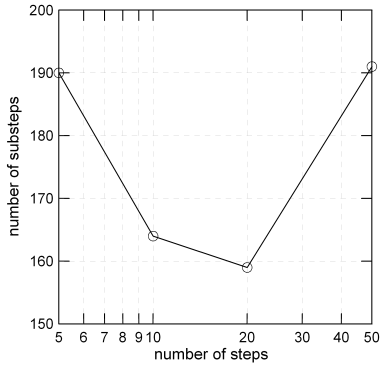

Fig. 9. Total number of substeps required to meet the prescribed tolerance (TOL = 1.0e-5) *vs.* number of steps.

To quantify the relative efficiency of the integration algorithm for the different cases considered, a suitable indicator is the total number of substeps required to complete the the simulations, including the rejected ones. This indicator is plotted in Fig. 9 as a function of the number of load steps (ranging from 5 to 100). From the figure it is clearly apparent that using either very small load steps or very large load steps leads to a relatively inefficient performance. In the first case, the number of substeps for each step is small and only a few substeps are rejected, but many time steps (100) are required to complete the simulations. In the second case, only a few (5) time steps are used, but each of them is quite expensive in terms of the number of substeps required to advance the solution in time. From the data in Fig. 9 it appears that the best compromise for the prescribed error tolerance (1.0e-5) is to use 10 to 20 steps, which allows to obtain an efficiency gain of about 16% with respect to the least efficient solutions.

In the last group of simulations (r05 to r08), the number of steps has been kept constant to the lowest value ($n = 5$) and the error tolerance TOL has been increased to investigate its influence on the solutions accuracy. This last property of the solutions obtained has been quantified by means

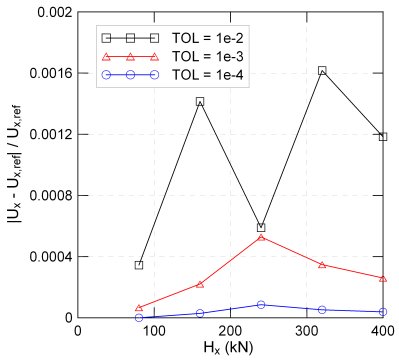

Fig. 10. Relative error E_U computed with different error tolerances (n = 5 steps).

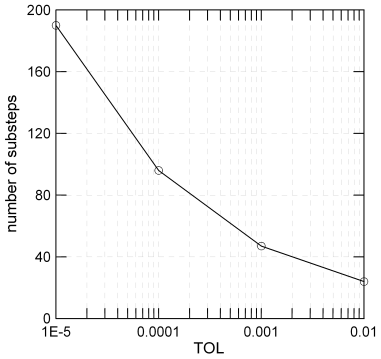

Fig. 11. Total number of substeps *vs*. prescribed tolerance (n = 5 steps).

of the following normalized relative error measure on computed horizontal displacements:

$$E_U(H_x) = \frac{|U_x(H_x) - U_{x,\text{ref}}(H_x)|}{|U_{x,\text{ref}}(H_x)|} \tag{16}$$

where $U_{x,\text{ref}}$ is the reference solution obtained with TOL = 1.0e-5.

The computed values of E_U at each load level for the three cases considered are plotted in Fig. 10. As expected, the error level increases with increasing TOL. However, the maximum relative error computed for an increase in TOL of 3 orders of magnitude is still quite low, only slightly larger than 0.1%. On the contrary, the increase in TOL allows for a dramatic increase in efficiency, as shown in Fig. 11 where the total number of substeps required in each simulations is plotted as a function of TOL. For the largest error tolerance considered, the reduction in the total number of substeps which can be achieved due to the less stringent accuracy requirements is about 84% of the substeps needed to obtain the reference solution .

5 CONCLUDING REMARKS

In this work an accurate and efficient integration scheme has been developed to implement the fully nonlinear, irreversible and hysteretic macroelement model for shallow foundations on sands recently proposed by Salciarini et al. (2011).

A series of parametric numerical simulations on a ideal problem – a medium size wind turbine subject to wind actions – has allowed to investigate the influence of the integration control parameters on the efficiency and accuracy of the algorithm. In particular, for a given error tolerance, the efficiency of the procedure tends to decrease for both very large and very small steps, with an optimum choice of the step size located in between the two extremes. For a given step size, the relative error tends to increase (as expected) with increasing TOL. However, a reasonable accuracy level is achieved even for relatively large tolerance values, with a significant advantage in terms of computational effort.

The implementation of the macroelement in a general purpose FE code allows the possibility of analyzing efficiently and accurately quite complex SFSI problems such as the seismic behavior of buildings and bridges (di Prisco et al. 2006; Grange et al. 2009; Grange et al. 2011), and of other slender structures like wind turbines, cable–stayed masts or offshore platforms subjected to cyclic wind or wave loading, see, *e.g.*, Byrne & Houlsby (2003), Materazzi & Venanzi (2007) and Martin (1994).

REFERENCES

Bienen, B., Byrne, B. W., Houlsby, G. T., & Cassidy, M. J. (2006). Investigating six–degree–of–freedom loading of shallow foundations on sand. *Géotechnique 56*, 367–379.

Buscarnera, G., Nova, R., Vecchiotti, M., Tamagnini, C., & Salciarini, D. (2010). Settlement analysis of wind turbines. In R. P. Orense, N. Chouw, & M. J. Pender (Eds.), *Proc. Int. Workshop on Soil–Foundation–Structure Interaction (SFSI 09)*, Auckland, New Zealand. CRC press.

Byrne, B. W. & Houlsby, G. T. (2003). Foundations for offshore wind turbines. *Philosophical Transactions of the Royal Society of London, Series A, 361*, 1257–1284.

di Prisco, C., Massimino, M. R., Maugeri, M., Nicolosi, M., & Nova, R. (2006). Cyclic numerical analysis of Noto Cathedral: soil–structure interaction modelling. *Rivista Italiana di Geotecnica 48*.

di Prisco, C. & Pisanò, F. (2011). Seismic response of rigid shallow footings. *European Journal of Environmental and Civil Engineering 15*, 185–221.

Grange, S., Botrugno, L., Kotronis, P., & Tamagnini, C. (2011). The effects of soil–structure interaction on a reinforced concrete viaduct. *Earthquake Engineering & Structural Dynamics 40*(1), 93–105.

Grange, S., Kotronis, P., & Mazars, J. (2009). A macro–element to simulate dynamic soil–structure interaction. *Engng. Structures 31*, 3034–3046.

Grange, S., Salciarini, D., Kotronis, P., & Tamagnini, C. (2010). A comparison of different approaches for the modelling of shallow foundations in seismic soil-structure interaction problems. In T. Benz & S. Nordal (Eds.), *Numerical Methods in Geotechnical Engineering NUMGE 2010*. Trondheim, June 2010.

Martin, C. M. (1994). *Physical and numerical modelling of offshore foundations under combined loads*. Ph. D. thesis, University of Oxford.

Materazzi, A. & Venanzi, I. (2007). A simplified approach for the wind response analysis of cable-stayed masts. *Journal of Wind Engineering and Industrial Aerodynamics 95*(9), 1272–1288.

Nova, R. & Montrasio, L. (1991). Settlements of shallow foundations on sand. *Géotechnique 41*, 243–256.

Salciarini, D., Bienen, B., & Tamagnini, C. (2011). A hypoplastic macroelement for shallow foundations subject to six–dimensional loading paths. In *Proc. International Symposium on Computational Geomechanics (ComGeo II), Cavtat-Dubrovnik, Croatia*.

Salciarini, D. & Tamagnini, C. (2009). A hypoplastic macroelement model for shallow foundations under monotonic and cyclic loads. *Acta Geotechnica 4*(3), 163–176.

Stoer, J. & Bulirsch, R. (1993). *Introduction to numerical analysis, 2nd. Ed.* Springer Verlag, New York.

Tamagnini, C., Viggiani, G., Chambon, R., & Desrues, J. (2000). Evaluation of different strategies for the integration of hypoplastic constitutive equations: Application to the CLoE model. *Mech. Cohesive–Frictional Materials 5*, 263–289.

SMALL STRAIN EFFECTS ON THE STIFFNESS OF MONOPILE FOUNDATIONS IN SAND

K. Thieken
Institute for Geotechnical Engineering, Leibniz University Hannover, Hannover, Germany

M. Achmus
Institute for Geotechnical Engineering, Leibniz University Hannover, Hannover, Germany

ABSTRACT:
Monopiles are currently the preferred foundation concept for Offshore Wind Energy Converters (OWECs) in water depths up to 30 meters. These large diameter steel piles have to withstand dynamic wind and wave loading. The stiffness of the monopile-soil system is decisive with respect to dynamic as well as quasi-static loading conditions. To evaluate the stiffness of the monopile-soil system in dependence of the acting load level, a three-dimensional numerical model is implemented which is able to account for a strain- dependent stiffness formulation. Results for a reference system are presented in detail. Furthermore the numerical model is validated on field tests. In a comprehensive study, the main influence parameters on monopile stiffness as the pile dimensions, loading conditions and relative density of soil are investigated systematically. Finally, a comparison of the numerical results with different approaches based on the p-y method is given. It can be shown that the existing approaches are valid only for special loading conditions.

1 INTRODUCTION

Within the next decades an enormous number of Offshore Wind Energy Converters (OWECs) shall be erected in wind farms in the North Sea and Baltic Sea. In German territorial waters water depths between 20m and 50m occur at possible areas for offshore wind farms. Monopiles are the preferred foundation concept for OWECs in water depths of up to about 30m due to a cost-effective and relatively simple manufacturing and installation process.

A monopile foundation (cf. Fig. 1) consists of a single steel pipe pile driven into the seabed. The monopile foundation has to withstand horizontal forces H and bending moments M caused by wind and wave loads. To guarantee the stability of this one-pile foundation, a large pile diameter is required, which is strongly dependent on water depth and wind turbine dimension. Piles diameters of more than 6m have already been realized and diameters of up to 7.5m are under planning. The relative pile length, i.e. the ratio of embedded pile length L to diameter D, lies usually around L/D=5.

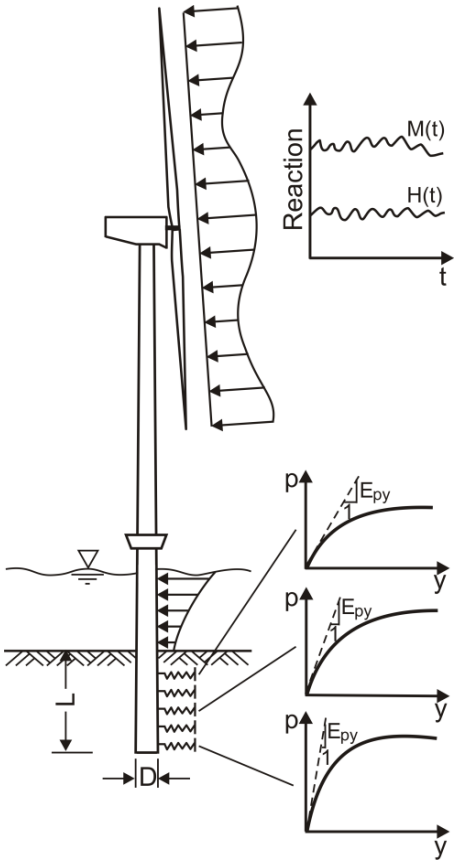

Fig. 1: Schematic sketch of an OWEC with monopile foundation

In the design, it has to be proved that the deflections and rotations under service loads (including the extreme load) stay below certain serviceability limits. In that, also an accumulation of deflections due to cyclic loading has to be considered. Besides, the stiffness of the foundation system under operational loads has to be analyzed. Considering this stiffness in a dynamic analysis of the whole OWEC structure, it must be ensured that the eigenfrequency of the wind turbine has a sufficient distance to the main excitation frequencies of the dynamic loading. In that, neither an overestimation nor an underestimation of the foundation stiffness is conservative. An incorrect estimation of soil stiffness results in an increase of uncertainties, leading to additional but unnecessary costs and decreasing the feasibility of the monopile foundation. Moreover, in the worst case it could have a strong negative influence on the structural lifetime (Kallehave et al., 2012).

To assess the current design practice for the estimation of the soil stiffness due to dynamic loading, Kallehave et al. (2012) evaluated frequency measurements on three operating wind turbines in the offshore wind farm Walney. Here monopiles of 6m diameter were located in predominately sandy soils. Kallehave et al. compared the measured frequencies of the OWECs with the calculated values. Based on the differences obtained the authors concluded that even by use of the initial stiffness of the soil-resistance curves in the current approaches the system stiffness is still under-predicted for large diameter piles.

In the present study, the finite element method (FEM) is used to investigate the monopile-soil stiffness due to loads of variable magnitude. Herein, a strain-dependent stiffness formulation is utilized.

2 STATE OF THE ART

2.1 Application of the p-y method in the monopile foundation design

For the design of monopiles, it is common practice to use the subgrade reaction method to simulate the occurring soil resistance. The soil is herein replaced by a number of spring elements along the pile shaft (cf. Fig. 1). In most cases the so-called p-y method, recommended in the offshore guidelines of the American Petroleum Institute (API, 2000) and Det Norske Veritas (DNV, 2011), is used. The suggested spring elements (p-y curves) have nonlinear, soil type- and depth-dependent load-displacement characteristics. For sand soils, the following approach for the dependence of soil resistance p on pile deflection y is used (API, 2000):

$$p = A\,p_u \tanh\left(\frac{k\,z}{A\,p_u}\,y\right) \tag{1}$$

Here, p_u is the maximum resistance, A is a calibration factor, z is the depth below ground surface and k is a stiffness value, which is dependent on the angle of internal friction φ' of the sand. k is termed the initial stiffness parameter and is given in a diagram in API (2000). Its dependence on the friction angle is given by the following equation (Augustesen et al., 2009):

$$k = 0.008085 \cdot \varphi^{2.45} - 26.09 \quad \text{for } 29° \le \varphi' \le 45° \tag{2}$$

It can be easily derived that $k\,z$ is the initial slope of the p-y curve, which is termed the initial soil stiffness E_{py}^{API}:

$$E_{py}^{API} = k\,z \tag{3}$$

The API p-y curve approach was derived based on several model and field tests. The first and most famous field tests with a pile diameter of D=0.61m were conducted at Mustang Island near to the Gulf of Mexico in 1974 (Reese et al., 1974, see also section 5). Experiences in the following decades showed that the approach was suitable for the design of piles with diameters of up to D=2m. In contrast, the validity of the current p-y method for large diameter monopiles stands in question. A number of numerical investigations (Wiemann et al., 2004; Achmus et al., 2008) indicated that in the calculation of maximum deflections under service loads, the monopile foundation stiffness is overestimated, i.e. the pile deflection is underestimated by the p-y method presented in the offshore guidelines. It was shown that the linear increase of the initial soil stiffness with depth (Eq. 3) overestimates soil stiffnesses in greater depths. This induces an under-estimation of deflection, since very stiff piles like monopiles exhibit substantial deflections in greater depths. Some researchers proposed new approaches for the initial soil stiffness (Wiemann et al., 2004; Soerensen, 2012) in order to give a more accurate prediction of monopile deflections under service loads.

2.2 Consideration of soil resistance in dynamic analyses

The determination of loads in a dynamic analysis of the whole OWEC system is usually carried out by considering a linear elastic system. Herein, the monopile system is idealized by a beam with linear elastic spring elements. Therefore it is necessary to derive constant spring stiffness values from the non-linear system which characterize the system behavior under usual dynamic operational loads.

Usually, a p-y calculation is carried out for typical operational loads, and from the resulting p and y-values in the considered depths the linear secant stiffnesses E_{py} = p/y are determined. In many design approaches, just the initial soil stiffness $E_{py}^{API} = k \cdot z$ (Eq. 3) is used in the dynamic analyses, assuming that the deflections under operational loads remain small.

A degradation of soil stiffness due to repeated (cyclic/ dynamic) loading is in general not taken into account. This assumption is supported by model tests of LeBlanc et al. (2010), which indicated that the un- and reloading system stiffnesses do not decrease, but even slightly increase with the number of load cycles.

2.3 Small strain effects in soil stiffness

Under high-frequency dynamic loads soil behaves like a perfectly elastic material. The main reason for this is that under such loads only very small shear strains occur due to inertia effects. In fact, the secant soil stiffness of soil under two-way loading is dependent on the shear strain amplitude (Fig. 2, left). In case of very small shear strains ($\gamma < 10^{-5}$), as induced under high-frequency loading, the soil stiffness is equivalent to the dynamic shear modulus G_0. If larger shear strains occur, the secant stiffness G_{sec} decreases as presented in Fig. 2 (right). The secant stiffness G_{sec} is thereby equivalent to the un- and reloading stiffness, which is needed in the dynamic analysis of the OWEC.

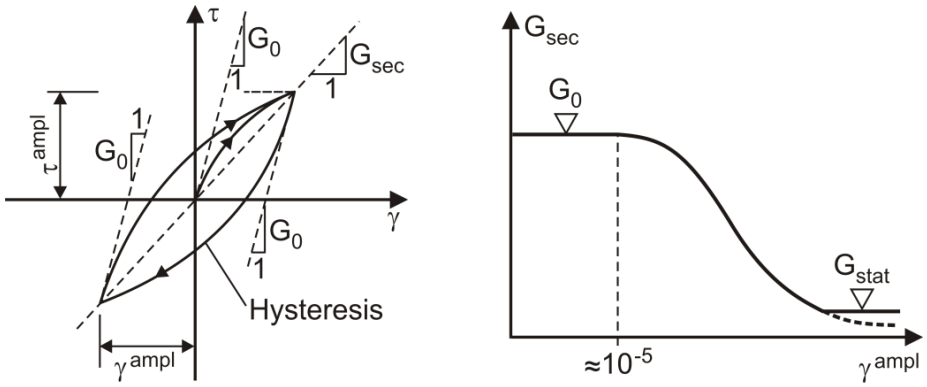

Fig. 2: τ-γ-hysteresis (left); Secant stiffness G_{sec} depending on shear strain (right)

For the description of the stiffness degradation, Santos & Correia (2001) suggested to use the following formulation:

$$\frac{G}{G_0} = \frac{1}{1 + \frac{a\,\gamma}{\gamma_{ref}}} \tag{4}$$

The ratio between actual shear modulus G and dynamic shear modulus G_0 depends on the value of shear strain γ. The shape factor a is proposed to a=0.385. The reference shear strain γ_{ref} corresponds to a secant shear modulus which is reduced to 72.2% of its initial value and is to be chosen dependent on soil type.

For large shear strains this formulation leads to unrealistic small soil stiffnesses. From Fig. 2 left it becomes apparent that the un- and reloading stiffness for two-way loading cannot be smaller than the static soil stiffness G_{stat}. Therefore, the minimum shear modulus is set here to $G=G_{stat}$, as shown in Fig. 2 right.

2.4 Equivalent soil stiffness method

The equivalent soil stiffness method accounts for the strain-dependence of soil stiffness by an iterative calculation procedure. The stress-strain behavior of soil is assumed linear elastic, but the elastic parameters are adapted iteratively to the occurring shear strains. This model is well-known in the field of earthquake analysis, but it was also successfully used for the estimation of shallow foundation stiffness of onshore wind turbines (Quast, 2010).

The model is based on the fact that the secant stiffness of the initial loading curves for the considered load level is identical to the secant stiffness of the corresponding τ-γ-hysteresis for (symmetrical) two-way loading. Therefore, the dynamic soil stiffness can be determined in a static calculation, if the soil stiffness is chosen corresponding to the occurring shear strains. Obviously, inertia forces and damping effects are not taken into account in this method. However, these effects are of minor importance for wind turbines due to the low-frequency of dynamic loading.

Apparently, this method is valid only for symmetrical two-way loading. Actually, real dynamic loads from wind are often swell loads. Consideration of swell loads, however, is much more complicated, since the equivalent soil stiffness then depends on both maximum load and load amplitude. Therefore, symmetrical two-way loading is assumed here. This is in line with current practice and should at least allow for a good first estimation of the un- and reloading stiffness.

3 NUMERICAL MODEL

3.1 Model and discretisation

A three-dimensional numerical model of a monopile foundation system was developed using the finite element program Abaqus Version V6.12 (Abaqus, 2012). With regard to the symmetry of both geometrical and loading conditions, only one half of the monopile foundation was modeled in order to reduce computational effort. Eight-node volume C3D8 elements were used to mesh both the monopile and the soil. Preliminary analyses focused on the mesh fineness and model dimensions to reach sufficiently accurate results and avoid the impact of boundary conditions. Finally, the soil model width was chosen forty-times the pile diameter and the model depth two-times the pile length, cf. Fig. 3. The model is discretized in 53505 elements. An exemplary mesh of the finite element model with geometrical parameters is presented in Fig. 3.

The monopile is modeled as an open tubular steel pile with a wall thickness t. An elasto-plastic contact according to the master-slave concept was implemented between inside and outside edges of the steel pile and the adjacent soil. The maximum shear stress τ_{max} results from the product of horizontal stress σ_H and contact friction angle δ, which was considered as two thirds of the internal friction angle φ'. The relative displacement, for which the mobilized shear stress is equal to the maximum shear stress, was set to $u_{el,slip}$=1mm.

3.2 Material modeling

The soil is modeled elasto-plastic, with the elastic parameters according to the equivalent soil stiffness method (see section 2.4). The shear strain- dependent stiffness degradation is implemented as presented in Equation 4. The assumed reference shear strain is set to γ_{ref} = 0.001, which is a typical value often used in practical applications. The respective shear strains have to be identified with the directional strain components ε_{ij} as presented in Eq. 5.

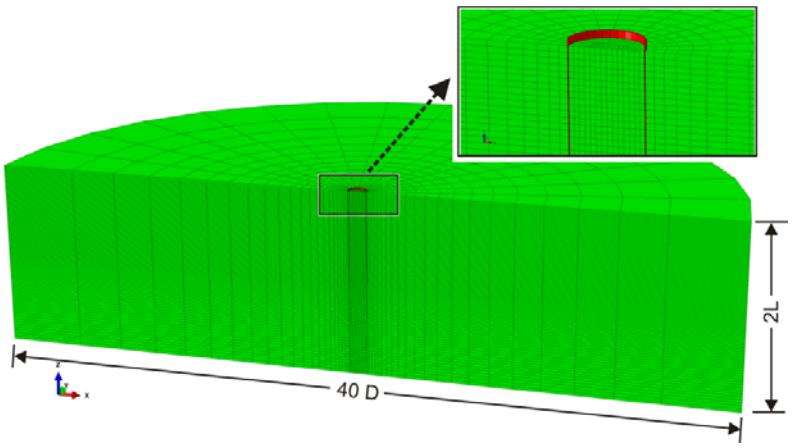

Fig. 3: Finite element mesh used in the simulations (Monopile D=5m; L=25m)

$$\gamma = \sqrt{\frac{4}{9}\left[\left(\varepsilon_{11}-\varepsilon_{22}\right)^2+\left(\varepsilon_{11}-\varepsilon_{33}\right)^2+\left(\varepsilon_{22}-\varepsilon_{33}\right)^2\right]+\frac{8}{3}\left[\varepsilon_{12}^2+\varepsilon_{13}^2+\varepsilon_{23}^2\right]} \quad (5)$$

The dynamic shear modulus G_0 was estimated based on an approach presented in DGGT (2002). This formulation is valid for poorly grained sandy soils with rounded grain shapes, which are mostly found in German offshore wind farm areas. The dynamic shear modulus depends on void ratio e and mean principal stress defined by the effective normal stress components σ_1', σ_2', σ_3'.

$$G_0 = 6.9\frac{(2.17-e)^2}{1+e}\left(\frac{\sigma_1'+\sigma_2'+\sigma_3}{3}\right)^{0.5} \quad (6)$$

It should be noted that the dynamic shear modulus for well-graded sandy soil can be significantly smaller (Wichtmann & Triantafyllidis, 2005). In contrast, the particle shape is of minor importance for the dynamic shear modulus.

As stated in section 2.3, a limitation of the stiffness degradation has to be considered. Therefore the static soil stiffness $E_{s,stat}$ is defined stress-dependent based on a formulation proposed by Ohde (1939):

$$E_{s,stat} = \kappa\sigma_{at}\left(\frac{\left(\sigma_1'+\sigma_2'+\sigma_3'\right)/3}{\sigma_{at}}\right)^{\lambda} \quad (7)$$

Here the reference stress σ_{at} is the atmospheric pressure 100 kPa, κ determines the soil stiffness at the reference stress state, and λ reflects the stress dependency of the soil stiffness. The average of the effective normal stress components σ_1', σ_2' and σ_3' defines the mean principal stress. Oedometric stiffness parameters κ and λ were selected corresponding to the bandwidth for sandy soils given in EAU (2012).

Additionally, a Mohr-Coulomb failure criterion was taken into account to ensure that no unrealistic soil resistance in the upper part of the monopile occurs. This is not in contrast with the soil model used due to the exclusive consideration of two-way loading. The parameters used in the simulations are presented in Table 1.

Tab. 1: Soil parameters used in the simulations

	γ' [kN/m³]	φ' [°]	c'[kN/m²]	ψ [°]	e [-]	ν [-]	κ [-]	λ [-]
Very loose	9.10	30.0	0.1	0.1	0.80	0.300	250	0.70
Loose	9.47	32.5	0.1	2.5	0.74	0.275	325	0.65
Medium dense	9.76	35.0	0.1	5.0	0.69	0.250	400	0.60
Dense	10.00	37.5	0.1	7.5	0.65	0.225	500	0.57
Very dense	10.31	40.0	0.1	10.0	0.60	0.200	700	0.55

In the FEM calculation, the stiffness has to be specified in terms of the elastic modulus E. The shear modulus G as well as the oedometric stiffness E_s can be converted into the elastic modulus under consideration of Poisson's ration ν as presented in Eq. 8.

$$\frac{1-\nu-\nu^2}{1-\nu} E_S = E = 2G(1+\nu) \tag{8}$$

The monopile steel is implemented as linear elastic material. The steel material properties E=210GPa, ν=0.2 were applied, where E and ν represent the modulus of elasticity and Poisson's ratio of steel material, respectively. The steel buoyant weight was set to γ'=68 kN/m³.

3.3 Calculation process

The FEM analyses were conducted in several steps. In the first step the initial stress state was generated by consideration of soil elements only. The horizontal stress σ_H was defined by a coefficient of horizontal earth pressure at rest k_0=1-sinφ'. Subsequently, the predefined elements defining the monopile geometry were replaced by steel elements representing the monopile structure. Additionally, the contact formulation between pile and surrounding soil was activated. Due to dead weight of the monopile a small initial settlement occured. The corresponding soil shear strains were neglected in the calculation of soil stiffness degradation. In the third step a horizontal force and a bending moment were applied by assigning the horizontal force to a reference node in the height of the desired load eccentricity. The transfer of the horizontal force and the corresponding bending moment to the monopile is arranged by a coupling condition which sets the displacements of the reference node to the head of the monopile in a relation.

The stiffness degradation in dependence of the shear strains is carried out iteratively. In a first calculation the dynamic shear modulus is used for all elements and set constant for the whole calculation. From the resulting shear strains a degraded stiffness distribution is calculated which is set as initial condition for the next iteration step. This process is carried out till the differences in the horizontal pile head deflection in two subsequent iterations becomes smaller than one percent.

4 RESULTS FOR A REFERENCE SYSTEM

First, the results for a reference system will be shown and discussed in detail. The reference system consists of a monopile with diameter D=5m, an embedded length L=25m and a wall thickness t=70mm in medium dense sand. The load eccentricity of the resultant horizontal load is set to h=50m, which is a realistic value for a load resulting from predominate wind and additional wave loads during operation of the turbine.

In Fig.4 the load-displacement curve (H-y curve) and the corresponding secant stiffnesses derived from K_{sec}=H/y are shown for different calculation approaches. Thereby the results of the current p-y method (API) are compared with the FEM results with different stiffness approaches. The curves for G_0 were calculated with a constant soil stiffness equal to the dynamic shear modulus and thus represent an upper limit of system stiffness. The calculation regarding the strain- dependent stiffness formulation as presented in section 3.2 is identified by G_{strain}. Considering a stress-dependent stiffness formulation excluding small strain effects (cf. Eq. 6) is presented as G_{static}.

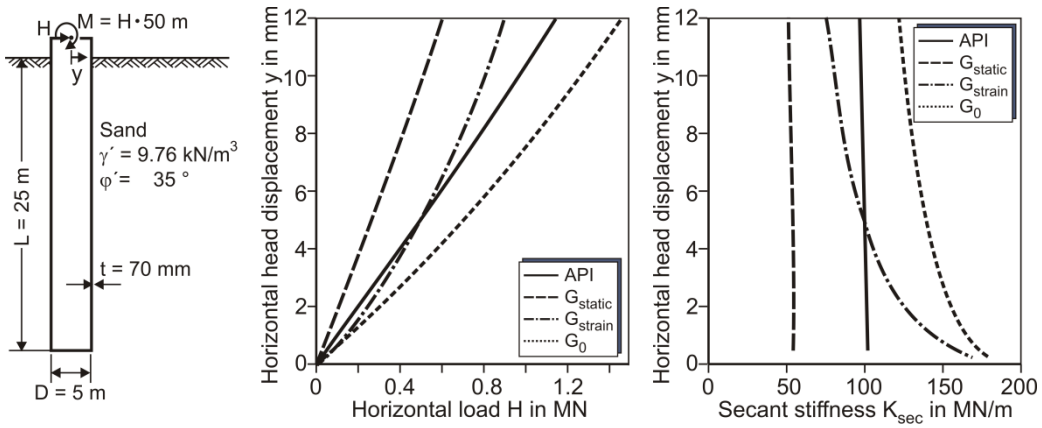

Fig. 4: Load-displacement curves and secant stiffnesses for the reference system

Evidently, the soil stiffness without small strain effects is significantly smaller than the stiffness resulting from the current design guidelines. This result corresponds to findings of other authors (Wiemann et al., 2004, Achmus et al., 2008; Soerensen, 2012) as mentioned in section 2.1. In contrast, the stiffness under consideration of the dynamic shear modulus is much larger than the results based on the p-y method, especially for small head displacements. The results for G_{strain} show almost identical results for very small head displacements as G_0, as to be expected. With increasing head displacement, the stiffness degrades and converges towards G_{static}. It can be concluded that the system stiffness for head displacements y<5mm is larger and for head displacements y > 5mm is smaller than based on p-y method.

It should be noted that even for constant soil stiffness the foundation stiffness is decreasing with increasing head displacement due to plastic failure in the upper part of the pile and a relative movement between pile and adjacent soil. The influence of plastic failure is thereby increasing with increasing soil stiffness. For the static calculation, these effects are overlain by the stress-dependent increase of soil stiffness.

Fig. 5 depicts the degradation of soil stiffness dependent on head displacement for the soil elements in the plane of symmetry. Evidently, the degradation increases with head displacement and becomes maximal close to the pile due to occurring shear strains. At a head displacement y=11.80mm an unsymmetrical distribution of stiffnesses is obtained, which is due to the degradation cut-off.

Additionally, the distribution of the secant slope of the p-y curves, which is termed here the bedding stiffness, representing the local soil stiffness along the pile shaft is presented in Fig. 6. Quite large stiffnesses are found from the numerical simulation results in the middle region of the pile. This is due to the point of pile rotation which leads to an inconstant stress spreading and a change of sign of pile displacement. However, the great stiffness is of minor importance due to the corresponding small deflections in this region and the small lever arm with respect to the point of rotation.

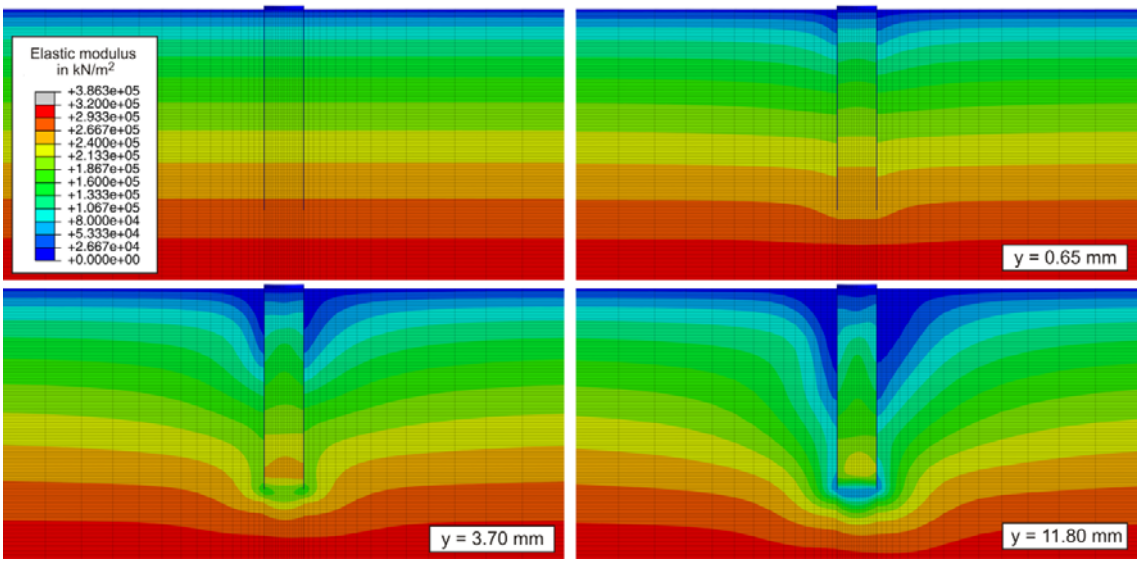

Fig. 5: Distribution of elastic modulus in dependence of pile head displacement for the reference system

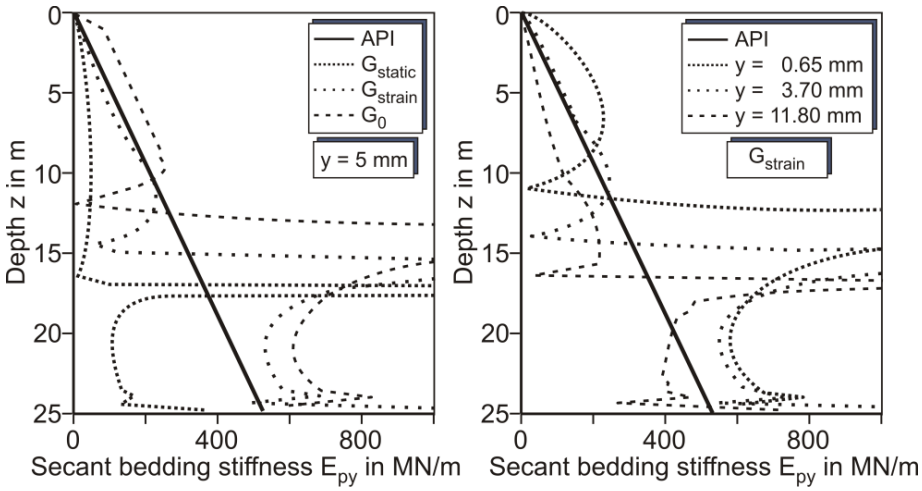

Fig. 6: Secant bedding stiffness along the pile shaft for the reference system

From Fig.6 (left), which shows the secant bedding stiffnesses for a pile head displacement of 5mm, it becomes evident that the local soil stiffnesses are affected in the same manner as the system secant stiffness shown in Fig. 4. Thereby, the strain- dependent stiffness formulation fits best with the p-y formulation, except for the case of very small displacement near to the point of rotation, which has minor effect on the system behavior. In Fig.6 (right) the influence of pile head displacement y on the bedding stiffness distribution is shown. Here, the degradation also of local soil stiffness due to increasing shear strains is obvious. The stiffness degradation for small head displacements is larger in the upper part of the pile. For a loading which causes a considerable movement also in the lower part of the pile length the degradation in this part becomes also relevant.

5 VALIDATION OF THE NUMERICAL MODEL

A back-calculation of pile tests at Mustang Island described and evaluated by Reese et al. (1974) was carried out to validate the numerical model. These tests were used as the basis of the original p-y formulation. Two tests with identical pile and soil conditions were conducted, one for static and one for cyclic loading. Tubular driven steel piles with an embedded length L=21m and a diameter D=0.61m were tested. For the cyclic load test only the results for the post-cyclic loading were presented. From the results it becomes apparent that the initial stiffness of the pile- soil system was not influenced by the cyclic loading. This is in good agreement with the findings of LeBlanc et al. (2010) as stated in section 2.2. Due to the focus on the initial stiffness in the present paper a consideration of the static test is therefore sufficient.

The soil conditions were specified as dense, poorly graded sand with a friction angle φ'=39° and a buoyant weight γ'=10.37 kN/m^2. Therefore the soil conditions are similar to the soil conditions assumed in this study. The dynamic shear modulus was calculated here according to Eq.5, and the oedometric stiffness parameters were set to κ=700 and λ=0.55.

Reese et al. presented a load deflection curve as well as a distribution of bending moments which were determined by strain measurements on the pile. The load displacement curve for the static test is presented in Fig. 7. For details of the field test see Cox et al. (1974).

Reese et al. developed a p-y formulation based on the results of the test. These p-y curves consist of four regions and are not identical with the p-y curves given in the offshore guidelines, which use a continuous tanh-function. With respect to initial stiffness and ultimate capacity the curves are almost identical, but the course in the middle section is different. The current API formulation is based on a comparative study of several model and field tests (Murchison & O'Neill, 1984). Both approaches are compared with the field tests results (Fig. 7, left). As expected, the approach of Reese et al. coincides with the field test very well. In contrast, the current API formulation of soil resistances predicts significantly stiffer behavior. For the calculation the program Lpile Plus V5.0 was used here (Reese et al., 2004).

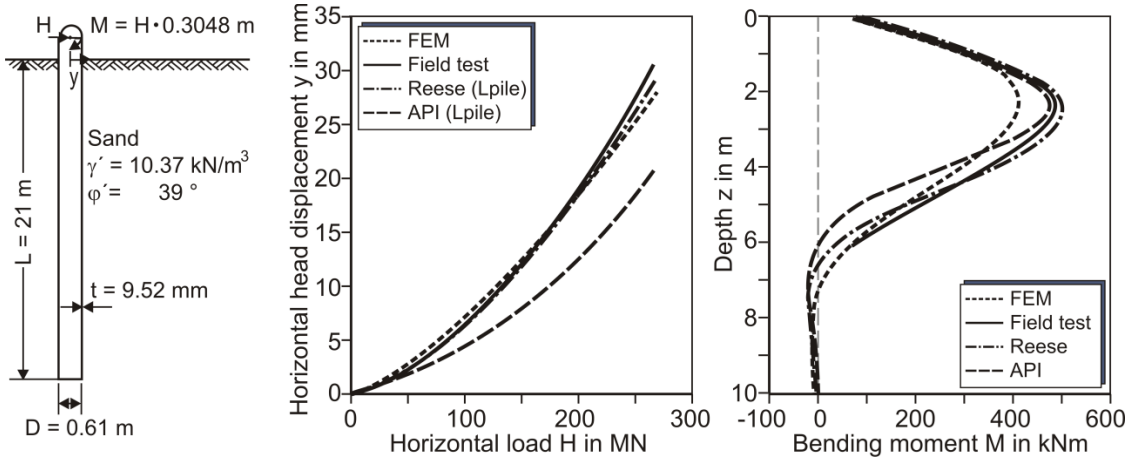

Fig. 7: Comparison of FEM and field test results for pile at "Mustang Island"

A comparison of the load displacement curves obtained by the FEM (accounting for strain-dependent stiffness) shows good agreement with the results of the field test, especially in the region of moderate pile head displacements. Also the distribution of bending moments fits very well with the results of the field tests. Therefore, it can be assumed that the implemented model is suitable for the calculation of monopile stiffness.

6 PARAMETRIC STUDY

In the following a comprehensive parametric study on the influence parameters on monopile stiffness is presented. Coming from the reference system, the relative density of sand, the pile dimensions and the load eccentricity are varied. In all calculations, the approach with strain-dependent soil stiffness was applied.

First, the relative density was varied, which is correlated with the angle of internal friction. The soil parameters used in the simulations are given in Table 1.

In Fig. 8 (left) the secant system stiffness of the monopile foundation is presented for different pile head displacements. The results are in the following designated as $K_{FEM.}$ The secant system stiffness increases almost linear with increasing friction angle.

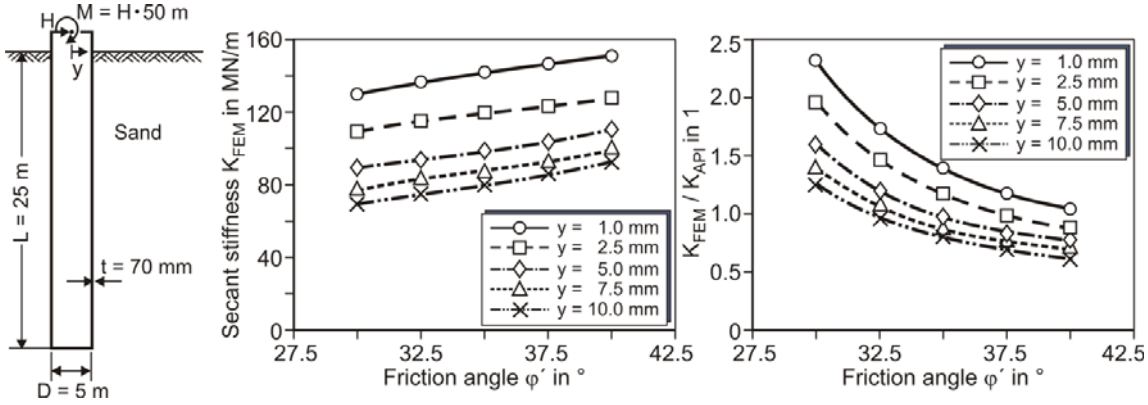

Fig. 8: Influence of relative density on secant system stiffness of monopile foundation

The FEM results are compared to the results from the API p-y method in Fig. 8 (right). As presented for the reference system in Fig. 4, the system stiffness based on the p-y method K_{API} is nearly constant for the adopted values of head displacements. It becomes apparent, that the p-y formulation is quite more sensitive against the variation of relative density. For small head displacements, the stiffness resulting from the FEM calculation is in all cases greater than the stiffness determined with the API formulation. For larger head displacement this depends on the relative density. Therefore, it cannot be generalized whether the API formulation behaves “stiffer” or “softer” than the FEM approach.

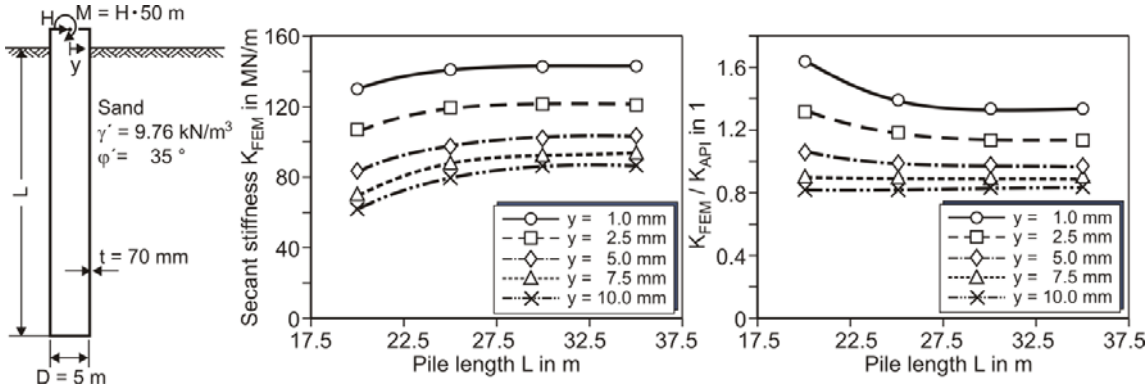

Fig. 9: Influence of pile length on secant system stiffness of monopile foundation

In Fig. 9 the effects of a variation of embedded pile length is shown. The stiffness of the monopile foundation is not affected by an increase of pile length above L=30m (L/D=6). This can be explained by a flexible behavior of long monopiles which occurs due to large initial soil stiffness for the considered small head displacements. It should be noted that the monopile behaves much stiffer for greater load levels or greater head displacements, respectively, due to the strain-dependent decrease of soil stiffness. A comparison with results based on the API formulation (Fig. 9 right) shows that similar system stiffness values are obtained for a pile head displacement of about 5mm.

Comparable results are achieved for variation of wall thickness (or pile stiffness, correspondingly). Under consideration of a pile head displacement y=5mm an almost identical secant stiffness results from both methods. Again it should be noted that the influence of pile head displacement is rather large. For example, for a head displacement of y=1mm the stiffness resulting from FEM is about 50% larger than based on the API formulation. In contrast, for a head displacement of y=10mm the stiffness based on FEM results is about 20% smaller.

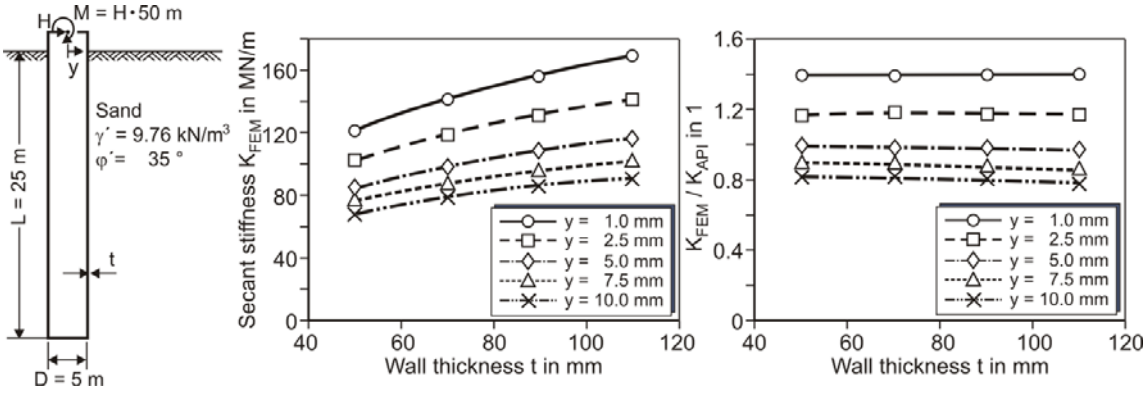

Fig. 10: Influence of pile stiffness on secant system stiffness of monopile foundation

In Fig. 11 the stiffness of the monopile-soil system for varied pile dimensions is presented. Here mainly the pile diameter is changed and the pile length, the wall thickness and the load eccentricity are adapted accordingly. This presentation shall account for typical monopile foundation situations at varying water depths. As to be expected, the secant stiffness increases strongly with a larger pile diameter. As before, for a pile head displacement of y=5mm the results from the FEM calculation are similar to the API formulation results.

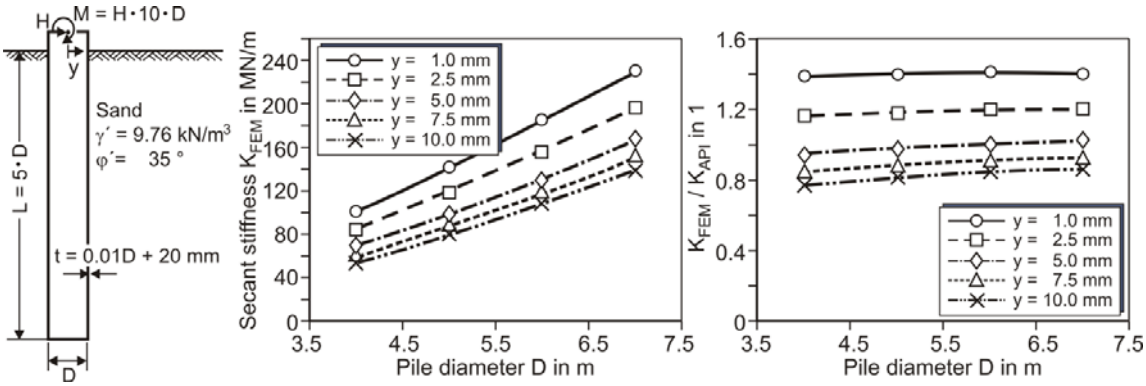

Fig. 11: Influence of pile dimension on secant system stiffness of monopile foundation

Finally, the effect of a variation of load eccentricity is shown in Fig. 12. An increasing load eccentricity leads to a significant decrease of the secant stiffness of the monopile. This results from an elevation of the point of rotation due to the additional moment acting at the pile head. Again, the API formulation results predicts almost identical stiffness of the monopile foundation if the applied loading results in a horizontal head displacement y=5mm.

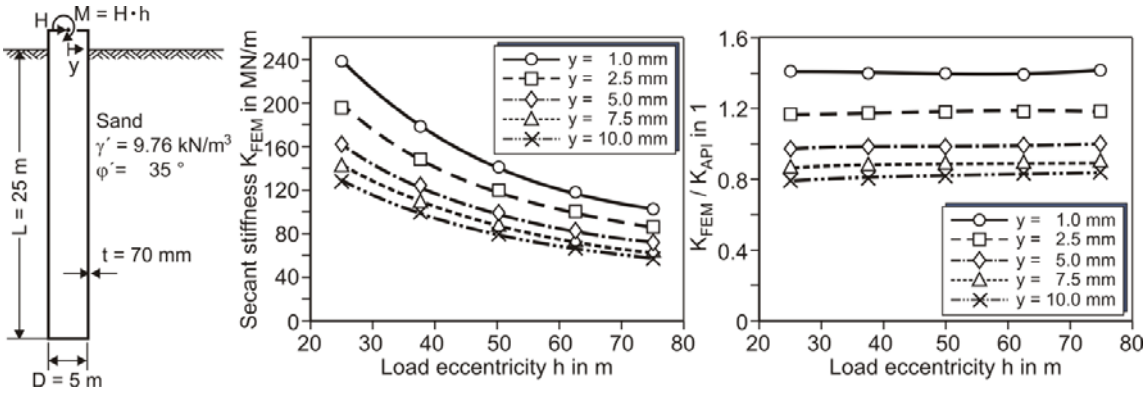

Fig. 12: Influence of load eccentricity on secant system stiffness of monopile foundation

7 COMPARISON WITH MODIFIED INITIAL STIFFNESS FORMULATIONS

A number of modified initial stiffness formulations for the consideration of large pile diameters exist in the literature. An approach proposed by Soerensen (2012) shall account for an overestimation of stiffness under service loads (see section 2.1). Soerensen did not change the p-y formulation in general but modified the equation to determine the initial stiffness of the p-y curve. Therefore, the initial stiffness is formulated in relation to the depth below surface z, soil stiffness E_s and pile diameter D as follows.

$$E_{py}^{Soerensen} = a\left(\frac{z}{z_{ref}}\right)^{b}\left(\frac{D}{D_{ref}}\right)^{c}\left(\frac{E_{s,ref}}{E_s}\right)^{d} \tag{9}$$

For the dimensionless constants b, c and d the values b=0.3, c=0.5 and d=0.8 are recommended. The reference stiffness a=1000 kPa is valid for a reference depth z_{ref}=1m, a reference pile diameter D_{ref}=1m and a reference soil stiffness $E_{s,ref}$=1kPa. Therefore Soerensen considered an under- linear increase of soil stiffness with depth and with pile diameter. Altogether, the approach of Soerensen leads to a significantly "softer" behavior of the monopile than resulting from the original API formulation.

A further modified initial stiffness formulation is suggested by Kallehave et al. (2012):

$$E_{py}^{Kallehave} = k\,z_0\left(\frac{z}{z_0}\right)^{m}\left(\frac{D}{D_0}\right)^{0.5} \tag{10}$$

This approach shall avoid an underestimation of stiffness under dynamic loading and should therefore also be valid for a primary initial loading in general. The recommended initial stiffness of the p-y curve E_{py} depends on the initial stiffness parameter k according to API and the relation of depth below surface z to a reference depth z_0=2.5m. The dimensionless parameter m is suggested to be 0.6, the reference diameter to D_0=0.61m. Overall, the proposed formulation results in a considerably "stiffer" behavior than the API formulation.

Fig. 13 presents a comparison of both modified formulations with the p-y method by API and the numerical results. The considered monopile-soil system is chosen to be in line with the system investigated by Kallehave et al. (2012). Unfortunately, many of the input parameters are not given in this paper. Missing parameters were thus assumed in a realistic range by general experience.

Regarding the secant soil stiffness distribution in Fig. 13 (left), large differences between the three formulations are evident. For all formulations, the soil stiffness is almost independent of the head displacement as it has been shown for the reference system in Fig. 4. This behavior can also be seen by the linear increase of the corresponding load-displacement curves in Fig. 13 (right).

In contrast, the stiffness resulting from the FEM approach strongly depends on the head displacement. For a head displacement of y=5mm the FEM results are in good agreement with the API formulation. This is reflected by the load-displacement diagram as well as in the distribution of initial bedding stiffness along the pile shaft. For smaller head displacements the stiffness is larger than based on the API approach. For head displacement y<1mm from the FEM a "stiffer" behavior results than from the formulation of Kallehave et al. For large head displacements the results converge towards the results of the Soerensen formulation.

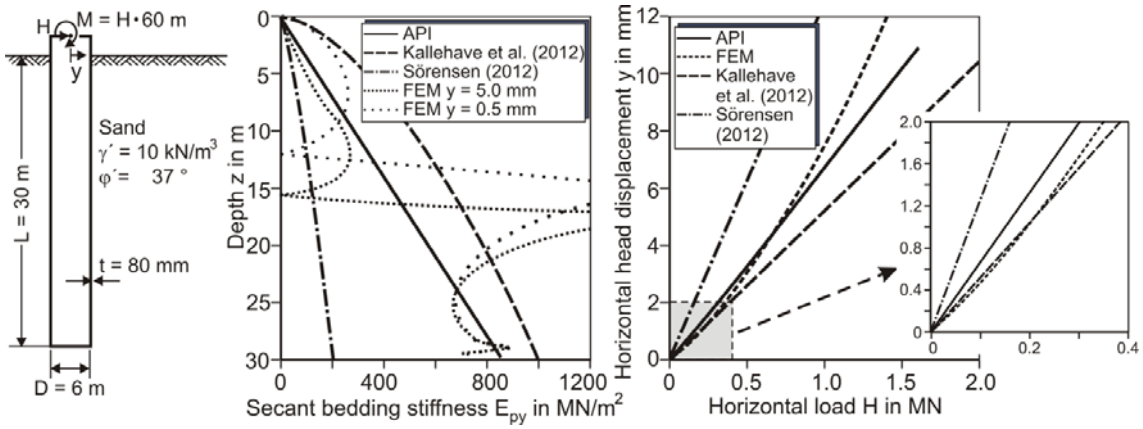

Fig. 13: Comparison of FEM results with approaches of Kallehave et al. (2012) and Soerensen (2012)

The results show that the proposed formulations (Eq. 9 and Eq. 10) have limited – and different – application ranges. The shortcomings of the original API approach are mainly induced by the fact that this approach was not calibrated and is thus not suitable for large diameter piles. The formulation of Soerensen (2012) is foreseen to correct the API method with respect to pile displacements under relatively great service loads. It cannot be used to predict the system stiffness under small operational loads. In contrast, the approach of Kallehave et al. is valid only for a very small pile head displacement. Therefore, the application of the current modified formulations lead to significant risks in the design process due to the limited validity for general load levels.

From these results it can be concluded that a new general formulation of p-y curves is urgently needed (Fig. 14). Such a new formulation has to take into account the overestimation of stiffness for large deflection as well as the underestimation of stiffness for small deflection obtained with the current approach.

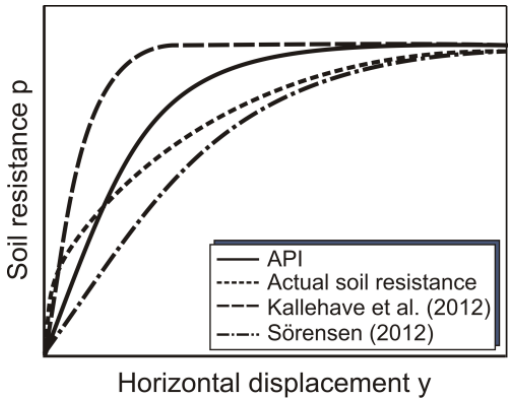

Fig. 14: General presentation of a realistic p-y curve in comparison with existing approaches

8 CONCLUSIONS

The p-y method is usually used in the design of monopile foundations. The p-y curves affect both the magnitude of monopile deformations under service loads and the system stiffness – which influences the OWEC's eigenfrequency – under dynamic operational loads. Previous investigations showed that the use of the original p-y curves stated in offshore regulations lead to an underestimation of maximum deformations under service loads, but to an overestimation of the system stiffness under dynamic operational loads.

The paper in hand presents results of numerical simulations which account for strain-dependent soil stiffness. The numerical model is validated by back-calculation of the Mustang Island pile tests performed by Reese et al. (1974) and gives very good agreement with the test results.

The model is then used for the identification of the effects of different parameters on the secant stiffness of the monopile-soil system. This secant stiffness can be used in the determination of eigenfrequencies, if perfect two-way loading is assumed. From this parametric study, the following conclusions can be drawn:

- The secant stiffness is strongly dependent on the pile head displacement occurring under the considered load, reflecting the non-linearity of the pile-soil system. It increases almost linear with the angle of internal friction of the sand. It also increases with embedded pile length, but non-linear in a way that from a certain length on no further increase occurs. The system stiffness also increases with pile wall thickness and – again almost linear – with pile diameter. The system stiffness decreases with increasing load eccentricity.
- A comparison with the currently usually applied approach (API p-y method) shows that this approach gives suitable results for pile head displacements in the order of 5 mm. If smaller head displacements occur, the API formulation underestimates, but for greater head displacements it overestimates stiffness, i.e. underestimates deformations.

A comparison with new p-y curve proposals from Soerensen (2012) and from Kallehave et al. (2012) shows that the latter can give reasonable results only for very small pile head displacements around 1 mm, whereas the first is suitable only for greater displacements, i.e. loading magnitudes.

A new p-y curve approach which gives reasonable results for arbitrary load levels is urgently needed. The numerical model used here, which accounts for small strain effects on soil stiffness, could be used to derive such a new approach. However, it is valid only for perfect two-way loading. A more sophisticated model is needed if the stiffness for swell loads

or non-symmetrical two-way loads shall be assessed. In any case, the results presented here show that small-strain stiffness effects considerably affect the monopile-soil system behavior.

Frequency measurements of operating wind turbines are also urgently needed to validate the numerical simulation results presented here. In order to do this, of course a precise description of the observed system, i.e. soil conditions, loading conditions and system geometry, is indispensable.

ACKNOWLEDGEMENT

The presented study was carried out as a part of a research project "GIGAWIND*life*" funded by the Federal Ministry for the Environment, Nature Conversation and Nuclear Safety, Germany (BMU). The authors sincerely acknowledge BMU support.

REFERENCES

Abaqus (2012), "Abaqus User's Manual", Version 6.12 (2012)

Achmus, M. (2008): "Bemessung von Monopiles für die Gründung von Offshore-Windenergieanlagen". Bautechnik 88 (9) (2011), S. 602-616 (in German).

Achmus, M., Abdel-Rahman, K., Kuo, Y.-S. (2008): "Design of Monopile Foundation for Offshore Wind Energy Plants". 11th Baltic Sea Geotechnical Conference, Gdansk, Poland, September 15-18, 2008.

American Petroleum Institute - API (2000): "Recommended Practice for Planning, Designing and Constructing Fixed Offshore Platforms - Working Stress Design, RP 2A-WSD". Version December 2000 and errata and supplement October 2007.

Augustesen A.H., Brodbaek, K.T., Moeller, M., Soerensen, S.P.H, Ibsen, L.B., Pedersen, T.S., Andersen, L. (2009): "Numerical Modeling of Large-Diameter Steel Piles at Horns Rev", Proceedings of the Twelfth International Conference on Civil, Structural and Environment Engineering Computing, Stirlingshire, UK, Paper No. 239, 2009.

Cox, W.R., Reese, L.C., Grubbs, B.R. (1974): "Field Testing of Laterally Loaded Piles in Sand". Proceedings of the Offshore Technology Conference, Houston, Texas, Paper No. OTC 2079, 1974.

Det Norske Veritas - DNV (2011): "Offshore Standard DNV-OS-J101, Design of Offshore Wind Turbine Structures". September 2011.

Deutsche Gesellschaft für Geotechnik e.V. - DGGT (2002): „Empfehlung des Arbeitskreises Baugrunddynamik". Eigenverlag: Grundbauinstitut der Technischen Universität Berlin 2002 (in German).

Empfehlungen des Arbeitsausschusses Ufereinfassungen - EAU (2004): „Häfen und Wasserstraßen (EAU 2004)", Ernst & Sohn, Germany 2005 (in German).

Kallehave D., LeBlanc Thilsted, C., Liingaard M.A. (2012): "Modification of the API p-y formulation of initial stiffness of sand". Proceedings of the 7th International Conference Offshore Site Investigation and Geotechnics, held 12–14 September 2012 at the Royal Geographical Society, London.

LeBlanc, C., Houlsby, G.T., Byrne, B.W. (2010): "Response of stiff piles in sand to long-term cyclic lateral loading, Geotechnique, Vol. 60, Issue 2, pp. 79-90, 2010.

Ohde, J., (1939): „Zur Theorie der Druckverteilung im Baugrund". Der Bauingenieur 20, H. 33/34, S.451-459, 1939 (in German).

Murchison, J.M., O'Neill, M.W. (1984): "Evaluation of p-y-Relationship in Cohesionless Soils". Analysis and Design of Pile Foundations, Editor J.R. Meyer, ASCE, NewYork, pp. 174-191, 1984.

Quast, A., (2010): "Zur Baugrundsteifigkeit bei der gesamtdynamischen Berechnung von Windenergieanlagen". Mitteilungen des Instituts für Grundbau, Bodenmechanik und Energiewasserbau, Leibniz Universität Hannover, Heft 69, 2010 (in German).

Reese, L.C., Cox, W.R., Koop, F.D. (1974): "Analysis of Laterally Loaded Piles in Sand". Proceedings of the Offshore Technology Conference, Houston, Texas, Paper No. OTC 2080, 1974.

Reese, L.C., Cox, Wang, S.T., Isenhower, W.M., Arrellaga, J.A., Hendrix, J. (2004): LPILEPlus, User's Manual and Technical Manual, Version 5.0 (2004).

Santos, J.A., Correia, A.G. (2001): "Reference threshold shear strain of soil and its application to obtain a unique strain-dependent shear modulus curve for soil". Proceedings of 15th International Conference on Soil Mechanics and Geotechnical Engineering. Istanbul, Turkey, Volume 1, 267-270.

Soerensen, S.P.H.: "Soil-structure interaction for non-slender, large-diameter offshore monopiles". PhD Thesis, Aalborg University / Denmark, Department of Civil Engineering, 2012.

Wichtmann, T., Triantafyllidis, T., (2005): "Über den Einfluss der Korngrößenverteilung auf das dynamische und das kumulative verhalten nichtbindiger Böden". Bautechnik 82 (6): 378-386, 2005 (in German).

Wichtmann, T., Triantafyllidis, T., (2006): "Über die Korrelation der ödometrischen und dynamischen Steifigkeit nichtbindiger Böden". Bautechnik 83 (7): 482-491, 2006 (in German).

Wiemann, J., Lesny, K., Richwien, W. (2004): "Evaluation of Pile Diameter Effects on Soil-Pile Stiffness". Proccedings of the 7th German Wind Energy Conference (DEWEK), Wilhelmshaven, Germany.

NUMERICAL ANALYSIS OF A PENETROMETER FREE-FALLING INTO A NON-UNIFORM SOIL LAYER

M. Moavenian, M. Nazem, and J.P. Carter

ARC Centre of Excellence for Geotechnical Science and Engineering, the University of Newcastle, Newcastle, NSW, Australia

ABSTRACT: *Evaluating the mechanical properties of soils is essential for successfully designing and constructing large infrastructure, including dams, bridges and offshore oil and gas platforms. The cone penetration test is utilized as an in situ test for exploring the geotechnical properties of the soils at these sites, but often it cannot be conducted or is difficult to conduct at relatively inaccessible sites, such as seabeds, riverbeds and wetlands. On the other hand, dynamic penetrometers have been used for offshore oil and gas industry applications such as pipeline feasibility studies and anchoring systems, and military applications including naval mine countermeasures and terminal ballistic studies. The main challenge of using dynamic penetrometers is the interpretation of their test results in order to deduce the mechanical properties of soil via experimental or theoretical relations. Recently, a robust numerical method based on the Arbitrary Langrangian-Eulerian (ALE) technique has been developed for analysing dynamic penetration problems and used to investigate a smooth penetrometer free falling into a uniform layer of clayey soil. Numerical as well as experimental results indicate that the penetration characteristics depend on the mechanical properties of the soil including its stiffness and strength parameters as well as the geometry of the penetrometer and its initial impact energy. In this study, the ALE method was employed to study the effect of shear strength increase with depth (a common condition of seabed deposits) on the penetration characteristics of a free falling penetrometer. This was achieved by conducting more than two thousand numerical experiments to accurately correlate the mechanical properties of the soil and penetrometer to the total time and total depth of penetration.*

1 INTRODUCTION

Free falling penetrometers (FFP) are one of the *in situ* devices employed in remote or inaccessible sites in order to measure the mechanical properties of soil. Testing of soils using these devices can provide vital information for the design of built infrastructure, such as bridges, dams, roads, landfills, pipelines, and offshore platforms. The measured information usually includes the total depth and time of penetration, and the deceleration characteristics of the falling penetrometer. Potentially, these data can then be used to deduce fundamental strength parameters for the soil in situ (Carter et al., 2010; Nazem et al., 2012).

The analysis of dynamic penetration is probably one of the most sophisticated and difficult problems in computational geomechanics, mainly due to challenges that arise from severe mesh distortion and the potential entanglement of elements caused by the large deformations. This usually motivates the application of adaptive finite-element techniques, such as the

Arbitrary Lagrangian–Eulerian (ALE) method, which can successfully overcome the mesh distortion issue. Important parameters such as the relative incompressibility of soil during the short period of penetration, the nonlinear stress–strain relations, and the rate-dependency of the material should also be considered in these analyses.

This study considers the effect of the inhomogeneity of soil on the penetration characteristic of a free-falling penetrometer. A preliminary study of this problem by Nazem & Carter (2011) indicated that, in the case of a FFP, inhomogeneity affects the dynamic response of soil. In this paper, a comprehensive parametric study is described in order to further understand the effect of shear strength increase of soil with depth on the penetration characteristics of a FFP. This is achieved by employing a validated numerical approach based on the ALE method previously developed by Nazem et al. (2006) and Nazem et al. (2009). Based on the numerical results obtained in this study, approximate closed-form relations between the mechanical properties of the soil, including its stiffness, strength, rate-dependency, and inhomogeneity, and the penetration characteristics, are established. These should prove useful in the interpretation of FFP tests conducted in the field.

2 ARBITRARY LAGRANGIAN-EULERIAN METHOD

The problems of soil penetration often involve large deformations causing severe mesh distortion and entanglement of elements. To avoid mesh distortion, the ALE method proposed by Nazem et al. (2006), and later improved by Nazem et al. (2009a and 2012), is employed in this study. In this method the analysis includes an Updated-Lagrangian (UL) step followed by an Eulerian step, which are explained as follows.

2.1 The Updated Lagrangian Method

In the UL method, the analysis starts at time 0 and all state variables that satisfy equilibrium at time t are known. Dynamic equilibrium will be achieved at time $t+\Delta t$ provided the equation of motion is satisfied by

$$\mathbf{M}\ddot{\mathbf{u}}^{t+\Delta t} + \mathbf{C}\dot{\mathbf{u}}^{t+\Delta t} + \mathbf{F}_{int}^{t+\Delta t} = \mathbf{F}_{ext}^{t+\Delta t} \tag{1}$$

where $\mathbf{M}$ and $\mathbf{C}$ are the mass and damping matrices, respectively, $\mathbf{u}$ represents the displacement vector, $\mathbf{F}_{int}$ and $\mathbf{F}_{ext}$ are the internal and the external force vectors, respectively, and the superimposed dot denotes the time derivative of a variable. To solve the momentum equation in (1), the implicit generalized-α method developed by Chung & Hulbert (1993) has been employed. The efficiency of this method in solving dynamic penetration problems has been demonstrated previously by Nazem et al. (2012).

2.2 Eulerian step

At the end of the UL step, the nodal coordinates are updated according to the incremental displacements which satisfy equilibrium. In problems with relatively large deformations, such as penetration problems, updating the nodal coordinates may lead to mesh distortion. Nazem et al. (2006) developed a robust method for mesh optimisation which makes use of an elastic static analysis. This method includes two steps: relocation of nodes along the boundaries and a subsequent elastic analysis. In this context the "boundaries" include the physical boundaries of the problem domain, the material interfaces and the loading boundaries. In the first step, the nodes on the boundaries are relocated along these boundaries (see Nazem et al.,2008 and Nazem et al., 2012 for details). The process of nodal relocation provides the spatial locations of mesh points, $\mathbf{x}_i^r$, for only those nodes along the boundaries. For these nodes, the incremental mesh displacements $\Delta\mathbf{u}_i^r$ are obtained from:

$$\Delta \mathbf{u}_i^r = \mathbf{x}_i^r - \mathbf{x}_i + \Delta \mathbf{u}_i \tag{2}$$

where x_i represents the spatial locations of material points (obtained at the end of UL step). The known displacements of all nodes on the boundaries, $\Delta \mathbf{u}_i^r$, are then applied to the undeformed domain as prescribed displacements and an elastic analysis using these boundary conditions is performed. This analysis assumes isotropic linear elasticity of a homogeneous medium and small deformation theory and aims to find the incremental mesh displacements for the remaining nodes of the continuum. The incremental displacement components computed for each node from this elastic analysis are then added to the nodal coordinates of the mesh to find the locations of the nodes in the new mesh. The new mesh and the old mesh share the same connectivity. Such an elastic analysis is very fast and will result in an optimum mesh if the nodes on the boundaries are optimally located.

After the mesh refinement, all state variables at nodal points as well as integration points are mapped from the old mesh to the new mesh. Remapping is usually performed using the ALE convection equation according to

$$\dot{f}^r = \dot{f} + \left(\dot{u}_i^r - \dot{u}_i\right) \cdot \frac{\partial f}{\partial x_i} \tag{3}$$

where $\dot{f}^r$ and $\dot{f}^r$ denote the time derivative of an arbitrary function f with respect to the mesh and material coordinates, respectively.

3 PROBLEM DEFINITION AND ASSUMPTIONS

A falling penetrometer with a conical tip is allowed to freely penetrate into a layer of soil in which the undrained shear strength increases linearly with depth. The initial impact velocity, the mass, and the diameter of the penetrometer are assumed to be v_0 , m, and d, respectively. The total depth and the total time of penetration are attained when the FFP stops, and are denoted by p and t_p, respectively. Due to the relatively rapid penetration, the soil behaviour is considered undrained and is modelled by the Tresca material with an associated flow rule. Poisson's ratio of the soil is assumed to be 0.49 to avoid any significant elastic volumetric changes, i.e., to approximate constant volume elastic behaviour. The undrained shear strength of the soil increases with the strain rate according to (Graham et al.,1983)

$$s_u = s_{u,ref}\left[1 + \lambda \log\left(\frac{\dot{\gamma}}{\dot{\gamma}_{ref}}\right)\right] \tag{4}$$

where s_u is the undrained shear strength of soil, $s_{u,ref}$ denotes the reference undrained shear strength measured at a reference strain rate of $\dot{\gamma}_{ref}$, λ is the rate of increase of strength per log cycle of time, and $\dot{\gamma}$ represents the strain rate. The value of $\dot{\gamma}_{ref}$ is assumed to be 0.01 per hour (Einav & Randolph, 2006). It is also assumed that the shear strength of the clay increases linearly with depth according to

$$s_{u,ref(z)} = s_{u,ref(0)} + k_s z \tag{5}$$

where $s_{u,ref(z)}$ and $s_{u,ref(0)}$ are respectively the undrained shear strength at depth z and ground surface, and k_s represents the rate of shear strength increase with depth. To avoid further complexities, the friction between penetrometer and soil as well as the material damping are ignored.

Nazem et al. (2009a) implemented the ALE method explained in previous section into SNAC, a finite element code developed at the University of Newcastle for geotechnical problems. For dynamic penetration problems, SNAC was validated by comparing its results with results obtained from experimental tests conducted at the University of Sydney (Nazem et al., 2012). SNAC is employed here for studying the dynamic penetration of a FFP in an inhomogeneous layer of soil in which the undrained shear strength increases linearly with depth. To study the effect of inhomogeneity of the soil on its dynamic behaviour as well as the penetration characteristics, a total of ~2300 specimens were analysed using different values of parameters as summarised in Table 1, in which I_r is the rigidity index of soil (the ratio between its shear modulus, G, and its undrained shear strength, $s_{u,ref}$) and $\bar{k}_s$ is a normalised inhomogeneity factor of soil defined as

$$\bar{k}_s = \frac{k_s d}{s_{u,ref(0)}} \qquad (6)$$

The finite element mesh and the boundary conditions of the problem are shown in Fig. 1. The mesh includes 10,252 and 4,988 6-node triangular elements. Due to axial symmetry, only the right half of the vertical cross section of the problem is considered in the analysis.

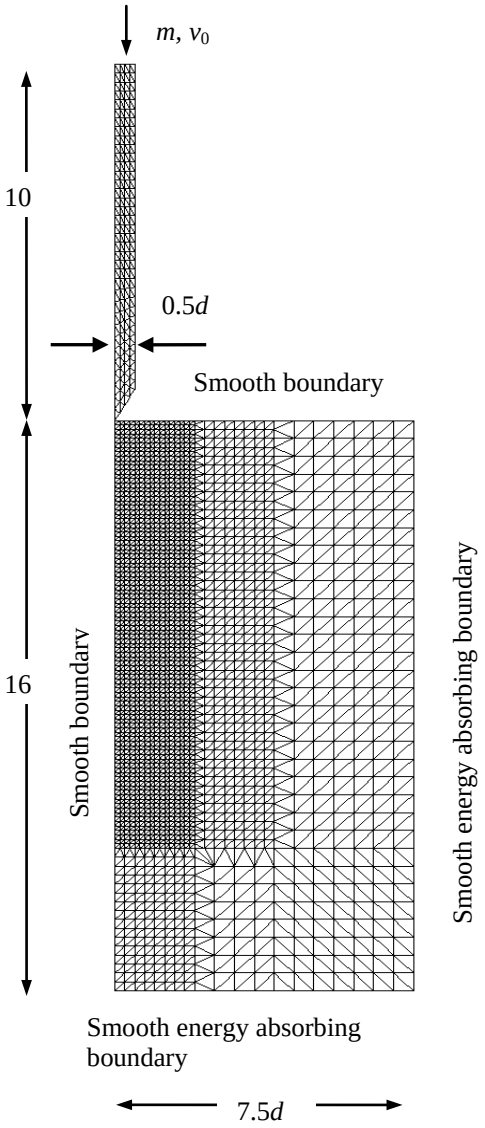

Fig. 1 Finite element mesh and boundary conditions of FFP problem.

4 NUMERICAL RESULTS

In a previous study, Nazem et al. (2012) showed that an appropriate strategy for studying the dynamic penetration problem is to plot the initial impact velocity of the penetrometer, $0.5mv_0^2$, normalised by $0.25\pi d^3 s_{u,ref(0)}$, versus the depth of penetration, normalised by diameter of penetrometer, $\bar{p}$. This normalised energy is defined by

$$E_n = 2\frac{mv_0^2}{\pi d^3 S_{u,ref(0)}} \qquad (7)$$

Table 1. Values of parameters used in parametric study.

Variable	Unit	Values
d	m	0.04, 0.06, 0.08, 0.1
m	kg	0.1, 0.5, 1.0, 5.0
v_0	m/s	5.0, 10.0
$s_{u,ref(0)}$	kPa	1.0, 2.0, 4.0
I_r		33, 67, 167
λ		0.0, 0.1, 0.2, 0.3, 0.4, 0.5
$\bar{k}_s$		0.0, 0.05, 0.1, 0.25, 0.5, 0.75, 1.0

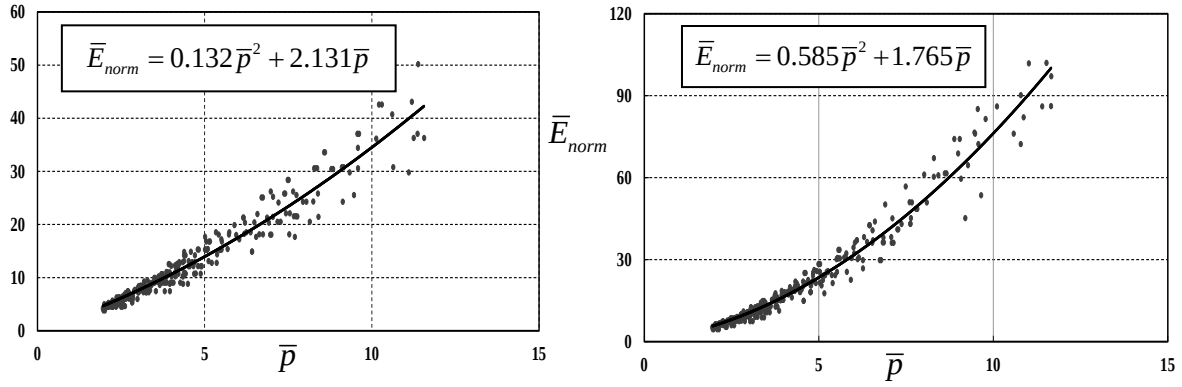

a. $\overline{k}_s = 0.1$ b. $\overline{k}_s = 0.5$

Fig 2. Normalised energy $\overline{E}_{norm}$ versus normalised penetration $\overline{p}$.

For an inhomogeneous layer of soil, however, a meticulous observation of the numerical results suggests that there is a quadratic relation between an alternative normalised energy, $\overline{E}_n$, given by

$$\overline{E}_n = \frac{E_n}{\left[0.1 + \ln\left(I_r\right)\right]\left(-4\lambda^2 + 8\lambda + 0.8\right)} \tag{8}$$

and $\overline{p}$, in the form of

$$\overline{E}_n = A_s \overline{p}^2 + B_s \overline{p} \tag{9}$$

where A_s and B_s are two variables depending on $\overline{k}_s$. To study this relationship in greater detail, the normalised energy $\overline{E}_n$ is plotted versus the normalised depth of penetration $\overline{p}$ in Fig. 2 for specimens where $\overline{k}_s = 0.1, 0.5$. For each value of $\overline{k}_s$, values of the variables A_s and B_s have been obtained and these are summarised in Table 2. According to this table, variables A_s and B_s can be estimated by

$$\begin{aligned} A_s &\approx 1.17\overline{k}_s \\ B_s &\approx 2.17 - \overline{k}_s \end{aligned} \tag{10}$$

Substituting the values of A_s and B_s from Equation (10) in Equation (9) provides

$$\overline{E}_n = 1.17\overline{k}_s \overline{p}^2 + \left(2.17 - \overline{k}_s\right)\overline{p} \tag{11}$$

To demonstrate the accuracy of Equation (11), the normalised energy $\overline{E}_n$ predicted by this equation and based on values of $\overline{p}$ obtained from the finite element analysis and the normalised energy calculated by Equation (8), is plotted in Fig. 3. According to Fig. 3, there is relatively good agreement between the values predicted by the proposed relation in (11) and the values of $\overline{E}_n$ used in the analyses.

To study the deceleration characteristics of the penetrometer, its velocity normalised by the initial impact velocity and its acceleration normalised by the gravitational acceleration, *g*, versus time are plotted in Fig. 4 and Fig 5, respectively, for penetrations into a non-uniform

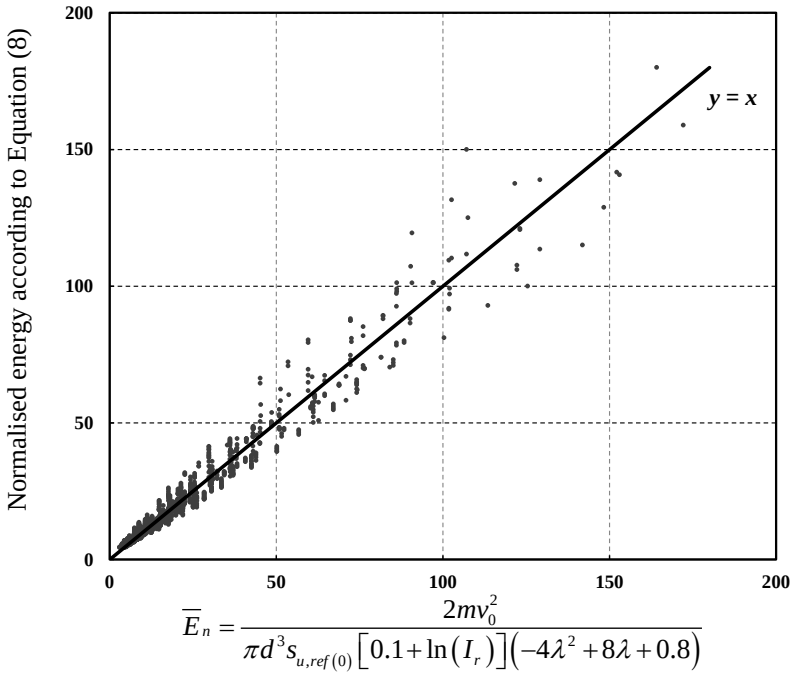

Fig. 3. Normalised energy $\overline{E}_n = 1.17\overline{k}_s\overline{p}^2 + \left(2.17-\overline{k}_s\right)\overline{p}$ (Equation (8)) versus the normalised energy according to finite element inputs.

as well as an uniform soil layer. On the plots in Fig. 5 a negative acceleration means that the penetrometer is slowing down. According to Figs 4 and 5, the magnitude of deceleration of a FFP penetrating into a uniform layer of soil is constant, whereas this magnitude linearly increases with time for a non-uniform layer of soil. Figs 4 and 5 also indicate that the velocity of FFP reduces linearly and quadratically for penetrations into an uniform and a non-uniform soil layer, respectively.

Table 2. Values of A_s and B_s

$\overline{k}_s$	A_s	B_s
0.05	0.08	2.131
0.1	0.132	2.116
0.25	0.334	1.808
0.5	0.585	1.765
0.75	0.919	1.285
1.0	1.18	1.165

Since the FFP is assumed to behave as a smooth rigid body, the applied force during penetration is proportional to its mass, and represents the dynamic soil response. To study the dynamic soil behaviour, the pressure

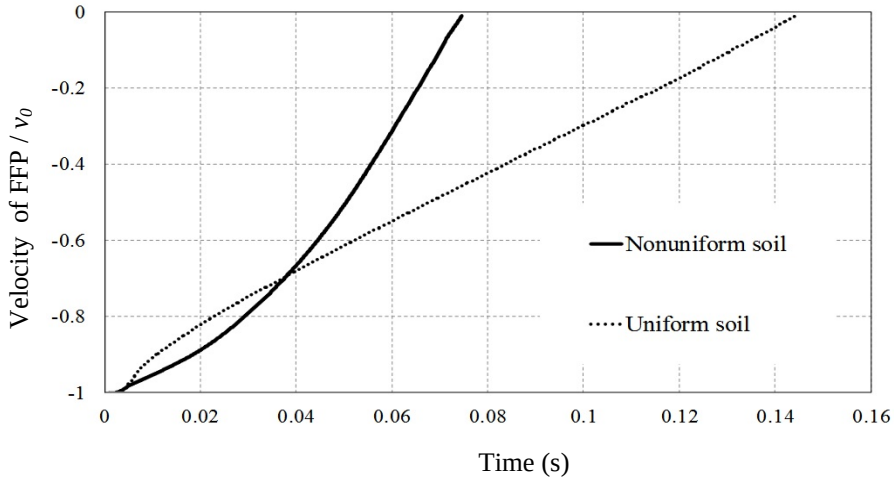

Fig. 4. Velocity profile of a FFP in non-uniform and uniform layers of soil.

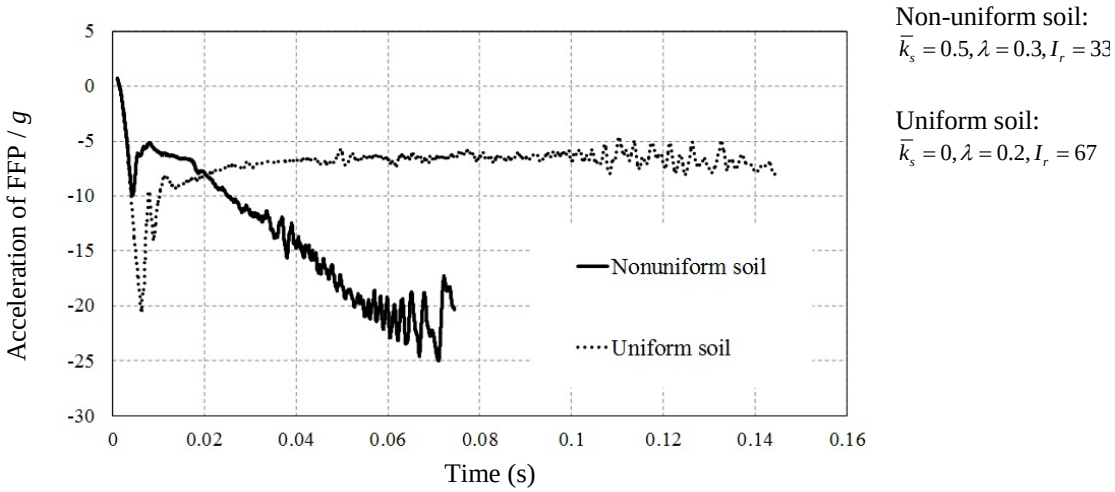

Fig. 5. Acceleration of a FFP in non-uniform and uniform layers of soil.

applied on penetrometer, normalised by $s_{u,ref(0)}$, is plotted versus the normalised penetration in Fig. 6. According to Fig. 6, the dynamic response of a non-uniform soil initially increases rapidly due to the inertia effect caused by the impact, and then increases more or less in a linear fashion with further penetration after the effects of the dynamic forces are diminished. This trend is observed for all penetrometers dropped onto an inhomogeneous layer of soil ($\bar{k}_s \neq 0$). On the other hand, as indicated in the previous study by Nazem et al. (2012), the resistance of a uniform layer converges to a constant value after the effect of the inertia forces has vanished.

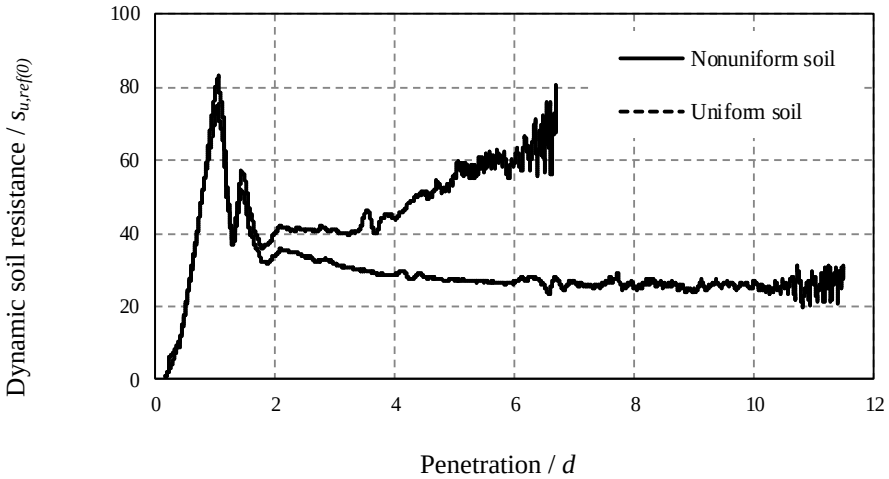

Fig. 6. Dynamic soil resistance versus penetration in non-uniform and uniform layers of soil.

5 CONCLUSIONS

Numerical analysis of free-falling penetrometers (FFPs) penetrating into an inhomogeneous layer of soil was considered in this study. A validated Arbitrary Lagrangian-Eulerian method was adopted to analyse these dynamic penetration problems. Numerical results indicate that the penetration characteristics of a FFP depend on the mechanical properties of the soil including its undrained shear strength, rate parameters, rigidity index, and inhomogeneity factor. Numerical results also indicated that the soil resistance increases linearly as the object penetrates into the soil layer.

6 REFERENCES

Carter, J.P., Nazem, M., Airey, D.W. & Chow, S.W. (2010), "Dynamic analysis of free-falling penetrometers in soil deposits". Proceedings of Geoflorida 2010, Advances in analysis, modelling and design, Geotechnical Special publication, No 199, ASCE, 53-68.

Chung J., & Hulbert, G.M. (1993), "A time integration algorithm for structural dynamics with improved numerical dissipation: the generalized-α method". J. Appl. Mech., Vol. 60, 371-375.

Einav, I. & Randolph, M. (2006), "Effect of strain rate on mobilised strength and thickness of curved shear bands". Geotechnique, Vol 56 (7), 501–504.

Graham, J., Crooks, J.H. A. & Bell, A.L. (1983), "Time effects on the stress–strain behaviour of natural soft clays". Geotechnique, Vol. 33(3), 327–340.

Liyanapathirana, D.S. (2009), "Arbitrary Lagrangian Eulerian based finite element analysis of cone penetration in soft clay". Comput. Geotech., Vol. 36(5), 851–860.

Nazem, M., Carter, J.P. (2011), "Parametric study of a free-falling penetrometer in clay-like soils". Proceedings of the 2nd International Symposium on Frontiers in Offshore Geotechnics, Perth, Australia, Frontiers in Offshore Geotechnics II – Gourvenec & White (eds), Taylor & Francis Group, London, 293-298.

Nazem, M., Carter, J.P., Airey, D.W. & Chow, S. H. (2012), "Dynamic analysis of a smooth penetrometer free-falling into uniform clay". Geotechnique, Vol. 62(10), 893–905.

Nazem, M., Sheng, D. & Carter, J.P. (2006), "Stress integration and mesh refinement in numerical solutions to large deformations in geomechanics". Int. J. Numer. Methods Engng Vol. 65(7), 1002– 1027.

Nazem, M., Sheng, D., Carter, J.P. & Sloan, S.W. (2008), "Arbitrary-Lagrangian-Eulerian method for large-deformation consolidation problems in geomechanics". Int. J. Numer. Anal. Meths. Geom., Vol. 32, 1023-1050.

Sheng, D., Nazem, M. & Carter, J.P. (2009), "Some computational aspects for solving deep penetration problems in geomechanics". Comput. Mech. 44, No. 4, 549–561.

Walker, J. & Yu, H.S. (2010), "Analysis of the cone penetration test in layered clay". Geotechnique, Vol. 60(12), 939–948.

LARGE DEFORMATION FINITE ELEMENT ANALYSIS OF SPUDCAN PENETRATION IN LAYERED SOILS

H.D.V. Khoa
Norwegian Geotechnical Institute, Oslo, Norway

ABSTRACT: *Spudcan foundations have been widely used to support jack-up rigs. Although the penetration behaviour of spudcan foundations on layered soils has received significant attention from researchers, punch-through failure during jack-up rig installation continues to be one of the major failure hazards of spudcan foundations. The paper presents results of 3D large deformation finite element analyses of the penetration response during installation of a spudcan foundation in layered soils. The penetration process is simulated by the Coupled Eulerian-Lagrangian method using Abaqus/Explicit. To approximately capture the effects of strain rate and strain softening on the penetration resistance the Mohr-Coulomb constitutive model is modified by introducing a hyperbolic evolution of the friction angle and cohesion as a function of the equivalent plastic strain. Using the CEL method together with the modified Mohr-Coulomb model makes it possible to successfully back-analyze the two centrifuge model tests of a spudcan foundation penetrating into stiff clay overlying soft clay (Hossain & Randolph, 2010a) and dense sand overlying clay (Teh, 2007). In fact, the CEL 3D FE-model is able to not only calculate the spudcan foundation resistance but also predict and capture well different failure mechanisms experimentally observed during the penetration process.*

1 INTRODUCTION

The offshore oil and gas industry continue to expand and move from shallow to deep water. Mobile jack-up units have considerable economic significance because they are used to carry out a large proportion of the word's oil and gas exploration in water depths up to 150 m. A modern jack-up rig typically consists of a buoyant triangular platform supported by three or four independent truss-work or cylindrical leg system with individual footings known as "spudcans". Spudcan foundations are generally circular or polygonal in plan view with shallow conical underside and sharp or truncated central. The equivalent diameters of these spudcans typically vary between 10 and 20 m. Different types of spudcans and installation methods are described in McClelland et al. (1981) and Menzies & Roper (2008). Spudcan foundations can be penetrated deeply into the seabed by up to three times of their diameters and pre-loaded by ballasting the hull of the rig.

When predicting the penetration behaviour of a spudcan at a site where layered soils are present, three foundation failure mechanisms are commonly considered (SNAME, 2002):

- General shear: this mechanism can occur where the thickness of the top layer is large when compared with the width of the footing or where the strength of the soil layers

do not vary significantly and an average (or similar) strength can be adopted in the bearing capacity equations;

- Squeezing: this mechanism occurs where a soft clay layer overlies a significantly stronger layer, in which case the bearing capacity of the soft layer can increase as the height of the soft soil layer decreases;
- Punch-through: this failure is usually observed in seabed sediments of a strong layer overlying a weak layer. With this mechanism, a small additional spudcan penetration may be associated with a significant abrupt reduction in bearing capacity within a short period, which can result in rapid (uncontrolled) leg penetration.

The research works presented in this paper are conducted with the aim of improving understanding of the penetration of spudcan foundations in a strong soil overlying a weak soil as well as prediction of the potential punch-through phenomena which continue to be a major problem during installation of jack-up units (Osborne, 2005).

To evaluate the depth of penetration and the bearing capacity for footings in layered soils several methods have been proposed ranging from a simplified projected area method (also known as load spread method) proposed by Terzaghi and Peck (1948) to more complex methods, for example:

- Limit equilibrium: Reddy & Srinivasan (1967), Okamura et al. (1998);
- Limit analysis (kinematic approach): Chen & Davidson (1973), Florkiewicz (1989), Michalowski & Shi (1995);
- Semi-empirical based on experimental studies: Brown & Meyerhof (1969), Meyerhof & Hanna (1978)), Craig & Chua (1990), Lee (2009), Teh (2010);
- Finite element method: Griffiths (1982), Merifield et al. (1999), Shiau et al. (2003), Edwards & Potts (2004), Szypcio and Dołżyk (2006).

However, almost all of these studies are limited to footings resting on the surface of the soil and are based on the assumption of small displacement. Thus, these methods cannot account for the soil heave formed gradually at the sides of the foundations as well as the distortion of the upper layer as it punches through into the lower layer. The effects of strain rate and strain softening on the bearing capacity of spudcan foundation have also been neglected in these methods.

Over the last decade, large deformation finite element (LDFE) analysis has extensively been applied to simulate spudcan foundation penetrating into layered soils. Using the LDFE analysis does not require any *a priori* assumption on failure mechanism, and thus it can reflect the natural development of the failure zone and provide good predictions of the bearing behaviour. Hossain & Randolph (2010b), Wang & Carter (2002) and Yu et al. (2012) have employed the Remeshing and Interpolating Technique with Small Strain (RITSS) developed by Hu & Randolph (1998) to simulate the penetration process of spudcan foundations in stratified soils. This RITSS method falls into the category of Arbitrary Lagrangian-Eulerian (ALE) methods. Qiu & Henke (2011), Qui & Grabe (2012) and Tho et al. (2012) have recently applied the Coupled Eulerian-Lagrangian (CEL) method in the finite element program Abaqus to simulate large installation of spudcan foundations. Andresen & Khoa (2013) have applied both the ALE and CEL methods available in Abaqus to model the deep penetration process and installation effects of offshore anchors and spudcan foundations. Through the comparison between the two approaches, it was concluded that in the Abaqus program, the ALE method is more flexible since it can be applied in planar, axisymmetric and three-dimensional boundary value problems whereas only the later is available for the CEL method. Moreover, the ALE method is also available for both Abaqus/Explicit and Abaqus/Standard, which largely expands its application fields such as:

steady-state transport analysis, couple pore fluid flow and stress analysis as well as couple temperature-displacement analysis. However, the main limitation of the ALE method in Abaqus is that it does not support the boundaries between different materials as they are considered as non-adaptive mesh (or Lagrangian) boundaries. In other words, this method cannot handle deep penetration of spudcan into layered soils where large deformations can occur at the material boundary regions.

In this paper the CEL method is employed to simulate a spudcan foundation penetrating into layered soils in which the top layer is assumed to be stronger than the bottom layer. A 3D FE-model is developed by using the Abaqus/Explicit program with the aim of back-analyzing two centrifuge model tests of a spudcan foundation penetrating into stiff clay overlying soft clay (Hossain & Randolph, 2010a) and dense sand overlying soft clay (Teh, 2007).

In particular the classical Mohr-Coulomb model in Abaqus/Explicit is modified by introducing a hyperbolic evolution of the internal variables (i.e. the friction angle and the cohesion) as a function of the Von Mises equivalent plastic strain which was proposed by Barnichon (1998). This simple modification allows the material to harden and/or soften isotropically. Thus the modified Mohr-Coulomb can be used to model gradual reduction in strength of granular material due to the cumulative shear strains during the penetration of spudcan foundations

2 NUMERICAL MODEL

The large deformation finite element (LDFE) analyses of vertical penetration process of spudcan foundations are undertaken by using the CEL method in Abaqus/Explicit. Three different cases of spudcan modelling are considered:

- Case 1: Spudcan foundation on homogeneous clay is modelled. The calculated bearing capacity results are compared with the centrifuge model test data reported by Hossain & Randolph (2009) in order to validate the CEL FE-model. Effect of penetration rate with respect to the bearing capacity is also studied;
- Case 2: it concerns about back-analysis of the centrifuge test E2UU-II-T5 conducted by Hossain & Randolph (2010a). In this laboratory test, a spudcan of prototype diameter 6 m was installed into stiff clay overlaying soft clay. The effects of strain rate and strain softening on the calculated bearing capacity of the spudcan is also numerically investigated;
- Case 3: the CEL FE-model is applied to back-analyze the centrifuge test Half_SP2 of a spudcan foundation on dense sand overlying relatively soft clay, which was carried out by Teh (2007). Special focus is addressed to the development of failure mechanisms during the penetration process.

Table 1 gives a summary of the three cases of LDFE analyses of the spudcan penetration process.

Table 1. Summary of three different cases of LDFE analyses of spudcan foundations.

Case	Soil domain	Material	Thickness of layer (m)	Submerged unit weight (kN/m^3)	Centrifuge model tests
1	Homogenous clay	Clay	30	7.4	Various tests conducted by Hossain & Randolph (2009)
2	Stiff clay over soft clay	Stiff clay	4.5	8.0	Test E2UU-II-T5 performed by Hossain & Randolph (2010a)
		Soft clay	22.5	7.4	
3	Dense sand over soft clay	Superfine silica sand	5	10.8	Test Half_SP2 conducted by Teh (2007)
		Kaolin clay	25	6.5	

2.1 Geometry and discretisation

Fig. 1 presents detailed information of a typical 3D FE-model used in the CEL FE analyses of the spudcan penetration in layered soils. The spudcan has a diameter D of 6 m. The dimensions of the FE-model are extended to 30 m in depth (equivalent to 5D) and 24 m in radius (equivalent to 4D) in order to minimize boundary effects.

The FE-model base boundary is fully fixed while its sides are constrained in motion only in the lateral direction. Owing to axisymmetry, only a 30-degree slice of the full 3D problem is considered so that the computational time is optimized without causing excessive skewing of the elements close to axis of symmetry. Thus the symmetric boundary conditions are in addition imposed on the two planes of symmetry by constraining the two in-plane rotations.

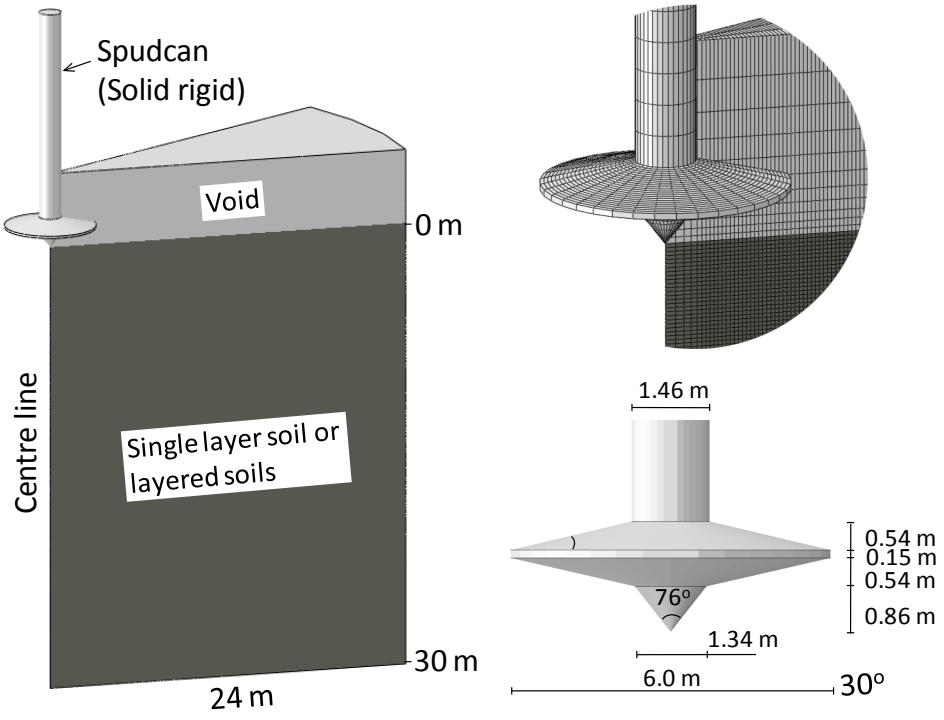

Fig. 1. Typical CEL finite element model of spudcan foundation.

In the CEL FE-model, the spudcan foundation is discretised by using Lagrangian elements whereas the soil and void domains are modelled with Eulerian elements. Since the spudcan is significant stiffer compared to the soil, it is modelled as rigid body which makes the model computationally more efficient. The purpose of the void layer is to capture the soil heave

during the spudcan installation process. The overall FE-mesh of the Eulerian domains composes of 68320 8-node linear brick elements with reduced integration and hourglass control. In order to minimize the discretisation effects as well as to well capture the failure mechanism the element size is gradually refine close to the spudcan.

The spudcan penetration process is simulated through the enforcement of displacement with a constant rate of 1 m/s, which is assumed slow enough so that the calculated results are not affected by inertia effects. The effect of the penetration rate with respect to the calculated bearing capacity of the spudcan is discussed in Section 3.

The interaction between the soils and the spudcan foundation is modelled using the "general contact" algorithm available in Abaqus/Explicit. Except if otherwise stated, the spudcan base and sides are assumed to be perfectly smooth.

All FE analyses presented in this paper are performed under the condition of free water by considering effective stress. The submerged unit weight is applied to generate the initial stress conditions. Table 1 presents a summary of all numerical analyses conducted.

2.2 Modification of Mohr-Coulomb constitutive model

This section presents a simple modification of the classical Mohr-Coulomb model in order to allow the material to harden and/or soften isotropically. Assuming that the plastic flow induces hardening/softening of the limit surface, Barnichon (1998) proposed a hyperbolic evolution of the internal variables (friction angle and cohesion) as a function of the Von Mises equivalent plastic strain ε_{eq}^{p}:

$$\varphi = \varphi_0 + \frac{\left(\varphi_f - \varphi_0\right)\varepsilon_{eq}^{p}}{B_p + \varepsilon_{eq}^{p}} \qquad \text{and} \qquad c = c_0 + \frac{\left(c_f - c_0\right)\varepsilon_{eq}^{p}}{B_c + \varepsilon_{eq}^{p}} \tag{1}$$

where the superscript p stands for plastic and the two subscripts 0 and f denote the initial and final values, respectively. The Von Mises equivalent plastic strain ε_{eq}^{p} is obtained by integration of the Von Mises equivalent plastic strain rate $\dot{\varepsilon}_{eq}^{p}$:

$$\varepsilon_{eq}^{p} = \int_0^t \dot{\varepsilon}_{eq}^{p}\,\mathrm{d}t = \int_0^t \sqrt{\frac{2}{3}\dot{\varepsilon}^{p} : \dot{\varepsilon}^{p}}\,\mathrm{d}t \tag{2}$$

Coefficients B_p and B_c represent, respectively, the values of the equivalent plastic strains for which half of the hardening/softening on the friction angle and cohesion is achieved (see Fig. 2)

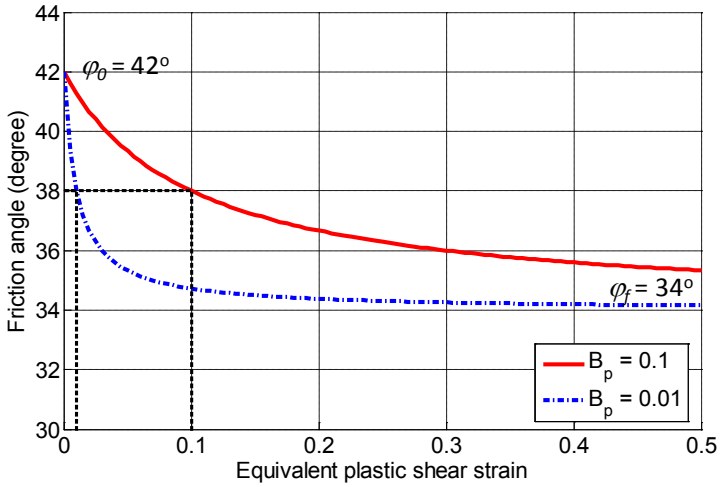

Fig. 2. Example of softening hyperbolic law for two values of coefficient *Bp* ($\varphi_0 = 42°$ and $\psi_f = 34°$).

Using the hyperbolic equation (1) the friction angle and the cohesion (or the undrained shear strength) at individual Gauss points can be modified according to the current accumulated equivalent plastic shear strain.

It's worth noting that the rate dependency effects are not directly accounted for in the modified Mohr-Coulomb constitutive model.

2.3 Material parameters

In all LDFE analyses the clay and sand behaviours are described by the modified Mohr-Coulomb constitutive model described in Section 2.2.

- Clay

The clay is assumed to be undrained and modelled using the Tresca material model which can be obtained by setting the modified Mohr-Coulomb model with $\varphi = \psi = 0$ and the value of cohesion, c, then represents the undrained shear strength s_u of the clay.

In Case 1 given in Table 1, the undrained shear strength is taken equal to 11 kPa.

In Case 2, the undrained shear strengths of the stiff and soft clay layers plotted in Fig. 3(a) is adopted from the T-bar test presented by Hossain & Randolph (2010a). In order to account for the effect of strain softening due to the soil gradually being remoulded as it flows around the spudcan and the effect of strain rate, Menzies & Roper (2008) and Randolph et al. (2008) suggested to reduce the intact undrained strength by about 15 % when computing vertical penetration resistance. Therefore, the values $c_0 = s_{u,intact}$, $c_f = 0.85 s_{u,intact}$ and $B_p = 0.001$ are used for the two clay layers in the CEL FE back-analysis of the centrifuge model test E2UU-II-T5 conducted by Hossain & Randolph (2010a).

In Case 3, the underlying kaolin clay was normally consolidated under the superfine silica sand overburden as well as soil self-weight. A number of penetration tests using miniature piezocone and ball were performed by Teh (2007) to evaluate the soil strength profile of the layered soils. In order to isolate the effect of dragged-down sand observed in the experimental tests in interpreting the strength parameter of the underlying clay, the shear strength profile can be conveniently described in the CEL FE back-analysis of the centrifuge model test Haft_SP2 (Teh, 2007) by the following relationship:

$$s_u = 17.3 + 1.2z \tag{3}$$

where z is the depth beneath the sand-clay interface (in meter). It can be seen in Fig. 3(b) that Eq (3) fits reasonably well to the experimental test results. It's worth noting that according to Hu & Randolph (1998), the typical values of the shear strength gradient for offshore soils generally lie in the range of 0.6-3.0 kPa/m, while the surface strengths may be as low as 10-20 kPa.

In all three cases the rigidity index G/s_u is taken as 150, where G is the shear modulus and s_u is the intact undrained shear strength. As an implication of undrained condition, a Poisson's ratio of 0.495 is used. This makes the material approximately incompressible.

Table 2 summarizes the clay parameters used in the CEL FE back-analyses.

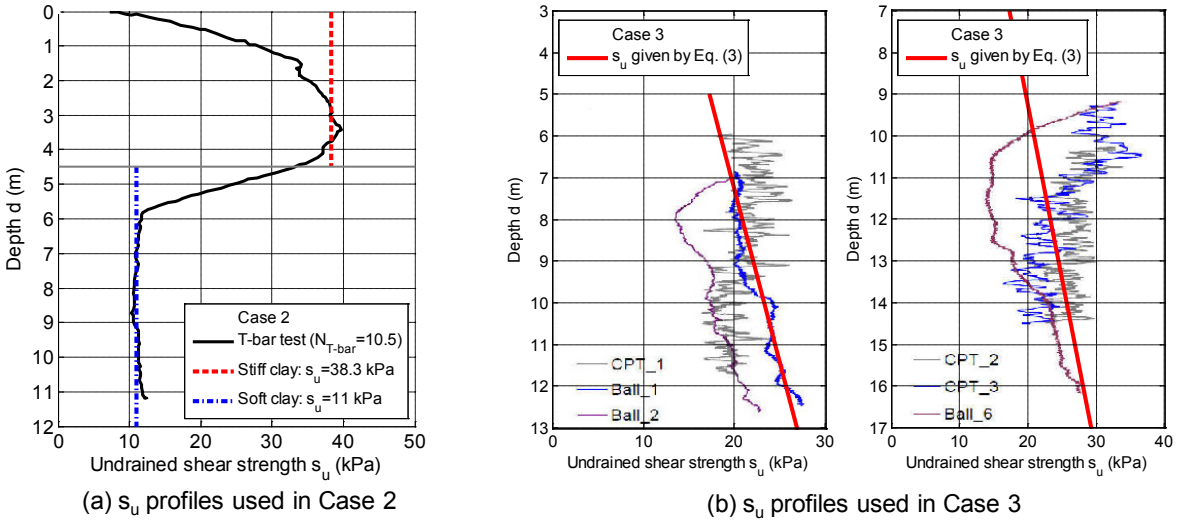

(a) s_u profiles used in Case 2 (b) s_u profiles used in Case 3

Fig. 3. (a) Typical undrained shear strength profiles s_u (a) from T-bar test reported by Hossain & Randolph (2009a) and (b) from miniature penetrometer test results reported by Teh (2007).

Table 2. Modified Mohr-Coulomb parameters of clay and sand materials used in LDFE analyses.

Case (see also Table 1)	Material	Friction angle (degree)		Dilatancy angle (degree)		B_p	Cohesion or undrained shear strength (kPa)		B_c
		φ_0	φ_f	ψ_0	ψ_f		c_0	c_f	
1	Soft clay						11		0
2	Stiff clay						38.3	$0.85*c_0$	0.001
	Soft clay						11	$0.85*c_0$	0.001
3	Dense sand	42.3	34	11	0	0.1	0.1		0
	Soft clay						$17.3+1.2z$	$0.85*c_0$	0.1

- Sand

In general practice, it is common to characterize the shear strength of sand by using the peak friction angle, φ_{peak}, and the critical state friction angle, φ_{cv}. Also, it is generally realized that φ_{peak} depends not only on the density but also on the stress path, including differences between plane strain and triaxial testing conditions. Assuming a unique critical state angle for both triaxial and plane strain Bolton (1986) proposed an empirical strength-dilatancy relationship in which the friction angle was computed as the sum of the critical state friction angle and a relative dilatancy index, I_R, which combined the influence of density, I_D, and the applied stress level:

$$\varphi_{peak} = \varphi_{cv} + mI_R \tag{4}$$

$$I_R = I_D\left(Q - \ln\left(p'\right)\right) - 1 \tag{5}$$

where Q (in kPa) is a material parameter depending on the grain crushing resistance and p' (in kPa) is the mean effective stress. The parameter m controls the amount of peak strength and dilatancy, and its values depend on the principal stresses orientation and mode of shearing (Randolph et al., 2004). Bolton suggested m = 3 for triaxial or general stresses and 5 for plane strain condition.

Bolton (1986, 1987) also limited the validity of Eq. (5) to $p' > 150$ kPa to avoid overestimation of dilatancy. In order to link the equations (4) and (5) with the bearing capacity analyses, the mean effect stress p' is approximately determined as follows:

$$p' = \lambda q_{peak} \tag{6}$$

where λ is a representative stress factor used to attenuate the peak penetration resistance, q_{peak}, down to a lower value which represents an appropriate mean stress within the failing soil.

Perkins (1995) found that the parameter λ lies between 0.1 and 0.25 for $30° < \varphi < 40°$. White et al. (2008) revealed that $\lambda = 0.15$ provided an excellent match with the data of the flat footing tests. This value is thus adopted for the sand layer in the LDFE analysis of Case 3 (see Table 2).

Based on experimental evidences, it states that the difference between the friction and dilatancy angles is constant, then any modification of the friction angle will affect the dilatancy angle. According to Bolton (1896), the peak dilatancy angle can be empirically related to the peak friction angle as follows:

$$\psi_{peak} = 1.25\left(\varphi_{peak} - \varphi_{cv}\right) \tag{7}$$

This type of relationship is called a flow rule. Note that the peak dilatancy angle decreases gradually and equals to zero as the soil reaches the critical state.

As reported in Teh's thesis (2007) the super fine silica sand used in the centrifuge model test Haft_SP2 has a density index I_D of 0.77 and a critical state friction angle φ_{cv} of 34^o. The material parameter Q shows minimal variation between different siliceous sands: $Q = 10 \pm 1$ kPa (Randolph et al., 2004). The most appropriate values $Q = 10$ kPa together with $m = 2.65$ are then adopted for the sand used in the CEL FE analysis of Case 3 given in Table 1.

The relative values of friction angle and dilatancy angle for the sand are chosen to be consistent with relationship (7) and the peak friction angle φ_{peak} is sought to match the peak resistance q_{peak} obtained from the centrifuge model test Haft_SP2 conducted by Teh (2007).

The sand behaviour is described by the modified Mohr-Coulomb constitutive model of which the parameters are detailed in Table 2. The strength reduction in the sand layer due to the effects of strain softening and strain rate is approximately taken into account by assigning $\varphi_f = \varphi_{cv} = 34^o$ and $B_p = 0.1$. To avoid numerical instability the cohesion of the sand was set as 0.1 kPa.

3 SPUDCAN FOUNDATION ON HOMOGENEOUS CLAY

This section presents the LDFE analysis of Case 1 given in Table 1. The spudcan foundation penetrating into the homogeneous clay is modelled using Abaqus/Explicit with the CEL method. The CEL FE-model and the soil parameters have been described in Section 2.1 and Section 2.3, respectively. The objective is to investigate the performance of the CEL FE-model in modelling of spudcan foundation response. The calculated bearing capacity results are compared to the centrifuges test results obtained by Hossain & Randolph (2009). Effect of penetration rate with respect to the bearing capacity is also studied.

The spudcan installation in soil with self-weight may cause back-flow above the spudcan at a relatively shallow depth, which affects the resulting penetration resistance. To account for the effect of back-flow the bearing capacity factors, N_c, are calculated as follows:

$$N_c = \frac{\gamma'\left(d + V_b/A\right) - q_u}{s_u} \qquad for\ d \le H_c$$
$$N_c = \frac{\gamma' V_b/A - q_u}{s_u} \qquad for\ d > H_c \tag{8}$$

where d is the penetration depth, H_c is the back-flow (or cavity) depth at which the soil starts to flow back in to the cavity. γ' is the effective unit weight of the soil. V_b is the volume of embedded spudcan (below the maximum diameter) and A is the spudcan largest cross-sectional area. q_u is the penetration resistance and s_u is the undrained shear strength at the current depth.

Fig. 4(a) plots the comparison between the calculated bearing capacity factor, N_c, and the centrifuge test data presented in the paper of Hossain & Randolph (2009). The penetration depth d is defined as zero from the level at which the maximum contact area of the spudcan is at the original soil surface. Both the results of smooth and rough soil-spudcan contacts are illustrated in this figure. The bearing capacity factor from the smooth contact is shown to agree well with the experimental data and the spudcan roughness has a significant effect on the calculated bearing responses. Thus, in all subsequent CEL FE analyses the contact between the soil and the spudcan foundation is modelled as smooth.

Fig. 4(a) also shows an excellent agreement between the depth of soil back-flow predicted by the CEL FE-model and those measured in the centrifuge tests.

In most real installation problems the rate of penetration is so slow that dynamic effects can be disregarded and the problem can be regarded as being static. Solving a static problem with Abaqus/Explicit requires choosing a penetration velocity that is artificial but which does not introduce inertia effects of significance for the solution. Fig. 4(b) compares the bearing capacity factors calculated with four different penetration rates of 1, 0.75, 0.5 and 0.25 m/s. It is observed that with the current FE discretisation the differences in N_c are minor (only about 2.6 % discrepancy between 1 m/s and 0.25 m/s). Hence the penetration rate of 1 m/s will be adopted in all further analyses.

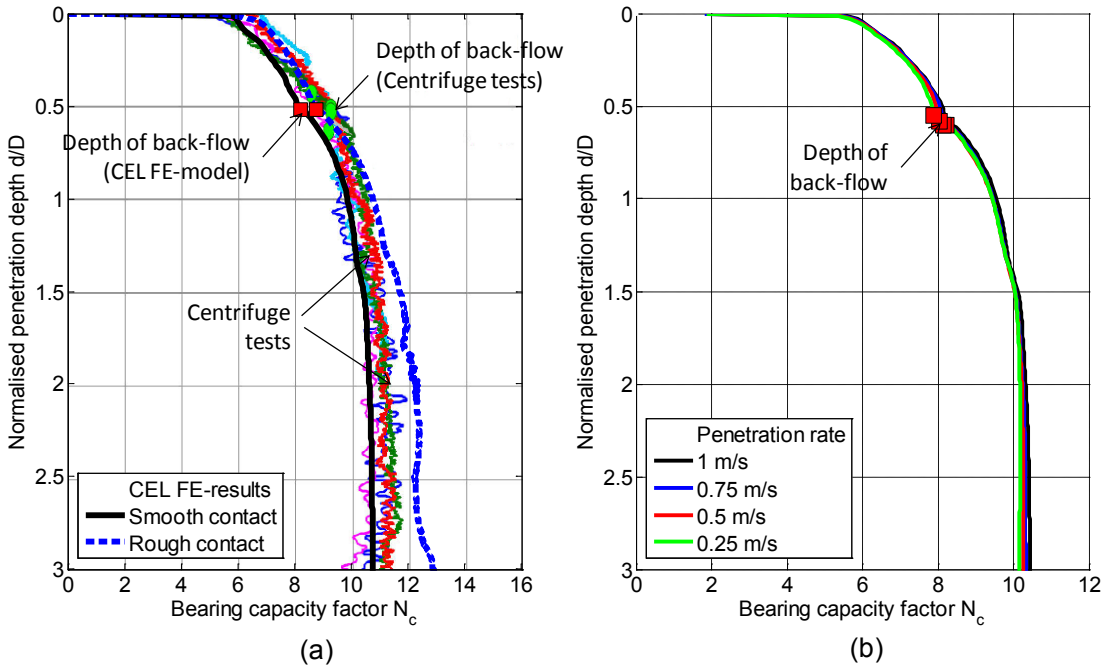

Fig. 4. Bearing capacity factors of spudcan foundation on homogeneous clay (Case 1 in Table 1)

4 SPUDCAN FOUNDATION ON STIFF CLAY OVERLYING SOFT CLAY

This section presents the LDFE back-analysis of the centrifuge test E2UU-II-T5 (Hossain and Randolph (2010a)) using the CEL method in Abaqus/Explicit. The study corresponds to Case 2 given in Table 1, in which the spudcan foundation is penetrated into stiff clay overlying soft clay. The CEL FE-model and the soil parameters have been described in Section 2.1 and Section 2.3, respectively.

Fig. 5(a) compares the numerically predicted bearing pressures against the centrifuge data. It can be seen from the figure that by taking into account the strength reduction due to the strain softening and strain rate effects the CEL FE-model predicts very well not only the magnitude of the punch-through load (peak load) but also the depth where the punch-through failure occurs (i.e. Stage A). Excellent agreement between the numerical and experimental spudcan responses is observed until the normalised depth d/D = 1. For penetration depth beyond d/D = 1 the two spudcan responses gradually diverge from each other. This mismatch could be explained by the fact that when the spudcan is displaced closer to the container base at 11.5 m (equivalent to d/D ≈ 1.92), the bottom boundary effects become more and more prominent. The bottom boundary in the CEL FE-model is, however, taken deep enough (d/D = 5) so that the spudcan response is not affected.

Fig. 5(b) to Fig. 5(f) compares the failure mechanisms observed from both the centrifuge test E2UU-II-T5 and the CEL FE-model during the penetration process. The velocity fields are presented at five different penetration stages: Stage A (d/D = 0.07), Stage B (d/D = 0.52), Stage C (d/D = 0.75), Stage D (d/D = 1.0) and Stage E (d/D = 1.6). Excellent agreement in terms of the flow mechanism including surface heave, soil displacements, and failure pattern can be observed at the first four stages.

- At Stage A (Fig. 5(b)): at this shallow penetration depth, a stiff clay wedge of truncated cone shape is formed from the edge of the spudcan base towards the interface between the two clay layers. Potential punching failure surfaces are observed and depicted by the black dash lines. This failure mechanism results in a significant reduction of the bearing capacity of the spudcan foundation as shown in Fig. (a).
- At Stage B (Fig. 5(c)): with this further penetration, the stiff clay wedge is gradually reformed in an inverted truncated cone and new inwards shear planes are observed in this upper stiff clay.
- At Stage C (Fig. 5(d)): when continuing to displace the spudcan deeper down until the spudcan base reaches the original stiff-soft clay interface, the stiff clay plug trapped beneath the spudcan continues to move down with the spudcan. The underlying soft clay is correspondingly forced to squeeze outward because of the inward sidewalls of the inverted truncated cone containing the stiff clay. The stiff clay wall above the spudcan edge is seen to remain standing thanks to its high cohesion. The bearing capacity reduces further at this stage as shown in Fig. 5(a).
- At Stage D (Fig. 5(e)): the cavity depth is now exceeding the thickness of the stiff top layer and the entire stiff clay plug is within the soft bottom layer. It can be seen that at this stage the CEL FE-model predicts a shallower depth of the trapped stiff clay than the experimental observation. Consistently with the difference in the failure predictions, the two bearing responses plotted in Fig. 5(a) also start to diverge.
- At Stage E (Fig. 5(f)): a complete deep penetration mechanism is revealed. Very good agreement in terms of the soil back-flow pattern and the cavity depth are observed from the CEL FE-model and the centrifuge data. It is also found from the figure that at this stage the numerical simulation predicts a localized deep failure mode while it is a more diffuse type of failure observed in the laboratory test. The difference of the failure modes can be attributed to the fact that since the penetration depth is very close

to the container base of the centrifuge test, the measurement results, especially beneath the spudcan base, are most likely affected by the boundary condition. The observation clarifies further the divergence of the two bearing pressure results obtained beyond Stage D as shown in Fig. 5(a).

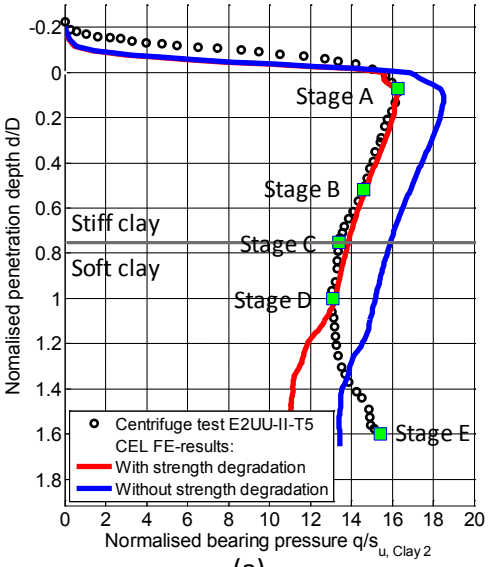

(a)

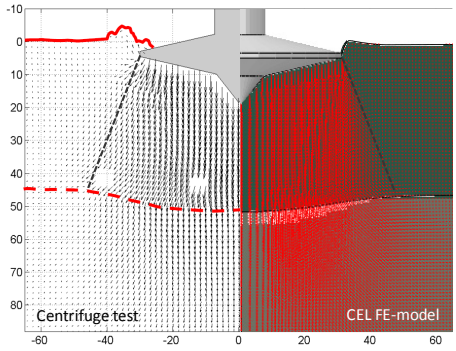

(b) Stage A (d/D = 0.07)

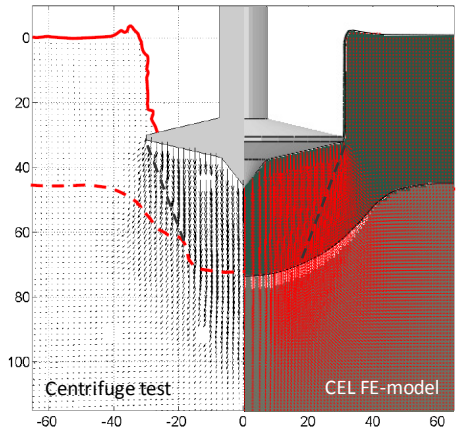

(c) Stage B (d/D = 0.52)

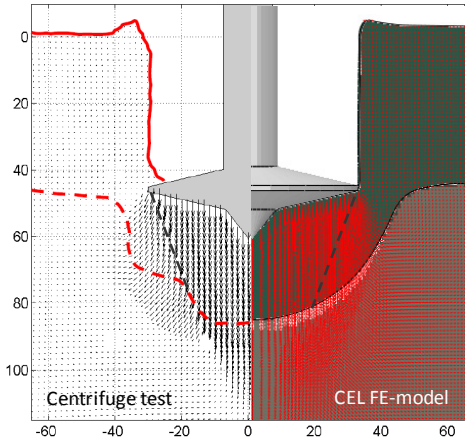

(d) Stage C (d/D = 0.75)

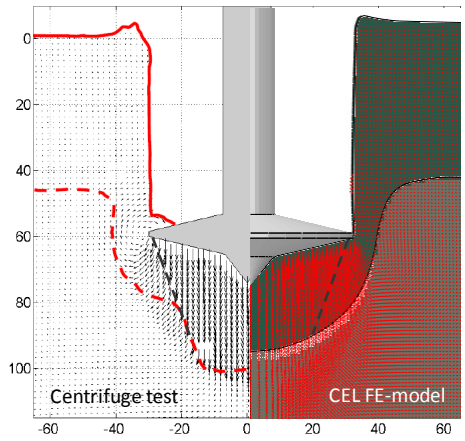

(e) Stage D (d/D = 1)

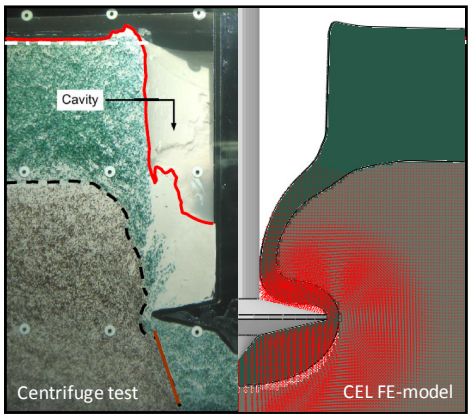

(f) Stage E (d/D = 1.6)

Fig. 5. Bearing capacity and failure mechanisms of spudcan foundation penetrating into stiff over soft clays. Comparison results between CEL FE-model and centrifuge model test E2UU-II-T5 (Case 2 in Table 1).

5 SPUDCAN FOUNDATION ON DENSE SAND OVERLYING SOFT CLAY

The section deals with the LDFE back-analysis of one of a series centrifuge tests of half spudcan penetrating into dense sand overlying relatively soft clay performed by Teh (2007). This study corresponds to Case 3 given in Table 1. The CEL FE-model and the soil parameters have been described in Section 2.1 and Section 2.3, respectively.

The comparison of the bearing response predicted by the CEL FE-model and the centrifuge model test is illustrated in Fig. 6(a). It is clearly observed that for both cases of with and without strength reduction the CEL FE-model predicts very well the maximum bearing capacity (Stage A) obtained from the centrifuge data. However, only by accounting for the strength reduction due to the strain softening and strain rate effects that the CEL FE-model can capture reasonably well the post-peak penetration resistance of the spudcan foundation measured in the centrifuge test.

Fig. 6(b) to Fig. 6(f) compare the failure mechanisms observed from the centrifuge test Half_SP2 and the CEL FE-model during the penetration process. The velocity fields are plotted at five penetration stages: Stage A (d/D = 0.07), Stage B (d/D = 0.31), Stage C (d/D = 0.43), Stage D (d/D = 0.84) and Stage E (d/D = 1.08). Excellent agreement in terms of the flow mechanism including surface heave, soil displacements, and failure pattern can be observed at the first four stages.

- At Stage A (Fig. 6(b)): both the CEL FE-model and the centrifuge test predict the same value of the maximum penetration resistance. It can be seen from the figure that a soil wedge of truncated cone shape is formed in the sand layer. The potential punching failure surfaces are approximately trumpet-shaped as also observed from the current centrifuge test.
- At Stage B (Fig. 6(c)): the soil starts to flow back at a penetration depth of d/D ≈ 0.25. With further penetration the outwards inclination of the shear surfaces are gradually reduced to the vertical shear plane. This indicates that the dilatancy angle of the sand layer continues to reduce with strains during the penetration process until it vanishes. This failure mechanism is observed in both the CEL FE-model and the centrifuge test.
- At Stage C (Fig. 6(d)): as the penetration continues, a soil plug with the shape of an inverted truncated cone is formed in the dense sand. Fig. 6(d) shows a very good agreement between the numerical and experimental predictions.
- At Stage D (Fig. 6(e)): the spudcan becomes fully embedded and the spudcan base starts to penetrate through the original level of the sand-clay interface. It is observed in both the numerical and experimental results that the sand plug sidewall is reformed in nearly vertical direction and is extended from the spudcan edge down to the deeper and stronger clay. A potential flow-around type of failure is also observed in the underlying clay layer and around the sand plug, which indicates a transition to a deep failure mechanism.
- At Stage E (Fig. 6(f)): the sand plug trapped beneath the spudcan continues to be forced down and tends to separate from the upper sand part at the spudcan edge. A deep failure mechanism has clearly developed. It can be seen that the depth of stable cavity above the spudcan is almost identical between the CEL FE-model and the centrifuge model test. However, the height of the sand plug (about 3.7 m) predicted by the numerical model is smaller than the measured value (about 5.0 m) in the centrifuge test. This discrepancy can be attributed to the boundary effect from the container base of the centrifuge test, which has also observed in Case 2.

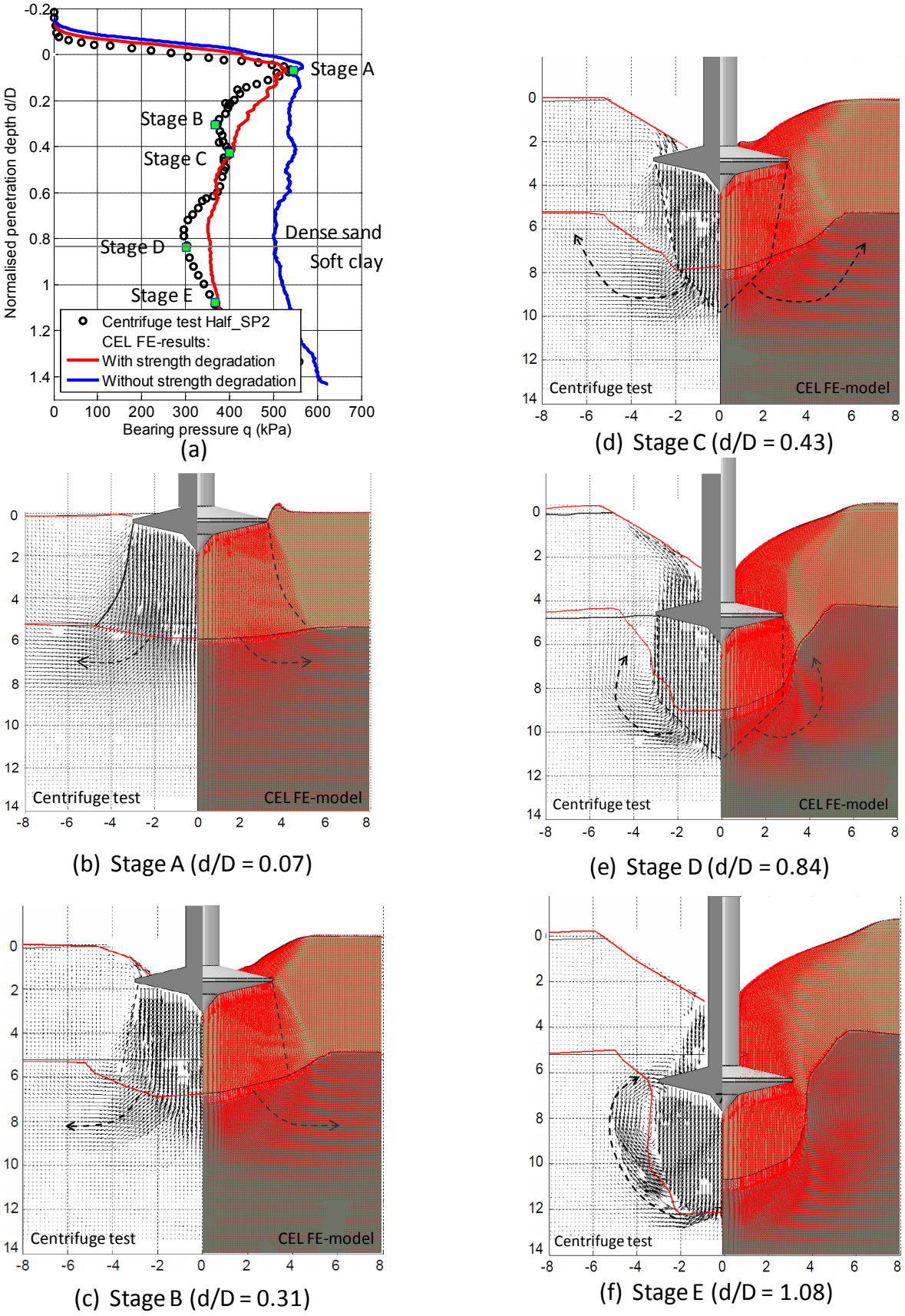

Fig. 6. Bearing capacity and failure mechanisms of spudcan foundation penetrating into dense sand over soft clay. Comparison results between CEL FE-model and centrifuge model test Half_SP2 (Case 3 in Table 1).

The development of the shear band in the sand layer during the penetration process can be investigated by plotting the incremental equivalent plastic strain $\Delta\varepsilon_{eq}^{p}$. Fig. 7 presents the shading plot of $\Delta\varepsilon_{eq}^{p}$ at the same five penetration stages, i.e. from Stage A to Stage E. It can be observed from the figure that at Stage A (peak resistance) a curved shear band is initially formed in the sand layer, starting from the spudcan edge down to the surface of the clay layer. It looks close to the failure surface assumed by the projected area method (Terzaghi & Peck, 1948). The curved shape may be due to the strain softening behaviour of the sand layer. This means due to larger plastic strains in the sand near to the spudcan the dilatancy angle is reduced and the failure surface tends to be more vertical, whereas the lower portions of the failure surface is more inclined due to lower plastic strains at the bottom, and hence large dilatancy angle. With further penetration (Stage B), a second shear band is gradually developed in the vertical direction. When continuing to penetration the spudcan foundation deeper down in the soil until Stages C the curved shear band merges into the vertical shear band. At the last two penetration stages (Stages D and E), the shear band angle in the upper side of the spudcan becomes align with the one beneath its base and a deep failure mechanism is observed.

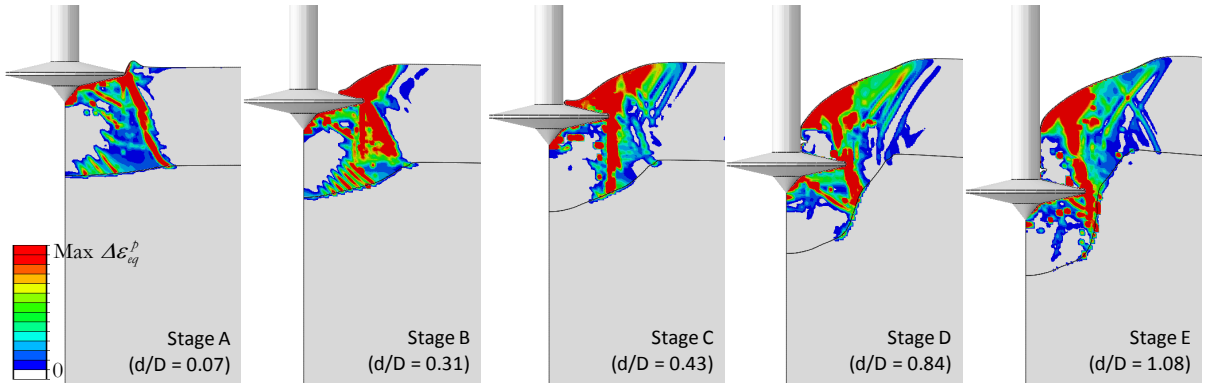

Fig. 7. Numerical prediction of development of shear bands in sand layer during penetration of spudcan foundation into dense sand overlying soft clay (Case 3 in Table 1).

6 CONCLUSIONS

This paper has investigated the capability of the large deformation finite element (LDFE) in modelling of the penetration process of spudcan foundations on layered soils, where a strong soil overlies a weak soil. The Coupled Eulerian-Lagrangian (CEL) method available in Abaqus/Explicit was employed. In order to capture the effects of strain rate and strain softening on the penetration resistance the Mohr-Coulomb constitutive model was modified by introducing a hyperbolic evolution of the friction angle and the cohesion as a function of the equivalent plastic shear strain. Using the CEL method together with the modified Mohr-Coulomb model makes it possible to successfully back-analyze the two centrifuge tests of a spudcan foundation penetrating into stiff clay overlying soft clay (Hossain & Randolph, 2010a) and dense sand overlying soft clay (Teh, 2007). Through the comparison results it was found that except for some later stages in the centrifuge test where the measured results were most likely affected by the container base boundary, the numerical predictions were in excellent agreement with the experimental data. In fact, the CEL 3D FE-model was able to not only calculate the spudcan foundation resistance but also predict and capture well the punch-through failure and the failure mechanisms experimentally observed during the penetration process.

ACKNOWLEDGEMENT

The research has been performed as a part of "GEO-INSTALL" (Modelling Installation Effects in Geotechnical Engineering) project. The work is partially funded by the European Community through the program "Marie Curie Industry-Academia Partnership and Pathways", under Contract No PIAP-GA-2009-230638 and partially supported by the Norwegian Research Council. The author would like to gratefully acknowledge all these supports.

REFERENCES

Andresen, L. & Khoa, H.D.V. (2013), "LDFE analysis of installation effects for offshore anchors and foundations", Proceeding of the International Conference on Installation Effects in Geotechnical Engineering, Rotterdam, 162-168.

Barnichon, J.D. (1998), "Finite element modelling in structural and petroleum geology", Ph.D thesis, University of Liège.

Bolton, M. (1986), "The strength and dilatancy of sands". Géotechnique, Vol. 36(1), 65-78.

Bolton, M. (1987), "The strength and dilatancy of sands: Discussion". Géotechnique, Vol. 37(2), 219-226.

Brown, J.D. & Meyerhof, G.G. (1969), "Experimental study of bearing capacity in layer clays", Proceedings 7th International Conference on Soil Mechanics and Foundation Engineering, Mexico, Vol. 2, 45-51.

Chen, W.F. & Davidson, H. L. (1973), "Bearing capacity determination by limit analysis". J. Soil Mech. and Found. Div., 99(SM6), 433-449.

Craig, W.H. & Chua, K. (1990), "Deep penetration of spud-can foundation on sand and clay". Géotechnique, Vol. 40(4), 541-556.

Edwards, D. & Potts, D. (2004), "The bearing capacity of a footing under "punch-through" failure", Proceedings 9th International Conference on Numerical Modelling in Geomechanics, Ottawa, Canada.

Florkiewicz, A. (1989), "Upper bound to bearing capacity of layered soils". Canadian Geotechnical Journal, Vol. 26, 730-736.

Griffiths, D.V. (1982), "Computation of bearing capacity on layered soils", Proceedings 4th International Conference on Numerical Methods in Geomechanics, Edmonton, Vol. 1, 163-170.

Hossain, M.S. & Randolph, M.F. (2009), "New mechanism-based design approach for spudcan foundations on single layer clay". J. Geotech. Geoenviron. Eng., Vol. 135(9), 1264-1274.

Hossain, M.S. & Randolph, M.F. (2010a), "Deep-penetrating spudcan foundations on layered clays: Centrifuge tests". Géotechnique. Vol. 60(3), 157-170.

Hossain, M.S. & Randolph, M.F. (2010b). "Deep-penetrating spudcan foundations on layered clays: Numerical analysis". Géotechnique, Vol. 60(3), 171-184.

Hu, Y., Randolph, M.F. (1998), "H-adaptive FE analysis of elasto-plastic nonhomogeneous soil with large deformation". Comput. Geotech. Vol. 23, 61-83.

Lee, K.K. (2009), "Investigation of potential spudcan punch-through failure on sand overlying clay soils", PhD thesis, The University of Western Australia, Perth.

McClelland, B., Young, A.G. & Remmes, B.D. (1981), "Avoiding jack-up rig foundation failures", Proc. Int. Symp. Geotechnical Aspects of Coastal and Offshore Structures, Bangkok.

Menzies, D., & Roper, R. (2008). "Comparison of jackup rig spudcan penetration methods in clay", Proc., Offshore Technology Conf., Houston.

Merifield, R.S., Sloan, S.W. & Yu, H.S. (1999), "Rigorous plasticity solutions for the bearing capacity of two-layered clays". Géotechnique, Vol. 49(4), 471-490.
Meyerhof, G.G. & Hanna, A.M. (1978), "Ultimate bearing capacity of foundations on layered soils under inclined load". Can. Geotech. J, Vol. 15, 565-572.
Michalowski, R. L., & Shi, L. (1995), "Bearing capacity of footings over two-layer foundation soils". J. Geotech. Eng., Vol. 121(5), 421-428.
Osbourne, J.J. (2005), "Are we good or are we lucky? Managing the mudline risk", Presentation slides for OGP/CORE Workshop: The jack-up drilling option-Ingredient for success, Singapore.
Okamura, M., Takemura, J., & Kimura, T. (1998), "Bearing capacity predictions of sand overlying clay based on limit equilibrium methods". Soils and Foundations, Vol. 38(1), 181-194.
Perkins, S.W. (1995), "Bearing capacity of highly frictional material". Geotech. Testing J., Vol. 18(4), 450-462.
Qiu, G. & Grabe, J. (2012), "Numerical investigation of bearing capacity due to spudcan penetration in sand overlying clay". Can. Geotech. J., Vol. 49, 1393-407.
Qiu, G. & Henke, S. (2011), "Controlled installation of spudcan foundations on loose sand overlying weak clay". Marine Structures, Vol. 24(4), 528-550.
Randolph, M. F., Jamiolkowski, M. B. & Zdravkovic, L. (2004), "Load carrying capacity of foundations", Proceedings of the Skempton Memorial Conference, London, Vol. 1, 207-240.
Randolph, M.F., Wang, D., Zhou, H., Hossain, M.S., & Hu, Y. (2008), "Large deformation finite element analysis for offshore applications", Proc., 12th Int. Conf. of Int. Association for Computer Methods and Advances in Geomechanics, India, 3307-3318.
Reddy, A.S. & Srinivasan, R.J. (1967), "Bearing capacity of footings on layered clays", Journal of Soil Mechanics and Foundations Division, ASCE, Vol. 93(2), 83-99.
Shiau, J.S., Lyamin, A.V. & Sloan, S.W. (2003), "Bearing capacity of a sand layer on clay by finite element limit analysis". Can. Geotech. J., Vol. 40, 900-915.
SNAME (2002), "Guidelines for Site Specific Assessment of Mobile Jack-Up Units", Technical & Research Bulletin 5-5A, Rev. 2, January 2002.
Szypcio, Z. & K. Dołżyk (2006), "The bearing capacity of layered subsoil", Studia Geotechnica et Mechanica, Vol. XXVIII(1), 45-60.
Teh, K.L. (2007), "Punch-through of spudcan foundation in sand overlying clay", Ph.D thesis, National University of Singapore.
Teh, K.L, Leung, C.F., Chow, Y.K & Cassidy, M.J. (2010), "Centrifuge model study of spudcan penetration in sand overlying clay". Géotechnique, Vol. 60(11), 825-842.
Tho, K., Leung, C.F., Chow, Y.K. & Swaddiwudhipong, S. (2012), "Eulerian finite element technique for analysis of jack-up spudcan penetration". Int. J. Geomech. Vol. 12(1), 64-73.
Terzaghi, K. & Peck, R.B. (1948), "Soil Mechanics in engineering practice", John Wiley and Sons, New York.
Wang, C. X., & Carter, J. P. (2002), "Deep penetration of strip and circular footings into layered clays". Int. J. Geomech., Vol. 2(2), 205-232.
White, D.J., Teh, K.L., Leung, C.F. & Chow, Y.K. (2008), "A comparison of the bearing capacity of flat and conical circular foundations on sand". Géotechnique, Vol. 58(10), 781-792.
Yu, L., Hu, Y., Liu, J., Randolph, M.F. & Kong, X. (2012), "Numerical study of spudcan penetration in loose sand overlying clay". Computers and Geotechnics Vol. 46, 1-12.

LOAD BEARING BEHAVIOR OF BUCKET FOUNDATIONS IN SAND

M. Achmus
Institute for Geotechnical Engineering, Leibniz University Hannover, Hannover, Germany

K. Thieken
Institute for Geotechnical Engineering, Leibniz University Hannover, Hannover, Germany

C.T. Akdag
Dokuz Eylül University, Torbali Vocational School of Higher Education, Izmir, Turkey

C. Schröder
Institute for Geotechnical Engineering, Leibniz University Hannover, Hannover, Germany

C. Spohn
Institute for Geotechnical Engineering, Leibniz University Hannover, Hannover, Germany

ABSTRACT: *The suction bucket foundation is a relatively new concept for the foundation of offshore wind energy converters. If only one bucket is installed (monopod), the structure is loaded by large horizontal forces and overturning moments. Besides the failure load and the initial stiffness, also the accumulation of head rotations of the foundation structure under cyclic loads has to be considered in the design. The behavior of buckets in sand under monotonic and cyclic horizontal loading is investigated in the paper by means of 3D finite element simulations. An elasto-plastic material law with stress-dependent stiffness approach is used herein. To investigate the behavior of a bucket under cyclic loading, a special numerical scheme originally developed for pile foundations (stiffness degradation method) is applied to the bucket system. The results of a parametric study show that the rate of accumulation of the bucket lid rotation depends on the relative skirt length of the bucket, on the relative density of the sand and also to a certain extent on the load level, i.e. the relative magnitude of the applied load.*

1 INTRODUCTION

In order to increase the portion of renewable energy in the total energy supply, a vast number of offshore wind energy converters (OWECs) shall be installed in the next decades in the North Sea and the Baltic Sea in Europe. The challenge for geotechnical engineers is to develop optimum foundation solutions for such structures. Experiences from offshore structures for the oil and gas industry cannot be used in every respect, since the loading conditions of OWECs significantly differ from such structures. Vertical loads are much smaller, which means that the horizontal loads due to wind and waves have greater impact on the design. Wind and wave loads are intensively cyclic. Therefore, the behavior of the foundation under cyclic loads is a very important issue in the design of OWECs. German regulations require an explicit calculation of accumulated displacements induced by the cyclic loads.

The suction bucket foundation is a relatively novel design concept for OWECs which seems to be favorable due to its potential cost-effectiveness and its advantages regarding environmental issues. A bucket structure consists of a steel cylinder with diameter D, skirt length L and skirt thickness t_s, closed by a generally heavily stiffened upper steel lid. A general view of a typical OWEC with a monopod bucket foundation – as considered in this paper – is shown in Figure 1.

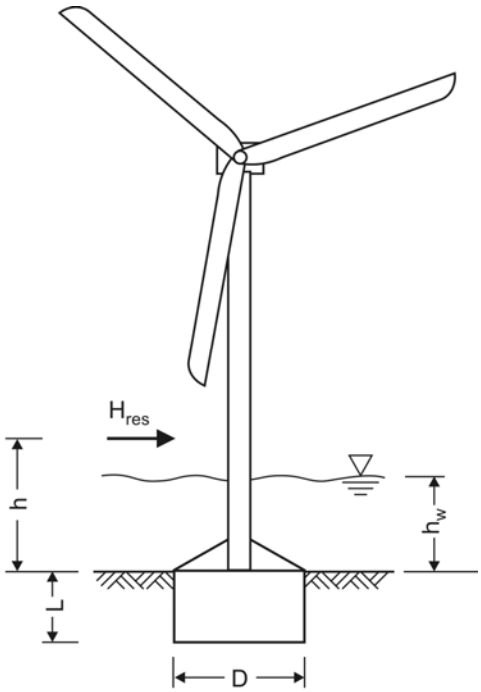

Fig. 1. Schematic sketch of an offshore wind energy converter with a monopod suction bucket foundation

Byrne (2000) and Feld (2001) first investigated the application of buckets as wind energy foundations, while Byrne & Houlsby (2003) as well as Ibsen et al. (2005) presented status reports on that topic. They denoted that there is a considerable uncertainty of the performance of suction bucket foundations for offshore wind farms under combined vertical and horizontal loading conditions. A few laboratory model tests (Villalobos et al., 2005 & 2009), field tests (Houlsby & Byrne 2000, Houlsby et al. 2005) and numerical analysis based studies (Abdel-Rahman & Achmus 2005) were performed to predict the loading response and the loading capacity of suction bucket foundations in sand.

Villalobos et al. (2009) carried out small-scale experiments on model buckets with L/D-ratios of 0.5 and 1.0 in loose dry sand. General loading conditions were examined, including also tensile vertical loads. Villalobos et al. defined a yield point from the load-deformation curves and derived moment-horizontal load interaction diagrams for this yield state. Villalobos et al. (2005) also presented model scale tests with buckets in dense, saturated sand under moment loading. One focus of the investigation was the effect of the installation process on the bucket behavior. It was found that installation by suction leads to considerably smaller capacities than installation by pushing.

Abdel-Rahman & Achmus (2005) presented results of numerical simulations regarding bucket foundations in medium dense sand. Load-deformation curves of bucket foundations under monotonic horizontal loading were calculated for two different bucket geometries and were compared with load-deformation curves of monopile foundations. For the considered systems, it was found that the suction buckets behaved stiffer than the monopiles under small loads but had smaller ultimate capacities. Zhang et al. (2010) investigated the load capacity of bucket foundations and developed an upper bound limit method for prediction. Using centrifuge tests for comparison, they showed that for the cases considered the method is capable of reasonably estimating the load capacity.

Although the behavior and ultimate capacity of suction bucket foundations in cohesionless soil for offshore wind energy systems has been studied as mentioned above, there are no design recommendations or guidelines available. Moreover, no investigations exist regarding the behavior of monopod buckets under cyclic horizontal loading.

In this paper, the finite element method (FEM) is used to investigate the bearing behavior of monopod buckets in sand under drained cyclic loading. Herein, a special calculation procedure originally developed for monopiles (Achmus et al. 2008 & 2009) is applied.

2 NUMERICAL MODELING

2.1 Finite Element Model

In this study, a three-dimensional finite element (FE) model of a monopod bucket foundation system was developed and utilized in the scope of a parametric study. The finite element program Abaqus Version (6.12) (Abaqus 2012) was used in the simulations. Considering the symmetry of both geometrical and loading conditions, only one half of the bucket foundation was modeled in order to reduce computational effort. Eight-node volume C3D8-elements were used to mesh both the bucket structure and the soil. Preliminary analyses were carried out for the determination of mesh fineness and model dimensions in order to reach sufficient accuracy of the results and avoid the influence of boundary conditions. Consequently, a soil model diameter of 6.67 times of the bucket diameter and a depth of the soil under the bucket of two times the bucket skirt length was chosen. An exemplary mesh of the finite element model with geometrical properties is presented in Figure 2.

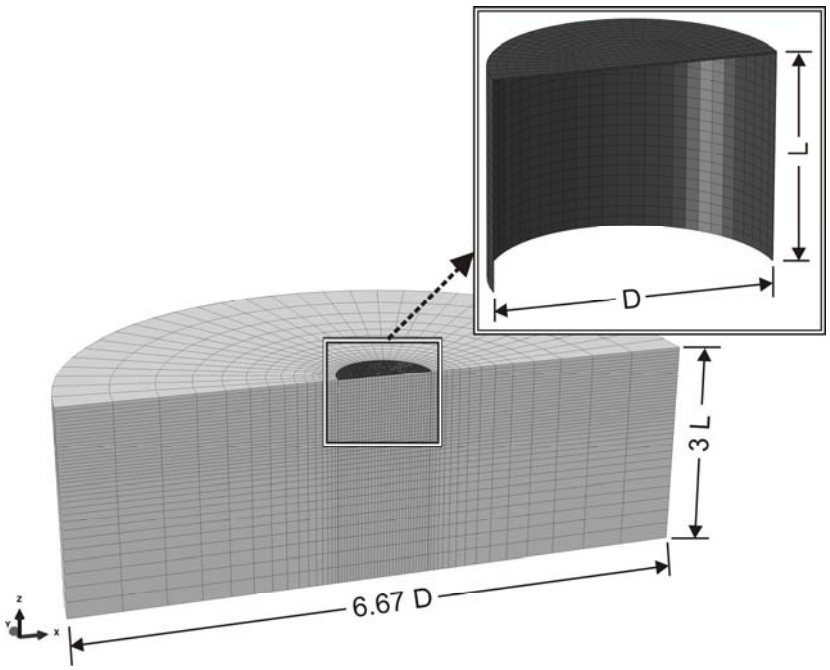

Fig. 2. Finite element model of a suction bucket foundation system

Displacements were fixed at the model boundaries as follows: in all directions at the bottom, in both horizontal directions on the periphery and in normal direction on the symmetry plane. Since relatively large deflections can occur during lateral loading, geometric non-linearity was considered, i.e. the coordinates of the element nodes were corrected during the loading steps with respect to the current deformations.

An elasto-plastic material law using Mohr-Coulomb failure criterion was utilized for the simulation of soil behavior. The stress-dependent oedometric modulus of elasticity, E_s, was implemented in order to simulate the non-linear soil response accurately (Equation 1):

$$E_S = \kappa \cdot \sigma_{at} \cdot \left(\frac{\sigma_m}{\sigma_{at}} \right)^{\lambda} \quad (1)$$

Here σ_{at} =100 kN/m^2 is reference stress; κ determines the soil stiffness at the reference stress state; λ rules the stress dependency of the soil stiffness and σ_m is the mean principal stress. Soil parameters for very dense and medium dense sand used in the numerical simulations are given in Table 1.

Table 1. Soil parameters used for very dense and medium dense sand

	Sand, very dense	*Sand, medium dense*
Buoyant unit weight γ'	11.0 kN/m³	9.0 kN/m³
Oedometric stiffness parameter κ	600	400
Oedometric stiffness parameter λ	0.55	0.60
Poisson´s ratio ν	0.25	0.25
Internal friction angle φ'	40.0°	35.0°
Dilation angle ψ	10.0°	5.0°
Cohesion c‘	0.1 kN/m^2	0.1 kN/m^2
Cyclic parameter b_1	0.12	0.12
Cyclic parameter b_2	0.32	0.32

This material law was also used for investigations on the behavior of monopiles (Achmus et al. 2009, Achmus & Thieken 2010), which showed its capability to realistically simulate the system behavior under monotonic loading.

In the modeling of the steel bucket, a skirt thickness of t_s= 0.03 m was considered. The steel material properties E = 210 GPa, ν = 0.2 were applied, where E and ν represent the modulus of elasticity and Poisson's ratio of steel material, respectively. The steel buoyant unit weight was set to γ'= 68 kN/m^3.

A thickness of t_L = 0.10 m and a very large modulus of elasticity ($E = 1 \cdot 10^9$ GPa) was applied to the lid in order to consider almost rigid behavior and additional dead weight (approximately 50% of the bucket's dead weight) due to stiffeners usually placed on the upper side connecting the bucket to the steel tower (see also Figure 1).

The FEM analyses were conducted in several calculation steps. In the initial step, geostatic stresses in the model consisting of soil elements only were calculated by application of gravity loading. Here a coefficient of earth pressure at rest, k_0 = 1-sin φ', was used. Subsequently, the predefined elements defining the bucket geometry were replaced by steel elements modeling the bucket structure. Interaction between the bucket surfaces and soil were activated using a "master-slave" modeling concept. Contact surfaces were defined with the contact friction angle, δ, considered as two thirds of the internal friction angle, φ', in the interaction properties. In the following steps, first the vertical load was applied on the bucket lid. Then, horizontal load (H) and bending moment (M) were applied simultaneously until the desired loading stage was reached. The bending moment can also be defined by an eccentricity (h) of the horizontal load with respect to the level of the lid bottom surface. In all calculations presented here, an eccentricity of h = 20 m, which lies inside a typical range for extreme wave load eccentricities, was considered. Furthermore, a typical vertical load of V = 10 MN for a large (e.g. 5 MW) wind turbine tower was applied in all calculations.

Actually, the relative density and the stresses in the soil in the vicinity of the bucket skirt are affected by the installation process consisting of suction-assisted penetration subsequent to self-weight penetration. However, it was assumed that these installation effects are of

minor importance regarding the general bucket performance under horizontal and moment loading, and therefore a "wished-in-place" procedure as described above was used in the simulation.

2.2 Procedure to account for cyclic loading

To investigate the deformation response of a foundation structure under cyclic loading, a method was originally developed for monopile foundations which yields the permanent displacements of a pile-soil system by numerical calculations, taking the behavior of soils under cyclic loading investigated in cyclic triaxial tests into account (Achmus et al. 2009, Kuo 2008). This method is based on the finite element model presented above and accounts for cyclic loading by a special stiffness degradation approach.

A sketch of principles of the results of a stress-controlled cyclic triaxial test under drained conditions is shown in Figure 3. The plastic portion of the axial strain ε_p^a increases with the number of load cycles. The increase rate of the plastic strain is mainly dependent on the initial stress state (confining stress) and on the magnitude of the cyclic load portion.

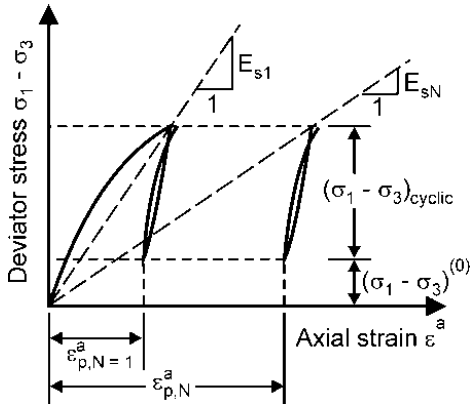

Fig. 3. Principle results of a cyclic triaxial test

The strain increase can be interpreted as a decrease in the secant stiffness modulus. When the elastic strain is negligible, the degradation of the secant modulus E_{sN} can be formulated in the following way dependent on the plastic strain in the first cycle $\varepsilon_{p,N=1}^a$ and in the N^{th} cycle $\varepsilon_{p,N}^a$:

$$\frac{E_{sN}}{E_{s1}} \cong \frac{\varepsilon_{p,N=1}^a}{\varepsilon_{p,N}^a} \tag{2}$$

The degradation of secant stiffness in a cyclic triaxial test with isotropic initial stress condition can be determined from the plastic strains measured with a regression equation. Due to an approach of Huurman (1996) used here, the increase in deformation or the decrease in stiffness, respectively, can be described by the following equation:

$$\frac{E_{sN}}{E_{s1}} = \frac{\varepsilon_{p,N=1}^a}{\varepsilon_{p,N}^a} = N^{-b_1(X)^{b_2}} \tag{3}$$

Here N is the number of cycles, X is a stress-dependent variable (cyclic stress ratio), and b_1, b_2 are regression parameters to be determined in cyclic triaxial tests. The cyclic stress ratio is defined as

$$X = \frac{\sigma_{1,cyclic}}{\sigma_{1,f}} \tag{4}$$

wherein $\sigma_{1,f}$ is the main principal stress at failure in a monotonic test (which is dependent on confining stress σ_3). Thus, the stress ratio is dependent on the initial stress state and on the cyclic load level.

A problem to be dealt with is that the Equations (3) and (4) are valid for triaxial test conditions with isotropic initial stress conditions and a constant confining pressure σ_3 during cyclic loading. In the soil-structure system, the initial stress conditions (before application of the horizontal load) are anisotropic and the minor principal stress in the elements as well as the directions of the principal stress axes in general change with the application of the load. To overcome this problem, a characteristic cyclic stress ratio X_c is defined here as

$$X_C = \frac{X^{(1)} - X^{(0)}}{1 - X^{(0)}} \tag{5}$$

Here the index $^{(1)}$ indicates the cyclic stress ratio at loading phase and the index $^{(0)}$ at unloading phase. At the initial (and unloading) phase, only the vertical load V due to the structure's weight is considered, and the lateral load H is applied subsequently in the loading phase. The characteristic cyclic stress ratio is derived from the difference between the stress ratios in the loading and the unloading phase. The accumulation of plastic strain and the degradation of stiffness of the soil element can be obtained from Equation (3) by replacing X by X_c.

It is possible either to repeat the calculation with the adapted stiffnesses or just to add calculation phases in which the stiffnesses of the elements are reduced. The first method is the more rigorous one. However, in the present paper the latter method was applied, since otherwise convergence problems occurred. These problems are induced by a tendency of back-rotation due to the vertical load of the bucket when the stiffnesses are adapted before the horizontal load is applied. Such an effect does not occur when piles are considered.

The described procedure is termed the "stiffness degradation method" (SDM). It is of course, from a theoretical point of view, a rather simple "engineering" approach to deal with cyclic loading effects. The method was proved capable, however, to predict the behavior of monopiles under one-way loading in a reasonable manner (Achmus et al. 2009, Achmus et al. 2010).

3 SIMULATION RESULTS

3.1 Behavior under monotonic loading

After application of the vertical load (V = 10 MN), horizontal load (H) and bending moment (M with h = M/H = 20 m) were applied simultaneously and increased gradually until the ultimate load capacity of the foundation system was reached.

For determination of ultimate load, the horizontal deflection of a rigid lever arm with the height h = 20 m was increased gradually, and the corresponding horizontal force was recorded. This means that a deformation-controlled loading was carried out to obtain the failure load of the system.

Figure 4 shows exemplary load-rotation curves for a bucket with a diameter D = 12 m and a skirt length L = 9 m, i.e. L/D = 0.75. The rotation of the bucket was derived from the difference of the vertical displacements of the bucket lid edges. The ultimate capacity H_u is 6.68 MN for medium dense sand and 11.76 MN for very dense sand.

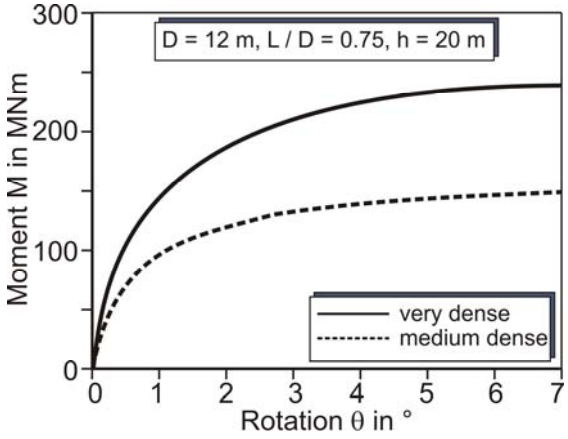

Fig. 4. Load-rotation curves for monotonic loading (D = 12 m, L/D = 0.75, h = 20 m)

In the simulations, the bucket diameter *D* was varied between 8 m and 20 m, and for each case skirt length-to-diameter ratios *L/D* of 0.5, 0.75 and 1.0 were considered. In total 24 calculations have been carried out. The ultimate capacities obtained are presented in Table 2.

It should be mentioned that in some simulations the ultimate capacity, i.e. a horizontal tangent in the load-rotation curve, could not be reached due to numerical instabilities. In such cases, an extrapolation of the load-displacement curve based on the hyperbolic method (Manoliu et al. 1985) originally derived for piles was carried out. In that, a correction factor of 0.92 on the capacity obtained from the original hyperbolic method proved to give reasonable results.

Table 2. Ultimate capacities of monopod buckets in sand (h = 20 m)

Diameter *D* in m	Skirt length *L* in m	*L/D*	Ultimate capacity H_u in MN	
			Very dense Sand	Medium dense sand
8	4	0.5	2.38	1.76
	6	0.75	3.85	2.50
	8	1.0	6.12	3.80
12	6	0.5	6.00	4.13
	9	0.75	11.76	7.37
	12	1.0	23.59	12.86
16	8	0.5	12.84	8.78
	12	0.75	29.09	17.79
	16	1.0	61.33	32.86
20	10	0.5	25.01	16.31
	15	0.75	60.50	35.19
	20	1.0	131.43	65.71

3.2 Behavior under cyclic loading

In all calculations with the stiffness degradation method the regression parameters were set to $b_1 = 0.12$ and $b_2 = 0.32$ independent of relative density (see Table 1). These parameters

were derived by Albiker & Achmus (2012) based on back-calculations of model tests with piles in sand.

In order to investigate the effect of the cyclic load amplitude on the bearing behavior, three different load levels were considered. Horizontal forces with a magnitude of 25%, 40% and 55% of the ultimate capacity of the considered system were applied, i.e. H/H_u = 0.25/ 0.40/ 0.55.

The results for the bucket lid rotation are shown in Figure 5, once in absolute values (left) and once as relative increase with respect to the static rotation (right). The dependence between rotation after N cycles θ_N and the static rotation θ_1 can be approximated by the following function:

$$\theta_N = \theta_1 N^m \tag{6}$$

Using this equation, the result of the SDM calculations for a system can be described only by the power m. m characterizes the behavior of the system under drained cyclic one-way loading and is termed here the cyclic accumulation parameter.

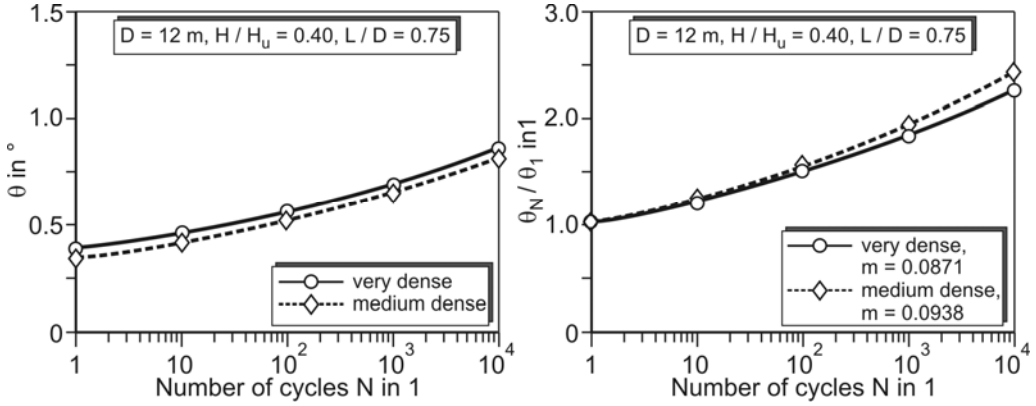

Fig. 5. Cyclic performance curves for buckets in sand (D = 12 m, L/D = 0.75, H/Hu = 0.40, h = 20 m)

For the example system with D = 12 m, L/D = 0.75 and H/H_u = 0.40 Figure 5 shows the effect of the sand's relative density on the accumulation parameter. For very dense sand a slightly greater static rotation (under equal relative load level) is obtained. The relative accumulation with respect to the static rotation, however, is slightly lower than for medium dense sand and yields therefore a smaller accumulation parameter m. From regression analysis m = 0.0871 is obtained for very dense sand, whereas m = 0.0938 is obtained for medium dense sand.

The effect of the relative skirt length L/D is shown in Figure 6. Here the results for a bucket with a diameter D = 16 m in medium dense sand are presented for different skirt lengths. It is evident that the cyclic behavior is more unfavourable for small skirt lengths. For L/D = 0.50 m = 0.1079 results, whereas for L/D = 0.75 and 1.0 very similar values of 0.0947 and 0.0966 apply. This tendency was confirmed also by calculations for other system conditions, see Table 3.

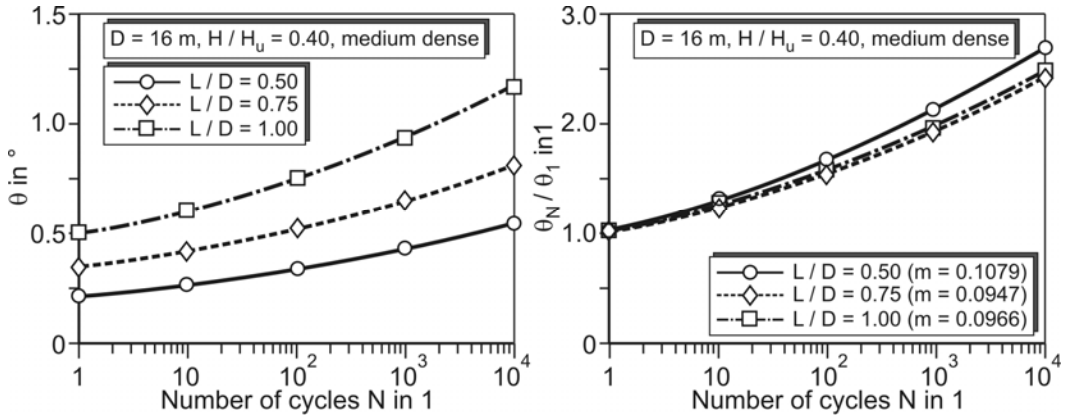

Fig. 6. Cyclic performance curves for buckets in medium dense sand (D = 16 m, H/H_u = 0.40, h = 20 m)

Figure 7 finally shows exemplarily the effect of the load level on the cyclic behavior for D = 20 m, L/D = 0.5 and medium dense sand. Surprisingly, the relative accumulation is the greater, the smaller the load level is. For H/H_u = 0.40 and H/H_u = 0.55 the differences are quite small, but for the lowest load level with H/H_u = 0.25 the parameter m is considerably increased. This trend was confirmed in all other calculations carried out (see Table 3).

The reason for that might be that at a small load level only minor non-linear effects like loss of contact between the bucket lid and the soil – which occurs at larger deflections, since the bucket heaves under lateral loading – or plastification of the soil in front of the bucket skirt occur. This leads to a rather stiff behavior under static loading (see Figure 4). However, the large stiffness is fully subject to degradation under cyclic loading. In contrast, at higher load levels loss of contact occurs or maximum bedding pressures are reached, which means that partly no further stiffness loss under cyclic loading is possible. This might be the reason for a reduced relative increase of displacements.

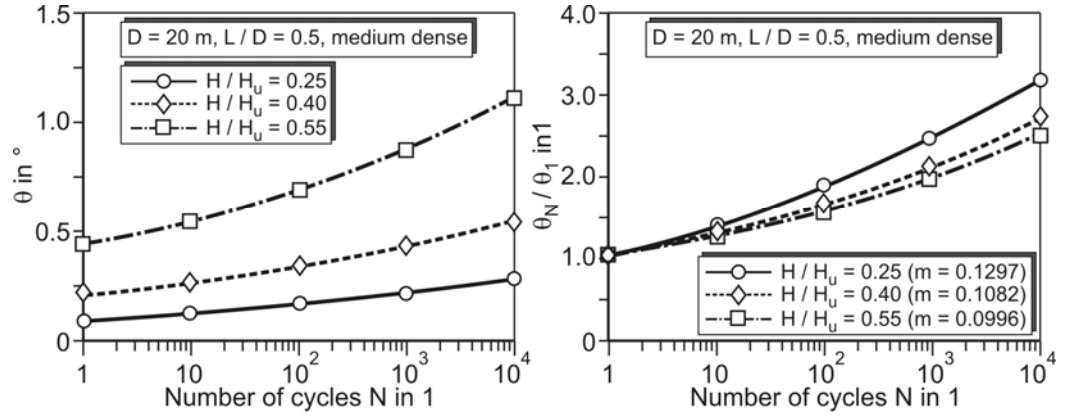

Fig. 7. Cyclic performance curves for buckets in medium dense sand (D = 20 m, L/D = 0.5, h = 20 m)

The m-values from all calculations carried out in the scope of the parametric study are collected in Table 3. A bandwidth of m-values between 0.088 und 0.130 is obtained.

Little & Briaud (1988) conducted field tests on flexible piles in non-cohesive soil and derived m-values between 0.04 and 0.09. For rigid piles, Long & Vanneste (1994) derived values between 0.10 and 0.25. Albiker & Achmus (2012) carried out calculations with the stiffness degradation method (SDM) also used here for a pile with a diameter of 1 m and a

length of 7.14 m and found values between m = 0.108 and m = 0.120, depending on load level and relative density of the sand. Here an increase of the *m*-values with increasing load level H/H_u was determined. Considering these results, the *m*-values for the bucket systems seem to be reasonable. With regard to cyclic performance, buckets seem to behave in a similar way as monopiles.

Table 3. Accumulation parameter *m* of monopod buckets in sand (h = 20 m)

D in m	*L* in m	*L/D*	m ($\theta_N/\theta_1 = N^m$) in 1					
			very dense sand			medium dense sand		
			0.25 H_u	0.40 H_u	0.55 H_u	0.25 H_u	0.40 H_u	0.55 H_u
8	4	0.5	0.1043		0.0957	0.1265	0.1150	0.108
	6	0.75	0.0941	0.0919		0.1144		0.108
	8	1.0	0.0914	0.0921		0.1040	0.1025	0.1038
12	6	0.5	0.1074	0.0952	0.0878	0.1278	0.1119	0.1049
	9	0.75	0.0947	0.0871		0.1067	0.0938	0.0952
	12	1.0	0.0911			0.1019	0.0932	0.1000
16	8	0.5	0.1122		0.0900	0.1275	0.1079	0.0996
	12	0.75	0.0974	0.0911		0.1116	0.0947	0.0970
	16	1.0	0.0942			0.1066	0.0965	
20	10	0.5	0.1157	0.0939	0.0944	0.1297	0.1082	0.0996
	15	0.75	0.0967	0.0926		0.1162	0.0966	0.0989
	20	1.0	0.0950			0.1088	0.0990	

4 CONCLUSIONS

In this study, the behavior of bucket foundations in sand under drained cyclic loading was investigated by means of the stiffness degradation method (SDM). The following main conclusions can be drawn:

- The accumulation parameter *m*, which describes the accumulation rate of the rotation of the bucket lid, was found to lie between 0.088 and 0.130, depending on bucket geometry, relative density of the sand and load level. Values of similar magnitude were found in previous investigations for monopile structures in sand. Thus, the cyclic performance, i.e. the relative increase of rotation, of a bucket structure is similar to that of a monopile.
- The accumulation rate is relatively large for a bucket with small skirt length (*L/D* = 0.5). It decreases with increasing skirt length. However, for relative skirt lengths *L/D* = 0.75 and 1.0 it is almost the same.
- The accumulation rates for loads of 40% and 55% of the ultimate capacity are very similar, but for a smaller load of 25% of the ultimate capacity significantly greater values were obtained. This surprising effect is perhaps induced by the special interaction between bucket skirt and bucket lid in the load bearing behavior.

The presented results give insight into the behavior of buckets under drained cyclic loading. However, validation of the findings by experimental studies is of course necessary and urgently needed.

ACKNOWLEDGEMENT

This study was partly carried out in the scope of the research project "WindBucket" funded by the Federal Ministry for the Environment, Nature Conversation and Nuclear Safety, Germany (BMU). The authors sincerely acknowledge BMU support.

REFERENCES

Abaqus (2012), Abaqus User's Manual, Version 6.12.

Abdel-Rahman, K. & Achmus, M. (2005), „Tragverhalten von Monopile-und Bucketgründungen", in: Gigawind Symposium, Hannover (in German).

Achmus, M., Kuo, Y.-S. & Abdel-Rahman, K. (2008), „Zur Bemessung von Monopiles für zyklische Lasten". Bauingenieur, Vol. 83, No. 7-8 (in German).

Achmus, M., Kuo, Y.-S. & Abdel-Rahman, K. (2009), "Behavior of monopile foundations under cyclic lateral load", Computers and Geotechnics, 36 (2009) 725-735.

Achmus, M. & Thieken, K. (2010), "On the behavior of piles in non-cohesive soil under combined horizontal and vertical loading", Acta Geotechnica, Vol. 5, No. 3, 2010, pp. 199-210.

Achmus, M., Albiker, J. & Abdel-Rahman, K. (2010), "Investigations on the behavior of large diameter piles under cyclic lateral loading", 2nd International Symposium on Frontiers in Offshore Geotechnics (ISFOG), Perth, Australia, November.

Albiker, J., Achmus, M. (2012), "Cyclic performance of horizontally loaded piles in layered subsoil", 12th Baltic Sea Geotechnical Conference, Rostock, Germany, May 31 - June 2.

Byrne, B.W. & Houlsby, G.T. (2003), "Foundation for offshore wind turbines", Phil. Trans. Roy. Soc. London. A 361 (2003), 2909-2930.

Byrne, B.W. (2000), "Investigations of Suction Caissons in Dense Sand", Ph.D. Thesis, University of Oxford, Oxford.

Feld, T. (2001), "Suction Buckets, A New Innovative Foundation Concept, Applied to Offshore Wind Turbines", Ph.D. Thesis ATV Project EF675, Aalborg University, Aalborg.

Houlsby, G.T., Ibsen, L.B. & Byrne, B.W. (2005), "Suction caissons for wind turbines", in: Proceedings of International Symposium on Frontiers in Geotechnics: ISFOG, Perth, Australia, pp. 75-94.

Houlsby, G.T. & Byrne, B.W. (2000), "Suction caisson foundations for offshore wind turbines and anemometer masts", Journal of Wind Engineering 24 (2000) 249-255.

Huurman, M. (1996), "Development of traffic induced permanent strains in concrete block pavements", Heron, Vol. 41, No.1. pp. 29-52.

Ibsen, L.B., Liingaard, M. & Nielsen, S.A., "Bucket foundation, a status", in: Proceedings of Copenhagen Offshore Wind 2005, 26-28 October 2005, Copenhagen, Denmark.

Kuo, Y.-S. (2008), "On the behavior of large-diameter piles under cyclic lateral load", Ph.D. Thesis, Leibniz Universität Hannover, Hannover, Heft 65.

Little, R.L., Briaud, J.L. (1988), "Full scale cyclic lateral load tests on six single piles in sand", Miscellaneous paper GL-88-27, Texas: Geotechnical Division, Texas A&M University.

Long, J.H., Vanneste, G. (1994), "Effect of cyclic lateral loads on piles in sand", Journal of the Geotechnical Engineering Division (ASCE), 120 (1) 1994, 33-42.

Manoliu, I., Dimitriu, D.V., Radulescu, N. & Dobrecu, D.H. (1985), "Load-deformation characteristics of drilled piers", in: Proceedings of 11th International Conference on Soil Mechanics and Foundation Engineering Vol.3. San Francisco, 1985, pp. 1553-1558.

Villalobos, F.A., Byrne, B.W. & Houlsby, G.T. (2009), “An experimental study of the drained capacity of suction caisson foundations under monotonic loading for offshore applications”, Soils and Foundations 49 (2009), 477-488.
Villalobos, F.A., Byrne, B.W. & Houlsby, G.T. (2005), “Moment loading of caissons installed in saturated sand”, in: Proceedings of International Symposium on Frontiers in Geotechnics, ISFOG, University of Western, Perth, Australia, pp. 411-416.
Zhang, J.H., Chen, Z.Y. & Li, F. (2010), “Three dimensional limit analysis of suction bucket foundations”, Ocean Engineering, 37 (2010) 790-799.

BEHAVIOUR OF SUCTION CAISSONS SUBJECTED TO STATIC AND DYNAMIC UPLIFT LOADS

Alper Turan
Material Engineering Research Office, Ontario Ministry of Transportation, Downsview, Ontario, Canada.

Zahid Khan
American University of Sharjah, Sharjah, UAE.

Hesham El Naggar
Western University, London, Ontario, Canada.

ABSTRACT: *Wind energy is becoming increasingly popular as a green and sustainable source of renewable power. There is a significant installed capacity and ongoing installations continue globally. Significant amount of the wind energy resources are available offshore. There is a considerable pool of knowledge and experience of foundation design for offshore structures used in oil and gas industry. However, the offshore foundations that support the wind turbines have some significant differences since the vertical loads are lower compared to other offshore foundations and the loading conditions are complicated by the dynamic nature of wind and wave loads. Another distinction is that the installations are typically done in shallow waters near shore. Suction caissons are simple steel units that are used economically as an alternative to the pile foundations.*

A number of numerical analyses were carried out to study the concentric uplift behavior as part of this paper. A 2D axisymetric finite element model was constructed using commercial finite element program PLAXIS 2D Dynamic. The undrained failure mechanism under uplift loads was studied for static and cyclic loading conditions. The results indicated that the ultimate uplift resistance of the suction caisson in soft clayey soils is largely contributed by the interface shear strength at the outer surface of caisson. The results also indicated that the radial stresses on the outer surface of caisson remain insensitive to the increasing uplift loads except for the loads approaching the ultimate limit. The cyclically applied uplift loads were seen to mobilize 14 % more interface strength relative to the statically applied loads. The research presented in this paper is considered to be of interest to designers and practitioners.

1 INTRODUCTION

Suction caissons, also known as suction cans, suction anchors, suction piles and bucket foundations are widely used in off-shore projects. Suction caissons emerged as a viable option due to the capacities they can provide and cost savings they can lead to. Suction caisson is a hollow circular tube closed by a lid at the upper end (see Figure 1). The maximum ratios of skirt length to diameter and wall thickness to diameter are

approximately less than 10 and in the range of 0.3% - 0.6%, respectively (Tran, 2005). Installation process comprises creating suction beneath the caisson by pumping the water from the hollow compartment, which results in a differential pressure beneath the caisson which assists the caisson penetration into the soil along with its gravity (see Figure 2). Distribution of initial stress in the soil plug inside the suction caisson and at the surrounding soil changes due to installation process. Displacement of the soil plug, remolding of the adjacent soil in the interface zone and generation of excess pore pressure contributes to the change in effective stress. Ring and longitudinal stiffeners that support the skirts can be added to the internal surfaces to prevent buckling during installation. Stiffeners are common in suction caissons in clay, where the maximum wall length to diameter ratio can be as high as 10 (Tjelta, 2001).

The suction caissons can be dated back to 1950s. However, first commercial application as a permanent foundation system did not take place until 1989, where a 22 m deep penetration of the concrete cell was achieved the Gullfaks C gravity platform (Tjelta et al., 1990). The experience gained during the subsequent field applications and academic studies led to a widespread and diverse use of suction caissons. They are currently used for various purposes including mooring anchorages to permanent foundations for platforms, support for ship salvages and as foundation systems for future offshore wind turbines. There are various advantages associated with the use of suction caissons such as speed and accuracy of installation and ability to remove.

Submerged weight of the caisson, suction pressure created across the caisson under tensile loading, skin friction, and soil tensile strength at the caisson's base, all of which determine the uplift capacity of caisson, are major considerations in the design. Depending on the rate of loading and drainage condition of soil, three different failure mechanisms are possible for pullout failure of suction caisson; i. bottom resistance failure, ii. reverse bearing failure, and iii. sliding failure (Thorel et al., 2005 and Huang et al., 2003). Bottom resistance failure mechanism is a semi-drained condition, where the soil plug inside the caisson moves along the caisson during failure. The pullout resistance is calculated by considering the outside friction on caisson wall and taking account for the weight of soil plug and caisson. Reverse bearing capacity mechanism takes place under undrained condition. It is similar to bottom resistance failure mechanism. Only difference is that soil failure capacity under caisson is deduced from the bearing capacity formula with reverse mechanism. The overall pullout capacity is calculated as sum of external wall friction and bearing capacity load of caisson. Sliding failure mechanism takes place under drained conditions. It occurs as the soil plug remains in its position. The resistance is calculated as the sum of internal and external skin friction of the caisson wall.

This paper presents the findings of some numerical investigations aimed at analyzing the behaviour of suction caissons subjected to uplift loads in soft cohesive soils.

Figure 1. (a) Caisson in fabrication yard (after Tran, 2005).

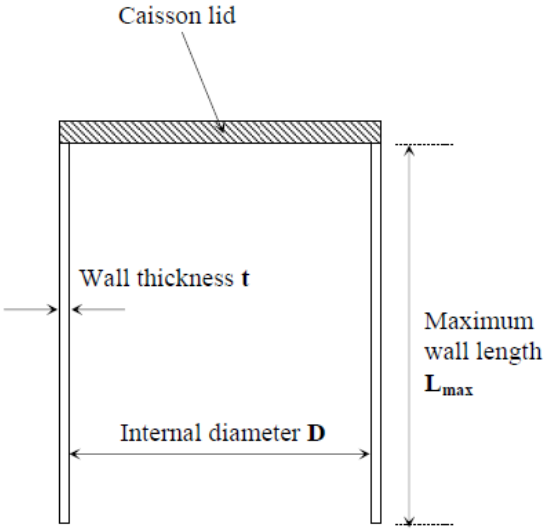

(a)

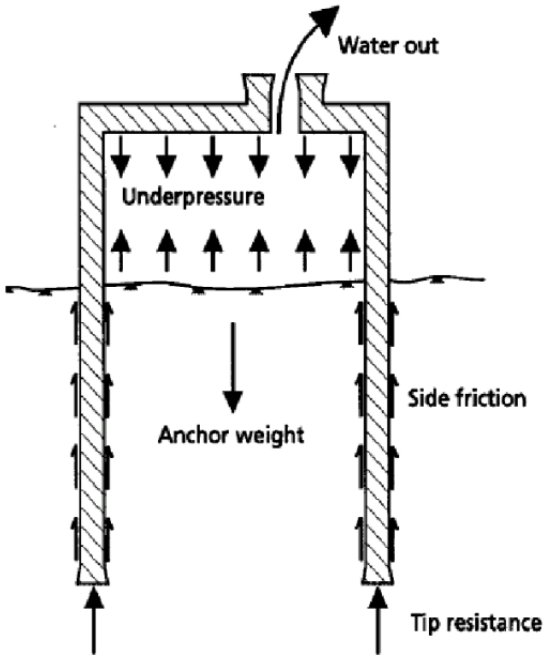

(b)

Figure 2. (a) Suction caisson components (after Tran, 2005) (b) Suction caisson with forces during installation (after Ulvestad, 2012)

2 METHODOLOGY

The methodology of the present study comprises a number of steps, which include; i. analytical estimation of the uplift capacity of the suction caisson, ii. 2D axisymetric FE analysis under static, concentric loads and calibration against the analytical solution. iii. 2D axisymetric FE analysis under cyclic concentric loads.

2.1. Problem Geometry

The problem investigated in this study is the behaviour of a suction caisson subjected to concentric static and cyclic loads in soft cohesive soils. The suction caisson considered in this study has a circular cross section with a diameter of 5m and depth of 7.5m. The caisson is considered to have fully penetrated into the seabed stratum.

2.2. Numerical Model and Boundary Conditions

Finite element model of suction caisson system was constructed using commercial FE program PLAXIS 2D Dynamic. The soil was modelled using 15-node axisymetric elements with three degrees of freedom per node. Figure 3 shows a view of FE model used in this study. The initial step comprised a geostatic analysis, which established initial geostatic equilibrium conditions long after the installation of suction caisson. This step is followed by a series of static analysis steps which were used to simulate

concentric uplift behaviour. Non-linear interface elements were used at the inner and outer surfaces of the skirts, which allowed slip on the interface. The concentric uplift load was increased incrementally until the failure was reached.

For dynamic analyses, the lateral soil boundaries were represented using absorbent boundaries (Lysmer and Kuhlemeyer, 1969), which are defined over a semi-infinite domain and were given a suitable decay function. The model base was assigned fully fixed boundary conditions. The infinite lateral boundaries were situated 10 times the diameter of suction caisson. The mesh refinement was done such that the largest element size remains smaller then $1/10^{th}$ of the wave length in accordance with Kramer (1996).

A series of static and dynamic analyses were also carried out using different mesh densities. The constitutive behaviour of the soil was modeled using simplified Mohr-Coulomb model. A single layer of normally consolidated soft clay was considered in the analyses for simplicity. Undrained soil behaviour was assumed in the analyses, since this is the predominant mode of behaviour for anticipated mode of failure. The increase of the undrained shear strength of soil with depth typically seen in normally consolidated clays was not taken into account. The nonlinear interface condition with interface factors of 1 was considered as part of the analyses.

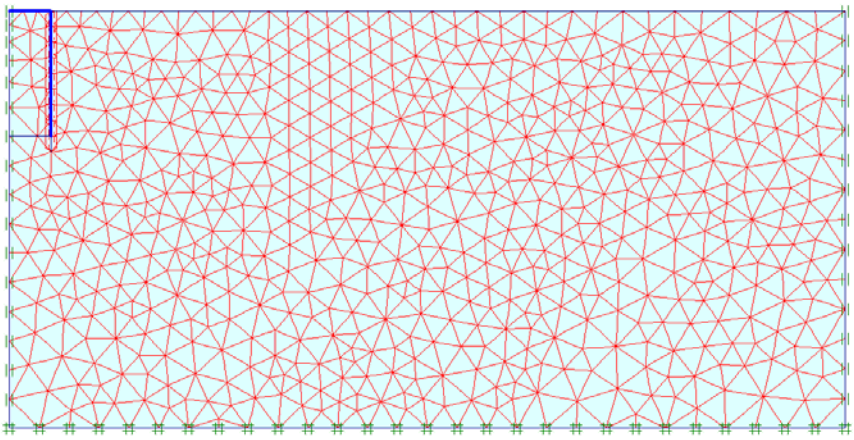

Figure 3. Axisymetric finite element model of suction caisson.

2.3. Static and Dynamic Loads

The vertical static and dynamic loads were applied at the axisymetry axis of the model. The static loads were applied incrementally as the vertical displacements in the suction caisson were monitored. The ultimate uplift resistance was determined from the point where non-linear behaviour was first observed in the load-displacement curves.

Harmonically varying dynamic loads acting vertically on the axisymetric axis were considered. An uplift load amplitude (4000 kN) varying harmonically was considered at

1 Hz frequency. The relative shear strengths on the interfaces resulting from dynamic excitations were compared to those resulted from static ones.

2.4. Verification of the Numerical Model

The verification of the results of FE model was conducted using the simplified procedure presented in Deng and Carter (1999). The ultimate vertical uplift load for suction caissons in uniform soil may be estimated from Equation 1.

$$V_0 = 2.7\pi d^2 \left(1 + 0.4\left(\frac{L}{d}\right)\right) S_u \quad (1)$$

where, V_0 is the ultimate uplift load, d is the caisson diameter, L is caisson embedded depth, and S_u is the undrained shear strength of the surrounding soil. The verification analyses were conducted using three models, which comprise uniform soil layers with undrained shear strength values of 10 kPa, 15 kPa and 20 kPa. The results indicated that the ultimate uplift load that can be carried by the suction caisson determined using FE model was in a reasonable agreement with the results produced using the analytical approach by Deng and Carter (1999). The ratio between the ultimate loads estimated by the FE method and Deng and Carter (1999) method were 0.98, 0.91 and 0.87 for models with undrained shear strength 10 kPa, 15 kPa and 20 kPa, respectively. Despite the increasing difference, there is a considerable agreement between the results of FE analyses and those of analytical solution.

3 RESULTS AND DISCUSSION

Both dynamic and static analyses were performed in this study described in this section. The analyses were conducted considering a uniform layer of soft clay with a 20 kPa undrained shear strength that is constant along the depth of the stratigraphy. The rigidity index of 100 was considered in determination of shear modulus of soil. The shear wave velocity of the soil was calculated as 33 m/s based on the shear modulus of 2000 kPa.

Initially, concentric static uplift loads were applied incrementally and the resultant deformations were computed. Then, the displacements resulting from each level of static uplift loads were applied harmonically with 1 Hz excitation frequency. The sheer stresses at the interface between soil and outer surface of suction caisson due to static and dynamic loads were compared. Figure 4 depicts the load deformation behaviour of suction caisson under static loads. The results show that a linear relationship was observed between the applied load and measured displacement when the loads were smaller then 6000kN. This pullout load was considered to be the ultimate pullout capacity of suction caisson investigated in this paper.

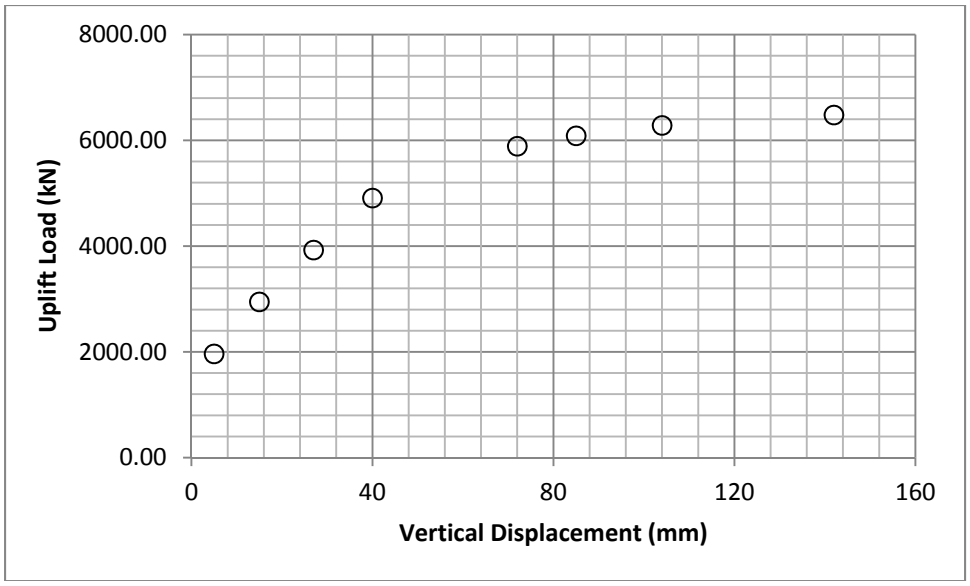

Figure 4. Static load-deformation behavior of suction caisson.

3.1. The Behavior under Static Loads

The failure mechanism of the suction caisson is complicated. The nonlinearity of the interfaces, plasticity of soft soil and generation of excess pore water pressures during the undrained loading further complicates this mechanism. The distribution of interface stresses and plastic points in the soils were depicted in Figures 5 and 6 for uplift loads of 2000, 4000 and 6000 kN. Figure 5 shows that the shear stresses in the interfaces inside and outside the suction caisson are significantly different. The shear stresses outside the caisson were fully mobilized during the incremental increase of uplift forces. However, the shear stresses inside the caisson showed slight increase during the incremental load increase. This observation indicates that the uplift resistance of the suction caisson was determined mainly by the outside surface of the caisson. The heave of the soil inside the caisson limits the development of shear stresses along the inner surface reducing the contribution of resistance from the inner surface. Figure 6 show the distribution of plastic points for three uplift loads. The results showed that the plastic zone started from the bottom of the caisson and propagate upwards along the soil-caisson interface and downwards to a depth of approximately equal to the diameter of the caisson. An interface failure rather than a passive wedge failure determined the ultimate uplift resistance of the suction caisson. The results in Figure 7 showed that the radial effective stress acting on the internal surfaces of caisson wall varied almost linearly along the penetration depth. The radial stresses on the inner face were seen to be independent of level of uplift load. The radial stresses on the outer face however, had the same peak stress resulting from gravitational forces but had an almost constant distribution with depth.

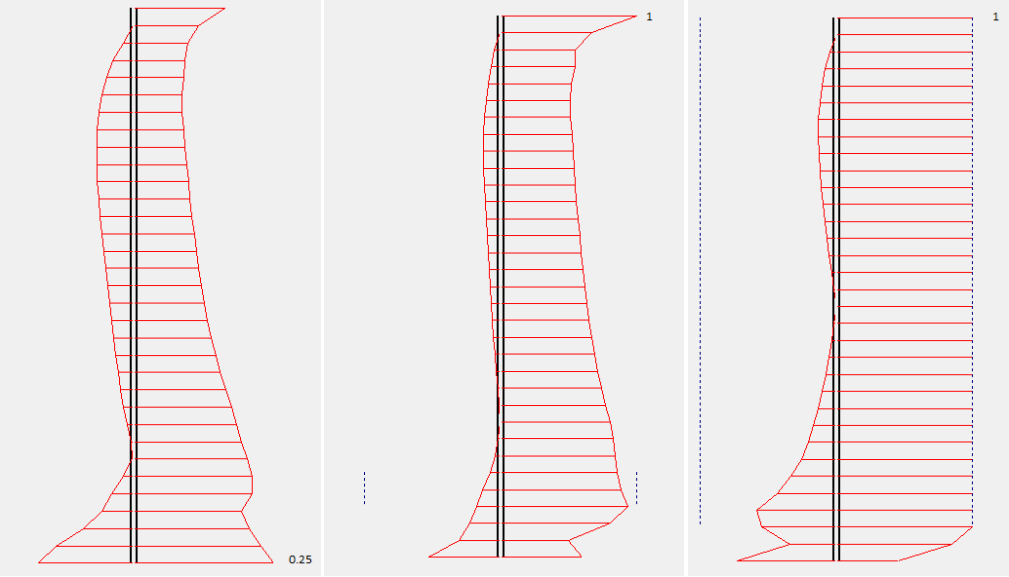

(a) (b) (c)

Figure 5. The relative shear strength of interfaces for (a) 2000 kN (b) 4000 kN (c) 6000 kN uplift force.

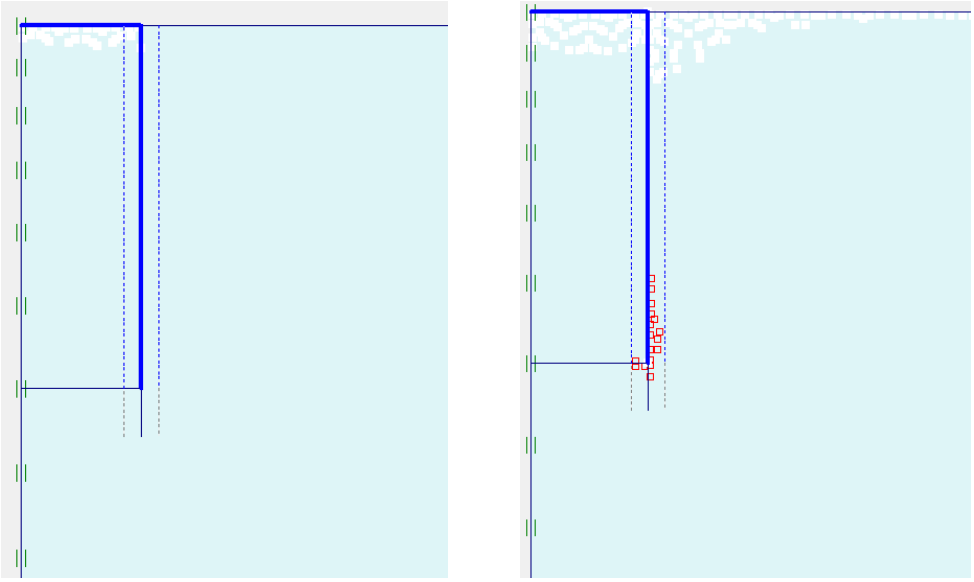

(a) (b)

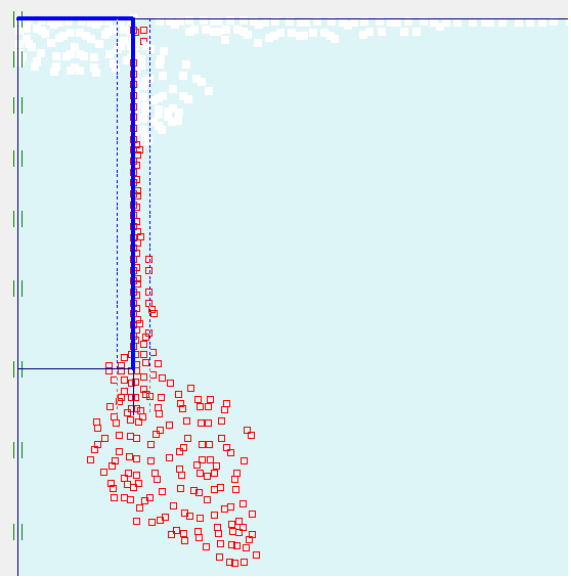

(c)

Figure 6. The plastic points for (a) 2000 kN (b) 4000 kN (c) 6000 kN uplift force.

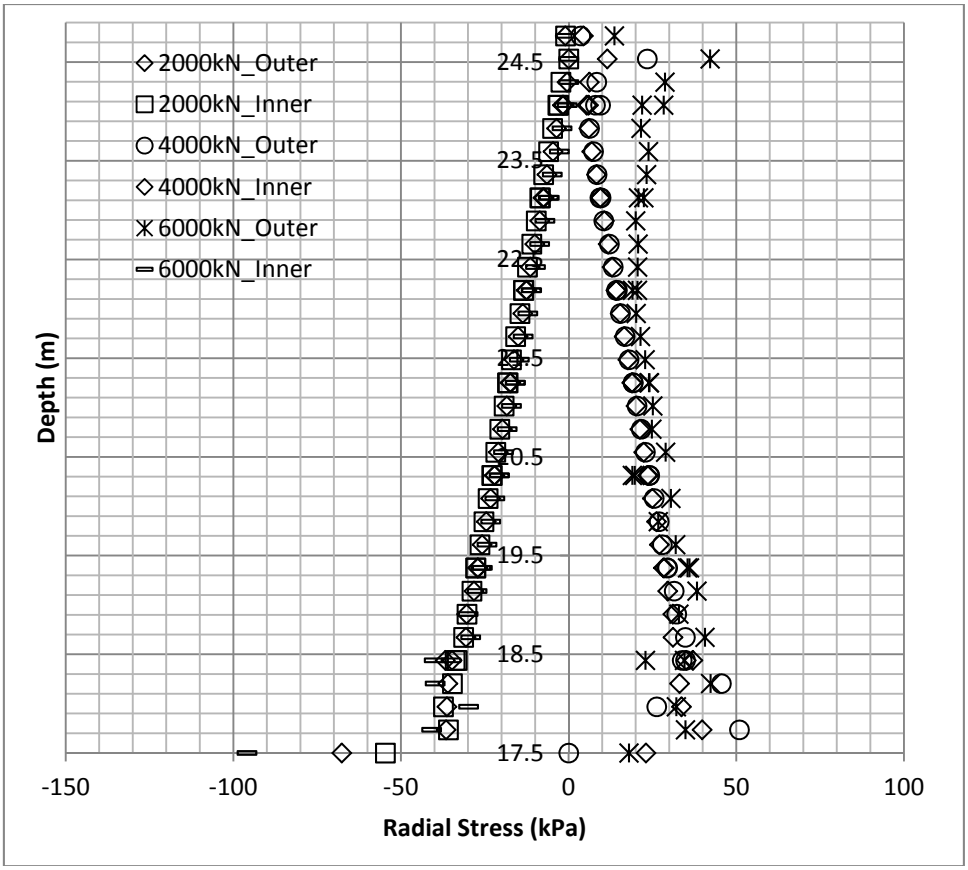

Figure 7. The variation of radial stresses on the suction caisson.

3.2 The Behavior under Dynamic Loads

The behaviour of the suction caisson was also studied under dynamic loading conditions. The comparison of the suction caisson behaviour under static and dynamic loading conditions was made considering an uplift load magnitude of 4000 kN. This comparison was made using a displacement controlled approach where, the suction displacement caused by the uplift force was applied cyclically in dynamic analyses. The uplift displacement caused by 4000kN uplift forces was 27 mm. Since the ultimate resistance of the caisson under static loading conditions was determined by the interface resistance at outer surface of the caisson, the relative shear strength of interfaces were compared for the same level of uplift displacement applied statically and cyclically. The relative shear strength of the interfaces can be defined as the ratio of shear stress at the interface between soil and the surfaces of the caisson and the maximum shear strength at the interface. Figure 8 compares the variation of the relative shear strength for static and dynamic loading conditions. The results in Figure 8 shows that the interface shear strength mobilized under cyclic loading is larger than that mobilized under short-term monotonic undrained loading for a uplift load of 4000 kN. The average values of mobilized interface shear strength along the outer face of caissons were calculated as 0.65 and 0.75 for 4000 kN uplift force applied statically and cyclically, respectively. This result indicates a 14 % increase in mobilized interface shear strength.

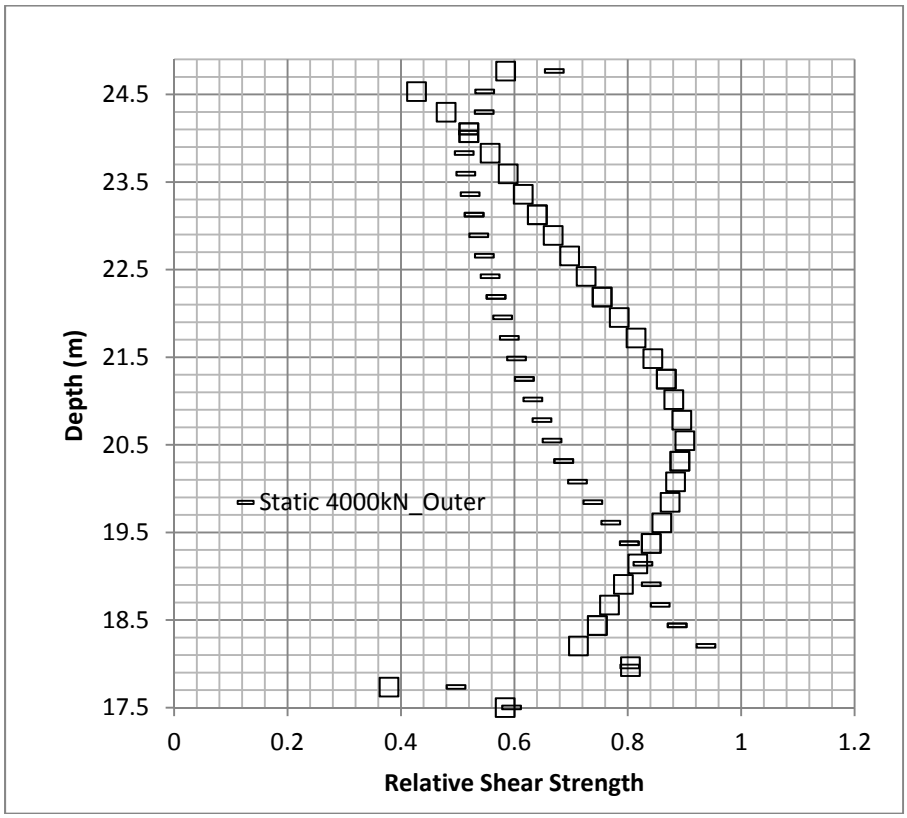

Figure 8. Variation of relative shear strength on the outer surface of suction caisson.

4. SUMMARY AND CONCLUSIONS

A series of finite element analyses were performed to study the uplift behaviour of suction caissons subjected to concentric loads. The behaviour under static and cyclic loads was evaluated. The conclusions arising from this study are outlined as follows;

- The results showed that the shear stresses mobilized on outer interface of suction caisson are significantly larger than that on the inner surfaces. The shear stresses on the outer surface of caisson are fully mobilized at the ultimate uplift forces. However, the shear stresses on the inner surface of caisson showed only a slight increase during load increase. Thus, the ultimate resistance of the suction caisson was determined by the shear resistance of the outer surface of the caisson.

- The heave of the soil inside the caisson during the pull out action limits the development of shear stresses along the inner surface reducing the contribution of resistance from the inner surface.

- The results show that the plastic zone in the soil started from the bottom of the caisson and propagated upwards along the soil-caisson's outer interface and downwards to a depth of approximately equal to one diameter of the caisson.

- It was observed that a shear failure on the outer interface rather than a passive wedge failure determined the ultimate uplift resistance of the suction caisson. Thus, the wall interface factor is of great importance for determining ultimate pullout resistance

- The radial effective stress acting on the inner and outer surfaces of caisson wall were seen to increase linearly with depth (triangular distribution) and remained unchanged during increased uplift forces. However, the radial stresses showed an almost constant distribution at ultimate limit.

- Results indicated that the interface shear strength mobilized under cyclic loading is larger than that developed under short-term monotonic undrained loading. The cyclically applied pullout load of 4000kN mobilized 14 % more interface shear strength relative to the static loading condition.

ACKNOWLEDGEMENTS

The research reported in this paper has been supported by the Western University Ontario Academic Development Fund.

REFERENCES

Tran, M.N. (2005). "Installation of Suction Caissons in Dense Sand and the Influence of Silt and Cemented Layers". PhD Thesis. The University of Sydney.

Tjelta, T.I. (2001). “Suction piles: Their position and application today”, Proc. 11th International Conference on Offshore and Polar Engineering, Stavanger, Norway, 2, 1-6.

Tjelta, T.I., Aas, P.M., Hermstad, J. and Andenaes, E. (1990). “The skirted piled Gullfaks C platform installation”, Offshore Technology Conference, Houston, USA. Paper: OTC 6473.

Ulvestad, A. (2012). "Consolidation Settlement of Suction Caissons". Master thesis.

Alavi, A. H., Gandomi, A. H., Mousavi, M., & Mollahasani, A. (2010). High-precision modeling of uplift capacity of suction caissons using a hybrid computational method. Geomechanics and Engineering, 2(4), 253–280.

S.K. Patel, S.K. and Singh, B ( ). "Study on Installation And Pullout of Suction Caisson Foundation for Offshore Wind Turbines". SAITM Research Symposium on Engineering Advancements.

L. Thorel, J. Garnier, G. Rault and A. Bisson, (2005). “Vertical uplift capacity of suction caisson in clay,” in: International Symposium on Frontier in Offshore Geotechnics, ISFOG, Perth, Australia.

J. Huang, J. Cao and Jean (2003). “Geotechnical design of suction caisson in clay,” in: Proceedings of 13th International Offshore and Polar Engg. Conference, pp. 770-779.

Lysmer J. and Kuhlmeyer, R.L. (1969). "Finite dynamic model for infinite media." ASCE J. of the Eng. Mech. Div., p.859-877.

Kramer S.L. (1996). "Geotechnical earthquake engineering." Prentice Hall. New Jersey.

Deng, W and Carter, J.P (1999). "Vertical pullout behavior of suction caissons" Centre for Geotechnical Research, The University of Sydney.

INVESTIGATION OF DIFFERENT SOLUTION STRATEGIES FOR NON-LINEAR 3D CONSOLIDATION PROBLEMS

H.P. Jostad
Norwegian Geotechnical Institute, Oslo, Norway

H.K. Engin
Norwegian Geotechnical Institute, Oslo, Norway

ABSTRACT: *Long term settlements of saturated soft soils subjected to effective stress changes are traditionally calculated by 1D consolidation programs or established consolidation diagrams. However, 3D effects such as non-uniform surface loads over a limited area and lateral pore pressure dissipations are easily included in a coupled 3D finite element formulation. A critical issue is then the computer processing time which depends on the element discretisation, the time stepping and iteration scheme and the solver strategy. For this type of 3D problems the computing time is generally governed by the time used to solve the global equation system. An optimal solution strategy can then be to reduce the need for updating the global system matrix. In this study, a solution scheme for typical 3D consolidation problems is proposed, in which the system matrix is updated only for a limited number of times during a simple automatic time stepping scheme. Simulations of the settlements of a quadratic loaded area on soft clay are used to demonstrate the performance of the proposed solution strategy, and the computer processing times are compared with other more traditional solution strategies.*

1 INTRODUCTION

Time dependent settlements of soft soils due to effective stress changes are traditionally solved by simple 1D consolidation programs as for instance Illicon (Mesri and Choi, 1985), Briscon (Nash and Brown, 2013), Geosuite Settlement (www.vianovasystems.com) or simple "in house" developed spread sheet programs or analytical consolidation diagrams. The effective stress changes are due to external loads (e.g. fills, foundation loads, etc.) or pore pressure changes (e.g. changes in ground water level, shear induced pore pressure, etc). The simplified methods are used in spite of the large limitations, such as idealized load spread with depth, and neglection of horizontal strains, lateral (3D) pore pressure dissipation, and lateral (3D) variations in geometry and material properties.

One possible reason for this is that establishing a 3D finite element model in commercial finite element programs as for instance Plaxis (www.plaxis.nl), ABAQUS (www.3ds.com), and Flac3D (www.itascacg.com) are time consuming, requires special skills in using these programs and knowledge of more complex general 3D soil models. In addition the computer time for these programs on standard PCs is typically several hours compared to only a few seconds for the simplified 1D methods. The reason for the long computer processing time in 3D finite element consolidation analyses is that the global equation system is generally solved (e.g. factorized) in each time step, while 10 to more than 100 time steps are usually required.

The main purpose of this paper is to study the possibility of reducing the need for updating the global system matrix and thus reduce the computer processing time in traditional 3D FE consolidation analyses.

2 GOVERNING EQUATIONS

The governing equations for coupled consolidation formulation are the stress equilibrium equations and the continuity (mass balance of pore fluid) equation. The governing field equations are then typically based on the following assumptions:

- Terzaghi's effective stress principle
- Fully saturated pores
- Incompressible grains
- Darcy's law for fluid flow
- No inertia effects (quasi-static response)

In the following, sign convention of stresses and strains are herein according to classical continuum theory, however, the pore pressure is positive. Index notations are employed in the formulation of the governing equations. A comma preceding a lower index implies differentiation with respect to a spatial coordinate. Matrices and vectors in the finite element formulation are written in bold.

2.1 Stress equilibrium

The equilibrium of an infinitesimal small soil element is given by:

$$(\sigma_{ij} - u\delta_{ij})_{,j} + f_i = 0 \tag{1}$$

Where $\sigma_{ij} = \sigma'_{ij} - u\delta_{ij}$ is the total (Cauchy) stress tensor, σ'_{ij} is the effective stress tensor, δ_{ij} is the Kronecker's delta, u is the pore pressure, and f_i is a body force per unit volume.

2.2 Continuity (mass balance of pore fluid)

The continuity equation, i.e. balance between the rate of the volumetric change of an infinitesimal small element, the rate of compression of the pore fluid within the element and the rate of net fluid flow out of an infinitesimal small element is given as:

$$\dot{v}_{i,i} - \frac{n}{K_w}\dot{u} + q_{i,i} = 0 \tag{2}$$

where v_i is a (spatial) displacement vector, and the superimposed dot $(\cdot)$ denotes derivative with respect to time, n is the porosity of the soil skeleton, K_w is the bulk modulus of the pore fluid, and q_i is the flow velocity vector. The flow velocity (specific discharge) q_i through the saturated porous medium is given by Darcy's law:

$$q_i = -\frac{1}{\gamma_w} k_{ij} u_{,j} \tag{3}$$

where k_{ij} is the permeability tensor, γ_w is the unit weight of the pore fluid, and $u_{,j}$ is the excess pore pressure gradient vector.

2.3 Finite element formulation

The finite element formulation for coupled consolidation problems are described in details in several text books e.g. Lewis et al. (1987), Potts and Zdravković (1999), and journals, e.g. Lewis et al. (1976), Borja (1989), and Prevost (1982), etc.. Therefore only a briefly presentation in order to define the different terms is presented below.

Applying Galerkin's weighted residual method to the equilibrium equations and the continuity equation, (1) and (2), and applying Gauss's divergence theorem gives:

$$\int_V \delta v_{i,j} \sigma'_{ij}\, dV - \int_V \delta v_{i,j} u \delta_{ij} dV = \int_V \delta v_i f_i dV + \int_S \delta v_i t_i dS \tag{4}$$

$$\int_V \delta u \dot{v}_{i,i} dV - \int_V \delta u \frac{n}{K_w} \dot{u} dV + \int_V \delta u_{,i} \frac{k_{ij}}{\gamma_w} u_{,j} dV = -\int_S \delta u q_n dS \tag{5}$$

where δv_i and δu are weighting functions (or virtual displacement vector and virtual pore pressure), $t_i = \sigma_{ij} n_j$ is a surface traction, and $q_n = -n_i k_{ij} u_{,j} / \gamma_w$ is the rate of fluid flow out of the surface, *S*.

Within an element the following standard finite element approximations are used: $v_i = N_\alpha v_{\alpha i}$, where the number of nodes with displacement degree of freedom is n_α, and $u = M_\beta u_\beta$, where the number of nodes with pore pressure degree is n_β. N_α is a vector of interpolation functions for the displacement and M_β is a vector of interpolation function for the pore pressure.

In order to establish the stiffness matrix of the soil skeleton one need to introduce a constitutive relationship between effective stress rates and strain rates, i.e. $\dot{\sigma}'_{ij} = D_{ijkl} \dot{\varepsilon}_{kl}$.

By incorporation the interpolation functions and the constitutive relationship into equations (4) and (5) the following governing finite element equations at the rate form are obtained:

$$\mathbf{K}\dot{\mathbf{v}} - \mathbf{L}\dot{\mathbf{u}} = \dot{\mathbf{R}} \tag{6}$$

$$\mathbf{L}^{\mathrm{T}}\dot{\mathbf{v}} - \mathbf{C}\dot{\mathbf{u}} + \mathbf{H}\mathbf{u} = -\mathbf{Q} \tag{7}$$

Where $\mathbf{K}$ is the stiffness matrix of the soil skeleton, $\mathbf{L}$ is the coupling matrix between the two equation systems, $\mathbf{R}$ is the external load vector, $\mathbf{C}$ gives the compressibility matrix of the pore fluid, $\mathbf{H}$ is the conductivity matrix and $\mathbf{Q}$ the vector of prescribed rate of nodal point outflow.

The above equation systems are solved by a time stepping procedure as described in the following chapter.

3 SOLUTION STRATEGY

3.1 Time stepping scheme

The solution of the time dependent coupled finite element equations is generally based on an implicit time stepping scheme. The linearised incremental equations from time, t_0 to $t_1 = t_0 + \Delta t$, may be expressed as:

$$\mathbf{K}\Delta\mathbf{v} - \mathbf{L}\Delta\mathbf{u} = \Delta\mathbf{R} \tag{8}$$

$$\mathbf{L}^{\mathrm{T}}\Delta\mathbf{v} - \mathbf{C}\Delta\mathbf{u} + \Delta t\mathbf{H}(\mathbf{u}_0 - \theta\Delta\mathbf{u}) = -\Delta t\mathbf{Q} \tag{9}$$

where, $\Delta\mathbf{v} = \Delta t \cdot \mathbf{v}$, $\Delta\mathbf{u} = \Delta t \cdot \mathbf{u}$, $\Delta\mathbf{R} = \Delta t \cdot \mathbf{R}$ and $\mathbf{u} = \mathbf{u}_0 + \theta\Delta t \cdot \mathbf{u}$

The 'average' excess pore pressure $\mathbf{u}$ over the time increment Δt, that by the pore pressure gradients control the fluid flow, is controlled by input of a time integration factor θ, which should be in the interval from 0 to 1 (explicit time stepping scheme, θ = 0, and fully implicit time stepping scheme, θ = 1).

3.2 Iteration scheme

For non-linear problems where the soil stiffness matrix $\mathbf{K}$ depends on the effective stresses (together with some history dependent state parameters) and the permeability *k* depends on the volumetric strain, the linearised equations, (8) and (9) may cause 'drift' from the correct solution curve. A corrector scheme based on a Modified Newton-Raphson iteration procedure is therefore used within each time increment.

The corrections in the unknown degree of freedoms for iteration number *i* are obtained from:

$$\mathbf{K}_{\alpha}\delta\mathbf{v}_i - \mathbf{L}\delta\mathbf{u}_i = \mathbf{R}_{ext} - \mathbf{R}_{\mathrm{int},i-1} \tag{10}$$

$$\mathbf{L}^{\mathrm{T}}\delta\mathbf{v}_i - \mathbf{C}\delta\mathbf{u}_i + \Delta t\theta\mathbf{H}\delta\mathbf{u}_i = -\mathbf{L}^{\mathrm{T}}\Delta\mathbf{v}_{i-1} + \mathbf{C}\Delta\mathbf{u}_{i-1} - \Delta t\mathbf{H}\mathbf{u}_{i-1} - \Delta t\mathbf{Q} \tag{11}$$

The permeabilities in the above equations are for simplicity kept fixed (equal to the value at the beginning of the time step). The internal force vector $\mathbf{R}_{\mathrm{int}}$ is calculated from the effective stresses and pore pressure in the previous iteration.

The coupled equation system is in the following for simplicity written in a compacted matrix form as:

$$\mathbf{G}\mathbf{x} = \mathbf{F} \tag{12}$$

Where $\mathbf{G}$ is the global system matrix, $\mathbf{F}$ is the unbalanced vector due to difference between external and internal nodal forces and incorrect fluid flow out/into the nodes, and $\mathbf{x}$ is the change in the node displacements and excess pore pressure. Different suitable expressions of the system matrix $\mathbf{G}$ (e.g. tangential, secant, initial, etc.) may be used in the solution process.

3.3 Equation solver

The equation system (10) is in this study solved by a factorization process (based on the Gaussian elimination method), where the global system matrix $\mathbf{G}$ is decomposed into an upper unit $\mathbf{U}$ and a lower $\mathbf{L}$ triangular matrix together with a diagonal matrix $\mathbf{D}$ as described in Dhatt and Touzot (1984). From the factorized matrix the solution vector $\mathbf{x}$ is found by forward and back-substitution.

Since the factorization process involves significantly more operations than the forward/back-substitution process (a factor times the total number of equations), the computer time is heavily affected by this process, i.e. number of factorizations compared to number of back- substitution.

As examples, the ratio between the time for factorization and back-substitution is calculated for a rectangular mesh with three different densities, namely, 13790, 23604 and

37226 numbers of equations. In Figure 1 the trend for factorization time and back-substitution time as functions of number of equations are given. The ratio between these times are found to be 0.0116 times the number of equations, i.e. $t_{fac}/t_{bs} = 0.0116 \cdot n_{eq}$. For a typical 3D element mesh as shown in Figure 2 with 41400 equations the ratio between the time for factorisation and back-substitution is then 482.

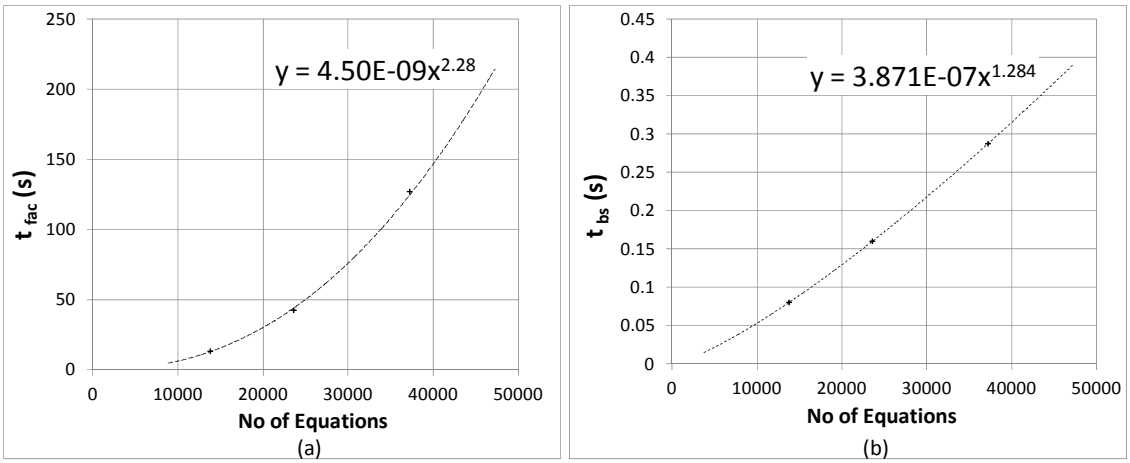

Fig. 1. Calculation time for a) factorisation, and b) back-substitution as function of number of equations

3.4 Automatic time stepping scheme

Specification of suitable time increments for a 3D non-linear consolidation problem is generally challenging without some initial trials and errors. Therefore, the time increments are in this study automatically controlled by the following input control parameters:

- *Minimum time increment*, $\Delta t_{\min}$. This time increment is at least used in the first time step and should be larger than a critical value as given later.
- *Maximum time increment*, $\Delta t_{\max}$. This is the maximum time increment used in the time stepping process.
- *Maximum time*, $t_{\max}$. The time stepping process is stopped when the accumulated time exceed this specified maximum time.
- *Minimum required pore pressure change*, $\Delta u_{\min}$. If the calculated pore pressure change in a time step in all nodes with pore pressure degrees of freedom is less than this specified value, the time increment in the following time step is increased as $\Delta t_k = t_{scale} \cdot \Delta t_{k-1}$.
- *Time increment scaling factor* t_{scale}, which is used to scale the time increment when required (see the bullet point above).
- *Maximum number of time steps*, N_{inc}. The time stepping process is stopped when the actual number of time steps exceed this specified value.

The convergence of the iteration process needs to be controlled by at least two criteria, the norm of the unbalanced force and the norm of the unbalanced flow of pore fluid out of the mesh. In addition one can also use criteria for changes in the displacement and pore pressure field. The iteration process is then stopped based on input of tolerance factors and a maximum allowed number of iteration within a time step.

This is one alternative procedure for automatic time stepping. Another procedure is for instance described in Sloan and Abbo (1997).

A critical minimum time step to be applied in order to secure stability in the solution process is for instance investigated by Vermeer and Verruijt (1981).

For a consolidation element with bi-linear interpolation functions for the pore pressure and 2nd order interpolation functions for the displacements, the minimum time step is recommended to be larger than:

$$\Delta t_{\min} \geq \frac{l^2}{3\theta c_v} \tag{13}$$

where l is the element length toward a drainage boundary (or a very permeable soil layer), c_v ($= M \cdot k / \gamma_w$) is the average coefficient of consolidation during the time step, and θ is the time integration factor. However, in order to avoid unrealistic initial changes in the pore pressure field it is recommended that the first time step is even larger than the above critical time step.

If the time step is smaller the pore pressure at the distance l from the drainage boundary may in the first step become larger than the correct solution.

4 CONSIDERED SOLUTION STRATEGIES

The following solution strategies are considered in this study:

- Optimum varying large time steps where each time step is increased such that the calculated error of the settlement curve is equal to or less than a) 3% of the "exact curve". Both a time integration factor of θ = 1 (backward Euler) and θ = 0.5 (Crank-Nicolson) are considered. Due to changes in the time increment the global system matrix $\mathbf{G}$ is updated and factorized at the beginning of each time step.
- Sequences (parcels) of constant time increments. The time step is automatically updated when the maximum pore pressure change in a time step becomes lower then a specified value. The global system matrix $\mathbf{G}$ is updated and factorized only when the time increment is changed.
- Initial global system matrix together with optimum varying large time steps. The initial global system matrix $\mathbf{G}_0$ is calculated using the maximum time increment in the time stepping process and the maximum stiffness of the soil during the consolidation process (here the initial stiffness). $\mathbf{G}_0$ is then factorized only once. The field equations are satisfied by iterations (corrector phase). The first trial solution for each time step is based on the solution using the initial global system matrix. This predictor will overestimate the displacements and pore pressure changes.

5 EXAMPLE STUDY

5.1 Considered problem

The consolidation settlement of an idealized problem is analysed in order to compare the different solution strategies presented in Section 4. The problem consists of a 35 m thick slightly over-consolidated clay (OCR=1.4) below a 5 m thick sand layer. The ground water table (GWT) is at the soil surface. The properties (effective unit soil weight γ', oedometer

modulus M before (oc) and after (nc) the pre-consolidation pressure σ'_{vc} and the permeability k) are presented in Figure 2.a. Both a surface load of 10 kPa (linear elastic problem) and 100 kPa (non-linear) are considered. In reality is the load applied over a limited area (10 m x 10 m), but for the purpose of this study it is for simplicity applied over the entire surface.

The element mesh used in the analyses is shown in Figure 2.b. The mesh consists of 13x13x18=3042 20-node consolidation element with pore pressure degree of freedom only in the corner nodes. The number of equation is then 41400.

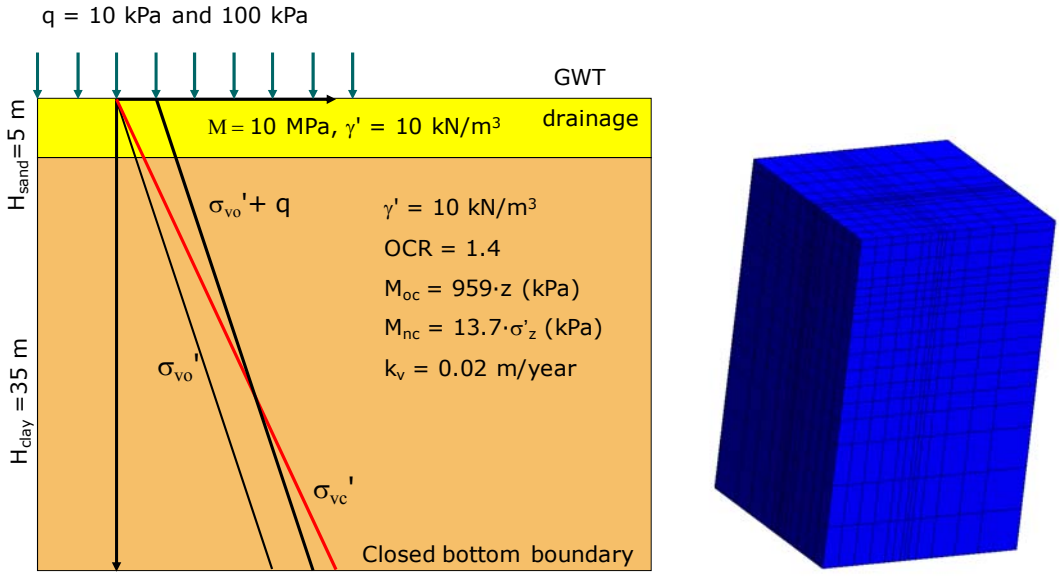

Fig. 2. a) Sketch and b) finite element mesh (number of degrees of freedom=41400) of the example problem considered in the analyses

Figures 3 and 5 present the calculated settlement curves of the reference ('exact') solution and the different solution strategies for a surface load of q = 10 and 100 kPa, respectively. It can be seen that all curves lie within the required 3% tolerance.

Figures 4 and 6 present the cumulative equivalent back-substitution times of the different solution strategies for a time of factorisation to time of back-substitution ratio of $t_{fac}/t_{bs} = 482$ and for elastic and non-linear loading ranges of q = 10 and 100 kPa, respectively. The equivalent back-substitution time is calculated using:

$$t_{eq}^{cum} = n_{bs} + (t_{fac}/t_{bs}) \cdot n_{fac} \tag{14}$$

where, n_{bs} and n_{fac} are the actual number of back-substitutions and factorizations, respectively. Using the relation given in Section 3.3, the ratio of the factorisation to back-substitution time is estimated to be, $t_{fac}/t_{bs} = 0.0116 \cdot n_{eq} = 482$.

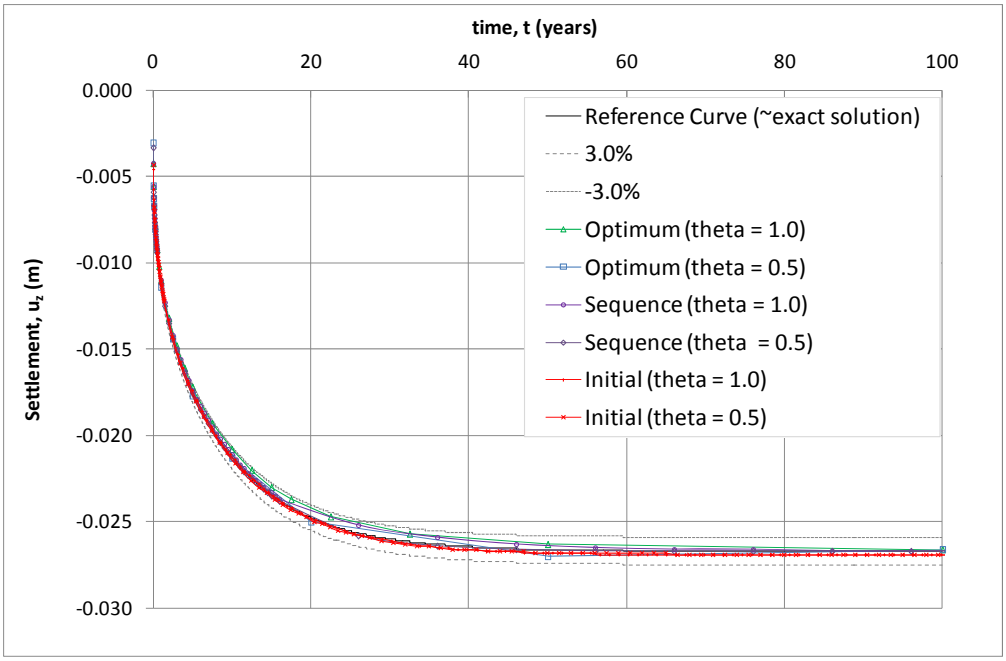

Figure 3. Settlement curves of different solution strategies (q=10kPa, linear elastic problem)

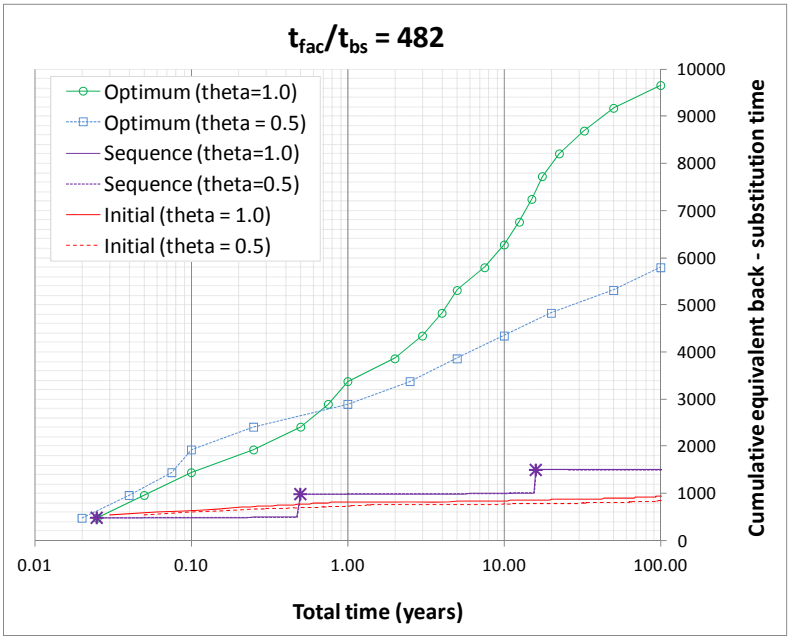

Fig. 4. Cumulative equivalent back-substitution times of the different solution strategies for the elastic loading range, q = 10 kPa for t_{fac}/t_{bs} = 482 (the factorisations are indicated by markers)

It can be seen from Figures 4 and 6 that the calculation time is reduced by a factor of ~5 to 11 due to reduced number of factorisations. The optimum strategy for both elastic and non-linear loading levels is the initial stiffness method. Sequential update of the global system matrix also reduces the calculation time considerably. As can be expected (Figure 1), the gain in calculation time increases with increasing number of equations (problem size).

The initial stiffness method can be further optimised by considering sequential updates.

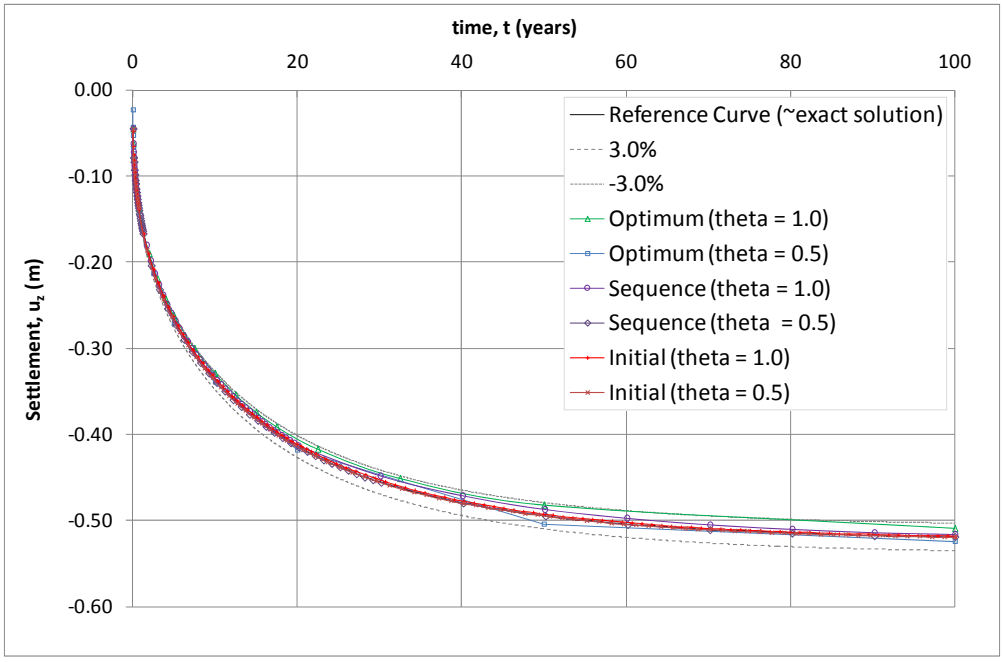

Fig. 5. Settlement curves of different solution strategies (q=100 kPa, non-linear problem)

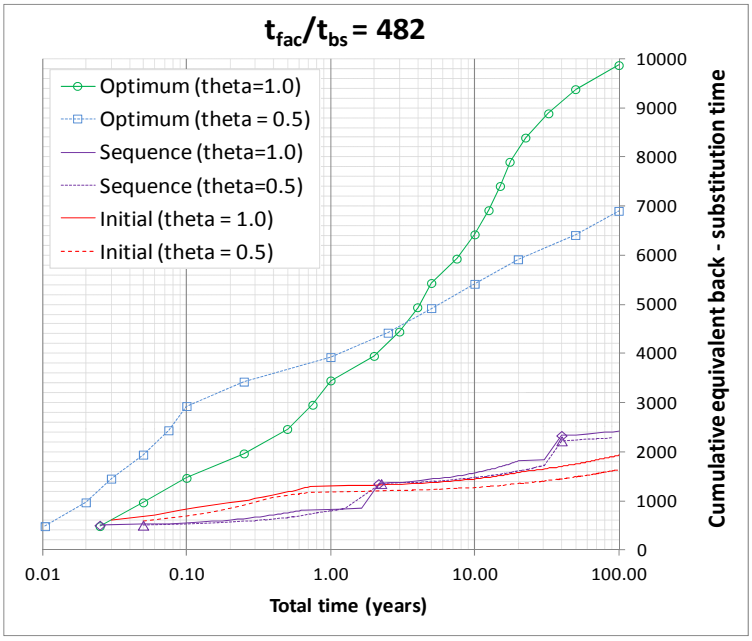

Fig. 6. Cumulative equivalent back-substitution times of the different solution strategies for the non-linear loading range q = 100 kPa for t_{fac}/t_{bs} = 482 (the factorisations are indicated by markers)

Table 1. Summary of calculation parameters of different solution strategies for linear elastic problem

Load = 10 kPa (elastic range)							
Solution Strategy	θ	number of steps	number of factorisations	number of iterations	number of back-substitutions	Normalised time for t_{fac}/t_{bs} = 100	Normalised time for t_{fac}/t_{bs} = 500
		n_{fac}	n_{step}	n_{iter}	n_{bs}	$=n_{fac}+n_{bs}/100$	$=n_{fac}+n_{bs}/500$
Optimum	1.0	20	20	-	20	20	20
Optimum	0.5	12	12	-	12	12	12
Sequences	1.0	60	3	-	60	3.6	3.1
Sequences	0.5	60	3	-	60	3.6	3.1
Initial	1.0	127	1	456	456	5.6	127.9
Initial	0.5	103	1	303	303	4.0	103.6

Table 1. Summary of calculation parameters of different solution strategies for non-linear problem

Load = 100 kPa (Non – linear range)							
Solution Strategy	θ	number of steps	number of factorisations	number of iterations	number of back-substitutions	Normalised time for t_{fac}/t_{bs} = 100	Normalised time for t_{fac}/t_{bs} = 500
		n_{fac}	n_{step}	n_{iter}	n_{bs}	$=n_{fac}+n_{bs}/100$	$=n_{fac}+n_{bs}/500$
Optimum	1.0	20	20	228	228	22.3	20.5
Optimum	0.5	14	14	154	154	15.2	14.3
Sequences	1.0	73	3	969	969	12.7	74.9
Sequences	0.5	61	3	842	842	11.4	62.7
Initial	1.0	125	1	1444	1444	15.4	127.9
Initial	0.5	87	1	1147	1147	12.5	89.3

6 CONCLUSIONS

A solution strategy that reduces the computer time for typical 3D FE consolidation analyses are considered in this study. For this type of problems the computer time is generally governed by the time used to solve the global equation system. In commercial software programs the global system matrix is generally established and solved in each step. This means that the equation system is solved (factorized) from 10 to more than 100 times. A more optimal solution strategy is therefore to reduce the need for updating the global system matrix to some few times and instead increasing the number of required time steps and iterations.

The benefit of this solution strategy increases with increasing number of degree of freedoms in the mesh.

In the example problem containing about 40 000 equations (unknown degrees of freedom), it was shown that the global system matrix can be updated only three times and still obtain a solution with only maximum 3% error. Due to a significant reduction of computational effort (e.g. factorizing the global system matrix 3 times instead of for instance 20 times), the calculation time was reduced by a factor of more than 5. The solution can be further optimised by using an initial stiffness method (described as solution strategy 3 in Section 4) together with sequential updates of the global system matrix.

In this study, the effect has been studied using a direct solver without parallel processing. The conclusion may therefore be somewhat different with other equation solvers.

ACKNOWLEDGEMENT

This study is part of the GeoFuture project (2012-2015) funded by The Research Council of Norway. The project consortium also sponsoring the project, is led by NGI and assembles Sintef Building and Infrastructure, the Norwegian University of Science and Technology (NTNU), the Norwegian Public Roads Administration, the Norwegian National Rail Administration, GeoVita AS, Multiconsult AS, Norconsult AS, Skanska AS and ViaNova Systems AS from Norway, and ViaNova GeoSuite AB and AG Programutveckling Ekonomisk förening (AGEF), both from Sweden.

REFERENCES

Borja, R. I. (1989), "Linearisation of elasto-plastic consolidation equations", Eng. Comput. 6, 163-168.

Dhatt, G. And Touzot, G. (1984), The Finite Element Method Displayed, Wiley and Sons, Inc. Chichester.

Lewis, R.W., Roberts, G.K. and Zienkiewicz, O.C. (1976), "A nonlinear flow and deformation analysis of consolidated problems", Proc. of 2nd Int. Conf. on Numerical Methods in Geomechanics, ASCE, New York.

Lewis, R.W. and Schrefler, B.A. (1987), The finite-element method in the deformation and consolidation of porous media, Wiley, Chichester.

Mesri, G. and Choi, Y.K. (1985), "Settlement analysis of embankments on soft clays", J. Geotech. Eng., ASCE, 111, 4, 441- 464.

Nash, D.F.T. and Brown, M.A. (2013), "The Influence of Destructuration of Soft Clay on Time-Dependent Settlements — A Comparison of Some Elastic Visco-Plastic Models." Int. J. Geomech., 10.1061/(ASCE) GM.1943-5622.0000281.

Potts, D. And Zdravkovic, L. (1999), Finite element analysis in geotechnical engineering: Theory, Thomas Telford, London.

Prevost, J. H. (1982), "Nonlinear transient phenomena in saturated porous media", Comput. Meth. Appl. Mech. Eng., 20, 3-18.

Sloan, S.W. & Abbo, A.J. (1997), "An automatic time stepping scheme for elastic and elastoplastic consolidation. Part 1: Theory and implementation", Int. J. Numer. Anal. Meth. Geomech., 492.

Vermeer, P.A. and Verruijt, A. (1981), "An accuracy condition for consolidation by finite elements", Int. J. Numer. Anal. Meth. Geomech., 5, 1-14.

NUMERICAL ANALYSIS OF TORPEDO ANCHORS

H. Sabetamal, M. Nazem, and J.P. Carter

ARC Centre of Excellence for Geotechnical Science and Engineering, The University of Newcastle, Newcastle, NSW, Australia

ABSTRACT: *This paper presents the development of a numerical framework based on the finite element method and its application in the analysis of torpedo anchors. The procedure is based on a mixture theory for the dynamic behaviour of saturated porous media. The nonlinear behaviour of the solid phase of soil is represented by the Modified Cam Clay material model and the interface between the soil and the structure is modelled by a mortar segment-to-segment frictional contact method. An Arbitrary Lagrangian-Eulerian (ALE) method is adopted to avoid mesh distortion throughout the numerical simulation. The generalised-α method is utilised to integrate the governing equations of motion in the time domain. Results obtained from the installation phase of a torpedo anchor reveal that the anchor decelerates at a constant rate during most of its penetration. Analysis results show a typical distribution of excess pore-water pressure during free falling installation, having higher magnitudes at the face and lower magnitudes along the shaft. The computational results for the setup phase indicate that for soil elements located within a radial distance of approximately one diameter from the centreline of the torpedo, 90% of consolidation takes place in a few days after installation, depending on the value of soil permeability.*

1 INTRODUCTION

Torpedo anchors have proven to be promising systems for anchoring taut mooring lines of floating offshore oil and gas exploration and production units due to their relatively easy installation process. The kinetic energy of a torpedo anchor attained by gravity throughout free fall through the water column provides the required dynamic penetration force, making it much more practical and cost-effective than other offshore structures such as suction piles, driven piles, drilled and grouted piles, and drag embedment anchors. The torpedo usually consists of a pipe pile (12 to 18m in length, 0.76 to 1.07m in diameter) filled with scrap metal and concrete, close ended and fitted with a conical tip and sometimes including fins at the top end which provide stability during free fall. The impact velocity of the torpedo piles reported by Medeiros (2002) varied between 10 to 22 m/sec, for hanging heights from which free fall commenced between 30 to 150 m as measured from the seabed, and the penetration depth usually varied between 8 m and 22 m.

The first step in the analysis of a torpedo anchor involves simulation of the installation phase in order to predict the penetration depth, soil resistance, and the development of excess pore water pressure. However, in the majority of research works devoted to the analysis of deep penetration anchors (DPA) the effect of installation on pullout or lateral capacity of the anchor is ignored. In other words, in most analyses conducted to date deep foundation systems are whished in place, with no effort to model the installation phase and hence a

perfect interface between the anchor system and the surrounding soil is assumed. The initial stress state of the soil is normally estimated based on the submerged unit weight, the lateral earth pressure coefficient at rest, and assumes zero excess pore-water pressure. Estimation of penetration depth of the anchor usually relies on the theoretical framework developed by True (1976).

Sturm and Andresen (2010) presented a finite element model for torpedo anchors using the commercial software package Abaqus, with a user defined contact algorithm and an Updated Lagrangian (UL) formulation. However, they simulated the installation process quasi-statically with a constant penetration rate and neglecting any inertia effects. They used the Tresca material model to simulate soil behaviour and evaluated the excess pore pressure using knowledge of the mean stress distribution and shear strain in the soil. Raie (2009) developed an alternative procedure based on Computational Fluid Dynamics (CFD) to predict the embedment depth as well as the installation effects, including shear distributions on the soil-anchor interface and the soil state parameters. This method is based on the principles of fluid dynamics where stress at any point of the media is equal to the pressure at that point independent of the direction, i.e., the vertical and horizontal stresses on soil elements are assumed to be identical, with this being an unrealistic assumption for soil.

The second stage in the simulation of torpedo anchors is the 'set up' analysis. With knowledge of the effective stresses and the excess pore water pressures, the set up analysis can be performed by reconsolidation of the soil in the vicinity of the anchor. In DPA systems excess pore pressure is generated due to two main factors: shearing of soil during installation and increase in total stress due to the vertical and mostly radial soil volume changes. The excess pore water pressures result in lower frictional resistance, which leads to lower pullout capacity of the anchor. As the soil consolidates, the pullout capacity of the anchor increases due to dissipation of excess pore water pressures and corresponding increases with time of the effective stresses.

The third and final step of the analysis includes estimation of the pullout capacity of the anchor. The finite element method (FEM) and the API (American Petroleum Institute, 2002) method are the two common techniques for estimating the holding capacity of torpedo anchors. The API method takes advantage of the conventional theory of pile bearing capacity based on the total stresses, and predicts the undrained holding capacity of DPA in cohesive soils. Randolph *et al.* (2005) applied this method to estimate the capacity of anchors embedded in calcareous sand. Richardson *et al*. (2009) employed the API method to study the skin friction ratio and fluke effects on the holding capacity by comparing its results with experimental results obtained by centrifuge tests. Modelling the soil as a Drucker-Prager material and assuming the anchor to be "wished in place", Sousa et al. (2010) employed the FEM to evaluate the long term load capacity of a typical torpedo anchor subjected to vertical and inclined loads.

A brief survey in the literature reveals that the analysis of dynamically penetrating objects needs further research to realistically model and evaluate their behaviour. Most available studies are based on experimental or approximate analytical solutions, and the current FEM simulations are generally based on a displacement formulation (neglecting the pore water pressures) and consider simplifying assumptions in the modelling. A more realistic model must incorporate pore fluid pressure development along with deformations, velocities and accelerations to facilitate a thorough understanding of soil response. Moreover, by providing the initial undrained or partially drained distributions of pore pressure, subsequent dissipation can be investigated. Such problems require a fully coupled analysis that takes into account the interaction between soil and pore fluid by incorporating the effect of the transient flow of the pore fluid through the inter-connected voids of the solid skeleton.

In this paper, a computational framework based on the FEM is developed and employed to simulate torpedo anchor systems. The procedure is based on a mixture theory for the

dynamic behaviour of saturated porous media. The nonlinear behaviour of the solid phase of soil is represented by the Modified Cam Clay material model and the interface between the soil and the structure is modelled by a mortar segment-to-segment frictional contact method. The Arbitrary Lagrangian-Eulerian (ALE) method is adopted to avoid mesh distortion throughout the numerical simulation. The generalised-α method is utilised to integrate the governing equations of motion in the time domain. Energy absorbing boundaries are used to model the radiation of waves towards infinity at the truncated finite element mesh boundaries. An automatic time stepping procedure for the dynamic consolidation algorithm is also employed to increase the efficiency of the method. In the following, we briefly explain the governing equations, the time-integration method, energy absorbing boundaries, modelling of contact, large deformation, and the strategy of mesh refinement. Then, a numerical example is presented to illustrate the effectiveness and utility of the proposed approach. Note that for brevity we only consider the analysis of the installation phase and the subsequent consolidation phase in this paper. The analysis of pullout behavior will be the subject of future studies.

2 FINITE ELEMENT FORMULATION

A saturated porous medium can be considered as a two phase mixture composed of a solid constituent as well as a fluid constituent in which the two phases in the assemblage interact with each other and affect the overall behavior of the medium. Here, a continuum approach based on the theory of mixtures (Truesdell & Touppin, 1960) is employed to derive the governing equations using the concept of volume fraction (Morland, 1972). The resulting equations guarantee the fulfillment of the local balance relations, for each individual constituent, as well as the balance relations of the entire mixture. The global finite element equations for a two phase saturated porous media might be written in the following matrix form

$$\begin{bmatrix} \mathbf{M}_s & 0 \\ \mathbf{M}_f & 0 \end{bmatrix} \begin{Bmatrix} \ddot{\mathbf{U}} \\ \ddot{\mathbf{P}} \end{Bmatrix} + \begin{bmatrix} \mathbf{C}_s & 0 \\ \mathbf{L}^T & \mathbf{S} \end{bmatrix} \begin{Bmatrix} \dot{\mathbf{U}} \\ \dot{\mathbf{P}} \end{Bmatrix} + \begin{bmatrix} \mathbf{K}_{ep} & \mathbf{L} \\ 0 & -\mathbf{H} \end{bmatrix} \begin{Bmatrix} \mathbf{U} \\ \mathbf{P} \end{Bmatrix} = \begin{Bmatrix} \mathbf{F}^u \\ \mathbf{F}^p \end{Bmatrix} \tag{1}$$

where $\mathbf{U}$, $\dot{\mathbf{U}}, \ddot{\mathbf{U}}$ and $\mathbf{P}$ denote the vectors of displacement, velocity, acceleration and pore water pressure, respectively, and $\mathbf{M}_s$, $\mathbf{M}_f$, $\mathbf{C}$ and $\mathbf{K}_{ep}$ are the solid mass, fluid mass, damping, and stiffness matrices, respectively. $\mathbf{L}$, $\mathbf{H}$, and $\mathbf{S}$ represent, respectively, the coupling matrix, the fluid flow matrix, and the compressibility matrix, and $\mathbf{F}^u$ and $\mathbf{F}^p$ are the vectors of external nodal forces. The system of second-order ordinary differential equations in (1) is usually solved using direct time integration methods. The selected time integration scheme should possess some form of numerical dissipation capability to attenuate the high frequency modes. Meanwhile, it should also allow the accurate capture of the low frequency behaviour of the system, so that it appears in the solution without attenuation. Among the various implicit time integration schemes we have used the generalised-α method, knowing that it is a second order accurate scheme and preserves the accuracy while providing the requisite numerical damping. In addition, it allows the analyst to control the amount of numerical dissipation at high frequencies.

The analysis of a torpedo anchor comprises a rapid installation phase as well as a subsequent consolidation phase in which the first phase requires relatively small time increments (to capture the rapid dynamic response) in comparison with the second phase which demands larger time steps. Typically, the size of the time steps in the consolidation phase can be up to 10,000 larger that the size of the increments in the installation phase. Therefore, an important characteristic of an efficient time stepping method is to adaptively choose small increments in the transient phase, while increasing the size of time steps as the

solution becomes smoother in the second phase. To devise such an automatic time stepping scheme, we use two different local truncation error estimators. One of the error estimators is based on Taylor's series and the other one takes advantage of a family of 4 stage-one step algorithms of Thomas and Gladwell (1988). A number of coarse time steps are defined at the beginning, which are then automatically sub-incremented into a number of smaller time increments if necessary. In order to increase the time increments, the estimated error has to be smaller than a percentage of a user defined tolerance. If the error is larger than this quantity, but smaller than the tolerance, the time increment will be held constant to minimise the number of rejected time sub-increments.

3 INTERFACE MODELLING

The so called node to segment (NTS) discretisation method is widely used to analyse large sliding and large deformation problems of contact mechanics. However, it has been highlighted that this approach cannot pass the contact patch test (Papadopoulos & Taylor, 1990), as coupling with higher order elements is not feasible without losing accuracy of displacements and stresses in the contact area. This can be a particular disadvantage in soil mechanics where higher order shape functions are often used to improve the accuracy and to avoid mesh locking. Oscillation of the contact force predicted by the NTS technique due to the non-smooth surface of the low order elements is another deficiency of this method. In order to overcome these issues, the mortar segment to segment approach has been developed which allows the interpolation functions of the contact elements to be of order *n*. (Wriggers, 2006). We use a contact algorithm based on the mortar method to model soil structure interactions in the torpedo problem. The interactions at a frictional contact interface for a two phase saturated porous media generally arise from the contact traction as well as the fluid flow. Therefore, when contact occurs between two deformable bodies, constraints have to be established to fulfill the continuity of the contact traction as well as the fluid flow across the interface. This means that in addition to applying constraints on displacements, two other constraints on the Darcy velocity and the pore fluid pressure must be enforced in order to guarantee, respectively, the linear momentum balance of the fluid phase and the conservation of mixture mass. In a frictional contact element, two conditions, stick and slip, are distinguished on the basis of the level of interface frictional force in comparison with the Coulomb's frictional force represented by

$$f_s = \|\mathbf{t}_T\| - \mu |t'_N| \tag{2}$$

where $\mathbf{t}_T$ and t'_N are, respectively, tangential and normal effective stress components of the total traction at the contact interface, and μ denotes the friction coefficient at the interface. In order to differentiate between stick and slip cases, we use the concept of a moving cone (Wriggers, 2006), which is a relatively efficient methodology in deriving the contact kinematics. For the coupled consolidation formulation presented in Section 2, Darcy's velocity does not appear explicitly in the formulation, so that pore pressures at the points of contact are used to derive the corresponding normal effective stress. Meanwhile, a constraint is applied to fulfil the balance condition of the pore pressure at the contact interface where necessary. Furthermore, the penalty method is used to enforce the contact constraints.

4 ABSORBING BOUNDARY

Another challenge in dynamic FE analyses is to cope with spurious wave reflection from artificial boundaries of the problem domain. Due to the fairly high wave velocity in soils and rocks, modelling a large portion of the domain does not seem to be an effective way to

proceed as the waves reflected from the boundaries will probably have enough time to return to the area of interest. Therefore, absorbing boundary conditions should be facilitated to absorb the outgoing waves. Generally, two types of bulk waves, including the dilatational waves (P- waves) as well as the shear waves (S- waves), appear in a saturated porous media (Biot, 1956). The dilatational waves can be decoupled into two waves, P1 and P2. The P1 waves propagate faster and attenuate slower compared to the P2 waves, known as Biot's slow wave. Shear waves are transmitted only in the solid constituent and are mainly governed by its shear stiffness while the propagation of acoustic waves essentially depends on the frequency of excitation, the hydraulic permeability and the mechanical properties of the constituent materials (Corapcioglu &Tuncay,1996; Straughan, 2008). For the dynamic problems concerned in this study, two types of the bulk waves, viz., P2 waves and S waves are predominant. This is mainly due to the conditions of low-frequency excitations and the relatively low permeabilities present in the problem. Under such circumstances, very low relative motions between the solid matrix and the viscous pore fluid are likely and body waves are mostly transmitted via the structure of the solid skeleton. Hence, a local transmitting boundary such as the standard viscous boundary of Lysmer & Kuhlemeyer (1969) can be utilised to ensure the absorption of the arriving elastic energy. However, as the standard viscous boundary embodies no static stiffness, it is not able to model a static problem and rigid body movement would occur for low frequencies. Alternatively, we use the cone boundary of Kellezi (2000) which consists of both dashpots and springs. The stiffness of the springs varies linearly along each boundary based on the radial distances of the boundary node from the source of excitation.

5 LARGE DEFORMATION AND MESH REFINEMENT

Penetration problems involve large deformations as well as rigid body rotations, which affect the soil stiffness and its permeability, and such special effects may not be simply disregarded in the analysis. The theory of large deformation has widely been used in the framework of the FEM to analyse large deformation problems of geomechanics on the basis of Lagrangian approaches. The effects of material and geometrical nonlinearities in the theory of consolidation were first presented by Small et al. (1976) and Carter et al. (1979), respectively. Dynamics of porous media at finite strain has also been elaborated and applied by others based on the theory of mixture (e.g., see Chao et al, 2004). The Updated-Lagrangian (UL) method is a more prevalent approach in handling geometrical nonlinearities comparing to the Total-Lagrangian (TL) method, especially where contact kinematics are invoked and formulated, since the UL methodology uses the last equilibrium configuration to evaluate the state variables. However, the Lagrangian methods are prone to failure and numerical errors where the finite element mesh undergoes excessive distortion, and are more likely to end up with a negative Jacobian of an individual element. This is due to the fact that the motion of the body and the mesh are the same in the Lagrangian approaches, viz., a given node remains coincident with the same material point throughout the analysis. However, numerical difficulties associated with excessive element distortion can be circumvented by combining the merits of the UL method and an Eulerian approach. In the literature, this strategy has provided two similar methods known as the Arbitrary Lagrangian-Eulerian (ALE) method and the Coupled Eulerian Lagrangian (CEL) method. In this study, we use the ALE technique and the mesh refinement strategy presented by Nazem et al. (2006) and Nazem et al. (2008). In this method the analysis comprises two steps; an UL step in order to obtain the material displacements, and an Eulerian step to find the mesh displacements. The separation of grid and material displacement and solving them in two different steps is usually referred as the decoupled ALE method. Following these steps, mesh refinement is performed and then all kinematic and static variables are transferred between the two meshes.

6 NUMERICAL EXAPMLE

The computational scheme explained here has been implemented into SNAC, a finite element code developed over many years by the geomechanics group at the University of Newcastle, Australia. SNAC was used to analyse the free falling penetration of a rigid finless torpedo anchor into a saturated soil layer. The aim of the analysis was to study the total penetration depth of the anchor, the mobilised soil resistance, the deceleration characteristics of the anchor during its installation phase, generation of the excess pore-water pressures in the surrounding soil, and its subsequent dissipation.

6.1 The installation of a torpedo anchor.

The geometry of the torpedo anchor, the finite element mesh containing 3433 axisymmetric triangular elements and 7079 nodal points, the boundary conditions, and the soil properties are presented in Figure 1. The material properties shown in Figure 1 are defined as K_0: the coefficient of earth pressure at rest, λ: the slope of the normal compression line (NCL) in the space of the logarithmic mean stress ($\ln p'$) versus the void ratio e, κ: the slope of the unloading-reloading line in the $\ln p' - e$ space, e_0: the intercept of the NCL on the e axis when $\ln p' = 0$, OCR: the over-consolidation ratio of the soil, ϕ': the drained friction angle, ν': the Poisson's ratio, k: the coefficient of permeability, and γ: the unit weight of the soil. The radial thickness of the soil elements underneath the anchor is equal to a third of the anchor shaft radius. The submerged weight of the anchor, W, its diameter, D, and its length, L, are assumed to be, respectively, 40 kN, 0.6 m, and 6.8 m. To avoid further material nonlinearity, the shear strength increase due to strain rate effects has been ignored in this example. The use of the mortar type method in the finite element contact model facilitates a curved surface between the torpedo and the soil due to quadratic shape functions. Therefore, the finite element discretisation of the pile does not include any sharp corners, thus reducing the numerical oscillations in the soil response. The coefficient of friction at the interface, μ, is 0.20 and a penalty parameter equal to 1×10^6 is used to enforce the contact constraints. The Modified Cam Clay soil model with a rounded Mohr Coulomb failure surface in the deviatoric plane was utilised to study the dynamic soil response. The plastic flow was governed by an associated flow rule and, for the stress states that are not at the critical state, plastic straining entails volumetric hardening of the material.

The simulation was started by applying a body force loading due to the self-weight of the soil. Then an overburden pressure of p_0 = 50kPa was applied to the surface of the soil layer over a long period of time to allow dissipation of excess pore pressures. After generating a non-zero stress field, the location of the yield surface at each integration point in the finite element mesh was adjusted according to the initial effective stresses and the value of the overconsolidation ratio (OCR). Finally, the torpedo was deployed and allowed to impact the soil vertically at an initial velocity of 15 m/sec, noting that the impact velocity is assumed to be less than its terminal velocity in water.

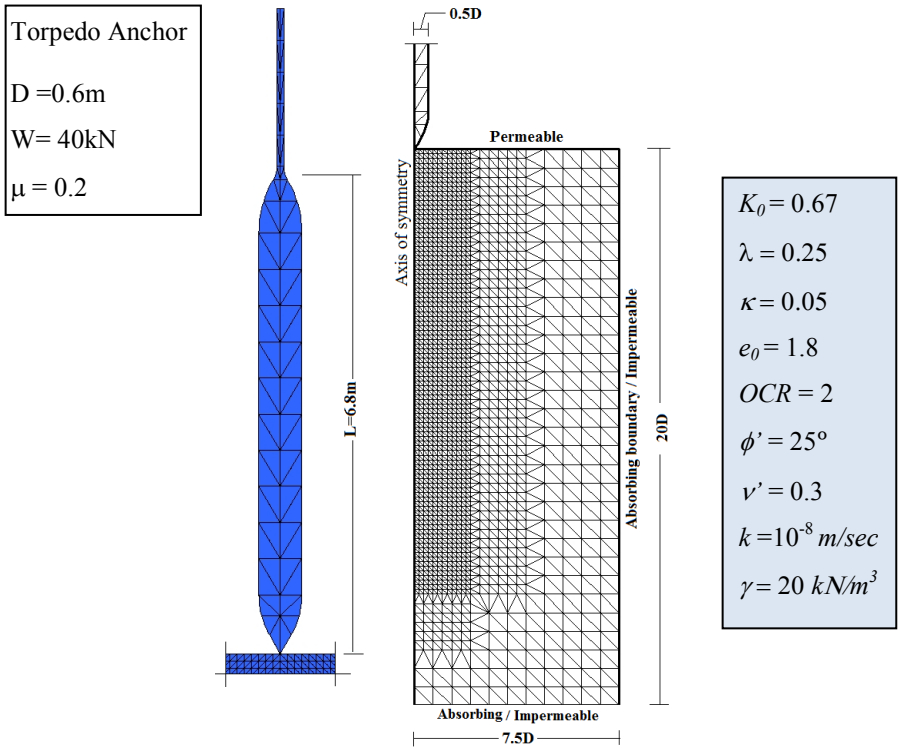

Figure 1. Finite element model of torpedo anchor

The predicted total dynamic soil resistance versus penetration, normalised by D, is plotted in Figure 1. According to Figure 1, the predicted response is reasonably free of oscillation. The energy absorbing boundaries, the numerical damping of the time-integration algorithm and, more importantly, incorporation of higher order mortar contact elements have all contributed to obtaining such a smooth curve. Numerical analyses have shown that smoothing the torpedo surface via the use of higher order contact elements probably makes the major contribution in decreasing these oscillations, while the effect of absorbing boundaries is further manifested when the analysis proceeded to the consolidation stage.

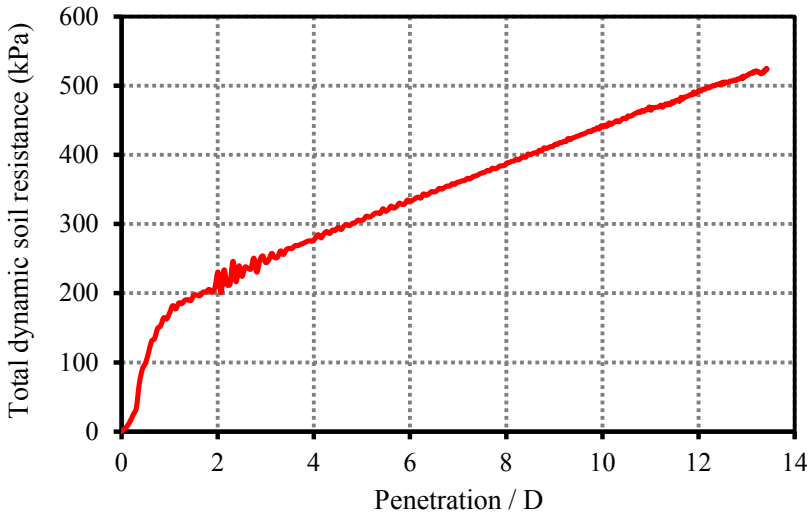

Figure 2. Total dynamic soil resistance profile

The deceleration characteristics of the torpedo can be investigated by plotting the velocity variations versus time, as depicted in Figure 3a, as well as by plotting velocity variations versus normalised penetration depth, as shown in Figure 3b. It is observed that the torpedo slightly accelerates at the early stages of penetration, mainly due to two reasons; (a) the sum of soil resistance and the frictional forces at the interface between the soil and torpedo is initially less than the weight of the torpedo, (b) the impact velocity of torpedo is less than its terminal velocity in water, allowing the torpedo to continue to accelerate even after the initial impact. The torpedo then starts to decelerate at an approximately linear rate, as shown in Figure 3a. This trend is consistent with the soil resistance profile plotted in Figure 2. Figure 3b indicates that the deceleration occurs after the torpedo has penetrated ~0.5D into the soil layer, and the predicted depth of installation is 13.4D.

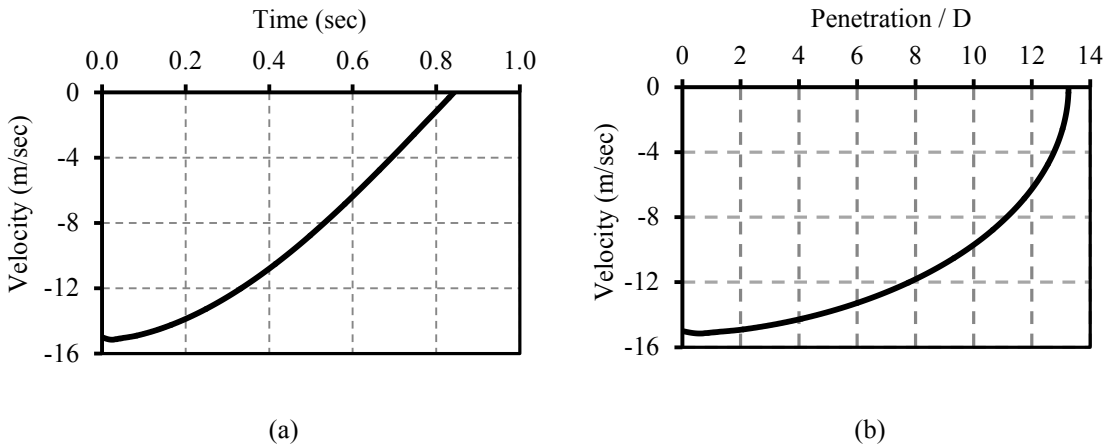

Figure 3. a- Velocity versus penetration; b - Velocity versus normalised penetration

5.2 Pore pressure generation and dissipation

To investigate the generation of excess pore pressures, we monitor the development of excess pore pressures at seven different points, located at depth of 5D and radial distances of 0.0, 0.17D, 0.33D, 0.5D, 0.67D, 1.5D, and 4.0D, throughout the installation process. The excess pore pressures developed at these seven points are plotted versus time in Figure 4, noting that the total installation time is 0.85 s. According to this figure, the excess pore water pressures experience a relatively steady state following a peak value in each case. Typically, the magnitude of excess pore water pressure at a point in the soil increases as the pile advances towards it, but once the pile passes that location the magnitude decreases sharply, and approaches the steady state value. The sudden drop in the excess pore water pressure is significant for the soil elements located within a radial distance of 1D from the pile shaft. It is also observed that the installation of pile only influences a region ~3D in the radial direction and ~1D in the vertical direction, measured from the pile tip. A contour plot of the excess pore water pressures developed at the end of pile installation is depicted in Figure 5.

When the full embedment depth is achieved and the torpedo comes to rest, the computational process automatically proceeds to the setup analysis and consolidation of the soil is permitted. The adopted automatic time stepping algorithm chooses very small time steps at the beginning of the set up analysis when high pore water pressure gradients occur, and then it gradually increases the time steps based on the estimated errors.

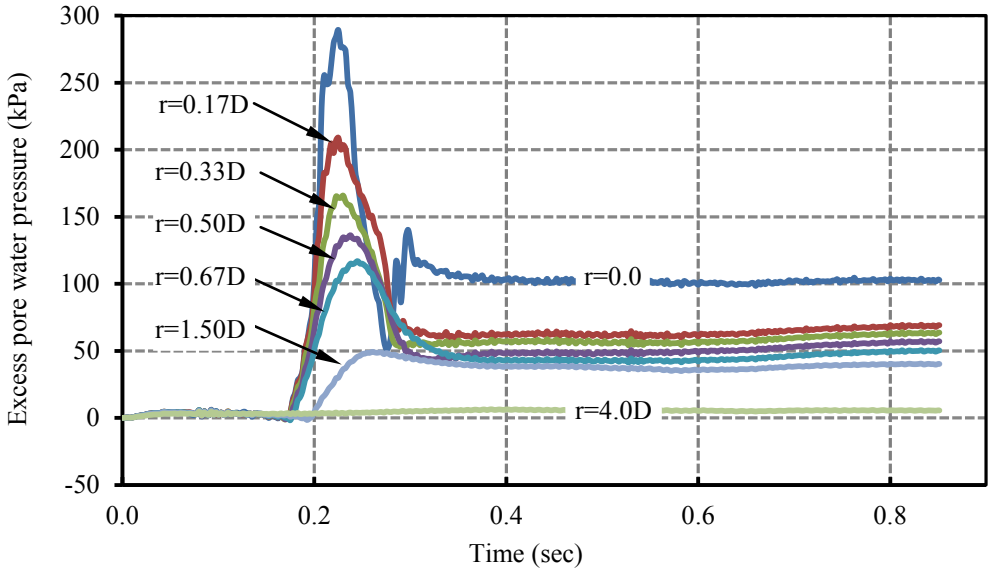

Figure 4. Excess pore water pressure evolution at depth 5D throughout the installation phase

This process is continued until the generated excess pore water pressures dissipate entirely. Figure 6 depicts the dissipation curves for the soil elements located at depth of 5D and different radial distances measured from the pile tip. It is observed that a degree of consolidation of 90% (the degree of consolidation is equal to 1 minus the ratio between the current excess pore water pressure and the initial excess pore water pressure) for elements within 1D radial distance from the torpedo shaft is achieved 13~33 days after installation. The same degree of consolidation takes place within 33~72 days for elements between 1D and 1.83D. Figure 6 also shows that a degree of consolidation of ~96% is attained for the entire affected zone at depth 5D after ~260 days. It is concluded that the most of the pullout capacity of the torpedo anchor (soil resistance) is available much earlier than the completion of consolidation as the most of the excess pore pressure dissipates within a matter of days or weeks.

7 CONCLUSION

A fully coupled dynamic consolidation procedure for analysing torpedo anchors, taking into account inertia effects, large deformation and the flow of pore water through the soil, was presented in this study. The evolution of soil resistance as well as the development of excess pore water pressures in the saturated soil due to the free falling penetration of a torpedo anchor was studied. The nonlinear behaviour of the solid soil skeleton was predicted by the Modified Cam Clay (MCC) soil model, and the mortar frictional contact method was used to model soil-structure interaction. The numerical results showed that for the lightly over consolidated soil simulated by the MCC material model, excess pore water pressures are generated in the soil surrounding the pile tip and its shaft. The magnitude of excess pore water pressure first increases when the pile tip is above or at the level of the point of interest in the soil, then decreases once the pile tip has moved below the evaluation point, and finally approaches a steady value at the end of the installation phase.

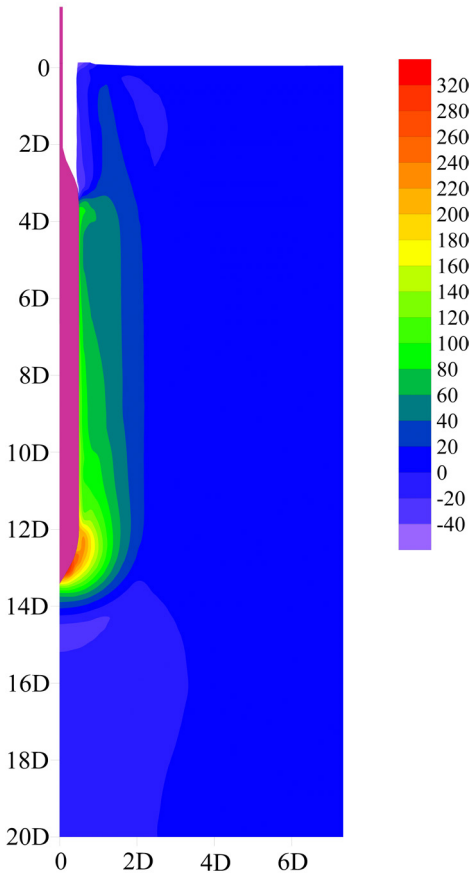

Figure 5. Excess Pore-water pressure contour at the end of installation

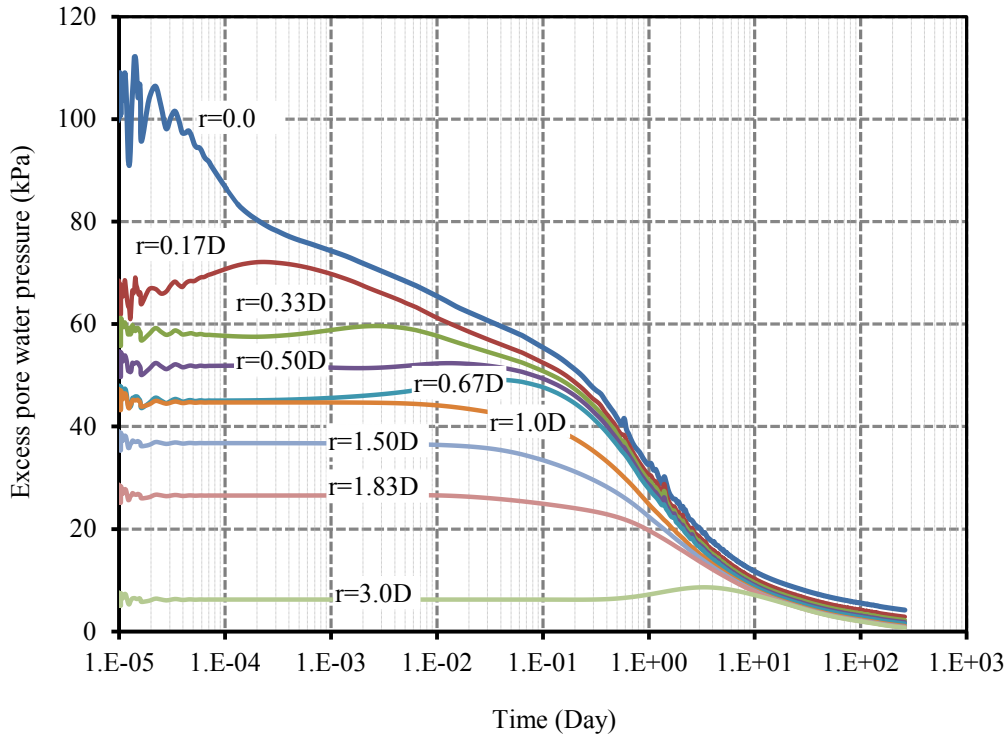

Figure 6. Excess pore water pressure dissipation versus time for elements at depth 5D

REFERENCES

API RP 2A, (2002), Recommended Practice for Planning, Designing and Constructing Fixed Offshore Platforms. 21st Edition, American Petroleum Institute, Washington, D.C.

Biot, M.A. (1956), "The theory of propagation of elastic waves in a fluid-saturated porous solid". J. Acous. Soc. Amer., 28, 168-191.

Carter, J.P, Booker JR, Small JC. (1979), "The analysis of finite elasto-plastic consolidation". Int. J. Numer .Anal. Meth .Geomech., 3,107–129.

Chao, L., Borja, R.I., Regueiro, R.A. (2004) "Dynamics of porous media at finite strain". Comput. Methods. Appl. Mech. Engrg., 193, 3837–3870

Corapcioglu, M.Y., Tuncay, K. (1996), Chapter 5- propagation of waves in porous media. Advances in porous media., Vol 3, Elsevier, New York., 361–440

Kellezi, L. (2000), "Local transmitting boundaries for transient elastic analysis". Soil Dynamics and Earthquake Engineering,. Vol.19 (7), 533–547

Lysmer, J. & R. L. Kuhlemeyer. (1969), "Finite dynamic model for infinite media". J. Engrg. Mech. Div., ASCE, Vol. 95, No. EM4 859-877.

Medeiros Jr, C. J. (2002), "Low Cost Anchor System for Flexible Risers in Deep Waters", Proceedings of '34 Annual Offshore Technology Conference, Houston, paper No. OTC 14151.

Morland, L. W. (1972), "A simple constitutive theory for a fluid-saturated porous solid". J. Geoph. Res., 77, 890–900.

Nazem, M., Sheng, D., Carter, J.P. (2006), "Stress integration and mesh refinement in numerical solutions to large deformations in geomechanics". Int. J. Numer .Meth .Engng. 65,1002-1027.

Nazem, M., Sheng, D., Carter, J.P. & Sloan, S.W. (2008), "Arbitrary-Lagrangian-Eulerian method for large-deformation consolidation problems in geomechanics". Int. J. Num. Anal. Meth. Geomech., Vol. 32, 1023-1050.

Papadopoulos, P. & Taylor, R.L. (1990), "A mixed formulation for the finite element solution of contact problems" Technical Report UCB/SEMM Report 90/18, University of California at Berkeley.

Raie, M. & Tassoulas, J. (2009). "Installation of Torpedo Anchors: Numerical Modeling". J. Geotech. Geoenviron. Eng., Vol. 135(12), 1805–1813.

Randolph, M; Richardson, M.D; O'Loughlin, C. D. (2005), "The geotechnical performance of Deep Penetrating Anchors in calcareous sand", Proceedings of the International Symposium on Frontiers in Offshore Geotechnics (IS-FOG 2005), Perth, WA, Australia

Richardson, M. D., O'Loughlin, C. D; Randolph, M. F; C. Gaudin. (2009), "Setup Following Installation of Dynamic Anchors in Normally Consolidated Clay". J. Geotech. Geoenviron. EngC

Small, J.C., Booker, J.R., Davis, E.H. (1976), "Elasto-plastic consolidation of soil". International Journal of Solids and Structures., 12, 431-448.

Sousa, J.R.M., Cristiano, S., de Aguiar., Ellwanger, G.B., Elisabeth, C.P., Foppa, D., Medeiros, J.C. (2010), "Undrained Load Capacity of Torpedo Anchors Embedded in Cohesive Soils". J. Offshore Mech. Arct. Eng., Vol. 133(2), 021102-021114

Straughan, B., (2008), Stability and wave motion in porous media, applied mathematical sciences, vol 165. Springer, New York

Sturm, H & Andresen, L. (2010), "Large deformation analysis of the installation of dynamic anchor", Proceedings of 7th European Conference on Numerical Methods in Geotechnical Engineering (NUMGE '10), pp. 255–260.

Thomas, R. M. & Gladwell, I. (1988), "Variable-order variable-step algorithms for second-order systems. Part 1: The methods" Int. J. Numer. Meth. Engng., 26, 39–53.

True, D. G. (1976), Undrained Vertical Penetration into Ocean Bottom Soils, PhD Dissertation, University of California, Berkeley, California.

Wriggers. P. (2006), Computational Contact Mechanics. 2nd ed. Springer, Heidelberg.

COMPARISON OF THE COMPUTED AND OBSERVED BEHAVIOR OF AN ANCHORED WALL UNDER LIMITED GEOTECHNICAL CHARACTERIZATION

H. Karatag
Department of Construction & Real Estate, Ministry of Family & Social Policies, Ankara, Turkey

S.O. Akbas, A.C. Gel
Department of Civil Engineering, Gazi University, Ankara, Turkey

ABSTRACT: *This study evaluates the behavior of an 15 m deep anchored contiguous pile wall in stiff overconsolidated fissured Ankara Clay. The wall consists of 650 mm diameter drilled shafts at 1000 mm spacing, with five rows of anchors. The geotechnical parameters of the soil had to be estimated by combining the results of very limited in-situ and laboratory tests with those obtained through empirical relationships. Plane strain finite element analyses were then performed to predict the wall behavior, focusing mainly on the deformations. The results of the numerical analyses were then compared with those obtained by in-situ measurements from three inclinometers and settlement benchmarks. The results indicate that, with the selection of appropriate constitutive model and soil parameters obtained through local correlations, plane strain finite element analyses are capable of predicting the behavior of anchored contiguous pile walls in a stiff overconsolidated clay with sufficient accuracy.*

1 INTRODUCTION

For the design of deep excavation retaining systems in stiff–hard clays, the use of soil models that are capable of incorporating both loading and unloading stiffness of the soil are recommended for realistic prediction of displacements. However, it is clear that the use of these more sophisticated soil models are justified only when an accurate estimate of soil modulus is available. Considering the relatively low quality of soil exploration studies for small to medium sized construction projects in Turkey, it is generally not expected to obtain the necessary deformation and strength parameters from laboratory test results for stiff-hard clays in which undisturbed sampling is already a difficult task. Thus, proper selection of correlations from the literature and the calibration of these correlations with local experience are of primary importance for soil parameter estimation in such design situations.

Within this context, this study examines the behavior of a 15 m deep anchored contiguous pile wall in stiff overconsolidated fissured Ankara Clay, which was constructed for supporting the 15 m deep basement excavation of a nursing house in Seyranbaglari district of Ankara. Plane strain finite element analyses were performed to predict the wall behavior, using geotechnical parameters that were estimated mostly by empirical relationships because of limited site characterization and laboratory test results. The calculated deformations were then compared with those obtained from in-situ inclinometer and settlement benchmark measurements. Also, a parametric study was performed using different strength and deformation parameters to obtain the soil modulus, use of which would result in actual displacements registered by the inclinometer readings.

2 GENERAL OVERVIEW OF THE EXCAVATION AND THE RETAINING WALL

Due to the natural slope of the ground in the northwest–southeast direction, only the two sides of the 1500 m^2 excavation with a maximum height of 13.6 m and a total length of 62.5 m was required to be supported. The retaining system was designed to consist of 650 mm diameter drilled shafts at 1.0 m spacing, with an embedment length of 4.4 m. Five rows of anchors at 2.5 m and 2.0 m vertical and horizontal spacing, respectively, and each with 8.00 m fixed length were utilized. Note that an old masonry nursery building, with bad maintenance conditions exists at about 4.0 m distance from the excavation face, which is deemed to be extra sensitive to ground displacements and settlements that could occur due to the proposed excavation. A typical cross section of the anchored pile wall and a photograph taken during the last excavation stage are given in Figures 1 and 2, respectively.

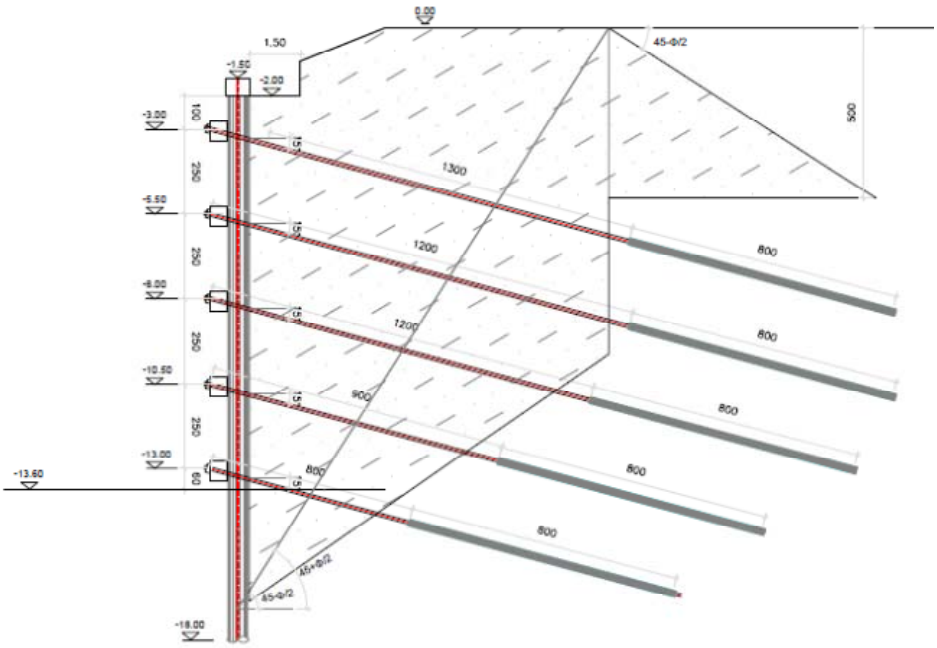

Fig. 1. A typical cross-section of the anchored pile wall

Fig. 2. A view of the retaining system at the last stage of the excavation

3 GEOTECHNICAL PROPERTIES

The geotechnical investigation originally involved drilling of three borings with depths ranging from 7.0 to 13.0 m. The top elevation of these borings are 948.00 m, which is 6.0 m lower than that of the retaining wall. Therefore, an additional boring at 953.00 m elevation with a depth of 16.0 m was also conducted. No in-situ test other than SPT were conducted, and only three undisturbed samples from elevations 946.00 m, 950.00 m, and 947.00 m, respectively, were recovered. SPT N values as a function of elevation is given in Figure 3.

According to the information gathered from the borings, following a 0.5 m thick artificial fill, the site is underlain by a silty clay deposit that was classified either as CL or CH according to USCS in the laboratory. This deposit, which is typical in the metropolitan area of Ankara, is characterized also by thin layers of sand, which was not reported for this case. In boring no. 4, greywacke deposits was reached at about 16.0 m. Only one consolidation test was performed, and the preconsolidation pressure was determined to be about 185 kPa at a depth of 2.5 m. The undrained shear strength (s_u) values were obtained from standard UU compression tests. A summary of the laboratory test results is given in Table 1.

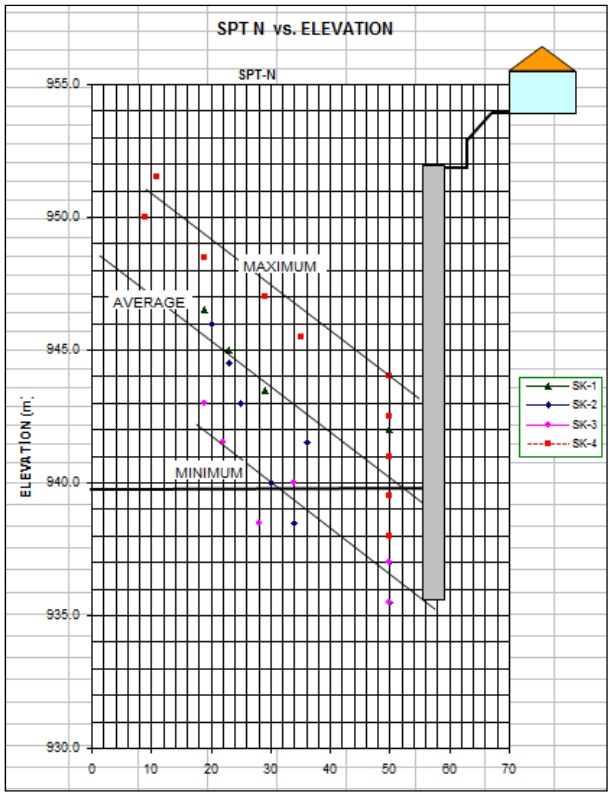

Fig. 3. Variation of SPT N values

Table 1. Summary of laboratory test results

Boring No.	Sample Depth (m)	γ_{nat} (kN/m^3)	<#200 (%)	USCS	PI	s_u (kPa)
1	2.0	18.2	90.4	CH	28	69.0
2	4.5	18.1	81.1	CH	22	-
3	4.0	-	83.1	CL	27	-
4	2.5-3.0	20.5	82.9	CL	25	75.5
4	5.5-6.0	18,9	96.9	CH	31	66.7

4 SELECTION OF DESIGN PARAMETERS AND NUMERICAL MODELING

As summarized in the previous section, the geotechnical exploration and the corresponding laboratory test results are limited both in terms of quality and suitability for the specific design case. It is well known that for retaining structures in stiff – hard, fissured clays, long term stability usually constitutes the more critical design phase, and accordingly the effective strength parameters are required for stability calculations. However, as can be seen from Table 1, the only available strength parameter for the clay is the undrained shear strength as obtained from UU tests, a value which is expected to be of low reliability. More importantly, except for a single consolidation test at a very shallow depth, no information about deformation parameters such as the modulus, which are needed for the estimation of wall deformations is given. Therefore, the geotechnical parameters that are required for the numerical analyses had to be estimated combining the results of very limited in-situ and laboratory tests with those obtained through empirical relationships. Experience from previous local studies had to be utilized in selecting the proper correlations, as they are numerous in the literature.

As a first step, the soil profile is subdivided into three layers based on the variation of SPT N values with depth, as summarized in Table 2.

Table 2. Basic soil layering assumption for design purposes

Layer No.	Depth, H (m)	N $(N_{60})_{ave}$	LL	PI	γ (kN/m^3)
Clay 1	< 4.0	10 (8)	50	28	19.1
Clay 2	4.0 < H < 9.0	25 (19)	47	22	
Clay 3	> 9.0	45 (34)	42	22	

Considering both the shallow sampling depths (Table 1), as well as the low reliability of the selected testing method, the undrained shear strength (s_u) values for the three layers given in Table 2 were determined using empirical correlations with the SPT N value. According to Stroud (1974), for insensitive clays, Equation 1 can be used to estimate s_u:

$$s_u = f_1 N \tag{1}$$

in which f_1 is a coefficient that is a function of the plasticity index (PI), and varies between 4.5 and 5.0 kPa for medium plasticity clays. Togrol and Sivrikaya (2007) estimated the same coefficient to be between 4.3 and 5.1 kPa, based on a statistical study using 185 clays from Turkey. Using the data obtained during the construction of the third section of the Ankara subway, Yaman (2007) recommended the use of Stroud's values for Ankara Clay. Based on these findings, f_1 was selected as 5, based on Stroud (1974) for the PI range of 22-28, in the current study.

In the literature, drained shear strength of clays have frequently been correlated with Atterberg Limits, especially the plasticity index (PI) (e.g., Kenney, 1967; Carter and Bentley, 1991). Due to its relatively limited effect on the deformation calculations, the effective stress friction angle for all layers were determined to be 25^o from Carter and Bentley (1991) for a mean PI of 25.

The experience from similar excavation and retaining structure design studies in Ankara Clay indicates that the ratio between the undrained elastic modulus E_u and s_u can be estimated to be between 400 and 500. These values is within the range recommended by Duncan and Buchignani (1976) considering the overconsolidation ratio and the average plasticity index of the soil. However, a more conservative value of 300, which corresponds to the lower bound value given by Duncan and Buchignani (1976), was selected to estimate design value of the

undrained soil modulus. The ratio between drained (E') and E_u was taken as 0.70, based on the recommendation given by Calisan (2009), specifically for Ankara Clay.

As stated previously, due to its capability of incorporating both loading and unloading stiffness of the soil, which is required for realistic prediction of displacements, hardening soil model (Schanz et al., 1999) was used to simulate the soil behavior in the finite element model. The main parameters employed for the hardening soil model are summarized in Table 3, for the three clay layers.

Note that the reference stiffness modulus, E_{50}^{ref}, and corresponding to the reference confining pressure, p_{ref}, of 100 kPa was back-calculated using Equation 2, after estimating the horizontal effective stress, which is assumed to be equal to σ_3', at the middle of each layer:

$$E' = E_{50}^{ref} \left(\frac{c'\cos\phi' - \sigma_3' \sin\phi'}{c'\cos\phi' + p^{ref} \sin\phi'} \right)^m \tag{2}$$

in which m is a parameter, which helps simulate the stress dependency of stiffness. The parameter m is reported by von Soos (1990) to take values between 0.5 and 1.0. A trial and error procedure was used to estimate the appropriate m value to be between 0.55 and 0.60 for Ankara Clay, using the modulus and stress values obtained from the single oedometer test available, within Equation 3:

$$E_{oed} = E_{oed}^{ref} \left(\frac{\sigma'}{p^{ref}} \right)^m \tag{3}$$

in which E_{oed} and E_{oed}^{ref} are the oedometric modulus and oedometric modulus corresponding to p_{ref}, respectively. The reference modulus for unloading was simply taken to be equal to $3E_{50}^{ref}$, which is the default setting in the finite element program.

Table 3. Basic hardening soil model parameters used in the finite element model

Layer No.	ϕ' (°)	c' (kPa)	E' (kPa)	E_{50}^{ref} (kPa)	E_{ur}^{ref} (kPa)	ν
Clay 1	25	5	10500	14000	52000	0.2
Clay 2		15	26250	24000	72000	
Clay 3		25	47250	29000	87000	

The 30 m x 72 m plane-strain finite element model consists of 1163 fifteen nodded triangular elements (Figure 4). The piles in the wall were modeled as beam elements, with interfaces around them to simulate soil-concrete interaction effects. The free and fixed anchor lengths were modeled by node to node anchors and using geotextile elements available in the finite element program, respectively. 370 kN prestressing force was applied to all of the anchors. The finite element mesh is finer around the fixed anchor length as well as around the piles and the pile tips for obtaining more accurate results with better convergence properties. The five excavation stages corresponding to each anchor elevation were simulated and the effect of the existing nearby building was modeled by an 80 kN surcharge load.

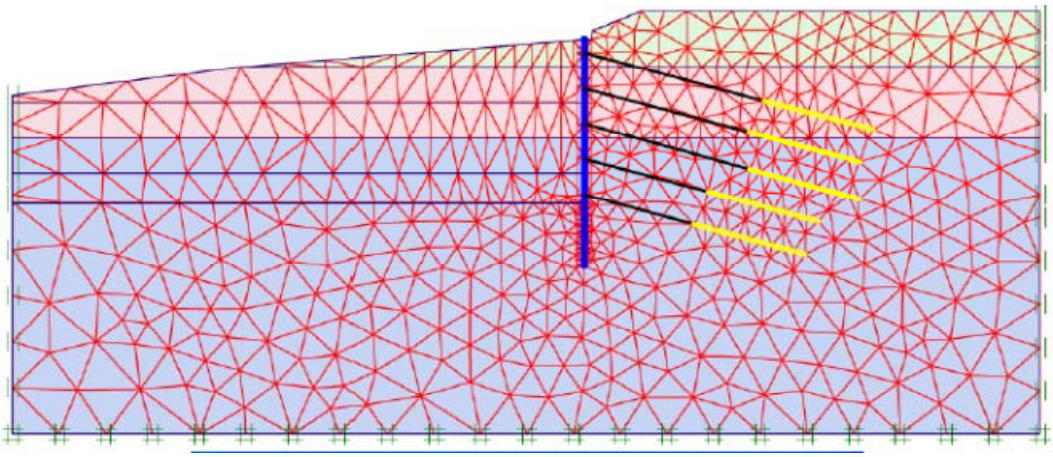

Fig. 4. General view of the finite element model for the wall

5 COMPARISON OF PREDICTED AND OBSERVED BEHAVIOR

Three inclinometers and three settlement reference points were used to monitor the performance of the retaining wall and the surrounding ground. The maximum horizontal and vertical displacements were measured to be around 9 mm and 16 mm, respectively. A comparison of the inclinometer measurements and finite element results are given in Figure 5.

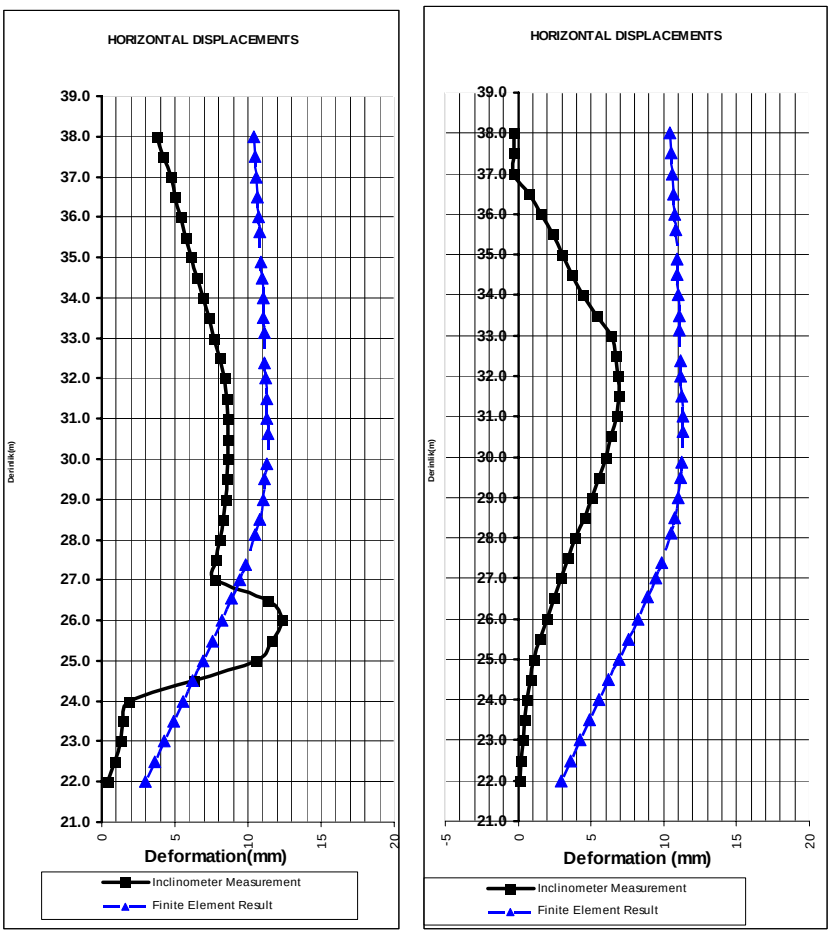

Fig. 5. Comparison of measured and calculated horizontal displacements

It can be seen from Figure 5 that, in general, the finite element model overestimated the horizontal displacements by about 30%. The difference is especially striking at higher elevations, which indicates that the numerical modeling could not take the effect of prestressing into account at the first excavation stages. It can also be observed that the location of the maximum horizontal displacement could be estimated pretty well with the numerical model. Note that the anomaly in the inclinometer measurements at around the excavation surface in Inclinometer 1 was ignored. The vertical displacements as measured from the settlement reference points were also overestimated by about 20% to 33% by the numerical model.

A back-analysis indicates that, with the parameters given in Table 4, a close to perfect agreement between the measured and calculated deformations can be obtained. Note that, in Table 4, the values in the parentheses are those that are measured.

Table 4. Results of the back analysis

Layer No.	ϕ' (^{o})	c' (kPa)	E_u / s_u	E' / E	Max. Horizontal Disp (mm)	Max. Vertical Disp (mm)
Clay 1	25	5	450	0.70	8.69 (8.33)	14.4 (15.6)
Clay 2		15				
Clay 3		25				

6 SUMMARY AND CONCLUSIONS

The deformation behavior of a 15 m deep retaining wall that consists of 650 mm diameter drilled shafts at 1000 mm spacing with five rows of anchors, was evaluated using inclinometer measurements and settlement reference point readings. The maximum horizontal and vertical displacements are in the order of 0.09% and 0.07% of the wall height, which are values within the range suggested by Long (2001) for stiff clays. The in-situ measurements were compared with those that were obtained by finite element modeling. The emphasis was given to geotechnical parameter estimation for numerical modeling, because of limited site investigation.

Using the geotechnical parameters obtained mostly by empirical relationships, the finite element model overestimated both the horizontal and vertical displacements by about 30%, but similar deformation patterns with inclinometer measurements were obtained. A back-analysis indicates that a close agreement between measured and calculated deformations could be obtained if E_u/s_u ratio was selected to be 450, with all other parameters remaining the same.

REFERENCES

Calisan, O. (2009), "Ankara kilinde yapilan 20 m derinligindeki bir kazinin geri analizi", Proceedings of 5. METU Geotechnical Symposium, 1-12, Ankara.

Carter, M. & Bentley, S.P. (1991), Correlations of Soil Properties, Pentech Press, London

Duncan, J.M. & Buchignani, A.L. (1976), An Engineering Manual for Settlement Studies, Department of Civil Engineering, University of California, Berkeley.

Kenney, T.C. (1967), Shearing Resistance of Natural Quick Clays, Ph.D. Thesis, University of London.

Long, M. (2001), "Database for retaining wall and ground movements due to deep excavation", Journal of Geotech. and Geoenviron. Engrg., ASCE, Vol. 127(3), 203-224.

Schanz, T., Vermeer, P. & Bonnier, P.G. (1999), "The hardening soil model: formulation and verification", Proceedings of Beyond 2000 in Computational Geotechnics – 10 Years of Plaxis, 5-17, Rotterdam.

von Soos, P. (1990), Properties of Soil and Rock, Grundbautaschenbuch, Part 4, Ed. 4, Ersnt & Sohn, Berlin.

Stroud, M.A. (1974), "The standard penetration test in insensitive clays and soft rock", Proceedings of 1st European Symposium on Penetration Testing, Vol. 2(2), 367-375, Stockholm.

Togrol, E. & Sivrikaya, O. (2007), "Relationship between SPT N values and the undrained shear strength for Turkish clays". Technical Journal, Vol. 18(4), 4229-4246.

Yaman, G. (2007), Prediction of Geotechnical Properties of Cohesive Soils from In-Situ Tests: An Evaluation of a Local Database, M.Sc. Thesis, Middle East Technical University, Ankara.

PROBABILISTIC ANALYSIS OF A BENCHMARK PROBLEM FOR SLOPE STABILITY IN 3D

Y. Li, M.A. Hicks & J.D. Nuttall
Department of Geoscience and Engineering, Delft University of Technology, Delft, The Netherlands

ABSTRACT: *A benchmark problem for 3D slope stability analysis with random undrained shear strength parameters has been analyzed by Vanmarcke's (1977b) simplified method and the more advanced Random Finite Element Method (RFEM), and the analytical and numerical results compared. Both methods lead to a statistical distribution of the factor of safety. However, they can give significantly different results, depending on the value of the Scale of Fluctuation (SOF) in the horizontal direction. It is shown that the computed response of the slope is weaker than the analytical solution in most cases. For large horizontal SOFs compared to the slope length the two methods agree, as most of the failure surfaces in the full 3D RFEM analyses then tend to be cylindrical and propagate along the entire length of the slope, thereby matching Vanmarcke's assumptions and resulting failure length. However, for more realistic ratios of the horizontal SOF to slope length, significant differences may be observed.*

1 INTRODUCTION

Studies of the effects of soil variability on slope stability have been done extensively in 2D, for example, Paice & Griffiths (1997), Hicks & Samy (2002), Fenton et al. (2003), Griffiths & Fenton (2004), Hicks & Onisiphorou (2005) and Griffiths et al. (2009), amongst others. However, the implicit assumption made in 2D analysis is that the scale of fluctuation in the out-of-plane direction is infinite. This is unrealistic in the sense that the spatial variability is inherently three-dimensional in character. Also, observations of actual failures indicate that the sliding bodies are of finite dimensions even under apparent plane strain conditions. It appears that local variations in soil properties are sufficient to exclude long failure mechanisms in most cases.

Three dimensional analyses become necessary when the heterogeneity of the soil is accounted for, although there is limited literature dealing with 3D slope reliability. However, Spencer & Hicks (2007), Hicks et al. (2008) and Hicks & Spencer (2010) considered the influence of anisotropic heterogeneity of undrained shear strength on the performance of a slope founded on a firm base and identified three possible failure modes depending on the horizontal scale of fluctuation relative to slope geometry. They showed that 2D analysis is only justified for long slopes with two dimensional failure mechanisms; moreover, discrete failures result from intermediate levels of anisotropy of the heterogeneity, demonstrating that the 3D nature of heterogeneity should be considered and that 3D analysis should be done to assess slope reliability in these situations.

The aforementioned studies were all based on numerical methods, because of the complexity of the mathematical optimization consisting of minimizing the reliability function involved in a probabilistic slope stability analysis, particularly in 3D. In contrast, Vanmarcke (1977b) considered, from an analytical point of view, the three-dimensional slope stability problem within a probabilistic framework by simplifying the complicated 3D problem to one involving a single cylindrical failure mechanism of finite length.

This paper benchmarks the methodology of Spencer & Hicks (2007) and Hicks & Spencer (2010) against Vanmarcke's (1977b) simplified theoretical 3D approach to slope stability and compares the relative performance for a range of inputs; these two approaches are primarily based on the same underlying (i.e. random field) theory (Vanmarcke 1977a), and they both incorporate anisotropy of the heterogeneity by taking a horizontal SOF that is different to that in the vertical direction. In particular, the circumstances in which the computed results approach the theoretical solution are discussed, as are those situations in which they are significantly different. This is particularly beneficial in indicating when Vanmarcke's (1977b) simplification is justified and may be appropriate as a tool in guiding design. Moreover, it indicates when the simpler approach is in error and where further research is needed to improve its performance.

In the following sections, Vanmarcke's (1977b) simplified 3D model will first be revisited and then the full 3D RFEM model briefly introduced. The relative performance of the two approaches in analyzing a simple 3D slope stability problem is then investigated and evaluated.

2 VANMARCKE'S SIMPLIFIED 3D MODEL REVISITED

Vanmarcke (1977b) considered the reliability of earth slopes in cohesive soils characterized by a stochastic undrained shear strength. Estimates of the mean and standard deviation of the factor of safety against slope failure for a single cylindrical failure mechanism of finite length were derived, assuming the spatially averaged shear strength over a finite length followed a Gaussian probability distribution. The equilibrium equation for a cylindrical failure in a 3D slope was proposed based on an extension of the circular arc method in 2D, but it also included a term for added end resistance.

Following the First Order Second Moment (FOSM) method, (Vanmarcke 1977b) first expressed the mean factor of safety, $\overline{F}_{Tb}$, for a cylindrical failure of length *b*, as

$$\overline{F}_{Tb} = \overline{F}_T\left(1+\frac{d_0}{b}\right) \tag{1}$$

where $\overline{F}_T$ is the mean traditional factor of safety for the plane strain condition, and d_0 is twice the cross sectional sliding area, *A*, divided by the arc length of the sliding plane, L_a, i.e.

$$d_0 = \frac{2A}{L_a} \tag{2}$$

An equation describing the standard deviation of F_{Tb}, $\widetilde{F}_{Tb}$, was given as

$$\widetilde{F}_{Tb} = \Gamma(b)V_{s_1}\overline{F}_T \tag{3}$$

where

$$\Gamma(b) = 1 \quad ; \ b \le \theta \tag{4a}$$

$$\Gamma(b) = \left(\frac{\theta}{b}\right)^{1/2} \quad ; \ b > \theta \tag{4b}$$

and

$$V_{s_1} = \Gamma(L_a) V_s \tag{5}$$

and where $\Gamma(b)$ is a variance reduction factor for the shear strength averaged over the length b, θ is the SOF in the horizontal plane, V_s is the coefficient of variation of the 'point' shear strength, V_{s1} is the coefficient of variation of the moving average s_1 over a unit length, and $\Gamma(L_a)$ can be found by replacing b with L_a and θ with θ_e, the equivalent SOF in the cross-sectional plane of unit thickness. Thus, as b increases relative to θ, $\Gamma(b)$ reduces and so does $\tilde{F}_{Tb}$. The equivalent SOF in the cross-sectional plane, θ_e, can be approximated by subdividing the failure arc L_a into segments (Vanmarcke 1977b).

Both $\overline{F}_{Tb}$ and $\tilde{F}_{Tb}$ are dependent on the length of the slope failure, b. For any b the probability of failure, for a slope section centered at some defined point along a longer slope, is the probability that F_{Tb} is less than or equal to 1.0, $P(F_{Tb} \le 1)$. As a Gaussian distribution is assumed for F_{Tb}, $P(F_{Tb} \le 1)$ can be calculated using the cumulative standard Gaussian distribution function Φ. Over the range of possible b, $P(F_{Tb} \le 1)$ varies due to the different influence of b on $\overline{F}_{Tb}$ and $\tilde{F}_{Tb}$. The probability of failure reaches a maximum for the critical length b_c, which, by considering a reliability function (Vanmarcke 1977b), was derived as

$$b_c = \frac{\overline{F}_T}{\overline{F}_T - 1} d_0 \quad ; \ b_c > \theta \tag{6a}$$

$$b_c = \theta \quad ; \ b_c \le \theta \tag{6b}$$

It is interesting to note that the probable failure length relies only on $\overline{F}_T$ and d_0 (the factor representing the end effects of the failure surface). One can therefore get a distribution for the factor of safety based on the most probable failure length.

3 FULL 3D RFEM MODELLING OF SLOPE RELIABILITY

The current implementation of RFEM, parallelized by Nuttall (2011), uses random fields generated using Local Average Subdivision (Fenton & Vanmarcke 1990) to model the spatial variability of material properties (in this case, the undrained shear strength) and finite elements to compute geo-structural response (in this case, the factor of safety against slope failure). The inputs include the property mean and standard deviation (which combine to give the coefficient of variation, V), and the scale of fluctuation (SOF). The anisotropy of the heterogeneity (ξ) is modelled by using different values of SOF in the vertical and horizontal directions (θ_v and θ_h, respectively), as has been previously reported and modelled, for example, by Hicks & Samy (2002) and Hicks & Spencer (2010) in 2D and 3D, respectively.

The random fields are generated using the exponential covariance function:

$$\beta(\tau_1,\tau_2,\tau_3)=\sigma^2\exp\left(-\frac{2|\tau_1|}{\theta_1}-\sqrt{\left(\frac{2\tau_2}{\theta_2}\right)^2+\left(\frac{2\tau_3}{\theta_3}\right)^2}\right) \quad (7)$$

where β is the covariance, τ is the lag distance, and subscripts 1-3 denote the vertical and two lateral coordinate directions, respectively. In this paper, the random field is initially generated for $\theta=\theta_1=\theta_2=\theta_3$, in which θ is taken to be equal to the largest SOF (i.e. θ_h). The anisotropic random field is then produced by post-processing the generated isotropic field (Vanmarcke 1983); that is, by squashing the field in the vertical direction to give the required value of θ_v. Note that a standard normal field is first generated, and then the target normal field is created from a simple transformation. The reader is referred to Spencer (2007) and Hicks & Spencer (2010) for more details about the implementation of the random field generation.

Based on multiple Monte Carlo realizations, a distribution for the realized factor of safety may be obtained.

4 ANALYSIS AND COMPARISON OF A BENCHMARK PROBLEM

In general, three failure mode categories have been identified in the analysis of a long 3D slope in a heterogeneous soil, as suggested by Hicks & Spencer (2010), with the likelihood of these different modes depending on the magnitude of θ_h relative to the slope geometry (characterized by the height H and length L). This previous finding constitutes a central component in understanding the results of this paper, and so they are summarized as follows:

- Mode 1: For $\theta_h<H$, failure goes through weak and strong zones alike, there is considerable averaging of property values over the failure surface (i.e. variance reduction due to averaging), and the slope fails along its entire length (initiating from the toe). This case is analogous to a conventional 2D deterministic analysis based on the property mean μ.
- Mode 2: For $H<\theta_h<L/2$, there is a tendency for failure to propagate through semi-continuous weaker zones, leading to discrete 3D failures and a wide range of possible factors of safety.
- Mode 3: For $\theta_h>L/2$, the predominant failure mechanism reverts to along the length of the slope, in a similar manner to Mode 1. However, in contrast to Mode 1, there is a wide range of solutions due to the location (i.e. depth) of the slide being influenced by the spatial distribution of the weaker layers. This case is analogous to a 2D stochastic analysis.

Note that the value of θ_h/L at which the predominant failure mode changes from 2 to 3 is rather subjective. Although $\theta_h/L=1/2$ seems reasonable, $\theta_h/L=1$ is more apparent from the results in the present study. Bearing in mind the above failure modes, a series of analyses are conducted to compare with Vanmarcke's (1977b) theoretical solution.

4.1 Problem description

The reliability assessment has been made for a 50m long slope of the same cross-sectional dimensions as the slopes studied by Hicks & Spencer (2010). The finite element mesh discretisation and boundary conditions are also the same as used previously. The slope is 5m high with a 45° slope angle, while the statistics of undrained shear strength are $V=0.2$, $\theta_v/H=0.2$ and a range of values considered for ξ ($\xi=\theta_h/\theta_v$). Moreover, the case of $\mu=40$ kPa has been considered, which corresponds to $F_T=2.458$ for a plane strain analysis based only on the mean property value. The clay behaviour is modeled by an elastic-perfectly plastic Tresca

soil model, with an elastic modulus E=1.0×10^{5}kPa and Poisson's ratio ν=0.3. The random field cell values are mapped onto the 8 Gaussian integration points within each 20-node finite element, instead of onto the element itself, in order to emulate the spatial variability as accurately as possible (Hicks & Samy 2002).

4.2 Analytical solution

An example for ξ=6 is used to demonstrate the theoretical calculation process, which is also applicable for other values of ξ. Calculating the slope's mean factor of safety, $\overline{F}_{Tb_c}$, for the most probable failure length b_c, can be considered equivalent to calculating the factor of safety against a 3D cylindrical failure with c_u=μ=40 kPa, taking account of the cylinder end contributions. The value of d_0 is calculated using Eq. (2); i.e. based on the estimates of L_a=12m and A=23m^2, obtained by analyzing a homogeneous slope. This gives d_0=3.83 m, which is substituted into Eq. (6) along with the factor of safety based on plane strain analysis, $\overline{F}_T$ =F_T=2.458, to give a most probable failure length of b_c=6.46m. This, in turn, is substituted into Eq. (1) to give the mean traditional factor of safety for a slope failure of that length, $\overline{F}_{Tb_c}$ =3.92. Note that this value is considerably higher than $\overline{F}_T$ =2.458, demonstrating a large increase in the resistance to failure, due to end resistance, for the predicted short failure length. Finally, the standard deviation of the factor of safety can be estimated using Eqs. (3)–(5), giving Γ(b)=0.96, and $\widetilde{F}_{Tb_c}$ =0.21, respectively. For other cases corresponding to different degrees of anisotropy of the heterogeneity, the mean and standard deviation of the factor of safety (FOS) are shown in Table 1.

Table 1. Means and standard deviations of theoretical and computed FOS

Anisotropy	ξ=1		ξ=2		ξ=6		ξ=12	
Statistics	Mean	SD	Mean	SD	Mean	SD	Mean	SD
Theoretical	3.92	0.056	3.92	0.097	3.92	0.205	3.24	0.228
RFEM	2.45	0.022	2.43	0.041	2.39	0.099	2.34	0.152

Anisotropy	ξ=50		ξ=100		ξ=1000	
Statistics	Mean	SD	Mean	SD	Mean	SD
Theoretical	2.65	0.241	2.55	0.243	2.47	0.246
RFEM	2.37	0.201	2.40	0.232	2.44	0.242

4.3 RFEM results and comparison with theory

Numerical simulations based on RFEM analyses comprising 500 realizations have been conducted for values of ξ ranging from 1-1000. The results are shown in Fig. 1 in terms of PDFs of factor of safety and, in Table 1, in terms of the mean and standard deviation of the realized factor of safety. The corresponding analytical solutions based on Vanmarcke's (1977b) simplified 3D model are also shown for comparison. Note that the legend shown in Fig. 1(a) applies to all cases considered.

Obviously, the computed results in Fig. 1(a) mainly fall into the Mode 1 failure category, as indicated by the narrow range of computed factors of safety. As ξ increases, Mode 2 becomes dominant (Fig. 1(b)), as indicated by the wider range of possible solutions. As ξ increases to even larger values (Figs. 1(c-d)), Mode 3 takes over as the dominant mechanism, with the PDF distributed over a still larger range of FOS. The results shown in Fig. 1(d) represent the limiting condition.

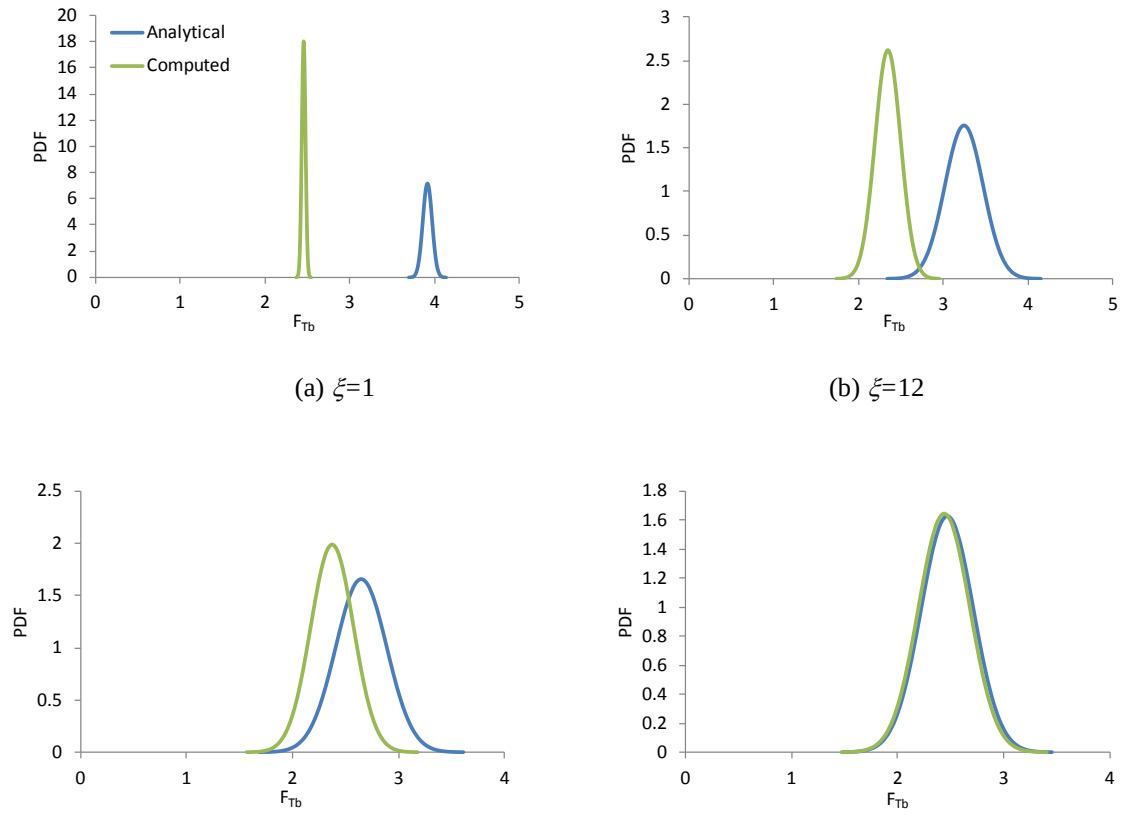

(a) ξ=1 (b) ξ=12

(c) ξ=50 (d) ξ=1000

Fig. 1. PDFs of factor of safety

The corresponding analytical solution is also plotted in Fig. 1. It is seen that, for Modes 1 and 2, the computed mean factor of safety is significantly lower than the analytical result (i.e. the predicted curve from the analytical solution has values well above FOS=3.0, while RFEM analyses have FOS values well below 3.0). For Mode 3, the analytical curve gets close to the computed response as ξ increases. For the limiting condition of ξ=1000, the computed and analytical curves show very close agreement.

The above observations can be explained by the nature of the evolution of the analytical solution. For $\theta_h \leq b_c$=6.46m (ξ=1 in Fig. 1), the mean of F_{Tbc} does not change (see. Eqs. (1) and (6a) and Table 1). In this case, the analytical solution predicts a most probable failure length of 6.46m, and thus $\overline{F}_{Tb_c}$=3.92. Eq. (1) implies that these predicted short slides are heavily influenced by the end resistance of the failure surface, leading to a very high factor of safety. In contrast, the computed results suggest a much greater (albeit still unlikely) chance of the slope falling down.

For $\theta_h \geq b_c$=6.46m (ξ=12, 50, 1000 in Fig. 1), the mean of F_{Tbc} decreases (Eqs. (1) and (6b) and Table 1). The case of ξ=6 (not shown in Fig. 1) can also be considered as the condition when the analytical PDF starts to move to the left. For the limiting condition of ξ=1000, the analytical PDF matches the computed curve due to the elimination of the end resistance effect (Eq. (1)). In this case, the computed failure mechanism generally fits the assumption made in Vanmarcke's (1977b) simplified model; that is, a cylindrical failure surface. Moreover, the slope failure propagates along the entire length of the slope, which is also consistent with Vanmarcke's model for this value of ξ.

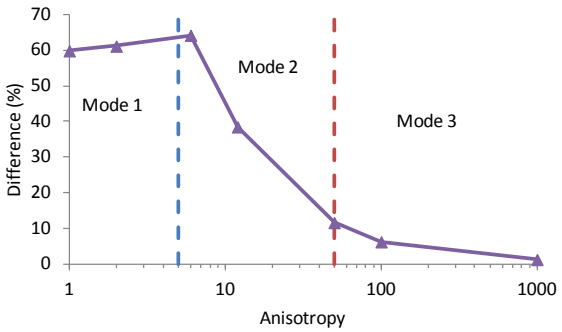

Fig. 2. Difference between analytical and RFEM solutions (expressed as a percentage of the RFEM solution and presented in terms of the mean factor of safety)

It is shown in Table 1 that the mean theoretical solution reduces as ξ increases, i.e. due to the reduced end contribution in Eq. (1); whereas the mean RFEM solution reduces as ξ increases to 12, due to its ability to seek out the weakest failure path resulting in a wide range of possible failure surfaces. The difference between the analytical and RFEM solutions, as a percentage of the RFEM solution, is shown in Fig. 2 as a function of the degree of anisotropy. It is seen that the difference generally reduces as ξ increases. It is also noted that the standard deviation of the computed results is less than that of the analytical results for lower values of ξ (Table 1). This may be partly due to the approximate form of the variance reduction factor used in Eq. (4) in Vanmarcke's (1977b) analytical model, compared to the variance function derived from the covariance function (Eq. (7)) used in the current numerical model. Moreover, Vanmarcke's (1977b) solution is based on an approximation of the equivalent SOF in Eq. (5). However, the short predicted failure length from the analytical model is believed to be the main reason for the large difference in standard deviation compared to the RFEM analyses (in particular, when compared to those RFEM analyses exhibiting Mode 1 failure).

5 CONCLUSIONS

A three dimensional benchmark slope stability problem has been analyzed by both Vanmarcke's (1977b) simplified 3D approach and a full 3D RFEM approach, and the results presented in terms of PDFs of the factor of safety. For Mode 3 failure (which occurs for large horizontal SOF) the two approaches agree, as most of the failure surfaces in the full 3D RFEM analyses tend to be cylindrical and propagate along the entire length of the slope, which matches Vanmarcke's assumption and resulting failure length. However, for Mode 1 and 2 failures (which occur for smaller horizontal SOF when using RFEM), with Mode 2 being the most probable situation encountered in practice, they give significantly different results depending on the value of the anisotropy of the heterogeneity. In these cases, the RFEM response of the slope is weaker than the analytical solution. The large difference between the results is due to 2 factors. Firstly, the ability of the RFEM simulation to seek out the weakest failure path through the slope, thereby reducing the average shear strength along the failure surface. This results in many possible failure surfaces of varying size and shape, and it is the spatial averages of material properties over these failure surfaces that count in practice, not simple spatial averages along a predefined failure surface such as a cylinder. Secondly, the end resistance plays a considerable role in increasing the resistance to failure in the theoretical analysis (i.e., as a multiplier of the plane strain solution, as defined in Eq. (1)), and thus the factor of safety may be greatly overestimated. It is likely that this has the greater effect on the difference between the solutions.

Overall, this paper presents as a basic validation of the current RFEM implementation for a simple 3D benchmark problem. The results show the capability of the full 3D analysis, which is more versatile than the simplified 3D model of Vanmarcke (1977b). However, the analytical solution serves as a useful bound for benchmarking the simulation results.

ACKNOWLEDGEMENT

This work is funded by the China Scholarship Council (CSC) and by the Section of Geo-Engineering, Delft University of Technology.

REFERENCES

Fenton, G.A. & Vanmarcke, E.H. (1990), "Simulation of random-fields via local average subdivision". ASCE J. Eng. Mech., Vol. 116(8), 1733-1749.

Fenton, G.A., Griffiths, D.V. & Urquhart, A. (2003), "A slope stability model for spatially random soils". Proceedings of 9th Int. Conf. Applications of Statistics and Probability in Civil Engineering (ICASP9), A. Kiureghian et al., Eds., Millpress, San Francisco, CA, 1263-1269.

Griffiths, D.V. & Fenton, G.A. (2004), "Probabilistic slope stability analysis by finite elements". ASCE J. Geotech. Geoenv. Eng., Vol. 130(5), 507-518.

Griffiths, D.V., Huang, J.S. & Fenton, G.A. (2009), "Influence of spatial variability on slope reliability using 2-D random fields". ASCE J. Geotech. Geoenv. Eng., Vol. 135(10), 1367-1378.

Hicks, M.A. & Samy, K. (2002), "Influence of heterogeneity on undrained clay slope stability". Quarterly J. Eng. Geology and Hydrogeology, Vol. 35(1), 41-49.

Hicks, M.A. & Onisiphorou, C. (2005), "Stochastic evaluation of static liquefaction in a predominantly dilative sand fill". Geotechnique, Vol. 55(2), 123-133.

Hicks, M.A. & Spencer, W.A. (2010), "Influence of heterogeneity on the reliability and failure of a long 3D slope". Computers and Geotechnics, Vol. 37(7-8), 948-955.

Hicks, M.A., Chen, J. & Spencer, W.A. (2008), "Influence of spatial variability on 3D slope failures". Proceedings of 6th Int. Conf. Computer Simulation in Risk Analysis and Hazard Mitigation, Kefalonia, Greece, 335-342.

Nuttall, J.D. (2011), Parallel implementation and application of the random finite element method. PhD thesis, University of Manchester, UK.

Paice, G.M. & Griffiths, D.V. (1997), "Reliability of an undrained clay slope formed from spatially random soil". Proceedings of 9th Int. Conf. Computer Methods and Advances in Geomech., Wuhan, China, Vol. 1, 543-548.

Spencer, W.A. & Hicks, M.A. (2007), "A 3D finite element study of slope reliability". Proceedings of 10th Int. Symp. Num. Models in Geomech., Rhodes, Greece, 539-543.

Spencer, W.A. (2007), Parallel stochastic and finite element modeling of clay slope stability in 3D. PhD thesis, University of Manchester, UK.

Vanmarcke, E.H. (1977a), "Probabilistic Modeling of Soil Profiles". ASCE J. Geotech. Eng., Vol. 103(11), 1227-1246.

Vanmarcke, E.H. (1977b), "Reliability of earth slopes". ASCE J. Geotech. Eng., Vol. 103(11), 1247-1265.

Vanmarcke, E.H. (1983), Random fields: analysis and synthesis, The MIT Press, Cambridge, Massachusetts.

MODELLING SOLID-FLUID TRANSITION IN SOILS DURING MUDFLOWS

Noémie Prime
Université de Liège, Dept. ArGEnCo, Chemin des Chevreuils 1, 4000 Liège, Belgium

Félix Darve, Frédéric Dufour
Grenoble INP / Universit Joseph Fourier / CNRS UMR 5521, 3SR laboratory, France

ABSTRACT: *This paper aims to propose a new constitutive model to describe the complex evolution of soil behaviour during landslides of the flow type, and notably its sudden solid-fluid transition. The constitutive model formulation can be justified from experimental observations as well as theoretical investigations in geomaterial solid-fluid transition. This model is based on the combination of two constitutive relations, an elasto-plastic one for the solid in-situ soils and a viscous one with a yield stress for the flowing mud or debris. The transition in between is defined at the material point by the second order work general failure criterion. The constitutive model is applied, by the way of a suitable numerical method, FEMLIP (Finite Element Method with Lagrangian Integration Points), to a simple heuristic model of an unstable soil with a slope geometry and a final obstacle. The simulations allow to distinguish the different phases of the mudflow, and to quantify its interaction with the obstacle.*

1 INTRODUCTION

Geomaterials result, at the micro-scale, from a complex assembly of grains with frictional, cohesive, viscous and even chemical interactions between each other, depending on the grains nature, the water content and the load applied. It implies that, at the macro-scale, they can appear under a wide range of states between a pure solid and a pure fluid form. This mechanical behaviour diversity is clearly manifest during landslides of the flow type, as mudflows, where the destabilized mass turns into a flow of very high velocity (about several m/s in those events).

This behaviour evolution represents a scientific key point for two main reasons. On one hand, this transition, although it is studied by many scientific communities (physicists, rheologists, etc.), is not yet well understood. On the other hand, modelling such a transition is very challenging since numerical methods are usually suitable for whether solid or fluid material, but rarely for both, which implies to deal with a high level of deformation but also to describe history dependant behaviours.

Because of these limitations, no constitutive model, as far as we know, has been formulated to describe the whole complex evolution of a soil during a landslide of the flow type. Let us specify that this evolution is characterized by an initial solid state of the in-situ soil (this last is usually described with elasto-plasticity), a transition, and a fluid phase (usually described with yield stress viscosity). The arrest of the flow for sufficiently low shear stresses can be considered as a last phase.

In this context, the present contribution proposes an original approach to model landslides of the flow type, and more generally to describe solid-fluid transition in geomaterials.

After some experimental and theoretical considerations about geomaterials loss of stability, we first expose the formulation of a global constitutive model able to describe the solid behaviour of in-situ soil, the transition, and the fluid behaviour of a mud or debris flow (section 2). Then, section 3 presents a simplified boundary value model on which the constitutive model can be tested. It has been realized thanks to a powerful numerical tool (the FEMLIP numerical method - Finite Element Method with Lagrangian Integration Points). Section 4 gathers the results obtained from the simulations. Lastly, section 5 draws some conclusions about the combined used of the new model and FEMLIP method.

2 SOLID-FLUID TRANSITION IN GEOMATERIALS

On the one hand, if a soil sample cannot sustain any more a constant stress state without being strained, it means that it has achieved a failure state. In the context of divergence instabilities (that is to say not flutter instabilities neither geometric ones), failure can develop with a localized mode, in which the plastic strains concentrate in a shear band, or with a diffuse one, in which plastic strains affect the whole bulk. The differences between these 2 modes are detailed in Khoa et al. 2006; Daouadji et al. 2011; Nicot & Darve 2011.

On the other hand, fluids are characterized by the fact that they cannot sustain non-zero deviatoric stresses without developing strain rates (for yield stress fluid, this is true if the second stress invariant is greater than the yield stress).

According to that similar characteristic between fluids and soils at failure, it is thus easy to conceive that when failure affects the whole bulk of a sample, the structure disorganization can lead to a fluidization of the material. An example of such a transformation during diffuse failure is liquefaction, in which the inter-granular stresses disappear due to the loss of contact between the grains. This response can be typically obtained during an undrained triaxial test led on a loose sand sample where, if the test is axially stress controlled, the sample suddenly collapses (see on Fig. 2 the final configuration observed for such a test).

Diffuse failure, which can induce this sudden behaviour change, is a very particular failure mode which happens typically in granular solids. Indeed, not only it affects the whole bulk of the material, but also it can occur even if the plastic critical stress state is not reached (Khoa et al. 2006). The classical plasticity criterion is thus not suitable to detect all diffuse failure cases, nor is the localized criterion (related to the failure pattern). However, the theory about general stability for solids developed by Hill (1958) stays appropriate in this context, as in all divergence instability cases even for non-associativity. In the hypothesis of small strains and negligible geometrical effects, the sufficient stability condition Hill expressed, for a material point, is:

$$d^2W = d\sigma_{ij} d\varepsilon_{ij} > 0, \qquad \forall ||\boldsymbol{d\varepsilon}|| > 0, \tag{1}$$

$\boldsymbol{d\varepsilon}$ and $\boldsymbol{d\sigma}$ being linked by the elasto-plastic relation ($\boldsymbol{d\sigma} = \boldsymbol{M}\,\boldsymbol{d\varepsilon}$) and d^2W being called second order work.

This criterion has been successfully applied to geomechanical issues, including landslides modelling (Darve & Laouafa 2000; Laouafa & Darve 2002). Furthermore, it has been shown that the bifurcation domain (complementary to the stability one) in which diffuse failure can take place is defined, in the stress space, by $(det\boldsymbol{M_s} < 0)$ ($\boldsymbol{M_s}$ being the symmetric part of the constitutive matrix $\boldsymbol{M}$). Finally, it can be demonstrated algebraically that conditions $(det\boldsymbol{M} < 0)$

(the plastic limit criterion) and $(det\boldsymbol{L} < 0)$ (the localization criterion with $\boldsymbol{L}$ the acoustic tensor) bring directly $(det\boldsymbol{M_s} < 0)$. From this result it can be stated that the second order work criterion is general (it includes the other criteria) and can detect all the divergence failures, including diffuse ones.

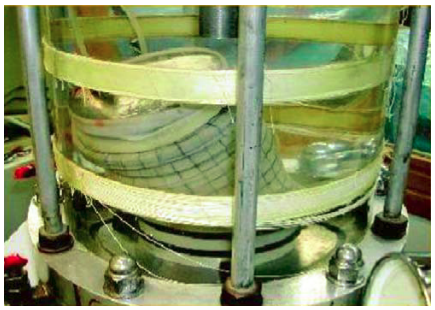

Fig. 1. Final configuration for an undrained triaxial test

3 A TRANSITION CONSTITUTIVE MODEL

We propose in this section the global formulation of a transition constitutive model based on: a constitutive relation for the solid in-situ soil, a constitutive relation for the fluid post failure phase and a transition criterion.

3.1 Transition criterion

As presented in section 1., the second order work criterion is well suited to predict solid bifurcation domain in the principal stress frame (it is obtained in practise by a 'directional search', that is to say the search -for a given point of the stress frame- of at least one negative value of d^2W with incremental loads applied in different directions). More than predicting this domain bounds, if only the direction of the current loading path is considered, the second order work can also be used as a failure criterion.

Besides, according to the literature, the vanishing of d^2W is linked to a burst a kinetic energy and a dynamic response, even if the perturbation of the system is infinitesimal (Nicot et al. 2011; Daouadji et al. 2012). That is why we consider, in the present approach, that the second order work, as it is a failure criterion for a given load increment, can also stand for a transition criterion between a solid behaviour and a fluid one, in the case of diffuse failures. In practice, the computation of d^2W can be led very simply for each material point and at each step, under a normalized form. It is expressed this way:

$$dW_n^2 = \frac{d\sigma_{ij}d\varepsilon_{ij}}{||\boldsymbol{d\sigma}||||\boldsymbol{d\varepsilon}||}, \tag{2}$$

the stress and strain increments being calculated explicitly, that is to say by a difference between the current state and the previous one.

3.2 The association of two constitutive relations

On the one hand, soils are classically described with elasto-plasticity with the specific features of hardening and non associativity. On the other hand, granular suspensions are mainly characterized by a yield stress viscous behaviour (Daido 1971; Coussot & Piau 1994; Roussel et al. 2007) and, to a lesser extent, by a non linearity of the viscous relation.

We propose to base, in a general manner, our transition model on the association of such elasto-plastic and viscous relations, for respectively the geomaterial in-situ phase and its flowing post failure one.

According to the sudden character of the collapse for the undrained triaxial test on a loose sand (if stress driven), and according to the well-known extremely fast development of mudflows, it can be considered that the solid→fluid transition in geomaterial during a diffuse failure is very sudden. We thus propose to consider, from an initial elasto-plastic behaviour, to activate instantaneously a viscous response (that is to say viscous strain rates if the threshold is overstepped) from the failure/transition state.

The fluid→solid transition which takes place when the flow stops (for example down a slope) is then described continuously since the stress state turns inside the stress threshold. As this point, the behaviour turns back solid.

Finally, the general scheme of the transition model is presented on figure 2. It can be used with various elasto-plastic or viscous (with yield stress) relations.

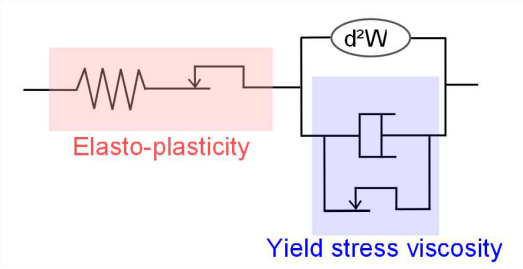

Fig. 2. Scheme of the proposed model in one dimension. The yield stress viscosity is activated as soon as d^2W becomes zero or negative.

3.3 First elasto-plastic and viscous chosen constitutive relations

a) Plasol elasto-plastic relation

Plasol (Barnichon 1998) is a well suited model for a wide range of soils, thanks to the following characteristics :

- Van Eekelen plastic criterion (VanEekelen 1980)
  This criterion, which depends on the three stress invariants, has a conical shape in the stress frame with a non circular base, whose radius is consistently larger in the compression direction than in the extension one. The equation of this criterion is:

$$f = J_{2\sigma} + m.\left(J_{1\sigma} - \frac{3C}{tan\varphi_c}\right) = 0 \tag{3}$$

  with : $J_{1\sigma} = tr(\boldsymbol{\sigma})$, $J_{2\sigma} = \sqrt{tr(\boldsymbol{s^2})}$, $J_{3\sigma} = \sqrt[3]{tr(\boldsymbol{s^3})}$ the three invariants of stress tensor $\boldsymbol{\sigma}$ ($\boldsymbol{s} = \boldsymbol{\sigma} - J_{1\sigma}/3.\boldsymbol{I}$ being the deviatoric part of tensor $\boldsymbol{\sigma}$), C the cohesion, φ_c the mobilized compression friction angle. m is a coefficient such as:

$$m = a(1 + b\sin(3\theta))^n,$$

where θ is the Lode angle defined as: $\sin(3\theta) = \sqrt{6}\left(J_{3\sigma}/J_{2\sigma}\right)^3$, n is a dimensionless parameter controlling the convexity of the criterion trace in the deviatoric plane and a and b are coefficient defined as:

$$b = \frac{(r_c/r_e)^{1/n} - 1}{(r_c/r_e)^{1/n} + 1} \quad \text{and} \quad a = \frac{r_c}{(1+b)^{1/n}},$$

with :

$$r_c = \frac{1}{\sqrt{3}}\left(\frac{2sin\varphi_c}{3 - sin\varphi_c}\right), \quad and \quad r_e = \frac{1}{\sqrt{3}}\left(\frac{2sin\varphi_e}{3 + sin\varphi_e}\right)$$

r_c and r_e are the compression and extension reduced radii define by $J_{3\sigma}/J_{2\sigma}$ for the triaxial test, and φ_e is the extension friction angle.

- Hardening of the yield surface
  Generally, softening is not used with Plasol, which means that the plastic parameters always increase with the plastic strains. This plastic parameter evolution (between initial values, symbolized with index '$_0$', and final ones, with index '$_f$') is defined as follows :

$$\begin{aligned} \varphi_c &= \varphi_{c0} + \frac{(\varphi_{cf} - \varphi_{c0})\varepsilon^p_{eq}}{B_p + \varepsilon^p_{eq}} \\ \varphi_e &= \varphi_{e0} + \frac{(\varphi_{ef} - \varphi_{e0})\varepsilon^p_{eq}}{B_p + \varepsilon^p_{eq}} \\ C &= C_0 + \frac{(C_f - C_0)\varepsilon^p_{eq}}{B_c + \varepsilon^p_{eq}}, \end{aligned} \tag{4}$$

  with B_p and B_c the hardening parameters, and ε^p_{eq} the equivalent plastic strain equal to $\sqrt{\frac{2}{3}e^p_{ij}e^p_{ij}}$ (with $\boldsymbol{e^p}$ the deviatoric part of plastic strain tensor $\boldsymbol{\varepsilon^p}$). The initial and final values of the plastic parameters define respectively the elastic domain bound and the plastic limit surface, beyond which no equilibrium can be found.

- Non-associativity
  In granular material the plastic potential (denoted g) is known to differ from the yield function f (see equation 3) and is expressed as follows:

$$g = J_{2\sigma} + m'.\left(J_{1\sigma} - \frac{3C}{tan\varphi_c}\right),$$

  where m' expression is similar to m one, but with dilatancy angles (ψ_e in extension and ψ_c in compression) instead friction ones. Dilatancy angles evolve in the same manner as friction ones during hardening, but as Plasol imposes a constant difference between ψ and ϕ, (Taylor law - Taylor (1948)), only the final values of ψ_e and ψ_c have to be given.

In total, as Plasol lastly considers an isotropic elastic relation in the elastic domain, 13 parameters are needed (E, ν and 11 plastic parameters).

b) Bingham viscous relation
Bingham is the simplest viscous constitutive relation with a stress threshold. In one dimension, it is expressed as follows:

$$\text{if} \quad |\tau| > s_o : \qquad \dot{\gamma} = (\tau - s_o \,\text{sgn}(\tau))/\eta, \qquad \text{else} : \quad \dot{\gamma} = 0, \tag{5}$$

with η the dynamic viscosity, τ the shear stress, $\dot{\gamma}$ the velocity gradient, and s_o the yield stress. Function $x \rightarrow \text{sgn}(x)$ returns the sign of scalar x. In three dimensions, and supported by the expression of Duvaut & Lions (1972), it can be expressed this way:

$$\text{if} \quad J_{2\sigma} > s_o : \qquad \dot{e}_{ij} = \frac{1}{2\eta}\left(s_{ij} - s_o \frac{s_{ij}}{J_{2\sigma}}\right) = \frac{J_{2\sigma} - s_o}{2\eta} . \frac{s_{ij}}{J_{2\sigma}}, \qquad \text{else} : \quad \dot{e}_{ij} = 0, \tag{6}$$

where $\boldsymbol{s}$ and $\dot{\boldsymbol{e}}$ are respectively the deviatoric stress and strain tensors, $J_{2\sigma}$ and $J_{2\dot{\varepsilon}}$ are the second invariants of stress and strain rate tensors (in other words, norms of $\boldsymbol{s}$ and $\dot{\boldsymbol{e}}$). The yield stress is thus equivalent to a tensor with a direction given by $\dot{s}_{ij}/J_{2\dot{\sigma}}$.

To conclude, this constitutive model, by describing the evolution between a solid and a fluid phase, allows to overstep a first limitation in mudflows whole modelling. The second constraint being numerical (cf. introduction), the following section starts to introduce the numerical tool we used before presenting the model we chose to simulate.

4 FIRST MODEL

4.1 FEMILP method

As one difficulty to simulate landslide lays in the ability to be describe both history dependent behaviours and high levels of strains, we used an original and very flexible numerical method with regard to these requirements, the FEMLIP method (Moresi & Solomatov 1995; Moresi et al. 2003), developed from Particle in Cell methods (Harlow 1964).

FEMLIP has the specificity to be based on a double discretisation: one related to the space (with classical finite elements) and one related to the material (with material points, also called 'particles', although they have nothing to do with physical entities). On one hand, as the finite element grid is Eulerian, it is fixed and it thus allows to deal with a high level of transformation. Nodal kinematical variables are solved in a classical way. On the other hand, the particles are handling the material properties (density, mechanical parameters, etc.) and variables (plastic strains, stresses, etc.). As they are associated with the material, they move according to the calculated displacement field for a given step. This way, material parameters and internal variables are conserved without space diffusion. FEMLIP is thus able to deal with history variables behaviours, as well as to accurately track frontiers between different materials (figure 3). The two discretization systems are disconnected after each step, since the material points advect across the fixed mesh. The link between them is temporarily re-established at every step since the particles are used as integration points. Each particle thus contributes to the integrals computation with its current coordinates and current numerical weight, re-computed at every step.

FEMLIP is thus well suited to describe the different phases of landslides: initiation, flow and arrest. It is important to underline that very few continuum methods are able to do so. SPH method, used in geomechanics for natural flows (Pastor et al. 2010), is also developed for elasto-plastic geomaterials (Bui et al. 2008). Besides, Material Point Method (Sulsky & Schreyer 1996)

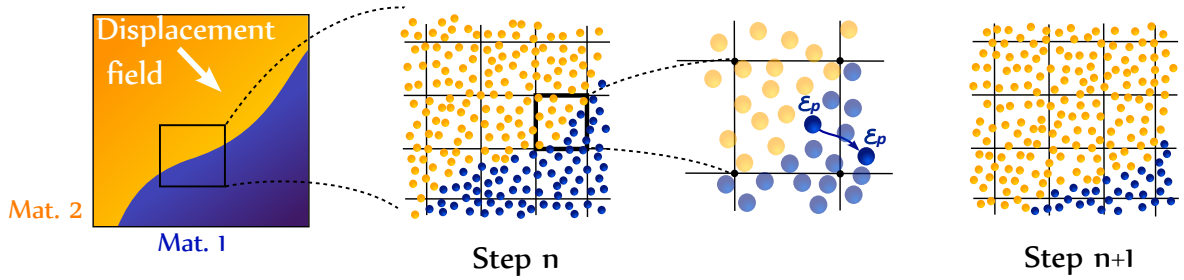

Fig. 3. Spatial and material discretizations in FEMLIP. Accurate tracking of the internal variables (as plastic strains) and parameters (represented here by the different colours) during the advection of two materials

has some common points with FEMLIP (as it also comes from Particle In Cell methods) but with a different integration process (see Moresi et al. 2003).

The FEMLIP code used in this contribution considers 2D plane strain conditions, no hydromechanical coupling and a viscous resolution matrix. The elastoplastic behaviour is taken into account by a modification of the global resolution matrix and of the force term (see Cuomo et al. 2012; Prime et al. 2011).

4.2 Geometry

The model we chose to simulate is a heuristic case with a simple geometry. It is made of a 27° slope on the top of which initially lays a metric square soil sample, and with a 50 cm high obstacle at its toe (Fig. 4). Three materials are described inside the model: the soil (initially elastoplastic, with a transitional behaviour), the obstacle (elastic), and a surrounding material (viscous). This last is not interesting for our analysis, but it need to be described: as the soil particles are moving through the fixed mesh, the initial grid must include all the domain they can potentially reach.

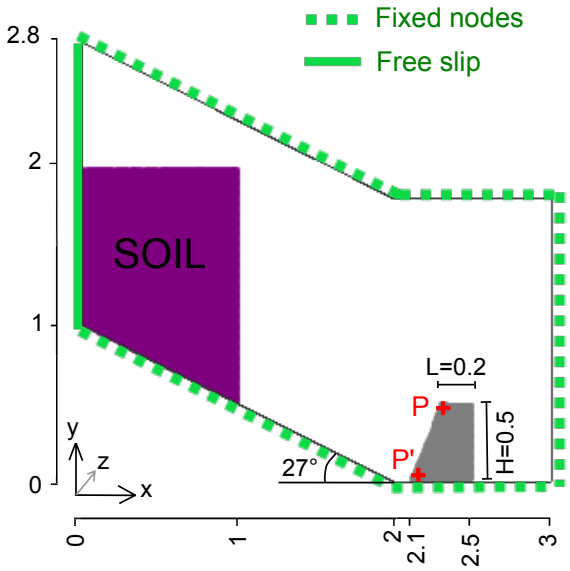

Fig. 4. Geometry and boundary conditions of the model studied

Displacements are prohibited on all boundaries, except on the left one where a free slip condition is applied. Finally, the model is divided in quadrilateral elements: 72 along x axis and 48 along y axis that follows the model boundaries (axes are shown in figure 4).

4.3 Parameters chosen

16 parameters are needed for the soil sample: 13 elasto-plastic, 2 viscous ones (the viscosity and the stress threshold, the granular suspension being supposed incompressible), and the density. They have been chosen as close as possible to those of the ash formation involved in the very investigated Sarno and Quindici mudflows (1998, Italy). E, ν, φ_f, C_f, γ_{nat} could be extracted from Olivares & Picarelli 2001; Cascini et al. 2010; Crosta & Negro 2003. Besides, we considered that friction and dilatation angles are the same in compression and extension and that there is a ratio of 5 between initial and final values of the plastic parameters. η and s_o were estimated through the velocity, the slope and the thickness of the flow on the one hand, and the order or magnitude for different mudflow events on the other hand (Jeyapalan et al. 1983; Pastor et al. 2008; Blasio et al. 2004). All these physical parameters are presented in table 1. Finally calibration coefficients n, B_p and B_c were chosen with realistic values of, respectively, -0.229, 0.01 and 0.02 (Lignon et al. 2009).

Table 1. Synthesis of parameters chosen

	γ_{nat} (kN/m^3)	E (MPa)	ν	C' (kPa)	$\varphi'_e = \varphi'_c$ (°)	$\psi_e = \psi_c$ (°)	η (Pa.s)	s_o (kPa)
Soil	16	5	0.29	2/10	8/38	-25/5	150	1.5
Obstacle		0.5	0.29					

Concerning the obstacle, E and ν have been chosen equal to 500 kPa and 0.29. The surrounding material viscosity has been chosen the lower possible, to not influence the result.

4.4 Load applied

A simple increase of gravity is considered, with a final value of 9.8 m/s^2 achieved in 50 steps.

5 RESULTS AND ANALYSIS

5.1 Initiation, propagation and arrest

First of all, for such a set of parameters, the computation led to a failure of the soil and a transition of its behaviour. Figure 5 highlights that various phases can be distinguished along the simulation.

Fig. 5a presents, in the initial configuration (no substantial strains have occurred yet), the pattern of the transition inside the sample for a gravity that has reached 7.8 m/s^2. The failure has a diffuse mode since the major part of the sample has achieved a zero second order work, and behaves viscously. That is consistent with the high initial contractancy ($\psi_0 = -25°$). Fig. 5b shows the propagation of the flow along the slope. The velocity of the front in this step is around 5 m/s which is a realistic order of magnitude compared to observed mudflows (notably in Sarno ans Quindici where it reaches more than 15 m/s). In Fig. 5c, the first contact of the flow with the obstacle is focused on, with a second stress invariant which starts to turn under the stress

threshold. According to that figure (and the figures of the other steps) one can observed that the immobilization occurs retrogressively from the top front of the flow, most likely less sheared. Finally, Fig. 5d presents the almost final configuration, on which the behaviour has turn back to be solid. The unique part that remains viscous is a thin band marking the direction of the higher second stress invariant.

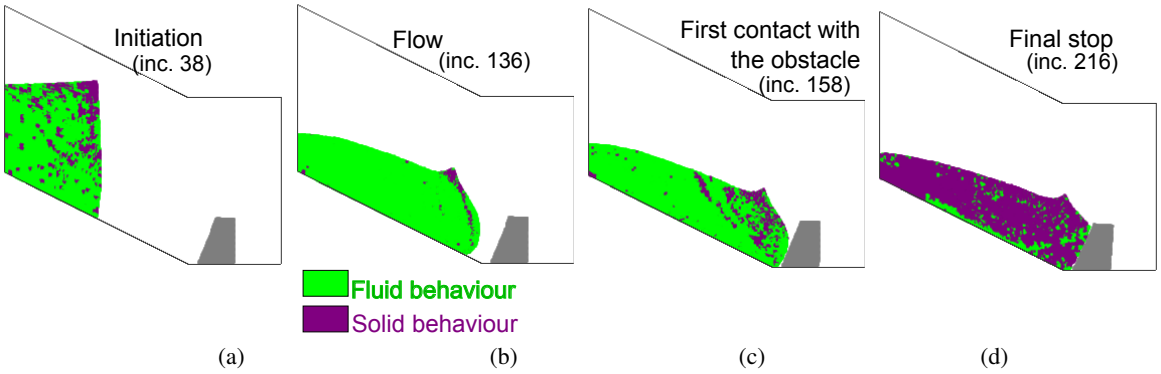

Fig. 5. Different stages of the flow: (a) diffuse failure, (b) general flow, (c) first solidification at the obstacle contact, (d) last remaining viscous band, in the most sheared zone.

Concerning the response of the obstacle, the horizontal displacement U_x of its top (that it to say the maximum displacement of the structure) and the second stress invariant $J_{2\sigma}$ on its base have been extracted on two specific particles (P and P' respectively on figure 4). It appears that the final (and maximum) values of displacement and second stress invariant respectively reached about 3 cm and 15 kPa. The temporal evolution of these quantities are visible on figure 6, for case E=0.5 MPa. According to the simulation, the first contact of the flow with the obstacle occurred at t=0.58 s. It means that the slight increase in U_x and $J_{2\sigma}$ between t=0.4 and t=0.58 s is only due to the surrounding 'air' material, whose negligible effect is thus verified.

5.2 Parametric analysis on the obstacle characteristics

One of the advantages of such a model, in addition to studying both the stability and the flow of a soil sample, is to calculate the optimum configuration of a solid obstacle interacting with the fluid mud. Following this idea, two parametric studies have been led, one on the obstacle Young modulus, and one on its height.

In the first case, U_x and $J_{2\sigma}$ have been extracted with a Young modulus varying between 500 kPa and 5 MPa. The results are presented in Fig. 6.

From these graphs, it appears first that an increase of E makes decrease the maximum displacement of the structure, which is consistent since flexion rigidity is proportional to E (it is equal to $\frac{EL^3}{12(1-\nu^2)}$). Secondly, it has no influence on the second stress invariant on its base. Indeed, the load applied on the obstacle by the flowing mass is always the same.

Besides, the influence of the obstacle's height H is an important parameter to study, in the context of a natural flow to contain. Height of 0.25, 0.3 and 0.4 m have been considered in addition to the case H=0.5 m. For each case, we determine if the obstacle was overhung or not by the flow. Configurations are presented for the three heights, after 300 to 350 increments. The zoning of solid and fluid behaviour highlights that, at this stage, stable configurations have been obtained for H=0.4 and H=0.3 m ('stable' in the sense that the viscous flow is almost stopped).

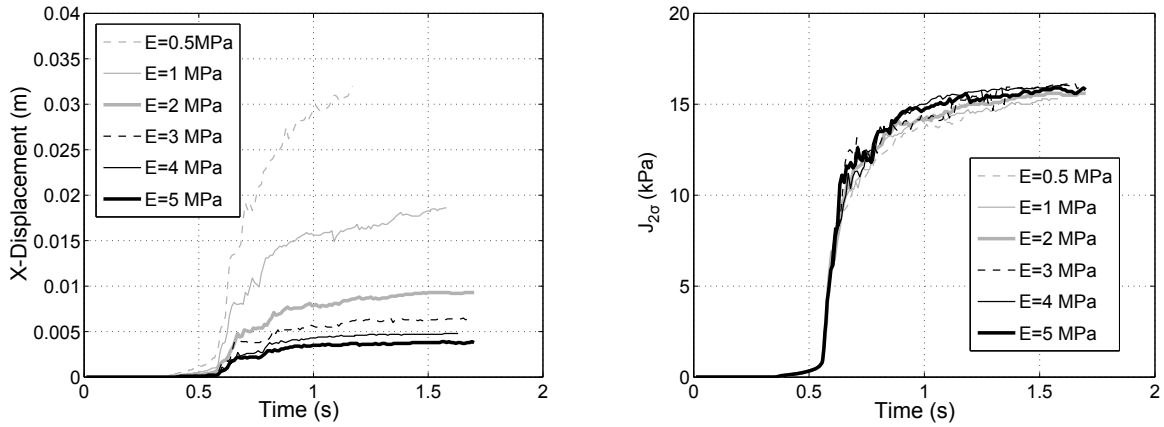

(a) Influence of E on the X-displacement of the obstacle's top

(b) Influence of E on $J_{2\sigma}$ of the obstacle's base

Fig. 6. Influence of the Young modulus E on the obstacle's response

On the contrary, for H=0.25 m, viscosity is still active, and the geomaterial flow is overhanging the obstacle.

For the present model, the minimum protection structure height is thus of 0.3 m (without considering any safety factor).

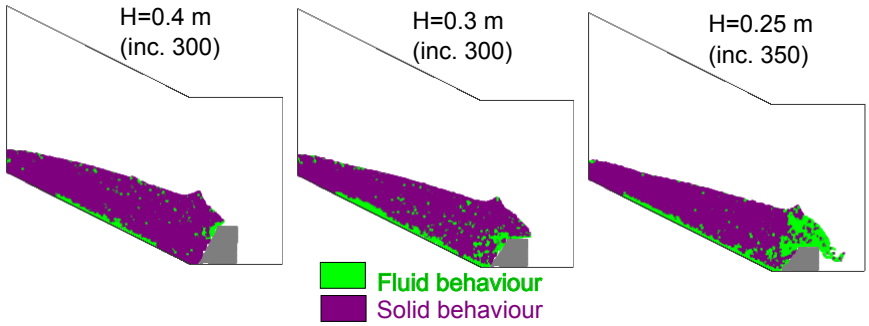

Fig. 7. Influence of height H on the obstacle efficiency

6 CONCLUSIONS

In conclusion, this contribution presented a new approach to describe solid→fluid transition for soils at failure (focusing on diffuse failure), but also for fluid→solid transition in granular suspensions. The model simulated is simple but gathers all the features necessary to describe more complex mudflows: a description of the elasto-plastic behaviour during the stable in-situ phase, an accurate detection of the failure state (which is considered also as a transition state), a description of the flow itself, and finally the arrest of the flow with eventual interactions with some structures. This last point is particularly interesting from an engineering point of view because it means that the efficiency of protection work can be predicted, according to the structure material strenght, to the volume of flow generated, etc.

The combination of the constitutive transition model and the FEMLIP method has thus proved its potential to describe phase transition in mudflow events, and has many prospects in numerous natural flows (mudflows, but also lahars, avalanches...)

REFERENCES

Balmforth, N. & Craster, R. (1999). A consistent thin layer theory for bingham plastics. *Journal of non-newtonian fluid mechanics 841*, 65–81.

Barnichon, J. (1998). *Finite Element Modeling in Structural and Petroleum Geology*. Ph. D. thesis, Universit de Lige.

Blasio, F. D., Elverhoi, A., Issler, D., Harbitz, C., Bryn, P., & Lien, R. (2004). Flow models of natural debris flows originating from overconsolidated clay materials. *Marine Geology 213*, 439–455.

Bui, H., Fukagawa, R., Sako, K., & Ohno, S. (2008). Lagrangian meshfree particles method (sph) for large deformation and failure flows of geomaterial using elastic–plastic soil constitutive model. *International journal for numerical and analytical methods in geomechanics 32*(12), 1537–1570.

Cascini, L., Cuomo, S., Pastor, M., & Sorbino, G. (2010). Modeling of rainfall-induced shallow landslides of the flow-type. *Journal of geotechnical and geoenvironmental engineering 136*, 85.

Coussot, P. & Piau, J. (1994). On the behavior of fine mud suspensions. *Rheological Acta 33*, 175–184.

Crosta, G. & Negro, P. D. (2003). Observations and modelling of soil slip-debris flow initiation processes in pyroclastic deposits: the sarno 1998 event.

Cuomo, S., Prime, N., Iannone, A., Dufour, F., Cascini, L., & Darve, F. (2012). Large deformation femlip drained analysis of a vertical cut (accept). *Acta Geotecnica ASCE 1*, 1.

Daido, A. (1971). On the occurence of mud-debris flow. *Bulletin of the Disaster Prevention Research Institute, Kyoto Univ 21*, 109–135.

Daouadji, A., Darve, F., Gali, H. A., Hicher, P., Laouafa, F., Lignon, S., Nicot, F., Nova, R., Pinheiro, M., Prunier, F., Sibille, L., & Wan, R. (2011). Diffuse failure in geomaterials: Experiments, theory and modelling. *International Journal of Numerical and Analytical Methods in Geomechanics 35(16)*, 1731–1773.

Daouadji, A., Jrad, M., Prunier, F., Sibille, L., Nicot, F., Laouafa, F., & Darve, F. (2012). Divergence instability and diffuse failure in granular media. *Procedia IUTAM 3*, 105–130.

Darve, F. & Laouafa, F. (2000). Instabilities in granular material and application to landslides. *Mechanics of Cohesive-Frictional Materials 5*, 627–652.

Duvaut, G. & Lions, J. (1972). Transfert de chaleur dans un fluide de bingham dont la viscosit dpend de la temprature. *Journal of Funtional Analysis 11*, 93–110.

Harlow, F. (1964). *The Particle-In-Cell Computing Method for Fluid Dynamics in Fundamental Methods in Hydrodynamics*. B. Lader and S. Fernbach and M. Rotenberg.

Hill, R. (1958). A general theory of uniqueness and stability in elasto-plastic solids. *Journal of the Mechanics and Physics of Solids 6*, 236–249.

Jeyapalan, J., Duncan, J., & Seed, H. (1983). Investigation of flow failures of tailing dams. *Journal of Geotechnical Engineering ASCE 109*, 172–189.

Khoa, H., Georgopoulos, I., Darve, F., & Laouafa, F. (2006). Diffuse failure in geomaterials: Experiments and modelling. *Computers and Geotechnics 33*(1), 1–14.

Laouafa, F. & Darve, F. (2002). Modelling of slope failure by material instability mechanism. *Computers and Geotechnics 29*, 301–325.

Lignon, S., Laouafa, F., Prunier, F., Khoa, H., & Darve, F. (2009). Hydro-mechanical modelling of landslides with a material instability criterion. *Geotechnique 59*(6), 513–524.

Moresi, L., Dufour, F., & Mühlhaus, H. (2003). A lagrangian integration point finite element method for large deformation modeling of viscoelastic geomaterials. *Journal of Computational Physics 184*(2), 476–497.

Moresi, L. & Solomatov, V. (1995). Numerical investigation of 2d convection with extremely large viscosity variations. *Physics of Fluids 7*, 2154.

Nicot, F., Daouadji, A., Laouafa, F., & Darve, F. (2011). Second-order work, kinetic energy and diffuse failure in granular materials. *Granular Matter 13,1*, 19–28.

Nicot, F. & Darve, F. (2011). Diffuse and localized failure modes, two competing mechanisms. *International Journal for Numerical and Analytical Methods in Geomechanics 35,5*, 586–601.

Olivares, L. & Picarelli, L. (2001). Suceptibility of loose pyroclastic soils to static liquefaction : some preliminary datas. In Khne M, Einstein HH, Krauter E, Klapperich H, Pttler R (Ed.), *Proceedings of International Conference on Landslides Causes, Impacts and Countermeasures, Davos*, pp. 75–85.

Pastor, M., Manzanal, D., Merodo, J. F., Mira, P., Blanc, T., Drempetic, V., Pastor, M., Haddad, B., & Sánchez, M. (2010). From solids to fluidized soils: diffuse failure mechanisms in geostructures with applications to fast catastrophic landslides. *Granular Matter 12*, 211–228.

Pastor, M., Merodo, J. F., Herreros, M., Pira, P., Gonzlez, E., Haddad, B., Quecedo, M., Tonni, L., & Drempetic, V. (2008). Mathematical, constitutive and numerical modelling of catastrophic landslides and related phenomena. *Rock Mechanics and Rock Engineering 41(1)*, 85–132.

Prime, N., Dufour, F., & Darve, F. (2011). Modeling of landslides with a finite element method with lagrangian integration points. In *International Symposium on Computational Geomechanics, Cavtat, Croatia*.

Roussel, N., Geiker, M., Dufour, F., Thrane, L., & Szabo, P. (2007). Computational modeling of concrete flow: General overview. *Cement and Concrete Research 37*(9), 1298–1307.

Sulsky, D. & Schreyer, H. (1996). Axisymmetric form of the material point method with applications to upsetting and taylor impact problems. *Computer Methods in Applied Mechanics and Engineering 139*(1), 409–429.

Taylor, D. (1948). *Fundamentals of Soil Mechanics - London Wiley*.

VanEekelen, H. (1980). Isotropic yield surface in three dimensions for use in soil mechanics. *International Journal for Numerical and Analytical Methods in Geomechanics 4*, 89–101.

A PROBABILISTIC STUDY OF A FILL IN GENTLY INCLINED AREA OF SENSITIVE CLAY USING FEA

P. Fornes
Norwegian Geotechnical Institute, Oslo, Norway

H.P. Jostad
Norwegian Geotechnical Institute, Oslo, Norway

ABSTRACT: *A probabilistic study was performed in order to improve the selection of a deterministic material coefficient to be used in the design of roads in areas of very sensitive clays. The material model NGI-ADPSoft was implemented into Plaxis 2D as a user-defined soil model. The model is a total stress model with anisotropic undrained shear stress-shear strain relationships including post peak strain softening, which makes it suitable for modelling the initiation of progressive failure in sensitive clays during undrained loading. The case study considered was the construction of a road fill in a long gently inclined slope. Monte Carlo simulation was performed using 1000 finite element analyses, both with and without strain softening behaviour, and Latin Hypercube sampling of 10 independent variables. The probability distributions of the input parameters are based on soil data from a project close to the historic quick clay slide in Rissa, Norway. A lognormal distribution function was fitted to the calculated failure loads, and used to estimate the probability of failure for different material coefficients. The material coefficient had to be increased from 1.4 to 1.7 (20 %), to obtain the same probability of failure for a strain-softening material as for a perfectly plastic material.*

1 INTRODUCTION

The Norwegian National Annex to Eurocode 7 (2008) states in Table NA.A.4 that the material coefficient should be increased when progressive failure is possible. However, the document does not provide guidelines of how much the material coefficient should be increased. In the Norwegian Public Road Administration's Handbook 016, the effect of brittle post peak behaviour is accounted for by increasing the required material coefficient γ_m in a total stress based limit equilibrium analysis. The increase is from 1.4 to 1.5 or from 1.5 to 1.6 (about 7 % increase), depending on the consequence of failure.

In the guidelines for evaluating overall stability of areas with quick clays by the Norwegian Water Resources and Energy Directorate (NVE), the required material coefficient γ_m should at least be 1.4 for construction works that increase the mobilization of the soil. The brittle behaviour of these clays should then be accounted for by reducing the peak shear strength by simple strain compatibility or a recommended percentage reduction when based on results from high quality block samples.

The purpose of this paper is to find the necessary increase in the material coefficient γ_m to indirectly account for the effect of strain-softening when analyzing such problems with conventional limit equilibrium methods and characteristic undrained peak shear strength.

Jostad et al. (2013) conducted a large sensitivity study to evaluate the reduction in capacity due to strain-softening for a large range of typical Norwegian soil conditions. In the present probability study, the required increase in γ_m was obtained by finding the same probability of failure when modelling with a strain softening material as for modelling with a perfectly plastic material. For a complex problem with many random variables, the Monte Carlo simulation accelerated with Latin Hypercube sampling is well suited (Lacasse & Nadim, 1996). The results from this study are meant as basis for a new guideline on how to perform safe design in areas with sensitive and quick clays in Norway.

2 SOIL MODEL

The material model NGI-ADPSoft (Grimstad & Jostad, 2010; Jostad & Grimstad, 2011) was used to model the sensitive clay in the probability study. The model is a user-defined special version of the NGI-ADP model (Grimstad et al., 2010), which was implemented as a standard material model into Plaxis (www.Plaxis.nl). The model is a total stress elasto-plastic model that describes the anisotropic behaviour of clays during undrained shear and includes post peak strain-softening. This makes the NGI-ADPSoft model suitable for modelling the initiation of progressive failure in sensitive clays under undrained loading.

The model uses as input the data from anisotropically consolidated undrained triaxial compression (CAUC) tests, constant volume direct simple shear (DSS) tests and undrained triaxial extension (CAUE) tests. The input data is the peak undrained shear strength s_{up} and the residual shear strength s_{ur} and the corresponding shear strains γ_p and γ_r along the shear stress-shear strain curves, as shown in Fig. 1. The curves start at an initial shear stress τ_o with the slope given by the initial shear modulus G_o. In the following, the plane strain "A=Active" behaviour is assumed to be equal to the triaxial compression behaviour, and correspondingly, the plane strain "P=Passive" behaviour is assumed to be equal to the triaxial extension behaviour. Using interpolation between the three input curves, the model describes the general 3D anisotropic behaviour of the clay that depends on the actual orientation of the maximum shear deformation.

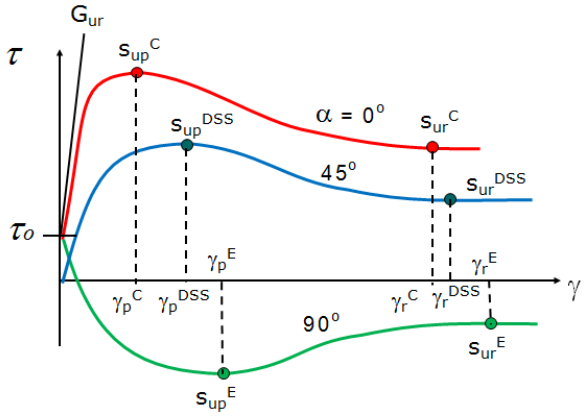

Fig. 1. Input parameters for the material model NGI-ADPSoft

The softening behaviour is regularized by introducing a "non-local plastic shear strain". The main idea of the so-called "non-local strain" (Eringen, 1981) is that the plastic strain in a stress point (Gaussian integration point) is replaced by an integrated weighted average plastic strain within a specified zone around the point. The result is that the plastic strain and ensuing reduction in the shear strength during softening becomes mesh independent. In this way, the shear band thickness and resulting brittleness are controlled by the input

parameters. More information about the non-local strain formulation used in the NGI-ADPSoft model is given in Grimstad & Jostad (2010) and Jostad & Grimstad (2011).

3 CASE STUDY

The case study considered is the construction of a road fill in a long natural slope with an inclination of only four degrees. The same Plaxis 2D FE model as in the Jostad et al. (2013) sensitivity study was used (Fig. 2). The boundary conditions were chosen to represent an unlimited slope. The element mesh is refined below the road fill, and consists in total of 2154 15-noded elements.

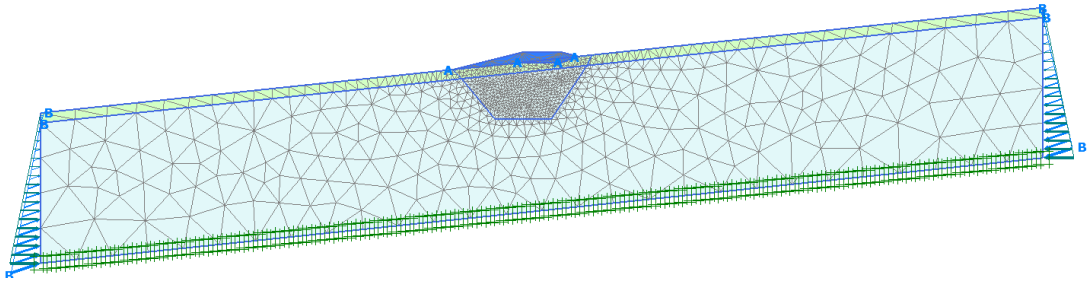

Fig. 2. FE model of slope with road fill in Plaxis 2D

The Mohr Coulomb constitutive law was used as soil model for the road fill with c_{ref} = 10 kPa and φ = 0 °. The user-defined soil model NGI-ADPSoft described in Section 2 was used for the clay slope. The top two meters were modelled as a non-sensitive clay, while the rest of the slope was modelled as a sensitive clay with strain softening behaviour. The slope started with an initial coefficient of lateral earth pressure K_0 = 0.6, and a calculation phase was done to gain equilibrium. Then, the road fill was added with zero unit weight to provide extra resistance, while a distributed load represented the weight from the road fill. This surface load was then gradually increased until failure.

4 SOIL DATA

The probability distributions of the input material parameters were based on soil data from an actual road project. The sensitive clay site is a planned road project (Fig. 3), which is close to the historic quick clay slide in Rissa in Norway (Gregersen, 1981). Example results of piezocone penetration tests (CPTU) and triaxial CAUC from the site are shown on Fig. 4.

Fig. 3. Location of the site (shown by black circle) close to Rissa and Trondheim, Norway.

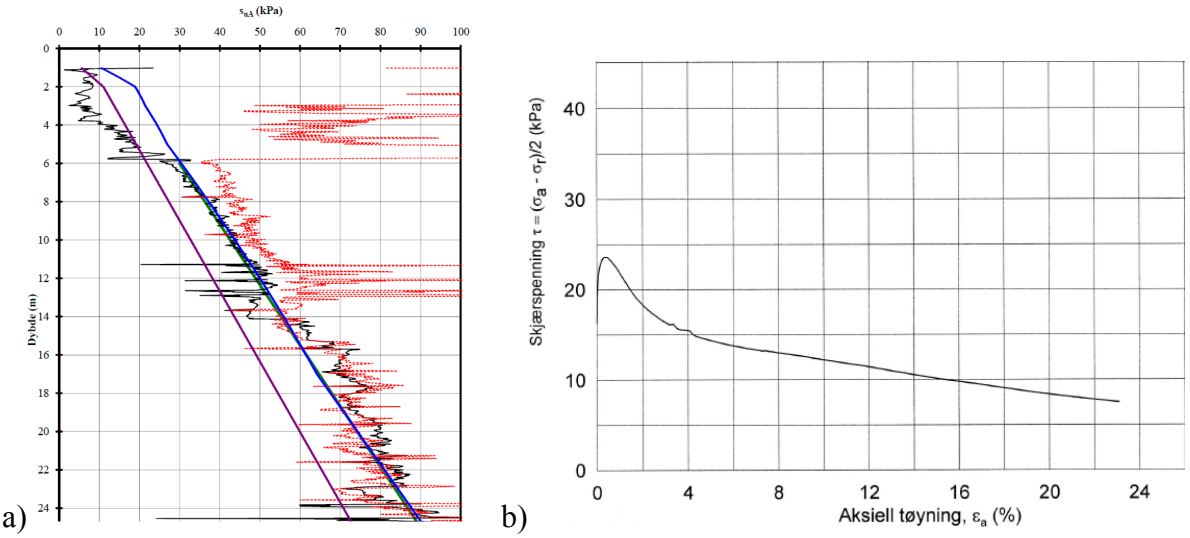

a) b)

Fig. 4. a) Undrained active shear strength profile s_{uA} from CPTU logs (black line is from pore pressure measurements, red line is from cone resistance measurements), and b) Triaxial CAUC test

5 MATERIAL PARAMETERS

The material model NGI-ADPSoft has 17 main input parameters. For the probability study all the input parameters were calculated from the 10 independent variables presented in Table 1. The standard deviation σ and mean values μ of each variable (Table 2) were based on the available soil data from the site: 5 CPTUs, 3 CAUC tests and 2 CAUE tests.

Table 1. Independent variables in NGI-ADPSoft model

Variable	Description	Based on
$s_u^A/s_u^A{}_{kar}$	Active undrained shear strength (s_u^A) normalized to characteristic undrained shear strength	CPTU
y_{ref}	Depth with constant strength	CPTU
G_{ur}/s_u^A	Initial shear stiffness normalized to s_u^A	CAUC
s_u^{DSS}/s_u^A	DSS strength normalized to s_u^A	CAUC, CAUE
s_u^P/s_u^A	Passive undrained shear strength normalized to s_u^A	CAUC, CAUE
γ_p^C	Shear strain at peak compression strength	CAUC
$\gamma_p^{DSS}/\gamma_p^C$	Shear strain at peak DSS strength normalized to γ_p^C	CAUC, CAUE
γ_p^E/γ_p^C	Shear strain at peak extension strength normalized to γ_p^C	CAUC, CAUE
γ_r^C-γ_p^C	Idealized shear strain from peak to residual compression strength	CAUC
-log(l_{int})	Internal length controlling shear band thickness	Assumed

Table 2. Probability distributions of independent variables in NGI-ADPSoft model

#	Variable	Mean value μ	Standard deviation σ	Unit	Distribution
1	$s_u^A/s_u^A{}_{kar}$	1.0	0.153	[-]	Lognormal
2	y_{ref}	6.0	0.860	[m]	Lognormal
3	G_{ur}/s_u^A	525	111	[-]	Lognormal
4	s_u^{DSS}/s_u^A	0.67	0.0089	[-]	Lognormal
5	s_u^P/s_u^A	0.33	0.0118	[-]	Lognormal
6	γ_p^C	1.0	0.532	[%]	Lognormal
7	$\gamma_p^{DSS}/\gamma_p^C$	2.0	0.70	[-]	Lognormal
8	γ_p^E/γ_p^C	3.0	1.24	[-]	Lognormal
9	γ_r^C-γ_p^C	21	11.6	[%]	Lognormal
10	-log(l_{int})	1.0	0.289	[-]	Uniform

Since the number of observations of each variable was limited, the standard deviation was estimated as the largest difference in the observations multiplied by a factor which is gradually reduced with additional observations according to Snedecor & Cochran (1964). For the present study, all the variables except the shear band thickness were assumed to have a lognormal probability distribution to avoid values below zero.

The strength profile is based on five CPTUs, shown on Fig. 5. A characteristic active undrained shear strength profile was determined by minimizing the difference between the CPTU data and an idealized straight line. Only the values below 6 m depth were considered in this idealization to account for the transition from the upper non-sensitive material to the sensitive clay. Fig. 4 indicates that the interpretations with the pore pressure response and with the cone resistance gave very different results down to 6 m depth. The constant shear strength $s_u^A{}_{ref}$ above y_{ref}, called the reference undrained shear strength, was therefore assumed and set equal to the strength at the top of the sensitive clay layer.

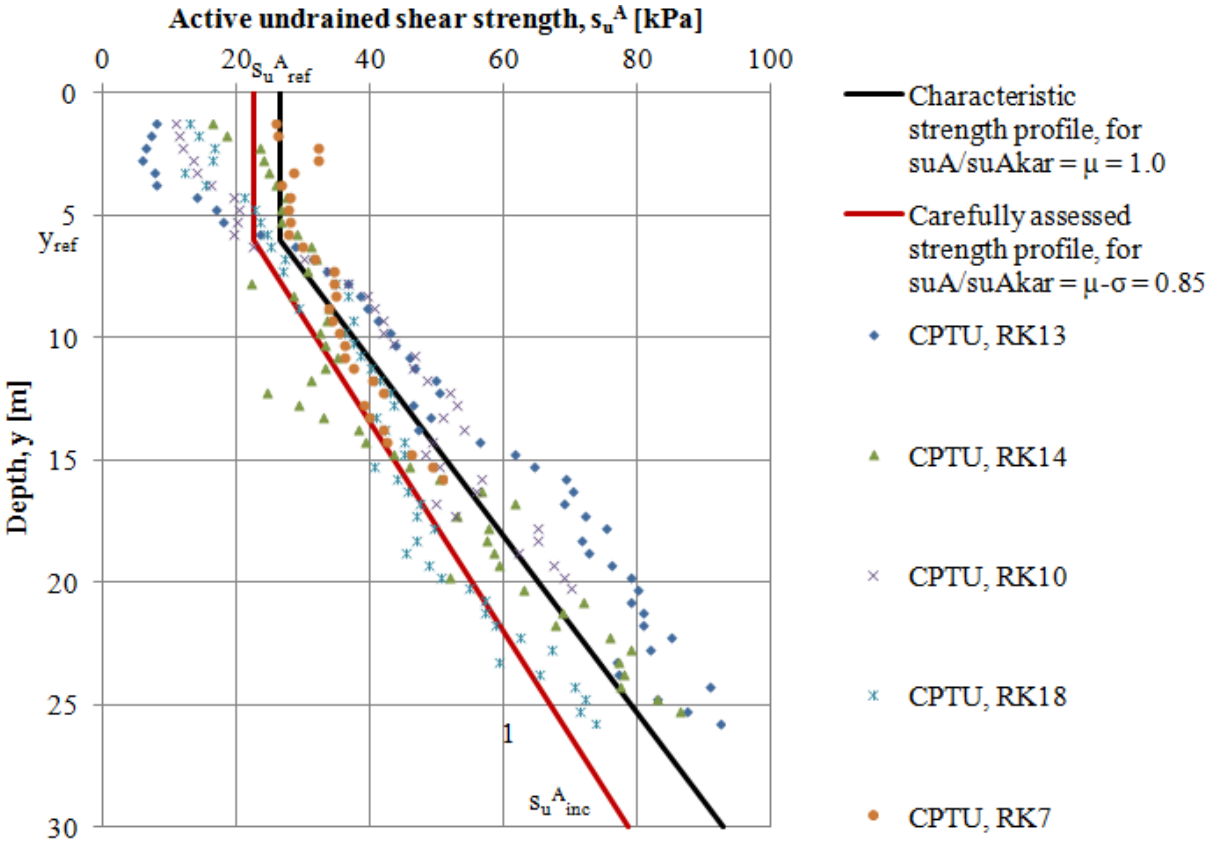

Fig. 5. Characteristic undrained shear strength profile and undrained shear strength interpreted from the pore pressure measurements from 5 different CPTU locations

For the characteristic active undrained shear strength profile, the increase of the characteristic $s_u^A{}_{inc,kar}$ strength with depth is 2.77 kPa/m and the reference characteristic $s_u^A{}_{ref,kar}$ strength is 26.5 kPa at 6 m depth (the mean value at depth y_{ref}). For the characteristic shear strength profile, the ratio s_u^A/σ_{v0}' is about 0.3, which is in the lower range of values from the NGI block sample database (Karlsrud & Hernandez-Martinez, 2013). The average standard deviation of the independent variable $s_u^A/s_u^A{}_{kar}$ was then determined from the CPTU data at each depth. Fig. 5 also presents a "carefully assessed" shear strength profile, for which the value of $s_u^A/s_u^A{}_{kar}$ was chosen as the mean value minus one standard deviation (Lacasse et al., 2007).

The reference shear strength $s_u{}^A{}_{ref}$ (at depth y_{ref}) and the increase of shear strength with depth $s_u{}^A{}_{inc}$ are calculated from the two independent variables $s_u{}^A/s_u{}^A{}_{kar}$ and y_{ref}:

$$s_{u\,inc}^{A} = s_{u\,inc,kar}^{A} \cdot \left[s_u^A / s_{u\,kar}^{A} \right] \tag{1}$$

$$s_{u\,ref}^{A} = \left(s_{u\,ref,kar}^{A} + \left(y_{ref} - 6\text{m} \right) \cdot s_{u\,inc,kar}^{A} \right) \cdot \left[s_u^A / s_{u\,kar}^{A} \right] \tag{2}$$

Eq. (1) and (2) indicate that there is a positive correlation between $s_u{}^A{}_{inc}$ and $s_u{}^A{}_{ref}$. This is not necessarily realistic for this type of material. The constant strength above y_{ref} is assumed as an approximation only which made it easier to run the Monte Carlo simulations. Otherwise the element mesh would have to be dependent on y_{ref}.

6 CALCULATIONS

The Monte Carlo simulation (MCS) (Metropolis & Ulam, 1949) was performed with 1000 finite element (FE) analyses. A script was used to run the FE program several times with new input parameter sets taken from input files. The analyses were performed with and without strain-softening behaviour, the latter called "Perfectly plastic". To obtain a reliable result with fewer simulations, Latin Hypercube sampling (LHS) was used for the 10 independent variables to generate the 1000 input parameter sets. This LHS technique ensures that the whole range of values of the probability distributions is used.

In addition to the Monte Carlo simulations, two sets of deterministic analyses were made to relate probability of failure to the material coefficient γ_m. The same case as in the Monte Carlo simulation with perfectly plastic behaviour was considered, and the undrained shear strengths were divided by different values of γ_m to obtain the failure loads. In the first set of analyses, the mean characteristic value of each variable was used. The same was done in the second set, but the independent variable $s_u{}^A/s_u{}^A{}_{kar}$ was selected as the mean value minus one standard deviation (as the "carefully assessed" shear strength profile in Fig. 5).

7 RESULTS

The results from the Monte Carlo simulations are shown in Fig. 6 with frequency diagrams of the failure load for the simulations with and without strain-softening. Out of the 1000 simulations without softening behaviour, 7 were unsuccessful due failure of the slope. These parameter sets were considered as unrealistic and thus removed from the data set.

The probability distributions of the failure load are shown in Fig. 7 for the Monte Carlo simulations with and without strain-softening (denoted "accumulated"). A lognormal probability distribution fitted very well the Monte Carlo simulation results (as expected since the random variables were mostly lognormal). The mean and the standard deviation of the failure load were 89.9 and 17.3 for the perfectly plastic soil, and 75.2 and 17.8 for the strain-softening soil.

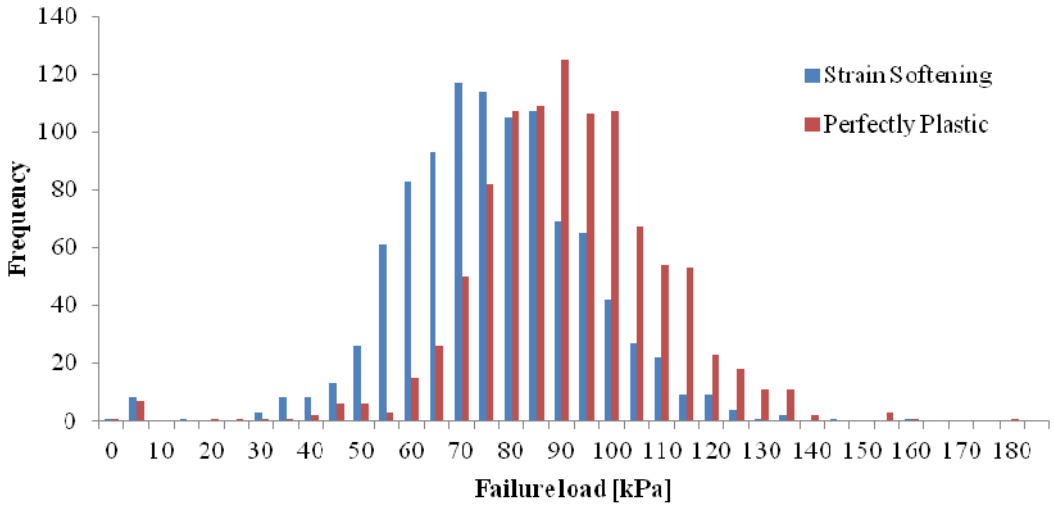

Fig. 6. Distribution of failure load with and without strain-softening

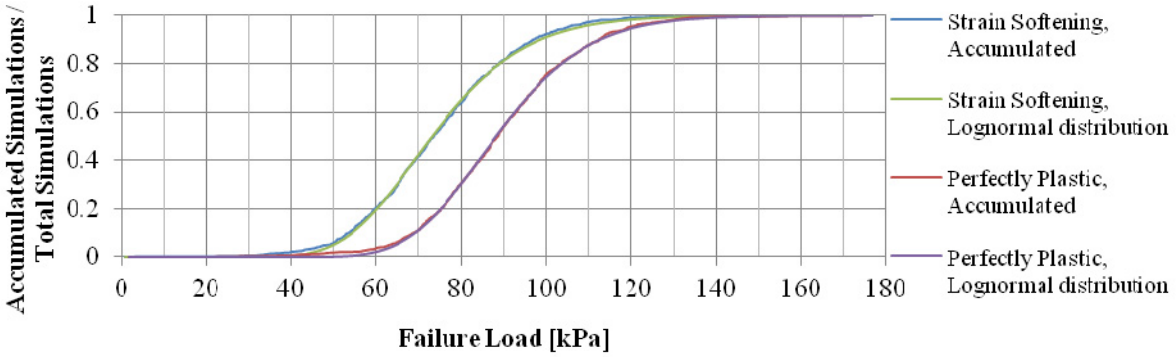

Fig. 7. Cumulative lognormal probability distributions fitted to the failure loads from MCS

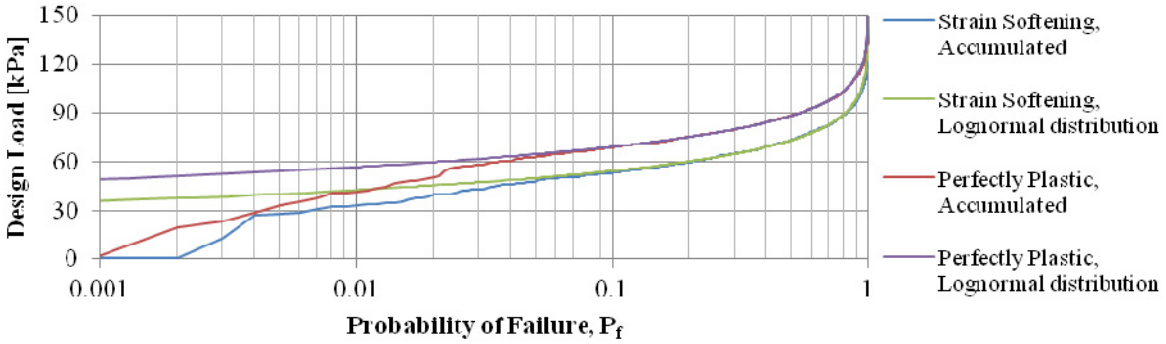

Fig. 8. Probability of failure for design loads, using the cumulative lognormal probability distributions

The cumulative lognormal distributions were then used to estimate the probability of failure for different design loads. The results are illustrated in Fig. 8. The lognormal probability distribution fitted well the results of the Monte Carlo simulations (denoted "Accumulated") for probabilities of failure greater than 5 %. To improve the accuracy in the tail of the distributions, a much larger number of simulations would have been needed. If one assumes that the lognormal distributions are also valid for lower probabilities of failure, the failure load is about 15 kPa higher for perfectly plastic behaviour than for strain softening.

The results from the deterministic analyses are shown in Fig. 9 in terms of the failure load versus the material coefficient γ_m, for both the characteristic and the "carefully assessed" shear strength profiles. The sudden drop in the failure loads at material coefficients of 1.8 and 1.5 is caused by the transition from local failure below the fill to global failure of the slope. For large material coefficients the reduced shear strength at the bottom of the model is lower than the shear stresses due to the weight of the soil, and the slope becomes unstable.

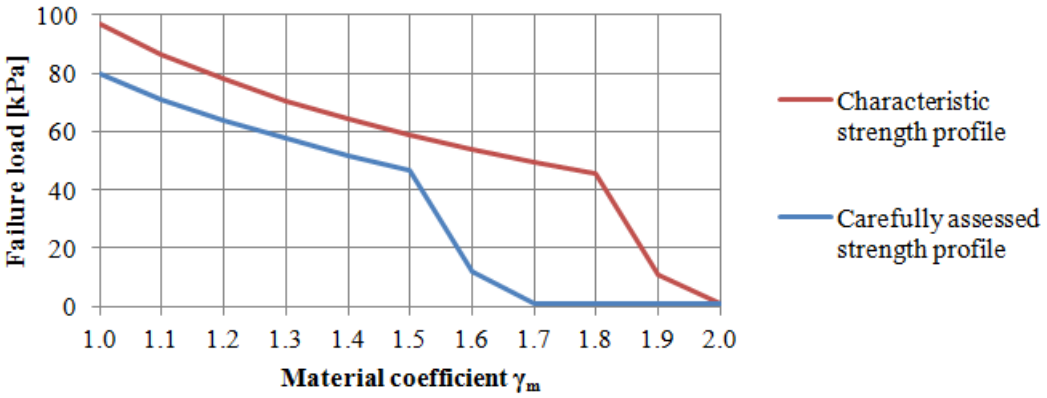

Fig. 9. Failure loads for material coefficient γ_m

By combining Fig. 8 and Fig. 9, the probability of failure (P_f) can be derived for different material coefficients γ_m. The increase in the material coefficient required to indirectly account for the strain-softening behaviour of the sensitive clay can be found by selecting the same probability of failure for the strain-softening material as for a perfectly plastic material. A material coefficient $\gamma_m = 1.4$ is required for construction work in non-sensitive clay areas according to the Norwegian guidelines. For the characteristic strength profile in Fig. 9, $\gamma_m = 1.4$ gave a failure load of 65 kPa, and $P_f = 5$ % in Fig. 8 for a perfectly plastic clay. For $P_f = 5$ %, the load for a strain-softening clay was 50 kPa. According to Fig. 9, a load of 50 kPa corresponds to $\gamma_m = 1.68$ (which is a 20 % increase in γ_m compared to γ_m of 1.4). Similarly for the "carefully assessed" undrained shear strength profile in Fig. 9, $\gamma_m = 1.4$ corresponds to a failure load of 52 kPa, and $P_f = 0.25$ % for a perfectly plastic clay in Fig. 8. For a sensitive clay, a load of 38 kPa has the same P_f. If the local failure mode for the "carefully assessed" undrained shear strength profile is extrapolated in Fig. 9, the load 38 kPa corresponds to $\gamma_m = 1.70$-1.75 (which is 21-25 % increase compared to 1.4).

The Monte Carlo simulations also provide sensitivity factors for each of the random variables in the analysis. The sensitivity factors quantify the relative contribution of the random variables to the probability of failure. Diagrams a) and b) in Fig. 10 present the sensitivity factors for the failure loads with perfectly plastic and with softening behaviour. Diagram c) in Fig. 10 presents sensitivity factors for the ratio of the perfectly plastic failure load to the strain-softening failure load. This ratio can be seen as the effect of including post peak softening in the material behaviour, the increase in failure load by not including strain softening.

The diagram shows that the variables controlling the shear strength profile, $s_u^A/s_u^A{}_{kar}$ and y_{ref} (variables 1 and 2), are the most significant parameters for the perfectly plastic behaviour. When strain-softening is included, the relative contribution of $s_u^A/s_u^A{}_{kar}$ is again the most significant, but less than for the perfectly plastic material. The relative contribution of the random variables 6 to 10 are, however, greatly increased compared to the perfectly plastic case. For the ratio between the failure loads, the effect of including post peak

softening, all the variables have similar relative contribution and the two brittleness variables (9 and 10) have about 20 % relative contribution together. The shear band thickness (variable 10) was the only parameter which probability distribution was assumed, due to lack of data. However, its contribution to the overall uncertainty is less than 10 %. It appears that the degree of mobilization is as important as the post peak strength reduction when softening behaviour is included.

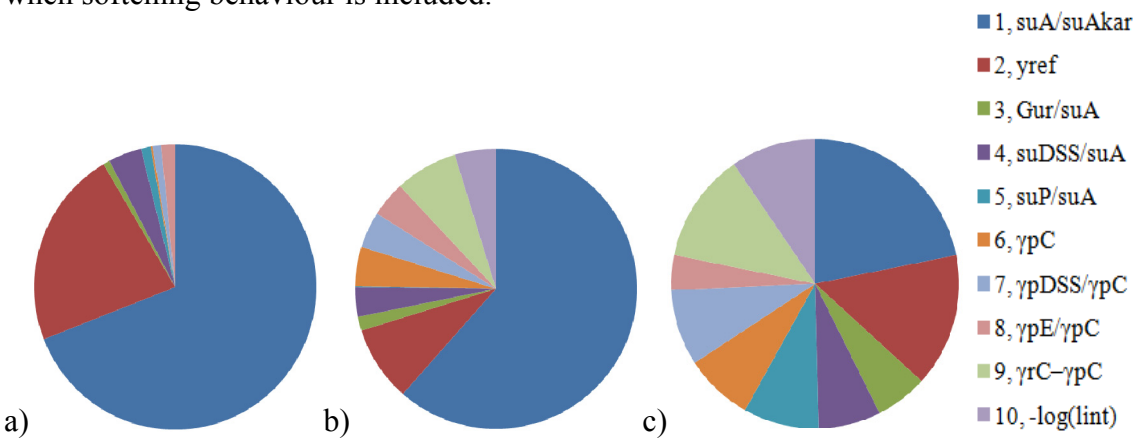

Fig. 10. Relative contribution of each random variable to the a) perfectly plastic failure load, b) strain-softening failure load, and c) ratio of perfectly plastic failure load to strain-softening failure load

8 CONCLUSIONS

The main conclusions from this probabilistic study of the material coefficient for perfectly plastic and strain-softening soil behaviour are:

- The material coefficient γ_m (used to scale the peak characteristic undrained shear strength profile) needs to be increased by 20 % (from 1.4 to 1.7) to obtain the same probability of failure when modelling a strain-softening sensitive clay as for a perfectly plastic clay.
- The probability of failure with this material coefficient was 5 % for the "characteristic" undrained shear strength profile, and 0.25 % for the "carefully chosen" strength profile.
- The effect of uncertainties in the shear band thickness (not measurable) was found to be of little significance for the initiation of progressive failure.

The results obtained are only valid for the case investigated with the given input distributions. It would be beneficial to do similar studies for typical construction projects in sensitive clay to further improve the selection of a new material coefficient. In this present paper, the input parameters and probability distributions of the random variables were determined from the site-specific soil data only. To reduce the uncertainty in the material input parameters in future probabilistic studies, one should also look into additional information, such as experience from block sample databases and reliable correlations with index parameters.

Other observations include:

- In an earlier sensitivity study (Jostad et al., 2013), only 2.5 % of approximately 500 simulations required more than a 20 % increase in the material coefficient to account for the strain-softening behaviour of sensitive clays.

- A lower probability of failure can be obtained by choosing a more careful strength profile, or by reducing the uncertainties in the input parameters. The latter requires more extensive soil investigations or more extensive studies of the soil parameters.
- To evaluate the increase in the material coefficient required to account for strain-softening, a high enough shear strength is required for the slope without the fill to not fail when it is divided by the new material coefficient.

ACKNOWLEDGEMENT

The authors would like to thank the Norwegian Public Road Administration and the Norwegian Water Resources and Energy Directorate for partly funding this research work. A special thank goes also to Dr. G. Grimstad at the Oslo and Akershus University College of Applied Sciences who developed the automated calculation procedure in Plaxis which was essential for performing this probability study. The authors also wish to acknowledge Dr. B.V. Vangelsten, Dr. S. Lacasse and Dr. F. Nadim, from NGI, NGI, for review and constructive feedback on this paper.

REFERENCES

Eurocode 7: Geotechnical design (2008). NS-EN 1997-1:2004+NA:2008. ICS 91.010.30; 93.020.

Eringen, A.C. (1981), "On non-local plasticity". Int. J. Eng. Science, 19, pp. 1461-1474.

Gregersen, O. (1981), "The Quick Clay Landslide in Rissa, Norway. The Sliding Process and Discussion of Failure Modes", International Conference on Soil Mechanics and Foundation Engineering, 10. Stockholm 1981. Proceedings, Vol. 3, pp. 421-426 .

Grimstad, G., Andresen, L. & Jostad, H.P. (2010), "NGI ADP: Anisotropic Shear Strength Model for Clay". International Journal for Numerical and Analytical Methods in Geomechanics, Vol. 36, No. 4, pp. 483-497.

Grimstad, G. & Jostad, H.P. (2010), "Undrained capacity analyses of sensitive clays using the nonlocal strain approach", 9th HSTAM International Congress on Mechanics Vardoulakis mini-symposia, Limassol, Kypros, 12. – 14. juli, 2010.

Jostad, H. P. & Grimstad, G. (2011), "Comparison of distribution functions for the nonlocal strain approach", Proc. 2nd International Symposium on Computational Geomechanics, Cavtat-Dubrovnik, Kroatia.

Jostad, H. P., Fornes, P. & Thakur, V. (2013), "Effect of strain-softening in design of fills on gently inclined areas with soft sensitive clays", Submitted to IWLSC2013, Québec. Oct. 2013.

Karlsrud, K. & Hernandez-Martinez, F.G. (2013), "Stress-strain-and strength characteristics of clays from high quality block samples". To be published in Can. Geot. Journal.

Lacasse, S. & Nadim, F. (1996), "Uncertainties in characterizing soil properties", Uncertainty in the Geologic Environment: From Theory to Practice. Proceedings of Uncertainty '96, Madison, Wisconsin, American Society of Civil Engineers, Geotechnical Special Publication, 58. pp. 49-75.

Lacasse, S., Nadim, F., Rahim, A. & Guttormsen, T.R. (2007), "Statistical Description of Characteristic Soil Properties", Offshore Technology Conference, 37, Houston, Proceedings paper 19117.

Metropolis N. & Ulam S. (1949), "The Monte Carlo Method". Journal of the American Statistical Association, number 247, September 1949, Volume 44, pp. 335-341.

Plaxis BV (2009), Plaxis manuals, Plaxis BV, www.plaxis.nl.

Snedecor, G.W. & Cochran, W. G. (1964), Statistical methods, Univ of Iowa Press, 140 p.

MODELING TRANSIENT GROUNDWATER FLOW UNDER DIKES AND DAMS FOR STABILITY ASSESSMENT

J.M. van Esch
Department of Geo-engineering, Deltares, Delft, The Netherlands

J.A.M. Teunissen
Department of Geo-engineering, Deltares, Delft, The Netherlands

D. Stolle
Department of Civil Engineering, McMaster University, Hamilton, ON, Canada

ABSTRACT: *Dikes and dams protect the land from flooding by mitigating high water levels. However, water penetrating the dike and the subsoil during high water periods reduces the strength of the dike due to the increase in pore pressure. Moreover, the raise in hydraulic head in deeper layers may lead to uplift of the top layer at the polder side of the dike, and finally an increase in the potential head gradient might lead to an internal erosion process called piping. To assess these effects it is important to have an adequate knowledge of the pore water pressure field. At present, pore water pressure fields are often obtained by solving the flow problem. This approach provides a computationally efficient method and requires less soil parameters than needed for solving the fully coupled flow-deformation problem. However, the flow formulation is not capable of correctly simulating the generation of pore water pressure due to hydraulic loading of the subsurface. This paper presents a numerical model for solving Biot's problem and compares the solution of the flow-deformation formulation to the solution of the flow formulation.*

1 INTRODUCTION

Groundwater flow simulations provide predictions of the pore water pressure fields in geotechnical structures, which can be used for the stability assessment of structures such as dike and dams. Stability analysis is most often based on effective stress, which corresponds to the difference between the total stress and water pressure. The finite element method is generally preferred for solving these problems because of the flexibility of this technique in capturing complex geometries (Brinkgreve et al. 2003). Pore water pressure fields are often obtained by considering Darcy flow and mass balance; i.e., the storage equation. This procedure provides a computationally efficient method and requires less soil parameters than the Biot approach that also considers the deformations of the soil. The Biot model couples the storage equation to the equilibrium equation and unlike the use of the storage equation by itself it is capable of simulating the generation and dissipation of pore water pressures as a result of hydraulic loading and compression of the subsurface.

Considerable research has been carried out to address problems that involve soil-pore fluid interaction, including those dealing with consolidation and wave loading. The equations describing two-phase flow were originally developed by Biot (1956a), Biot (1956b), with Zienkiewicz

et al. (1990) investigating the numerical implementation in terms of various formulations. For a comprehensive review of various formulations within the context of mixture theory, the reader is referred to Gidaspow (1994). This paper briefly reviews the two-phase flow equations and then presents two one-dimensional examples and one two-dimensional application to demonstrate the significance of various simplifications.

2 MATHEMATICAL MODEL

It is assumed in this paper the soil is saturated. The coupled equilibrium and storage equations form Biot's model. The equilibrium equation follows from conservation of moment of momentum and linear momentum, Terzaghi's effective stress principle, Hooke's linear elastic constitutive law, and the strain-displacement equation (Verruijt 1995). The storage equation follows from mass conservation and Darcy's law, which is an approximation for the equilibrium of the fluid. In this article a Galerkin finite element methodology is adopted to develop the weak formulation with regard to spatial variations of the unknown variables. Compressive stresses as well as saturated pore pressures are considered to be positive, and index notation is used, x_i (m) denotes Cartesian coordinates in space, t (s) time, Ω (m^2) represents the flow-deformation domain and Γ (m) its boundary. The primary field variables are soil displacement u_i (m) and pore pressure p (N/m^2) (Hughes 2000; Belytschko et al. 2008).

2.1 Equilibrium Equation

The equilibrium equation (Verruijt 1995) reads

$$\frac{\partial \sigma_{ij}}{\partial x_i} - \rho g_j = 0 \,, \quad \sigma_{ij} = -\tfrac{1}{2} D_{ijkl} \left(\frac{\partial u_k}{\partial x_l} + \frac{\partial u_l}{\partial x_k} \right) + p \delta_{ij} \quad \text{on} \quad \Omega \,, \tag{1}$$

where σ_{ij} (N/m^2) denotes the total Cauchy stress, ρ (kg/m^3) is the soil density, g_j (m/s^2) represents the gravitational acceleration vector, D_{ijkl} (N/m^2) is the fourth order tensor of elastic moduli and δ_{ij} $(-)$ denotes the Kronecker delta. For a y-coordinate pointing in opposite direction of the gravitational vector g_y is $-9.81\,\mathrm{m/s^2}$. The soil density follows from the solid phase density ρ^s (kg/m^3) and the liquid phase density ρ^l (kg/m^3) as $\rho = (1-n)\,\rho^s + n\rho^l$, where n $(-)$ is the porosity of the soil. Terzaghi's principle states that the total stress follows from the effective stress σ'_{ij} (N/m^2) and pore pressure as $\sigma_{ij} = \sigma'_{ij} + p\delta_{ij}$. The material stiffness tensor for an isotropic elastic material formulated with Lamé constants λ (N/m^2) and μ (N/m^2) reads

$$D_{ijkl} = \mu \left(\delta_{ik}\delta_{jl} + \delta_{il}\delta_{jk} \right) + \lambda \delta_{ij}\delta_{kl} \,. \tag{2}$$

Alternatively the bulk modulus of the skeleton K (N/m^2) and its shear modulus G (N/m^2) could be used as $K = \lambda + \frac{2}{3}\mu$ and $G = \mu$. Two types of boundary conditions that close the equilibrium equation are the Dirichlet and Cauchy conditions. The first prescribes the displacement $\overline{u}_i$ (m) and the second specifies the stress by a compressive force $\overline{\tau}_i$ (N/m^2) according to

$$u_j = \overline{u}_j \quad \text{on} \quad \Gamma_1^u \,, \quad \sigma_{ij} n_i = \overline{\tau}_j \quad \text{on} \quad \Gamma_2^u \,. \tag{3}$$

The weak form of the momentum balance equation reads

$$\int_\Omega N_a^u \frac{\partial \hat{\sigma}_{ij}}{\partial x_i} d\Omega - \int_\Omega N_a^u \hat{\rho} g_j d\Omega = 0 \,, \tag{4}$$

where $N_a^u\ (-)$ denotes the weighting function and the caret above a symbol implies that the variable is an approximation. Application of Green's theorem and imposing Cauchy boundary conditions gives

$$\int_\Omega \frac{\partial N_a^u}{\partial x_i}\hat{\sigma}_{ij}d\Omega = \int_{\Gamma_2^u} N_a^u \overline{\tau}_j d\Gamma - \int_\Omega N_a^u \hat{\rho} g_j d\Omega \ . \tag{5}$$

The incremental form of this second weak form of the momentum balance equation then reads

$$\int_\Omega \frac{\partial N_a^u}{\partial x_i}\Delta\hat{\sigma}_{ij}d\Omega = \int_{\Gamma_2^u} N_a^u \Delta\overline{\tau}_j d\Gamma - \int_\Omega N_a^u \Delta\hat{\rho} g_j d\Omega + R_{aj}^u \ , \tag{6}$$

where the residual $R_{aj}^u\ (\mathrm{N})$ is given by

$$R_{aj}^u = \int_{\Gamma_2^u} N_a^u \overline{\tau}_j^k d\Gamma - \int_\Omega N_a^u \hat{\rho}^k g_j d\Omega - \int_\Omega \frac{\partial N_a^u}{\partial x_i}\hat{\sigma}_{ij}^k d\Omega \ . \tag{7}$$

The residual, which vanishes at equilibrium, corresponds to the end of the previous (pseudo) time step, indicated by the superscript k. The internal stress increment $\Delta\hat{\sigma}_{ij}\ (\mathrm{N/m^2})$ relates to the external load increment $\Delta\overline{\tau}_j\ (\mathrm{N/m^2})$ and the internal load increment $\Delta\hat{\rho}g_j\ (\mathrm{N/m^2})$. The Cauchy stress at the new state $k+1$ is given by $\sigma_{ij}^{k+1} = \sigma_{ij}^k + \Delta\sigma_{ij}$. After making substitutions the weak form of the equilibrium equation reads

$$-\tfrac{1}{2}\int_\Omega \frac{\partial N_a^u}{\partial x_i} D_{ijkl}\left(\frac{\partial \Delta\hat{u}_k}{\partial x_l} + \frac{\partial \Delta\hat{u}_l}{\partial x_k}\right) d\Omega + \int_\Omega \frac{\partial N_a^u}{\partial x_j}\Delta\hat{p} d\Omega = \int_{\Gamma_2^u} N_a^u \Delta\overline{\tau}_j d\Gamma - \int_\Omega N_a^u \Delta\hat{\rho} g_j d\Omega + R_{aj}^u \ . \tag{8}$$

The displacement for the new state follows from the previous state of the system and the incremental displacement as $u_i^{k+1} = u_i^k + \Delta u_i$, with the updated pressure $p^{k+1} = p^k + \Delta p$. Including the interpolation of displacement and pressure, equation (8) becomes

$$-\tfrac{1}{2}\int_\Omega \frac{\partial N_a^u}{\partial x_i} D_{ijkl}\left(\frac{\partial N_b^u}{\partial x_l}\Delta u_{bk} + \frac{\partial N_b^u}{\partial x_k}\Delta u_{bl}\right) d\Omega + \int_\Omega \frac{\partial N_a^u}{\partial x_j} N_b^p \Delta p_b d\Omega = \int_{\Gamma_2^u} N_a^u N_b^u \Delta\overline{\tau}_{bj} d\Gamma - \int_\Omega N_a^u \Delta\rho g_j d\Omega + R_{aj}^u \ . \tag{9}$$

The total stress at the integration points follows from

$$\sigma_{ij} = -\tfrac{1}{2} D_{ijkl}\left(\frac{\partial N_b^u}{\partial x_l}u_{bk} + \frac{\partial N_b^u}{\partial x_k}u_{bl}\right) + \delta_{ij} N_b^p p_b \ . \tag{10}$$

A combination of quadratic shape functions for displacement interpolation $N_b^u\,(-)$ and linear shape functions for pressure interpolation $N_b^p\,(-)$ provides a consistent stress approximation.

2.2 Storage Equation

The storage equation (Van Esch 2010) reads

$$\frac{\partial \epsilon_v}{\partial t} + n\beta\frac{\partial p}{\partial t} + \frac{\partial q_i}{\partial x_i} = 0 \ , \quad q_i = -\frac{\kappa_{ij}}{\mu}\left(\frac{\partial p}{\partial x_j} - \rho^l g_j\right) \quad \text{on} \quad \Omega \ , \tag{11}$$

where $\epsilon_v\,(-)$ denotes volumetric strain, $\kappa_{ij}\,(\mathrm{m}^2)$ represents the intrinsic permeability tensor, $\mu^l\ (\mathrm{kg/ms})$ is the dynamic viscosity of the liquid phase, $\rho^l\,(\mathrm{kg/m}^3)$ represents its density and $\beta\,(\mathrm{m}^2/\mathrm{N})$ is the compressibility of the liquid phase. Here the assumption is made that the density of the liquid phase depends on the liquid phase pressure given by an equation of state that reads $\rho^l = \rho_0^l \exp\left[\beta(p-p_0)\right]$, where $\rho_0\ (\mathrm{kg/m}^3)$ expresses the density of the fluid at reference pressure $p_0\ (\mathrm{N/m}^2)$. Two types of boundary conditions close the storage equation: Dirichlet boundary conditions prescribe the pressure $\overline{p}\ (\mathrm{N/m}^2)$ and Neumann boundary conditions impose a volumetric flux $\overline{q}\ (\mathrm{m/s})$ into the flow domain according to

$$p = \overline{p} \quad \text{on} \quad \Gamma_1^p\,, \quad q_i n_i = -\overline{q} \quad \text{on} \quad \Gamma_2^p\,. \tag{12}$$

Here $n_i\ (-)$ denotes the outward pointing normal to the boundary.

If the storage equation is used for solving the decoupled flow problem instead of solving the fully coupled flow-deformation problem then the left hand side of equation (11) becomes $(\alpha + n\beta)\,\partial p/\partial t$, where $\alpha\,(\mathrm{m}^2/\mathrm{N})$ denotes the compressibility of the solid phase matrix. The compressibility of the soil skeleton can be written as $\alpha = 1/(\lambda + 2\nu)$.

The weak form of the storage equation that contributes to the coupled formulation follows from

$$\int_\Omega N_a^p \frac{\partial \hat{\epsilon}_v}{\partial t} d\Omega + \int_\Omega N_a^p n\beta \frac{\partial \hat{p}}{\partial t} d\Omega = \int_\Omega N_a^p \frac{\partial}{\partial x_i}\left[\frac{\kappa_{ij}}{\mu}\left(\frac{\partial \hat{p}}{\partial x_j} - \hat{\rho}^l g_j\right)\right] d\Omega\,, \tag{13}$$

where $N_a^p\ (-)$ denotes the weighting function, which differs from the weighting function that was used for the discretization of the equilibrium equation. Using Green's theorem and substituting Neumann boundary conditions gives

$$\int_\Omega N_a^p \frac{\partial \hat{\epsilon}_v}{\partial t} d\Omega + \int_\Omega N_a^p n\beta \frac{\partial \hat{p}}{\partial t} d\Omega = - \int_\Omega \frac{\partial N_a^p}{\partial x_i}\left[\frac{\kappa_{ij}}{\mu}\left(\frac{\partial \hat{p}}{\partial x_j} - \hat{\rho}^l g_j\right)\right] d\Omega + \int_{\Gamma_2^p} N_a^p \overline{q}^{k+1} d\Gamma\,. \tag{14}$$

Galerkin weighting and substitution of the interpolation functions gives

$$\int_\Omega N_a^p \frac{\partial N_b^u}{\partial x_i} \frac{du_{bi}}{dt} d\Omega + \int_\Omega n\beta N_a^p N_b^p \frac{dp_b}{dt} d\Omega = - \int_\Omega \frac{\partial N_a^p}{\partial x_i} \frac{\kappa_{ij}}{\mu} \frac{\partial N_b^p}{\partial x_j} p_b d\Omega + \int_\Omega \frac{\partial N_a^p}{\partial x_i} \frac{\kappa_{ij}}{\mu} \rho^l g_j d\Omega + \int_{\Gamma_2^p} N_a^p N_b^p \overline{q}_b^{k+1} d\Gamma\,. \tag{15}$$

Implicit linear integration in time together with a consistent mass matrix formulation gives a set of algebraic equations that may be written as

$$\int_\Omega N_a^p \frac{\partial N_b^u}{\partial x_i} \Delta u_{bi} d\Omega + \int_\Omega n\beta N_a^p N_b^p \Delta p_b d\Omega + \Delta t \int_\Omega \frac{\partial N_a^p}{\partial x_i} \frac{\kappa_{ij}}{\mu} \frac{\partial N_b^p}{\partial x_j} \Delta p_b d\Omega = \Delta t \int_\Omega \frac{\partial N_a^p}{\partial x_i} \frac{\kappa_{ij}}{\mu} \Delta \rho^l g_j d\Omega + \Delta t \int_{\Gamma_2^p} N_a^p N_b^p \Delta \overline{q}_b d\Gamma + \Delta t R_a^p\,, \tag{16}$$

where the residual $R_a^p\ (\mathrm{N})$ reads

$$R_a^p = - \int_\Omega \frac{\partial N_a^p}{\partial x_i} \frac{\kappa_{ij}}{\mu} \frac{\partial N_b^p}{\partial x_j} p_b^k d\Omega + \int_\Omega \frac{\partial N_a^p}{\partial x_i} \frac{\kappa_{ij}}{\mu} \rho^{lk} g_j d\Omega + \int_{\Gamma_2^p} N_a^p N_b^p \overline{q}_b^k d\Gamma\,. \tag{17}$$

Equations (9) and (16) provide a coupled sets of algebraic equations that must be solved numerically.

3 NUMERICAL SIMULATIONS

This section presents predictions for two oedometer tests on a clay material followed by an analysis of a simplified dam supported by a layered soil consisting of clay and sand sub-layers. With regard to the oedometer test, a surface traction (total stress) is applied on the first sample, with the second sample experiencing an increase in pore pressure (total stress plus water pressure) at the upper surface. These are termed mechanically and hydraulically loaded, respectively. The vertical boundaries of both samples are closed for flow and the horizontal displacement is fixed. Along the bottom, zero displacement is prescribed in both vertical and horizontal directions. At the top and the bottom the pore pressure is prescribed.

The density of water is set to $10^3\,\mathrm{kg/m^3}$, with a dynamic viscosity of $10^{-3}\,\mathrm{Ns/m^2}$. The compression modulus is $2\cdot10^9\,\mathrm{N/m^2}$, implying a compressibility of $5\cdot10^{-10}\,\mathrm{m^2/N}$ given $\beta = 1/K^l$. The gravitational acceleration is assumed to be $10\,\mathrm{m/s^2}$. For the clay, the Young's modulus E $(\mathrm{N/m^2})$ is $10^7\,\mathrm{N/m^2}$, the Poisson's ratio ν $(-)$ is 0, the porosity equals 0.33, the density of wet clay is $2\cdot10^3\,\mathrm{kg/m^3}$ and its intrinsic permeability reads $1.157\cdot10^{-17}\,\mathrm{m^2}$. From these values the following parameters for the clay material can be derived: the bulk modulus of the skeleton equals $3.33\cdot10^6\,\mathrm{N/m^2}$ and its shear modulus is $5\cdot10^6\,\mathrm{N/m^2}$ as $K = \frac{1}{3}E/(1-2\nu)$ and $G = \frac{1}{2}E/(1+\nu)$. The compressibility of the clay is $10^{-7}\,\mathrm{m^2/N}$ as $\alpha = 1/(K+\frac{4}{3}G)$. Its hydraulic conductivity is $10^{-5}\,\mathrm{m/d}$, and the void ratio is 0.4925. For the sand, the Young's modulus is $10^8\,\mathrm{N/m^2}$, the Poisson's ratio is 0.3, the porosity equals 0.33, the density of wet sand is $2\cdot10^3\,\mathrm{kg/m^3}$ and its intrinsic permeability reads $1.157\cdot10^{-10}\,\mathrm{m^2}$. The hydraulic conductivity of sand then equals $100\,\mathrm{m/d}$, the bulk modulus of the skeleton is $8.33\cdot10^7\,\mathrm{N/m^2}$, its shear modulus is $3.846\cdot10^7\,\mathrm{N/m^2}$, with the compressibility of sand being $7.429\cdot10^{-9}\,\mathrm{m^2/N}$.

3.1 Mechanical Loading

Dissipation of water pressure for a one-dimensional consolidation problem (Verruijt 1995) follows from

$$\frac{\partial p}{\partial t} = c_v \frac{\partial^2 p}{\partial y^2}\,, \tag{18}$$

where the consolidation coefficient c_v $(\mathrm{m^2/s})$ reads $1.157\cdot10^{-7}\,\mathrm{m^2/s}$ as $c_v = k/\left[\rho^l g\,(\alpha+n\beta)\right]$. The analytical solution for this one-dimensional consolidation equation is given by

$$\frac{p(t)}{p_0} = \frac{4}{\pi}\sum_{j=1}^{\infty}\frac{(-1)^{j-1}}{2j-1}\cos\left[(2j-1)\,\frac{\pi}{2}\left(\frac{h-y}{h}\right)\right]\exp\left[-(2j-1)^2\,\frac{\pi^2}{4}\,\frac{c_v t}{h^2}\right]\,, \tag{19}$$

where h (m) is the sample height. This expression holds for a two phase liquid-solid material, although the effect of a small amount of dissolved gas may be accounted for by an increase of the liquid phase compressibility.

The first example considers the pore water dissipation process for the case of gravity loading followed by the application of a vertical traction to the surface of 1 m thick clay sample. The top is at atmospheric pressure $(0\,\mathrm{kN/m^2})$ with the bottom pore pressure set at $10\,\mathrm{kN/m^2}$, which produces a hydrostatic pressure distribution at beginning and end of the simulation corresponding to no flow situation. Given a soil unit weight of $20\,\mathrm{kN/m^3}$, gravity loading gives a total stress of $0\,\mathrm{kN/m^2}$ at the top and $20\,\mathrm{kN/m^2}$ at the bottom. The initial displacements were set to zero. Mechanical loading generated water pressures and negligible increase in effective stresses at the beginning of the process.

The load was applied as a ramp such that the maximum stress at the top is $50\,\mathrm{kN/m^2}$, with $70\,\mathrm{kN/m^2}$ at the bottom. For ramp loading the pressure and effective stress increase follow from the total stress increase as $dp = \alpha/(\alpha + n\beta)\; d\sigma$ and $d\sigma' = n\beta/(\alpha + n\beta)\; d\sigma$. At the final stage effective stress varies linearly from $50\,\mathrm{kN/m^2}$ at the top to $60\,\mathrm{kN/m^2}$ at the bottom.

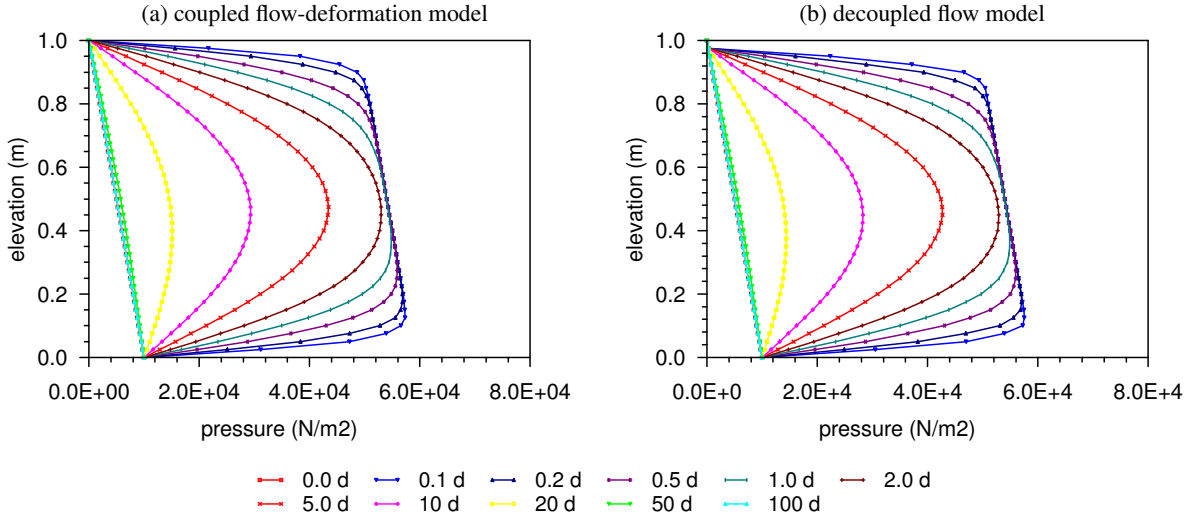

Fig. 1. Mechanical loading test.

As shown in Figure 1, the excess pore pressure dissipates in time until a constant flow situation occurs. The figure compares the predictions of the proposed coupled model (a) to those obtained from equation (19), shown in the plot on the right (b). The agreement is seen to be excellent.

3.2 Hydraulic Loading

For the second problem, the water pressure at the top of the sample was increased linearly while water pressures at the bottom remained constant. A linear head increase of 5 m per day was imposed at the top until a value of $50\ \mathrm{kN/m^2}$ for pore pressure and total stress was attained. Thereafter the pore pressure remained constant. The hydraulic load increased the total stress and depending on the ratio of soil skeleton compressibility and liquid phase compressibility, water pressures and effective stress where generated. As a result pore water flowed in downward direction increasing in time until the maximum load was reached and then decreased until the steady state situation was established. The pore pressure at the bottom boundary was set at $10\ \mathrm{kN/m^2}$ throughout the analysis.

The plot on the left of Figure 2 corresponds to the fully coupled storage-equilibrium formulation that captures the compression of the soil skeleton by the equilibrium equation and the compressibility of the pore water fluid by the storage equation. The displacements, which varied nonlinearly, were maximum when steady state was attained. At steady state the pore pressure distribution was linear as shown in the figure. The plot on the right corresponds to the solution of the decoupled storage equation. While the steady state solution (about 100 days) is similar to that obtained by the proposed model, it is clear that the storage equation could not follow the pore pressure generation process properly. Compressibility of the pore water and compressibility of the soil skeleton are added to a storage coefficient in the decoupled formulation, which delayed the generation of pore water pressure as can be seen in the plot on the right of Figure 2.

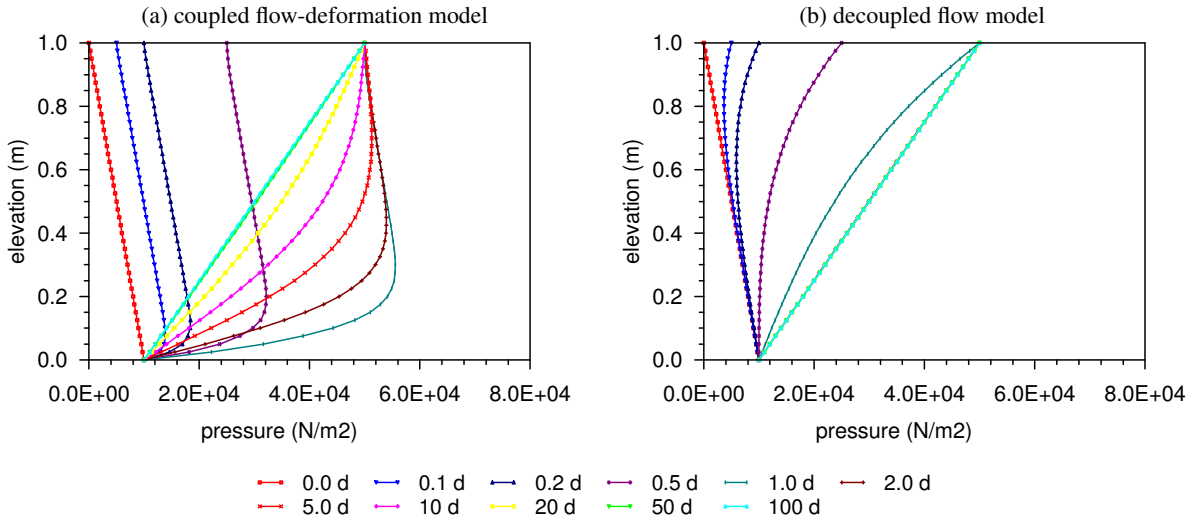

Fig. 2. Hydraulic loading test.

3.3 Model Application

Figure 3 shows the finite element mesh of a problem where a dam is supported by a layered subsoil. To the left side of the dam the river water level imposes a hydraulic (water pressure) load on the upper surface of the clay layer that covers the high permeability aquifer. Hydraulic head $\phi\,(\mathrm{m})$ relates to pore water pressure as $\phi = p/(\rho^l g) + y$, where $y\,(\mathrm{m})$ is the elevation level. To the right a constant polder water level is applied. Non-flow conditions were assumed along the vertical aquifer boundaries, as well at the base of the aquifer. The idealized dam had low hydraulic conductivity thus minimizing groundwater flow. Water flowed underneath the dam through the aquitard and aquifer from the river side towards the polder side. Equipotential lines that connect points of the same piezometric head are shown in Figure 3. Given that the soils are isotropic, the flow direction is normal to these lines. The picture displays the position of two monitoring points at the inner side and the outer side just underneath the cover layer. At these positions groundwater heads are observed as a function of time. Figures 4 and 5 compare the

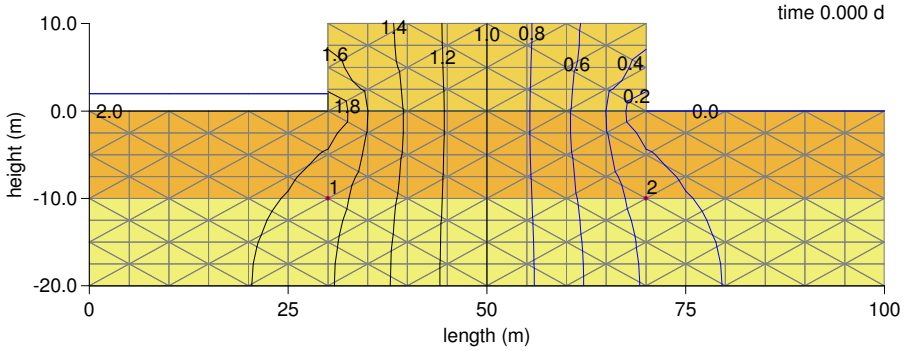

Fig. 3. Simplified geometry.

total head predicted by the proposed model (a) and decoupled model (b) as a function of time for two combinations of soil permeability. It is clearly shown that both models do not predict the same response. The decoupled flow formulation overestimates the effect of damping and delay associated with storage and resistance in the geo-hydrological system.

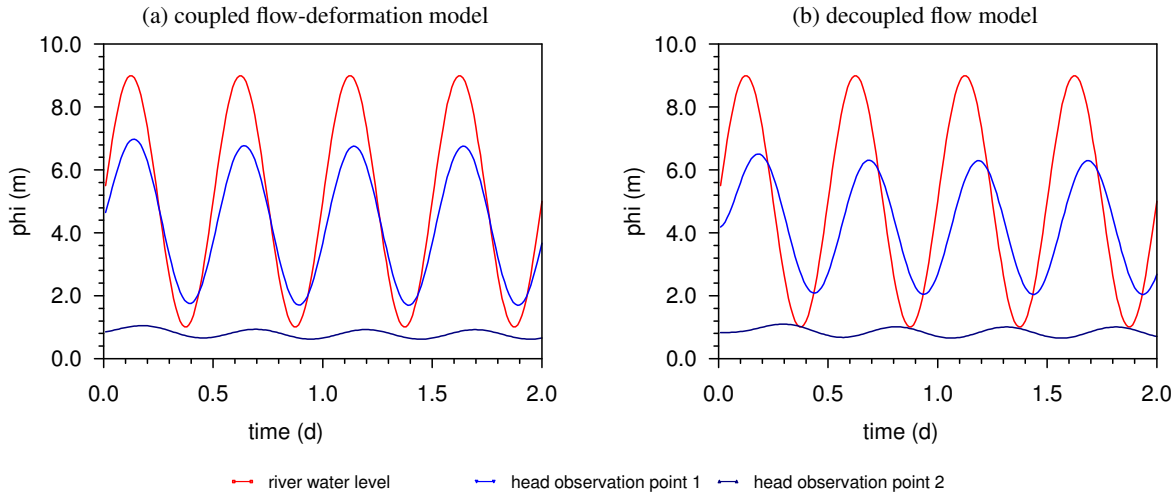

Fig. 4. Model application 1; $k_{\text{aquifer}} = 1\text{m/d}$, $k_{\text{cover}} = 1\text{m/d}$.

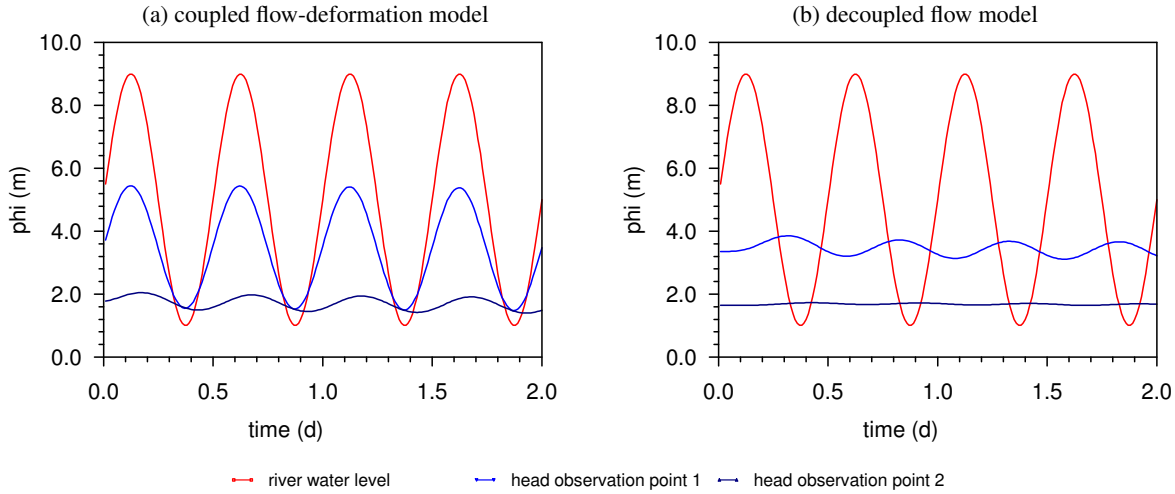

Fig. 5. Model application 2; $k_{\text{aquifer}} = 1\text{m/d}$, $k_{\text{cover}} = 0.1\text{m/d}$.

4 CONCLUSIONS

In general, modeling transient groundwater flow provides less conservative pore water pressure fields for the stability assessment of dikes and dams than steady state simulations do. At the present these pressure fields are obtained by solving the storage equation. This procedure provides a computationally efficient method and requires less soil parameters than required by the Biot formulation. The downside is that the storage equation is not able to simulate the generation of pore water pressure due to hydraulic loading at the subsurface correctly. The Biot model couples the storage equation to the equilibrium equation and is therefore able to simulate both the generation and dissipation process.

ACKNOWLEDGEMENTS

This research was carried out as part of the Wettelijk Toets Instrumentarium program (WTI2017). This program was funded by the Rijkswaterstaat; the executive arm of the Dutch Ministry of Infrastructure and the Environment.

REFERENCES

Belytschko, T., Liu, W. K., & Moran, B. (2008). *Nonlinear Finite Elements for Continua and Structures*. Wiley.

Biot, M. A. (1956a). Theory of propagation of elastic waves in a fluid-saturated porous solid. i. low-frequency range. *Journal of the Acoustical Society of America 28*(2), 168–178.

Biot, M. A. (1956b). Theory of propagation of elastic waves in a fluid-saturated porous solid. ii. higher frequency range. *Journal of the Acoustical Society of America 28*(2), 179–191.

Brinkgreve, R. B. J., Al-Khoury, R., & Van Esch, J. M. (2003). *Plaxflow*. Plaxis B.V.

Gidaspow, D. (1994). *Multiphase Flow and Fluidization Continuum and Kinetic Theory Descriptions*. Academic Press.

Hughes, T. J. R. (2000). *The Finite Element Method, Linear Static and Dynamic Finite Element Analysis*. Dover Publications.

Van Esch, J. M. (2010). *Adaptive Multiscale Finite Element Method for Subsurface Flow Simulation*. Ph. D. thesis, Delft University of Technology.

Verruijt, A. (1995). *Computational Geomechanics*. Kluwer Academic Publishers.

Zienkiewicz, O. C., Chan, A. H. C., Pastor, M., Paul, D. K., & Shiomi, T. (1990). Static and dynamic behaviour of soils: A rational approach to quantitative solutions, part i: Fully saturated problems. *Proceedings of the Royal Society 429*, 285–309.

MODELING TRANSIENT GROUNDWATER FLOW AND PIPING UNDER DIKES AND DAMS

J.M. van Esch
Department of Geo-engineering, Deltares, Delft, The Netherlands

J.B. Sellmeijer
Department of Geo-engineering, Deltares, Delft, The Netherlands

D. Stolle
Department of Civil Engineering, McMaster University, Hamilton, ON, Canada

ABSTRACT: *Dikes and dams are water mitigating structures that protect the land from floods and high tides. In the Netherlands these structures are often constructed of impervious clays and are built on a sandy aquifer as subsoil. Foundations of such geotechnical structures are vulnerable to an erosion effect called piping that refers to the development of small flow channels that begin at the downstream side of the structure where the seepage pressure is high. The internal erosion process works its way to the upstream side. If the erosion process continues the structure may collapse. This paper presents a new numerical formulation of the piping mechanism based on Poiseuille flow through a piping slit and White's limit equilibrium for particle movement, in combination with a groundwater flow simulator capable of resolving the transient behavior of the groundwater pressure field based on Richard's equation. Simulations demonstrate that the compressibility of the aquifer delays the increase of water pressures in time. This delay hampers the growth of the piping channel.*

1 INTRODUCTION

In delta regions dikes protect the land from floods and high tides. In the Netherlands dikes are generally constructed of impervious clays and are built on a sandy aquifer as subsoil. The foundations of these geotechnical structures are vulnerable to an erosion process called piping. In literature, the piping mechanism is also referred to as backward erosion or underseepage erosion (Blight 1915; Lane 1935; Wolfs 2002). At present the most advanced design rule for piping is the rule proposed by Sellmeijer (1988). This rule is based on the analysis of the mechanism under an impervious structure of base length L (m) on top of a single aquifer of constant height D (m). Sellmeijer's rule predicts the critical head difference H_c (m) between the outer river water level at one side of the structure and polder water level to the other side of the structure. If the actual head difference is larger than the critical head difference, a piping channel will propagate until the channel reaches the upstream side. The rule in the current form (Sellmeijer et al. 2011) is given by

$$H_c = F_r F_s F_g L \ , \tag{1}$$

where L (m) denotes the horizontal potential piping length, which corresponds to the structure length, F_r $(-)$ expresses the resistance term, F_s $(-)$ denotes the scaling term, and F_g $(-)$ ex-

presses the geometry term, in which

$$F_r = \frac{\rho^s - \rho^l}{\rho^l}\eta \tan\vartheta \;, \quad F_s = \frac{d_{70}}{\sqrt[3]{\kappa L}} \;, \quad F_g = 0.91\left(\frac{D}{L}\right)^{\varsigma} \;, \quad \varsigma = \frac{0.24}{\left(\frac{D}{L}\right)^{2.8} - 1} \;. \tag{2}$$

In the expression of the resistance term ρ^s (kg/m^3) corresponds to the density of the soil particles, ρ^l (kg/m^3) denotes the density of the water phase, η $(-)$ expresses White's constant, and ϑ (deg) is the bedding angle. The scaling term includes the intrinsic permeability κ (m^2) of the sand under the structure, the 70% grain diameter d_{70} (m) and the potential piping length. The coefficient ς $(-)$ has a value of 1.08 for $D/L = 1$ as follows from a limit analysis. The geometry term relates the thickness of the aquifer to the potential piping length and includes a coefficient 0.91, which was determined using numerical modeling. According to Sellmeijer's rule larger values of L, ρ^s, η, ϑ, d_{70}, and smaller values for D, κ and ρ^l increase the critical head difference H_c and reduce the risk of piping.

2 MATHEMATICAL MODEL

The storage equation according to Richard's model follows from the mass balance equation, Darcy's law and empirical relations for water content and relative permeability as a function of pore pressure. This article adopts a Galerkin finite element discretization in space, in which the primary field variable is pore pressure p (N/m^2) (Hughes 2000; Belytschko et al. 2008). Pore pressures are considered to be positive in compression, with index notation being used, x_i (m) denotes Cartesian coordinates in space, t (s) denotes time, and Ω (m^2) represents the flow domain with Γ (m) its boundary.

2.1 Subsurface Flow Equation

Flow through a partly saturated porous medium can be modeled considering conservation of mass and a generalization of Darcy's law (Van Esch 2010), which can be written as

$$(\alpha + n\beta)\, S\frac{\partial p}{\partial t} + n\frac{dS}{dp}\frac{\partial p}{\partial t} + \frac{\partial q_i}{\partial x_i} = 0 \;, \quad q_i = -\frac{k_r \kappa_{ij}}{\mu}\left(\frac{\partial p}{\partial x_j} - \rho^l g_j\right) \quad \text{on} \quad \Omega^p \;, \tag{3}$$

where α (m^2/N) is the compressibility of the soil skeleton, β (m^2/N) represents the compressibility of the pore water, n $(-)$ denotes porosity and S $(-)$ expresses the degree of saturation of the liquid phase in the void space. The compressibility for elastic behavior of the soil skeleton can be written as $\alpha = 1/(\lambda + 2\nu)$, where λ (N/m^2) and ν (N/m^2) denote Lamé's constants. Specific discharge q_i (m/s) relates to relative permeability k_r $(-)$, intrinsic permeability κ_{ij} (m^2), dynamic viscosity of the liquid phase μ (kg/ms) and its density ρ^l (kg/m^3). For a y-coordinate pointing in the opposite direction than the gravitational vector g_y is $-9.81\,\mathrm{m/s^2}$. Equation (3) is known as the storage equation. Two types of boundary conditions complete the problem definition; Dirichlet conditions prescribe the pressure on parts of the boundary and Von Neumann boundary conditions prescribe the derivative of the pressure or flux on the boundary. These first-type and second-type boundary conditions read

$$p = \overline{p} \quad \text{on} \quad \Gamma_1^p \;, \quad q_i n_i = -\overline{q} \quad \text{on} \quad \Gamma_2^p \;, \quad q_i n_i = -s \quad \text{on} \quad \Gamma_3^p \;, \tag{4}$$

where Γ_1^p, Γ_2^p and Γ_3^p are disjoint parts of the boundary where the conditions apply, n_i $(-)$ denotes the outward pointing normal to the boundary, $\overline{p}$ (N/m^2) is the prescribed pressure, $\overline{q}$

$(\mathrm{m/s})$ denotes the volumetric water flux over the boundary into the flow domain as a source term, and s $(\mathrm{m/s})$ expresses a source term that will be used for coupling the subsurface flow equation to the flow equation for piping.

A weak form of equation (3) follows from multiplication by weighting functions N_a $(-)$, which are attached to nodes of a finite element mesh and integration over the flow domain. The first weak form is given by

$$\int_{\Omega^p} N_a \left(\alpha + n\beta\right) S \frac{\partial \hat{p}}{\partial t} d\Omega + \int_{\Omega^p} N_a n \frac{dS}{dp} \frac{\partial \hat{p}}{\partial t} d\Omega = \int_{\Omega^p} N_a \frac{\partial}{\partial x_i} \left[\frac{k_r \kappa_{ij}}{\mu} \left(\frac{\partial \hat{p}}{\partial x_j} - \rho^l g_j \right) \right] d\Omega \,, \quad (5)$$

where the caret above a symbol implies that the variable is an approximation. Application of Green's theorem to the term on the right hand side of equation (5) leads to

$$\begin{aligned} \int_{\Omega^p} N_a \left(\alpha + n\beta\right) S \frac{\partial \hat{p}}{\partial t} d\Omega + \int_{\Omega^p} N_a n \frac{dS}{dp} \frac{\partial \hat{p}}{\partial t} d\Omega = \\ - \int_{\Omega^p} \frac{k_r \kappa_{ij}}{\mu} \frac{\partial N_a}{\partial x_i} \left(\frac{\partial \hat{p}}{\partial x_j} - \rho^l g_j \right) d\Omega + \int_{\Gamma^p_{2\cup 3}} N_a \frac{k_r \kappa_{ij}}{\mu} \left(\frac{\partial \hat{p}}{\partial x_j} - \rho^l g_j \right) n_i d\Gamma \,. \end{aligned} \quad (6)$$

Galerkin weighting and substitution of the interpolation functions gives

$$\begin{aligned} \int_{\Omega^p} N_a N_b \left(\alpha + n\beta\right) S \frac{dp_b}{dt} d\Omega + \int_{\Omega^p} N_a N_b n \frac{dS}{dp} \frac{dp_b}{dt} d\Omega = - \int_{\Omega^p} \frac{k_r \kappa_{ij}}{\mu} \frac{\partial N_a}{\partial x_i} \frac{\partial N_b}{\partial x_j} p_b d\Omega \\ + \int_{\Omega^p} \frac{k_r \kappa_{ij}}{\mu} \frac{\partial N_a}{\partial x_i} \rho^l g_j d\Omega + \int_{\Gamma^p_2} N_a N_b \overline{q}_b d\Gamma + \int_{\Gamma^p_3} N_a N_b s_b d\Gamma \,, \end{aligned} \quad (7)$$

after the Neumann boundary conditions were incorporated. Prescribed boundary fluxes are given at the nodal points. Implicit time integration yields

$$\begin{aligned} \int_{\Omega^p} N_a N_b \left(\alpha + n\beta\right) S^{k+1} \left(p_b^{k+1} - p_b^k \right) d\Omega + \int_{\Omega^p} N_a N_b n \left(\frac{dS}{dp} \right)^{k+1} \left(p_b^{k+1} - p_b^k \right) d\Omega = \\ - \Delta t \int_{\Omega^p} \frac{k_r^{k+1} \kappa_{ij}}{\mu} \frac{\partial N_a}{\partial x_i} \frac{\partial N_b}{\partial x_j} p_b^{k+1} d\Omega + \Delta t \int_{\Omega^p} \frac{k_r^{k+1} \kappa_{ij}}{\mu} \frac{\partial N_a}{\partial x_i} \rho^l g_j d\Omega \\ + \Delta t \int_{\Gamma^p_2} N_a N_b \overline{q}_b^{k+1} + \Delta t \int_{\Gamma^p_3} N_a N_b s_b^{k+1} d\Gamma \,, \end{aligned} \quad (8)$$

where Δt is the time step size, k denotes the current time step and $k+1$ indicates the new step.

2.2 Flow Equation for Piping

Modeling of piping follows from the application of conservation of mass and considering Poiseuille flow (Huyakorn & Pinder 1983) through a horizontal erosion slit and can be written as

$$\frac{dq}{dx} + s = 0 \,, \quad q = -\frac{a^3}{12\mu} \frac{dp}{dx} \quad \text{on} \quad \Omega^c \,, \quad (9)$$

where a (m) denotes the height of the channel and s expresses a sink term. Here the extension of the pipe flow domain Ω^c (m) corresponds to the boundary of the subsurface flow domain Γ^p (m) as equation (9) holds for a one-dimensional flow domain. Dirichlet conditions hold on the

inflow and outflow point of the piping domain. Boundary conditions for the piping domain are given by

$$p = \overline{p} \quad \text{on} \quad \Gamma_1^c \,. \tag{10}$$

The condition of limit equilibrium for the horizontally oriented erosion channel (Sellmeijer 1988) reads

$$a\frac{dp}{dx} = \frac{\pi}{3}\left(\rho^s - \rho^l\right) g d_{70} \eta \tan\vartheta \,. \tag{11}$$

The height of the erosion channel varies in between 0 and 3 grains in an experimental setup, 0 to 10 grains in a field test and 0 to 30 grains for an embankment.

Discretization of equation (9) follows the same steps as the discretization of equation (3), and the first weak form reads

$$\int_{\Omega^c} N_a \frac{d}{dx}\left(\frac{\kappa_p}{\mu}\frac{d\hat{p}}{dx}\right) d\Omega = \int_{\Omega^c} N_a s d\Omega \,, \tag{12}$$

where the equivalent intrinsic permeability κ_p (m^3) has a scalar value that is given by $\kappa_p = a^3/12$. The second weak form is given by

$$\int_{\Omega^c} \frac{\kappa_p}{\mu}\frac{dN_a}{dx}\frac{d\hat{p}}{dx} d\Omega = -\int_{\Omega^c} N_a s d\Omega \,, \tag{13}$$

and the final form follows from the substitution of interpolation functions

$$\int_{\Omega^c} \frac{\kappa_p^{k+1}}{\mu}\frac{dN_a}{dx}\frac{dN_b}{dx} p_b^{k+1} d\Omega = -\int_{\Omega^c} N_a N_b s_b^{k+1} d\Omega \,. \tag{14}$$

The condition of limit equilibrium for a horizontally oriented erosion channel is evaluated at the integration points and is given by

$$\kappa_p^{k+1} = \tfrac{1}{12}\left(a^{k+1}\right)^3, \quad a^{k+1}\frac{dN_b}{dx} p_b^{k+1} = \frac{\pi}{3}\left(\rho^s - \rho^l\right) g d_{70} \eta \tan\vartheta \,. \tag{15}$$

2.3 Coupled Flow Equation

The sink term in equation (14), where s is positive for flow out of the channel, provides a source term in equation (8), where s is positive for flow into the subsurface, and vice versa. Linear one-dimensional elements are used for solving equation (14), whereas linear triangular elements discretize the flow domain attached to equation (8). Combining both equations yields

$$\begin{aligned}\int_{\Omega^p} N_a N_b \left(\alpha + n\beta\right) S^{k+1}\left(p_b^{k+1} - p_b^k\right) d\Omega + \int_{\Omega^p} N_a N_b n \left(\frac{dS}{dp}\right)^{k+1}\left(p_b^{k+1} - p_b^k\right) d\Omega = \\ - \Delta t \int_{\Omega^p} \frac{k_r^{k+1}\kappa_{ij}}{\mu}\frac{\partial N_a}{\partial x_i}\frac{\partial N_b}{\partial x_j} p_b^{k+1} d\Omega + \Delta t \int_{\Omega^p} \frac{k_r^{k+1}\kappa_{ij}}{\mu}\frac{\partial N_a}{\partial x_i}\rho^l g_j d\Omega \\ - \Delta t \int_{\Gamma_3^p} \frac{\kappa_p^{k+1}}{\mu}\frac{\partial N_a}{\partial x_i}\frac{\partial N_b}{\partial x_j} p_b^{k+1} d\Omega + \Delta t \int_{\Gamma_2^p} N_a N_b \overline{q}_b^{k+1} \,.\end{aligned} \tag{16}$$

The interface elements align along the horizontal axis. Picard iteration over κ_r^{k+1} and S^{k+1} are used to resolve the non-linearities in the system of equations. Nonlinearities in κ_p^{k+1} are resolved sequentially. For a given trial channel height, equation (15) provides the equivalent intrinsic

permeability, which is attached to the relevant interface element. The product of channel height and pressure gradient are then compared with the equilibrium condition given by the second part of expression (15).

Figure 1 provides the sequential procedure graphically for a sample problem that includes two interface elements that are in series. The height of the channel is presented as a function of hydraulic head gradient. Hydraulic head $h\,(\mathrm{m})$ is presented as $h = p/(\rho^l g) + y$, where $y\,(\mathrm{m})$ is the elevation level. The dark blue line represents the limit equilibrium condition; below this line stable grain conditions apply and above the equilibrium line unstable conditions hold.

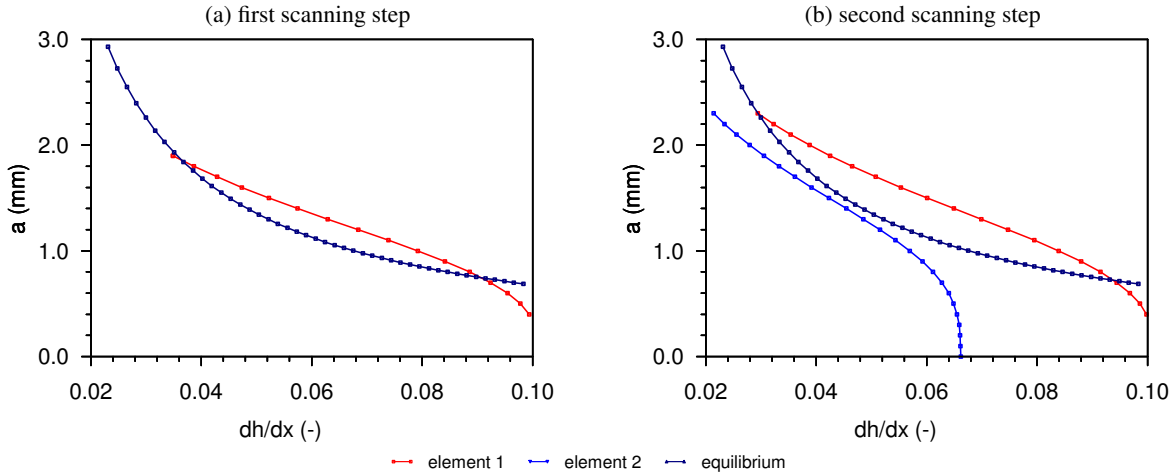

Fig. 1. Activation algorithm.

The calculation process starts by checking the interface element located to the downstream side of the channel (element 1) next to the exit point. For a thickness of 0 mm the head gradient is due to the flow process through the subsurface. Increasing the thickness of the element increases the effective permeability of the element and decreases the gradient over the element leading to the red line in Figure 1 (a). The height of the channel is increased stepwise until the condition becomes unstable. This unstable situation is associated with the first (right) point where the red line intersects the equilibrium line. At this point the element becomes active for the given head difference over the structure; a small increase in the channel height pushes the element in the unstable zone. The permeability of the element is increased until the element becomes stable again. The element thickness for which equilibrium holds is obtained by means of a bisection algorithm. This second (left) intersection point denotes a stable situation. If the height of the channel increases above this point, the element enters the stable zone.

The procedure continues by checking the element on the upstream side (element 2) of the first element (element 1). The plot on the right of Figure 1 illustrates this process. The height is increased sequentially until the line enters the unstable zone and the second intersection point is found, or a threshold value for the maximum channel height has been reached indicating that the element will not be activated. For the depicted situation, the applied head difference over the structure will not activate the second element. If equilibrium is not satisfied for the trial element however, then the height of the already activated elements is modified accordingly until equilibrium is satisfied within the entire pipe domain.

3 NUMERICAL SIMULATIONS

Figure 2 shows the layout of a simplified dam geometry with a low permeable structure that is supported by an aquifer of high permeability, as well as the finite element mesh used for the flow simulation. To the left side of the structure the water level imposes a hydraulic head condition on the horizontal edge of the aquifer and to the right side of the structure a constant water level applies. The vertical boundaries and base of the aquifer are considered impervious as well as external dam boundaries. The structure itself has a low permeability, hardly supporting groundwater flow. Thus, water flows under the structure through the aquifer from the river side towards the polder. Sellmeijer (1988) considered an impermeable structure on top of an aquifer with the same hydraulic loading conditions.

The numerical experiments outlined in this section consider a set microscale material parameters given by: particle diameter that is $2.08 \cdot 10^{-4}$ m; density of the grains of $2.65 \cdot 10^{3}\,\mathrm{kg/m^3}$; White's constant of 0.25 and bedding angle that is assumed to be 37 deg. The geometry of the problem is given by the thickness of the aquifer of 20 m and the potential piping length of 40 m. The solid skeleton has an intrinsic permeability of $1.157 \cdot 10^{-10}\,\mathrm{m^2}$. The pore water has a unit weight of $10^{4}\,\mathrm{N/m^3}$and dynamic viscosity of $10^{-3}\,\mathrm{Ns/m^2}$. The gravitational acceleration is set to $10\,\mathrm{m/s^2}$, which sets the hydraulic conductivity K $(\mathrm{m/s})$ of the aquifer to $100\,\mathrm{m/d}$, as $K = \kappa\rho^{l}g/\mu$. For this sample problem equation (2) provides a resistance term of 0.311, yielding a scale term of 0.125 and sets the geometry term to 1.110. Using these terms, Sellmeijer's rule (1) predicts a critical head difference of 1.726 meter for which the pipe grows progressively.

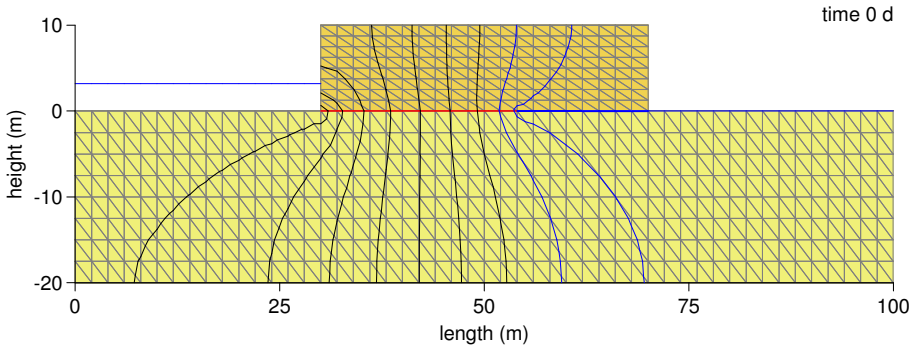

Fig. 2. Simplified dam geometry.

Figure 2 shows the result of a steady state computation where the piping channel did not reach the upstream side and the structure remains stable for the imposed head difference. The channel is captured by interface elements located at predefined position under the dam. Current inactive interface elements are colored red and active interface elements that support Poiseuille flow through the channel are colored blue. The flow direction is normal to the equipotential lines as the permeability tensor is isotropic. The active 15 meter long piping channel that drains the aquifer to some extent, cause a shift in the otherwise symmetrically arranged equipotential lines as shown.

3.1 Steady State Simulation

Steady-state calculations were carried out for five cases of head loss across the dam. Figure 3 shows the results along the interface elements. The variation of the hydraulic head over the interface is continuous in space as groundwater pressures are linearly interpolated over the elements,

whereas the head gradient being discontinuous between the elements. As the channel height relates to the head gradient, it is discontinuous as well.

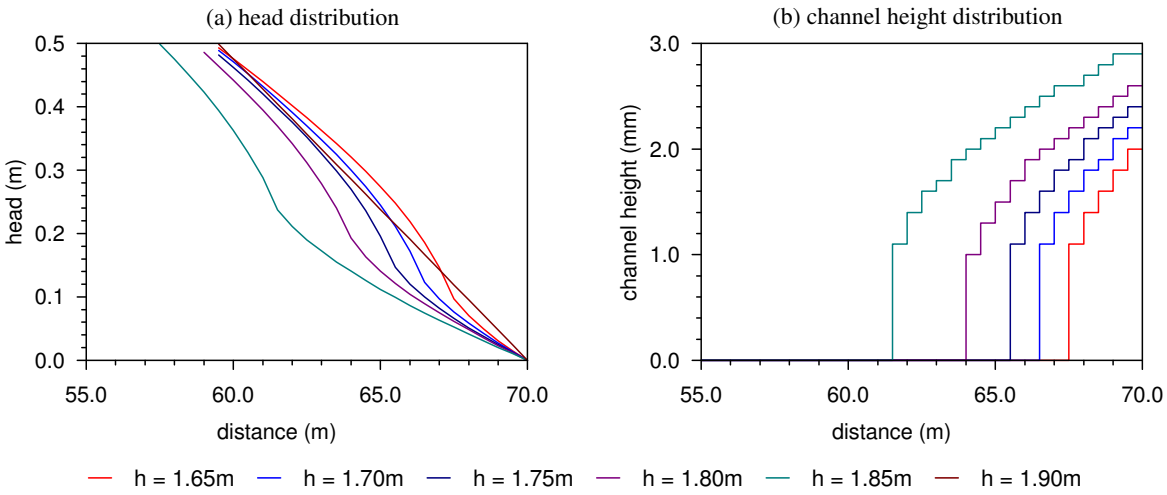

Fig. 3. Steady state results along the interface.

In this simulation a temporal linear increase of the river level was imposed. The storage in the system due to wetting and drying above the phreatic line and due to compression and swelling of the soil was neglected.

3.2 Transient Flow Simulation

Transient simulations were also performed where the compressibility of the aquifer was taken into account. Compression, which was mainly due to clay inclusions in the sandy aquifer delayed the water pressure generation. This delay was found to hamper the growth of the piping channel in time and increase the critical head difference for rapid changes of river water level. The response in the interface elements was assumed to be instantaneous with regard to changes within the adjacent triangular elements as the model does not simulate the transport process of the grains within the channel. For the transient simulation the compressibility of the aquifer was set to $2 \cdot 10^{-7}$ m^2/N and calculations were carried out for a period of one hour over which the river level changed linearly from 1.0 m to 2.0 m. Figure 4 presents the predictions for six moments in time corresponding to head differences 1.65, 1.70, 1.75, 1.80, 1.85 and 1.90 meters.

3.3 Comparison with Sellmeijer's Rule

A set of numerical computations were run to compare the prediction with Sellmeijer's rule and results obtained by the prescribed model. The particle diameter of either $1.0 \cdot 10^{-4}$ m or $3.0 \cdot 10^{-4}$ m and the hydraulic conductivity of the aquifer was set to 1 m/d or 100 m/d. The thickness of the aquifer varied from 10 m to 30 m and the potential piping length ranged from 30 m to 90 m. This implies that D/L varied from 1/9 to 1, where the upper bound yields the lowest value for the critical head difference.

Given a length of the dam L, the geometry of the flow problem was extended 150 m left of the structure, where infiltration of water took place at the horizontal upper aquifer boundary. On the inland side of the structure a strip of 50 m was added. Here exfiltration was concentrated at a single point at the structure boundary. To the right side of this point the boundary is closed

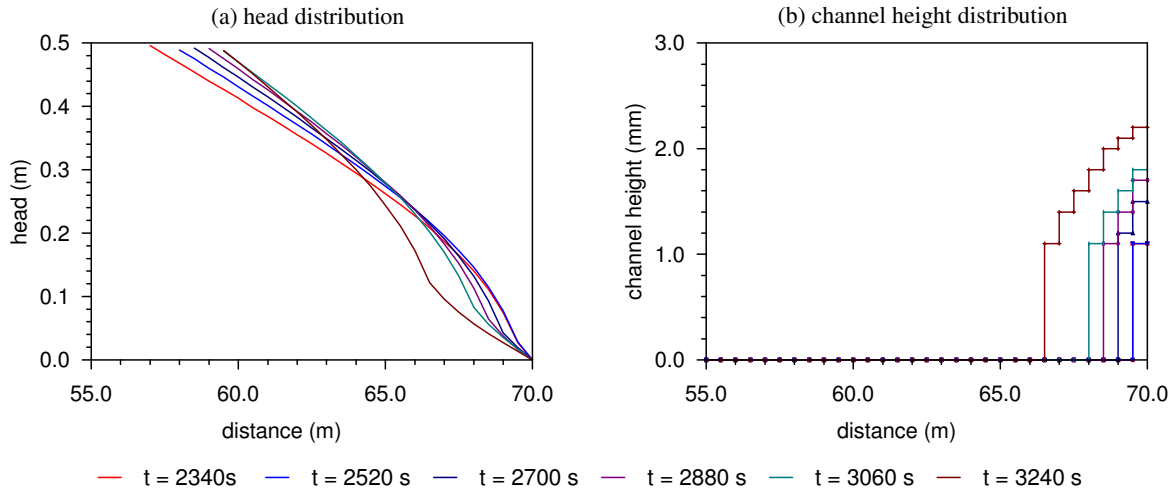

Fig. 4. Transient results along the interface.

for flow. A uniform mesh of elements with a height of 2.5 m and width of 5 m was adopted. This discretization resulted for the smallest model of $230 \times 10\,\mathrm{m}^2$ in 235 nodes, 4 interface elements capture the piping channel. The largest model of $290 \times 30\,\mathrm{m}^2$ generates 767 nodes with 12 interface elements for the erosion channel. Tables 1, 2, 3 and 4 compare the results from Sellmeijer's rule H_c and the numerical predictions H_n.

Table 1. $d_{70} = 1.0 \cdot 10^{-4}$ m, $\kappa = 1.157 \cdot 10^{-12}$ m^2

L (m)	D (m)	H_c (m)	H_n (m)	H_c/H_n $(-)$
30.000	10.000	3.430	3.500	0.980
60.000	10.000	6.367	6.900	0.923
90.000	10.000	9.179	10.600	0.866
30.000	20.000	3.003	3.100	0.969
60.000	20.000	5.444	5.800	0.939
90.000	20.000	7.806	8.600	0.908
30.000	30.000	2.601	2.900	0.897
60.000	30.000	5.015	5.400	0.929
90.000	30.000	7.134	7.900	0.903

Table 2. $d_{70} = 3.0 \cdot 10^{-4}$ m, $\kappa = 1.157 \cdot 10^{-12}$ m^2

L (m)	D (m)	H_c (m)	H_n (m)	H_c/H_n $(-)$
30.000	10.000	10.289	10.700	0.962
60.000	10.000	19.100	20.900	0.914
90.000	10.000	27.538	32.000	0.861
30.000	20.000	9.008	9.300	0.969
60.000	20.000	16.333	17.500	0.933
90.000	20.000	23.418	25.900	0.904
30.000	30.000	7.804	8.900	0.877
60.000	30.000	15.045	16.300	0.923
90.000	30.000	21.403	23.700	0.903

Table 3. $d_{70} = 1.0 \cdot 10^{-4}$ m, $\kappa = 1.157 \cdot 10^{-10}$ m^2

L (m)	D (m)	H_c (m)	H_n (m)	H_c/H_n $(-)$
30.000	10.000	0.739	0.700	1.056
60.000	10.000	1.372	1.500	0.914
90.000	10.000	1.978	2.200	0.899
30.000	20.000	0.647	0.600	1.078
60.000	20.000	1.173	1.200	0.977
90.000	20.000	1.682	1.800	0.934
30.000	30.000	0.560	0.600	0.934
60.000	30.000	1.080	1.100	0.982
90.000	30.000	1.537	1.600	0.961

Table 4. $d_{70} = 3.0 \cdot 10^{-4}$ m, $\kappa = 1.157 \cdot 10^{-10}$ m^2

L (m)	D (m)	H_c (m)	H_n (m)	H_c/H_n $(-)$
30.000	10.000	2.217	2.200	1.008
60.000	10.000	4.115	4.500	0.914
90.000	10.000	5.933	6.800	0.872
30.000	20.000	1.941	2.000	0.970
60.000	20.000	3.519	3.700	0.951
90.000	20.000	5.045	5.600	0.901
30.000	30.000	1.681	1.900	0.885
60.000	30.000	3.241	3.500	0.926

The piping rule provides lower bound values for the critical head within the range of river levels investigated. Given the time step size a value of 1.0 m states that the piping channel reached the upstream boundary for a head difference of 1.1 m as the step size was 0.1 m. The H_c/H_n ratio suggests that the fit parameter (0.91) in equation (1) could be removed and the system might be more resistant to piping during high water periods. The fit parameter resulted from calculations

with a less accurate numerical code. At present the factor also represents a model factor that fits predictions to validation test results that were carried out both at laboratory and field scale.

4 CONCLUSIONS

This article presents a new numerical formulation of the piping mechanism that is capable of simulating groundwater flow and piping through more complex geotechnical structures. Storage of water above the phreatic surface is taken into account by simulating flow through the unsaturated zone by means of Richards' equation. Elastic storage in the saturated zone is included in the model by considering the compressibility of the solid matrix and the compressibility of the pore water. The transient simulation demonstrates that the compressibility of the aquifer delays the increase of water pressures in time. This delay hampers the growth of the piping channel and increases the critical head difference if the frequency of river water level variations is high compared to the groundwater response time. Numerical simulations demonstrate that Sellmeijer's rule predicts critical head differences quite well. The rule however applies for simplified impervious geotechnical problems only and considers a single homogeneous aquifer.

The implementation enables the definition of a physical criterion for the onset of particle movement and facilitates the extension of the current equilibrium formulation for grain movement in the erosion channels to a fully transient formulation. This will be the topic for future work.

ACKNOWLEDGEMENTS

The authors would like to thank Cristina Jommi for her valuable comments on the article. The research was carried out as part of the Wettelijk Toets Instrumentarium program (WTI2017). This program was funded by the Rijkswaterstaat; the executive arm of the Dutch Ministry of Infrastructure and the Environment.

REFERENCES

Belytschko, T., Liu, W. K., & Moran, B. (2008). *Nonlinear Finite Elements for Continua and Structures*. Wiley.

Blight, W. G. (1915). Submerged weirs founded on sand. *Dams and weirs*.

Hughes, T. J. R. (2000). *The Finite Element Method, Linear Static and Dynamic Finite Element Analysis*. Dover Publications.

Huyakorn, P. S. & Pinder, G. F. (1983). *Computational Methods in Subsurface Flow*. Academic Press.

Lane, E. W. (1935). Security from under-seepage-masonry dams on earth foundations. *Transactions of the American Society of Civil Engineers 100*(1), 1235–1272.

Sellmeijer, J. B. (1988). *On the mechanism of piping under impervious structures*. Ph. D. thesis, Delft University of Technology.

Sellmeijer, J. B., Lopez De La Cruz, J., Van Beek, V. M., & Knoeff, J. G. (2011). Fine-tuning of the piping model through small-scale, medium-scale and ijkdijk experiments. *European Journal of Environmental and Civil Engineering 15*(8), 1139–1154.

Van Esch, J. M. (2010). *Adaptive Multiscale Finite Element Method for Subsurface Flow Simulation*. Ph. D. thesis, Delft University of Technology.

Wolfs, T. F. (2002). *Performance of Levee Underseepage Controls: A Critical Review*, Volume ERDC/GSLTR-02-19. Michigan State University.

A QUANTITATIVE COMPARISON OF THE EFFECTS OF DESIGN PARAMETERS OF LANDFILL LINERS ON INORGANIC CONTAMINATION OF GROUNDWATER

A.H. El-Zein
School of Civil Engineering, University of Sydney, NSW 2006, Australia

I. McCarroll
School of Civil Engineering, University of Sydney, NSW 2006, Australia

ABSTRACT: *Geo-environmental engineers aim to minimize the leaching of contaminants from waste repositories into underlying aquifers, using cost-effective designs. Hence, the relative effects on pollution levels of various design parameters in landfill liners are of primary importance. However, there is very little in the literature by way of direct quantitative comparison of the impacts of these parameters. We build coupled hydro-chemical models of inorganic transport (cadmium and chloride) through geosynthetic clay liners (GCLs) in 2D. We take into account defects in the geomembrane and the quality of contact between the geomembrane and the underlying liner. We use the finite-element code Soil Pollution Analysis System (SPAS) to conduct simulations and develop a set of variability ratios which allow us to compare the amplitude of change of environmental outcomes per unit of change of a given design parameter. We find that the design parameters with the strongest effects on contaminant levels are the depths of the liners and the attenuation layers rather than the hydraulic conductivities of the GCL. Finally, we find configurations with similar leakage rates can lead to very different patterns of chemical concentration in groundwater.*

1 INTRODUCTION

Designers of waste containment systems typically aim to achieve a number of performance objectives: environmental (organic and inorganic contamination levels in groundwater; methane emissions), hydraulic (leakage rates; leachate management) and operational (construction and durability; access to site). In addition, they must respect a set of regulatory, budgetary and time constraints. Given these multiple considerations, understanding the relative effects on pollution levels of various design parameters in landfill liners, quantitatively and qualitatively, are of primary importance. While we do understand how the most important parameters affect environmental outcomes in typical design configurations, very few studies have attempted to make direct comparisons of various design parameters (e.g., Rowe et al., 2004; Kandris and Pantazidou, 2012). Such a comparison would allow designers to make a more informed decision about which parameter to focus on in attempting to improve their solutions.

Most landfill liners include, in addition to a compacted clay liner (CCL) or a geosynthetic clay liner (GCL), a high density geomembrane which is extremely effective in preventing water and inorganic contaminants from travelling from the waste into the subsurface. However, given the large surface areas over which the liner is deployed and the challenging

chemical, physical and climate conditions under which it must operate, it is very difficult to prevent damage from occurring to the geomembrane before, during and after waste placement, which leads to some leakage into the underlying layers (e.g., Nosko and Touze-Foltz, 2000). Over the last decade, our ability to build more realistic models taking into account both hydraulic and chemical behavior, as well as typical patterns of defects in the geomembrane, has improved significantly (Foose et al., 2002; El-Zein and Rowe, 2008; El-Zein et al., 2005; El-Zein et al., 2012). One of the interesting findings of some of these studies is that leakage rates, often taken as reflective of levels of contamination, do not always correlate well with chemical concentrations in the aquifer, at least not for organic contaminants.

In this paper, we use the purpose-built finite-element code Soil Pollution Analysis System (SPAS) (El-Zein and Balaam, 2012) to simulate coupled hydro-chemical transport of sorptive and non-sorptive inorganic contaminants—cadmium and chloride—through geosynthetic clay liners (GCLs) in 2D. We take into account defects in the geomembrane and the quality of contact between the geomembrane and the underlying liner.

Our aims are to:

a) quantify the effects of various design parameters on leakage rates and concentrations of inorganic contaminants in the aquifer in order to identify those parameters with the biggest impact on the liner's performance, and
b) assess the extent to which leakage rates are good predictors of maximum concentrations of inorganic contaminants in the aquifer.

To this end, we develop a set of variability ratios which allow us to compare the amplitude of change of environmental outcomes per unit of change of a given design parameter.

2 THEORY AND SIMULATIONS

The steady-state flow of water in saturated, incompressible soil can be represented by the following equations, based on Darcy's law and a mass conservation statement:

$$k_x \frac{\partial^2 H}{\partial x^2} + k_y \frac{\partial^2 H}{\partial y^2} = 0 \tag{1}$$

$$v_x = -\frac{k_x}{n}\frac{\partial H}{\partial x} \tag{2}$$

$$v_y = -\frac{k_y}{n}\frac{\partial H}{\partial y} \tag{3}$$

where (x,y) is a Cartesian coordinate system [L], H is the total hydraulic head [L], k_x, k_y are the two diagonal components of the hydraulic conductivity tensor [$L.T^{-1}$], v_x and v_y are the two components of the seepage velocity vector [$L.T^{-1}$], and n is the medium porosity. The transport of inorganic, non-radioactive species dissolved in water in the soil is governed by processes of mechanical dispersion, molecular diffusion, advection and linear sorption and can be described by the following equation:

$$\frac{\partial}{\partial x}\left(nD_{xx}\frac{\partial c}{\partial x}\right)+\frac{\partial}{\partial x}\left(nD_{xy}\frac{\partial c}{\partial y}\right)+\frac{\partial}{\partial y}\left(nD_{yx}\frac{\partial c}{\partial x}\right)+\frac{\partial}{\partial y}\left(nD_{yy}\frac{\partial c}{\partial y}\right) - nv_x c - nv_y c = (n+\rho K_d)\frac{\partial c}{\partial t} \tag{4}$$

$$D_{xx} = D_0 + \alpha_T |v| + (\alpha_L - \alpha_T)\frac{v_x^2}{|v|} \tag{5}$$

$$D_{xy} = D_{yx} = (\alpha_L - \alpha_T)\frac{v_x v_y}{|v|} \quad (6)$$

$$D_{yy} = D_0 + \alpha_T |v| + (\alpha_L - \alpha_T)\frac{v_y^2}{|v|} \quad (7)$$

$$f_x = -nD_{xx}\frac{\partial c}{\partial x} + nv_x c \quad (8)$$

$$f_y = -nD_{yy}\frac{\partial c}{\partial y} + nv_y c \quad (9)$$

where t is time [T], c(t,x,y) is the solute concentration [$M.L^{-3}$], D_{xx} and D_{yy} are the two diagonal components of the hydrodynamic dispersion tensor for the solute in the medium [$L^2.T^{-1}$], D_0 is the coefficient of molecular diffusion of the solute in the soil water [$L^2.T^{-1}$], α_L and α_T are the longitudinal and transverse dispersivities, respectively [L]; K_d is the linear sorption distribution coefficient of the solute in the medium [$L^3.M^{-1}$], ρ is the dry density of the soil [$M.L^{-3}$], f_x and f_y are the solute fluxes, or specific discharges, in the two directions [$M.L^{-2}.T^{-1}$]. To characterize the relationship between landfill liner design parameters and contamination levels in groundwater, we simulate a typical composite landfill liner configuration shown in figure 1.

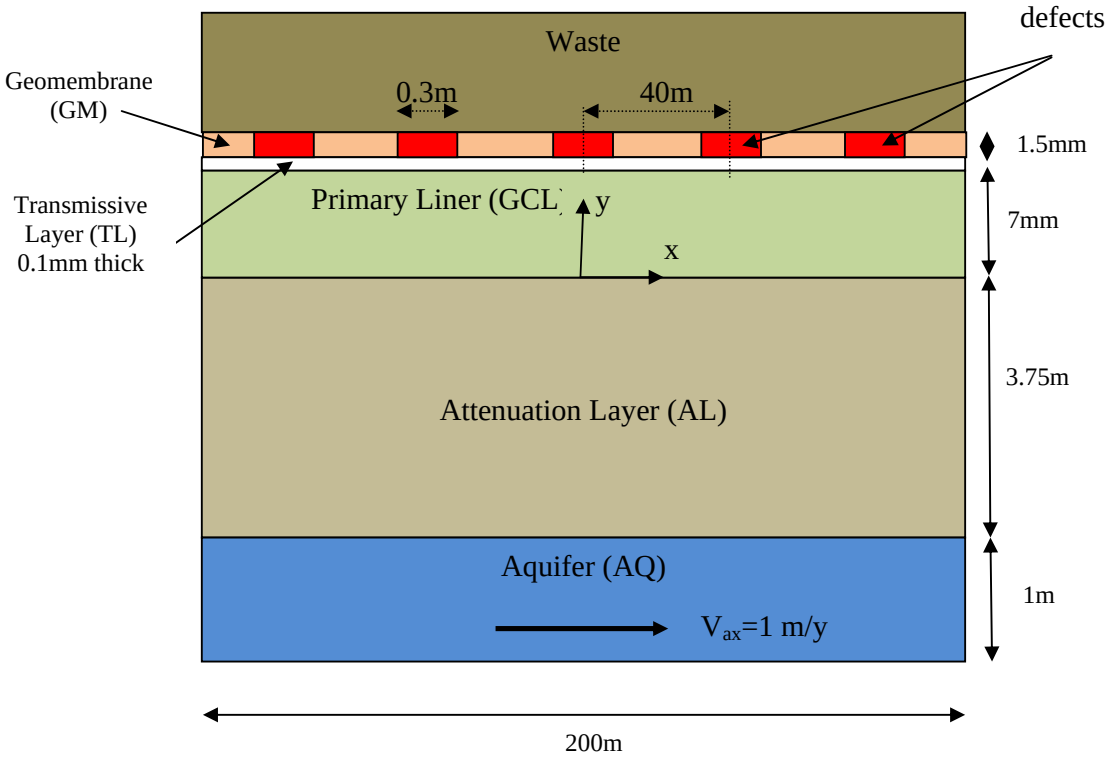

Figure 1. Cross-section of base model of landfill liner-soil system (figure not to scale)

We use the 2D version of the Soil Pollution Analysis System (SPAS), a purpose-built finite element method (FEM) program which simplifies the generation of landfill liner features (El-Zein and Balaam, 2012). It is based on a weighted-residual Galerkin solution of the above equations. A time-marching scheme is used to solve the coupled hydro-chemical equations shown above. Two degrees of freedom are adopted at each node: the total hydraulic head H

and the solute concentration C. H, v_x, and v_y are first obtained from the steady-state seepage analysis. Next, the spatially-variable seepage velocities become part of the input parameters for the time-dependent mass-transport problem which, when solved, yields C, f_x and f_y. Leakage rates are calculated as the integral of the vertical Darcy velocity function over the interface between the primary liner and the attenuation layer, divided by the surface area of that interface. The hydraulic steady-state assumption is justified because of the long time scales (decades and centuries) of solute transport processes in clay soils.

Two base cases are simulated:

a) chloride transport through a composite geosynthetic clay liner (GCL-Cl);
b) cadmium transport through a composite geosynthetic clay liner (GCL-Cd).

Chloride is adopted because data on its diffusion properties are widely available and it has negligible sorption capacity in soil, leading to fewer variables in the analyses and a worst-case scenario. Cadmium on the other hand is a heavy metal with some sorptive affinity to clay and known diffusion parameters.

Material properties used in the analyses are given in Table 1. A transmissivity of 10^{-10} m^2/s for the GCL/Geomembrane interface is adopted. The thickness of the high-density polyethylene (HDPE) geomembrane is assumed to be 1.5 mm with rectangular defects of width 0.3 m, as observed by Pelte et al. (1994). This is consistent with works by Touze-Foltz et al. (2001) and, more recently, Chappel et al. (2008). All layers are fully saturated and the aquifer is assumed to be 1 m deep. Sorption in all layers is negligible, except for cadmium in the primary liner. Pressure heads of 30cm are applied at each defect, and 3.75m in the aquifer. All other surfaces have zero flow hydraulic boundary conditions. For the chemical transport problem, initial contaminant concentrations are taken to be identically zero, everywhere except in the waste. To simulate a specified mass of contaminants at the inlet, a waste layer is included in the mass transport problem with a specified initial concentration C_0 and a thickness equal to the equivalent height of leachate H_f. At the downstream edge of the aquifer, an advective discharge boundary condition is applied, i.e. contaminants are assumed to leave the system at a flux rate of nv_xc. All other surfaces have zero flux boundary conditions.

The analyses are conducted in 2 stages. First, the two base cases are simulated as benchmark references. Second, the effect on leakage rates and chemical concentrations in the aquifer of relevant design parameters is studied. Convergence analyses are conducted to ensure the robustness of the predictions. Eight-noded quadratic elements are used throughout.

Key boundary conditions in our analyses are clearly oversimplifications of likely site conditions. This is especially the case for the aquifer downstream boundary condition (and aquifer hydraulic regime) which assume that contaminants are discharged from the system at the advective rate, hence neglecting dispersive effects at the boundary. On the positive side, the condition is likely to be conservative, keeping more contaminants in the system than would otherwise be the case. The assumption of regular and parallel defects can have an important effect on the results; however, deviating from this assumption would lead to a wide range of possible scenarios that are difficult to cover. In addition, we have made two assumptions that are likely to have the most significant impacts on our conclusions. First, the contaminants in the waste were taken to be fully available for migration into the underlying liner when in fact inorganic chemicals can become immobilized at the source. This is,

Table 1. Parameters Used in Simulations: Four Base Cases and Variability Ranges

	Description	Units	Source	GCL-Cl	GCL-Cd
C_0	Initial concentration in the waste	g/m^3	[1] p56	11950	0.05
d	Waste density	g/m^2	[2]	$2.5x10^7$	$2.5x10^7$
p_0	Contaminant density in the waste	g/g	[1] p64	$1.5x10^{-3}$	$2.4x10^{-9}$
H_f	Equivalent height of leachate	m	dp_0/C_0	3.14 (1-5)	1.2 (0.5-2)
N_{GCL}	Primary liner porosity		[4]	0.7	0.7
n_{AL}	Attenuation layer porosity			0.35	0.35
n_{AQ}	Aquifer porosity			0.3	0.3
w	Width of defect	m		0.3 (0.1-0.5)	0.3 (0.1-0.5)
f	Frequency of defects	defect/ha	[1] p427	2.5 (1-5)	2.5 (1-5)
k_{GCL}	Primary liner hydraulic conductivity	m/s		$5x10^{-11}$ ($5x10^{-12}$-$5x10^{-9}$)	$5x10^{-11}$ ($5x10^{-12}$-$5x10^{-9}$)
k_{AL}	Attenuation layer hydraulic conductivity	m/s		10^{-7} (10^{-8}-10^{-6})	10^{-7} (10^{-8}-10^{-6})
θ_x	Transmissivity geomembrane-primary liner	m^2/s	[3]	10^{-10} (10^{-11}-10^{-9})	10^{-10} (10^{-11}-10^{-9})
D_{GM}	Diffusion coefficient in geomembrane	m^2/s	[1] p295	$5x10^{-15}$	$5x10^{-16}$
D_{GCL}	Diffusion coefficient in primary liner	m^2/s	[1] p270,394	$3x10^{-10}$ ($6x10^{-11}$-$3x10^{-9}$)	$3x10^{-10}$ ($6x10^{-11}$-$3x10^{-9}$)
D_{AL}	Diffusion coefficient in attenuation layer	m^2/s	[1] p270	$7.5x10^{-10}$ ($4.2x10^{-11}$-$7.5x10^{-9}$)	$4.2x10^{-10}$ ($4.2x10^{-11}$-$7.5x10^{-9}$)
D_{AQ}	Mechanical dispersion in aquifer	m^2/s	[1] p270	100	100
ρ_{GCL}	Primary liner dry density	kg/m^3		790	790
k_{dGCL}	Primary liner sorption coefficient	m^3/kg	[4]	0	0.072

[1] Rowe et al. (2004); [2] O. Reg 232/98; [3] Touze-Foltz and Barroso (2006) ($\log\theta = -2.2322 + 0.7155\log K_{GCL}$); [4] Shackelford and Daniel (1991)

however, a conservative assumption. Second, the parameters we have used in the analyses were taken to be time-independent, as though no deterioration of the system components take place over time. This is clearly not the case, especially since peak concentrations in the aquifer, according to our analyses, are sometimes reached hundreds of years after waste placement on landfill closure. Therefore, it is important to interpret our results as guidance for comparative designs under idealized conditions, rather than predictions of actual behavior for centuries to come.

In order to be to able to compare quantitatively the impacts of various design parameters on the performance of the liners, we develop a set of definitions for variability ratios shown in Table 2. Variability ratios R_{vL} and R_{vC} provide an estimate of the average percentage change

Table 2. Definitions of Variability Ratios

Variable	Description			Definition
P*	Design parameter range	p_{min}	p_{max}	
L	Leakage rate calculated at the 2 ends of the parameter range	L_1	L_2	
C_{max}	Maximum concentration in aquifer calculated at the 2 ends of the parameter range	C_{max1}	C_{max2}	
Δp	Percent change in p			$\frac{p_{max} - p_{min}}{p_{min}}$
ΔL	Percent change in L			$\frac{L_2 - L_1}{L_1}$
ΔC	Percent change in C			$\frac{C_{max2} - C_{max1}}{C_{max1}}$
$R_{vLeakage}$	Variability ratio for leakage rate	Average % change in leakage rate per 1% change in design parameter		$\frac{\Delta L}{\Delta p}$
R_{vCmax}	Variability ratio for maximum concentration in aquifer	Average % change in aquifer maximum concentration per 1% change in design parameter		$\frac{\Delta C}{\Delta p}$
R_{LC}	Ratio of variability ratios	Average % change in leakage rate per 1% change in aquifer maximum concentration		$\frac{R_{vLeakage}}{R_{vCmax}}$

in leakage rates and maximum concentration in the aquifer, respectively, per percentage change in a given design parameter. Clearly, the larger R_{vL} and R_{vC}, the more impact the design parameter in question has on environmental outcomes. R_{LC}, on the other hand, captures the extent to which leakage rates and maximum chemical concentrations in the aquifer are correlated, between the extremes of no correlation (R_{LC}=0) and perfect correlation (R_{LC}=1).

3 RESULTS

The general hydraulic and chemical behaviors of each landfill liner for the base case are shown in Figures 2, 3 and 4.

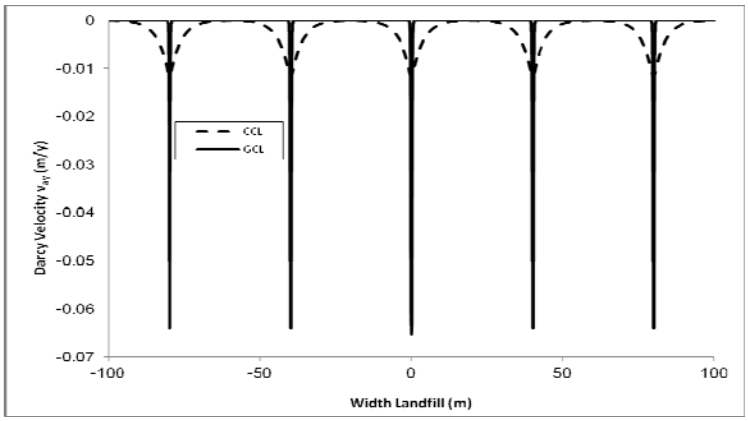

Figure 2. Downward Darcy velocity along the horizontal axis at the interface between the primary liner and attenuation layer, at hydraulic steady-state in comparison with a CCL case

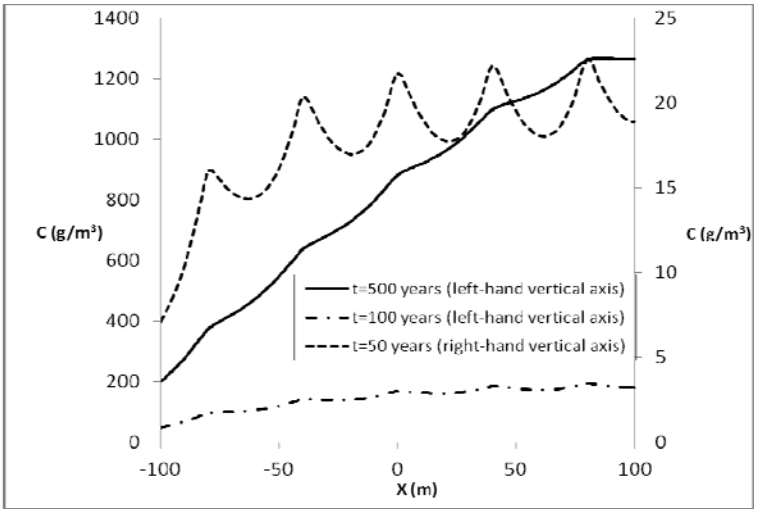

Figure 3. Chemical concentrations of chloride along the horizontal axis in the aquifer

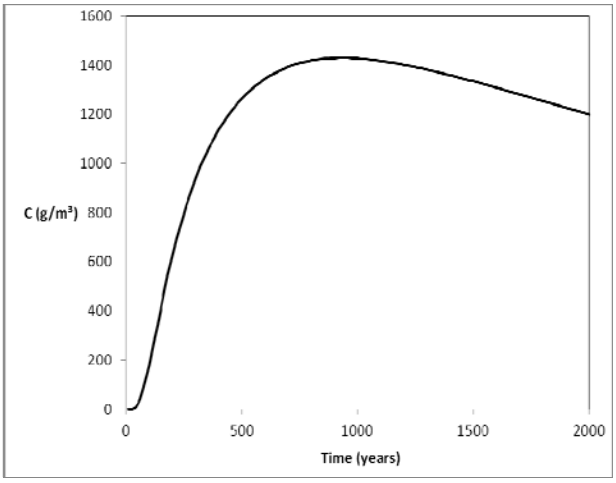

Figure 4. Change in chemical concentrations of chloride in the aquifer with time

From figure 2, it can be seen that leakage occurs over a narrower area in the case of a GCL liner, in comparison with a CCL liner. This is due to the GCL's low transmissivity at the interface with the geomembrane. It is also evident from figure 3 that as time progresses the maximum peak concentrations that occur beneath the wrinkles in earlier years are smoothed out. This is indicative of strong effect of mechanical dispersion in the aquifer. The concentration levels are also affected by the magnitude of groundwater flow in the aquifer and the maximum contamination levels are reached at, or close to, the downstream end of the landfill. Figure 4 shows the buildup and decline of concentrations in the aquifer, as the contaminant is flushed out of the system. Similar effects were found by El-Zein and Rowe (2008) and El-Zein et al. (2012) for organic contaminants, except that, owing to the effect of biodegradation, maximum concentrations of organic contaminants are reached much earlier. In reality, inorganic peaks are likely to be reached earlier than our simulations reveal because of immobilization of inorganic contaminants at source and diffusive discharge from the aquifer, both of which we neglect in our analyses (see our discussion of assumptions at the end of section 2 of the paper).

Next, the effects of changing a number of different design parameters are considered. Table 3 shows calculated variability ratios for different design parameters. Key parameters are the thicknesses of the primary liner and attenuation layer, the frequency of defects, the hydraulic conductivity of the primary liner, the transmissivity and the diffusion coefficient in the primary liner. The effect of increasing the GCL thickness is particularly pronounced, leading to a large drop in both leakage rates and chemical concentrations in the aquifer. The width of the defect has a strong effect on both leakage rates and chemical concentrations because it determines the extent of direct contact between leachate in the waste and the primary liner. Clearly, combining variability ratios with some measure reflecting cost per unit change in a given design parameter would allow landfill designers to optimize designs in order to achieve desired environmental outcomes are the lowest possible cost.

Table 3 also shows the ratio $R_{LC}=R_{vL}/R_{vC}$ which reflects the extent to which changes in leakage rates are proportional to changes in chemical concentrations. Predictably, H_f and diffusion coefficients have no impact on leakage rates, therefore yielding $R_{LC}=0$. Changes in leakage rates as a result of changes in the thickness of the attenuation layer, frequency of defects and hydraulic conductivity of the primary liner correlate well with corresponding changes in maximum chemical concentrations in the aquifer. Especially significant is the steeper change in concentrations, relative to leakage rates, when it comes to transmissivity. This is especially surprising since no such effect is observed when varying k_{GCL}. This observation can be explained by the fact that the same leakage rates can be obtained from Darcy velocity profiles exhibiting very different peak velocities and lateral extent of leakage penetration under the geomembrane. This is because the leakage rate is a measure of the Darcy velocity *averaged* over the surface area of the liner. Hence, leakage rates do not reveal the full picture and chemical concentrations need to be considered in critical cases.

Table 3. Calculated Variability Ratios R_v

		H_f	t_{GCL}	t_{AL}	w	F	k_{GCL}	k_{AL}	θ	D_{GCL}	D_{AL}
Range	**Interval End 1**	1m (Cl) 0.5m (Cd)	7mm	3.75 m	0.1 m	1 /ha	10^{-12}m/s	10^{-8}m/s	10^{-11}m/s	$6x10^{-11}$m^2/s	$4.2x10^{-11}$m/s
	Interval End 2	5m (Cl) 2m (Cd)	10mm	7m	0.5m	5 /ha	10^{-9}m/s	10^{-6}m/s	10^{-9}m/s	$3x10^{-9}$ m^2/s	$7.5x10^{-9}$m^2/s
Output GCL-Cl	**L_1 (10^{-4} m/year)**	8.96	8.96	8.96	5.72	3.6	1.83	6.59	6.3	8.96	8.96
	L_2 (10^{-4} m/year)	8.96	1.91	103	12.10	17.9	141	9.3	17.3	8.96	8.96
	C_1 (g/m^3)	1133	1430	1430	886	744	628	1169	1317	1344	1108
	C_2 (g/m^3)	1326	598	8488	1928	2449	15104	1466	1530	1531.9	2932
	$R_{vLeakage}$	0	**-12.3**	**1.98**	0.66	1	0.99	0.29	0.64	0	0
	R_{vCmax}	0.18	**-4.63**	**1.8**	0.68	0.87	0.96	0.2	0.14	0.13	0.63
	$R_{LC}=R_{vLeakage}/R_{vCmax}$	**0**	**1.35**	1.1	0.97	1.15	1.03	**1.45**	**4.57**	0	0
Output GCL-Cd	**L_1 (m/year)**	8.96	8.96	8.96	5.72	3.6	1.83	6.59	6.3	8.96	8.96
	L_2 (m/year)	8.96	1.91	103	12.1	17.9	141	9.3	17.3	8.96	8.96
	C_1 (10^{-3} g/m^3)	2.96	3.81	3.81	2.22	1.88	1.21	3.05	3.49	3.61	4.11
	C_2 (10^{-3} g/m^3)	4.29	0.74	29.30	5.36	6.41	45.4	3.97	4.24	4.15	8.77
	$R_{vLeakage}$	0	**-12.3**	**1.98**	0.66	1	0.99	0.29	0.64	0	0
	R_{vCmax}	0.41	**-13.8**	**1.89**	0.73	0.88	0.97	0.23	0.18	0.13	0.54
	$R_{LC}=R_{vLeakage}/R_{vCmax}$	**0**	0.97	1.05	0.9	1.14	1.02	**1.26**	**3.56**	**0**	**0**

4 CONCLUSIONS

We have simulated the transport of chloride and cadmium through composite liners with multiple defects in the geomembrane. We have developed definitions of change ratio which allow us to compare the amplitude of change of environmental outcomes per unit of change of a given design parameter. We have found that the levels of inorganic contamination in the aquifer is most sensitive to the depths of the primary liners and attenuation layers, more so than the hydraulic conductivities of the two layers. It is also clear from these results that the use of the hydraulic regime to estimate the levels of contamination in the aquifer can, in some instances, be insufficient. This is most pronounced in the effects of change in transmissivity: reductions in leakage rates as a result of a decrease in the value of transmissivity (i.e., improvement in the quality of contact between geomembrane and primary liner) does not translate into a proportionate decline in maximum inorganic contamination levels in the aquifer.

REFERENCES

Chappel, M.J., W.A. Take, W.A., Brachman, R.W.I., Rowe, R.K., 2008. A case study of wrinkles in a textured HDPE geomembrane on a slope. *GEOAMERICAS 2008*, Cancun, Mexico, March, 452-458.

El-Zein A, Carter JP, Airey DW. 2005. Multiple-porosity contaminant transport by finite-element method. *International Journal of Geomechanics* 5, 24.

El-Zein, A., Rowe, R.K., 2008. Impact on groundwater of concurrent leakage and diffusion of dichloromethane through geomembranes in landfill liners. *Geosynthetics International* **15**(1):55-71.

El-Zein, A., McCarroll, I., Touze-Foltz, N., 2012. Three-dimensional finite-element analyses of seepage and contaminant transport through composite geosynthetics clay liners with multiple defects. *Geotextiles and Geomembranes* **33**:34-42.

El-Zein A and Balaam N. 2012. Saturated-unsaturated flow and solute transport in engineered liner systems: a new special-purpose finite-element analysis software. *Australian Geomechanics Journal*, **47**(3):11-126.

Foose JG, Benson CH, Tunser BE. 2002. Comparison of solute transport in 3 composite liners. *Journal of Geotechnical and Geoenvironmental Engineering* **128**(5):391-403.

Kandris K. and Pantazidou M. 2012. Landfill Base Liners: Assessment of Material Equivalency and Impact to Groundwater. *Geotechnical and Geological Engineering* **30**:27-44.

Nosko, V., Touze-Foltz, N., 2000. Geomembrane liner failure: modelling of its influence on contaminant transfer. *Proceedings Eurogeo 2, Second Eare uropean Conference on Geosynthetics*, Bologna, Italia, 15-18 October 2000, 557-560.

Pelte, T., Pierson, P., Gourc, J.P., 1994. Thermal analysis of geomembrane exposed to solar radiation. *Geosynthetics* International **1**:21-44.

Rowe, R.K., Quigley, R.M., Brachman, R.W.I., Booker, J.R., 2004. *Barrier Systems for Waste Disposal Facilities*. Spon Press, London and New York, 587 pages.

Rowe, R.K., 2005. Long term performance of contaminant barrier systems. *Géotechnique* **9**:631-678.

Shackelford, C. D., and Daniel, D. E. (1991). Diffusion in saturated soil: I. Background. *Journal of Geotechnical Engineering*, ASCE, 117(3), 467-484.

Touze-Foltz, N., Schmittbuhl, J., Memier, M., 2001. Geometric and spatial parameters of geomembrane wrinkles on large scale model tests. *Geosynthetics Conference 2001*, Portland, USA, 715-728.

Touze-Foltz, N., Barroso, M., 2006. Empirical equations for calculating the rate of liquid flow through geosynthetic clay liners–geomembrane composite liners. Geosynthetics International, 13(2), 73-82.

MODELLING OF SAND COLUMN COLLAPSE WITH MATERIAL POINT METHOD

W.T. Sołowski
ARC Centre of Excellence for Geotechnical Science and Engineering, Department of Civil Surveying and Environmental Engineering, Newcastle University, Callaghan, NSW, Australia

S.W. Sloan
ARC Centre of Excellence for Geotechnical Science and Engineering, Department of Civil Surveying and Environmental Engineering, Newcastle University, Callaghan, NSW, Australia

ABSTRACT: *The paper shows numerical analysis of sand column collapse. The simulation was performed with the material point method and the results are compared to experiment. The problem considered involves extreme deformations and is difficult to model with more traditional numerical approaches like the finite element method.*
In the analysis, the sand is modelled with a rate-independent Mohr-Coulomb model. Despite the use of a simple constitutive model, the computed results agree with the experimental observations reasonably well. This agreement is satisfactory both during and after the collapse.

1 INTRODUCTION

The paper models the collapse of a sand pile using the material point method. The analysis aims to reproduce the experimental results of Lube et al. (2007).
The material point method is an extension of the FLIP method (Brackbill & Ruppel 1986), and was first developed by Sulsky *et al.* (1994). In the method, the material points contain all the information required for the calculations, and the problem is solved in an explicit manner. In each time step, the information stored in the material points is transferred to the grid nodes. After solution on the grid, the updated information is returned to the material points, where some additional updates may occur.
The generalised interpolation material point method (GIMP) was introduced by Bardenhagen & Kober (2004). In GIMP, unlike in the original formulation of Sulsky *et al.* (1994), material points are not just points in space; they have a fixed domain instead (see Figure 1). This corresponds to a fixed grid shape function for all the particles.

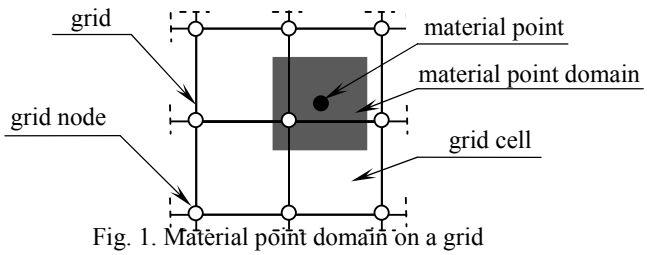

Fig. 1. Material point domain on a grid

As the particle domain (or the grid shape function) is fixed, the material points can still separate from each other once the material deformation is large enough. As the material points interact through the grid nodes, material separation occurs when no part of the two

neighbouring material point domains contribute to a common node. This usually undesirable behaviour is greatly reduced when compared to the original material point method formulation. The more advanced versions of the material point method (e.g. Ma *et al*. 2006, Sadeghirad *et al*. 2011) aim to remove the possibility of material separation. The computational cost, however, may be significant. Moreover, due to an increase in their complexity, these more advanced methods may be less robust numerically.

The material point method is particularly suited to problems with very large deformations. That is why it has been chosen for simulation of sand pile collapse. Such a problem would be difficult to solve using a traditional finite element method.

2 SAND COLUMN COLLAPSE EXPERIMENT

The sand pile collapse experiment by Lube et al. (2007) is shown in Figure 2. It consists of a 20 cm deep channel, the release system (adjustable for different column widths) and a table on which the sand can spread after the mechanism is released.

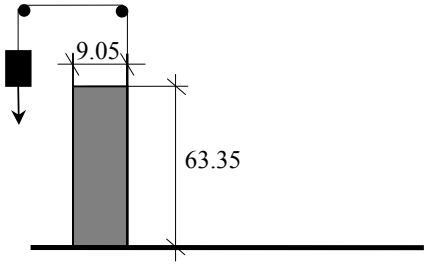

Fig. 2. Experimental setup (after Lube et al. 2005). Falling weight lifts the front gate and releases the sand.

The results of the experiment were filmed through a transparent side of the channel. The particular experiment modelled was performed with a column of initial width equal to 9.05 cm and height 63.35 cm. This experiment was chosen as it is the only one for which evolution of the column free surface during the experiment was given.

The free surface evolution of the collapsing sand pile is shown in Figure 3. These results were obtained by filming the experiment with a high speed camera (120 frames/s). Every fifth frame was taken, leading to a time difference between the lines in Figure 3 of approximately 0.0417s. Note that the initial time t_0 is not related to the moment the experiment began, but rather some later moment after releasing the sand.

3 NUMERICAL ANALYSIS

The experiment was modelled with the GIMP version of the material point method using a modified version of the Uintah software developed at the University of Utah. The grid and the initial position of the material points are given in Fig 1. The dimensions of the column were exactly the same as in the experimental setup, i.e. 633.5 x 90.5 mm. The grid cell size was set to 5 mm. In each cell, nine (3x3) material points were placed, so that the simulation was made with a total of 25,920 material points.

The sand was modelled as a Mohr-Coulomb material. This model was implemented using the procedure of Clausen et al. (2006, 2007), which ensures that the stresses are integrated accurately.

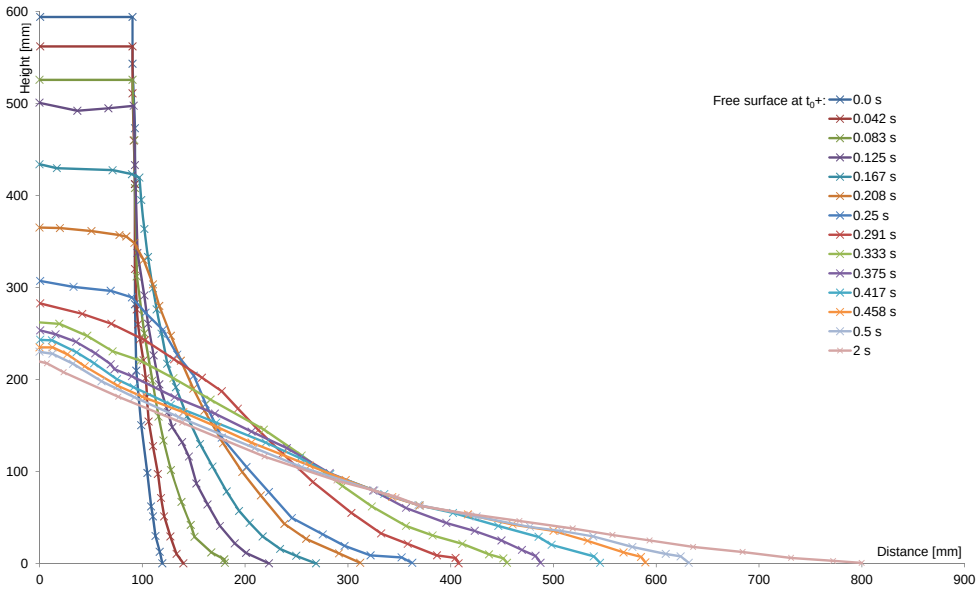

Fig. 3. Evolution of the free surface of the collapsing sand column in time. Data digitised from Lube et al. 2007 (crosses indicates the points where data was taken).

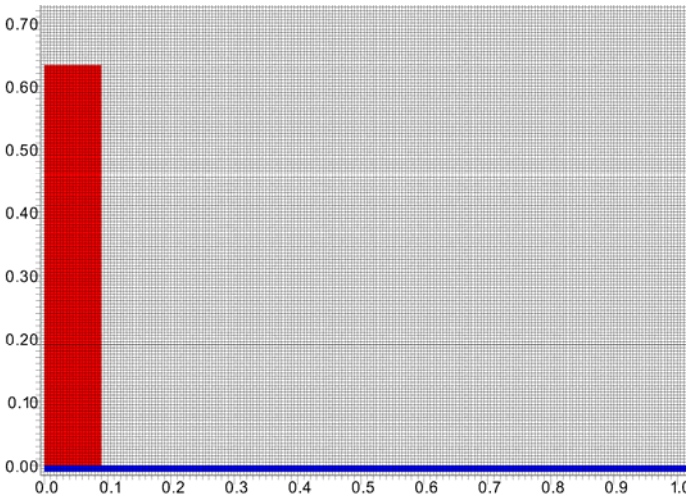

Fig. 4. Material point grid and initial material point setup.

The sand used in the experiment was an industrial sand with a grain-size of 1.4±0.4 mm. Unfortunately, Lube et al. (2007) does not provide much more information on the properties of the sand used. Therefore, the friction angle was approximated by the angle of repose while typical values were assumed for the dilation angle, the elastic properties and the density (see Table 1)

Table 1: Material parameters for sand (Mohr – Coulomb model)

Shear modulus [MPa]	Bulk modulus [MPa]	Cohesion [kPa]	Friction angle [deg]	Dilation angle [deg]	Density [kg/m^3]
0.323	0.7	0	31	1	2650

The release mechanism used in the experiment was not modelled, since little information was given on it. Consequently, modelling the frictional contact between the gate and the sand pile would thus have been rather arbitrary. Moreover, the computational resources needed for modelling the release mechanism accurately would be significant. Instead of modelling the release mechanism, the sand is assumed to be released fully at the beginning of the analysis (i.e. at time zero). This will cause some discrepancies between the experimental observations and the predictions in the first few tenths of seconds of the sand pile collapse (as the release takes around 0.08s).

Lube et al. (2005) (where more details on the test setup is given) suggested that the roughness of the table surface on which the sand spreads has a negligible effect on the experiment results. This can be explained by the fact that the majority of the actual flow generally occurs over the sand already deposited. Therefore rough contact, inherent in the material point method, was used in the analysis.

4 RESULTS

The numerical analysis aimed to replicate the experimental results over the full range of movement, up to an including the final state. However, as the initial data were disturbed by the releasing mechanism, only the data from t_0+0.125s are compared. The correlation between the time counted from the beginning of the numerical analysis and time from the experiment is given in Table 2. As such, the earliest compared experimental result (from t_0+0.125s) corresponds to 0.17s of the performed analysis (see Fig 5 left). Further results are given in Figures 7-10. In these figures, the material points are coloured according to their initial position.

Table 2: Correlation between time in the numerical analysis and experiment

Analysis [s]	0.17	0.21	0.25	0.29	0.33	0.37	0.41	0.46	0.5	0.54	2.0
Experiment t_0+… [s]	0.125	0.167	0.208	0.25	0.291	0.333	0.375	0.417	0.458	0.5	2.0

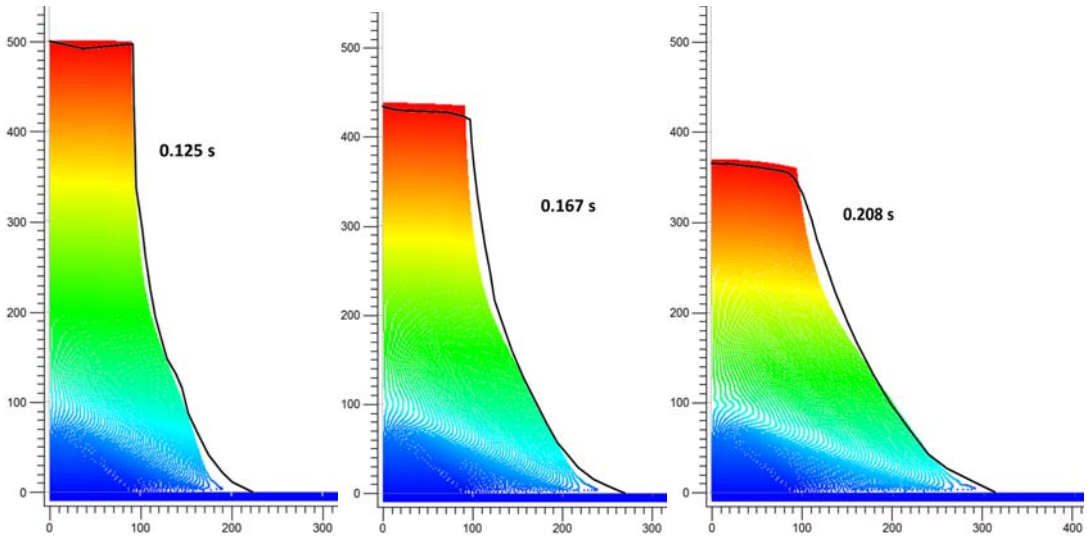

Fig. 5. Comparison of simulation with the experimental results at t_0+0.125 to t_0+0.208 s.

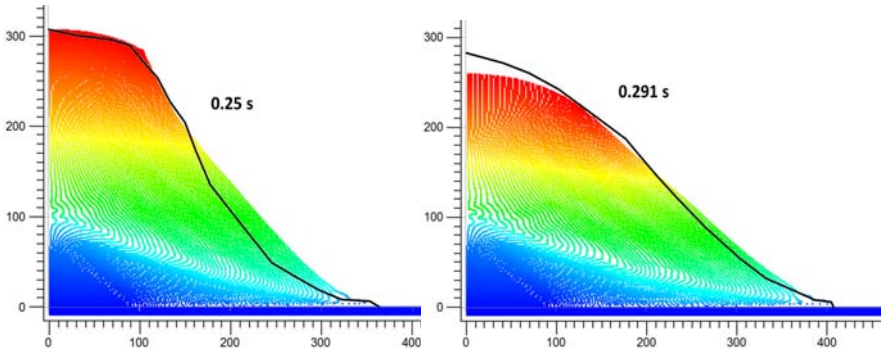

Fig. 6. Comparison of simulation with the experimental results at t0+0.25 to t0+0.291 s.

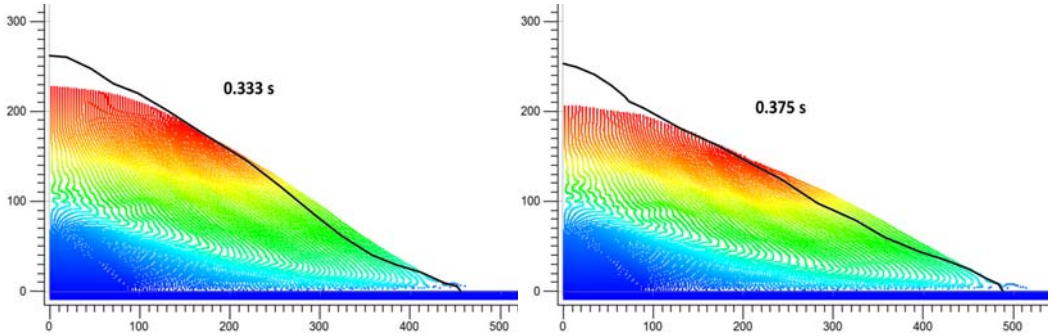

Fig. 7. Comparison of simulation with the experimental results at t_0+0.333 to t_0+0.375 s.

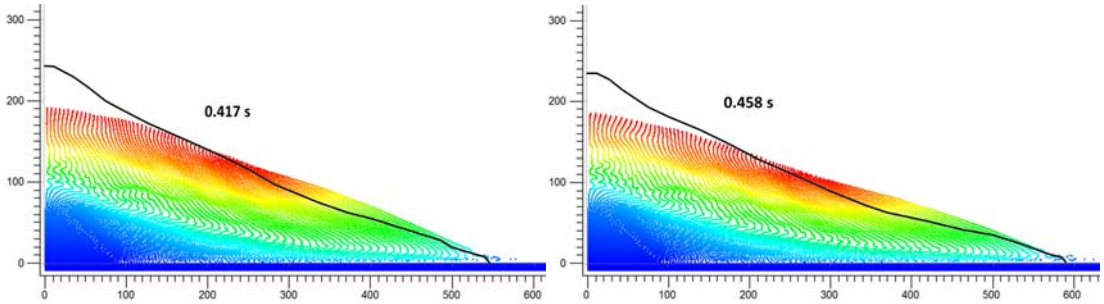

Fig. 8. Comparison of simulation with the experimental results at t_0+0.417 to t_0+0.458 s.

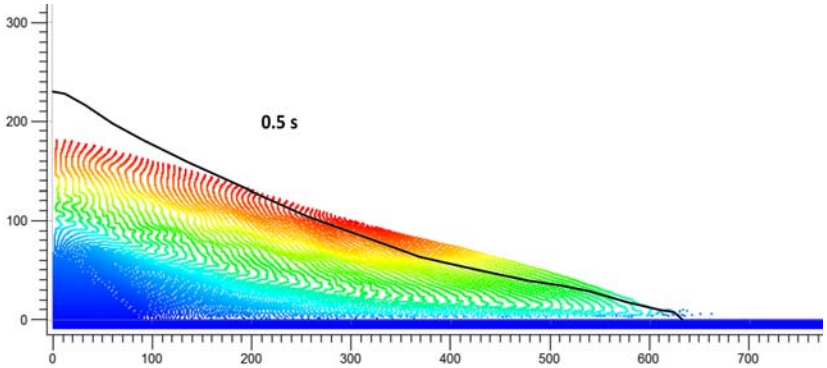

Fig. 9. Comparison of simulation with the experimental results at t_0+0.5 s.

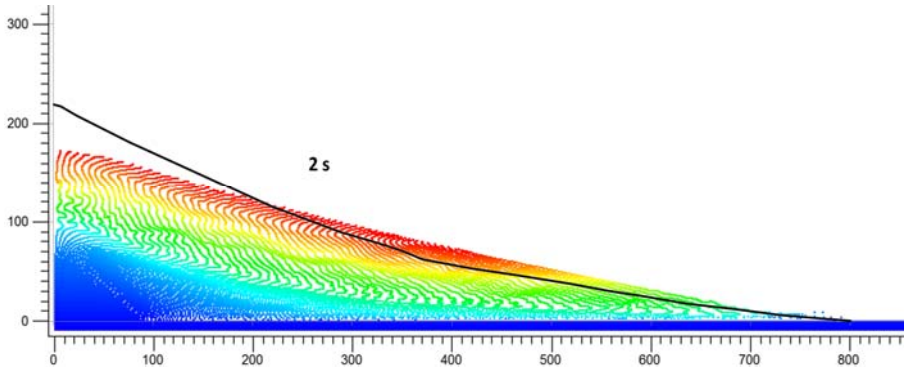

Fig. 10. Comparison of final simulation results with the experiment.

.

These results indicate a relatively good agreement between theory and experiment. To achieve this good agreement, some additional numerical dissipation was needed in the analysis. This numerical dissipation replicates the loss of energy of the sand upon moving without any change in strain. Such energy loss is observed in reality and is mostly a result of friction when the sand grains rotate during movement.

To compare, some results computed without additional numerical dissipation are shown in Figures 11-13. It can be noted that initially the results are remarkably similar, but at the end of the simulation where no additional dissipation was used, the predicted granular deformation spreads much further than that which is observed in the experiment.

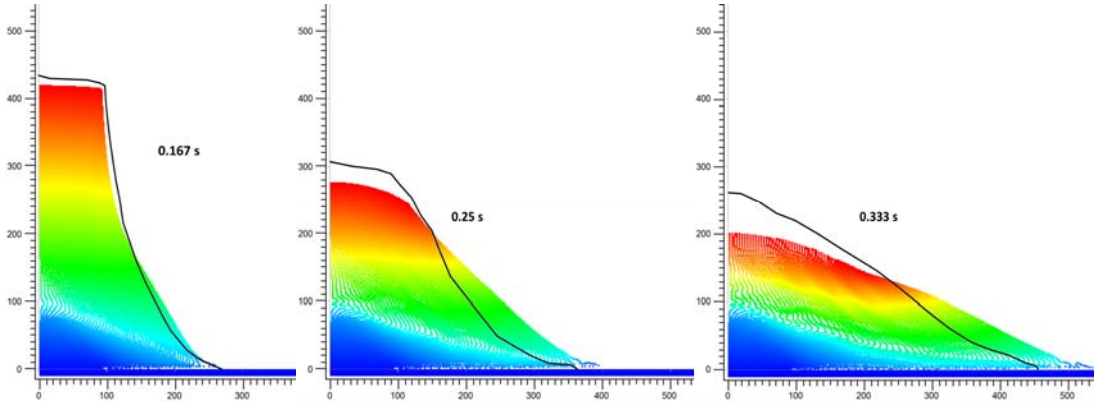

Fig. 11. Comparison of simulation with the experimental results at t_0+0.167 to t_0+0.333 s. No numerical dissipation used.

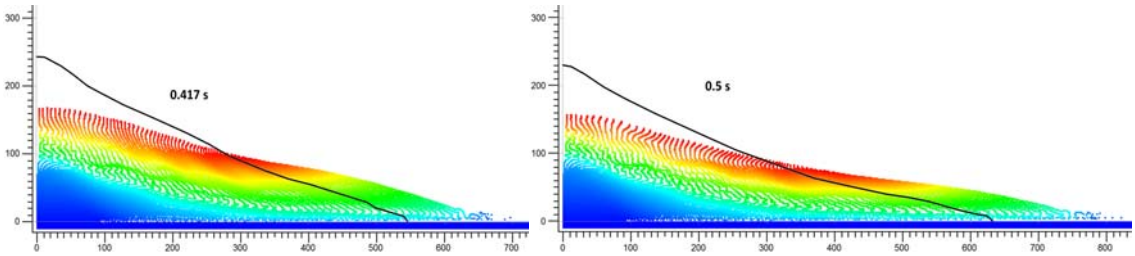

Fig. 12. Comparison of simulation with the experimental results at t_0+0.417 to t_0+0.5 s. No numerical dissipation used.

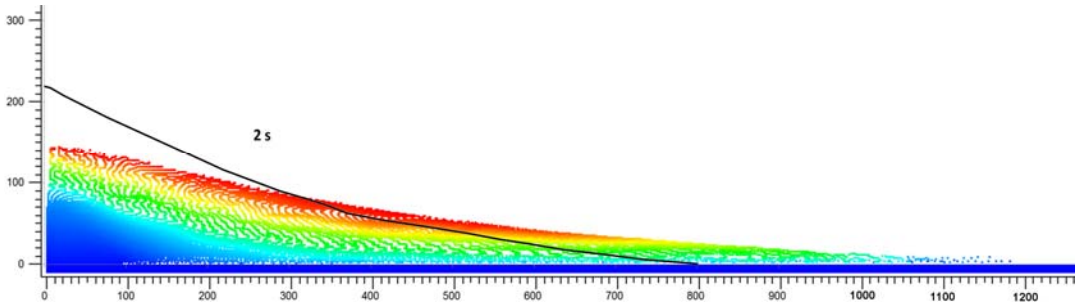

Fig. 13. Comparison of final results of simulation with the experimental results. No numerical dissipation used.

During the calculations, some mesh dependency is expected as certain material points separate. For example, the material points at the tip of the collapsing pile (Figures 7-10) seem to have lost connection with their initial neighbours. It appears that these points were initially close to the bottom of the sand pile (thus their blue colour), but during collapse they were pushed out and stayed at the front of the sand mass. The final result of the simulation with a coarser mesh (150x75) is shown in Figure 14.

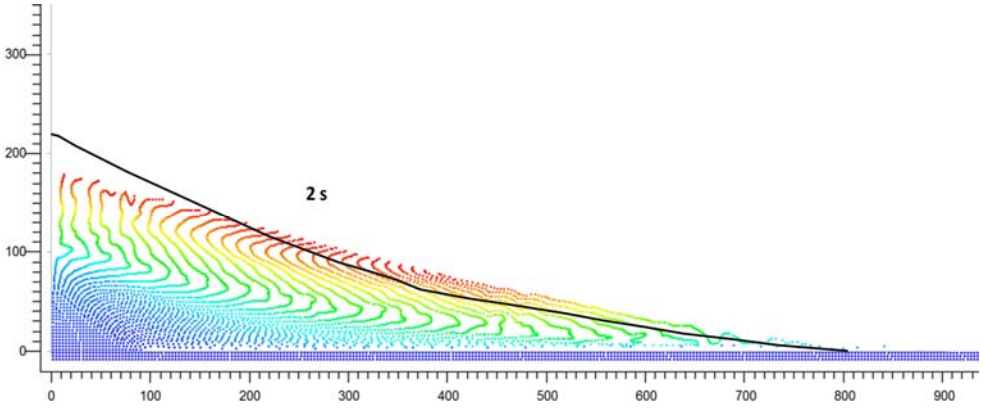

Fig. 14. Comparison of final results of simulation with the experimental results. Results obtained with numerical dissipation and coarser grid (150x75).

To further improve the results, a more advanced constitutive model could be used instead of the classical Mohr-Coulomb model. The Mohr-Coulomb model is a simple one which does not capture some of the more complex facets of sand behaviour (like rate dependency). Still, the predictions agree with the experimental data reasonably well, especially taking into account how simple it is to calibrate the constitutive model used.

5 CONCLUSIONS

The paper shows a material point method simulation of a sand pile collapse. The results obtained are compared to the experimental results of Lube et al. (2005), with show a satisfactory agreement. The calculations were made to confirm the ability of the material point method to model granular media, thus validating its applicability in geomechanics. The material point method appears to be very capable in such problems where extreme deformations and dynamic behaviour are encountered. The simulation proved to be relatively robust and few numerical issues were experienced. In contrast, to solve this problem with the finite element method, very advanced techniques would have to be used and many numerical problems could occur.

6 ACKNOWLEDGEMENTS

This research was supported by the ARC Centre of Excellence for Geotechnical Science and Engineering, headquartered at the University of Newcastle, Australia. The computations were partially undertaken at the NCI National Facility in Canberra, Australia, which is supported by the Australian Commonwealth Government. These computational resources were provided by Intersect Australia Ltd.

REFERENCES

Bardenhagen, S.G. & Kober, E.M. (2004), "The Generalized Interpolation Material Point Method". Computer Modeling in Engineering & Sciences Vol. 5(6):477-495.

Brackbill, J.U. & Ruppel, H.M. (1986), "FLIP: a method for adaptively zoned, particle-in-cell calculations of fluid flows in two dimensions". Journal of Computational Physics Vol 65:314-346.

Clausen, J., Damkilde, L. & Andersen, L. (2006), "Efficient return algorithms for associated plasticity with multiple yield planes". Int. J. Numer. Meth. Engng. Vol. 66:1036–1059.

Clausen, J., Damkilde, L. & Andersen, L. (2007), "An efficient return algorithm for non-associated plasticity". Computers and Structures Vol. 85:1795–1807.

Lube, G, Huppert, H.E., Sparks, R.S.J. & Freundt A. (2005), "Collapses of two-dimensional granular columns". Physical Review E. Vol. 72, 041301.

Lube, G, Huppert, H.E., Sparks, R.S.J. & Freundt A. (2007), "Static and flowing regions in granular collapses down channels". Physics of Fluids Vol. 19, 043301.

Ma J., Lu H. & Komanduri R. (2006), "Structured mesh refinement in generalized interpolation material point method (GIMP) for simulation of dynamic problems". Computer Modeling in Engineering and Sciences Vol. 12:213–227.

Sadeghirad A., Brannon R.M. & Burghard J. (2011), "A convected particle domain interpolation technique to extend applicability of the material point method for problems involving massive deformations". Int. J. Num. Meth. Engn. Vol. 86:1435-1456.

NUMERICAL MODELING OF GAS FRACTURING WITH THE EXTENDED FINITE ELEMENT METHOD

M. Goodarzi
Department of Civil Engineering, Newcastle University, Newcastle Upon Tyne, United Kingdom

E. F. Salmi
Department of Civil Engineering, University of Newcastle, Newcastle, Australia

S. Mohammadi
Department of Civil Engineering, University of Tehran, Tehran, Iran

A. Jafari
Department of Mining Engineering, University of Tehran, Tehran, Iran

ABSTRACT: *In this paper, the fractures propagation around a pressurized hole was simulated as a quasi-static phenomenon. The gas flow through the cracks has been assumed as a one-dimensional transient flow, the equations of which are governed by conservation of mass and momentum. The fractured media was modeled with the extended finite element method, and stress intensity factor was calculated by using displacement extrapolation method which is simple but sufficiently accurate. To evaluate the proposed algorithm, two field tests were simulated; the unknown parameters have been determined through calibration. By considering the high level of uncertainties in these types of engineering problems, the obtained results are satisfactory. Sensitivity analyses were performed to find out the effective parameters on the simulation results. Numerical findings indicate that in the process of blasting which consists of two subsequent stages of the action of shock wave and gas pressurization, the second stage is the crucial item on crack propagation.*

1 INTRODUCTION

High Energy Gas Fracturing (HEGF) is a technique to stimulate wellbores by producing several radial cracks around the hole. The cracks are normally generated by high pressure gas produced by burning a propellant. In addition, this method has been successfully used in other application such as enhancing the injectivity of gas-injection wells (Salazar et al., 2002), pre-fracturing before hydraulic fracturing to reduce the friction pressure losses in the near wellbore (Jaimes et al., 2012), stimulating geothermal wells. Simplicity of its procedure and low cost of this approach can be mentioned as its advantages.

In HEGF, the aim is to extend cracks without causing considerable damage to the wellbore wall. In a conventional blasting process, there are two major causes which contribute to the crack propagation and rock fragmentation, shock wave and gas pressure. The role of shock wave is to create initial cracks and the gas pressure leads to their propagations. In fact, the shock wave can only generate some cracks and crush the surrounding rock near the borehole while the length of these initial cracks would not exceed more than several hole diameters (Kutter & Fairhurst, 1971). According to some field and laboratory experiments, McHug (1983) concluded that the effects of gas pressure may be more noticeable than the effects of shock wave. This result was admitted by others as well (Daehnke et al., 1997).

Although so far numerous attempts have been devoted on the simulation of the mechanism of dynamic rock breakage and fragmentation, because of the complicated nature of this phenomenon, none of them could capture all the aspects of this process well. Therefore, still simplification of this problem into different stages of the action of the blast load is the only

method for analyzing the problem. Since the main aim of this paper is to investigate the effects of gas pressurization on the extension of the pre-existed cracks which are caused by shock wave, only those literature related to gas fracturing are going to be reviewed. Nilson et al. (1985) developed precise equations of gas penetrating through a crack based on conservation of mass and momentum. The equations were solved numerically, and analytical solutions were proposed for crack propagation. Munjiza et al. (2000) suggested a simple model for evaluation of the gas pressure through the cracks. Gas pressure was only considered in a specific area around the source, and the combined finite/discrete element method was used for the analysis of the solid part. The Nilson's equations were implemented by Cho et al. (2004), to investigate the dynamic fracture process of rock. A dynamic FEM code equipped with re-meshing algorithm was used to consider crack growth, and gas pressure was estimated as a one dimensional flow through cracks. Mohammadi & Bebamzadeh (2005) also proposed an approach to model gas-solid interaction. This model used two separate but coupled meshes for the analysis of solid and gas phases based on mechanics of porous media.

Similar to blasting, gas fracturing also has two stages; rapid rising of gas pressure which causes some cracking around the hole and the gas penetration which leads to crack's extension. In this paper, the second stage of gas fracturing, gas penetration into pre-existing cracks is analyzed. This process can be considered as a quasi-static phenomenon that allows using static algorithm (Paine & Please, 1994; Nilson et al., 1985).

For simulation of the solid media, the Extended Finite Element Method (XFEM) was implemented. This method simulates cracks independent of mesh generation, thus it avoids the time-consuming and technically difficult re-meshing algorithm. To consider the gas flow through the fractures, a one-dimensional transient flow governed by conservation of mass and momentum (Nilson et al., 1983 &1985) which was verified by lab tests (Cho et al., 2003) was implemented. These equations were solved with the explicit finite difference method (FDM). In each time step, the geometrical parameters of the fractures are given to the FDM code, and the gas pressure along the crack is taken back and applied as the boundary conditions on the solid medium.

Moreover, after introducing the gas flow and XFEM equations, the provided XFEM code was validated. The proposed algorithm was evaluated by simulating two field experiments of gas fracturing. A comprehensive sensitivity analyses were carried out to observe the effect of each parameter.

2 NUMERICAL MODELING OF GAS FLOW

Due to the action of shock wave a small zone with lots of cracks is generated around the blast-hole, while a few of these cracks can finally surpass others and extend; the other ones are halted. Experimental investigations also showed that the number of major cracks around a blast-hole is between 3 to 8 (Garnsworthy, 1990).

Accordingly, in this research the gas flow is only considered in those surpassing fractures. The gas penetration through the cracks is assumed to be a one-dimensional transient flow. Moreover, because of the insignificant loss of mass and heat into the surrounding rock, it is reasonable to presume that gas expansion is an adiabatic process, and the rock is impermeable (Nilson et al., 1985; Hustrulid, 1999).

The one-dimensional equations of gas flow governed by the laws of conservation of mass and momentum can be written as:

$$\frac{\partial(\rho h)}{\partial t} + \frac{\partial(\rho v h)}{\partial x} = 0 \tag{1}$$

$$\rho h\left(\frac{1}{\rho}\frac{\partial P}{\partial x}+\psi\right)=0 \tag{2}$$

where ρ is the density, v is the velocity, P is the gas pressure, and ψ is the viscous shear stress which can be approximated from Eq. (3a) and (3b) for laminar and turbulent flow, respectively (Pine & Please, 1994).

$$\psi=\frac{12\mu v}{\rho h^2} \tag{3a}$$

$$\psi=a\left(\frac{\varepsilon}{h}\right)^b\frac{v^2}{h} \tag{3b}$$

where μ is the viscosity of fluid, h is the aperture of fracture, and based on the experimental results $a=0.1$ and $b=0.5$ (Nilson et al., 1985). For the friction factor $f_t=a(\varepsilon/h)^b$, Eq. (3) can be rewritten as:

$$v=\frac{h^2}{12\mu}\left(-\frac{\partial P}{\partial x}\right) \tag{4a}$$

$$v=\sqrt{\frac{h}{f_t\rho}\left(-\frac{\partial P}{\partial x}\right)} \tag{4a}$$

Cho et al. (2004) showed that turbulent gas flow through the fracture is much more reasonable, Therefore Eq. (4b) was chosen for the rest of this study. By substituting Eq. (4b) into Eq. (1) and discretizing it on the mesh shown in Fig. 1, we have:

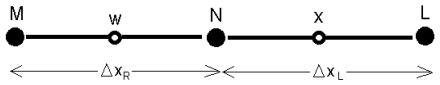

Fig. 1. The Finite Difference mesh, *w* and *x* are in the middle of the elements.

$$\rho_N^{t+\Delta t}-\rho_N^t=-\frac{4\Delta t}{(\Delta x_R+\Delta x_L)(h_w+h_x)}\left(h_x\sqrt{-\rho^t{}_x\frac{h_x}{f}\frac{(P^t{}_L-P^t{}_N)}{\Delta x}}-h_w\sqrt{-\rho^t{}_w\frac{h_w}{f}\frac{(P^t{}_N-P^t{}_M)}{\Delta x}}\right) \tag{5}$$

where h is a constant input data along an element, and the density of elements are calculated as the average of the densities of their nodes.

To estimate the detonation gas pressure along the fractures, an equation of state should be used. The equation of state of an ideal gas is used for this purpose (Eq. (6)).

$$P=P_0\left(\frac{\rho}{\rho_0}\right)^\gamma \tag{6}$$

where P_0 and ρ_0 are the initial pressure and density of the gas, P and ρ are the current ones and γ is the coefficient of the ideal gas. Capability of these equations to simulate gas pressure inside cracks was evaluated by comparing their results with some experiments (Cho et al., 2002).

3 EXTENDED FINITE ELEMENT EMTHOD

The Finite Element Method is one of the powerful methods in engineering analyses, frequently used to model cracks in solid medium. One of the main approaches of FEM is to use an adaptive mesh for simulating cracks physically. This re-meshing process is technically difficult and time-consuming. The Extended Finite Element Method simulates the cracks by enriching the shape functions of the elements which are involved with cracks. In this way, after each step of crack propagation, there is no need to change the initial mesh, and just the new involved elements should be detected for proper enrichments.

There are two types of enrichments for cracked elements. When an element takes part in crack simulation, its displacement approximation can be defined as (Mohammadi, 2008):

$$u^h(x) = \sum_{j=1}^{n} N_j(x)u_j + \sum_{h=1}^{m} N_h(x)H(\xi(x))a_h + \sum_{k=1}^{mt} N_k(x)\left(\sum_{l=1}^{mf} F_l(x)b_k^l\right) \tag{7}$$

in which n is the number of the nodes of the element, m is the number of nodes which are involved with the crack length, mt is the number of nodes being related to the crack tip, mf is the number of functions that are used for enriching the crack tip element, and a and b are the additional degrees of freedom. N is the usual shape functions of FEM, H is the Heaviside function, and F is a set of functions which are obtained from analytical solution of displacement around a crack tip.

$$F_\alpha(r,\theta) = \left\{\sqrt{r}\sin\frac{\theta}{2}, \sqrt{r}\cos\frac{\theta}{2}, \sqrt{r}\sin\theta\sin\frac{\theta}{2}, \sqrt{r}\sin\theta\cos\frac{\theta}{2}\right\} \tag{8}$$

The suitable enrichments of nodes according to the crack position are shown in Fig. 2.

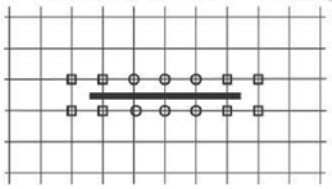

Fig. 2. The squares show the crack tip enrichment, and the circles are related to Heaviside enrichment.

Because of those additional degrees of freedom, the common FEM formulation should be updated. If the cracked solid, shown in Fig. 3, is assumed, the unknown vectors u, the global stiffness matrix K, and the external force vector f in Eq. (9), will change to (QingWen et al., 2008):

$$u = Kf \tag{9}$$

$$u = \left\{u_j, a_h, b_k^1, b_k^2, b_k^3, b_k^4\right\} \tag{10}$$

$$k_{ij}^e = \begin{bmatrix} k_{ij}^{uu} & k_{ij}^{ua} & k_{ij}^{ub} \\ k_{ij}^{au} & k_{ij}^{aa} & k_{ij}^{ab} \\ k_{ij}^{bu} & k_{ij}^{ba} & k_{ij}^{bb} \end{bmatrix} \tag{11}$$

$$f_i^e = \left\{f_i^u, f_i^a, f_i^{b1}, f_i^{b2}, f_i^{b3}, f_i^{b4}\right\} \tag{12}$$

$$k_i^e = \int_{\Omega^e} \left(B_i^e\right)^T DB_j^s d\Omega \quad (r,s = u,a,b) \tag{13}$$

$$f_i^u = \int_\Omega N_i b d\Omega + \int_{L_F} N_i t d\Gamma \tag{14}$$

$$f_i^a = \int_\Omega N_i H b d\Omega + \int_{L_F} N_i H t d\Gamma + 2\int_{L_c} n.N_i p d\Gamma \tag{15}$$

$$f_i^{b_l} = \int_{\Omega} N_i F_l b d\Omega + \int_{L_F} N_i F_l t d\Gamma + 2\int_{L_c} n\sqrt{r}.N_i p d\Gamma \ (l = 1-4) \tag{16}$$

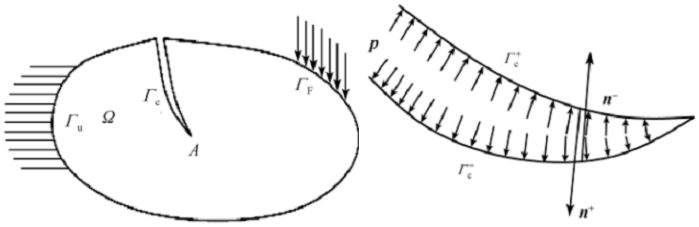

Fig. 3. A cracked solid (left) and details of the crack (right) (QingWen et al., 2008).

4 COUPLING PROCESS AND CRACK PROPAGATION

In each step, the equations of gas and solid phase are solved separately and the obtained data are exchanged between them. At first, an initial length should be assumed for the cracks as a result of the action of the shock wave, which is not considered in this paper directly. This initial length can also be estimated based on rock blasting literatures (Hustrulid, 1999). The initial FDM mesh is generated on the existing cracks and the gas flow algorithm is performed for a small time-span which is called time-step here. Then, the calculated gas pressure is applied as boundary conditions into the XFEM code. The new cracks length and the cracks opening displacement (COD) along them are imported to the gas algorithm for the next step of calculation.

A criterion is also required for crack propagation. The stress intensity factor is implemented, and compared with the critical value in each step. There are several methods for numerical calculation of SIF, but inasmuch as it is not necessary to be highly accurate, the simple thought sufficiently accurate displacement extrapolation method is adopted.

Following a linear elastic analysis, the stress intensity factors are determined by equating the numerically obtained displacements with their analytical expressions in terms of the SIF. Such a correlation is performed along a radial line emanating from the crack tip (Saouma, 2000). In addition, the crack propagation is assumed to be under pure Mode I.

As the problem is solved in a quasi-static condition, cracks propagate equal to a specific value when the criterion is satisfied. In the other word, a velocity is assumed for the crack propagation, and the specific value of propagation for each step is equal to this velocity times the time-step.

5 NUMERICAL RESULTS

5.1 Loading on Crack Surface

To verify the accuracy of the present XFEM code, the results are compared with the available analytical solution. A pressurized hole with two radiating cracks in an infinite plate has a closed-form solution for stress intensity factor presented in Eq. (17).

$$K = \beta P\sqrt{\pi a} \tag{17}$$

where β is a coefficient which is related to the ratio of the distance of the crack tip from the center of the hole to the hole radius. A hole with 5 cm radius and a 15 cm radiating crack is considered, the ratio mentioned above is 4, thus β would be 0.9976 (Saouma, 2000). A

uniform pressure equals to 1 MPa is applied inside the hole and the cracks. Based on the closed form solution, the stress intensity factor for this problem is $7.9076*10^6$.

This example is simulated with the provided code; to reduce the amount of calculation, only half of the model is considered. Fig. 4 shows the generated mesh and the enriched nodes around the cracks. The calculated stress intensity factor is $7.6949*10^6$, so the error is around 2.7% which completely acceptable for this study.

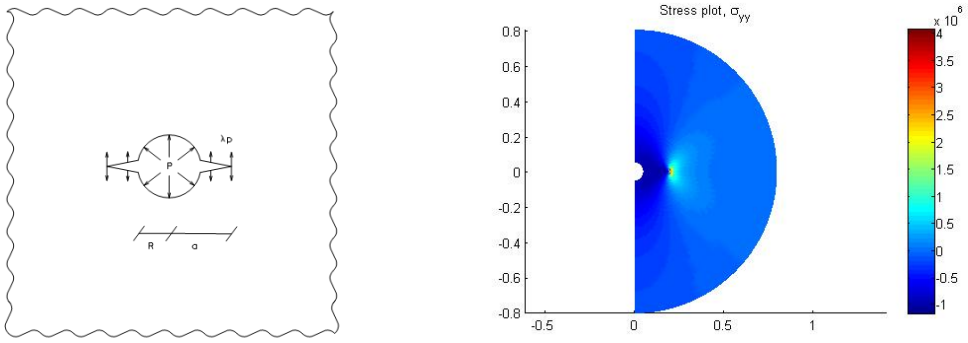

Fig. 4. Geometry (Left), Vertical stress (σ_{yy}) contour (right).

5.1 Gas Fracturing

In order to investigate the capability of the proposed approach to simulate gas-fracturing, the experimental studies conducted by Sandia National laboratory in US were modeled. These experiments were carried out in some deep tunnels excavated in a homogenous Tuff with 10 MPa hydrostatic stresses. Two of these examples were chosen for this study. One of them is a low-power fracturing which produced only two fractures and the other one is a high-energy fracturing with 6 major radiating cracks. The details of experiments and the rock are presented in Table 1 and 2.

Here, the produced gas from propellant burning and its expansion are considered as ideal gas and adiabatic expansion, respectively. In addition, the generated pressure is applied simultaneously. For the first experiment, named D1, aside from the final cracks' lengths and initial conditions, the well-hole pressure is also available. Because this code is not capable of initiating the cracks, some small cracks are assumed around the bore-hole. There are also two unknown parameters in this simulation which should be determined based on calibration, the constant of equation of state (γ) and the crack velocity.

Fig. 5 shows the generated model for this example which contains 3000 nodes. The initial crack length is 2 cm, the time-step for analyzing the solid media is 100 μs and the crack velocity is assumed to be 100 m/s.

According to the observation of this experiment, the average final crack's lengths is equal to 0.7 m, thus the constant of equation of state could be calibrated with this available data. This coefficient for the produced gas in the blast-holes with high temperature and high density is taken in the range of 1.2-3 (Mortazavi & Katsabanis, 2001). By back analyzing, this value for this specific experiment is 1.29 which is in the expected range (Fig. 6). The obtained value for the constant of equation of state might not be exactly equal to the real value because there are too many uncertainties in these types of experiments which are unavoidable.

To understand the effect of other influential parameters, sensitivity analyses should be carried out. The effects of assumed parameters such as the crack velocity, the initial crack length and the time-step were examined. The magnitudes of these parameters were changed

in reasonable ranges and the sensitivity of the final crack length to them was observed. Fig. 7 shows the results of the sensitivity analyses; as it can be seen through these graphs the sensitivity of the final crack length to these parameters is not noticeable.

Table 1. Properties and results of the selected experiments (Nilson et al., 1985).

Experiment Name	GF2	D1
Pressure Peak (MPa) Rise time (msec) Decay time (msec)	 90 0.5 16	 40 3 18
Well-bore Diameter (m)	 0.2	 0.048
Propellant Diameter (m) Density (gr/cm^3) Type	 0.2 0.7 0.5 M5B	 0.04 1 0.5 M5B
Cracks Number Length range (m) Length mean (m)	 7 0.9 – 2.5 1.7	 2 0.4 – 0.9 0.7
Crack Shape 1m	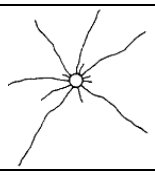	

Table 2. Properties of host rock (Nilson et al., 1985).

Parameters	Values
Toughness (MPa.m0.5)	0.5
Shear Modulus (GPa)	3
Poisson's Ratio	0.3
Crack Roughness (mm)	0.4
Shear Wave Velocity (m/s)	1200

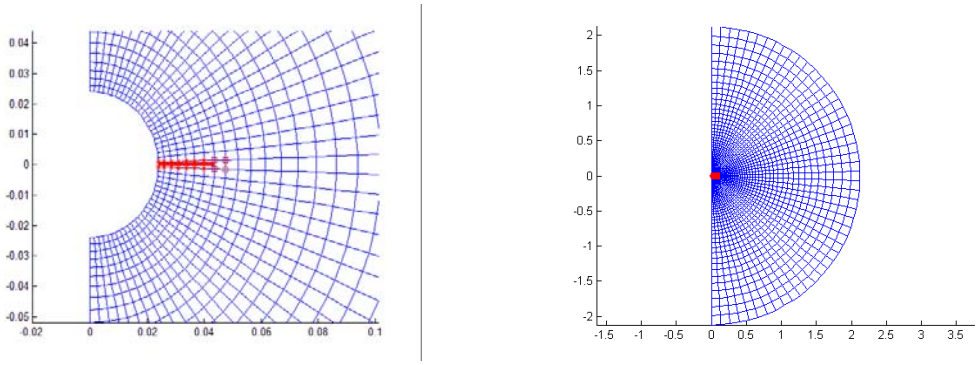

Fig. 5. Initial enriched nodes (left); Generated mesh (right) for D1.

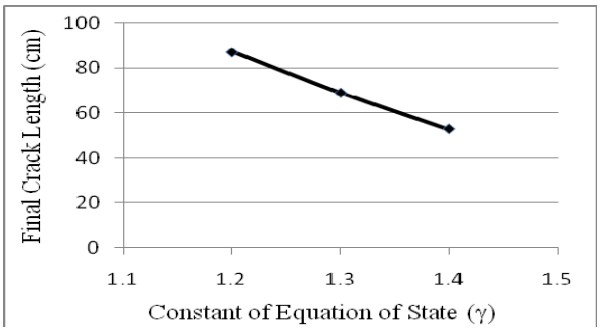

Fig. 6. Calibration of the constant of the equation of state.

Although assumed crack propagation velocity is not influential on the final results, its value should be in an acceptable range. In fact, this investigation helps us to see whether the parameters determined by back analyzing, are reasonable. In dynamic mode the maximum velocity for crack propagation is 50% of Rayleigh speed (which is 600 m/s for this type of rock). In contrast, in hydraulic or gas fracturing, the fluid-dynamic considerations control the speed of the crack growth because the driving pressure cannot push fluid into the narrow crack fast enough, and it becomes slower than the dynamic mode (Nilson et al., 1985). This velocity is changed and its effect is observed on the second field data, borehole pressure. Fig. 8 shows the effect of crack velocity on the borehole pressure decay. It can be concluded that the values of different unknown parameters which were estimated from the field data are within the expected ranges.

The second experiment (GF2) is simulated based on the results obtained from the first experiment (D1) because the host rock and the propellant are the same for both tests. Fig. 9 shows the generated mesh for GF2 experiment which has 2750 nodes. The crack propagation velocity and initial crack length will be assumed 200 m/s and 5 cm which may not be the real values, but their effects are not that significant. After 16 ms the final crack length becomes 2.3 m. The enriched nodes and the contour of tangentional stress, at the end of the test, are plotted in Fig. 10.

The observed difference between the numerical and the experimental result is completely foreseeable, because there are some unavoidable sources that can cause such an error. Firstly, material properties involve with uncertainties, especially toughness which would clearly be very influential in the results. Secondly, due to the short raise time (0.5 ms) in this experiment, some small cracks generated around the hole; a portion of the gas penetrates into these small spaces, and affects the final suppressed cracks length. Generally, Because of the high level of uncertainties, a model that can predict even with 2 times differences is acceptable for practice (Nilson et al., 1985).

6 CONCOLUSIONS

In this paper a simple model is proposed to estimate the results of gas fracturing operation. The gas flow through the cracks was computed with FDM and the XFEM method was implemented to model the fractures in solid media. The proposed equations to calculate gas pressure inside crack have been verified in the literature. The XFEM code was also validated by an analytical solution. Two experimental studies were chosen to calibrate and evaluate the model. Although the simulated results could not be perfectly matched with the experimental study, it is still acceptable for practice because of the high level of uncertainties which are involved in HEGF. In addition, this study shows that the final lengths of the cracks is not dependant on the initial lengths of them which means that in a blasting process, the role of

gas pressure is more important than the role of shock wave on extension of cracks. This was also observed before through some experimental studies.

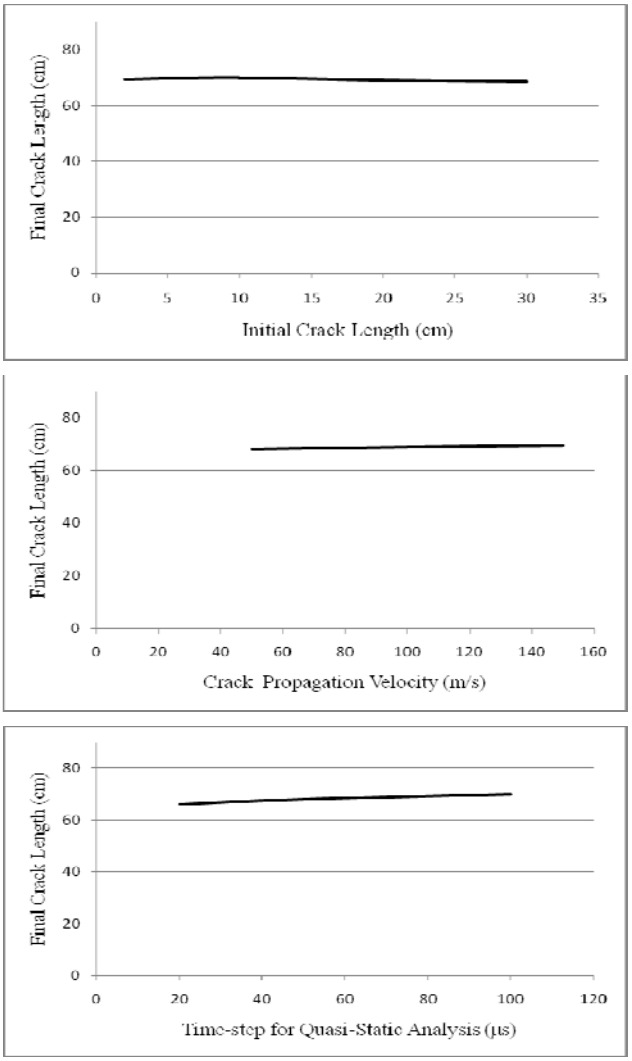

Fig. 7. Sensitivity analyses with respect to final crack length.

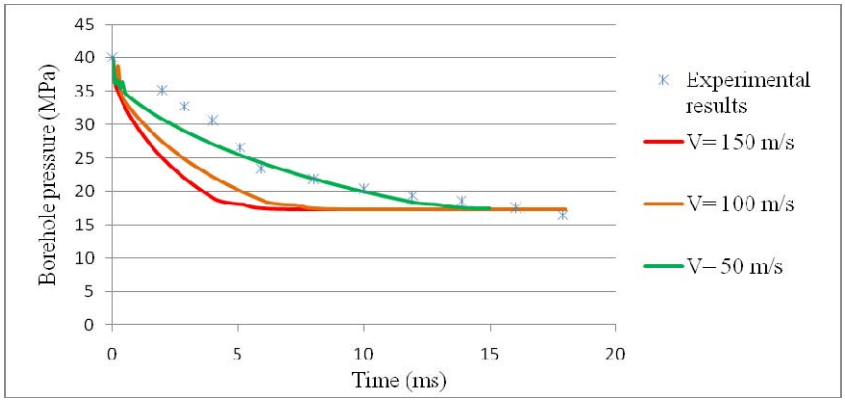

Fig. 8. The effect of crack propagation velocity on the decay of bore-hole pressure.

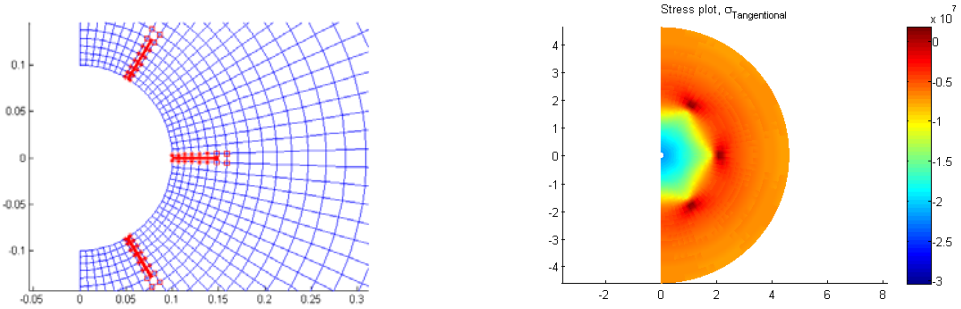

Fig. 10. Initial enriched nodes (Left) and tangentional stress at GF2 model after 16 ms (Right).

REFERENCES

Cho, S.H, Risei, K., Kato, M., Nakamura, Y. & Kaneko, K. (2002), "Development of numerical simulatin method for dyanmic fracture propagation due to gas pressurization and stress wave", Proc. 2002 ISRM Regional Sym.(3nd Korea-Japan Joint Symposium) on Rock Engineering Problem and Approaches in Underground Construction, Jul. 22-24, Seoul, Korea.

Cho, S.H., Nakamura, Y. & Kaneko, K. (2004), "Dynamic fracture process analysis of rock subjected to stress wave and gas pressurization". Int. J. Rock Mech. Min. Sci, Vol. 41(3), 2A 20.

Daehnke, A., Rossmanith, H.P. & Napier, A.L. (1997), "Gas pressurization of blast-induced conical cracks". Int. J. Rock Mechanics and Mining Science, Vol. 34(3), 226-226(1).

Garnsworthy, R.K. (1990), "The mathematical modeling of rock fragmentation by high pressure arc discharges", 3rd Int. Symp. On Rock Frag. Blasting, Brisbane, Australia.

Jaimes, M.G., Castillo, R.D. & Mendoza, S.A. (2012), "High Energy Gas Fracturing: A Technique of Hydraulic Prefracturing To Reduce the Pressure Losses by Friction in the Near Wellbore - A Colombian Field Application", The SPE Latin American and Caribbean Petroleum Engineering Conference held in Mexico City, Mexico, 16–18 April. SPE 152886.

Kutter, H. K. & Fairhurst, C. (1971), "On the fracture process in blasting". Int. J. Rock Mech. Min. Sci., Vol. 8, 181-202.

McHugh, S. (1983), "Crack extension caused by internal gas pressure compared with extension caused by tensile stress", Int. J. of Fracture, Vol. 21, 163-176.

Mohammadi, S. & Bebamzadeh, A. (2005), "A coupled gas-solid interaction model for FE/DE simulation of explosion". Finite element in analysis and design, Vol. 41, 1289-1308.

Mohammadi S. (2008), Extended finite element method for fracture analysis of structure, Blackwell Publishing.

Mortazavi, A. & Katsabanis, P.D. (2001), "Modeling burden size and strata dip efects on the surface blasting process". Int. J. Rock Mech. Min. Sci., Vol. 38, 481-498.

Munjiza, A., Latham, J.P. & Andrews, K.R.F. (2000), "Detonation gas model for combined finite-discrete element simulation of fracture and fragmentation". Int. J. Numer. Meth. Engng., Vol. 49, 1495-1520.

Nilson, R.H. & Griffiths, S.K. (1983), "Numerical analysis of hydraulically-driven fractures". Computer Method in Applied Mechanics and Engineering, Vol. 36, 359-370.

Nilson, R.H., Proffer, W.J. & Duff, R.E. (1985), "Modeling of gas-driven fracture induced by propellant combustion within a borehole". Int. J. Rock Mech. Min. Sci & Geomech., Vol. 22, 1, 3-19.

Paine, A.S. & Please, C.P. (1994), "An improved model of fracture propagation by gas during rock blasting - some analytical results". Int. J. Rock Mech. Min. Sci & Geomech., Vol. 31(6), 699-706.

QingWen, J.L., YuWen, D. & TianTang, Y.U. (2009), "Numerical modeling of concrete hydraulic fracturing with extended finite element method". Science in china series E: Technological science, Vol. 52(3), 559-565.

Saouma, V.E. (2000), Lecture notes in fracture mechanics, Department of Civil Environmental and Architectural Engineering, University of Colorado.

Salazar, A., Almanza, E. & Folse, K. (2002), "Application of propellant high-energy gas fracturing in gas-injector wells at El Furrial field in Northern Monagas State – Venezuela", The SPE international syposium and exhibition on formation damage control, Lafayette, Louisiana, 20-21 Feb. SPE 73756.

Hustrulid, W. (1999), Blasting Principles for Open Pit Mining- Volume 2-Theoritical Foundations, A. A. Balkema/ Roterdam/ Brookfield.

MODELING THE TWO-DIMENSIONAL FAILURE OF DRY-STONE RETAINING WALL

James OETOMO
Université de Lyon, LTDS, CNRS-UMR 5513, Ecole Centrale de Lyon, Ecully, France

Eric VINCENS
Université de Lyon, LTDS, CNRS-UMR 5513, Ecole Centrale de Lyon, Ecully, France

Fabian DEDECKER
ITASCA SAS, Ecully, France

Jean-Claude MOREL
Université de Lyon, LTDS, CNRS-UMR 5513, ENTPE, Vaux en Velin, France

ABSTRACT: *The development of reinforced concrete early in the XXth century has revolutionized the civil engineering practice and progressively led to the disappearance of the use of dry stone retaining walls (DSRW) for slope reinforcement. Nevertheless these structures present significant advantages such as deformability, natural drainage and lesser grey energy requirement for their construction. The lack of regulation for this kind of construction has also led the local authorities to discard technological solutions for the rehabilitation of damaged DSRW. Over the few decades extensive research has also been conducted to improve the understanding of their behaviour. In this work, we focus on the planar failure of DSRW due to an excessive pressure from backfill. A Discrete Element Method is used for the modelling of the entire soil-wall system. The objective is to find both the water and backfill critical height and corresponding failure mode that were previously obtained throughout several full scale experiments involving various types of block material for the wall, i.e. limestone and schist.*

1 INTRODUCTION

Dry-stone retaining wall is an ancient construction technique, widely used across the world to retain the slopes, making plain areas for agriculture and thus reducing the erosion process. During the industrial age, this construction technique was widely used for creating the retaining wall along the road/railway. In France, based on the survey by Odent (2000) held by the Ministry of Public Works, 18% of retaining wall structures are classified as dry-stone retaining wall (DSRW), equivalent with an area of 410000 m^2. However, early in the 20^{th} century, new industrialized processes for construction requiring fewer workers emerged. Reinforced concrete is one of these new technologies which led to the progressive abandonment of dry-stone structures. Meanwhile, even if the know-how was maintained by some artisan builders, the scientific knowledge related to this technology was totally lost.

DSRW is a discrete structure composed of rigid stone blocks. The “dry” term is related to the dry-joint contacts between the stone blocks which implies that no intermediary substance is used to stick the stone blocks altogether. The surface of blocks in contact mobilizes the dry friction between them which explains the global stability of this wall. In addition, it allows irreversible sliding movements between blocks that dissipate energy creating a highly deformed shape before the failure.

Two types of DSRW failures have been observed: 1. An excessive lateral force from the backfill leads to a velocity jump in the wall along a “sliding” surface creating a failure plane. This plain strain phenomenon appears as sliding or toppling failure (see Fig. 1), thus

classified as two-dimensional rupture; 2. If the top part of the backfill is loaded by a concentrated force (e.g. wheel of a vehicle), this loading will diffuse in the backfill before being transferred to the DSRW. If the DSRW experiences an excessive loading of this type, it will deform according to typical three dimensional belly shape.

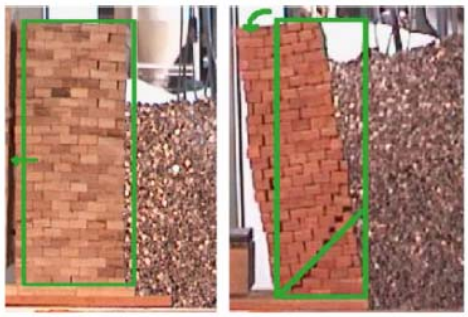

(a) (b)

Fig. 1. Two-dimensional mode of failure of DSRW
(a) Sliding, (b) Toppling (Colas et al., 2010a)

In the last few years, there is a resurgence of interest towards the DSRW; first of all because it requires less embodied energy for construction compared to the reinforced concrete wall; secondly, the wall may let the water flowing through inside its body due to the high porosity of the wall. As a consequence, it would never bear extra hydrostatic pressure which is definitely an advantage.

2 EXPERIMENTAL STUDY

The first real scale experimental test addressing the DSRW system was carried out by Burgoyne in 1834. Four walls have been tested with different geometries and the corresponding critical height was measured in each case. However, Burgoyne's experiments are inadequately documented.

In 2007, five DSRW of 2-4 m with different geometries and constitutive materials have been tested by Villemus et al. (2007). The geometrical variation involves height, width, wall batter, and base inclination. Two materials have been used for the blocks, limestone ($\phi = 36°$) and schist ($\phi = 28.5°$). A hydrostatic loading was used, restricting the loading to a pure horizontal component.

Fig. 2. Experimental wall of Villemus et al. (2007)
(a) Before loading, (b&c) After loading

More recently, Colas et al. (2010b) have tested four DSRW loaded by a backfill (gravel). Two construction methods have been studied: 1. One created less carefully in order to reproduce walls encountered in the countryside, they are denoted herein “rural” wall; 2. Other created with much care according to the rules followed by expert artisan builders, they are denoted as “engineered” wall.

(a) (b)

Fig. 3. DSRW tested by Colas et al. (2010b)
(a) Failure of a “rural” wall (b) Failure of a “engineered” wall

The last two experiments described above are well documented, and the involved experimental results constitute the scope of the study presented herein. A numerical modeling corresponding to the loading of DSRWs towards failure is provided. The modes of failure as well as the backfill critical height (maximum backfill height bearable by the DSRW) will be compared with the results obtained on full scale experiments

3 NUMERICAL STUDY

DSRW exhibits a continuum model limitation as every block can move or rotate freely which allows high energy dissipation before failure. In this case the Discrete Element Method (DEM), a numerical method introduced by Cundall (1971) is more appropriate to study the behavior of DSRW. Late in the 90s, following their observation on free-standing medieval dry-stone walls in Zimbabwe (Walker & Dickens, 1995), Dickens & Walker (1996) have used UDEC (an ITASCA software) to carry out a tentative study of dry-stone wall focusing on finding the origin of the bulging shape of free-standing walls.

In the last decade, DEM approach is gaining popularity, thanks to the exponential growth of hardware computing capability. During this time, Burgoyne’s experiments have successfully been reproduced by Harkness et al. (2000) using UDEC™, in the sense that he found a critical backfill height similar to the one reported by Burgoyne. It was followed by a parametric study of the same wall by Powrie et al. (2002) and Claxton et al. (2005), in search of the parameters influencing the wall failure.

In this paper, the authors will use PFC^{2D} (ITASCA, 2008). It allows addressing the whole system with a single approach, say, by using only disk clusters in order to model both the wall blocks and the backfill grains.

3.1 CONTACT MODELS

The wall blocks are rebuilt with an assembly of overlapping disks forming rigid clumps of particles. The contact surface between blocks is elastic and deformable, additionally it uses an averaged Coulomb’s dry-friction contact law along its surface known as smooth-joint contact law. Using this contact law, the particles from two different blocks will "slide" as

expected along the joint, rather than be forced to move around one another like in contact grain-grain.The orientation of this contact is defined according to a global axes reference of blocks (here the vertical and the horizontal). As the contact is deformable, therefore the normal and tangential stiffness must be defined alongside with the contact friction coefficient.

The backfill consist of elongated rounded grains formed from rigid clusters of two disks. The contact between grains is deformable (based on normal and tangential stiffness) and capped with a Coulomb's friction law.

The minimum local friction will be considered for contacts between wall and backfill. Exceeding this value will lead to the contact slip.

Both normal and tangential stiffness (k_n & k_s) of wall and backfill are set to 10^8 N/m^2, a sufficiently high stiffness to retain a rigid behavior, but small enough to keep a reasonable critical time step. We checked that in the range of typical stiffness for stone grains (10^8 N/m^2-10^{10} N/m^2), the specified value for k_n and k_s has a few influence on the results. The mechanical parameters are identified using numerical tests which allowed characterizing the proper local parameters on the basis of data provided by actual experimental tests.

3.2 TILT TEST

This test is used to identify the average Coulomb's friction coefficient between two blocks. If the average contact shear force between two blocks is greater than Coulomb's friction criterion, in consequence the top block will slide on the bottom block. The slip force limit depends on tan (ϕ^b_{local}) the corresponding friction coefficient between contacts, where ϕ^b_{global} refers to the inclination of the bottom block which is increased progressively.

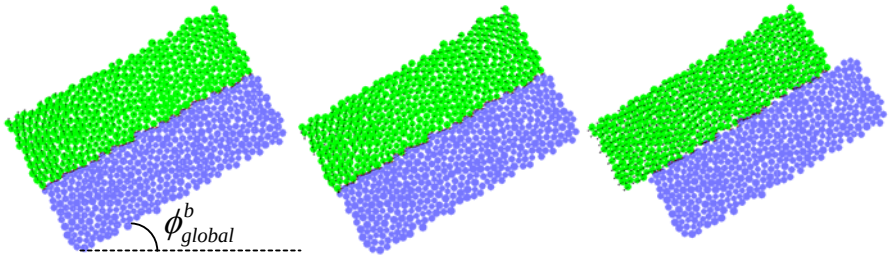

Fig. 4. Block tilt test with ϕ^b_{local} = 30°

(a) ϕ^b_{global} = 29°, (b) ϕ^b_{global} = 30°, (c) ϕ^b_{global} = 31°

Suppose that contacts have ϕ^b_{local} equal to 30°, in Fig. 4a, the shear force acting on the contacts is still inferior to the Coulomb's criterion, thus contact adhesion is maintained. An incremental tilting-angle is added in Fig. 4b, in this state $\phi^b_{global} = \phi^b_{local}$ and consequently contact shear force is now equal to the resisting force, however no slip occurs because the criterion has not been exceeded. As shown in Fig. 4c, slip arises when a new increment is added. Based on the smooth joint model used here, the block-block contact is not affected by the block roughness due to the outer geometrical frontier of the block; this result was expected.

3.3 ROTATING BOX TEST

In the experimental test by Colas et al. (2010b), the backfill material is poured progressively from a dumpster, forming a natural angle of repose (ϕ^s_{repose}). This natural angle of repose is associated to the local friction between the grains of the backfill (ϕ^s_{local}) and their natural shape. Finding the relation of known natural angle of repose and the corresponding local friction is the main objective of this simulation.

To reach this goal, simulations have been conducted using several ϕ^s_{local} values. Elongated grains are generated inside a 75 cm x 75 cm box, and then the box is incrementally rotated up to an angle of 90°. Fig. 5 illustrates the principle steps of the simulation where the backfill grains automatically rearrange during the rotation. Finally, the natural angle of repose is measured. A local friction (ϕ^s_{local}) equal to 20° is found to reach a natural angle of repose equal to 32° [Colas et al. (2010b)].

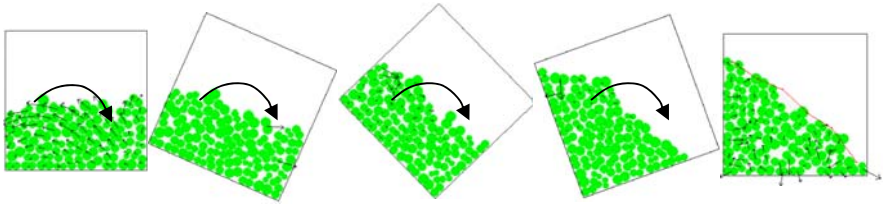

Fig. 5. Schematic layout for the rotating box test in order to find the natural angle of repose

4 RESULTS

The modeling of different DSRW loaded either by a hydrostatic loading model or by a backfill is performed. Using Intel® Xeon® processors, depending on the complexity of the model and the rate of the incremental load, it takes a couple of hours up to 2 days to simulate the DSRW model loaded by a hydrostatic force. In contrast, the DSRW model loaded with a granular backfill requires about 3 days of computation to reach the wall failure.

The stability is based on the average global unbalanced force (AUF) in the whole wall-backfill system. This value is set to 1% which means the model will run indefinitely till either the AUF reaches a value smaller than 1% or if the failure in DSRW is detected. When AUF < 1%, thus a new load is added and new cycles are done until reaching a new equilibrium state. If this criterion is not satisfied, the failure criterion is checked. Failure is stated when the kinetic energy in the wall exceeds a certain prescribed value.

A general view of the DSRW model based on Villemus et al. (2007)'s experimental campaign is shown in Fig. 6a. The hydrostatic force was incremented constantly until the failure of the DSRW. The toppling failure is noticeable in Fig. 6b as well as its failure surface, leaving the bottom part immobile while the top part is mobilized in a monolithic fashion.

These simulations were carried out for all the 5 walls tested by Villemus et al. (2007) in full scale experiments. The results are summarized in Table 1, we found a relative error of water critical height smaller than 8% compared to the experimental results. This small discrepancy shows the capability of DEM to simulate and find the phenomena observed onsite.

In order to model Colas et al (2010b)'s experimental campaign, the backfill must be created in the same way to the method used on site. Since the gravel was gently dropped from a dumper, the numerical particles are generated in a container located at the right hand part of the system and released under gravity. The release from a rather concentrated point on the

horizontal plane creates a natural slope characterized by the natural angle of repose (Fig. 7a). The backfill is created according successive layers of grains and equilibrium of the whole system is obtained before the release of further grains that will compose the subsequent layer. The number of released grains per layer was defined in order to obtain a layer thickness approximately equal to a wall block height. Fig. 7b depicts the velocity field for the backfill grains during the toppling failure. One can note that a top triangular part of grains is mobilized at failure (similar to the well-known Coulomb corner) whereas a bottom triangular part is quasi-immobile.

The results for the simulations (3 different walls) are shown in Table 2. One can note a larger discrepancy between the critical heights found through the simulations with the experimental results. Since the previous simulations of Villemus' experimental campaign tend to prove that the wall behavior is correctly addressed, a specific study involving the interface of wall-backfill was undertaken to explain such a discrepancy.

Table 1. Comparison of water critical height (m) of Villemus's experimental tests and DEM results

Wall Height (m)	2	1.95	4	2	4.25
Wall Name / Critical Height	V1L	V2L	V3L	V4L	V5S
Experiment	1,74*S*	1,90*S* 1,78*T*	3,37*S*	1,94*S* 1,90*T*	3,62*S*
DEM (PFC)	1,76*T*	1,79*T*	3,52*T*	1,79*T*	3,71*T*
Error (%)	1%	6%	5%	8%	3%

S = Schist C = Colas *S*= Sliding e = engineered
L = Limestone V = Villemus *T*= Toppling r = rural

Table 2. Comparison of backfill critical height (m) of Colas's experimental tests and DEM results

Wall Height (m)	2.5	2.5	2.5
Wall Name / Critical Height	C2Se	C3Sr	C4Lr
Experiment	2,3*S* 2,3*T*	2,78*T*	2,72*T*
DEM (PFC)	1.76*T*	1.96*T*	1.63*T*
Error (%)	23%	29%	40%

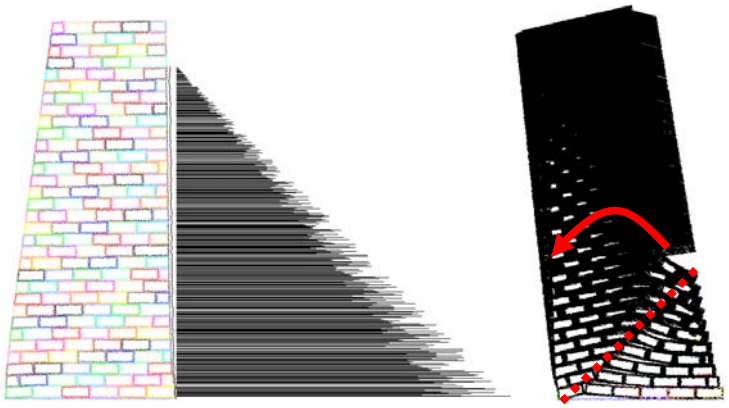

Fig. 6. Discrete model of DSRW loaded with a hydrostatic loading
(a) General view, (b) Kinematic of failure

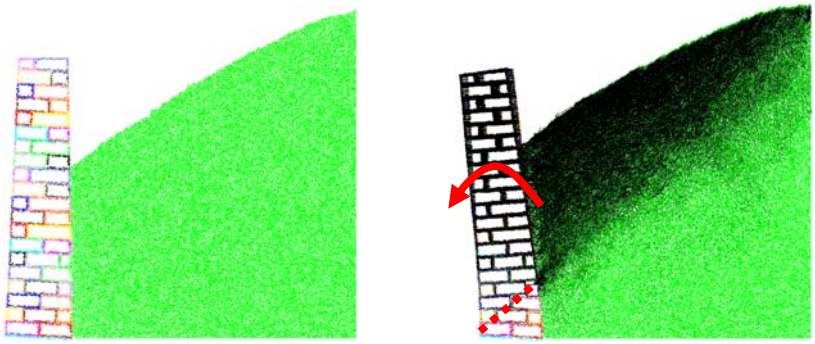

Fig. 7. Discrete model of DSRW loaded with a granular backfill
(a) General view, (b) Kinematic of failure

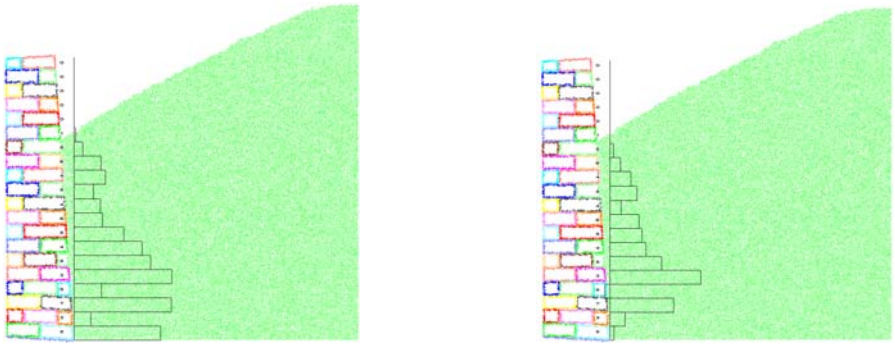

Fig. 8. Interface force field per block just before failure for wall C2se
(a) Horizontal forces, (b) Vertical forces

Fig 8 depicts the mean force (horizontal and vertical) per block applied on the wall due to the backfill loading. The state corresponds to a state for C2se wall which could be qualified at the limit of failure. Indeed, a further layer of soil that is subsequently added on the backfill has induced the toppling failure of the wall. We found an average value interface friction coefficient $\delta_{C2se}^{20} = 29°$ while the default local friction coefficient is $\delta_{local} = 20°$ (corresponding to the local friction angle for backfill particles). The geometrical roughness of the wall blocks contributes to the overall wall-soil friction which explained why the global interface friction angle is greater than 20°. A former computation showed that a lower friction angle for the interface soil-wall (equal to $\delta_{C2se}^{0} = 21°$) was obtained for $\delta_{local} = 0°$. The corresponding backfill critical height was found equal to 1.56m. Actually, the behavior of the interface has definitely a great influence on the expected backfill critical height and a meaningful interface friction angle is required in order to find a correct backfill critical height (2.3m).

During the experimental campaign, no measurement was performed in order to identify the property of the interface. Boussinesq's theory for retaining walls could be used as a substitute to real experiments. First, simulations of biaxial tests involving the backfill grains were performed in order to identify the backfill internal friction angle. For a local grain-grain friction angle of 20°, the internal friction angle ϕ_{global}^{s} for the backfill was found equal to 37.7°. In the case of sheet piles or reinforced concrete retaining wall, the friction between the wall and the soil is generally approximated by $\delta_{Bous\sin esq} = \frac{2}{3}\phi_{global}^{s}$. Then, for the system studied herein, the wall-soil friction angle is equal to 25°, which is smaller than 29° derived from the simulation. It seems that a friction angle greater than 29° is required to find the backfill critical height found onsite. Consequently, further research is required in order to find a relationship for the friction wall-soil of the same type as in Boussinesq theory but valid for the DSRW. This angle must be found in the interval $\left[\frac{2}{3}\phi_{global}^{s};\phi_{global}^{s}\right]$.

5 CONCLUSIONS

A 2D discrete element method has been used to model a series of full scale experiments performed to study the plane deformation failure of dry stone retaining walls. The simulations of tests involving a pure hydrostatic loading show the capability of DEM to model the actual test. Indeed, the simulations provided the phenomena at failure observed onsite and the water critical height shows a discrepancy with onsite results that does not overpass 8%, which is very little.

The phenomena observed onsite are also found through the simulations when the dry stone retaining walls are loaded by a backfill. However, considerable discrepancy between the experimental and numerical backfill critical height have been observed. This could be due to the underestimation of the interface wall-soil friction effect which seems to play a very important role into the wall stabilization process. Ongoing research is currently undertaken to study this wall-backfill friction.

ACKNOWLEDGEMENT

This study is part of the project C2D2 PEDRA 10 MGC S 01 (*Ouvrages en pierre faiblement maçonnés*) and project RESTOR (*Restauration des murs de soutènement en pierre sèche*). The authors would like to thank the *Ministère de l'Ecologie* (MEDDE) and *Ministère de la Culture* (MCC) for their financial support.

REFERENCES

Claxton M., Hart R.A., McCombie P.F., Walker P.J. (2005), "Rigid Block Distinct-Element Modeling of Dry-Stone Retaining Walls in Plane Strain". Journal of Geotechnical and Geoenvironmental Engineering, Vol. 131(3), 381-389.

Colas A.S., Morel J.C., Garnier D. (2010a), "2D Modelling of dry joint masonry wall retaining a pulverulent backfill", Vol. 34(12), 1237-1249.

Colas A.S., Morel J.C., Garnier D. (2010b), "Full-scale field trials to assess dry-stone retaining wall stability", Engineering Structures, Vol. 32, 1215-1222.

Dickens J.G., Walker P. J. (1996), "Use of distinct element model to simulate behaviour of dry-stone walls", Structural Engineering Review, Vol 8(2/3), 187-199.

Cundall P.A. (1971), "A computer model for simulating progressive large-scale movements in blocky rock systems", Proceedings of the Symposium of the International Society of Rock Mechanics, paper n° II-8, Nancy.

Harkness R.M., Powrie W., Zhang X., Brady K.C., O'Reilly M.P. (2000), "Numerical modeling of full-scale tests on drystone masonry retaining wall", Géotechnique, Vol. 50(2), 165-179.

ITASCA Consulting Group. (2008), "PFC2D Particle Flow Code in 2 Dimensions - Theory and Background 4th ed".

Odent N. (2000), "Recensement des ouvrages de soutènement en bordure du réseau routier national", Ouvrages d'art, n° 34, Mai 2000, pp. 15-18.

Powrie W., Harkness R.M., Zhang X., Bush D.I. (2002), "Deformation and failure modes of drystone retaining walls", Géotechnique, Vol. 52(6), 435-446.

Villemus B., Morel J.C., Boutin C. (2007), "Experimental assessment of dry stone retaining wall stability on a rigid foundation", Engineering structures, Vol. 29, 2124-2132.

Walker P.J., Dickens J.G. (1995), "Stability of medieval dry-stone walls in Zimbabwe", Géotechnique, Vol 45, 141-147.

ANALYTICAL AND NUMERICAL STUDIES ON THE MECHANISM OF MINING SUBSIDENCE

E. Fathi Salmi[a], M. Nazem[a], and A. Giacomini[b]

[a]*Australian Research Council Centre of Excellence for Geotechnical Science and Engineering, the University of Newcastle, NSW, Australia*

[b]*Centre for Geotechnical and Materials Modelling, The University of Newcastle, Callaghan, NSW 2308, Australia*

ABSTRACT: *Ground subsidence due to mining is a very complicated geomechanics phenomenon, particularly in the longwall mining method. Due to the adverse consequences of subsidence on surface structures, facilities, and environment, subsidence prediction has attracted interest in geotechnical engineering over the past few decades. Previous research has indicated that the thickness and inclination of seam, depth of working panel, and ground characteristics are the main factors which should be considered in estimating the subsidence. Methods for predicting the subsidence are: empirical, analytical and/or numerical. The geotechnical characteristics of ground affect the caving, collapse, and bulking of goaf and the extent of the cavity toward the surface. The main aim of this paper is to investigate the mechanism of ground surface subsidence based on analytical and numerical simulations. Analytical solutions are based on the theory of elasticity. The Distinct Element Method, which can simulate jointed and stratified rock mass, is used for numerical modelling of subsidence due to mining. In this paper, numerical and analytical results are obtained for two different cases of isotropic and transverse isotropic (layered) strata. Outcomes of this study indicate that the weak planes and stratification not only play a significant role in geotechnical behavior of the rock mass, but they affect the mechanism of ground movement. Results also show that considering the real structure and properties of ground will lead to more accurate estimation of measured subsidence in the field.*

1 INTRODUCTION

Longwall mining is widely used for extracting relatively horizontal coal seams with acceptable widths and thicknesses. A cut along the coal face is initiated, and the unsupported overburden is held in place by hydraulic roof supports. As the coal shearer progresses cutting a new coal face each pass, the roof supports move forward to support the new overburden and the panel left unsupported caves in, creating the goaf. The caving of overlaying strata causes ground movement and subsidence, as depicted in Fig. 1. In modern coal mining, especially longwall mining method, subsequent panels are exploited according to the schedule and production plan, where numerous economic and technical items are considered (SME, 1992). Extractions of significant panels of longwall are accompanied by deformation of ground. This deformation depends on the size of the underground excavation, the complex behaviour of the rock mass, and it is affected by the process of collapse and caving of overlying strata.

The mechanisms of caving and fragmentation of spanning strata, the collapse and bulking of goaf, its re-compaction, the time-dependent behaviour of the process and the direct effects of all of the above-mentioned items on ground movement create an extremely complex problem that is not trivial to simulate. Therefore, simplifying assumptions are usually considered for investigating this phenomenon. Subsidence pre-calculation methods are generally divided into three categories; (i) empirical techniques, (ii) influence functions, and (iii) analytical modelling. Empirical techniques depend on the experience gained from large number of field measurements. The influence function methods are based on model propositions and mathematical assumptions to a greater or lesser degree; whereas analytical methods are established on the rheology of subsiding materials and their response to changing mining geometries (Bahuguna et al, 1991; Kratzsch, 1983).

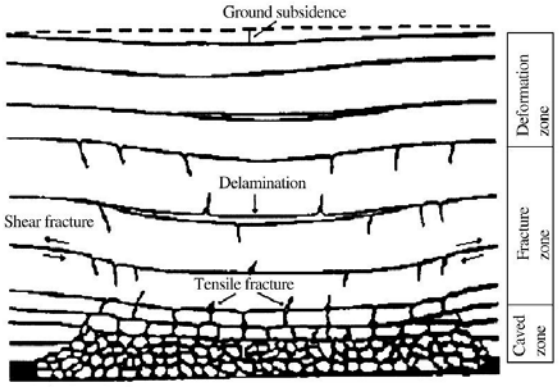

Fig.1. Caving of the overlaying strata and extension of the mining subsidence (after Peng & Chiang, 1984)

In this paper the effect of stratification on subsidence is investigated by analytical and numerical simulations. Analytical simulations are based on the theory of elasticity. The Distinct Element Method (DEM) is employed for numerical analysis of the effect of stratification on ground surface subsidence. The main aim of the paper is to investigate the effects of the geotechnical charactristics of rock mass on accurately predicting the amount of ground surface subsidence caused by extraction of an underground coal seam.

2 ROCK MASS CHARACTERISTICS

Generally speaking, the bending, sagging and fragmentation of the strata and the development of the cavity toward the surface are related to the deformational and strength characteristics of strata. Therefore, the first step in conducting an analytical study or a numerical modelling for mining subsidence is to estimate the mechanical characteristics of rock mass. The incorporation of sophisticated constitutive laws that govern the mechanical behaviour of the rock mass within such models requires a range of engineering parameters for each distinctive strata horizon to be specified. The strength of rock mass and its deformability are probably the most dominant characteristics of the rock mass as they represent the response of rock mass around underground excavations. These characteristics of rock mass are associated with the properties of intact rock materials as well as discontinuities. Although several methods have been proposed for estimating rock mass characteristic, it is still a very challenging task for engineers (Bieniawski, 2011), mainly due to the complexities and uncertainties associated with the response of jointed and bedded rock masses. Rock mechanics studies have shown that the elastic properties of sedimentary rocks, particularly coal rocks, are inhomogeneous in the mass and are normally anisotropic even in small samples (Salamon,1968), affecting the mechanical behaviour of sedimentary rocks.

In order to consider a stratified ground as an isotropic continuous, it is necessary to determine the properties of an equivalent medium, where the characteristics of intact rock and bedding planes are taken into account. To date, numerous direct and indirect methods have been proposed to determine the mechanical properties of rock mass, such as in-situ tests and back calculation of rock mass parameters based on the measured data (Hoek, 2007). Predicting the rock mass properties by the conventional rock mass classifications is an

acceptable and simple method (Zhang, 2004). Therefore, in this study the rock mass classification has been used for predicting the geotechnical parameters of rock mass. Although numerous empirical formulation have been proposed to predict the strength and deformation characteristics of rock mass (Zhang, 2004), most of these relations are only valid for the isotropic rocks. In addition, the conventional rock mass classifications systems usually ignore the fact that the strength and deformation of a bedded rock mass varies depend on the loading direction relative to the orientation of the lamination planes. Perhaps, none of the conventional classification systems have been developed according to the Australian coal mine conditions. Thus, traditional rock mass classifications are not suitable for underground coal mining applications because (a) they tend to focus on the properties of joints, whereas bedding is generally the most significant discontinuity affecting coal mine roof, and (b) they rate just one rock unit at a time, while coal mine roof often consists of several layers (Mark & Molinda, 2005). In other words, methods such as Rock Mass Rating (RMR), Barton's Q-system, and Geological Strength Index (GSI), can be used to classify bedded rock masses, but they fail to estimate the variation in the strength and deformation characteristics due to the bedding (Whittles et al, 2007).

A brief review of the underground coal literature indicates that there are a few rock classification systems which have been developed for stratified grounds in coal mining applications. For instance, Coal Measure Classification (CMC) is a suitable method developed for coal rock masses to be used for empirically prediction of the engineering properties of the stratified rock masses. The output of this classification system is two numerical ratings representing the different engineering properties of the strata in directions parallel and perpendicular to stratification (Whittles et al, 2007). Because of this capability, CMC has been selected for estimating the characteristics of rock mass in this study. Whittles et al (2007) stated that the empirical equation proposed by Mitri (1994) can estimate the deformation modulus of the stratified rocks within an acceptable range, according to

$$\frac{E_m}{E_i} = \frac{1}{2}\left[1 - cos\left(\frac{\pi \mathrm{RMR}}{100}\right)\right] \tag{1}$$

where E_m and E_i represent the modulus of deformation of the rock mass and the intact rock, respectively, and RMR indicates the Rock Mass Rating classification system. Whittles et al. (2007) also proposed the following equation relating CMC to RMR

$$\mathrm{RMR}_{89} = 0.8835\mathrm{CMC} + 10 \tag{2}$$

where RMR_{89} is the 1989 version of the RMR system (Whittles et al, 2007).

Anisotropy is one of the most important mechanical properties that governs the behaviour of rock masses. Although significant research has been devoted to investigate the effects of anisotropy on strength and mechanical response of geo-materials (Pietruszczak & Mroz, 2000; Lydzba et al, 2003; Lee and Pietruszczak, 2008), mining and geotechnical engineers normally neglect the role of anisotropy in a daily practice. The main reason for overlooking anisotropy is that the anisotropic theory of elasticity is complex, and anisotropy increases the number of unknowns. Moreover, difficulties associated with reliable sampling methods and testing procedures for anisotropic geo-materials increase the demand for simplifying the anisotropic materials into equivalent homogeneous media (Exadaktylos, 2001). In equivalent continuum models for jointed rock masses it is assumed that the rock mass consists of a single set or multiple sets of parallel joints, and the accurate position of the joints or bedding is not important for predicting the mechanical parameters of the equivalent medium. In the literature, one of the most convenient methods of deriving an equivalent medium is based on

the volumetric average of the stresses and strains over a representative volume of the corresponding laminated medium (Salamon, 1968; Wardle & Gerrard, 1972; Gerrard, 1982; Pande et al, 1989). Usually quantifiable mechanical characteristics of a stratified rock mass are simplified to an equivalent homogeneous transversely isotropic elastic solid. Transversely isotropic materials are fully characterised by six elastic constants, which reduce to five due to arguments of invariance of the strain energy density of isotropic materials under coordinates transformation (Exadaktylos, 2001). Salamon (1968) proposed the following equations for deriving the equivalent properties of a stratified rock mass based on the relevant thickness and the elastic properties of each layer:

$$\nu = \frac{\sum \frac{t_i \nu_i E_i}{1-\nu_i^2}}{\sum \frac{t_i E_i}{1-\nu_i^2}} \qquad \nu' = (1-\nu)\sum \frac{t_i \nu_i'}{1-\nu_i^2}$$

$$E = (1-\nu^2)\sum \frac{t_i E_i}{1-\nu_i^2} \qquad E' = \frac{1}{\sum \frac{t_i}{E_i}\left(\frac{E_i}{E_i'} - \frac{2\nu_i'^2}{1-\nu_i}\right) + \frac{2\nu'^2}{(1-\nu)E}} \tag{3}$$

$$G = \frac{E}{2(1+\nu)} = \sum t_i G_i \qquad G' = \frac{1}{\sum \frac{t_i}{G_i'}}$$

where ν, E, and G represent the Poission's ratio, deformation modulus, and shear modulus of the equivalent medium in the direction perpendicular to the bedding planes, respectively, ν', E', and G' are similarly defined for the equivalent medium parallel to the bedding planes, and t_i is the relevant thickness of i^{th} layer.

3 SUBSIDENCE OF ISOTROPIC GROUNDS

Although the behaviour of the disturbed ground in longwall mining is complex and cannot be described in terms of conventional ideal media, it is believed that the fragmentation of the overlaying rocks does not often occur close to the ground surface. Therefore, it can be assumed that deformation of the surface is mainly elastic. For instance, Berry (1960) mentioned that if the excavation is fairly deep the development of the severely disturbed ground will form a small fraction of the entire area, and therefore it can be considered as a continuous medium for mining engineering designs. Field observations and measurements have revealed that subsidence is a very complicated time dependent phenomenon, which cannot be exactly studied by the theory of elasticity (Berry, 1964; Kratzsch, 1983). Therefore, visco-elastic or visco-plastic models have been employed for analysing the time-dependent subsidence (Berry, 1964; Kratzsch, 1983). Nonetheless, the elastic analysis is still valid for the final status of the deformation when creep and time effects are ceased (Berry, 1960). Berry (1960) derived an elastic solution for estimating the surface subsidence in isotropic ground. Considering a sufficiently wide excavation and neglecting the effects of caving and goaf materials, the floor and roof would meet in some middle part of the opening and the amount of ground convergence (closure) in this interval will be equal to the whole thickness of the excavated seam. However, because of the caving followed by bulking of goaf materials, the amount of ground closure is significantly less than the thickness of the extracted seam. The seam thickness can be considered infinitesimal as long as the coal mine overburden is relatively high. Thus, it is reasonable to assume that the opposing points of roof and floor possess the same coordinate. The ground closure at these opposing points can be

treated as a discontinuity in displacement at a single point. Berry (1960) probed this problem and extracted a series of closed-form solutions based on the theory of elasticity and the status of the ground closure. Three different conditions were considered for this problem:

i. Non-closure: in which the roof and floor do not have contact at any point,
ii. Partial closure: where the roof and floor meet over some parts of the longwall panel, and
iii. Complete closure: in which there is a connection between the roof and floor all over the excavation.

Considering the above circumstances for the ground closure, Case (i) can be hypothesized as an inverse crack problem, where the edges of the crack move toward each other instead of drawing apart. Case (ii) can be treated as a double reversed crack problem where the interval between the two cracks is subjected to a constant displacement discontinuity. In Case (iii) the constant discontinuity covers the whole distance representing the excavation.

The deformation due to an underground excavation is accompanied by induced stresses. The final state of stresses after excavation is the sum of initial stresses and the induced stresses. For simplicity, it is assumed that the induced stresses exert a normal and a constant traction *P* on the unclosed parts of the panel (Berry, 1960). To fulfill this condition it is necessary to consider a horizontal seam or a tilted panel where the difference between the depths of sides is negligible and the initial stresses have hydrostatic condition.

Considering an infinite medium, an analytical solution has been proposed based on the theories of crack in elastic bodies (Muskhelishvili, 1954). This method results in an exact solution for Case (iii), but the results are only approximations for open and partially closed cases. The ground surface is assumed to be remote enough from the panel of extraction which covers the distance $-a<x<a$, as depicted in Fig. 2. In addition, due to the closure of the ground, roof and floor can meet at the interval $-b<x<b$ (Fig. 2). However, in intervals $-a<x<-b$ and $b<x<a$ the induced stress can exert a normal traction.

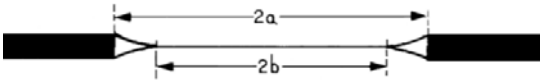

Fig. 2. A schematic view of coal seam and parameters *a* and *b* (after Berry, 1960.)

$$\begin{cases} \Delta v = -t & |x| \le b \\ \Delta v = 0 & |x| > a \end{cases} \qquad \begin{cases} \sigma_y = p & b \le |x| < a \\ \tau_{xy} = 0 & b \le |x| < a \end{cases} \tag{4}$$

where *a* and *b* are the half widths of the longwal panel and the closed interval, respectively, *t* depicts the thickness of the seam, σ_y is the vertical stress, and τ_{xy} is the component of the shear stress. The following expressions were proposed to assess the ground surface subsidence caused by underground coal exploitation in an isotropic and homogeneous medium.

Non-closure:

$$u_x + iu_y = -2pa^2 \frac{1-\nu}{G}\left(\frac{hCos\alpha - xSin\alpha}{x^2+h^2}\right)^2 (x+ih)\left[1+O\left(\frac{a^2}{h^2}\right)\right] \tag{5}$$

Partial closure:

$$u_x + iu_y = -2p\left(a^2 - b^2\right)\frac{1-\nu}{G}\left(\frac{hCos\alpha - xSin\alpha}{x^2 + h^2}\right)^2 (x + ih)\left[1 + O\left(\frac{a^2}{h^2}\right)\right] \quad (6)$$

Complete closure:

$$u_x + iu_y = -\frac{4at}{\pi}\left(\frac{hCos\alpha - xSin\alpha}{x^2 + h^2}\right)^2 (x + ih)\left[1 + \frac{a^2 q(x)}{3(x^2 + h^2)} + O\left(\frac{a^2}{h^2}\right)\right] \quad (7)$$

where u_x and u_y represent the horizontal and the vertical displacements, respectively, α is the inclination of the coal seam, h is the depth of the panel, x represents the horizontal distance from the centre of the panel, and i is the imaginary unit. $O(a^2/h^2)$ contains negligible terms provided a^2/h^2 approaches zero. In Equation (7), $q(x)$ is defined by

$$q(x) = \frac{x - ih}{x + ih}e^{2i\alpha} - 2 + 3\frac{x + ih}{x - ih}e^{-2i\alpha}a \quad (8)$$

Thus in overall the following single expression can be used to describe the subsidence caused in all different cases:

$$(u + i\,v)_0 = -\frac{2}{\pi}A\left(\frac{hCos\alpha - xSin\alpha}{x^2 + h^2}\right)(x + ih)\left[1 + O\left(\frac{a^2}{h^2}\right)\right] \quad (9)$$

where A is the area of the discontinuity or the volume of closure per unit length of the longwall panel. According to the above solution proposed by Berry (1960), for non-closure and partial closure cases, the amount of surface subsidence is a function of the elastic properties of the rock mass including its deformation modulus and Poisson's ratio, while for Case (iii) the expression for the surface displacement is independent of the elastic characteristics of the rock. The case of complete closure can be considered as an upper bound for the magnitude of subsidence. This case cannot happen since the caved rocks prohibit the complete closure of the excavation.

In this study, Equations (5)-(8) are employed for analysing the subsidence caused by a horizontal longwall panel with a width of 110 m and a depth of 300 m. This panel is located near Wollongong, Australia (Lee, 2005). The deformation modulus is calculated based on CMC classification (CMC=55), and is approximately equal to 3.5 GPa. The Poission's ratio of the overlaying sandstone is approximately 0.25 (Lee, 2005; Keilich, 2009). The profiles of the vertical and horizontal subsidence of the ground surface are plotted in Fig. 3. According to Fig. 3, the maximum vertical displacement is ~7.5 cm and the maximum horizontal movement is approximately 2.5 cm, which occurs at ~170 m from the centre of the subsidence trough.

4 SUBSIDENCE OF TRANSVERSELY ISOTROPIC GROUNDS

Ground movement in stratified rock masses is directly affected by the characteristics of the planes of discontinuity. Sliding of strata along bedding planes and their separation at interfaces play critical roles in extension of the cavity toward surface. Comparing the results obtained by the isotropic elastic model with the measured subsidence indicates that the fundamental assumptions for deriving the elastic model are not appropriate for the stratified rocks (Berry, 1960). Therefore, complex variable formulation of anisotropic bodies given by

Green and Zerna (1958) were employed for deriving the analytical solution of the mining subsidence in transversely isotropic grounds (Berry & Sales, 1961; Berry & Sales, 1962; Berry & Sales, 1963; Berry, 1964 a & b). In order to avoid complex quantities, two parameters k_1 and k_2 have been defined as follows (Berry & Sales, 1961):

$$k_1 = \left(1-\nu^2\right)^{\frac{1}{2}}\left(\frac{E}{E'}-\nu'^2\right)^{-\frac{1}{2}} \qquad k_2 = \left[\frac{E}{2G}-\nu'\left(1+\nu\right)\right]\left(\frac{E}{E'}-\nu'^2\right)^{-1} \tag{10}$$

Berry and Sales (1961) proposed the following general expressions to estimate the magnitude of the surface subsidence due to exploitation of a horizontal coal seam based on the parameter k_1 and k_2:

$$\left(u+iv\right)_0 = -\frac{2^{\frac{1}{2}}Ah^2\left(k_1+k_2\right)^{\frac{1}{2}}\left(k_1x+ih\right)}{\pi\left(k_1^2x^4+2k_2h^2x^2+h^4\right)}\left[1+O\left(\frac{a^2}{h^2}\right)\right] \tag{11}$$

where A is defined as follows:

Non-closure:

$$A = \sqrt{2}\pi a^2 p\left(\frac{1}{E'}-\frac{\nu'^2}{E}\right)\left(k_1+k_2\right)^{\frac{1}{2}} \tag{12}$$

Partial closure:

$$A = \sqrt{2}\pi\left(a^2-b^2\right)p\left(\frac{1}{E'}-\frac{\nu'^2}{E}\right)\left(k_1+k_2\right)^{\frac{1}{2}} \tag{13}$$

Complete closure:

$$A = 2at \tag{14}$$

Berry (1963) suggested k_1=2 and k_2=10 for stratified rock masses.
Fig. 3 represents the profiles of the vertical and horizontal displacements for the longwall panel in Section 3, considering a transversely isotropic ground. In this case the Young's modulus of the intact rock is 20 GPa (Keilich, 2009). According to the profiles in Fig. 3, the maximum vertical subsidence is ~8 cm, whereas the maximum horizontal displacement is approximately 2 cm, which occurs ~70 m from the centre of the subsidence trough.

5 NUMERICAL ANALYSIS

In this section, numerical analyses are carried out for 2 different cases of isotropic and stratified grounds by the Discrete Element Method (DEM). A commercial DEM package, UDEC (Itasca Consulting Group, 2004), is employed for this purpose. The mechanical response of the longwall panel host rock is predicted by the Mohr-Coulomb material model. Similar to analytical analysis, Case 1 represents the isotropic ground, whereas Case 2 represents the stratified ground. In the first case, the equivalent characteristics of the rock

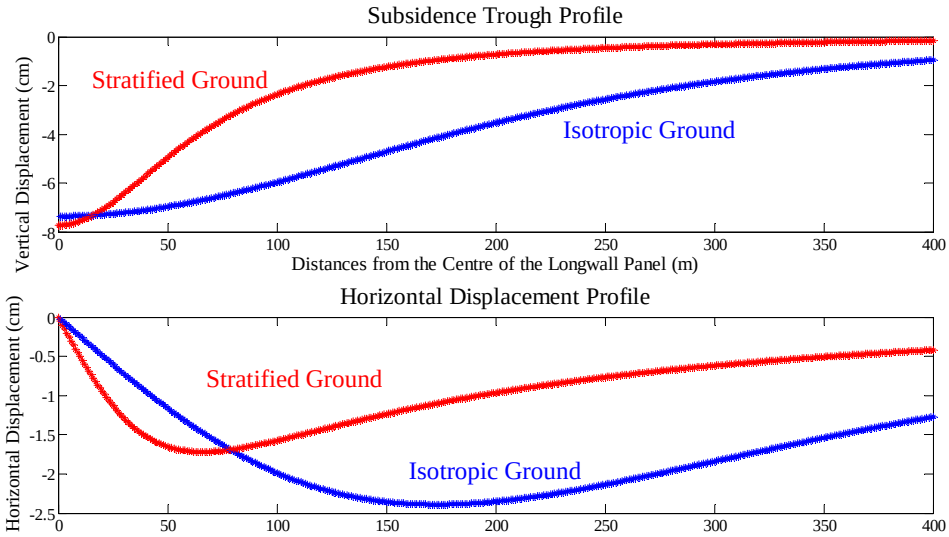

Fig. 3. Profiles of the vertical and horizontal displacements (a=55 m, b= 15 m)

mass are estimated based on CMC and its relation with GSI. The Mohr-Coulomb parameters are driven based on the Hoek-Brown failure criterion (Hoek, 2007).

$$\mathrm{GSI} = 0.8835\mathrm{CMC} + 10 \tag{15a}$$

$$s = \exp\left(\frac{\mathrm{GSI}-100}{9-3D}\right) \qquad a = \frac{1}{2} + \frac{1}{6}\left(e^{-\frac{\mathrm{GSI}}{15}} - e^{-\frac{20}{3}}\right) \qquad m_b = m_i \exp\left(\frac{\mathrm{GSI}-100}{28-4D}\right) \tag{15b}$$

$$\varphi = Sin^{-1}\left[\frac{6am_b\left(s+m_b\sigma_{3n}\right)^{a-1}}{2(1+a)(2+a)+6am_b\left(s+m_b\sigma_{3n}\right)^{a-1}}\right] \tag{15c}$$

$$c = \frac{\sigma_{ci}\left[(1+2a)s+(1-a)m_b\sigma_{3n}\right]\left(s+m_b\,\sigma_{3n}\right)^{a-1}}{(1+a)(2+a)\sqrt{1+\left(6am_b\left(s+m_b\sigma_{3n}\right)^{a-1}\right)/\left((1+a)(2+a)\right)}} \tag{15d}$$

where ϕ and c are the friction angle and cohesion of the rock mass, respectively, and s, a, D, m_b and m_i are constants in the Hoek-Brown failure criterion, which are estimated based on Geological Strength Index (GSI). To avoid further complexities, the overburden material only consists of sandstone. Similar to analytical solution, a longwall panel with 110 m width, 3 m thickness, and 300 m overburden is considered (Lee, 2005; Keilich, 2009). The input parameters for the numerical simulation for Case 1 are presented in Table 1, where ρ is density, and σ_{mt} represents the tensile strength of rock mass. The average of the ratios of the horizontal to vertical stresses in most Australian coal mines is ~2, so for the numerical models, a horizontal to vertical stress ratio of 2 is considered (Keilich, 2009). In Case 2, we consider the effect of stratification on subsidence. In this case each individual stratum is considered as a block of intact rock, and the rock mass is a set of bonded strata. The Mohr-Coulomb material model is used for predicting the elastoplastic behavior of the blocks of intact rocks. Therefore, the characteristics of the rock mass are obtained by considering the parameters of intact blocks as well as the parameters of bedding planes. The input parameters of the intact rock and the bedding planes used for numerical modeling of Case 2 are presented in Tables 2 and 3, respectively. In Table 2, σ_{it} represents the tensile strength of intact rock. According to the rock mechanics literature, the shear modulus of the stratified rock masses dominantly govern their mechanical behaviour. Different studies suggest that the shear

modulus of a stratified rock mass must be a relatively small value (Singh, 1973; Yao et al, 1993; Singh et al, 1998; Alejano et al, 1999). Here, the shear modulus of the stratified rock mass is assumed to be *E*/20 (Singh, 1973).

Table 1. Equivalent parameters of rock mass (after Lee, 2005)

Parameter	$\rho\left(\mathrm{kg/m^3}\right)$	$E\left(\mathrm{GPa}\right)$	υ	$c\left(\mathrm{MPa}\right)$	$\varphi\left(\mathrm{deg}\right)$	$\sigma_{mt}\left(\mathrm{MPa}\right)$
Overburden Sandstone	2500	3.5	0.25	2.8	30	0.12
Coal	1500	2	0.3	1.5	25	0.09

Table 2. Parameters of intact rock (after Keilich, 2009)

Parameter	$E\left(GPa\right)$	σ_c(MPa)	$c\left(\mathrm{MPa}\right)$	$\varphi\left(\mathrm{deg}\right)$	$\sigma_{it}\left(\mathrm{MPa}\right)$
Overburden Sandstone	20	72	4	40	3.5
Coal	10	40	3	30	0.8

Fig. 4 shows the profiles of the vertical and the horizontal displacements of isotropic ground and stratified ground. According to Fig. 4, the maximum subsidence of the isotropic ground (~9 cm) is significantly less than the maximum subsidence of the stratified ground (15 cm). Moreover, the slope of the vertical displacement in the stratified rock mass is larger than the slope of vertical displacement in the isotropic ground. It is notable that the domain of the region affected by the excavation in isotropic ground is larger than the affected region in stratified ground, which has been shown by Berry (1960). Also, Berry (1964) observed that the surface subsidence trough produced by coal mining is restricted to a smaller area than the surface subsidence predicted by the isotropic continuum model.

6 CONCLUSIONS

After extracting the coal seam the roof strata bend due to their weight. Then, breakage and fragmentation of the roof strata occur which progress toward the ground surface. Due to this phenomenon the cavity is extended toward the surface and causes subsidence unless its progress is stopped by strong strata in upper layers. The characteristics of mine host rock play a critical role in the ground subsidence. Structural integrity of the mine roof is greatly affected by the natural weaknesses such as bedding planes, fractures, and small faults. Therefore, it is essential to consider the effects of the discontinuities on rock mass behavior. A stratified rock mass is highly anisotropic because the shear stiffness of bedding planes are much less than their normal stiffness.

Table 3. Properties of the bedding plane (after Keilich, 2009)

Parameter	**Value**
Friction Angle (°)	25
Residual Friction Angle (°)	15
JRC	5
JCS	4
Cohesion (MPa)	0.3
Residual Cohesion (MPa)	0
Dilation Angle (Deg)	0
Tensile Strength (MPa)	0
Bedding Plane Spacing (m)	4
Normal Stiffness (GPa/m)	80
Shear Stiffness (GPa/m)	8

The mechanism of ground movement in the longwall mining method is a very complicated phenomenon which involves the time-dependent behavior of the strata and the goaf materials. In this study the mechanism of ground movement was investigated by conducting analytical as well as numerical simulations for two different cases of isotropic and transversely isotropic grounds. To estimate the equivalent characteristics of the ground, rock mass classification was implemented for reducing the characteristics of the intact rock into the characteristics of the rock mass. Analytical simulation was carried out based on the elastic solutions proposed by Berry et al. (1960; 1961; 1962; 1963 and 1964). Analytical results indicate that the equivalent continuum medium can estimate the maximum amount of subsidence, but the extension of the horizontal

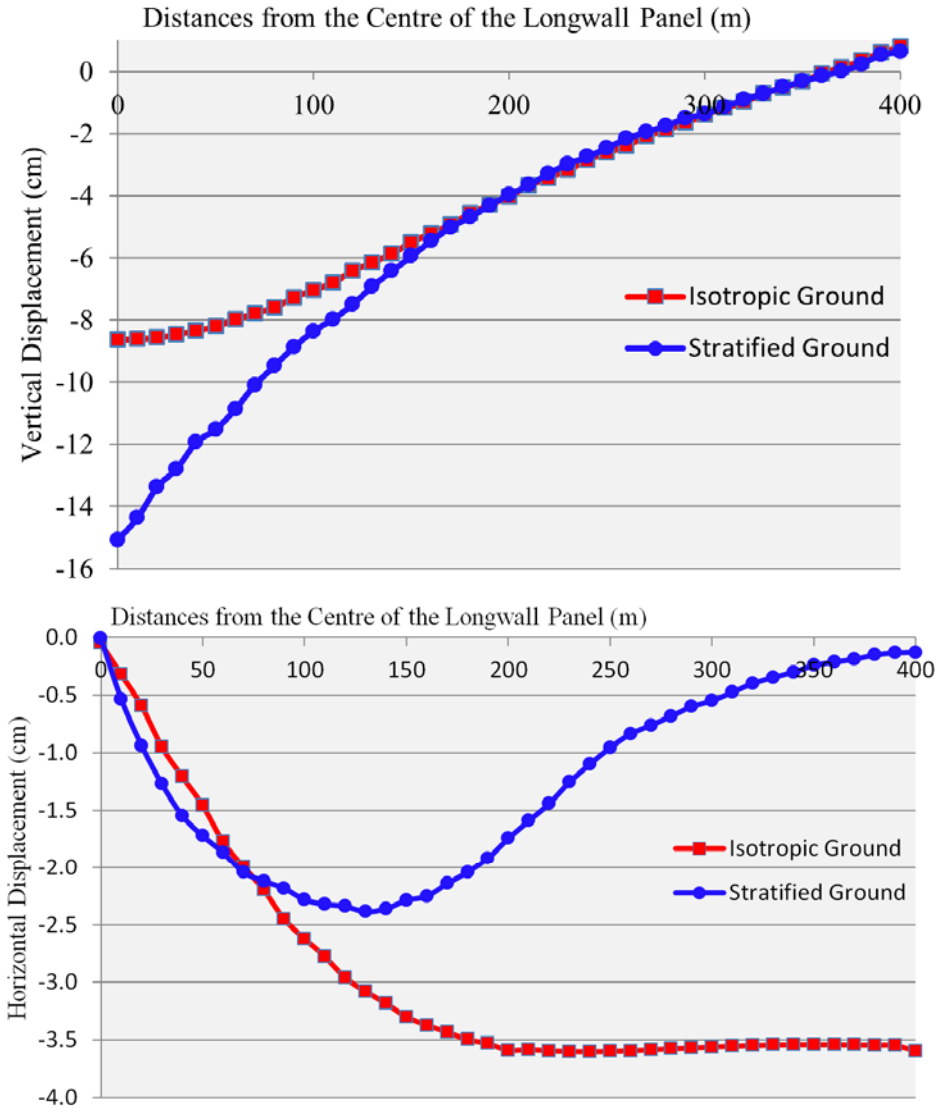

Fig.4.Profiles of the vertical and horizontal displacements

displacement for an isotropic ground is significantly greater than the extension of the horizontal displacement for a transversely isotropic ground.

The Mohr-Coulomb material model was selected for predicting the mechanical behaviour of the rock mass. The outcomes of the numerical simulations indicated that the subsidence predicted by the isotropic model is less than the ground movement observed in the stratified model. Similar to the analytical simulation, the isotropic model predicted the horizontal displacements over a larger area compared to the area obtained by the stratified model. A very good agreement between the results of the numerical and analytical simulations was observed. Results of this study indicate that the bedding plays an important role on subsidence and the development of the cavity toward the ground surface. Therefore, it is concluded that the stratified grounds are more vulnerable to ground movements than the isotropic grounds.

REFERENCES

Alejano, L.R., Ramirez-Oyanguren, P. & Taboada, J. (1999), "FDM predictive methodology for subsidence due to flat and inclined coal seam mining". Int. J. Rock Mech. Min. Sci.,Vol. 36, 475-491.

Bahuguna, P.P., Srivastava, A.M.C. & Saxena, N.C. (1991), A critical review of mine subsidence prediction methods, Elsevier Science Publishers B.V., Amsterdam, Mining Science and Technology, Vol. 13, 369-382.

Berry, D.S. (1960), "An elastic treatment of ground movement due to mining. I- Isotropic ground". J. Mech. & Phy. Sol., Vol. 8, 280-292.

Berry, D.S. & Sales. I.W. (1961),"An elastic treatment of ground movement due to mining. II- Transversely isotropic ground". J. Mech. & Phy. Sol., Vol.9, 52-62.

Berry, D.S. & Sales, I.W. (1962), "An elastic treatment of ground movement due to mining. III- Three dimensional problem, transversely isotropic ground". J. Mech. & Phy. Sol., Vol. 10, 73-83.

Berry, D.S. (1963), Anelastic treatment of ground movement due to mining – Corrigendum**,** J. Mech. & Phy. Sol., Vol.11, 373-375.

Berry, D.S. (1964), "The ground considered as a transversely isotropic material". Int. J. Rock Mech. Mining Sci. Vol. 1, 159-167.

Berry, D.S. (1964), "A theoretical elastic model of the complete region affected by mining a thin seam". The 6th U.S Symposium on Rock Mechanics (USRMS), 310-329, October 28 - 30, Rolla, Missouri.

Bieniawski, Z.T. (1989), Engineering rock mass classifications, a complete manual for engineers and geologists in mining, civil and petroleum engineering, John Wiley & Sons, New Yourk, Chichester, Brisbane, Toronto, Singapore.

Bieniawski, R.Z.T. (2011), "Misconceptions in the applications of rock mass classifications and their corrections", ADIF Seminar on Advanced Geotechnical Characterization for Tunnel Design Madrid, Spain, 1-32.

Exadaktylos, G.E. (2001), "On the constraints and relations of elastic constants of transversely isotropic geomaterials**"**.Pergamon, Int. J. Rock Mech. Min. Sci., Vol. 38, 941–956.

Gerrard, C.M. (1982), "Equivalent elastic moduli of a rock mass consisting of orthorhombic layers", Pergamon, Int. J. Rock Mech. Min. Sci. & Geomech. Abstr. Vol. 19, 9-14.

Greent, A.E & Zerna, W. (1968), Theoretical elasticity, Second Edition, Dover Publication, INC, New York.

Hartman, H.L. (1992), SME Mining Engineering Handbook, Society for Mining, Metallurgy, and Exploration, Inc. Littleton, Colorado.

Hoek, E. (2007), Practical rock engineering, Toronto, Rocscience.

Itasca Consulting Group (2004). UDEC Universal Distinct Element Code Version 4.0, Users' manual.

Keilich, W. (2009), Numerical modelling of mining subsidence, upsidence and valley closure using UDEC, PhD Thesis, School of Civil, Mining and Environmental Engineering University of Wollongong.

Kratzsch, H. (1983), Mining Subsidence Engineering, Springer-Verlag, Berlin Heidelberg New York.

Lee, J.W. (2005), Development of a numerical model of rock failure mechanisms associated with the impact of lateral displacement, Masters Thesis, School of Civil, Mining and Environmental Engineering, University of Wollongong.

Lee, Y.K & Pietruszczak, S. (2008), "Application of critical plane approaches to the prediction of strength anisotropy in transversely isotropic rock masses". Elsevier, Int. J. Rock Mech. Min. Sci., Vol. 45, 513–523.

Lydzba, D., Pietruszczak, S. & Shao, J.F. (2003), “On anisotropy of stratified rocks: homogenization and fabric tensor approach”. Elsevier, Comput. Geotec., Vol. 30, 289–302

Mark, C. & Molinda G.M. (2005), “The coal mine roof rating (CMRR)-A decade of experience”, Elsevier, Int. J. Coal Geol., Vol. 64, 85– 103

Mitri, H.S. & Edrissi, R. & Henning, J. (1994),“Finite element modeling of cable bolted stopes in hard rock underground mines”, In: Proceedings of the SME Annual Meeting, Albuquerque, NM, Paper no. 94–116 (Case 33).

Muskhelishvili, N.I. (1954), Some basic problems of the mathematical theory of elasticity-fundamental equations, plane theory of elasticity, torsion and bending, Fourth Corrected and Augmented Edition, Moscow.

Pande, G.N., Liang, J.X & Middleton, J. (1989), Equivalent elastic moduli for brick masonry, Comput. Geotec., Vol. 8, 243-265.

Peng, S. & Chiang H.S. (1984), Longwall mining. New York, Wiley.

Pietruszczak, S. & Mroz, Z. (2000), “Formulation of anisotropic failure criteria incorporating a microstructure tensor”, Comput. Geotec., Vol. 26, 105-112.

Salamon, M.D.G. (1968), “Elastic moduli of a stratified rock mass”, Int. J. Rock Mech. Min. Sci., Vol. 5, 519-527.

Singh, B. (1973) ‘Continuum Characterization of Jointed Rock Masses. Part I-The Constitutive Equations’, Int. J. Rock Mech. Min. Sci. & Geomech. Abstr., Vol. 10, 311 - 335.

Singh, B. (1973), ‘Continuum Characterization of Jointed Rock Masses. Part II-Significance of Low Shear Modulus’, Int. J. Rock Mech. Min. Sci. & Geomech. Abstr., Vol. 10, 337 - 349.

Singh, B., Goel, R.K., Mehrotra, V.K., Garg, S.K., & Allu, M.R. (1998), "Effect of intermediate principal stress on strength of anisotropic rock mass". Pergamon, Tunnelling and Underground Space Technology, Vol. 13 (1), 71-79.

Wardle, L.J. & Gerrard, C.M. (1972), “The equivalent anisotropic properties of layered rock and soil masses**”**, Rock Mechanics, Vol. 4, 155-175.

Whittles, D.N., Reddish, D.J. & Lowndes, I.S. (2007), “The development of a coal measure classification (CMC) and its use for prediction of geomechanical parameters”. Int. J. Rock Mech. Min. Sci., Vol. 44, 496–513.

Yao, X.L., Reddish, D.J. & Whittaker, B.N. (1993), "Non-linear finite element analysis of surface subsidence arising from inclined seam extraction". Int. J. Rock Mech. Min. Sci. & Geomech. Abstr., Vol. 30(4), 431-441.

Zhang, L. (2003), Engineering properties of rocks, Elsevier Geo-Engineering Book Series, Edit. Hudson. J. A., Vol. 4.

A PRACTICAL APPROACH TO CONSTITUTIVE MODELS FOR THE ANALYSIS OF GEOTECHNICAL PROBLEMS

K.N.Vakili, T. Barciaga, A.A. Lavasan, T. Schanz
Institute for Foundation Engineering , Soil and Rock Mechanics, Ruhr-Universität Bochum, Germany

ABSTRACT: *Numerical modeling of complex geotechnical problems usually requires an advanced 3D-discretization and requires a sophisticated constitutive soil model. Some complex constitutive models lead to analyses of practical structures becoming computationally expensive. Hence, it would be wiser to assign the more sophisticated hierarchical models to the zones which are highly influenced by geotechnical processes spatially and temporally. On the other hand, the regions with less stress/strain concentration can be numerically solved using simpler models. This approach which reduces the computational effort considerably is called here 'adaptive' constitutive modeling. It leads to an optimum-accurate numerical analysis by concentrating on the important selected factors of soil behavior such as stress dependent stiffness, hardening and softening plasticity, stiffness at small strains, anisotropy etc. in a small region of the mesh. This paper presents the first step to develop a conceptual approach for adaptive constitutive modeling of soils in numerical analyses with finite element method (FEM). To achieve this, a number of numerical soil element tests were simulated to assess the effects of employing the adaptive constitutive soil modeling on the results and the features which should be precisely taken into account in this process. The results of present study provides the basic and initial concept of proposed approach. Finally, a sample geotechnical application that can be simplified by the use of this approach is introduced.*

1 INTRODUCTION AND MOTIVATION

Due to recent advances in computational technology, numerical analysis has become a standard tool to investigate the geotechnical problems. However, numerical simulations and their contributing physical-mechanical parameters are becoming increasingly difficult to obtain. On one hand the adequate results for numerical analysis of the complicated geotechnical problems (especially those involve in multi-phase calculations) can be acquired only by generating an effective three dimensional numerical model; on the other hand the behavior of soils subjected to complicated stress paths can only be predicted by employing appropriate advanced constitutive models. For the two aspects to be adequately addressed analyses require enormous computational time. The physical-mechanical parameters required for numerical modeling might be measured from complex tests or from curve-fitting of results from one-element numerical simulations. For the sake of simplicity in such cases, an innovative idea of adaptive constitutive soil modeling is developed. This approach advocates the different regions of the mesh, though having same material to have different constitutive models with respect to existing conditions and the applied stress/strain path at different times. Accordingly, this adaptive approach deals with changing the

constitutive model of the material spatially and temporally. Furthermore, by the simultaneous use of simple to complex constitutive models in a single model with several regions, a balance between the computational complexity, calculation accuracy and the computer processing time will be achieved. In order to conduct an accurate analysis, these zones with some complexities (usually form the smaller part of the global model) are allocated advanced hierarchical soil constitutive models whilst the rest of the regions are modelled using simpler soil models. This approach leads to an optimum computational solution in which the complexity and accuracy have been precisely balanced. The proposed approach avoids using advanced soil models for the whole global model which evidently leads to a longer computational time and more parameters to be measured in laboratory.
One of the most relevant applications of this approach is for numerical simulation of staged construction procedures in which the stress concentration within the elements is time dependent. As mentioned before, in such cases the adaptive constitutive modeling becomes a spatially and temporally progressive process. As a consequence, the appropriate advanced model can be defined to the particular zones at specific times. Hence, by the absence of the features acting on these particular regions due to getting staged construction further, the simple but still convenient model may be assigned back to the zone again. This process may become more significant when stress-induced anisotropy or dynamic loading is partly involved in numerical analyses.
In numerical analysis of a domain, the global model will be discretized to a number of elements and corresponding nodes. During calculations by the new method, some of these nodes are subjected to exchange the constitutive model (from one soil model to another). Hence, an attempt is made in the present paper to demonstrate the numerical response of the soil due to manual adaptive exchange in constitutive models by taking a number of numerical soil element tests (oedometer test and triaxial test) into account. Furthermore, calibration of the soil constitutive parameters in numerical model analysis is conducted to obtain the results of soil element test. Evaluation of the results will form the fundamental framework of the adaptive constitutive modeling of soils.

This paper aims to provide a framework to present adaptive constitutive modeling of soil by the use of Finite Element Method (FEM). The proposed approach provides an insight into the potential advantages of adaptive constitutive modeling and its features which should be considered during the model exchange. Thereafter, the advanced aspects of adaptive constitutive soil modeling are generally described in a complex geotechnical works such as staged tunneling construction as an application of the proposed method.

2 CONSTITUTIVE MODELING OF SOILS

The following section specifies the numerical procedure for adaptive constitutive modeling. In this study three elastic-plastic soil models with different complexity, but from the same hierarchical model family (see section 2) are selected for the description of the constitutive soil behavior. For all analyses a synthetic soil parameter set is chosen. Before using the constitutive soil models in the analysis of adaptive constitutive modeling, a calibration of the soil models and their soil parameters, especially because of the different stiffnesses and Elastic moduli is needed. For this reason, the numerical soil element tests (triaxial and oedometer test) are conducted. A detailed description of the boundary and loading conditions of the soil tests is given. The calibration analyses aim to result in equivalent stress-strain and volumetric behavior of the soil for all three soil models. Differences in the soil behavior are reported and discussed. It follows by

a detailed explanation of the general concept for the adaption of constitutive soil models and its corresponding influences on the soil parameters and on the plasticity properties of soil while changing the constitutive soil model from the simple model (MC) to the advanced model (HS) and vice versa. As a first step and based on the obtained parameter sets from the calibration, the manual adaption of soil models is applied to soil element tests. The soil models are manually exchanged during stress paths what means during loading and un/reloading of the soil sample. The results from the performed element tests are discussed with respect to differences in the stress-strain and volumetric behavior of the soil.

2.1 Linear Elastic - Perfectly Plastic Mohr-Coulomb Model

The Mohr-Coulomb model (MC) is one of the mostly referenced constitutive models which numerically offers reasonable results for porous media specially frictional soils (Fig. 1). This model is most relevant for simple stress paths and provides a linear elastic-perfectly plastic prediction for soil behavior.
The model involves four parameters, i.e. Young's modulus (E) and Poisson's ratio (ν) for soil elasticity; friction angle (φ) and cohesion (c) for soil plasticity. In order to evaluate the accurate direction for plastic strain vectors, a non-associated flow rule has been taken into account in this model. This non-associativity arises from having different yield and potential surfaces by defining ψ as an angle of dilatancy. These parameters can be directly measured by routine laboratory experiments. Furthermore, the numerical calculation for the constitutive model is quite simple and a constant average stiffness or a stiffness that increases linearly with depth is estimated by this model for each layer. Due to this constant stiffness, computations tend to be relatively fast [1]. Accordingly, the time required to proceed the numerical calculation with this model is reasonable. Results of existing studies on numerical simulation of the problems by MC constitutive model revealed that this model offers reasonably accurate results for frictional materials such as sand and gravel as well as cured concrete [2].

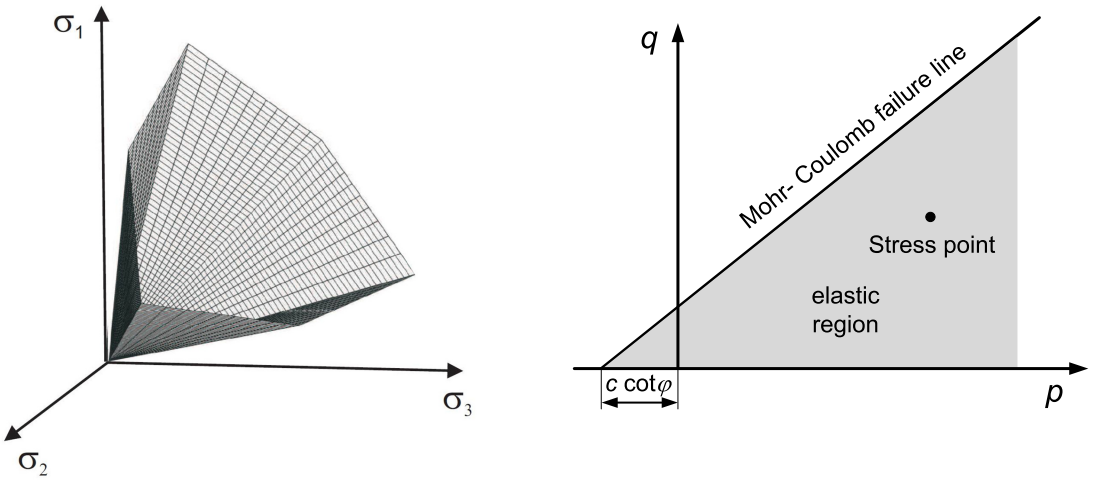

Fig. 1: Mohr-Coulomb yield surface in principal stress and q-p stress space [3]

2.2 *Isotropic Hardening Model*

The Hardening Soil model (HS) is an advanced model which is formulated in the framework of classical theory of plasticity. This model is appropriate to be considered for simulating the behavior of different types of soil, both soft soils and stiff soils. Since the failure criteria in this model obeys Mohr-Coulomb failure criteria, the state of stress in plastic range is described by means of φ, c as for the MC model. However, soil stiffness is described much more accurately by defining three different stiffnesses corresponding to the loading condition as: (a) the triaxial loading stiffness (E_{50}^{ref}), (b) the triaxial unloading stiffness ($E_{\text{ur}}^{\text{ref}}$), and (c) the oedometer loading stiffness ($E_{\text{oed}}^{\text{ref}}$).

The HS model also accounts for stress-dependency of stiffness modulus so that all stiffnesses increased when the stress level is increased. The plastic strains are calculated by introducing a multi-surface yield criterion. Hardening is assumed to be isotropic depending on both the plastic shear and volumetric strains. For the deviatoric hardening section, a non-associated flow rule was assumed by taking dilation angle (ψ) different from friction angle (φ). For the cap yield surface (volumetric hardening part), an associated flow rule is assumed.

In this constitutive model, a distinction between shear hardening and compression hardening can be taken into account. Shear hardening is used to numerically simulate irreversible strains due to primary deviatoric loading. However, the compression hardening is used to model irreversible plastic strains due to primary compression in oedometer loading. The use of HS model generally results in longer calculation times, since the material stiffness matrix is formed and decomposed in each calculation step ([1, 2]).

In contrast to MC model, the yield surface of a hardening plasticity model is not fixed in principal stress space, but it can expand due to plastic straining (Fig. 2). Thus, it is to be noted that the current stress point which has shown to be in elastic domain in Fig. 2 may place in plastic region when the constitutive model exchange from MC to HS. Nevertheless, the point which is already in plastic domain may be located back in elastic region by exchange of the model from HS to MC. Thus, adaptive constitutive modeling is not an arbitrary process which can happen by turning constitutive model from one to another. In consequence, a thorough consideration should be taken into account on what this process may lead to.

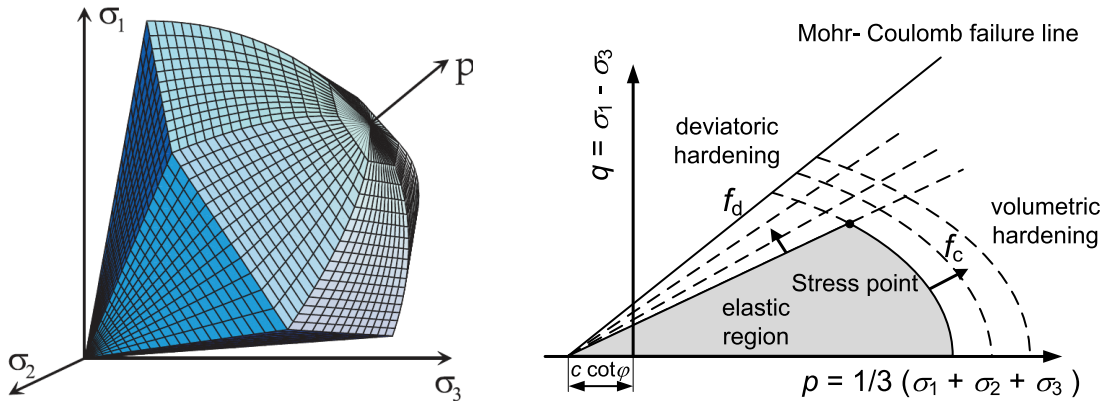

Fig. 2: Hardening soil model is principal stress space and its double hardening yield surfaces [4,5]

2.3 Isotropic Hardening Model with Consideration of Small Strain Stiffness

As mentioned in former section, the original HS model assumes fully linear material behavior during unloading and reloading. However, the strain range in which soil can be considered truly linear, is very small. With increasing strain amplitude, soil stiffness decays non-linearly (Fig. 3). The Hardening Soil model with small strain stiffness (HSS) is a modification of the HS model that accounts for increased stiffness of soils at small strains. At low strain levels most soils exhibit a higher stiffness than at engineering strain levels, and this stiffness varies non-linearly with strain level. This behavior is described in the HSS model using an additional strain-history parameter and two additional material parameters, G_0^{ref} (the small-strain shear modulus) and $\gamma_{0.7}$ (the shear strain level at which the shear modulus has reduced to about 70% of the small-strain shear modulus). The HSS constitutive model is based on the same framework proposed for HS model with Mohr-Coulumb failure criteria. However, the variation of the shear modulus regarding the small-strain condition can be evaluated by this model.

The advanced features of the HSS model are most apparent in working load conditions. Here, the model gives more reliable displacements than the MC and HS models. The use of HSS will generally result in calculation times than are even longer than those of the HS model [4,6]. In present study, this model is categorized as advanced constitutive model. It is to be noted that, in addition to the complexity of the model and the time required to follow the calculation, there are some extra parameters which should be defined via a sensitivity analysis or further laboratory testing. These extra investigation process and the longer analysis time, makes the numerical study with this model expensive. This may become more important when there are several layers with different materials in the numerical model.

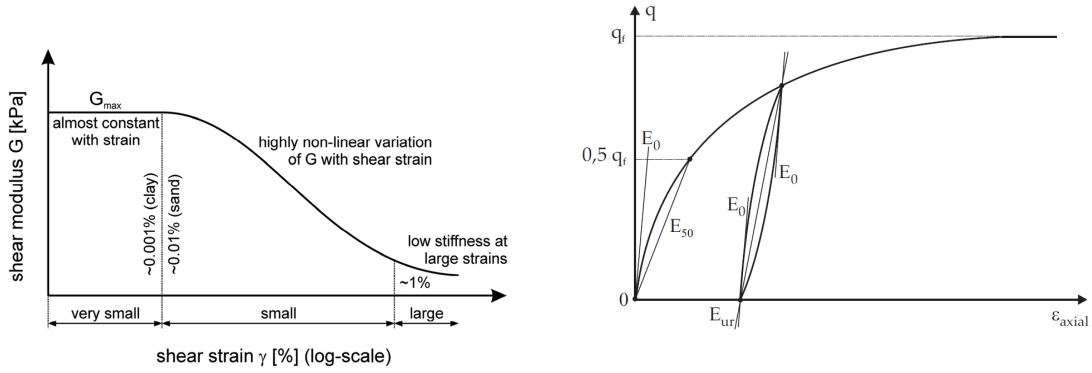

Fig. 3: Hardening soil model with small strain stiffness and shear modulus variation [4,5]

3 NUMERICAL ANALYSIS OF SOIL ELEMENT TESTS

The following section specifies the numerical procedure for adaptive constitutive modeling. In this study three elastic-plastic soil models with different complexity, but from the same hierarchical model family, as shown in section 2, are selected for the description of the constitutive soil behavior. For all analyses a synthetic soil parameter set is chosen. Before using the constitutive soil models in the analysis of adaptive constitutive modeling, a calibration of the soil models and their soil parameters, especially because of the different stiffnesses and Elastic moduli is needed. For this reason, numerical soil element tests (triaxial and oedometer test) are conducted.

A detailed description of the boundary and loading conditions of the soil tests is given. The calibration analyses aim to result in equivalent stress-strain and volumetric behavior of the soil for all three soil models. Differences in the soil behavior are displayed and discussed. It follows a detailed explanation of the general concept for the adaption of constitutive soil models and its corresponding influences on the soil parameters and on the plasticity properties of soil while changing the constitutive soil model from the simple model (MC) to the advanced models (HS model) and vice versa. As a first step and based on the obtained parameter sets from the calibration, the manual adaption of soil models is applied to soil element tests. The soil models are manually exchanged during stress paths what means during loading and un/reloading of the soil sample. The results from the performed element tests are discussed with respect to differences in the stress-strain and volumetric behavior of the soil.

3.1 Numerical Soil Element Tests

In this study, two soil element tests namely oedometer test (one-dimensional compression) and triaxial test are numerically analyzed by the use of Finite Element Method (FEM). The geometrical boundaries of the cylindric soil sample are given through the ratio of the model height to the model diameter with a value of two. The initial geometry and the mesh discretization are kept constant for both tests as shown in Fig. 4. However, the tests differ in their boundary conditions and fixities (see Fig. 4). In general, the boundary conditions for both tests allow vertical displacements of the soil sample, but the bottom surface is fixed in its vertical position. In oedometer condition, the lateral expansion is constrained ($\varepsilon_3 = 0$). In triaxial condition, a confining pressure σ_3 is applied and from this follows that horizontal deformations of the soil sample can occur. Both tests are performed under stress controlled loading condition, whereat the increasing vertical stress σ_1 is applied at the top surface of the soil sample. With respect to the analysis of adaptive modeling in section 3.3, the following stress path has been selected. In the oedometer test the soil sample is loaded in two phases from 0 kPa to 100 kPa and 200 kPa. It is followed by two unloading phases to 100 kPa and finally 50 kPa. The loading pattern in triaxial test is divided into five phases. Two phases of loading to $q = 0.5\, q_\mathrm{f}$ and $q = 0.9\, q_\mathrm{f}$, continues with two unloading phases to $q = 0.5\, q_\mathrm{f}$ and $q = 0.25\, q_\mathrm{f}$ and ends up with a reloading phase until failure at $q = q_\mathrm{f}$, where q_f refers to deviatoric stress at failure. In all analyses, the compressive load is assumed to be positive. The synthetic soil sample has homogeneous and isotropic material properties and it is normally consolidated. The soil parameter sets for the three constitutive soil models from section 2 will be shown after their calibration in section 3.2.

3.2 Calibration of Constitutive Soil Parameters in the Simulation of Laboratory Tests

For adequate adaptive modeling an equivalent stress-strain and volumetric behavior of the soil must be ensured. For that reason, the constitutive parameters of all three different soil models have to be calibrated in soil element tests (oedometer and triaxial tests). The MC model parameters are calibrated with the model parameters of the advanced reference models HS and HSS. Due to the fact that this study is based on a hierarchical soil model family, it is required that some common parameters have identical values. For example a common failure criterion leads to the choice of equal shear strength parameters (φ and c). Consequently the calibration would be limited to the variation of the different types of modulus of elasticity for the MC, HS and HSS model, as described in section 2. The Youngs modulus E' in the MC model, which is stress independent and constant for one stress path (no difference between virgin compression and

un/reloading of the soil sample), varies and set to the values of the different and stress dependent moduli of elasticity in the HSS model ($E_{\text{oed}}^{\text{ref}}, E_{50}^{\text{ref}}, E_{\text{ur}}^{\text{ref}}$ and E_{0}^{ref} at certain reference stress p^{ref}. In the framework of this study $E_{\text{oed}}^{\text{ref}}$ and E_{50}^{ref} are equal. The results of the calibration in the oedometer and the triaxial tests are given in Figs. 5 and 6.

Using different values for E' in the MC model results in significantly different values for the vertical strains ε_1 and therefore in the volumetric behavior of the soil sample. The main conclusion of the calibration in the oedometer test is that by selecting the equivalent E-modulus for the MC model a fit of single parts of the stress path (virgin compression or un/reloading at reference stress level) in comparison to the more advanced models HS and HSS is possible only. But with increasing complexity of the stress path the results in displacements are not sufficient, because of the mentioned limitations of the MC model. These results are confirmed in the triaxial test. The selection of the appropriate value of E' for the MC model depends on the stress path of the in situ application.

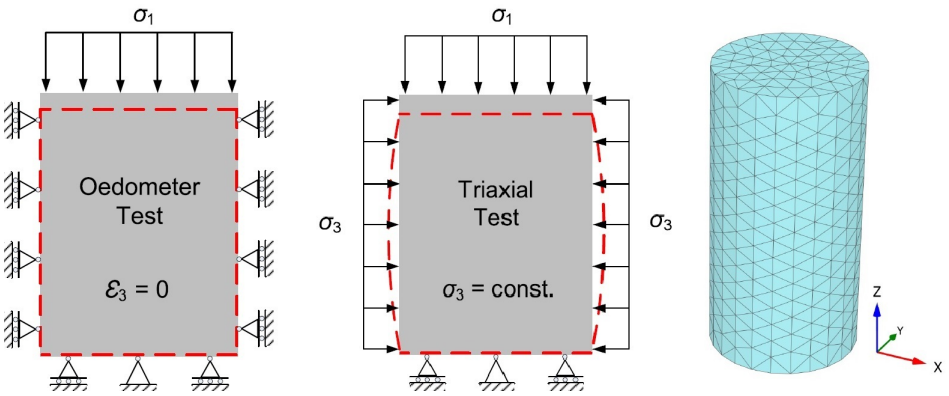

Fig. 4: Schematic boundary condition and mesh discretization for numerical simulation of oedometer and triaxial tests of the numerical model

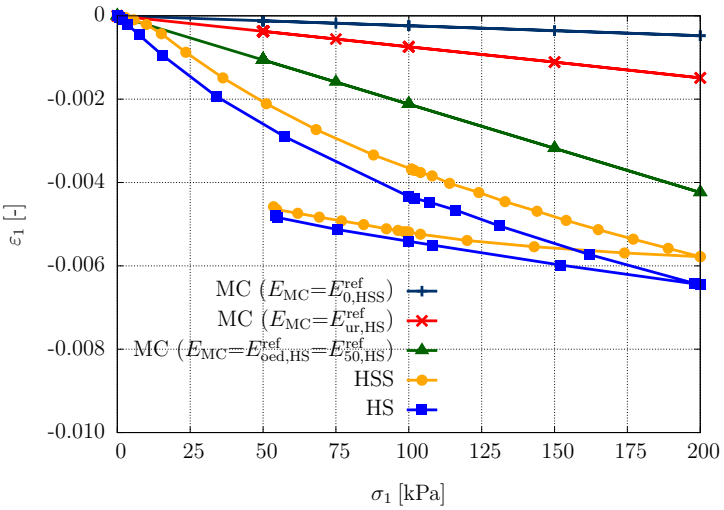

Fig. 5: Calibration of soil parameters of MC to HS and HSS models in oedometer test

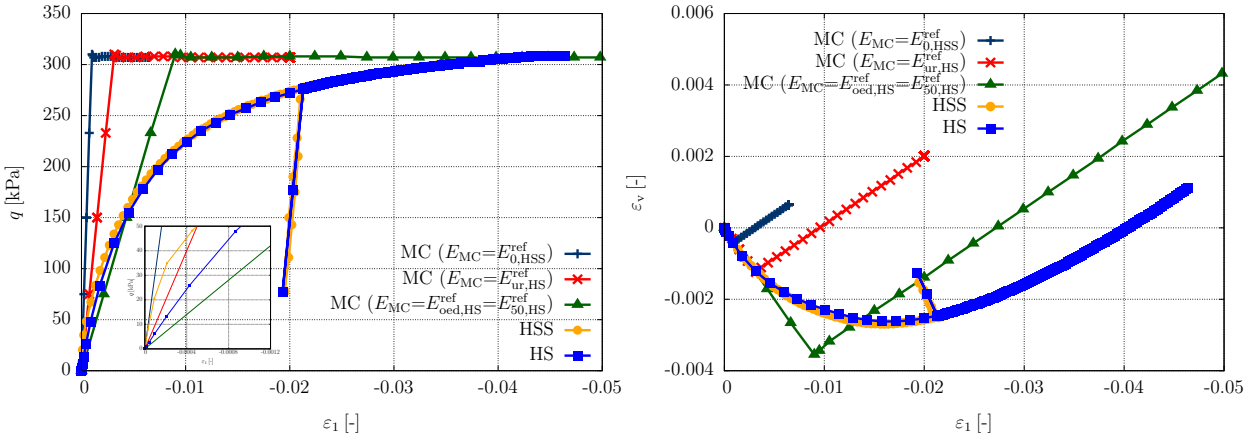

Fig. 6: Calibration of soil parameters of MC, HS and HSS models in Triaxial test

According to Figs. 5 and 6, the best consistency between MC and advanced HS models is observed when the constant elastic modulus of soil in MC model is assumed to be equal to E_{50}^{ref}=$E_{\text{oed}}^{\text{ref}}$ for both oedometer and triaxial tests. The calibrated soil parameters which are further used in adaptive constitutive modeling are presented in Table 1.

Table 1: Calibrated soil parameter sets for the different constitutive soil models

Soil model	φ [°]	ψ [°]	c [kPa]	E' [MPa]	E_{50}^{ref} [MPa]	$E_{\text{oed}}^{\text{ref}}$ [MPa]	$E_{\text{ur}}^{\text{ref}}$ [MPa]	E_{0}^{ref} [MPa]	G_{0}^{ref} [MPa]	$\gamma_{0.7}$ [-]	p^{ref} [kPa]	m [-]	R_{f} [-]	ν [-]	ν_{ur} [-]
MC	35	5	10	35	-	-	-	-	-	-	-	-	-	0.3	-
HS	35	5	10	-	35	35	100	64	-	-	100	0.7	0.9	-	0.2
HSS	35	5	10	-	35	35	100	312	130	0.00015	100	0.7	0.9	-	0.2

3.3 Adaptive Modification of the Subsoil Properties in Element Tests

The results of numerically modeled oedometer and triaxial tests considering manual adaptive constitutive soil modeling have been presented in this section. The MC and HS models are taken as simple and advanced constitutive models, respectively. To evaluate the results for variable loading situations, two cases were taken into account in adaptive modification analyses. Based on the results obtained from calibration section, the elastic modulus of the soil for MC model in oedometer and triaxial tests in this section is assumed to be equal to $E_{\text{oed}}^{\text{ref}}$ and $E_{50,\,\text{HS}}^{\text{ref}}$in HS model to avoid high un/reloading stiffness. The other parameters of MC and HS models are taken form Table 1. In the analyses conducted in this section, the same load patterns as defined in section 3.1 for oedometer and triaxial tests are considered. The manual constitutive modeling adaption in each loading step was performed as HS-MC-MC-HS (case 1) and MC-HS-HS-MC (case 2), four loading steps for oedometer test, and as HS-MC-MC-HS-HS (case 1) and MC-HS-HS-MC-MC (case 2), five loading steps for triaxial test. The numerical results of oedometer soil element test subjected to soil model exchange have been illustrated in Fig. 7.

As seen in Fig. 7, the soil model exchange during loading and unloading conditions has a significant effect on strain mobilization and stress path. Despite of MC model, the stress paths in loading and unloading are not coincided in HS model due to having different elastic modulus in loading and unloading phases. Regarding the comparisons between the stress-strain curves

for adapted and homogeneous constitutive models, it can be seen that when the loading starts with HS model then follows by MC model (case 1), the results of adaptive model becomes in a fairly good agreement with those obtained from homogeneous HS model. However, the difference between the final axial strain at the end of last unloading phase, arises from considering the same elastic modulus for loading and unloading. As seen, if unloading was conducted by HS model from beginning, the results of adaptive constitutive modeling would completely fit to the result of homogeneous HS model. According to the second loading/unloading pattern (case 2), since the loading has been started with MC model, the loading part of the stress-strain is much more closer to MC rather than HS. Results of the adaptive constitutive modeling in oedometer test shows that exchange of soil model from HS to MC after disappearing the the complex stress path does not make any undesired change in the numerical analysis procedure such as stress path and strain values. By exchanging the model, the stress/strain level is saved by the code but the numerical calculations are performed based on recently defined constitutive model. Furthermore, when the constitutive model exchanges from MC to HS for normally consolidated soil, the size of the yield surfaces are precisely determined based on the initial condition in which the test has been started. It also shows that the use of MC model for unloading does not lead to accurate results due to loading and unloading paths coincidence.

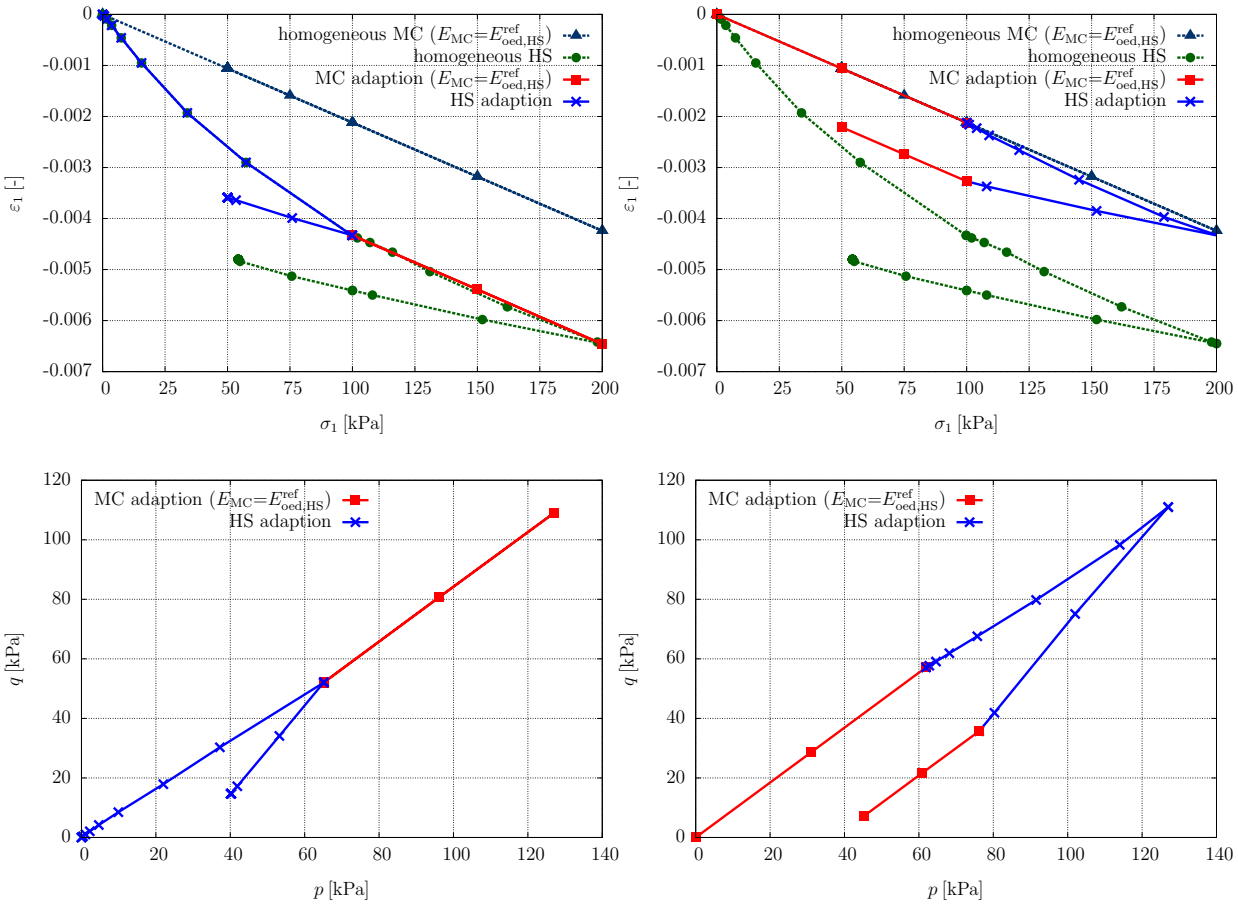

Fig. 7: Oedometer test results for material exchange

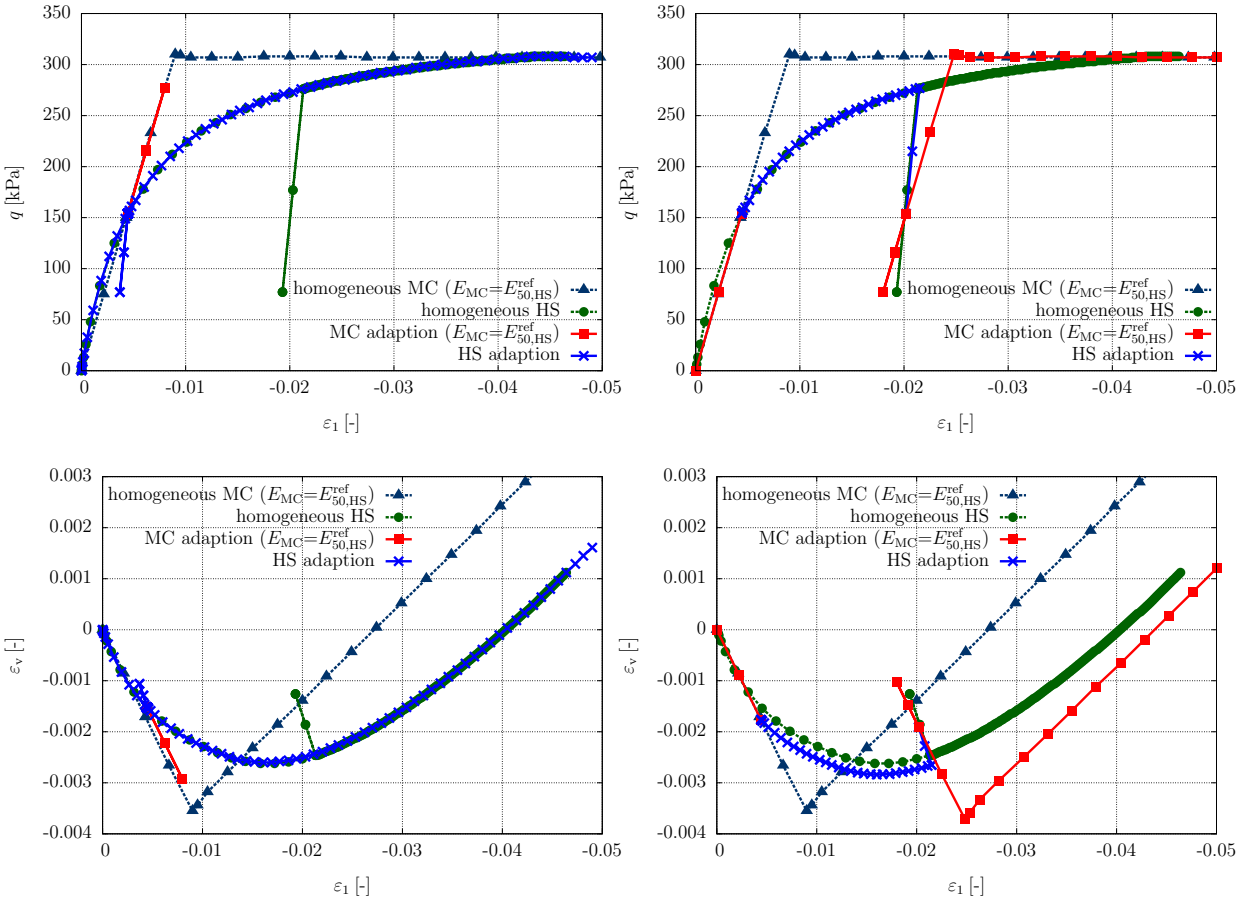

Fig. 8: Triaxial test results for material exchange

According to Fig. 8, the results relate to the case 1 of loading pattern is fully fitted to what obtained from homogeneous HS model. However when the constitutive model manually exchanged from MS to HS then to MC, the results are still in a good agreement. Regarding the variation of the volumetric-axial strain for loading case 2, exchanging model from HS to MC during un/reloading caused a difference between results of case 2 and HS model. As mentioned in oedometer test, use of MC model during un/reloading can results in inaccurate prediction of soil behavior. However, it seems that the results obtained from triaxial shear test is less sensitive to adaptive constitutive modeling that oedometer test.

4 APPLICATION OF ADAPTIVE CONSTITUTIVE MODELING IN GEOTECHNICAL PROBLEMS

The adaptive constitutive soil modeling can potentially be employed in a wide range of geotechnical problems. All numerical models with staged construction, progressive stress/strain mobilization, local strain/stress concentration and any other time/location variation in the behavior of the material might be numerically categorized in the range of adaptive constitutive modeling range. Applications of adaptive constitutive modeling of soils are mostly apparent in complex geotechnical models.

One of the most challenging geotechnical problems, which are recently taken into account by geotechnical engineers, is deep excavation and tunneling. In last two decades, the technology of mechanized tunneling by the use of Tunnel Boring Machine (TBM) has been significantly grown.

In boring a tunnel with TBM as a progressive staged constructional process, some features are involved. In a simple description, mechanized tunnel excavation consists of three stages: 1. excavation with TBM, 2. lining installation 3. grouting adhesive viscous material between lining and soil material. Numerical analysis of a tunnel excavation process usually requires relatively a large geometric model with sophisticated soil constitutive models to obtain adequate results. This usually leads to a considerable time consumption, complex calculations and large number of constitutive parameters for different types of materials. Furthermore, uncertainty in the constitutive parameters can result in unreliable results. As a considerable consequence, this complexity may lead to questionable results instead of obtaining more accurate ones. Hence, it would be more wise to allocate the more advanced hierarchical soil models time dependently to the subareas which are highly influenced by tunnel excavation process. This approach simplifies the computational progress considerably. Regarding this construction procedure, different constitutive models might be assigned to different zones. Furthermore, the location of these zones vary by progressing the staged excavation. Accordingly, the constitutive models which are allocated to different zones should be selected by a thorough temporal and spatial consideration. Apparently, the excavation of the deep or shallow tunneling generally requires multi-phase calculations. The schematic sketch of the subarea subjected to different stress paths have been shown in Fig. 9.

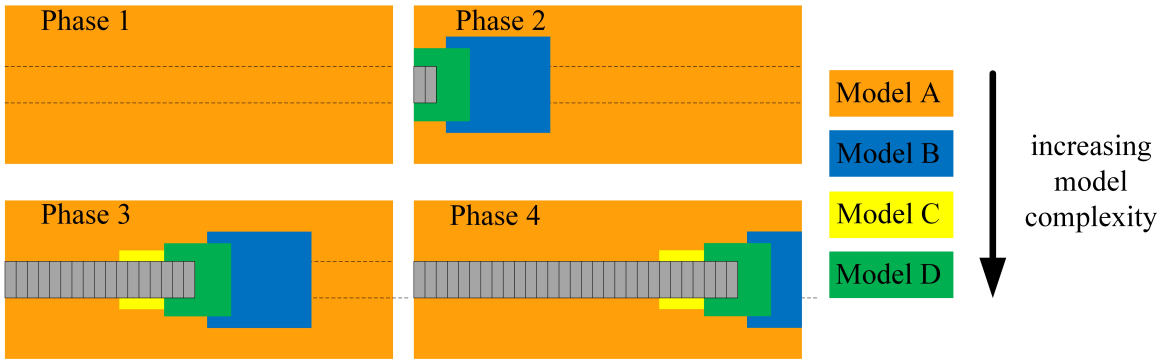

Fig. 9: Application of adaptive constitutive soil models in tunneling

As seen in Fig. 9, four different subareas can be defined due to mechanized tunnel excavation. Taking an adaptive constitutive modeling approach into account, the behavior of these subareas might be predicted by different constitutive models. For the main soil body which is far from tunnel's head, a simple constitutive model (Model A) can be used. For the zone that is not still being directly excavated but subjected to excavation effects transferring from neighboring subarea, a more sophisticated constitutive model (Model B) should be allocated. Since this subarea is mainly under unloading stress path, a relevant constitutive model for unloading is needed. For the subarea around tunnel length which has been recently stabilized with lining ring, a more complex model should be assigned. This model should be able to investigate the soils behavior under mechanical (or even hydraulic) un/reloading due to excavation, lining installation and grouting. On the other hand, grouting and lining installation are occurring in this zone. Depending on the type of material and construction method, a constitutive model having the ability to consider the chemical interaction between soil and concrete or mechanical-thermal behavior of concrete during curing process, can be used (Model C). For the subarea that is directly subjected to TBM excavation, the stress path includes loading un/reloading cycles. With respect to the soil type and its mechanical properties, some complex features such as damage in the soil structure,

rotational hardening, dynamic stress path might become necessary to be considered in numerical Analysis (Model D).

5 CONCLUSION AND RECOMMENDATION

This paper presents the first step to develop a conceptual approach for adaptive constitutive modeling of soils in finite element method (FEM). This approach can be used in numerical analysis of complex geotechnical problems. The constitutive models considered in present study were introduced. These three soils models were taken as hierarchical Mohr-Coulomb constitutive family. Thereafter, the constitutive parameters of soil were calibrated through soil element test with unit models during loading and un/reloading. The main framework of adaptive constitutive modeling was introduced in a number of oedometer and triaxial test by manual model exchange. Finally, a potential application of the proposed approach in mechanized tunneling was describe. Base on the analyses conducted in present study, the following general remarks can be made: 1. The results obtained from numerical simulation of oedometer test are more sensitive to adaption those relate to triaxial test. 2. For oedometer case, the results of adaptive approach in loading phase are close to homogeneous simple and advanced models if the loading process starts with simple and advanced models, respectively. 3. For both oedometer and triaxial tests, the best agreement between adaptive constitutive model and homogeneous advanced model will be obtained when un/reloading is conducted by an advanced model.

6 ACKNOWLEDGMENT

Financial support was provided by the German Science Foundation (DFG) in the framework of project A5 of the Collaborative Research Center SFB 837 and the third writer was sponsored through a scholarship by Alexander von Humboldt Foundation, Germany. These supports are gratefully acknowledged.

REFERENCES

[1] Schanz, T., Vermeer, P. A., Bonnier, P. G. (1999). The hardening soil model formulation and verification. In: Brinkgreve, R. (Hrsg.): Beyond 2000 in computational geotechnics, Rotterdam: Balkema. 281-296.

[2] Vermeer, P., & de Borst, R. (1984). Non-associated Plastisity for Soils, *Concrete and Rock., HERON.*, 29(3), 16-26.

[3] Brinkgreve, R.B.J., Engin, E. & Swolfs, W.M. (2011). Material models manual, Plaxis 3D. Plaxis bv, Delft, Netherlands.

[4] Benz, T., Schwab, R. & Vermeer, P. (2009). Small-strain stiffness in geotechnical analyses. *Bautechnik special issue.* 16-26.

[5] Vermeer, P.A., (1978). A double yield hardening model for sand. *Geotechnique*, 28(4), 413-433.

[6] Hai-Sui Yu. (2006). Plasticity and geotechnics. Advances in mechanics and mathematics. volume 13. Springer Science+Business Media, LLC.

[7] Potts, D.M., Zdravkovic, L. (1999). Finite element analysis in geotechnical analysis. 1st. Ed. Thomas Telford Ltd, 1 Heron Quay London.

[8] Duncan, J.M., Chang, C. (1970). Nonlinear analysis of stress and strain in soils. J. Soil mechanics and foundation division, ASCE. 1629-1654.

NUMERICAL MODELING OF FRACTURE PATTERNS AROUND DEEP UNDERGROUND DRIFTS

D. Seyedi
Department of Fluid and Solid Mechanics, Research and Development Division, ANDRA, Chatenay-Malabry, France

G. Armand
Department of Fluid and Solid Mechanics, Research and Development Division, ANDRA, M/HM URL, Bure, France

ABSTRACT: *Extensive experimental observations have been performed around drifts and shafts at the Meuse Haute-Marne underground research laboratory (North-Eastern France) to assess the extension and pattern of the induced fracture networks in Callovo-Oxfordian claystone. Two types of fractures can be distinguished, namely; shear (mode II) and extension unloading (mode I) fractures. The main goal of the present paper is to provide insights on the pattern of fracture networks around the drifts by numerical simulations. A two-step approach is considered. First, 2D elastic calculations are performed. Considering two directions for the drifts, namely; parallel to the major and minor in situ principal stresses, the evolution of the stress and strain tensors around drifts are calculated. Two failure criteria are then verified for shear and extension induced fractures. A generalized Hoek and Brown and an equivalent strain criteria are considered. The obtained results show that the employed simplified approach provides rather good results for extension fracturing for drifts parallel to minor horizontal stress. It seems that post-processing elastic results leads to underestimating the extent of shear fractures. Finally, it seems that taking into account the anisotropy of elastic parameters cannot explain the important anisotropy of the observed fracture networks around drifts parallel to major horizontal stress.*

1 INTRODUCTION

The excavation of underground openings induces fracture networks in the surrounding rock called Excavation Damaged Zone (EDZ). The pattern and extent of fractured zone depend on several parameters such as mechanical properties of the host rock, geometry of drift, excavation technique and initial stress state. Definition of the EDZ varies depending on the design needs. In the context of radioactive geological disposals EDZ is usually considered as "a zone in which hydromechanical and geochemical modifications induce significant changes in flow and transport properties. These changes can, for example, include one or more orders of magnitude increase in flow permeability'' (Tsang et al., 2005).

The impact of fractures on hydraulic permeability of a fractured rock mass depends on the fracture conductivity and fracture density (e.g., Vu et al., 2012). The fracture conductivity is usually modeled by a Poiseuille's type law relating the fracture conductivity to its opening. Extension and tensile induced (mode I) fractures represent generally larger opening than shear induced (mode II) fractures. It can thus be supposed that mode I fractures influence the equivalent permeability of a fractured zone more than shear fractures (i.e., mode II).

The extent of the fractured zone has a direct impact on the loading transferred to the drift's lining. Laboratory and in situ experimental observations show also that damage amplify the

time-dependent effects (e.g., creep strains). The extent and nature of the fractured zone affect in this manner support system design.

Understanding damage mechanisms and the possible pattern and extent of induced fracture zone around the repository structures constitute thus a main issue in the context of radioactive waste disposals. Extensive experimental observations have been performed around drifts and shafts at the Meuse Haute-Marne underground research laboratory (M/H-M URL) at Bure (North-Eastern France) to assess the EDZ extension and pattern in Callovo-Oxfordian claystone. Fracture networks induced around the excavated drifts consist of shear and extension unloading fractures. The main goal of the present paper is to provide useful insights for understanding the extent of each failure mechanism through simple numerical analysis. It is worth noting that the fractures and fractured zones are regarded only from a mechanical point of view in the present work. In this view after a brief presentation of observed fracture networks at M/H-M URL, a set of simplified numerical simulations of excavation operations are proposed. Two failure criteria are then considered in order to check the extent of shear and extension induced fractures through post-processing the results of simplified (i.e., linear elastic) simulations. It is worth noting that due to simplifications considered in the modeling process, the obtained results must be considered in a qualitative manner, which can be useful for understanding and distinguishing the fundamental phenomena that must be taken into account in more realistic simulations.

2 THE MEUSE/HAUTE-MARNE UNDERGROUND RESEARCH LABORATORY

The construction of the Meuse/Haute-Marne underground research laboratory (M/HM URL) has been launched in 2000 in Bure located about 300 km North-East of Paris by the French national radioactive waste management agency (ANDRA). The main goal of the URL is to demonstrate the feasibility of a radioactive waste repository. A Callovo-Oxfordian claystone, located between 420 and 550 m depth, is selected as the host formation. The clayey formation is overlain and underlain by poorly permeable carbonate formations.

An important experimental program is planned to characterize different properties of the host rock and to study its response to different shaft and drift excavation. Numerous experiments and direct measurements have been performed in the laboratory drifts excavated at -445 m and then at -490 m (i.e., the main level). Figure 1 shows a global view of different drifts and shafts of the M/HM URL. Extensive surveys have been accomplished to investigate the EDZ around the excavated drifts. These studies provided fruitful insights on the effect of the drift geometry, the in situ stress state and rock properties on the pattern and the extent of the induced fracture networks. Moreover, using different excavation and support techniques allowed investigating their influences on the short and long term behavior of the constructions.

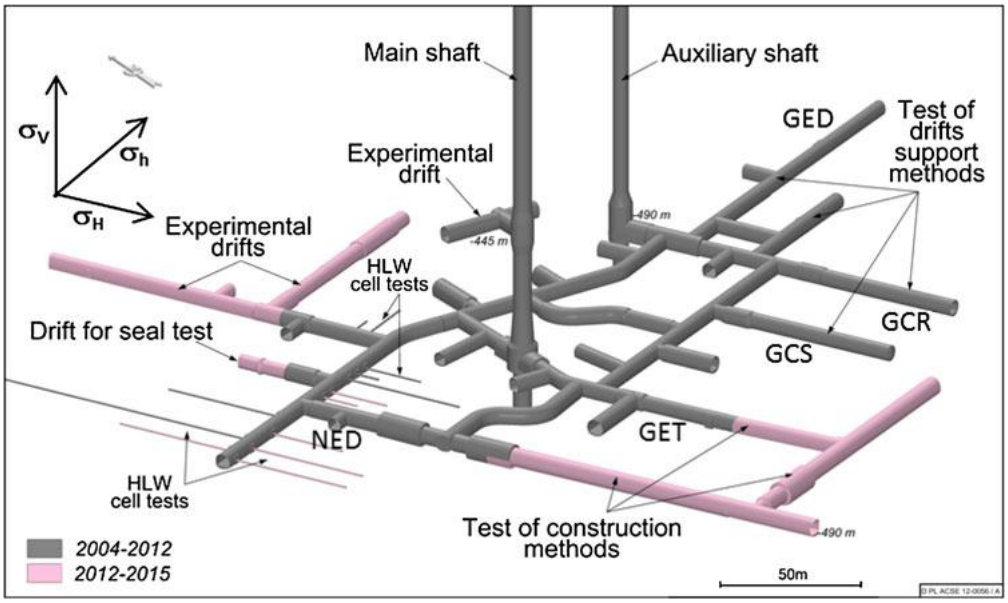

Figure 1. Meuse/Haute-Marne URL. Grey drifts and shafts are already excavated and the pink ones are planned to be constructed

It is worth noting that at the main level of the URL (i.e., -490 m) any natural joints or fracture has not been detected in the cores obtained from the boreholes drilled from the surface. It is thus considered that all fractures observed around drifts constructed at the main level are induced due to the excavation operations.

2.1 Mechanical properties of Callovo-Oxfordian claystone

Mineralogical composition of the Callovo-Oxfordian claystone (COX) varies slightly within the stratigraphic level. Mineralogical studies showed a rather homogeneous composition at the main level constituted mainly by tectosilicates (20%), carbonates (20 – 25%) and clay minerals (50 – 55%). The clay minerals are composed by about 55% illite-smectite, 30% illite and 15% kaolinite and chlorite. Even if claystone exhibits a relatively high porosity (between 14 and 21%), has a very low permeability (5E-20 to 5E-21 m²) due to its very small mean pore size (~0.02 µm). Table 1 summarizes the principal mechanical characteristics of the claystone at the URL's main level.

Table 1. Principal mechanical characteristics of the claystone at of the URL's main level

Rock parameter	Value
Density	2.39 g/cm^3
Porosity	18 ± 1 %
Young modulus	4000 ± 1470 MPa
Poisson ratio	0.29 ± 0.05
Uniaxial compressive strength	21 ± 6.8 MPa

2.2 In situ stress state

The largest principal stress is horizontal and the vertical and the smallest horizontal stresses are close to each other (Wileveau et al. 2007). The major horizontal stress (σ_H) is oriented at NE150°. The vertical stress (σ_v) and the horizontal minor stress (σ_h) read respectively

$$\sigma_v = \rho g Z \ , \sigma_h \approx \sigma_v \tag{1}$$

where ρ designates the density, g the gravity and Z the depth.

The ratio between the major horizontal stress and vertical stress varies with depth and mineralogical composition of different layers. This ratio is close to 1.3 at the main level of the URL.

3 FRACTURE NETWORKS AROUND DRIFTS AT M/HM URL

As it can be seen on Figure 1, most of the drifts are excavated following the horizontal principal stresses at the main level of the URL. Different techniques are employed for characterizing the induced damage around the drifts. The main investigation techniques are:

- Structural analysis of the core samples drilled from the drifts
- Geological survey of the drift face and sidewalls
- Seismic measurements (measuring the evolution of P and S wave velocities due to damage)
- Permeability measurements
- Overcoring of resin-filled fractures

Performed analysis showed that the fracture patterns and the extent of the fractured zone around the drifts depend essentially on the drift orientation, i.e., on the in situ stress state. The extent of the fractured zone was determined taking into account all available data in different directions (Armand et al., 2013). Two kinds of fractures are distinguished namely; shear fractures (mode II) and "extension" fractures (mode I). In the following, the obtained results for drifts excavated parallel to σ_H and σ_h are briefly presented.

3.1 Drifts Parallel to the Horizontal Major Stress (σ_H)

Table 2 shows the lateral extent of the induced fracture zones around two drifts (GCS and GET) excavated parallel to σ_H. The vertical extent of the fracture network is not significant in this direction. GCS and GET are excavated with the same technique (road header technique) but are supported with different systems. GCS is supported by rock bolts and shotcrete with compressive wedges, which allow deformation of the concrete support while GET is supported by rock bolts, shotcrete and sliding steel arches. The results exhibit a large variability showing that the extent of the fractured zones varies along the drifts. However, it can be seen that the support system has not a significant influence on the extent of the induced fracture network.

Table 2. Lateral extent (diameter ratio) of the induced fracture zone around drifts parallel to σ_H (Armand et al., 2013)

	Shear Fractures			Extension fractures		
Drift	Min	Average	Max	Min	Average	Max
GCS	0.71D	0.83D	0.96D	0.01D	0.18D	0.31D
GET	0.71D	0.77D	0.83D	0.07D	0.18D	0.36D

Based on the observed results a conceptual fracturing model is proposed for drifts parallel to σ_H (Armand et al., 2013). Shear fractures constitute the majority of the observed fractures (Figure 2). They are longer and expand deeper in the rock. Extension fractures are concentrated near the drift's wall with a more heterogeneous dip and strike.

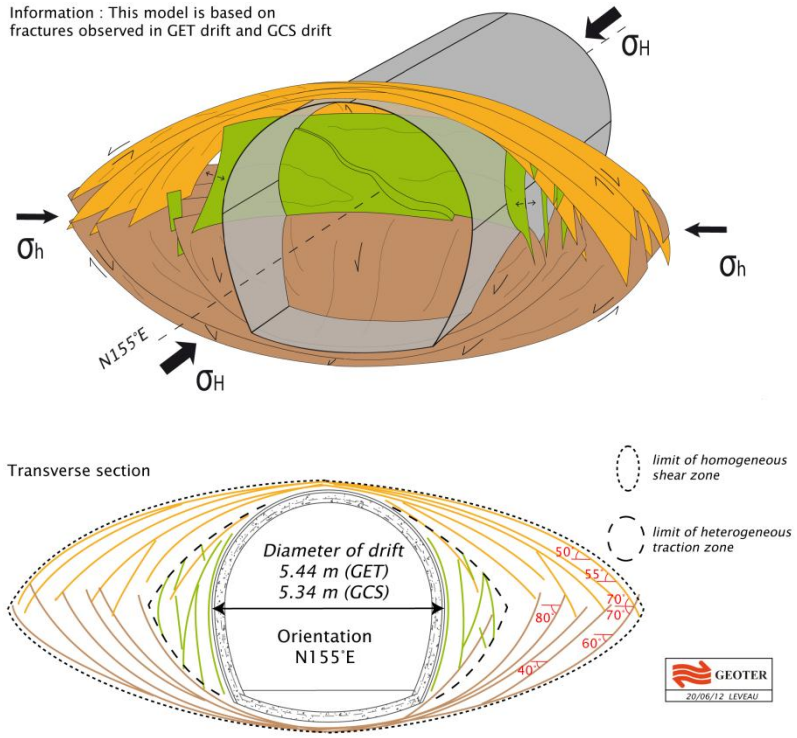

Figure 2. Conceptual model of the induced fractures network around drifts parallel to σ_H. dark and light brown surfaces show shear fractures and green ones extension unloading fractures (Armand et al., 2013)

3.2 Drifts Parallel to the Horizontal Minor Stress (σ_h)

Table 3 shows the extent of the induced fracture zones around a drift (GED) excavated parallel to σ_h. The investigations show three types of fracture families:

1. Shear "chevron" fractures initiated in front of the excavation face extended until about 1 drift diameter
2. Shear vertical and oblique fractures initiated beyond the chevron fractures
3. Extension (unloading) fractures initiated parallel to the drift's walls extended to a maximum depth of 0.5 – 0.7 m in the rock.

In the same manner as for drifts parallel to σ_H, a conceptual model representing fracture systems around drifts parallel to σ_h is presented in figure 3 (Armand et al., 2013).

Table 3. Extent (diameter ratio) of the induced fracture zone around drifts parallel to σ_h (Armand et al., 2013)

	Shear Fractures			Extension fractures		
Location	Min	Average	Max	Min	Average	Max
Ceiling	0.5D	0.6D	0.8D	0.2D	0.3D	0.4D
Wall	-	-	-	0.1D	0.1D	0.2D
Floor	0.5D	0.8D	1.1D	0.2D	0.4D	0.5D

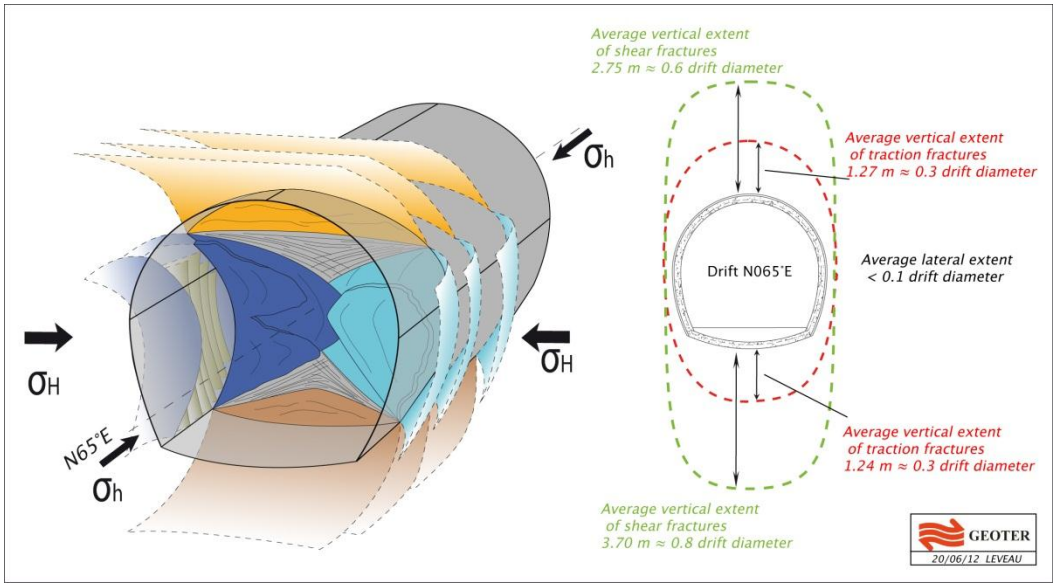

Figure 3. Conceptual model of the induced fracture networks around a drift parallel to σ_h (Armand et al., 2013)

4 NUMERICAL MODELING OF THE EXCAVATION OPERATIONS

The main goal of this section is to provide insightful information on the extent of the induced fracture zones around drifts excavated in the M/HM URL. Two configurations are thus considered; drifts parallel to the major horizontal stress and those parallel to minor horizontal stress. To this end, a two-step modeling approach is employed. First, 2D elastic calculations are performed in two directions. Anisotropy of the initial stress state is considered for drifts parallel to σ_h. Furthermore, the effect of the anisotropy of elastic parameters is investigated. Indeed, the laboratory experiments exhibit anisotropy of the Young modulus for the specimens drilled parallel and perpendicular to the bedding. Back analysis of P and S-wave measurements performed on samples, demonstrates a ratio of 1.3 on elastic modulus. The results of triaxial tests show that parallel Young modulus can reach two times the perpendicular one. The second ratio ($E_p = 2\,E_v$) is considered in the following.

A 5.2 m diameter circular drift is considered for both directions. Figure 4 shows the geometry of the model, considered boundary conditions and the used mesh. The numerical simulations have been performed within Code_Aster (2010). As it can be seen, a quarter of the drift and its surrounding rocks are modeled. Horizontal displacements are blocked on the vertical boundaries and vertical displacements on the lower horizontal one. A vertical stress equal to -12 MPa is applied on the upper boundary to simulate the overburden weight. The excavation procedure is idealized through an experimental unconfinement curve representing the effect of the excavation progress on the radial stress around the opening. No support system is considered in the simulations thus the radial stresses reach zero at the end of the excavation works on the drift surface.

Principal and von Mises equivalent stresses at the end of excavation are plotted on Figure 5 and 6 for a drift excavated parallel to σ_h and σ_H respectively. As it can be seen the anisotropy of the initial stresses in the plane of a drift parallel to σ_h has a significant effect on the stress field around the drift (Figure 5). More particularly, the von Mises equivalent stress, which can be considered as a measure of the intensity of shear stresses develops deeper on the vault than on the side walls (Figure 5). The anisotropy of the Young modulus has a less significant effect when the drift is excavated parallel to σ_H, i.e., with an isotropic initial stresses field (Figure 6).

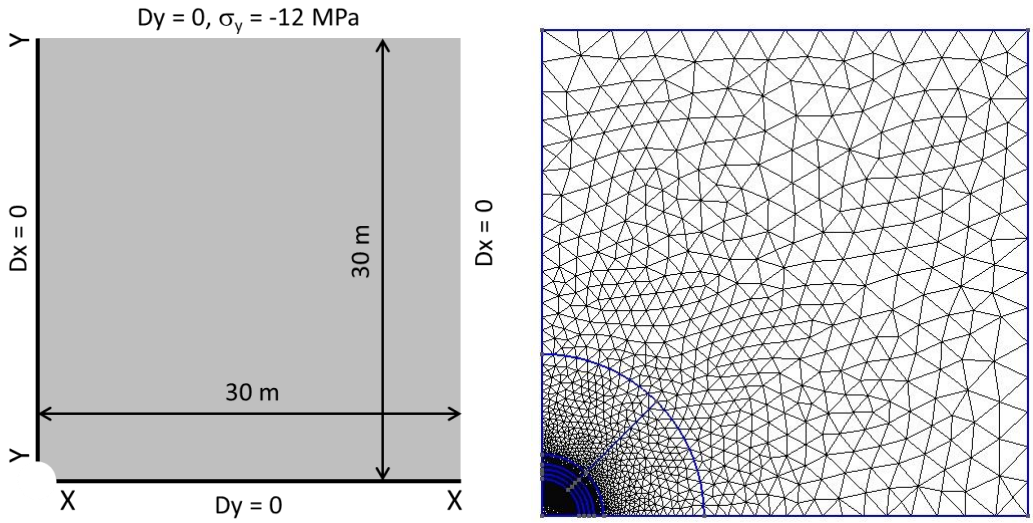

Figure 4, Geometry, boundary conditions and mesh of the model

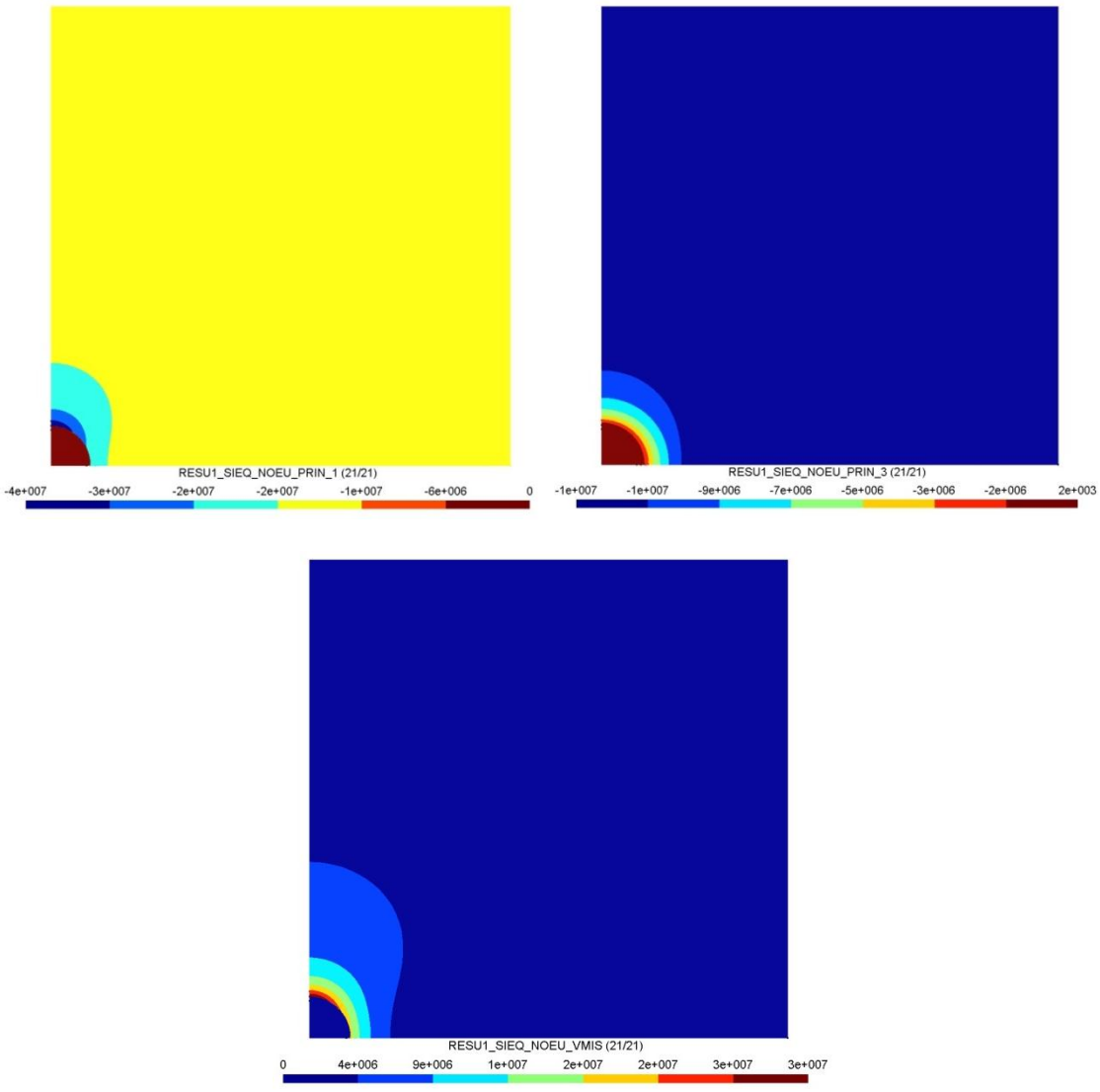

Figure 5. Principal major stresses (top left), principal minor stresses (top rigth) and von Mises equivalent stresses at the end of excavation around a drift parallel to σ_h.

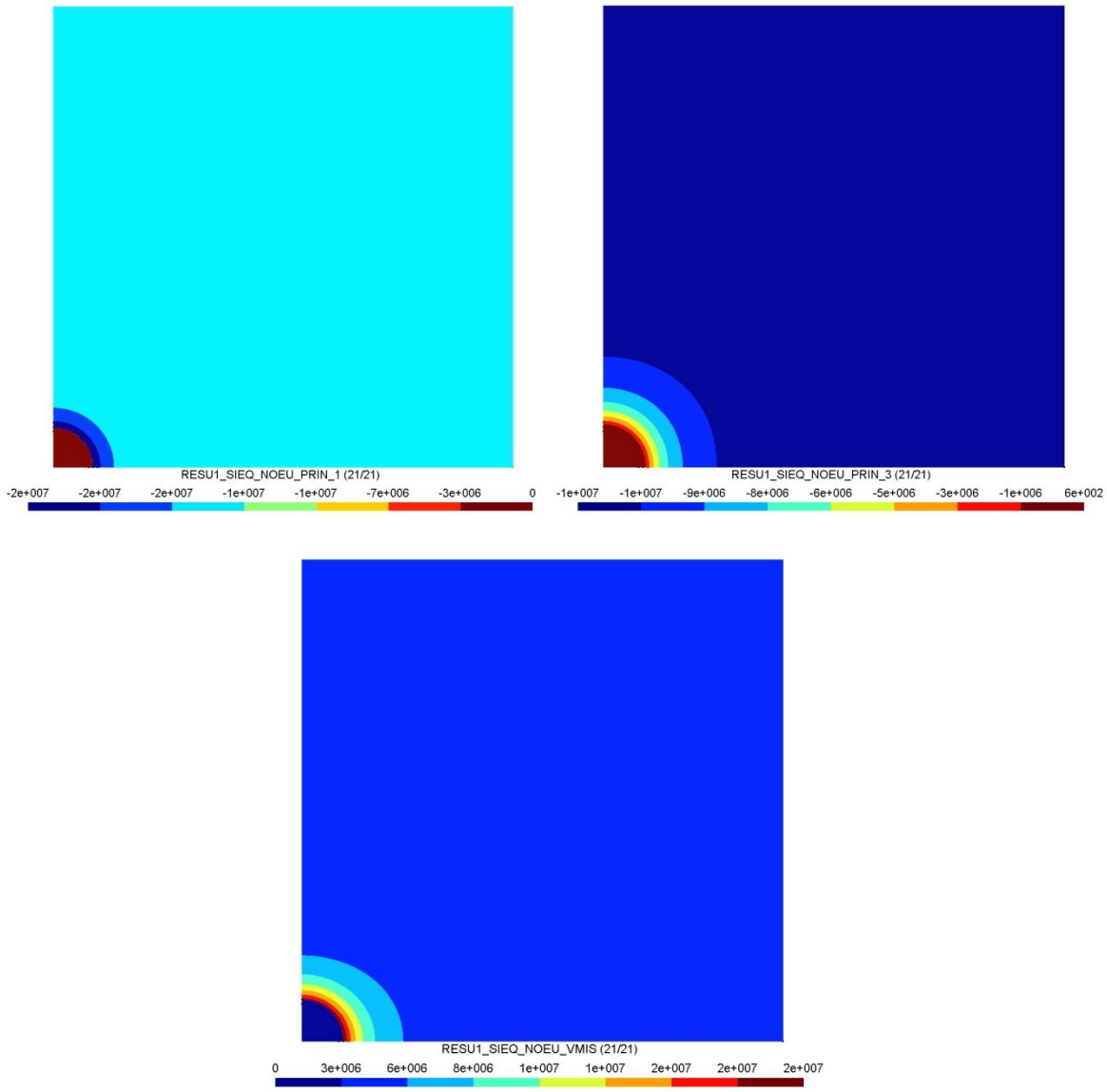

Figure 6. Principal major stresses (top left), principal minor stresses (top rigth) and von Mises equivalent stresses at the end of excavation around a drift parallel to σ_H.

5 STUDY OF FRACTURE PATERNS

As it has been mentioned in section 3, two major failure mechanisms can be distinguished around the drifts, namely shear fracturing and extension unloading fracturing. Present section is devoted to evaluate the extent of the damaged zones based on the obtained results of elastic simulation performed in the previous section. Two distinguished failure criteria are considered for shear and extension fracturing.

5.1 Shear fractures

An elstoplastic constitutive law with hardening and softening mechanisms has been already developed to evaluate the short-term behavior of the claystone (Souley et al., 2011). A generalized Hoek and Brown criterion (Hoek and Brown, 1980; Hoek et al., 2002) is used to evaluate the overall extent of the fractured zone. The yield function reads

$$\sigma_1 = \sigma_3 + \left[m_b \frac{\sigma_3}{\sigma_c} + s \right]^{1/2} \quad (2)$$

where σ_1 and σ_3 are principal major and minor stresses respectively, σ_c uniaxial compression strength of the intact rock, m_b and s the constants.

A hardening mechanism is considered to reproduce damage initiation and propagation before the pic. A linear function of the hardening parameter is used to translate from damage initiation to the failure pic. Shear plastic strain is considered as the hardening parameter in this framework. The post-pic behavior is then modeled through a strain softening mechanism yielding to a residual behavior (Souley et al., 2011).

By post-processing the results obtained through linear elastic analysis, the initiation of damage can only be evaluated. The yield function expressed in equation (1) is thus used within the material parameters corresponding to the damage initiation (see Table 4). It is expected that a Hoek and Brown type criterion explains better the shear failure of the claystone and thus evaluates the overall extent of the damaged zone.

Table 4. Shear damage initiation parameters (Souley et al., 2011)

S	m_b	σ_c (MPa)
1.0	1.5	9.6

5.2 Extension unloading fractures

From a macroscopic point of view, it can be reasonably supposed that the excavation operations do not provoke tensile stresses in the host rock. A fracture mechanics or tensile stress based model cannot be used to simulate the mode I fracture initiation at this level. A phenomenological constitutive law based on the extension (i.e., positive) strains could be more appropriate. The damage model proposed by Mazar (1986) is used in the present work.

Damage initiation is governed by an equivalent strain taking into account the three-dimensional state of the strain tensor. In principal strain system, the equivalent strain reads

$$\epsilon_{eq} = \sqrt{\langle\varepsilon_1\rangle_+^2 + \langle\varepsilon_2\rangle_+^2 + \langle\varepsilon_3\rangle_+^2} \tag{3}$$

where ε_i designates principal strains and $<\varepsilon_i>_+$ the positive part of ε_i. When the equivalent strain reaches a threshold value, ε_{d0}, damage is initiated. A correction coefficient is usually added to taking into account the effect of compressive stresses on the damage initiation:

$$\varepsilon_{eq}^{cor} = \gamma\epsilon_{eq} \tag{4}$$

Among different existing correction coefficients, the following expression is used: $\gamma = -\sqrt{\sum_i\langle\sigma_i\rangle^2}\Big/\sum_i\langle\sigma_i\rangle_-$ when at least one compressive principal stress exists and $\gamma = 1$ if not.

Specific experiments must be performed to identify the value of ε_{d0} corresponding to the damage onset. As a first estimate value, ε_{d0} is considered equal to 0.1%.

5.3 Estimation of the fractured zone extent

Considering the aforementioned criteria, the extent of the fractured zone is estimated for two drifts parallel to σ_h and σ_H respectively. For each drift, Hoek and Brown criterion and equivalent strain criterion are calculated on two perpendicular axes (XX and YY on figure 4) to estimate lateral and vertical extent of the fractured zone respectively (Table 5).

Table 5. Lateral and vertical extent of fractured zone

Drift direction	Lateral extent		Vertical extent	
	H&B	ε_{eq}	H&B	ε_{eq}
Parallel to σ_h	0.16D	0.15D	0.3D	0.18D
Parallel to σ_H	0.18D	0.1D	0.16D	0.19D

6 CONCLUDING REMARKS

A series of simplified calculations are presented in this paper to provide information on the extent and patterns of the induced fracture networks around excavated drifts in the M/HM URL. The employed modeling approach consists in verifying two distinguished failure criteria respectively for shear and extension induced fractures considering stress and strain tensors calculated through linear elastic simulations. A generalized Hoek and Brown and an equivalent strain criteria are considered in this framework.

Table 5 shows that the employed simplified method provides rather good results concerning the extent of extension unloading fractures for a drift parallel to σ_h. The obtained results underestimate the global extent of the fractured zone, governed by shear fractures. However, the vertical calculated extent reaches twice the horizontal extent for a drift parallel to σ_h.

Indeed, when a plastic zone is induced around a drift, the stresses will be redistributed in the rock mass and may induce damage by provoking new plastic zones. A linear elastic analysis ignores completely the stress redistribution and thus may underestimate the extent of shear damaged zone. In contrary, the initiation of mode I fractures produces a stress relaxation zone around the propagating fractures and prevents initiation of new fractures. This shielding effect is not considered in the present work.

The obtained results show that the anisotropy of the elastic properties, i.e., Young modulus, is not sufficient to explain the anisotropy of the induced fracture networks for drifts parallel to σ_H. Furthermore, if an inelastic behavior is considered, one can expect that larger strain occur in the damaged zones. Using an elastic model, this effect is not taken into account and leads to underestimating lateral strains, e.g., the case of a drift parallel to σ_H.

Additional investigations must be conducted to study the potential resistance anisotropy both in shear and extension fracturing and in all directions. More accurate models must be used for estimating the extent of the induced fracture networks. However, the simplified calculations are useful to examine different hypothesis and to provide insights for deeper investigations.

REFERENCES

Armand, G., Leveau, F., Nussbaum, C., de La Vaissiere, R., Noiret, A., Jaeggi, D., Landrein, P. & Righini, C. (2013) “Geometry and properties of the excavation induced fractures at the Meuse/Haute-Marne URL drifts”. Rock Mech. Rock Eng., DOI 10.1007/s00603-012-0339-6.

Code_Aster (2010) http://www.code-aster.org EDF R&D.

Hoek E. & Brown E.T., (1980) “Emprical strength criterion for rock masses”. J. Geotech. Engng. Div., ASCE, Vol. 106(GT9), 1013-1035.

Hoek E., Carranza-Torres C., Corkum B. (2002) “Hoek-Brown failure criterion – 2002 edition”. Proceedings of NARMS-TAC Conference, Toronto, Vol 1, 267-273.

Mazar J. (1986) “A description of micro- and macroscale damage of concrete structures”. J. Engng Frac. Mech., Vol. 25, 729-737.

Souley M., Armand G. Su K., Ghoreychi M. (2011) “Modeling the viscoplastic and damage behavior in deep argillaceous rocks”. Phys. Chem. Earth, Vol. 36, 1949–1959

Tsang C.F., Bernier F., Davies C. (2005) “Geohydromechanical processes in the excavation damaged zone in crystalline rock, rock salt, and indurated and plastic clays—in the context of radioactive waste disposal”. Int. J. Rock Mech. Min. Sci. 42(1): 109–125.

Vu M.N., Pouya A., Seyedi D.M. (2012) “Modelling of steady-state fluid flow in 3D fractured isotropic porous media: Application to effective permeability calculation”, Int. J. Num. Analy. Methods in Geomech., DOI: 10.1002/nag.2134.

Wileveau Y., Cornet F.H., Desroches J., Blumling P. (2007) “Complete in situ stress determination in an argillite sedimentary formation”. Phys. Chem. Earth, Vol. 32, 866–878.